Friends of the Pleistocene Annual Field Trip 2023

Salt Creek Offset Reconstruction

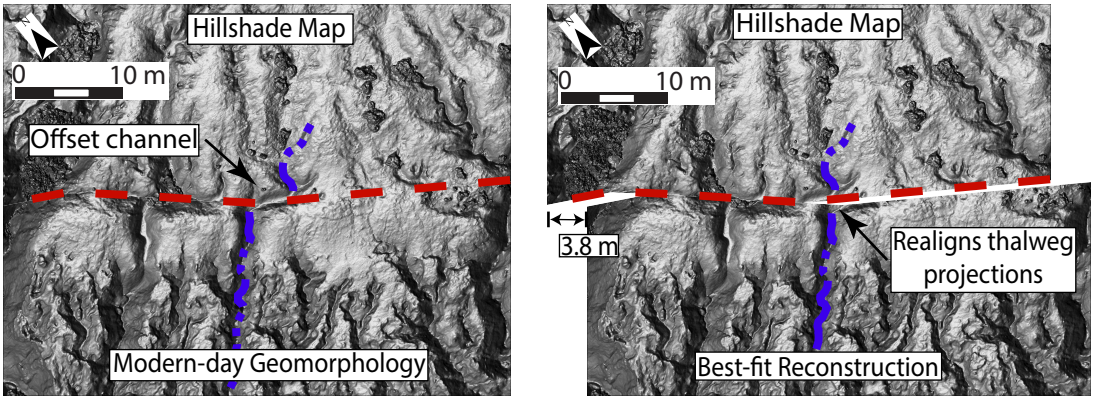

Offset reconstruction representing the Most Recent Event (MRE) for a feature located at Salt Creek with modern-day geomorphology (left) and inferred reconstruction (right). Offset location: 33.4436464, -115.8366745

Salt Creek Trench Log

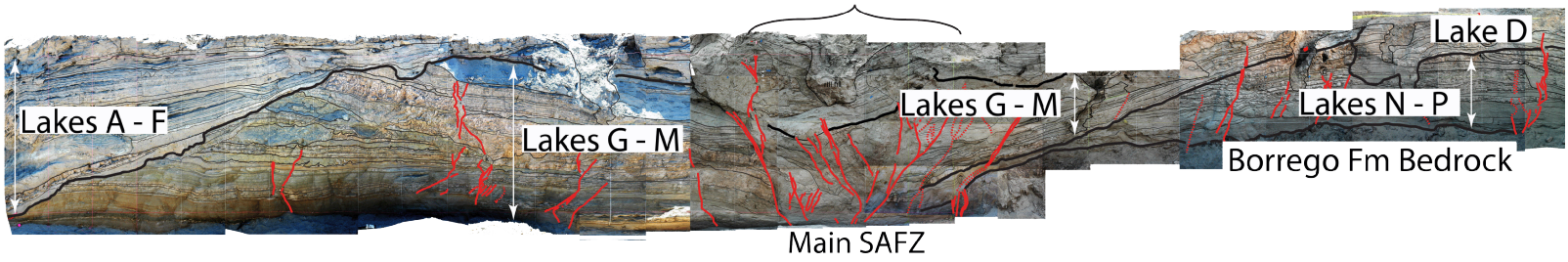

Trench log exhibiting the complex, 5,000-year lake history across the southern San Andreas Fault (sSAF) at Salt Creek.

FOP 2023 Pacific Cell Guidebook Table of Contents

1. *Road Log (description of stops and how to get to/from stops) – pages 3-16*

2. *Day 1 Papers Relevant to Each Stop – pages 17-316*

3. *Day 2 Papers Relevant to Each Stop – pages 317-462*

4. *Day 3 Papers Relevant to Each Stop – pages 463-570*

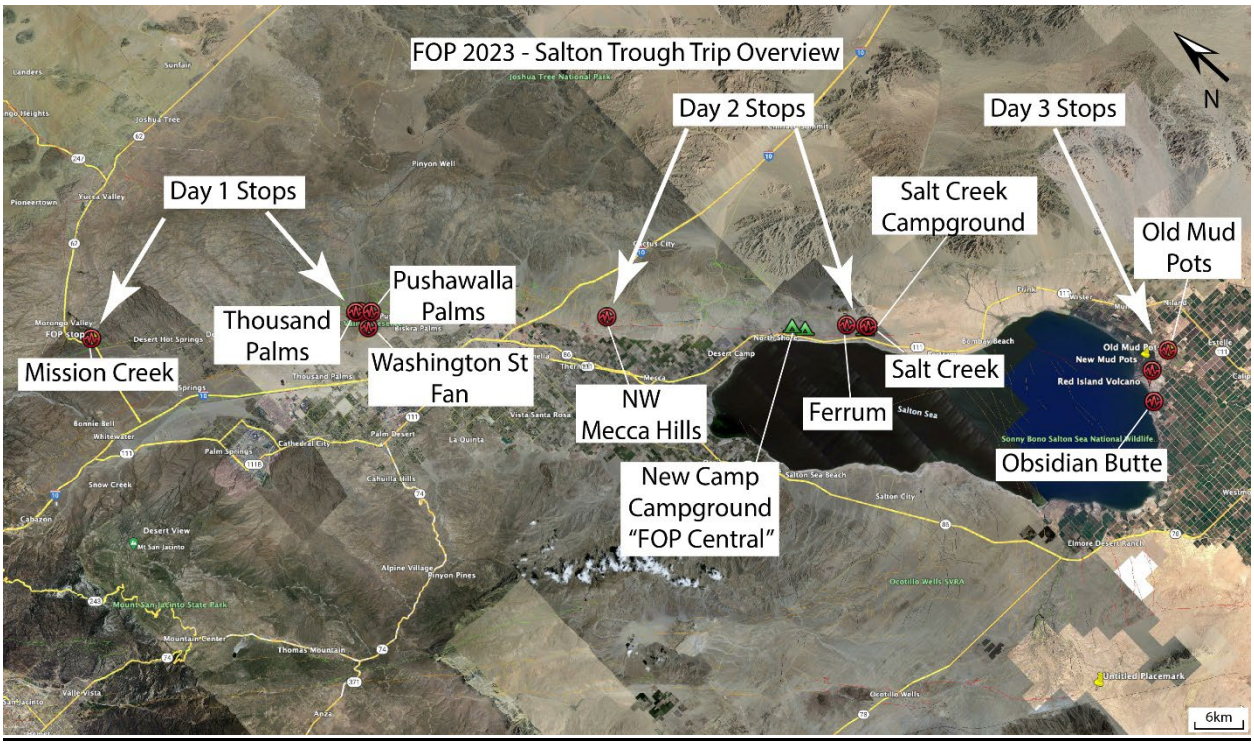

FOP Field Trip Stops

First and foremost, we will be congregating at 'FOP Central' which is located at the New Camp Campground, located along the northeastern shoreline of the Salton Sea. Camping in this area is covered via the FOP registration fee. This campground includes plenty of shade, bathrooms, and even showers! We will ideally be congregating together at 'FOP Central' before and after our field stops each day.

FOP Central coordinates: 33.501701, -115.912130

Day 1

To kick off the trip, we will be heading into the Indio Hills where the San Andreas Fault splits off into two strands – the Mission Creek and Banning strands! First, we will be meeting at the Pushawalla Palms Trailhead (Blisnuk). We will plan to leave New Camp Campground at 8:30am on Friday morning.

Pushawalla Palms Trailhead coordinates: 33.8353, -116.3069

Drive time from 'FOP Central': ~45 minutes

Details on how to get there from 'FOP Central' at New Camp are as follows:

1. *Make your way out of the campground toward the main road (CA-111)*
2. *Turn left onto CA-111 (follow for 13.1 miles)*
3. *Turn right onto 62nd Avenue (follow for 0.2 miles)*
4. *Turn right onto CA-86 (follow for 10.3 miles)*
5. *Merge onto I-10 W (follow for 6.6 miles)*
6. *Take exit 137 toward Washington Street (follow for 0.3 miles)*
7. *Use the middle lane to turn left onto Varner Road (follow for 0.2 miles)*

8. *Use the right 2 lanes to turn right onto Washington Street (follow for 5.0 miles)*
9. *Turn right onto Thousand Palms Canyon Road (follow for 1.8 miles)*
10. *Park at the dirt lot near the Pushawalla Palms Trailhead. If the parking lot becomes full, park along the dirt shoulders on either side of the road.*

Next, we will be heading to the Thousand Palms Oasis Preserve (Seitz).

Thousand Palms Oasis Preserve coordinates: 33.8370, -116.3101

Walking / driving time: ~5 minutes walking / ~1 minute driving

Details on how to get there from Pushawalla Palms Trailhead are below.

1. *Driving here isn't necessary, as it is a short walk from the trailhead (~0.3 miles). If you do wish to drive, follow the same instructions as below. There is a parking lot but space is not guaranteed for everyone.*
2. *From the trailhead, begin walking northeast along Thousand Palms Canyon Road for about ¼ mile.*
3. *You will then see a sign on the left-hand side of the road which says 'The Coachella Valley Preserve'.*
4. *Follow the sign by turning left onto the gravel road, and walk ~500 feet (~150 meters) towards the cluster of palm trees.*

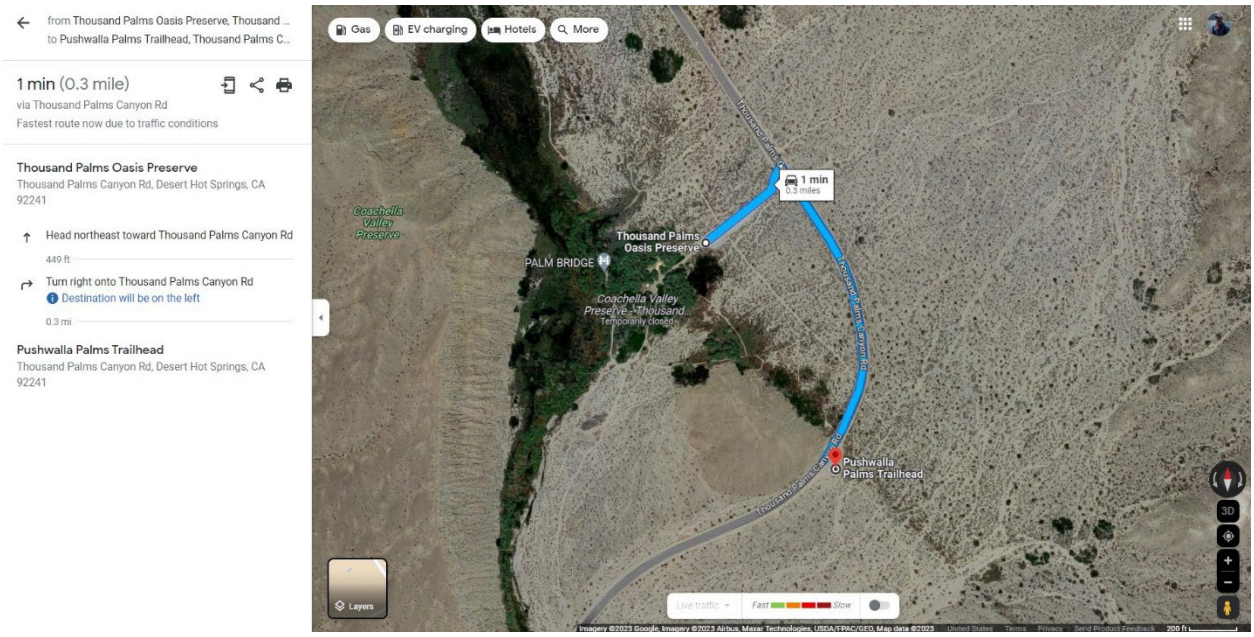

After this, we will be heading to the Washington Street Fan/Banning Fault Site (Scharer, Blisniuk).

Washington Street Fan/Banning Fault Site coordinates: 33.8160, -116.3121

Drive time from Pushawalla Palms Trailhead: ~3 minutes

Details on how to get there from Pushawalla Palms Trailhead are as follows:

1. *Travel southwest down Thousand Palms Canyon Road (follow for 1.8 miles)*
2. *Turn left onto Washington Street (follow for 0.8 miles)*
3. *Park along the dirt shoulders on either side of the road.*
4. *Hike ~300 feet (~91 meters) northeast towards the Washington Street Fan.*

from Coachella Valley Preserve, California
to Coachella Valley Preserve, California
5 min (3.0 miles)
via Thousand Palms Canyon Rd and Washington St
Fastest route now due to traffic conditions
Coachella Valley Preserve
California
Head northeast toward Thousand Palms Canyon Rd
449 ft
Turn right onto Thousand Palms Canyon Rd
2.0 mi
Turn left onto Washington St
Destination will be on the left
0.8 mi
Coachella Valley Preserve
California
Gas
EV charging
Hotels
More
Indio Hills
Coachella Valley Preserve
Thousand Palms Oasis Preserve
Coachella Valley Preserve
Pushwalla Palms Trailhead
5 min
3 miles
Willis Palms
Willis Palm Trailhead
Thousand Palms Canyon
Shadow Mountain Ranch
Coachella Valley Preserve
Layers
3D

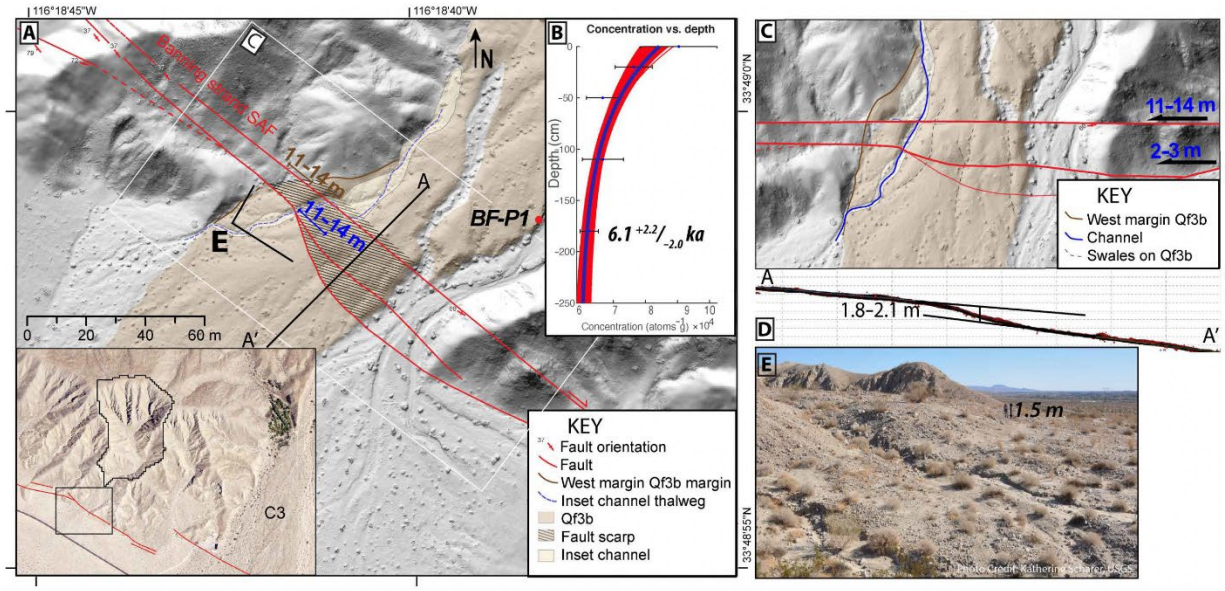
116°18'45"W
116°18'40"W
A
B
C
D
E
Reinforced Segment SAF
11-14 m
11-14 m
BF-P1
N
A
A'
E
0
20
40
60 m
C3
Concentration vs. depth
Depth (cm)
0
-50
-100
-150
-200
-250
6
7
8
9
10
Concentration (atoms g-1) ×10^4
6.1 +2.2/-2.0 ka
KEY
Fault orientation
Fault
West margin Qf3b margin
Inset channel thalweg
Qf3b
Fault scarp
Inset channel
33°49'0"N
33°48'55"N
11-14 m
2-3 m
KEY
West margin Qf3b
Channel
Swales on Qf3b
A
A'
1.8-2.1 m
1.5 m
Photo Credit: Katherine Scharer, USGS

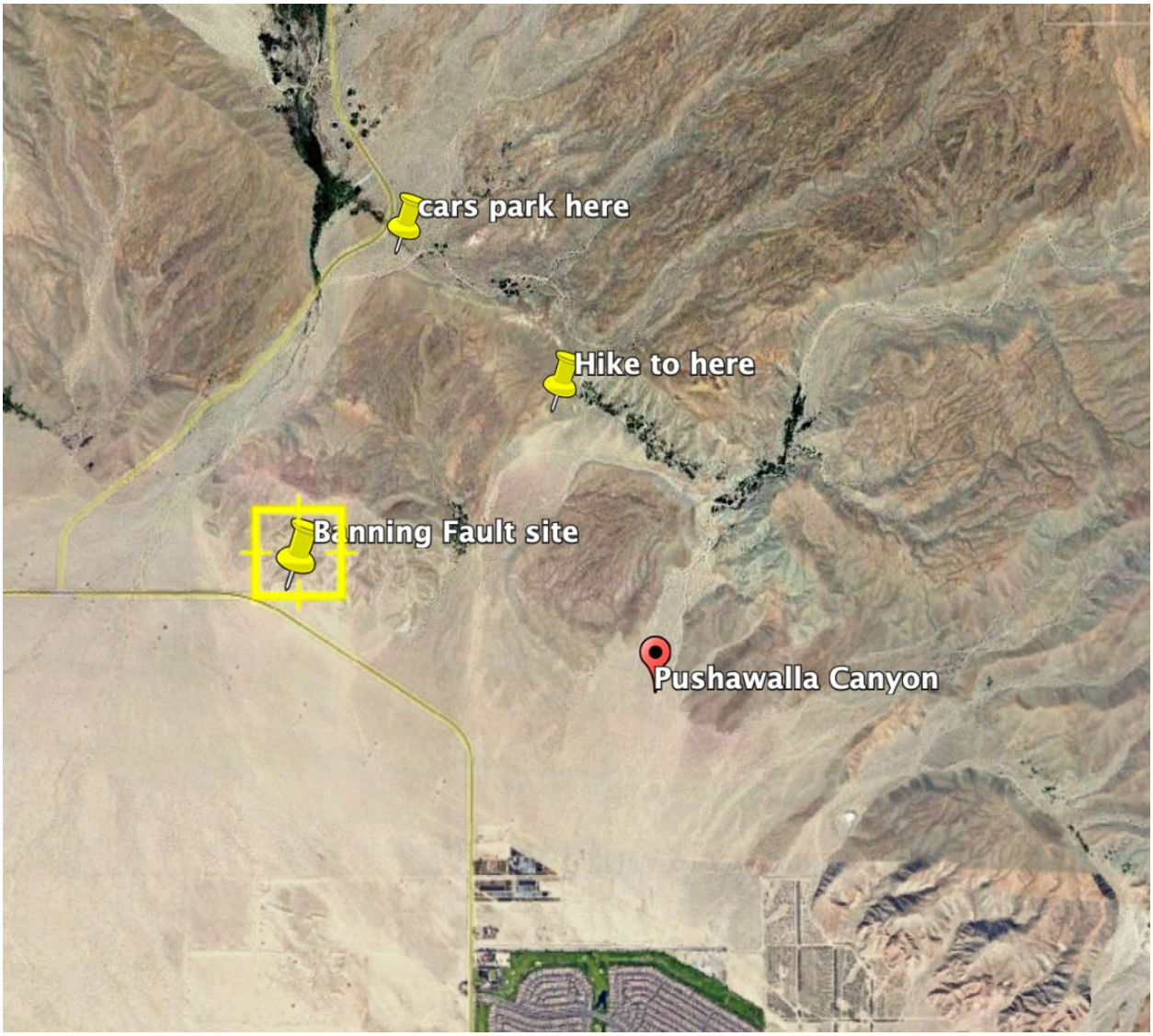

We will then head up to Mission Creek to explore/debate recent slip history along the Mission Creek strand of the San Andreas Fault (Matti et al).

Mission Creek coordinates: 34.0087, -116.5806

Drive time from Washington Street Fan: ~28-35 minutes

Details on how to get there from Washington Street Fan are as follows:

1. *Head northwest on Washington Street toward Thousand Palms Canyon Road (follow for 1.0 miles)*
2. *Continue onto E Ramon Road (follow for 3.5 miles)*
3. *Turn left onto Monterey Avenue (follow for 0.6 miles)*
4. *Turn right to merge onto I-10 W (follow for 14.2 miles)*
5. *Take exit 117 for CA-62/29 Palms toward Yucca Valley (follow for 0.4 miles)*
6. *Continue onto CA-62 E/29 Palms Highway (follow for 6.1 miles)*
7. *Slight left toward N Indian Canyon Drive/Kolbe Road (0.1 miles)*

8. *Continue onto N Indian Canyon Drive/Kolbe Road (0.2 miles)*
9. *Turn right along a restricted usage road for 0.2 miles (there are two dirt roads to turn right onto…turn right onto the 2nd possible option) and park somewhere along the dirt road.*

That will be a wrap for Day 1 at FOP! The only thing left to do is go back to FOP Central, drink some beer, and discuss/debate some of the things that have been brought up today. Slip activity along the Mission Creek strand of the fault might facilitate some interesting discussion!

Details on how to get back to FOP Central from here are as follows:

Drive time from Mission Creek to FOP Central: ~1 hour 20 minutes

1. *Head back to CA-62 W and turn right onto the highway (follow for 6.2 miles)*
2. *Keep right at the fork, follow signs for I-10 E/Indio/Palm Springs and merge onto I-10 E (follow for 28.5 miles)*
3. *Use the right 2 lanes to take exit 145 for California 86 toward Brawley/El Centro (500 ft)*
4. *Continue straight onto CA-86 S (follow for 12 miles)*
5. *Use the left lane to take the 66th Avenue ramp to CA-111 S/Niland/Calipatria (follow for 0.2 miles)*
6. *Turn left onto 66th Avenue (follow for 0.7 miles)*
7. *Turn left onto Lincoln Street (follow for 0.1 miles)*
8. *Turn right toward CA-111 S and make a slight right onto CA-111 S (follow for 10 miles)*
9. *Turn right onto State Park Road*

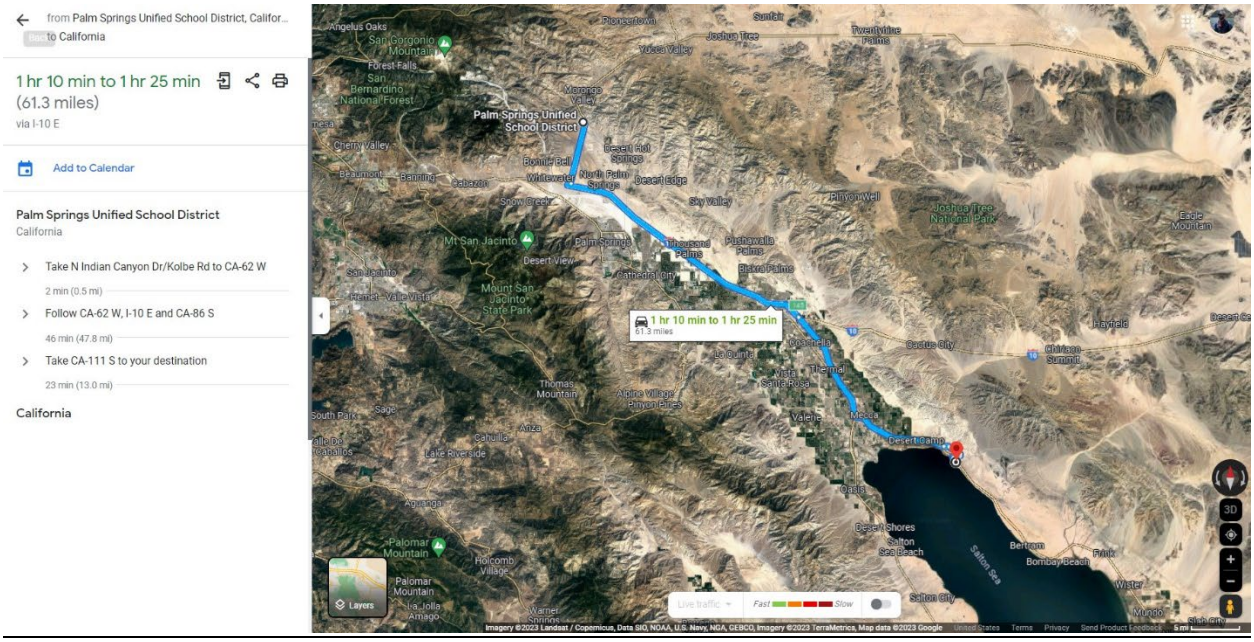

Day 2

We will kick off Day 2 by heading down to the Salt Creek Paleoseismic Site (Rockwell, Williams, Scharer).

Salt Creek Parking Area: 33.4457, -115.8430

Salt Creek Paleoseismic Site: 33.4460, -115.8398

Drive time to the Paleoseismic Site: ~10 minutes

Details on how to get to the parking area from FOP Central are as follows:

1. *Make your way out of the campground toward the main road (CA-111)*
2. *Turn right onto CA-111 S (follow for 6.2 miles)*

You will see a large dirt shoulder on the left-hand side of the road, shortly after you drive past a railroad bridge on the left. Park anywhere in this dirt area. The hike to the paleoseismic site from here will take roughly 5-10 minutes.

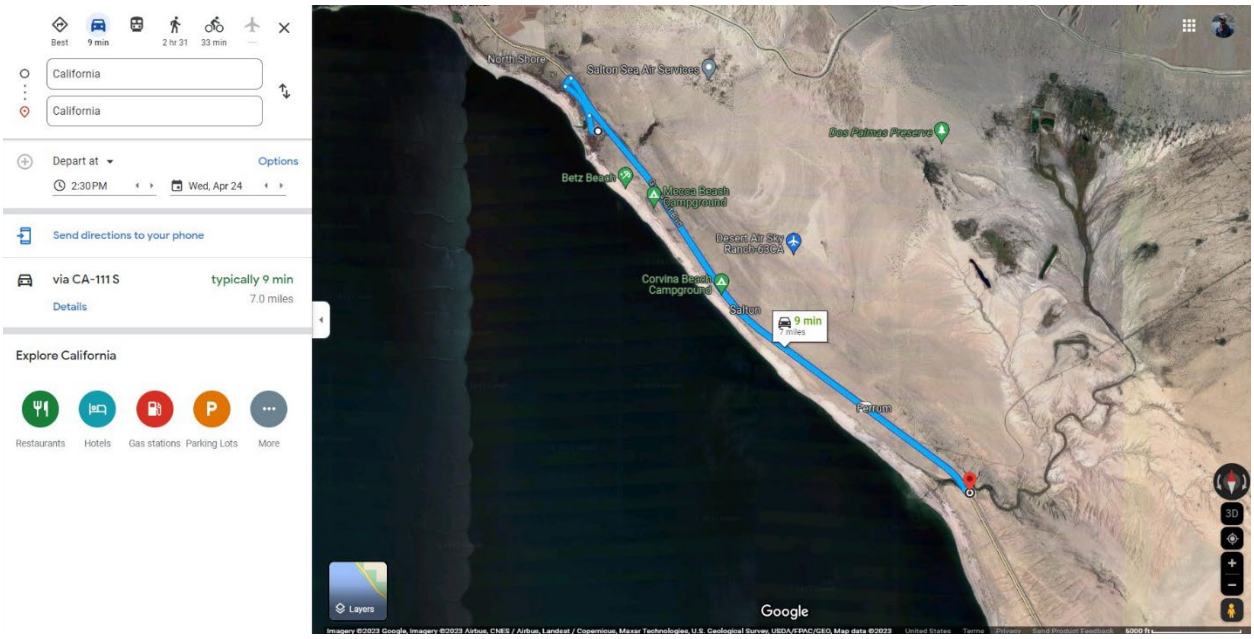

After this, we will head to one of Roger Bilham's creepmeters.

Creepmeter coordinates: 33.4485, -115.8436

Directions to the creepmeter are as follows:

1. *We won't need to drive, as Roger's creepmeter is fairly close to the paleoseismic site. We will instead walk over to the site, which is roughly a 0.5 mile walk from the parking area.*
2. *From the parking area, walk north-northwest along the highway until you cross the bridge.*
3. *Once you cross the bridge, walk into the large open dirt area on the right-hand side and make your way towards the railroad bridge.*
4. *Walk underneath the railroad bridge and turn left onto the existing dirt road/path.*
5. *Follow the dirt road/path for ~500 feet and you should see the creepmeter on the left-hand side.*

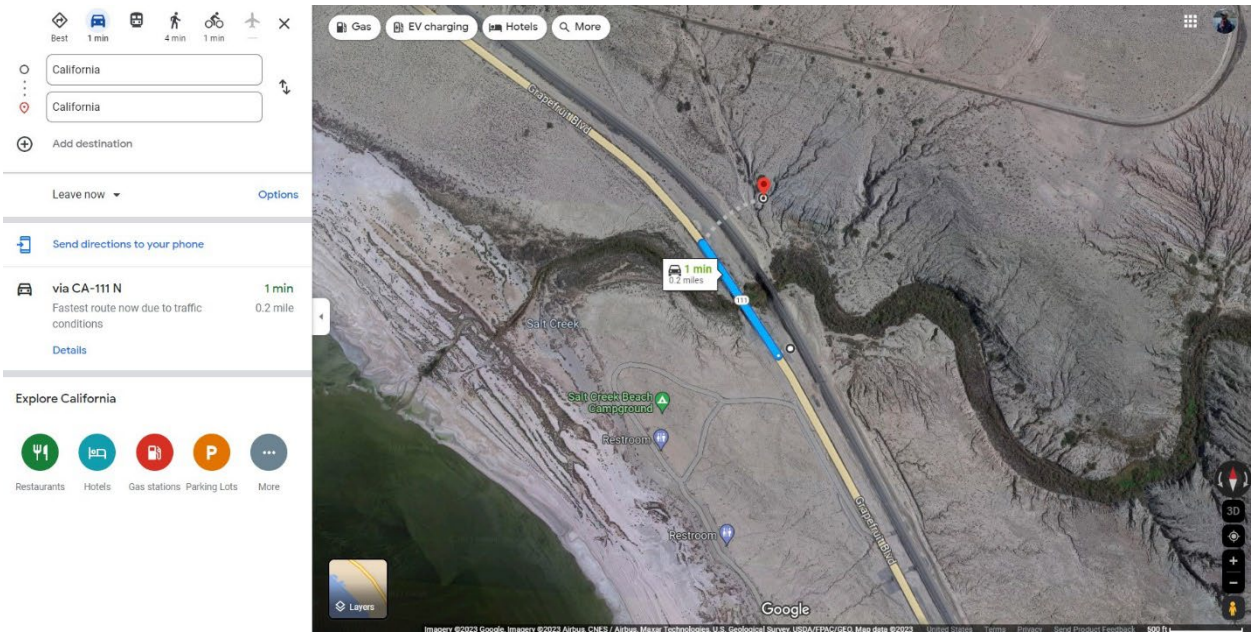

After the creepmeter, we will begin looking at geomorphology along the fault in the form of offset channels/streams by first starting at Ferrum (Buckley et al.). We will have to hop back in our cars briefly to meet up at this next spot.

Ferrum parking area coordinates: 33.4578, -115.8603

Ferrum offset coordinates: 33.4615, -115.8583

Drive time to Ferrum from Salt Creek: ~1 minute

Details on how to get to the parking area at Ferrum are as follows:

1. *Head northwest along CA-111 N for 1.3 miles.*
2. *You will see several turnouts on the right-hand side of the road which lead into a large open dirt area.*
3. *Turn in anywhere you see fit for parking.*
4. *To get to the offset, we will have to hike ~1/4 mile to the north-northwest.*

After Ferrum, we'll head over to the northwestern side of the Mecca Hills to look at more geomorphic offsets (Blanton et al).

Northwestern Mecca Hills parking spot coordinates: 33.6450, -116.0774

Drive time: ~26 minutes

Details on how to get to this next parking area from Ferrum are as follows:

1. *Head northwest on CA-111 N (follow for 19.4 miles)*
2. *Turn right onto 62nd Avenue (follow for 0.5 miles)*
3. *Turn left onto Buchanan Street (follow for 3 miles)*
4. *Turn right onto Airport Blvd (follow for 0.2 miles)*
5. *Turn right after crossing the canal and follow the road through the existing facilities (follow for 1 mile)*
6. *You'll see a large open dirt area on the left-hand side of the road, where we will park and meet.*

from California
to Thermal, California 92274

26 min (22.0 miles)
via CA-111 N

Add to Calendar

California

Head northwest on CA-111 N
18.1 mi

Turn right onto 62nd Ave
0.5 mi

Turn left onto Buchanan St
3.0 mi

Turn right onto Airport Blvd
0.2 mi

Turn left
Destination will be on the left
0.2 mi

Thermal
California 92274

That's a wrap for Day 2 at FOP! We will meet back at FOP Central for more beer and discussion.

Drive time back to FOP Central: ~35 minutes

Directions back to FOP Central are as follows:

1. *Make your way back across the canal and head west along Airport Blvd (follow for 0.2 miles)*
2. *Turn left onto Buchanan Street (follow for 1.0 miles)*
3. *Tur right at the 2nd cross street onto Avenue 58 (follow for 1.9 miles)*
4. *Turn left onto CA-111 S (follow for 15 miles)*
5. *Turn right onto State Park Road into the campground*

Day 3

We will be closing off this FOP trip with a couple unique stops, the first of which is Obsidian Butte along the southern shoreline of the Salton Sea.

Obsidian Butte coordinates: 33.1711, -115.6375

Drive time from FOP Central: ~50 minutes

Details on how to get to Obsidian Butte from FOP Central are as follows:

1. *Make your way out of the campground toward the main road (CA-111)*
2. *Turn right onto CA-111 S (follow for 37.0 miles)*
3. *Turn right onto Estelle Road/W Sinclair Road (follow for 5.5 miles)*
4. *Turn left onto Gentry Road (follow for 0.5 miles)*
5. *Turn right onto McKendry Road (follow for 1.1 miles)*
6. *Turn right onto the first dirt road that you see and follow for 0.2 miles.*
7. *Park anywhere you see fit. We will take a brief hike (~500 feet) up Obsidian Butte*

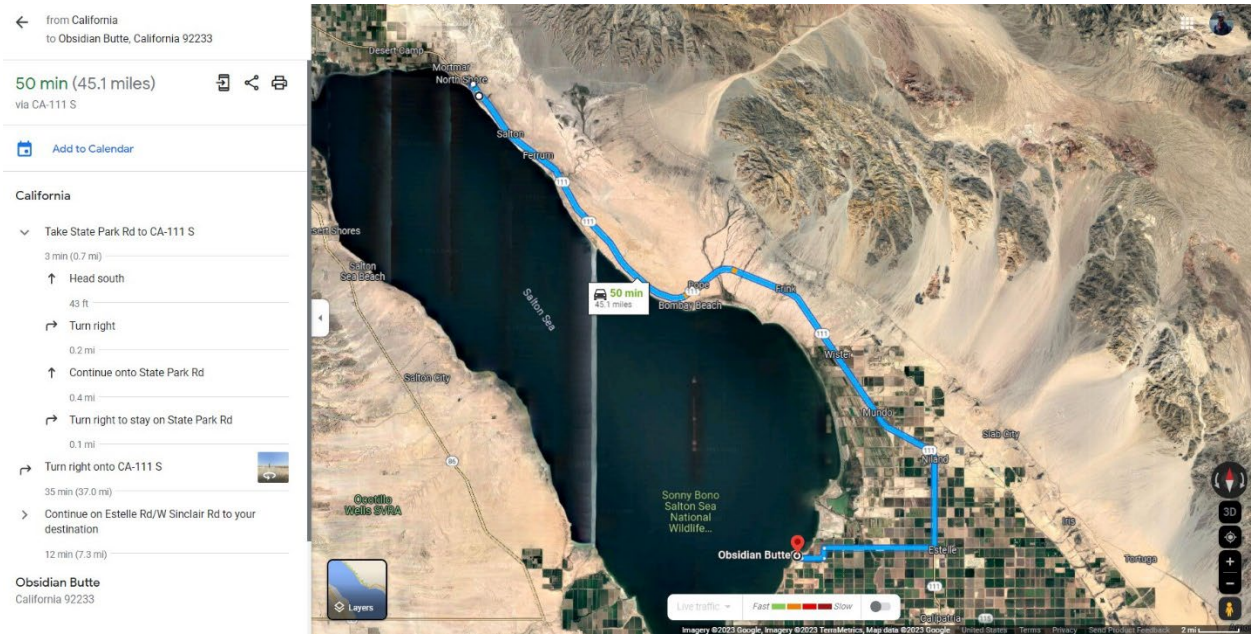

We will then head to the 'Old Mud Pots' aka mud volcanoes. These mud volcanoes are continuously flowing (erupting, if you want to call it that) and the mud temperature is relatively mild, up to about 100 degrees F or so.

Old Mud Pots coordinates: 33.2006, -115.5781

Drive time to Old Mud Pots: ~20 minutes

Details on how to get to the Old Mud Pots are as follows:

1. *Head back towards McKendry Road and turn left onto McKendry Road (follow for 1.1 miles)*
2. *Turn left onto Gentry Road (follow for 0.5 miles)*
3. *Turn right onto Estelle Road/W Sinclair Road (follow for 4.0 miles)*
4. *Turn left onto English Road (follow for 1.5 miles)*
5. *Turn left onto W Schrimpf Road (follow for 2.0 miles…….weird name for a road huh??)*
6. *Turn right onto Davis Road (follow for 0.2 miles)*
7. *Park anywhere you see fit along the dirt shoulders on either side of the road.*
8. *We will have to take a brief hike (~1/4 mile) to the mud volcanoes.*

from Obsidian Butte, California 92233
to Old Mud Pots, Calipatria, CA 92233

20 min (9.5 miles)
via Estelle Rd/W Sinclair Rd

Add to Calendar

Obsidian Butte
California 92233

- Head northeast toward McKendry Rd — 0.2 mi
- Turn left onto McKendry Rd — 1.1 mi
- Turn left onto Gentry Rd — 0.5 mi
- Turn right onto Estelle Rd/W Sinclair Rd — 4.0 mi
- Turn left onto English Rd — 1.5 mi
- Turn left onto W Schrimpf Rd — 2.0 mi
- Turn right onto Davis Rd — 0.2 mi

Old Mud Pots
Calipatria, CA 92233

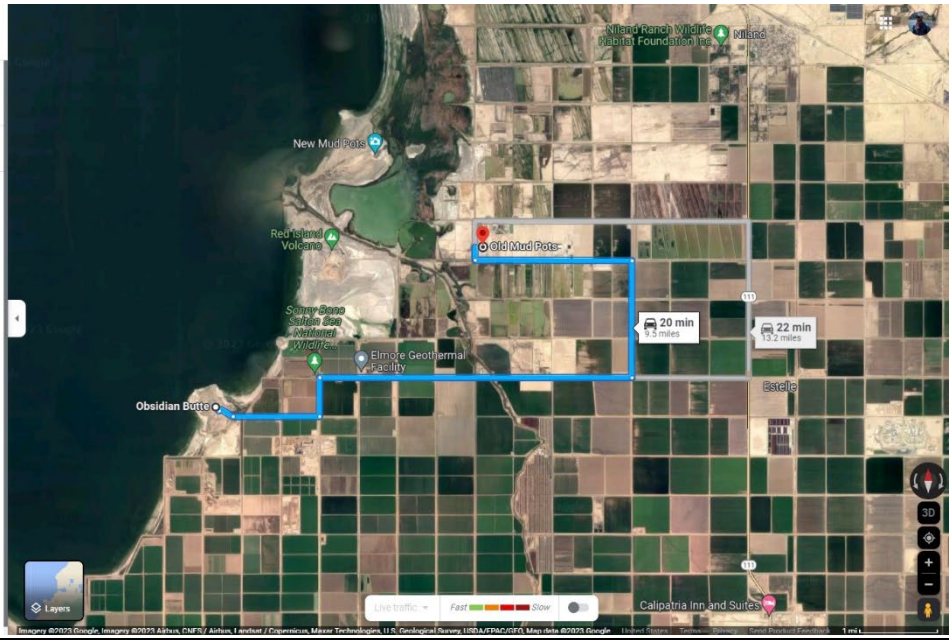

DAY 1 PAPERS

GEOLOGY

A revised position for the primary strand of the Pleistocene-Holocene San Andreas fault in southern California

Kimberly Blisniuk[1]*, Katherine Scharer[2], Warren D. Sharp[3], Roland Burgmann[4], Colin Amos[5], Michael Rymer[6]

Copyright © 2021 The Authors, some rights reserved; exclusive licensee American Association for the Advancement of Science. No claim to original U.S. Government Works. Distributed under a Creative Commons Attribution NonCommercial License 4.0 (CC BY-NC).

The San Andreas fault has the highest calculated time-dependent probability for large-magnitude earthquakes in southern California. However, where the fault is multistranded east of the Los Angeles metropolitan area, it has been uncertain which strand has the fastest slip rate and, therefore, which has the highest probability of a destructive earthquake. Reconstruction of offset Pleistocene-Holocene landforms dated using the uranium-thorium soil carbonate and beryllium-10 surface exposure techniques indicates slip rates of 24.1 ± 3 millimeter per year for the San Andreas fault, with 21.6 ± 2 and 2.5 ± 1 millimeters per year for the Mission Creek and Banning strands, respectively. These data establish the Mission Creek strand as the primary fault bounding the Pacific and North American plates at this latitude and imply that 6 to 9 meters of elastic strain has accumulated along the fault since the most recent surface-rupturing earthquake, highlighting the potential for large earthquakes along this strand.

INTRODUCTION

Landforms offset along faults by surface-rupturing earthquakes preserve a cumulative record of fault motion over time. When combined with their ages of formation, these offset landforms may be used to calculate average long-term fault-slip rates. Slip rate data, especially over multiple time intervals, are fundamental to understanding the kinematic partitioning of deformation along an evolving plate boundary. These slip rate data are also important when evaluating earthquake hazard because in most long-term probabilistic seismic hazard models, the faster a fault slips, the greater the likelihood of a future earthquake [e.g., (*1*, *2*)].

The faults of the southern San Andreas fault system, inclusive of the San Andreas fault (SAF), San Jacinto fault, and Elsinore fault (Fig. 1A), all accommodate Pacific–North American (PA-NA) plate motion and all pose seismic hazard (*1*). Of these, the SAF poses the greatest hazard potential because the southernmost section has not ruptured since ca. 1726 CE (Fig. 1A) (*3*), and geodetic data suggest that the fault accumulates interseismic strain of up to 25 mm/year, roughly half of the motion across the PA-NA plate boundary [(*4*) and references therein]. However, the SAF is multistranded along this section so it is uncertain which strand of the SAF carries the most slip and poses the greatest rupture likelihood [e.g., (*5*, *6*)]. Furthermore, obtaining geologic slip rates for some strands of the fault has proven challenging, while geodetic slip rate models have limited resolution in places where faults are closely spaced or multistranded, as the SAF is in southern California.

In the Coachella Valley in southern California near the Indio Hills, at the Biskra Palms site, the SAF is estimated to slip at a rate of ~12 to 22 mm/year (14 to 17 mm/year, preferred) (Fig. 1A) (*7*). Northwest of this location, the SAF bifurcates into the Mission Creek and Banning strands (Fig. 1A). Farther northwest, the SAF further partitions and encompasses the Mission Creek, Banning, and Garnet Hill strands and San Gorgonio Pass fault zone (Fig. 1A). Here, the relative proportion of plate boundary deformation accommodated by each strand of the SAF remains unresolved (*7*–*11*), despite the distinct implications that slip rates would have on earthquake rupture forecasts and understanding the tectonic configuration of this complex region. Several studies suggest that the majority of plate boundary deformation is localized along the Banning and Garnet Hill strands and the San Gorgonio Pass fault zone (Fig. 1B) because kinematic models for the region infer that the Mission Creek strand and its northwest continuation as the Mill Creek strand is inactive [(*8*–*11*) and references therein]. The Banning and Garnet Hill strands and San Gorgonio Pass fault zone are assumed by current hazard models (*1*) to take up most of the lateral strain at this latitude and, therefore, are considered most likely to rupture in a future SAF earthquake (*12*).

Many kinematic models indicate that as the SAF bifurcates northwestward into the Mission Creek and Banning strands at Biskra Palms, slip on the Mission Creek strand diminishes to the northwest. For example, slip rates on the Mission Creek strand are thought to decrease from values of 14 to 17 mm/year at Biskra Palms (*7*) to ~2 to 6 mm/year (*13*) at the Thousand Palms site located in the Indio Hills and 0 to 3 mm/year near the San Bernardino Mountains ~30 km to the northwest (Fig. 1A) [(*1*) and references therein]. Near Thousand Palms, the majority of SAF slip has been inferred to occur along the Banning strand [(*7*–*11*) and references therein]. The postulated reduction in slip rate and, therefore, diminished rupture likelihood on the Mission Creek strand has been explained by a model of regional fault reorganization that attributes transfer of slip off the Mission Creek strand to a change in fault geometry as the SAF evolves to a restraining bend near the southern Little San Bernardino Mountains (*9*–*11*). This transfer of plate boundary deformation off of the Mission Creek strand is thought to have occurred ~500 to 100 ka, as deformation migrated westward onto the Banning and Garnet Hill strands, San Gorgonio Pass fault zone, and northward into the Eastern

[1]Geology Department, San Jose State University, San Jose, CA 95192-0201, USA. [2]U.S. Geological Survey, Earthquake Science Center, Pasadena, CA 91106, USA. [3]Berkeley Geochronology Center, Berkeley, CA 94709, USA. [4]University of California, Berkeley, Berkeley, CA 94720-4767, USA. [5]Western Washington University, Bellingham, WA 98225, USA. [6]U.S. Geological Survey, Earthquake Science Center, Menlo Park, CA 94025, USA.
*Corresponding author. Email: kimberly.blisniuk@sjsu.edu

Downloaded from http://advances.sciencemag.org/ on April 1, 2021

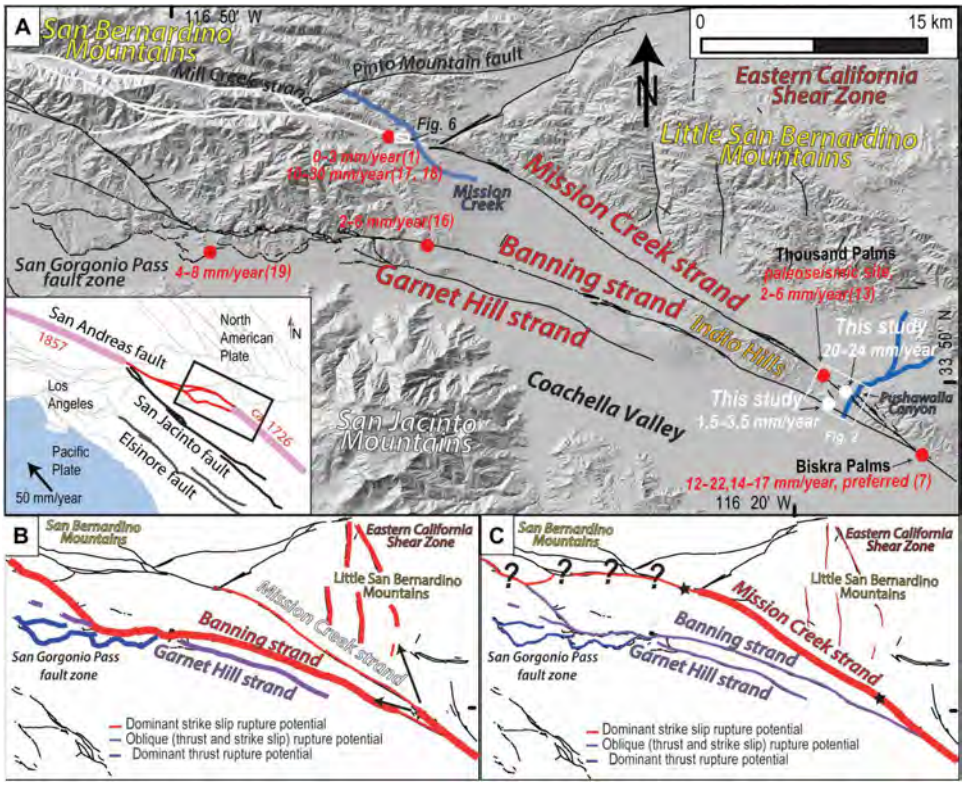

Fig. 1. Location map of study area on the southern SAF. (**A**) Map showing the location of the Mission Creek strand, Banning strand, Garnet Hill strand, and San Gorgonio Pass fault zone of the southern SAF. The white circles show the locations of slip rate sites in this study, and red circles show the locations of prior studies. The white rectangles show the locations of Figs. 2 and 6. Black lines show the location of active faults, and white lines show the location of inactive faults proposed in previous studies of the southern SAF (*9*–*11*). The thick blue lines identify the key drainages discussed in the text and show the source of sediment for channel and terrace deposits from the Little San Bernardino Mountains through Pushawalla Canyon. Topography derived from 10-m NED (National Elevation Dataset) data, U.S. Geological Survey. Inset map shows the southern SAF system, defined by the SAF, San Jacinto fault, and Elsinore fault. Thick pink lines delineate portions of the SAF that last ruptured in 1857 and after 1726 CE (*3*). Black box outlines location of (A). (**B**) Illustration of current kinematic and rupture forecast models that reduce likelihood of Mission Creek strand ruptures and emphasize hazard posed by the strands to the southwest; symbolized here by thickness of lines (black arrows indicating alternative rupture pathways). (**C**) Simplified kinematic and rupture forecast model based on the results from this study, emphasizing constraints from slip rates at either end of the Mission Creek strand (locations shown by black stars). (B) and (C) are modified from (*16*).

California Shear Zone near the Little San Bernardino Mountains (Fig. 1B) [e.g., (*10*, *11*)]. This kinematic model of fault slip distribution suggests that primary plate boundary faults may evolve fairly rapidly by transferring strain across wide zones onto new or reactivated faults. It also informs official earthquake forecasts and has focused attention on the potential for ruptures through the San Gorgonio Pass. Consequently, estimates of 30-year probabilities of a >M (moment magnitude) 6.7 rupture on the Mission Creek strand are low (1.5%) compared to a westerly route linking the Banning and Garnet Hill strands to the San Gorgonio Pass fault zone (12 to 18%), as illustrated in Fig. 1B (*1*). Accordingly, the inferred higher rupture likelihood along the Banning strand, Garnet Hill strand, and San Gorgonio Pass fault zone is used in regional earthquake response planning as exemplified in the ShakeOut Scenario (*12*).

Here, we challenge the consensus that most of the slip is transferred off of the Mission Creek strand and onto other structures. We investigate the long-term deformation rate of the Mission Creek and Banning strands of the SAF in the Coachella Valley, a section of the SAF that has yet to produce a substantial historical earthquake, but where paleoseismic studies suggest frequent ground-rupturing earthquakes (Fig. 1A) (*13*). We then compare our study with dynamic rupture models (*14*), paleoseismic data (*13*, *15*), and fault slip studies (*7*, *16*–*19*) to (i) reevaluate the relative roles of the Mission Creek and Banning strands in accommodating surface deformation across the PA-NA plate boundary and (ii) discuss the impact of slip rates on rupture likelihood forecasts for the region.

Study location and approach

Between the drainages of Thousand Palms and Pushawalla Canyon in the Indio Hills, the Mission Creek and Banning strands (Fig. 1A) are well expressed (*20*) and separated by ~4 km at the surface but likely connect at a depth of between 12 and 15 km (*21*). These strands are identified by vegetation lineaments, shutter ridges, beheaded channels, and offset alluvial fans (Figs. 2 to 4). The Mission Creek strand is exposed within the channel walls of Pushawalla Canyon as two prominent fault splays (Figs. 2 to 4), and the subparallel Banning strand is expressed by an offset alluvial fan along the range front of the Indio Hills (Fig. 5). A previous study of the Mission Creek strand at this location by Keller *et al.* (*20*) identified the fault and an abandoned channel (C3; Fig. 2) originating from Pushawalla Canyon that was subsequently offset by ~1 km. In this study, we identify that two more previously unrecognized beheaded channels also offset from

Downloaded from http://advances.sciencemag.org/ on April 1, 2021

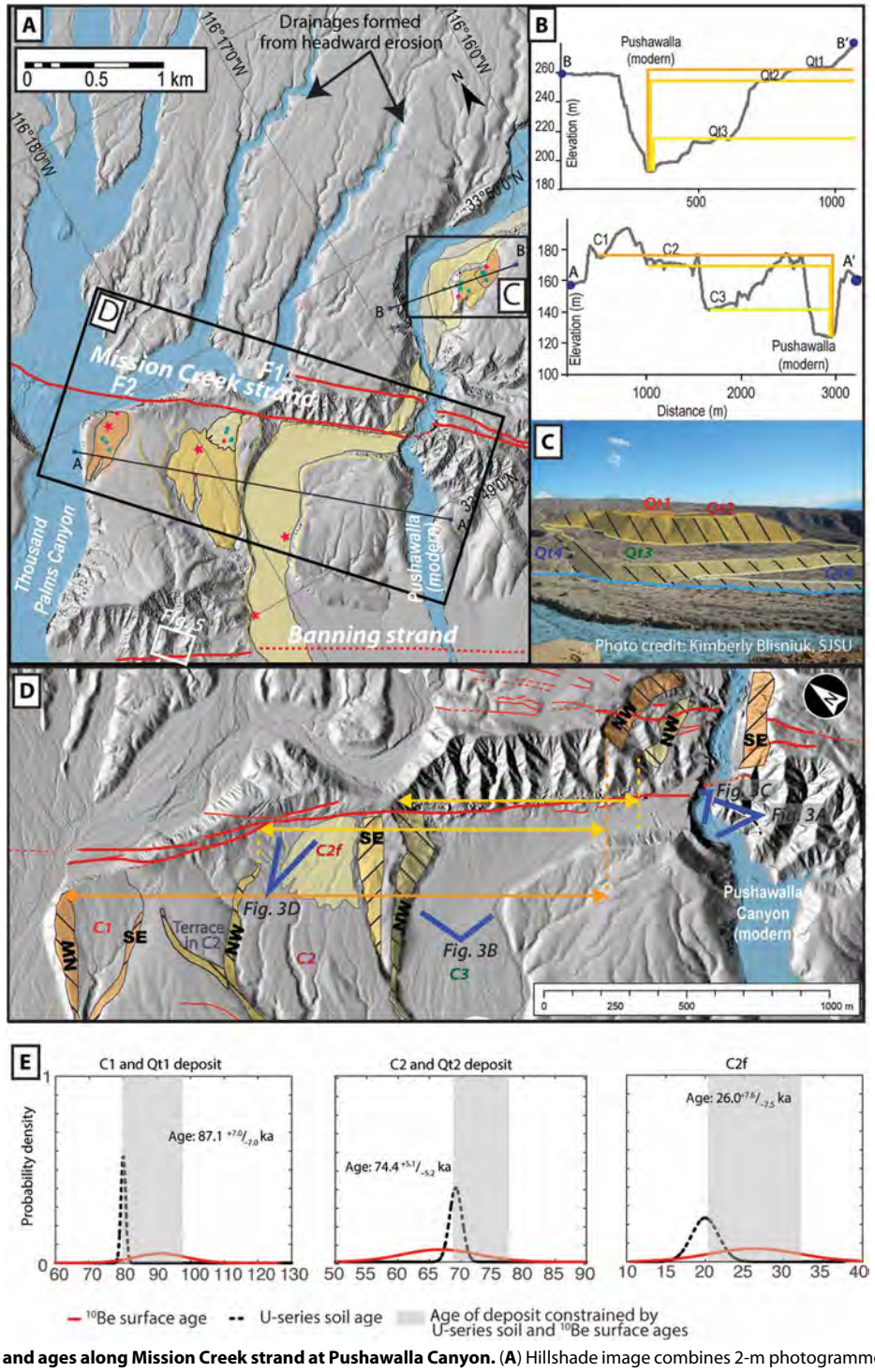

Fig. 2. Summary of offsets and ages along Mission Creek strand at Pushawalla Canyon. (**A**) Hillshade image combines 2-m photogrammetric and 1-m lidar data (*22*). Modern drainages are highlighted in blue, including Pushawalla Canyon, Thousand Palms Canyon (TPC) and two drainages tributary to Thousand Palms Canyon formed by headward erosion. Faults F1 and F2 (red lines) show splays of Mission Creek strand. Locations of dated samples include amalgamated ^{10}Be surface samples (red stars), ^{10}Be samples of individual resistant surface clasts (green circles), and U-Th pedogenic carbonate samples from soil pits and excavated channel walls (red circles). Profiles A-A′ and B-B′ are shown in (B). Black rectangles show locations of (C) and (D) of this figure. White rectangle shows location of Fig. 5. (**B**) Topographic profiles show relief of dated, offset landforms relative to modern Pushawalla Canyon. Note similar relief of terrace treads upstream of fault (B-B′) and channel floors downstream of fault (A-A′). (**C**) Photo looking east across Pushawalla Canyon upstream of the fault showing flight of terraces. (**D**) Image showing offsets inferred for channels C1, C2, and C3. Offsets (yellow and orange arrows) are based on restoring channel walls upstream and downstream of the main fault trace (thick red line). Channel walls are highlighted in colored fills and hachuring. SE, southeast walls; NW, northwest walls. Full reconstructions with uncertainties are given in the text and in Fig. 4 and fig. S5. Blue triangles show view direction of photos in Fig. 3. (**E**) Summary of landform ages. Age distributions of ^{10}Be ages (red) and U-Th ages (black) are modeled using Gaussian probability distributions; gray bars show preferred landform age ranges. See fig. S4 for a plot of all ages. Photo credit: Kimberly Blisniuk, SJSU.

Downloaded from http://advances.sciencemag.org/ on April 1, 2021

Pushawalla Canyon along the Mission Creek strand (C1 and C2; Fig. 2) and an alluvial fan offset along the Banning strand. We use offsets of these landforms and dates calculated for them using the U-Th soil carbonate and ^{10}Be surface exposure techniques to calculate slip rates for each fault strand and sum them to obtain the cumulative slip rate across the SAF.

Because of a lack of age control and refined piercing points, a slip rate for the Mission Creek strand was not estimated at Pushawalla Canyon by Keller *et al.* (*20*). However, these authors did estimate a slip rate of 23 to 35 mm/year for the SAF where it is single stranded at the Biskra Palms site, ~5-km southeast of Pushawalla Canyon (Fig. 1). More recent studies that applied multiple numerical dating techniques to the Biskra Palms fan site revised the slip rate there to 12 to 22 mm/year, with preferred rates of 14 to 17 mm/year (Fig. 1) (*7*). The only published slip rate for the Mission Creek strand near Pushawalla Canyon was developed at Thousand Palms Canyon. There, a slip rate of 2 to 6 mm/year since 1000 CE was estimated on the basis of a channel offset of 2.0 ± 0.5 m (*13*).

RESULTS

Mission Creek strand at Pushawalla Canyon

Two fault splays of the Mission Creek strand form a left step at Pushawalla Canyon that produces local folding, uplift, and an angular unconformity between older, mid-Quaternary Ocotillo Formation and younger, overlying cobble-rich fluvial gravels (Fig. 2) (*20*). This deformation appears to have constrained the path of the stream forming Pushawalla Canyon upstream of the fault. The northern fault splay (F1) becomes inactive and is absent at the surface ~1-km northwest of Pushawalla Canyon, and deformation is transferred to the southern fault splay (F2), where the Mission Creek strand is clearly delineated and continues along the northern side of the Indio Hills (Figs. 2A and 3).

Pushawalla Canyon carves a single path through older sediment of the Ocotillo Formation, delivering younger granitoid-rich cobbly sediment from the Little San Bernardino Mountains across the Mission Creek strand via an ephemeral stream (Fig. 1A). The canyon is ~500-m-wide upstream of the fault and abruptly narrows to ~200 m at the fault, which it crosses at a high angle (Fig. 2). Upstream of the Mission Creek strand, a flight of terraces is preserved in the canyon as mantled deposits overlying Ocotillo Formation (*20*), where we mapped four main surfaces (Qt1, Qt2, Qt3, and Qt4) in the field and from lidar data (*22*). The deposits that make up the terraces are distinctly different from those of the Ocotillo Formation. These deposits are 1 to 3 m in thickness, fluvial in nature, and rich in Cretaceous granitoid and gneissic sediment that are derived from the Little San Bernardino Mountains and were likely left behind when the terrace surfaces were abandoned. Downstream of the Mission Creek strand, we identified three beheaded and abandoned paleochannels (C1, C2, and C3) and an alluvial fan (C2f) (Figs. 2 and 3B) that are also incised into the Ocotillo Formation (Fig. 3). Sediment deposits in these paleochannels are also 1 to 3 m in thickness, fluvial in nature, and rich in granitoid and gneissic sediment. Both upstream terrace deposits and downstream deposits

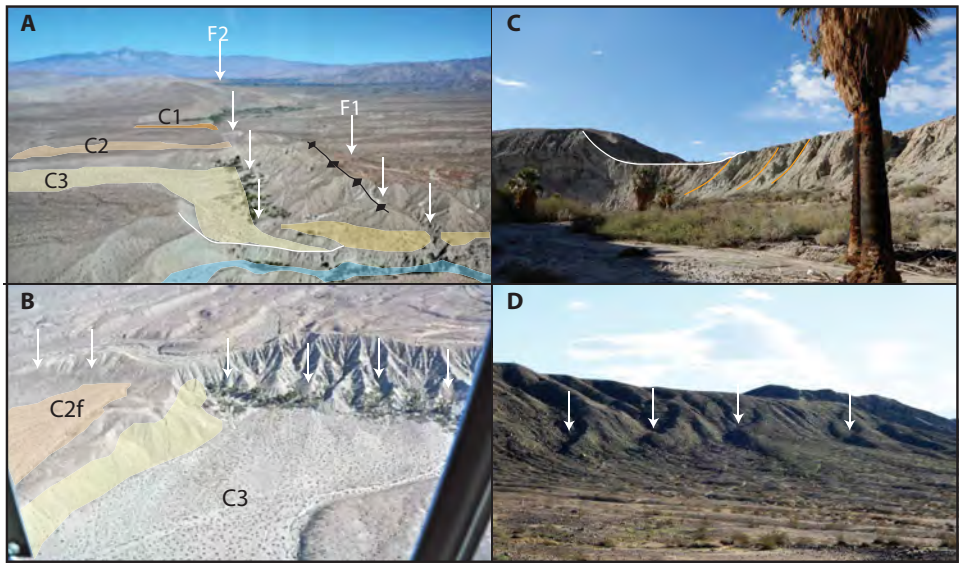

Fig. 3. Photos of Mission Creek strand at Pushawalla Canyon. The white arrows delineate primary geomorphic traces of the fault. Locations shown in Fig. 2. (**A**) Oblique aerial photo looking northwest. The fault here forms a left step, producing a compressional ridge in between the two fault splays, F1 and F2 (*20*). The ridge is shown by the black line with diamonds. The main fault splay, F2, is delineated by a vegetation lineament formed by palm trees and shrubs. Highlighted in blue is present day Pushawalla Canyon. Highlighted in pale yellow, light orange, and dark orange are offset channel deposits, C3, C2, and C1, respectively. The yellow surface is Qt2. All highlighted surfaces are sourced from Pushawalla Canyon. The white line marking the outline of C3 highlights the channel form of C3. Photo credit: Katherine Scharer, USGS. (**B**) Photo taken from above channel C3 looking north showing the geometry of C3 and the Mission Creek strand. The channel wall of C3, highlighted in yellow, is relatively straight and intersects the fault at a high (~90°) angle, indicating that abandonment of C2 and incision of C3 did not occur until this edge was in front of Pushawalla Canyon. Combined with this linear edge, the fault-parallel section of C3 indicates that the channel was first incised across the fault and then deflected before the more recent incision into the modern channel. Highlighted in orange is the fan, C2f, in C2. Photo credit: Katherine Scharer, USGS. (**C**) Photo showing the northwest wall of present day Pushawalla Canyon exposing steeply tilted and folded bedding of the Ocotillo Formation along the fault, indicated by the orange lines. White line is the channel bottom of C3 [see (A)]. (**D**) Photo showing southwest-facing ridge in C2. The white arrows show the location of the fault and shutter ridges produced along it. Photo Credit: Kimberly Blisniuk, SJSU.

Downloaded from http://advances.sciencemag.org/ on April 1, 2021

in the paleochannels unconformably overlie the Ocotillo Formation and can be observed where more recent erosion has incised into the paleochannels (fig. S2).

We provide multiple lines of geomorphic evidence to support the interpretation that Pushawalla Canyon is the source of incision and subsequent deposition of fluvial deposits into the three paleochannels (C1, C2, and C3). These observations are the following:

1) The topography shows that Pushawalla Canyon is currently the closest through-going stream channel that would have most recently supplied sediment from the Little San Bernardino Mountains, in the form of terrace and fluvial deposits, into those paleochannels (Fig. 2 and fig. S1). The channels are incised into mid-Quaternary Ocotillo Formation, and they are mantled by 1 to 3 m of younger sediment deposited by the stream issuing from Pushawalla Canyon, their only plausible source given their elevations. We note that Fig. 2 and fig. S1 show two other tributary channels on the upstream side of the fault just northwest of Pushawalla Canyon, which were considered as possible sources of channel alluvium across the fault for C2 and C1, respectively. However, we concluded that these were not sources because (i) the tributary channels end in the surface north of the fault and do not connect all the way to the Little San Bernardino Mountains; (ii) the tributary channels do not have evidence for older, higher elevation terrace remnants preserved along them that would be correlative with the elevations of C1 and C2; and (iii) a previous study that examined longitudinal profiles for each of these drainages noted that the tributaries do not show evidence of the uplift associated with the left step between F1 and F2 (*20*). We therefore interpret this absence of uplift to indicate that the tributaries are younger than the deformation caused by transfer of slip between F2 and F1 of the Mission Creek strand.

2) The basis of the elevations and morphology of the beheaded channels relative to the tributary channels and the absence of sediment similar to those in C1, the tributary channels cannot be sources of alluvium for the offset paleochannels. We interpret the tributary channels to be formed more recently by processes of headward erosion on the fan surface (Fig. 2 and fig. S1).

3) Folding and tilting of mid-Quaternary Ocotillo Formation on the northeast side of the fault produced the ridge between F1 and F2 that effectively blocks drainage flow from upstream into the three paleochannels (Fig. 2 and fig. S1). This ridge constrains Pushawalla Canyon to a relatively narrow width of 200 m on the northeast side of the fault. Evidence of this constriction is shown by the deflection of the modern drainage near the fault (Fig. 2 and fig. S1).

4) The relief between each terrace riser from Qt1 to Qt2 to Qt3 in Pushawalla Canyon is similar to the progressive decrease in elevation of channel bottoms from C1 to C2 to C3 (Fig. 2B). Specifically, the relief between surfaces C1-C2 and Qt1-Qt2 (~10 m) and the relative elevation of surfaces C2-C3 and Qt2-Qt3 (30 to 35 m) are similar in magnitude (Fig. 2B). This pattern indicates long-term downcutting in response to regional uplift and repeated channel avulsion driven by dextral slip.

Surface characteristics and geochronology of paleochannels and associated terraces

Below, we summarize that field observations and geochronological data indicating that beheaded paleochannels offset by the Mission Creek strand can be correlated with penecontemporaneous terrace surfaces preserved upstream of the Mission Creek strand in Pushawalla Canyon, thereby supporting the fault offsets and landform ages that underlie our new slip rate calculations.

Paleochannel C1 and terrace Qt1. Qt1 is the highest strath terrace within Pushawalla Canyon, preserved at the inside corner of a meander ~1-km upstream from the Mission Creek strand (Fig. 2 and fig. S1). The Qt1 terrace is spatially restricted (150 m by 250 m) and sits ~18 m below a higher Ocotillo Formation pediment. The surface of Qt1 is planar in form, with no bar and swale microtopography evident. Surface clasts are dominated by moderate-sized cobbles. Sparse gneissic and amphibolite cobbles exhibit strong parting along foliations or are disaggregated. Varnish is strong (medium brownish gray), and rubification is strong (dark orange with red-orange rims) on granitic clasts. Many cobbles show rubification on both sides of the clast, indicating that they have been overturned, suggesting reworking and/or inheritance.

We analyzed ^{10}Be concentrations on the tops of four resistant boulders from Qt1 (PT-1, PT-5, PT-11, and PT-15) and applied U-Th dating to soil carbonate clast coatings from a carbonate-rich horizon 1.3 to 1.0 m below the surface (PT-P1) (fig. S1). The photo of the boulder in fig. S3 from Qt1 provides an example of boulders from which ^{10}Be surface samples were collected. ^{10}Be exposure ages range from 89.4 ± 8.5 to 105 ± 8.8 ka (table S1 and fig. S4). Two carbonate clast coatings yielded dates of pedogenesis, and therefore minimum estimates for deposition of host alluvium, of 80.1 ± 0.7 and 65.4 ± 1.5 ka (table S2). The younger U-Th age postdates all ^{10}Be ages from Qt1 and is younger than U-Th samples collected from soils of C2, so it was not used to bracket the minimum age of deposit Qt1.

C1 is identified as the highest fluvial deposit that is contained within channel wall downstream of the Mission Creek strand (Figs. 2B and 3A). The C1 deposit is located 1900 to 2300 m from its upstream source, Pushawalla Canyon, and is the westernmost of the beheaded channels preserved (Fig. 4 and see the "Offset and slip rate estimates" section under Methods). C1 is 300 m in width at its upstream edge (Fig. 2 and fig. S1), where lateral incision by a tributary of Thousand Palms Canyon has eroded part of the channel near the Mission Creek strand (Fig. 2, A and D). Incision by this tributary exposes bright red soils of the C1 deposit overlying light tan colored Ocotillo Formation (fig. S2F). The surface of C1 is incised by a deep gully near its downstream end, reflecting headward erosion from Thousand Palms Canyon below. Otherwise, the surface of the C1 deposit is relatively planar with no bar and swale microtopography evident (figs. S2E and S3). Surface clasts are dominated by small boulders and cobbles (fig. S3). Amphibolite and gneissic boulders appear strongly varnished (shiny and black) and are commonly split along foliation planes. Weathering characteristics of granitic boulders on the surface are variable; some are deeply grusified, while others preserve a deep strong varnish. Surface clasts exhibit strong rubification with many cobbles showing a deep orange red color on their undersides. Many cobble clasts exhibit rubification on both sides. (fig. S3, C1 surface).

We analyzed ^{10}Be from five samples taken from C1: three boulder tops (PW-1, PW-3, and PW-4) and two amalgamated samples (PW-5 and PW-6) (fig. S1). The amalgamated samples yielded ^{10}Be dates of 82.1 ± 6.2 and 90.6 ± 2.0 ka, respectively. While one boulder top (PW-4) yielded a much older age (346.2 ± 30.3 ka), two other boulders yielded ages of 76 ± 6.7 and 94.2 ± 5.9 ka, respectively, which are similar to those of the amalgamated samples (table S1). The photos labeled C1 surface in fig. S3 show the typical clast size sampled from the C1 surface.

Given the similarities in the Qt1 and C1 surfaces and underlying alluvium, including the types and weathering characteristics of

Downloaded from http://advances.sciencemag.org/ on April 1, 2021

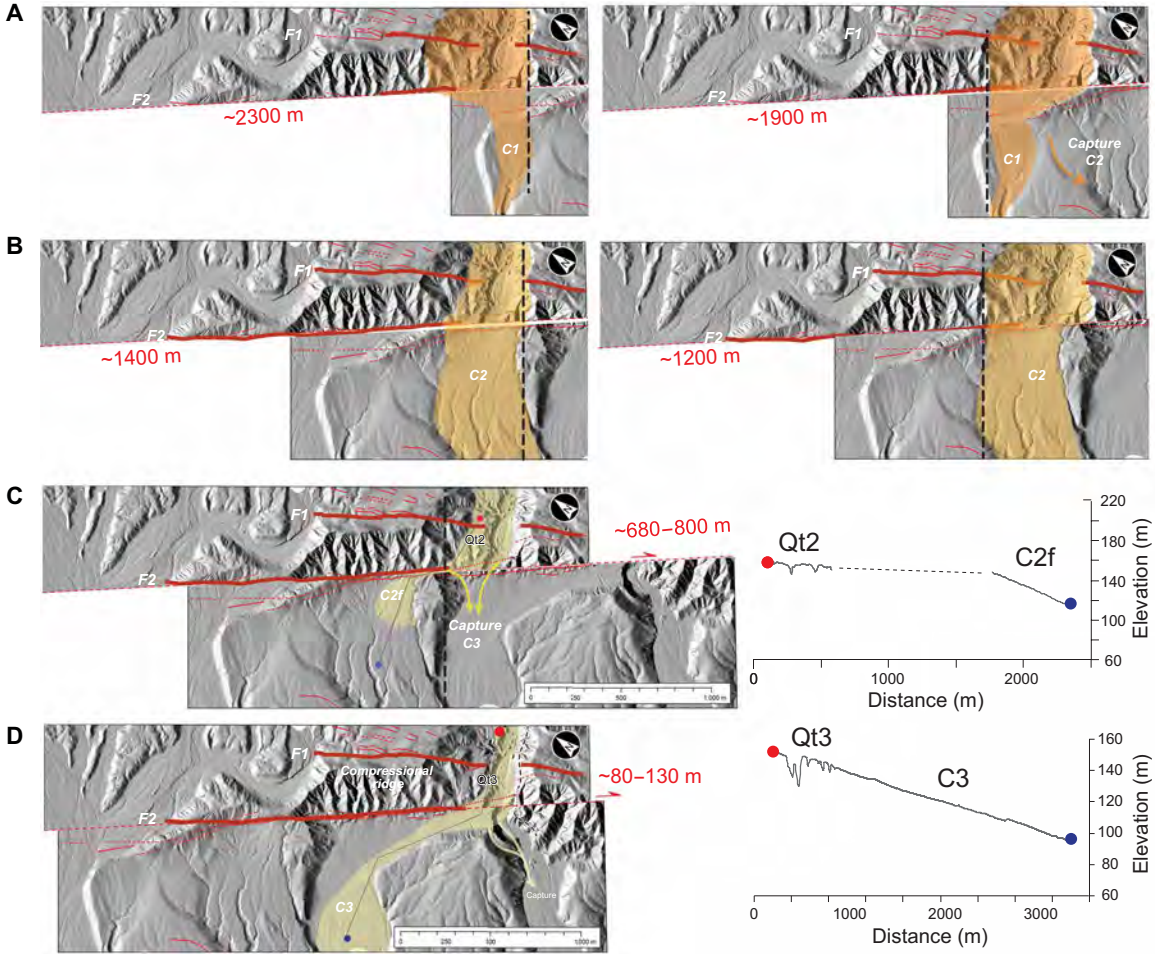

Fig. 4. Digital topography of terrain between Pushawalla and Thousand Palms Canyons along the Mission Creek strand (same area as Fig. 2D) and the reconstruction of preferred offsets of paleochannels C1, C2, C3, and the fan deposit, C2f, in C2 from Pushawalla Canyon. (**A**) Restored view showing preferred offset range needed to realign C1 with Pushawalla Canyon. (**B**) Restored view showing preferred offset range needed to realign C2 with Pushawalla Canyon. (**C**) Reconstruction showing the capture of stream flow by C3 from C2f in C2, with topographic profile showing the gradient of Qt2 and C2f. Red and blue dots show the location of profile across topography connecting Qt2 and C2f (right). (**D**) Reconstruction showing the present capture of stream flow from C3 by modern Pushawalla Canyon, with topographic profile showing the gradient of Qt3 and C3 (right). Limiting minimum and maximum ranges are provided in fig. S5.

surface clasts, microtopography, and their ^{10}Be and U-Th ages (~80 to 100 ka; fig. S4), we interpret that Qt1 and C1 were incised and abandoned approximately synchronously. We note that ^{10}Be surface exposure dates of amalgamated pebbles (PW-5 and PW-6) and the tops of individual boulders (samples PW-1, PW-3, PT-1, PT-5, PT-11, and PT-15) are similar, suggesting that the dates are not severely biased by partial shielding, erosion, or inherited ^{10}Be, since these processes are unlikely to affect the different sample types equally. We calculate an error-weighted mean ^{10}Be age of 90.4 ± 3.8 ka for Qt1 and C1 from eight similar ^{10}Be dates (table S1). We interpret boulder PW-4 to be an outlier affected by inheritance because it yielded a ^{10}Be date of 346.2 ± 30.2 ka; this date is also a statistical outlier. Because we cannot completely rule out inheritance in the ^{10}Be ages, we adopt a conservative approach to assigning a preferred age to the Qt1 and C1 landforms. That is, we consider the oldest U-series date of 80.1 ± 0.7 ka to provide a minimum age for the Qt1/C1 landform and the upper limit of the mean ^{10}Be exposure age of 90.4 ± 3.8 ka as the landform's maximum age, yielding an estimated age of 80.1 to 94.1 ka, or 87.1 ± 7.0 ka for the Qt1/C1 landform (Fig. 2E, fig. S4, and tables S1 and S2).

Paleochannel C2 and terrace Qt2. Qt2 is the second highest strath terrace within Pushawalla Canyon upstream of the Mission Creek strand and is inset into the Qt1 terrace (Fig. 2B). The preserved patch of Qt2 is about 200 m by 200 m, and the terrace is ~10 m below Qt1 in elevation (Fig. 2B). The Qt2 surface is planar, with many pebble clasts interlocking and forming a moderate pavement (fig. S3). The surface of Qt2 is dominated by cobbles up to 35 cm in length. Granitic cobbles are moderately varnished (pinkish brown color), while gneissic and amphibolite cobbles exhibit varnish that is medium dark gray in color. A few medium-grained granitic and porphyroblastic gneissic clasts show spallation, producing grus on the surface around the clasts. However, most surface clasts appear smooth and varnished, suggesting little to no weathering of these clasts. Some gneissic and amphibolite clasts show parting along foliations. The underside of many surface cobbles on the Qt2 surface shows moderate orange to pink rubification, and few clasts on the surface exhibit rubification of both sides.

From Qt2, four individual ^{10}Be surface boulder-top samples were collected (samples PT-16, PT-18, PT-19, and PT-20; table S1 and

Downloaded from http://advances.sciencemag.org/ on April 1, 2021

fig. S1). The photos labeled Qt2 surface in fig. S3 show the typical boulder sampled from the Qt2 surface. The dates for these samples are 71.2 ± 5.9, 75.8 ± 6.4, 96.9 ± 8.9, and 105.1 ± 8.8 ka (fig. S4). These dates scatter more than expected from their analytical errors, and the two older dates equal or exceed our preferred age for the geologically older C1/Qt1 landform pair, suggesting that the two older samples contain inherited ^{10}Be. U-Th dating of eight carbonate clast coatings from near the basal contact of Qt2 with the underlying Ocotillo Formation (table S2) yielded dates of 7.0 ± 0.8 to 27.6 ± 0.8 ka, younger than the ^{10}Be dates, and too young to represent deposition of Qt2 (table S2).

C2 is the second highest fluvial deposit identified as a paleochannel floor downstream of the Mission Creek strand (Fig. 2). The C2 deposit is located 1200 to 1400 m from the active stream issuing from Pushawalla Canyon and is the second oldest beheaded channel, following C1 (Fig. 4 and see Methods offset reconstruction). The surface of C2 is broad, flat, and ~600 m in width where it terminates against a high ridge along the Mission Creek strand (fig. S2C). Higher terraces are present along the northwest channel wall of C2, preserving an intermediate terrace elevation between C1 and C2 (Fig. 2 and fig. S6). Headward erosion of the C2 deposit has deeply incised the paleochannel floor, locally exposing bright red soils developed in C2 alluvium (fig. S2D). Where not incised by younger erosion, the surface of C2 is fairly smooth, containing poorly sorted subangular pebbles, cobbles, and sparse boulders (fig. S3). Most fine-to-medium–grained granitoid cobbles are grusified in place. Amphibolite and gneissic clasts have rust to almost black varnish developed on their exposed surfaces, with the presence of parting along foliation planes. The undersides of cobble clasts show a range of color intensity from strong to moderate rubification.

From C2, we analyzed one ^{10}Be sample consisting of >100 amalgamated surface clasts (PW-P2-S), which produced an age of 72.6 ± 6.9 ka. No boulders were found that were considered suitable for cosmogenic dating. Four carbonate clast coatings from ~2.2 to 2.4 m in depth yielded mutually consistent U-Th ages with a weighted mean of 69.2 ± 1.4 ka. (table S2 and fig. S4), in good agreement with the ^{10}Be age. On the basis of their similar surface morphology, weathering characteristics, and ^{10}Be and U-series dates, we infer that terrace Qt2 and channel C2 were incised and abandoned synchronously. We consider the mean U-Th age of 69.2 ± 1.4 ka to be a minimum estimate for the Qt2/C2 landform and the mean of three concordant ^{10}Be ages (71.2 ± 5.9, 72.6 ± 6.9, and 75.8 ± 6.4 ka), 72.6 ± 6.9 ka, to provide a maximum estimate for the Qt2/C2 landform. Accordingly, we assign the landform a preferred age range of 69.2 to 79.5 ka or $74.4^{+5.1}/_{-5.2}$ ka. We exclude from consideration ages of two boulders from Qt2 (PT-18 and PT-20) that yielded ^{10}Be dates of 96.9 ± 8.8 and 105.1 ± 8.8 ka, respectively, much older than other ^{10}Be and U-Th dates for C2 and Qt2 but similar to ages calculated for Qt1, suggesting that they were inherited from Qt1.

The northeast corner of C2 contains an alluvial fan, C2f, that abuts the high ridge along the fault and covers part of the interfluve between C2 and C3 (Figs. 2, 3B, and 4). This fan is significant as it is interpreted as the youngest deposit from Pushawalla Canyon in C2. The apex of the fan grades to the elevation of the Qt2 surface, which is located on the northeast side of the fault 680 to 800 m from C2f in Pushawalla Canyon (Fig. 4 and see Methods offset reconstruction). On the basis of the presence of the high-ridge north of the Mission Creek strand, which would block sediment from the tributary canyons (Figs. 2 and 3A), the shape of the fan (bordering the interfluve and down into the C2 drainage), the elevation of its apex (Fig. 4C), and the similarity of clast size and composition of the fan to that of C1 and C2 deposits, we conclude that Pushawalla Canyon is the source for this fan. In contrast, hillslopes of the high ridge along the Mission Creek strand expose Palm Springs and Ocotillo Formation (Fig. 3C), which consist of mudstones and sandstone, unlike the C2f alluvium that consists of larger cobbles and pebbles of rocks lithologically similar to those of the Little San Bernardino Mountains.

The surface of C2f is undulating and hummocky with preserved but muted bar-and-swale microtopography (fig. S3). Surface clasts are lightly to moderately varnished with bars consisting dominantly of cobble clasts, with some boulders present on the surface. Clast sizes on the surface range from boulders to gravel with 30- to 40-cm-long cobbles as the dominant clast size (fig. S3, C2f surface). Granitic clasts exhibit pinkish-brown varnish, with medium-grained clasts showing evidence of spallation and grusification. Rubification is moderate on well-seated clasts, and some parting is observed in gneissic cobbles.

From C2f, we collected five boulder- and cobble-top samples (PW-9, PW-10, PW-11, PW-13, and PW-14) for ^{10}Be dating and analyzed six pebbles with pedogenic carbonate coatings from the soil at ~1.5 to 1.7 m in depth. The photos labeled C2f surface in fig. S3 show the clast sampled from bars of the C2f surface and a photo of a boulder from C2f. ^{10}Be dates of four of the five samples from the C2f fan surface indicate a mean exposure age of 27.3 ± 6.3 ka. One older ^{10}Be sample (PW-10, 48.4 ± 4.1 ka) is a statistical outlier and likely reflects the presence of inherited ^{10}Be (fig. S4). U-Th dating yielded dates ranging from 11.1 ± 3.0 to 18.9 ± 4.6 ka. The two oldest U-Th ages are concordant with the ^{10}Be dates, and we interpret their mean age of 18.5 ± 4.8 ka as a minimum estimate of the depositional age of the C2f alluvium. Combining this U-series age with the ^{10}Be exposure age for the surface indicates that C2f was abandoned $26.0^{+7.6}/_{-7.5}$ ka (table S1).

Paleochannel C3 and terrace Qt3. The largest preserved patch of Qt3 in Pushawalla Canyon is about 700 m in length by about 100 m in width. Bar and swale microtopography is preserved on the surface, with relative amplitudes (40 cm) similar to the modern wash. The surface is dominated by very coarse gravel to cobble-sized clasts. Cobbles are rounded to subrounded, and felsic-rich clasts are smooth with pale pink to medium pale pink varnish. Rubification on felsic rocks is subtle, dominantly pale orange or pale pink. Scattered about the surface are dark, highly varnished cobbles that are presumed to reflect reworking and inheritance from older deposits. Some bars on the surface include boulders 1 m or more in size. Using ^{10}Be, we dated the tops of two such boulders from Qt3, PT-7 and PT-8, which yielded ages of 31 ± 2.6 and 13.0 ± 1.1 ka, respectively. The date of the older boulder overlaps with the age estimated for C2f (27.3 ± 6.3 ka), and the date of the younger boulder is similar to the date estimated for C3 (fig. S4 and table S1).

C3 is a ~400-m-wide channel deposit lying between steep bedrock side walls that form the paleochannel floor of C3, the most recent beheaded channel from Pushawalla Canyon along the Mission Creek strand (fig. S1) (*20*). The surface is light gray to pale pink, with muted bar and swale microtopography. The bars are dominated by 20-cm cobbles of subrounded granitoids, amphibolite, and gneiss. Surface clasts are weakly varnished with a pale pink color, and darker clasts appear to be more weathered, or darker on their sides, suggesting that these clasts were likely toppled or had prior exposure. Approximately 10 to 15% of the granitic clasts show surface erosion,

Downloaded from http://advances.sciencemag.org/ on April 1, 2021

while most are smooth with no apparent weathering observed on their surface. Undersides of granitic clasts are pale orange showing weak to moderate rubification. No parting is observed in more mafic, foliated clasts. Boulders up to 1 m are common in some debris flow bars; some of these boulders have moderate pink varnish that is locally flaking off.

We collected amalgamated samples consisting of >100 pebbles (PW-P7-S and PW-P1-S) from two young debris flow bars that were formed during channel aggradation of C3, one from each side of the channel walls of C3 (Fig. 2A and fig. S1). Sample PW-P7-S (13.7 ± 1.1 ka) was collected from near the west channel wall of C3 to potentially constrain older debris flow deposits, and sample PW-P1-S (11.5 ± 1.1 ka) was collected near the east channel wall of C3 to potentially bracket younger debris flow deposits. ^{10}Be exposure dating of these two amalgamated samples overlaps within their respective uncertainties, yielding a mean age of 12.7 ± 1.4 ka (table S1 and fig. S4).

Given the similarity in their surface weathering, including weak to moderate varnish development and rubification, lack of parting in amphibolite clasts, and their consistent elevation relative to the gradient of Pushawalla Creek, we infer that Qt3 and C3 were formed and abandoned around the same time. The age of incision postdates the C2f deposit ($26.0^{+7.6}/_{-7.5}$ ka), and abandonment is dated by the mean date of two amalgamated samples of cobble bars within C3 (12.7 ± 1.4 ka) and a single boulder date from Qt3 (PT-8, 13 ± 1.3 ka)

Interpretation of paleochannel reconstruction and displacement

We interpret the similarities of the absolute ages, relative elevations, observed surface characteristics of fluvial deposits, and age-related surface properties between the terraces and paleochannel deposits across the fault to indicate synchronous deposition of Qt1 and C1, Qt2 and C2, and Qt3 and C3, respectively (Fig. 2 and fig. S4). These results indicate that C1 and Qt1 were incised and abandoned by 87.1 ± 7.0 ka and C2 and Qt2 were incised and abandoned by $74.4^{+5.1}/_{-5.2}$ ka. Terrace Qt3 in Pushawalla Canyon yielded dates between 13.0 ± 1.0 and 31.0 ± 2.6 ka, which overlap with the dates for both the incision of C3 and abandonment of C2f (fig. S5).

To determine offset along the Mission Creek strand, we summarize the progression of drainage capture and slip along the fault over time based on dates estimated in this study. The best example of progressive drainage capture and downcutting comes from the youngest of the paleochannels (C3) at Pushawalla Canyon (Fig. 4C) (*20*). We interpret that C3 was cut and then accrued dextral slip, resulting in a large deflection of C3 of at least 680 m (Fig. 4C). This occurred sometime after ~26 ka based on the ages in C2f, C3, and Qt3. Avulsion has produced a weak left jog in the present Pushawalla Canyon. Restoring the modern channel, where Pushawalla Canyon has recently incised ~20 m, to the width of the canyon upstream of the fault permits 80 to 130 m of slip since C3 was abandoned (Fig. 4D).

Before channel avulsion and downcutting to create C3, deposition of a fan in C2, C2f, occurred along the southeast edge of C2 near the fault (Figs. 3B and 4C). The similarity in elevation of the strath of the Qt2 terrace near the fault and the apex of the C2f surface provides strong evidence that C2f graded to Qt2 (Fig. 4C and fig. S1). Deposition of a fan across and then along the fault (Fig. 4C) may reflect the reduced slope produced as C2 was translated away from the canyon mouth, or a climatic period of reduced transport. Accordingly, the last time that alluvium was deposited in C2 from Pushawalla Canyon should be closely constrained by the age of the C2f fan surface. Reconstruction of the incised western channel wall of C3 suggests that at least 680 m (and as much as ~800 m) of dextral slip has accumulated since abandonment of the C2f fan. This range in displacement values reflects possible reconstructions that allow drainage connectivity between Qt2 (i.e., the width of the upstream channel during Qt2 time) and the C2f surface. The slip rate calculated from this offset uses the abandonment age of the C2f surface (i.e., $26.0^{+7.6}/_{-7.5}$ ka) and the offset range of 680 to 800 m (table S4).

Incision and deposition of the C2 surface into the Ocotillo Formation resulted in a prominent, arcuate fluvial scarp bounding the northwestern channel margin of C2 (fig. S5). Realignment of this scarp with the back edge of the Qt1 terrace across the fault suggests a maximum offset of 1800 m since original cutting of C2 (fig. S5A). A similar value of 1800 m of slip realigns the southeast channel wall of Pushawalla Canyon to the west channel wall of C2 (fig. S5B). A minimum offset for C2 of 1050 m is determined by aligning the back edge of the Qt2 terrace with the west edge of the alluvial fan deposit, C2f (fig. S5C). The preferred offset reconstruction of 1200 to 1400 m simply aligns the channel walls of Pushawalla Canyon with the preserved channel walls of paleochannel C2 north and south of the fault, respectively (Fig. 4B). The preferred slip rate is calculated using this offset value, 1200 to 1400 m, and the dates from C2 and Qt2 of $74.4^{+5.1}/_{-5.2}$ ka (Fig. 2E and fig. S4).

C1 is smaller and has a narrower width than the other paleochannels (Fig. 2). The edge of C1 closest to the fault has been eroded back about 150 m from the fault by tributaries of Thousand Palms Canyon. Evidence of alluvial deposition from Pushawalla Canyon into C1 is preserved where we observed (i) a reddish younger soil on top of older mid-Quaternary light colored alluvium (fig. S2F), (ii) the form of C1, which has gently sloped channel walls that grade toward the flat channel bottom (fig. S1B), (iii) intermediate small terrace remnants that are inset into the channel walls within C1 (fig. S3), and (iv) the presence and age of a Qt1 terrace located on the upstream side of the fault that provides evidence that flow from Pushawalla Canyon likely shaped the topographic form of C1. Reconstruction of the gently sloped northwest channel wall of C1 with the 500-m-wide mouth of Pushawalla Canyon suggests between 1900 and 2300 m of slip occurred since original cutting of C1 (Fig. 4A). The preferred slip rate calculated for C1 uses this offset value of 1900 to 2300 m and the age of 87.1 ± 7.0 ka for the C1 surface (Fig. 4 and table S4). We also calculate a minimum slip rate for C1 using the maximum offset of C2 (1700 to 1800 m); the uncertainty is determined by realigning the terrace riser of C2 across the fault, which we interpret to represent the initial incision of C2 (fig. S5 and table S4). The minimum slip rate for C1 combines this 1700- to 1800-m offset of C2 with the age of the C1 surface (fig. S6B and table S4).

We calculated preferred and minimum slip rates for the Mission Creek strand over three time intervals, since 87.1 ± 7.0, $74.4^{+5.1}/_{-5.2}$, and $26.0^{+7.6}/_{-7.5}$ ka (fig. S6) based on ages of offset paleochannels and an offset alluvial fan. Projection and realignment of the channel walls of C1, C2, and C3 yield preferred offsets of 2300 to 1900 m and 1400 to 1200 m for C1 and C2, respectively (Fig. 4). The offset of each reconstruction is the midpoint value between the range of displacements, and the uncertainty of each offset is the distance from this midpoint to the maximum and minimum displacements (table S4). The calculated average slip rate applies a linear fit to the offsets and ages of all offset channels, using code provided in (*23*) and using uniform probability distributions based on maximum and minimum values for age and offset distance, and calculates the probability distribution of the fault's slip rate using Monte Carlo sampling. The

Downloaded from http://advances.sciencemag.org/ on April 1, 2021

linear average preferred slip rate on the Mission Creek strand for these three time intervals since ~95,000 years is 21.6 ± 2 mm/year (2σ) (fig. S6A). A limiting minimum slip rate of 20.7 ± 2 mm/year (2σ) is also calculated by combining the age of C1 with the maximum offset of C2 and by combining the age of the alluvial fan, C2f, with the maximum offset of C3 (fig. S6B and table S4). Slip rates of 20.7 ± 2 mm/year (2σ) provide a minimum rate for the Mission Creek strand during this time interval because aggradation of the channel floor in C1 and the C2f fan in C2 must predate or be synchronous with the incision of the west channel walls of C2 and C3, respectively (Fig. 4 and fig. S5). This minimum rate is similar to calculated estimates of 20.7 ± 3.6 mm/year, when applying ^{10}Be surface dates of the oldest clasts from each offset landform and the limiting maximum and limiting minimum offset values, demonstrating that slip rates appear to be relatively insensitive to the details of the age interpretations.

To encompass all rates for the Mission Creek strand consistent with our data, we also calculate limiting maximum and limiting minimum rates based on dextral offsets of 2500 to 1800 m, 1800 to 1050 m, and 800 to 680 m for C1, C2, and C3, respectively, which yields estimated slip rates of 22.6 ± 4 mm/year (2σ). See offset reconstruction shown in fig. S5.

Banning strand, Indio Hills

Just south of the Mission Creek strand at Pushawalla Canyon, three closely spaced traces of the Banning strand were identified and mapped at the Washington Street site (*24*). These splays vertically and horizontally offset an alluvial fan along the Indio Hills (Fig. 5). The alluvial fan, Qf3b, is sourced locally from a small catchment that delivers reworked mid-Quaternary sediment and alluvium from the Ocotillo and Palm Springs Formations (Fig. 5). The surface of the Qf3b fan is light tan in color and is hummocky with preserved but muted bar-and-swale microtopography (Fig. 5E). Cobble to gravel clasts are scattered on the surface, with 15- to 20-cm-long cobbles as the dominant clast size within bars. These clasts appear fresh, angular to subangular, and unvarnished to lightly varnished, indicating a Holocene age deposit.

The subsurface alluvium of the fan is characterized by a silty matrix with many interbedded pebble lenses. We collected six gravel samples for a ^{10}Be depth profile model age, including one from the surface on a bar and five samples from the subsurface (table S2). ^{10}Be concentrations of profile samples decrease exponentially with depth, yielding a model age of $6.1^{+2.2}/_{-2.0}$ ka for the fan surface (Fig. 5A and table S3). One sample, BF-P1-b, was not used in the model age calculation because the uncertainty of the measured ^{10}Be concentration of this sample was significantly larger (~2×) than the remaining five samples. We also applied U-Th dating to nine samples of soil carbonate clast coatings collected at two different depth intervals, from 100 to 120 cm and 160 to 190 cm (table S2). The mean of the four oldest reproducible clast-coat ages is 139.9 ± 8.1 ka. Unlike samples from the Pushawalla slip rate site on the Mission Creek strand, where U-series dates either overlapped or were younger than the ^{10}Be exposure dates, U-series dates of 139.9 ± 8.1 ka from the Qf3b deposit are significantly older than the $6.1^{+2.2}/_{-2.0}$ ka ^{10}Be

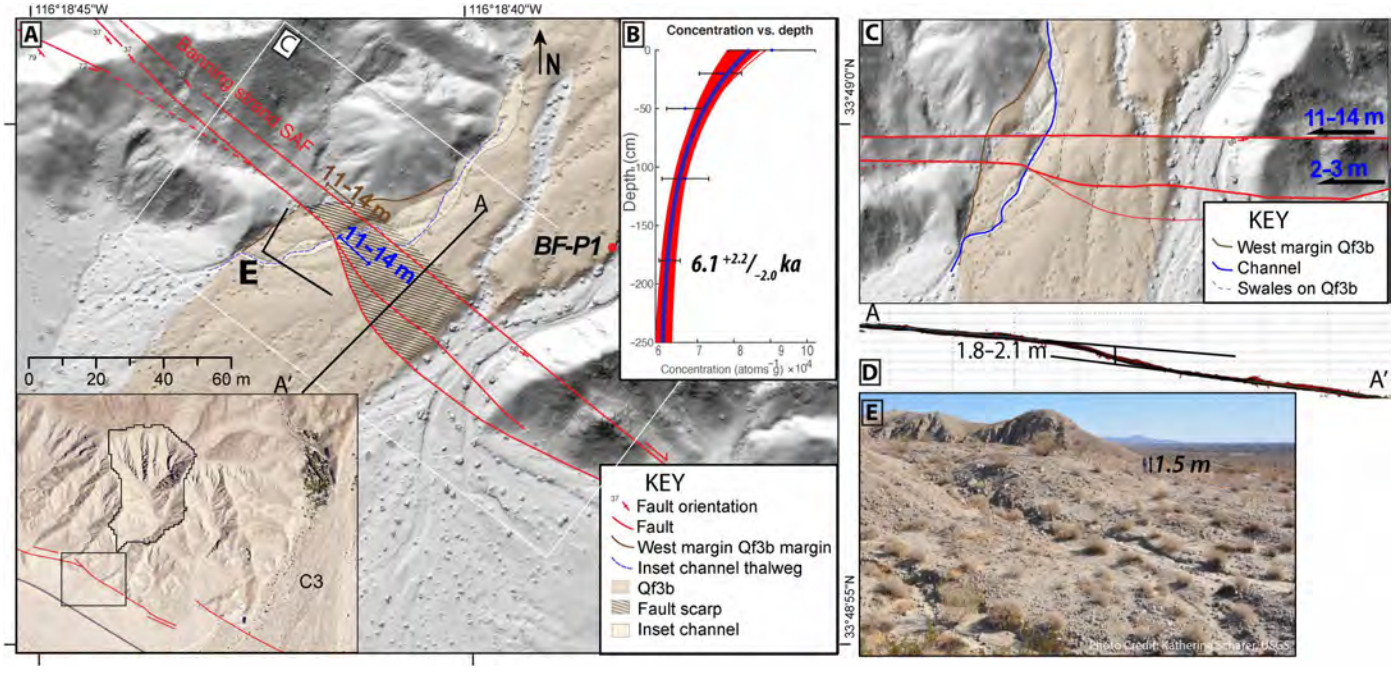

Fig. 5. Summary of Banning strand, Washington Street site in the Indio Hills showing offset landforms and ages. (**A**) Composite hillshade image on the Banning strand showing a mapped Qf3b alluvial fan offset along three splays of the fault. The red circle shows the location of the ^{10}Be depth profile and U-series samples collected from the surface and subsurface. Blue and brown offsets of 11 to 14 m are based on reconstruction of northwestern fan margin and a channel thalweg shown in (B). Image produced from data in (*24*) and (*22*). Inset map is aerial image showing the location of this site near southern end of paleochannel C3. Black line demarks drainage area of Qf3b. See Fig. 2A for location. (**B**) Modeled ^{10}Be depth profile (and associated age range) showing a decrease in ^{10}Be concentration with depth following procedures summarized in (*34*). (**C**) Reconstruction of the offset alluvial fan, aligning the edge of the fan and an incised channel thalweg (indicated by brown and blue lines, respectively). (**D**) Topographic profile A-A′ across the Qf3b fan in (A) showing vertical displacement of the fan. (**E**) Field photo of the fault scarp offsetting the Qf3b alluvial fan, with person for scale. Location shown in (A). Photo credit: Katherine Scharer, USGS.

Downloaded from http://advances.sciencemag.org/ on April 1, 2021

depth profile model age. On the basis of overall surface morphology, the relatively young appearance of the Qf3b surface, and the position of the Qf3b fan in the landscape, we interpret the $6.1^{+2.2}/_{-2.0}$ ka to best represent the age of the deposit. We interpret our results to indicate that the sampled carbonate was derived primarily from clasts reworked from older deposits, given the small catchment size and proximal source of the alluvial fan.

Observed faulting of the Qf3b alluvial fan is distributed over an ~20-m-wide zone that includes two distinct southwest-facing scarps, offsets of bars and swales, and offset of an incised channel (Fig. 5A). The northeastern-most fault splay exhibits the largest horizontal displacement of the Qf3b fan surface. A maximum horizontal offset of 14 m is measured across this splay by realigning the west edge of the Qf3b fan where it is in contact with Ocotillo Formation bedrock (brown lines in Fig. 5, A and C). A minimum offset of 11 m on the northern splay realigns the thalweg of a deflected channel that is incised into the Qf3b fan (Fig. 5C). A second, central splay of the Banning strand right-laterally offsets swales and an intervening bar by 2 to 3 m (Fig. 5, A and C). The third (southwestern) splay of the Banning strand does not exhibit measurable lateral displacement of the Qf3b surface. A topographic profile measured across all three splays indicates 1.8 to 2.1 m of vertical displacement (Fig. 5D). Combining the ^{10}Be depth profile model age of $6.1^{+2.2}/_{-2.0}$ ka with the cumulative horizontal offset of 13 to 17 m and vertical displacement of 1.8 to 2.1 m yields a Holocene lateral slip rate of 2.5 ± 1 mm/year (2σ) mm/year and vertical slip rate of $0.3^{+0.2}/_{-0.1}$ mm/year for the Banning strand at the Washington Street site.

DISCUSSION

Our new slip rate for the SAF in the Indio Hills is 24.1 ± 3 mm/year (2σ), obtained by summing rates across the Mission Creek (21.6 ± 2 mm/year) and Banning strands (2.5 ± 1 mm/year). This is similar to rates on the SAF ~125 km to the northwest at Cajon Pass (*25*) and to the high end of rates of 12 to 22 mm/year reported a few km to the south at Biskra Palms, although we note that the preferred rate of 14 to 17 mm/year at Biskra Palms is somewhat lower (Fig. 1) (*7*). A slip rate of 24.1 ± 3 mm/year is also similar to present-day geodetic slip rates at this latitude (*4*) estimated across the entire southern SAF. Our calculated slip rate represents about half of the deformation across the PA-NA plate boundary.

These results support a model in which the Mission Creek strand is the primary plate boundary fault at the latitude of our study, 33° 50′, and show that SAF surface ruptures from past and potentially future earthquakes are likely to be larger and more frequent on the Mission Creek strand in the northern Coachella Valley than currently inferred in earthquake forecasts (*1*). This emerging picture stands in contrast to previous interpretations of the SAF at this latitude.

Previous kinematic models for this region of the SAF inferred that slip rates decrease along the Mission Creek strand to a few millimeters per year northwest of Biskra Palms as the SAF bifurcates and begins to form a restraining bend near the Little San Bernardino Mountains (*7*–*11*) and, furthermore, that slip along the Mission Creek strand is transferred to the west onto the Banning strand, Garnet Hill strand, and San Gorgonio Pass fault zone and to the north onto the Eastern California Shear Zone (Fig. 1B). The inference of a marked decrease in Mission Creek strand slip was apparently supported by a slip rate of 2 to 6 mm/year proposed at Thousand Palms (*13*) and a rate of 0 to 3 mm/year estimated for the continuation of the strand to the northwest (*1*) and has been attributed to the geometric complexity of the SAF in the San Gorgonio Pass region (*9*–*10*). The Banning strand, Garnet Hill strand, and San Gorgonio Pass fault zone are therefore predicted by existing models to take up most of the lateral displacement and seismic hazard potential at this latitude. In particular, the combined Banning and Garnet Hill strands through Coachella Valley are considered to have the highest slip rate (4 to 16 mm/year) among the SAF strands in this region in recent earthquake forecasts (*1*).

Here, we question those models and contend that the majority of slip on the Mission Creek strand does not transfer westward onto the Banning strand and that the Mission Creek strand may remain active along its restraining bend near the San Bernardino Mountains. Below, we develop several considerations relevant to this possibility.

Our preferred (21.6 ± 2 mm/year) and minimum (20.7 ± 2 mm/year) slip rate estimates for the Mission Creek strand are notably faster than a slip rate of 2 to 6 mm/year just north of Pushawalla Canyon at Thousand Palms Canyon calculated in an earlier study (Fig. 1) (*13*). However, we note that the slip rate of 2 to 6 mm/year at Thousand Palms is the result of displacement from only two to three earthquakes on fault strands exposed in trenches and may not include other deformation across a broader aperture on the strand given the discontinuous nature of surface faulting expressed in the trenches (*13*). Accordingly, we conclude that this earlier study does not provide a robust long-term average for all slip on the Mission Creek strand.

On the Banning strand, our new Holocene slip rate of 2.5 ± 1 mm/year is within the range of a Holocene slip rate of 2 to 6 mm/year estimated at a location ~30 km to the northwest along this fault, as it enters the San Gorgonio Pass (Fig. 1) (*16*). Given the overlap in these two rates for the Banning strand, it is possible that the Holocene slip rate remains constant along the fault between the two sites, although an increase in as much as a factor of two along the 30-km length of the fault strand cannot be ruled out with the present data. However, our new Banning strand slip rate of 2.5 ± 1 mm/year at Indio Hills and rates of 2 to 6 mm/year (*16*) near the San Bernardino Mountains account for only a small fraction (~$^1/_5$) of total SAF slip as the fault enters the San Gorgonio Pass. These relatively slow Holocene slip rates along the Banning strand do not support a model where the majority of plate boundary motion is accommodated by this structure.

In contrast, an active Mission Creek strand from the Indio Hills to the San Bernardino Mountains is consistent with more frequent ground-rupturing earthquakes observed at the Thousand Palms paleoseismic site (average repeat time, ~215 years) than on the Banning strand or San Gorgonio Pass fault zone (average repeat times, ≥500 years) (*13*, *15*). This idea is supported by several other studies, including dynamic rupture models that show ruptures readily transfer from the Coachella section to the Mission Creek strand, but not the Banning strand (*14*); geodetic studies that include an active Mission Creek strand (*4*); and recent geologic studies that suggest mid to late Pleistocene slip rates of 10 to 30 mm/year on the Mission Creek strand near its restraining bend in the San Bernardino Mountains (Fig. 1A), based on 2.4 to 2.5 km of displacement since ~260 to 100 ka (*17*, *18*).

Previous studies (*8*, *10*–*11*, *26*) note observations of the subdued tectonic expression of offset landforms in Holocene to late Pleistocene deposits northwest of the Indio Hills to infer inactivity of the Mission Creek strand. To address the apparent paradox between previous studies and more recent data, we highlight evidence of recent active

Downloaded from http://advances.sciencemag.org/ on April 1, 2021

faulting along the Mission Creek strand based on our observations and consultant paleoseismic trenches (*27*). Just west of Mission Creek, we find ~50-m offsets of ephemeral drainages incised into late Pleistocene surfaces (*17*) and offsets of gullies in steep-walled canyons, which we infer to likely be Holocene in age (Fig. 6). Although these offsets are not yet dated, their presence on the Mission Creek strand provides evidence of more recent faulting at this latitude than previously thought. We suggest that the range in offset amounts observed and apparent ages based on regional geochronology of alluvial fan surfaces (*26*) to indicate that the Mission Creek strand is active as it enters the San Bernardino Mountains along the restraining bend of the SAF. Last, trenching investigations along the Mission Creek strand just east of Mission Creek show faulting in alluvium on some of the mapped strands, although clear expression of the faults is not present on the surface (*27*). We speculate that scarps along the Mission Creek strand are less apparent in the topography because the Mission Creek strand is closer to the range front, where streams more readily bury and erode scarps, while vertical separation across the Banning strand enhances its appearance at its more distal position.

The combination of a high slip rate on the Mission Creek strand in the Coachella Valley from the Indio Hills to possibly the southern San Bernardino Mountains and evidence of late Quaternary activity

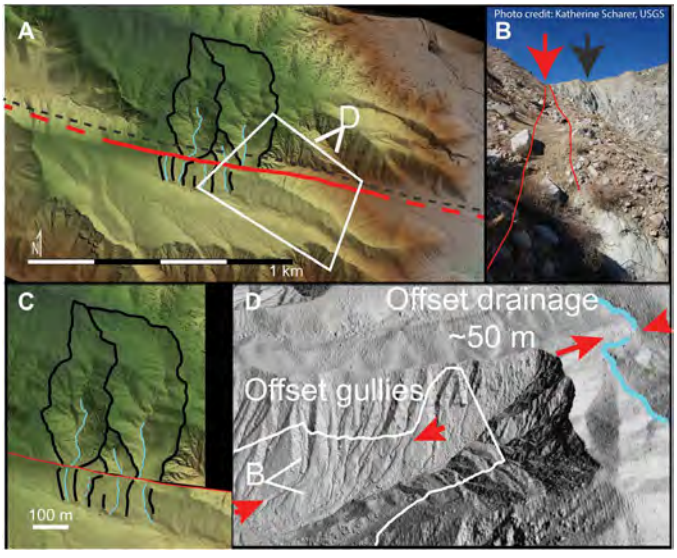

Fig. 6. Evidence of late Quaternary offsets on the Mission Creek strand west of Mission Creek (see Fig. 1A for location). (**A**) Shaded topography of area from lidar (*22*). Red line shows fault trace offsetting features; gray dashed line bounds northern edge of fault zone based on a damage zone mapped in the field. Four catchments (black lines) and thalwegs (light blue) incised into late Pleistocene (*26*) surface deposits are highlighted. (**B**) Field photograph looking northwest along recent trace. View location shown in (C). Oblique view to southwest highlights right lateral offsets of steep Holocene gullies that establish recent fault motion on the Mission Creek strand (red arrows). (**C**) Backslipping catchments by 50 to 60 m restores geometry of catchments and channel thalwegs across the Mission Creek strand (red). Note that in Fig. 1A, the Mission Creek strand has been considered inactive at this location west of Mission Creek. Black arrow marks northern extent of damage zone; note crushed rocks in lower right. Beheaded and deflected drainages and consistent right-lateral displacement in this area indicate tectonic motion. (**D**) Image is composite of lidar from (*22*) and photogrammetric model provided by K. Johnson outlined in white, scale variable but shows ~0.5 km of the fault. Processing as in (*24*). Photo credit: Katherine Scharer, USGS.

in the area of Mission Creek (Fig. 6) may shed light on the three-dimensional geometry of the SAF, where the complex tectonic history led to the appellation of the "San Gorgonio Knot" (*9*–*10*). Many workers have tried to unravel the knot with geologic (*9*, *10*) and geophysical investigations (*28*), and interpretations of the structure have varied over time (*6*). A major challenge in deciphering the subsurface geometry of the SAF near the San Gorgonio Pass is the paucity of seismicity along the major fault strands. Neither the Mission Creek nor Banning strands are illuminated by microseismicity in the upper crust, although a ~5-km step in the base of seismicity below the surface trace of the Mission Creek strand (*29*) suggests a subvertical discontinuity there. Recent seismicity in the northern Coachella Valley, such as the moderate 1986 North Palm Springs event (moment magnitude, 6.0) and its aftershocks, is generally interpreted as the down-dip expression of the Banning or Mission Creek strands (*29*). Alternatively, other studies have emphasized a major north-dipping structure tied to the Banning strand and San Gorgonio Pass fault zone and dismissed activity on an upper crustal extension of a steeply dipping Mission Creek strand (*30*). A recent study of seismic wave speeds along the Mission Creek strand supports continuity of fault structure through this region but proposes that ruptures would not traverse the full length of the strand (*31*). In combination, a fast-slipping Mission Creek strand in the Indio Hills, evidence of late Quaternary to recent offsets at Mission Creek (Fig. 6) (*17*, *18*), and recent seismic reflection studies (*21*) indicate that the geometry of the SAF at seismogenic depths is likely a hybrid of a steeply dipping, through-going Mission Creek strand and north-dipping faults associated with the Banning and Garnet Hill strands and the San Gorgonio Pass fault zone. We do not propose that the Banning strand, Garnet Hill strand, or the San Gorgonio Pass fault strands are inactive; rather, we suggest that up to half of the strain from PA-NA horizontal plate motion is accommodated by slip along the Mission Creek strand in the northern Coachella Valley. If so, then our new results and interpretations suggest that continental transform plate boundaries, such as the mature SAF, may remain relatively stable over tens of thousands of years and plate boundary deformation may migrate more slowly than suggested by existing evolution models (*10*).

It remains unclear where slip is transferred from the Mission Creek strand to the northwest into the San Bernardino Mountains. We speculate that some slip may continue along the Mission Creek and Mill Creek strands or other, unidentified fault strands to the west, and then link to the San Bernardino strand and some may be transferred onto the Eastern California Shear Zone through motion on the Pinto Mountain fault (*11*). More work is needed to constrain fault slip rates in this region and to examine the accommodation by broadly distributed or plastic deformation and uplift within the San Bernardino Mountains (*32*). While our study results may not affect existing models of shaking for the Los Angeles region modeled for ruptures along the Banning strand and San Gorgonio Pass fault zone [e.g., (*33*)], we are not aware of studies that examine the effects of rupture directivity along a more northerly route. An increased slip rate for the Mission Creek strand will likely affect fault displacement hazard estimates for major infrastructure in the area (*6*, *12*). We suggest that the Mission Creek strand may have a higher rupture likelihood than is currently estimated (*1*) and that a future SAF earthquake could link the Mission Creek strand with other faults in the San Bernardino Mountains (Fig. 1). Given the elapsed time since the ca. 1726 CE earthquake (*3*) and the high slip rates found in

Downloaded from http://advances.sciencemag.org/ on April 1, 2021

this study, 6 to 9 m of elastic strain may have accumulated on the Mission Creek strand. The Mission Creek strand transects major water and power infrastructure that serves the greater Los Angeles region but has received less attention than other faults such as the Banning strand, Garnet Hill strand, and San Gorgonio Pass fault zone in regard to earthquake effects.

METHODS

We completed field mapping of the Mission Creek and Banning strands and the Indio Hills on hillshade maps derived from lidar data (*22*) at 1:1000 scale to identify the best slip rate site for the region. Field mapping revealed multiple locations for slip rate studies. Pushawalla Canyon was selected as the main site for detailed mapping and geochronologic studies because it preserves multiple landforms offset across the fault at a single location and dateable features on both sides of the Mission Creek and Banning strands of the SAF.

Channel and terrace deposits, C1, C2, C2f, C3, Qt1, Qt2, and Qt3, were differentiated in the field based on overall geomorphologic character and the degree of weathering exhibited by surface clasts to establish relative ages of deposits. Observations made of each surface included the degree of desert pavement development, the preservation of bar-and-swale morphology, relative smoothness and texture of surface clasts, and the degree of channel dissection. Observations made of surface clasts for each deposit included the degree of grusification and fracturing, the degree of desert varnish development, and the degree of rubification on the undersides of surface clasts. Numerical ages of paleochannels, alluvial fans, and terraces were estimated by dating the uppermost alluvium preserved on each landform via ^{10}Be surface exposure dating and U-Th dating of pedogenic carbonate clast coatings.

^{10}Be surface exposure dating

Three sampling protocols were used to obtain material for ^{10}Be dating (table S1). Boulders and large cobbles were sampled by collecting chips from the top 2 cm of the largest clasts available from each surface. These samples were collected from clasts exhibiting smooth surfaces, minimal postdeposition eolian erosion, and minimal grusification. Sampled boulders were embedded into their respective surfaces, suggesting that they had remained stable since deposition. A second sampling technique involved amalgamating many pebbles and small cobbles (8 to >100 clasts) from the surface of the deposit into a single sample, thereby providing an average ^{10}Be exposure date for the landform. The third sampling technique involved collecting sand and gravel samples from the surface and subsurface for a cosmogenic depth profile. Rock types of sampled clasts include quartz-rich rocks, including quartzites, gneisses, and granitoids, such as tonalities and quartz monozonites, originating from the Little San Bernardino Mountains. All chemical and analytical processing for cosmogenic exposure ages followed the procedures described in (*34*). The ^{10}Be depth profile model age was calculated following procedures and a MATLAB code summarized in (*35*). All ^{10}Be surface exposure ages were calculated using the CRONUS Age Calculator version 3 (*36*). Ages are reported at the 2σ level.

Except for a single depth profile age, ^{10}Be dates in this study are not corrected for inheritance. This correction, which typically consists of subtracting the ^{10}Be present in samples taken from an active wash from dating samples, was not applied in this study because a previous study in the region found that these corrections for ^{10}Be inheritance yielded anomalously young exposure ages of landforms, probably because the landscape is not in steady state (*34*).

U-Th dating

Field and laboratory sampling protocols for U-Th dating of pedogenic carbonate were similar to those of (*37*). For "no-chem." samples (see table S2), solutions were aliquoted to yield fractions containing 0.1 to 0.2 mg of carbonate and analyzed via inductively coupled plasma mass spectrometer (ICP-MS). For most samples, U and Th were separated from matrix elements using anion exchange chemistry, reacted with HNO_3 and $HClO_4$ to remove residual organic material, and analyzed via ICP-MS. Samples were analyzed using both conventional and no-chem. procedures and yielded ages in good agreement (table S2).

Carbonates were analyzed using a Thermo Fisher Scientific Neptune Plus ICP-MS in solution mode using analytical protocols described in (*38*). Activity ratios and ages were calculated using the half-lives of (*39*) for ^{238}U, (*40*) for ^{232}Th, and (*41*) for ^{230}Th and ^{234}U. Correction for U and Th from detritus was made assuming activity ratios of $(^{232}Th/^{238}U) = 1.2 \pm 0.5$, $(^{230}Th/^{238}U) = 1.0 \pm 0.1$, and $(^{234}U/^{238}U) = 1.0 \pm 0.1$. Ages and uncertainties were calculated with Isoplot 3.75 (*42*). Uncertainties of corrected ages are reported at the 2σ level and include measurement errors, procedural ^{230}Th blanks, and uncertainties associated with detritus corrections but not decay constants (*43*). U-Th data and ages are reported in table S2.

Estimating final landform ages

If postdepositional erosion has not significantly modified a geomorphic surface, then ^{10}Be exposure dates should yield the maximum age of the surface when no correction is made for inheritance, as for the Mission Creek strand samples in this study. U-series dating of pedogenic carbonate, in contrast, provides minimum estimates of depositional age since pedogenic carbonate forms after deposition of host alluvium. Accordingly, where both ^{10}Be and U-Th ages are available (i.e., channel-terrace pairs C1/Qt1 and C2/Qt2, and fan C2f), we estimated ages of landforms as follows. We interpret their mean ^{10}Be exposure age (excluding outliers) as a maximum age estimate and the oldest U-Th age or ages as a minimum age estimate. Where multiple mutually consistent U-Th ages defined the oldest U-Th age (i.e., C2), we used their weighted mean age as the minimum landform age. For the remaining landforms where no U-Th ages were available, ages were inferred from bracketing ^{10}Be ages (C3/Qt3) or from a ^{10}B depth profile (Qf3). Note that detailed interpretations of the ^{10}Be and U-Th ages of each landform are given on a case-by-case basis in the "Surface characteristics and geochronology of paleochannels and associated terraces" section.

Offset and slip rate estimates

To estimate the amount of displacement on the Mission Creek strand at Pushawalla Canyon, we realigned offset features based on image reconstruction and geomorphic interpretation of progressive channel avulsion driven by dextral slip (Fig. 4 and fig. S5). Eroded remnants of Ocotillo Formation on the southwest side of the fault appear to periodically block upstream drainage and flow from Pushawalla Canyon (Fig. 4). Figure 4 shows our preferred interpretation of the long-term downcutting in response to this uplift and the avulsion of channels C1, C2, and C3 and present day Pushawalla Canyon. Figure S5 shows the maximum and minimum interpretation of the long-term downcutting in response to this uplift and the avulsion of channels C1, C2, and C3 and present day Pushawalla Canyon.

Downloaded from http://advances.sciencemag.org/ on April 1, 2021

To determine the magnitude of displacement for each beheaded paleochannel, the preserved northwestern and southeastern channel walls of C1, C2, and C3 were projected to the Mission Creek strand and aligned to Pushawalla Canyon along the fault on a composite 1-m lidar basemap in ArcMap (Fig. 4). Paleochannel walls of C1, C2, and C3 are defined by their relief and geomorphology and correlated with terrace risers within Pushawalla Canyon upstream of the fault (Figs. 1A and 2, B and D). Preferred maximum displacement values for C1 and C2 are estimated by aligning the present southeast channel wall of Pushawalla Canyon upstream of the fault with the southeast channel walls of C1 and C2 (Fig. 4). Preferred minimum displacement values for C1 and C2 align the high terrace risers along the northwest wall of Pushawalla Canyon upstream of the fault with the northwest channel walls of C1 and C2 (Figs. 2 and 4). We also estimate limiting maximum and limiting minimum offset measurements for the incision of beheaded channels C1 and C2. The limiting maximum offset measurement values align the northwest channel wall downstream of the fault to the preserved southeast channel wall of modern Pushawalla Canyon (fig. S5). The limiting minimum offset measurement for beheaded channel C1 aligns the highest terrace riser (representing capture of C2) in C2 downstream of the fault to Pushawalla Canyon upstream of the fault (fig. S5). The minimum offset measurement for beheaded channel C2 is determined by aligning the alluvial fan C2f in C2 downstream of the fault to its preserved terrace floor upstream of the fault (fig. S5).

SUPPLEMENTARY MATERIALS

Supplementary material for this article is available at http://advances.sciencemag.org/cgi/content/full/7/13/eaaz5691/DC1

REFERENCES AND NOTES

1. E. H. Field, G. P. Biasi, P. Bird, T. E. Dawson, K. R. Felzer, D. D. Jackson, K. M. Johnson, T. H. Jordan, C. Madden, A. J. Michael, K. R. Milner, M. T. Page, T. Parsons, P. M. Powers, B. E. Shaw, W. R. Thatcher, R. J. Weldon II, Y. Zeng, Long-term time-dependent probabilities for the third Uniform California Earthquake Rupture Forecast (UCERF3). *Bull. Seismol. Soc. of Am.* **105**, 511–543 (2015).
2. M. Gerstenberger, B. Fry, Preface to the focus section on the joint Japan–Taiwan–New Zealand National Seismic Hazard Model Collaboration. *Seismol. Res. Lett.* **87**, 1236–1239 (2016).
3. T. K. Rockwell, A. J. Meltzner, E. C. Haaker, Dates of the two most recent surface ruptures on the southernmost San Andreas fault recalculated by precise dating of Lake Cahuilla Dry Periods. *Bull. Seismol. Soc. Am.* **108**, 2634–2649 (2018).
4. K. A. Guns, R. A. Bennett, J. C. Spinler, S. F. McGill, New geodetic constraints on southern San Andreas fault-slip rates, San Gorgonio Pass, California. *Geosphere* **17**, 39–68 (2020).
5. J. Beyer, M. L. Cooke, S. T. Marshall, Sensitivity of deformation to activity along the Mill Creek and Mission Creek strands of the southern San Andreas fault. *Geosphere* **14**, 2296–2310 (2018).
6. R. Weldon, G. de Lamare, D. Yule, W. Hammond, A. Streig, A. Sarmiento, S. Freeman, J. Shamma, M. Beikae, A. Rodriguez, San Andreas fault – South Branch surface deformation modeling and risk to the Colorado River Aqueduct, in *Applied Geology in California*, R. Anderson, H. Ferriz, Eds. (Association of Environmental and Engineering Geologists, 2016), pp. 147–219.
7. W. M. Behr, D. H. Rood, K. E. Fletcher, N. Guzman, R. Finkel, T. C. Hanks, K. W. Hudnut, K. J. Kendrick, J. P. Platt, W. D. Sharp, R. J. Weldon, J. D. Yule, Uncertainties in slip-rate estimates for the Mission Creek strand of the southern San Andreas fault at Biskra Palms Oasis, southern California. *Geol. Soc. Amer. Bull.* **122**, 1360–1377 (2010).
8. C. R. Allen, San Andreas fault zone in San Gorgonio Pass, southern California. *Geol. Soc. Amer. Bull.* **68**, 315–350 (1957).
9. D. Yule, K. Sieh, Complexities of the San Andreas fault near San Gorgonio Pass: Implications for large earthquakes. *J. Geophys. Res.* **108**, 2548 (2003).
10. J. C. Matti, D. M. Morton, Paleogeographic evolution of the San Andreas fault in southern California: A reconstruction based on a new cross-fault correlation, in *The San Andreas Fault System: Displacement, Palinspastic Reconstruction, and Geologic Evolution*, R. E. Powell,R. E. Weldon II, J. C. Matti, Eds. (Geological Society of America, 1993), **178**, pp. 107–159.
11. K. J. Kendrick, J. C. Matti, S. A. Mahan, Late quaternary slip history of the Mill Creek strand of the San Andreas fault in San Gorgonio Pass, southern California: The role of a subsidiary left-lateral fault in strand switching. *Geol. Soc. Am. Bull.* **127**, 825–849 (2015).
12. L. M. Jones, R. L. Bernknopf, D. A. Cox, J. Goltz, K. W. Hudnut, D. S. Mileti, S. Perry, D. J. Ponti, K. A. Porter, M. S. Reichle, H. A. Seligson, K. Shoaf, J. Treiman, A. M. Wein, "The ShakeOut Scenario: Effects of a potential M7. 8 earthquake on the San Andreas fault in southern California" (USGS Open-File Report 2008-1150, California Geological Survey, 2008).
13. T. E. Fumal, M. J. Rymer, G. G. Seitz, Timing of large earthquakes since AD 800 on the Mission Creek strand of the San Andreas fault zone at Thousand Palms Oasis, near Palm Springs, California. *Bull. Seismol. Soc. Am.* **92**, 2841–2860 (2002).
14. R. Douilly, D. D. Oglesby, M. L. Cooke, J. L. Hatch, Dynamic models of earthquake rupture along branch faults of the eastern San Gorgonio Pass region in California using complex fault structure. *Geosphere* **16**, 474–489 (2020).
15. K. M. Scharer, D. Yule, A maximum rupture model for the Southern San Andreas and San Jacinto faults, California, derived from paleoseismic earthquake ages: Observations and limitations. *Geophys. Res. Lett.* **47**, e2020GL088532 (2020).
16. P. Gold, W. M. Behr, D. Rood, W. D. Sharp, T. Rockwell, K. J. Kendrick, A. Salin, Holocene Geologic slip rate on the Banning strand of the southern San Andreas fault, southern California. *J. Geophys. Res.* **120**, 5639–5663 (2015).
17. J. C. Fosdick, K. Blisniuk, Sedimentary signals of recent faulting along an old strand of the San Andreas fault, USA. *Sci. Rep.* **8**, 12132 (2018).
18. G. Balco, K. Blisniuk, A. Hidy, Chlorine-36/beryllium-10 burial dating of alluvial fan sediments associated with the Mission Creek strand of the San Andreas fault system, California, USA. *Geochronology* **1**, 10.5194/gchron-2019-2, (2019).
19. R. Heermance, D. Yule, Holocene slip rates along the San Andreas fault system in the San Gorgonio Pass and implications for large earthquakes in southern California. *J. Geophys. Res.* **44**, 5391–5400 (2017).
20. E. A. Keller, M. S. Bonkowski, R. J. Korsch, R. J. Shlemon, Tectonic geomorphology of the San Andreas fault zone in the southern Indio Hills, Coachella valley, California. *Geol. Soc. Am. Bull.* **93**, 46–56 (1982).
21. R. D. Catchings, M. J. Rymer, M. R. Goldman, G. Gandhok, San Andreas fault geometry at desert hot springs, California, and its effects on earthquake hazards and groundwater. *Bull. Seismol. Soc. Am.* **99**, 2190–2207 (2009).
22. M. Bevis, K. Hudnut, R. Sanchez, C. Toth, D. Grejner-Brzezinska, E. Kendrick, D. Caccamise, D. Raleigh, H. Zhou, S. Shan, W. Shindle, A. Yong, J. Harvey, A. Borsa, F. Ayoub, R. Shrestha, B. Carter, M. Sartori, D. Phillips, F. Coloma, "The B4 project: Scanning the San Andreas and San Jacinto fault zones" (Fall Meeting: abstract #H34B-01, American Geophysical Union, 2005).
23. R. Styron, Slip Rate Calculator, v. 0.1.2. Zenodo (2015); http://dx.doi.org/10.5281/zenodo.33360.
24. K. Johnson, E. Nissen, S. Saripalli, J. R. Arrowsmith, P. McGarey, K. Scharer, P. Williams, K. Blisniuk, Rapid mapping of ultrafine fault zone topography with structure from motion. *Geosphere* **10**, 969–986 (2014).
25. R. Weldon II, K. Sieh, Holocene rate of slip and tentative recurrence interval for large earthquakes on the San Andreas fault, Cajon Pass, southern California. *Geol. Soc. Am. Bull.* **96**, 793–812 (1985).
26. L. A. Owen, S. J. Clemmens, R. C. Finkel, H. Gray, Late Quaternary alluvial fans at the eastern end of the San Bernardino Mountains, southern California. *Quat. Sci. Rev.* **87**, 114–134 (2014).
27. Leighton and Assoc. Geologic Fault and Seismic Investigation, Mission Creek Fault, T2S, R3E, Riverside County, California, Project 6790444-05, 106 p, 2 plates (1981).
28. V. E. Langenheim, R. C. Jachens, J. C. Matti, E. Hauksson, D. M. Morton, A. Christensen, Geophysical evidence for wedging in the San Gorgonio Pass structural knot, southern San Andreas fault zone, southern California. *Geol. Soc. Am. Bull.* **117**, 1554–1572 (2005).
29. C. Nicholson, Seismic behavior of the southern San Andreas fault zone in the northern Coachella valley, California: Comparison of the 1948 and 1986 earthquake sequences. *Bull. Seismol. Soc. Am.* **86**, 1331–1349 (1996).
30. S. Carena, J. Suppe, H. Kao, Lack of continuity of the San Andreas fault in southern California: Three-dimensional fault models and earthquake scenarios. *J. Geophys. Res.* **109**, B04313 (2004).
31. P.-E. Share, Y. Ben-Zion, Bimaterial interfaces in the south San Andreas fault with opposite velocity contrasts NW and SE from San Gorgonio Pass. *Geophys. Res. Lett.* **43**, 10,680–10,687 (2016).
32. M. L. Cooke, L. C. Dair, Simulating the recent evolution of the southern big bend of the San Andreas fault, Southern California. *J. Geophys. Res.* **116**, B04405 (2011).
33. K. B. Olsen, S. M. Day, J. B. Minster, Y. Cui, A. Chourasia, M. Faerman, R. Moore, P. Maechling, T. Jordan, Strong shaking in Los Angeles expected from southern San Andreas earthquake. *Geophys. Res. Lett.* **33**, L07305 (2006).
34. K. Blisniuk, M. Oskin, K. Fletcher, T. Rockwell, W. Sharp, Assessing the reliability of U-series and ^{10}Be dating techniques on alluvial fans in the Anza Borrego Desert, California. *Quat. Geochron.* **13**, 26–41 (2012).
35. A. J. Hidy, J. C. Gosse, J. L. Pederson, J. P. Mattern, R. C. Finkel, A constrained Monte Carlo approach to modeling exposure ages of cosmogenic nuclides: An example from the Lees Ferry, Arizona. *Geochem. Geophys. Geosyst.* **11**, Q0AA10 (2010).
36. G. Balco, J. O. Stone, N. A. Lifton, T. J. Dunai, A complete and easily accessible means of calculating surface exposure ages or erosion rates from ^{10}Be and ^{26}Al measurements. *J. Quat. Geochronol.* **3**, 174–195 (2008).

Downloaded from http://advances.sciencemag.org/ on April 1, 2021

37. K. E. K. Fletcher, W. D. Sharp, K. J. Kendrick, W. M. Behr, K. W. Hudnut, T. C. Hanks, ^{230}Th/U dating of a late Pleistocene alluvial fan along the southern San Andreas fault. *Geol. Soc. Am. Bull.* **122**, 1347–1359 (2010).
38. W. D. Sharp, C. A. Tryon, E. M. Niespolo, N. D. Fylstra, A. Tripathy-Lang, J. T. Faith, ^{230}Th/U burial dating of ostrich eggshell. *Quat. Sci. Rev.* **219**, 263–276 (2019).
39. J. L. Bischoff, R. W. Williams, R. J. Rosenbauer, A. Aramburu, J. L. Arsuaga, N. García, G. Cuenca-Bescós, High-resolution U-series dates from the Sima de los Huesos hominids yields $600^{+\infty}_{-66}$ kyrs: Implications for the evolution of the early Neanderthal lineage. *J. Archaeol. Sci.* **34**, 763–770 (2007).
40. J. L. Arsuaga, N. García, G. Cuenca-Bescós, Precise measurement of half-lives and specific activities of ^{235}U and ^{238}U. *Phys. Rev.* **C4**, 1889–1906 (1971).
41. N. E. Holden, Total and spontaneous fission half-lives for uranium, plutonium, americium and curium nuclides. *Pure Appl. Chem.* **61**, 1483–1504 (1989).
42. H. Cheng, R. Lawrence Edwards, C.-C. Shen, V. J. Polyak, Y. Asmerom, J. Woodhead, J. Hellstrom, Y. Wang, X. Kong, C. Spötl, X. Wang, E. Calvin Alexander Jr., Improvements in ^{230}Th dating, ^{230}Th and ^{234}U half-life values, and U–Th isotopic measurements by multi-collector inductively coupled plasma mass spectrometry. *Ear. & Plan. Sci. Lett.* **371-372**, 82–91 (2013).
43. K. R. Ludwig, Using Isoplot/Ex, version 3.75: A geochronological toolkit for Microsoft Excel, *Berkeley Geochronology Center Special Publication 1a* (Berkeley Geochronology Center, 2010), p. 47.

Acknowledgments
Funding: Funding for this project came from the National Science Foundation Earth Science Postdoctoral Fellowship to K.B. (award #1049688), the National Earthquake Hazards Reduction Program (grant #G13AP00031) and the Southern California Earthquake Center (grant #13132). We thank U.S. Geological Survey (USGS) internal reviewers A. Cyr, D. Yule, K. Kendrick, S. Hecker, and K. Knudsen, editor K. Hodges, R. Arrowsmith, and two anonymous reviewers for thoughtful and thorough comments. R. Gold produced the photogrammetric digital elevation model (DEM) in Fig. 2 using NASA Ames Stereo Pipeline software with WorldView satellite imagery acquired under the NextView license. **Author contributions:** K.B. designed and performed the investigation, conducted the field work, collected the samples for dating, processed and analyzed the geochronologic data, and wrote the paper. K.S. conducted the field work and collected the samples. W.D.S. conducted the field work, collected the U-series samples, conducted the U-series analyses, and analyzed the geochronologic data. R.B. conducted the field work. C.A. analyzed offset data. All authors contributed to the preparation of the final manuscript. **Competing interests:** The authors declare that they have no competing interests. **Data and materials availability:** All data needed to evaluate the conclusions in the paper are present in the paper and/or the Supplementary Materials. Any use of trade, firm, or product names is for descriptive purposes only and does not imply endorsement by the U.S. government. Additional data related to this paper may be requested from the authors.

Submitted 19 September 2019
Accepted 3 February 2021
Published 24 March 2021
10.1126/sciadv.aaz5691

Citation: K. Blisniuk, K. Scharer, W. D. Sharp, R. Burgmann, C. Amos, M. Rymer, A revised position for the primary strand of the Pleistocene-Holocene San Andreas fault in southern California. *Sci. Adv.* **7**, eaaz5691 (2021).

Downloaded from http://advances.sciencemag.org/ on April 1, 2021

ScienceAdvances

A revised position for the primary strand of the Pleistocene-Holocene San Andreas fault in southern California

Kimberly Blisniuk, Katherine Scharer, Warren D. Sharp, Roland Burgmann, Colin Amos and Michael Rymer

Sci Adv **7** (13), eaaz5691.
DOI: 10.1126/sciadv.aaz5691

ARTICLE TOOLS http://advances.sciencemag.org/content/7/13/eaaz5691

SUPPLEMENTARY MATERIALS http://advances.sciencemag.org/content/suppl/2021/03/22/7.13.eaaz5691.DC1

REFERENCES This article cites 35 articles, 11 of which you can access for free
http://advances.sciencemag.org/content/7/13/eaaz5691#BIBL

PERMISSIONS http://www.sciencemag.org/help/reprints-and-permissions

Use of this article is subject to the Terms of Service

Science Advances (ISSN 2375-2548) is published by the American Association for the Advancement of Science, 1200 New York Avenue NW, Washington, DC 20005. The title *Science Advances* is a registered trademark of AAAS.

Copyright © 2021 The Authors, some rights reserved; exclusive licensee American Association for the Advancement of Science. No claim to original U.S. Government Works. Distributed under a Creative Commons Attribution NonCommercial License 4.0 (CC BY-NC).

Downloaded from http://advances.sciencemag.org/ on April 1, 2021

Downloaded from gsabulletin.gsapubs.org on July 6, 2010

Geological Society of America Bulletin

Uncertainties in slip-rate estimates for the Mission Creek strand of the southern San Andreas fault at Biskra Palms Oasis, southern California

W.M. Behr, D.H. Rood, K.E. Fletcher, N. Guzman, R. Finkel, T.C. Hanks, K.W. Hudnut, K.J. Kendrick, J.P. Platt, W.D. Sharp, R.J. Weldon and J.D. Yule

Geological Society of America Bulletin 2010;122;1360-1377
doi: 10.1130/B30020.1

Email alerting services click www.gsapubs.org/cgi/alerts to receive free e-mail alerts when new articles cite this article

Subscribe click www.gsapubs.org/subscriptions/ to subscribe to Geological Society of America Bulletin

Permission request click http://www.geosociety.org/pubs/copyrt.htm#gsa to contact GSA

Copyright not claimed on content prepared wholly by U.S. government employees within scope of their employment. Individual scientists are hereby granted permission, without fees or further requests to GSA, to use a single figure, a single table, and/or a brief paragraph of text in subsequent works and to make unlimited copies of items in GSA's journals for noncommercial use in classrooms to further education and science. This file may not be posted to any Web site, but authors may post the abstracts only of their articles on their own or their organization's Web site providing the posting includes a reference to the article's full citation. GSA provides this and other forums for the presentation of diverse opinions and positions by scientists worldwide, regardless of their race, citizenship, gender, religion, or political viewpoint. Opinions presented in this publication do not reflect official positions of the Society.

Notes

© 2010 Geological Society of America

THE GEOLOGICAL SOCIETY OF AMERICA

Downloaded from gsabulletin.gsapubs.org on July 6, 2010

Uncertainties in slip-rate estimates for the Mission Creek strand of the southern San Andreas fault at Biskra Palms Oasis, southern California

W.M. Behr[1,†], D.H. Rood[2], K.E. Fletcher[3], N. Guzman[4], R. Finkel[2], T.C. Hanks[5], K.W. Hudnut[6], K.J. Kendrick[6], J.P. Platt[1], W.D. Sharp[7], R.J. Weldon[8], and J.D. Yule[4]

[1]*Department of Earth Sciences, University of Southern California, Los Angeles, California 90089, USA*
[2]*Center for Accelerator Mass Spectrometry, Lawrence Livermore National Laboratory, Livermore, California 94550, USA*
[3]*Department of Earth and Planetary Science, University of California, 307 McCone Hall, Berkeley, California 94720-4767, USA*
[4]*Department of Earth Sciences, California State University, 18111 Nordhoff Street, Northridge, California 91330, USA*
[5]*U.S. Geological Survey, 345 Middlefield Road, Menlo Park, California 94025, USA*
[6]*U.S. Geological Survey, 525 South Wilson Avenue, Pasadena, California 91106, USA*
[7]*Berkeley Geochronology Center, 2455 Ridge Road, Berkeley, California 94709, USA*
[8]*Department of Geological Sciences, 1272 University of Oregon, Eugene, Oregon 97403, USA*

ABSTRACT

This study focuses on uncertainties in estimates of the geologic slip rate along the Mission Creek strand of the southern San Andreas fault where it offsets an alluvial fan (T2) at Biskra Palms Oasis in southern California. We provide new estimates of the amount of fault offset of the T2 fan based on trench excavations and new cosmogenic ^{10}Be age determinations from the tops of 12 boulders on the fan surface. We present three alternative fan offset models: a minimum, a maximum, and a preferred offset of 660 m, 980 m, and 770 m, respectively. We assign an age of between 45 and 54 ka to the T2 fan from the ^{10}Be data, which is significantly older than previously reported but is consistent with both the degree of soil development associated with this surface, and with ages from U-series geochronology on pedogenic carbonate from T2, described in a companion paper by Fletcher et al. (this volume). These new constraints suggest a range of slip rates between ~12 and 22 mm/yr with a preferred estimate of ~14–17 mm/yr for the Mission Creek strand of the southern San Andreas fault. Previous studies suggested that the geologic and geodetic slip-rate estimates at Biskra Palms differed. We find, however, that considerable uncertainty affects both the geologic and geodetic slip-rate estimates, such that if a real discrepancy between these rates exists for the southern San Andreas fault at Biskra Palms, it cannot be demonstrated with available data.

[†]E-mail: behr@usc.edu

INTRODUCTION

This study builds upon a long history of estimating the geologic slip rate of the Coachella Valley segment of the southern San Andreas fault where it offsets an alluvial fan at Biskra Palms Oasis, California (Fig. 1) (Keller et al., 1982; Dorsey, 2003; van der Woerd et al., 2006). Keller et al. (1982) first used displaced fan remnants at Biskra Palms to propose a late Quaternary mean slip rate of 23–35 mm/yr, a rate that for more than two decades remained the benchmark for long-term geologic slip on the southern San Andreas fault. Because of increasing interest in late Quaternary strain budgets and seismic hazard evaluation for the southern San Andreas fault zone, the Biskra Palms site has been recently reevaluated, leading to conflicting interpretations of both the amount of offset and the age of the fan, and to apparent discrepancies of up to 10 mm/yr between geologic and geodetic slip rates for this region (Dorsey, 2003; van der Woerd et al., 2006).

We continue this reevaluation and complement existing geologic and geochronologic data with new estimates of the amount of offset based on new trench excavations and new age determinations for the T2 fan. This unusually complete and diverse data set allows us to focus on the uncertainties in the geologic slip rate at this important location on the Coachella Valley segment of the southern San Andreas fault. Rather than choosing a single estimate of fault offset, for example, we present three alternative offsets. We also consider different surface-exposure–age sampling strategies, which provide different ages of the offset fan surface, and we compare these results to those obtained from U-series age determinations of pedogenic carbonate developed in the deposits of this fan, described in a companion paper by Fletcher et al. (this volume). The different offsets and ages we consider here lead to a wide range of permissible geologic slip rates for the Coachella Valley segment of the southern San Andreas fault at Biskra Palms, 12–22 mm/yr.

This study also revisits the "slip-rate discrepancy" at Biskra Palms, as it is thus far the only site on the southern San Andreas fault where a long-term (millennial) slip-rate estimate can be obtained and compared to short-term (decadal) slip-rate estimates from geodesy. Recent comparisons of slip-rate data worldwide have highlighted discrepancies between long-term and short-term slip-rate estimates. The best-known examples are for the great strike-slip faults of Tibet, where geologic slip-rate estimates are commonly greater than those inferred from geodetic data (Meriaux et al., 2004, Meriaux et al., 2005; Thatcher, 2007). These discrepancies, if common for active crustal faults, have profound implications for how the crust accumulates and releases elastic strain and potentially for seismic clustering and seismic hazard (Peltzer et al., 2001; Dolan et al., 2007; Oskin et al., 2008). In many instances, however, a more fundamental question is whether these slip-rate discrepancies are real, given the uncertainties in geodetic modeling choices and capabilities and in the offsets and ages from which geologic slip rates are calculated. On the Altyn Tagh fault, for instance, considerable concern has recently arisen as to whether the slip-rate discrepancy of ~15 mm/yr is more a function of uncertainties in the geologic data rather than temporal variations in slip rate (e.g., England and Molnar, 1997; Brown

GSA Bulletin; September/October 2010; v. 122; no. 9/10; p. 1360–1377; doi: 10.1130/B30020.1; 15 figures; 3 tables.

For permission to copy, contact editing@geosociety.org
© 2010 Geological Society of America

Downloaded from gsabulletin.gsapubs.org on July 6, 2010

et al., 2005; Hanks and Thatcher, 2006; Cowgill, 2006; Thatcher, 2007). In general, answers to this question are beyond the scope of this paper, for each slip-rate discrepancy must be considered on a case-by-case basis. We argue in this paper, however, that considering the uncertainties in the presently available data, geologic and geodetic slip rates in the Coachella Valley overlap within error and any case for a slip-rate discrepancy is unsubstantiated.

REGIONAL GEOLOGY

The southern San Andreas fault zone in the Coachella Valley displays considerable complexity, and we therefore use the following nomenclature throughout this paper. The terms *segment*, *strand*, and *splay* are used in a hierarchical fashion, with *segment* representing a regional domain of San Andreas–related fault *strands* that themselves may be split into two or more fault *splays*. We refer to the entire San Andreas fault zone in the Coachella Valley as the Coachella Valley segment and to the various strands that compose it according to previously used classifications that are cited accordingly.

The Biskra Palms alluvial fan is situated within the Indio Hills where the relatively simple, northwest-striking Indio strand of the Coachella Valley segment of the southern San Andreas fault splits into the Mission Creek strand and the more westward-striking Banning strand (Fig. 1) (Allen, 1957; Dibblee, 1964, 1967). Of these, the Mission Creek strand is the longest lived and has large dextral displacement, nearly 160 km (Matti and Morton, 1993). The Banning strand has only a few kilometers of dextral displacement, appears to be no older than late Quaternary, and clearly has absorbed right slip that has stepped left (west) from the Mission Creek strand (Matti and Morton, 1993). The Indio Hills formed within the stepover zone, suggesting that the Banning strand has a significant dip-slip component, which it may have if it roots into the Mission Creek strand (Fig. 2). The Indio Hills are bounded on the north by the dextral-reverse Indio Hills fault (Fig. 2) (Rymer, 1989).

Northwest of the Indio Hills, the Banning strand continues toward the San Gorgonio Pass region, where it interacts with the San Gorgonio Pass fault zone (Matti et al., 1985; Matti and Morton, 1993; Yule and Sieh, 2003). The Mission Creek strand continues northwest from Biskra Palms toward the southeastern San Bernardino Mountains (Fig. 2). It loses surface expression beneath Quaternary alluvial deposits in Morongo Wash and is inactive beyond Desert Hot Springs (Matti and Morton, 1993). As discussed by van der Woerd et al. (2006), the geomorphology at Biskra Palms suggests that the Mission Creek strand is the most active fault, where it is locally split into two splays, which we refer to as the NE and SW fault splays.

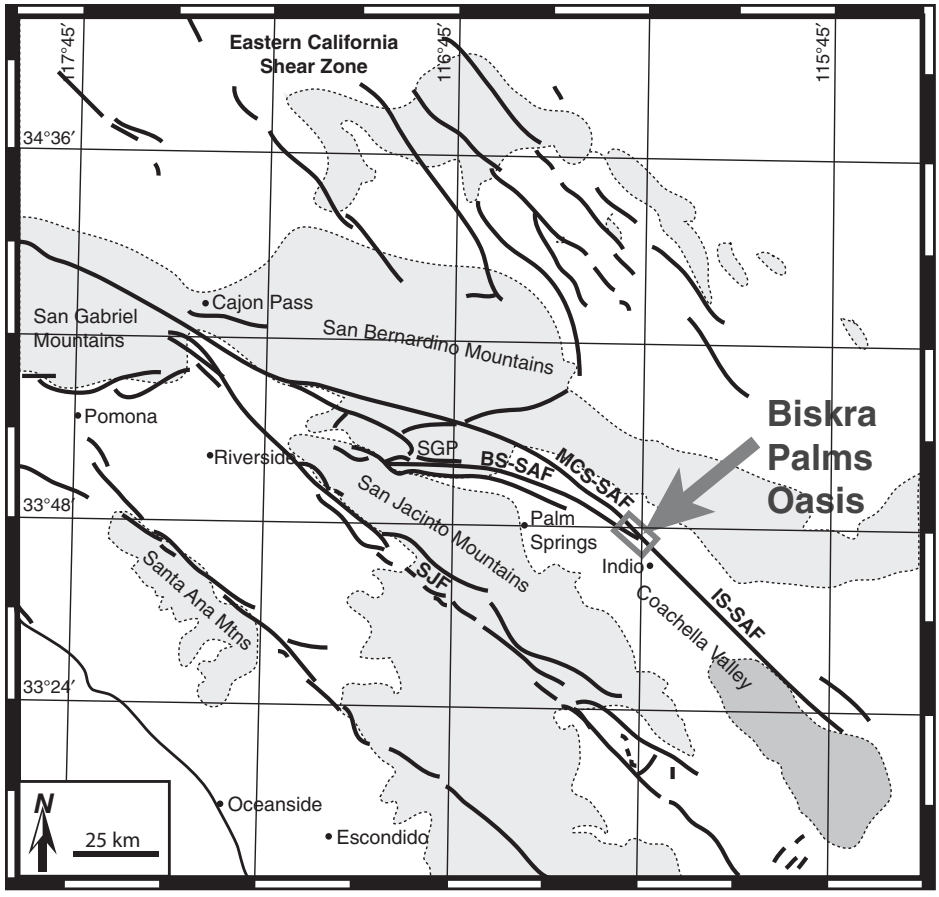

Figure 1. Schematic map of southern California showing the major faults of the San Andreas fault system (in red) and regions of high relief (in gray). Blue box shows the location of Figure 2. SGP—San Gorgonio Pass; BS-SAF—Banning strand San Andreas fault; MCS-SAF—Mission Creek strand San Andreas fault; IS-SAF—Indio strand San Andreas fault; SJF—San Jacinto fault.

The Indio Hills consist of deformed Pleistocene sedimentary rocks of the nonmarine, fluviodeltaic Palm Spring Formation and Quaternary conglomerates of the fluvial Ocotillo Formation (Dibblee, 1954; Proctor, 1968). The catchment in which the Biskra Palms fan was deposited originates at the crest of the Indio Hills and extends to the south where it is presently deflected slightly eastward by operations in a gravel quarry. The drainage erodes through local bedrock of the Palm Spring Formation, which here includes siltstone, sandstone, and conglomerate.

ALLUVIAL FAN DEPOSITS

For the following discussion of features and structures at the Biskra Palms site, we have, for the most part, adopted the terminology used by van der Woerd et al. (2006) for ease of comparison to previous work. This terminology includes four separate alluvial fan remnants labeled T0 (youngest) through T3 (oldest) (Fig. 3), which represent sequential episodes of fan deposition through time.

T0 refers to the floor of the modern active channel, which has eroded through bedrock of the Palm Spring Formation on the east, and through older alluvial deposits on the west.

The T1 fan remnant has been quarried away within the past 15 years, but it was mapped by van der Woerd et al. (2006) using 1969 aerial photograph stereo pairs. It was topographically higher than T0 and less incised than T2 (van der Woerd et al., 2006).

T2 is the well-defined fan remnant that has been offset by two splays of the Mission Creek fault strand (Fig. 3). Following van der Woerd et al. (2006), we refer to the lowermost, downstream portion of T2 as T2d, the intermediate portion between the two fault strands as T2i, and

Downloaded from gsabulletin.gsapubs.org on July 6, 2010

Figure 2. Annotated satellite image from Google Earth of the southeastern Indio Hills showing faults (black) and major drainages (white) that are visible on the image and in the field (faults are dashed where inferred). Box shows location of Figure 3. Original base image is U.S. Department of Agriculture digital aerial photography.

the upstream portion as T2u (Fig. 4). A considerable part of the T2d section of the fan has been quarried away, to a depth of ~80 m. The entire T2 fan, including the intermediate and upstream portions, is scheduled to be quarried over the next decade.

The surface of the T2 fan remnant throughout its extent consists of numerous clasts ranging in size from pebbles to boulders (Fig. 5). Major clast compositions include, in decreasing order of abundance based on a clast count, medium-grained biotite tonalite, biotite granodiorite, mafic migmatitic gneiss, pegmatitic granite, equigranular granite, and quartzite. Overall, clasts with granitoid compositions are the most abundant, and the majority of boulders are composed of this lithology. The T2 fan surface also has some isolated patches of moderately well developed desert pavement, which is best developed where pebble-size clasts are concentrated (Fig. 5B). In other areas with more variable clast sizes, there is a crude pavement formation.

At the start of this research, T2d (Fig. 4A) was the most distinctive section of the T2 fan, but in November 2007, this part of the fan surface was leveled in preparation for quarrying. Fortunately, much of our mapping, sample collection, and soil descriptions were performed before the surface was destroyed, and high-resolution light detection and ranging (LiDAR) data acquired by the B4 project provided a high-resolution image of the original morphology (Bevis et al., 2005; Shan et al., 2007). Prior to quarrying, the T2d fan surface was incised by several prominent longitudinal gullies that were either (1) fluvial and/or debris flow channels relict from the aggradation of sediment underlying the T2 fan surface, or (2) arroyos incised into the T2 surface during later erosional episodes. Several of these gullies had gently curved walls and desert varnished boulders at their bases, suggesting they were older, relict features, whereas others had steep-sided walls and were filled with fresh clasts and plant debris indicating they were active washes. These active washes were fed by groundwater that ponds behind the SE splay of the Mission Creek fault strand and breaches the surface during flash floods.

The T2i section of the fan (Fig. 4B) is somewhat less well preserved than the former fan remnant, T2d, as a result of faulting and warping, but is still easily recognizable. It has some subtle swales that are difficult to differentiate from morphology associated with abundant small-scale extensional faults and fractures present on its eastern extent (Fig. 3). One prominent paleochannel cuts this section of the fan from northeast to southwest (labeled C in Fig. 3).

The T2u section of the fan (Fig. 4C) also has some 0.2- to 0.5-m-deep swales but has been modified in some places by roads and drill pads. At the northern tip of T2u, the fan surface is relatively flat, and several large boulders of the associated deposit are preserved at the surface. The western edge of the modern channel is incised into the head of T2u forming a terrace riser up to 4 m in height.

There is a distinctive difference in orientation between the northward-trending, main drainage that forms the headwaters for the T2 fan, and the northeast-trending, modified channel remnants preserved on the T2d section of the fan, indicating that the original axial crest and fan structure curved toward the southwest. Some channel remnants on T2i, although significantly modified by faulting and warping, also show a gradual change in trend and overall curvature toward the southwest. Curved axial crests on alluvial fans are not uncommon in the Coachella valley, and some active examples can be seen in the Indio Hills northwest and southeast of Biskra Palms.

The characteristics of the intermediate T3 fan remnant (T3i) are noticeably different than the adjacent T2i remnant (Fig. 3). The surface of T3i is undulating, in contrast to the relatively planar surface of T2i. T3i also has clasts that display a greater degree of desert varnish, has several grussified granitoid boulders that protrude less than 0.15 m above the surface, and has numerous boulder and cobble-size clasts that are stacked on top of each other in isolated piles, rather than embedded within the finer grained matrix. All of these observations suggest that T3i displays a greater degree of surface degradation than the T2 fan remnants.

Soils have been described on fan remnants T2u, T2i, and T2l (after the methodology and terminology of Soil Survey Staff, 1951, 1999; Birkeland, 1999; refer to pedons A through E in Fletcher et al., this volume, for complete descriptions). The degree of soil development provides additional understanding of the character and magnitude of surficial modification since the time of stability of the T2 fan surface. Pedogenesis in this area is characterized by reddening, accumulation of $CaCO_3$, and eolian influx. The soils associated with T2 surfaces attain maximum colors of brown to light yellowish brown (10YR5/3-6/4). Soils developed on the western edge of T2 have brighter and redder colors (7.5YR hues) and contain clay films along pedon faces and within pores. Calcium carbonate accumulation reaches maximum development at depths of 1–1.5 m in the soil profile, and there are no abrupt transitions that would indicate a complex pedogenic and depositional history. Rather, the steady and gradual increase in $CaCO_3$ with depth suggests that the soil has experienced a climatic shift since stabilization of the surface, but not burial by younger deposition. Very thin Av horizons and variable Bw and Bt horizon thicknesses indicate that the fan has experienced variable amounts of surface lowering since stabilization, with up to ~1 m of erosion in some areas (refer to pedons D and E in Fletcher et al., this volume). In general, the soils are comparable with previously described soils of similar age (Reheis et al., 1989; McDonald, 1994; McDonald et al., 1996).

STRUCTURES AND LOCAL KINEMATICS

We used field observations, high-resolution LiDAR data from the B4 data set (Bevis et al., 2005), Google Earth base imagery, and aerial photographs to produce the geologic map shown in Figure 3. We also excavated several trenches that helped constrain the locations of subsidiary

Downloaded from gsabulletin.gsapubs.org on July 6, 2010

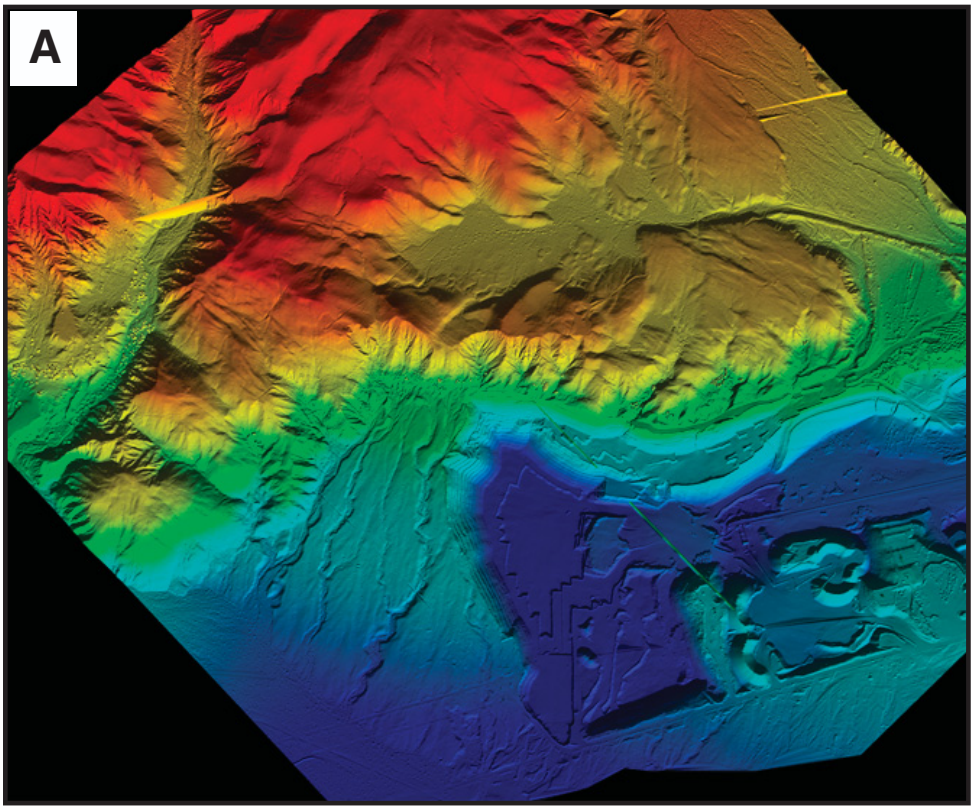

Figure 3. (A) One-meter–resolution, light detection and ranging (LiDAR) digital elevation model (DEM) of the Biskra Palms site at the time of acquisition of the B4 data, color-shaded by elevation, at same scale and orientation as in (B). (B) Quaternary geologic map of the Biskra Palms offset alluvial fan (T2, in blue) superimposed on a combined 1-m–resolution LiDAR DEM image from the B4 data set and a 1969 low-sun–angle aerial photograph. The two images are merged together to show the original geomorphology of the fan complex and surroundings prior to quarrying. The triple-black line shows the extent of the quarry pit as of the time of acquisition of the B4 data set. Currently, the T2d section of the fan is no longer preserved, and the quarry pit is considerably larger. Teeth on faults are on upper plate.

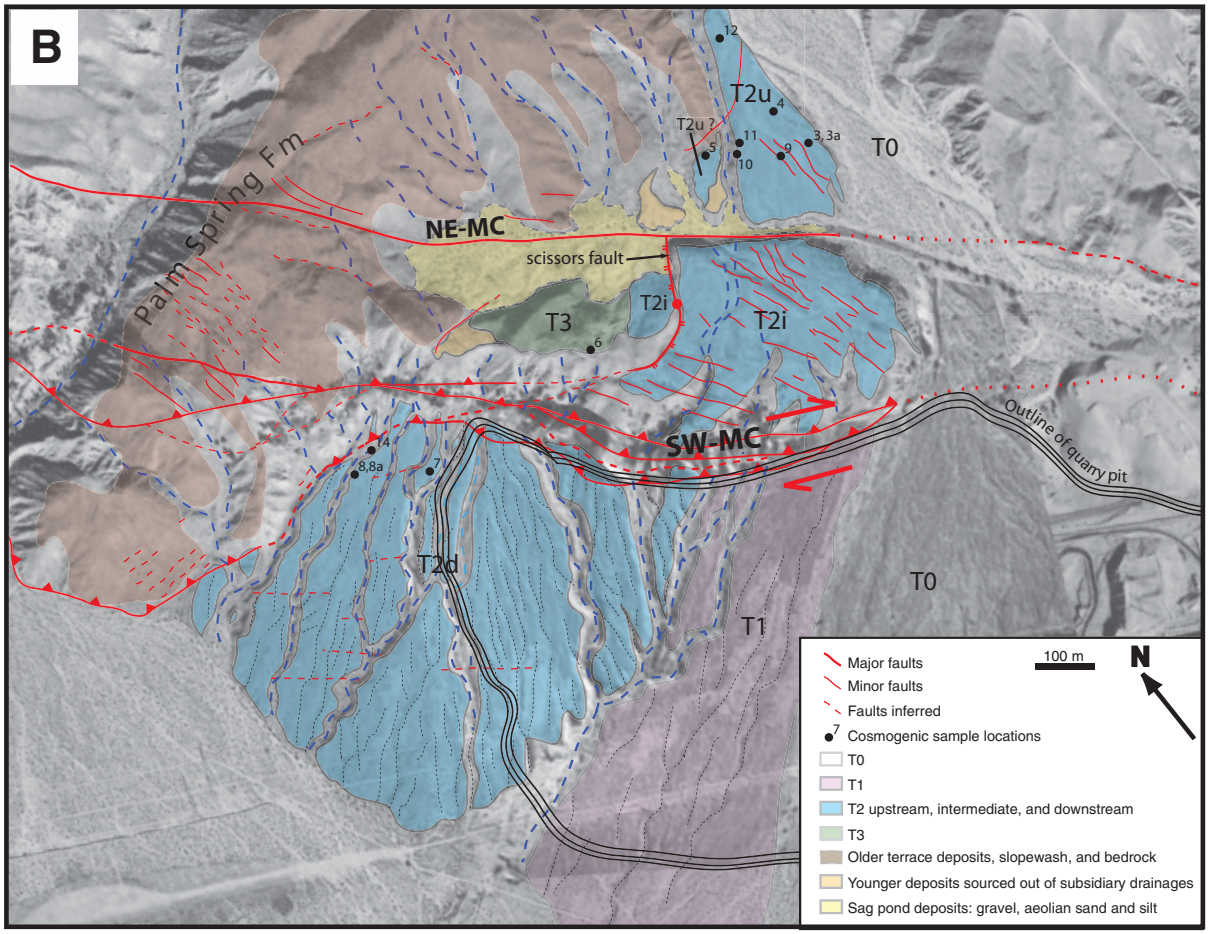

Downloaded from gsabulletin.gsapubs.org on July 6, 2010

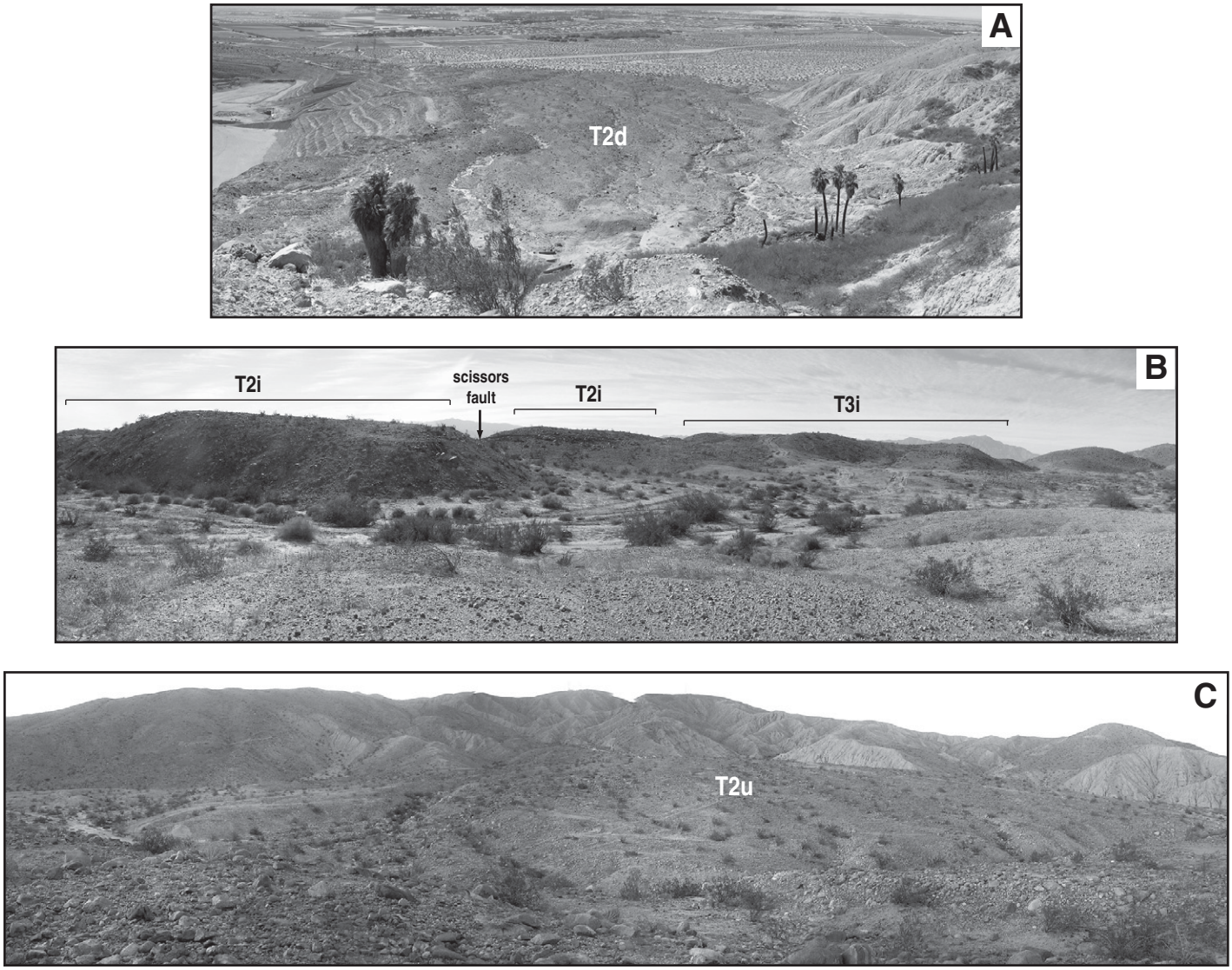

Figure 4. Photographs of all three fault-separated remnants of the T2 fan. (A) T2d looking toward the southwest. Palm trees delineate the main trace of the Mission Creek fault. (B) T2i and T3i looking toward the southwest. T2i remnant is offset by a steep scissors fault. See text for details. (C) T2u looking toward the northeast.

faults that deform the T2 fan as well as rule out the presence of faulting on some ambiguous geomorphic features. A total of 11 trenches were excavated with a track hoe; six were pit trenches used for soil descriptions and sampling for geochronology. Five of the trenches are specifically relevant to the fault offset and general interpretation of the T2 fan; these are discussed below (Fig. 6).

Splays of the Mission Creek Fault Strand

Figure 3 illustrates the complex faulting at the Biskra Palms site. The Mission Creek strand consists of two subparallel fault splays, here referred to as the NE and SW splays. As described by previous workers, the NE splay appears to have accommodated primarily dextral strike-slip motion, whereas the SW splay has a reverse-slip component that has formed the prominent, 50-m-high scarp visible in Figures 3 and 4 (Keller et al., 1982; van der Woerd et al., 2006). Northwest of Biskra Palms, the NE splay immediately loses surface expression within Holocene fluvial deposits and presumably merges with the SW fault splay or dies out (Fig. 3), whereas the SW splay is the main trace of the Mission Creek strand and can be traced continuously northwest from Biskra Palms to Thousand Palms Oasis (Fig. 2).

The SW splay and several associated anastomosing faults function as a groundwater barrier, and are delineated along the steeply dipping fault scarp by rows and clusters of palm trees (Fig. 3). Immediately northwest of the T2d segment of the fan, the SW splay, marked by vegetation lineaments, forms a broad "v" across the ridgeline (northwest corner of Fig. 3, colored as Palm Spring Formation) and into the adjacent catchment, suggesting that the fault dips moderately toward the northeast. Several additional color and vegetation lineaments trending approximately N-S traverse this ridgeline uphill from the main fault trace and appear to be traces of minor faults and fractures. Minor faults associated with the SW splay, identified by subtle vegetation lineaments and small escarpments, branch off at a slightly more easterly trend, but

Downloaded from gsabulletin.gsapubs.org on July 6, 2010

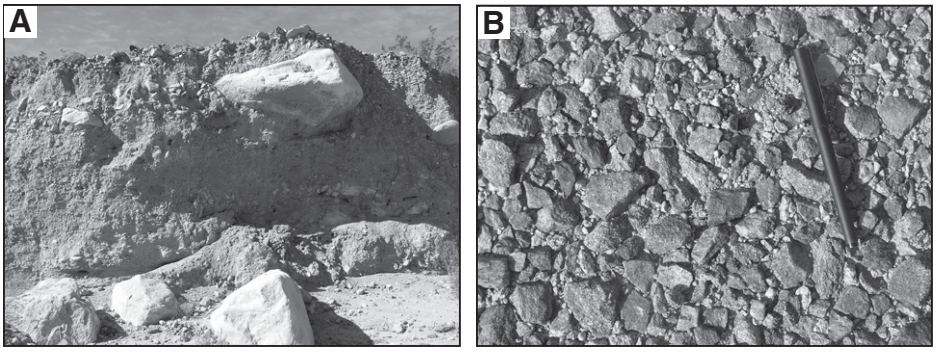

Figure 5. Detailed photographs of the T2 alluvial fan. (A) The T2u section of the fan in cross section where exposed in the active wash. (B) Varnished cobbles of the T2u section of the fan showing a moderate degree of pavement development.

do not appear to be continuous, and therefore are likely not significant in accommodating slip.

The NE fault splay is delineated by rows of small bushes where it crosses some younger fluvial deposits, and by lineaments in the hillslopes northwest of the T2 fan. As discussed in a later section, displacement along the NE splay since deposition of the T2 fan may be negligible in comparison to the SW splay, and in general it appears to be a subsidiary structure of little regional significance. Another curvilinear fault trace trending generally E-W has vertically offset the head of the T2u fan remnant by ~1 m, but otherwise T2u appears undeformed.

Between the NE and SW splays of the Mission Creek fault strand, two opposite-facing escarpments represent the trace of a subvertical "scissors" fault that intersects the NE splay at a high angle (Fig. 3). We investigated this feature by trenching because van der Woerd et al. (2006) had interpreted one of the escarpments that defines it as a delta foreset deposit and the other as a terrace riser and used it to reconstruct fault offset. Trench E1 (Fig. 6) was excavated across the northeastern scarp and revealed this fault crosscutting the T2i fan remnant (Fig. 7). The relationship between this scissors fault and the SW fault splay is unclear, but the scissors fault appears to curve significantly and merge with a minor thrust splay, in which case we interpret the scissors fault to be a vertical tear in the edge of a thrust ramp. Regardless of the geometry at depth, this structure clearly separates pieces of the T2i segment of the fan that have been differentially tilted. Southeast of the scissors fault, the T2i fan surface is clearly defined but has been uplifted ~10 m, tilted toward the southwest, and broadly warped. It is also cut by north-south–striking, minor normal faults that are likely related to flexural slip during warping. The other distinct fragment of T2i, northwest of the scissors fault, dips ~22° toward the northeast, and in Trench E1b, can be traced into the subsurface beneath northeast-dipping eolian sand and silt beds, and fluvial deposits with bedding that shallows upward toward the surface (labeled FD in Fig. 7).

Splays of the Banning Fault

The exact location of the intersection between the Mission Creek and Banning fault strands has not been previously documented. For several kilometers northwest of Biskra Palms, a linear series of escarpments traverse the southwestern foot of the Indio Hills, and several appear to be associated with offset Holocene alluvium; we interpret these to represent the trace of the Banning fault (Fig. 2). Immediately west of the T2d fan remnant several escarpments are also present, some of which are associated with right-lateral offset of local drainages (see star in Fig. 6). Van der Woerd et al. (2006) recognized these escarpments at Biskra Palms and mapped some of them as the trace of the Banning fault strand, but did not consider them to override the

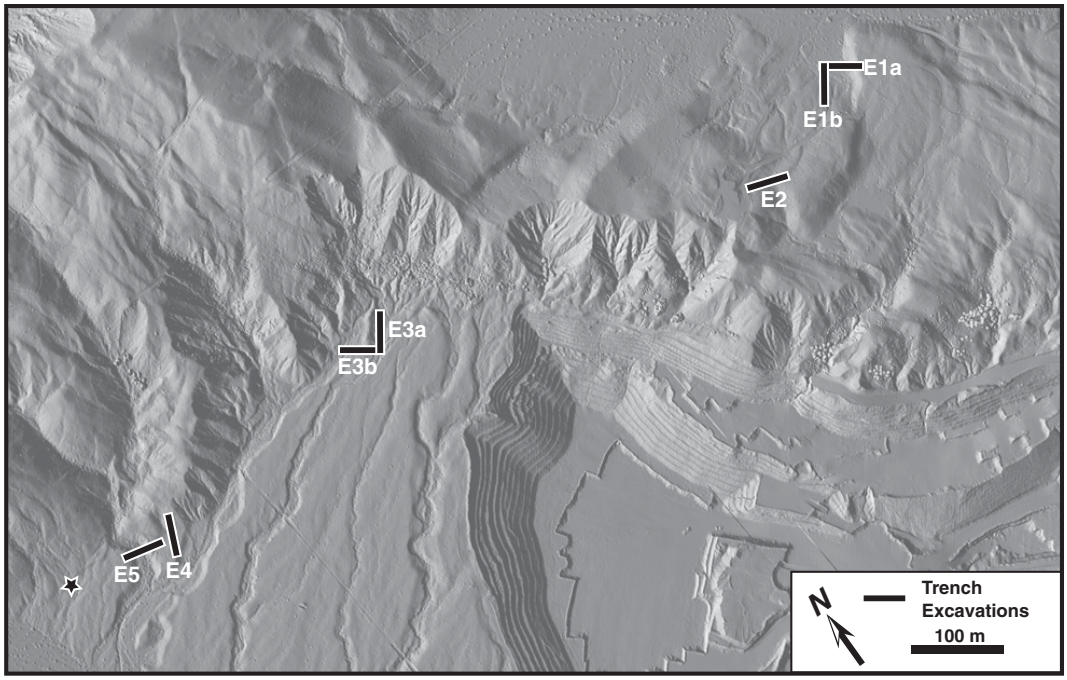

Figure 6. Locations of trench excavations pertinent to reconstructing the original extent of the T2 fan. The black star marks the location of some small gullies that are right-laterally offset by the Banning fault. Digital elevation model (DEM) is from the B4 light detection and ranging (LiDAR) data set.

Downloaded from gsabulletin.gsapubs.org on July 6, 2010

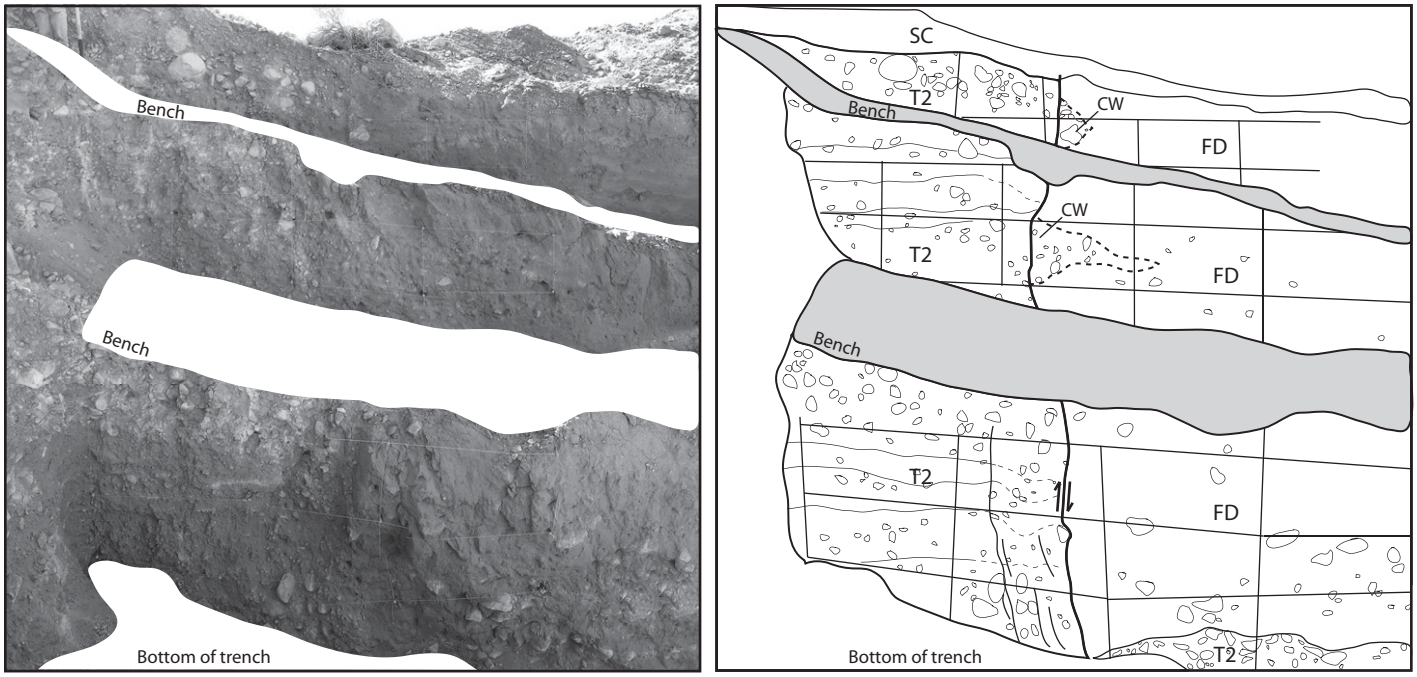

Figure 7. Photomosaic and trench log of SW wall of trench E1a where the subvertical scissors fault is exposed. Grid spacing is 1 m in the horizontal and 0.5 m in the vertical direction. The scissors fault is subvertical and offsets the T2 fan by ~10 m at this location, forming the prominent escarpment that this trench is carved into (shown in Fig. 6). The top of T2 on the downthrown side of the fault in this figure can be traced continuously out of trench E1b to the surface, where it is preserved as a planar fan surface dipping ~N 22° E. Within the trench, the down-thrown part of T2 is covered by eolian and fluvial fill deposits (FD) that are mostly poorly consolidated and massive sands and silts. Some small colluvial wedges (CW) with coarser material sourced from the upthrown side of this structure have formed adjacent to the fault. T2 on the upthrown side of the fault is well bedded and consists primarily of pebbly sands and conglomerates.

western edge of the T2 fan. Trenches E3, E4, and E5 were excavated across several of these escarpments, and each revealed a low-angle (0°–15°) structure juxtaposing bedrock of the Palm Spring Formation over gravels of the T2 fan (Fig. 8).

This low-angle structure can be interpreted as either the toe of a landslide, or the tip of a propagating thrust fault, namely the Banning fault. While we cannot rule out either possibility, our preferred interpretation is that this structure is the tip of the Banning fault, based on several observations.

The first of these observations is that a 0.25 m, steeply dipping escarpment just to the west of trench E5 projects along strike into the low-angle structure preserved in the trenches and is associated with offsets of several small streams and gullies in a right-lateral sense (labeled with a star on Fig. 6). This landform is consistent with oblique-slip faulting but more difficult to reconcile as a feature associated with a landslide.

A second observation is that lineations on the slip plane, revealed in trench E4, are oriented toward the south or southeast, oblique to the dip direction of the slip plane, which is consistent with a component of right-lateral motion but inconsistent with down-slope motion.

Additionally, where this low-angle structure is exposed in trench E4, it overrides some young, unconsolidated sands, and therefore appears to be an active structure. If it is an active landslide, however, we would expect to find a fresh and active headscarp uphill, which we have not found. And finally, this low-angle structure exposed in the trenches occurs exactly along the strike of the Banning fault, if projected from its known location northwest.

Regardless of whether this structure is a landslide or fault, the implications are the same—the western edge of the T2d section of the fan is overridden by bedrock, and therefore cannot be used as a piercing line (a linear feature that can be restored across the fault) in restoring the fan across the Mission Creek fault, as has been attempted by all previous workers (Keller et al., 1982; Dorsey, 2003; van der Woerd et al., 2006). In the following section, we describe the potential piercing lines that *can* be used to restore the fan, which include both the western edge of the fan on T2i and T2u, as well as the axial crests of the fan surfaces where preserved on T2d and inferred on T2u.

FAN MORPHOLOGY AND PIERCING LINES

Keller et al. (1982) and van der Woerd et al. (2006) used slightly different reconstructions to arrive at offsets of the T2 fan of ~700 m and 595 m, respectively. However, exploratory trenches excavated for this study invalidate some geomorphic features that were used as piercing lines in these previous studies. Of particular importance, the trenches reveal that the current western margin of the T2d segment of the fan is not a depositional feature as previously reported, but is a structurally modified fan margin, and thus cannot be used as a piercing line. We therefore use two geomorphic elements to estimate the fan offset—the longitudinal axial crest of each fan remnant, augmented where possible by its western depositional edge.

Geomorphic Evidence for Fan Axial Crests

The longitudinal axial crest of each fan segment provides the best criterion for reconstructing the original morphology of T2 and constraining the offset. In this section we

Downloaded from gsabulletin.gsapubs.org on July 6, 2010

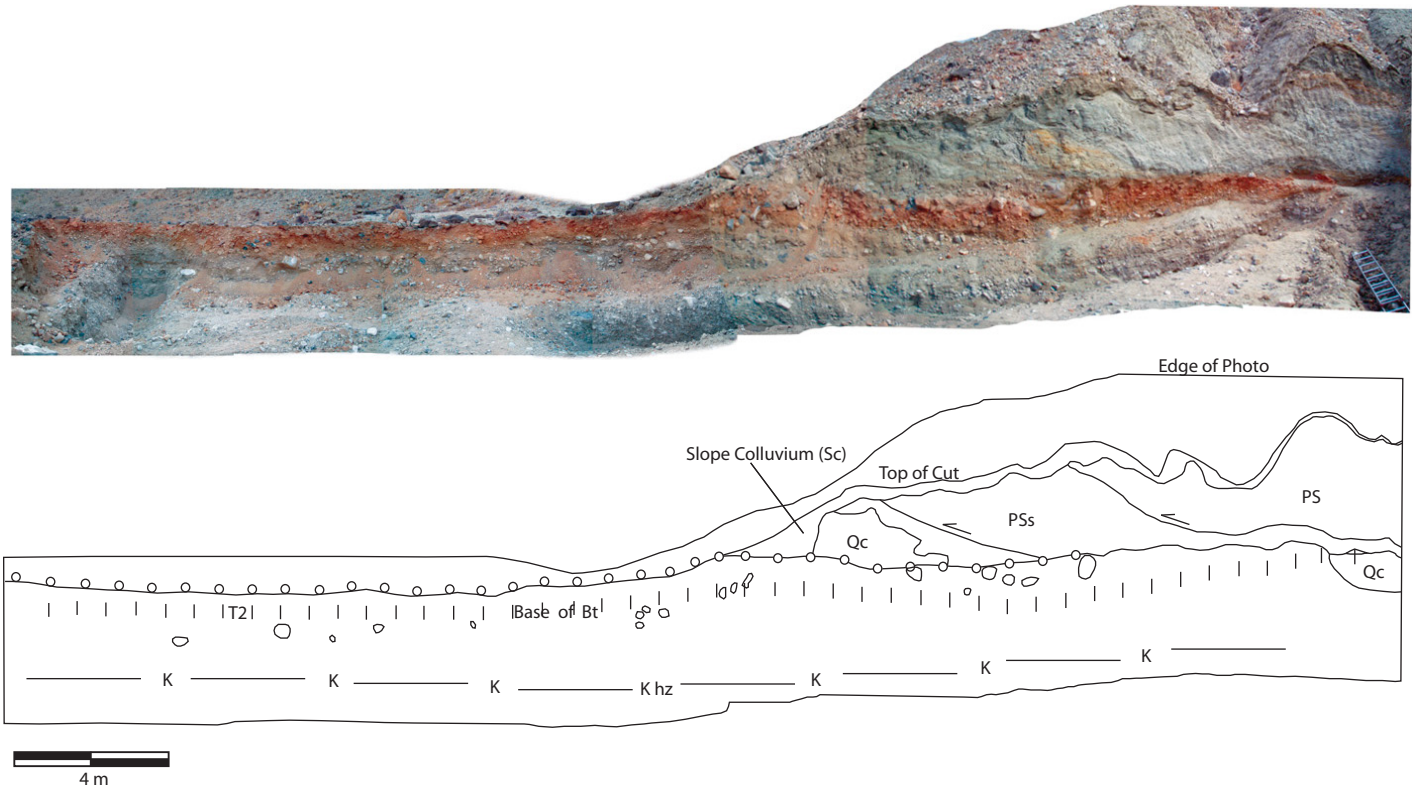

Figure 8. Photomosaic (looking toward the north) and simplified trench log of trench E5 showing the T2 alluvial fan overridden by sheared Palm Spring Formation. Contact between these units may be base of large landslide or the Banning fault. Units include: PS—Palm Spring Formation (sands and fine gravels); PSs—sheared Palm Spring Formation, lenses of fine- to medium-grained sands, fine gravels and silty to fine clay; T2—pebbly sand interbedded with coarse cobble to boulder gravel and a well-developed rubified, clay-rich soil pedon (laterally continuous with Pedon G, Fletcher et al., this volume), locally sheared along contact with PSs; Qc—colluvial material beneath PSs, non-bedded chaotic cobbles, gravel in fine-sand matrix; Sc—slope colluvium; Qc—colluvial material; K hz—K horizon soil layer characterized by thick sequence of coarse stacked cobbles and small boulders with pedogenic carbonate rinds.

describe the position and attributes of the axial crest for each of the three T2 fan remnants and discuss the ease or difficulty with which these geomorphic elements can be recognized and constrained.

T2 Upstream

Erosion by the modern channel has removed the axial crest of the T2u segment of the fan, but topographic contour lines on the T2u remnant define a "half-fan" geometry that allows one to infer that the approximate location of the eroded axial crest coincides with the terrace riser cut by the modern channel (Fig. 9A).

T2 Intermediate

Locating the axial crest of the T2 fan on the T2i remnant is difficult for several reasons. Firstly, there are numerous high-angle faults that strike subparallel to the trend of the axial crest and dominate the small-scale topography (Fig. 9B). This introduces the possibility that any high point currently on the topography may reflect collective displacement on those faults, rather than the actual crest of the fan remnant. Secondly, as with T2u, much of the eastern edge of this part of the fan has been eroded away, but we cannot use the geometry of the modern channel to constrain the location of the axial crest because the modern channel widens significantly and diverts off toward the east. If, however, the NE splay of the Mission Creek fault strand has little to no offset (an offset model discussed in the next section), then the axial crest of the T2i remnant would parallel the same trend as the axial crest of T2u.

T2 Downstream

Quarrying over the past decade removed the eastern half of the T2d segment of the fan. Fortunately, the axial crest on T2d can be located visually to within ~10 m using 1969 aerial photographs. These images show a clear topographic crest from which drainages radiate outward toward the fan edges (van der Woerd et al., 2006).

Geologic and Geomorphic Evidence for Western Fan Edges

The western depositional edge of the fan can also be used as a piercing line in conjunction with the axial crest, but only for segments T2u and T2i. Uncertainties in restoring the western fan edge stem primarily from distinguishing geomorphic elements that have been modified by erosion, warping, and/or minor faulting. Our reconstructions are based on detailed observation of fan surface characteristics, morphologic features, and subsurface geology as revealed by trenching.

T2 Upstream

The western edge of T2u is not uniquely defined, and we consider two possible piercing lines: (1) the western edge of T2u coincides with channel A (Fig. 9A), as suggested by Keller et al. (1982) and van der Woerd et al. (2006), and (2) the western edge of T2u coincides with channel B (Fig. 9A). We consider option 2 a viable

Downloaded from gsabulletin.gsapubs.org on July 6, 2010

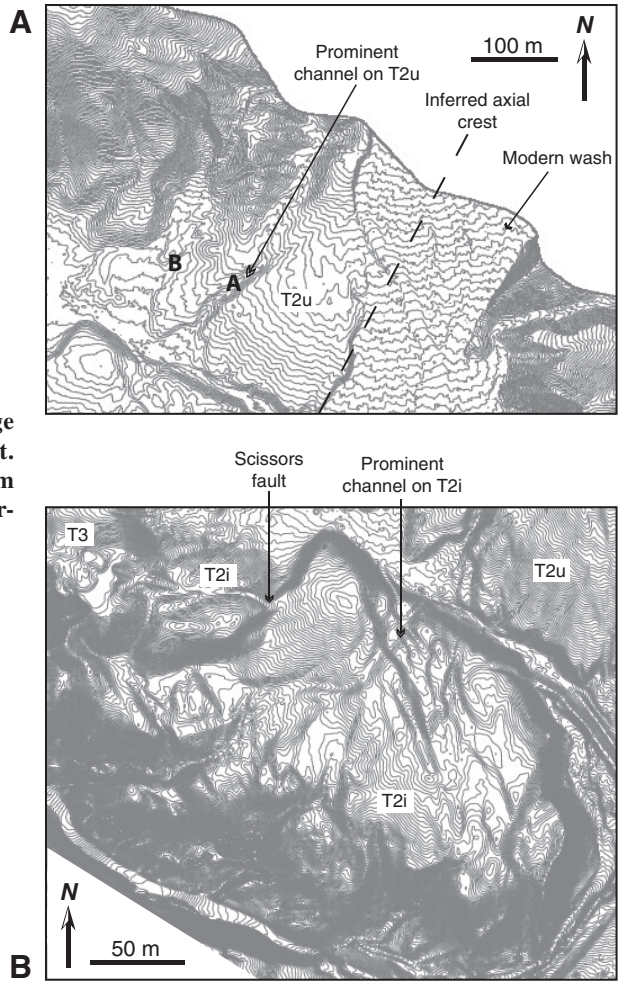

Figure 9. (A) Contour image of T2u from the B4 data set. (B) Contour image of T2i from the B4 data set. Contour intervals are less than 0.5 m.

possibility because a smooth patch of varnished boulders and pavement to the west of channel A slopes away from the main T2u surface at an angle consistent with a tapering fan edge, and because a boulder-top sample we dated using cosmogenic ^{10}Be (sample BP5, discussed in the following section) yields an age consistent with the samples taken from the main T2u remnant.

T2 Intermediate

Trench E2 revealed deposits associated with T2i pinching out onto bedrock, and thus constraining its western edge and providing a useful piercing line (Fig. 10). Northwest of trench E2, the terrace remnant labeled T3 is slightly higher, is more deformed, has more weathered clasts, and is considerably older, as suggested by van der Woerd et al. (2006). The older age of T3 is confirmed by our cosmogenic dating discussed in the next section. From trench E2 eastward, the edge of T2i trends approximately northeast to where it is buried by fluvial and eolian fill deposits. From here we project the edge of T2i ~70 m to the NE fault strand and allow for a possible change in trend of up to 10°. From trench E2 westward, we project the edge of T2i toward the SW strand of the Mission Creek fault (also allowing for a possible change in trend of up to 10°).

T2 Downstream

Prior to quarrying, the T2d surface was well preserved and relatively undeformed. Previous interpretations considered the edge of T2d near the SW splay of the Mission Creek fault strand to coincide with the prominent channel just west of trenches E3a and E3b (Fig. 6) (Keller et al. 1982; van der Woerd et al., 2006). However, as discussed previously, the T2 fan has been overridden by what we are interpreting to be the Banning strand of the San Andreas fault, and the amount of displacement along the Banning strand since the formation of T2 has not been measured. Exposures due to future quarrying, however, may allow us to quantify the extent to which T2 is overridden. Currently, we have no constraints on the location of the fan's original western margin on T2d.

OFFSET MODELS

We use the piercing lines described above to develop the maximum, minimum, and preferred offset models shown in Figure 11. All three models assume that the fan was roughly symmetrical around the crest and incorporate both the axial crest and fan edge as piercing lines wherever possible. The models reflect the range of uncertainty in each piercing line, such that the maximum offset model is derived from piercing lines providing upper bound offsets, and the minimum offset is derived from piercing lines providing lower bound offsets. The preferred model falls in between the two and was chosen based on detailed observations of the geologic relationships.

Maximum Offset

For the maximum offset model (Fig. 11B), we interpret a trend for the axial crest of the T2u portion of the fan of ~N 12° E, which represents the maximum possible angle between the fan axial crest and the margins of the modern channel based on its current geometry and orientation. We project this trend across T2i to meet the axial crest on T2d, which we assign a trend of ~N 44° E. We allow for some curvature of the two projections to give the axial crest a more realistic geometry. Since the location of the axial crest on the T2i remnant is unknown, we have used its western edge to estimate its maximum offset. This results in 170 m of offset on the NE fault splay and 810 m of offset on the SW fault splay, for a total offset of 980 m.

Minimum Offset

The minimum offset model (Fig. 11C) utilizes a more northeasterly trend for the axial crest of the fan on T2u of N 22° E, and for the axial crest on T2d of N 50º E. For this minimum estimate we assume negligible offset on the NE splay of the Mission Creek fault strand and project the axial crest from T2d up to T2u where they meet at a moderate angle. This results in 660 m of offset on the SW fault splay.

Preferred Offset

We prefer a model in which the axial crest of the fan curves westward more gradually than shown in the maximum and minimum offset reconstructions. Thus, for our preferred model (Fig. 12D) we curve the axial crest between the two fault strands at an angle consistent with the curvature of visible channel remnants on T2i. As in the minimum offset model, we assume negligible offset on the NE fault splay for the

Downloaded from gsabulletin.gsapubs.org on July 6, 2010

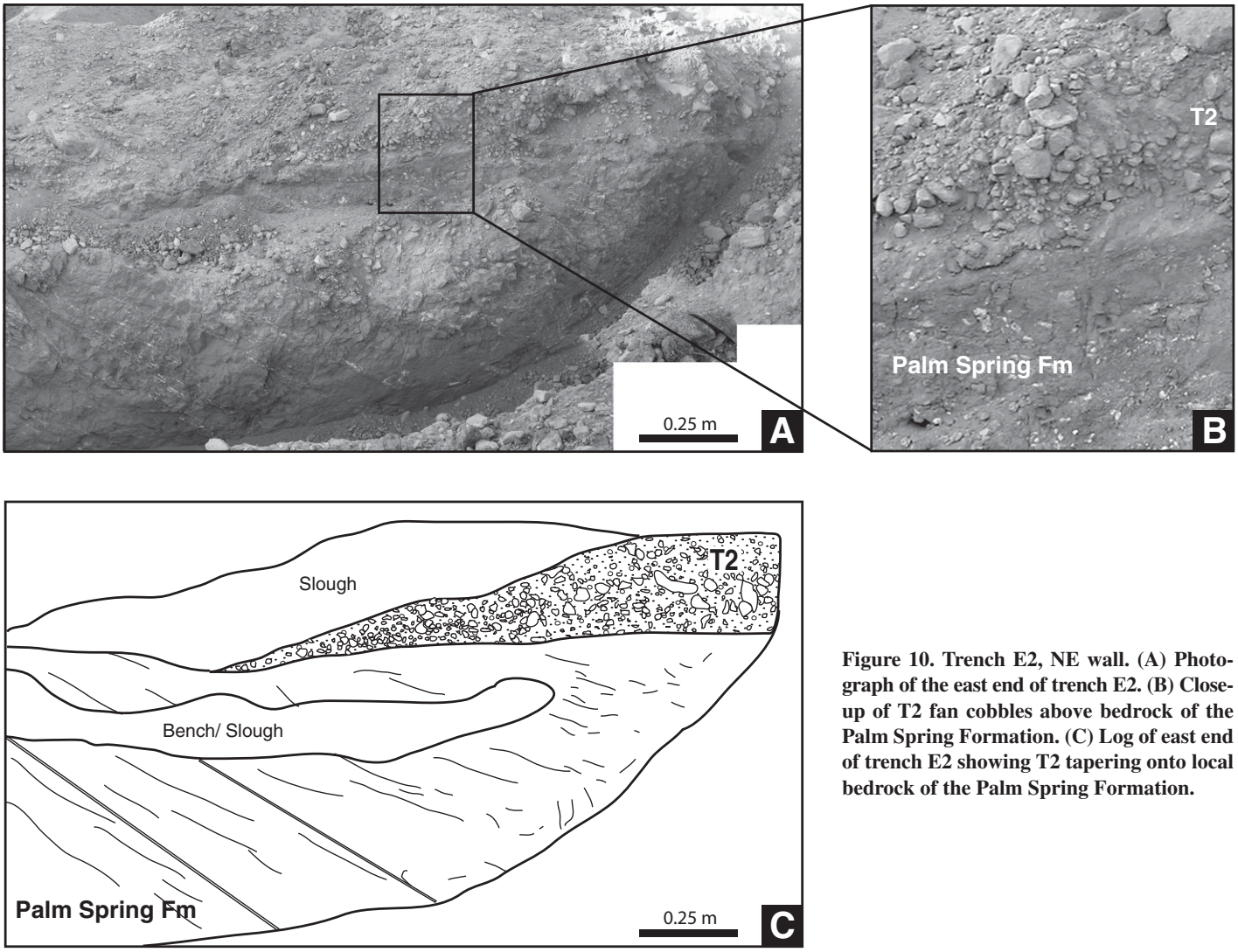

Figure 10. Trench E2, NE wall. (A) Photograph of the east end of trench E2. (B) Close-up of T2 fan cobbles above bedrock of the Palm Spring Formation. (C) Log of east end of trench E2 showing T2 tapering onto local bedrock of the Palm Spring Formation.

following two reasons. (1) The only prominent, through-going channel on T2i matches up with the only similar-size channel upstream (Fig. 9B). (2) Results from our cosmogenic dating (discussed in the following section) suggest the unit labeled T2u? on Figure 3 is indeed part of the T2 fan. This means that no offset is necessary on the NE fault splay (since deposition of T2) to project the fan edge across the NE fault splay. In this case, the NE splay of the Mission Creek strand may be a structural break separating the warped and faulted T2i remnant from the coherent T2u remnant upstream. Our preferred offset model results in 770 m of total horizontal offset.

COSMOGENIC DATING

Scatter in cosmogenic exposure ages can be attributed to either variable exposure before deposition (inheritance) or to postdepositional processes such as surface erosion, burial, or clast spalling (e.g., Brown et al., 2005). This has proven particularly important for the interpretation of boulder ages on glacial moraines along the Karakoram fault (Brown et al., 2002) and in the Sierra Nevada (Phillips et al., 1996), for instance. At Biskra Palms, van der Woerd et al. (2006) interpreted the T2 fan to be 35.5 ± 2.5 ka based on cosmogenic ^{10}Be ages determined from 19 cobble-size clasts gathered from the ground surface. The scatter in their cobble ages was attributed to variable inheritance, and one clast with an age of ca. 45 ka was excluded as an outlier (van der Woerd et al., 2006). Several studies, however, have indicated that boulder tops yield older ages than cobble-size clasts and have described a general correlation of boulder age with height above the fan surface (e.g., Hanks et al., 2001; Putkonen and Swanson, 2003; Garvin et al., 2005; Blard et al., 2007). In these instances, the scatter in exposure ages can be attributed to postdepositional processes, particularly to surface lowering in which shorter clasts are exhumed through time, rather than continuously exposed (Hanks et al., 2001; Putkonen and Swanson, 2003; Garvin et al., 2005; Blard et al., 2007).

A second goal of this study then is to explore the sources of uncertainty that arise from different cosmogenic sampling strategies, focusing on comparing ^{10}Be concentrations in samples from different clast sizes. We supplement the cobble data of van der Woerd et al. (2006) with 12 samples from large, lithologically similar boulders that retained relatively flat tops, were situated at high points on the T2 fan surface away from secondary surface erosional features, and exhibited only minor amounts of spalling and other evidence of erosion (Fig. 12). This ensures that local effects such as

Downloaded from gsabulletin.gsapubs.org on July 6, 2010

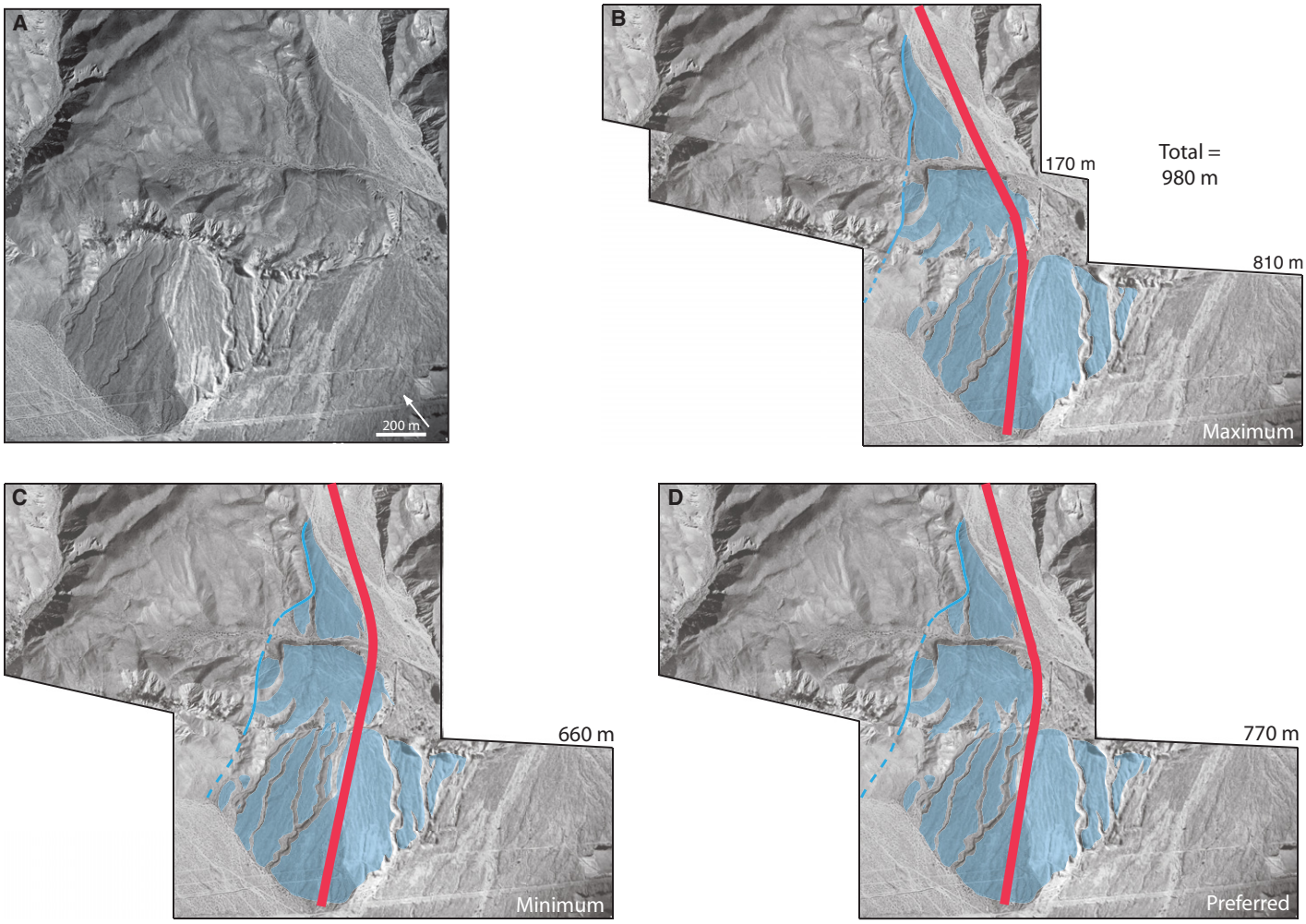

Figure 11. Maximum, minimum, and preferred offset models for the T2 fan. Only strike-slip component of slip is restored on the Mission Creek strands in these reconstructions. Banning fault is not shown or restored. Red line represents the estimated axial crest of the fan for each offset model, and the blue line represents the western edge of the T2 fan (dashed where projected from known locations) for each offset model. The T2 fan remnants included for each offset model are shown in blue.

self-shielding, local topographic shielding, and differential erosion have less influence on the ^{10}Be concentrations in the boulders.

Six samples were taken from boulders on T2u, four from T2d, one from the unit labeled T2u?, and one from T3 (Fig. 3). The majority of samples were granitoids, and most were medium-grained biotite tonalites. BP6 and BP3a, however, were foliated migmatitic gneisses. BP3a was located adjacent to BP3 and was selected specifically to compare two boulders with similar shapes and heights from the ground surface, but different lithologies, to test the effect of lithology (and weathering) on ^{10}Be concentrations (Fig. 12B).

Only the upper 5 cm of each sample was used for extracting ^{10}Be. Each sample was crushed and sieved to the 250–500 µm size fraction. Quartz was separated and etched by acid

Figure 12. Sample BP4 viewed from the SW—this is the largest boulder on the T2 surface.

Downloaded from gsabulletin.gsapubs.org on July 6, 2010

leaching (e.g., Kohl and Nishiizumi, 1992), and beryllium was separated from quartz using ion-exchange chromatography and precipitated as BeO. The concentration of ^{10}Be in the samples was measured on the accelerator mass spectrometer at Lawrence Livermore National Laboratory.

Results and Interpretations

Beryllium concentrations and model ages were calculated assuming zero erosion rate using the CRONUS-Earth online calculator (Balco et al., 2008) and a constant production rate model and scaling scheme for spallation of Lal (1991) and Stone (2000) (Table 1). The model minimum exposure ages from boulders collected on T2 range from 32.3 ± 0.8 ka to 53.9 ± 1.3 ka and the single boulder from T3 yield a model minimum age of 66.6 ± 1.6 ka. These data are reported with both 1-sigma internal uncertainties, which is the conventional format for ^{10}Be ages, and 2-sigma uncertainties, which allow comparison between the ^{10}Be data and the U-series ages in Fletcher et al. (this volume). To calculate the 2-sigma error, we combined the systematic or external uncertainty, which includes variable production rate of ~±6%, with the 2-sigma internal uncertainty summed quadratically (Table 1).

Sample BP3a suggests that mechanical anisotropy of boulders may play a significant role in the ultimate concentration of cosmogenic nuclides by enhancing boulder weathering. It is a foliated migmatitic gneiss with a layering defined by quartz-feldspar–rich leucosomes and biotite-rich melanosomes. Although the leucosomes contain a significant amount of quartz, and the height of this boulder is similar to sample BP3, the nuclide concentrations are considerably lower. This can be explained by the presence of well-developed platy foliation in this rock that acts as planes of weakness and facilitates both mechanical and chemical weathering, such that this boulder has lost more mass (and height) to erosion. Because of this apparent effect of weathering, we exclude BP3a from the rest of the boulder-top ages that define the age of T2.

Although there is scatter in the rest of the zero-erosion–rate boulder-top ages for T2, they are consistently and significantly older than the mean cobble age discussed in van der Woerd et al. (2006) of 35.5 ka. Furthermore, the boulder-top ages systematically correlate with height above the current fan surface such that the shortest boulders yield the youngest ages, and the ages increase progressively with boulder height up to at least 1 m (Fig. 13).

An important first consideration is whether the boulder-top ages reflect ~15–20 k.y. worth of inheritance and the mean cobble age represents the true depositional age of T2. We consider this unlikely for several reasons. First and foremost, the pedogenic carbonate ages of Fletcher et al. (this volume) indicate that this fan has a minimum depositional age of 45 ka. Second, inheritance alone would not explain the increase in ages with boulder height. Third, although the boulders and cobbles in the Indio Hills are second-generation clasts sourced originally from the San Bernardino Mountains, and incorporated into the 0.9–4.0 m.y. Palm Spring and 0.75–1.2 m.y. Ocotillo Formations that now comprise the Indio Hills, any inherited cosmogenic nuclides from this earlier phase of exposure, transport, and burial should affect both the cobble and boulder-top ages and can therefore not explain the differences in age between them. Finally, the cluster of larger boulder ages at ca. 50 ka is difficult to explain by inheritance; boulders are self-shielding, and those that are exposed before being deposited will generally accumulate large amounts of nuclides only on the face that is oriented favorably. When the boulders are transported, there is a chance they will land in this same orientation when redeposited. However, in order for the older boulder ages to be explained by major inheritance, they must have each had similar amounts of prior exposure, and they must have each been redeposited in the same orientation they were in prior to transport and redeposition. As an example of how unlikely this is for at least one boulder, a small trench adjacent to BP4 indicates that this 3 × 2 × 2 m boulder is embedded in the fan matrix with its long axis vertical and its smallest-area face facing upward; it is unlikely to have resided in this unstable position at another time upstream.

The second consideration is the observation that boulder-top ages correlate systematically with boulder height (Fig. 13). This suggests that the shorter boulders and cobbles are composed of more erodible material than the taller boulders, the shorter boulders and cobbles have experienced different rates of weathering due to differences in surface processes, or there has been incremental surface lowering through

TABLE 1. SAMPLE INFORMATION AND RESULTS OF ^{10}Be GEOCHRONOLOGY

Sample	Lithology*	Height (m)	Location Latitude (°N) /longitude (°W)	Elevation (m)	Thickness (cm)	Shielding correction†	Measured ^{10}Be (10^3 atoms g^{-1})§	Exposure age (k.y.)#	2-σ uncertainty (k.y.)**
					T2 fan				
BP3a	B	0.65	33.7848/116.2361	148	5	0.999	141.5 ± 3.3	32.3 ± 0.8	3.0
BP3	A	0.78	33.7855/116.2362	149	5	0.999	171.1 ± 3.3	39.1 ± 0.8	3.6
BP4	A	1.5	33.7856/116.2377	144	5	0.999	214.2 ± 4.1	49.3 ± 1.0	4.5
BP5	A	0.72	33.7856/116.2377	144	5	0.999	168.9 ± 3.3	38.8 ± 0.8	3.6
BP7	A	0.50	33.7847/116.2458	91	5	0.999	147.1 ± 4.6	35.2 ± 1.1	3.5
BP8	C	1.10	33.7854/116.2466	91	4	0.999	203.2 ± 3.9	48.4 ± 0.9	4.5
BP9	C	1.08	33.7849/116.2367	149	5	0.999	231.1 ± 4.6	53.0 ± 1.1	4.9
BP10	A	0.85	33.7854/116.2373	144	5	0.999	199.0 ± 4.7	45.7 ± 1.1	4.3
BP11	A	0.94	33.7855/116.2371	146	5	0.999	234.5 ± 5.5	53.9 ± 1.3	5.1
BP12	A	1.05	33.7870/116.2360	163	5	0.999	191.8 ± 3.2	43.4 ± 0.7	4.0
BP14	A	1.17	33.7856/116.2464	94	5	0.999	206.2 ± 4.9	49.4 ± 1.2	4.7
					T3 fan				
BP6	B		33.78465/116.24200	145	5	0.999	288.9 ± 6.7	66.6 ± 1.6	6.3

*Lithology: A—medium-grained biotite tonalite; B—migmatitic gneiss; C—coarse-grained granite.

†Ratio of the production rate at the shielded site to that for a 2π surface at the same location calculated using the cosmic-ray–produced nuclide systematics on Earth project (CRONUS-Earth) Geometric Shielding Calculator Version 1.1.

§Calculated using 07KNSTD ^{10}Be measurement standard and calibration (Nishiizumi et al., 2007).

#Nominal exposure age assuming no inheritance, zero erosion, density 2.7 g/cm^3, and standard atmosphere calculated using the CRONUS-Earth ^{10}Be-^{26}Al exposure age calculator (Balco et al., 2008). This version of the CRONUS calculator uses a reference spallogenic ^{10}Be production rate of 4.96 ± 0.43 atoms g^{-1} yr^{-1} (±1 σ, sea level and high latitude [SLHL]) and muogenic production after Heisinger et al. (2002a, 2002b). The quoted uncertainty is the 1-σ internal error, which reflects measurement uncertainty only.

**2-σ error is calculated by combining the external uncertainty, which includes a variable production rate of ~±6%, with the 2-σ internal uncertainty summed quadratically.

Note: Be carriers used at Lawrence Livermore National Laboratory are low-background carriers prepared from beryl with 4 ± 4 x 10^{-16} ^{10}Be/^{9}Be ratios. Process blanks were ~38,000 ± 7000 ^{10}Be atoms, 0.8%–1.7% of the total number of ^{10}Be atoms in the samples. 1-σ analytical uncertainties for ^{10}Be/^{9}Be ratios were 1.7%–3.1%.

Downloaded from gsabulletin.gsapubs.org on July 6, 2010

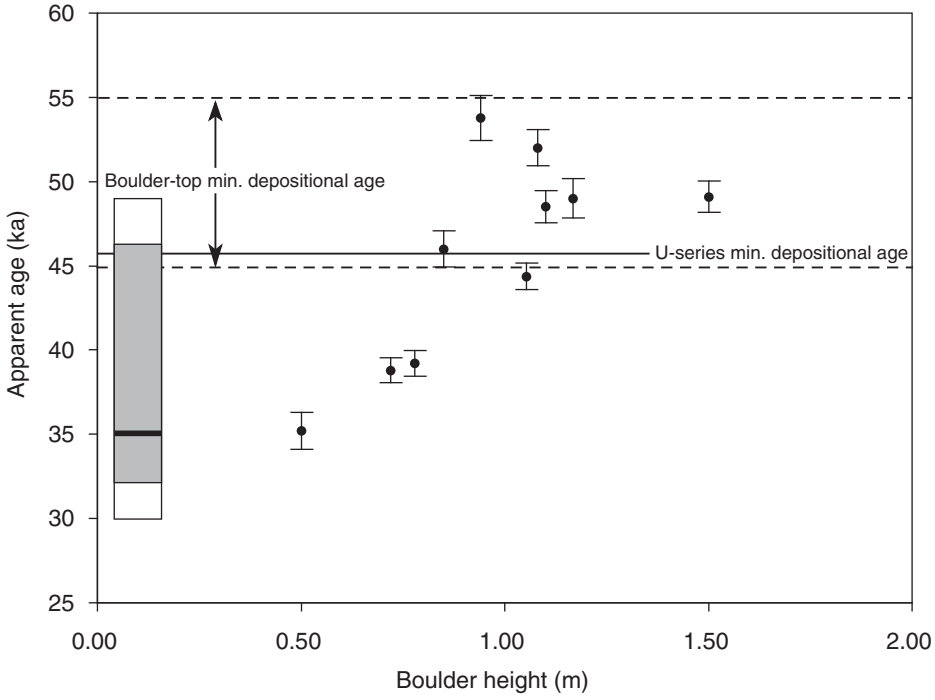

Figure 13. Apparent age of boulder-top samples (assuming zero erosion rate with 2-sigma error bars) plotted against boulder height relative to the current fan surface. Boulders less than ~1.0 m appear to scale with height, whereas those greater than ~1.0 m cluster at around 50 ± 5 ka, as discussed in text. Dashed lines bracket our conservative estimate of the minimum depositional age of T2. Gray rectangle represents the range of ages from cobble-size clasts from van der Woerd et al. (2006); outer rectangle is the full range in the van der Woerd data set including 1-sigma errors; bold black line is the mean cobble age of 35.5 ka. Solid line shows the minimum depositional age from U-series on pedogenic carbonate from Fletcher et al. (this volume).

time, or some combination of these. Because each of the boulders are composed of the same lithology, we temporarily neglect the effects of differential erosion between boulders and examine below a simplified surface-lowering model assuming zero-erosion rate for the cobbles and boulders embedded in a finer grained matrix (Fig. 14). That surface lowering plays a role in the postdepositional evolution of the T2 fan is supported by detailed soil profile descriptions presented in Fletcher et al. (this volume). In particular, the soils show evidence of having been stripped to varying depths, including very thin maximum-B horizons near to the current fan surface and shallow depths to maximum carbonate accumulation (Fletcher et al., this volume).

Our model setup is illustrated in Figure 14, with a total amount of surface lowering (x_0) and a depositional age (t_0) as independent variables. The average surface-lowering rate around the cobbles and boulders is $\varepsilon = x_0/t_0$ and is assumed constant through time, t_1 represents the amount of time any boulder is buried, and $t_2 = t_0 - t_1$ represents the amount of time the boulder top is fully exposed. We use the following equations to calculate concentrations, N_1 for t_1 and N_2 for t_2, representing accumulation of ^{10}Be while buried by matrix material and accumulation once exhumed, respectively, which we add together to estimate a total predicted concentration for different values of x_0 and t_0:

$$N_1 = S_{el} S_T S_s \sum_q \frac{J_q}{\varepsilon/(AL)_{q_s} + \lambda_m} \left[\exp\left(-\frac{x_1 - \varepsilon t_1}{(AL)_{q_s}} \right) - \exp\left(-\lambda_m t_1 - \frac{x_1}{(AL)_{q_s}} \right) \right],$$

$$N_2 = S_{el} S_T S_s \sum_q \frac{J_q}{\lambda_m} \left[1 - \exp\left(-\lambda_m t_2 \right) \right].$$

In these equations S_{el}, S_T, and S_s are scaling relations for ^{10}Be production as a function of elevation and latitude, topographic shielding, and surface coverage, respectively, q refers to the relevant production reactions (spallogenic and muogenic), J_q is the production rate for that reaction, and $(AL)_q$ is the absorption length of the reaction in sediment, given in terms of the mass-attenuation length divided by density. The surface erosion rate (ε) is equal to x/t, and λ_m is the radioactive decay constant for ^{10}Be.

Input values of x and t are inferred from Figure 13. Values for t of less than 45 ka and greater than 54 ka are unlikely because the majority of boulder-top ages cluster at ca. 50 ka, particularly those that are higher from the ground surface. Thus, we choose values for t that are in the range from 45 to 55 ka. Similarly, values for x of less than 0.8 m fail to explain the boulder concentrations scaling with height, so we input values only from the range 0.8–1.5 m. The results of the model calculations are shown in Figure 15.

Forward modeling such as this allows us to isolate the effects of specific variables in what is clearly a multivariable system. These calculations provide a simple and broad explanation of both the cobble and boulder-top data and support our interpretation that the depositional age of the T2 fan is between 45 and 56 ka, but they also demonstrate that the system is quite complex. In considering both the boulder-top and cobble data, note that there are considerable tradeoffs between estimated depositional age and amount of surface lowering, such that no combination fits the data perfectly (Fig. 15). For example, the model for an age of 50 ka and 1.5 m surface lowering fits the boulder concentrations (Fig. 15B) but predicts a cobble concentration much lower than that which is observed in the cobble data from van der Woerd et al. (2006), and indicates a greater amount of surface lowering than recognized in the soil profiles (Fletcher et al., this volume). On the other hand, the model for 1.0 m surface lowering and 50 ka matches the larger boulders and comes close to the cobble ages but overpredicts the concentrations of the smaller boulders.

The inability of these models to exactly predict the clast concentrations can be explained by considering several additional variables besides surface erosion and depositional age. Firstly, the general overestimation of concentrations for the small boulders in the models shown in Figure 15 can be attributed to differences in the density of the matrix material surrounding the boulders during surface lowering, to spatial and temporal variations in the erosion rate of the matrix material, and/or to surface processes that affected only specific clast sizes. As an example, wildfires during the Pleistocene are thought to have been fueled by intermittent herbaceous growth among the low shrub community (Minnich, 1988, 2007), which may have enhanced clast erosion for small boulders and cobbles but left the larger boulders relatively unscathed. Small boulders could also have been

Downloaded from gsabulletin.gsapubs.org on July 6, 2010

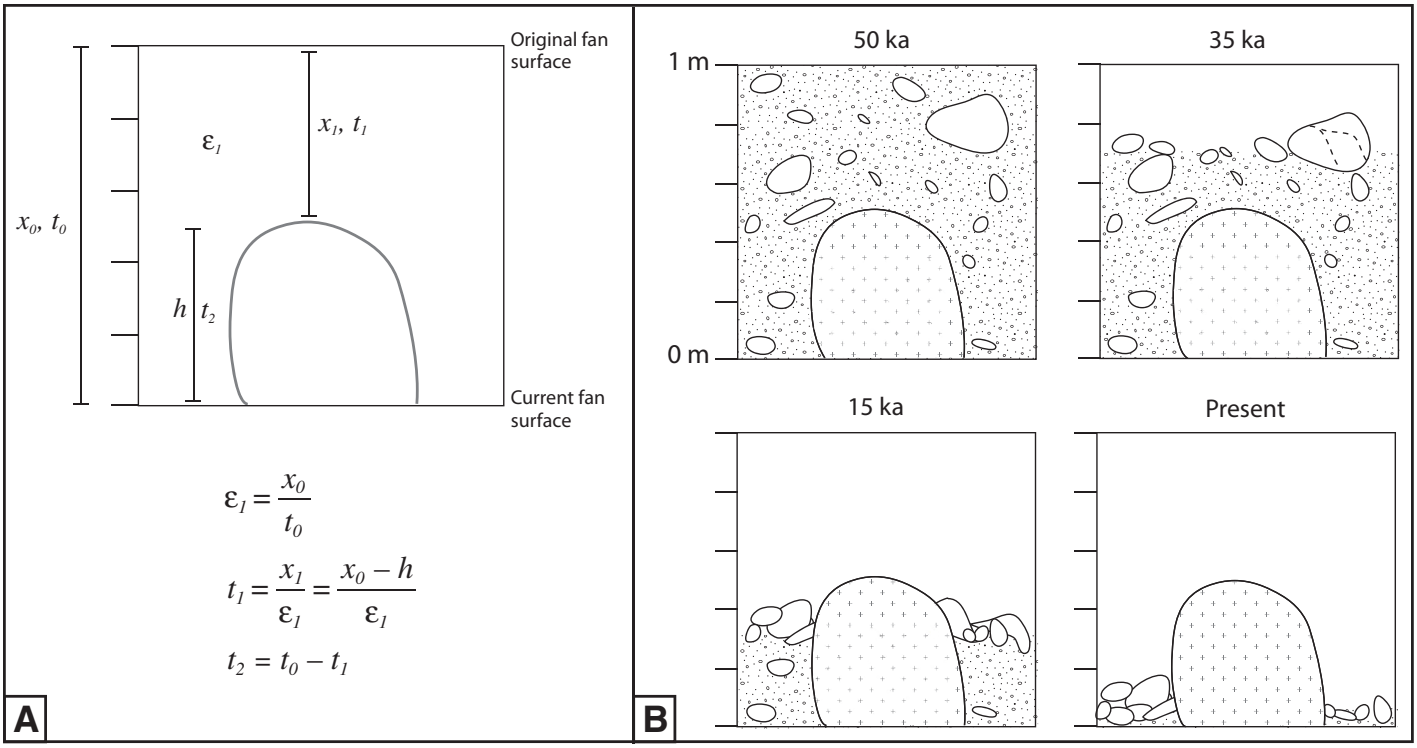

Figure 14. (A) Parameters used in surface lowering model and discussed in text. (B) Schematic cartoon of surface lowering model described in text and used to explain boulder and cobble ages. Cartoon shows the matrix around a 0.5 m boulder continuously eroding through time until the boulder is exhumed and the matrix continues to erode around it.

more affected by saltating particles during high wind-erosion events. Secondly, the overall scatter of the concentrations of boulders greater than 0.8 m in height can be explained by differential erosion of the boulders based on their proximity to dominant agents of erosion (e.g., surface runoff and wind activity) and/or variable amounts of inheritance for the boulders ranging from 0 to 9 ka. For example, sample BP11, which is ca. 54 ka, can have as much as 9 k.y. worth of inheritance, if the depositional age is equal to the minimum depositional age of 45 ka constrained by the U-series data. Thirdly, the observed scatter in the cobble ages is to be expected from a surface-lowering model because the cobbles were once distributed throughout the sediment column that surrounded the boulders, and individual cobbles were progressively exhumed through time. This suggests that the oldest cobble with an age of ca. 45 ka, which was discarded by van der Woerd et al. (2006) due to apparent inheritance, was likely close to the original depositional surface when first exposed and is the cobble age that best approximates the age of deposition, whereas the youngest cobble with an age of ca. 31 ka was likely deeper in the original deposit at the time of deposition and was exhumed more recently by surface lowering.

Summary of Age Constraints from Cosmogenic Dating

The primary observation from the age data described above is that the cobble ages are incompatible with the U-series minimum depositional age of 45 ka (Fletcher et al., this volume), whereas the majority of boulder-top ages are compatible. The differences between the cobble and boulder-top ages can be broadly explained by incremental surface lowering. Some amount of surface lowering is indicated by the soil profile descriptions (Fletcher et al., this volume). In detail, however, because of the competing effects of variables such as amount of surface lowering, matrix erosion rate, matrix density, boulder erosion rate, and boulder inheritance, we cannot justify increasing the precision in our depositional age estimate by choosing a mean boulder age. We therefore consider the age of the T2 fan to lie between 45 ka—the minimum depositional age determined from U-series in Fletcher et al. (this volume), and 54 ka—the age of the oldest boulder measured in this study. We have no basis by which to select a preferred age estimate that is more precise, and we thus use the full age range to calculate minimum, maximum, and preferred slip rates.

DISCUSSION

New Slip-Rate Estimate at Biskra Palms

Our offset estimates of between 660 and 980 m, coupled with the revised age of the alluvial fan of between 45 and 54 ka result in minimum, maximum, and preferred slip rates of 12.2 mm/yr, 21.7 mm/yr, and between 14 and 17 mm/yr, respectively. If, however, we also consider the ^{10}Be sampling strategy to be a source of uncertainty, such that the age of the T2 fan is between 35 and 54 ka, the range of geologic slip rates increases to between 12.2 and 27.6 mm/yr. There has been a range of geologic slip-rate estimates suggested for this site to date, summed across both the NE and SW splays of the Mission Creek fault strand (Table 2). The large variation of slip rates between ~10 and 35 mm/yr represents the total uncertainty and reflects the range of offset models, age dating techniques, and sampling strategies applied. Since the assessment of Keller et al. (1982), we have successfully reduced some of the uncertainty in the age of the T2 alluvial fan. Additionally, although our revised slip-rate estimate is less precise than, and spans the estimates of both Dorsey (2003) and van der Woerd et al.

Downloaded from gsabulletin.gsapubs.org on July 6, 2010

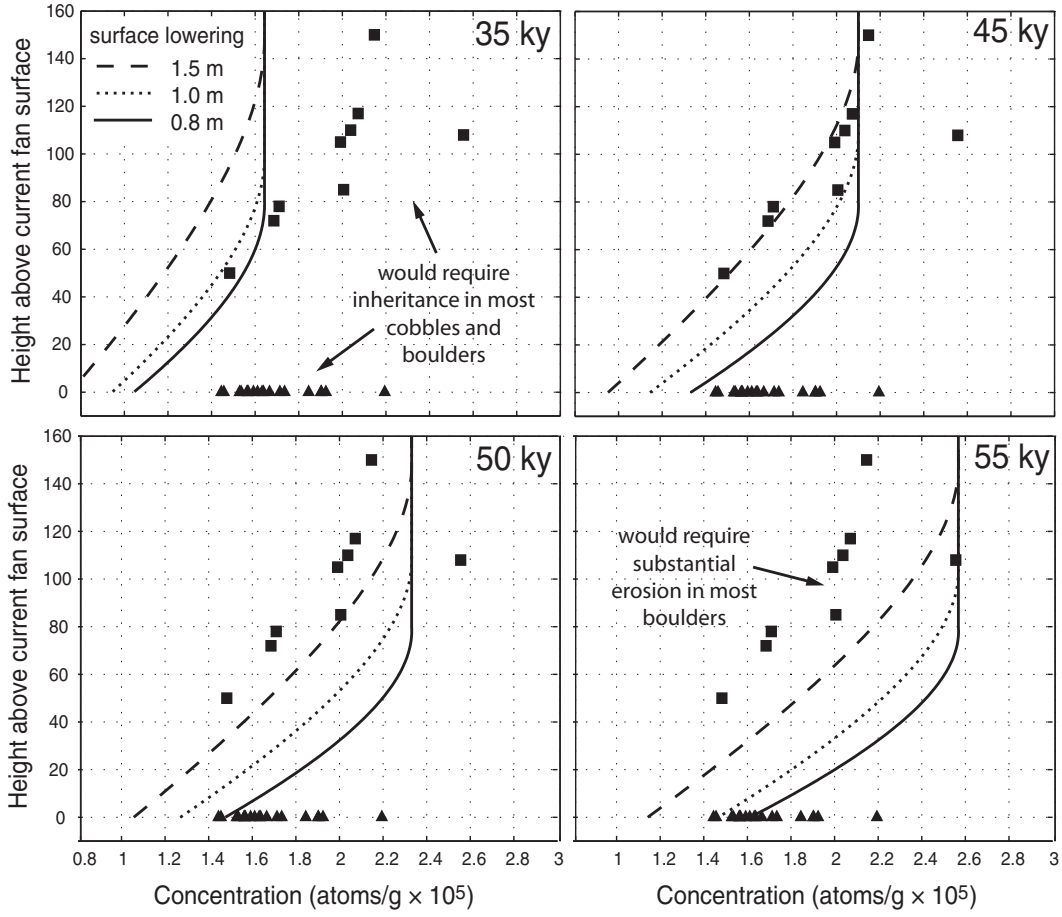

Figure 15. Plots of ^{10}Be concentration versus height, with the current fan surface at zero. Boulder concentrations are depicted as black squares and cobble concentrations from van der Woerd et al. (2006) as black triangles. The curves represent the calculated concentrations for the forward model described in the text and in Figure 15, for which we assign a depositional age (35, 45, 50, and 55 ka) and variable amounts of surface lowering. Dashed lines, dotted lines, and solid lines represent 1.5 m, 1.0 m, and 0.8 m of surface lowering, respectively. The model curves are calculated using the following values for the relevant parameters: $J_{spallation} = 4.66$, $J_{muogenic} = 0.207$, $S_{el} = 0.969$, density (ρ) = 2.0 g/cm^3, and $\lambda_m = 4.62 \times 10^{-7}$ s^{-1}.

(2006), it is based on a much more robust data set, and can therefore be more confidently applied to seismic hazard analyses.

TABLE 2. SLIP-RATE ESTIMATES FOR BISKRA PALMS OASIS

Reference	Offset	Fan age	Slip rate
Keller et al. (1982)	700 m	20–70 ka; 20–30 ka preferred; based on soil descriptions	10–35 mm/yr; 23–35 mm/yr preferred
Dorsey (2003)	450 ± 40 m	30.1 ± 2.4 ka (from van der Woerd et al., 2001, cosmogenic ^{10}Be dating)	15 ± 3 mm/yr
van der Woerd (2006)	565 ± 80 m	35.5 ± 2.5 ka; based on cosmogenic ^{10}Be dating of cobbles	15.9 ± 3.4 mm/yr
This study	770 +210/–90 m	50 ± 5 ka	12.0–21.7 mm/yr; 14.0–17.0 mm/yr preferred

Implications for Slip Transfer between the Mission Creek–San Andreas Fault and Banning Strand–San Andreas Fault

This study leaves open two important questions regarding the kinematics of the major faults at Biskra Palms. How do the Banning and Mission Creek strands of the southern San Andreas fault link together at depth, and how much displacement is currently being transferred from one fault to the other at this complex intersection? Detailed mapping and further geomorphological and structural investigation in the Indio Hills are needed to trace the displacement and geometrical relationships along strike between these two important components of the Coachella Valley segment of the southern San Andreas fault. It is clear, however, that the Biskra Palms site marks the transition from a dextral strike-slip fault system on the southeast to a dextral-reverse fault system on the northwest. The Mission Creek–San Andreas fault retains its surface expression northwest of Biskra Palms until exiting the Indio Hills, where it dies out in Morongo Wash, suggesting that the transfer of slip onto the Banning strand–San Andreas fault is largely completed within the Indio Hills. The left-stepping pattern of dextral strike-slip to dextral reverse faulting continues into San Gorgonio Pass (Yule and Sieh, 2003). Geologic slip rates from faults in the Coachella Valley northwest of Biskra Palms and from San Gorgonio Pass must therefore be treated as partial slip rates for the Coachella Valley segment of the southern San Andreas fault in this region.

A very crude estimate of the minimum slip rate on the Banning strand–San Andreas fault can be made at Biskra Palms by assuming an approximately horizontal dip for the Banning fault—as seen in the trenches and as indicated by the intersection of the fault with topography—and by assuming a slip vector for the Banning strand–San Andreas fault oriented toward the south-southeast, as inferred from fault slickenlines. Using the current western edge of the fan as the location of the original western fan margin, along with the above assumptions, gives a minimum displacement of ~100 m. Combined with the age range of the T2 fan (45–54 ka), this yields a very crude estimate of the minimum slip rate for the Banning fault of ~1–3 mm/yr. A more accurate estimate of the slip rate on the Banning strand–San Andreas fault at Biskra Palms could potentially be

Downloaded from gsabulletin.gsapubs.org on July 6, 2010

obtained from further trenching, but this crude estimate supports the interpretation that the Mission Creek–San Andreas fault has accommodated most of the displacement at Biskra Palms over the past ~50 k.y.

Comparisons with Geodetic Data

Several recent studies have drawn attention to potential discrepancies between geologic and geodetic slip-rate estimates for faults in southern California (e.g., Carena et al., 2004; Oskin and Iriondo, 2004; Meade and Hager, 2005; Fialko, 2006; van der Woerd et al., 2006; Johnson et al., 2007; Oskin et al., 2008). For the Mission Creek–San Andreas fault in particular, van der Woerd et al. (2006) indicated a discrepancy of ~10 mm/yr between the long-term geologic slip rate at Biskra Palms and shorter term geologic and geodetic slip-rate estimates, and interpreted this as either temporal changes in slip rate or faulting behavior. In detail, however, geologic estimates on the Coachella Valley segment (including the Indio, Mission Creek, and Banning fault strands) range from 4 to 35 mm/yr (Keller et al., 1982; Fumal et al., 2002; Dorsey, 2003; van der Woerd et al., 2006), and geodetic model estimates vary from ~15 to 30 mm/yr (Table 3) (Bennett et al., 1996; Becker et al., 2005; Fay and Humphreys, 2005; Meade and Hager, 2005). There are several explanations for such large variations in both geologic and geodetic slip-rate estimates.

One explanation is that many geodetic models for this region focus on the southern San Andreas and San Jacinto faults and do not model the Eastern California shear zone (e.g., Bennett et al., 1996; Fay and Humphreys, 2005; Fialko, 2006). But both geologic and geodetic observations indicate that some slip is transferred from the Coachella Valley segment of the southern San Andreas fault onto the Eastern California shear zone, yet there is no consensus as to how much and on which faults. Excluding the Eastern California shear zone in geodetic models can lead to higher slip rates on the faults that are more outboard, especially the San Andreas fault.

Additionally, it is important to recognize that geodetic and geologic slip-rate estimates fundamentally examine not only different time scales, but perhaps more importantly, different length scales. Geologic models capture slip at points and do not account for additional deformation that is distributed throughout the fault zone. This is clearly the case at Biskra Palms, where slip can be directly estimated on splays of the Mission Creek fault strand, but off-fault deformation and slip on numerous minor faults have not been quantified. Geodetic models have the opposite limitation—the density and resolution of global positioning system (GPS) station coverage currently requires modeling relatively large, undeformed (elastic) blocks with few faults bounding them such that the slip rates are average estimates of strain accumulation on all faults within the blocks and not a direct measurement of the slip rates on any particular fault. The model from Meade and Hager (2005), for instance, requires ~21 mm/yr of slip transfer from the Coachella Valley segment onto the Eureka Peak fault in order to allow for the drastic reduction in slip rates from ~23 mm/yr on the Coachella Valley segment to ~5 mm/yr on the San Bernardino segment. In actuality, however, the transfer of slip from the southern San Andreas fault onto the southern Eastern California shear zone is distributed along numerous faults of differing slip senses that approach the Coachella Valley segment along strike (Allen, 1957; Dibblee, 1967; Matti and Morton, 1993; Rymer, 2000) but that are not included in the Meade and Hager model. Until the various length scales begin to approach one another, they are major sources of uncertainty that produce large variations in slip-rate estimates and that make it difficult to compare geodetic and geologic slip rates directly.

Finally, among geodetic models alone, there are numerous input parameters that are essential sources of uncertainty, including locking depth, rheology structure, and the selection and size of individual blocks (for block models), among others (e.g., Savage and Burford, 1973; Savage, 1990; Dixon et al., 2003; Meade and Hager, 2004; Johnson et al., 2007). The station density can also affect the model results and resolution (Segall and Davis, 1997). There is currently no systematic way of estimating the effects of changing these parameters such that they factor into the total uncertainty in the geodetic slip rates.

The fundamental conclusion in comparing all of the various slip-rate determinations (Table 3) is that considerable uncertainty affects both the geologic and geodetic slip-rate estimates. If a real discrepancy between these rates exists for the Mission Creek–San Andreas fault at Biskra Palms, it cannot be demonstrated with available results (Table 3).

TABLE 3. SLIP-RATE ESTIMATES FOR THE SOUTHERN SAN ANDREAS FAULT

Reference	Model type	Time scale	Slip rate (mm/yr)
	Entire sSAF		
Fialko et al. (2005)	INSAR	Decadal	25 ± 3
	sSAF—Indio segment		
Bennett et al. (1996)	GPS—elastic block model	Decadal	22 ± 2
Becker et al. (2005)	GPS and stress inversions	″	23.0 ± 8
Meade and Hager (2005)	GPS—elastic block model	″	23.3 ± 0.5
Fay and Humphreys (2005)	GPS—elastic and viscoelastic	″	22.3 ± 0.7
Keller et al. (1982)	Geology—offset alluvial fan	~50,000	10–35
Dorsey (2003)	″	″	15 ± 3
van der Woerd et al. (2006)	″	″	15.9 ± 3.4
This study	″	″	11–22
Fumal et al. (2002)	Geology—paleoseismology on MC-SAF	~900 yr	>4 ± 2
	Transfer from sSAF onto ECSZ		
Meade and Hager (2005)	Eureka Peak fault	Decadal	21.3 ± 1.6

Note: ECSZ—Eastern California shear zone; GPS—global positioning system; INSAR—interferometric satellite aperture radar; MC-SAF—Mission Creek–San Andreas fault; sSAF—Southern San Andreas fault.

CONCLUSIONS

Our reexamination of a well-studied site on the southern San Andreas fault has demonstrated that large geologic uncertainties in both fan offset models and cosmogenic sampling techniques affect slip-rate estimates. Through detailed examination of the geology at Biskra Palms using high-resolution mapping and several trenches, we determined that the T2 fan is cut by a high-angle scissors fault in its central section and is overridden by the Banning fault at its western extent. The recognition that the T2 fan margin is structurally modified highlights the importance of subsurface exploration for constraining slip rates, even when the geomorphic relationships appear relatively straightforward. Additionally, through collecting boulder-top samples and comparing them to cobble-size clasts analyzed by van der Woerd et al. (2006) and U-series ages from pedogenic carbonate (Fletcher et al., this volume), we find that the T2 fan is at least 10 k.y. older than previously recognized, and we demonstrate that systematic errors in dating surface cobbles are considerably larger than the errors included in choosing a mean age and considering only measurement errors. This study emphasizes the importance of cosmogenic sampling strategies and indicates that boulder tops may yield a closer approximation of the depositional age of a geomorphic feature than cobble-size clasts, particularly in instances where the cobbles have been exhumed sometime after deposition during erosional lowering of the fan surface. This work also

Downloaded from gsabulletin.gsapubs.org on July 6, 2010

illustrates that alluvial fan surfaces are dynamic features that should be approached using several different techniques, partly to extract information about their postdepositional histories, and ultimately to assign a meaningful depositional age. The revised age and offset models from this study yield a range of slip rates of between 12 and 22 mm/yr, with our preferred range being 14–17 mm/yr; these rates are entirely compatible with short-term slip-rate estimates from geodetic models for this region, themselves subject to large uncertainties.

ACKNOWLEDGMENTS

We thank Becky Dorsey, Mike Oskin, and Kurt Frankel for several very helpful discussions. We also thank numerous other Southern California Earthquake Center (SCEC) community researchers who participated in discussions and review during field trips to Biskra Palms, especially on January 31, 2008. Jonathan Matti, Doug Morton, and Patricia McCrory provided preliminary internal U.S. Geological Survey (USGS) reviews that greatly improved this paper prior to submission. Kurt Frankel, Eric Kirby, and an anonymous reviewer also provided formal reviews that led to significant improvements to this paper. We would also like to thank the employees at Granite Construction Company, Indio, California, particularly Sterling Wainscott for providing us with nearly unlimited access to the gravel quarry in which the Biskra Palms fan is located. This research was supported by the SCEC, which is funded by National Science Foundation cooperative agreement EAR-0106924 and USGS cooperative agreement 02HQAG0008. The SCEC contribution number for this paper is 1292.

REFERENCES CITED

Allen, C.R., 1957, San Andreas fault zone in San Gorgonio Pass, southern California: Geological Society of America Bulletin, v. 68, no. 3, p. U315, doi: 10.1130/0016-7606(1957)68[315:SAFZIS]2.0.CO;2.

Balco, G., Stone, J., Lifton, N., and Dunai, T., 2008, A simple, internally consistent, and easily accessible means of calculating surface exposure ages and erosion rates from Be-10 and Al-26 measurements: Quaternary Geochronology, v. 3, p. 174–195, doi: 10.1016/j.quageo.2007.12.001.

Becker, T.W., Hardebeck, J.L., and Anderson, G., 2005, Constraints on fault slip rates of the southern California plate boundary from GPS velocity and stress inversions: Geophysical Journal International, v. 160, no. 2, p. 634–650, doi: 10.1111/j.1365-246X.2004.02528.x.

Bennett, R.A., Rodi, W., and Reilinger, R.E., 1996, Global positioning system constraints on fault slip rates in southern California and northern Baja, Mexico: Journal of Geophysical Research: Solid Earth, v. 101, no. B10, p. 21,943–21,960, doi: 10.1029/96JB02488.

Bevis, M., Hudnut, K., Sanchez, R., Toth, C., Grejner-Brzezinska, D., Kendrick, E., Caccamise, D., Raleigh, D., Zhou, H., Shan, S., Shindle, W., Yong, A., Harvey, J., Borsa, A., Ayoub, F., Elliot, B., Shrestha, R., Carter, B., Sartori, M., Phillips, D., Coloma, F., and Stark, K., 2005, The B4 project: Scanning the San Andreas and San Jacinto fault zones: San Francisco, California, 2005 American Geophysical Union Fall Meeting Abstracts for Poster Presentations, December 5–9.

Birkeland, P.W., 1999, Soils and Geomorphology: New York, Oxford University Press.

Blard, P.H., Lave, J., Pik, R., Wagnon, P., and Bourles, D., 2007, Persistence of full glacial conditions in the central Pacific until 15,000 years ago: Nature, v. 449, no. 7162, p. 591–U10, doi: 10.1038/nature06142.

Brown, E.T., Bendick, R., Bourles, D.L., Gaur, V., Molnar, P., Raisbeck, G.M., and Yiou, F., 2002, Slip rates of the Karakorum fault, Ladakh, India, determined using cosmic ray exposure dating of debris flows and moraines: Journal of Geophysical Research: Solid Earth, v. 107, no. B9, 2192, doi: 10.1029/2000JB000100, p. 7-1–7-9.

Brown, E.T., Molnar, P., and Bourlès, D.L., 2005, Comment on "Slip-Rate Measurements on the Karakorum Fault May Imply Secular Variations in Fault Motion," Science, v. 309, no. 5739, p. 1326, doi: 10.1126/science.1112508.

Carena, S., Suppe, J., and Kao, H., 2004, Lack of continuity of the San Andreas fault in southern California: Three-dimensional fault models and earthquake scenarios: Journal of Geophysical Research, v. 109, no. B04313, doi:10.1029/2003JB002643.

Cowgill, E., 2007, Impact of riser reconstructions on estimation of secular variation in rates of strike-slip faulting: Revisiting the Cherchen River site along the Altyn Tagh fault, NW China: Earth and Planetary Science Letters, v. 254, no. 3–4, p. 239–255.

Dibblee, T.W., Jr., 1954, Geology of the Imperial Valley region, California, *in* Jahns, R.H., ed., Geology of southern California: California Division of Mines Bulletin 170, p. 21–28 and plate 2 of Chapter II, Geology of the natural provinces.

Dibblee, T.W., Jr., 1964, Geologic map of the San Gorgonio Mountain quadrangle, San Bernardino and Riverside Counties, California: U.S. Geological Survey Miscellaneous Geologic Investigations Map I-431, scale 1:62,500.

Dibblee, T.W., Jr., 1967, Geologic map of the Morongo Valley quadrangle, San Bernardino and Riverside Counties, California: U.S. Geological Survey Miscellaneous Geologic Investigations Map I-517, scale 1:62,500.

Dixon, T., Norabuena, E., and Hotaling, L., 2003, Paleoseismology and global positioning system: Earthquake-cycle effects and geodetic versus geologic fault slip rates in the Eastern California shear zone: Geology, v. 31, no. 1, p. 55–58, doi: 10.1130/0091-7613(2003)031<0055:PAGPSE>2.0.CO;2.

Dolan, J.F., Bowman, D.D., and Sammis, C.G., 2007, Long-range and long-term fault interactions in southern California: Geology, v. 35, no. 9, p. 855–858, doi: 10.1130/G23789A.1.

Dorsey, B., 2003, Late Pleistocene slip-rate on the Coachella Valley segment of the San Andreas fault and implications for regional slip partitioning: Geological Society of America Abstracts with Programs, 99th Annual Meeting, v. 35, no. 4, p. 22.

England, P., and Molnar, P., 1997, The field of crustal velocity in Asia calculated from Quaternary rates of slip on faults: Geophysical Journal International, v. 130, no. 3, p. 551–582, doi: 10.1111/j.1365-246X.1997.tb01853.x.

Fay, N.P., and Humphreys, E.D., 2005, Fault slip rates, effects of elastic heterogeneity on geodetic data, and the strength of the lower crust in the Salton Trough region, southern California: Journal of Geophysical Research, v. 110, p. B09401, doi: 10.1029/2004JB003548.

Fialko, Y., 2006, Interseismic strain accumulation and the earthquake potential on the southern San Andreas fault system: Nature, v. 441, no. 7096, p. 968–971, doi: 10.1038/nature04797.

Fumal, T.E., Rymer, M.J., and Seitz, G.G., 2002, Timing of large earthquakes since A.D. 800 on the Mission Creek strand of the San Andreas fault zone at Thousand Palms Oasis, near Palm Springs, California: Bulletin of the Seismological Society of America, v. 92, no. 7, p. 2841–2860, doi: 10.1785/0120000609.

Garvin, C.D., Hanks, T.C., Finkel, R.C., and Heimsath, A.M., 2005, Episodic incision of the Colorado River in Glen Canyon, Utah: Earth Surface Processes and Landforms, v. 30, p. 973–984, doi: 10.1002/esp.1257.

Hanks, T.C., and Thatcher, W., 2006, The slip-rate discrepancy for the Altyn Tagh fault: An example of epistemic uncertainty: San Francisco, California, 2006 American Geophysical Union Fall Meeting Abstracts for Poster Presentations, December 5–9.

Hanks, T.C., Lucchitta, I., Davis, S.W., Davis, M.E., Lefton, S.A., and Garvin, C.D., 2001, The Colorado River and the age of Glen Canyon, *in* Young, R.A., and Spamer, E.E., eds., The Colorado River: Origin and Evolution: Grand Canyon, Arizona, Grand Canyon Monograph 12.

Johnson, K., Hilley, G., and Burgmann, R., 2007, Influence of lithosphere viscosity structure on estimates of fault slip rate in the Mojave region of the San Andreas fault system: Journal of Geophysical Research, v. 112, B7, p. 15.

Keller, E.A., Bonkowski, M.S., Korsch, R.J., and Shlemon, R.J., 1982, Tectonic geomorphology of the San Andreas fault zone in the Southern Indio Hills, Coachella Valley, California: Geological Society of America Bulletin, v. 93, no. 1, p. 46–56, doi: 10.1130/0016-7606(1982)93<46:TGOTSA>2.0.CO;2.

Kohl, C.P., and Nishiizumi, K., 1992, Chemical isolation of quartz for measurements of in-situ–produced cosmogenic nuclides: Geochimica et Cosmochimica Acta, v. 56, p. 3583–3587, doi: 10.1016/0016-7037(92)90401-4.

Lal, D., 1991, Cosmic-ray labeling of erosion surfaces—In situ nuclide production rates and erosion models: Earth and Planetary Science Letters, v. 104, no. 2–4, p. 424–439, doi: 10.1016/0012-821X(91)90220-C.

Matti, J.C., and Morton, D.M., 1993, Paleogeographic evolution of the San Andreas fault in southern California: A reconstruction based on a new cross-fault correlation, *in* Powell, R.E., Weldon, R.J., and Matti, J.C., eds., The San Andreas fault system: Displacement, palinspastic reconstruction, and geologic evolution: Geological Society of America Memoir 178, p. 107–159.

Matti, J.C., Morton, D.M., and Cox, B.F., 1985, Distribution and geologic relations of fault systems in the vicinity of the central Transverse Ranges, southern California: U.S. Geological Survey Open-File Report 85-365, 27 p., scale 1:250,000.

McDonald, E.V., 1994, The relative influences of climatic change, desert dust, and lithologic control on soil-geomorphic processes and hydrology of calcic soils formed on Quaternary alluvial-fan deposits in the Mojave Desert, California [Ph.D. thesis]: Albuquerque, New Mexico, University of New Mexico.

McDonald, E.V., Pierson, F.B., Flerchinger, G.N., and McFadden, L.D., 1996, Application of a process-based soil-water balance model to evaluate the influence of Late Quaternary climate change on soil-water movement in calcic soils: Geoderma, v. 74, p. 167–192, doi: 10.1016/S0016-7061(96)00070-5.

Meade, B.J., and Hager, B.H., 2004, Viscoelastic deformation for a clustered earthquake cycle: Geophysical Research Letters, v. 31, p. L10610, doi: 10.1029/2004GL019643.

Meade, B.J., and Hager, B.H., 2005, Block models of crustal motion in southern California constrained by GPS measurements: Journal of Geophysical Research, Solid Earth, v. 110, no. B3, B03403, doi: 10.1029/2004JB003209.

Meriaux, A.S., Ryerson, F.J., Tapponnier, P., Van der Woerd, J., Finkel, R.C., Xu, X.W., Xu, Z.Q., and Caffee, M.W., 2004, Rapid slip along the central Altyn Tagh fault: Morphochronologic evidence from Cherchen He and Sulamu Tagh: Journal of Geophysical Research, Solid Earth, v. 109, no. B6, B06401, doi: 10.1029/2003JB002558.

Meriaux, A.S., Tapponnier, P., Ryerson, F.J., Xu, X.W., King, G., Van der Woerd, J., Finkel, R.C., Li, H.B., Caffee, M.W., Xu, Z.Q., and Chen, W.B., 2005, The Aksay segment of the northern Altyn Tagh fault: Tectonic geomorphology, landscape evolution, and Holocene slip rate: Journal of Geophysical Research, Solid Earth, v. 110, no. B4, B04404, doi: 10.1029/2004JB003210.

Minnich, R.A., 1988, The biogeography of fire in the San Bernardino Mountains of California: A historical study: University of California Publications in Geography 27, p. 1–121.

Minnich, R., 2007, Southern California coniferous forest, *in* Barbour, M., Keeler-Wolf, T., and Schoenherr, A., eds., Terrestrial Vegetation of California, third ed.: Berkeley, CA, USA, University of California Press, p. 502–538.

Oskin, M., and Iriondo, A., 2004, Large-magnitude transient strain accumulation on the Blackwater fault, Eastern California shear zone: Geology, v. 32, no. 4, p. 313, doi: 10.1130/G20223.1.

Downloaded from gsabulletin.gsapubs.org on July 6, 2010

Oskin, M., Perg, L., Shelef, E., Strane, M., Gurney, E., Singer, B., and Zhang, X., 2008, Elevated shear zone loading rate during an earthquake cluster in eastern California: Geology, v. 36, no. 6, p. 507.

Peltzer, G., Crampe, F., Hensley, S., and Rosen, P., 2001, Transient strain accumulation and fault interaction in the Eastern California shear zone: Geology, v. 29, no. 11, p. 975–978, doi: 10.1130/0091-7613(2001)029<0975:TSAAFI>2.0.CO;2.

Phillips, F.M., Zreda, M.G., Benson, L.V., Plummer, M.A., Elmore, D., and Sharma, P., 1996, Chronology for fluctuations in late Pleistocene Sierra Nevada glaciers and lakes: Science, v. 274, p. 749–751, doi: 10.1126/science.274.5288.749.

Proctor, R.J., 1968, Geology of the Desert Hot Springs-Upper Coachella Valley area, California: California Division of Mines and Geology Special Report, v. 94, p. 50.

Putkonen, J., and Swanson, T., 2003, Accuracy of cosmogenic ages for moraines: Quaternary Research, v. 59, no. 2, p. 255–261, doi: 10.1016/S0033-5894(03)00006-1.

Reheis, M.C., Harden, J.W., McFadden, L.D., and Shroba, R.R., 1989, Development rates of Late Quaternary soils, Silver Lake Playa, California: Soil Science Society of America Journal, v. 53, p. 1127–1140.

Rymer, M.J., 1989, New Quaternary age control for strata within the Indio Hills, southern California: San Bernardino County Museum Quarterly, v. 36, no. 2, p. 64.

Rymer, M.J., 2000, Triggered surface slips in the Coachella Valley area associated with the 1992 Joshua Tree and Landers, California, earthquakes: Bulletin of the Seismological Society of America, v. 90, no. 4, p. 832–848, doi: 10.1785/0119980130.

Savage, J.C., 1990, Equivalent strike-slip earthquake cycles in half-space and lithosphere-asthenosphere Earth models: Journal of Geophysical Research, v. 95, p. 4873–4879, doi: 10.1029/JB095iB04p04873.

Savage, J.C., and Burford, R.O., 1973, Geodetic determination of relative plate motion in central California: Journal of Geophysical Research, v. 78, p. 832–845, doi: 10.1029/JB078i005p00832.

Segall, P., and Davis, J.L., 1997, GPS applications for geodynamics and earthquake studies: Annual Review of Earth and Planetary Sciences, v. 25, p. 301–306, doi: 10.1146/annurev.earth.25.1.301.

Shan, S., Bevis, M., Kendrick, E., Mader, G.L., Raleigh, D., Hudnut, K., Sartori, M., and Phillips, D., 2007, Kinematic GPS solutions for aircraft trajectories: Identifying and minimizing systematic height errors associated with atmospheric propagation delays: Geophysical Research Letters, v. 34, no. 23, L23S07, doi: 10.1029/2007GL030889.

Soil Survey Staff, 1951, Soil Survey Manual: Department of Agriculture Handbook, no. 18.

Soil Survey Staff, 1999, Soil Taxonomy: 2nd edition: U.S. Department of Agriculture Handbook, no. 436.

Stone, J.O., 2000, Air pressure and cosmogenic isotope production: Journal of Geophysical Research, Solid Earth, v. 105, no. B10, p. 23,753–23,759, doi: 10.1029/2000JB900181.

Thatcher, W., 2007, Microplate model for the present-day deformation of Tibet: Journal of Geophysical Research, Solid Earth, v. 112, no. B01401, doi: 10.1029/2005JB004244, p. 1–13.

van der Woerd, J., Klinger, Y., Sieh, K., Tapponnier, P., Ryerson, F.J., and Meriaux, A.S., 2006, Long-term slip-rate of the southern San Andreas fault from Be-10-Al-26 surface exposure dating of an offset alluvial fan: Journal of Geophysical Research, Solid Earth, v. 111, B04407, doi: 10.1029/2004JB003559, p. 1–17.

Yule, D., and Sieh, K., 2003, Complexities of the San Andreas fault near San Gorgonio Pass: Implications for large earthquakes: Journal of Geophysical Research, Solid Earth, v. 108, no. B11, p. 9-1–9-23.

Manuscript Received 2 February 2009
Revised Manuscript Received 24 August 2009
Manuscript Accepted 26 August 2009

Printed in the USA

Solid Earth, 13, 1169–1190, 2022
https://doi.org/10.5194/se-13-1169-2022
© Author(s) 2022. This work is distributed under
the Creative Commons Attribution 4.0 License.

Solid Earth Open Access EGU

Tectonic evolution of the Indio Hills segment of the San Andreas fault in southern California, southwestern USA

Jean-Baptiste P. Koehl[1,2], **Steffen G. Bergh**[3], **and Arthur G. Sylvester**[4]

[1]Centre for Earth Evolution and Dynamics (CEED), University of Oslo, 0315 Oslo, Norway
[2]Department of Earth and Planetary Sciences, McGill University, H3A 0E8 Montreal, Canada
[3]Department of Geosciences, UiT The Arctic University of Norway in Tromsø, 9037 Tromsø, Norway
[4]Department of Earth Science, University of California, California, 93106, Santa Barbara, USA

Correspondence: Jean-Baptiste P. Koehl (jeanbaptiste.koehl@gmail.com)

Received: 17 January 2022 – Discussion started: 2 February 2022
Revised: 3 July 2022 – Accepted: 5 July 2022 – Published: 1 August 2022

Abstract. Transpressional uplift domains of inverted Pliocene–Pleistocene basin fill along the San Andreas fault zone in Coachella Valley, southern California (USA), are characterized by fault linkage and segmentation and deformation partitioning. The Indio Hills wedge-shaped uplift block is located in between two boundary fault strands, the Indio Hills fault to the northeast and the main San Andreas fault to the southwest, which merge to the southeast. Uplift commenced about or later than 0.76 million years ago and involved progressive fold and faulting stages caused by a change from distributed strain to partly partitioned right-slip and reverse/thrust displacement on the bounding faults when approaching the fault junction. Major fold structures in the study area include oblique, right-stepping, partly overturned en echelon macro-folds that tighten and bend into parallelism with the Indio Hills fault to the east and become more open towards the main San Andreas fault to the west, indicating an early and close relationship of the macro-folds with the Indio Hills fault and a late initiation of the main San Andreas fault. Sets of strike-slip to reverse step-over and right- and left-lateral cross faults and conjugate kink bands affect the entire uplifted area, and locally offset the en echelon macro-folds. Comparison with the Mecca Hills and Durmid Hills uplifts farther southeast along strike in Coachella Valley reveals notable similarities, but also differences in fault architectures, spatial and temporal evolution, and deformation mechanisms. The present work contributes to better understand the structure and tectonic history of a major fault system along a transform plate boundary.

1 Introduction

This paper describes and evaluates structural patterns of the Indio Hills uplift in the northwestern part of Coachella Valley along the San Andreas fault zone (SAFZ) in California, southwestern USA (Fig. 1), where the fold–fault architecture, evolution, and partitioning of deformation compared to Mecca Hills and Durmid Hills are not well understood (e.g., Keller et al., 1982; Dibblee and Minch, 2008). The main goal of this study is to analyze internal macro- and meso-scale folds and related faults and to outline the kinematic evolution in relation to major SAFZ-related fault strands in the area (Fig. 1: Keller et al., 1982; Guest et al., 2007). These include the Indio Hills fault in the northeast (Allen, 1957; Tyley, 1974) and the main San Andreas fault along the southwest flank of the Indio Hills and of the Mecca Hills, and along the northeast flank of the Durmid Hills (Janecke et al., 2018; Fig. 1). The progressive tectonic evolution model for the Indio Hills uplift is then compared and correlated with other major uplifts and SAFZ-related fault strands along strike in the Mecca Hills and Durmid Hills (Sylvester and Smith, 1987; McNabb et al., 2017; Janecke et al., 2018; Bergh et al., 2019). We also briefly discuss the potential northwestward continuation of the Indio Hills fault into the eastern California shear zone and its role as a possible transfer fault (Dokka and Travis, 1990a, b; Thatcher et al., 2016). The variable fault and fold architectures and associated ongoing seismic activity in these uplift areas underline the need for persistent along-strike studies of the SAFZ to characterize the fundamental geometry, resolve the kinematic development, and correlate regionally major fault strands (see Janecke et

al., 2018). Such studies are essential to explain the observed lateral variations in fold and fault architectures and to resolve mechanisms of transpression, fault linkage, and areal segmentation in continental transform settings.

2 Geological setting

The Coachella Valley segment of the SAFZ in southern California is expressed as multiple, right-lateral fault strands, which uplifted blocks in the Indio Hills, Mecca Hills, and Durmid Hills (Fig. 1; Sylvester, 1988). These domains comprise thick successions of Pliocene–Pleistocene sedimentary strata uplifted and deformed in Pleistocene–Holocene time due to oblique convergence of the Pacific and North American plates and movement along the SAFZ and related faults (e.g., Atwater and Stock, 1998; Spotila et al., 2007; Dorsey et al., 2011). Recent structural studies in the Mecca Hills (McNabb et al., 2017; Bergh et al., 2019), and Durmid Hills at the southern termination of the SAFZ (Janecke et al., 2018), show that individual fault strands are linked and that the deformation splits into abruptly changing fold and fault geometries (Fuis et al., 2012, 2017). These recent works call for further characterization of the understudied Indio Hills segment in order to compare its structural development with other uplifted features along a major transform plate boundary fault zone. Below we summarize local and regional fault nomenclature, distribution, and fault movement history (Table 1) throughout the greater Coachella Valley region (Fig. 1), the stratigraphy of the Indio Hills area, and previous structural work in the main Indio Hills, Mecca Hills, and Durmid Hills uplift areas.

2.1 Regional faults

The southeastern Indio Hills are a WNW–ESE-trending tectonic uplift situated in a small restraining bend northeast of the main San Andreas fault (Figs. 1 and 2 and S1 in the Supplement). The studied uplift is located along strike about 25–50 km northwest of the Mecca Hills and Durmid Hills and to the southeast of the major left bend in the SAFZ trace near San Gorgonio Pass (Matti et al., 1985, 1992; Matti and Morton, 1993; Dair and Cooke, 2009).

The main faults in the southeastern Indio Hills include the Indio Hills fault in the northeast (Allen, 1957; Tyley, 1974) and the main San Andreas fault in the southwest (we refrain from using the name "Indio strand" ascribed to this fault by Gold et al., 2015, to avoid confusion with the Indio Hills fault). Regionally, the Indio Hills fault possibly merges with the Landers–Mojave Line and the eastern California shear zone in the north (Dokka and Travis, 1990a, b; Nur et al., 1993a, b; Thatcher et al., 2016). The Landers–Mojave Line is believed to be the locus of several recent earthquakes aligned in a NNW–SSE trend, including the 1992 Joshua Tree earthquake (Fig. 1b; Nur et al., 1993a, b). These earthquakes were tentatively ascribed to movement along a through-going NNW–SSE-striking fault, possibly the west-dipping Quaternary West Deception Canyon fault (Sieh et al., 1993; Rymer, 2000). This fault is thought to crosscut the E–W- to ENE–WSW-striking, left-lateral, Holocene Pinto Mountain fault, which merges with the main strand of the San Andreas fault in the west at the intersection of the right-lateral Mission Creek and Mill Creek strands (Allen, 1957; Bryant, 2000; Kendrick et al., 2015; Blisniuk et al., 2021). The former is thought to correspond to the continuation of the main San Andreas fault to the northwest (Gold et al., 2015) and may have accommodated ca. 89 km of right slip in the past 4 million years, whereas the latter accommodated about 8 km right slip at 0.5–0.1 Ma and is offset ca. 1 km by the Pinto Mountain fault (Kendrick et al., 2015).

The main San Andreas fault continues to the southeast where it bounds the Mecca Hills to the southwest. The Painted Canyon fault, a previous (late Miocene?–) Pliocene southwest-dipping normal fault reactivated as a right-lateral-reverse oblique-slip fault in the Pleistocene–present day, bounds the Mecca basin to the northeast (Sylvester and Smith, 1987; McNabb et al., 2017; Bergh et al., 2019). Farther southeast, the main San Andreas fault proceeds along the northeast flank of the Durmid Hills opposite the Pleistocene (ca. 1 Ma) right-lateral East Shoreline fault (Babcock, 1969, 1974; Bürgmann, 1991; Janecke et al., 2018). There, the main San Andreas fault merges with the Brawley seismic zone (Lin et al., 2007; Hauksson et al., 2012; Lin, 2013) and, together with the right-lateral San Jacinto fault zone, they merge into the right-lateral Imperial fault (Rockwell et al., 2011). In the north, the main San Andreas fault splays into the Banning strand and the Mission Creek fault in the northwestern part of the Indio Hills (Keller et al., 1982; Gold et al., 2015). The Banning strand is much younger than the Mission Creek fault and may have accommodated approximately 3 km of right slip in the past 0.1 million years (Kendrick et al., 2015).

Northwest and west of the Coachella Valley, Miocene–Pleistocene sedimentary strata are structurally bounded by the San Bernardino and San Jacinto fault strands of the SAFZ (Bilham and Williams, 1985; Matti et al., 1985; Morton and Matti, 1993; Spotila et al., 2007). To the southwest, Miocene–Pleistocene strata are bounded by the West Salton Detachment fault (Dorsey et al., 2011). The San Jacinto fault is typically believed to have slipped ca. 25 km right-laterally in the past 1.5 million years (Matti and Morton, 1993; Kendrick et al., 2015), whereas the West Salton Detachment fault is a low-angle normal fault that accumulated ca. 8–10 km of normal-oblique movement starting in the mid-Miocene and is related to the opening of the Gulf of California (Prante et al., 2014, and references therein).

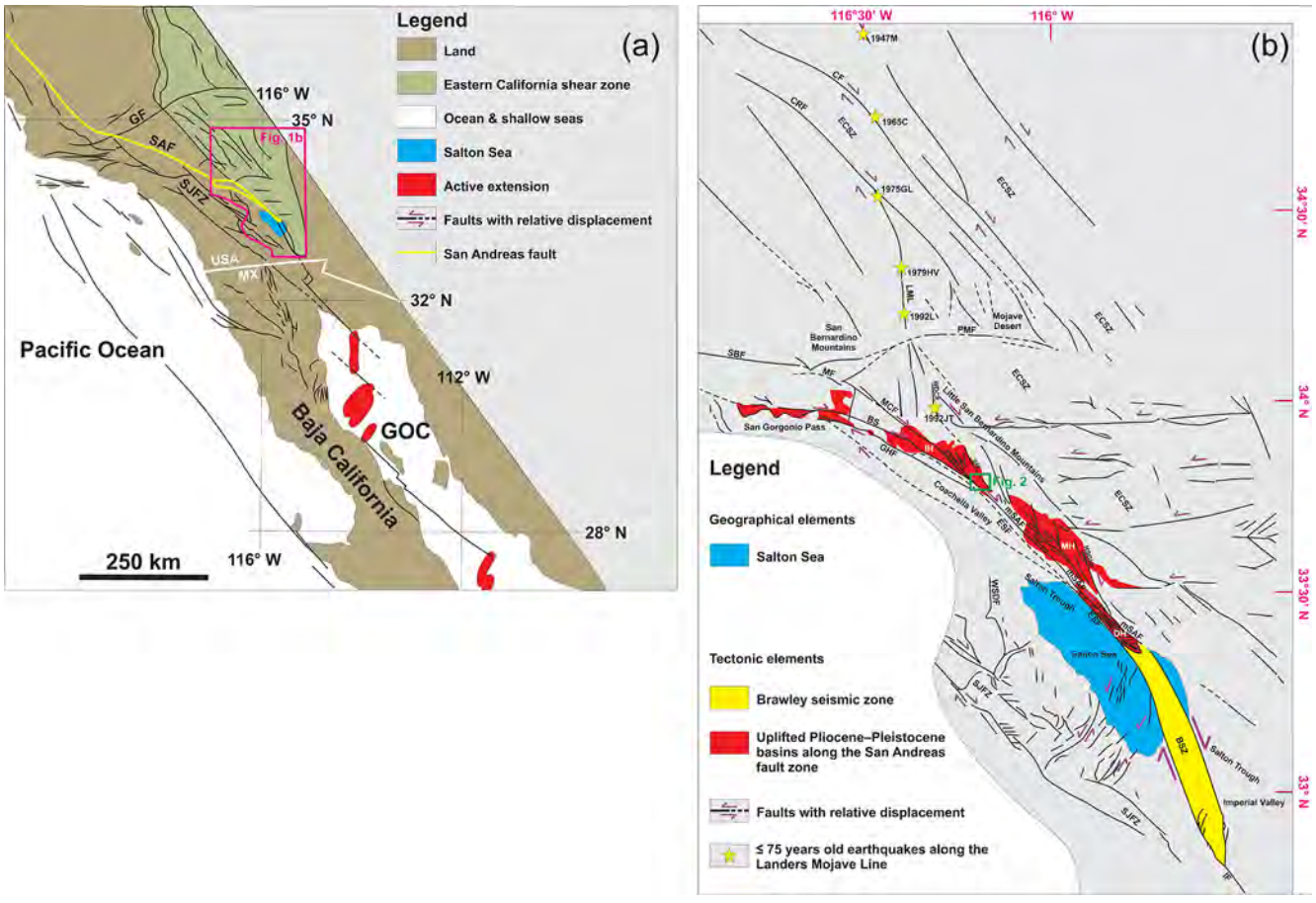

Figure 1. **(a)** Map of the main geological features of southern California, Baja California, and the Gulf of California. The location of **(b)** is shown as a fuchsia polygon. Modified after Janecke et al. (2018). **(b)** Simplified geological map of the Coachella Valley and Salton Trough, southern California, showing the three main transpressional uplift areas along the SAFZ: the Indio Hills (IH), Mecca Hills (MH), and Durmid Hills (DH). Note the link of the SAFZ with the Brawley seismic zone to the south. The study area is shown in a green rectangle. Recent earthquakes ($\leq$ 75 years) along the Landers–Mojave Line (LML) are shown as yellow stars with associated year of occurrence. Faults are drawn after Rymer (2000), Guest et al. (2007), Janecke et al. (2018), and Bergh et al. (2019). Earthquakes after Nur et al. (1993a, b). Abbreviations: 1947M: 1947 Manix earthquake; 1965C: 1965 Calico earthquake; 1975GL: 1975 Galway Lake earthquake; 1979HV: 1979 Homestead Valley earthquake; 1992JT: 1992 Joshua Tree earthquake; 1992L: 1992 Landers earthquake; BS: Banning strand; BSZ: Brawley seismic zone; CF: Calico fault; CRF: Camp Rock fault; DH: Durmid Hills uplift; ECSZ: eastern California shear zone; ESF: East Shoreline fault; GF: Garlock fault; GHF: Garnet Hill fault; GOC: Gulf of California; HSGHF: Hidden Springs–Grotto Hills fault; IF: Imperial fault; IH: Indio Hills uplift; IHF: Indio Hills fault; LML: Landers–Mojave Line; MCF: Mission Creek fault; MF: Mill Creek fault; MH: Mecca Hills uplift; mSAF: main San Andreas fault; PCF: Painted Canyon fault; PMF: Pinto Mountain fault; SBF: San Bernardino fault; SCF: Skeleton Canyon fault; SJFZ: San Jacinto fault zone; WDCF: West Deception Canyon fault; WSDF: West Salton detachment fault.

2.2 Stratigraphy of the Indio Hills and adjacent areas

The Indio Hills uplift is an inverted Pliocene–Pleistocene sedimentary basin lying upon Mesozoic granitic basement rocks, which we regard as an analog to the inverted Mecca basin farther southeast (Keller et al., 1982; Damte, 1997; McNabb et al., 2017; Bergh et al., 2019). In the Mecca basin, alluvial, fluvial, and lacustrine deposits of the Mecca and Palm Spring formations are truncated unconformably by the middle to upper Pleistocene Ocotillo Formation (Dibblee, 1954; Sylvester and Smith, 1976, 1987; Boley et al., 1994; Rymer, 1994; Sheridan et al., 1994; Sheridan and Weldon, 1994; Winker and Kidwell, 1996; Kirby et al., 2007; McNabb et al., 2017; Table 1). Similar uplifted strata at Durmid Hills (Fig. 1) belong to the Pliocene–Pleistocene Borrego Formation and are overlain by middle to upper Pleistocene deposits of the Brawley and Ocotillo formations (Dibblee, 1997; Herzig et al., 1988; Lutz et al., 2006; Kirby et al., 2007; Dibblee and Minch, 2008).

Leuco-granitic rocks crop out near gently SW-dipping conglomerates along the northeastern flank of the Indio Hills, near the trace of the Indio Hills fault (Fig. 2). Despite proximity of the conglomerates to segmented granite outcrops,

Table 1. Summary of the timing of the main events in the Coachella Valley and Gulf of California. Note the presumed timing phases (1–3) of fold-faulting and uplift events in the Indio Hills (this work). The stratigraphy is common to the Mecca Hills and Indio Hills, although some features are only observed in one area (e.g., unconformities 1 and 2 in the Mecca Hills but not in the Indio Hills).

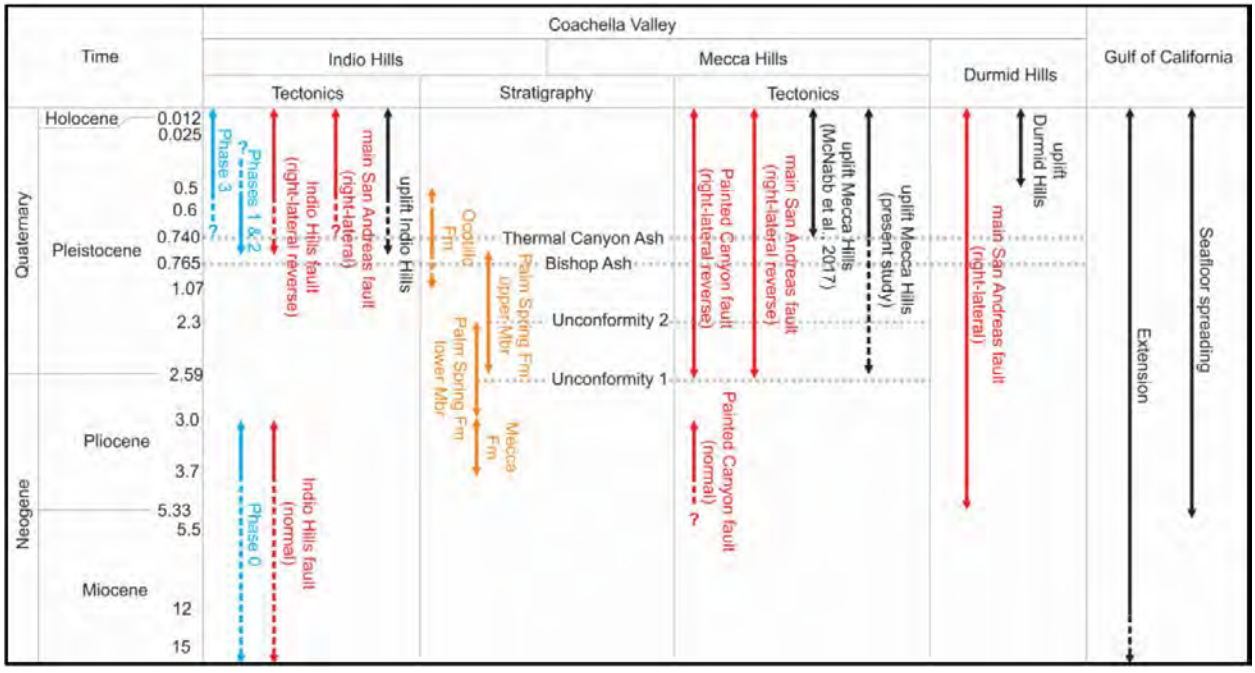

the contact itself is not exposed. The conglomerates are the lowermost stratigraphic unit exposed in the Indio Hills and are characterized by a succession of meter-thick beds of very coarse, poorly sorted blocks of gneissic and granitic rocks more than a meter in size. Previous mapping in the area (Dibblee, 1954; Lancaster et al., 2012) considered the conglomerates to be stratigraphic equivalents to the middle to upper Pliocene Mecca Formation in the Mecca Hills (Sylvester and Smith, 1987; McNabb et al., 2017; Bergh et al., 2019), and at least part of the clasts are from the leuco-granitic rocks, which must correspond to basement rocks of the inverted Indio Hills basin. Up-section toward the southwest, the conglomerate gradually is succeeded by coarse-grained sandstone, which defines the transition from the Mecca Formation to the lower Palm Spring Formation.

The Palm Spring Formation in the Indio Hills consists of moderately to well-consolidated alluvial fan deposits (Dibblee and Minch, 2008), with some interbedded gypsum layers and red-colored calcareous mudstone, as in the Mecca Hills (Sylvester and Smith, 1987). The main rock types include beds of light-colored, medium- to coarse-grained sandstone, gray–brown silty sandstone, and dark biotite-rich mudstone. The southwestwards increase in silt–clay toward the main San Andreas fault (also recorded in the Mecca Hills; Bergh et al., 2019) may indicate a gradual transition from the lower to the upper member of the Palm Spring Formation. By contrast, the transition between the lower and upper members of the Palm Spring Formation in the Mecca Hills is marked by two angular unconformities that signal further steps in uplift and inversion of the Mecca basin (Table 1; McNabb et al., 2017; Bergh et al., 2019).

Ages of 3.0–2.3 Ma (latest Pliocene–early Pleistocene) and 2.6–0.76 Ma (earliest Pleistocene to earliest late Pleistocene) were obtained respectively for the lower and upper member of the Palm Spring Formation in the Mecca Hills based on reversed magnetic polarity data (Chang et al., 1987; Boley et al., 1994; McNabb, 2013; McNabb et al., 2017; Table 1). We infer a similar age range for the Palm Spring Formation in the southern Indio Hills.

In contrast to other uplift areas in Coachella Valley, the Ocotillo Formation has not been mapped in the Indio Hills in the present study. However, based on the occurrence of the Bishop Ash at the northwestern edge of the study area and the occurrence of the volcanic deposit within the uppermost Palm Spring Formation or at the base of the overlying Ocotillo Formation in the Mecca Hills, it is likely that the Ocotillo Formation is present just northwest of the area mapped (Fig. 2). In addition, it is deposited on the flank northeast of the Indio Hills fault, and southwest of the main San Andreas fault (Figs. 1 and 2), indicating that this unit was either not deposited or eroded in the area that recorded the most uplift in Indio Hills.

Additional dating constraints on transpressional uplift in the Coachella Valley include tephrochonology of the 0.765-million-year-old Bishop Ash layer (Sarna-Wojcicki et al., 2000; Zeeden et al., 2014; Table 1). This volcanic deposit is

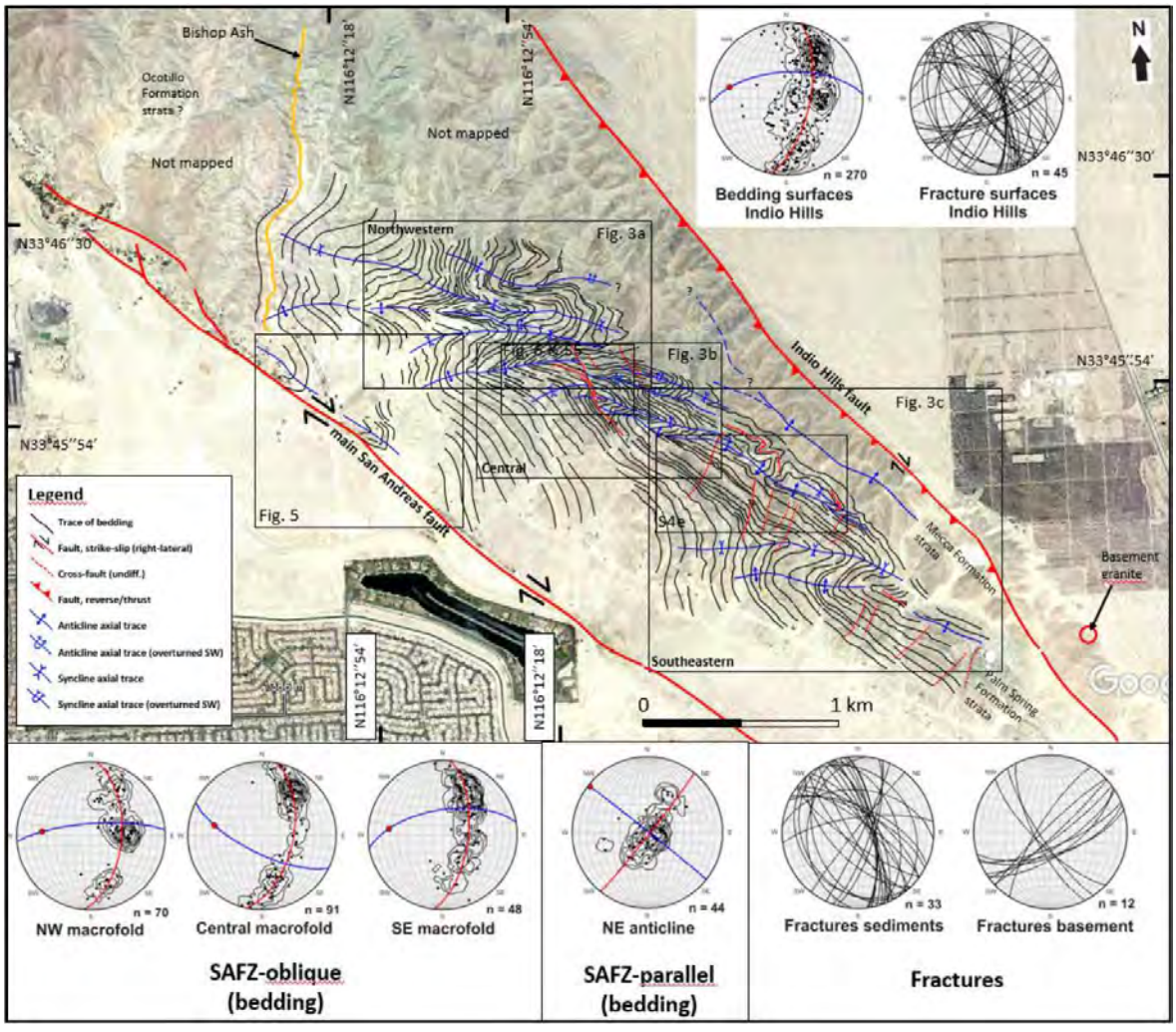

Figure 2. Interpreted Google Earth image in the southeastern part of the Indio Hills uplift area. Three main SAFZ-oblique macro-folds (northwestern, central, southeastern) are mapped in between the bounding Indio Hills and main San Andreas faults, whereas one SAFZ-parallel anticline is present close to the Indio Hills fault. More detailed figures are numbered and framed. Structural datasets are plotted in lower hemisphere Schmidt stereonets via the Orient software (Vollmer, 2015). Note that faults are also included as fractures in the stereonets. Bedding surfaces are shown as pole to plane with frequency contour lines, with average πS great circle (red great circles), fold axial surface (blue great circles), and fold axis (red dots). Brittle fractures in sedimentary strata and basement rocks are plotted as great circles. Source: Google Earth historical imagery November 2011. Uninterpreted version of the image available as Fig. S1. © Google Earth 2011.

found within the upper member of the Palm Spring Formation (which is unconformably overlain by the Ocotillo Formation) in the hanging wall of the Painted Canyon fault away from the fault, and within the base of the Ocotillo Formation in the hanging wall of the Painted Canyon fault near the fault (Ocotillo and uppermost Palm Spring formations interfingering near the fault) and in the footwall of the fault (McNabb et al., 2017; Bergh et al., 2019). The unconformable contact between the Palm Spring and Ocotillo formations away from the Painted Canyon fault towards the southwest and their interfingering relationship near the fault suggest that uplift had already initiated prior to deposition of the Ocotillo Formation (i.e., before 0.76 Ma, in the mid-Pleistocene), possibly during the formation of the lower unconformity between the lower and upper members of the Palm Spring Formation (McNabb et al., 2017; Table 1). Complementarily, the involvement of the Bishop Ash in deformation suggests that deformation continued past 0.76 Ma (in the late Pleistocene).

2.3 Major tectonic uplifts in the Coachella Valley

2.3.1 Indio Hills

The southeastern end of the Indio Hills is an uplifted domain of deformed strata of the Mecca and Palm Spring formations situated in between the main San Andreas and Indio Hills fault (Fig. 2). The main San Andreas fault corresponds to a

major oblique strike-slip fault segment at the eastern end of San Gorgonio Pass (Matti et al., 1985; Morton et al., 1987). It is easily traced to Indio Hills (Figs. 1 and 2) since its main trace provides preferential pathways for groundwater flow and growth of wild palm trees along strike.

The Indio Hills fault was mapped north of the study area (Dibblee and Minch, 2008) extending into the Landers–Mojave Line (Nur et al., 1993a, b), a NNW–SSE-striking right-lateral fault system extending hundreds of kilometers northward from the southeastern Indio Hills into the eastern California shear zone and related fault segments such as the Calico and Camp Rock faults (Fig. 1; Dokka et al., 1990a; Nur et al., 1993b). The Indio Hills fault may correspond to a major fault splay of the SAFZ (Dokka and Travis, 1990a, b; Thatcher et al., 2016). Southeast of the Indio Hills, however, the geometry of the Indio Hills fault remains elusive, and the fault either dies out or merges with structures like the main San Andreas fault, the Skeleton Canyon fault, and/or the Painted Canyon fault in the Mecca Hills (Fig. 1).

The transpressional character of the Indio Hills uplift was suggested by Sylvester and Smith (1987). However, detailed structural analyses documenting this hypothesis for the uplift as a whole have not been conducted. Gold et al. (2015) explore tectonogeomorphic evidence for dextral-oblique uplift, and Keller et al. (1982) and Blisniuk et al. (2021) focus on landscape evolution near the intersection of the Banning strand and Mission Creek fault (northwest of the study area), which merge into the main San Andreas fault (Fig. 1). In addition to investigating soil profiles, offset drainage systems, and recent (a few thousand years old) displacement along the SAFZ, Keller et al. (1982) called attention to a strong dominance of gently plunging and upright macro-folds in bedrock strata along the Mission Creek fault and at the southeastern end of the Banning strand where these faults merge. Their study showed that bends and steps along the main fault traces were consistently located near brittle fault segments and zones of uplift. The study also showed that drainage systems were offset recently (at ca. 0.03–0.02 Ma) and indicate relatively high slip rates along the Mission Creek fault on the order of 23–35 cm yr^{-1}, i.e., comparable to the more recent ca. 23 cm yr^{-1} estimate by Blisniuk et al. (2021).

2.3.2 Mecca Hills

Farther south, the Mecca Hills uplift was previously defined as a classic flower structure (Sylvester and Smith, 1976, 1987; Sylvester, 1988), in which all folds and faults formed synchronously and merged at depth. Recent analyses (Bergh et al., 2014, 2019) indicate a modified flower-like structure, consisting of a steep SAFZ fault core zone to the southwest, a surrounding approximately 1–2 km wide damage zone expressed by en echelon folds and faults oblique to the SAFZ (including left-slip cross faults), steeply plunging folds, and SAFZ-parallel fold and thrust belt features (including right- and left-slip and oblique-reverse faults) formed in kinematic succession. In addition to the steep shallow portion of the SAFZ (Fuis et al., 2012, 2017), two other major NW–SE-striking faults occur in the Mecca Hills (Fig. 1). One is the Skeleton Canyon fault, which initiated as a steep SAFZ-parallel strike-slip fault and was reactivated as a reverse fault dipping gently northeastwards in the late kinematic stages (Sylvester and Smith, 1976, 1979, 1987; Bergh et al., 2019). The other is the Painted Canyon fault, which is a former Miocene–Pliocene basin-bounding normal fault (McNabb et al., 2017) and is now reactivated as a NE-directed thrust fault with dip to the southwest (Bergh et al., 2019; Table 1). The polyphase evolution and reactivation of internal oblique, step-over faults, and SAFZ-parallel faults were explained by a series of successive–overlapping events involving a change from distributed and locally partitioned into fully partitioned strain in a changing oblique-plate convergence regime (Bergh et al., 2019).

2.3.3 Durmid Hills

The Durmid Hills are an elongate ridge that parallels the main strand of the SAFZ at the south edge of the Salton Sea in Imperial Valley (Fig. 1). Farther south, this deformation zone and the SAFZ project towards the Brawley seismic zone, an oblique transtensional rift area with particularly high seismicity (Lin et al., 2007; Hauksson et al., 2012; Lin, 2013). The main San Andreas fault (mSAF) is located on the northeast side of the Durmid Hills and has been thoroughly studied (Dibblee, 1954, 1997; Babcock, 1969, 1974; Bilham and Williams, 1985; Bürgmann, 1991; Sylvester et al., 1993; Lindsey and Fialko, 2013; Janecke et al., 2018). The rocks southwest of the mSAF consist of highly folded Pliocene–Pleistocene deposits (Babcock, 1974; Bürgmann, 1991; Markowski, 2016; Janecke et al., 2018) bounded to the southwest by the subsidiary East Shoreline fault strand of the SAFZ. Northeast of the mSAF, the formations are much less deformed (Janecke et al., 2018). The overall structure (Fig. 1) resembles a right-lateral strike-slip duplex (Sylvester, 1988), but the geometry is not fully consistent with a duplex model due to abundant left-lateral cross faults and internal block rotations. Instead, the Durmid Hills structure was interpreted as a ladder structure (Janecke et al., 2018), as defined by Davis (1999) and Schultz and Balasko (2003), where overlapping, E–W- to NW–SE-striking step-over faults rotated along multiple connecting cross faults. The 1–3 km wide Durmid ladder structure consists of multiple internal clockwise-rotating blocks bounded by major en echelon folds and right- and left-lateral cross faults in between the right-slip mSAF and East Shoreline fault strand, indicating a complex termination of the SAFZ around the Brawley Seismic Zone to the southeast (Fig. 1).

3 Methods and data

In our investigation of the Indio Hills, we used Google Earth images and aerial photographs (© Google Earth 2011) as a basis for detailed field and structural analyses (Fig. 2). We mapped and analyzed individual macro- and meso-scale folds and associated faults in Miocene–Pliocene strata both in the field and via imagery analysis. Key horizons of light-colored quartz sandstone and carbonate rocks in the Palm Spring Formation provide structural markers, notably to correlate bed displacement and fault–fold geometries and kinematics. We address crosscutting relations of the main San Andreas and Indio Hills faults and nearby fold structures. Structural orientation data are obtained from meso-scale folds and faults and are integrated between the areal segments to link a prevalent pattern of deformation into a wider structural architecture (Fig. 2).

4 Results

4.1 Structural overview of the Indio Hills

The study area comprises three major SAFZ-oblique, asymmetric, E–W-trending, moderately west-plunging fold systems having multiple smaller-scale parasitic folds (Fig. 2). The main folds affect most of the Palm Spring Formation in a zone approximately 2 km wide between the main San Andreas and Indio Hills faults (Fig. 2). The northeastern flank of the Indio Hills is structurally different by consisting of a sub-horizontal, NW–SE-trending, open, upright anticline, which trends parallel to the Indio Hills fault (Fig. 2). Similarly, close to the main San Andreas fault, tilted strata of the Palm Spring Formation are folded into a tight, steeply plunging shear fold (folds involving shearing along a plane that is parallel to subparallel to the fold's axial plane; Groshong, 1975; Meere et al., 2013; Fig. 2). At a smaller scale, several subsidiary reverse faults and mostly right-slip step-over faults having orientations both parallel (E–W to NW–SE) and perpendicular (NNE–SSW) to the bounding faults exist within the macro-folded domain. Most of these faults truncate individual SAFZ-oblique folds.

4.2 SAFZ-oblique macro-folds

SAFZ-oblique macro-folds are consistently asymmetric and mostly south-verging, and their axial surfaces are arcuate and right-stepping (Fig. 2). Fold geometries change from open and nearly upright near the main San Andreas fault to kink/chevron styles in the middle part to very tight (isoclinal) and overturned fold styles adjacent to the Indio Hills fault (Figs. 3a–c and S2a–c). These changes in geometry correspond to a change in obliquity of the fold axial surface trace from approximately 60–70° to less than 20° with the Indio Hills fault (Fig. 2). All three macro-folds have axial trends that bend and partly merge into parallelism with the Indio Hills fault. In contrast, moderate to steeply WSW-dipping strata of the Palm Spring Formation are obliquely truncated by the main San Andreas fault. Tighter fold hinges are mapped in the central macro-fold and on the back limb (stretched long limb in an overturned fold) of the Z-shaped southeastern macro-fold (Fig. 2). These folds were not observed northeast of the Indio Hills fault or southwest of the main San Andreas fault.

4.2.1 Northwestern and central macro-folds

The northwestern and central macro-folds define two major compound and arcuate fold systems that affect the entire Palm Spring Formation between the main San Andreas and Indio Hills faults (Fig. 3a–b). They consist of eight subsidiary Z- and S-shaped south-verging anticline–syncline pairs and show fold axes plunging variably but mostly about 30° to the west (Fig. 2). At a large scale, both folds tighten northeastward and display clockwise bend of axial traces from ENE–WSW near the main San Andreas fault to E–W and NW–SE as they approach the Indio Hills fault (Figs. 2 and 3c). Fold hinges in the west are typically symmetric, concentric, and open (Fig. S3a–b), and they become gradually tighter and dominantly Z-shaped kink folds eastward (Fig. S3c). The folds transform into tight, isoclinal, and inverted geometries (Fig. S3d–e) when approaching the central macro-fold back limb (Fig. 3b), and they potentially merge with the SAFZ-parallel anticline less than 200 m from the Indio Hills fault (Fig. 2). From southwest to northeast, the central macro-fold hinge zone displays a corresponding change in geometry, i.e., from symmetric to kink/chevron and to isoclinal overturned styles (Fig. S4a–b), until the folds of the central macro-fold flank the back limb of the southeastern macro-fold (Fig. S4c–d). Bedding surfaces on the fore limb (the shortened inverted limb indicating the direction of tectonic transport in an overturned fold) of the central macro-fold dip steeply or are inverted, whereas strata on the back limb mostly dip gently to the north or northwest, i.e., at a high angle to the bounding faults, and gradually change to northward dip when approaching the Indio Hills fault (Fig. 3c).

Another feature of the central macro-fold is that it is offset by a system of both layer-parallel and bed-truncating faults (Fig. 3b). Strata east of the fault system are affected by a large shear fold having thickened hinges and thinned limbs. The next fold to the north-northeast changes from open to tight, overturned, and locally isoclinal (Fig. S4a–c) and merges with the inverted NE-dipping back limb of the southeastern macro-fold (Fig. 3c). Notably, the consistent eastward tightening of fold hinges occurs within the lower stratigraphic parts of the Palm Spring Formation, whereas conglomerates of the underlying Mecca Formation are only weakly folded (see Sect. 4.4). Furthermore, beds in tighter folds (especially in relatively weak clayish–silty dark mudstone layers) are commonly accompanied by disharmonic folds and

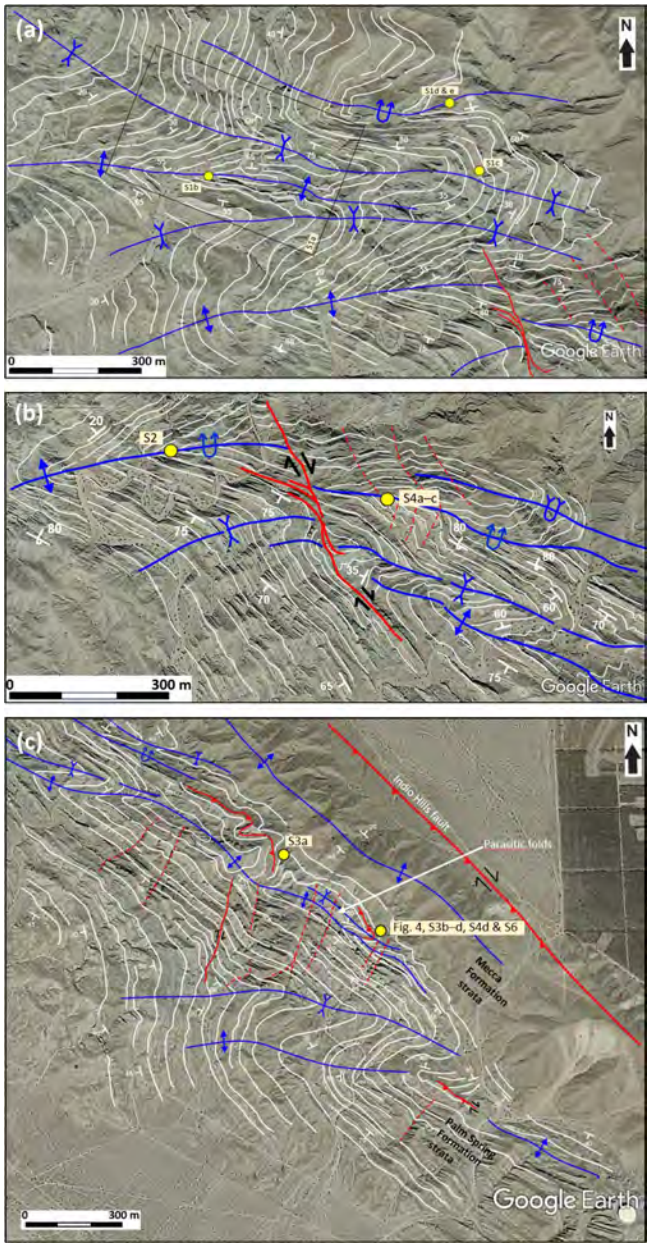

Figure 3. Detailed structural maps showing the architecture and outline of anticline–syncline pairs, traces of bedding and strike and dip orientation, axial surface traces, and fold-related faults in **(a)** the northwestern, **(b)** central, and **(c)** southeastern macro-folds. Note tighter and consistently asymmetric (Z-shaped) geometries of the macro-folds to the east, whereas folds to the west are more open and symmetric. Traces and orientation of bedding show a back limb composed of attenuated shear folds merging from the central macro-fold in the north, whereas the fore-limb is much shorter and more regularly folded. The yellow dots show the location of field photographs. See Fig. 2 for legend and location. Uninterpreted version of the images available as Fig. S2a–c. © Google Earth 2011.

internal structural disconformities. By contrast, more rigid and thicker sandstone beds are more commonly fractured.

4.2.2 Southeastern macro-fold

The southeastern macro-fold is expressed as a kilometer-wide, Z-shaped, open to tight, south-verging syncline–anticline pair showing moderately west-plunging axes and steeply north-dipping axial surfaces (Fig. 3c). Most of the Palm Spring Formation strata on the back-limb trend parallel to the Indio Hills fault and dip about 50–70° to the north, whereas strata in the hinge and fore limb dip about 40–70° to the west-southwest (Fig. 3c). Combined with a relatively narrow hinge zone, these attitudes define the southeastern macro-fold as a chevron type. The axial trend of the syncline–anticline pair is at a low angle (< 20°) to the Indio Hills fault but bends into a NE–SW trend westward with a much higher (oblique) angle to the main San Andreas fault, which cuts off the fore-limb strata (Fig. 2). The southeastern macro-fold is very tight in the north and east and has several smaller-scale tight to isoclinal, strongly attenuated folds on the main back limb that merge from the central macro-fold, thus indicating increasing strain intensity northeastward (see discussion). In contrast to the tightly folded beds of the Palm Spring Formation, bedding surfaces in conglomerates of the underlying Mecca Formation are only weakly folded northeastward and become part of the open SAFZ-parallel anticline close to the Indio Hills fault.

A macro-folded siltstone layer of the lower Palm Spring Formation more than 200 m southwest of the Indio Hills fault (Fig. 4a) contains centimeter-scale upright (sub-horizontal) and disharmonic folds having E–W trend and western plunge (Fig. 4b). These intra-layer folded strata are cut by low-angle reverse faults yielding a NE-directed sense of shear. The upright geometry and the sub-horizontal fold axes (about 5° plunge) of these intra-bed minor folds differ from the SAFZ-oblique folds but resemble those of the macro-scale, SAFZ-parallel NW–SE-trending anticline near the Indio Hills fault. These disharmonic folds are interpreted as intra-detachment folds (see discussion).

4.3 SAFZ-parallel macro-folds

About 100–200 m southwest of the trace of the Indio Hills fault, the conglomerates of the Mecca Formation are folded into a major open anticline, whose axis is parallel to slightly oblique (< 20°) to the Indio Hills fault. This macro-fold is traceable northwestward to where the Indio Hills fault bends northward (Fig. 1). The southwestern limb of the fold marks the transition from the Mecca Formation conglomerate with the overlying Palm Spring Formation on the back limb of the southeastern and central macro-folds (Figs. 2 and S4c). The conglomerate beds are thicker, nearly unconsolidated, and much less internally deformed than the strata of the Palm Spring Formation. The major anticline displays an open,

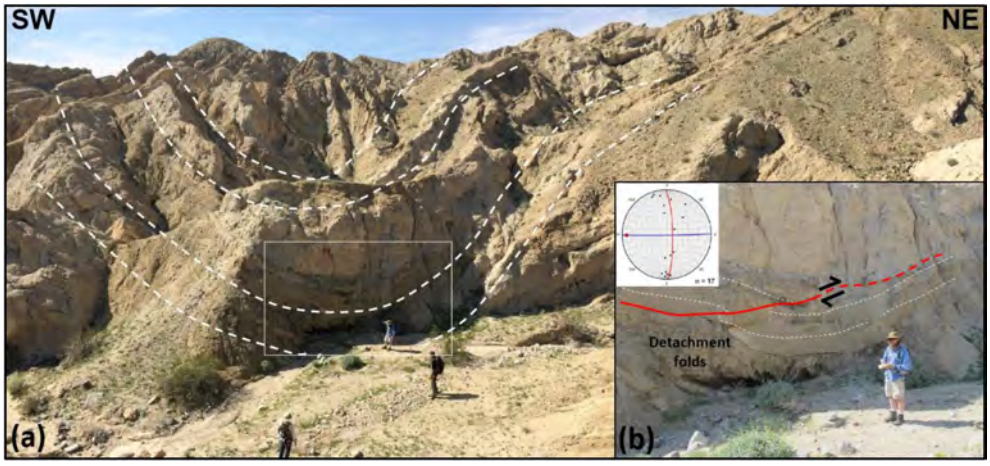

Figure 4. Meso-scale folds and related faults on the back limb of the southeastern macro-fold. See location in Fig. 3c. **(a)** Syncline in upper Palm Spring Formation units adjacent to the SAFZ-parallel macro-fold near the Indio Hills fault. **(b)** Close-up view of the synclinal fold hinge in **(a)**, where a meter-thick sandstone bed is slightly offset by a minor low-angle thrust fault (red line) with NE-directed sense of shear. The minor thrust faults die out in the overlying sandstone bed. The mudstone bed below acts as a décollement layer with internal plastically folded lamination, including disharmonic intra-detachment folds. Structural orientation data of minor centimeter-scale fold limbs in the décollement zone are plotted in a lower hemisphere Schmidt stereonet, indicating E–W-trending fold axes and a sub-horizontal axial surface (average great circle in red and fold axis as a red dot).

symmetric, partly box-shaped, NW–SE-trending, upright geometry with 2–3° plunge of the fold axis to the northwest. Outcrops on the SW-dipping limb of the anticline (Fig. 3c) are cut by a SW-dipping reverse fault system that is subparallel to the Indio Hills fault (Fig. S5a). These reverse faults may be linked with the reverse fault in folded strata of the Palm Spring Formation on the southeastern macro-fold back limb described above (Fig. 4). The upright geometry and sub-horizontal NW–SE-trending axes of related small-scale folds in a mudstone layer (Fig. 4) resemble that of the SAFZ-parallel anticline.

A couple of major synclines showing axial traces parallel to the main San Andreas fault are also well displayed on Google Earth images (Figs. 5 and S6). These folds affect WSW-dipping strata of the Palm Spring Formation on the broadened western part of the northwest and central macro-folds. Fold geometries are tight and asymmetric, with wavelengths less than 200 m, and presumably steep NW-plunging axes. The local appearance and sheared geometry of these folds contrast both with the broad SAFZ-oblique folds near the main San Andreas fault and with that of the upright SAFZ-parallel anticline near the Indio Hills fault.

4.4 Major and minor faults

Fold-related brittle faults exist both in granitic basement and in sedimentary rocks of the Mecca and Palm Spring formations in the study area. Such faults display narrow damage zones less than 1 m wide and are geometrically related to either SAFZ-oblique or SAFZ-parallel macro- and meso-scale folds, or they are orthogonal to the SAFZ and related faults. With the exception of the main San Andreas and Indio Hills faults, brittle faults are generally difficult to trace laterally, but, where preserved, they display centimeter- to meter-scale strike-slip and/or reverse dip-slip displacement. Macro-scale fault orientations and kinematics in sedimentary rocks are more variable than in basement rocks but commonly strike WNW–ESE to N–S and show moderate–steep dips to the northeast (Fig. 2). Subsidiary meso-scale faults include high-angle SW- and SE-dipping strike-slip faults and low-angle SW-dipping thrust faults. We describe the Indio Hills and main San Andreas faults, strike-slip faults, and thrust faults in sedimentary strata, and fractures in basement rocks northeast of the Indio Hills fault.

4.4.1 Indio Hills and main San Andreas faults

Along the Indio Hills fault, poor exposures make it difficult to measure fault strike and dip directly, but Google Earth images suggest a rectilinear geometry in map view relative to the uplifted sedimentary strata to the southwest (Fig. 2). The fault strikes mainly NW–SE and is subparallel to the northeastern flank of the Indio Hills. Farther southeast, it probably merges with the main San Andreas fault (Fig. 1; Tyler, 1974). In the southeastern part of the study area (Fig. 2), the Indio Hills fault is most likely located between an outcrop of basement granite and the first outcrops of overlying strata of the Palm Spring Formation. The granite there is highly fractured and cut by vein and joint networks (see description below), as may be expected in the damage zone of a major brittle fault.

Like the Indio Hills fault, fault-plane dip and strike of the main San Andreas fault must be inferred indirectly. The main

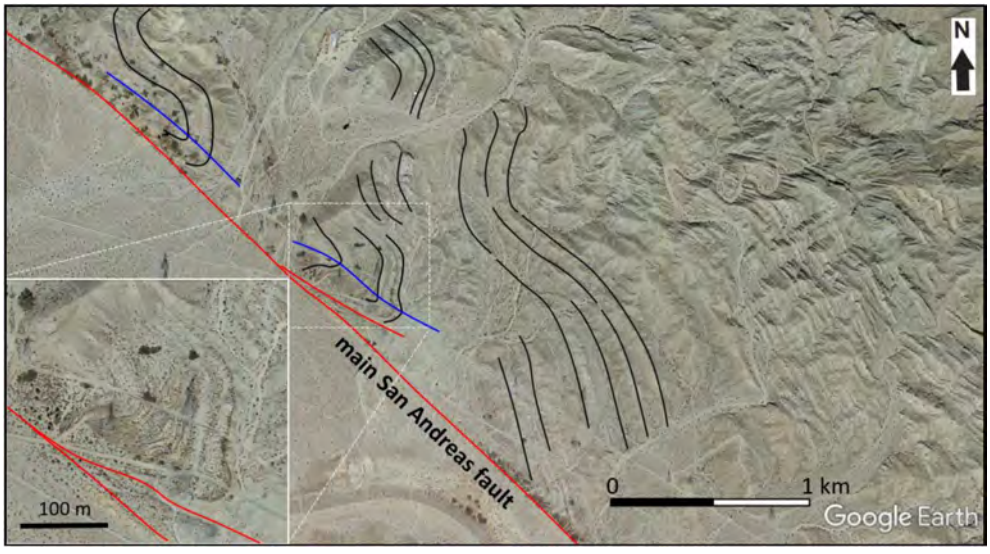

Figure 5. Interpreted SAFZ-parallel macro-folds (synclines) adjacent to the main San Andreas fault, which affect the southern limb of earlier (en echelon) macro-folded and tilted strata of the Palm Spring Formation. Note shear fold geometry in the inset map with a thickened hinge zone and thinned limb to the south, steeply plunging axis, and axial trace parallel to the main San Andreas fault. See Fig. 2 for location. Uninterpreted version of the image available as Fig. S4. © Google Earth 2011.

San Andreas fault in the study area strikes WNW–ESE and is sub-vertical based on its consistent rectilinear surficial trace and because it truncates both back- and fore-limb strata on most of the SAFZ-oblique macro-folds (Fig. 2). Thus, the main San Andreas fault does not seem to have had major impact on the initial geometry and development of the macro-folds in the Indio Hills. However, notable exceptions include displacement by the main San Andreas fault of the two shear folds on the southern flank of the macro-folds (Fig. 5), and a consistent counterclockwise bend of most axial traces of the macro-folds (Fig. 2).

4.4.2 Strike-slip faults in folded sedimentary strata

One major brittle fault set striking NW–SE and dipping steeply to the northeast has developed on the central macro-fold (Figs. 3b and 6). The faults splay out from a bedding-parallel core zone subparallel to steeply SW-dipping mudstone–siltstone layers on the southern limb of the central macro-fold and then proceed to truncate NW-dipping sedimentary strata and offset the hinge of a macro-fold by ca. 70 m right-laterally before dying out (Fig. S7a–b). The fault damage zone is traceable for more than 1 km along strike as a right-slip fault which displaces the hinge of a major, tight, asymmetric, shear-like (similar style) fold (Figs. 6 and S8). The shear-folded sedimentary strata bend clockwise toward the main fault, thus supporting dominant right-lateral slip (Fig. 6). Minor faults branch out from the fault core zone and either die out in the macro-fold hinge and/or persist as bedding-parallel faults for some distance on the southern limb of the macro-fold (Fig. 6).

At a smaller scale, the folded and tilted strata of the Palm Spring Formation are commonly truncated by sets of steep NW–SE-striking right-lateral and NNE–SSW-striking left-lateral faults, displaying meter- to centimeter-scale offsets (Fig. S7b–d). These minor faults generally dip steeply to the northeast to east-northeast, i.e., opposite to most bedding surfaces, which dip southwest (Fig. 3b) and, in places, develop reddish fault gouge along strike. Furthermore, these minor faults typically cut sandstone beds and flatten, and/or die out within, mudstone beds, which restricts their lateral extent to a few decimeters–meters. Kinematic indicators, such as offset of bedding surfaces and fold axial surfaces, yield mostly right-slip displacements, in places with minor reverse components. In some localities, on fold limbs within thick and competent sandstone beds, such minor right- and left-slip faults appear to form conjugate sets (Fig. S7b and d) that may have developed simultaneously. In addition, NNE–SSW-striking, ESE-dipping faults and/or semi-brittle kink bands sub-orthogonal to the SAFZ are well displayed in the southeastern macro-fold (Figs. 3c and S7e) and cut bedding surfaces at high angles with left-slip displacement, therefore potentially representing cross faults between segments/splays of the SAFZ system.

4.4.3 Reverse and thrust faults in folded sedimentary strata

Reverse and thrust faults are common and traceable on the back limb of the central and southeastern macro-folds near the SAFZ-parallel anticline and the Indio Hills fault, but not recorded in areas close to the main San Andreas fault.

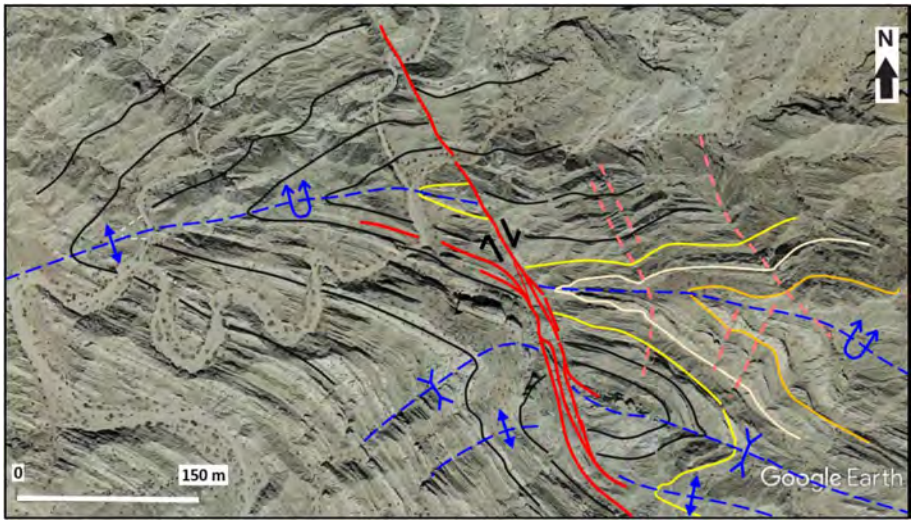

Figure 6. Interpreted satellite image of the central macro-fold showing right-lateral offset of the entire fold hinge/axial surface (upper left dashed blue line) by a NNW–SSE-trending, NE-dipping strike-slip fault (red lines). Note that the fault merges out from a layer in the southern limb of the macro-fold (black lines) and continues as a right-lateral fault. Offset geological markers include thick sandstone beds (yellow, white, light brown lines) and the fold axial surfaces of a second syncline fold farther south (lower right, dashed blue lines). Note that the syncline axial trace dies out to the southwest and that kink bands acting as cross faults crop out in the eastern part of image (dashed pink lines). Uninterpreted version of the image available as Fig. S8. © Google Earth 2011.

Reverse faults strike mainly NW–SE and dip gently to the southwest, although subsidiary gently NE-dipping faults exist. An example is the low-angle reverse fault that propagates out of the syncline on the southeastern macro-fold (Fig. 4) and yields a NE-directed sense of shear. This thrust fault may continue westward into the central macro-fold (Fig. 3b), where reverse offset of SW-dipping strata of the Palm Spring Formation constrains vertical displacement from about 10–15 m (Fig. S5a), though offset is only a few centimeters in the southeast (Fig. 4). This fault system has a listric geometry, and internal splay faults die out in thick silt- to mudstone layers. The low-angle faults seem to develop almost consistently near major fold hinge zones and propagate northeastward as out-of-the-syncline thrusts (Figs. 4 and S5a).

In sandstone beds on the north-dipping limb of the major syncline, minor-scale thrust faults offset asymmetric fold hinges (Fig. S7c) and yield down-to-the-north (normal) sense of shear if the strata are rotated to a horizontal position (Fig. S9). An opposite effect is apparent for a conjugate set of minor normal faults in a small-scale graben structure on the steep, north-dipping layer, which defines a set of reverse faults when rotating the sedimentary strata to horizontal (Figs. S7d and S9).

4.4.4 Fractures and faults in basement rocks north of the Indio Hills fault

Basement-rock exposures in the Indio Hills are limited to a single, approximately 50 m long chain of outcrops located in the southeasternmost part of the study area (Fig. 2). These outcrops of massive granite are heavily fractured with mostly steep to sub-vertical sets that strike dominantly NE–SW to ENE–WSW and subsidiary NW–SE to NNW–SSE (see stereoplot in Fig. 2). Kinematic indicators are generally lacking, but in highly fractured areas, centimeter-thick lenses of unconsolidated reddish gouge are present, comparable to fault rocks observed in Palm Spring Formation sedimentary rocks and corresponding to similar small-scale strike-slip and reverse faults in the basement granite. The fault sets in granitic basement rocks trend parallel to fault sets in sedimentary strata southeast of the Indio Hills fault (see stereoplots in Fig. 2) and are therefore suggested to have formed due to similarly oriented stress.

5 Discussion

5.1 Structural evolution of SAFZ-oblique folds

We mapped and analyzed three macro-scale fold systems between the Indio Hills and main San Andreas faults. In map view (Fig. 2), the folds are right-stepping, and each fold set is increasingly asymmetric (Z-shaped) and sigmoidal towards the Indio Hills fault in the northeast. Based on these properties, we interpret the fold sets as modified SAFZ-oblique en echelon macro-folds. Various investigators (Babcock, 1974; Miller, 1998; Titus et al., 2007; Janecke et al., 2018; Bergh et al., 2019) describe similar fold geometries in sedimentary strata from many other segments of the SAFZ and are interpreted as structures formed by right-lateral displacement between two major fault strands. However, the

present fold-orientation data in the Indio Hills (Fig. 2) do not correspond with a uniform simple shear model in between two active strike slip faults because the long axis of the strain ellipse is not consistently about 45° to the shear zone as expected (Sanderson and Marchini, 1984; Sylvester, 1988). Instead, fold geometries vary both across and along strike; e.g., axial surface traces of dying-out macro-fold hinges are at high obliquity angles (> 50–$65°$) in the southwest, whereas they are at much lower angles (< 20–$30°$) and merge with sigmoidal-shaped patterns against the Indio Hills fault (Fig. 2). Thus, we propose that the SAFZ-oblique macro-folds in Indio Hills rather evolved from a single boundary fault (Indio Hills fault) being progressively more active through time. For example, a model in which the folds initially splayed out from an early active Indio Hills fault through right-laterally distributed displacement (compare with Titus et al., 2007) is consistent with fold hinges extending outward south of the Indio Hills fault and dying out (broadening) away from the fault in a several-kilometer-wide damage zone (Fig. 2). Fold propagation outward from the Indio Hills fault is supported by the increased structural complexity of the fold geometries towards the Indio Hills fault. Furthermore, the initial upright en echelon folding clearly occurred after deposition of the entire Palm Spring Formation because of the involvement in folding of the Bishop Ash and of adjacent strata possibly of the Ocotillo Formation (i.e., maximum age of 0.76 Ma – earliest late Pleistocene; Fig. 2 and Table 1). Should the whole Ocotillo Formation be folded in the Indio Hills, the maximum age constraints could be narrowed to < 0.6–0.5 Ma based on magnetostratigraphic ages for the upper part of the Ocotillo Formation (Kirby et al., 2007). By contrast, the main San Andreas fault truncates both limbs of the open-style en echelon folds (Fig. 2), which therefore indicates younger deformation along this fault.

The moderate–steep westward plunge of all three macro-folds ($\geq 30°$), however, shows that the presumed initial horizontal fold hinges rotated into a steeper plunge. Such steepening may be due to, e.g., progressive shortening above a deep-seated fault, a hidden splay of the Indio Hills fault, or an evolving stage of distributed shortening (folding) adjacent to the master strike-slip faults (e.g., Bergh et al., 2019), with gradually changing stress–strain orientation through time and/or due to structural tilting in the hanging wall of the Indio Hills fault. This kind of fold reworking favors a situation where the northwestern and central macro-folds were pushed up and sideways (right-laterally), following the topography and geometry of an evolving transpressional uplift wedge (i.e., a contractional uplift formed synchronously with successively simple shear transpression to balance internal forces in a crustal-scale critical taper; Dahlen, 1990). The corresponding eastward-tightening, enhanced shear folding and recurrent SW-directed overturned geometries of the central macro-fold on the back limb of the southeastern macro-fold near the Indio Hills fault (Fig. 3b) support this idea.

We propose a progressive model that changes from distributed (en echelon folding) to partly partitioned, i.e., pure shear (shortening) plus simple shear (strike-slip) deformation (Fig. 7), as inferred for other parts of the SAFZ, e.g., in the Mecca Hills (Bergh et al., 2019). In this model, the tight to isoclinal fold geometries to the northeast (Fig. 3b) may account for progressively more intense shortening near the Indio Hills fault, whereas coeval strike-slip faulting affected the already folded and steeply dipping strata of the lower Palm Spring Formation (Fig. 6). This model would favor shortening to have evolved synchronously with renewed strike-slip shearing adjacent to the Indio Hills fault and/or on a blind fault below the contact between the Mecca Formation and overlying Palm Spring Formation, because the Mecca Formation is much less deformed (Fig. 3c). Alternatively, the more mildly deformed character of the Mecca Formation conglomerate may arise from its homogeneity, which contrasts with alternating successions of mudstone–siltstone and sandstone of the Palm Spring Formation prone to accommodating large amounts of deformation and to strain partitioning. Regardless, such reshaping of en echelon folds is supported by analog modeling (McClay et al., 2004; Leever et al., 2011a, b), suggesting that partly partitioned strain may lead to a narrowing of fold systems near a major strike-slip fault (i.e., Indio Hills fault), whereas widening away from the fault indicates still ongoing distributed deformation. Partly partitioned deformation is supported by the tight to isoclinal and consistent Z-like geometry of smaller-scale folds present on the back limb of the central and southeastern macro-folds (Fig. 3b–c), indicating that they are all parasitic folds and related to the same partly partitioned shear-folding event. Where S- and Z-like fold geometries are present, these minor folds may have formed by buckling in an early stage of en echelon folding. An alternative interpretation is that the tight, reshaped parasitic folds are temporally linked to the SAFZ-parallel macro-fold south of the Indio Hills fault (Fig. 3c; see next section).

5.2 Structural evolution of SAFZ-parallel folds

The SAFZ-parallel anticline differs significantly in geometry from the en echelon macro-folds and associated parasitic folds by having an upright and symmetric geometry $< 20°$ oblique to the Indio Hills fault. Thus, it resembles that of a fault-propagation fold in a more advanced partitioned transpressional segment of the SAFZ (e.g., Titus et al., 2007; Bergh et al., 2019). We suggest that this fold formed by dominant NE–SW-oriented horizontal shortening, i.e., at high obliquity to the main Indio Hills fault (near-orthogonal pure shear), and/or as a fault-related fold above a buried major reverse (SW-dipping) oblique-slip splay of the Indio Hills fault at depth (e.g., Suppe and Medwedeff, 1990). The timing might be after the tight reworking of en echelon folds in the late Pleistocene. The idea of a late-stage highly oblique pure-shear overprint onto the macro-folds is supported by small-

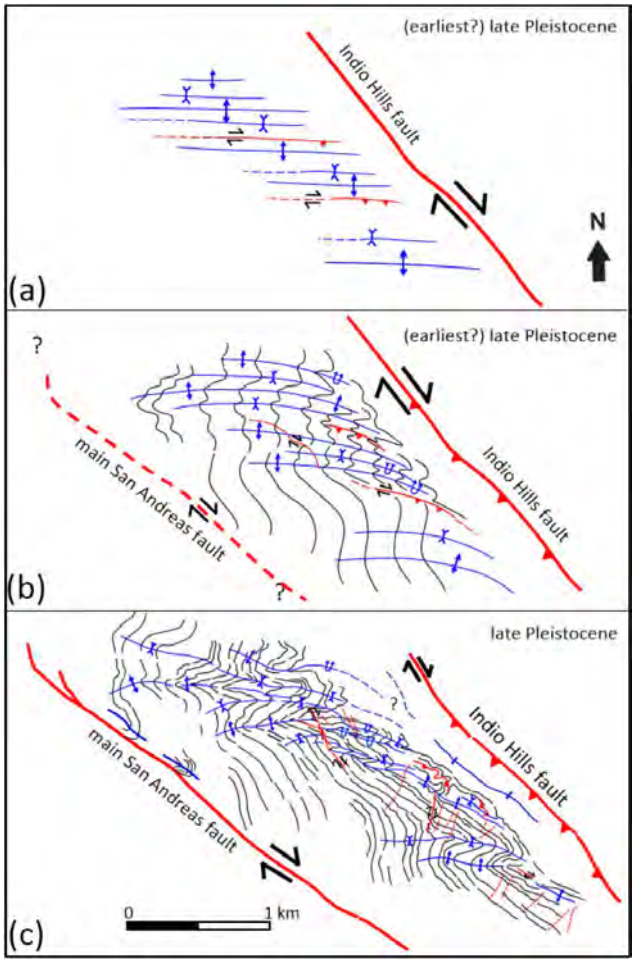

Figure 7. Model illustrating the progressive uplift/inversion history of the Indio Hills presuming a narrow time interval between formation of all structures in the area, except for the main San Andreas fault and associated folds. **(a)** Early distributed transpressional strain and formation of three major en echelon-oriented macro-folds, several subsidiary parasitic anticline–syncline fold pairs, and bed-parallel strike-slip and reverse (décollement) faults initiating at a high angle (ca. 45°) to the Indio Hills fault. **(b)** Incremental partly partitioned transpression when the Indio Hills fault started to accommodate oblique-reverse movement forcing previous horizontal en echelon macro-folds and parasitic folds to tighten, overturn, and rotate into steeper westward plunges. Note also sigmoidal rotation of axial traces on the back limbs of the macro-folds to low angle (< 20–30°) with the Indio Hills fault. **(c)** Late-stage advanced strain partitioning with dominant shortening component on the oblique-reverse Indio Hills fault and right-lateral slip on the main San Andreas fault. Notice the formation of the anticline parallel to the Indio Hills fault, subsidiary fold-internal strike-slip faults, and conjugate cross faults and kink bands that overprinted the macro-folds. Legend as in Fig. 2.

scale upright folds located within the tight en echelon syncline on the back limb of the modified central macro-fold system (Fig. 4). The NW–SE trend, upright style, and negligible plunge of the fold axes indicate that these folds may be superimposed on the steeper plunging and reshaped en echelon folds and/or that they formed in progression to an increased component of NE–SW shortening on the Indio Hills fault. Nonetheless, these folds may have formed simultaneously with the en echelon macro-folds in the (earliest?) late Pleistocene (Table 1) due to uncertain (not fully understood) crosscutting relationships.

Progressive NE–SW-oriented contraction may have triggered formation of the upright SAFZ-parallel anticline adjacent to the Indio Hills fault (Figs. 2 and 3c). The fault then acted as a SW-dipping thrust fault with top-NE displacement. The oblique shortening then led to a certain amount of uplift near the Indio Hills fault and possibly also accomplished the overturning of folds on the northeastern back limb of the central and southeastern macro-fold. A similar mode of advanced partitioned shortening was proposed for SAFZ-parallel fold structures in central and southern California (Mount and Suppe, 1987; Titus et al., 2007; Bergh et al., 2019). Our results are supported by stress orientation data acquired by Hardebeck and Hauksson (1999) along a NE–SW-trending profile across the Indio Hills. They recorded an abrupt change in the maximum horizontal stress direction from about 40° oblique to the SAFZ around the main San Andreas fault to about 70° oblique (i.e., sub-orthogonal) farther northeast, near the Indio Hills fault, which supports the change in attitude and shape of macro-fold geometries that we have outlined. Shortening and strike-slip partitioning, however, would require synchronous right slip on another major fault strand, e.g., the main San Andreas fault, a hypothesis that is supported by the recorded late-stage (i.e., late Pleistocene) shear folding there (Fig. 5).

5.3 Fold and fault interaction, evolution, and relative timing

In this section we use the geometry and kinematics of folds and faults in the southern Indio Hills to reconstruct the tectonic history of the area, not only of the inverted late Cenozoic basin but also about strike-slip and dip-slip faults that bound the basin. Essential tectonic events include (1) extensional normal faulting along the Indio Hills fault in the mid-Miocene–Pliocene (ca. 15–3.0 Ma), (2) reactivation of the Indio Hills fault as a right-lateral to oblique-reverse fault in the (earliest?) late Pleistocene to present day (< 0.76 Ma), and (3) right-lateral movement along the main San Andreas fault in the late Pleistocene to present day (< 0.76 Ma; Table 1).

Prior to inversion and uplift of the Indio Hills, the Indio Hills fault most likely acted as a SW-dipping, extensional, basin-bounding normal fault. Indications of an early-stage episode of extension are shown by micro-fault grabens in steeply dipping layers (Figs. S5d and S6); by the deposition

and preservation of sedimentary strata of the Palm Spring and Mecca formations southwest of the Indio Hills, whereas they were eroded or never deposited northeast of the fault; and by fining upwards of the stratigraphic units from conglomerates in the Mecca Formation to coarse-grained sandstone in the lower parts of the Palm Spring Formation. In addition, the flat geometry of micro thrust faults (e.g., Fig. S5b–c) suggests that they were rotated during macro-folding. Restoration of all micro faults in their initial position prior to macro-folding shows that some of these faults exhibit normal kinematics with associated syn-tectonic growth strata (Figs. S5d and S9). Alternatively, the Indio Hills fault dips northeast and uplifted the granitic basement rocks in the hanging wall to the northeast, followed by erosion of the overlying Mecca, Palm Spring, and Ocotillo formations there (Fig. 1). We favor a basin geometry and formation similar to that of the Mecca Hills, where down-SW slip along the Painted Canyon fault was inferred in the (Miocene?–) Pliocene (McNabb et al., 2017), and of the transtensional Ridge Basin though having opposite vergence (Crowell, 1982; Ehman et al., 2000) with a steep SW-dipping normal fault that was progressively reactivated as an oblique-slip reverse/thrust fault during basin inversion. Formation of the Indio Hills fault as a normal fault probably occurred in mid-Miocene times during extension related to the opening of the Gulf of California (Stock and Hodges, 1989; Stock and Lee, 1994) as proposed for the Salton Trough (Dorsey et al., 2011, and references therein).

Right-lateral to right-lateral-reverse movement along the Indio Hills fault that led to the formation of the SAFZ-oblique en echelon macro-folds also supports a steeply dipping character for the precursory Indio Hills fault. The change to a right-lateral-reverse fault is further supported by the presence of both meso-scale strike-slip and thrust faults having similar NW–SE strikes (Figs. 4, S4c, and S5a). The increased reverse (and decreasing right-lateral) component of faulting may have triggered rotation of the en echelon macro-fold axes to a steeper plunge, reshaped the open asymmetric folds into tight overturned folds, and caused gentle buckling of strata in the nearby SAFZ-parallel anticline. Hence, the Indio Hills fault ultimately functioned as an oblique-slip thrust oblique to the transform plate boundary in the late Pleistocene, which is supported by oblique maximum horizontal stress near the Indio Hills fault (ca. 70°; Hardebeck and Hauksson, 1999), while the main San Andreas fault simultaneously accommodated right slip during this period.

By contrast, the last episode of movement along the main San Andreas fault clearly postdates en echelon folding, from its truncating attitude (Fig. 2). In addition, the counterclockwise bending of the axial traces into an ENE–WSW trend towards the southwest suggests that a distributed component of off-fault deformation affected the area around the main San Andreas fault in its early kinematic stages in the late Pleistocene. The refolding of the southwest limb of the central macro-fold near the main San Andreas fault (Fig. 5) also favors a late-stage activation of this fault in the late Pleistocene (i.e., after the initial transpressional slip events along the Indio Hills fault in the – earliest? – late Pleistocene). Possibly as a consequence of a longer period of activity, and as suggested by relatively higher topographic relief and more intensely folded sedimentary strata in the vicinity of and along the Indio Hills fault than along the main San Andreas fault, the former probably accommodated significantly larger amounts of uplift than the latter. This implies a southwest-tilted geometry for the Indio Hills uplift.

Minor faults in the Indio Hills provide additional input to resolve the spatial, temporal, and kinematic relations between macro-fold and fault interaction. We analyzed minor fault-related folds (Fig. S5c), which, in their current position on steep north-dipping beds, define down-to-the-north displacement. However, when rotating the sedimentary strata to horizontal (Fig. S9), the fault-related folds define a low-angle fold-and-thrust system. These geometric relationships suggest that the minor folds and faults (other than right-slip faults) pre-date (or were coeval with) the SAFZ-oblique macro-folding event and that they formed initially as internal fractures due to N–S-oriented shortening when the sedimentary strata were still horizontal. This implies that some partitioning (e.g., SAFZ-parallel small-scale thrust faults) occurred simultaneously with distributed deformation (e.g., SAFZ-oblique en echelon macro-folds).

Further, our field data suggest that minor right-slip faults evolved synchronously and parallel with the E–W-trending en echelon fold limbs, propagating through rheologically weaker mudstone beds that flowed plastically and acted as slip surfaces during distributed deformation. Later or simultaneously, these faults escaped from the mudstone beds and propagated as NW–SE-striking right-slip faults adjacent to tightened shear folds during partly partitioned deformation and finally ended up with truncation of the SAFZ-oblique folds (Figs. 6 and S7a–c).

The presence of out-of-the-syncline reverse/thrust faults relative to the reshaped and tightened SAFZ-oblique macro-folds (Figs. 4 and S5a and d), where SW-dipping thrust faults formed (sub-) parallel to the Indio Hills fault, and the related upright anticline (Fig. 3c) suggests successive distributed and partly partitioned strain in the study area. The proximity and superimposed nature of reverse/thrust faults relative to the reshaped en echelon folds suggest that they utilized modified fold hinges and steeply tilted limbs as preexisting zones of weakness. Despite the uncertainty around the crosscutting relationship between the SAFZ-parallel anticline and the SAFZ-oblique en echelon macro-folds, the low-angle thrust and intra-detachment folds in the southeastern macro-fold (Fig. 4) indicate that such thrust detachments may have already formed during (early?) distributed deformation, i.e., that distributed and partitioned deformation occurred simultaneously and/or progressively (see phases 1 and 2 in Table 1).

The conjugate WNW–ESE- to NNW–SSE-striking right-slip and NNE–SSW-striking left-slip faults and kink band

feature truncate strata on both macro-fold limbs (Fig. 3b–c) with an acute angle perpendicular to the macro-folded and tilted Palm Spring Formation strata (e.g., Fig. S7e). Thus, they formed together with or after the en echelon macro-folding (< 0.76 Ma).

5.4 Tectonic model

In this section we use detailed structural analysis of folds and faults in the southeastern Indio Hills to outline the structural history of the tectonic uplift itself, evaluate it in terms of what is known about strain budgets within the southern San Andreas fault system, link it to nearby structures (eastern California shear zone and Landers–Mojave Line), and integrate the local structural history into a structural synthesis for the southern San Andreas fault zone in the past 4 Myr.

Our field and structural data support inversion and uplift of the Indio Hills involving progressive or stepwise stages of folding and faulting, incorporating a switch from distributed to partly partitioned transpression (Fig. 7). Prior to inversion in late Pleistocene time, the Indio Hills fault may have been a steep SW-dipping normal fault that downthrew (Miocene?–) Pliocene sedimentary strata against granitic basement rocks in its footwall to the northeast. These basement rocks were partly eroded in the footwall of the fault. In the hanging wall of the fault, strata of the Mecca Formation were deposited in the Pliocene, most likely at 3.7–3.0 Ma, and the lower and upper members of the Palm Spring Formation respectively at 3.0–2.3 and 2.6–0.76 Ma, as suggested from paleomagnetic studies in the Mecca Hills (Chang et al., 1987; Boley et al., 1994; McNabb et al., 2017).

Early inversion involved distributed transpressional strain triggered by right-lateral slip along the Indio Hills fault (Fig. 7a). Three macro-scale upright en echelon folds and associated parasitic folds formed in loosely consolidated sedimentary rocks of the Mecca and Palm Spring formations after the latter was deposited (< 0.76 Ma), i.e., probably in earliest late Pleistocene time (Table 1). The fold set evolved oblique to the main strand of the SAFZ and formed a right-stepping pattern of E–W-oriented axial surfaces that trend at a high angle (45°) to the bounding Indio Hills fault due to uniform simple shear (e.g., Sanderson and Marchini, 1984; Sylvester, 1988). This is notably observed in the less deformed southwestern part of the study area (Fig. 2) near the main San Andreas fault, where the macro-folds still display their initial non-plunging geometries. Bed-internal minor fold and fault systems in weak mudstone beds (Figs. 4 and S5a) may have formed parallel to the E–W-trending en echelon fold traces, as thrust detachments due to oblique N–S shortening when strata were horizontal and/or strike-slip faults on the fold limbs. In addition, minor (bed-internal) SAFZ-parallel thrusts and folds formed prior to or together with the en echelon macro-folds (Figs. S4b–c and S9a–b), thus suggesting minor strain partitioning.

Further deformation in the late Pleistocene led to gradual change from mostly distributed with minor partitioned deformation to partly partitioned shortening and right-lateral faulting and folding (Fig. 7b), probably since the Indio Hills fault started to accommodate an increasing amount of reverse slip, thus acting as an oblique-slip right-lateral-reverse fault, and where the main San Andreas fault did not yet play a major role. The main result was tightening of the macro-folds toward the Indio Hills fault and clockwise rotation of fold axes to a steeper westerly plunge due to increased shear folding, whereas en echelon upright folding continued in the southwest (Fig. 7b). Increased shortening and shearing reshaped the macro-folds and their back limb folds to tight, isoclinal, and partly overturned folds with consistent Z-style and sigmoidal axial-surface traces near the Indio Hills fault (Fig. 7b). The sigmoidal pattern of the WNW–ESE-trending en echelon macro-folds formed at a much lower angle with the Indio Hills fault (< 20–30°) than farther southwest (60–70°). Furthermore, the incremental component of lateral strain is recorded as progressively cross-cutting NW–SE-striking strike-slip shear faults terminating with local truncation of the central macro-fold (see Fig. 7c and Sect. 5.5). Uplift of the Indio Hills in the late Pleistocene (because the earliest late Pleistocene 0.765 Ma Bishop Ash is involved in folding; Sarna-Wojcicki et al., 2000; Zeeden et al., 2014) was marked by a gradual switch to more kinematically evolved transpressional strain partitioning, where the dominant shortening component was accommodated by right-lateral-oblique top-NE thrusting along the Indio Hills fault and major strike-slip movement along the main San Andreas fault (Fig. 7c and phase 3 in Table 1). NE-directed oblique thrusting on the Indio Hills fault and related minor, reverse, out-of-the-syncline faults led to uplift, which resulted in formation of a major anticline parallel to the Indio Hills fault in sediments of the Mecca Formation (see anticline closest to Indio Hills fault in Figs. 3c and 7c). With increasing partitioning, slip parallel to the transform plate boundary was accommodated by right slip along the linear main San Andreas fault, where sub-vertical folds formed locally, and presumed antithetic conjugate kink band sets of right- and left-slip cross faults affected the entire uplifted area.

We favor a progressive evolution from distributed to partly partitioned deformation as presented in Fig. 7a–c, although overlapping and synchronous formation of various structures may have occurred (overlapping of phases 1 and 2 in Table 1), at least locally (except for the late-stage main San Andreas fault and related shear folds; phase 3 in Table 1). The overlapping and synchronous formation of structures is based on uncertainties in our field data, e.g., variable cross-cutting relations of early bedding-parallel strike-slip and thrust faults and en echelon macro-folds (Figs. 4, 6, and S5c–d and S7), and also based on the spatial variations in the direction of maximum horizontal stress across the Indio Hills at present, from 40° oblique to the boundary faults near the main San

Andreas fault to 70° oblique near the Indio Hills fault (Hardebeck and Hauksson, 1999).

Our observations of mostly lateral movement along the main San Andreas fault (i.e., southeastern continuation of the Mission Creek fault) and the proposed late Pleistocene to present-day age for deformation in the southeastern Indio Hills are consistent with work by Keller et al. (1982). A major difference between the northwestern and southeastern Indio Hills is the relatively tighter macro-folding over a narrower area and more intense character of deformation in between the two bounding faults in the southeastern Indio Hills (Figs. 2 and 3; Keller et al., 1982; Lancaster et al., 2012).

The right-lateral-reverse character of the Indio Hills fault and its role in our kinematic model for basin inversion in the southern Indio Hills are further supported by the relationship of the Indio Hills fault with the eastern California shear zone, which merge together north of the study area where the Indio Hills fault bends into a NNW–SSE strike along the Landers–Mojave Line (Dokka and Travis, 1990a, b; Nur et al., 1993a, b; Thatcher et al., 2016). Recent activity along the Landers–Mojave Line recorded as six–seven earthquakes with $M > 5$ between 1947 and 1999 (Fig. 1; Nur et al., 1993a, b; Du and Aydin, 1996; Spinler et al., 2010) indicates that a throughgoing NNW–SSE-striking fault crosscuts the Pinto Mountain fault (Nur et al., 1993a, b; Rymer, 2000). Notably, the 1992 Joshua Tree earthquake occurred along the NNW–SSE-striking, west-dipping West Deception Canyon fault (Rymer, 2000 and references therein), which merges with the (probably southwest-dipping) Indio Hills fault in the south (see Fig. 1 in Rymer, 2000). Therefore, we propose that the Indio Hills fault may be one of several faults to transfer displacement from unsuitably oriented NW–SE-striking right-slip faults in the north, such as the Calico and Camp Rock faults, to the main SAFZ strand in the south (Fig. 1).

Farther southeast along strike, the Indio Hills and main San Andreas faults merge along a dextral freeway junction, i.e., a junction of three dextral fault branches (sensu Platt and Passchier, 2016, and Passchier and Platt, 2017), which may have enhanced wedge-shaped transpressional uplift of the Indio Hills after the late formation of the main San Andreas fault in the late Pleistocene (Fig. 8a–c and Table 1). However, counterclockwise rotation of the Indio Hills block and related structures in map view as predicted in a dextral freeway junction (Platt and Passchier, 2016; Passchier and Platt, 2017) were not recorded by our field data (except along the main San Andreas fault due to localized right-slip along the fault; see sub-vertical shear fold in Fig. 5). This may be due in part to the late formation of the main San Andreas fault (< 0.76 Ma, i.e., late Pleistocene), i.e., clockwise rotation (in map view) of the fold and fault structures due to right-lateral slip along the Indio Hills fault and to the oblique-slip character of the Indio Hills fault. Thus, the dextral freeway junction in the Indio Hills may be more of a transitional nature. Instead of major counterclockwise rotation of the Indio Hills block in map view, the accretion of material toward the fault junction due to right slip along the main San Andreas fault is probably partly accommodated by the dominant vertical slip component along the Indio Hills fault, leading to further uplift near the junction (i.e., clockwise rotation in cross section).

5.5 Regional comparison and implications

The proposed progressive tectonic model for the Indio Hills uplift has wide implications when compared and correlated with other fault strands of the SAFZ bounding uplifted domains along strike in the Coachella and Imperial valleys (Fig. 8a–c) and in explaining lateral variations in fault architectures, kinematic evolution and timing, deformation mechanisms, and areal segmentation (Sylvester and Smith, 1987; McNabb et al., 2017; Janecke et al., 2018; Bergh et al., 2019). Here we compare and contrast the structural evolution of the southeastern Indio Hills with that of nearby tectonic uplifts (Mecca Hills and Durmid Hills).

5.5.1 Comparison with the Mecca Hills

Previous studies of SAFZ-related uplifts between the Indio Hills and Durmid Hills in Coachella Valley suggest that the Indio Hills and main San Andreas faults link up in the southeasternmost Indio Hills and proceed as the main San Andreas fault in the Mecca Hills (Fig. 8c), which then, together with the subsidiary Skeleton Canyon and Painted Canyon faults, bound a much wider flower-like uplift area than in the Indio Hills (Fig. 8c; Sylvester and Smith, 1976, 1987; Sylvester, 1988; McNabb et al., 2017; Bergh et al., 2019). In contrast to the Indio Hills fault, however, the main San Andreas fault in Mecca Hills has an anastomosing geometry with thick (10–500 m) red-stained fault gouge. Regardless, we consider these faults to be correlative and infer the lack of fault gouge along the Indio Hills fault to be due to more localized strain on the Indio Hills fault than on the SAFZ in Mecca Hills. This is supported by a more rectilinear geometry and lack of fold–fault linkage in Indio Hills, which may have allowed initial lubrication of the fault surface in basement rocks with high contrasting rheology (e.g., Di Toro et al., 2011; Fagereng and Beall, 2021), and which hampered fluid circulation and extensive cataclasis. Another possible explanation may be the presence of coarse-grained deposits of the Mecca Formation, which may have partitioned/decoupled deformation along the Indio Hills fault from that in overlying Palm Spring sedimentary strata.

Both the Indio Hills and Mecca Hills uplift areas are bounded to the northeast by a presumed Miocene–Pliocene SW-dipping normal fault (Fig. 8a), which later acted as major SAFZ-parallel oblique-reverse faults and which significantly contributed to the uplift of these areas in (late) Pleistocene time (Sylvester and Smith, 1976, 1987; McNabb et al., 2017; Bergh et al., 2019). In the Mecca Hills (Fig. 8c), the Painted Canyon fault is flanked in the hanging wall to the southwest

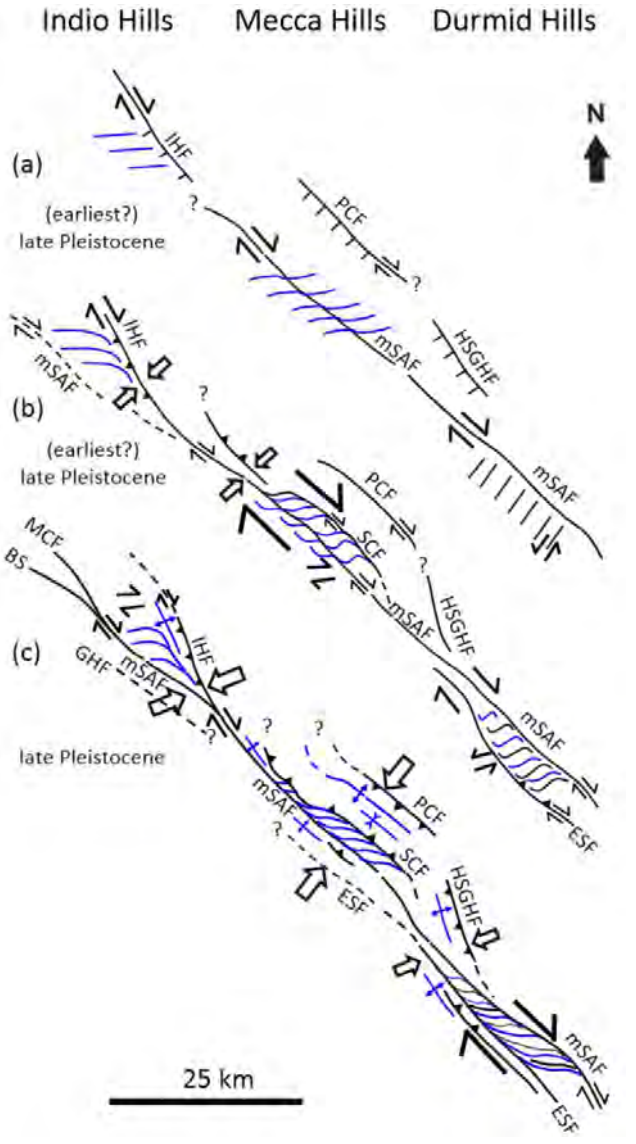

Figure 8. Kinematic evolution, timing, and along-strike correlation of the Indio Hills, Mecca Hills, and Durmid Hills uplift domains and bounding master faults in the Coachella Valley, southern California. We present a progressive kinematic evolution from **(a)** distributed, through **(b)** partly partitioned, to **(c)** advanced partitioned strain events. See text for further explanation. Black lines are faults (full or stippled). Blue lines are fold axial traces. Wide arrows indicate main shortening direction, and half-arrows indicate lateral (strike-slip) shearing. Abbreviations: BS: Banning strand; ESF: East Shoreline fault; GHF: Garnet Hill fault; HSGHF: Hidden Springs–Grotto Hills fault; IHF: Indio Hills fault; mSAF: main San Andreas fault; MCF: Mission Creek fault; PCF: Painted Canyon fault; SCF: Skeleton Canyon fault.

by a basement-cored, macro-fold (Mecca anticline), which is similar to the upright anticline that parallels the Indio Hills fault and adjacent minor thrust faults (Figs. 2, 3c, and S5a). Similar folds appear adjacent to the Hidden Springs–Grotto Hills fault (Sheridan et al., 1994; Nicholson et al., 2010), a NW–SE-striking, now reverse splay fault of the main SAFZ between the Mecca Hills and Durmid Hills (Fig. 8c). It is, however, unlikely that these marginal faults link up directly along strike. Rather, they merge or splay with the SAFZ and SAFZ-oblique faults.

The inversion and main uplift history of the Mecca Hills segment of the SAFZ (Bergh et al., 2019) initiated with right-lateral slip on a steep SAFZ, from where SAFZ-oblique en echelon folds and dominantly right-slip faults splayed out in a 1–2 km wide damage zone on either side of the SAFZ (Fig. 8a). The subsidiary Skeleton Canyon fault initiated as a steep right-lateral and SAFZ-parallel strike-slip fault along a small restraining bend (Fig. 8b). Successive lateral shearing reshaped the en echelon folds into steeply plunging folds with axial traces parallel to the SAFZ. The final kinematic stage generated SW-verging fold and thrust structures parallel to the SAFZ (Fig. 8c), which truncated the en echelon folds and the NE-dipping Skeleton Canyon fault. The resulting wedge-like flower structure thus records a polyphase kinematic evolution from distributed, through locally partitioned, to fully partitioned strain (Bergh et al., 2019).

Based on the geometric similarities, we consider that the en echelon macro-folds in both Indio Hills and Mecca Hills formed coevally, but not on the same regional right-lateral fault strand (Fig. 8a). In both areas, the en echelon folds and faults are strongly reworked and tightened into sigmoidal shapes where they merge with the Indio Hills and Skeleton Canyon faults, respectively (Fig. 8b; Bergh et al., 2019), and SAFZ-parallel thrust faults formed early (i.e., prior to macro-folding) both in the Indio Hills (Fig. S5c–d) and in the Mecca Hills (Rymer, 1994), thus supporting continuous, partly partitioned strain field in both areas. Strain partitioning caused major uplift of the Mecca Hills block along the Skeleton Canyon, Painted Canyon, and Hidden Springs–Grotto Hills faults (Fig. 8c), all acting as SAFZ-parallel oblique-slip thrust faults (Sheridan et al., 1994; Bergh et al., 2019). The partitioned right-slip component was partly transferred to the main San Andreas fault in Indio Hills, and/or to an unknown hidden fault southwest of the SAFZ (e.g., in Mecca Hills; Hernandez Flores, 2015; Fuis et al., 2017), possibly the East Shoreline fault (Janecke et al., 2018).

Based on paleomagnetic and structural field studies, uplift of the SAFZ-related Mecca basin started at ca. 2.6–0.76 Ma (i.e., earliest to mid-Pleistocene) with partial and local erosion of the Palm Spring Formation (see lower and upper unconformities in McNabb et al., 2017) and culminated after 0.76 Ma (see unconformity between the uppermost Palm Spring Formation and base of the Ocotillo Formation southwest of the Painted Canyon fault in McNabb et al., 2017), i.e., after deposition of the whole Palm Spring Formation (McN-

abb et al., 2017; Janecke et al., 2018). Uplift is still ongoing at present (Fattaruso et al., 2014; Janecke et al., 2018). Fault activity and tectonic uplift of the Mecca Hills therefore most likely initiated earlier (earliest Pleistocene) than in the Indio Hills (earliest late Pleistocene; Table 1), where the transition from the lower to the upper member of the Palm Spring Formation is gradual and does not show any major unconformity.

5.5.2 Comparison with Durmid Hills

The Durmid ladder structure along the southern 30 km of the SAFZ in Imperial Valley defines a similar but oppositely merging, 1–3 km wide wedge-shaped uplift as in Indio Hills, bounded by the right-lateral and reverse East Shoreline fault to the southwest and the main SAFZ to the northeast (Fig. 8c; Janecke et al., 2018). Internally, the ladder structure comprises en echelon folds (Babcock, 1974; Bürgmann, 1991) that merge in a sigmoidal pattern with the main SAF and subsidiary sets of conjugate SAFZ-parallel right-lateral and SAFZ-oblique E–W-striking left-slip cross faults, which accommodated clockwise rotation of internal blocks (Janecke et al., 2018). The en echelon folds formed at a comparable time, i.e., < 0.76 Ma in the Indio Hills and at ca. 0.5 Ma in the Durmid Hills (Table 1). By assuming a northwest continuation of the main SAFZ with the SAFZ in Mecca Hills, the East Shoreline fault has no exposed correlative fault in the Mecca Hills and Indio Hills (Fig. 8c; Damte, 1997; Bergh et al., 2019). Nevertheless, the East Shoreline fault may continue at depth southwest of the main San Andreas fault (Janecke et al., 2018).

A significant difference between the Indio Hills–Mecca Hills and the Durmid Hills, however, is the large number of cross faults in the Durmid ladder structure. Such faults are interpreted as early-stage (ca. 1 Ma – early or mid-Pleistocene), NE–SW-striking, left-lateral faults (Fig. 8a), which were rotated clockwise by progressive right-lateral motion into sigmoidal parallelism with the SAFZ and East Shoreline fault (Fig. 8b–c; Janecke et al., 2018). In contrast, cross faults in Indio Hills are much less common and, where present, probably formed late, but prior to the main San Andreas fault (i.e., in the earliest or middle part of the late Pleistocene). Thus, in the Indio Hills, there is no evidence of clockwise rotation of early-stage cross faults as in the Durmid Hills, but rather clockwise rotation of fold axial traces is common, which may be a first step in the formation of ladder-like fault blocks (e.g., Davis, 1999; Schultz and Balasko, 2003).

A major outcome of the comparison with Durmid Hills is that the wedge-shaped uplift block between the Indio Hills and main San Andreas faults may represent a failed uplift and/or the early stage of formation of a ladder structure. This idea is supported by the presence of similar master faults and structures with comparable kinematics in both the Indio Hills and Durmid Hills, including oblique en echelon macro-folds, strike-slip faults acting as step-over faults, and reverse faults. Younger non-rotated, conjugate cross faults exist in the Indio Hills but not in the Durmid Hills where such faults are more evolved features due to larger strain and more advanced stage of ladder structure formation. From these observations, one should expect to find ladder structures operating at different evolution stages among the many, yet unexplored, uplifts in Coachella Valley.

6 Conclusions

The Indio Hills fault likely initiated as a SW-dipping, basement-seated normal fault during the opening of the Gulf of California in the mid-Miocene and was later inverted as a right-lateral reverse, oblique-slip fault in the (earliest?–) late Pleistocene due to transpression along the transform plate boundary, whereas the main San Andreas fault initiated probably as a dominantly right-slip fault during the later stages of uplift in the late Pleistocene.

The Indio Hills segment of the SAFZ in Coachella Valley, southern California, evolved as a wedge-shaped uplift block between two major SAFZ-related fault strands, the Indio Hills and main San Andreas faults, which merge in a dextral freeway junction of a transitional nature to the southeast.

Transpressive deformation triggered uplift and inversion of the Indio Hills through a progressive change from distributed en echelon folding to partly partitioned right-slip thrusting. We favor a progressive rather than stepwise model in which the main uplift was related to late shortening at the freeway junction where the Indio Hills and main San Andreas faults merge.

The Indio Hills fault is a splay fault of the SAFZ that merges to the north with the Landers–Mojave Line and contributes to transfer slip from unsuitably oriented faults of the eastern California shear zone to the main San Andreas fault in the southeast.

A significant difference of the Indio Hills from the Durmid Hills is that left-lateral step-over and cross faults in the Durmid Hills rotated subparallel with the mSAF, whereas in Indio Hills, all cross faults are oblique with the SAFZ and, thus, may reflect an earlier stage of a still evolving ladder structure.

The initiation of right-lateral to right-lateral-reverse slip along major SAFZ-parallel faults and the main San Andreas fault in the Coachella Valley is younger towards the northwest (Pliocene in the Durmid Hills, early Pleistocene in the Mecca Hills, and late Pleistocene in the Indio Hills). The onset of uplift, however, appears to be coeval in all tectonic uplifts (late to latest) Pleistocene.

Data availability. The structural dataset and field photographs used in the present study are available on DataverseNO (Open Access repository) at https://doi.org/10.18710/TM18UZ (Koehl, 2022). Satellite and aerial images are from Google Earth (© Google Earth 2011).

Supplement. The supplement related to this article is available online at: https://doi.org/10.5194/se-13-1169-2022-supplement.

Author contributions. All authors contributed to collect structural measurements in the Indio Hills. JBPK wrote the first draft of the manuscript and designed half the figures and Supplement (35 % workload). SGB made major revision to the initial draft and designed half the figures and Supplement (35 % workload). AGS also revised the manuscript and provided major input about the local geology (30 % workload).

Competing interests. The contact author has declared that none of the authors has any competing interests.

Disclaimer. Publisher's note: Copernicus Publications remains neutral with regard to jurisdictional claims in published maps and institutional affiliations.

Acknowledgements. The staff at the University of California–Santa Barbara and San Diego State University provided great hospitality during Steffen G. Bergh's sabbatical leaves in 2011–2012 and 2016–2017 while working with the San Andreas fault. We thank all the persons from these institutions that were involved in this project. The authors thank Arild Andresen (University of Oslo) and Holger Stunitz (UiT) for helpful comments and Jack Brown (San Diego State University) for fieldwork collaboration. Susanne Janecke (Utah State University) and Miles Kenney (Kenney Geoscience) provided fruitful discussion. We thank the reviewers (Jonathan Matti and the anonymous reviewer) for their extended helpful comments on the manuscript.

Financial support. The present study is part of the CEED (Centre for Earth Evolution and Dynamics) and ARCEx projects (Research Centre for Arctic Petroleum Exploration), which are funded by grants from UiT The Arctic University of Norway in Tromsø and the Research Council of Norway (grant nos. 223272 and 228107) together with eight academic and six industry partners, and part of the ArcTec project funded by the European Union's Horizon 2020 research and innovation program under the Marie Skłodowska-Curie grant (agreement no. 101023439).

Review statement. This paper was edited by Stefano Tavani and reviewed by Jonathan Matti and one anonymous referee.

References

Allen, C. R.: San Andreas fault zone in San Gorgonio Pass, southern California, GSA Bull., 68, 315–360, 1957.

Atwater, T. and Stock, J.: Pacific-North America Plate Tectonics of the Neogene Southwestern United States: An Update, Int. Geol. Rev., 40, 375–402, 1998.

Babcock, E. A.: Structural Geology and Geophysics of the Durmid Area, Imperial Valley, California, PhD Thesis, University of California, Riverside, 149 pp., 1969.

Babcock, E. A.: Geology of the northeast margin of the Salton Trough, Salton Sea, California, GSA Bull., 85, 321–332, 1974.

Bergh, S. G., Sylvester, A. G., Damte, A., and Indrevær, K.: Evolving transpressional strain fields along the San Andreas fault in southern California: implications for fault branching, fault dip segmentation and strain partitioning, Geophys. Res. Abstr., EGU2014-2066, EGU General Assembly 2014, Vienna, Austria, 2014.

Bergh, S. G., Sylvester, A. G., Damte, A., and Indrevær, K.: Polyphase kinematic history of transpression along the Mecca Hills segment of the San Andreas fault, southern California, Geosphere, 15, 901–934, 2019.

Bilham, R. and Williams, P.: Sawtooth segmentation and deformation processes on the southern San Andreas fault, California, Geophys. Res. Lett., 12, 557–560, 1985.

Blisniuk, K., Scharer, K., Sharp, W. D., Burgmann, R., Amos, C., and Rymer, M.: A revised position for the primary strand of the Pleistocene-Holocene San Andreas fault in southern California, Sci. Adv., 7, eaaz5691, https://doi.org/10.1002/2015JB012004, 2021.

Boley, J.-L., Stimac, J. P., Weldon II, R. J., and Rymer, M. J.: Stratigraphy and paleomagnetism of the Mecca and Indio Hills, southern California, in: Geological Investigations of an Active Margin, edited by: McGill, S. F. and Ross, T. M., GSA, Cordilleran Section Guidebook, 27th Annual Meeting, San Bernardino County Museum Associations, AAPG Bull., USA, 60, 12, 336–344, 1994.

Bryant, W. A.: Fault number 118, Pinto Mountain fault zone (includes Morongo Valley fault), Quaternary fault and fold database of the United States, USGS website, https://earthquakes.usgs.gov/hazards/qfaults (last access: 5 March 2022), 2000.

Bürgmann, R.: Transpression along the southern San Andreas fault, Durmid Hills, California, Tectonics, 10, 1152–1163, 1991.

Chang, S.-B. R., Allen, C. R., and Kirschvink, J. L.: Magnetic stratigraphy and a test for block rotation of sedimentary rocks within the San Andreas fault zone, Mecca Hills, southeastern California, Quaternary Res., 27, 30–40, 1987.

Crowell, J. C.: The tectonics of the Ridge Basin, southern California, in: Geologic History of Ridge Basin, Southern California, edited by: Crowell, J. C. and Link, M. H., SEPM, Pacific Section, Vol. 22, 25–42, 1982.

Dahlen, F. A.: Critical Taper Model of Fold-and-Thrust Belts and Accretionary Wedges, Annu. Rev. Earth Planet. Sc., 18, 55–99, 1990.

Dair, L. and Cooke, M. L.: San Andreas fault geometry through the San Gorgonio Pass, California, Geology, 37, 119–122, 2009.

Damte, A.: Styles of deformation in zones of oblique convergence: Examples from the Mecca Hills, southern San Andreas fault, PhD thesis, University of California, Santa Barbara, 164 pp., 1997.

Davis, G. H.: Structural geology of the Colorado Plateau region of southern Utah, with emphasis on deformation bands, GSA Spec. Pap., 342, 157 pp., https://doi.org/10.1130/SPE342, 1999.

Di Toro, G., Han, R., Hirose, T., De Paola, N., Nielsen, S., Mizoguchi, K., Ferri, F., Cocco, M., and Shimamoto, T.: Fault lubrication during earthquakes, Nature, 471, 494–498, 2011.

Dibblee Jr., T. W.: Geology of the Imperial Valley, California, Californian Division of Mines Bulletin, 170, 21–28, 1954.

Dibblee Jr., T. W.: Geology of the southeastern San Andreas fault zone in the Coachella Valley area, Southern California, in: Southern San Andreas fault, Whitewater to Bombay Beach, Salton Trough, California, edited by: Baldwin, J., Lewis, L., Payne, M., and Rocquemore, G., South Coast Geological Society, Annual Field Trip Guide Book, Vol. 25, 35–56, 1997.

Dibblee Jr., T. W. and Minch, J. A.: Geological map of the Thousand Palms & Lost Horse Mountain 15 minutes quadrangles, Riverside County, California, Dibblee Foundation, Map DF-372, 2008.

Dokka, R. K. and Travis, C. J.: Late Cenozoic strike-slip faulting in the Mojave Desert, California, Tectonics, 9, 311–340, 1990a.

Dokka, R. K. and Travis, C. J.: Role of the Eastern California Shear Zone in accommodating Pacific-North American plate motion, Geophys. Res. Lett., 17, 1323–1326, 1990b.

Dorsey, R. J., Housen, B. A., Janecke, S. U., Fanning, C. M., and Spears, A. L. F.: Stratigraphic record of basin development within the San Andreas fault system: Late Cenozoic Fish Creek–Vallecito basin, southern California, GSA Bull., 123, 771–793, 2011.

Du, Y. and Aydin, A.: Is the San Andreas big bend responsible for the Landers earthquake and the eastern California shear zone, Geology, 24, 219–222, 1996.

Ehman, K. D., Sullivan, M. D., and May, S. R.: Ridge Basin Field Trip Guidebook, Tectonic Controls on Facies Distribution and Stacking Patterns, Ridge Basin, southern California, SEPM, Pacific Section, Los Angeles, California, USA, Vol. 87, 50 pp., 2000.

Fagereng, Å. and Beall, A.: Is complex fault zone behavior a reflection of rheological heterogeneity, Philos. T. Roy. Soc. A, 329, 20190421, https://doi.org/10.1098/rsta.2019.0421, 2021.

Fattaruso, L. A., Cooke, M. L., and Dorsey, R. J.: Sensitivity of uplift patterns to dip of the San Andreas fault in the Coachella Valley, California, Geosphere, 10, 1–12, 2014.

Fuis, G. S., Scheirer, D. S., Langenheim, V. E., and Kohler, M. D.: A New Perspective on the Geometry of the San Andreas Fault in Southern California and Its Relationship to Lithospheric Structure, B. Seismol. Soc. Am., 102, 236–251, 2012.

Fuis, G. S., Bauer, K., Goldman, M. R., Ryberg, T., Langenheim, V. E., Scheirer, D. S., Rymer, M. J., Stock, J. M., Hole, J. A., Catchings, R. D., Graves, R. W., and Aagaard, B.: Subsurface Geometry of the San Andreas Fault in Southern California: Results from the Salton Seismic Imaging Project (SSIP) and Strong Ground Motion Expectations, B. Seismol. Soc. Am., 107, 1642–1662, 2017.

Gold, P. O., Behr, W. M., Rood, D., Sharp, W. D., Rockwell, T. K., Kendrick, K., and Salin, A.: Holocene geologic slip rate for the Banning strand of the southern San Andreas Fault, southern California, J. Geophys. Res.-Sol. Ea., 120, 5639–5663, https://doi.org/10.1002/2015JB012004, 2015.

Groshong, R. H.: Strain, fractures, and pressure solution in natural single-layer folds, GSA Bull., 86, 1363–1376, 1975.

Guest, B., Niemi, N., and Wernicke, B.: Stateline fault system: A new component of the Miocene-Quaternary Eastern California shear zone, GSA Bull., 119, 1337–1346, 2007.

Hardebeck, J. L. and Hauksson, E.: Role of fluids in faulting inferred from stress field signatures, Science, 285, 236–239, 1999.

Hauksson, E., Yang, W., and Schearer, P. M.: Waveform Relocated Earthquake Catalog for Southern California (1981 to June 2011), B. Seismol. Soc. Am., 102, 2239–2244, 2012.

Hernandez Flores, A. P.: Paleosismologia del sistema de fallas imbricado en la Sierra Cucapah, Baja California, Mexico, Master's Thesis, Centre for Scientific Research and Higher Education, Ensenada, Mexico, 254 pp., 2015.

Herzig, C. T., Mehegan, J. M., and Stelting, C. E.: Lithostratigraphy of the State 2-14 Borehole: Salton Sea Scientific Drilling Project, J. Geophys. Res., 93, 12969–12980, 1988.

Janecke, S. U., Markowski, D. K., Evans, J. P., Persaud, P., and Kenney, M.: Durmid ladder structure and its implications for the nucleation sites of the next $M > 7.5$ earthquake on the San Andreas fault or Brawley seismic zone in southern California, Lithosphere, 10, 602–631, 2018.

Keller, E. A., Bonkowski, M. S., Korsch, R. J., and Schlemon, R. J.: Tectonic geomorphology of the San Andreas fault zone in the southern Indio Hills, Coachella Valley, California, GSA Bull., 93, 46–56, 1982.

Kendrick, K. J., Matti, J. C., and Mahan, S. A.: Late Quaternary slip history of the Mill Creek strand of the San Andreas fault in San Gorgonio Pass, southern California: The role of a subsidiary left-lateral fault in strand switching, GSA Bull., 127, 825–849, 2015.

Kirby, S. M., Janecke, S. U., Dorsey, R. J., Housen, B. A., Langenheim, V. E., McDougall, K. A., and Steely, A. N.: Pleistocene Brawley and Ocotillo Formations: Evidence for Initial Strike-Slip Deformation along the San Felipe and San Jacinto Fault Zones, Southern California, J. Geol., 115, 43–62, 2007.

Koehl, J.-B. P.: Replication data for "Tectonic evolution of the Indio Hills segment of the San Andreas fault in southern California", DataverseNO [data set], https://doi.org/10.18710/TM18UZ, 2022.

Lancaster, J. T., Hayhurst, C. A., and Bedrossian, T. L.: Preliminary geologic map of Quaternary surficial deposits in southern California: Palm Springs $30' \times 60'$ quadrangle, in: Geologic compilation of Quaternary surficial deposits in southern California, edited by: Bedrossian, T. L., Roffers, P., Hayhurst, C. A., Lancaster, J. T., and Short, W. R., California Geological Survey, Sacramento, https://www.conservation.ca.gov/cgs/fwgp/Pages/sr217.aspx#palmsprings (last access: 27 April 2022), 2012.

Leever, K., Gabrielsen, R. H., Sokoutis, D., and Willingshofer, E.: The effect of convergence angle on the kinematic evolution of strain partitioning in transpressional brittle wedges: Insight from analog modeling and high-resolution digital image analysis, Tectonics, 30, TC2013, https://doi.org/10.1029/2010TC002823, 2011a.

Leever, K., Gabrielsen, R. H., Faleide, J. I., and Braathen, A.: A transpressional origin for the West Spitsbergen fold- and thrust belt: Insight from analog modeling, Tectonics, 30, 1–24, 2011b.

Lin, G.: Three-Dimensional Seismic Velocity Structure and Precise Earthquake Relocations in the Salton Trough, Southern California, B. Seismol. Soc. Am., 103, 2694–2708, 2013.

Lin, G., Schearer, P. M., and Hauksson, E.: Applying a three-dimensional velocity model, waveform cross correlation, and cluster analysis to locate southern California seismicity from 1981 to 2005, J. Geophys. Res., 112, B12309, https://doi.org/10.1029/2007JB004986, 2007.

Lindsey, E. O. and Fialko, Y.: geodetic slip rates in the southern San Andreas Fault system: Effects of elastic heterogeneity and fault geometry, J. Geophys. Res., 118, 689–697, 2013.

Lutz, A. T., Dorsey, R. J., Housen, B. A., and Janecke, S. U.: Stratigraphic record of Pleistocene faulting and basin evolution in the Borrego Badlands, San Jacinto fault zone, Southern California, GSA Bull., 118, 1377–1397, 2006.

Markowski, D. K.: Confirmation of a New Geometric and Kinematic Model of the San Andreas Fault at Its Southern Tip, Durmid Hill, Southern California, Master's Thesis, Utak State University, Logan, USA, 151 pp., 2016.

Matti, J. C. and Morton, D. M.: Paleogeographic evolution of the San Andreas fault in southern California: a reconstruction based on a new cross-fault correlation, in: The San Andreas fault system: displacement, palinspastic reconstruction, and geologic evolution, edited by: Powell, R. E., Weldon, R. J., and Matti, J. C., GSA Mem., Geological Society of America Vol. 178, 107–159, https://doi.org/10.1130/MEM178-p107, 1993.

Matti, J. C., Morton, D. M., and Cox, B. F.: Distribution and geologic relations of fault systems in the vicinity of the Central Transverse Ranges, southern California, USGS Report, 85–365, 31 pp., 1985.

Matti, J. C., Morton, D. M., and Cox, B. F.: The San Andreas fault system in the vicinity of the central Transverse Ranges province, southern California, U.S. Geological Survey Open-File, Report 92-354, 40 pp., https://doi.org/10.3133/ofr92354, 1992.

McClay, K. R., Whitehouse, P. S., Dooley, T., and Richards, M.: 3D evolution of fold and thrust belts formed by oblique convergence, Mar. Petrol. Geol. Bull., 21, 857–877, 2004.

McNabb, J. C.: Stratigraphic record of Pliocene-Pleistocene basin evolution and deformation along the San Andreas fault, Mecca Hills, California, Master's Thesis, University of Oregon, 70 pp., 2013.

McNabb, J. C., Dorsey, R. J., Housen, B. A., Dimitroff, C., and Messé, G. T.: Stratigraphic record of Pliocene–Pleistocene basin evolution and deformation within the Southern San Andreas Fault Zone, Mecca Hills, California, Tectonophysics, 719–720, 66–85, 2017.

Meere, P. A., Mulchrone, K. F., and Timmerman, M.: Shear fodling in low-grade metasedimentary rocks: Reverse shear along cleavage at a high angle to the maximum compressive stress, Geology, 41, 879–882, 2013.

Miller, D. D.: Distributed shear, rotation, and partitioned strain along the San Andreas fault, central California, Geology, 26, 867–870, 1998.

Morton, D. and Matti, J. C.: Extension and contraction within an evolving divergent strike-slip fault complex: The San Andreas and San Jacinto fault zones at their convergence in southern California, in: The San Andreas fault system: displacement, palinspastic reconstruction, and geologic evolution, edited by: Powell, R. E., Weldon, R. J., and Matti, J. C., GSA Mem., Geological Society of America Vol. 178, 217–230, https://doi.org/10.1130/MEM178-p217, 1993.

Morton, D., Matti, J., and Tinsley, J.: Banning fault, Cottonwood canyon, San Gorgonio pass, southern California, in: Cordilleran Section of the Geological Society of America, edited by: Hill, M., 191–192, Geol. Soc. of Am., Boulder, Colorado, USA, https://doi.org/10.1130/0-8137-5401-1.191, 1987.

Mount, V. S. and Suppe, J.: State of stress near the San Andreas fault: implications for wrench tectonics, Geology, 15, 1143–1146, 1987.

Nicholson, C., Hauksson, E., and Plesch, A.: Revised 3D Fault Models for the Southern San Andreas Fault System Extending from San Gorgonio Pass to the Salton Sea, 27–29 May 2010, 106th Annual Meeting AAPG, American Association of Petroleum Geologists, 2010.

Nur, A., Hagai, R., and Beroza, G. C.: The Nature of the Landers-Mojave Earthquake Line, Science, 261, 201–203, 1993a.

Nur, A., Hagai, R., and Beroza, G. C.: Landers-Mojave earthquake Line: A New Fault System?, GSA Today, 3, 255–258, 1993b.

Passchier, C. W. and Platt. J. P.: Shear zone junctions: Of zipper and freeways, J. Struct. Geol., 95, 188–202, 2017.

Platt, J. P. and Passchier, C. W.: Zipper junctions: A new approach to the intersections of conjugate strike-slip faults, Geology, 44, 795–798, 2016.

Prante, M. R., Evans, J. P., Janecke, S. U.. and Steely, A.: Evidence for paleoseismic slip on a continental low-angle normal fault: Tectonic pseudotachylyte from the West Salton detachment fault, CA, USA, Earth Planet. Sc. Lett., 387, 170–183, 2014.

Rockwell, T., Meltzner, A., and Tsang, R.: A Long Record of Earthquakes With Timing and Displacements for the Imperial Fault: A Test of Earthquake Recurrence Models, Geological Sciences San Diego State University, technical report, 70 pp., 2011.

Rymer, M. J.: Quaternary Fault-Normal Thrusting in the Northwestern Mecca Hills, Southern California, GSA Cordilleran Section Guidebook, Trip 15, AAPG Bull., 60, 12, 268–272, 1994.

Rymer, M. J.: Triggered Surface Slips in the Coachella Valley Area Associated with the 1992 Joshua Tree and Landers, California, Earthquakes, B. Seismol. Soc. Am., 90, 832–848, 2000.

Sanderson, D. J. and Marchini, W. R. D.: Transpression, J. Struct. Geol., 6, 449–458, 1984.

Sarna-Wojcicki, A. M., Pringle, M. S., and Wijbrans, J.: New $^{40}Ar/^{39}Ar$ age of the Bishop Tuff from multiple sites and sediment rate calibration for the Matuyama-Brunhes boundary, J. Geophys. Res., 105, 21431–21443, 2000.

Schultz, R. A. and Balasko, C. M.: Growth of deformation bands into echelon and ladder geometries, Geophys. Res. Lett., 30, 2033, https://doi.org/10.1029/2003GL018449, 2003.

Sheridan, J. M. and Weldon II, R. J.: Accomodation of compression in the Mecca Hills, California, GSA Cordilleran Section Guidebook, Trip 15, AAPG Bull., 60, 12, 273–279, 1994.

Sheridan, J. M., Weldon II, R. J., Thornton, C. A., and Rymer, M. J.: Stratigraphy and Deformational History of the Mecca Hills, Southern California, GSA Cordilleran Section Guidebook, Trip 15, AAPG Bull., 60, 12, 262–268, 1994.

Sieh, K., Jones, L., Hauksson, E., Hudnut, K., Eberhart-Phillips, D., Heaton, T., Hough, S., Hutton, K., Kanamori, H., Lilje, A., Lindvall, S., McGill, S. F., Mori, J., Rubin, C., Spotila, J. A., Stock, J., Kie Thio, H., Treiman, J., Wernicke, B., and Zachariasen, J.:

Near-Field Investigations of the Landers Earthquake Sequence, April to July 1992, Science, 260, 171–176, 1993.

Spinler, J. C., Bennett, R. A., Anderson, M. L., McGill, S. F., Hreinsdottir, S., and McCallister, A.: Present-day strain accumulation and slip rates associated with southern San Andreas and eastern California shear zone faults, J. Geophys. Res., 115, B11407, https://doi.org/10.1029/2010JB007424, 2010.

Spotila, J. A., Niemi, N., Brady, R., House, M., Buscher, J., and Oskin, M.: Long-term continental deformation associated with transpressive plate motion: The San Andreas fault, Geology, 35, 967–970, 2007.

Stock, J. M. and Hodges, K. V.: Pre-Pliocene extension around the Guld of California and the transfer of Baja California to the Pacific plate, Tectonics, 8, 99–115, 1989.

Stock, J. M. and Lee, J.: Do microplates in subduction zones leave a geological record?, Tectonics, 13, 1472–1487, 1994.

Suppe, J. and Medwedeff, D. A.: Geometry and kinematics of fault-propagation folding, Eclogae Geol. Helv., 83, 409–454, 1990.

Sylvester, A. G.: Strike-slip faults, GSA Bull., 100, 1666–1703, 1988.

Sylvester, A. G. and Smith, R. R.: Tectonic Transpression and Basement-Controlled Deformation in San Andreas Fault Zone, Salton Trough, California, Treatise of Petroleum Geology, 60, 2081–2102, 1976.

Sylvester, A. G. and Smith, R. R.: Structure section across the San Andreas fault zone, Mecca Hills, in: Tectonics of the juncture between the San Andreas fault system and the Salton Trough, southeastern California, edited by: Crowell, J. C. and Sylvester, A. G., Annual Meeting Geological Society of America, San Diego, California, USA, 125–139, 1979.

Sylvester, A. G. and Smith, R. R.: Structure section in Painted Canyon, Mecca Hills, southern California, in: GSA Centennial Field Guide, Cordilleran Section, edited by: Hill, M. L., Geological Society of America Field Guide, 103–108, 1987.

Sylvester, A. G., Bilham, R., Jackson, M., and Barrientos, S.: Aseismic Growth of Durmid Hill, Southeasternmost San Andreas Fault, California, J. Geophys. Res., 98, 14233–14243, 1993.

Titus, S. J., Housen, B., and Tikoff, B.: A kinematic model for the Rinconada fault system in central California based on structural analysis of en echelon folds and paleomagnetism, J. Struct. Geol., 29, 961–982, 2007.

Thatcher, W., Savage, J. C., and Simpson, R. W.: The Eastern California Shear Zone as the northward extension of the southern San Andreas Fault, J. Geophys. Res.-Sol. Ea., 121, 2904–2914, 2016.

Tyley, S. J.: Analog model study of the ground-water basin of the upper Coachella Valley, California, U.S. Geological Survey Water-Supply, 2027, https://doi.org/10.3133/OFR71287, 1974.

Vollmer, F. W.: Orient 3: a new integrated software program for orientation data analysis, kinematic analysis, spherical projections, and Schmidt plots, GSA Abstracts with Programs, 47, 9, 2015.

Winker, C. D. and Kidwell, S. M.: Stratigraphy of a marine rift basin: Neogene of the western Salton Trough, California, in: Field Conference Guide, edited by: Abbott, P. L. and Cooper, J. D., AAPG National Convention, San Diego, California, USA, 295–336, https://doi.org/10.32375/1996-GB73.16, 1996.

Zeeden, C., Rivera, T. A., and Storey, M.: An astronomical age for the Bishop Tuff and concordance with radioisotopic dates, Geophys. Res. Lett., 41, 3478–3484, 2014.

Earthquake Geology and Paleoseismology of Major Strands of the San Andreas Fault System

Thomas Rockwell
Geological Sciences, San Diego State Univ., San Diego, CA 92182
Katherine Scharer
U.S. Geological Survey, Pasadena, CA 91106
Timothy Dawson
California Geological Survey, Menlo Park, CA 94025

ABSTRACT

The San Andreas fault system in California is one of the best-studied faults in the world, both in terms of the long-term geologic history and paleoseismic study of past surface ruptures. In this paper, we focus on the Quaternary to historic data that have been collected from the major strands of the San Andreas fault system, both on the San Andreas Fault itself, and the major sub-parallel strands that comprise the plate boundary, including the Calaveras-Hayward- Rogers Creek-Maacama fault zone and the Concord-Green Valley-Bartlett Springs fault zone in northern California, and the San Jacinto and Elsinore faults in southern California. The majority of the relative motion between the Pacific and North American lithospheric plates is accommodated by these faults, with the San Andreas slipping at about 34 mm/yr in central California, decreasing to about 20 mm/yr north of its juncture with the Calaveras and Concord faults. The Calaveras-Hayward-Rogers Creek-Maacama fault zone exhibits a slip rate of 10–15 mm/yr, whereas the rate along the Concord-Green Valley-Bartlett Springs fault zone is lower at about 5 mm/yr. In southern California, the San Andreas exhibits a slip rate of about 35 mm/yr along the Mojave section, decreasing to as low as 10–15 mm/yr along its juncture with the San Jacinto fault, and about 20 mm/yr in the Coachella Valley. The San Jacinto and Elsinore fault zones exhibit rates of about 15 and 5 mm/yr, respectively. The average recurrence interval for surface-rupturing earthquakes along individual elements of the San Andreas fault system range from 100–500 years and is consistent with slip rate at those sites: higher slip rates produce more frequent or larger earthquakes. There is also evidence of short-term variations in strain release (slip rate) along various fault sections, as expressed as "flurries" or clusters of earthquakes, as well as periods of relatively fewer surface ruptures in these relatively short records. This is reflected by non-periodic coefficients of variation in earthquake recurrence of 0.4 to 0.7 for the various paleoseismic sites.

Introduction

General tectonic setting – The San Andreas Fault is the primary boundary between the Pacific and North American lithospheric plates, although the 50 mm/yr of relative motion between these plates is accommodated by many faults that trend sub-parallel to or splay away from the San Andreas Fault. In north and central California, the onshore elements of the

San Andreas Fault system include the San Andreas, Hayward-Rodgers Creek-Maacama fault zone, the Concord-Green Valley-Bartlett Springs fault system, and the Nacimiento fault zone, with additional slip in the offshore accommodated by the San Gregorio-San Simeon-Hosgri fault zone (Figure 1). These faults accommodate about 80% of the relative motion; the remaining 20% is accommodated by smaller subsidiary structures. In central California, the San Andreas is the dominant fault strand, and creeps at 25–35 mm/yr. In southern California north of the Transverse Ranges, plate motion is accommodated largely by the San Andreas Fault with ~20% of the deformation accommodated by oblique motion in the southernmost Walker Lane and the Eastern California Shear Zone (Figure 1). The San Andreas Fault takes a left bend through the Transverse Ranges, an east-west trending fold and thrust belt with rapid convergence resulting from this "Big Bend" in the southern San Andreas Fault (Figure 1). South of the Transverse Ranges, the principal strands include the San Andreas, San Jacinto, and Elsinore fault zones inland from the coast, the Rose Canyon-Newport-Inglewood and Palos Verdes fault zones at the coast and in the near offshore, and the San Diego Trough, and San Clemente faults farther offshore.

This article focuses primarily on the slip rates and paleoseismology of the onshore principal strands of the system in the San Francisco Bay Area (SFBA) region and south of the creeping section in southern California. In the creeping section in central California, the San Andreas creeps at or near the long-term slip rate and no large earthquakes are known to have occurred. The long-term history and evolution of the San Andreas Fault system is briefly discussed, followed by a summary of slip rate and paleoseismic information in the northern and southern regions, with a focus on the longest records available. We separate the discussion into the northern and southern San Andreas fault regions, with detailed discussions on the slip rates on a fault by fault basis. The slip rate summaries are then followed by discussions on the current state of knowledge on the paleoseismology of each fault. We focus on the principal strands of the system because these are the faults for which the most information has been collected, and because they transfer most of the plate margin motion. We also did not include the Imperial Fault, which is the primary plate boundary fault that crosses the international border into Mexico, because there are few published data and because there are abundant new data that are expected to be available in the next few years.

Age of initiation, long-term history, and total slip – Transform motion initiated in the late Oligocene about 28–30 Ma when the spreading center between the Farallon and Pacific plates collided with the subduction zone off the west coast of North America (Atwater 1970). Due to the relative motion between the Pacific and North American plates, the San Andreas transform fault developed as two triple junctions that migrated to the northwest and southeast (Figure 2), resulting in a growing or lengthening transform boundary.

Total displacement on the San Andreas Fault system is reasonably well-constrained at several hundred kilometers (Crowell 1962; Powell 1993; Sims 1993). Depending on the configuration of now-displaced terranes, the total plate slip in north-central California is on the order of 500 km. Of this, the offshore Hosgri-San Simeon-San Gregorio fault system has sustained about 120 km of slip since the Miocene (Dickenson et al., 2005). Onshore, total basement offset in central California on the San Andreas Fault itself is estimated at about 300-320 km based on correlation of fan deposits in the Temblor Range with the Vaqueros Sandstone in the Santa Cruz Mountains (Graham et al., 1989) and correlation of the Neenach and Pinnacle volcanics (Matthews 1976), with a best estimate of 315 km based on offset of seismically-observed basement structures (Ravenaugh and Reasoner 1997), and a detailed reconstruction of exotic blocks in the Parkfield region (Sims, 1993). Other major faults, including the Rinconada fault with 56 km of lateral displacement (Hart et al., 1986), support large total displacement since early Miocene time.

In southern California, total slip on the San Andreas Fault (sensu stricto) is estimated to be 240 km, based on the reconstruction of PreCambrian, Oligocene and Miocene rocks (Crowell 1962; Ehlig 1981).

Figure 1. Map of major (and some minor) faults of the San Andreas Plate Boundary Fault System. In northern California, MF=Macaama fault, RCF=Rodgers Creek fault, SAF=San Andreas Fault, HF=Hayward fault, CF=Calaveras fault. In central and southern California, H_SS_SGFZ=Hosgri-San Simeon-San Gregorio fault zone, EF=Elsinore fault, RCF=Rose Canyon fault, SJF=San Jacinto Fault, LSF=Laguna Salada fault, GF=Garlock fault, PVF=Palos Verdes fault, CPF=Cerro Prieto fault, IF=Imperial fault. Significant historical earthquakes indicated by stars with year and magnitude.

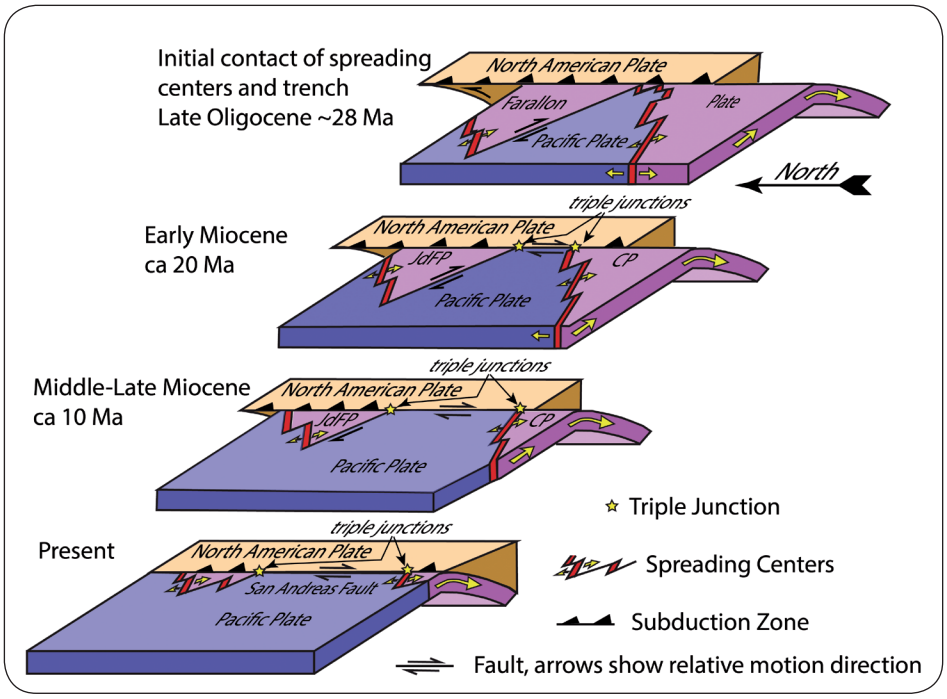

Figure 2. Progressive subduction of the spreading ridge system between the Pacific and Farallon - Juan de Fuca (JdFP)-Cocos(CP) plates led to a lengthening transform margin that initiated in the late Oligocene and evolved into the modern San Andreas Fault system of today (derived from Atwater, 1970; Irwin, 1990).

An alternative interpretation of 160 km of offset is proposed based on reconstruction of crystalline rock bodies (Matti and Morton 1993). An analysis incorporating the role of the rotation of blocks in the Mojave Desert region, adjacent to the San Andreas Fault, is used to reconcile these alternative models, and results in an estimate of total slip of 180 km (Powell 1993). A similar analysis, though one that did not use total offset along the sinistral faults of the Mojave Desert to constrain rotation, suggests approximately 200 km to resolve these disparate estimates (Darin and Dorsey 2013). Other major strands include the San Gabriel fault with ~45 km of slip (Powell and Weldon 1992), the San Jacinto with ~25–30 km of slip (Sharp 1967; Baird et al., 1970; Bartholomew 1970; Hill, 1981), the Elsinore fault with ~10 km of slip (Rockwell 1988), and the coastal system of faults that may have sustained as much as 250 km of slip (Abbott and Smith 1989; Nicholson et al., 1994). Altogether, cumulative slip across the main plate boundary faults in southern California sums to at least 480 km of plate margin dextral shear, generally consistent with estimates farther north.

Northern San Andreas System

The northern San Andreas system is composed of multiple northwest-trending strike slip faults that accommodate dextral shear in the Coast Ranges of northern California and collectively carry about 40 mm/yr of slip, or about 80% of the relative motion between the Pacific and North American plates (Figure 1) (Kelson et al., 1992). North of the Pinnacles, the SAF splays into three major zones of sub-parallel dextral faults that extend north to the Mendocino Triple Junction. From west to east, these are: the main trace of the San Andreas Fault; the Calaveras – Hayward – Rodgers Creek – Maacama system; and the Concord – Green Valley – Bartlett Springs system (Figures 1 and 3). Other significant faults include the mostly off-shore San Gregorio fault, which joins the SAF near Bolinas Lagoon, and the Greenville fault, which is the easternmost fault of the system in the San Francisco Bay Region (SFBR).

Northern San Andreas Slip Rate - Estimates of late Quaternary slip rates along the northern SAF system are spatially sparse, limited to a few key sites along strike (Figure 3). At Point Arena, offset

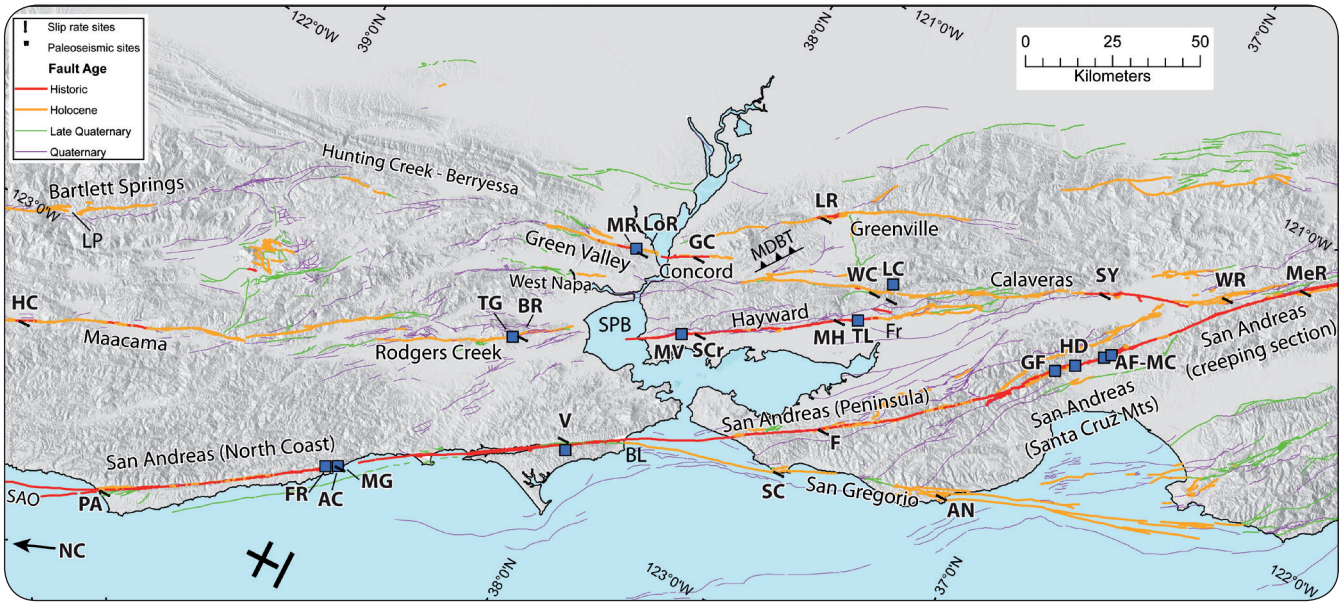

Figure 3. Key slip rate and paleoseismic sites on the northern San Andreas System. Site names are as follows: AC, Archae Camp; AN, Ano Nuevo; AF-MC, Arano Flat-Mill Canyon; BR, Beebe Ranch; F, Filoli; FR, Fort Ross; GC, Galindo Creek; GF, Grizzly Flat; HC, Haehl Creek; HD, Hazel Dell; LC, Leyden Creek; LR, Laughlin Road; LoR, Lopes Ranch; MeR, Melendy Ranch; MG, Mill Gulch; MH, Masonic Home; MR, Mason Road;, MV, Mira Vista; NC, Noyo Canyon; PA, Point Arena, SC, Seal Cove; SCr, Strawberry Creek; SY, San Ysidro; TL, Tyson's Lagoon; V, Vedanta; WC, Welch Creek; WR, Winfield Ranch. Place names are as follows: BL, Bolinas Lagoon; Fr, Fremont; LP, Lake Pillsbury; MDBT, Mount Diablo Blind Thrust; SAO, San Andreas Offshore section; SPB, San Pablo Bay.

marine terraces, dated to 80 ka and 120 ka, yield preferred slip rates of 19 – 20 mm/yr (Prentice and Kelson, 2006). At Mill Gulch, Prentice and Kelson (2006) report a slip rate of 19 ± 4mm/yr, based on a stream offset 80 -100 meters over the past ~5000 years. Niemi and Hall (1992) report a best-estimate slip rate of 24 ± 3 mm/yr at the Vedanta site over the past ~1800 years. South of Vedanta, the slip rate decreases due to the rate being partitioned between the SAF and San Gregorio faults. On the Peninsula section of the San Andreas Fault (SAP), Hall et al., (1999) report a slip rate of 17 ± 4 mm/yr over the past 2000 years at the Filoli site. South of the SAP, the slip rate is unconstrained by geologic studies, although slip is likely partitioned between the SAF and other oblique slip faults, as the fault passes through a broad restraining bend forming the Santa Cruz Mountains (Working Group on California Earthquake Probabilities (WGCEP 2003)). South of the Santa Cruz Mountains, the fault transitions from being fully locked to the north to being dominated by steady state aseismic creep to the south (Johanson and Bürgmann, 2005). The slip rate also increases north to south as the fault merges with the Calaveras fault in a ~25 km-long transition zone. At the Melendy Ranch site, situated within the creeping section of the SAF, Perkins et al., (1989) report a minimum slip rate of 21 mm/yr, based on an offset stream terrace riser. Geodetic studies and alignment arrays suggest a 25 ± 1 mm/yr slip rate along the creeping section of the fault (Titus et al., 2004). However, larger aperture GPS arrays away from the fault give fault parallel rates up to 30 ± 2 mm/yr, which suggests some elastic strain is accumulating on the fault. This suggests the potential for damaging earthquakes on a section previously assumed as largely aseismic due to a lack of documented moderate or larger earthquakes.

Calaveras – Hayward – Rodgers Creek – Maacama Slip Rate - The Calaveras – Hayward – Rodgers Creek – Maacama fault system is located east of the SAF and forms the active traces of a fault system that has been evolving since about 8 Ma (McLaughlin et al., 1996). The active traces are characterized by relatively high slip rates (> 8 mm/yr), as well as some parts of the fault system that creep aseismically. The degree of creep relative to the full slip rate is thought to vary from fully

creeping (parts of the Calaveras, Hayward, and Maacama faults), to partially locked (portions of the Calaveras, Hayward, Rodgers Creek and Maacama faults) to nearly fully locked, such as along other parts of the Rodgers Creek fault (Galehouse and Lienkaemper 2003). Locations of slip rate sites are shown on Figure 3. The slip rate for the southern Calaveras fault is poorly constrained, with a minimum rate of > 9 mm/yr (Perkins and Sims 1988). A best-estimate rate of 14 ± 5 mm/yr, based on a series of offset channels, is reported by Kelson et al., (1998) for the central Calaveras fault. In the vicinity of Fremont, the slip rate on the Calaveras decreases as the central Calaveras fault splits into the Hayward fault and northern Calaveras fault. The slip rate at the Leyden Creek site on the northern Calaveras is 5 ± 2 mm/yr (Kelson et al., 1996). The reported rate at the Welch Creek site, located 2.5 km northwest of Leyden Creek, is similar, between 3 – 8 mm/yr (Simpson et al., 1999). At the northern end of the mapped northern Calaveras fault, slip may step east to the Concord – Green Valley – Bartlett Springs system, while some unknown amount may continue through the East Bay hills to the West Napa fault. On the southern Hayward fault, at the Masonic Home site, Lienkaemper and Borchardt (1996) report a minimum slip rate of 7 – 11 mm/yr over the past 4600 years. The slip rate to the north is similar, with a longer-term (32 ka) rate of 10 mm/yr reported at the Strawberry Creek site on the northern Hayward fault (Williams 1998). A ~5 km extensional step, located within San Pablo Bay, separates the northern Hayward fault from the Rodgers Creek fault to the north, and is thought to be a possible segmentation point for earthquake ruptures (WGCEP 2003). Schwartz et al., (1992) report a slip rate of 6 – 10 mm/yr over the past 900 years at the Beebe Ranch site, located on the Rodgers Creek fault.

For the Maacama fault, Larson and others (2005) report a minimum rate of 8 mm/yr over the past 3400 years at the Haehl Creek site whereas Prentice et al., (2014) document a creep rate at Willits of 5.7+/–0.1 mm/yr, and a slightly lower, 560–690 year slip rate of 6.4–8.6 mm/yr.

The Maacama fault becomes progressively more difficult to map north of the Haehl Creek site due to landslide prone terrain and a less integrated fault system, but the fault system may progressively step west to join the Mendocino Triple Junction (Wakabayashi 1999).

Concord – Green Valley – Bartlett Springs Slip Rate - The Concord – Green Valley – Bartlett Springs fault system is the eastern-most system of faults in the northern Coastal Ranges. Slip in this system is fed from the south by the northern Calaveras fault (WGCEP 2003) and by the Greenville fault – Mt Diablo Blind Thrust system (Unruh and Lettis 1998). The Bartlett Springs fault system may be the most recently developed, with low cumulative slip (Wakabayshi, 1999) and a less integrated geomorphic character at the surface (Lienkaemper, 2012). Late Quaternary slip rates are poorly resolved, or nonexistent, along much of this system (sites are located on Figure 3). On the Concord fault, Borchardt and Wills (1999) report minimum rates of 3.4 ± 0.3 mm/yr over the past 6 ka and 5.4 mm/yr over the past 2.4 ka, based on offset buried channels of Galindo Creek. These rates are similar to the reported creep rate of 2.5 – 3.3 mm/yr measured over two decades (Galehouse and Lienkaemper, 2003). The Green Valley fault is the northward continuation of the Concord fault, with a reported minimum slip rate over the past 300 years of 3.8 – 4.8 mm/yr (Baldwin and Lienkaemper 1999) at the Lopes Ranch site. As with the Concord fault, the reported geologic rate on the Green Valley fault is similar to the reported creep rate (4.4 mm/yr) (Galehouse and Lienkaemper, 2003). Late Quaternary slip rates have not been developed for other faults in this system such as the Hunting Creek – Berryessa or the Bartlett Springs faults. However, geodesy, in the form of continuous and survey-mode GPS arrays, suggest creep rates as high as 8 mm/yr for parts of the Bartlett Springs fault northwest of Lake Pillsbury, although creep rates are somewhat lower at Lake Pillsbury and to the south (Murray et al., 2013).

San Gregorio and Greenville slip rates - The San Gregorio fault is the westernmost recognized active fault and is part of a system of faults that accommodate dextral shear west of the SAF, south of where they merge with the SAF near Bolinas Lagoon. The San Gregorio fault is largely offshore,

but is exposed on land at Point Ano Nuevo as well as at Seal Cove. At Seal Cove, Simpson et al., (1997) report a slip rate of 3.5 – 4.5 mm/yr over the past 80 ka, but note that this may be a minimum rate for the zone, due to additional, unaccounted for slip on offshore strands of the fault. At Año Nuevo, Weber and Nolan (1995) report a slip rate of 3–9 mm/yr, based on a stream incised into a ~100 ka marine terrace that is offset across multiple strands of the fault. The Greenville fault is the easternmost strike slip fault in the San Francisco Bay Region (SFBR). Berger et al., (2010) report a minimum rate of 2 mm/yr, averaged over the past 10 ka, based on an offset buried channel.

Northern San Andreas Paleoseismology – The northern San Andreas System has been the focus of numerous paleoseismic studies (Figure 3) in an attempt to understand the timing, spatial extent and recurrence of large, surface rupturing earthquakes. Such information is used extensively in seismic hazard studies such as those produced by the WGCEP (WGCEP 2003; WGCEP 2008; Field et al., 2013). Published earthquake ages and recurrence estimates at key paleoseismic sites are summarized by Weldon et al., (2013) as part of the most recent WGCEP study (Field et al., 2013). Despite the number of attempts to develop long term chronologies, only a handful of studies have produced records of more than a few earthquakes, although the timing of the most recent and penultimate events are known for most of the major faults in the SFBR (Schwartz et al., 2014).

On the northern San Andreas Fault, paleoseismic studies have focused on the timing of past earthquakes and how similar these earthquakes were to the 1906 earthquake, in terms of rupturing the entire northern SAF, from Point Arena to San Juan Bautista. The Vedanta site, located north of San Francisco on the North Coast Section (SAN) of the SAF has one of the longest records of paleoseismic surface ruptures on the northern SAF. Zhang et al., (2006) identify 12 surface rupturing earthquakes in the past ~3 ka, yielding an average recurrence interval of about 250 years between earthquakes. Near Fort Ross, Kelson et al., (2006) present a composite record from two sites, the Fort Ross Orchard and Archae Camp sites, and identify five surface rupturing earthquakes over the past ~1500 years. At the Fort Ross Orchard site, event evidence is expressed in the trenches as scarp derived colluvial wedges, upward terminations, and fissure fills. Kelson et al., (2006) also summarize paleoseismic studies for other onshore sites on the northern SAF, including sites with shorter and less well-resolved records, and present a correlation diagram for earthquakes on the northern SAF (Figure 4).

Indirect evidence of large northern SAF earthquakes comes in the form of marine turbidites, observed in cores taken from submarine channels (Goldfinger et al., 2007). The turbidites are thought to be the product of strong shaking related to large earthquakes on the SAN and offshore section of the San Andreas Fault (SAO). While marine turbidites can be triggered in a number of ways (e.g. storms, sediment loading), researchers working in Cascadia have developed a number of criteria that attempt to distinguish earthquake-triggered turbidites from those triggered by other mechanisms (Adams, 1990). For the turbidites found offshore of California, Goldfinger et al., (2007) rely primarily on a test of synchroneity, arguing that simultaneous triggering of turbidites over a large area is likely due to earthquake shaking, rather than other causes. Another key test is employed at the confluences of submarine channels, where cores show multiple turbidite pulses within a short period of time, each with a unique mineralogy related to the source area of the onshore drainage. This is further evidence that the turbidites were triggered by the same mechanism over a large area. In their study, Goldfinger et al., (2007) establish synchronous triggering in individual channels along 320 km of coastal California. For the northern SAF earthquake chronology, Goldfinger et al., (2007) rely primarily on cores collected at Noyo Canyon, in which 15 turbidites are recognized and have been deposited in the past ~2800 years, yielding an average repeat time of ~200 years (Figure 5). Using radiocarbon dating and hemipelagic sedimentation rates as dating constraints, Goldfinger et al., (2007) also developed a chronologic age model in order to derive individual turbidite ages, and to compare these ages to the long onshore paleoseismic records at the Vedanta and Fort Ross sites. While the average repeat times of the turbidite and onshore records are similar (~200 years versus ~230 years),

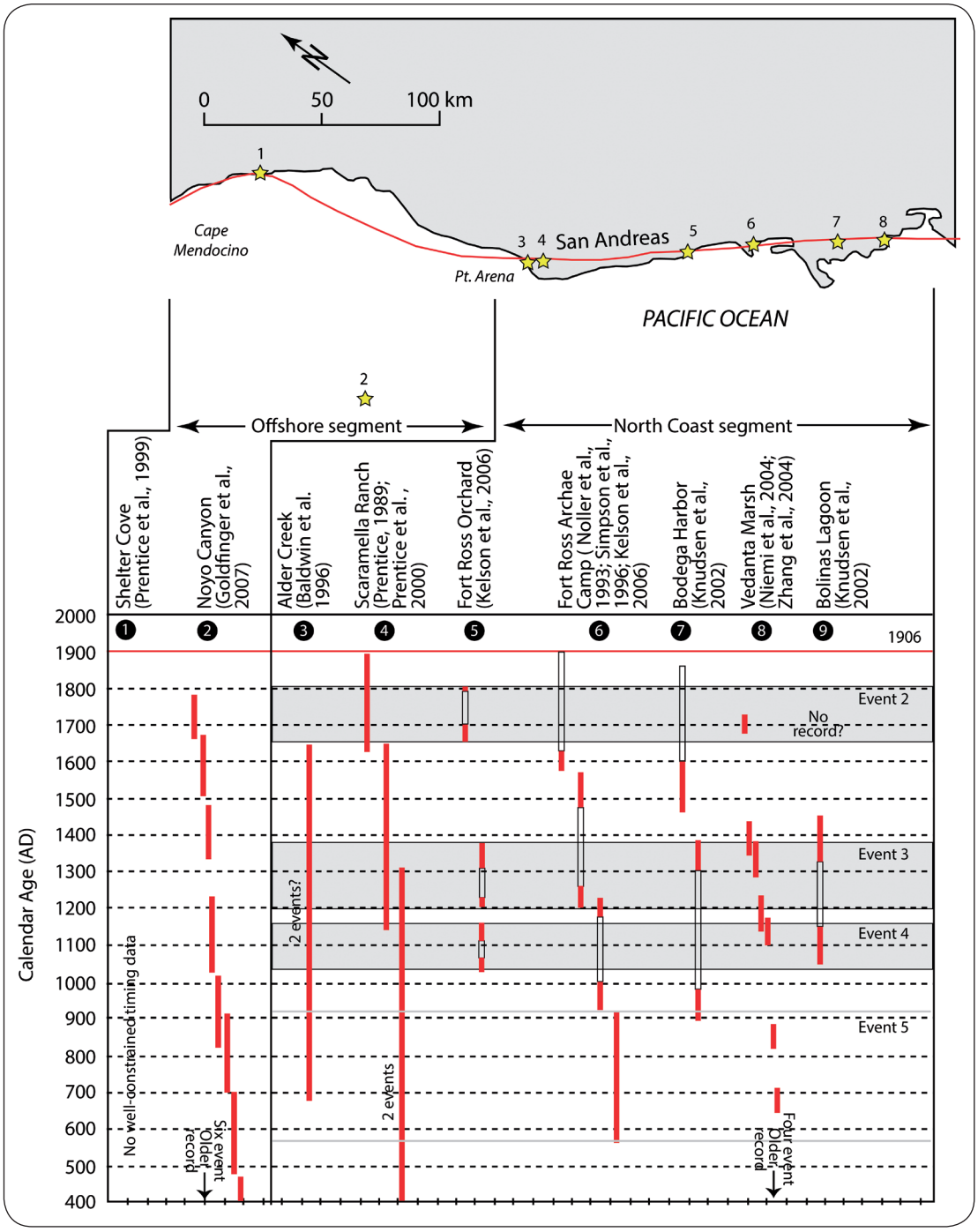

Figure 4. Event ages and proposed earthquake correlations for sites on the northern San Andreas Fault. Open rectangles show 1-sigma calibrated age ranges. Solid rectangles are 2-sigma calibrated event ages. Grey horizontal rectangles are proposed event correlations of Kelson et al., (2006). Modified from Kelson et al., (2006).

correlation of individual event ages of the onshore and offshore records is more difficult (Figure 5). Goldfinger et al., (2007) argue that the ages of offshore events are in reasonably good agreement with those observed at Fort Ross, although they note that Turbidite 3/4 does not have a corresponding earthquake at Fort Ross. Comparison of the turbidite record with events at the Vedanta site is even more problematic, as the individual event age ranges are too broad to uniquely correlate between the two records and it is unclear whether this issue is a function of limitations in stratigraphic resolution, poorly resolved age dating, or actual differences in the earthquake record between the sites.

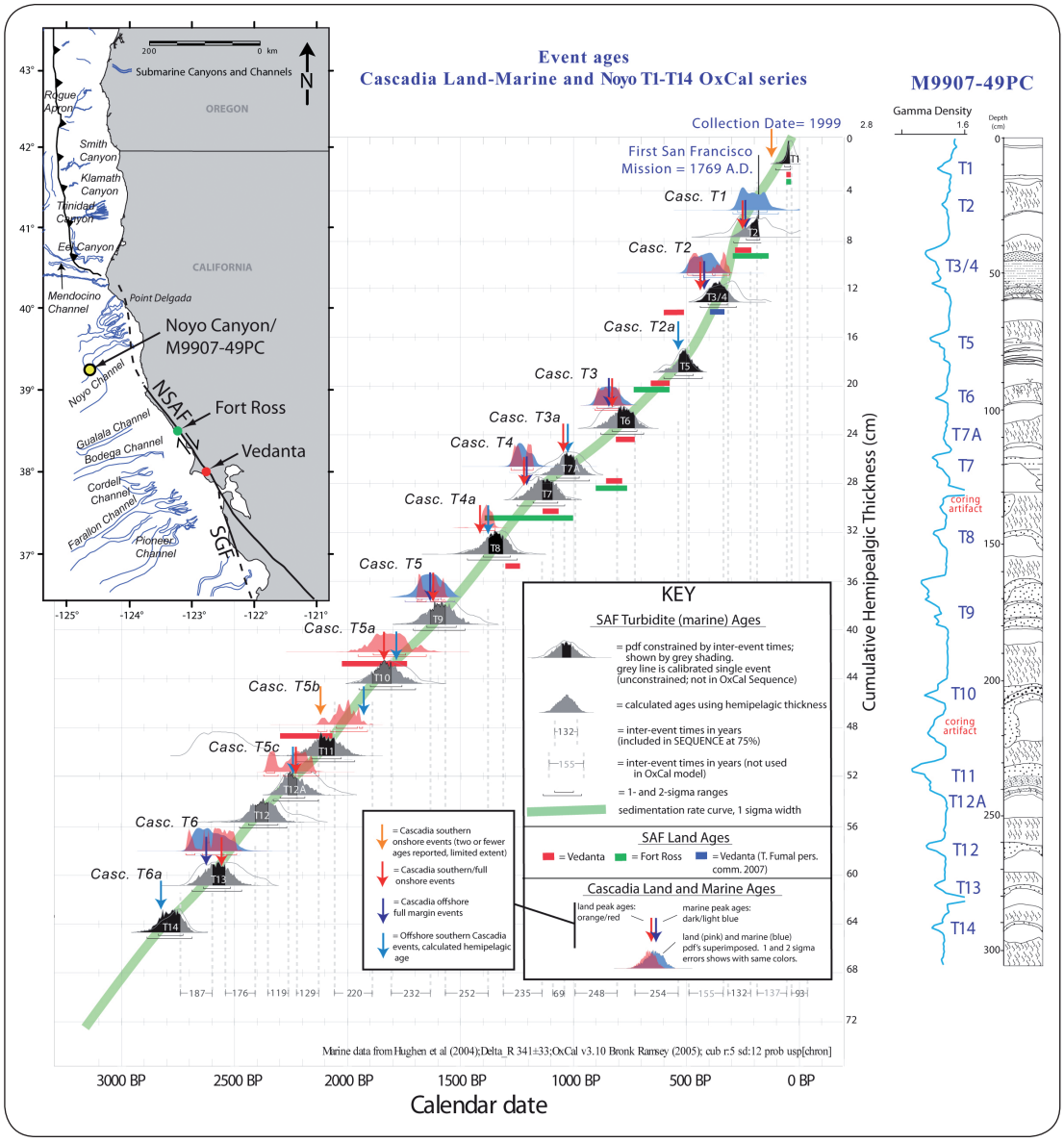

Figure 5. OxCal age model for the youngest 15 events in the northern SAF offshore system, and comparison to onshore ages. Inter-event times based on hemipelagic sediment thickness (represented by gray bars) were used to constrain original 14C calendar age distributions (gray traces) using the SEQUENCE option in OxCal. Inter-event times were estimated by converting hemipelagic sediment thickness between each pair of events to time using the sedimentation rate. Events dated more than once were combined in OxCal prior to calibration if results were in agreement; if not in agreement, the younger radiocarbon age was used in the final model. Five ages are calculated from sedimentation rates where not enough forams were present for 14C dating. The resulting probability distributions (filled black, gray for undated events) are mostly in good agreement with land ages from Fort Ross except for T3-4 and T7a (green lines) and Vedanta (red lines). From Goldfinger et al., (2007).

Long event records are not available on the Peninsula section of the San Andreas (SAP) (Figure 3). At the Filoli site (Figure 3), Hall et al., (1999) interpret one earthquake prior to 1906, inferred on the basis of a channel offset of 4.1 ± 0.5 m,which is 1.6 meters more than the 2.5 meters of slip that occurred in 1906. Based on historical accounts in the area, Hall et al., (1999) attribute this 1.6 meters

of excess slip to an earthquake that occurred in A.D. 1838, although the event age is not well-constrained by radiocarbon dating and could have occurred anytime after A.D. 1450. Based on this apparently smaller earthquake, Hall et al., (1999) argue that, in addition to large 1906-type earthquakes, the SAP may fail in smaller (Mw 7.0 – 7.4) 1838-type earthquakes.

On the Santa Cruz Mountains section (SAS) of the SAF, four paleoseismic sites provide insights into the behavior of the fault as it transitions from being fully locked to mostly creeping (Figures 3, 6).The northernmost site is Grizzly Flat, where Schwartz et al., (1998) present evidence for 1906 and one earlier earthquake dated between A.D. 1632 and 1659, based on a combination of dendrochronology of a tree stump located on the fault and radiocarbon ages of charcoal taken from the trenches. Fumal (2012) reevaluated the Grizzly Flat data and noted possible problems with the dating of the earlier event, and concluded that the trench and the tree rings may not be recording the same event. Fumal (2012) also reinterpreted the trench logs of Schwartz et al., (1998) and identified two additional possible earthquakes that occurred after the older earthquake reported by Schwartz et al., (1998) and before 1906. Based on this reinterpretation and a revised age model, Fumal (2012) reports earthquake ages of 1906 for GF-1, 1828 – 1906 for GF-2, 1733 – 1872 for GF-3, and 1105 – 1545 for GF-4, although he notes the record may be incomplete due to poor stratigraphic resolution at the site.

Six kilometers southeast of Grizzly Flat is the Hazel Dell site, where in addition to the 1906 earthquake, paleoseismic excavations have uncovered evidence of two pre-1906 nineteenth-century earthquakes and an earlier earthquake dated to between A.D. 760 and 1318 (Streig et al., 2014) (Figure 6). The ages of the two 19th century earthquakes are constrained by archeological artifacts, in the form of cut woodchips found below the Event 3 horizon in the trenches. Based on historical accounts, the area was settled in the early 1800's and logging in the area of the site probably began no later than 1832, with the construction of a sawmill by the land grantee. Streig et al., (2014) interpret the two 19th century earthquakes to be the April 1890 and June 1838 earthquakes, based on historical accounts of

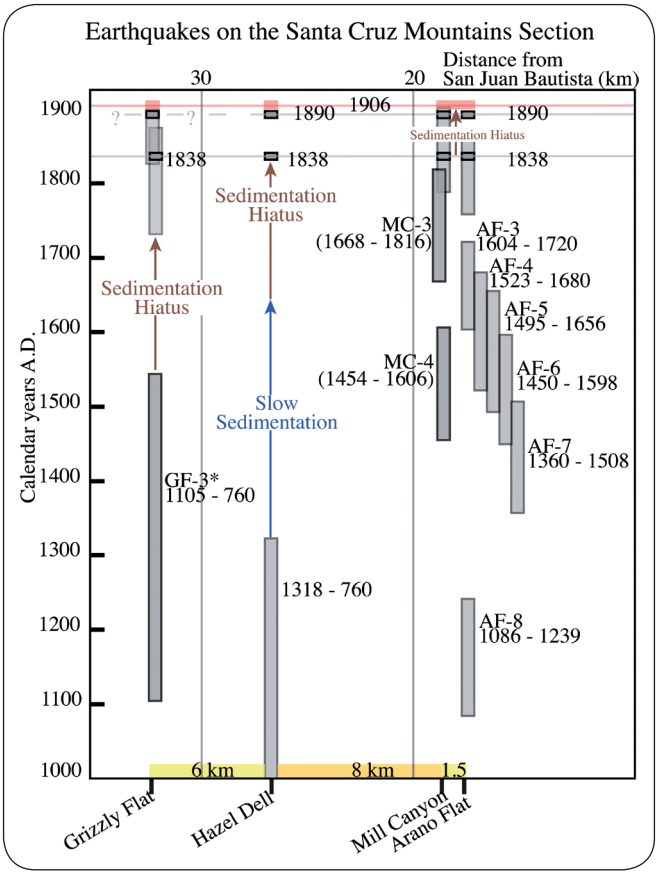

Figure 6. Time space diagram for the SAS showing the distribution of paleoseismic investigation sites. Distance north of San Juan Bautista shown at the top of the figure. Sites from north to south are: Grizzly Flat (Schwartz et al., 1998; Fumal 2012), Hazel Dell (Streig et al., 2014), Arano Flat (Fumal et al., 2003a, 2003b), and Mill Canyon (Fumal, 2012). Distance between adjacent sites shown at the bottom of the figure. Modeled event age ranges are shown as rectangles for all four sites, horizontal lines are event correlations between sites. From Streig et al., (2014).

earthquakes in the region, which likely were both located on the San Andreas Fault (Bakun, 1999). Streig et al., (2014) note that without the historical constraints provided by the archeological artifacts and the exceptional stratigraphy during this timeframe, it would be impossible to precisely date these two earthquakes using radiocarbon, as the radiocarbon uncertainties for samples below the E3 horizon are large. The sedimentation rate is low during the time period of the fourth earthquake identified in the exposures at Hazel Dell (A.D. 760 and A.D. 1318), and thus the paleoseismic record may be incomplete during this time interval.

The Mill Canyon and Arano flat sites lie, respectively, 8 km and 9.5 km southeast of the Hazel Dell Site (Figure 3). At the Mill Canyon site, Fumal (2012) identified five earthquakes during the past 500 years, including the 1906 earthquake. Earthquake evidence at the site includes buried scarps, fissure fills, and colluvial wedges. Earthquake age constraints are provided by radiocarbon dates along with historical constraints from non-native pollen (*Erodium cicutarium*) found in thestratigraphic section, which was introduced to the area by Spanish settlers. Average recurrence for the past five earthquakes is about 125 years (100 – 150 years). The earthquake prior to 1906 occurred either about A.D.1711–1770 or A.D. 1789–1904, depending on assumptions incorporated into two alternative age models. If the later age range is correct, the 1789 – 1904 earthquake may be the June 1838 earthquake, which likely ruptured the SAF Peninsula and Santa Cruz Mountains sections of the fault, based on reports of shaking in the region (Toppozada and Borchardt 1998). The Arano Flat site, located about 1.5 km southeast of Mill Canyon, has a longer record of earthquakes, with evidence of nine earthquakes in the past ~900 years and an average recurrence interval of about 106 years (Fumal et al., 2003; Weldon et al., 2013).

The four sites on the SAS section of the fault all appear to exhibit shorter recurrence times between earthquakes than observed on the SAN and SAO sections, with the recurrence interval at the Arano Flat and Mill Canyon sites being about half of what is implied by the onshore and offshore records on the northern SAF. One possible explanation for this discrepancy is that these sites are located near the zone where the fault transitions from aseismic creep to the south to being fully locked in the area near Arano Flat (Johanson and Bürgmann, 2005) and may be failing in smaller, more frequent surface-rupturing earthquakes. Earthquake recurrence for the Hazel Dell and Grizzly Flat sites may be somewhat longer than for the sites farther south, although the records may be incomplete over the same time interval preserved at the Mill Canyon and Arano Flats sites (Figure 6).

Calaveras – Hayward – Rodgers Creek – Maacama Paleoseismology – Earthquake records on the Calaveras fault are complicated by high creep rates along the length of the fault, which may overprint evidence of coseismic surface ruptures. At the Leyden Creek site (Figure 3), past earthquake ruptures are primarily identified based on scarp-derived colluvial wedges, inferred to have formed as a result of discreet ruptures (Kelson et al., 1996). Kelson et al., (1996) identify five or six events during the past 2500 years and calculate an average recurrence of 500 ± 300 years.

On the southern Hayward fault, the record at the Tyson's Lagoon site (Figure 3) is the longest and perhaps best resolved record of paleoearthquakes on the northern San Andreas Fault system. The site, located in a structural graben along the Hayward fault, is ideally suited to record earthquakes, with continuous deposition and abundant datable material that has accumulated in a sag pond for much of the Holocene (Lienkaemper and Williams 2007). Evidence for individual earthquakes is discussed by Lienkaemper et al., (2002), Lienkaemper and Williams (2007), and Lienkaemper et al., (2010), and comes in the form of scarp-derived blocky colluvium, discrete increases in vertical separation, and liquefaction at horizons also associated with faulting. Active creep may complicate the interpretation of discrete faulting events, although Lienkaemper et al., (2002) note that creep is unlikely to produce scarp-derived colluvium, and liquefaction related features cause by seismic shaking is further evidence that these are coseismic events. Lienkaemper et al., (2010) report that 12 events have occurred during the past 1900 years and calculate an average recurrence of 161 ± 65 years, with a coefficient of variation for the past 12 earthquakes of 0.40, suggesting earthquakes on the fault are somewhat periodic.

On the northern Hayward fault, a record of four to seven earthquakes over the past ~2000 years has been developed at the Mira Vista site, located in a small graben (Hayward Paleoearthquake Group (HPEG), 1999) (Figure 3). Four of the earthquakes are considered well resolved with clear evidence, while three other possible earthquakes were identified with weaker evidence in the exposures. Based

on radiocarbon ages and pollen studies, the most recent event occurred after A.D. 1640, but before ~1776, suggesting this part of the fault did not rupture during the 1868 earthquake, which ruptured the southern part of the fault. HPEG (1999) note that the record may be incomplete and that the radiocarbon constraints are not precise enough to evaluate variability in recurrence. However, event ages from HPEG (1999) data were reevaluated and are presented in Weldon et al., (2013) with an average recurrence of about 400 years.

Farther north, along the Rodgers Creek and Maacama faults, long, well-resolved paleoseismic records are lacking. On the Rodgers Creek fault, Schwartz et al., (1992) identify three events during the past 1100 years at the Triangle G site, but were unable to obtain ages of individual earthquakes. Using radiocarbon and pollen constraints, Hecker et al., (2005) report the most recent event on the Rodgers Creek fault at the Triangle G site probably occurred after A.D. 1715 and before A.D. 1776. A buried channel is offset a minimum of $2.2^{+1.2/-0.8}$ meters by this earthquake. This is similar to an offset measurement of 1.8-2.3 meters at the Beebe Ranch site (Budding et al., 1991) about 1 km to the south. Hecker et al., (2005) note that the age range for this most recent earthquake (MRE) on the Rodgers Creek fault is similar to the reported age range for the MRE at the Mira Vista site on the northern Hayward fault, as well as the penultimate earthquake at Tyson's Lagoon, suggesting that the Hayward – Rodgers Creek fault system may have failed together in one earthquake, or within a short period of time during multiple earthquakes. Prentice et al., (2014) infer two, and possibly as many as three, paleoearthquakes on the Maacama fault at the Haehl Creek site after about A.D. 770, supporting the idea that the fault is partially locked and supports infrequent large earthquakes.

Concord – Green Valley – Bartlett Springs Paleoseismology – Two sites located on the Green Valley fault provide the only record of multiple earthquakes on the Concord – Green Valley - Bartlett Springs fault system. Lienkaemper et al., (2013) present evidence of four earthquakes at the Mason Road site during the past ~1000 years (Figure 3). At the Lopes Ranch site, 12 km south of the Mason Road site, Lienkaemper et al., (2013) present evidence of three earthquakes: an earthquake around A.D. 1609, and two earlier earthquakes between 18 BCE – 238 CE (Figure 3). A period of low sedimentation prior to the most recent earthquake makes this record incomplete, although Lienkaemper et al., (2013) use the intervals between earthquakes from both sites to calculate a composite average recurrence interval of 199 ± 82 years.

Insights into behavior from paleoseismology of the northern San Andreas Fault system – While long, well-resolved records for individual faults within the northern San Andreas system are few, making it difficult to understand the long term history of each fault, ages of the most recent earthquake and penultimate events are known for most of the major faults and provide some insight into how stress accumulates and has been released across the region. Schwartz et al., (2014) present a compilation of these SFBR earthquakes, estimate seismic moments for each of these earthquakes, and estimate moment release rates for different time intervals between A.D. 1600 and 2012. From this record, they infer that moment release during this period is dominated by either great earthquakes, such as the 1906 earthquake, or is distributed in multiple, smaller magnitude earthquakes on other faults within the system. Figure 7 shows three models proposed by Schwartz et al., (2014) for rupture scenarios between 1600 to 1690 and 1690 to 1776. During the period from 1690 to 1776, Schwartz et al., (2014) suggest that a cluster of earthquakes on several faults (northern San Andreas, Santa Cruz section of the San Andreas, Hayward, Rodgers Creek, northern Calaveras, and San Gregorio) dominate moment release in the region, while the 1906 earthquake dominates moment release in the region during the historical period from 1776 to 1906. This paleoseismic data has also been used to model stress changes in the SFBR at different times (Figure 8) and according to this model, following the cluster of earthquakes in the 1600 to 1776 interval, stress was relaxed on most faults within the system, similar to a regional

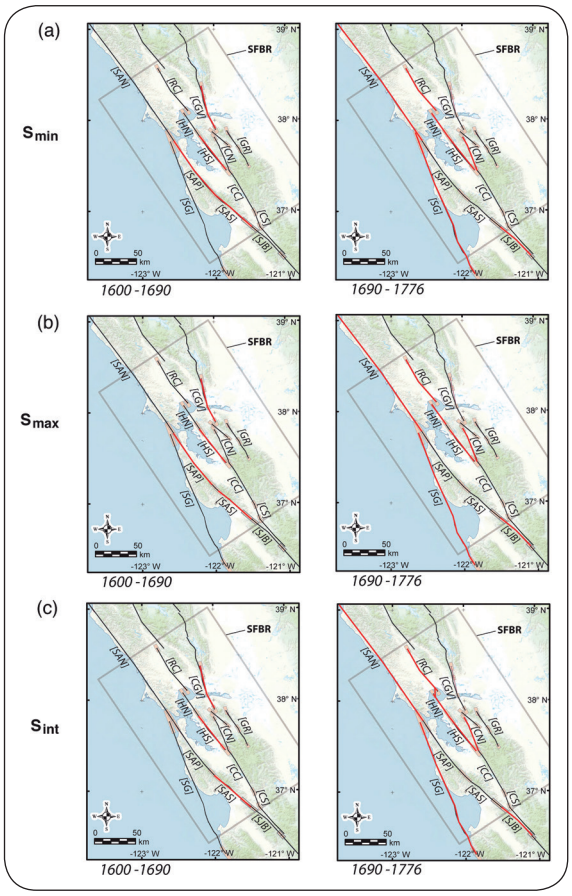

Figure 7. Map of proposed paleoseismic surface ruptures for time interval 1600-1776. a) minimum source model, Smin; b) maximum source model, Smax; c) preferred source model, Sint as proposed by Schwartz et al., (2014). There are no data on timing of the most recent surface rupture on the Greenville fault (GR) or the northern extension of the Concord-Green Valley fault (CGV). The Central Calaveras fault (CC) is creeping at or near its long-term plate rate and it is uncertain whether it produces large surface ruptures; none has been interpreted for the paleoseismic time interval of interest here. From Schwartz et al., (2014).

decrease in stress following the 1906 earthquake (Pollitz and Schwartz, 2008). Figure 8 also shows that in the past 100 years, stress has increased across the region, and is particularly high on the Hayward and Rodgers Creek faults. In general, these observations suggest a model of stress build-up, then release of some stress on faults in moderately large earthquakes, followed by rupture of the San Andreas Fault in 1906-type earthquakes, followed by a period of lower seismicity while the region remains in a stress shadow.

Southern San Andreas System – The southern San Andreas Fault system is an evolving complex of faults with considerably disparate histories whose individual components each play a distinct role. The SAF (sensu stricto) appears to be Pliocene and younger with about 180-200 km of total displacement in southern California (Powell, 1993; Powell and Weldon 1992; Darin and Dorsey 2013). An additional ~50 km of displacement occurred in the late Miocene between about 12 and 5 Ma on the present-day San Gabriel fault. (Crowell 1979; 1982; Powell 1993). Geometric complexity and accompanying changes in the fault trace is documented through the activation and cessation of several ancestral strands of the San Andreas Fault in the central Transverse Ranges (Matti et al., 1992). During the Miocene, an ancestral strand called the Banning Fault accommodated motion near the San Bernardino Mountains; this fault is now inactive. At the end of Miocene time, slip was transferred onto the Wilson Creek strand and then onto the Mission Creek strand in the Pliocene, which have a total of 44 and 89 km of slip, respectively. In the Quaternary, at least 14 km of slip has been accommodated on several strands active within and at the periphery of the central Transverse Ranges: the San Gorgonio Pass Fault zone, and four strands of the San Andreas: the Mill Creek, San Bernardino, Banning and Garnet Hill faults ((Figure 9)(Matti et al., 1992; Matti and Morton 1993).

The San Jacinto and south-central Elsinore faults, and probably some elements of the coastal zone of strike slip faults, including the Rose Canyon fault in San Diego and the Agua Blanca fault in northern Baja California, initiated motion in the early Quaternary (Rockwell et al., 1990; Hull and Nicholson 1992; Morton & Matti 1993; Magistrale and Rockwell 1996; Albright 1999; Janecke et al., 2010; Dorsey et al., 2012). Bennett et al., (2004) suggest that the San Andreas and San Jacinto Faults may have experienced a variable slip rate history, although new slip rate data on the San Jacinto Fault suggests no discernable change in rate for at least the past half million years (Blisniuk et al., 2013). In any case, the southern San Andreas Fault system experienced a profound change and reorganization in distribution of slip in the early Quaternary, setting the stage for

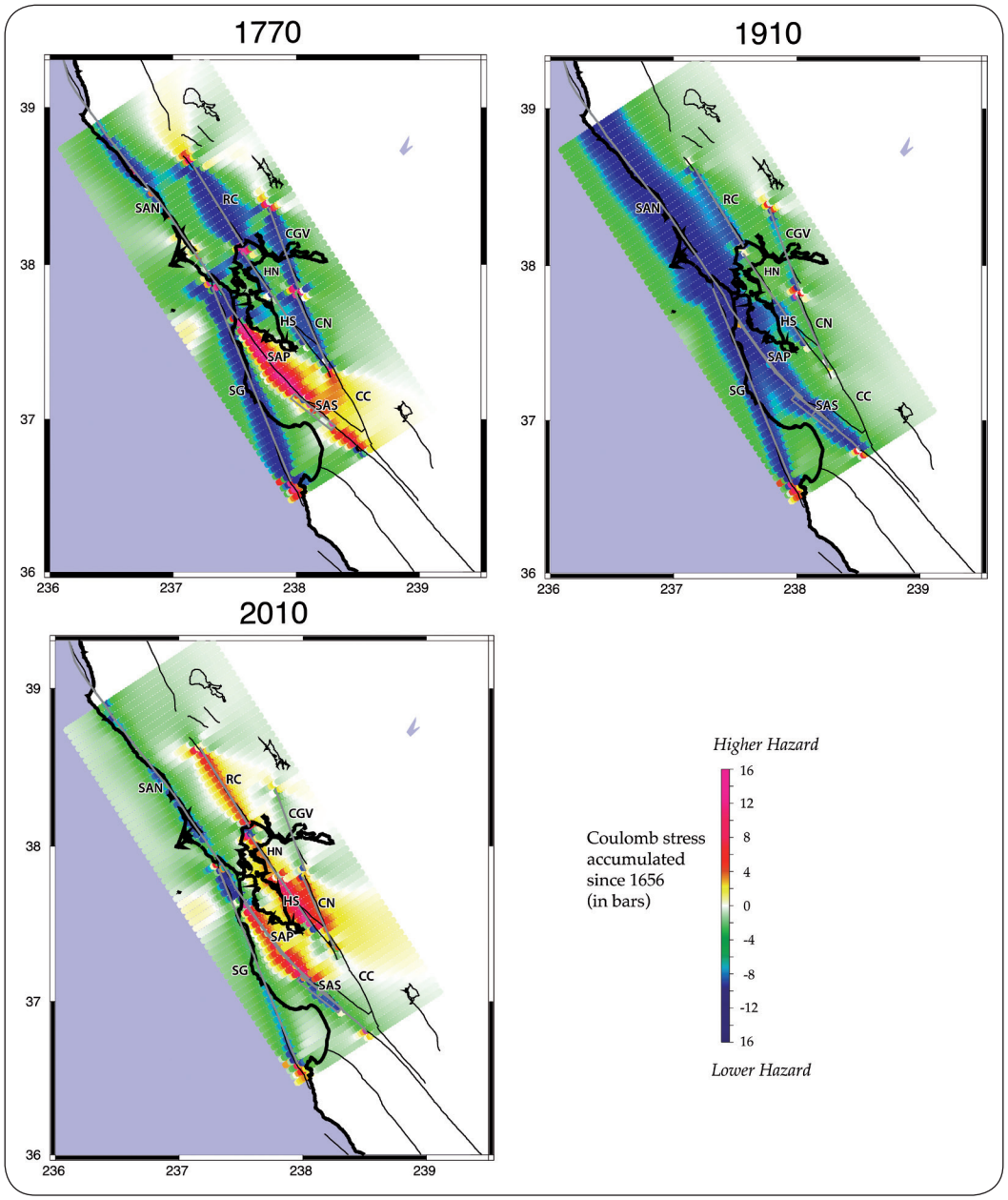

Figure 8. Snapshots of modeled cumulative stress changes in the SFBR. Three time slices from a stress evolution model extending from 1660 to 2040 are shown (modified from Pollitz and Schwartz, 2008). The warmer colors indicate increased Coulomb stress and the cooler depict decreased stress. The time slice for 1770 shows the regional decrease in stress following a sequence of large earthquakes. The time slice for 1910 shows the modeled stress in the SFBR following the 1906 earthquake. The time slice at 2010 reflects the general increase in stress across the SFBR at essentially the present time. From Schwartz et al., (2014).

the modern tectonic environment (Matti et al., 1985; Matti et al., 1992; Matti and Morton 1993; Morton and Matti 1993; Yule and Sieh 2003).

Southern San Andreas Fault slip rate - Estimates of the slip rate for the south-central San Andreas Fault vary along fault strike (Figure 10), with 33+3 mm/yr in the Carrizo Plain (Sieh and Jahns 1984), ~3 cm/yr in the central portion of the Mojave section (Matmon et al., 2005), decreasing to 24.5 +3.5 mm/yr at the southeast end of the section near Cajon Pass (Weldon and Sieh 1985), decreasing further to 12-13 mm/yr near San Bernardino

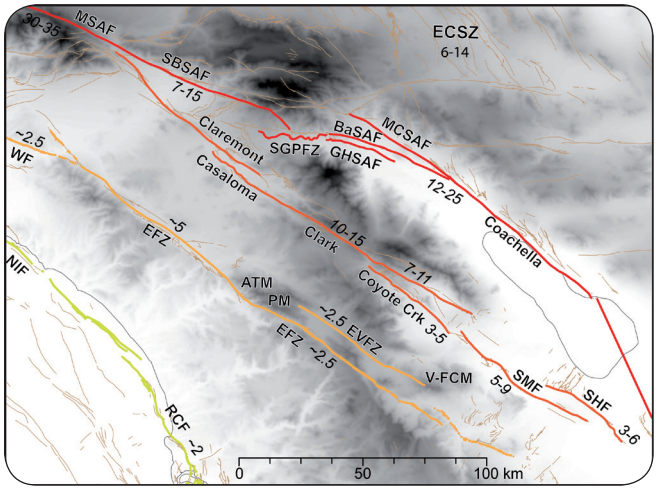

Figure 9. Fault map highlighting primary strands of the San Andreas Fault (red), San Jacinto Fault (dark orange), Elsinore Fault (yellowish orange) and Rose Canyon Fault Zone (greenish yellow). The SAF includes: MSAF-Mojave section; SBSAF-San Bernardino section; SGPFZ-San Gorgonio Pass Fault Zone; BaSAF-Banning strand; MCSAF-Mission Creek strand; GHSAF-Garnet Hill strand. EVFZ=Earthquake Valley fault zone, EFZ=Elsinore fault zone, WF=Whittier fault zone, RCF=Rose Canyon fault zone, NIF=Newport-Inglewood fault zone. ATM=Agua Tibia Mountain, PM=Palomar Mountain, V-FCM=Vallecitos-Fish Creek Mountains. Simplified fault slip rates in mm/yr, see text for references. Base map generated from GMTED2010 digital elevation from the U.S. Geological Survey.

(McGill et al., 2013), and increasing again to 16-22 mm/yr in the Salton Trough (Fletcher et al., 2010; Behr et al., 2010). Geodetic measurements yield similar rates, although they are, in part, model-dependent (e.g., Chuang and Johnson 2011). The geodetic rate based on continuous GPS measurements in the Carrizo Plain is a little slower than the geologic rate at 29 mm/yr, but there is a similar pattern of decrease in rate in the San Bernardino area. The slowest geodetic rate is in the vicinity of San Gorgonio Pass at 9 mm/yr, and the rate increases southward into the Salton Trough (Parsons et al., 2013; Bennett et al., 2004b; Fialko, 2006). Part of these variations in rate can be explained by the distribution of displacement between the San Andreas and San Jacinto Faults, with a higher rate north of their juncture. Part of the reduction to the south is attributed to 6-14 mm/yr of motion being transferred to the Eastern California Shear Zone (Sauber 1986; Rockwell et al., 2000a).

San Jacinto Fault slip rate - The San Jacinto Fault also exhibits variations or gradients in slip rate (Figure 10), with about 12–13 mm/yr accommodated by the main strand of the fault at Anza, where nearly all of the long term slip is concentrated (Sharp 1967; Rockwell et al., 1990; 2014; Blisniuk et al., 2013). Southward, the slip rate decreases along the Clark strand of the fault to about 9 mm/yr at Rockhouse Canyon and less than 2 mm/yr near the southern end of the fault near the southeastern end of the Santa Rosa Mountains (Blisniuk et al., 2010). There is a concomitant increase in rate along the sub-parallel Coyote Creek strand from zero at its northern end to about 5 mm/yr at Ash Wash (Blisniuk et al., 2010). Farther south, the Coyote Creek fault splits into the Superstition Mountain and Superstition Hills faults, with slip rates estimated at 5–9 mm/yr (Gurrola and Rockwell 1996) and 3–6 mm/yr (Hudnut and Sieh 1989), respectively.

The slip rate for the northern San Jacinto Fault is less well constrained, with estimates ranging from 3 to 22 mm/yr (Figure 10; Wesnousky et al., 1991; Morton and Matti 1993; Kendrick et al., 2002). Onderdonk et al., (2015) resolved a rate of 12 to 19 mm/yr and suggest that a best-estimated rate of 15+/2 mm/yr satisfies almost all geologic and geodetic slip rates for the entire length of the fault, with the slightly lower rate at Anza explained by minor slip on the secondary strands of the fault zone to the northeast of Anza (Hot Springs and Thomas Mountain faults).

Elsinore fault slip rate - The Elsinore fault zone is relatively simple in the north, but splits into at least two major strands along the central and southern parts of the fault zone (Magistrale and Rockwell 1996), with both the western Elsinore strand and the eastern Earthquake Valley strand accommodating a similar amount of the slip rate (Figure 9; Rockwell et al., 2013). The northern Elsinore transfers about 5 mm/yr based on dating offset alluvial fans using soil development for chronologic control (Millman and Rockwell 1986; Vaughan and Rockwell 1986), albeit with large age uncertainties. A similar rate of $4.9^{+1/-0.6}$ mm/yr was estimated by Rockwell et al., (2000b) on the northern Elsinore based on 3D trenching

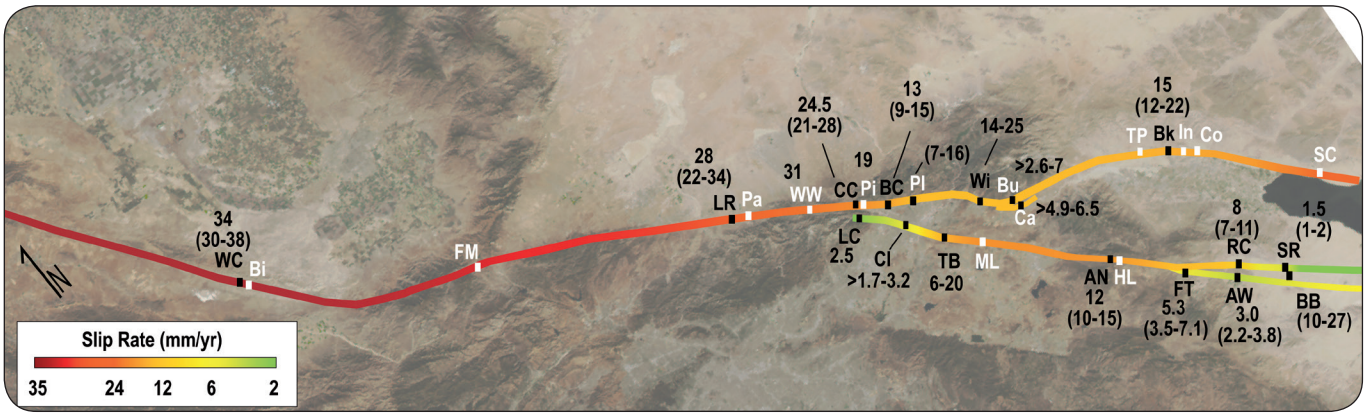

Figure 10. Simplified slip rate map for the southern San Andreas and San Jacinto Faults. Sites identified with black label are slip rate sites, white labels indicate paleoseismic event sites. Slip rates adapted from McGill et al., (2013) and Blisniuk et al., (2013). Site names: WC-Wallace Creek; Bi-Bidart Fan; FM-Frazier Mountain; LR-Littlerock; Pa-Pallett Creek; WW-Wrightwood; CC-Cajon Creek; Pi-Pitman Canyon; BC-Badger Canyon; Pl-Plunge Creek, Wi-Wilson Creek; Bu-Burro Flats; Ca-Cabazon; TP-Thousand Palms; Bk-Biskra Palms; In-Indio; Co-Coachella; SC-Salt Creek; LC-Lytle Canyon; Cl-Colton; TB-San Timoteo Badlands; ML-Mystic Lake; An-Anza; HL-Hog Lake; RC-Rockhouse Canyon; SR-Santa Rosa; FT-Fishcreek; AW-Ash Wash; BB-Borrego Badlands. Detailed references provided in text.

of a 1.9 ka fluvial channel that is offset about 10 m. This rate also has a large uncertainty because it is determined for a short period of time, during which there have likely been only a few surface ruptures. Southward, transfer of 2.5 mm/yr of the slip rate to the Earthquake Valley fault has produced uplift of Palomar and Agua Tibia Mountains, and similarly, transfer of slip from the Earthquake Valley to the southern San Jacinto Fault has produced uplift of the Vallecito and Fish Creek Mountains (Figure 9).

Slip Rates on Other Faults - The coastal and offshore faults of the plate boundary system are generally slower than the three main strands of the southern San Andreas system (Figure 9), with the Rose Canyon fault accommodating 1.5–2 mm/yr of slip (Lindvall and Rockwell 1995; Rockwell 2010), the Palos Verdes fault coming in at about 3 mm/yr (McNeilan et al., 1998; Stephenson et al., 1995), and the onshore Newport-Inglewood fault slipping at about 0.5 mm/yr (brittle slip - Freeman et al., 1992), with an additional component of warping or folding deformation. Rates on other offshore faults are poorly constrained, but the total rate probably does not exceed the 6 mm/yr measured on the Agua Blanca fault in northern Baja California, to which these faults connect (Rockwell et al., 1993).

Finally, slip rates for most faults of the Eastern California Shear Zone (Figure 1) fall in the 0.5–1 mm/yr range (Rockwell et al., 2000b), with the total rate of shear estimated at 6–14 mm/yr based on geologic and geodetic measurements (Sauber et al., 1986; Rockwell et al., 2000b). Geodetic rates in this region generally are higher than the geologic rates (Oskin, 2008), possibly explained by distributed, off-fault deformation (Herbert et al., 2013).

Southern San Andreas Fault Paleoseismology - The Carrizo section of the southern San Andreas Fault extends southward from the creeping section for ~100 km. In this section, the fault is fairly straight, oriented parallel to the plate motion, and compared to other sections, isolated from other structures. The longest paleoseismic record on this section is at Bidart Fan (Figure 10), which has been investigated for over a decade due to the presence of a narrow fault zone that crosses excellent fan stratigraphy containing abundant dateable material (Akciz et al., 2009; Akciz et al., 2010; Grant and Sieh 1994) (Figure 11). The earthquake ages for this location have been refined over time due to improvements in accelerator mass spectrometry (AMS) radiocarbon dating that permit analysis of smaller samples, which increases the number of sampled sediment layers that can be used to constrain the earthquake age. Fissures and faulting

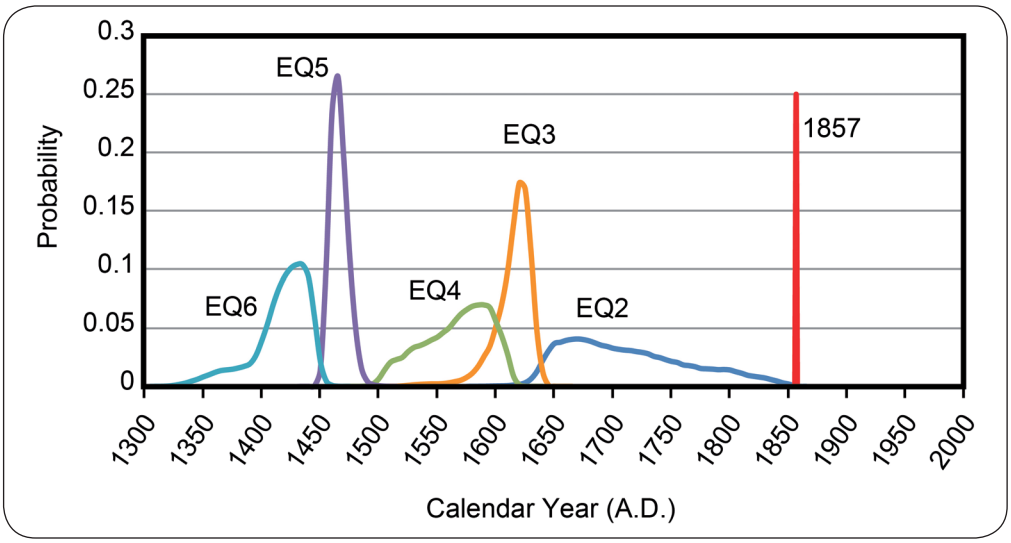

Figure 11. Probability distribution functions (PDFs) for earthquake ages determined at Bidart Fan, on the Carrizo section of the San Andreas Fault. Data from Akciz et al., (2010).

exposed in the trenches and dated with 33 radiocarbon samples constrain the 1857 rupture and five previous events to post ca. 1360 A.D. (Akciz et al., 2010) (Figure 11). The most significant change due to the AMS dating was an alteration in the understanding of the statistics of earthquake recurrence on the Carrizo. Due to the limitation from the dating, the previous study (Grant and Sieh 1994) concluded that earthquake recurrence was clustered; yet the new dates showed that the pace of earthquakes was more regular, consistent with a quasi-periodic behavior (Biasi 2013).

The additional dating at Bidart Fan also demonstrated that the average recurrence interval for the Carrizo section was significantly shorter than previously interpreted, from 160 years to only 88 (+/– 41) years for the period between 1360 and 1857 A.D. (Akciz et al., 2010). This reduction in interval length is supported by work at the Frazier Mountain paleoseismic site, located about 100 km to the southeast (Figure 10). Trenching investigations at Frazier Mountain show that since ca. 1400 A.D., there have been six ruptures, resulting in an average interval of ~90 years (Scharer et al., 2014). Preliminary work at Frazier suggests, however, that the short interval may not reflect the longer-term record of these sections, as only five earthquakes are preserved at the site in the period from ca. 500 to 1400 A.D.; resulting in an average recurrence interval of ~135 years, when averaged over the past ~1500 years.

The first long record of paleoearthquakes on the San Andreas Fault was developed on the Mojave section at the Pallett Creek paleoseismic site (Sieh 1978; Sieh 1984; Sieh et al., 1989) (Figure 10). The site is located at the base of the San Gabriel Mountains, where distal fan and sheet flow deposits alternate with charcoal-rich soil layers. This setting is ideal for paleoseismic studies as the high sedimentation rate (typically 0.1–1 cm/yr) helps to isolate a high-resolution record of ground rupturing earthquakes from disturbance due to burrowing animals. In the pioneering work done at the site, Sieh excavated a series of parallel cuts to track the deformation across the site, revealing the types of ground deformation seen in modern ruptures: broad folding, fissures, vertical offsets. Sieh et al., (1989) used conventional radiocarbon dating to constrain the earthquake ages. This technique offered the advantage of high-precision dating, but requires large samples and thus limited the number of layers that were dated. Later work by Scharer et al., (2011) re-dated the section with AMS techniques. Since AMS can be completed on smaller samples, more layers, and specific organic material from each layer (rather than a mix of radiocarbon sources), was dated. The re-dating found that although the total time span represented by the section was unchanged, several of the earthquake ages were slightly younger than previously reported (Figure 12). Overall, the slight changes in the ages

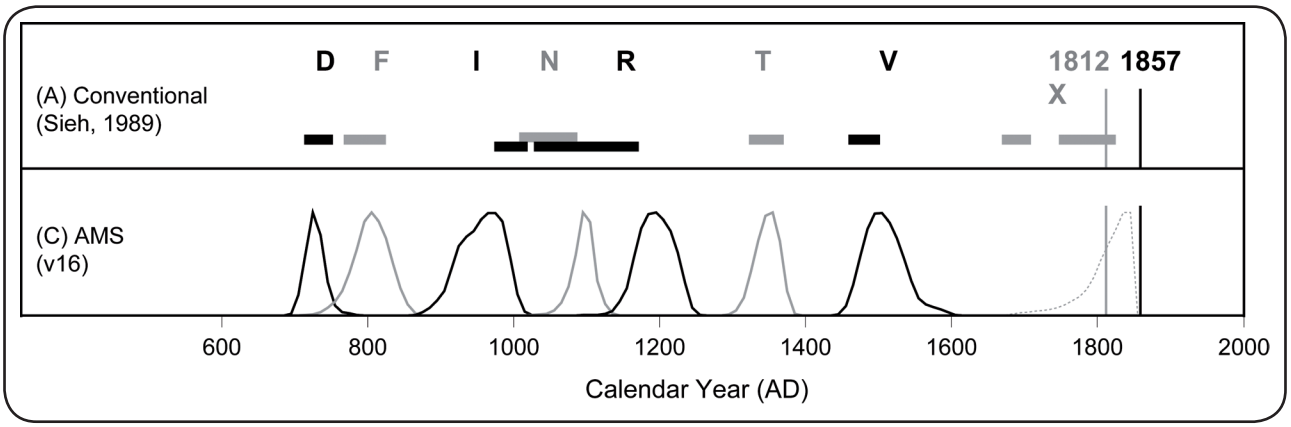

Figure 12. Comparison of earthquake ages from Pallett Creek. Upper panel shows age ranges provided by Sieh et al., (1989) based on conventional dates; lower panel shows PDFs of earthquake ages from Scharer et al., (2011) from AMS dates. The new technique permitted more layers to be dated and caused slight changes in the earthquake ages, revealing a more regular sequence.

produced a temporal recurrence that is more regular than the original estimate, with a quasi-periodic recurrence pattern (Scharer et al., 2011).

The longest record of paleoearthquakes on the SAF is from the Wrightwood paleoseismic site (Fumal et al., 1993; 2002; Biasi et al., 2002; Weldon et al., 2004; Scharer et al., 2007; 2010) (Figure 10). This site is located high in the San Gabriel Mountains, at the base of a steep catchment that provides a source for debris and mudflows that are deposited across the site. The clastic units are interbedded with organic and charcoal-rich horizons; pollen and macroflora analysis of organics indicates that upland marsh conditions were common until the early-1800s when a stream down cut across the debris fan and lowered the water level. Evidence for earthquake deformation at the site was documented in over 1 km of excavated trenches across the debris fan, which showed zones of complex vertical deformation and folding across the site during each earthquake (Weldon et al., 2002; Scharer et al., 2007). At present, two time periods have been fully investigated, from ca. 3000 to 1500 B.C. and ca. 500 A.D. to present. The old and younger periods have similar average recurrence intervals of ~100–120 years (Figure 13). Statistical examination of these records (Scharer et al., 2010) shows that no major rate changes have occurred across these periods. The number of earthquakes in the combined record (~30) was large enough that robust tests of the impact of paleoearthquake event quality and interpretation on the resulting recurrence behavior could be tested. The nonparametric tests showed that even if weakly expressed earthquakes were removed, or hypothetical earthquakes added during periods of slower sediment accumulation, the Wrightwood record is more consistent with a time-dependent or unimodal behavior, and is not clustered (Figure 13) (Scharer et al., 2010; Biasi, 2013).

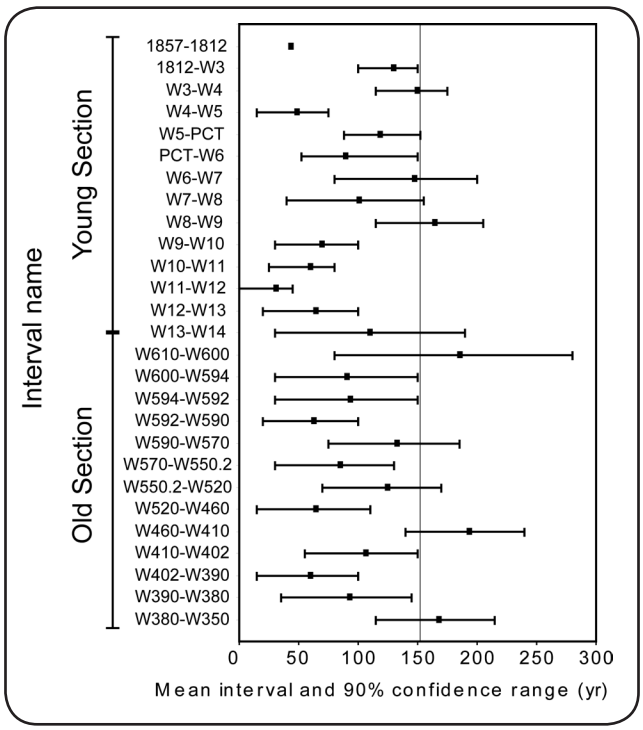

Figure 13. Comparison of time since historic 1857 earthquake (157 years ago) with the time interval between earthquakes at Wrightwood. Modified from Scharer et al., (2010).

The Wrightwood site is one of the few locations on the SAF system where slip-per-event data are available. By measuring discrete features such as channels or fold crests offset along the fault, and combining this with measurements of extension across subsidiary faults with normal separation, Weldon et al., (2002; 2004) determined the slip accrued during individual earthquakes with offsets ranging from 0.7–6.6 m; the average offset for the last 14 earthquakes was ~3 m. If the individual slip values are assumed to represent the average slip for each event, the associated magnitudes would range from ~M6.9 to ~M7.7. The average offset combined with the recurrence interval is internally consistent with the long-term slip rate of the Mojave section (25–35 mm/yr). In order to examine how strain release and earthquake timing co-vary, Weldon et al., (2004) compared the amount of time between successive earthquakes with the preceding or resulting offset. These comparisons found that there was no evidence of time-predictable or slip-predictable behavior (i.e., the slip of the past event does not determine the amount of time until the next, nor does the amount of time since the last event predict the amount of slip in the following earthquake), and suggest that the timing and size of successive earthquakes is not a simple renewal process.

Three paleoseismic sites have been investigated on the San Bernardino Strand of the SAF: Pitman Canyon, Plunge Creek, and Burro Flats. (Seitz et al., 1999; McGill et al., 2002; Yule et al., 2012) (Figure 10). The depositional setting at Pitman Canyon is similar to that at Wrightwood, resulting in a section of alternating organic rich marsh deposits and debris flow gravels. Upward termination of faulting, fissures, folding, and increases in down-fault separation were used to identify seven separate earthquakes, including the historic 1812 earthquake, that have occurred since ca. 900 A.D. (Seitz et al., 2000). This event record produces an average return period of ~140 years (Biasi, 2013), an increase from sites to the northwest that reflects the general reduction in slip rate from the Mojave section to the San Bernardino section (McGill et al., 2012). The Plunge Creek site (McGill et al., 2002) had evidence for two events that are compatible with the ages of the three prehistoric events at Pitman Canyon. Limited dating precludes further differentiation of these events, but suggests that only two events since ca. 1300 A.D. spanned the 30 km between these sites (McGill et al., 2002).

The Burro Flats site is located about 60 km southeast of Pitman Canyon and less than a dozen km northwest of the San Gorgonio Pass Thrust Fault System (Yule and Sieh 2010) (Figures 9 and 10). Paleoearthquakes at the site produced abundant fissures, ground folding that is preserved as growth strata in subsequent deposits, and minor faulting of the alternating peat and alluvial gravel and mud layers. The most recent event breaks a peat layer that contains abundant European pollen, indicating the earthquake occurred after the arrival of settlers in the mid-1700s; this earthquake is interpreted to be the historic 1812 event known to have ruptured Wrightwood. Four earlier earthquakes are well constrained by existing dating to have occurred since 1060 A.D. (Yule and Sieh, 2010). In sum, the recurrence interval for Burro Flats is very similar to that of Pitman Canyon, about 160 years (Biasi, 2013).

The only published paleoseismic record for the Mission Creek Strand is from the Thousand Palms site (Figure 10), where fluvial gravels are interbedded with fine charcoal derived from in-situ burn horizons (Fumal et al., 2002). This record includes good evidence for three earthquakes and weak evidence for two additional earthquakes since A.D. 800. If all of these earthquakes did rupture the Mission Creek Strand, then the average recurrence here is on the order of 230 years. The Coachella paleoseismic site is located 8 km southeast of the junction of the Mission Creek and Banning Strands (Figure 10) (Philibosian et al., 2011). This location is just below the highstand of Lake Cahuilla, a large, shallow lake produced by intermittent diversion of the Colorado River into the Salton Trough. The resulting stratigraphic record includes lake deposits, aeolian and fluvial sands that are interbedded with local organic mats and charcoal-rich burn horizons. Aseismic creep of 2–5 mm/yr is documented for this section of the SAF (Sieh and Williams 1990; Tong et al., 2013), so small upward terminations of faults were not considered evidence for coseismic rupture at the site (Philibosian et al., 2011). Careful dating of charcoal and other organic fractions provide the chronologic control for seven

earthquakes since A.D. 900, five of which were characterized by robust evidence of ground rupturing. If all seven earthquakes are considered, the average interval at the site is ~130 years, or ~160 years if the five probable earthquakes best reflect the coseismic ruptures on this section.

San Jacinto Paleoseismology – Several paleoseismic sites have yielded information on the past history of surface ruptures along the San Jacinto Fault (Figure 10). In the north, a long record is being developed at Mystic Lake, which lies along the Claremont strand north of a 2.5 km-wide releasing step (Onderdonk et al., 2013; Marliyani et al., 2013). The average interval between ground rupturing earthquakes at Mystic Lake is 151±72 years; Figure 14 shows the timing of past events documented at the site, with a longer record currently under development (Onderdonk et al., 2013, Rockwell et al., 2014). Two other sites (Figure 10) in San Bernardino and Colton have been studied and yielded useful information; the two most recent earthquakes were dated at both the Walnut site in San Bernardino and a site in Colton (Kendrick and Fumal, 2005; Fumal and Kendrick, 2008). The Walnut site also recorded several middle Holocene earthquakes, although a hiatus in deposition did not allow for dating of earthquakes between about 4 and 0.5 ka.

Along the middle section of the San Jacinto Fault zone, a long earthquake record has been developed at Hog Lake near Anza (Figure 10). This site, on the Clark Fault, has as many as 21 surface ruptures in the past 4 ka (Rockwell et al., 2014). Excavation of a dozen trenches and trench slices provide the exposures that were used to define the rupture history. The 1918 earthquake ruptured to the north and produced only minor displacement at Hog Lake (Rolfe and Strong 1918; Rockwell et al., 2014), whereas event 2 is interpreted as the November 22, 1800 earthquake that produced damage at San Juan Capistrano and San Diego (Toppozada et al., 1981; Salisbury et al., 2012; Rockwell et al., 2014) and is inferred to have ruptured from at least Hemet to Clark Valley. Thus, there are at least two broadly different types or sizes of earthquakes recognized at Hog Lake: smaller, 1918-type earthquakes with magnitudes in the high M6's, and 1800-type events with magnitudes in the low to moderate M7's. Figure 15 shows probability distributions for the interpreted ages of earthquakes that have ruptured through the Hog Lake site, although some events such as the 1918 M6.9 earthquake are inferred to be smaller than the penultimate November 22, 1800 event.

At face value, the long-term recurrence interval at Hog Lake is estimated at about 186 years, although the coefficient of variation (CoV) is

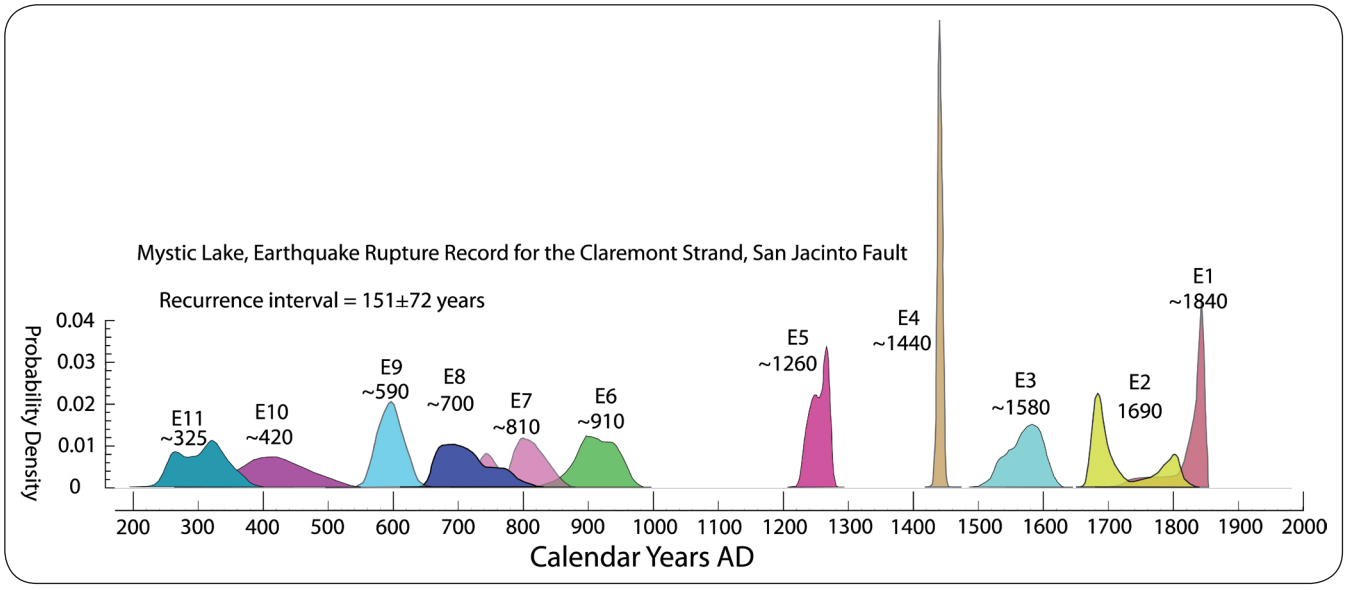

Figure 14. PDFs of event ages determined at Mystic Lake, Claremont strand of the San Jacinto Fault. Event ages represent the age of the peak of the distribution (Data from Rockwell et al., in review, 2013; Onderdonk et al., 2013).

fairly large, between 0.5 and 0.6. Using only the ruptures that are inferred to represent large earthquakes, Rockwell et al., (2014) infer a longer recurrence interval of 260 years for ruptures that extend the length of the south-central Clark strand of the San Jacinto Fault, and the CoV drops to about 0.3, suggesting much more periodic rupture behavior for the largest events (Figure 16).

Marliyani et al., (2013) suggest that the "Hemet Step-over", a large releasing step between the Claremont and Casa Loma faults at Mystic lake (figure 9) has been reorganizing or straightening its course and may allow for rupture of the entire south-central and northern San Jacinto Fault in single events. Onderdonk et al., (2013) find support for this idea in that some Mystic Lake and Hog Lake events are indistinguishable in their ages. Comparison of the Hog Lake and Mystic Lake records also demonstrates that many earthquakes at each site have no correlation at the other, indicating that these two main segments often rupture independently.

Figure 17 shows some plausible rupture scenarios that involve the Clark, Casa Loma and Claremont strands (Rockwell et al., 2014). There are events that clearly have no match between the sites and are assumed to represent rupture of only part or all of the individual fault strands but not the entire fault. Those that have ages that may correlate could have ruptured all three strands together, although the limits of radiocarbon dating cannot distinguish between such "cascade" ruptures or two closely-spaced large earthquakes.

Paleoseismic investigations in the southern San Jacinto Fault zone include studies along the Superstition Mountain fault (Gurrola and Rockwell 1996; Rockwell et al., 2000; Faneros 2005), Superstition Hills and related faults (Hudnut and Sieh 1989; Hudnut et al., 1989), and the Coyote Creek fault (Pollard and Rockwell 1995; Ragona et al., 2001; Rockwell et al., 2000). None of the sites in the southernmost San Jacinto Fault zone yielded long records, but most have yielded information on the past two to five ruptures. For the Superstition Hills fault, Hudnut and Sieh (1989)

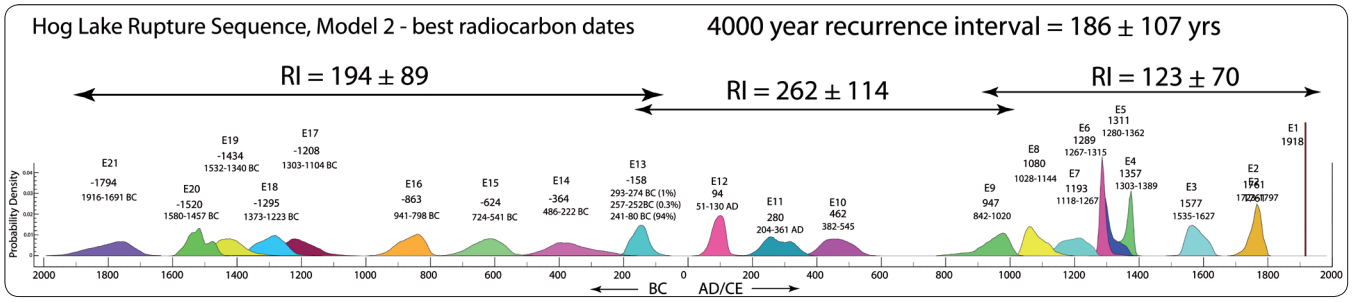

Figure 15. Probability distribution functions (PDFs) of surface ruptures interpreted from the Hog Lake record near Anza. Note that the ca. 1765 event is almost certainly the November 22, 1800 earthquake (Salisbury et al., 2012). Also note that the recurrence interval (RI) varies for different time periods, implying short-term variations in earthquake production, and possibly slip rate.

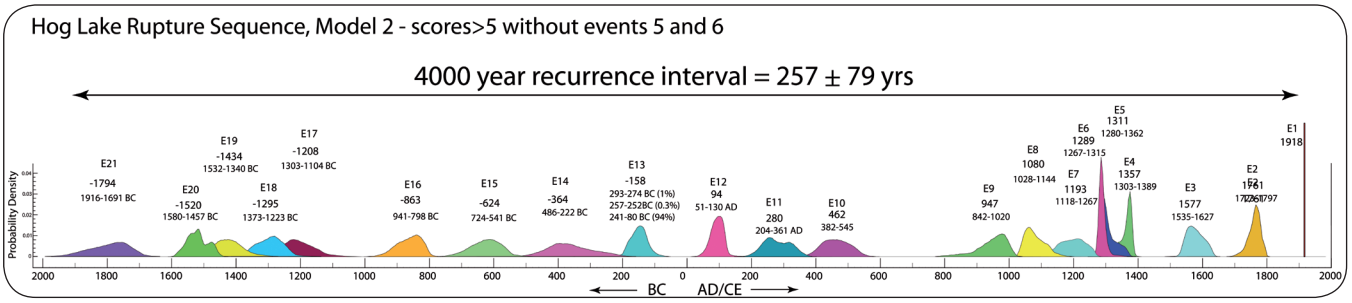

Figure 16. PDFs of the Hog Lake events that appear to have the best expression at the site and are interpreted as major surface ruptures similar to the 1800 earthquake (Rockwell et al., 2014).

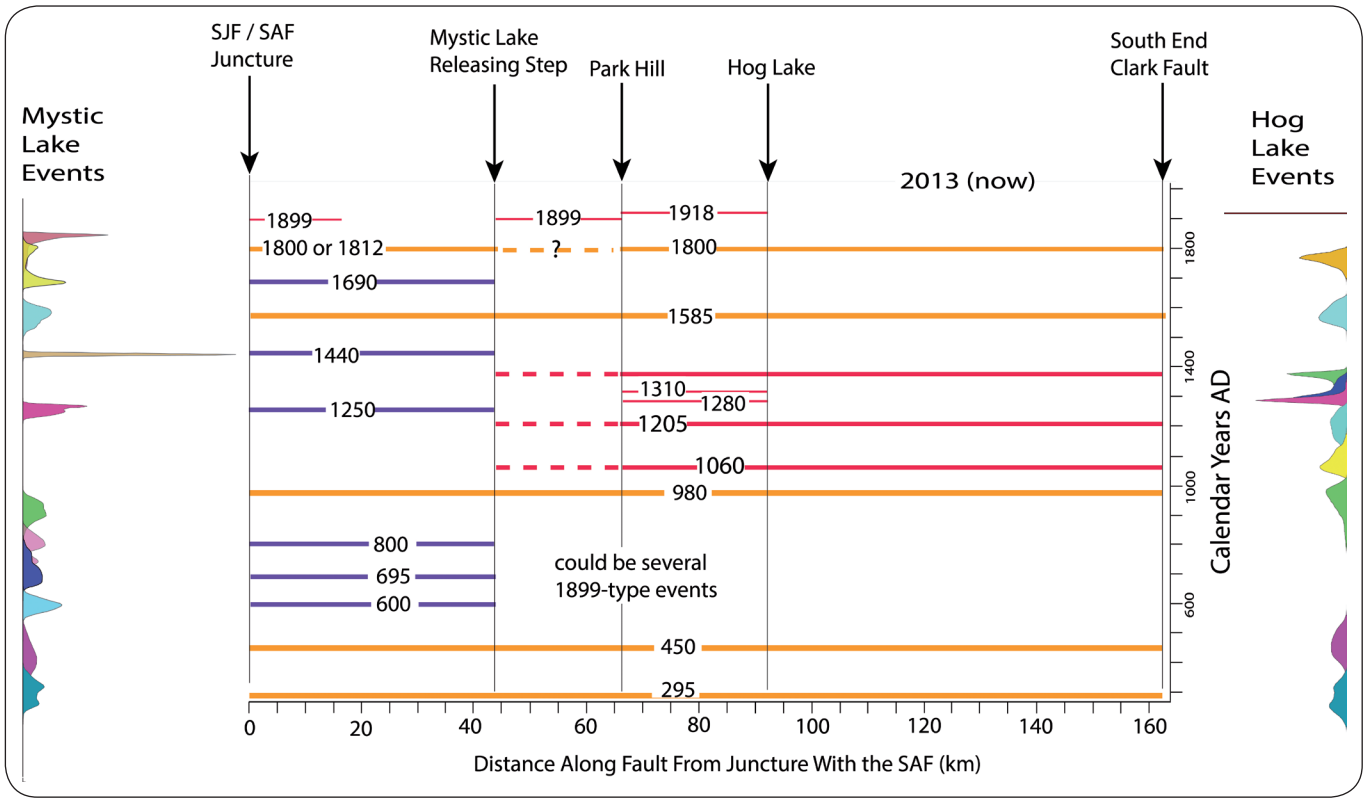

Figure 17. Plausible rupture history of the Clark, Casa Loma and Claremont strands of the San Jacinto Fault for the past 1800 years. Earthquake ages given are the peaks of the probability distributions. Note that some Mystic Lake ruptures definitely have no correlation at Hog Lake, and vice versa (red and blue lines), where as some may correlate between the sites (orange bands) although radiocarbon dating does not have the precision to demonstrate a correlation (Rockwell et al, 2014).

excavated a recessional shoreline that was ruptured through during the 1987 earthquake to resolve that a similar rupture with similar displacement had occurred in the past 300 years. Gurrola and Rockwell (1996) dated the three most recent ruptures on the Superstition Mountain fault to between about AD 850 and 1450, with no surface ruptures in at least the past 500 years, suggesting that this section of the fault is ripe for a future earthquake. The southern part of the Coyote Creek fault ruptured in 1968, producing a maximum of 50 cm of lateral displacement at the surface. The rupture crosses a paleo-shoreline to ancient Lake Cahuilla, which experienced 25–30 cm of displacement. 3-dimensional trenching by Pollard and Rockwell (1995) on the Coyote Creek fault determined the occurrence of only two events in the past 300 years, but with the penultimate event having more than a meter of lateral slip, suggesting a larger earthquake than occurred in 1968. Information is currently too sparse to develop likely rupture scenarios for paleoseismic events by correlation of events from site to site.

Insights into behavior from paleoseismology of the southern San Andreas and San Jacinto Faults - The intersection of the San Andreas and San Jacinto Faults presents a unique location to study fault interaction and fault splays. These two faults converge at a 20 degree junction, although the San Jacinto trends more parallel to the San Andreas Fault in its northernmost ~10 km (Figure 9). Recent work from the Burro Flats, Mystic Lake, and Hog Lake sites brings paleoseismic data to within 25 km of this intersection, and correlations based on the dates of events at these sites permits insight into the patterns of past behavior (Figure 18). For example, each of the earthquake ages from Pitman Canyon can be matched to an earthquake age at the Wrightwood and Pallett Creek sites to the northwest, suggesting that the San Bernardino section of the fault and the southern end of the Mojave section rupture together. Further, of the

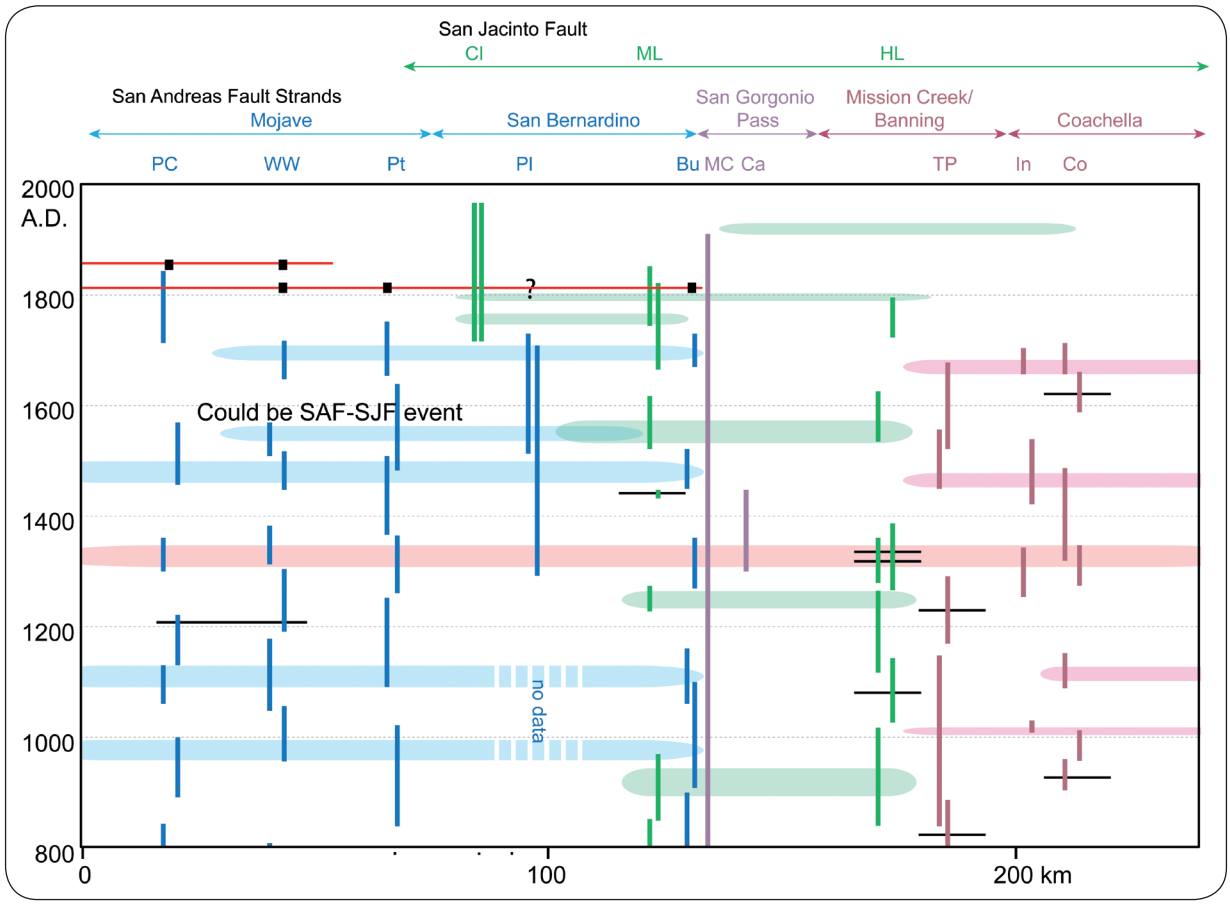

Figure 18. Space-time diagram of San Andreas and San Jacinto Fault earthquakes. Vertical bars represent 95% confidence limits on individual earthquake ages at each site. Horizontal bars connect earthquake ages that correlate from site to site, blue are ruptures north of San Gorgonio Pass, pink are for ruptures south of San Gorgonio Pass, red is a rupture that could have spanned both sides; green are ruptures on the San Jacinto Fault. Thin black bars show earthquakes that do not correlate and are interpreted to be restricted in length. These rupture correlations represent one of many possible scenarios; long ruptures spanning a couple sites could for example be split into two or more separate ruptures. This example was created to assess the frequency of earthquakes crossing from the San Jacinto to the San Andreas. Assuming that each Bu earthquake that correlates with a Pt earthquake is a San Bernardino strand rupture that does not cross onto the San Jacinto Fault, only one San Jacinto rupture, about 1550 A.D. could connect to the San Bernardino strand. (PC: Pallett Creek, Scharer et al., 2011; WW: Wrightwood, Weldon et al., 2004; Pt: Pitman Canyon, Seitz et al., 2000; Pl: Plunge Creek, McGill et al., 2002; Bu: Burro Flats, MC: Millard Canyon, and Ca: Cabazon, Yule et al., 2012; TP: Thousand Palms, Fumal et al., 2012; In: Indio, Co: Coachella, Philibosian et al., 2012, CI: Colton, Kendrick and Fumal, 2005; ML: Mystic Lake, Onderdonk et al., 2013; HL: Hog Lake, Rockwell et al., in review).

seven possible San Bernardino strand ruptures since ~1000 A.D., six of them are consistent with an earthquake age at Burro Flats, and at least one may have ruptured onto the San Gorgonio Pass Fault Zone (Yule et al., 2012). It is intriguing that the single Pitman Canyon rupture not correlative with an earthquake at Burro Flats is temporally consistent with an earthquake that could span the Hog Lake and Mystic Lake ruptures on the San Jacinto Fault. This pattern suggests that at least one event ruptured from the San Jacinto on to the San Andreas (or vice versa), or two events within a short time occurred on these faults (Figure 18). It is important to emphasize that the scenario shown in Figure 18 represents an interpretation that favors longer (bigger) earthquakes; it is possible that each proposed rupture is in fact more than one, smaller earthquake.

Elsinore Fault Paleoseismology – The earthquake history of the Elsinore fault is not as well resolved as that of the San Andreas or San Jacinto Faults. Nevertheless, several important sites have been explored and the timing of the most recent events is known for most segments. The Elsinore trend includes, from north to south, the Whittier, Chino, Glen Ivy, Wildomar, and Elsinore faults, with the parallel Earthquake Valley fault to the east, and to the south of Palomar Mountain (Figure 9). The Whittier fault has ruptured two times in the past 3400 years, the most recent event occurring between 1400 and 2200 years ago with lateral displacement of at least 1.9 m (Weldon et al., 1996). The fault was well expressed in the geomorphology prior to massive earth moving for construction of housing, evidenced by several streams that have right-lateral displacements of about 400 m. The offset streams are incised into a fluvial terrace that is estimated at 125–220 ka based on soil development and correlation of the terraces to coastal marine terraces (MIS stage 5e or 7), indicating a long-term rate of 1.9–3.2 mm/yr (Rockwell et al., 1988).

To the south, the Glen Ivy North fault has been explored at Glen Ivy Marsh, where evidence for six surface ruptures having occurred in the past 1 ka has been documented (Figure 19) (Rockwell et al., 1986). The most recent rupture is inferred to be the May 1910 M6 earthquake, because there is about 25 cm of lateral slip on a circa 1890's concrete flume (Rockwell 1988) but no lateral displacement of a 1914 terracotta drainage pipe (Figure 20).

Two paleoseismic sites were developed on the western flank of Agua Tibia Mountain near Pala (Thorup 1997; Vaughan et al., 1999). One site dated the timing of the most recent rupture to after AD 1655 but prior to the construction of the Pala Mission in 1810. The other site yielded an incomplete record, as the currently active strand apparently lies beneath a major roadway and could not be trenched. Study of secondary strands indicated the timing of four surface ruptures between 2.7 ka and just before 4.5 ka, yielding an average recurrence interval of 550–600 years for the middle Holocene time period (Vaughan et al., 1999). They considered it likely that additional events occurred between 2.7 ka and the most recent, near-historical

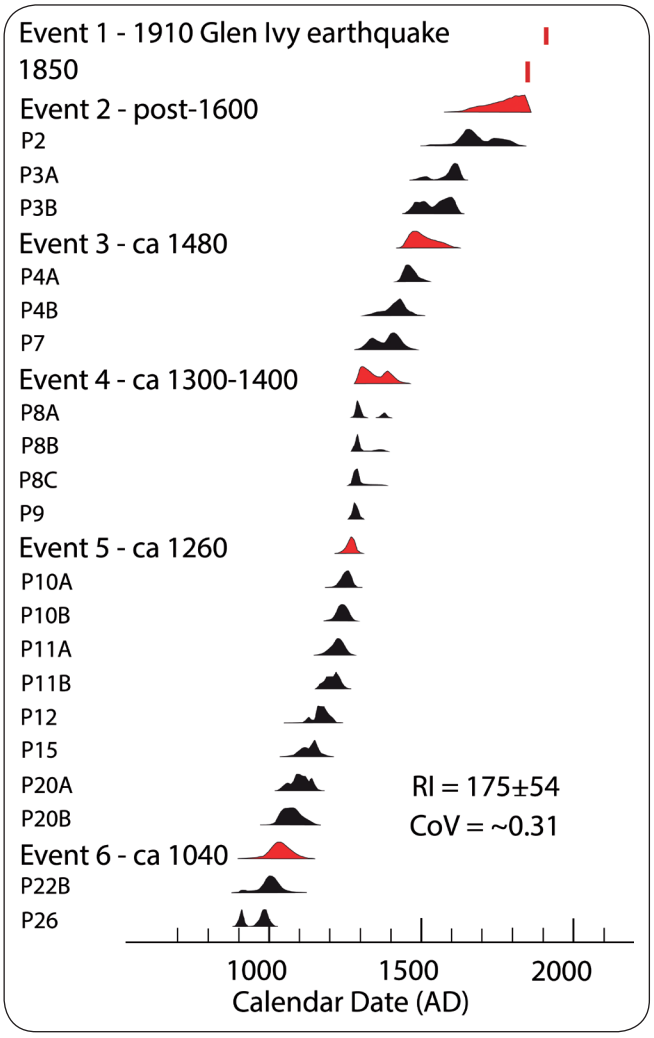

Figure 19. PDFs of radiocarbon dates and inferred ages of surface ruptures at Glen Ivy Marsh (data and interpretations from Rockwell et al., 1985; 1986). The coefficient of variation is estimated by using the peak probabilities as the event ages.

rupture. This inference is supported by another paleoseismic site along the same fault strand at Murrieta in the Elsinore Trough; Rockwell et al., (2000) excavated an offset channel and found that 9.5 m of right-lateral displacement has occurred in the past 1.9 ka. It is unlikely that the entire 9.5 m occurred in a single event, supporting the occurrence of additional events in the past 2 ka.

Two sites located about 12 km apart were explored along the central portion of the Elsinore fault, one near Lake Henshaw and one near Julian, but both had poor stratigraphy and did not yield a long record (Thorup 1997). At Lake Henshaw, two

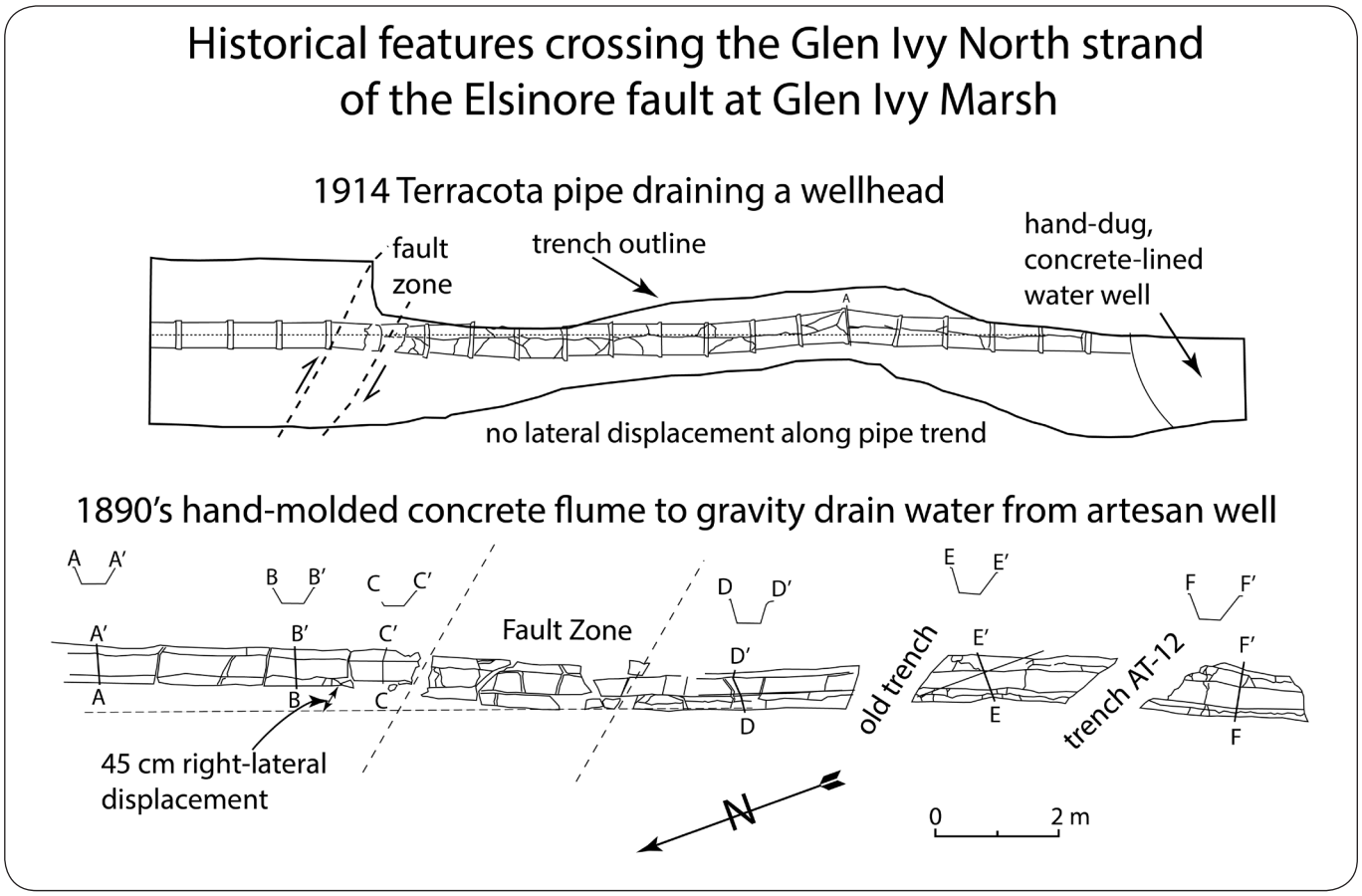

Figure 20. A ca. 1890's hand-molded concrete flume used to drain an artisan well is offset about 45 cm in a right lateral sense, whereas a 1914 terracotta pipe used to drain another well is not laterally offset. The wells are located about 100 m apart. Rockwell (1988) attributed the flume offset to the 1910 M6.1 Glen Ivy earthquake.

ruptures were interpreted to have occurred in the past 5 ka, with the most recent in the past 1.5–2 ka, suggesting a recurrence interval as long as 3–3.5 ka (Thorup 1997). At Julian, only the most recent rupture was dated, with the event age constrained to between 0.7 and 1.8 ka. Taken together, and considering the close proximity of the two sites, Thorup (1997) interpreted the most recent events at each site to be the same rupture, with a best-estimated age of about 1.5–1.8 ka.

Farther south, the rupture history of the Elsinore fault is recorded in geomorphic offsets of small alluvial bars and channels in the Coyote Mountains (Rockwell 1990). The most recent earthquake is dated to have occurred in the past 300 years, using radiocarbon, and luminescence dating suggests three events in the past 2000 years (Rockwell 1990). The slip rate has been determined at Fossil Canyon to be about 1.8 mm/yr (Fletcher et al., 2010). Slip in the past large earthquake increases from about 1.5 m at Fossil Canyon to 2.7 m in the central part of the range (Rockwell 1990), consistent with an increase in slip rate to the northwest. A recurrence interval of about a thousand years is consistent with the slip rate, timing of past events, and displacement in the most recent event.

South of the international border, the Elsinore trend continues as the Laguna Salada and related faults. The Laguna Salada fault ruptured with an M7.1 in 1892 (Mueller and Rockwell 1995; Hough and Elliot 2004), and portions of the Laguna Salada, Pescadores, Borrego and Paso Superior faults ruptured in the M7.3 El Mayor-Cucapa earthquake in 2010 (Fletcher et al., 2014). Paleoseismic investigations of offset alluvial fans suggest a recurrence interval of a couple thousand years for the Laguna Salada fault (Mueller and Rockwell 1995).

Summary

The San Andreas Fault system comprises a complex of sub-parallel faults in northern and southern California that collectively transfer about 80% of the relative motion between the Pacific and North American lithospheric plates. Numerous paleoseismic studies have been conducted on most elements of this fault system over the past 40 years; the timing of the most recent earthquake is known for nearly all fault segments, and long records have been developed for several sections of the fault system. In northern California, the system is apparently coming out of the stress shadow caused by the 1906 earthquake, and other major faults in the northern system are expected to rupture in moderately large earthquakes in the near term.

In southern California, nearly all sections of the San Andreas Fault are at or beyond their average recurrence interval, by 50–100%. Together with the San Jacinto Fault, which also has sections that have not ruptured for over 200 years, most earthquake scientists believe the southern San Andreas Fault system is due for a major earthquake.

REFERENCES

Abbott P.L., Smith T.E., 1989, Sonora, Mexico, source for the Eocene Poway Conglomerate of southern California: *Geology*, v. **17**, p. 329–332.

Akciz S. O., Grant Ludwig L., Arrowsmith J. R., 2009, Revised dates of large earthquakes along the Carrizo section of the San Andreas Fault, California, since A.D. 1310 ± 30: *Journal of Geophysical Research* v. **114** (B1), B01313.

Akçiz S.O., Ludwig L.G., Arrowsmith J.R., Zielke, O., 2010, Century-long average time intervals between earthquake ruptures of the San Andreas Fault in the Carrizo Plain, California: *Geology*, v. **38** (9), p. 787–790.

Adams, J., 1990, Paleoseismicity of the Cascadia subduction zone: evidence from turbidites off the Oregon-Washington margin: *Tectonics*, v. **9,** p. 569–583.

Albright, 1990, Biostratigraphy and vertebrate paleontology of the San Timoteo Badlands, southern California: *University of California Publications*, Geological Sciences 144.

Atwater, T., 1970. Implications of plate tectonics for the Cenozoic evolution of western North America: *Geological Society of America Bulletin,* v. **81**, p. 3513–3536.

Bakun, W.H., 1999, Seismic Activity of the San Francisco Bay Region: *Bulletin of the Seismological Society of America*: v. **89**, p. 764–784.

Baldwin J. N., Lienkaemper J. J., 1999, Paleoseismic investigations along the Green Valley fault, Solano County, California: Unpublished report-Bay Area Paleoseismological Experiment Contract No. 98WRCN1012, 18 p.

Baird A.K., Welday E.E., Baird K.W., 1970, Chemical variations in batholithic rocks of southern California: Geological Society of America Abstracts with Programs, v. **2**, p. 69.

Bartholomew, M.J., 1970, San Jacinto fault zone in northern Imperial Valley, California: *Geological Society of America Bulletin*, v. **81**, p. 3161–3166.

Behr W.M., Rood D.H., Fletcher K.E., Guzman N., Finkel R., Hanks T.C., Hudnut K.W., Kendrick K.J., Platt J.P., Sharp W.D., Yule J.D., 2010, Uncertainties in slip-rate estimates for the Mission Creek strand of the southern San Andreas Fault at Biskra Palms Oasis, southern California: *Geological Society of America Bulletin*, v. **122**, p. 1360–1377.

Bennett R.A., Friedrich A.M., Furlong K.P., 2004a, Codependent histories of the San Andreas and San Jacinto Fault zones from inversion of fault displacement rates: *Geology,* v. **32**, p. 961–964.

Bennett R.A., Rodi W., Reilinger R.E., 2004b, Global positioning system constraints on fault slip rates in southern California and northern Baja California: *Journal of Geophysical Research,* v. **101**, B10, p. 21,943–21,960.

Berger G. W., Sawyer T. L., Unruh J. R., 2010, Single- and multigrain luminescence dating of sediments related to the Greenville Fault, eastern San Francisco Bay Area, California: *Bulletin of the Seismological Society of America*, v. **100**, 3, p. 1051–1072

Biasi G.P., Weldon R.J., Fumal T.E., Seitz G.G., 2002, Paleoseismic event dating and the conditional probability of large earthquakes on the southern San Andreas Fault, California: *Bulletin of the Seismological Society of America*, v. **92**, 7, p. 2761–2781.

Biasi G. P., 2013, Maximum likelihood recurrence intervals for California paleoseismic sites: In *Uniform California Earthquake Rupture Forecast, Version 3 (UCERF3) - The Time-Independent model*, edited by E. Field, *U.S. Geological Survey Open-File Report* **2013–1165**, 97 p., *California Geological Survey Special Report* **228**, and Southern California Earthquake Center Publication 1792, http://pubs.usgs.gov/of/2013/1165/.

Blisniuk K., Rockwell T., Owen L., Oskin M., Lippincott C., Caffee M., Dortch J., 2010, Late Quaternary slip rate gradient defined using high-resolution topography and 10Be dating of offset landforms on the southern San Jacinto Fault zone, California: *Journal of Geophysical Research,* v. **115**, B08401, doi:10.1029/2009JB006346.

Blisnuik K., Oskin M., Mériaux A-S., Rockwell T., Finkel R., Ryerson F. J., 2013, Stable, rapid rate of slip since inception of the San Jacinto Fault, California: *Geophysical Research Letters*, v. **40**, p. 4209–4213.

Borchardt G.S., Wills C.J., 1999, Holocene slip rate of the Concord Fault at Galindo Creek in Concord, California: U. S. Geological Survey, Library, Reston, Va., National Earthquake Hazards Program, final technical report, 30 p.

Chuang R.Y., Johnson K.M., 2011, Reconciling geologic and geodetic fault-slip-rate discrepancies in southern California: consideration of non-steady mantle flow and lower crustal fault creep: *Geology*, v. **39** (7), p. 627–630.

Crowell, J.C., 1962, Displacement along the San Andreas Fault, California: *Geological Society of America Special Paper* **71**, 61 p.

Crowell, J.C., 1979, The San Andreas Fault system through time: *Geological Society of London Journal*, v. **136**, p. 293–302.

Crowell, J.C., 1982, The tectonics of Ridge Basin, southern California: *in* Crowell, J.C., and Link, M.H., eds. Geologic history of Ridge Basin, southern California: *Pacific Section, Society of Economic Paleontologists and Mineralogists*, Field trip guide and volume, p. 25–42.

Darin M.H., Dorsey R.J., 2013, Reconciling disparate estimates of total offset on the southern San Andreas Fault: *Geology*, v. **41**, 9, p. 975–978.

Dickinson W.R., Ducea M., Rosenberg L.I., Greene H.G., Graham S.A., Clark J.C., Weber G.E., Kidder W.S., Ernst W.G., Brabb E.E., 2005, Net dextral slip, Neogene San Gregorio-Hosgri fault zone, coastal California: Geologic evidence and tectonic implications: *Geological Society of America Special Paper* **391**, 44 p.

Dickinson W.R., Snyder W.S., 1979, Geometry of triple junctions related to the San Andreas transform: *Journal of Geophysical Research*, v. **84**, B2, p. 561–572.

Dorsey R.J., Axen G.J., Peryam T.C., Kairouz M.E., 2012, Initiation of the southern Elsinore fault at ~1.2 Ma: Evidence from the Fish Creek-Vallecito Basin, southern California: *Tectonics*, v. **31**, TC2006, doi:10.1029/2011TC003009.

Ehlig P.L., 1981, Origin and tectonic history of the basement terrane of the San Gabriel Mountains, central Transverse Ranges: *in* Ernst, W.G., ed., The geotectonic development of California (Rubey Volume I): Englewood Cliffs, New Jersey, Prentice-Hall, p. 253–283.

Ehlig P.L., Ehlert K.W., Crowe B.M., 1975, Offset of the Upper Miocene Caliente and Mint Canyon Formations along the San Gabriel and San Andreas Faults: *in* Crowell, J.C., ed., San Andreas Fault in southern California: *California Division of Mines and Geology Special Report* **118**, p. 83–92.

Faneros G.A., 2005, Structure and neotectonics of the Superstition Mountain fault, Imperial County, California: M.S. thesis, San Diego State University, 182 p.

Fialko Y., 2006, Interseismic strain accumulation and the earthquake potential on the southern San Andreas Fault system: *Nature*, v. **441**, p. 968–971.

Field E.H., Biasi G.P., Bird P., Dawson T.E., Felzer K.R., Jackson D.D., Johnson K.M., Jordan T.H., Madden C., Michael A.J., Milner K.R., Page M.T., Parsons T., Powers P.M., Shaw B.E., Thatcher W.R., Weldon R.J., II, Zeng Y., 2013, Uniform California earthquake rupture forecast, version 3 (UCERF3)—The time-independent model: *U.S. Geological Survey Open-File Report* **2013–1165**, 97 p., *California Geological Survey Special Report* **228**, and Southern California Earthquake Center Publication 1792, http://pubs.usgs.gov/of/2013/1165/.

Fletcher J.M., Grove M., Kimbrough D., Lovera O., Gehrels G.E., 2007, Ridge-trench interactions and the Neogene tectonic evolution of the Magdalena shelf and southern Gulf of California: Insights from detrital zircon U-Pb ages from the Magdalena fan and adjacent areas: *Geological Society of America Bulletin*, v. **119**, p. 1313–1336.

Fletcher J. M., Rockwell T. K., Teran O. J., Masana E., Faneros G., Hudnut K. W., Gonzalez J., Gonzalez A., Spelz R. M., Mueller K. J., Chung L., Akciz S. O., Galetzka J., Stock J. M., Sharer K., 2010, The surface ruptures associated with the El Mayor-Borrego earthquake sequence: *Eos,* T*ransactions of the American Geophysical Union* Abstract SE05-1 presented at 2010 Fall Meeting.

Fletcher K.E.K., Sharp W.D., Kendrick K.J., Behr W.M., Hudnut K.W., Hanks T.C., 2010, ^{230}Th/U dating of a late Pleistocene alluvial fan along the southern San Andreas Fault: *Geological Society of America Bulletin*, v. **122**, p. 1347–1359.

Fletcher K.E.K., Rockwell T.K., Sharp W.D., 2011, Late Quaternary slip rate of the southern Elsinore fault, southern California: Dating offset landforms via 230TH/U on pedogenic carbonate: *Journal of Geophysical Research,* v. **116**, F02006, doi:10.1029/2010JF001701.

Freeman S.T., Heath E.G., Guptil P.D., Waggoner J.T., 1992, Seismic hazard assessment, Newport-Inglewood fault zone: *in Engineering Geology Practice in southern California*. B.W. Pipkin and R.J. Proctor (eds.), Association of Engineering Geologists, Star Publishing Company, Belmont, California, p. 211–231.

Frizzell V.A. Jr., Mattison J.M., Matti J.C., 1986, Distinctive Triassic megaporphyritic monzogranite: Evidence for only 160 km offset along the San Andreas Fault, southern California: *Journal of Geophysical Research*, v. **91**, p. 14,080–14,088.

Fumal T.E., 2012, Timing of Large Earthquakes during the Past 500 Years along the Santa Cruz Mountains segment of the San Andreas Fault at Mill Canyon, near Watsonville, California: *Bulletin of the Seismological Society of America,* v. **102**, doi:10.1785/0120110161.

Fumal T.E., Heingartner G. F., Dawson T. E., Flowers R., Hamilton J. C., Kessler J., Reidy L. M., Samrad L., Seitz G. G., Southon J., 2003, A 100-Year average recurrence interval for the San Andreas Fault, southern San Francisco Bay Area, California: *Eos,* T*ransactions of the American Geophysical Union*, S12B-0388.

Fumal T.E., Rymer M.J., Seitz G.G., 2002a, Timing of large earthquakes since A.D. 800 on the Mission Creek strand of the San Andreas Fault zone at Thousand Palms Oasis, near Palm Springs, California: *Bulletin of the Seismological Society of America*, v. **92** (7), p. 2841–2860.

Fumal T.E., Schwartz D.P., Pezzopane S.K., Weldon R.J., 1993, A 100-year average recurrence interval for the San Andreas Fault at Wrightwood, California: *Science*, v. **259**, p. 199–203.

Fumal T.E., Weldon R.J., Biasi G.P., Dawson T.E., Seitz G.G., Frost W.T., Schwartz D.P., 2002b, Evidence for large earthquakes on the San Andreas Fault at the Wrightwood, California, paleoseismic site: A.D. 500 to present: *Bulletin of the Seismological Society of America*, v. **92** (7), p. 2726–2760.

Fumal T.E., Kendrick K.J., 2008, Appendix O; Paleoseismic investigations of the Walnut site on the San Jacinto Fault: *In*, The Uniform California Earthquake Rupture Forecast, version 2 (UCERF 2): *U.S. Geological Survey Open-File Report* 2007–1437, *California Geological Survey Special Report* 203, and *Southern California Earthquake Center Publication* 1138, 3 sheets.

Grant L.B., Sieh K., 1994, Paleoseismic evidence of clustered earthquakes on the San Andreas Fault in the Carrizo Plain, California: *Journal of Geophysical Research*, v. **99** (B4), p. 6819–6841.

Galehouse J.S., Lienkaemper J.J., 2003, Inferences drawn from two decades of alignment array measurements of creep on faults in the San Francisco Bay region: *Bulletin of the Seismological Society of America*, v. **93**, p. 2415–2433.

Goldfinger C, Morey A., Hans Nelson C., Gutiérrez-Pastor J., Johnson J.E., Karabanov E., Chaytor J., Eriksson A., and the Shipboard Scientific Party, 2007, Rupture lengths and temporal history of significant earthquakes on the offshore and North Coast Segments of the Northern San Andreas Fault based on turbidite stratigraphy: *Earth and Planetary Science Letters,* v. **254**, p. 9–27.

Graham S.A., Stanley R.G., Best J.V., Carter J.B., 1989, Oligocene and Miocene paleogeography of central California and displacement along the San Andreas Fault: *Geological Society of America Bulletin*, v. **101**, p. 711–730.

Gurrola L.D., Rockwell T.K., 1996, Timing and slip for prehistoric earthquakes on the Superstition Mountain fault, Imperial Valley, southern California: *Journal of Geophysical Research*, v. **101**, B3, p. 5977–5985.

Hall N.T., Wright R.H., Clahan K.B., 1999, Paleoseismic studies of the San Francisco peninsula segment of the San Andreas Fault zone near Woodside, California: *Journal of Geophysical Research*, v. **104**, B10, p. 23, 215–23, 236.

Hart E.W., Bryant W.A., Manson M.W., Kahle J.E., 1986, Summary report: Fault evaluation program, 1984–1985, southern Coast Ranges region and other areas: *California Division of Mines and Geology Open-File Report* **86-3**, 26 p., 1 plate.

HPEG (Hayward Fault Paleoearthquake Group: Lienkaemper J.J., Schwartz D.P., Kelson K.I., Lettis W.R., Simpson G.D., Southon J.R., Wanket J.A., Williams P.L.), 1999, Timing of paleoearthquakes on the northern Hayward Fault -- Preliminary evidence in El Cerrito, California: *U.S. Geological Survey Open-File Report*, **99–318**, 34 p.

Hecker S., Pantosti D., Schwartz D.P., Hamilton J.C., Reidy L.M., Powers T.J., 2005, The most recent

large earthquake on the Rodgers Creek Fault, San Francisco Bay Area: *Bulletin of the Seismological Society of America*, v. **95**, 3, p. 844–860.

Herbert J., Cooke M., Oskin M., Difo O., 2014, How much can off-fault deformation contribute to the slip rate discrepancy within the eastern California shear zone?: *Geology*, v. **42**, 1, p. 71–75.

Hill R.L., 1981, Geology of Garner Valley and vicinity: In Brown, A.R. & Ruff, R.W., eds., Geology of the San Jacinto mountains, Santa Ana, California. *South Coast Geological Society Annual Field Trip Guidebook* v. **9**, p. 90–99.

Hough S.E., Elliot A., 2004, Revisiting the 23 February 1892 Laguna Salada earthquake: *Bulletin of the Seismological Society of America,* v. **94**, 4, p. 1571–1578.

Hudnut K.W., Sieh K.E., 1989, Behavior of the Superstition Hills fault during the past 330 years: *Bulletin of the Seismological Society of America*, v. **79** (2), p. 304–329.

Hudnut K.W., Seeber L., Rockwell T., 1989, Slip on the Elmore Ranch fault during the past 330 years and its relation to slip on the Superstition Hills fault: *Bulletin of the Seismological Society of America*, v. **79**, 2, p. 330–341.

Hull A.G., Nicholson C., 1990, Seismotectonics of the northern Elsinore fault zone, southern California: *Bulletin of the Seismological Society of America*, v. **82**, p. 800–818.

Irwin W.P., 1990, Quaternary deformation: in Wallace, R.E. (ed.), The San Andreas Fault system, California. *U.S. Geological Survey Professional Paper* **1515**, online at: http://pubs.usgs.gov/pp/1990/1515/.

Janecke S.U., Dorsey R.J., Forand D., Steely A.N., Kirby S.M., Lutz A.T., Housen B.A., Belgarde B., Langenheim V.E., Rittenour T.M., 2010, High geologic slip rates since early Pleistocene initiation of the San Jacinto and San Felipe fault zones in the San Andreas Fault system, southern California, USA: *Geological Society of America Special Paper* **475**, 48 p.

Johanson I.A., Bürgmann R., 2005, Creep and quakes on the northern transition zone of the San Andreas Fault from GPS and InSAR data: *Geophysical Research Letters*, v. **32**, L143056, doi:10.1029/2005GL023150.

Kelson K.I., Lettis W.R., Lisowski M., 1992, Distribution of geologic slip and creep among faults in the San Francisco Bay Region: In Borchardt, G and others, eds., Proceedings of the Second Conference on Earthquake Hazards in the Eastern San Francisco Bay Area: *California Division of Mines and Geology Special Publication* **113**, p. 31–38.

Kelson K.I., Simpson G.D., Lettis W.R., Haraden C.C., 1996, Holocene slip rate and recurrence of the northern Calaveras fault at Leyden Creek, eastern San Francisco Bay region: *Journal of Geophysical Research*, v. **101**, B3, p. 5961–5975.

Kelson K.I., and others, 1998, Late Holocene slip rate and amounts of coseismic rupture along the central Calaveras fault, San Francisco Bay area, California. Final Technical Report, U.S. Geological Survey National Earthquake Hazard Reduction Program, Award Number 1434-HQ-97-GR-03151, 26 p.

Kelson K.I., Streig A.R., Koehler R.D., 2006, Timing of late Holocene paleoearthquakes on the northern San Andreas Fault at the Fort Ross Orchard Site, Sonoma County, California: *Bulletin of the Seismological Society of America*, v. **96**, p. 1012–1028.

Kendrick K.J., Morton D.M., Wells S.G., Simpson R.W., 2002, Spatial and temporal deformation along the northern San Jacinto Fault, southern California; Implications for slip rates: *Bulletin of the Seismological Society of America*, v. **92**, 7, p. 2782–2802.

Kendrick K.J., Fumal T.E., 2005, Paleoseismicity of the northern San Jacinto Fault, Colton and San Bernardino, Southern California; preliminary results: *Geological Society of America Abstracts with Programs*, v. 37, 7, p. 559.

Larsen M., Prentice C.S., Kelsey H.M., Zachariasen J., Rotberg G.L., 2005, Paleoseismic investigation of the Maacama fault at the Haehl Creek site, Willits, California: *Geological Society of America Abstracts with Programs*, v. 37, p. 68.

Lienkaemper J.J., Borchardt G., 1996, Holocene slip rate of the Hayward fault at Union City, California: *Journal of Geophysical Research*, v. **101**, B3, p. 6099–6108.

Lienkaemper J.J., Dawson T.E., Personius S.F., Seitz G.G., Reidy L.M., Schwartz D.P., 2002, A record of large earthquakes on the southern Hayward fault for the past 500 years: *Bulletin of the Seismological Society of America*, v. **92**, p. 2637–2658.

Lienkaemper J.J., Williams P.L., 2007, A record of large earthquakes on the southern Hayward fault for the past 1800 years: *Bulletin of the Seismological Society of America*, v. **97**, p. 1803–1819.

Lienkaemper J. J., Williams P. L., Guilderson T. P., 2010,_Evidence for a twelfth large earthquake on the southern Hayward fault in the past 1900 years: *Bulletin of the Seismological Society of America*, v. **100**, p. 2024 – 2034.

Lienkaemper J. J., Baldwin J.N., Turner R. Sickler R.R., Brown J., 2013, A record of large earthquakes during the past two millennia on the southern Green Valley Fault, California: *Bulletin of the Seismological Society of America*, v. **103**, p. 2386 – 2403.

Lienkaemper J.J., 2012, Recently Active Traces of the Berryessa Fault, California. A Digital Database: U.S. Geological Survey Data Series **710**, http://pubs.usgs.gov/ds/710/.

Lindvall S., Rockwell T.K., 1995, Holocene activity of the Rose Canyon fault, San Diego, California: *Journal of Geophysical Research*, v. **100**, B12, p. 24121–24132.

Magistrale H., Rockwell T., 1996, The central and southern Elsinore fault zone, southern California: *Bulletin of the Seismological Society of America*, v. **86**, 6, p. 1793–1803.

Marliyani G.I., Rockwell T.K., Onderdonk N., McGill, S., 2013, Straightening of the northern San Jacinto Fault, California as seen in the fault structure evolution of the San Jacinto Valley step-over: *Bulletin of the Seismological Society of America*, v. **103**, 3, p. 2047–2061.

Matmon A., Schwartz D.P., Finkel R., Clemmens S., Hanks T., 2005, Dating offset fans along the Mojave section of the San Andreas Fault using cosmogenic Al-26 and Be-10P: *Geological Society of America Bulletin*, v. **117**, p. 795–807.

Mathews V., III, 1976, Correlation of the Pinnacles and Neenach volcanic formations and their bearing on San Andreas Fault problem: *American Association of Petroleum Geologists Bulletin*, v. **60**, p. 2128–2141.

Matti J.C., Morton D.M., 1993, Paleogeographic evolution of the San Andreas Fault in southern California: A reconstruction based on a new cross-fault correlation: *in* Powell, R.E., Weldon, R.J.,II, and Matti, J.C., eds., The San Andreas Fault system: Displacement, palinspastic reconstruction, and geologic evolution: *Geological Society of America, Memoir* **178**, Chapter 2, p. 107–160.

Matti J.C., Morton D.M., Cox B.F., 1985, Distribution and geologic relations of fault systems in the vicinity of the central Transverse Ranges, southern California: *U.S. Geological Survey Open-File Report* **85-365**, 27 p., scale 1:250,000.

Matti J.C., Morton D.M., Cox B.F., 1992, The San Andreas Fault system in the vicinity of the central Transverse Ranges province, southern California: *U.S. Geological Survey Open-File Report* **92-354**, 40 p, scale 1:250,000.

McGill S., Dergham S., Barton K., Berney-Ficklin T., Grant D., Hartling,C., Hobart K., Minnich R., Rodriguez M., Runnerstrom E., Russell J., Schmoker K., Stumfall M., Townsend J., Williams J., 2002, Paleoseismology of the San Andreas Fault at Plunge Creek, near San Bernardino, Southern California: *Bulletin of the Seismological Society of America*, v. **92**, 7, p. 2803–2840.

McGill S. F., Owen L. A. , Weldon R. J., Kendrick K. J., 2012, Latest Pleistocene and Holocene slip rate for the San Bernardino strand of the San Andreas Fault, Plunge Creek, Southern California: Implications for strain partitioning within the southern San Andreas Fault system for the last ~35 k.y: *Geological Society of America Bulletin,* v. **125**, p. 48–72, doi:10.1130/b30647.1.

McLaughlin R.J., Sliter,W.V., Sorg D.H., Russell P.C., Sarna-Wojcicki A.M., 1996, Large-scale right-slip displacement on the East San Francisco Bay region fault system: Implications for the location of late Miocene to Pliocene plate boundary: *Tectonics*, v. **15**, p. 1–18.

McNeilan T., Rockwell T.K., Resnick G., 1996, Sense and rate of Holocene slip, Palos Verdes fault, southern California: *Journal of Geophysical Research*, v. **101**, B4, p. 8317–8334.

Millman D.E., Rockwell T.K., l986, Neotectonics of the Elsinore fault in Temescal Valley, California: *in* Guidebook and Volume on Neotectonics and Faulting in Southern California (P. Ehlig, ed.), *Cordilleran Section, Geological Society of America*, p. 159–166.

Morton D. M., Matti J. C., 1993, Extension and contraction within an evolving divergent strike-slip fault complex: the San Andreas and San Jacinto Fault zones at their convergence in southern California: *in* The San Andreas Fault System: Displacement, Palinspastic Reconstruction, and Geologic Evolution. R. E. Powell, R. J. Weldon, and J. C. Matti (Editors), *Geological Society of America Memoir*, **178**, p. 217–230.

Mueller K. J., Rockwell T. K., 1995, Late Quaternary activity of the Laguna Salada fault in northern Baja California, Mexico: *Geological Society of America Bulletin*, v. **107**, 1, p. 8–18.

Murray J.R., Svarc J.L., Minson S.E., 2012, Spatially Variable Creep Rate on the Bartlett Springs and Maacama Faults, Northern California, Estimated via Bayesian Inversion of Global Positioning System Data: *Eos, Transactions of the American Geophysical Union,* 2012 Fall Meeting

Nicholson C., Sorlien C.C., Atwater T., Crowell J.C., Luyendyk B.P., 1994, Microplate capture, rotation of the western Transverse Ranges, and initiation of the San Andreas transform as a low-angle fault system: *Geology*, v. **22**, p. 491–495.

Niemi T.M., Hall N.T., 1992, Late Holocene slip rate and recurrence of great earthquakes on the San Andreas Fault in northern California: *Geology*, v. **20**, 3, p. 196–198.

Onderdonk N., Rockwell T.K., McGill S., Marliyani G., 2013, Evidence for seven surface ruptures in the past 1600 years on the Claremont fault at Mystic Lake, northern San Jacinto Fault, California: *Bulletin of the Seismological Society of America*, v. **103**, 1,

Onderdonk, N., McGill, S. and Rockwell, T.K., 2015, Short-term variations in slip rate and size of prehistoric earthquakes during the past 2000 yr on the northern San Jacinto fault zone, a major plate-boundary structure in southern California. Lithosphere, v. **7**, 3, p. 211–234, doi: 10.1130/L393.1

Oskin M., Perg L., Shelef E., Strane M., Gurney E., Singer B., Zhang X., 2008, Elevated shear one loading rate during an earthquake cluster in eastern California: *Geology* v. **36**, 6, p. 507–510.

Oskin M., Stock J., 2003, Pacific–North America plate motion and opening of the Upper Delfin basin, northern Gulf of California, Mexico: *Geological Society of America Bulletin*, v. **115**, p. 1173–1190.

Parsons T, Johnson K., Bird P, Bormann J., Dawson T., Field E., Hammond W., Herring T., McCaffrey R., Shen Z-K., Thatcher W., Weldon R., Zeng Y., 2013, Deformation models for UCERF3, Appendix C of the Uniform California earthquake rupture forecast, version 3 (UCERF3)—The time-independent model. *U.S. Geological Survey Open-File Report* **2013–1165**, 97 p., *California Geological Survey Special Report* **228**, and *Southern California Earthquake Center Publication* **1792**, http://pubs.usgs.gov/of/2013/1165/.

Perkins J.A., Sims J.D., 1988, Late Quaternary slip along Calaveras fault near Hollister, California: *Eos* (American Geophysical Union, Transactions), v. **69**, 44, p. 1420.

Perkins J.A., Sims J.D., Sturgess S.S., 1989, Late Quaternary movement along the San Andreas Fault at Melendy Ranch--Implications for the distribution of fault slip in central California: *Journal of Geophysical Research*, v. **94**, B8, p. 10,217–10,230.

Philibosian B., Fumal T., Weldon R., 2011, San Andreas Fault Earthquake Chronology and Lake Cahuilla History at Coachella, California: *Bulletin of the Seismological Society of America,* v. **101** (1), p. 13–38.

Pollard W.J., Rockwell, T.K., 1995, Late Holocene slip rate for the Coyote Creek fault, Imperial County, California: *Geological Society of America, Abstracts With Programs*, v. **27**, 5, p. 72.

Pollitz F.R., Schwartz D.P, 2008, Probabilistic seismic hazard in the San Francisco Bay area based on a simplified viscoelastic-cycle: *Journal of Geophysical Research*, v. **113** B05409.

Powell R.E., 1993, Balanced palinspastic reconstruction of pre-late Cenozoic paleogeology, southern California: Geologic and kinematic constraints on evolution of the San Andreas Fault system: In Powell, R.E., et al., eds., The San Andreas Fault system: Displacement, palinspastic reconstruction, and geologic evolution. *Geological Society of America Memoir* **178**, p. 1–106.

Powell R.W., Weldon R.J., Matti, J.C., 1993, The San Andreas Fault system: Displacement, palinspastic reconstruction, and geologic evolution: *Geological Society of America Memoir* **178**, 332 p.

Powell R.E., Weldon R.J., II, 1992, Evolution of the San Andreas Fault: *Annual Review of Earth and Planetary Sciences*, v. **20**, p. 431–468.

Prentice, C.S., 1989, Earthquake geology of the northern San Andreas Fault near Point Arena California: California Institute of Technology, Pasadena, unpub. Ph.D. dissertation, 252 p.

Prentice C.S., Kelson K.I., 2006, The San Andreas Fault in Sonoma and Mendocino counties: *in* Prentice, C.S., Scotchmoor, J.G., Moores, E.M., & Kiland, J.P., eds., 1906 San Francisco Earthquake centennial field guides—Field trips associated with the 100th anniversary conference, April 18–23, 2006, San Francisco, Calif.: *Geological Society of America Field Guide* **7,** p. 127–156, doi:10.1130/206.1906SF(11).

Prentice, C.S., Larsen, M.C., Kelsey, H.M., and Zachariasen, J., 2014, Late Holocene slip rate and ages of prehistoric earthquakes along the Maacama fault near Willits, Mendocino County, northern California. *Bulletin of the Seismological Society of America*, **104** (6), p. 2966–2984.

Ragona D., Rockwell T.K., Orgil A., 2001, Fault segmentation and earthquake behavior: A high-resolution paleoseismic study in the southern San Jacinto Fault zone. *Eos, Trans*actions of the American Geophysical Union, **83**, p. 47, Fall Meet. Suppl., Abstract S52D-0668.

Revenaugh J., Reasoner C., 1997, Cumulative offset of the San Andreas Fault in central California: A seismic approach: *Geology*, v. **25**, p. 123–126.

Richard S.M., 1993, Palinspastic reconstruction of southeastern California and southwestern Arizona for the Middle Miocene: *Tectonics*, v. **12**, p. 830–854.

Rockwell T.K., McElwain R.S., Millman D.E., Lamar D.L., l986, Recurrent late Holocene faulting on the Glen Ivy North strand of the Elsinore fault at Glen Ivy Marsh: *in* Guidebook and Volume on Neotectonics and Faulting in Southern California (P. Ehlig, ed.), *Cordilleran Section, Geological Society of America*, p. 167–176.

Rockwell T.K., Gath E.M., Cook K.D., 1988, Sense and rate of slip on the Whittier fault zone near Yorba Linda, California: *Geological Society of America Abstracts With Programs*, v**. 20**, 3, p. 224.

Rockwell T.K., 1989, Behavior of individual fault segments along the Elsinore-Laguna Salada fault zone, southern California and northern Baja California: Implications for the characteristic earthquake model: U.S. Geological Survey Redbook on Fault Segmentation and the Controls of Rupture Initiation and Termination: *U.S. Geological Survey Open File Report* **89-315**, p. 288–308.

Rockwell T., 1990, Holocene activity of the Elsinore fault in the Coyote Mountains, southern California: *in* Western Salton Trough Soils and Tectonics, *Friends of the Pleistocene Guidebook*, p. 30–42.

Rockwell T.K., Loughman C., Merifield P., 1990, Late Quaternary rate of slip along the San Jacinto Fault zone near Anza, southern California: *Journal of Geophysical Research*, v. **95**, p. 8593–8605.

Rockwell T.K., Schug D.L., Hatch M.E., 1993, Late Quaternary slip Rates along the Agua Blanca fault, Baja California, Mexico: *in* (P.L. Abbott, ed.) Geological Investigations of Baja California. *South Coast Geological Society, Annual Field Trip Guidebook* **No. 21**, p. 53–92.

Rockwell T.K., Lindvall S., Herzberg M., Murbach D., Dawson T., Berger G., 2000a, Paleoseismology of the Johnson Valley, Kickapoo and Homestead Valley faults of the Eastern California Shear Zone: *Bulletin of the Seismological Society of America*, v. **90**, 5, p. 1200–1236.

Rockwell T., Bergmann M., Kenney M., 2000b, Holocene slip rate of the Elsinore fault in Temecula Valley, Riverside County, California: *in* Geology and Enology of the Temecula Valley (B. Birnbaum and K. Cato, eds), p. 105–118.

Rockwell T.K., Dewhurst J.A., Walls C.W., Pollard W.J., Orgil A., Faneros G., Dawson T.E., 2000c, High-resolution paleoseismology in southern California: Investigation of segment controls on the rupture history of the southern San Jacinto Fault: *in* Active Fault Research for the New Millenium, Proceedings of the Hokudan International Symposium and School on Active Faulting, (K. Okumura, K Takada, and H. Goto, eds.), Letter Press Ltd., Hiroshima, Japan, p. 413–419.

Rockwell T.K., 2010, The Rose Canyon Fault in San Diego. Proceedings of the Fifth International Conference on Recent Advances in Geotechnical Earthquake Engineering and Soil Dynamics, May 24–29, 2010, San Diego, California, Paper No. 7.06C, 9 p.

Rockwell T., Akciz S., Gordon E., 2013, Paleoseismology of the Aqua Tibia - Earthquake Valley fault, eastern strand of the Elsinore Fault Zone: *Seismological Research Letters*, v. **84**, p. 332.

Rockwell T.K., Dawson T.E., Young J., Seitz G., 2014, A 21 event, 4,000-year history of surface ruptures in the Anza Seismic Gap, San Jacinto Fault: Implications for long-term earthquake production on a major plate boundary fault: *Pure and Applied Geophysics*. doi:10.1007/s00024-014-0955-z

Rolfe F., Strong A. M., 1918, The earthquake of April 21, 1918, in the San Jacinto Mountains: *Bulletin of the Seismological Society of America*, v. **8**, p. 63–67.

Ross D.C., Wentworth C.M., McKee E.H., 1972, Cretaceous mafic conglomerate near Gualala offset 350 miles by San Andreas Fault from oceanic crustal source near Eagle Rest Peak, California: *U.S. Geological Survey Journal of Research*, v. **1**, 1, p. 43–

Salisbury J.B., Rockwell T.K., Middleton T.J., Hudnut K.W., 2012, LiDAR and Field Observations of Slip Distribution for the Most Recent Surface Ruptures Along the Central San Jacinto Fault: *Bulletin of the Seismological Society of America*, v. **102**, 2, p. 598–619.

Sauber J., Thatcher W., Solomon S.C., 1986, Geodetic measurements of deformation in the central Mojave Desert, California: *Journal of Geophysical Research*, v. **91, p.** 12683–12693.

Scharer K.M., Biasi G.P., Weldon R.J., 2011, A reevaluation of the Pallett Creek earthquake chronology based on new AMS radiocarbon dates, San Andreas Fault, California: *Journal of Geophysical Research*: *Solid Earth,* v. **116** (B12), B12111, doi:10.1029/2010JB008099.

Scharer K.M., Biasi G.P., Weldon R.J., Fumal T.E., 2010, Quasi-periodic recurrence of large earthquakes on the southern San Andreas Fault: *Geology*, v. **38** (6), p. 555–558.

Scharer K.M., Fumal T.E., Weldon R.J., Streig A., 2014, Photomosaics and Event Evidence from the Frazier Mountain Paleoseismic Site, Trench 1, Cuts1-4, San Andreas Fault, Southern California (2007-2009): *U.S. Geological Survey Open-File Report* **2014-1002**.

Scharer K.M., Weldon R.J., Fumal T.E., Biasi G.P., 2007, Paleoearthquakes on the Southern San Andreas Fault, Wrightwood, California, 3000 to 1500 B.C.: A New Method for Evaluating Paleoseismic Evidence and Earthquake Horizons: *Bulletin of the Seismological Society of America*, v. **97** (4), p. 1054–1093.

Schwartz D.P., Pantosti D., Hecker S., Okumura K., Budding K.E., Powers T., 1992, Late Holocene behavior and seismogenic potential of the Rodgers Creek Fault Zone, Sonoma County, California: *in* Borchardt, G., (chief ed.), Proceedings of the second conference on earthquake hazards in the eastern San Francisco Bay Area. *California Department of Conservation, Division of Mines and Geology Special Publication* **113**, p. 393–398.

Schwartz D.P., Pantosti D., Okumura K., Powers T. J., Hamilton J., 1998, Paleoseismic investigations in the Santa Cruz Mountains, California: implications for recurrence of large magnitude earthquakes on the San Andreas Fault: *Journal of Geophysical Research,* v. **103**, p. 17,985–18,001, doi:10.1029/98JB00701

Schwartz D.P., Lienkaemper J.J., Hecker S., Kelson K.I., Fumal T.E., Baldwin J.N., Seitz G.G., Niemi T.M., 2014, The Earthquake Cycle in the San Francisco Bay Region: AD 1600-2012: *Bulletin of the Seismological Society of America*, v. 104, 3, doi: 10.1785/0120120322

Seitz G. G., Biasi G. P., Weldon R. J., 2000, An Improved Paleoseismic Record of the San Andreas Fault at Pitman Canyon: *in* Noller, J. S., Sowers, J. M., and Lettis, W. R., eds. *Quaternary Geochronology*, American Geophysical Union, p. 563–566.

Sharp R.V., 1967, San Jacinto Fault zone in the Peninsular Ranges of southern California: *Geological Society of America Bulletin*, v. **78**, p. 705–729.

Sieh,K., Stuiver M., Brillinger D., 1989, A more precise chronology of earthquakes produced by the San Andreas Fault in southern California: *Journal of Geophysical Research*: *Solid Earth*, v. **94** (B1), p. 603–623.

Sieh K. E., 1978, Slip along the San Andreas Fault associated with the great 1857 earthquake: *Bulletin of the Seismological Society of America*, v. 68 (5), p. 1421–&.

Sieh K. E., 1984, Lateral offsets and revised dates of large prehistoric earthquakes at Pallett Creek, southern California: *Journal of Geophysical Research: Solid Earth*, v. **89** (B9), p. 7641–7670.

Sieh K. E., Jahns R.H., 1984, Holocene activity of the San Andreas Fault at Wallace Creek, California: *Geological Society of America Bulletin*, v. **95** (8), p. 883–896.

Sieh K.E., Williams, P.L., 1990, Behavior of the southernmost San Andreas Fault during the past 330 years: *Journal of Geophysical Research*, v. **95**, p. 6629–6645.

Simpson G.D., Thompson S.C., Noller J.S., Lettis W.R., Williams, 1997, The northern San Gregorio fault zone: Evidence for the timing of late Holocene earthquakes near Seal Cove, California: *Bulletin of the Seismological Society of America*, v. **87**, 5, p. 1158–1170.

Simpson G.D., Baldwin J.N., Kelson, K.I., Lettis W.R., 1999, Late Holocene slip rate and earthquake history for the northern Calaveras fault at Welch Creek, eastern San Francisco Bay area, California: *Bulletin of the Seismological Society of America,* v. **89**, 5, p. 1250–1263.

Sims J.D., 1993, Chronology of displacement on the San Andreas Fault in central California: Evidence from reversed positions of exotic rock bodies near Parkfield, California: *in* Powell, R.E., Weldon, R.J.,II, and Matti, J.C., eds., The San Andreas Fault system: Displacement, palinspastic reconstruction, and geologic evolution. *Geological Society of America, Memoir* **178**, Chapter 6, p. 231–256.

Stephenson W.J., Rockwell T.K., Odum J.K., Shedlock K.M., Okaya D.A., 1995, Seismic reflection and geomorphic characterization of the onshore Palos Verdes fault zone, Los Angeles, California: *Bulletin of the Seismological Society of America*, v. **85**, 3, p. 943–950.

Stoffer P.W., 2006, Where's the San Andreas Fault? A guidebook to tracing the fault on public lands in the San Francisco Bay region: *U.S. Geological Survey General Interest Publication* **16**, 123 p., online at http://pubs.usgs.gov/gip/2006/16/.

Streig A.R., Dawson T.E., Weldon II R.J., 2014, Paleoseismic evidence of the 1890 and 1838 earthquakes on the Santa Cruz Mountains Section of the San Andreas Fault, near Corralitos, California: *Bulletin of the Seismological Society of America*, v. **104**.

Thorup K.M., 1997, Paleoseismology of the central Elsinore fault in southern California: Results from three trench sites: M.S. thesis, San Diego State University, 94 p.

Titus S.J., DeMets C., Tikoff B., 2006, Thirty-Five-Year Creep Rates for the Creeping Segment of the San Andreas Fault and the Effects of the 2004 Parkfield Earthquake: Constraints from Alignment Arrays, Continuous Global Positioning System, and Creepmeters: *Bulletin of the Seismological Society of America*, v. **96**, 4B, S250–S268.

Tong X., Sandwell D.T., Smith-Konter B., 2013, High resolution interseismic velocity data along the San Andreas Fault from GPS and InSAR: *Journal of Geophysical Research*, v. **118**, doi:10.1029/2012JB009442.

Toppozada T. R, Real C.R., Parke D.L., 1980, Preparation of isoseismal maps and summaries of reported effects for pre-1900 California earthquakes: *California Division of Mines and Geology Open-File Report* **81-11 SAC**, 182 p.

Toppozada T. R., Borchardt G., 1998, Re-evaluation of the 1836 "Hayward Fault" and the 1838 San Andreas earthquakes: *Bulletin of the Seismological Society of America*, v. **88**, p. 140–159.

Unruh J.R., Lettis W.R., 1998, Kinematics of transpressional deformation in the eastern San Francisco Bay region, California: *Geology*, v. **26**, 1, p. 19–22.

Vaughan P., Rockwell T., l986, Alluvial stratigraphy and neotectonics of the Elsinore fault zone at Agua Tibia Mountain, southern California: *in* Guidebook and Volume on Neotectonics and Faulting in Southern California (P. Ehlig, ed), *Cordilleran Section, Geological Society of America*, p. 177–192.

Vaughan P.R., Thorup K.M., Rockwell T.K., 1999, Paleoseismology of the Elsinore fault at Agua Tibia Mountain, southern California: *Bulletin Seismological Society of America*, v. **89**, 6, p. 1447–1457.

Weldon R.J., Sieh K.E., 1985, Holocene rate of slip and tentative recurrence interval for large earthquakes on the San Andreas Fault in the Cajon Pass, southern California: *Geological Society of America Bulletin,* v. **96**, p. 793–812.

Weldon R.J., McCalpin J.P., Rockwell T.K., 1996, Paleoseismology in strike-slip tectonic environments. *Paleoseismology* (J. McCalpin, ed), Academic Press, San Diego, p. 271–330.

Weldon R. J., Fumal T. E., Powers T. J., Pezzopane S. K., Scharer K. M., Hamilton J. C., 2002, Structure and earthquake offsets on the San Andreas Fault at the Wrightwood, California, paleoseismic site: *Bulletin of the Seismological Society of America*, v. **92**, 7, p. 2704–2725.

Wagner D.L., Saucedo G.J., Clahan K.B., Fleck R.J., Lagenheim V.E., McLaughlin R.J., Sarna-Wojcicki A.M., Allen J.R., Deino A.L., 2011, Geology, geochronology, and paleogeography of the southern Sonoma volcanic field and adjacent areas, northern San Francisco Bay region, California: *Geosphere*, v. **7**, 3, p. 658–683.

Wakabayashi J., 1999, Distribution of displacement on and evolution of a young transform fault system: The northern San Andreas Fault system: *Tectonics*, v. **18**, p. 1245–1274.

Weber G.E., Nolan J.M., 1995, Determination of late Pleistocene-Holocene slip rates along the San Gregorio fault zone, San Mateo County, California: *U.S. Geological Survey Open-File Report* **95-210**, p. 805–807.

Weldon R.J., Scharer K.M., Fumal T.E., Biasi G.P., 2004, Wrightwood and the earthquake cycle: What a long recurrence record tells us about how faults work, *GSA Today*, v. **14** (9), p. 12–16.

Weldon R.J., Dawson T.E., Biasi G., Madden C., Streig A.R., 2013, Appendix G-Paleoseismic Recurrence Database *in* Field, E.H., Biasi, G.P., Bird, P., Dawson, T.E., Felzer, K.R., Jackson, D.D., Johnson, K.M., Jordan, T.H., Madden, C., Michael, A.J., Milner, K.R., Page, M.T., Parsons, T., Powers, P.M., Shaw, B.E., Thatcher, W.R., Weldon, R.J., II, Zeng, Y., Uniform California earthquake rupture forecast, version 3 (UCERF3)—The time-independent model: *U.S. Geological Survey Open-File Report* **2013–1165**, 97 p., *California Geological Survey Special Report* **228**, and *Southern California Earthquake Center Publication* **1792**, http://pubs.usgs.gov/of/2013/1165/.

Yule D., 2009, The enigmatic San Gorgonio Pass: *Geology*, v. **37** (2), p. 191–192.

Yule D., Sieh K., 2010, Ruptures of the San Andreas Fault system in San Gorgonio Pass, Abstract T41C-03 presented at 2010 Fall Meeting, AGU, San Francisco, Calif., 13-17 Dec.

Yule D., Sieh K., 2003, Complexities of the San Andreas Fault near San Gorgonio Pass: Implications for large earthquakes: *Journal of Geophysical Research*, v. **108**, p. 2548.

Yule D., McBurnett P., Ramzan S., Sieh K., 2012, Comparing the size and frequency of ruptures of the San Andreas Fault system at the Burro Flats, Millard Canyon, and Cabazon paleoseismic sites: 2012 SCEC Annual Meeting, Palm Springs Calif.

Wesnousky S. G., Prentice C. S., Sieh K., 1991, An offset Holocene stream channel and the rate of slip along the northern reach of the San Jacinto Fault zone, San Bernardino Valley, California: *Geological Society of America Bulletin*, v. **103**, p. 700–709.

WGCEP (Working Group on California Earthquake Probabilities) (2003) Earthquake probabilities in the San Francisco Bay region: 2002-2031: *U.S. Geological Survey Open-File Report* **03-214**.

WGCEP (Working Group on California Earthquake Probabilities) (2008) The uniform California earthquake rupture forecast: *U.S. Geological Survey Open-File Report* **2007-1437**, http://pubs.usgs.gov/of/2007/1437/

Williams P.L., 1998, Hayward Fault Slip Vector and Rate Constraints at Berkeley: Reinterpretation of East Bay Landforms and Tectonic Hazards: *U.S. Geological Survey Final Technical Report*, Award Number 1434-HQ-97-GR-03080, 17 p.

Zhang H., Niemi T., Fumal T., 2006, A 3000-year record of earthquakes on the northern San Andreas Fault at the Vedanta marsh site, Olema, California: *Seismological Research Letters*, v. **77**, p. 176.

Kate Scharer is a Research Geologist with the Earthquake Science Center at the U.S. Geological Survey in Pasadena, California. She holds a B.S. in Geological Sciences from the University of Washington, Seattle, and a Ph.D. in Geological Sciences from the University of Oregon, Eugene. She studies the effects of large earthquakes on the landscape, specializing in paleoseismology along the San Andreas Fault and the dating and reconstruction of Quaternary surfaces deformed by active structures.

Timothy Dawson is a Senior Engineering Geologist in the Seismic Hazards Assessment Program at the California Geological Survey (CGS). He holds a Bachelor of Science degree from the University of Oregon and a Masters of Science from San Diego State University. He specializes in studies of active faults and has conducted paleoseismic studies in California, Alaska, Panama, Portugal, and Turkey. He serves on the Executive Committee of the Working Group on California Earthquake Probabilities (WGCEP), which is responsible for producing authoritative forecasts of earthquake probabilities in California. Currently, he is manager of the Fault Zonation Program at CGS, which is responsible for producing regulatory maps of earthquake fault zones as required by the Alquist-Priolo Act. He is a Professional Geologist and a Certified Engineering Geologist in the State of California.

Dr. Thomas Rockwell is a professor of geology at San Diego State University. He has conducted neotectonic and paleoseismic studies in many countries throughout the world, including in Asia, Europe, Central and South America as well as the U.S and Mexico, resulting in over 160 journal articles, dozens of guidebook articles and conference papers, and hundreds of presentations at professional meetings. He has served on the Board of Directors for the Seismological Society of America and the Planning Committee for the Southern California Earthquake Center (SCEC), and currently serves on the Board of Directors for SCEC.

Long-term slip rate of the southern San Andreas Fault from ^{10}Be-^{26}Al surface exposure dating of an offset alluvial fan

Jérôme van der Woerd,[1,2] Yann Klinger,[3,4] Kerry Sieh,[3] Paul Tapponnier,[5] Frederick J. Ryerson,[1] and Anne-Sophie Mériaux[1,3,6]

Received 30 November 2004; revised 21 December 2005; accepted 12 January 2006; published 15 April 2006.

[1] We determine the long-term slip rate of the southern San Andreas Fault in the southeastern Indio Hills using ^{10}Be and ^{26}Al isotopes to date an offset alluvial fan surface. Field mapping complemented with topographic data, air photos and satellite images allows precise determination of piercing points across the fault zone that are used to measure an offset of 565 ± 80 m. A total of 26 quartz-rich cobbles from three different fan surfaces were collected and dated. The tight cluster of nuclide concentrations from 19 samples out of 20 from the offset fan surface implies a simple exposure history, negligible prior exposure and erosion, and yields an age of 35.5 ± 2.5 ka. The long-term slip rate of the San Andreas Fault south of Biskra Palms is thus 15.9 ± 3.4 mm/yr. This rate is about 10 mm/yr slower than geological (0–14 ka) and short-term geodetic estimates for this part of the San Andreas Fault, implying changes in slip rate or in faulting behavior. This result puts new constraints on the slip rate of the San Jacinto and on the Eastern California Shear Zone for the last 35 kyr. Our study shows that more sites along the major faults of southern California need to be targeted to better constrain the slip rates over different timescales.

Citation: van der Woerd, J., Y. Klinger, K. Sieh, P. Tapponnier, F. J. Ryerson, and A.-S. Mériaux (2006), Long-term slip rate of the southern San Andreas Fault from ^{10}Be-^{26}Al surface exposure dating of an offset alluvial fan, *J. Geophys. Res.*, *111*, B04407, doi:10.1029/2004JB003559.

1. Introduction

[2] The rate of horizontal translation between the Pacific and North American plates has averaged at about 50 mm/yr over the past 3 Myr [*DeMets*, 1995; *DeMets and Dixon*, 1999] and 48 ± 5 mm/yr over the past decade [*Bennett et al.*, 1996]. Many have attempted to understand how this deformation is partitioned between the numerous active faults of southern California because such knowledge is critical to understand the mechanics of this complex plate boundary. The details of slip rates distribution are also important input for estimating local seismic hazards because seismic productivity generally increases with increasing fault slip rate.

[3] Attempts to measure the partitioning of slip across the plate boundary have relied on either short- or long-term measurements. Geodetic data enable calculation of rates spanning a few years or decades; stratigraphic, geomorphologic and geochronologic information yield rate averages that span thousands to tens of thousands of years. Heretofore, measurements of long-term slip rates have been sparse because they have depended on the presence of clearly offset landforms datable by the radiocarbon method. Only at Cajon Pass and Wallace Creek (Figure 1, inset) is the millennially averaged slip rate well constrained along the San Andreas Fault (SAF) [*Weldon and Sieh*, 1985; *Sieh and Jahns*, 1984]. The rates there, 24.5 ± 3.5 and 34 ± 3 mm/yr, respectively, suggest that the fault currently bears about 50 to 70% of the entire relative plate motion.

[4] Use of the Cajon Pass rate to establish the nature of slip partitioning farther south in southern California is probably inappropriate because the geometry of active faults there differs greatly from their geometry at the latitude of Cajon Creek (Figure 1, inset). South of Cajon Pass, several other active strike-slip faults lie west of and subparallel to the San Andreas [*Allen*, 1957]. Structural, stratigraphic and geochronologic data show that among these faults, the San Jacinto and San Andreas have long been the principal structures. Geodetic measurements show that this continues to be the case, with the two faults carrying well over half of the total relative plate motion.

[5] The relative degree of current activity of these two faults remains controversial, however. Although the total Miocene slip across the SAF (215 km) is clearly much larger than that across the San Jacinto fault (SJF) (20 km), some interpretations suggest that the slip rate of the SJF

[1] Institute for Geophysics and Planetary Physics, Lawrence Livermore National Laboratory, Livermore, California, USA.
[2] Now at Ecole et Observatoire des Sciences de la Terre, Institut de Physique du Globe de Strasbourg, Strasbourg, France.
[3] Division of Geological and Planetary Sciences, California Institute of Technology, Pasadena, California, USA.
[4] Now at Laboratoire de Tectonique, Institut de Physique du Globe de Paris, Paris, France.
[5] Laboratoire de Tectonique, Institut de Physique du Globe de Paris, Paris, France.
[6] Now at School of Geosciences, Institute of Geography, Edinburgh, UK.

Copyright 2006 by the American Geophysical Union.
0148-0227/06/2004JB003559$09.00

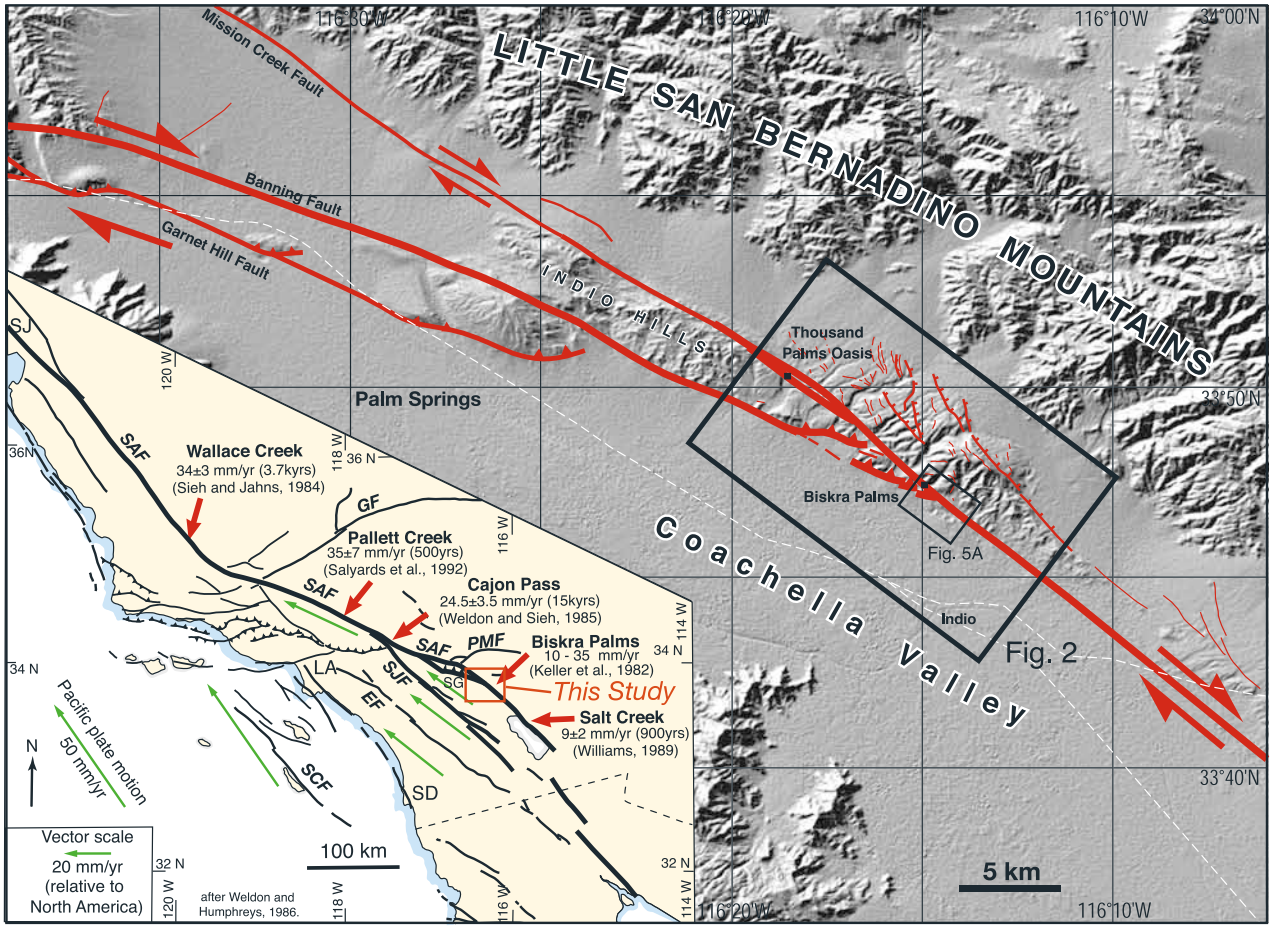

Figure 1. Map of San Andreas Fault system in the Coachella Valley. Fault map in eastern Indio Hills is modified from *Clark* [1984]. Biskra Palms site is located along southwestern Indio Hills, just southeast of the Biskra Palms oasis. Background is shaded DEM derived from Shuttle Radar Topography Mission data (30 m pixel). Inset, modified from *Weldon and Humphreys* [1986], shows Biskra Palms site in relation to other sites where geological long-term slip rate have been already determined. Gray arrows [*Weldon and Humphreys*, 1986] indicate relative motion of various crustal blocks relative to North American plate (SCF, San Clemente Fault; EF, Elsinore Fault; SJF, San Jacinto Fault; SAF, San Andreas Fault; GF, Garlock Fault; PMF, Pinto Mountain Fault; SG, San Gorgonio Pass fault zone; SJ, San Jose; LA, Los Angeles; SD, San Diego).

over the past 30,000 years is equal to or greater than that of the SAF [e.g., *Merrifield et al.*, 1987; *Kendrick et al.*, 2002; *Matti and Morton*, 1993; *Bennett et al.*, 2004]. Inversion of GPS geodetic vector fields [*Bennett et al.*, 1996; *Meade and Hager*, 2005] yields best fit slip rates of about 23–26 and 9–12 mm/yr for the southern San Andreas (SSAF) and SJF, respectively. *Meade and Hager* [2005] allowing for more than 1 cm/yr of slip to be accommodated in the Eastern California Shear Zone (ECSZ) obtain a slow rate of 5 mm/yr for the SAF across the San Gorgonio bend north of the Indio Hills, between Cajon Pass and the Indio Hills (Figure 1).

[6] More precise constraints on the millennially averaged slip rate of the SAF south of Cajon Pass would eliminate another degree of freedom in inversions of geodetic or structural data. Furthermore, a well-constrained slip rate would enable more realistic estimations of the average length of the seismic cycle. The current 300-year-long period of dormancy [*Sieh*, 1986; *Fumal et al.*, 2002], for example, could be an aberration from a normal, shorter interval, or it could be typical and reflect a low rate of elastic loading.

[7] A significant hindrance to determination of well-constrained long-term slip rates has been the difficulty of dating offset surfaces. Until recently, radiocarbon dating had been the most common and reliable means for acquiring an age. Unfortunately, carbonaceous materials are rare in offset strata, and the method is limited by the short half-life of ^{14}C to features that are younger than about 50,000 years. The development of methods to date offset geomorphic surfaces by measurement of cosmic ray produced ^{10}Be and ^{26}Al has created new possibilities for quantifying deformation in tectonically active regions [e.g., *Bierman et al.*, 1995a; *Ritz et al.*, 1995; *Repka et al.*, 1997; *van der Woerd et al.*, 1998, 2002; *Zehfuss et al.*, 2001; *Mériaux et al.*, 2004, 2005; *Chevalier et al.*, 2005; *Matmon et al.*, 2005]. The value of these methods is clear from their successful application in recent studies of the kinematics of the Indian-Asian colli-

sion. Age determinations from ^{10}Be and ^{26}Al of offset alluvial fans and glacial moraines have enabled calculation of slip rates for major strike-slip faults there [*Tapponnier et al.*, 2001, and references therein]. Cosmogenic dating allows for dating of surfaces as old as about several 100,000 years and does not rely on the recovery of carbonaceous material. Here we constrain the slip rate along the southern SAF by measuring the age of previously undatable surfaces using ^{10}Be and ^{26}Al.

2. Biskra Palms Site

[8] We focused our attention on an offset alluvial fan just southeast of Biskra Palms oasis, near the southeastern tip of the Indio Hills (Figure 1). For ease of reference, we will call this the Biskra Palms fan, even though it is in the drainage immediately southeast of the actual oasis. *Keller et al.* [1982] recognized that the Biskra Palms alluvial fan (Figure 2) might enable determination of a slip rate. They estimated an offset of about 700 m, but could not find carbonaceous materials for dating the fan surface. In lieu of radiocarbon analyses, they used the degree of soil development to estimate a 20,000- to 70,000-year age of the fan surface. Their estimated slip rate was thus poorly constrained between 10 and 35 mm/yr, although they had reasons to favor a rate range between 23 and 35 mm/yr [*Keller et al.*, 1982].

[9] In sections 2.1–2.3, we will present the geology and our mapping of the site, then discuss the offsets, and finally determine the age of the offsets.

2.1. Geologic Setting and Mapping

[10] The Biskra Palms fan is immediately southeast of the junction of two major strands of the SAF (Figures 1 and 2). To the southeast, the SAF continues 75 km to the Salton Sea as a relatively simple, straight structure. To the northwest, the fault divides into two principal strands, the Mission Creek (MCF) and Banning (BF) faults. Offset channels and terraces between the Biskra and Thousand Palms oases indicate that the MCF is the more active of the two near the site. The BF does not traverse the site, but becomes the principal fault farther northwest [*Allen*, 1957; *Keller et al.*, 1982; *Yule and Sieh*, 2003]. Near and northwest of Biskra Palms oasis, scarps demonstrate that the BF has a significant thrust component, up on the north (Indio Hills) side. Scarps also belie the existence of many secondary faults within and along the northeastern flank of the Indio Hills (Figure 2) [e.g., *Powell et al.*, 1993; *Clark*, 1984]. Among these faults, the Indio Hills fault, which appears to have a significant vertical component of slip. At the Biskra Palms fan, the MCF consists of two parallel strands, 400 m apart (Figure 2). Both clearly offset the alluvial fan horizontally and vertically (Figure 3). The Biskra Palms fans are fed by a small stream, nowadays intermittent, that extends about 3 km into the Indio Hills (Figure 2). The stream erodes the Ocotillo formation [*Rogers*, 1965] from a small (2.5 km^2) drainage basin. This formation contains different type of sediments from fine sandy units to coarser conglomerates providing the mostly granitic and quartzitic pebbles and cobbles found downstream on the fan surfaces.

[11] The fan consists of a sequence of alluvial surfaces, all well preserved northwest of the modern channel until recent years (Figure 4). Quarrying operations had removed most of the younger and much of the older fan deposits by the beginning of our study in 2000 (Figure 3). Nevertheless, we were able to map the fan surfaces from old and new aerial photographs augmented by mapping in the field. To characterize the different fan surfaces and their offsets better we mapped them in the field using stereo air photos taken in both 1969 and 2004, 10-m pixel SPOT images (KJ 545-282, 13 November 1999), and SRTM digital topographic data. Several different surfaces are distinguishable on the images by the different hues that have resulted from differing degrees of development of desert pavement and varnish. The surfaces are also distinguishable by their distinct heights relative to the active streambed.

[12] Figure 5 shows our field and remote mapping of the alluvial surfaces and faults, superimposed on the USGS 24,000-scale topographic contours and the USGS orthophoto (26 September 1996). Cross sections, derived from the topographic map and field mapping, display deformation of the surfaces across the fault zone and the relative heights of the terraces (Figure 5b). The cross sections indicate a common pattern of fan agradation with slopes becoming shallower from the oldest to the youngest surface [e.g., *van der Woerd et al.*, 2001]. Note that most of the vertical offset occurs along the southwestern strand of the MCF (SMCF) due to upslope tilting or rotation of the block separated by the SMCF and northeastern MCF (NMCF), with almost no net vertical offset of the fan surfaces across the whole fault zone (Figure 5b). Four distinct surfaces are (or were) present. From youngest to oldest, these are T0, T1, T2 and T3. Quarrying has obliterated T1 and much of the active streambed TO. T3 is clearly preserved only as a solitary remnant upstream from the fault zone, although slopes between the two fault traces may also be chaotically deformed remnants of T3. T2 is the most prominent surface and the one from which we are able to determine an offset and a slip rate. To avoid confusion, we labeled the different surfaces depending on their position upstream (u), downstream (d), or intermediate (i) when located northeast, southwest, or in between, respectively, the two MCF strands, the NMCF and the SMCF (Figure 5).

[13] Cobbles and boulders on the T2 surface are varnished and at places embedded in pavement (Figure 6). Rounded pebbles and cobbles up to 50 cm in size are common. A discrete sublevel (T2'd) existed downstream in 1969 (Figures 4 and 5a). Unfortunately, T2'd had been completely quarried away by the time of our fieldwork. Between the two main faults, T2i is pervasively disrupted by small, oblique normal faults, oriented about 30° clockwise relative to the principal strike-slip faults [*Keller et al.*, 1982]. The normal faults crosscut abandoned drainage rills and locally offset them vertically by as much as ~10 m (Figure 5a). Only two of these faults offset the western T2 terrace riser.

[14] The youngest abandoned surface, T1, appears clearly on the 1969 vintage stereo air photos. It is lower than T2 and less incised by secondary rills. It has a lighter tone than the T2 and T3 surfaces, probably because its bears less varnished pebbles and cobbles. Unfortunately, it had been almost totally removed by quarrying by 2000. Only a small

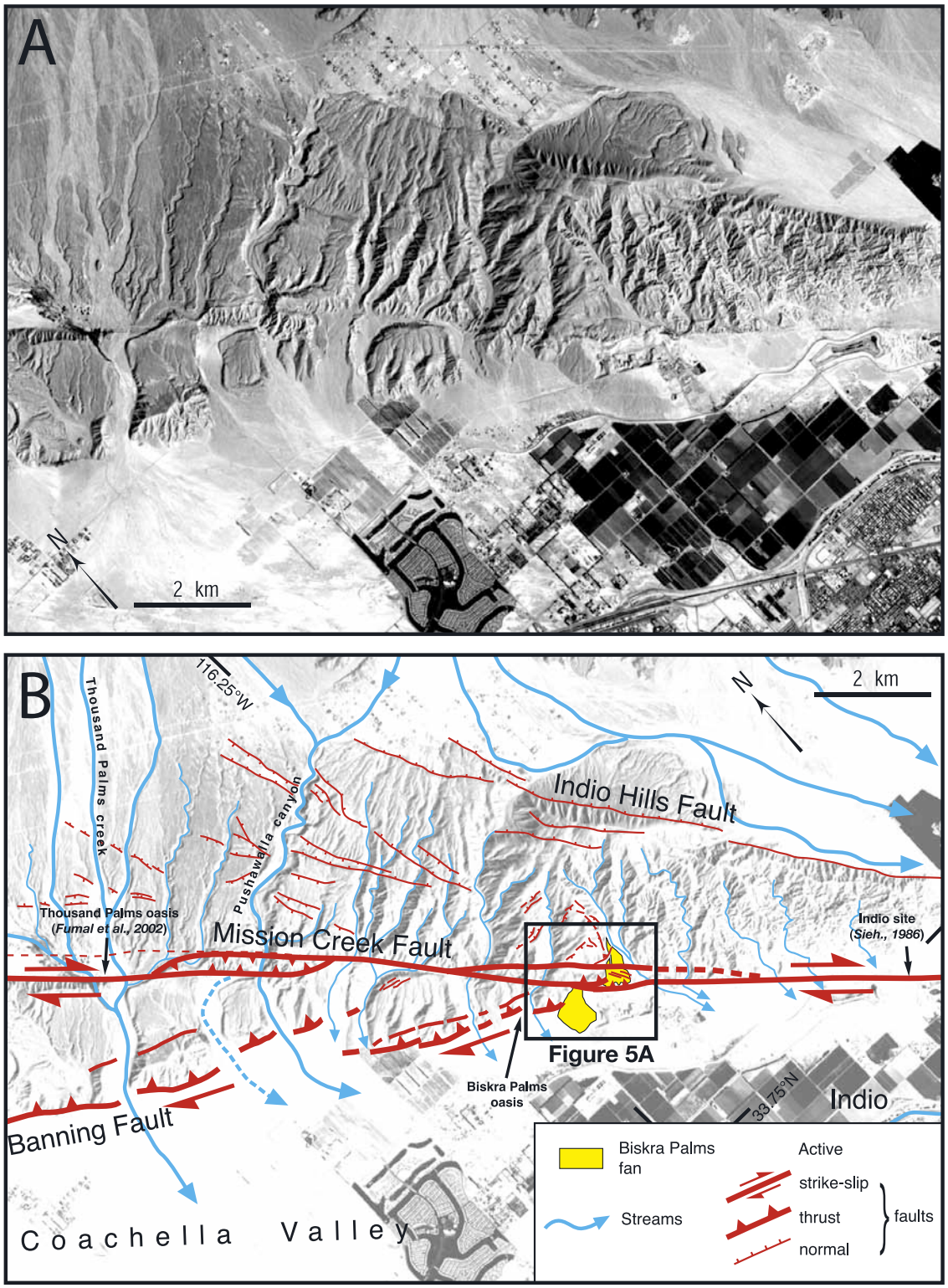

Figure 2. (a) SPOT image (KJ 545-282, 13 November 1999) of the southeastern Indio Hills. Main trace of San Andreas Fault is visible across uplifted and dissected alluvial sands and gravels of the Indio Hills. Streams that cross the main fault trace have jogs that are characteristic of right-lateral motion along the fault. (b) Interpretation of SPOT image outlining main strands of San Andreas Fault and faults across Indio Hills (modified from *Clark* [1984]).

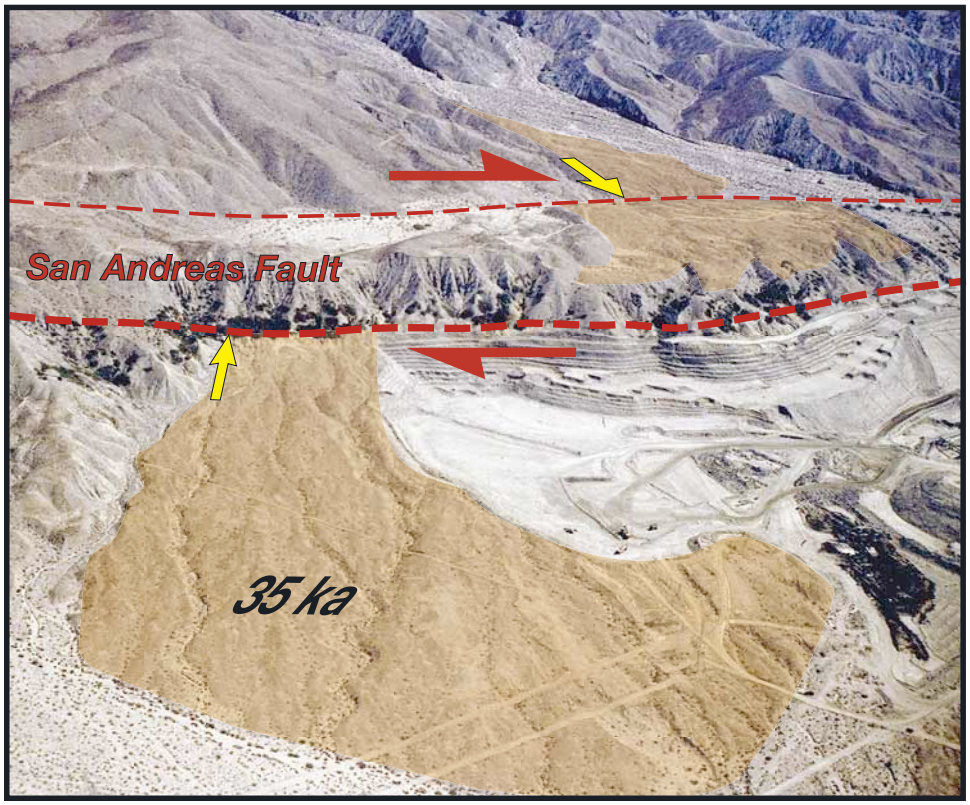

Figure 3. Oblique aerial view of the Biskra Palms fan surface, offset by two strands of the Mission Creek fault. By the time the photo was taken, in 2002, most of the fan downstream from the principal strand of the fault had been removed by quarrying. White arrows are piercing points of offset fan surface (dark gray) across two strands of San Andreas Fault.

patch of T1 remained, downstream from the fault zone (Figure 5a).

2.2. Offset Measurements

[15] *Keller et al.* [1982] recognized that the T2 surface has been offset by both strands of the MCF and proposed a cumulative offset of 700 m. This value appears to be an overestimate and has recently been challenged [*Dorsey*, 2002]. Thus we discuss below in some detail the nature of the piercing lines and conclude with a reassessment of the offset measurement.

[16] From the two parallel strands of the MCF, the SMCF is the more prominent in part because its vertical offset across T2 and T3 is several tens of meters high (Figures 3, 4, 5, and 6). In detail, the fault trace consists of a set of right-stepping traces that form an arcuate zone. Several of the gullies that incise the fault scarp are offset right laterally (Figure 5b). *Keller et al.* [1982] attributed the 50-m-high scarp to a component of reverse faulting caused by the curvature of the fault. Our observations confirm this view, and we suggest a similar interpretation on the cross section of Figure 5b. The NMCF is more subdued and does not continue more than a couple kilometers eastward from the offset fan. To the west, it joins the main MCF strand (Figure 2). It is followed locally by an ephemeral stream course, which crosses a small playa west of T2i (Qal in the work by *Keller et al.* [1982]). It accommodates mostly right-lateral motion (Figure 5b).

[17] Both faults offset the western edge of T2. This is the only marker that enables us to quantify a total MCF offset precisely and accurately. In the following we describe the piercing points used to assess the total right-lateral offset of T2 (Figure 5a). First, let us consider the offset across the NMCF. North of the NMCF, the western edge of T2u is nearly linear and trends N35E (Figures 5a and 7a). For most of its length however, a younger rill has eroded the western fan margin T2u. The bed of this small channel widens downstream, toward the northern fault. On Figure 7, piercing points A and C represent the intersections with the fault of the present eastern and western edges of this widening channel. They bracket the range of plausible piercing points for T2u. Piercing point B, between these two extremes, would represent the intersection of the western edge of T2u with the fault, if the original channel edge near the fault did not deviate from its upstream trend of N35E.

[18] South of the NMCF, the western edge of T2i consists, to the northeast, of a straight, 100-m-long, northwest facing N35E trending scarp (Figures 4 and 5a). To the southwest the scarp bends to become N78E for 300 m and faces southeast. It clearly separates two different terraces. T3i to the northwest is represented by a chaotic surface of eroded hills, dipping on average to the northeast due to upslope tilting. T2i to the southeast is a much smoother surface, although dissected by recent small normal faults, it is less back-tilted and still dips to the southwest (Figure 5b). Several possible explanations for the existence of the

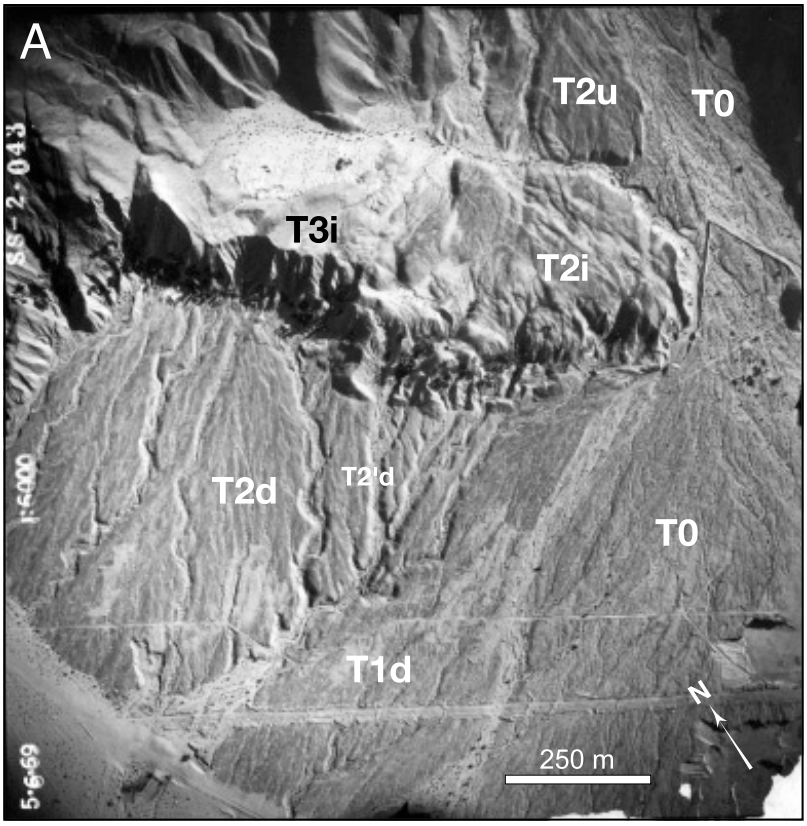

Figure 4. Vertical aerial photo of Biskra Palms site (6 May 1969). Main fan surface T2d, south of the fault, has been disconnected from its upstream counterparts T2i and T2u by right-lateral motion along the fault. Youngest alluvial surfaces are T0. T1d is an intermediate terrace.

northeastern western T2i fan margin may be suggested, as it may not be only the result of stream incision (Figure 5a). The fan margin may represent the largely uneroded front of a fan delta that abutted a small lake that occupied the valley formed after tilting of T3i (Figure 5b). Fine sands and silts on the valley floor attest to the former presence of a lake (Qal in the work by *Keller et al.* [1982]). The fan margin may be a fault scarp, due, to a reverse fault [*Keller et al.*, 1982], or to differential tilting of the T3i and T2i units as we suggest occurs between the NMCF and SMCF (Figure 5b). However, there is no field evidence that supports a faulted contact. Whatever the actual origin of the present shape of the scarp between D and F, it is interpreted as the western margin of T2i [*Keller et al.*, 1982]. The fan margin T2i intersects the NMCF at piercing point D.

[19] The offsets between D and A, B, and C are 90, 130 and 180 m, respectively (Figure 7a). The most likely actual offset is D-B (130 m) because in this case the upstream and downstream segments of the western edge of T2 have the same strike (Figure 5b). The two other piercing points (A and C) are probably beyond the extreme lower and upper bounds for the offset, since these yield poorly matching trends for the upstream and downstream fan edges. In actuality, the upper and lower bounds for the offset of T2 across the northern strand must be closer to B than to A and C.

[20] We turn now to an evaluation of the offset of T2 across the SMCF. North of the SMCF, the western edge of T2i abuts a 10- to 15-m-high topographic scarp (Figures 3 and 5a). Following our interpretation of the contact between T3i and T2i (see above), depending on the tilting amount of T3i when T2i was deposited, this scarp may partly or totally be a riser, reflecting incision by the T2 stream into a preexisting ridge of T3i alluvial conglomerate. Both the riser and the edge of the T2i tread are gently arcuate and collinear with the portion of the northeastern T2i margin described above.

[21] TheT2i riser is cut and offset right laterally about 30 m by a minor fault that splays off of the SMCF (Figure 5a). The intersection of the T2i terrace edge and this fault are labeled E and F in Figure 7. From piercing point E the base of the terrace riser trends S78W toward the SMCF, until it is cut by another minor strand of the SMCF.

[22] Beyond this intersection, erosion has eliminated the terrace riser. Thus one must extrapolate to the trace of the SMCF to estimate the position of the piercing point. Linear extrapolation to the main southern strand yields a position for the piercing point at H (Figure 7a).

[23] This piercing point may not reflect the total offset across the SMCF, however. The arcuate nature of the riser between the NMCF and SMCF suggests that it and T2 may be right laterally warped. The en échelon field of minor faults that cuts the T2i surface also suggests that warping may have occurred (Figure 5a). However, only one of these little faults clearly offsets the terrace riser. That offset is no more than a few meters, too small to be depicted on

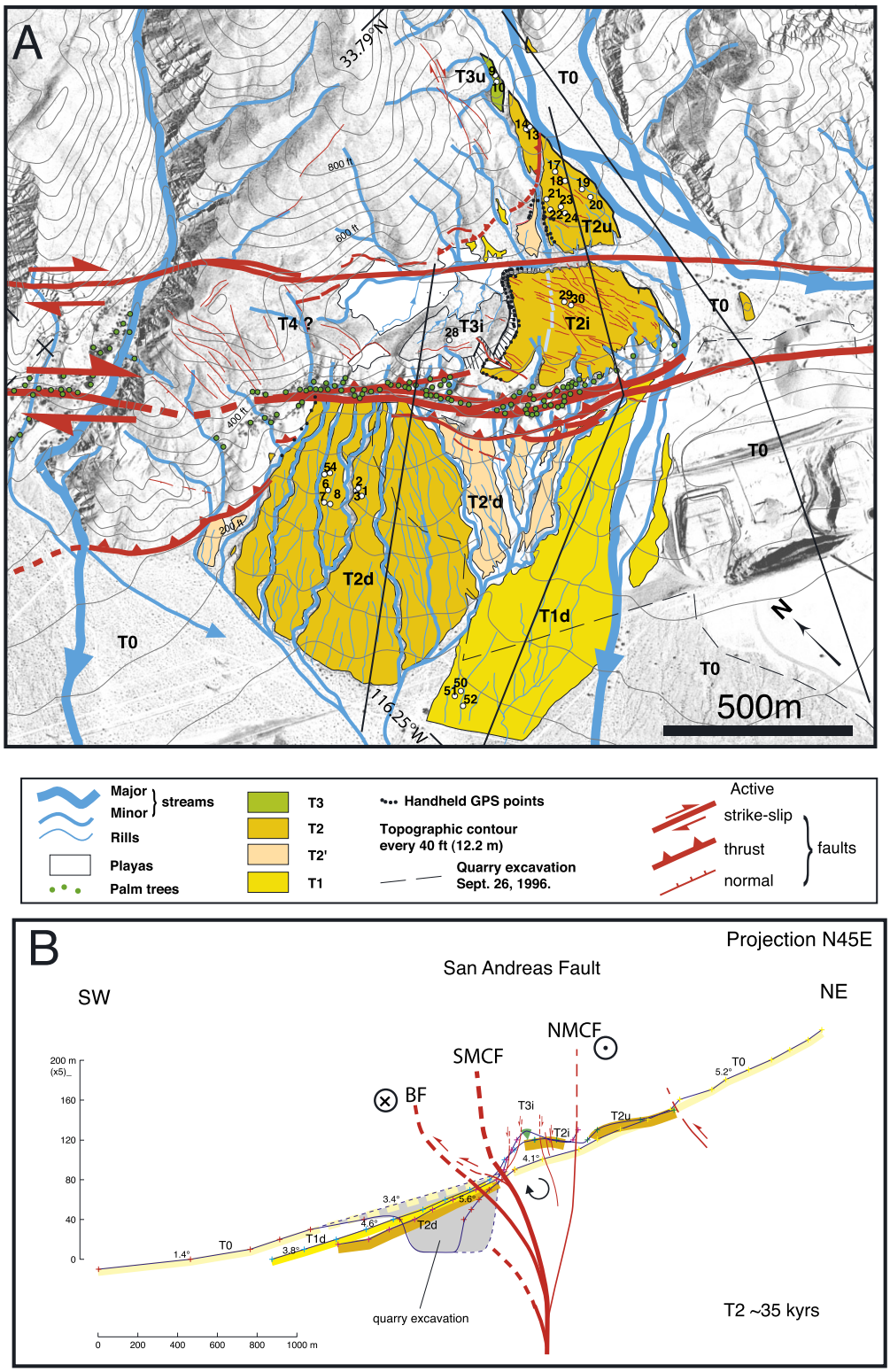

Figure 5. (a) Map of fault traces and alluvial surfaces superimposed on topographic contours and USGS orthophoto (26 September 1996). Numbered dots show locations of samples collected for cosmogenic dating. Straight lines indicate positions of topographic profiles plotted in Figure 5b. (b) Superimposed topographic profiles across main alluvial levels, projected to a line perpendicular to strike of the fault zone. Match between surfaces northeast and southwest of central fault zone is clear. Main scarp along the principal strike-slip fault is likely due to thrust component and uplift of block between the two strike-slip faults. Fault geometry at depth, though hypothetical, is consistent with this interpretation.

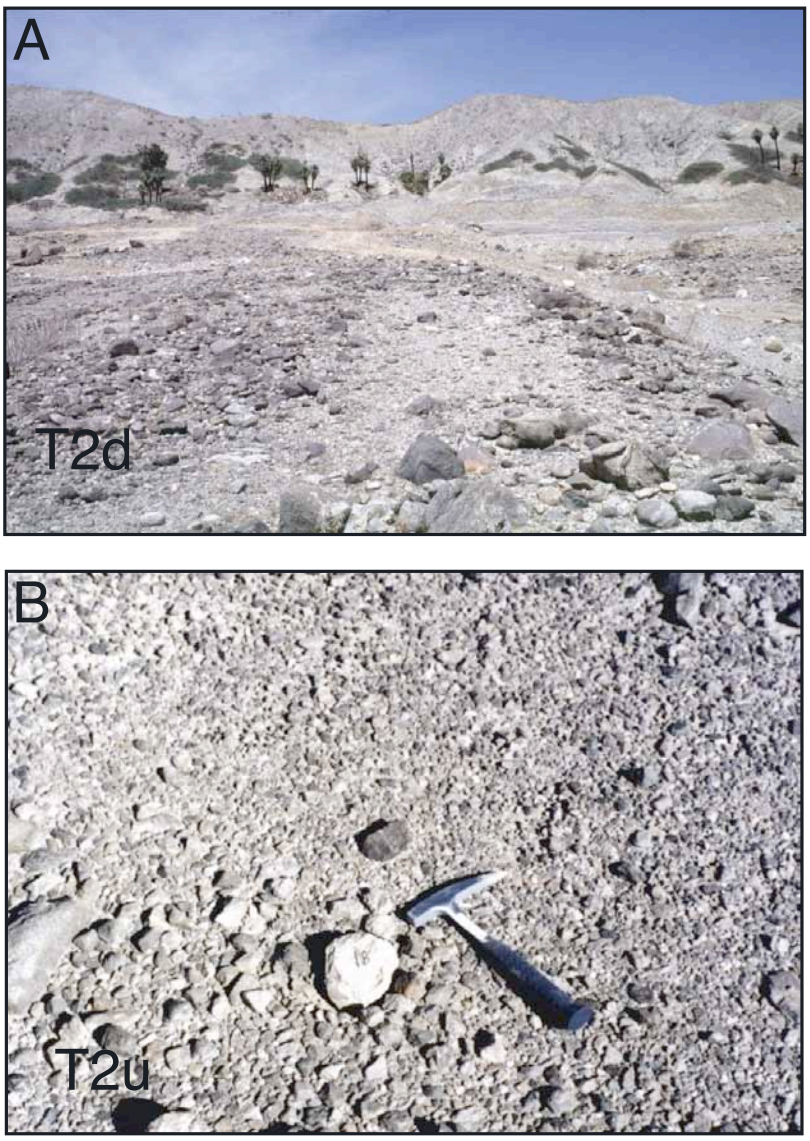

Figure 6. (a) The surface of terrace T2d, downstream of the fault zone. View to northeast, toward principal fault zone marked by aligned palm trees and by scarp. Lightly varnished cobbles paving the alluvial surface are typical of those sampled for surface exposure dating. (b) Close-up of desert pavement on T2u surface northeast of fault. The white cobble near the head of the rock hammer is sample 18 (^{10}Be age of 35.4 ± 3.9 ka).

Figure 5a. This suggests that the family of minor faults is principally a superficial feature that cuts only the thin T2i fill and not the underlying older materials. Nonetheless, these superficial faults may belie the existence of significant broad right-lateral shearing of the block between the two principal faults.

[24] If we assume that the entire curvature of the terrace riser between the two principal fault strands is due to right-lateral warping, then we can extrapolate the N35E trend of the riser near the NMCF all the way to the SMCF to infer a piercing point at G. Since this point is about 200 m SE of piercing point H, warping could, conceivably, account for 200 m of the offset across the fault zone.

[25] Determination of the piercing point on the southwestern side of the SMCF is less complicated. The T2 fan south of the fault has a simple geometry and is cleanly offset. Five major rills incise the fan surface south of the SMCF, including one along the fan's western margin (Figure 5a). All of these rills intersect the fault zone at a high angle and together exhibit a slightly radial pattern across the fan. These rills probably fed by the springs along the fault zone have reused or slightly widened preexisting channels at the surface of the fan surface, therefore indicating no major surface change since T2 was beheaded and abandoned.

[26] Adjacent to the western edge of the T2d terrace is a small intermittent active stream channel. This channel is too small and services too small a drainage basin to have had the power to significantly erode the western margin of the T2d fan. Thus the current mapped edge of the T2d fan is probably within a few meters of the original fan edge. The

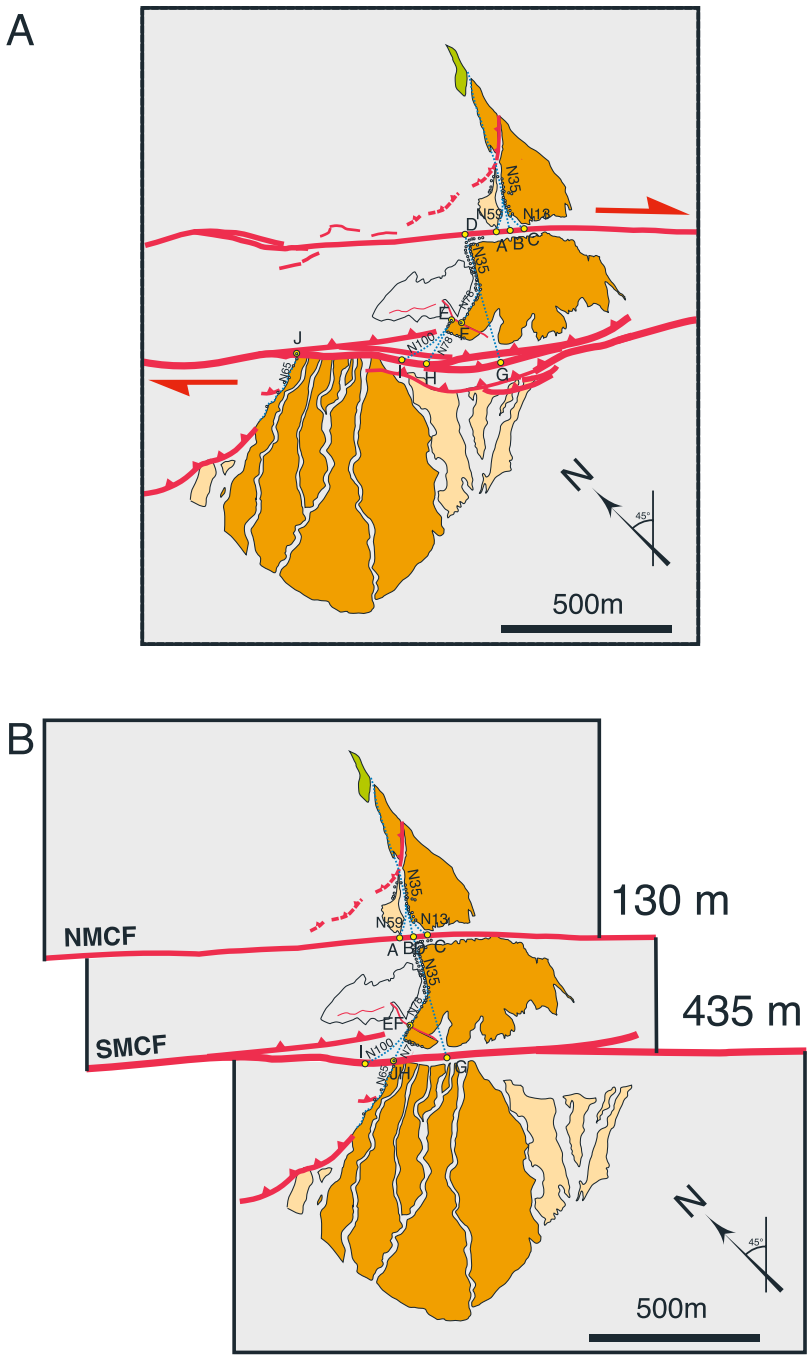

Figure 7. (a) Map of alluvial unit T2, faults and various considered piercing points. Small white dots are points surveyed in the field along piercing lines. Dashed lines are western edges of T2 that we consider for offset estimation. Lettered circles are piercing points defined by intersection of dotted lines with fault traces. (b) Preferred reconstruction of T2 surface and corresponding total offset values.

fan edge projects N65E into the fault zone at point J (Figure 7a).

[27] One might argue that the original fan margin and piercing point lie farther to the west and have been overridden by the thrust fault in Figure 5a. This cannot be the case, however. First, there are no young scarps that would indicate the fault has been recently active. Second, small remnants of the T2d surface present at the mouth of tributary canyons on the hanging wall block still grade to the main T2d fan.

[28] The distance between piercing point J and piercing points H is 405 m. Addition of the 30-m offset between points E and F yields a total offset of 435 m. If we were to allow for an extreme amount of warping by matching up piercing point J and G, the offset would be 600 m. (Figure 7a).

[29] The true offset across the southern fault zone must be close to the 435-m value because the trends of the western edges of T2 are similar in this reconstruction. The trend of the T2 fan south of the fault zone is N65E, and the trend of the T2 terrace riser immediately north of the fault zone is N78E. Even if we allow for some rotation north of the southern fault zone, by rotating the latter so that it has a N65E trend, the offset increases only by about 40–50 m. The 600-m offset, based upon 200 m of warping, is indefensible because it creates an enormous mismatch between the trend of the T2 terrace riser north of the fault zone and the T2 fan south of the fault. We suggest that the uncertainty in offset across the southern main fault is no more than 50 m or so because of the similarity in trend of the offset features north and south of the fault zone.

[30] Figure 7b illustrates our reconstruction of offsets across the fault zone. The reconstruction assumes that no rotation has occurred. The total offset across the fault zone is 565 m, 130 m across the northern strand and 435 m across the southern strand. Allowance for enough warp to restore the trend of the T2i terrace riser to the N65E trend of the T2d fan edge increases the total offset by about 50 m, to 615 m. Offsets across the southern fault zone much smaller than 435 m [e.g., *Dorsey*, 2002] must be considered unlikely because they require piercing lines with grossly conflicting trends. In addition, the geomorphic expression of the NMCF and SMCF are quite different implying more displacement along the southern branch. The NMCF is discontinuous and difficult to map both in the field and from air photos. The SMCF is a clear cut across the landscape, underlined with numerous springs and palm trees and at our site forms a several tens of meter high topographic scarp (Figures 3–6). It therefore appears unlikely to accumulate most of the displacement along the NMCF as implied by the interpretation of *Dorsey* [2002]. Arguments that unrecognized sinuosity in the western margin of T2 could make smaller offsets plausible are also difficult to defend. First, the western edge of the T2 surface is well preserved along most of its length, and there are no preserved abrupt changes in trend. Variations in its trend occur over hundreds, not tens of meters. Second, rills cut into T2 upstream and downstream support this inference because they too tend to have rather uniform trends over short distances. The trends of the western margin of the T2 surface and the major rills cut into the T2 surface vary from N30E to N45E. If we allow this much variation in the piercing line where it has been obliterated by erosion near each of the two main fault zones, we derive an estimate of 80 m for the uncertainty in our measurement. Note that, ignoring the trend of the northwestern margin of T2i in the more chaotic zone between the two MCF strands implies to estimate an offset between piercing points B and J (Figure 7a) with varying extreme trends from N35 to N65 across the 430 m large fault zone. This would result in an average offset of 600 ± 100 m, only slightly larger than the one determined here (Figure 7b) with a similar uncertainty. In the discussion below, we take the value of 565 ± 80 m as the best estimate of the offset of the T2 surface at the site.

2.3. Cosmogenic Dating

[31] Alluvial fan and terrace surfaces, which are abandoned streambeds, may be dated with surface exposure dating techniques if deposition and incision are events of relatively short duration. Exposure of clasts to cosmic rays before deposition on a surface (also called inheritance [e.g., *Anderson et al.*, 1996; *Repka et al.*, 1997]) is largely a function of transport time and storage within the drainage basin. At Biskra Palms, the headwaters of the drainage basin are only 3 km away from the site of deposition. This suggests that inheritance related to exposure during transport is likely to be small [e.g., *van der Woerd et al.*, 1998]. Exposure on eroding slopes may occur, however, and can be responsible for inherited components in the total cosmogenic nuclide content [e.g., *Anderson et al.*, 1996]. This is also the case of cobbles previously deposited and then reworked and transported into the drainage basin. To detect such potential age bias we collected multiple samples from each surface [*Bierman et al.*, 1995a; *van der Woerd et al.*, 1998, 2000, 2002; *Mériaux et al.*, 2004; *Zehfuss et al.*, 2001].

[32] Erosion is usually advocated to be the source of uncertainties in surface exposure dating [e.g., *Gosse and Phillips*, 2001]. In comparable climatic conditions, bedrock surfaces [*Bierman*, 1994; *Small et al.*, 1997; *Matmon et al.*, 2005] or large boulders [*Bierman et al.*, 1995b; *Phillips et al.*, 1997; *Zehfuss et al.*, 2001] have been found to erode at rates of 0.002–0.017 and 0,002–0.004 mm/yr, respectively. We think that these rates are maximum when transposed at our site. The surface targeted here are loose conglomerates and we sampled in general cobbles (the most common rock size of the surfaces) avoiding large protruding boulders. Away from recent rills the flat fan surfaces we targeted, although they are loosely compacted conglomerates, show no evidence of erosion, cobbles look pretty much the same as those from the present-day streambed. In general, the well-preserved cobbles showed no evidence of mass wasting due to frost or fire spalling. However, paved surfaces clearly indicate that surface weathering occurred resulting in patches of smooth surfaces. Desert pavement development and evolution is critical to assess the exposure evolution with time of the surface cobbles. Rapid development of desert pavement followed by stabilization of the surface may in fact reduce the erosion factor as a source of uncertainty [e.g., *Wells et al.*, 1995; *Quade*, 2001]. If pavements develop in relatively short times, a few centuries or a few thousand years [*Quade*, 2001], the duration of surface exposure may be close to the true age of abandonment of the surface. Hence we consider that erosion of the samples or of the surfaces occurs at a rate slow enough to be neglected.

[33] We dated a total of 26 quartz-rich, rooted cobbles, ranging in size from about 10 to 20 cm in diameter (Figure 6b and Table 1). Three cobbles were collected from older surfaces (two on T3u, north of the fault zone, and one on the irregular surface west of T2i; Figure 5a). From the T2 complex, we dated 20 cobbles (10 from T2u, 2 from T2i and 8 from T2d). From the youngest abandoned terrace, T1, we dated 3 cobbles (Figure 5a and Table 1). Samples locations were plotted in the field on the aerial photos, and some of them were determined with a handheld GPS. Elevation of each sample has been checked with the USGS 24,000-scale topographic contours and shielding due to surrounding relief determined for each sample (the Indio Hills crest line is the main

Table 1. The ^{10}Be and ^{26}Al Nuclide Concentration and Modeled Age for 26 Surface Samples at the Biskra Palms Site

Sample	Elevation, m above sea level	^{10}Be, 10^4, atoms g^{-1}	^{26}Al, 10^4 atoms g^{-1}	^{26}Al/^{10}Be	Lat/Alt Correction	Depth/Topo Correction	^{10}Be Age,[a] ka	Mean Terrace Age,[b] ka
			Terrace T3u					
9	170	14.544 ± 2.079	87.769 ± 11.783	6.03	1.0076	0.9549	30.7 ± 4.47	
10	170	17.169 ± 2.001	80.138 ± 9.414	4.67	1.0076	0.9549	35.96 ± 4.31	33.33 ± 3.72
			Terrace T2u					
13	165	19.026 ± 1.892	87.789 ± 11.432	4.61	1.0034	0.9550	39.66 ± 4.1	
14	165	18.453 ± 2.238	114.348 ± 14.083	6.20	1.0034	0.9550	38.55 ± 4.8	
17	155	21.943 ± 1.925	109.06 ± 12.482	4.97	0.9950	0.9555	45.81 ± 4.22[c]	
18	155	16.66 ± 1.788	81.015 ± 9.528	4.86	0.9950	0.9555	35.37 ± 3.92	
19	150	14.449 ± 1.674	76.224 ± 9.451	5.28	0.9909	0.9554	30.98 ± 3.7	
20	150	19.035 ± 1.964	89.438 ± 10.576	4.70	0.9909	0.9555	40.13 ± 4.29	
21	150	19.246 ± 1.273	84.108 ± 10.157	4.37	0.9909	0.9554	40.54 ± 2.92	
22	150	15.624 ± 1.131	75.772 ± 9.028	4.85	0.9909	0.9555	33.4 ± 2.6	
23	150	15.353 ± 1.117	86.771 ± 11.62	5.65	0.9909	0.9555	32.84 ± 2.56	
24	150	17.133 ± 1.204	73.357 ± 12.197	4.28	0.9909	0.9555	36.44 ± 2.76	37.37 ± 4.44
			Terrace T3i					
28	150	18.179 ± 1.314	73.916 ± 19.572	4.07	0.9909	0.9558	38.45 ± 2.98	38.45 ± 2.98
			Terrace T2i					
29	140	17.35 ± 1.2	86.018 ± 10.346	4.96	0.9825	0.9558	37.13 ± 2.77	
30	140	15.679 ± 1.181	80.765 ± 10.841	5.15	0.9825	0.9558	33.78 ± 2.72	35.45 ± 2.37
			Terrace T2d					
1	84	15.287 ± 0.561	84.65 ± 9.573	5.54	0.9367	0.9533	34.6 ± 1.6	
3	84	16.378 ± 0.586	102.963 ± 7.337	6.29	0.9367	0.9533	36.9 ± 1.68	
7	75	15.639 ± 0.547	91.353 ± 11.1	5.84	0.9295	0.9533	35.62 ± 1.6	
2	84	14.561 ± 1.702	91.357 ± 7.346	6.27	0.9367	0.9534	33.02 ± 3.97	
4	84	16.11 ± 1.857			0.9367	0.9534	36.34 ± 4.31	
5	84	16.315 ± 1.874	82.935 ± 6.668	5.08	0.9367	0.9533	36.77 ± 4.35	
6	80	15.9192.582	81.591 ± 8.387	5.13	0.9335	0.9533	36.06 ± 5.94	
8	75	14.984 ± 1.871	75.843 ± 14.617	5.06	0.9295	0.9534	34.2 ± 4.38	35.44 ± 1.37
			Terrace T1					
50	30	7.253 ± 0.265	63.346 ± 7.857	8.73	0.8938	0.9534	17.52 ± 0.81	
51	30	4.576 ± 0.184	31.98 ± 5.048	6.99	0.8938	0.9532	11.08 ± 0.54	14.30 ± 4.56
52	30	15.679 ± 0.503	117.253 ± 14.841	7.48	0.8938	0.9534	37.02 ± 1.58	
				5.48 ± 1.07[d]				35.53 ± 2.48[e]

[a]The ^{10}Be age is calculated with corresponding geographic and topographic correction factors (see text for details).
[b]Mean is average of ^{10}Be age, and error is standard deviation.
[c]Not included in average calculation.
[d]Average.
[e]Average T2.

shielding factor at the site, an horizon at about 10–15°, less than 3 km away).

[34] We separated quartz and removed meteoric components using the chemical isolation method of *Kohl and Nishiizumi* [1992]. We separated beryllium and aluminum from the dissolved quartz by anion and cation exchange chromatography, precipitated the hydroxides and ignited them to form oxides. We measured the ^{10}Be/Be and ^{26}Al/Al ratios by accelerator mass spectrometry (AMS) at the Lawrence Livermore National Laboratory AMS facility [*Davis et al.*, 1990]. Measurements were normalized to the ICN ^{10}Be and NBS ^{26}Al standards prepared by K. Nishiizumi (personal communication, 2005).

[35] In cases of negligible erosion and inheritance, model ages for ^{10}Be and ^{26}Al can be calculated from

$$N(0,t) = (P_0/\lambda)\left(1 - e^{-\lambda t}\right) \quad (1)$$

where $N(0, t)$ is the nuclide concentration at time t, P the surface production rate (atom/g/yr) and λ the decay constant of the nuclide (yr^{-1}). Zero-erosion model ages were calculated using a sea level high-latitude (SLHL) ^{10}Be production rate of 5.06 atoms/g quartz/yr, based on measurements of glacial surfaces in the Sierra Nevada [*Nishiizumi et al.*, 1989], recalculated using the revised 13,000 yr glacial retreat ages reported by *Clark et al.* [1995], and rescaled for latitude and altitude using the coefficients of *Lal* [1991], as described by *Owen et al.* [2002]. An uncertainty of 6% on the production rate [*Stone*, 2000] is taken into account. At the latitude of our site, the variations in the geomagnetic field and pole position produce changes in the production rate. These changes can be expressed in terms of an equivalent change in geomagnetic latitude and evaluated using the data from *Ohno and Hamano* [1992], *McElhinny and Senanayake* [1982] and the Sint-800 intensity record of *Guyodo and Valet* [1999]. For all our samples, which are at most 1.5 km apart, we use the same latitude and longitude coordinates (33.8°N, 116.2°W) and the ages were calculated using the *Stone* [2000] latitude and altitude correction factors.

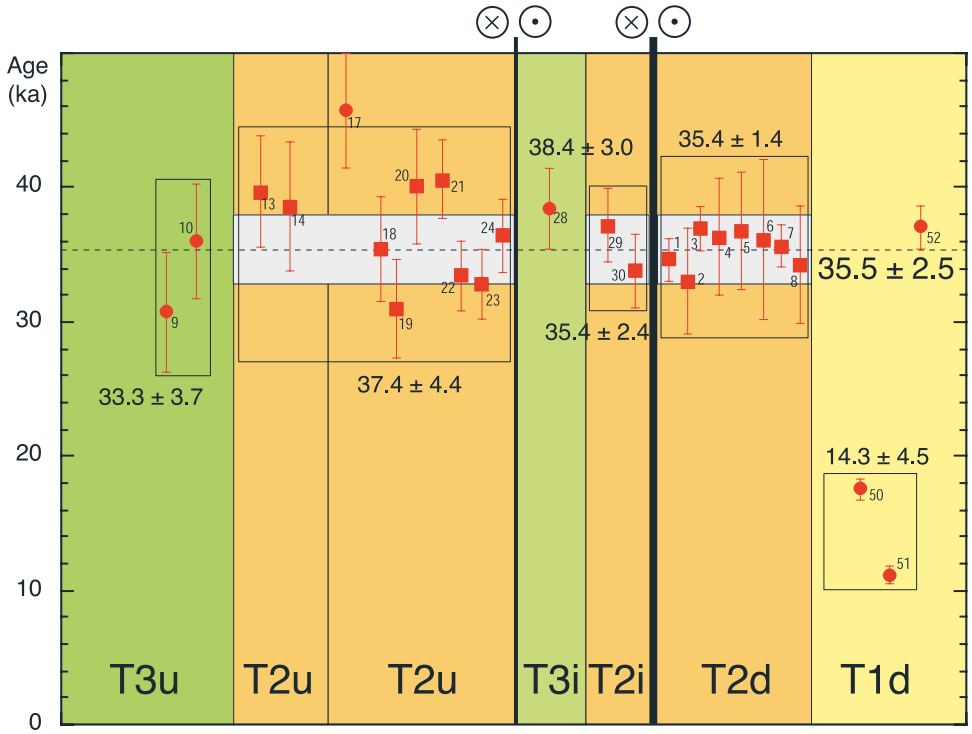

Figure 8. Plot of ^{10}Be model ages for each surface. The positions of each principal fault strand relative to the surfaces appear as vertical lines. Dotted line represents average age for T2. Light gray stripe is average standard deviation for samples represented by squares. Data are tabulated in Table 1.

[36] The isotopic concentrations and calculated model ages appear in Table 1. For all samples, save one, both ^{10}Be and ^{26}Al measurements were performed. While for most of the samples the ratio between ^{10}Be and ^{26}Al concentrations is close to 6, we observe systematically lower concentrations for ^{26}Al. We are more confident in the ^{10}Be ages because they rely on a single ratio measurement, whereas the ^{26}Al determination requires two measurements, the ^{26}Al/^{27}Al ratio and the ^{27}Al concentration. For these reasons, we use only the ^{10}Be data in the final age calculations, which include the geomagnetic correction (Table 1). As such, these ages are calibrated and can be compared to dates derived from other dating methods (calibrated radiocarbon dating, for example).

[37] South of the main fault (Figure 5a), 8 samples from T2d yield ages of 33 to 37 ka. The averaged value of these ages is 35.4 ± 1.4, with no outliers (Figure 8). The 3 samples from T1 yield ages ranging from 11 to 37 ka (Figure 8). Since T1 cannot be older than T2, the oldest sample could be a reworked cobble from T2. The average age of the two youngest samples of T1, 14 ± 4 ka, is our best estimate of the age of this surface.

[38] Between the two main faults, the average of the two cobble exposure ages obtained for T2i (33.8 and 37.1 ka) is 35.4, in good agreement with the average age of cobbles on T2d. The age of the one sample from the surface west of T2i (38.4 ka) is only slightly greater than the average age of T2.

[39] North of the faults we sampled two surfaces, T2u and T3u. Nine of the 10 samples from T2u yield ages between 31 and 40 ka, average 37.4 ± 4.4 ka, in keeping with the ages on T2i and T2d. However, one sample is significantly older (45.8 ka). The two samples from T3u have ages comparable to that of T2u, even though this terrace level stands several meters higher than T2.

[40] In summary, the age of T2 is well constrained by 19 sample ages that cluster tightly and yield an average age of 35.5 ± 2.5 ka (Figure 8 and Table 1). The 45 ka age of one sample from T2u is clearly an outlier and probably indicates reworking of a previously exposed clast. T1 (~14 ka) is at least 20 kyr younger than T2, and might be as young as 11 ka. The age of T1 indicates emplacement of T1 after the end of the Last Glacial Maximum.

3. Long-Term Slip Rate

[41] We may conclude confidently that the T2 surface was emplaced 35.5 ± 2.5 kyr ago. Subsequent to that date of deposition, the surface has been offset 565 ± 80 m. Dividing this offset by this age yields an average slip rate of 15.9 ± 3.4 mm/yr at the Biskra Palms fan. This rate is lower than the geological rates determined to the north along the SAF at Cajon Pass (24.5 ± 3.5 mm/yr [*Weldon and Sieh*, 1985]). However, as discussed below, the rate calculated here may be considered a minimum bound.

[42] In any case, it is presently the only and best direct estimate of the rate of right-lateral displacement on the main branch of the SAF across the Indio Hills. Despite fault related deformation along the two main fault branches the reconstruction of the geometry of the northwestern limit of T2 we propose is realistic. Conservatively, we have considered a simple, almost linear, shape for this limit (Figure 7b) in agreement with the present-day geomorphic characters of the surface suggested both from topographic contours and postdepositional rill incisions. Such characters require that

the total offset of the T2 limit, mapped on Figure 5a, must have accrued after the T2 conglomeratic fan was abandoned. Because of overlapping fan deposits downstream of the fault coupled with a component of thrusting (Figure 5a), the southeastern limit of T2 is less well defined, but overall the total offset is unlikely to be less than 500 m.

[43] The abandonment age of T2 (35.5 ± 2.5 ka), determined from sets of samples from various parts of the surface upstream and downstream from the two fault strands yields strong constraints on the age of the total offset of T2. The large number of surface samples (a total of 19, Figures 5a and 8), distributed over large areas of the three T2 remnants, with well clustered ages, confirm that predepositional exposure or postdepositional erosion were negligible and that the 35.5 ± 2.5 ka age is statistically representative of the timing of abandonment of T2. In addition, this age, which is calibrated and integrates topographic and geomagnetic corrections, corresponds to a well-known interstadial at 35 ka, a warm pluvial separating Marine Isotope Stages 3 and 2, also described in lake sediments at Owens Lake [e.g., *Bischoff and Cummins*, 2001] and Mono Lake [*LaJoie*, 1968]. This would have been a period propitious to fan aggradation and fairly rapid abandonment.

[44] While the rate we find is low, we argue that it is a minimum bound for the total slip rate across the entire fault zone at Biskra Palms. As shown above, there is additional faulting and deformation at the site that is difficult to assess quantitatively. In particular, there are numerous N160°–170° trending normal faults [*Keller et al.*, 1982] visible across T2 and between the two major strike-slip faults (Figure 5a). A few of these faults have dextral offsets of several meters. They probably accommodate internal deformation of the block between the main faults and ought to be responsible for additional right lateral slip at the site. While motion on these faults might attest to counterclockwise rotation of the small blocks they separate, clockwise rotation of the entire block between the two major strike-slip faults may also occur. A rotation of only 7° of this 400 m wide block would add up to 50 m to the total right-lateral offset and would increase the slip rate by more than 10%. Furthermore, as shown on Figures 1 and 2, faults north of the most prominent strands may accommodate additional right-lateral motion in the Indio Hills. They might easily account for another 10% increase in the slip rate.

[45] The major problem at Biskra Palms is to assess how the BF connects to the MCF and where. Clearly, the BF accommodates most of the right-lateral motion of the SAF as one moves 15 km northwest of the Indio Hills. The slip transfer must occur within the Indio Hills, but is probably not complete at Biskra Palms. The BF becomes less and less clear as it approaches its southeastern termination, with stepping en échelon segments that have a thrust component (Figure 2), responsible for uplift and upslope tilting of the hills southwest of the MCF. Such uplift terminates at Biskra Palms, as evidenced by the disappearance of the hills immediately to the southeast, and no additional faulting is observed across the fans farther south.

[46] Therefore the actual rate could reach a value closer to that determined at Cajon Pass, north of the San Gorgonio bend along the main trace of the San Andreas Fault. Such a rate would be in keeping with recent geodetic (GPS or VLBI) data that estimate the rate along the MCF to range between 21 and 28 mm/yr [*Feigl et al.*, 1993; *Bennett et al.*, 1996]. Note that the highest rate estimate is provided by the GPS data (26 ± 2 mm/yr [*Bennett et al.*, 1996]), which integrates strain over a wide area, with the eastern most stable points being as far as 100 km away from the SAF [*Bennett et al.*, 1996]. If a few millimeters per year of strain is taken up east of the Indio Hills, then a better agreement between our rate and the GPS data ensues.

[47] Alternatively, the slip rate along the SAF from Cajon Pass to the Indio Hills might not be constant and a decrease in slip could be envisaged as the fault crosses the San Gorgonio bend [e.g., *McGill et al.*, 2002], and could decrease even more toward Salton Sea [e.g., *Shifflett et al.*, 2002; *Sieh and Williams*, 1990]. If this were the case, then some form of distributed strain transfer might occur among the different faults that make up the plate boundary. In particular, the San Jacinto Fault (SJF) might become faster and could take up as much as 10–15 mm/yr of slip, in agreement with the fastest slip estimate along it [e.g., *Sharp*, 1981; *Merrifield et al.*, 1987; *Rockwell et al.*, 1990; *Bennett et al.*, 2004; *Kendrick et al.*, 2002; *Anderson et al.*, 2003; *Becker et al.*, 2005].

[48] To further assess the validity of our rate within the broader, regional active deformation framework, we show on Figure 9 the rates of slip on most of the faults across southern California. The rates compiled are from a variety of sources and were determined by different methods (Table 2) [e.g., *Wesnousky*, 1986; *Petersen and Wesnousky*, 1994; *Jennings*, 1994; *Dokka and Travis*, 1990; *McGill and Sieh*, 1993; *Lee et al.*, 2001; *Salyards et al.*, 1992; *Williams*, 1989]. When possible we show geologically determined rates, which provide information over comparable time spans. Considering the total slip budget across the plate boundary along three different paths (1–3, Figure 9), we obtain similar values of about 40–51 mm/yr. This first order calculation likely underestimates the total motion of the Pacific plate relative to North America, which probably explains the difference with the NUVEL-1A predictions of 45–55 mm/yr [*DeMets*, 1995; *DeMets and Dixon*, 1999] (Figure 9). If one considers that the total rates across the three paths have to be the same, we may infer the rates across other faults of the plate boundary. Either the SJF moves fast, up to 20 mm/yr (path 3B in Figure 9), i.e., 40% of the plate motion [e.g., *Kendrick et al.*, 2002]. Or, the SJF moves at 12 mm/yr and up to 1 cm/yr is already accommodated toward the northeast, in the ECSZ, (path 3A in Figure 9) [e.g., *Meade and Hager*, 2005].

4. Conclusion

[49] The slip rate we obtain at Biskra Palms using cosmogenic dating (15.9 ± 3.4 mm/yr) spans a 35,000 years period, and places a strong new constraint on slip distribution amongst the faults of southern California.

[50] To a first order, this rate is slower than even the lower bounds of the geological rate at Cajon Pass, 24.5 ± 3.5 mm/yr [*Weldon and Sieh*, 1985], and of the VLBI [*Feigl et al.*, 1993] and GPS [*Bennett et al.*, 1996; *Meade and Hager*, 2005] rates of 26 ± 2 mm/yr and 23 ± 2 mm/yr, respectively. Yet, it confirms that near Indio, the MCF is the principal strand of the SAF, accommodating most (35%) of the relative motion between the Pacific and North American

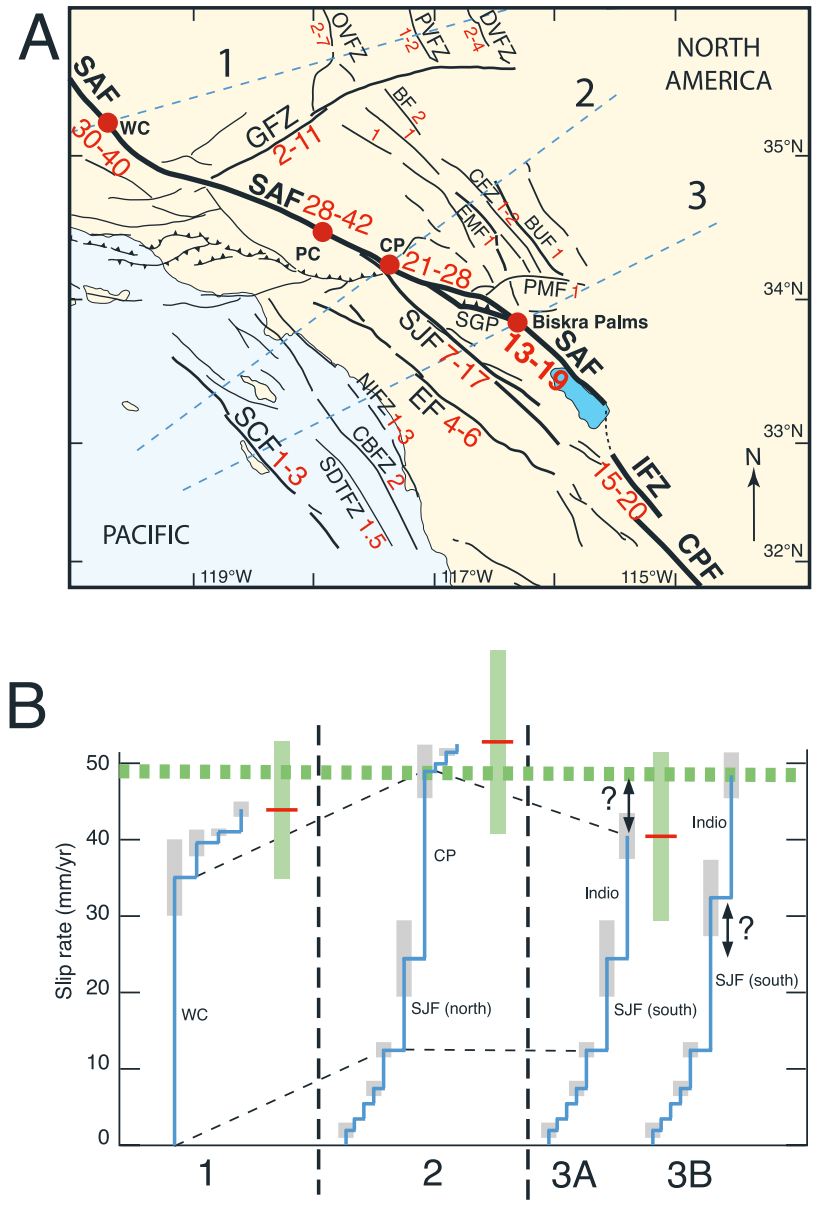

Figure 9. (a) Map of Southern California active faults. Values for slip rates on various faults and sites along SAF are from the literature (Table 2). Rates are expressed for right-lateral slip in mm/yr, except for GFZ and PMF, which are left-lateral faults. New rate at Biskra Palms is from this study. Dotted lines 1, 2, and 3 are paths along which we summed slip rates across plate boundary. WC, Wallace Creek; PC, Palett Creek; CP, Cajon Pass; OVFZ, Owens Valley Fault Zone; PVFZ, Panamint Valley Fault Zone; DVFZ, Death Valley Fault Zone; BF, Blackwater Fault; BUF, Bullion Fault; CFZ, Calico Fault Zone; EMF, Emerson Fault; PMF, Pinto Mountain Fault; SGP, San Gorgonio Pass; IFZ, Imperial Fault Zone; CPF, Cerro Prieto Fault; SJF, San Jacinto Fault; EF, Elsinore Fault; NIFZ, Newport-Inglewood Fault Zone; CBFZ, Coronado Bank Fault Zone; SDTFZ, San Diego Trough Fault Zone; SCF, San Clemente Fault. (b) Total slip of Pacific-America plate boundary for paths 1, 2, and 3 shown in Figure 9a. Considering an average plate boundary rate of 48–50 mm/yr (thick gray dotted line), the rate found in this study implies that either slip transfer (5–10 mm/yr) occurs toward the Eastern California Shear Zone east of our site (path 3A) or that the SJF is fast (>20 mm/yr; path 3B).

plates. The relatively slow rate on the main branch of the SAF at Biskra Palms suggests that the slip rate on the San Jacinto Fault maybe closer to the upper bounds of rates determined along this fault (12–20 mm/yr). Because it remains on the low side of all other rates determined on the southern SAF, we suspect that it is a minimum bound. This inference is supported by the fact that we obtain this rate at a rather complex location where the SAF splits into two branches (BF and MCF), with a significant change in strike (~10° toward west). Some motion must be accommodated by thrusting at Biskra Palms, and probably some more by adjacent normal faults. Also, the rates at Cajon

Table 2. Amount and Source of Slip Rates Along the Faults of Southern California as Discussed in the Text and Plotted in Figure 9

Fault	Slip Rate, mm/yr	Time Range	Reference
		Geologic	
San Andreas Fault			
Wallace Creek (WC)	34 ± 3	37 kyr	*Sieh and Jahns* [1984]
Pallet Creek (PC)	35 ± 7	500 years	*Salyards et al.* [1992]
Cajon Pass (CP)	24.5 ± 3.5	15 kyr	*Weldon and Sieh* [1985]
Thousand Palms Oasis	4 ± 2	900 years	*Fumal et al.* [2002]
Indio	15.9 ± 3.4	35.5 kyr	this study
	10–35	20–70 kyr	*Keller et al.* [1982]
Mecca Hills	6.5 ± 1.5	34 kyr	*Shifflett et al.* [2002]
Salt Creek	9 ± 2	900 years	*Williams* [1989] and *Sieh and Williams* [1990]
Imperial Fault Zone (IFZ)	15–20	300 years	*Thomas and Rockwell* [1996]
West of San Andreas			
San Jacinto Fault	20	100 kyr	*Kendrick et al.* [2002]
	6–23	50 kyr	*Rockwell et al.* [1990]
	1–12	700 kyr	*Sharp* [1981]
Elsinore Fault	4–6	600 kyr	*Petersen and Wesnousky* [1994]
Newport-Inglewood Fault Zone (NIFZ)	1–3	NA[a]	*Petersen and Wesnousky* [1994]
Coronado Bank Fault Zone (CBFZ)	2	NA	*Jennings* [1994]
San Diego Trough Fault Zone (SDTFZ)	1.5	NA	*Jennings* [1994]
San Clemente Fault	1–3	NA	*Jennings* [1994]
East of San Andreas			
Owens Valley Fault Zone (OVFZ)	2–4	4 kyr	*Lee et al.* [2001]
Panamint Valley Fault Zone (PVFZ)	1–2	10 kyr	*Hart et al.* [1989]
Death Valley Fault Zone (DVFZ)	2–4	NA	*Wesnousky* [1986]
Garlock Fault Zone (GFZ)	2–11	14 kyr	*McGill and Sieh* [1993]
Lockhard Fault	1	NA	*Jennings* [1994]
Harper Fault Zone	1	20 kyr	*Petersen and Wesnousky* [1994]
Blackwater Fault (BF)	2	20 kyr	*Dokka and Travis* [1990]
Emerson Fault (EMF)	1	20 kyr	*Dokka and Travis* [1990]
Calico Fault zone (CFZ)	1–2	20 kyr	*Dokka and Travis* [1990]
Bullion Fault (BUF)	1	NA	*Jennings* [1994]
Pinto Mountain Fault (PMF)	1	5–20 Myr	*Wesnousky* [1986]
Plate boundary (NUVEL-1A)	52 ± 2	3.16 Myr	*DeMets* [1995] and *DeMets and Dixon* [1999]
		Geodetic	
San Andreas Fault			
Southern SAF	23 ± 2	15 years	*Bennett et al.* [1996]
Southern SAF (VLBI)	26 ± 2		*Feigl et al.* [1993]
Salton Sea	23.3 ± 0.5	15 years	*Meade and Hager* [2005]
San Jacinto Fault	11.9 ± 1.2	15 years	*Meade and Hager* [2005]
San Jacinto Fault	9 ± 2	10 years	*Bennett et al.* [1996]
Elsinore Fault	6 ± 2	15 years	*Bennett et al.* [1996]
Owens Valley Fault Zone (OVFZ)	2.1 ± 0.7	15 years	*Dixon et al.* [2003]
Plate Boundary	49 ± 3	15 years	*Bennett et al.* [1996]
Plate Boundary (VLBI)	47 ± 1		*Feigl et al.* [1993]

[a]NA, data not available.

Pass and Biskra, on either side of the San Gorgonio restraining bend, need not be precisely the same, if diffuse strain transfer occurs across the San Bernardino and San Jacinto mountains [e.g., *Spotila et al.*, 1998; *Kendrick et al.*, 2002]. Finally, space geodesy rates span only the last 15 years and, as observed elsewhere [e.g., *Peltzer et al.*, 2001], millennial slip rates, especially spanning as much as 35,000 years, need not be identical if strain buildup varies through the seismic cycle and on larger timescales [*Bennett et al.*, 2004; *Friedrich et al.*, 2003; *Dixon et al.*, 2003].

[51] **Acknowledgments.** We like to thank Granite Corporation for allowing unlimited access to the fans and especially to Lola Green and Lilburn Corporation for sharing topographic data. Tom Rockwell was kind enough to take one of us in his plane to fly over the Indio Hills. We thank S. Mitchell and B. Dorsey for their critical reviews and comments that improved the final version of the manuscript. We thank R. C. Finkel and M. W. Caffee at Lawrence Livermore National Laboratory for their help in analyzing the samples. The Lawrence Livermore National Laboratory (LLNL) group acknowledges support from the Laboratory Directed Research and Development Program at LLNL, operating under the auspices of the U.S. Department of Energy contract W-7405-Eng-48. This research was supported in part by the Gordon and Betty Moore Foundation. This is Caltech Tectonic Observatory contribution 9.

References

Allen, C. R. (1957), San Andreas fault zone in San Gorgonio Pass, southern California, *Bull. Geol. Soc. Am.*, *68*, 315–350.

Anderson, G., D. C. Agnew, and H. O. Johnson (2003), Salton Trough regional deformation estimated from combined trilateration and survey-mode GPS data, *Bull. Seismol. Soc. Am.*, *93*, 2402–2414.

Anderson, R. S., J. L. Repka, and G. S. Dick (1996), Explicit treatment of inheritance in dating depositional surfaces using in situ ^{10}Be and ^{26}Al, *Geology*, *24*, 47–51.

Becker, T. W., J. L. Hardebeck, and G. Anderson (2005), Constraints on fault slip rates of the southern California plate boundary from GPS velocity and stress inversions, *Geophys. J. Int.*, *160*, 634–650, doi:10.1111/j.1365-246X.2004.02528.x.

Bennett, R. A., W. Rodi, and R. E. Reilinger (1996), Global Positioning System constraints on fault slip rates in southern California and northern Baja, Mexico, *J. Geophys. Res.*, *101*, 21,943–21,960.

Bennett, R. A., A. M. Friedrich, and K. P. Furlong (2004), Codependent histories of the San Andreas and San Jacinto fault zones from inver-

sion of fault displacement rates, *Geology*, *32*, 961–964, doi:10.1130/G20806.1.

Bierman, P. R. (1994), Using in situ cosmogenic isotopes to estimate rates of landscape evolution: A review from the geomorphic perspective, *J. Geophys. Res.*, *99*, 13,885–13,896.

Bierman, P. R., A. R. Gillespie, and M. W. Caffee (1995a), Cosmogenic ages for earthquake recurrence interval and debris flow fan deposition, Owens Valley, California, *Science*, *270*, 447–450.

Bierman, P. R., A. R. Gillespie, M. W. Caffee, and D. Elmore (1995b), Estimating erosion rates and exposure ages with ^{36}Cl produced by neutron activation, *Geochim. Cosmchim. Acta*, *59*, 3779–3798.

Bischoff, J. L., and K. Cummins (2001), Wisconsin glaciation of the Sierra Nevada (79,000–15,000 yr B.P.) as recorded by rock flour in sediments of Owens Lake, California, *Quat. Res.*, *55*, 14–24.

Chevalier, M. L., F. J. Ryerson, P. Tapponnier, R. C. Finkel, J. van der Woerd, H. Li, and Q. Liu (2005), Slip-rate measurements on the Karakorum fault may imply secular variations in fault motion, *Science*, *307*, 411–414.

Clark, D. H., P. R. Bierman, and P. Larsen (1995), Improving in-situ cosmogenic chronometers, *Quat. Res.*, *44*, 367–377.

Clark, M. M. (1984), Map showing recently active breaks along the San Andreas fault and associated faults between Salton Sea and Whitewater River-Mission Creek, California, *U.S. Geol. Surv. Misc. Invest. Map*, *I-1483*, scale 1:24,000.

Davis, J. C., I. D. Proctor, J. R. Southon, M. W. Caffee, D. W. Heikkinen, M. L. Roberts, K. W. Turteltaub, D. E. Nelson, D. H. Loyd, and J. S. Vogel (1990), LLNL/UC AMS facility and research program, *Nucl. Instrum. Methods Phys. Res., Sect. B*, *52*, 269–272.

DeMets, C. (1995), Reappraisal of seafloor spreading lineations in the Gulf of California: Implications for the transfer of Baja California to the Pacific plate and estimates of Pacific-North America motion, *Geophys. Res. Lett.*, *22*, 3545–3548.

DeMets, C., and T. H. Dixon (1999), New kinematic models for Pacific–North America motion from 3 Ma to present, I: Evidence for steady motion and biases in the NUVEL-1A model, *Geophys. Res. Lett.*, *26*, 1921–1924.

Dixon, T. H., E. Norabuena, and L. Hotaling (2003), Paleoseismology and Global Positioning System: Earthquake cycle effects and geodetic versus geologic fault slip rates in the Eastern California shear zone, *Geology*, *31*, 55–58.

Dokka, R. K., and C. J. Travis (1990), Late Cenozoic strike-slip faulting in the Mojave desert, California, *Tectonics*, *9*, 311–340.

Dorsey, B. (2002), Late Pleistocene slip-rate on the Coachella Valley segment of the San Andreas fault and implications for regional slip partitioning, paper presented at Cordilleran Section GSA 99th Annual Meeting, Puerto Vallarta, Jalisco, Mexico, 1–3 April.

Feigl, K. L., et al. (1993), Space geodetic measurement of crustal deformation in central and southern California, 1984–1992, *J. Geophys. Res.*, *98*, 21,677–21,712.

Friedrich, A. M., B. P. Wernicke, N. A. Niemi, R. A. Bennett, and J. L. Davis (2003), Comparison of geodetic and geologic data from the Wasatch region, Utah, and implications for the spectral character of Earth deformation at periods of 10 to 10 million years, *J. Geophys. Res.*, *108*(B4), 2199, doi:10.1029/2001JB000682.

Fumal, T. E., M. J. Rymer, and G. G. Seitz (2002), Timing of large earthquakes since AD 800 on the Mission Creek strand of the San Andreas fault zone at Thousand Palms Oasis, near Palm Springs, California, *Bull. Seismol. Soc. Am.*, *92*, 2841–2860.

Gosse, J. C., and F. M. Phillips (2001), Terrestrial in situ cosmogenic nuclides: Theory and application, *Quat. Sci. Rev.*, *20*, 1475–1560, doi:10.1016/S0277-3791(00)00171-2.

Guyodo, Y., and J. P. Valet (1999), Global changes in intensity of the Earth's magnetic field during the past 800 kyr, *Nature*, *399*, 249–252.

Hart, E. W., W. A. Bryant, C. J. Wills, J. A. Treiman, and J. E. Kahle (1989), Summary report: Fault Evaluation Program, 1987–1988, southwestern Basin and Range Region and supplemental areas, *Open File Rep., 89-16*, Dep. of Conserv., Div. of Mines and Geol., Sacramento, Calif.

Jennings, C. W. (1994), Fault activity map of California and adjacent areas with location and ages of recent volcanic eruptions, *Calif. Geol. Data Map Ser., Map 6*, Calif. Div. of Mines and Geol., Sacramento.

Keller, E. A., M. S. Bonkowski, R. J. Korsch, and R. J. Shlemon (1982), Tectonic geomorphology of the San Andreas fault zone in the southern Indio Hills, Coachella Valley, California, *Geol. Soc. Am. Bull.*, *93*, 46–56.

Kendrick, K. J., D. M. Morton, S. G. Wells, and R. W. Simpson (2002), Spatial and temporal deformation along the northern San Jacinto fault, southern California: Implications for slip rates, *Bull. Seismol. Soc. Am.*, *92*, 2782–2802.

Kohl, C. P., and K. Nishiizumi (1992), Chemical isolation of quartz for measurement of in-situ produced cosmogenic nuclides, *Geochim. Cosmochim. Acta*, *56*, 3583–3587.

LaJoie, K. R. (1968), Quaternary stratigraphy and geologic history of Mono Basin, eastern California, thesis, Ph.D. thesis, Dep. of Geol. and Geophys., Univ. of Calif., Berkeley.

Lal, D. (1991), Cosmic ray labeling of erosion surfaces: In situ production rates and erosion models, *Earth Planet. Sci. Lett.*, *104*, 424–439.

Lee, J., J. Spencer, and L. Owen (2001), Holocene slip rates along the Owens Valley fault, California: Implications for the recent evolution of the Eastern California Shear Zone, *Geology*, *29*, 819–822.

Matmon, A., D. P. Schwartz, R. Finkel, S. Clemmens, and T. Hanks (2005), Dating offset fans along the Mojave section of the San Andreas fault using cosmogenic ^{26}Al and ^{10}Be, *Geol. Soc. Am. Bull.*, *117*, 795–807, doi:10.1130/B25590.

Matti, J. C., and D. M. Morton (1993), Paleogeographic evolution of the San Andreas fault in southern California: A reconstruction based on a new cross-fault correlation, in *The San Andreas Fault System: Displacement, Palinspastic Reconstruction, and Geologic Evolution*, edited by R. E. Powell, R. J. Weldon, and J. C. Matti, *Mem. Geol. Soc. Am.*, *178*, 107–159.

McElhinny, M. W., and W. E. Senanayake (1982), Variations in the geomagnetic dipole 1: The past 50,000 years, *J. Geomagn. Geoelectr.*, *34*, 39–51.

McGill, S., and K. Sieh (1993), Holocene slip rate of the central Garlock Fault in southeastern Searles valley, California, *J. Geophys. Res.*, *98*, 14,217–14,231.

McGill, S., et al. (2002), Paleoseismology of the San Andreas fault at Plunge Creek, near San Bernardino, southern California, *Bull. Seimol. Soc. Am.*, *92*, 2803–2840.

Meade, B. J., and B. H. Hager (2005), Block models of crustal motion in southern California constrained by GPS measurements, *J. Geophys. Res.*, *110*, B03403, doi:10.1029/2004JB003209.

Mériaux, A.-S., F. J. Ryerson, P. Tapponnier, J. van der Woerd, R. C. Finkel, X. Xu, Z. Xu, and M. W. Caffee (2004), Rapid slip along the central Altyn Tagh Fault: Morphochronologic evidence from Cherchen He and Sulamu Tagh, *J. Geophys. Res.*, *109*, B06401, doi:10.1029/2003JB002558.

Mériaux, A.-S., et al. (2005), The Aksay segment of the northern Altyn Tagh fault: Tectonic geomorphology, landscape evolution, and Holocene slip rate, *J. Geophys. Res.*, *110*, B04404, doi:10.1029/2004JB003210.

Merrifield, P. M., T. K. Rockwell, and C. C. Loughman (1987), Slip rate on the San Jacinto fault zone in the Anza seismic gap, southern California, *Geol. Soc. Am. Abstr. Programs*, *19*, 431.

Nishiizumi, K., E. L. Winterer, C. P. Kohl, J. Klein, R. Middleton, D. Lal, and J. R. Arnold (1989), Cosmic ray production rates of ^{10}Be and ^{26}Al in quartz from glacially polished rocks, *J. Geophys. Res.*, *94*, 17,907–17,915.

Ohno, M., and Y. Hamano (1992), Geomagnetic poles over the past 10,000 years, *Geophys. Res. Lett.*, *19*, 1715–1718.

Owen, L. A., R. C. Finkel, M. W. Caffee, and L. Gualtieri (2002), Timing of multiple glaciations during the Late Quaternary in the Hunza Valley, Karakoram Mountains, Northern Pakistan: Defined by cosmogenic radionuclide dating of moraines, *Geol. Soc. Am. Bull.*, *114*, 5, 593–604.

Peltzer, G., F. Crampe, S. Hensley, and P. Rosen (2001), Transient strain accumulation and fault interaction in the Eastern California Shear Zone, *Geology*, *29*, 975–978.

Petersen, M. D., and S. G. Wesnousky (1994), Fault slip rates and earthquake histories for active faults in southern California, *Bull. Seismol. Soc. Am.*, *84*, 1608–1649.

Phillips, F. M., M. G. Zreda, J. C. Gosse, J. Klein, E. B. Evenson, R. D. Hall, O. A. Chadwick, and P. Sharma (1997), Cosmogenic ^{36}Cl and ^{10}Be ages of Quaternary glacial and fluvial deposits of the Wind River Range, Wyoming, *Geol. Soc. Am. Bull.*, *109*(11), 1453–1463.

Powell, R. E., R. J. Weldon, and J. C. Matti (1993), The San Andreas Fault system: Displacement, palinspastic reconstruction, and geologic evolution, *Mem. Geol. Soc. Am.*, *178*, 332 pp.

Quade, J. (2001), Desert pavements and associated rock varnish in the Mojave Desert: How old can they be?, *Geology*, *29*, 855–858.

Repka, J. L., R. S. Anderson, and R. C. Finkel (1997), Cosmogenic dating of fluvial terraces, Fremont River, Utah, *Earth Planet. Sci. Lett.*, *152*, 59–73.

Ritz, J. F., E. T. Brown, D. L. Bourlès, H. Phillip, A. Schlupp, V. M. Raisbeck, F. You, and B. Enkhtuvshin (1995), Slip rates along active faults estimated with cosmic-ray-exposure dates: Application to the Bogd fault, Gobi-Altaï, Mongolia, *Geology*, *23*, 1019–1022.

Rockwell, T., C. Loughman, and P. Merrifield (1990), Late Quaternary rate of slip along the San Jacinto fault zone near Anza, Southern California, *J. Geophys. Res.*, *95*, 8593–8605.

Rogers, T. H. (1965), Geologic map of California, Santa Ana Sheet, fifth printing 1985, Olaf P. Jenkins edition, Calif. Div. of Mines and Geol., Sacramento.

Salyards, S. L., K. E. Sieh, and J. L. Kirschvink (1992), Paleomagnetic measurements of non-brittle deformation across the San Andreas fault at Pallett Creek, *J. Geophys. Res.*, *97*, 12,457–12,470.

Sharp, R. V. (1981), Variables rates of late Quaternary strike-slip on the San Jacinto fault zone, southern California, *J. Geophys. Res.*, *86*, 1754–1762.

Shifflett, H., M. G. Gray, R. Grannell, and B. L. Ingram (2002), New evidence on the slip rate, renewal time, and late Holocene surface displacement, southernmost San Andreas fault, Mecca Hills, California, *Bull. Seimol. Soc. Am.*, *92*, 2861–2877.

Sieh, K. (1986), Slip rate across the San Andreas fault and prehistoric earthquakes at Indio, California, *Eos Trans. AGU*, *67*, 1200.

Sieh, K., and R. Jahns (1984), Holocene activity of the San Andreas fault at Wallace Creek, California, *Geol. Soc. Am. Bull*, *95*, 883–896.

Sieh, K. E., and P. L. Williams (1990), Behavior of the southernmost San Andreas fault during the past 300 years, *J. Geophys. Res.*, *95*, 6629–6645.

Small, E. E., R. S. Anderson, J. L. Repka, and R. C. Finkel (1997), Erosion rates of alpine bedrock summit surfaces deduced from in situ ^{10}Be and ^{26}Al, *Earth Planet. Sci. Lett.*, *150*, 413–425.

Spotila, J. A., K. A. Farley, and K. Sieh (1998), Uplift and erosion of the San Bernardino Mountains associated with transpression along the San Andreas fault, California, as constrained by radiogenic helium thermochronometry, *Tectonics*, *17*, 360–378.

Stone, J. O. (2000), Air pressure and cosmogenic isotope production, *J. Geophys. Res.*, *105*, 23,753–23,759.

Tapponnier, P., F. J. Ryerson, J. van der Woerd, A.-S. Mériaux, and C. Lasserre (2001), Long-term slip rates and characteristic slip: Keys to active fault behaviour and earthquake hazard, *C. R. Acad. Sci., Ser. II*, *333*(9), 483–494.

Thomas, A. P., and T. K. Rockwell (1996), A 300– to 550–year history of slip on the Imperial fault near the U.S.-Mexico border: Missing slip at the Imperial fault bottleneck, *J. Geophys. Res.*, *101*, 5987–5998.

van der Woerd, J., F. J. Ryerson, P. Tapponnier, Y. Gaudemer, R. Finkel, A. S. Mériaux, M. Caffee, G. Zhao, and Q. He (1998), Holocene left slip-rate determined by cosmogenic surface dating on the Xidatan segment of the Kunlun Fault (Qinghai, China), *Geology*, *26*, 695–698.

van der Woerd, J., F. J. Ryerson, P. Tapponnier, A. S. Mériaux, Y. Gaudemer, B. Meyer, R. C. Finkel, M. W. Caffee, G. Zhao, and Z. Xu (2000), Uniform slip-rate along the Kunlun Fault: Implications for seismic behaviour and large-scale tectonics, *Geophys. Res. Lett.*, *27*, 2353–2356.

van der Woerd, J., X. Xu, H. Li, P. Tapponnier, B. Meyer, F. J. Ryerson, A. S. Mériaux, and Z. Xu (2001), Rapid active thrusting along the northwestern range front of the Tanghenan Shan (western Gansu, China), *J. Geophys. Res.*, *106*, 30,475–30,504.

van der Woerd, J., P. Tapponnier, F. J. Ryerson, A. S. Mériaux, B. Meyer, Y. Gaudemer, R. C. Finkel, M. W. Caffee, G. Zhao, and Z. Xu (2002), Uniform postglacial slip-rate along the central 600 km of the Kunlun Fault (Tibet), from ^{26}Al, ^{10}Be and ^{14}C dating of riser offsets, and climatic origin of the regional morphology, *Geophys. J. Int.*, *148*, 356–388.

Weldon, R. J., and E. Humphreys (1986), A kinematic model of southern California, *Tectonics*, *5*, 33–48.

Weldon, R. J., and K. E. Sieh (1985), Holocene rate of slip and tentative recurrence interval for large earthquakes on the San Andreas fault, Cajon Pass, southern California, *Geol. Soc. Am. Bull.*, *96*, 793–812.

Wells, S. G., L. D. McFadden, J. Poths, and C. T. Olinger (1995), Cosmogenic ^{3}He surface-exposure dating of stone pavements: Implications for landscape evolution of deserts, *Geology*, *23*, 613–616.

Wesnousky, S. G. (1986), Earthquakes, Quaternary faults, and seismic hazards in California, *J. Geophys. Res.*, *91*, 12,587–12,631.

Williams, P. L. (1989), Aspects of the earthquake geology and seismotectonics of the southern San Andreas and related fault, southern California, Ph.D. thesis, Columbia Univ., New York.

Yule, D., and K. Sieh (2003), Complexities of the San Andreas fault near San Gorgonio Pass: Implications for large earthquakes, *J. Geophys. Res.*, *108*(B11), 2548, doi:10.1029/2001JB000451.

Zehfuss, P. H., P. R. Bierman, A. R. Gillespie, R. M. Burke, and M. W. Caffee (2001), Slip rates on the Fish Spring fault, Owens Valley, California, deduced from cosmogenic ^{10}Be and ^{26}Al and soil development on fan surfaces, *Geol. Soc. Am. Bull.*, *113*, 241–255.

Y. Klinger and P. Tapponnier, Laboratoire de Tectonique, IPG Paris, 4 place Jussieu, F-75252 Paris Cedex 05, France. (klinger@ipgp.jussieu.fr; tapponnier@ipgp.jussieu.fr)

A.-S. Mériaux, School of Geosciences, Institute of Geography, Drummond Street, EH8 9XP, Edinburgh, UK. (meriaux1@mac.com)

F. J. Ryerson, IGPP-LLNL, L202, 7000 East Avenue, Livermore, CA 94550, USA. (ryerson@llnl.gov)

K. Sieh, Division of Geological and Planetary Sciences 100-23, California Institute of Technology, Pasadena, CA 91125, USA. (sieh@gps.caltech.edu)

J. van der Woerd, EOST-IPGS, 5 Rue R. Descartes, F-67000 Strasbourg, France. (jeromev@eost.u-strasbg.fr)

2023 FRIENDS OF THE PLEISTOCENE FIELD TRIP, PACIFIC CELL, SALTON TROUGH

DAY 1: SLIP RATES FOR THE SAN ANDREAS FAULT SYSTEM

STOP 3: San Andreas Fault, Mission Creek strand in the NW Coachella Valley—San Gorgonio Pass regions: fast slip or slow slip?

Intersection of California State Highway 62 and Indian Canyon Drive (dirt road leading northwest from Highway 62)

Discussion leaders (honoring the memory & contributions of J. Douglas Yule)

Jonathan C. Matti, U.S. Geological Survey (emeritus), Geology, Minerals, Energy, and Geophysics Science Center, Tucson, AZ 85719, USA (jmatti@usgs.gov)

Richard V. Heermance, Department of Geological Sciences, California State University Northridge, Northridge, CA 91330-8266, USA (richard.heermance@csun.edu)

Katherine J. Kendrick, U.S. Geological Survey (emeritus), Earthquake Science Center, Pasadena, CA 91106, USA (kjkendrick1499@gmail.com)

Michael E. Oskin, Department of Earth and Planetary Sciences, University of California, Davis, Davis, CA 95616 (meoskin@ucdavis.edu)

BACKGROUND

How does the 20-25 had mm/yr slip rate in Imperial and Coachella Valley (from geologic and geodetic studies) make it through the San Gorgonio Pass "knot"? Here, slip rates are controversial: some workers conclude that principal SAF strands (Mission Creek and Mill Creek faults) have minimal rates during the last 500 ka or longer (Matti and others, 1992; Matti and Morton, 1993; Kendrick and others, 2015, 2022; Matti and Yule, 2020); alternatively, recent workers (Fosdick and Blisniuk, 2018; Balco and others, 2019; Blisniuk and others, 2021) suggest that 20-25 mm/yr rates interpreted for the main San Andreas strand in the Indio Hills region (Mission Creek Fault) persist northwestward to the eastern San Gorgonio Pass portal, thence connecting directly to the modern SAF trace northwest of the Pass (San Bernardino strand). Implicit in the recent work is that the Mission Creek Fault in the northwestern Coachella Valley and San Gorgonio Pass regions remains a major plate boundary susceptible to future throughgoing large-magnitude earthquakes. Alternatively, in the vicinity of the SG Pass "knot", is strain now accommodated mainly by structures other than the major SAF strands? At STOP 3 we explore some of these issues—recognizing that field-trip time does not allow us to visit specific sites 5-10 km northwest where geologic and geomorphic evidence in support of fast-slip or slow-slip paradigms can be evaluated. Hence, STOP 3 represents a "teaser" that hopefully will promote friendly discussion among field-trip participants.

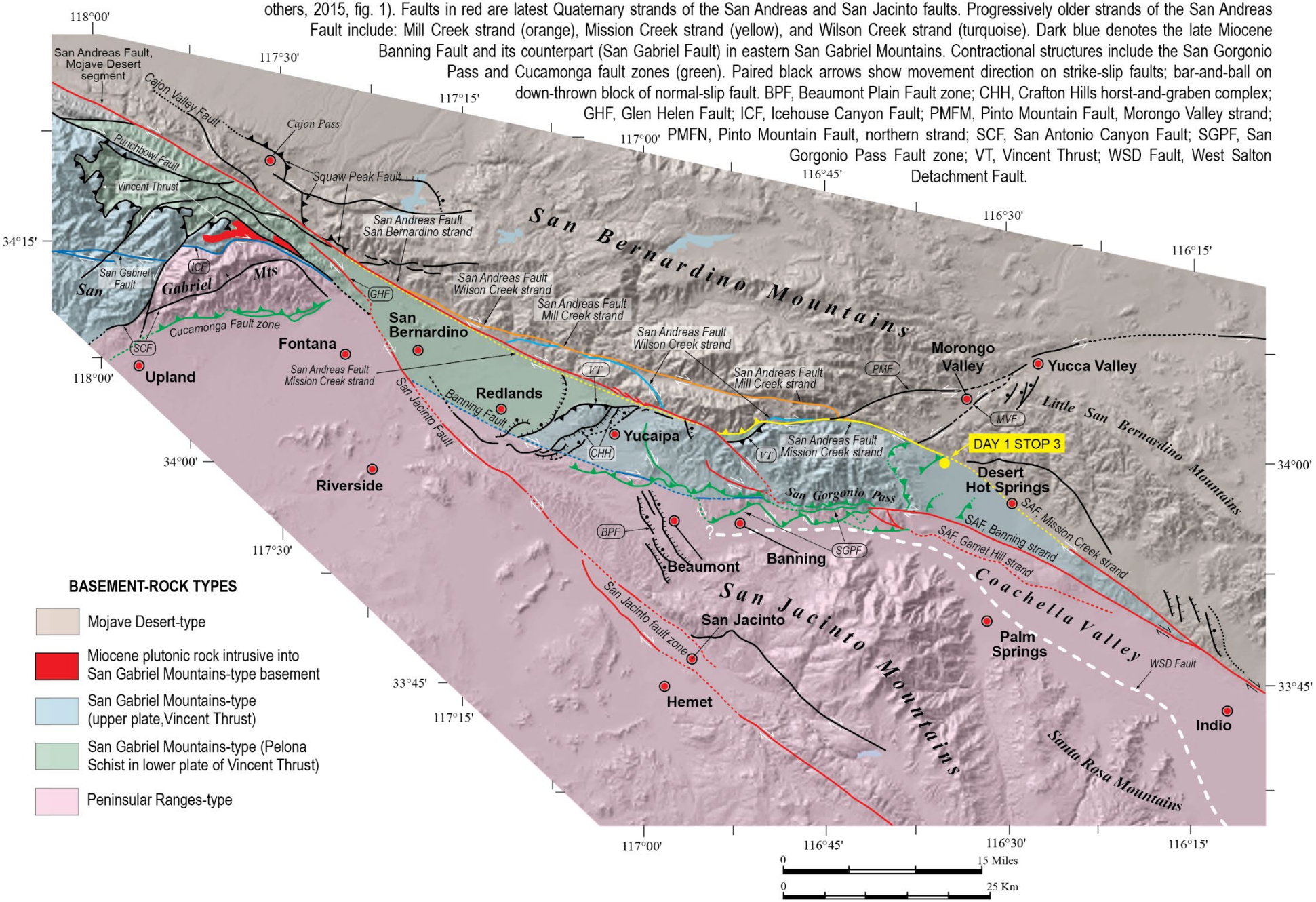
Friends of the Pleistocene DAY 1 STOP 3 location (yellow dot) relative to major faults and regional basement terranes (revised slightly from Kendrick and others, 2015, fig. 1). Faults in red are latest Quaternary strands of the San Andreas and San Jacinto faults. Progressively older strands of the San Andreas Fault include: Mill Creek strand (orange), Mission Creek strand (yellow), and Wilson Creek strand (turquoise). Dark blue denotes the late Miocene Banning Fault and its counterpart (San Gabriel Fault) in eastern San Gabriel Mountains. Contractional structures include the San Gorgonio Pass and Cucamonga fault zones (green). Paired black arrows show movement direction on strike-slip faults; bar-and-ball on down-thrown block of normal-slip fault. BPF, Beaumont Plain Fault zone; CHH, Crafton Hills horst-and-graben complex; GHF, Glen Helen Fault; ICF, Icehouse Canyon Fault; PMFM, Pinto Mountain Fault, Morongo Valley strand; PMFN, Pinto Mountain Fault, northern strand; SCF, San Antonio Canyon Fault; SGPF, San Gorgonio Pass Fault zone; VT, Vincent Thrust; WSD Fault, West Salton Detachment Fault.
118°00'
117°30'
117°15'
117°00'
116°45'
116°30'
116°15'
34°15'
34°00'
33°45'
San Andreas Fault, Mojave Desert segment
Cajon Valley Fault
Cajon Pass
Punchbowl Fault
Vincent Thrust
Squaw Peak Fault
San Andreas Fault San Bernardino strand
San Bernardino Mountains
San Gabriel Fault
ICF
San Gabriel Mts
GHF
San Andreas Fault Wilson Creek strand
San Andreas Fault Mill Creek strand
Cucamonga Fault zone
SCF
Upland
Fontana
San Bernardino
San Andreas Fault Mission Creek strand
San Andreas Fault Wilson Creek strand
VT
PMF
Morongo Valley
Yucca Valley
San Andreas Fault Mill Creek strand
MVF
Little San Bernardino Mountains
Redlands
San Jacinto Fault
Banning Fault
Yucaipa
CHH
VT
San Andreas Fault Mission Creek strand
DAY 1 STOP 3
Desert Hot Springs
Riverside
San Gorgonio Pass
SAF, Mission Creek strand
SAF, Banning strand
SAF, Garnet Hill strand
BPF
SGPF
Beaumont
Banning
Coachella Valley
San Jacinto Mountains
San Jacinto
San Jacinto fault zone
Palm Springs
WSD Fault
Hemet
Indio
Santa Rosa Mountains
BASEMENT-ROCK TYPES
Mojave Desert-type
Miocene plutonic rock intrusive into San Gabriel Mountains-type basement
San Gabriel Mountains-type (upper plate,Vincent Thrust)
San Gabriel Mountains-type (Pelona Schist in lower plate of Vincent Thrust)
Peninsular Ranges-type
0
15 Miles
0
25 Km

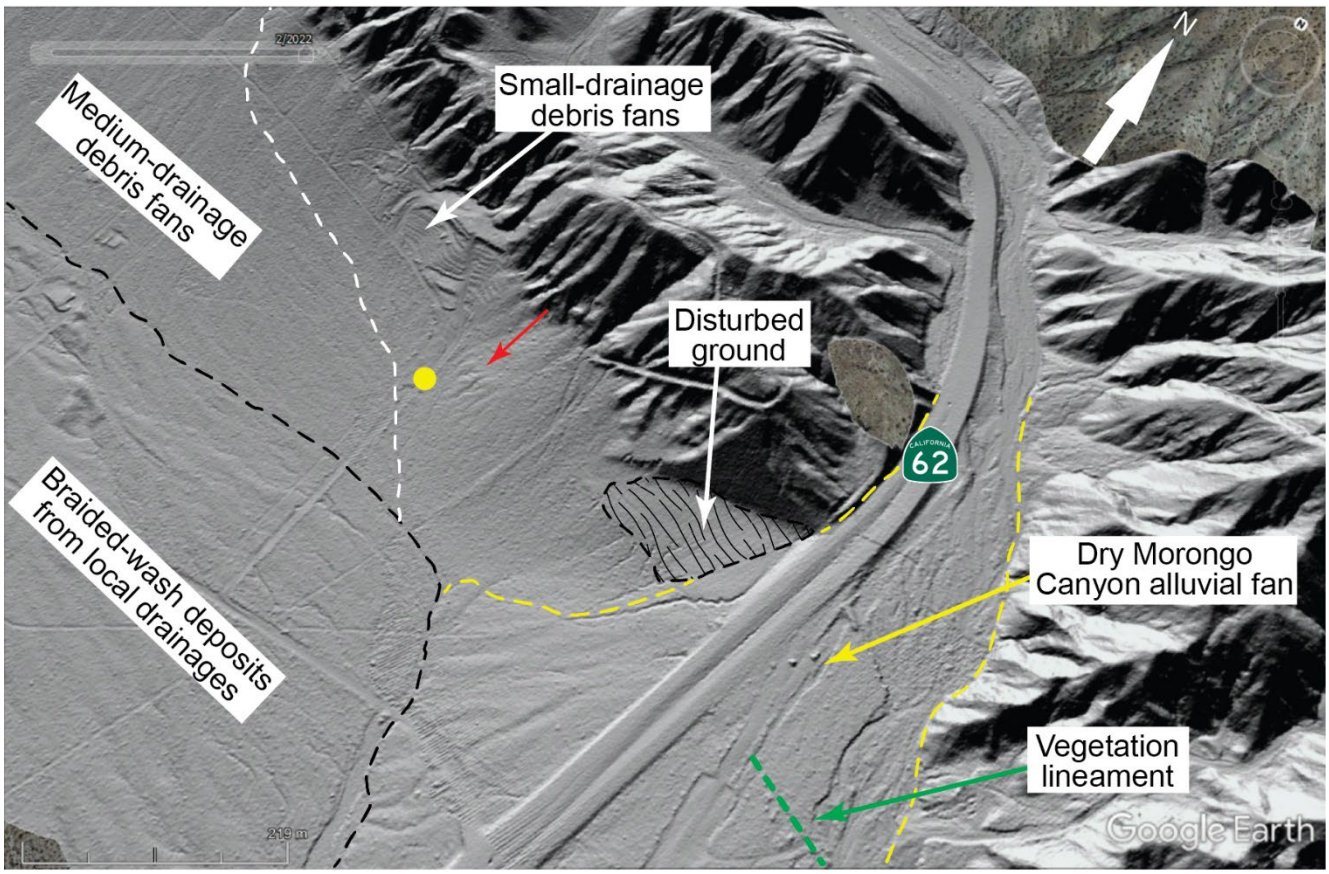

DAY 1 STOP 3 (Jonathan C. Matti, Richard V. Heermance, Katherine J. Kendrick, Michael E. Oskin, discussion leaders)—Bare-earth image from B4 lidar (45° sun angle) processed to remove vegetation (Bevis and others, 2017). Yellow dot indicates stop location. Squiggly black lines = disturbed ground that obscures original geologic and geomorphic features; 1953 Agricultural Stabilization and Conservation Service ASCS AXM imagery reveals that the disturbed area originally consisted of crystalline basement rocks of Mojave Desert-type. Red arrow points to a degraded fault scarp discernable in this image and on 1953-vintage Agricultural Stabilization and Conservation Service aerial photographs (ASCS, 1953, series AXM). The north-facing scarp bounds an area of warped ground underlain by dissected youthful surficial deposits. Younger surficial materials (debris-fan deposits) derived from the adjacent hillslope of crystalline rocks buttress depositionally against the warped landform, and elevation contrasts between the higher- and lower-standing land surfaces are so slight that the scarp is difficult to discern. The buttressing materials are part of a restricted domain of localized debris fans radiating from small gullies and canyons heading into the crystalline mountain front; the white dashed line bounds the toes of the localized debris fans and separates them from debris-fan deposits derived from somewhat larger drainages to the northwest. The black dashed line separates all the mountain-front debris-fan deposits from throughgoing braided-wash deposits sourced to the northwest. Where State Highway 62 enters the mountain front a large alluvial-fan landform debouches from the mouth of Dry Morongo Canyon (referred to by Fosdick and Blisniuk, 2018, as “Morongo Valley Canyon”); yellow dashed lines demarcate the approximate boundary of the fan landform. All surficial materials at STOP 3 appear to be Holocene in age, although no dates here have been published.

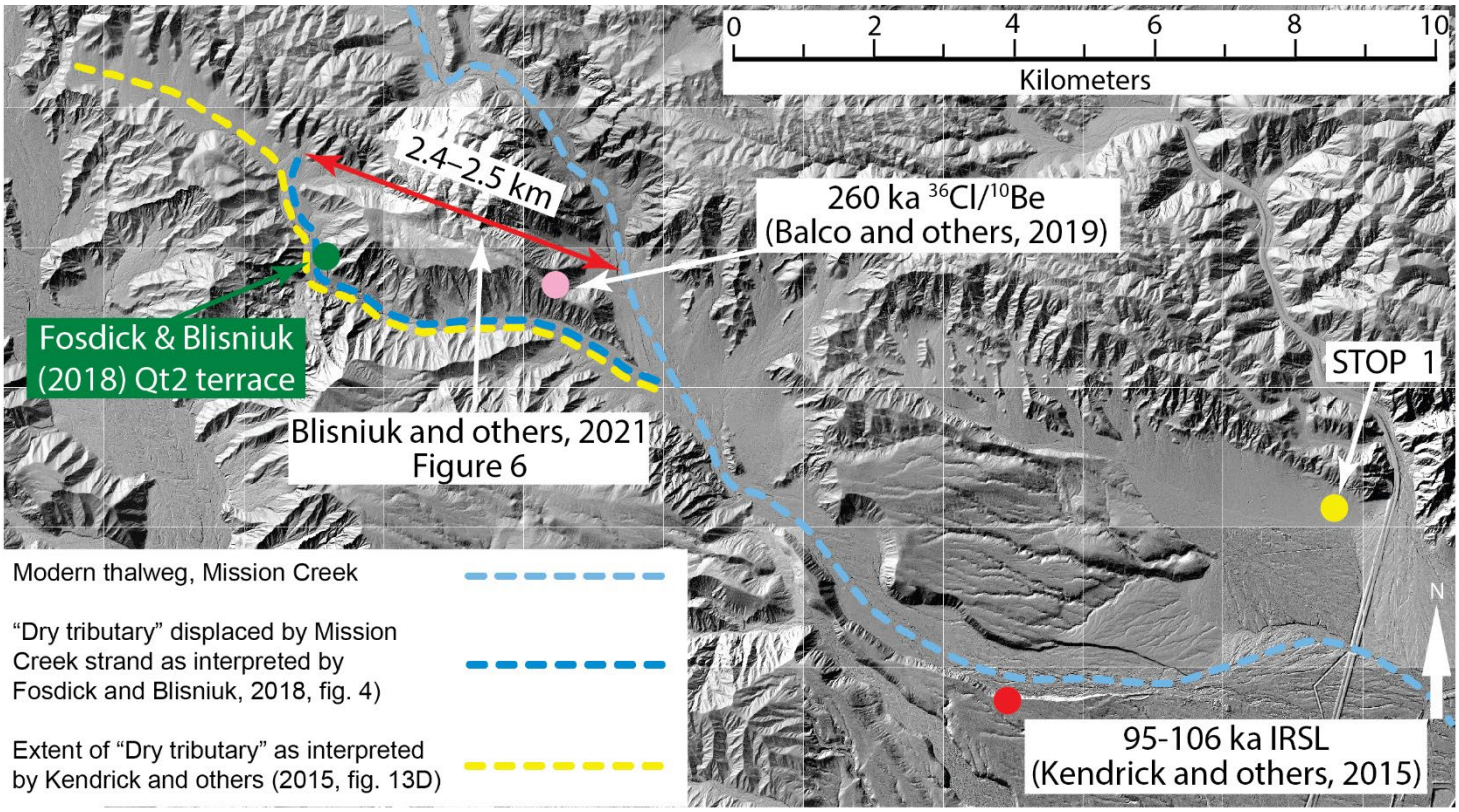

Lidar image of the Mission Creek area, showing geomorphic and geochronologic information pertaining to the age and displacement history for the Mission Creek strand of the San Andreas Fault as interpreted by Fosdick and Blisniuk (2018), Balco and others (2019), and Blisniuk and others (2021). Lidar source: U.S. Geological Survey, 2017).

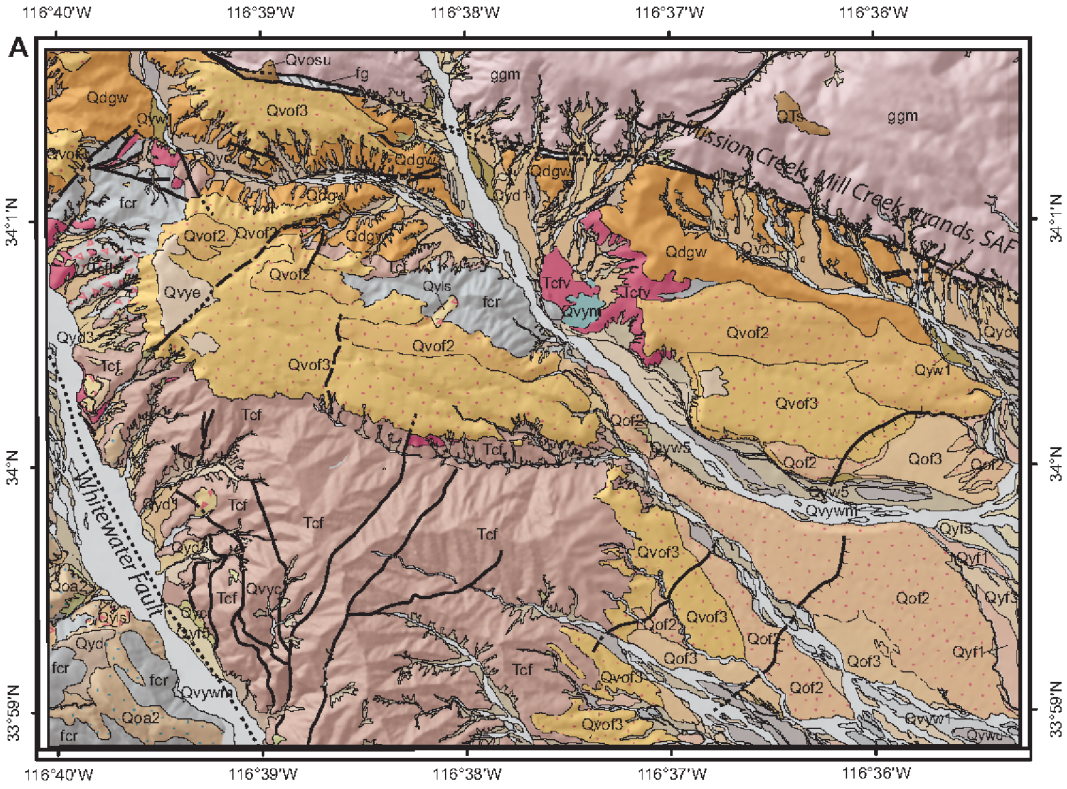

Qvywm	Very young wash deposits, modern (latest Holocene)	Qyls	Young landslide deposits (Holocene and latest Pleistocene)	Qdgw	Deformed gravels of Whitewater River (early Pleistocene)
Qvyw1	Very young wash deposits, unit 1 (latest Holocene)	Qoa2	Old axial-valley deposits, unit 2 (late Pleistocene)	QTs	Sedimentary rocks, undifferentiated (Quaternary and Tertiary)
Qvyc	Very young colluvial deposits (latest Holocene)	Qof3	Old alluvial-fan deposits, unit 3 (late Pleistocene)	Tcf	Coachella Fanglomerate (Miocene)
Qvye	Very young eolian deposits (latest Holocene)	Qof2	Old alluvial-fan deposits, unit 2 (late and middle Pleistocene)	Tcfv	Coachella Fanglomerate, volcanic unit
Qvym	Very young marsh deposits (latest Holocene)	Qvof3	Very old alluvial-fan deposits, unit 3 (middle Pleistocene)	Tcfls	Coachella Fanglomerate, landslide unit
Qyc	Young colluvial deposits, undifferentiated (Holocene and latest Pleistocene)	Qvof2	Very old alluvial-fan deposits, unit 2 (middle Pleistocene)	fcr	Foliated crystalline rocks of San Gabriel Mountains-type (Cretaceous and older)
Qywu	Young alluvial-wash deposits, undifferentiated (Holocene and latest Pleistocene)	Qvosu	Very old surficial deposits, undifferentiated (middle Pleistocene)	ggm	Granitic and gneissic rock of Mojave Desert-type (Cretaceous and older)
Qyw5	Young alluvial-wash deposits, unit 5 (late Holocene)			fg	Crushed and sheared rock in fault zone
Qyw1	Young alluvial-wash deposits, unit 1 (early Holocene and latest Pleistocene)				
Qyf5	Young alluvial-fan deposits, unit 5 (late Holocene)				
Qyf3	Young alluvial-fan deposits, unit 3 (middle Holocene)				
Qyf1	Young alluvial-fan deposits, unit 1 (early Holocene and latest Pleistocene)				
Qyd	Young debris-fan deposits, undifferentiated (Holocene and latest Pleistocene)				
Qyd3	Young debris-fan deposits, unit 3 (middle Holocene)				
Qyd1	Young debris-fan deposits, unit 1 (early Holocene and latest Pleistocene)				

Contact—Solid where meets map-accuracy standard; dashed where may not meet map-accuracy standard; dotted where concealed

Fault—Solid where meets map-accuracy standard; dashed where may not meet map-accuracy standard. Dotted where concealed by mapped covering unit. Hachures indicate scarp, with hachures on down-dropped block.

Geologic map of the Mission Creek Preserve of the Wildlands Conservancy (figure 7A of Kendrick and others, 2015). Note that Pleistocene stratigraphic units mapped here as various subunits of Qo and Qvo are shown as “Cabezon Fanglomerate” by Fosdick and Blisniuk (2018; Balco and others, 2019; Blisniuk and others, 2021). Application of the “Cabezon” nomenclature follows Allen (1957) and Proctor (1968), but we doubt correlation of the Mission Creek Pleistocene deposits with the “type” Cabezon Fanglomerate in San Gorgonio Pass because the unit there occupies a different stratigraphic position than deposits mapped as “Cabezon Fanglomerate” in the Mission Creek drainage, and by correlation throughout the San Gorgonio Pass region most of the formation can be shown to have reversed magnetic polarity (Matti and others, 2015).

Yule, D., Matti, J., Kendrick, K., and Heermance, R., 2019, Evidence for inactivity since ~100 ka on the northern route of the San Andreas fault , southern California: Geological Society of America Cordilleran Section Meeting, Paper 16-8 https://gsa.confex.com/gsa/2019CD/meetingapp.cgi/Paper/329441.

From San Bernardino to Indio, CA, the San Andreas fault (SAF) follows two distinct routes. A northern route (NR) follows the Mill Creek and Mission Creek strands and a southern route (SR) follows the San Bernardino, Banning, and Garnet Hill strands, and San Gorgonio Pass (SGP) fault zone. We think that reconfiguration of the SAF zone in the SGP region at ~100 ka shifted motion from the NR to the SR. Surprisingly, the complex SR has experienced low slip rates and relatively infrequent paleoearthquakes, particularly in SGP. SR complexity and low slip rates in part led Fosdick & Blisniuk (F&B) (2018) to propose that the NR has generated 2.5 km of dextral slip since ~100 ka, yielding a slip rate of 20-30 mm/yr. Their offset and its timing are based on correlating a small strath terrace (Qt2) with an expansive fill terrace (Qf2) 5-7 km away that has a published OSL age of ~100 ka, then using those deposits to define a paleodrainage that has been offset along the NR since that 100 ka—thereby showing that the NR remains a major active plate boundary. We question this proposal using four arguments that support little, if any, slip on the NR since ~100 ka: (1) The Qt2/Qf2 correlation is implausible because of (a) differences in soil development, elevation above modern channel, and genetic terrace styles (strath vs fill), (b) the lag on Qt2 consists of material cannibalized from older alluvial deposits into which the strath was carved, and (c) a profile connecting the Qt2-Qf2 terraces defines a gentle gradient much different from steeper profiles on Pleistocene fan remnants in the area. (2) The NR does not deform Holocene units for most of its route (Matti et al., this session). In contrast there is abundant evidence for Holocene deformation along the SR over the same distance. (3) Stream deflections of ~50 m in >>60 ka fill proposed on the NR near Mission Creek (F&B, 2018) equate to slip rates of <<1 mm/yr. (4) Dextral motion of ~6 mm/yr on the SR through SGP (Heermance & Yule, 2017) matches estimates from geodetic models for SAF motion here. Thus, there is no reason to require significant motion on the NR. Though the NR once carried ~20 mm/yr of SAF motion, it shut down following the latest SAF reorganization at ~100 ka. This relatively recent event created the geometrically complex SR and its traits characteristic of a poorly organized, youthful fault system.

Geological Society of America Abstracts with Programs. Vol. 51, No. 4, ISSN 0016-7592
doi: 10.1130/abs/2019CD-329441

© Copyright 2019 The Geological Society of America (GSA), all rights reserved.

Matti, J.C., Kendrick, K.J., Yule, J.D., and Heermance, R.K., 2019, The Mission Creek Fault in the San Gorgonio Pass region—A long-abandoned strand of the San Andreas Fault, or a major player in the latest Quaternary San Andreas strain budget? Geological Society of America Cordilleran Section Meeting, Paper 329432 https://gsa.confex.com/gsa/2019CD/meetingapp.cgi/Paper/329432.

The San Andreas Fault (SAF) zone in the San Gorgonio Pass (SGP) region is geologically and geomorphically more complex than perhaps anywhere else in southern California. Here, the zone consists of at least six separate strands that, acting together, record the fault's entire movement history since inception at ~6 Ma. In addition, interaction between the SAF and associated sinistral, contractional, and extensional fault sets has significantly impacted the geometry and slip history of individual SAF strands—especially the Mission Creek strand (MCS), which generated most of the total SAF slip during Pliocene and Pleistocene time. Many workers view the MCS in SGP as an abandoned structure that has produced no dextral slip for >0.5 Ma. This contrasts with the MCS in the Indio Hills, where the fault has generated 12-22 mm/yr of slip during the late Pleistocene. Slip-rate contrasts between SGP and the Indio Hills suggest that—between the two regions—latest Quaternary slip on the MCS does not project NW through SGP but instead must step left (and/or right) from the MCS onto other components of the SAF system. Recently, Fosdick & Blisniuk (F&B) (2018) challenged this paradigm, based on work in the Mission Creek area of NE SGP. They conclude that the MCS here has generated ~20-30 mm/yr of dextral slip over the last 100 ka. A companion abstract (Yule et al., this session) explores the basis for this proposal, and presents detailed evidence refuting the idea that the MCS in SGP has generated significant dextral slip over the last 100 ka. We also refute F&B (2018) by citing the MCS's geologic character between the Indio Hills and San Gorgonio River in northern SGP: (1) Throughout much of this 45-km extent, the MCS trace is concealed by undisrupted Holocene surficial deposits. (2) Fault scarps and other tectonogeomorphic features occur locally along the strand's extent, but these are discontinuous and are not convincingly youthful. (3) We see no evidence for young Quaternary dextral slip on the MCS in the critical footprint between Mission Creek and the headwaters of San Gorgonio River. (4) Some workers propose that—in NE SGP—20-30 mm/yr of slip steps abruptly south off the MCS and onto faults in crystalline rocks that connect directly to the SAF San Bernardino strand to the NW. We see no evidence for this, but we do see slip stepping left well SE of SGP.

Geological Society of America Abstracts with Programs. Vol. 51, No. 4, ISSN 0016-7592
doi: 10.1130/abs/2019CD-329432

© Copyright 2019 The Geological Society of America (GSA), all rights reserved.

Matti, J.C., and Yule, J.D., 2020, Does a “structural knot” in the Quaternary San Andreas Fault exist in San Gorgonio Pass? Traditional and recent views provide conflicting answers: Geological Society of America Cordilleran Section Meeting, Paper 17-1 https://gsa.confex.com/gsa/2020CD/meetingapp.cgi/Paper/347317.

Abstract

Traditional geologic models for Quaternary (Q) strain within the southern San Andreas Fault (SAF) zone invoke a “structural knot” centered on San Gorgonio Pass (SGP). The “knot” concept grew out of Allen’s (1957) recognition that Q thrusting now predominates in SGP: older dextral-slip faults have been disrupted, and the “modern” SAF trace is disguised. We now know that several SAF strands occur in the SGP region and have evolved sequentially (“switched on and off”) throughout the zone’s ~6-Ma lifespan. Later workers also have shown that late Q SAF motion carries through SGP in complex but understandable ways *via* oblique thrust and tear faults of the SGP Fault Zone (SGPFZ). Oblique convergence in SGP also is supported by the first-order observation that its mountainous landscape rises abruptly above adjacent lowlands. These factors all led to a traditional time-space model where the SAF system at SGP is a left-oblique regime within which Q slip steps progressively from the Mission Creek strand (MCS, on the NE) to the Banning and Garnet Hill strands (to the SW), accompanied by the following constraints: (1) in mid-Pleistocene (PL) time the MCS in SGP was abandoned, leading to mid-PL contraction within the SGPFZ and uplift of high-standing parts of the SGP landscape; (2) in mid-PL time the Mill Creek strand bypassed this older “knot” in the SAF, but ultimately even it was abandoned by the SAF; (3) today, the late Q framework of SGP reflects left-oblique SAF slip trying to work through SGP in order to “connect” young SAF strands to the NW and SE. Recent reports by Fosdick and Blisniuk, 2018 (https://doi.org/10.1038/s41598-018-30622-3) and Balco et al., 2019 (https://doi.org/10.5194/gchron-1-1-2019) challenge this paradigm. These reports assert that—over the last ~100 ka years—20-30 mm/yr of SAF slip projects through SGP on the MCS and on fault structures associated with the MCS. To us, this poses a pressing question: is there any need for a late Q San Gorgonio Pass “knot” in the SAF? We answer “yes”: (1) interaction among ALL geologic structures in the SGP region is consistent with a long-lived Q knot; (2) in SGP we see no evidence for youthful dextral offset on the MCS itself; (3) in SGP we see no evidence for dextral-slip faults SW of the MCS (e.g., Waco et al., 2017, https://files.scec.org/s3fs-public/SCEC2017Proceedings.pdf).

Geological Society of America Abstracts with Programs. Vol. 52, No. 4, 2020
doi: 10.1130/abs/2020CD-347317

© Copyright 2020 The Geological Society of America (GSA), all rights reserved.

Heermance, R., Matti, J.C., and Kendrick, K.J., 2023, Holocene slip rates along the San Andreas Fault through the San Gorgonio Pass: Geological Society of America Cordilleran Section Meeting, Paper 15-9, https://gsa.confex.com/gsa/2023CD/meetingapp.cgi/Paper/387451.

Abstract

As it traverses NW Coachella Valley the San Andreas fault (SAF) splits into multiple, divergent strands that enter the “enigmatic” San Gorgonio Pass (SGP). Large, historical earthquakes have not ruptured through SGP, thus creating debate about the rupture length and location of a future event on the southern SAF. Relatively continuous faults have been mapped in two zones through the SGP: a *southern-route* (SR) involving the Banning strand, Garnet Hill strand, and San Gorgonio Pass Fault zones and a *northern route* (NR) involving the Mission Creek and Mill Creek strands and/or associated structures. Any large earthquake on the southern SAF through SGP must follow one of these two routes, and only the southern route shows convincing geologic and geomorphic evidence for repeated throughgoing earthquake ruptures during the Holocene. Only two sites provide published Holocene slip-rates within SGP: along the Banning strand and the San Gorgonio Pass fault zone, both along the SR. An oblique slip rate of 5.7 (+2.5, -1.5) mm/yr was calculated across fault scarps within Millard Canyon in the central SGP, where fan terraces were dated (10Be exposure) as Holocene. At the eastern edge of SGP the Banning strand has a comparable slip rate of 3.9-4.9 mm/yr from an offset mid-Holocene fan surface. Together, these data suggest that the SR is active but accommodates <50% of slip along the SAF system. In contrast, there are no published Holocene slip rate sites along the NR through SGP. Notably, fault scarps and dextral stream offsets are sparse, discontinuous and developed in alluvium of undocumented age; dextral stream offsets developed on one uplifted Pleistocene terrace NW of Mission Creek cannot convincingly be attributed to Holocene slip. At Dry Tributary, a 45 m-deep canyon reveals a strath surface beneath 25 m sedimentary fill that buries the Mission Creek strand of the SAF. Although the NR undoubtedly was active during the Pleistocene, during the Holocene it has shut down and slip has been transferred to the southern route or is accommodated by diffuse off-fault deformation.

Geological Society of America Abstracts with Programs. Vol. 55, No. 4, 2023
doi: 10.1130/abs/2023CD-387451

© Copyright 2023 The Geological Society of America (GSA), all rights reserved.

Matti, J.C., Kendrick, K.J., and Powell, R.E., 2023, Tectonic evolution at the intersection of the San Andreas, Pinto Mountain, and Morongo Valley Fault zones, southern California: implications for Quaternary San Andreas Fault slip rates: Geological Society of America Cordilleran Section Meeting, Paper 15-7, https://gsa.confex.com/gsa/2023CD/meetingapp.cgi/Paper/387523.

Abstract

In the San Gorgonio Pass (SGP) region, dextral slip rates for northern strands of the San Andreas Fault Zone (SAFZ) are hotly debated. Some workers maintain that dextral slip on the Mission Creek strand (MiCS) of the northern route (NR) slowed at ~1.5 Ma as a "structural knot" evolved in the SAFZ, with slip approaching zero before ~500 ka (Matti and Morton, 1993); in SGP the MiCS has an E-W bend that formed a 9-15 km left step in the Pleistocene SAFZ. At ~500 ka, slip initiated on the Mill Creek strand (MCS) and produced ~8 km of displacement before ~100 ka, when slip ended (Kendrick and others, 2015). In contrast, recent workers contend that the SAF NR has 20-30 mm/yr of slip during the last 100 ka and longer (e.g., Blisniuk and others, 2021). Here, we argue that interaction between the SAF NR and intersecting sinistral faults (Pinto Mountain Fault [PMF] and Morongo Valley Fault [MVF]) allows only minimal slip on the SAF NR over the last 1.5 Ma. Specifically: when slip on the MCS is reconstructed, the MiCS left bend aligns with the MVF—suggesting that sinistral slip on the latter is coeval with and caused the MiCS left bend (Kendrick and others, 2022). We use these relations to propose the following tectonic scenario: (1) At ~1.5 Ma, dextral slip on the MiCS gradually was impeded by sinistral slip on the MVF. (2) During this period, the MiCS was deformed into its E-trending bend. (3) The MVF thus is as a major strand of the PMFZ. (4) The PMFZ is widely viewed as the northern boundary for clockwise-rotating blocks of the Eastern Transverse Ranges (ETR); we see the MVF as part of that boundary during middle Pleistocene time. (5) Following interaction between the MVF and the MiCS, dextral slip punched through the "structural knot" in the SAFZ, allowing the MCS to displace the MiCS left bend NW to its current location. (6) In late Pleistocene time, sinistral slip on the PMF truncated and displaced an abandoned MCS by ~1.2 km. (7) Geometric relations and sequencing of major dextral and sinistral faults at the NE portal to SGP suggest that they have interacted together for the last ~1.5 Ma to produce the current geologic framework. *Implication*: The original spatial arrangement of these faults has been disrupted only by 8 km of dextral slip on the MCS, requiring that the SAF NR has not produced significant dextral slip in middle and late Quaternary time.

Geological Society of America Abstracts with Programs. Vol. 55, No. 4, 2023
doi: 10.1130/abs/2023CD-387523

© Copyright 2023 The Geological Society of America (GSA), all rights reserved.

RERENCES FOR DAY 1, STOP 3

Allen, C.R., 1957, San Andreas fault zone in San Gorgonio Pass, southern California: Geological Society of America Bulletin, v. 68, p. 319-350.

Balco, G., Blisniuk, K., and Hidy, A., 2019, Chlorine-36/beryllium-10 burial dating of alluvial fan sediments associated with the Mission Creek strand of the San Andreas Fault system, California, USA: Geochronology, v. 1, 16 p. accessed at https://doi.org/10.5194/gchron-1-1-2019.

Bevis, M., Hudnut, K.W., Sanchez, R., Toth, C.K., Grejner-Brzezinska, D., Kendrick, E., Caccamise, D., Raleigh, D., Zhou, H., Shan, S., Shindle, W., Yong, A., Harvey, J., Borsa, A.A., Ayoub, F., Shrestha, R.L., Carter, B., Sartori, M., Phillips, D.A., Coloma, F., and S. B. DeLong, S.B., 2017, Classified point cloud and gridded elevation data from the 2005 B4 Lidar Project, southern California, USA (data accessed at https://opentopography.org/news/reprocessed-version-b4-lidar-southern-san-andreas-and-san-jacinto-faults-dataset-released).

Blisniuk, K., Scharer, K., Sharp, W.D., Burgmann, R., Amos, C., and Rymer, M., 2021, A revised position for the primary strand of the Pleistocene-Holocene San Andreas fault in southern California: Science Advances, v. 7, no. 13, accessed at https://advances.sciencemag.org/content/7/13/eaaz5691.

Fosdick, J.C., and Blisniuk, K.D., 2018, Sedimentary signals of recent faulting along an old strand of the San Andreas Fault, USA: Scientific Reports 8:12132DOI:10.1038/s41598-018-30622-3, accessed at https://doi.org/10.1038/s41598-018-30622-3.

Heermance, R., Matti, J.C., and Kendrick, K.J., 2023, Holocene slip rates along the San Andreas Fault through the San Gorgonio Pass: Geological Society of America Cordilleran Section Meeting, Paper 15-9, https://gsa.confex.com/gsa/2023CD/meetingapp.cgi/Paper/387451.

Kendrick, K.J., Matti, J.C., and Mahan, S.A., 2015, Late Quaternary slip history of the Mill Creek strand of the San Andreas fault in San Gorgonio Pass, southern California: The role of a subsidiary left-lateral fault in strand switching: Geological Society of America Bulletin, v. 127, p. 825-849, accessed at https://doi.org/10.1130/B31101.1.

Kendrick, K.J., Matti, J.C., and Barth, N.C., 2022, Geologic and geomorphic evidence for multi-phase history of strands of the San Andreas fault through the San Gorgonio Pass structural knot, southern California: Geosphere, v. 18, no. X, p. 1–34, accessed at https://doi.org/10.1130/GES02424.1.

Matti, J.C., and Yule, J.D., 2020, Does a “structural knot” in the Quaternary San Andreas Fault exist in San Gorgonio Pass? Traditional and recent views provide conflicting answers: Geological Society of America Cordilleran Section Meeting, Paper 17-1 https://gsa.confex.com/gsa/2020CD/meetingapp.cgi/Paper/347317.

Matti, J.C., Cox, B.F., and Iverson, S.R., 1983, Mineral resource potential map of the Raywood Flat Roadless Area, San Bernardino and Riverside Counties, California: U.S. Geological Survey Miscellaneous Field Studies Map MF–1563–A, scale 1:62,500, accessible at https://pubs.er.usgs.gov/publication/mf1563A

Matti, J.C., Cox, B.F., Obi, C.M., Powell, R.E., Hinkle, M.E., Griscom, A., and McHugh, E.L., 1982, Mineral resource potential map of the Whitewater Wilderness Study Area, Riverside and

San Bernardino Counties, California: U.S. Geological Survey Miscellaneous Field Studies Map MF–1478, scale 1:24,000, accessible at https://pubs.er.usgs.gov/publication/mf1478A

Matti, J.C., Kendrick, K.J., and Powell, R.E., 2023, Tectonic evolution at the intersection of the San Andreas, Pinto Mountain, and Morongo Valley Fault zones, southern California: implications for Quaternary San Andreas Fault slip rates: Geological Society of America Cordilleran Section Meeting, Paper 15-7, https://gsa.confex.com/gsa/2023CD/meetingapp.cgi/Paper/387523.

Matti, J.C., Morton, D.M. and Cox, B.F., 1992, The San Andreas fault system in the vicinity of the central Transverse Ranges province, southern California: U.S. Geological Survey Open-File Report 92-354, 40 p., scale 1:250,000. https://pubs.er.usgs.gov/publication/ofr92354. NOTE: Oversize plates 1 and 2 can be downloaded at the URL for this citation.

Matti, J.C., Morton, D.M., and Langenheim, V.E., 2015, Geologic and geophysical maps of the El Casco 7.5' quadrangle, Riverside County, southern California, with accompanying geologic-map database: U.S. Geological Survey Open-File Report 2010–1274, 152 p., 3 sheets, scale 1:24,000, accessed at https://pubs.er.usgs.gov/publication/ofr20101274.

Matti, J.C., Kendrick, K.J., Yule, J.D., and Heermance, R.K., 2019, The Mission Creek Fault in the San Gorgonio Pass region—A long-abandoned strand of the San Andreas Fault, or a major player in the latest Quaternary San Andreas strain budget? Geological Society of America Cordilleran Section Meeting, Paper 329432 https://gsa.confex.com/gsa/2019CD/meetingapp.cgi/Paper/329432.

Proctor, R.J., 1968, Geology of the Desert Hot Springs-Upper Coachella Valley, Salton Sea, and vicinity: California Geological Survey [formerly California Division of Mines and Geology], Special Report 94, 50 p.

Rasmussen, G.S., and Reeder, W.A., 1986, What happens to the real San Andreas fault at Cottonwood Canyon, San Gorgonio Pass, California? *in* Kooser, M.A., and Reynolds, R.E., eds., Geology around the margins of the eastern San Bernardino Mountains: Redlands, California, Publications of the Inland Geological Society, v. 1, p. 57-62.

Reeder, W.A. and Rasmussen, G.S., 1986, Character and Holocene activity of the Mission Creek fault in the vicinity of Desert Hot Springs, Riverside County, California, *in* Kooser, M.A., and Reynolds, R.E., eds., Geology around the margins of the eastern San Bernardino Mountains: Redlands, California, Publications of the Inland Geological Society, v. 1, p. 71-73.

U.S. Geological Survey, 2017, 3D Elevation Program Lidar Point Cloud Project CA_SE_Fault_Zone_Lidar_2017 (published 20180803), accessed at https://apps.nationalmap.gov/lidar-explorer/#/.

Yule, D., Matti, J., Kendrick, K., and Heermance, R., 2019, Evidence for inactivity since ~100 ka on the northern route of the San Andreas fault , southern California: Geological Society of America Cordilleran Section Meeting, Paper 16-8 https://gsa.confex.com/gsa/2019CD/meetingapp.cgi/Paper/329441.

Matti, J.C., Morton, D.M. and Cox, B.F., 1992, The San Andreas fault system in the vicinity of the central Transverse Ranges province, southern California: U.S. Geological Survey Open-File Report 92-354, 40 p., scale 1:250,000. https://pubs.er.usgs.gov/publication/ofr92354. NOTE: Oversize plates 1 and 2 can be downloaded at the URL in this citation.

DEPARTMENT OF THE INTERIOR

U.S. GEOLOGICAL SURVEY

THE SAN ANDREAS FAULT SYSTEM IN THE VICINITY OF THE CENTRAL TRANSVERSE RANGES PROVINCE, SOUTHERN CALIFORNIA

By

Jonathan C. Matti[1], Douglas M. Morton[2], and Brett F. Cox[3]

OPEN-FILE REPORT 92-354

This report is preliminary and has not been reviewed for conformity with U.S. Geological Survey editorial standards or with the North American Stratigraphic Code. Any use of trade, product, or firm names is for descriptive purposes only nd does not imply endorsement by the U.S. Government.

[1]U.S. Geological Survey
Department of Geosciences
Gould-Simpson Building
University of Arizona
Tucson, Arizona 85721

[2]U.S. Geological Survey
Department of Earth Sciences
University of California
Riverside, California 92521

[3]U.S. Geological Survey
345 Middlefield Road, MS 975
Menlo Park, California 94025

1992

SUMMARY

The vicinity of the central Transverse Ranges is a structurally complex region that is traversed by several major fault zones. The Banning, San Jacinto, and San Andreas faults are right-lateral strike-slip faults of the San Andreas transform system. The San Gorgonio Pass and Cucamonga fault zones are compressional thrust- and reverse-fault complexes. The Crafton Hills horst-and-graben complex, the Tokay Hill and Peters faults in the Cajon Pass region, and the Beaumont Plain fault complex are extensional fault zones. The compressional and extensional fault complexes owe their origin and kinematics to complications within the San Andreas transform fault system.

The Banning fault has had a complex history that includes both left- and right-lateral displacements. During middle Miocene time the ancestral Banning fault zone may have generated left-lateral displacements that juxtaposed the Peninsular Ranges block against the San Gabriel Mountains block along a regionally extensive fault system that included the Malibu Coast-Santa Monica fault. During late Miocene time the Banning fault was incorporated into the San Andreas transform system and generated 16 to 25 km of right-lateral displacement; during this period the Banning probably was the eastward continuation of the San Gabriel fault in the San Gabriel Mountains. The Banning fault was abandoned by the San Andreas system in earliest Pliocene time. In San Gorgonio Pass the Banning fault has been obscured and reactivated by low-angle Quaternary faulting of the San Gorgonio Pass fault zone. In the Coachella Valley the Banning fault has been reactivated by Quaternary strike-slip faulting related to the San Andreas fault, and has generated about 3 km of right-lateral displacement that largely has been absorbed by convergence within the San Gorgonio Pass fault zone.

The San Andreas fault in the vicinity of the central Transverse Ranges consists of three segments--the Mojave Desert, Coachella Valley, and San Bernardino Mountains segments. The complex San Bernardino Mountains segment consists of multiple strands that had sequential movement histories. To the northwest and southeast these strands merge to form the simpler Mojave Desert and Coachella Valley segments.

The San Bernardino Mountains segment of the San Andreas fault consists of three paleotectonic strands (the Wilson Creek, Mission Creek, and Mill Creek faults) and a neotectonic strand (the San Bernardino strand). Together, these four strands have generated about 160 km of right-lateral displacement and record the total history of the San Andreas fault (*sensu stricto*) since its inception 4 or 5 m.y. ago. The Wilson Creek and Mission Creek faults together generated about 130 km of right-lateral displacement during Pliocene and Pleistocene time. The Wilson Creek fault, the older strand, generated about 40 km of displacement before it was deformed into a sinuous trace in the vicinity of the San Bernardino Mountains; this displacement estimate is based on our proposal that the Wilson Creek fault is the offset continuation of the Punchbowl fault in the San Gabriel Mountains--a structure that has about 40 km of right slip documented by other workers. In Pliocene time the Wilson Creek strand was succeeded by the Mission Creek strand, which generated the balance of the 130-km displacement before it was deformed and abandoned in late Pleistocene time. The Mill Creek strand subsequently evolved inboard (east) of the locked-up Mission Creek fault and generated about 8 km of right-slip during late Pleistocene time. Ultimately, the Mill Creek strand was abandoned as right-lateral activity shifted to the southwest front of the San Bernardino Mountains, where the neotectonic San Bernardino strand developed. The San Bernardino strand is aligned with the Coachella Valley segment of the Banning fault, but these two neotectonic right-lateral faults are separated by the San Gorgonio Pass fault zone and it is not clear that they ever formed a single throughgoing trace between the Coachella and San Bernardino valleys.

Two compressional fault complexes and an extensional fault system have evolved in the vicinity of the south-central Transverse Ranges in association with the San Andreas fault. The San Gorgonio Pass and Cucamonga fault zones consist of late Quaternary thrust and reverse faults that have evolved where neotectonic strands of the San Andreas and San Jacinto faults interact with the southeastern San Bernardino Mountains and San Gabriel Mountains, respectively. Northwest of the San Gorgonio Pass fault zone, crustal extension in the San Bernardino valley and vicinity has created normal dip-slip fault complexes like the Beaumont Plain fault zone, the Crafton Hills horst-and-graben complex, and the Tokay Hill and Peters faults in the Cajon Pass region.

The Quaternary tectonic framework of the central Transverse Ranges can be viewed as a regionally integrated response to an evolving left step in the San Andreas transform-fault system. The left step was initiated during Pleistocene time, and was accompanied by left-slip on the Pinto Mountain fault that gradually projected the San Bernardino Mountains westward across the path of the Mission Creek strand of the San Andreas fault and offset the Coachella Valley and Mojave Desert segments of the fault. The modern San Andreas fault has adjusted to this inherited left step, and various neotectonic fault complexes in the vicinity of the central Transverse Ranges have evolved in response to this adjustment. During latest Quaternary time, right-slip on the San Andreas fault has stepped left from the Coachella Valley segment to the Banning fault and thence into San Gorgonio Pass, where right-slip is absorbed by convergence within the San Gorgonio Pass fault zone. Some slip may step farther west onto the San Jacinto fault, where accelerated right-slip may have contributed to subsidence of the San Jacinto graben. Ultimately, slip steps back from the San Jacinto fault to the modern San Andreas fault, giving rise to the San Bernardino strand by reactivation of the Mission Creek fault. This right step has created a right-lateral shear couple and extensional strain field in the greater San Bernardino valley, with extension giving rise to normal dip-slip faults like those in the Crafton Hills horst-and-graben complex and the Tokay Hill and Peters faults.

INTRODUCTION

In this report we describe the tectonic framework and geologic history of faults in the vicinity of the central Transverse Ranges, southern California (fig. 1). The fault zones discussed include right-lateral faults of the San Andreas transform system (including the San Andreas fault itself), associated reverse and thrust faults in the vicinity of San Gorgonio Pass and the southeastern San Gabriel Mountains, and associated normal faults that occur between the San Jacinto and San Andreas faults in the vicinity of the San

Bernardino valley. The San Andreas fault has received much attention because it has played such an important role in the geological history of southern California. However, associated contractional and extensional fault zones have not been studied as thoroughly, even though they play important roles in the geologic framework and history of the central Transverse Ranges.

This review of paleotectonic and neotectonic fault complexes provides a geologic framework for studies of regional seismicity, earthquake potential, and earthquake hazards, and for our ongoing reconstruction of strike-slip displacements on faults of the San Andreas transform system. Our purpose is fourfold: (1) to describe various right-lateral strands of the San Andreas fault zone in the vicinity of the central Transverse Ranges; (2) to outline the geologic history of these strands; (3) to identify fault zones that are not part of the San Andreas zone but that have interacted with it in the context of the overall transform-fault system; and (4) to present a model that relates modern faults of the central Transverse Ranges within a coherent regional framework.

This study is a status report that updates a similar study released in 1985 as U.S. Geological Survey Open-File Report 85-365 (Matti and others, 1985). The update reflects ongoing geological studies conducted under the auspices of two U.S. Geological Survey programs--the National Geologic Mapping Program (GEOMAP and COGEOMAP Components) and the National Earthquake Hazards Reduction Program (Regional Geologic Hazards Element). This status report is the result of geologic-mapping investigations that are delineating the geologic framework of various fault complexes (Morton, 1978a,b,c; Morton and Matti, 1990a,b; Matti and others, 1992) and topical investigations that address the geologic history and strain budget of these fault complexes (Matti and others, 1982b; Morton and Matti, 1987; Harden and Matti, 1989; Morton and Matti, in press; Matti and Morton, in press).

MAJOR STRUCTURAL BLOCKS

The diverse basement terranes of southwestern California can be grouped into rocks of Peninsular Ranges-type, San Gabriel Mountains-type, and San Bernardino Mountains-type (fig. 2).

Basement rocks of ***San Gabriel Mountains-type*** (fig. 2A) consist of two crustal layers separated by a low-angle tectonic contact--the Vincent thrust (Ehlig, 1982). The upper thrust plate consists of Mesozoic plutons of various compositions, ages, and deformational styles that have intruded prebatholithic crystalline rocks. One distinctive Mesozoic granitoid unit is the Lowe pluton of Triassic age (Joseph and others, 1982a). The prebatholithic rocks largely are Proterozoic, and include orthogneisses and the anorthosite-syenite complex that is so well known from the western San Gabriel Mountains (Silver, 1971; Ehlig, 1981; Carter, 1982). The lower plate of the Vincent thrust consists of Pelona Schist--Mesozoic quartzofeldspathic sandstone and siltstone, limestone, quartzite, chert, and mafic volcanic rocks that have been metamorphosed to greenschist and lower amphibolite facies, presumably during late Mesozoic to early Tertiary emplacement of the upper plate (Ehlig, 1968b, 1981, 1982). From the Frazier Mountain region southeast to the Salton Trough, Pelona Schist occurs as windows and fault-bounded blocks (Ehlig, 1968b), including: (1) the Sierra Pelona window in the western San Gabriel Mountains; (2) the Lytle Creek window in the eastern San Gabriel Mountains; (3) the Blue Ridge slice between the Punchbowl and San Andreas faults; (4) a large window that mostly has been buried beneath sedimentary fill of the San Bernardino Valley; and (5) the Orocopia Mountains and Chocolate Mountains windows of Pelona-type schist that are referred to as Orocopia Schist and that are separated from rocks of San Gabriel Mountains-type by the Orocopia-Chocolate Mountain thrust. Both lower and upper plates are intruded by high-level Miocene granitoid plutons and dikes that were emplaced after initial juxtaposition of the two plates (Miller and Morton, 1977; Crowe and others, 1979).

Basement rocks of ***Peninsular Ranges-type*** (fig. 2B) consist of Jurassic and Cretaceous granitoid rocks (granodiorite, quartz diorite, tonalite, gabbro) that have intruded prebatholithic metasedimentary rocks (pelitic schist, metaquartzite, marble, quartzofeldspathic gneiss and schist). Along its north and northeast edge, the Peninsular Ranges block is bordered by a mylonitic belt of ductile deformation that separates lower plate plutonic and metasedimentary rocks of typical Peninsular Ranges type from broadly similar upper-plate rocks that appear to be parautochthonous equivalents of the more typical Peninsular Ranges suite; the autochthonous and parautochthonous suites have been telescoped along the mylonite zone (Sharp, 1979; Erskine, 1985). The ductile zone is referred to by different names locally, but Sharp (1979) recognized its regional significance and named it the Eastern Peninsular Ranges mylonite zone. The ductile zone probably continues westward into the southeastern San Gabriel Mountains, where mylonitic rocks have been mapped a few km north of the Mountain front (Alf, 1948; Hsu, 1955; Morton and Matti, 1987); if so, then the San Gabriel mylonitic belt may separate lower and upper plate rocks of Peninsular Ranges type--a speculative proposal we adopt here. Juxtaposition of Peninsular Ranges-type and San Gabriel Mountains-type rocks in the southeastern San Gabriel Mountains represents either (1) original intrusive relations between the two suites or (2) their tectonic juxtaposition by Neogene strike-slip displacements or (3) their tectonic juxtaposition by Paleogene or latest Cretaceous thrust faulting (May and Walker, 1989), or (4) a combination of some or all of these mechanisms.

Basement rocks of ***San Bernardino Mountains-type*** (fig. 2C) are similar to those in the Mojave Desert, and consist of Triassic through Cretaceous granitoid rocks of various compositions that have intruded prebatholithic orthogneiss (Proterozoic) and metasedimentary rocks (late Proterozoic and Paleozoic metaquartzite, marble, pelitic schist, and gneiss). The metasedimentary rocks are comparable with rocks of the Cordilleran miogeocline (Stewart and Poole, 1975). The Mesozoic plutonic rocks include both deformed and undeformed suites that extend southeastward into the Little San Bernardino Mountains, where they intrude rocks of San Gabriel Mountains-type. Strongly deformed Mesozoic granodiorite, tonalite, and quartz diorite form a discrete belt in the southeastern San Bernardino Mountains and along the western margin of the Little San Bernardino Mountains. Like rocks of San Gabriel Mountains-type, rocks of San Bernardino Mountains-type may be a layered terrane with batholithic and prebatholithic rocks in an upper plate separated from Pelona Schist in a lower plate by a low-angle fault comparable to the Vincent thrust.

RIGHT-LATERAL STRIKE-SLIP FAULTS

In the vicinity of the central Transverse Ranges, rocks of Peninsular Ranges type, San Gabriel Mountains type, and San Bernardino Mountains type are traversed by a series of northwest-trending strike-slip faults (fig. 1) that most workers assign to the San Andreas transform-fault system--a family of right-lateral faults that has evolved along the continental margin of western North America since middle Miocene time in response to interactions between the North American plate and various oceanic plates to the west (Atwater, 1970; Crowell, 1979; Dickinson and Snyder, 1979a,b). Youthful faults commonly viewed as modern components of the San Andreas system include the San Andreas fault proper; the San Jacinto, Whittier-Elsinore, and Newport-Inglewood faults; and various northwest-trending faults occurring in the offshore continental borderland (see Allen, 1957, p. 346; Crowell, 1975a, p. 10-11, 1981, p. 593). Older faults commonly viewed as abandoned components of the San Andreas system include the Punchbowl, San Gabriel, and Banning faults (Allen, 1957; Crowell, 1962, 1975a, 1981; Ehlig, 1976, 1981). Even older right-lateral faults that may belong to the San Andreas system include the San Juan-St. Francis and San Francisquito-Fenner-Clemens Well fault zones proposed in various forms by Smith (1977), Powell, (1981, 1986), and Joseph and others (1982b).

Right-lateral strike-slip faults in southern California are named and classified according to a hierarchical nomenclature that includes fault "strand", fault "zone", and fault "system" (Crowell, 1975a, p. 10-12): thus, the Mission Creek and Mill Creek strands (along with other fault strands) occur within the San Andreas fault zone that (along with other fault zones) occurs within the San Andreas fault system. Within this hierarchical classification, we adopt the fault nomenclature identified in Table 1 and map sheets 1 and 2.

SAN JACINTO FAULT ZONE

Within the Peninsular Ranges Province, the San Jacinto fault zone separates the San Jacinto Mountains and San Timoteo Badlands from the Perris block. In the San Jacinto Mountains the fault forms a series of en-echelen segments that locally are complicated by thrust faults (Sharp, 1967, 1972). A major right step in the fault zone occurs to the northwest in the San Jacinto Valley. There, the eastern right-stepping strand (Claremont fault) is located along the northeast side of the Valley and locally forms scarps in late Quaternary deposits; however, youngest Quaternary units are not broken and the fault largely must be inferred beneath sediment deposited by the San Jacinto River and by alluvial fans derived from the San Timoteo Badlands. To the west, a left-stepping strand of the San Jacinto zone (Casa Loma fault) is located along the southwest side of the San Jacinto Valley. The fault forms a scarp that Sharp (1972, map sheet 2) traced almost continuously from Hemet to north of the Lakeview Mountains. However, to the northwest the fault has no surface expression in youthful alluvium of the northern San Jacinto Valley, and slip must step right (east) onto the Claremont strand of the San Jacinto zone (J.C. Matti and D.M. Morton, in prep.). Within the Perris block, the San Jacinto fault has generated about 25 km of right-lateral displacement since early Pliocene time (Sharp, 1967; Matti and Morton, 1975).

Between the San Jacinto Valley and the San Gabriel Mountains the San Jacinto fault zone traverses Quaternary alluvial units and sedimentary rocks. In the Reche Canyon area the fault displaces strongly folded Quaternary deposits of the San Timoteo Badlands, and has a pronounced bow convex to the west that forms a restraining bend (Morton and Matti, in press); the main trace is flanked by subparallel faults (Morton, 1978a,b) that may be right-lateral in origin. Southeast of metropolitan San Bernardino the main trace displaces older and younger Quaternary units, but southeast and northwest of this break the youngest floodplain deposits of the Santa Ana River and Cajon and Lytle Creeks are not broken.

The distribution and geologic history of the San Jacinto fault in the southeastern San Gabriel Mountains are problematical. The name "San Jacinto" traditionally has been applied to a northwest-oriented fault zone developed in crystalline rocks east of the mouth of Lytle Creek canyon (fig. 3). There, the zone consists of two or more closely spaced fault strands that form impressive shear zones in crystalline bedrock but do not displace Quaternary alluvial deposits (Morton and Matti, 1987, plate 12.1). To the east, the Glen Helen fault forms scarps and sag ponds in alluvial deposits that probably are as young as Holocene (Sharp, 1972, map sheet 3; Morton and Matti, 1987, pl. 12.1), and to the west the Lytle Creek fault forms a scarp in alluvial materials that are latest Pleistocene in age (Morton and Matti, 1987, pl. 12.1). Mezger and Weldon (1983) documented a late Quaternary right-slip rate of about 2 mm/yr for the Lytle Creek fault. The Glen Helen fault probably is the active strand of the San Jacinto fault zone in the San Gabriel Mountain region, but it is unclear if this fault records the total history of the fault that developed southeast of the San Gabriel Mountains.

Models for the long-term history of the San Jacinto fault in the southeastern San Gabriel Mountains depend on how various bedrock faults that occur there are mapped and interpreted. Some workers indicate that the fault zone east of the mouth of Lytle Creek continues to the northwest and joins the San Andreas fault by way of the Punchbowl fault (Noble, 1954b; Ehlig, 1975, fig. 1, 1981, fig. 10-2). This interpretation leads to the idea that the San Jacinto fault feeds into the San Andreas, and that total slip on the San Andreas northwest of this junction includes displacements on the San Jacinto (Ehlig, 1982, p. 375; Weldon, 1984). However appealing, this model is questioned by other workers (Dibblee, 1968a, fig. 1, p. 266; 1975b, p. 156; Morton, 1975a, figs. 1, 2, p. 175) who conclude that the San Jacinto fault cannot be mapped into either the Punchbowl or San Andreas faults; instead, faults attributed to the San Jacinto zone appear to splay into several branches that curve west into the San Gabriel Mountains without joining the San Andreas fault at the surface (Morton, 1975a; Morton and others, 1983). This difference in structural interpretation has led to uncertainty about how the San Jacinto fault participates in the San Andreas fault system.

We propose that fault strands in the southeastern San Gabriel Mountains that originated by Quaternary right-slip on the San Jacinto fault can be understood only in the context of earlier Neogene faults that juxtaposed and rejuxtaposed rocks of Peninsular Ranges-type and San Gabriel Mountains-type. Figure 3 illustrates the pattern of Neogene faults in the southeastern San Gabriel Mountains and our interpretation of basement-rock provincial affinities (discussed below). In our discussion of the San Gabriel and Banning faults, we propose that the east- to northeast-oriented Evey Canyon, Icehouse Canyon, and Stoddard Canyon faults are segments of

throughgoing structures that formerly were regionally extensive--namely, the middle Miocene left-lateral Malibu Coast-Raymond-Banning fault and the late Miocene San Gabriel-Banning fault. Moreover, we propose that these older faults separate rocks of San Gabriel Mountains-type on the west, north, and east from rocks of Peninsular Ranges-type on the south (fig. 3). In our model, these older structures trend essentially eastward until they enter the Lytle Creek drainage, where they converge and trend southeastward down Lytle Creek Canyon. There, they are represented by the fault zone that occurs east of the mouth of Lytle Creek Canyon. In our view, then, the name "San Jacinto fault" in Lytle Creek Canyon has been applied to an ancient fault zone that has witnessed multiple episodes of strike-slip faulting--only the latest of which can be attributed to the movement history of the fault called "San Jacinto" that traverses the Peninsular Ranges Province to the southeast. This composite movement history is consistent with the broad crush zone that marks the trace of the San Jacinto fault between the Icehouse Canyon fault and the mountain front, and accounts for the pronounced contrast in basement-rock types on either side of the crush zone (fig. 3; Morton and Matti, 1987, Plate 12.1).

Thus, earlier Neogene faulting in the southeastern San Gabriel Mountains established a structural template that has been modified by Quaternary right-slip within the San Jacinto zone. But where and how did Quaternary displacements occur in the mountains? To the southeast, within the Peninsular Ranges, 25 km of Quaternary right slip can be documented for the San Jacinto fault on the basis of displaced basement rocks (Sharp, 1967) and displaced Pliocene sedimentary rocks of the San Timoteo Badlands (Matti and Morton, 1975). The San Jacinto thus should be viewed as a strand of the San Andreas system, and an easy solution would have right-slip faults of the San Jacinto in the southeastern San Gabriel Mountains connect with the San Andreas northwest of Cajon Pass. However, we reiterate here that faults attributable to the San Jacinto cannot be mapped beyond the southeastern San Gabriel Mountains. Instead, right-lateral faults that might be attributable to the San Jacinto zone in Lytle Creek Canyon curve westward and southwestward into the San Gabriel Mountains and turn into east- to northeast-trending north-dipping faults that have reverse left-slip displacements (Morton, 1975a, figs. 1, 2). Morton (1975b) viewed the curving fault splays in the southeastern San Gabriel Mountains as a schuppen-like structure within which right slip on northwest-oriented strands of the San Jacinto is transformed into reverse left slip on east- and northeast-oriented faults that appear to be continuations of the San Jacinto zone.

We adopt Morton's (1975b) proposal here, but modify it to fit our notion that these curving faults were not pioneered by Quaternary slip but instead are older Neogene strands of the Malibu Coast-Banning and San Gabriel-Banning fault systems that have been reactivated and deformed during Quaternary time due in part to the 15° angular convergence between the San Jacinto and San Andreas faults (Morton and Matti, in press). We propose that one of these curving structures is the reactivated Stoddard Canyon segment of the San Gabriel fault that originally was a right-lateral structure but now has latest-movement indicators interpreted by Morton (1975a) as evidence for oblique left slip. A second oblique left-lateral fault (the San Antonio) trends down San Antonio Canyon and has displaced three fault segments of the old Malibu Coast-Banning system and the San Gabriel-Banning system (fig. 3): (1) the north branch of the San Gabriel fault about 3 km from the Icehouse Canyon fault, (2) the Evey Canyon fault about 3 km from the Icehouse Canyon fault, and (3) the south branch of the San Gabriel fault about 3 km from the Stoddard Canyon fault.

The oblique left-lateral faults all root eastward or northeastward into the northwest-oriented fault zones of Lytle Creek drainage that traditionally have been assigned to the San Jacinto fault. One of these strands apparently has generated at least 8 to 13 km of Quaternary right slip that has displaced plutonic contacts between Miocene granitoid rock and Pelona Schist (fig. 3; Morton, 1975a). However, even this displacement cannot be mapped northwestward out of the Lytle Creek drainage basin.

The structural complexity in the southeastern San Gabriel Mountains makes it unclear to us exactly how right slip on the San Jacinto has been transferred to the San Andreas. Two extreme interpretations apply: (1) right slip on the San Jacinto is transferred entirely to the San Andreas by way of a right-step that takes place between San Gorgonio Pass and the southeastern San Gabriel Mountains, or (2) right slip on the San Jacinto fault is transformed entirely into oblique left slip along faults within the southeastern San Gabriel Mountains, and thereby does not contribute at all to right slip on the Mojave Desert segment of the San Andreas. We suspect that kinematic interaction between the San Jacinto and San Andreas faults has involved both right-stepping slip transfer and left-stepping slip bypass, but until the relative scale of either process is documented, the amount of slip transfer from the San Jacinto to the Mojave Desert segment of the San Andreas can only be inferred. In the absence of actual data, we arbitrarily infer that 20 km of slip has been transferred between the two faults by way of the right step across the San Bernardino Valley; we infer that the remaining 5 km has been transformed into oblique left slip within the southeastern San Gabriel Mountains, where this transformation has led to convergence, uplift, block rotations, and severe shape changes of blocks bounded by brittle faults.

SAN ANDREAS FAULT ZONE

The main strand of the San Andreas fault in southern California consists of two segments (fig. 1): (1) the Mojave Desert segment that mainly separates rocks of San Gabriel Mountains-type from rocks of San Bernardino Mountains-type, and (2) the Coachella Valley segment that separates rocks of Peninsular Ranges-type from rocks of San Bernardino Mountains- and San Gabriel Mountains-type. In plan view the main strand has a left-stepping geometry: the Mojave Desert segment has been stepped left (west) about 15 km from the Coachella Valley segment, with the step occurring in the San Gorgonio Pass region of the southeastern San Bernardino Mountains (Matti and others, 1985). This left step forms a structural knot in the San Andreas that has influenced the evolution of the entire transform-fault system and has led to multiple fault strands that evolved sequentially. Multiple strands also have developed along the Mojave Desert segment of the San Andreas (Barrows and others, 1985, 1987). This strand complexity has made it difficult to identify the distribution and displacement history of faults in the San Andreas family, and has led to variable fault nomenclature and to conflicting fault-movement scenarios.

FAULT NOMENCLATURE

The complex pattern of late Cenozoic right-lateral faults in southern California has led to nomenclature for the San Andreas fault that is more complex than for central California. There, most if not all Miocene and younger displacement on the San Andreas has occurred within a narrow, singular (although complex) zone that extends the length of central California to Hill and Dibblee's (1953) "Big Bend" at the latitude of the Garlock fault. The name "San Andreas fault" has been used by most workers in central California (Hill, 1981), and little confusion has arisen with regard to which geologic structure bears the name "San Andreas fault" or whether multiple fault strands have generated sequential displacements. By contrast, the San Andreas fault in southern California consists of multiple strands, each representing some portion of the geologic history allocated to the more singular zone in central California (Noble, 1932; Dibblee, 1954, 1968a; Allen, 1957; Crowell, 1962; Woodburne, 1975; Matti and others, 1985). This structural complexity has presented two challenges: (1) to document the distribution of the various fault strands and to determine their sequencing and amount of right-lateral displacement, and (2) to establish nomenclature that provides a logical framework for understanding faulting history and for relating fault segments having similar and/or dissimilar movement histories.

A nomenclatural framework for the San Andreas fault in southern California has evolved through the efforts of many workers (see the historical review by Hill, 1981). Early workers recognized that the characteristic geomorphic and geologic features of the San Andreas rift zone in central California extend southeast beyond Hill and Dibblee's Big Bend region and intervene between the Mojave Desert and the massifs of Liebre Mountain and the San Gabriel Mountains. On this basis, the name "San Andreas fault" originally was extended into southern California. However, Noble (1926, 1932) was among the first to observe that the San Andreas in southern California splays into several major branches--some occurring close to each other within the narrow Mojave Desert zone, others forming discrete strands that follow independent traces many kilometers apart. As Allen (1957) pointed out, this strand complexity creates a dilemma: which strand should bear the name San Andreas fault and which strand generated the large displacements proposed by Hill and Dibblee (1953) for the fault in central California?

Whenever possible, we refer to the San Andreas fault proper in southern California by one of the specific strand names identified in Table 1. However, because each of these strands merged with or fed into the San Andreas fault in central California, each southern California strand during its lifetime represented the San Andreas before it was abandoned and succeeded by the next "San Andreas." This iterative pattern has culminated in the modern San Andreas fault in southern California--the genetically related set of strands that most workers believe originated onshore in reponse to Pliocene opening of the Gulf of California by sea-floor spreading and transform faulting (Atwater, 1970). The name San Andreas fault usually is applied to this modern strand. Within this complex geologic and nomenclatural framework, we use the term "San Andreas (*sensu lato*)" for all strands of the San Andreas in southern California that have fed into the central California segment of the fault and contributed to its total history; we use the term "San Andreas (*sensu stricto*)" for those strands in southern California that have contributed to displacements on the fault only in Pliocene and Quaternary time. Thus, we can refer to the San Andreas fault generically without reference to a particular strand, but at the same time distinquish between broader vs. narrower interpretations of the name.

MOJAVE DESERT SEGMENT

The Mojave Desert segment of the San Andreas fault extends from Tejon Pass to the San Bernardino valley, where it passes into the San Bernardino strand. The modern break forms a singular trace that runs the entire length of the segment (Ross, 1969) and describes a gently-curving arc having a regional strike of about N 60 W; in Tejon Pass the trace is deflected into the big bend of Hill and Dibblee (1953, p. 453). Ground rupture associated with the 1857 earthquake on the San Andreas fault occurred along the Mojave Desert segment from Tejon Pass to about Wrightwood (Sieh, 1978a), and the modern trace has been the site of recurring Holocene ground rupture (Sieh, 1978b, 1984; Weldon and Sieh, 1985).

The Mojave Desert segment has been described thoroughly by Barrows and others (1985, 1987) on the basis of detailed mapping by the California Division of Mines and Geology (Barrows, 1975; Kahle, 1975; Barrows, 1979, 1980; Barrows and others, 1976; Beeby, 1979; Kahle and others, 1975; Kahle, 1979; Kahle and Barrows, 1980). Their mapping shows that from Tejon Pass southeast to Elizabeth Lake the modern trace coincides with older traces to form a narrow fault zone having a relatively simple faulting history. By contrast, between Elizabeth Lake and Cajon Pass the modern trace is but one of several fault strands that form a zone several kilometers wide (see similar interpretations by Noble, 1926, 1933, 1954a,b; Wallace 1949; Dibblee, 1967a, 1968a, 1975b). Within this wide zone, fault strands like the Punchbowl, Nadeau, and Little Rock faults have evolved sequentially and been abandoned, culminating in the modern trace that apparently evolved no earlier than the Pleistocene (Barrows and others, 1985, p. 105-106).

Geologic setting in the San Gabriel Mountains

In the San Gabriel Mountains Barrows and others (1985, 1987; Barrows, 1987) recognize five discrete strands of the San Andreas fault including, from west to east, the Punchbowl, Nadeau south, Nadeau north, Mojave Desert, and Little Rock strands (we use the term "Mojave Desert strand" to designate the "main San Andreas trace" of Barrows and others, 1985, 1987). Careful mapping by Barrows and others (1985) shows that the Punchbowl, Nadeau (north and south branches), and Little Rock faults all are truncated on their northwest and southeast ends by the Mojave Desert strand of the San Andreas. Thus, they can be viewed as anastomosed and abandoned strands of the San Andreas that probably are related to strands of the fault farther to the southeast in the San Bernardino Mountains and (or) Salton Trough.

Regional correlation of the Punchbowl fault is of particular interest because the fault appears to be a significant strand of the San Andreas, and yet its isolated position outboard (west) of the main San Andreas trace makes its role in the overall history of the San Andreas difficult to evaluate. The fault extends for about 75 km along the northeast flank of

the San Gabriel Mountains (fig. 1; Barrows and others, 1987). The strand is characterized by its locally sinuous trace and west-dipping reverse dips, a geometry attributed by Barrows and others (1987) to deformation following its right-slip history. The Punchbowl fault originally was identified by Noble (1953), who interpreted it as a reverse dip-slip fault and implied that it merged with the San Jacinto fault by way of the Glen Helen fault (Noble, 1954a,b). Subsequently, Dibblee (1967a, 1968a) showed that the Punchbowl fault is a right-lateral fault that he interpreted as an old strand of the San Andreas family. Because it is truncated on the southeast and northwest by younger strands of the San Andreas zone, the Punchbowl should be viewed like any other linear structure that has been displaced by a strike-slip fault: its northwest and southeast terminations have been displaced from cross-fault counterparts that should be identifiable after right slip is restored on younger strands of the San Andreas. This interpretation motivated us to search southeastward for a possible displaced counterpart for the Punchbowl fault on the opposite side of the main trace of the San Andreas.

Faulting chronology.--The multiple San Andreas strands in the San Gabriel Mountains evolved sequentially about 5 m.y. ago (Barrows and others, 1985, 1987). The Punchbowl fault appears to be the oldest strand, although Barrows and others (1987, p. 2, 84, 86) indicate that sequencing relations between the Punchbowl and Little Rock strands are not completely clear. According to Barrows (1987, p. 149-153, figs. 6-8), stratigraphic relations bertween the Punchbowl fault and sediments of the Juniper Hills Formation (of Barrows, 1987) indicate that the Punchbowl fault may have generated right slip continuously between early Blancan (5 Ma) and late Blancan time (2 Ma). However, the age of the Juniper Hills Formation is poorly constrained (Barrows, 1987, p. 129-130), and relevent beds in the unit cannot be confidently assigned to a particular part of the Blancan (A.G. Barrows, oral communication, 1990). The Nadeau faults appear to be Pliocene in age, while the Mojave Desert strand may have originated in middle Pleistocene time.

Displacement history.--Barrows and others (1985, Table 4, 1987 p. 86) were able to document no more than 102 km of right slip on all strands of the San Andreas fault in the eastern San Gabriel Mountains: 21 km on the main or Mojave Desert strand of the San Andreas; 16 km on the Nadeau fault (north and south branches); 21+ km on the Little Rock fault; and 44 km on the Punchbowl fault. Their estimates for the Punchbowl fault are comparable with those proposed by other workers. Dibblee (1967a, fig. 72; 1968a, p. 263-264, fig. 1) recognized between 32 and 48 km of displacement on the Punchbowl based on cross-fault correlations between the San Francisquito and Fenner faults, between marine rocks of the San Francisquito Formation, and between the Sierra Pelona and Blue Ridge windows of Pelona Schist. Farley and Ehlig (1977) and Ehlig (1981, fig. 10-4) proposed about 40 km of displacement based on their suggestion that the Punchbowl fault has displaced strata in Ridge Basin that contain polka-dot granite clasts from strata in the Punchbowl Formation that contain similar clasts. Barrows and others (1985, 1987) acknowledge that their total displacement for the San Andreas (102 km) is considerably less than the widely accepted displacement (240 km), and they point out that displacement on the Little Rock strand may be greater than the 21 km they were able to document. Their displacement estimate for the main San Andreas strand (21 km) also is considerably less than most workers would infer for the strand.

COACHELLA VALLEY SEGMENT

The Coachella Valley segment of the San Andreas fault is a relatively simple fault zone, although locally it is complicated by en-echelon strands and lateral splays (Clark, 1984). The segment is relatively straight and generally has a uniform regional strike of about N 45° W, although Bilham and Williams (1985) identified alternating segments 9 to 14 km long that have trends of N 40° W and N 48° W, repectively. Youthful tectonic landforms and faulted Holocene alluvial deposits indicate that the Coachella Valley segment is a modern neotectonic element (Keller and others, 1982), but the antiquity and tectonic significance of the segment cannot be judged because Quaternary and late Tertiary sediments of the Salton Trough conceal older rocks bearing evidence for its full history.

In the southern Indio Hills the Coachella Valley segment of the San Andreas fault is joined by another right-lateral fault (map sheet 1). Dibblee (1954, p. 26, pl. 2; 1968a; 1975a) referred to these two faults as north and south branches of the San Andreas fault, but Allen (1957, p. 336-339, p. 346) cited geologic relations that discouraged him from assigning the name San Andreas to any of the faults in this region. Accordingly, Allen (1957, fig. 1) applied the names Mission Creek fault and Banning fault, respectively, to Dibblee's north and south branches of the San Andreas.

We share Dibblee's view that the northern of his two branches is the main strand of the San Andreas fault in the Salton Trough, and that the name "San Andreas" can be properly applied to the strand. However, we are not certain that his south branch is a throughgoing strand of the San Andreas. Our nomenclature reflects these interpretations (map sheet 1). We refer to Dibblee's north branch as the Coachella Valley segment of the San Andreas fault, and we apply that nomenclature to the entire extent of the fault in the Salton Trough. Like Allen (1957), we refer to Dibblee's south branch as the Banning fault, and we believe that it is a reactivated segment of the ancestral late Miocene Banning fault (an idea proposed by Dibblee, 1975a, p. 134).

The southeast and northwest terminations of the Coachella Valley segment of the San Andreas involve complex interactions with other fault zones. To the southeast, surface expression of the segment terminates near the southeast margin of the Salton Sea, where it interacts with the Brawley seismic zone and the Imperial fault (Sharp, 1982; Johnson and Hill, 1982). Some workers view this segment of the San Andreas fault as the northwesternmost of a series of right-stepping transform faults that extend from the Gulf of California onshore into the Salton Trough (Moore and Buffington, 1968, fig. 4; Elders and others, 1972, fig. 1; Crowell and Ramirez, 1979; Lonsdale and Lawver, 1980, fig. 1; Crowell, 1981, fig. 18-4; Johnson and Hill, 1982, fig. 6; Curray and Moore, 1984, figs. 1, 9).

At its northwest end the regional strike of the Coachella Valley segment is deflected westward, and it splays into the Mission Creek and Mill Creek strands of the southeastern San Bernardino Mountains. We cannot prove that these multiple strands merge beneath the Coachella Valley because they are buried by unfaulted Quaternary alluvium where they exit the San Bernardino Mountains. However, their map pattern in the mountains strongly suggests that the strands coalesce southeastward, and by the simplest

interpretation they ultimately form a single fault zone--the Coachella Valley segment of the San Andreas fault.

Northwest of Desert Hot Springs the Coachella Valley segment of the San Andreas fault loses its clear surface expression, and Holocene displacements have not been demonstrated for the segment. The fault forms conspicuous scarps in Quaternary alluvium southeast of Desert Hot Springs, and discontinuous scarps can be traced northwestward where they disrupt young (but not youngest) alluvium in the center of town (Clark, 1984). However, to the northwest, latest Quaternary alluvial fans that flank the Little San Bernardino Mountains are not disrupted by the fault. The late Quaternary history of the Coachella Valley segment has not been worked out in this region.

Displacement history.--Although small youthful displacements on the Coachella Valley segment of the San Andreas fault have been recognized on the basis of cross-fault correlations between Quaternary alluvial materials (e.g., Keller and others, 1982; Matti and others, 1985), large older displacements recognized on the basis of cross-fault correlation between Cenozoic and pre-Cenozoic units generally have not been recognized. In part this reflects the fact that older rocks of appropriate age containing evidence for large-scale displacements largely are buried by young Quaternary sediment that has filled the Salton Trough. In addition, the widely cited model for 240 km of Pliocene and Quaternary displacement on the San Andreas fault in effect has dampened the search for pre-Pliocene cross-fault counterparts in the Salton Trough because the 240-km model requires that pre-Pliocene rocks have been displaced completely out of the Salton Trough region.

A study by Dillon (1975) suggests that this may not be the case. In his study of the southern Chocolate Mountains, Dillon (1975, fig. 70, p. 334-365) proposed that rocks in the southeastern San Bernardino Mountains have been displaced from the southern Chocolate Mountains by 180 ± 20 km of right slip on the Coachella Valley strand of the San Andreas (Dillon's north branch of the San Andreas). Dillon's proposal is based on three cross-fault correlations: (1) crystalline rocks of San Gabriel Mountains-type northeast of San Gorgonio Pass correlated with similar rocks in the vicinity of Mammoth Wash in the Chocolate Mountains (Dillon, 1975, p. 59-60, 351-353); (2) the Miocene Coachella Fanglomerate in the Whitewater area correlated with the fanglomerate of Bear Canyon in the southern Chocolate Mountains (Dillon, 1975, p. 341-346); and (3) the inferred strandline position of the marine Imperial Formation in the Whitewater area correlated with the inferred strandline position for the marine Bouse Formation in the Chocolate Mountain region (Dillon, 1975, p. 347-350, fig. 69). Dillon's reconstruction contrasts with that of Peterson (1975), who restores the Coachella Fanglomerate farther south in the Salton Trough and calls for 215 km of displacement on the Coachella Valley strand of the San Andreas.

San Bernardino Mountains segment

The San Andreas fault within and adjacent to the San Bernardino Mountains consists of several strands that evolved sequentially and then were abandoned; to the northwest and southeast, these strands merge to form the Mojave Desert and Coachella Valley segments.

PREVIOUS INVESTIGATIONS

In his geologic reconnaissance of the eastern San Bernardino Mountains, Vaughan (1922) recognized that the region was traversed by two important faults--the San Andreas fault, which he projected through San Gorgonio Pass and eastward into the Coachella Valley, and a fault he named the Mission Creek fault, which he projected through the southeastern San Bernardino Mountains. Hill (1928) discussed the San Andreas fault and related faults in the vicinity of the San Bernardino Mountains and named the Pinto Mountain and Mill Creek faults.

Following the observation by Noble (1932) that the San Andreas fault zone southeast of Cajon Pass splits into several major branches, Allen (1957) and Dibblee (1968) addressed the distribution and nomenclature of faults in the vicinity of the San Bernardino Mountains. Allen (1957, fig. 1, p. 336-343) reviewed fault nomenclature used by earlier workers in the San Gorgonio Pass region and clarified the distribution of the Mill Creek fault (adopted from Hill, 1928), the Mission Creek fault (modified from Vaughan, 1922), the Banning fault (recognized originally by Vaughan, 1922, and defined and extended by Hill, 1928), and the modern San Andreas fault. Allen showed that the Mill Creek and Mission Creek faults are strands of the San Andreas fault zone, although he was unable to confirm or refute large right-lateral displacements on the strands. Between Cajon Pass and San Gorgonio Pass, Allen followed tradition by applying the name San Andreas fault to "the most aligned and obvious prolongation" of the San Andreas that extends southeast of Cajon Pass--that is, "the fault that lies at the foot of the San Bernardino Mountains and continues into San Gorgonio Pass. Within the Pass area, however, various structural complications make the continuity of the fault through this region doubtful" (Allen, 1957, p. 337). Allen's last sentence epitomizes the notion that San Gorgonio Pass is the site of a knot in the modern San Andreas fault system.

Dibblee modified the distribution and nomenclature of Allen's fault strands in the southeastern San Bernardino Mountains. In his geologic map of the San Gorgonio Mountain quadrangle, Dibblee (1964) equated his north branch of the San Andreas fault with Allen's Mill Creek fault, an interpretation he reiterated later (Dibblee, 1968a, p. 269). Dibblee apparently viewed Allen's Mission Creek fault as a splay of his north branch (Dibblee, 1968a, figs. 3, 4; 1975a, p. 127, figs. 1, 2) and it is not clear from these papers which structure has the greater displacement. Dibblee's recent work (Dibblee, 1982, p. 152, 161-165, figs 1, 4, and 8) clearly equates his north branch with Allen's Mill Creek fault and states that it generated large right-lateral displacements. Dibblee (1968a, p. 268) applied the term south branch of the San Andreas fault to the modern trace along the foot of the San Bernardino Mountains, and projected this trace southeastward through San Gorgonio Pass to join his south branch in the Coachella Valley (Dibblee, 1954). Dibblee's discussion of offsets on the south branch is confusing: he indicates minor displacements on the south branch between San Gorgonio River and San Gorgonio Pass but large displacements on the same strand along the base of the San Bernardino Mountains (Dibblee, 1968a, p. 268), without elaborating on this discrepancy.

Our concept of basement terranes and their bounding faults in the southeastern San Bernardino Mountains borrows some elements from both Allen and Dibblee, but departs from

both in the details of fault distribution and movement history. Our view of fault relations is closer to Allen's scheme than to Dibblee's. Despite the unifying appeal of Dibblee's nomenclature, his concept of north and south branches of the San Andreas fault is too simplified and partly is in error as shown by later mapping (Ehlig, 1977; Farley, 1979; Matti and others, 1982a, 1983). Allen's (1957) interpretation of the Mill Creek and Mission Creek faults as independent strands that follow separate routes through the San Bernardino Mountains more accurately delineates the boundaries of crystalline terranes native and exotic to the southeastern San Bernardino Mountains, even though Allen was unable to use the significance of these terranes to reconstruct a comprehensive movement history for his fault strands. Although many workers have adopted Dibblee's nomenclature for the San Andreas fault in the south-central Transverse Ranges, we recommend that this nomenclature be abandoned because it does not accurately reflect the geologic relations.

GEOLOGIC SETTING

Wilson Creek and Mission Creek faults

The Wilson Creek and Mission Creek faults are major strands of the San Andreas fault in the south-central Transverse Ranges: both juxtapose exotic, far-travelled crystalline and sedimentary rocks against rocks native to the San Bernardino Mountains. Our recognition of two major fault strands in a region where only the Mission Creek fault has been mapped previously is based on relations in the Raywood Flat area of the southeastern San Bernardino Mountains (Matti and others (1983) and in the Mill Creek area (Matti and others, 1992).

Wilson Creek and Mission Creek faults in the southeastern San Bernardino Mountains

Within crystalline rocks of the southeastern San Bernardino Mountains, the Wilson Creek and Mission Creek faults are closely spaced and traverse the range along a gently bowed, east-trending arc. At the southwest end of this arc, the Wilson Creek and Mission Creek faults diverge and follow separate paths within and adjacent to the mountains. At the east end of this arc, the two faults apparently coalesce to form a single fault that continues southeastward beneath alluvium of the Coachella Valley (Matti and others, 1982a). There, the combined Wilson Creek-Mission Creek strands merge with the Mill Creek strand to form the Coachella Valley segment of the San Andreas fault.

Throughout the southeastern San Bernardino Mountains, the Mission Creek fault occurs outboard (south) of the Wilson Creek fault and bounds a distinctive terrane of crystalline rocks similar to those of the lower and upper plates of the Vincent thrust in the San Gabriel Mountains. These relations can be seen best in the headwaters of San Gorgonio River, where rocks outboard of the Mission Creek fault form two suites separated by a steeply dipping fault that probably originated as a low-angle segment of the region-wide Vincent-Orocopia-Chocolate Mountain thrust system. Lower-plate rocks are Pelona Schist that consist mainly of chlorite-albite-actinolite greenstone; upper-plate rocks are hornblende-bearing granitoid rocks and granitic gneiss that have strongly foliated and layered fabrics created by ductile and brittle-ductile deformation. Small bodies and lenses of the Triassic Lowe plutonic complex (of Joseph and others, 1982) occur locally in the upper-plate sequence (Farley, 1979). These lower- and upper-plate rocks are similar to those that occur in the same structural block in the nearby Crafton Hills, and both sequences in turn are similar to those in the eastern San Gabriel Mountains (Ehlig, 1968b, p. 301, fig. 1, locs. 6-8). These correlations form the basis for our interpreting rocks in the southeastern San Bernardino Mountains as San Gabriel Mountains-type.

Relations between the Mission Creek and Wilson Creek faults can be seen best in the vicinity of Raywood Flat north of San Gorgonio Pass, where the two faults parallel each other closely and separate three different assemblages of crystalline rock. The Wilson Creek fault separates granitoid and gneissic rocks native to the San Bernardino Mountains to the north from a slice of crystalline rocks of unproven provincial affinity to the south; we refer to this enigmatic slice as the Wilson Creek block. The Mission Creek fault bounds the Wilson Creek block on the south and separates it from rocks of San Gabriel Mountains type.

Our interpretations in the Raywood Flat area differ in detail from those of Ehlig (1977) and Farley (1979), who recognized that the Mission Creek fault zone is an important structural boundary but suggested a different interpretation for geologic features that we use to identify the Wilson Creek fault. Critical to any interpretation is the structural position of Pelona Schist and associated crystalline rocks that we believe are bounded by the Wilson Creek and Mission Creek faults.

Pelona Schist forms two bodies in the headwaters of San Gorgonio River (map sheet 2). We agree with Farley (1979), who includes the main Pelona Schist body with rocks of San Gabriel Mountains-type and separates this package from non-related rocks to the north by the Mission Creek fault (map sheet 2; Matti and others, 1983). A second slice of Pelona Schist and associated crystalline rocks just west of Raywood Flat is more problematical, and forms the basis for our recognition of the Wilson Creek fault as a structure distinct from the Mission Creek fault. Farley (1979) viewed the Raywood Flat Pelona Schist body as a fault-bounded slice caught up between two branches of his Mission Creek fault zone, and he concluded that this and the main Schist body belong together as one coherent terrane south of the main Mission Creek strand. In contrast, we believe that the two Pelona Schist bodies and associated crystalline rocks constitute two different assemblages bounded by two major strike-slip faults. The schist bodies differ in their pre-metamorphic stratigraphy, and crystalline rocks in fault contact with the Raywood Flat body are different from rocks of either San Gabriel Mountains-type or San Bernardino Mountains-type.

We use these differences to suggest that the Raywood Flat Pelona Schist body is not a slice caught up in a right-lateral fault zone (Farley, 1979) but instead is a window through crystalline rocks of the Wilson Creek block. By this interpretation, high-angle faults now bounding the window have reactivated and modified a thrust surface (the Vincent-Orocopia-Chocolate thrust) that formerly had a low-angle geometry. Upper-plate rocks of this window constitute rocks of the Wilson Creek block that appear to be unlike those native to the San Bernardino Mountains or those in the upper-plate of the Vincent-Orocopia thrust to the south. These observations lead to our conclusion that two exotic crystalline terranes separated by two major strands of the San Andreas fault occur in the southeastern San Bernardino Mountains: (1)

a terrane of San Gabriel Mountains-type rocks outboard (south) of the Mission Creek fault and (2) the Wilson Creek block between the Mission Creek and Wilson Creek faults.

At the west margin of the southeastern San Bernardino Mountains the Wilson Creek-Mission Creek couplet has been modified by low-angle faulting and cannot be recognized in its original configuration. In the headwater region of San Gorgonio River, crystalline rocks native to the San Bernardino Mountains have been thrust southeastward across the Wilson Creek-Mission Creek fault zone and across exotic crystalline rocks outboard of the zone (Farley, 1979; Matti and others, 1983). Low-angle faulting probably evolved as the Wilson Creek-Mission Creek fault couplet was rotated from its original northwest strike into the anomalous east to northeast strike it presently displays in this vicinity. Although the low-angle faults obscure the original course of the Wilson Creek and Mission Creek faults, our mapping and palinspastic reconstructions indicate that they originally continued through and beyond Banning Canyon.

Wilson Creek fault along the southwest margin of the San Bernardino Mountains

Faults we assign to the Wilson Creek strand of the San Andreas occur along the southwest base of the San Bernardino Mountains between Wilson Creek and Cook Creek (map sheets 1, 2). Along this reach, the strand forms a curving, locally sinuous trace sandwiched between the San Bernardino and Mill Creek strands of the San Andreas. Southeast of this reach, between Wilson Creek and Banning Canyon, the Wilson Creek fault either is concealed by Quaternary alluvium or is truncated and displaced by the younger Mission Creek or San Bernardino strands of the San Andreas fault. To the northwest, beyond Cook Creek, the Wilson Creek strand is truncated by the Mission Creek and San Bernardino strands.

Near Wilson Creek, its namesake, the fault enters the San Bernardino Mountains and traverses Yucaipa Ridge before descending into Mill Creek Canyon. To the west, the Wilson Creek fault adopts a more westerly trend and converges with the younger Mill Creek fault. The two faults parallel each other for a few miles before the Wilson Creek strand diverges in the Cook Creek drainage near San Bernardino and exits the San Bernardino Mountains. Along this segment the fault dips between 35° and 65° to the southwest. The 35° dip occurs near the Cook Creek drainage, where the Wilson Creek strand juxtaposes gneissic crystalline rocks against Tertiary sedimentary rocks. There, the low-angle movement zone has been interpreted as a landslide surface (Gary Rasmussen and Associates, unpublished geotechnical report on file with San Bernardino County; G. Rasmussen, oral commun., 1984); however, we interpret it as a segment of the Wilson Creek fault that has acquired a low-angle geometry. West of City Creek, isolated masses of gneissose rock mapped as landslide masses by Morton and Miller (1975, fig. 1c) may be klippe of Wilson Creek block emplaced along a south-dipping and locally north-dipping thrust segment of the Wilson Creek fault.

The distribution, movement sense, and signficance of the Wilson Creek fault are interpreted in different ways by different workers. In the vicinity of Yucaipa Ridge and Mill Creek Canyon, faults we assign to the Wilson Creek strand were mapped by Owens (1959), and by R.E. Smith (1959) who identified two fault segments (his South fault and Yucaipa Ridge fault) that he thought were unrelated. Matti and others (1985) combined Smith's South and Yucaipa Ridge faults into their throughgoing Wilson Creek fault. The distribution and displacement history of the fault were examined by Demirer (1986), by West (1987) who referred to the structure as the Yucaipa Ridge fault and restricted the name "Wilson Creek" to another fault zone in the Yucaipa Ridge area, and by Hillenbrand (1990) who mapped the Wilson Creek fault northwest to the Cook Creek area. All previous workers conclude that faults we assign to the Wilson Creek fault are minor structures having a dip-slip geometry.

Stratigraphic comparisons between Tertiary nonmarine sedimentary rocks traversed by the Wilson Creek fault have influenced investigators who view the fault as a minor structure. These rocks originally were grouped by Vaughan (1922) into his vaguely defined Potato Sandstone. In the Mill Creek area the rocks have been mapped and investigated by various graduate students (Smith, 1959; Owens, 1959; Gibson, 1964; Demirer, 1986; West, 1987; Hillenbrand, 1990). Recently, Matti and others (1992) proposed that Vaughan's Potato Sandstone can be separated into the Mill Creek Formation (modified from Gibson, 1964, 1971) and the Formation of Warm Springs Canyon, and they indicate that the two units are separated by the Wilson Creek fault (map sheet 2 of this report). Most workers (Dibblee, 1982; Demirer, 1986; Sadler and Demirer, 1986; West, 1987) recognize strong lithostratigraphic similarities between the units that we separate into two formations, and therefore see no need to juxtapose them along a fault having significant strike-slip movement. We believe that stratigraphic differences between the Mill Creek and Warm Springs Formations outweigh stratigraphic similarities between them (Matti and others, 1992). Moreover, basement rocks of the Wilson Creek block that underlie the Mill Creek Formation are dissimilar to those in the San Bernardino Mountains east of the Wilson Creek and Mill Creek faults, and if the Mill Creek fault is a relatively minor strand of the San Andreas (discussed below), then either the Wilson Creek fault or some other (unrecognized) fault is required to bring the Wilson Creek block into the region.

Mission Creek fault along the southwest margin of the San Bernardino Mountains

Matti and others (1985) inferred the existence of the Mission Creek fault along the southwestern base of the San Bernardino Mountains in order to explain the juxtaposition of San Gabriel Mountains-type basement rocks (upper- and lower-plate rocks of the Vincent thrust) against the Wilson Creek block and rocks of San Bernardino Mountains-type. Juxtaposition of these distinctive crystalline terranes can be documented in the southeastern San Bernardino Mountains where the Mission Creek fault separates rocks of San Gabriel Mountains-type from rocks native to the San Bernardino Mountains and from rocks of the Wilson Creek block (discussed above). Matti and others (1985) reasoned that the Mission Creek strand continues in the subsurface along the southwestern base of the San Bernardino Mountains, where the structure continues to separate outboard rocks of San Gabriel Mountains-type from rocks of the San Bernardino Mountains and the Wilson Creek block. Just as in the southeastern San Bernardino Mountains, where the Mission Creek fault is an older abandoned strand of the San Andreas (Matti and others, 1983, 1985), so too along the southwestern

base of the San Bernardino Mountains the Mission Creek fault is an older fault either (1) buried under Quaternary surficial materials or (2) reactivated by the late Quaternary San Bernardino strand. In the latter case, the trace of the San Bernardino strand would mark the trace of the older Mission Creek strand.

Mill Creek strand

The Mill Creek fault was named by Hill (1928), but modern discussions of the fault date from Allen's (1957) clarification of its distribution and geologic setting; our mapping of the fault is similar to Allen's. Within the San Bernardino Mountains the Mill Creek fault occurs inboard (east) of the Wilson Creek and Mission Creek faults, and traverses the mountains along a relatively straight to slightly curving trace that has a regional strike of about N 70° W. The fault zone is relatively simple and narrow. Southeast of the San Bernardino Mountains the Mill Creek fault and the Wilson Creek and Mission Creek faults coalesce to form the Coachella Valley segment of the San Andreas fault. To the northwest the Mill Creek fault exits the mountains near San Bernardino and merges with the San Bernardino strand of the San Andreas fault.

At the southeast end of the San Bernardino Mountains, near the confluence of the North and South Forks of the Whitewater River, we map the Mill Creek fault differently than either Allen (1957) or Dibblee (1967b). Allen (1957, pl. 1) thought that the Mill Creek fault terminated in this vicinity after having traversed much of the San Bernardino Mountains to the west. Dibblee recognized that the fault (his north branch) must continue to the southeast; he (Dibblee, 1967b, 1975a) projected the Mill Creek fault eastward beneath alluvium of the Whitewater River and suggested that it truncates the Pinto Mountain fault. We map the Mill Creek fault differently, and propose that it is deflected by the Pinto Mountain fault (Matti and others, 1982a, 1983). Where it obliquely exits the San Bernardino Mountains southeast of the Whitewater River, the Mill Creek fault flanks the mountain front and is located close to but north of the combined traces of the Mission Creek and Wilson Creek faults (Matti and others, 1982a, 1983).

San Bernardino strand

As defined by Matti and others (1985), the San Bernardino strand denotes the modern trace of the San Andreas fault in the vicinity of the San Bernardino Mountains. The fault extends for 60 km along the base of the Mountains from Cajon Pass southeast to the vicinity of Banning Canyon, and describes a gently curving arc that is convex to the south. To the northwest the San Bernardino strand is continuous with the modern trace of the Mojave Desert segment of the San Andreas; to the southeast the strand appears to terminate within the San Gorgonio Pass fault zone.

The San Bernardino strand coincides spatially with the projected trace of the Mission Creek fault, and probably evolved by reactivation of that older strand. By this interpretation, the Mission Creek fault is responsible for juxtaposing exotic far-travelled Pelona Schist bedrock of the San Bernardino valley against the Wilson Creek block to the north, and the San Bernardino strand is only a relatively recent break that developed within or close to the older fault.

We recognize three segments of the San Bernardino strand: a segment extending from Cajon Pass to the vicinity of Mill Creek, a segment extending from Mill Creek to the vicinity of Banning Canyon, and a segment extending from Banning Canyon to the Burro Flats area north of San Gorgonio Pass. Distinction between these three segments is based on contrasts in geologic structure and tectonic geomorphology.

Cajon Pass-Mill Creek segment.--The San Bernardino strand between Cajon Pass and Mill Creek is characterized by its conspicuous geologic and geomorphic expression, by its overall simplicity, and by abundant evidence for youthful activity: (1) The segment is relatively continuous and only slightly curved, and is not sinuous. It does not have significant left or right steps along its trace, although minor steps between overlapping fault segments occur locally. (2) Youthful activity along the segment is indicated by well developed primary fault features (scarps, sag ponds, pressure and shutter ridges) and by youthful geologic and physiographic features (alluvial fans, landslides, drainage lines) that have been offset by the fault throughout Holocene time. The fault cuts and forms scarps in all Holocene alluvial units, except for the youngest active stream alluvium. In the active sediments, shallow ground water is backed up behind the fault and its trace is marked by linear vegetation lines. (3) The San Bernardino Mountain front along the segment generally has low topographic relief, particularly to the northeast (Weldon and Meisling, 1982; Weldon, 1983), although relief gradually increases southeastward toward Mill Creek. These relations indicate that this segment of the San Bernardino strand has not generated significant amounts of vertical displacement (Weldon, 1985b). (4) In Cajon Pass the segment has a well documented Holocene slip rate of about 25 mm/year (Weldon and Sieh, 1985). Rasmussen (1982) indicates a similar rate of Holocene slip near San Bernardino.

Mill Creek-Banning Canyon segment.--Between Mill Creek and Banning Canyon the San Bernardino strand is characterized by its lack of clear continuous geomorphic expression and by its structural complexity locally.

Between Santa Ana River and the canyon mouth of Mill Creek, the San Bernardino strand maintains its regional strike of about N 70° W but becomes increasingly complex. Directly west of Mill Creek, bedrock and surficial units are traversed by several parallel fault strands, some of which are part of the San Andreas zone; locally, these strands have north-facing scarps (Matti and others, 1992). None of these faults breaks youngest deposits of Mill Creek wash, but on the east side of the wash vintage aerial photographs reveal a scarp that disrupts surficial deposits that have attributes of soil-stage S6 or S7 of McFadden (1982), and the unit probably is middle to late Holocene in age.

Southeast of Mill Creek the San Bernardino strand adopts a regional trend of about N 55° W, is complex structurally, and is complicated by landslide masses that have been shed from the Mill Creek Formation on Yucaipa Ridge (map sheet 2; Matti and others, 1992). These landslides have numerous crown scarps that resemble scarps created by faults, and it is difficult to associate any of these geomorphic features with the San Bernardino strand. The antiquity of the landslide masses is unknown. Whatever their age, right-slip on the San Bernardino strand has not displaced them laterally to any measurable degree. This reflects either (1) the youthfulness of the landslides or (2) the fact that the San Bernardino strand may step left around and beneath the

landslide masses (Matti and others, 1992), in the process leaving most of them effectively attached to the Yucaipa Ridge block. We favor the latter hypothesis.

The left-stepping geometry is more conspicuous to the southeast toward Wilson Creek (Harden and Matti, fig. 2). In plan view, the fault pattern here consists of short northwest-trending fault segments that pass into northeast-trending fault-like scarps. The latter probably are north-dipping reverse faults, but we have not confirmed this speculation; in other fault systems, reverse dip-slip fault segments are common within left-stepping right-lateral strike-slip fault zones, and their occurrence in this vicinity would be compatible with the apparent left-stepping geometry of the San Bernardino strand along this reach. Locally, stream gullies and other geomorphic features have been displaced right-laterally by the northwest-trending fault segments. This evidence for youthful right-slip on the San Bernardino strand southeast of Mill Creek Canyon is complemented by convincing evidence for longer term right-slip throughout the latest Pleistocene and Holocene (Harden and Matti, 1989).

Between Wilson Creek and Banning Canyon the trace of the San Bernardino strand is not well defined, and it may have local left steps. Primary fault features generally are not common between Wilson Creek and Banning Canyon, and geologic and geomorphic evidence for youthful right-lateral activity is not obvious. The segment does not appear to cut or form scarps in youngest Holocene alluvial units, and the fault trace locally is overlapped by unfaulted landslide deposits. The San Bernardino Mountain front along the segment has considerable topographic relief, culminating in a 5,000-foot escarpment near Banning Canyon. This suggests that significant vertical movements have occurred along the segment.

Banning Canyon-Burro Flats segment.--Along the Banning Canyon-Burro Flats segment the regional strike of the San Bernardino strand turns abruptly southeastward toward San Gorgonio Pass. Southeast of Banning Canyon the fault zone is marked by springs, bedrock scarps, and lineaments, and Allen (1957), Dibblee (1975a, 1982), and Farley (1979) report that the fault forms a gouge zone in the crystalline rocks. Farther southeast, in an alluviated intermontane area known as Burro Flats, youthful-appearing northwest-trending en-echelon scarps that disrupt Holocene alluvial deposits and Pleistocene landslide debris may have been formed by the modern San Andreas fault. However, the origin of these scarps is questionable: they face northeast and have trends that are similar to other northeast-facing scarps in the region that are not part of the San Andreas fault zone (for example, the family of northeast-facing scarps on the Beaumont Plain), and it is possible that they formed within an extensional strain field rather than by right-slip along the trace of the modern San Andreas fault. If so, then there may be no evidence for recent activity on the San Bernardino strand (modern San Andreas) southeast of Banning Canyon. If they were formed by the San Andreas, these scarps are the southeasternmost evidence for a surface trace of the San Bernardino strand: between Burro Flats and the Banning fault, alluvial deposits are not cut by faults attributable to the San Andreas, and bedrock exposures are not traversed by major fault zones.

Lack of fault features led Allen (1957) to conclude that the modern San Andreas fault (our San Bernardino strand) dies out before reaching San Gorgonio Pass, although Dibblee (1968a, 1975a, 1982) concluded that the fault (his south branch) continues through San Gorgonio Pass and into the Coachella Valley. We do not know if the San Bernardino strand is continuous between Banning Canyon and San Gorgonio Pass or if it has generated the full right-lateral displacement (3 km) that we recognize in the vicinity of Mill Creek (discussed below). The total displacement gradually may fall off between Mill Creek and Burro Flats, so that the fault in the vicinity of San Gorgonio Pass has considerably less displacement and may not have been active recently. We tentatively agree with Allen's conclusion that the modern San Andreas fault dies out southeastward before it reaches San Gorgonio Pass.

GEOLOGIC HISTORY, SAN BERNARDINO MOUNTAINS SEGMENT, SAN ANDREAS FAULT

The San Bernardino Mountains segment of the San Andreas fault consists of four separate fault strands that evolved sequentially; each strand generated right-lateral displacements during a specific period and then was abandoned and succeeded by a younger strand. We have determined the sequence in which the four strands evolved, but we have not confirmed the timing and amount of displacement for all of them. Even though some elements of their movement history are ambiguous, however, one fact seems clear: together, the four strands record the total history of the San Andreas fault (*sensu stricto*) since its inception 4 or 5 m.y. ago.

Sequencing relations

The relative sequence in which the four strands evolved can be determined from structural relations between them and by the alluvial units that overlap the strands or are broken by them. The Wilson Creek fault is the oldest strand, followed sequentially by the Mission Creek, Mill Creek, and San Bernardino strands.

The Wilson Creek fault is demonstrably older than the Mission Creek fault because the Mission Creek truncates faults we interpret as part of the Wilson Creek strand and because the trace of the Wilson Creek everywhere is more curving and discontinuous than that of the Mission Creek. These relations suggest that the Wilson Creek fault is an older strand that was deformed and then succeeded by the less sinuous Mission Creek fault. The Mill Creek fault is younger than either the Wilson Creek or Mission Creek faults because it displaces late Quaternary gravel units that are not broken by either of the older faults (discussed below). The San Bernardino strand is the youngest of the four strands, and forms the modern trace of the San Andreas fault in the San Bernardino Mountains segment.

Faulting chronology

Wilson Creek and Mission Creek faults.--Our conclusion that the four strands of the San Bernardino Mountians segment record the full history of the San Andreas fault (*sensu stricto*) requires that the oldest strand--the Wilson Creek fault--developed when the San Andreas first evolved. The timing of initial movements on the Wilson Creek fault cannot be determined directly from relations in the San Bernardino Mountains but can be inferred from relations elsewhere in the region.

In the Whitewater area, south of all strands of the San Andreas fault but north of the Banning fault, Miocene and Pliocene sedimentary units all record about the same amount of right-lateral displacement from their probable depositional positions. Relevant units include the Coachella Fanglomerate, which is about 10 m.y. old (Peterson, 1975), and unconformably overlying beds of the Painted Hill and Imperial Formations, older parts of which are 6 m.y. old and older (Table 2). Dillon (1975, p. 334-365, fig. 70) proposed that the San Andreas fault has displaced the Coachella Fanglomerate and Imperial Formation from cross-fault counterparts in the southern Chocolate Mountains, a proposal we accept here. Moreover, conglomeratic beds of the Painted Hill Formation contain clasts that indicate source areas east of the southern Salton Trough. The fact that the Miocene Coachella Fanglomerate and unconformably overlying late Miocene and Pliocene units all record the same displacement requires that the San Andreas fault displaced them together during an episode of right-lateral faulting that commenced after 6 Ma. This timing is compatible with the proposed inception of the San Andreas fault (*sensu stricto*) in southern California, which most workers link with the onset of seafloor spreading in the Gulf of California and northwestward propagation of the East Pacific Rise (Moore and Buffington, 1968; Larson and others, 1968; Atwater, 1970; Elders and others, 1972; Moore, 1973; Crowell, 1979, 1981). The precise timing of this event is disputed, but about 4 or 5 Ma is a widely cited figure. Thus, initial movements on the Wilson Creek strand of the San Andreas fault occurred after 6 Ma and probably during the earliest Pliocene, 4 or 5 m.y. ago.

Initiation of the San Andreas fault (*sensu stricto*) also has been linked with termination of movement on the San Gabriel fault. According to Crowell (1982, p. 35, fig. 12), major right-lateral activity on the San Gabriel fault ceased about 5 m.y. ago when the Pliocene Hungry Valley Formation began to accumulate in Ridge Basin. Crowell suggests that right-slip was initiated on the San Andreas at or slightly before that time, although sequencing relations between deposition of the Hungry Valley Formation and initial movements on the San Andreas fault have not been documented.

Eclipse of the San Gabriel fault by the San Andreas fault about 5 m.y. ago corresponds nicely with the maximum age suggested for opening of the Gulf of California (4.9 m.y. ago according to Curray and Moore, 1982). Curray and Moore (1984) proposed a two-phase model for the geologic history of the Gulf: an early phase of diffuse extension, crustal attenuation, and rifting that may have been accompanied by formation of oceanic crust without lineated magnetic anomalies, followed time-transgressively by a later phase of opening accompanied by formation of lineated magnetic anomalies. The early extensional phase commenced 5.5 m.y. ago, but the actual opening phase commenced at about 4.9 Ma and culminated at about 3.2 Ma. Thus, the San Gabriel fault waned, the San Andreas fault (*sensu stricto*) evolved, and the Gulf of California opened--all about 4.9 m.y. ago. Linkage between these events needs to be documented, however, and this scenario has problems. For example, Curray and Moore (1984, p. 29) conclude that 300 km of right-slip on the combined San Andreas and San Gabriel faults correponds with the 300-km separation of Baja California from mainland Mexico, and that right-slip along the onshore faults commenced 5.5 m.y.B.P. This interpretation is in conflict with the onshore evidence (Crowell, 1981, 1982; Ehlig, 1981; Matti and others, 1986; Matti and Morton, 1992), and illustrates the lack of congruence between onshore and offshore histories.

We have not documented the timing of critical events like the duration of right-slip activity on the Wilson Creek and Mission Creek faults or when the Wilson Creek fault was eclipsed by the Mission Creek fault. These elements of faulting history require information about total displacement, rate of slip, and (or) the age of sedimentary units that date the critical events--questions that presently are unanswered by our studies.

The timing of latest strike-slip displacements on the Wilson Creek and Mission Creek faults is clearer than the timing of their early activity. In the vicinity of Whitewater River and Mission Creek, both faults are buried by Pleistocene gravel deposits (Matti and others, 1982a) that bear stage-S2 soils of McFadden (1982) and thus are at least 0.5 m.y. old (McFadden, 1982, p. 55-64, 344-349, 352-354, fig. 16). Farther west, in the Raywood Flat area, the two faults are buried by Pleistocene gravels that appear to correlate with those in the Whitewater-Mission Creek region. Farther northwest, between Banning Canyon and the Cajon Pass region, the Wilson Creek and Mission Creek faults are buried wherever they are associated with Quaternary alluvium.

The absence of primary fault features provides additional evidence for inactivity on the Wilson Creek and Mission Creek faults during late Quaternary time: neither fault displays scarps, sag ponds, shutter or pressure ridges, or right-laterally offset drainage lines. A degraded north-facing scarp that traverses Pleistocene gravels in the Raywood Flat area (Matti and others, 1983) is a possible exception. The scarp is associated with a north-dipping fault noted by Ehlig (1977) and mapped by Farley (1979); the fault breaks the Raywood Flat gravels at their east margin and drops them down to the north. Both Ehlig (1977) and Farley (1979) cite this fault as evidence for youthful right-lateral activity within the Mission Creek-Wilson Creek fault zone. However, we interpret it as a normal dip-slip fault that is part of a family of late Quaternary dip-slip faults in the region that have northeast- or north-facing scarps. The fault coincides with, and has reactivated, the Wilson Creek-Mission Creek fault zone in the vicinity of Raywood Flat, but diverges from it farther west (Matti and others, 1983). Thus, we conclude that the Wilson Creek and Mission Creek strands are abandoned right-lateral faults that have been bypassed by the San Andreas system.

Mill Creek fault.--The Mill Creek fault is a late Quaternary strand that is younger than the Wilson Creek and Mission Creek strands but older than the San Bernardino strand. The fault probably has not been a throughgoing right-lateral strand of the San Andreas during Holocene and latest Pleistocene time, and we propose that it has been abandoned and bypassed by the San Andreas system. Locally, the strand has been reactivated by dip-slip movements that have formed north-facing scarps in alluvium and in bedrock.

If our observation is correct that it has displaced Pleistocene gravel deposits and pre-Pleistocene crystalline rocks by about the same amount (discussed below), then the Mill Creek fault generated all of its right-slip displacement during late Pleistocene time. Faulting occurred more recently than about 0.5 Ma, the minimum age for Pleistocene gravel deposits displaced the full amount by the fault: (1) Gravels in the vicinity of Mission Creek and Whitewater River that are displaced 8 to 10 km from possible cross-fault counterparts north of Desert Hot Springs bear stage-S2 soils (McFadden,

1982, p. 55-64) and are at least 0.5 m.y. old; (2) gravels in the vicinity of Raywood Flat that have been displaced about 8 km from Hell For Sure Canyon and the North Fork of the Whitewater River are late Pleistocene, and probably are the same age as those in the vicinity of Mission Creek.

The Mill Creek fault is not a modern neotectonic strand of the San Andreas fault. For most of its extent, the fault is buried by Holocene and latest Pleistocene alluvial deposits. This relation can be observed at several localities between Waterman Canyon and the head of Mill Creek Canyon. Moreover, the strand does not form primary fault features such as sag ponds, shutter and pressure ridges, and right-laterally offset drainage lines. Scarps occur along some segments of the fault: for example, in the Harrison Mountain and San Bernardino North 7.5' quadrangles (Morton and Miller, 1975; Miller, 1979), north- and northeast-facing scarps disrupt bedrock and older Pleistocene alluvial deposits (Allen, 1957, p. 343); the sense of displacement indicated by scarps and faulted contacts is down on the north. Latest displacements on the Mill Creek fault in this vicinity probably represent dip-slip reactivation of the strand, and the north-side-down movements may be related to partial subsidence of the San Bernardino Mountains following their uplift during the Pleistocene (Weldon and Meisling, 1982; Meisling, 1984; Weldon, 1983, 1985b).

North of Raywood Flat the Mill Creek fault zone may have been the site of modern movements, but we have not determined their recency or sense of displacement. At the head of the Middle Fork of Whitewater River (the Middle Fork Jumpoff), alluvial units overlying the crush zone of the Mill Creek fault are broken by a conspicuous fault plane that dips steeply to the north and drops alluvial deposits to the north against crystalline rocks to the south (Allen, 1957, pl. 1; Farley, 1979, p. 86-88, fig. 9). This fault appears to form a degraded north-facing scarp that can be traced a short distance west from the Middle Fork Jumpoff (J.C. Matti and J.W. Harden, unpubl. data). The faulted alluvial deposits are a north- and south-thinning wedge of colluvial sand and gravel derived from highlands to the north and south. Uppermost layers of the north-thinning wedge are youthful and have only incipient soil-profile development. It is not clear if these youngest deposits are faulted, or if they buttress depositionally against the degraded fault scarp.

Several problems plague this locality: (1) The age of the faulted alluvial deposits has not been determined, nor have their stratigraphic and paleogeographic relations to Pleistocene fluvial gravels of the nearby Raywood Flat area that have been displaced 8 km by the Mill Creek fault. (2) It is not clear that the obvious fault plane represents strike-slip movements on the Mill Creek fault--most of whose crush zone is buried by the alluvial deposits--or activity on one of the other numerous faults that traverse the Raywood Flat region. It is possible that the fault plane, with its north-facing scarp and down-on-the-north separation, represents dip-slip displacements like those that have occurred on the Mill Creek fault farther to the west. Available data do not confirm or refute Holocene right-slip displacements on the Mill Creek fault here or to the east. Farley (1979) explored the possibility that youthful displacements have occurred on the fault east of the Middle Fork Jumpoff, but have died out to the west. Our data cannot rule out this proposal. However, because of the absence of primary fault features throughout most of the alluvial cover here, we suspect that the fault in this region has not generated throughgoing right-lateral displacements since latest Pleistocene time.

San Bernardino strand.--The San Bernardino strand is the modern neotectonic component of the San Andreas fault in the vicinity of the south-central Transverse Ranges, and has generated right-lateral displacements throughout Holocene and latest Pleistocene time. If the strand has maintained the 25 mm/year Holocene slip rate determined for the fault in Cajon Pass (Weldon and Sieh, 1985), and if it has generated no more than about 3 km of displacement, then right-slip on the modern neotectonic trace of the San Andreas fault in the Transverse Ranges segment commenced about 120,000 yr. ago.

Although the San Bernardino strand apparently did not generate ground ruptures during the 1857 earthquake (Sieh, 1978a,b), it should be viewed as a fault capable of generating large or even great earthquakes (Allen, 1968, 1981; Sieh, 1981; Rasmussen, 1981; Raleigh and others, 1982; Lindh, 1983; Nishenko and Sykes, 1983; Sykes and Seeber, 1982; Sykes and Nishenko, 1984; Ziony and Yerkes, 1985; Wesson and Wallace, 1985; National Earthquake Prediction Evaluation Council, 1988). Most earthquake scenarios for this part of southern California incorporate ground-rupture lengths of several hundred kilometers and moment magnitude of 8 or greater (Raleigh and others, 1982; Sykes and Nishenko, 1984; Lindh, 1983). Some workers suggest that an earthquake comparable to the 1857 event might lead to ground rupture on the San Bernardino strand northwest through Cajon Pass and onto the Mojave Desert segment, and possibly southeast through San Gorgonio Pass and into the Coachella Valley region where other neotectonic components of the San Andreas fault would be activated. Such scenarios need to be tested in a rigorous way, however, and other scenarios may be possible (Rasmussen, 1981; Weldon and Sieh, 1985, p. 811-812). Ground-rupture patterns within the San Andreas fault zone will become more predictable only when we understand the overall fabric of a region where the San Andreas fault is only one of several neotectonic elements.

Amount of displacement: previous interpretations

Following Crowell's (1962) proposal that the San Andreas fault in southern California has 210 km of right-lateral displacement, many workers have attempted to apportion this displacement among various San Andreas strands in the southeastern San Bernardino Mountains. Gibson (1964, 1971) inferred on the basis of paleocurrent and clast-provenance studies that the Mill Creek fault has displaced the Miocene Mill Creek Formation (of Gibson, 1971) about 120 km from its original position adjacent to the Orocopia Mountains. Dibblee (1968a, p. 269) concluded that, if Crowell's 210 km of right slip has occurred along strands of the San Andreas in the San Bernardino Mountains, then the largest movement probably occurred along his north branch (Mill Creek fault). Later, Dibblee (1975a, p. 134) proposed that the north branch generated about 96 km of right slip and displaced crystalline rocks in the southeastern San Bernardino Mountains from presumed cross-fault counterparts in the Orocopia Mountains. Dibblee (1982b, p. 164) subsequently increased this value to 120 km--a displacement identical to Gibson's (1964, 1971) and presumably based on Gibson's palinspastic restoration of the Mill Creek strata to the Orocopia Mountains region.

Neither Gibson (1964, 1971) nor Dibblee (1968a, 1975a) accounted for the large difference between their proposed displacements on the Mill Creek fault (96 to 120 km) and Crowell's (1962) proposal for total displacement on the San Andreas (210 km). This difference presumably was made up by other faults in the region. However, Dibblee (1968a, p. 168) had ruled out his south branch of the San Andreas because the fault has only a few km of right slip in the San Gorgonio Pass area, leaving only the Banning and San Jacinto faults to take up the missing 90 km. However, neither of these faults qualifies for the following reasons: (1) the Banning did not generate right-lateral displacements at the same time as the San Andreas (*sensu stricto*) and therefore does not figure into the 210-km reconstruction proposed by Crowell (1962); (2) the San Jacinto has no more than 25 or 30 km of displacement (Sharp, 1967); and (3) neither fault figures into palinspastic reconstruction of rocks in the southeastern San Bernardino Mountains because both faults pass outboard of that region.

Dillon's (1975) proposal that the north branch of the San Andreas has displaced rocks in the southeastern San Bernardino Mountains from counterparts in the southern Chocolate Mountains (discussed above) provided a major alternative to the proposals by Gibson and Dibblee. Dillon's displacement on Dibblee's north branch (180±20 km) is considerably greater than the displacements proposed by Gibson and Dibblee (96 to 120 km), but both estimates seemed equally attractive based on the merits of their underlying cross-fault correlations.

This conflict was resolved by later studies in the San Bernardino Mountains that reinterpreted the bounding faults between distinctive basement terranes. Ehlig (1977), Farley (1979), and Matti and others (1983a, 1985) showed that the Mill Creek fault (Dibblee's north branch) does not form a major break between crystalline rocks as Gibson (1971) and Dibblee (1968a, 1975a, 1982a) believed. Instead, lithologic similarities between crystalline rocks on either side of the fault preclude large right-lateral displacements on this strand of the San Andreas (Matti and others, 1985, p. 9). Thus, the Mill Creek fault could not have displaced Gibson's Mill Creek strata by more than a few kilometers from their depositional position. Building on Ehlig's (1977) earlier work, Farley (1979) demonstrated that the major lithologic break between crystalline rocks is formed by the Mission Creek fault of Allen (1957)--an interpretation refined by Matti and others (1983a, 1985). This fault--not the Mill Creek strand (Dibblee's north branch)--was shown to be the San Andreas strand that juxtaposed rocks of San Gabriel Mountains-type against rocks of San Bernardino Mountains-type as proposed by Dillon (1975; see Farley, 1979, p. 120-129; Matti and others, 1985, p. 9-10). This clarified the distribution of major basement terranes and their bounding faults and set limits on displacements for individual strands, but left two factors still unresolved: (1) the palinspastic position of the Mill Creek Formation alleged to have originated near the Orocopia Mountains and (2) the 40-km to 80-km discrepancy between Dillon's estimate of 180±20 km of displacement on the San Andreas and the widely cited estimate of 240 km (upgraded by Crowell, 1975a, 1981, and Ehlig, 1981, from Crowell's original estimate of 210 km).

The slip discrepancy was reemphasized when Matti and others (1985, 1986) proposed that total right slip on the San Andreas fault in the vicinity of the San Bernardino Mountains may be no more than 160±10 km. This estimate corresponds nicely with the lower limit of Dillon's estimate of 180±20 km, and both proposals indicate that estimates of 210 to 240 km for total right slip on the San Andreas fault (*sensu stricto*) in southern California may be too large. We adopt this position, and use the 160-km displacement together with estimates for displacement on other strands of the San Andreas zone to reconstruct fault-movement histories for individual strands of the San Andreas in the vicinity of the San Bernardino Mountains.

Amount of displacement: new possibilities

Our conclusion that the Wilson Creek, Mission Creek, Mill Creek, and San Bernardino strands record the full history of the San Andreas fault (*sensu stricto*) requires that their individual displacements sum to the total displacement on the fault in southern California. Estimates for this total range from less than 100 km to 270 km, but the most widely cited studies have focused on a range of 210 km (Crowell, 1962) to 240 km (Crowell, 1975a; Ehlig and others, 1975; Ehlig, 1981, 1982). By contrast, Matti and others (1985, 1986; Frizzell and others, 1986) concluded that the San Andreas fault in southern California probably has no more than 160±10 km of total displacement. This smaller displacement is based on the proposal that distinctive bodies of Triassic megaporphyritic monzogranite that occur in the Mill Creek region of the San Bernardino Mountains (Monzodiorite of Manzanita Springs of Morton and others, 1980; unit Trm of Matti and others, 1992) and in the Liebre Mountain area on the opposite side of all strands of the San Andreas fault represent segments of a formerly continuous pluton that was severed and displaced by the fault. We adopt the 160-km displacement, and apportion it between the four strands of the San Bernardino Mountains segment of the San Andreas fault.

San Bernardino strand.--We propose that the San Bernardino strand has no more than 3 km of displacement. This hypothesis is based on evidence from Pleistocene alluvial deposits and crystalline bedrock that occur south of the fault between Mill Creek and the Santa Ana River. The gravels were deposited by ancestral streamflows of Mill Creek, and contain several distinctive clast types traceable to bedrock sources drained by the modern stream Since their deposition, the gravels have been displaced no more than 3 km by the San Bernardino strand (Matti and others, 1992). The gravel deposits are capped by soil profiles that have thick, well developed, red argillic horizons comparable to those in old Pleistocene soils (stage S2 soils of McFadden, 1982). The bedrock is a slice of crystalline rock from the Wilson Creek block; although we cannot identify an exact cross-fault counterpart for this slice, it constrains right-lateral displacements on the San Bernardino strand to no more than 3 km.

Mill Creek strand.--Available evidence suggests that the Mill Creek fault has no more than 8 to 10 km of right-lateral displacement. This conclusion is based on four separate geologic relations:

(1) In the vicinity of Raywood Flat, thick deposits of Quaternary gravel appear to have been displaced about 8 km by the Mill Creek fault (Sheet 2, A-A', B-B'). The gravel was derived primarily from crystalline-rock sources north of the fault and was deposited in an intermontane-valley setting. The bilobate shape of the gravel body suggests that the alluvial fill was derived from two large converging drainages lying to the north of the Mill Creek fault. Such drainages do

not exist north of the present position of the Raywood Flat area, but two drainages with the appropriate size, orientation, and spacing do exist east of this area and north of the Mill Creek fault--the North Fork of the Whitewater River and Hell For Sure Canyon. These two large drainages most likely were the source for the Quaternary fill in the Raywood Flat area--a paleogeographic reconstruction requiring about 8 km of right-slip on the Mill Creek fault since deposition of the Raywood Flat gravels.

(2) Bodies of metaquartzite, marble, and minor schist that occur on both sides of the fault on the north and south flanks of Mill Creek Canyon appear to be parts of a single metasedimentary sequence that has been severed by the fault and displaced no more than 10 km (Sheet 2, C-C'). The metasedimentary bodies, first mapped by Dibblee (1964), occur in Mill Creek Canyon on the north side of the Mill Creek fault and on Yucaipa Ridge on the south side of the fault. Farley (1979, p. 107, fig. 13) reasoned that the two metasedimentary bodies could be displaced counterparts, but he discounted their exact cross-fault correlation because of differences in lithologic detail; instead, he cited them as evidence for the overall lithologic similarity of rocks on either side of the Mill Creek fault. Detailed differences in lithology and stratigraphic sequence exist between the two bodies, but we attribute these to metamorphic modification that occurs along strike in both areas and we interpret the two bodies as displaced counterparts.

(3) Bodies of distinctive granodioritic orthogneiss (orthogneiss of Alger Creek of Matti and others, 1992) that occur on both sides of the fault in Mill Creek Canyon appear to be severed parts of a single pluton that have been displaced no more than about 10 km (Sheet 2, D-D').

(4) Pleistocene gravel deposits overlying the Coachella Fanglomerate in the vicinity of the Whitewater River and Mission Creek drainages (Matti and others, 1982a) are similar to, and have some clast types in common with, gravel deposits north of the Coachella Valley segment of the San Andreas fault near Desert Hot Springs (Sheet 2, E-E'). Dibblee (1967b) originally assigned the Desert Hot Springs gravels questionably to the Miocene Coachella Fanglomerate, but they probably are Quaternary (Proctor, 1968). Restoration of about 8 to 10 km on the Mill Creek fault and the Coachella Valley segment of the San Andreas aligns the gravels north of Desert Hot Springs with those in the vicinity of Mission Creek and Whitewater River, which suggests that the two deposits may be parts of a coalescing alluvial-fan complex that since has been displaced by the Mill Creek strand.

Thus, available evidence from both crystalline rocks and Quaternary alluvial deposits indicates that the Mill Creek strand of the San Andreas fault has no more than 8 to 10 km of right-lateral displacement, and is not a major strand of the San Andreas fault.

Mission Creek and Wilson Creek strands.– Displacements on the Mission Creek and Wilson Creek faults presently cannot be determined directly on the basis of specific cross-fault correlations. Originally, we proposed that the two faults are major strands of the San Andreas that in combination have brought exotic rocks against the San Bernardino Mountains from original positions as much as 150 km farther southeast in the Coachella Valley region (Matti and others, 1985, p. 9-10). We proposed that the Wilson Creek strand had considerably more displacement than the Mission Creek strand, but we acknowledged the uncertainties in this model and pointed out that an equally likely reconstruction of displaced crustal blocks could be achieved if the Mission Creek fault, rather than the Wilson Creek fault, had the larger displacement. We now favor this role reversal between the two fault strands.

We assign right-slip estimates to the Mission Creek and Wilson Creek faults based on three arguments: (1) the hypothesis that these two faults, along with other strands of the San Andreas system, have displaced the Mill Creek and Liebre Mountain Triassic megaporphyry bodies by no more than 160 km; (2) cross-fault correlation between rocks of San Gabriel Mountains-type in the southeastern San Bernardino Mountains and similar rocks in the Chocolate Mountains (Dillon, 1975); and (3) correlation of fault segments in the San Bernardino Mountains with other fault strands of the San Andreas zone in the San Gabriel Mountains.

As discussed by Matti and Morton (in press), total displacement on the San Andreas fault (*sensu stricto*) in the vicinity of the San Bernardino Mountains is the sum of displacements on individual faults that jointly have displaced the Liebre Mountain megaporphyry body away from its cross-fault counterpart in the Mill Creek region:

$$A + B + C + D + E = 160 \text{ km},$$

where A = San Bernardino strand, B = Mill Creek strand, C = San Jacinto fault, D = Mission Creek strand, and E = Wilson Creek strand.

The slip equation can be partly solved using the following values:

A = about 3 km of right slip on the San Bernardino strand. This displacement has fed into the Mojave Desert segment of the San Andreas.

B = about 8 km of right slip on the Mill Creek strand. This displacement fed into the Mojave Desert segment of the San Andreas.

C <25 km of right slip on the San Jacinto fault. Our original estimate for strand displacements in the San Bernardino Mountains (Matti and others, 1985) did not incorporate the notion that slip on the San Jacinto fault has contributed to northwestward displacement of the Liebre Mountain megaporphyry body away from the San Bernardino Mountains. Our current interpretation is that most of the 25 km of right-slip proposed by Sharp (1967) for the San Jacinto fault in the Peninsular Ranges steps right from the San Jacinto fault to the San Andreas fault between San Gorgonio Pass and Cajon Pass, and thereby contributes to total slip on the Mojave Desert segment of the San Andreas (Matti and others, 1985; Morton and Matti, in press). The full 25 km may not have been transferred, however, because an unknown percentage of slip on the San Jacinto has been dissipated by extension within the right-stepping region of the San Bernardino Valley and absorbed by convergence within the Cucamonga fault zone and uplift of the southeastern San Gabriel Mountains (Matti and others, 1982b, 1985; Morton and Matti, 1987; Morton and Matti, in press). In this report we arbitrarily apportion 20 km of right slip on the San Jacinto fault to the San Andreas and 5 km to contractional and extensional deformation related to strain transfer between the San Jacinto and San Andreas faults.

Using slip data for A, B and C, the displacement equation is complete except for D and E, displacements on the Mission Creek and Wilson Creek faults:

$$3 \text{ km} + 8 \text{ km} + 20 \text{ km} + D + E = 160 \text{ km}.$$

Assuming values A, B, and C are correct and sum to 31 km, then values D and E (the combined displacements on the Mission Creek and Wilson Creek faults) sum to 129 km. Compare this value with the 150-km displacement we originally proposed for combined slip on the Mission Creek and Wilson Creek faults when we did not take into account slip contributed by the San Jacinto fault.

To arrive at values for D and E in the displacement equation, we turn to strike-slip faults in the San Gabriel Mountains that might be counterparts of either the Mission Creek fault or the Wilson Creek fault. Given our conclusion that the Mission Creek strand is middle Pliocene and younger in age and is a major fault that juxtaposed rocks of San Gabriel Mountains-type and San Bernardino Mountains-type, its counterpart in the San Gabriel Mountains should include faults of the same age that also juxtapose the two crystalline suites. By these criteria the Mission Creek strand is correlative with the Mojave Desert strand, which must be viewed as a major strand of the San Andreas that has a right-slip history extending from the present back to at least middle Pleistocene (Barrows and others, 1985, 1987). Although Barrows and others (1987, p. 2, 83, 85) indicated that the Mojave Desert strand (their "main trace") may be no older than 1 to 1.4 Ma, they (1987, p. 82) also pointed out that ". . . all rock units older than late Pleistocene that are juxtaposed along the main trace are dissimilar. . . ." We take this to mean that the Mojave Desert strand is the major trace of the San Andreas in the vicinity of the San Gabriel Mountains, and is responsible for juxtaposing rocks of San Gabriel Mountains-type against rocks of San Bernardino Mountains-type. Like other workers, we suspect that the Mojave Desert strand has a longer-lived history than proposed by Barrows and others (1985, 1987). Thus, we correlate the Mission Creek strand (and the younger Mill Creek and San Bernardino strands) with the Mojave Desert strand (and potentially with the Pliocene Nadeau faults).

If the Mission Creek and Mojave Desert strands are the major throughgoing traces of the San Andreas, then restoration of significant slip on that strand together with restored slip on the Mill Creek and San Bernardino strands would bring the northwest termination of the Punchbowl fault near Palmdale (fig. 1) closer to the southeast termination of the Wilson Creek fault in the southeastern San Bernardino Mountains. We propose that the Wilson Creek and Punchbowl faults originally formed a single throughgoing structure that was severed by younger strands of the San Andreas fault; the displaced segments of the once-continuous structure now are situated in the San Bernardino and San Gabriel Mountains. Comparison of the Wilson Creek and Punchbowl faults is supported by three lines of evidence: (1) they generated right-lateral displacements during the same time period (5 or 6 Ma to about 3.5 Ma, although Barrows, 1987, would have activity on the Punchbowl fault be as young as 2 Ma); (2) they both have sinuous traces and west-dipping reverse dips; and (3) they both bound crystalline-rock slices (the Wilson Creek block and crystalline rocks of Pinyon Ridge in the San Gabriel Mountains) that have no documented affinity with particular crystalline terranes in southern California but are broadly similar to each other. We propose that the Punchbowl and Wilson Creek strands of the San Andreas once formed a continuous throughgoing right-lateral fault that had about 40 to 45 km of displacement based on estimates for the Punchbowl fault in the San Gabriel Mountains. In this report, we use the 40-km figure and insert this value for E in the displacement equation.

Using slip data for A, B, C, and E, the displacement equation

$$3 \text{ km} + 8 \text{ km} + 20 \text{ km} + D + 40 \text{ km} = 160 \text{ km}$$

can be solved for D, yielding a displacement of 89 km for the Mission Creek strand of the San Andreas fault.

SYNTHESIS

Available data lead to a preliminary history of the San Andreas fault in the vicinity of the Transverse Ranges (fig. 4):

(1) Following inception of the San Andreas fault 4 or 5 m.y. ago, about 40 km of right-slip on the throughgoing Wilson Creek-Punchbowl fault juxtaposed exotic crystalline and sedimentary rocks of the Wilson Creek block against the San Bernardino Mountains (fig. 4A). Rocks native to the San Bernardino Mountains, including Triassic megaporphyritic monzogranite discussed by Matti and others (1986; Frizzell and others, 1986), were displaced to the northwest by these offsets, and the Wilson Creek block and Mill Creek Formation were juxtaposed against rocks native to the San Bernardino Mountains. During this period, the Wilson Creek-Punchbowl fault probably was a straight throughgoing strand that was continuous to the northwest and the southeast with the Mojave Desert and Coachella Valley segments of the San Andreas fault.

(2) Right-slip on the Wilson Creek-Punchbowl fault terminated when it was deformed into a sinuous trace and was bypassed by the Mission Creek fault (fig. 4B). This event occurred adjacent to the left-lateral Pinto Mountain fault, and left the Wilson Creek block stranded against the San Bernardino Mountains block. Thereafter, the San Bernardino and Wilson Creek blocks functioned as a single structural unit, with the Wilson Creek block behaving as though it was native to the region.

(3) The Mission Creek fault juxtaposed Pelona Schist and associated upper-plate rocks like those in the eastern San Gabriel Mountains against the Wilson Creek block (fig. 4C). The throughgoing Mission Creek fault was continuous to the northwest and southeast with the Mojave Desert and Coachella Valley segments of the San Andreas. Ultimately, the Mission Creek fault and adjacent rocks were deflected to the west and southwest as a left step developed in the San Andreas fault (fig. 4D), and the strand was abandoned and bypassed by the San Andreas transform system.

(4) The Mill Creek fault evolved inboard of the locked up Mission Creek fault (fig. 4E), and generated about 8 km of right-lateral displacement during the late Pleistocene (after about 0.5 Ma). Subsequently, the Mill Creek fault was deformed and apparently abandoned as a throughgoing right-lateral fault.

(5) The San Bernardino strand marks the trace of the modern neotectonic strand of the San Andreas fault within the Transverse Ranges segment (fig. 4F). This strand probably has reactivated the older Mission Creek strand in the vicinity of the San Bernardino valley.

Discussion

Several questions can be asked about the history of the San Andreas fault in the vicinity of the south-central Transverse Ranges. Why did several strands evolve? By what mechanism was each strand deformed and succeeded by a younger strand, and how much time did such a transition involve? Were there gaps in right-slip activity on the San Andreas fault during these periods? If so, did right-slip transfer from the San Andreas to some other fault in the San Andreas transform system? What impact did deformation of the Wilson Creek and Mission Creek faults have on the region? Or alternatively, were these two faults deformed in passive response to other events in the region? Does the Pliocene and early Pleistocene history of the San Andreas fault provide a precedent for the modern neotectonic framework? Some of these questions can be addressed on the basis of existing data.

Several unique Pliocene-Pleistocene structural and physiographic elements coincide in the vicinity of the south-central Transverse Ranges--a juxtaposition that implies a cause-and-effect relation. The most important elements are (1) the multiple deformed strands of the San Andreas fault; (2) the Pinto Mountain fault, a major left-lateral structure that generated about 16 km of displacement (Dibblee, 1968b); and (3) the San Bernardino Mountains, a major physiographic element created by Pleistocene orogenesis (Meisling, 1984; Meisling and Weldon, 1989). Various authors have discussed the history of the San Andreas fault in the context of these unique structural and physiographic elements.

Allen (1957) contributed many original concepts, including (1) the idea that the present surface geometry of faults in the San Gorgonio Pass region differs from their original orientation parallel to the northwest regional strike of the San Andreas fault, and (2) the idea that faults of the San Andreas system are vying with east-oriented faults of the Transverse Ranges for structural control of the region. Allen (1957, p. 344-346, fig. 3) evaluated the structural setting of the San Gorgonio Pass region from the viewpoint of a regional triaxial strain field incorporating a principal stress direction oriented N-S and an intermediate stress direction that alternates between the E-W and vertical axes. Allen proposed that right-slip on San Andreas-type faults predominated when the intermediate stress was oriented vertically, but thrust faulting (and presumably left-slip on structures like the Pinto Mountain fault) predominated when the intermediate stress was oriented E-W. Allen's analysis applied mainly to Quaternary thrust faulting in San Gorgonio Pass, but by implication extends to the paleotectonic history of the Banning and San Andreas faults. The triaxial-strain concept was embellished by Farley (1979, p. 115-120) and by Crowell and Ramirez (1979, p. 31-32, 39), who evaluated relations between the San Andreas fault and the Pinto Mountain fault from the viewpoint of conjugate shear within a region undergoing simple shear.

Dibblee (1975a) evaluated the history of the south-central Transverse Ranges by relating deformation of the San Andreas fault to left-lateral displacements on the Pinto Mountain fault, and by relating these events in turn to uplift of the San Bernardino Mountains. In his analysis, left-lateral displacements on the Pinto Mountain fault impinged on the San Andreas and created a bottleneck that impeded throughgoing right slip; as a consequence, the Banning fault and segments of his north and south branches in the San Gorgonio Pass region were bent into east-west orientations, and the San Bernardino Mountains evolved through compressional uplift (Dibblee, 1975a, p. 134-135; 1982b). He suggested that these events occurred in late Quaternary time. Farley (1979, p. 115-129) envisioned a similar scenario, although he interpreted strands of the San Andreas fault differently than Dibblee and suggested that deformation of the San Andreas and Banning faults by left-slip on the Pinto Mountain fault occurred during late Pliocene time.

We agree that structural and physiographic elements in the south-central Transverse Ranges are linked in their evolution, but we differ from earlier workers in our view of how the various elements interacted with each other. For example, Dibblee (1975a, p. 134-135) and Farley (1979, p. 115-129) both suggest that left-slip on the Pinto Mountain fault deflected the Banning fault and all strands of the San Andreas fault during a single period of deformation. By contrast, we believe that the Banning fault acquired its east-trending orientation prior to inception of the San Andreas fault 5 m.y. ago, and that the Wilson Creek, Mission Creek, and Mill Creek faults each were deformed separately during compressional episodes that were followed by right-slip on the succeeding strand.

It seems certain that deformation of the San Andreas fault in the south-central Transverse Ranges is linked with orogenic uplift of the San Bernardino Mountains, but linkage between the two events cannot be documented in detail because their timing is known only in a general way. Recent studies suggest that uplift of the mountains commenced less than about 2.6 m.y. ago (Sadler, 1982a,b; May and Repenning, 1982; Weldon and Meisling, 1982; Meisling and Weldon, 1982, 1989; Sadler and Reeder, 1983; Meisling, 1984). We can demonstrate that the Mission Creek fault was being deformed during the Pleistocene and was abandoned before 0.5 m.y. ago, thus linking uplift and strand deformation during later parts of the Quaternary.

The Pinto Mountain fault probably played a role in the interaction between the San Andreas fault and the San Bernardino Mountains--although more likely as an effect than as a cause. The history of the Mission Creek fault may have bearing on the history of the Pinto Mountain fault. In the southeastern San Bernardino Mountains, the Mission Creek fault has a concave-south trace that occurs outboard of crystalline rocks native to the region. This curving geometry apparently was achieved as a bulge of San Bernardino Mountains basement was projected west and southwest across the path of the fault during the late stages of its activity--an event that accompanied deformation of the strand into its curving trace (fig. 4B,C, fig. 5). Left-slip on the Pinto Mountain fault could have achieved this effect by displacing the southeastern corner of the San Bernardino Mountains west and southwest relative to the little San Bernardino Mountains. The Pinto Mountain fault need not have truncated and offset the Mission Creek fault by this process: instead, gradual projection of the San Bernardino Mountains across the path of the San Andreas merely could have deflected or bowed the Mission Creek strand into a curved trace (fig. 5). When the curvature became too great to sustain right-slip, the Mission Creek was succeeded by other faults in the San Andreas family, including the San Jacinto fault zone and the Mill Creek strand (fig. 4C).

It is unclear whether left-slip on the Pinto Mountain fault continued throughout the history of the Mission Creek fault, thereby causing slow progressive deformation of the

strand, or whether the Mission Creek fault enjoyed an early history of right-slip unimpeded by regional compression. Ultimately, however, continued left-slip on the Pinto Mountain fault projected the San Bernardino Mountains farther across the path of the San Andreas fault, and the Mission Creek strand was abandoned and bypassed by the San Andreas transform system before 0.5 Ma (fig. 4D). The evolving intersection between the Mission Creek and Pinto Mountain faults probably resembled the curving intersection between the modern San Andreas fault and the Garlock fault in the Big Bend of the Tejon Pass region. Westward projection of the San Bernardino block created a significant geometric effect (fig. 5): the Mojave Desert and Coachella Valley segments of the San Andreas fault have been stepped left from each other by about 15 km, which is about the amount of left-lateral displacement on the Pinto Mountain fault (Dibblee, 1968b).

The Mill Creek fault did not exist when the Mission Creek fault was deformed, but subsequently broke in behind the barrier imposed by the bent and locked-up Mission Creek strand. This event occurred after about 0.5 Ma. Subsequent displacements on the Mill Creek fault sliced off the westward projection of the San Bernardino Mountains block created by left-lateral displacements on the Pinto Mountain fault. Ultimately, renewed left-slip on the Pinto Mountain fault kinked the Mill Creek fault in the vicinity of the Whitewater River Forks, and the Mill Creek fault, too, has been abandoned by the San Andreas system.

The history of the San Bernardino Mountains segment of the San Andreas fault may have included one or more slip gaps filled by other faults in southern California. For example, some authors have suggested that the San Jacinto fault evolved when right-slip on the San Andreas was impeded in the vicinity of the southeastern San Bernardino Mountains (for example, Crowell, 1981, p. 597), and that accelerated or deccelerated slip on these two faults may have alternated through time (Sharp, 1981, p. 1761). The long-term slip rate for the San Bernardino Mountains segment of the San Andreas fault may well have varied through time, but such a scenario can be documented only when the timing and amount of right-lateral displacements on the Mission Creek and Mill Creek strands of the segment are better understood.

SAN GABRIEL FAULT

Geologic setting

The San Gabriel fault extends southeastward from Ridge Basin to the western San Gabriel Mountains, where most workers recognize north and south branches (fig. 1). The north branch curves eastward through the San Gabriel Mountains to the southeastern part of the range, where its eastward continuation is obscured by a complex network of faults (Morton, 1975a). The south branch traverses the south flank of the San Gabriel Mountains, where the fault is obscured by the Quaternary frontal-fault zone that bounds the south margin of the mountains. Most workers suggest that the south and north branches rejoin in the vicinity of the eastern San Gabriel Mountains, but this structural reunion has not been documented and each worker has suggested a different arrangement of linking faults (contrast the views of Dibblee, 1968a, fig. 1, 1982a, fig. 1; Ehlig, 1973, fig. 1 and 1981, fig. 10-2; Crowell, 1975a, fig. 1; 1975c, p. 208-209; 1982a, fig. 1). According to the generally accepted view, the combined south and north branches of the San Gabriel fault must work their way through the structural complexity of the eastern San Gabriel Mountains and continue eastward.

Continuity of the San Gabriel fault southeast and northwest of its mapped distribution is problematical. Matti and others (1985) proposed that the Banning fault forms the southeastward continuation of the San Gabriel fault. We elaborate this proposal below. Northwestward continuation of the San Gabriel fault beyond Ridge Basin is obscured by Quaternary thrust faults that carry crystalline rocks of the Frazier Mountain region southward over the San Gabriel fault and associated sedimentary rocks of Ridge Basin. There, most workers follow Crowell (1950, 1975a, 1982a, figs. 3, 4) who proposed that the San Gabriel fault at depth continues northwestward beneath the thrust sheets to join the San Andreas fault (Crowell, 1982a, p. 29). We interpret this junction as a meeting point where an older fault (the San Gabriel) intersects a younger fault (the San Andreas, *sensu stricto*), and we view the northwest end of the San Gabriel fault as a piercing point whose palinspastic position should be identifiable after right-slip is restored on the San Andreas (*sensu stricto*). When we restore 160 km of right slip on the Mojave Desert segment of the San Andreas, the northwest end of the San Gabriel fault restores to the Cajon Pass region where the Cajon Valley fault (fig. 1) may represent a former continuation of the San Gabriel fault (Matti and Morton, 1992).

Displacement history

Estimates for right slip on the San Gabriel fault range from 0 to 70 km. Crowell (1952) first proposed large lateral displacements based on his recognition that distinctive Precambrian basement clasts in the upper Miocene Violin Breccia of Crowell (1954a) in Ridge Basin and in upper Miocene marine beds of the Modelo Formation have been displaced 30 to 35 km from likely cross-fault sources in the Frazier Mountain region and western San Gabriel Mountains, respectively. However, Paschall and Off (1961) discounted the role of right slip on the San Gabriel fault and instead accounted for the distribution of basement clasts in the sedimentary units purely on the basis of vertical dip-slip movements. Crowell (1962, p. 39-40) reiterated his proposal that clasts in sedimentary rocks require about 32 km of displacement on the San Gabriel fault, and also suggested that basement rocks in the Frazier Mountain region may have been displaced by as much as 48 km from cross-fault counterparts in the western San Gabriel Mountains (Crowell, 1962, p. 41). Carman (1964) called for about 32 km of right slip on the fault based on his proposal that upper Miocene nonmarine deposits of the Caliente Formation in the Lockwood Valley area were part of the same fluvial drainage that deposited the Mint Canyon Formation in Soledad basin; the two parts of the fluvial system since have been displaced by the San Gabriel fault. This proposal was expanded and refined by Ehlig and others (1975), who used stratigraphic patterns of distinctive volcanic clasts and basement-rock clasts to propose that the Caliente-Mint Canyon drainage was disrupted by as much as 56 to 65 km of right slip on the San Gabriel fault. Ehlert (1982b) subsequently increased this estimate to 70 km. Ehlig and Crowell (1982) subsequently refined the basement-rock correlations originally cited by Crowell (1962), and concluded that the San Gabriel fault has displaced these rocks by about 60 km. This figure has become widely accepted as the total

displacement on the San Gabriel fault. In the San Gabriel Mountains, the 60-km displacement presumably is split between the north and south branches of the fault: about 22 km on the north branch, as shown by displaced crystalline rock units (Ehlig, 1968a), and the remaining 38 km presumably on the south branch, although this displacement has not been proven by cross-fault correlations. We propose that the San Gabriel fault has no more than about 44 km of displacement: 22 km on the north branch (Ehlig, 1973), and 22 km on the south branch based on our proposal that the fault has displaced the left-lateral Malibu Coast-Santa Monica-Raymond fault from the Evey Canyon-Icehouse Canyon fault in the southeastern San Gabriel Mountains (discussed below).

Crowell (1982a, fig. 12) proposed that right slip on the San Gabriel fault was initiated in the late Miocene (about 10 m.y. ago) and largely was completed by the end of the Miocene (about 5 Ma). Late Miocene onset of faulting is interpreted from interfingering stratigraphic relations between the syntectonic Violin Breccia and marine sediments of late Miocene age. Termination of strike-slip displacements on the San Gabriel fault by earliest Pliocene time is interpreted from relations in Ridge Basin, where the Pliocene Hungry Valley Formation of Crowell (1950) has been mapped as a depositional cap that seals the main displacement history of the San Gabriel fault (Crowell, 1982c). The basal part of the Hungry Valley Formation is about 5 m.y. old, and Crowell (1982a,b) concluded that right slip within the San Andreas transform system switched from the San Gabriel fault to the San Andreas fault at about this time. However, this conclusion has been questioned by some workers, most notably Weber (1982) who indicates that the Hungry Valley sequence is disrupted by the San Gabriel fault and that a few km of right slip on the San Gabriel occurred after the Hungry Valley was deposited.

BANNING FAULT

Previous Investigations

Vaughan (1922) first mapped faults later referred to the Banning fault; his map shows these as unnamed faults that extend west from their juncture with the San Andreas fault in the east part of San Gorgonio Pass. It is clear from Vaughan's text (1922, p. 399-401) that he viewed the San Andreas fault as the dominant structure in San Gorgonio Pass; he attached no particular significance to the unnamed faults that he recognized to the west. Hill (1928) reinterpreted fault relations in San Gorgonio Pass and introduced the name "Banning fault" for the fault segments that Vaughan (1922) first identified. Although Hill (1928, plate II) did not specifically designate the Banning fault on his map, he evidently applied the name to a fault he showed extending from the east part of San Gorgonio Pass west to the San Jacinto fault and beyond; he did not indicate an identifiable extension of the Banning fault eastward into the Coachella Valley. Hill (1928, p. 142) indicated that the fault Vaughan had called the San Andreas in the east part of San Gorgonio Pass did not extend to the northwest as Vaughan believed, but instead continued west to the fault segment that Vaughan had not named or evaluated.

Allen (1957) clarified many of the geologic and nomenclatural problems associated with the Banning fault zone, and his report has formed the basis for all later discussions of the zone. Allen recognized that the Banning fault not only is an important zone of crustal convergence, as indicated by the zone of thrust and reverse faults associated with the fault in San Gorgonio Pass, but also is an important strike-slip fault with as much as 11 to 19 km of right-lateral offset. Reexamination of the Banning fault by Matti and Morton (1982) enlarged on Allen's studies by refining the geologic history and tectonic role of the fault zone.

Distribution and geologic setting

The Banning fault can be identified or inferred over a distance of about 100 km between the Indio Hills and the San Jacinto fault. The fault zone today consists of western, central, and eastern segments, each having a unique geologic and geomorphic setting and each recording a distinctive depositional and tectonic history during Quaternary time. These Quaternary events have obscured the distribution and history of an ancestral strike-slip fault that originally formed a single continuous trace throughout the three geographic segments.

Western segment.--The western segment of the Banning fault extends from the San Jacinto fault east to the Calimesa area. This segment has no surface expression because it is covered by late Pliocene and Quaternary sediments, and the position of the ancestral strand can only be inferred on the basis of gravity data (Willingham, 1971, 1981) and indirect geologic evidence.

Central segment.--The central, or San Gorgonio Pass, segment of the Banning fault extends from Calimesa to the vicinity of Whitewater Canyon. This segment largely is obscured by Quaternary sedimentary deposits, and has been modified by Quaternary reverse, thrust, and wrench faults of the San Gorgonio Pass fault zone. Where it crops out east of Calimesa and north of Banning, the Banning fault dips steeply to the north and juxtaposes crystalline rocks of San Gabriel Mountains-type against late Cenozoic sedimentary rocks; these exposures probably represent the ancestral trace of the fault. East of Banning, the ancestral trace is enmeshed in the San Gorgonio Pass fault zone and has been reactivated and obscured by Quaternary reverse and thrust faults of that system. For example, between Cabazon and Whitewater canyon, crystalline sheets have been thrust southward over the ancestral Banning fault and over Tertiary and Quaternary sedimentary deposits along low-angle fault surfaces that locally are flat or even south-dipping (Allen, 1957; D.M. Morton and J.C. Matti, unpublished data).

Eastern segment.--The eastern, or Coachella Valley, segment of the Banning fault extends from the vicinity of Whitewater canyon southeastward to the southern Indio Hills, where it merges with the San Andreas fault. The trace of the segment is well defined by conspicuous linear vegetation traces (Allen, 1957, fig. 1 of pl. 6) and forms degraded scarps in alluvial units that are late Pleistocene and Holocene in age. No published studies address the Quaternary history of this segment of the fault.

Geologic history

Late Cenozoic right-lateral history.--Evidence for at least 16 to 25 km of late Cenozoic right slip on the Banning fault is provided by geologic relations among Tertiary sedimentary rocks in the San Gorgonio Pass region. There, uppermost Miocene strata of the marine Imperial Formation south of the Banning fault have been displaced at least 11 km

in a right-lateral sense from Imperial beds in the Whitewater area on the north side of the fault (Allen, 1957, p. 329). The 11-km separation is a minimum displacement, however, because the two sequences are not exact cross-fault counterparts: they differ in details of their physical stratigraphy and in their relations with underlying rocks. Moreover, their benthic foraminiferal assemblages suggest different paleogeographic settings for the two sequences (K. A. McDougall and J. C. Matti, unpublished data): Imperial beds south of the Banning fault represent a more offshore facies than beds north of the fault in the Whitewater area, which suggests that the southern sequence should be restored to a palinspastic position at least several kilometers farther offshore (southeast) from the more onshore Whitewater section.

In San Gorgonio Pass, the Painted Hill and Hathaway Formations (of Allen, 1957) provide additional evidence for right slip on the Banning fault. South of the fault, many conglomeratic beds in these units contain north-derived volcanic, plutonic, and gneissic clasts that could not have been derived from bedrock sources presently cropping out north of the fault (J. C. Matti and D. M. Morton, unpublished data). After about 140 km of right slip is restored on the Coachella Valley segment of the San Andreas fault (described above), restoration of 16 to 25 km of right slip on the Banning fault positions the Hathaway and Painted Hill Formations south of the southern Chocolate Mountains, where bedrock sources for some of their volcanic, plutonic, and metamorphic clasts can be found. However, the Hathaway Formation must have been deposited in a two-sided depositional basin having both northern and southern source areas because many of the unit's conglomeratic beds contain clasts of Peninsular Ranges-type from both lower and upper plates of the Eastern Peninsular Ranges mylonite belt (Matti and Morton, 1992).

Available evidence restricts right slip on the Banning fault to the late Miocene and earliest Pliocene. Displacements occurred after about 8 Ma because sedimentary and volcanic rocks displaced by the fault in San Gorgonio Pass are that age and younger (D. M. Morton, J. C. Matti, and J. L. Morton, unpublished data). Right slip occurred after about 7 Ma because the Banning fault has displaced the Imperial Formation 16 to 25 km and the unit appears to be about 7 m.y. old (Table 2). The late Miocene displacement episode may have extended into earliest Pliocene time, but recognition of Pliocene right slip on the Banning fault (if any) must await improved age control and facies analysis in the San Timoteo and Painted Hill Formations.

Quaternary history.--After the Banning fault was abandoned as a right-lateral strike-slip fault in earliest Pliocene time, the three segments of the fault had different geologic histories.

(1) The western segment did not generate ground ruptures of any kind during the Quaternary.

(2) The San Gorgonio Pass segment has been overprinted by compressional tectonism that created the San Gorgonio Pass fault complex--a later deformation that has been superimposed along the trend of the ancestral Banning fault but is not related kinematically to it.

(3) Unlike the western and central segments, the Coachella Valley segment has generated right-lateral displacements during Quaternary time. Paleocurrent directions and cobble compositions in Quaternary gravels of the eastern San Gorgonio Pass area indicate deposition by an ancestral Whitewater River; the clasts include a variety of bedrock stones of San Gabriel Mountains and San Bernardino Mountains type, and have southeasterly paleocurrents (J.C. Matti and B.F. Cox, unpubl. data). These data suggest that during late Quaternary time the gravels have been displaced about 2 to 3 km into San Gorgonio Pass by right slip on the Coachella Valley segment of the Banning fault (Sheet 2, F-F'). This figure probably represents the total amount of right slip on the segment since its Quaternary reactivation. Additional evidence for late Quaternary displacements on the Coachella Valley segment include right-laterally offset stream gullies cut into Pleistocene gravels between Whitewater Canyon and U.S. Highway 92 (Clark, 1984) and late Pleistocene gravel deposits in the Coachella Valley that may have been offset by the fault (Sheet 2, G-G'). The neotectonic trace of the segment probably correponds to the position occupied by the ancestral Banning/San Gabriel fault in late Miocene and early Pliocene time.

Although the age span for late Quaternary displacements has not been established, the Coachella Valley segment of the Banning fault probably has generated Holocene as well as late Pleistocene displacements. The fault appears to have been the source for the M=5.9 1986 North Palm Springs earthquake. However, although secondary ground failures developed in the vicinity of the surface trace of the Banning fault (Morton and others, 1989), the earthquake did not generate tectonic ground ruptures. The hypocenter for the 1986 event was located approximately halfway between Banning fault and the Coachella Valley segment of the San Andreas fault, and focal-plane solutions indicate reverse dip-slip as well as right-slip movements (Jones and others, 1988). If the 1986 earthquake originated on the Banning fault, the structure must dip moderately to the north beneath the Coachella Valley and may join the Coachella Valley segment of the San Andreas at depth.

Regional correlation.--Its late Miocene right-lateral history indicates that the ancestral Banning fault was a strand of the San Andreas transform system during the same period when the San Gabriel fault was an active component of the system. Many workers have proposed that the west end of the Banning fault has been displaced by the San Jacinto fault, and that its offset conterpart must continue to the west. Allen (1957, p. 339) may have been the first to suggest that the Banning is "the offset segment of one of the prominent east-west faults of the San Gabriel Mountains", but he did not cite the San Gabriel fault by name. Sharp (1967, p. 726) suggested that the Sierra Madre-Cucamonga fault may be the offset counterpart of the Banning fault, a view shared by Dibblee (1975a, p. 134).

We conclude that the San Gabriel and Banning faults originally formed a single throughgoing right-lateral fault, and suggest that the 22 km of right-lateral displacement suggested by Ehlig (1968a; 1975, p. 184) for the north branch of the San Gabriel fault corresponds to the 16 to 25 km of displacement we recognize for the Banning fault between 7.5 and 4 or 5 Ma. This right-slip activity would have coincided with latest Miocene displacements on the San Gabriel fault in Ridge Basin, where major right-lateral activity on the San Gabriel fault ceased about 5 m.y. ago (Crowell, 1982, p. 35, fig. 12). In the earliest Pliocene, the San Gabriel-Banning strand was bypassed by the San Andreas system as the San Andreas fault (*sensu stricto*) evolved to the east.

The Banning-San Gabriel connection via Neogene faults in the southeastern San Gabriel Mountains

Our conclusion that the Banning and San Gabriel faults once were continuous does not follow obviously from what is known about the two faults because (1) the north and south branches of the San Gabriel fault cannot be traced easily through and beyond the eastern San Gabriel Mountains, (2) the Banning fault cannot be traced easily west of the San Gorgonio Pass region, and (3) Quaternary right slip on the San Jacinto fault has rearranged and obscured any throughgoing connection between the two older faults.

Rocks and structures in the southeastern San Gabriel Mountains provide insight into possible relations between the San Gabriel and Banning faults. In the southeasternmost part of the range, two distinct suites of crystalline rock occur (fig. 3; Dibblee, 1968a, 1982a, figs. 1, 2; Morton, 1975a, fig. 1; especially see Ehlig, 1975, fig. 1, and 1981, fig. 10-2): (1) Pelona Schist and structurally overlying granitoid and gneissic rocks that respectively form lower and upper plates of the Vincent thrust, and (2) a suite of granitoid rocks and prebatholithic metasedimentary rocks of uncertain provincial affiliation. Lower- and upper-plate rocks of the Vincent thrust are typical of those elsewhere in the San Gabriel Mountains (Ehlig, 1975, fig. 1; 1981, fig. 10-2). However, granitoid and metasedimentary rocks in the southeasternmost part of the range have enigmatic provincial affinities and are structurally isolated from typical rocks of San Gabriel Mountains-type. The two suites evcrywhere are separated by high-angle faults (fig. 3): (1) on the east, the two suites are separated by northwest-trending right-lateral faults traditionally assigned to the San Jacinto[1] fault zone; (2) on the north, the two suites are separated by an east-trending zone of strike-slip faults referred to as the Icehouse Canyon fault; (3) on the west, the two suites are separated by the poorly studied Evey Canyon and San Antonio faults that traverse San Antonio Canyon (Ehlig, 1975, fig. 1; Morton, 1975a, figs. 1, 2; Dibblee, 1982a, fig. 1). We propose that these three fault zones and the granitic and metasedimentary terrane they enclose can be used to establish a connection between the San Gabriel and Banning faults.

Our correlation of the San Gabriel and Banning faults depends heavily on two inferences: (1) the enigmatic terrane of granitoid and metasedimentary rock in the southeastern San Gabriel Mountains is Peninsular Ranges-type rock that has been juxtaposed against San Gabriel Mountains-type rock (Matti and others, 1985; Matti and Morton, 1992), and (2) right-lateral displacement on a throughgoing San Gabriel-Banning fault contributed to this juxtapostion. In order to defend the San Gabriel-Banning connection we must defend these two propositions.

Provincial affinities.--Crystalline rocks enclosed by the "San Jacinto", Icehouse Canyon, and Evey Canyon faults are broadly similar to rocks of Peninsular Ranges-type. The granitoid rocks consist mainly of foliated biotite-hornblende quartz diorite and tonalite (Ehlig, 1975, 1981; Morton, 1975a; Evans, 1982; Morton and others, 1983; Morton and Matti, 1987, Plate 12.1, rock units Kqd and Kd; May and Walker, 1989) that locally are intruded by small bodies of monzogranite and garnetiferous muscovite-bearing monzogranite (Morton and Matti, 1987, Plate 12.1, unit Kqm). These granitoids probably all are Cretaceous, although emplacement ages of about 87 Ma (May and Walker, 1989) have been moderately to strongly reset by an early Tertiary thermal event (Miller and Morton, 1980). The quartz dioritic and tonalitic rocks are progressively more deformed southward toward the San Gabriel Mountain front, culminating in an east-trending zone of mylonite and mylonitic quartz diorite first studied by Alf (1948) and Hsu (1955) and later mapped by Morton (1975a, 1976; Morton and others, 1983; Morton and Matti, 1987, Plate 12.1). At the mountain front, crystalline rocks structurally beneath the mylonite belt consist of multiply-deformed gneiss, quartz diorite, and garnetiferous hypersthene-bearing retrograded granulite rocks. Most workers assign a Precambrian age to these deformed rocks based on their unique structural and metamorphic history, but Ehlig (1975, fig. 1; 1981, fig. 10-2) believed them to be younger and grouped them with other granitoid rocks in this part of the southeastern San Gabriel Mountains that he inferred to be Mesozoic in age. Granulite-facies metamorphism appears to be early Cretaceous in age on the basis of a 108-Ma U-Pb age obtained by May and Walker (1989) from a late-stage syntectonic pyroxene-plagioclase pegmatite associated with the retrograded granulite rocks.

Prebatholithic metasedimentary rocks intruded by the granitoids consist of amphibolite-grade marble, metaquartzite, and pelitic gneiss and schist that locally is graphitic. North of the main mylonite belt the metasedimentary rocks occur as large bodies and pendants; south of the mylonite belt the metasedimentary rocks occur only as thin septa and xenoliths. Most workers assign a late Proterozoic or early Paleozoic age to the sedimentary protoliths based on their general similarities to rocks known to be that age elsewhere in southern California.

Matti and others (1985, p. 3) speculated that the crystalline terrane enclosed by the "San Jacinto", Icehouse Canyon, and Evey Canyon faults is part of the Peninsular Ranges block. We reiterate this proposal here, and support it with several lines of evidence:

(1) Quartz diorite and tonalite in the southeasternmost San Gabriel Mountains are similar to quartz diorite and tonalite in the northeastern Peninsular Ranges block: the granitoids appear to have similar intrusive ages that have been reset by a younger thermal event (Miller and Morton, 1980, and unpublished K/Ar data), and they have similar major and minor element compositions (Baird and others, 1974, 1979).

(2) The mylonitic belt of ductile deformation that separates foliated granitoid rocks from highly deformed retrograded granulites in the San Gabriel Mountains is similar to the Eastern Peninsular Ranges mylonite zone of Sharp (1979), except that mylonitic lineations are oriented down-dip in most parts of the Eastern Peninsular Ranges mylonite zone (Erskine, 1985) but are oriented parallel to strike in the San Gabriel Mountains (Morton and Matti, 1987; May and Walker, 1989). This discrepancy could reflect either spatial differences in the orientation of the syntectonic strain field within the regionwide mylonite belt (May and Walker, 1989) or localized post-tectonic rotation of the mylonite fabrics around vertical and/or horizontal axes. Other workers have

[1]Because of confusion between Quaternary displacements [if any] and older displacements within the San Jacinto fault zone in the southeastern San Gabriel Mountains, we use the term "San Jacinto fault" to refer to Miocene displacements.

pointed out similarities between the two mylonite belts (Hsu, 1955; Ehlig, 1975, p. 183; Erskine, 1985).

(3) Bodies of garnetiferous muscovite monzogranite structurally overlying the mylonite belt in the southeastern San Gabriel Mountains (Morton and Matti, 1987, Plate 12.1, units Kg and Kgc) are comparable to similar bodies structurally above and beneath the Eastern Peninsular Ranges Mylonite Belt in the Santa Rosa Mountains (Matti and others, 1983b, unit Mzlm).

(4) Prebatholithic metasedimentary rocks in the southeasternmost San Gabriel Mountains are broadly similar to metasedimentary rocks structurally above and beneath the mylonite belt in the San Jacinto and Santa Rosa Mountains (Powell, 1982a; Matti and others, 1983b, units gsc, mq, and mc; Erskine, 1985). Powell (1982a) has grouped these and similar prebatholithic metasedimentary rocks into his Placerita terrane.

Correlation of faults.--If the enigmatic granitoid and metasedimentary rocks in the southeastern San Gabriel Mountains are rocks of Peninsular Ranges-type, then their present tectonic juxtaposition against rocks of San Gabriel Mountains-type must be explained by identifiable structures--ductile, brittle, or both. May and Walker (1989) proposed that the enigmatic suite (their Cucamonga and San Antonio terranes) was juxtaposed against rocks of San Gabriel Mountains-type in late Cretaceous or early Paleogene time by ductile oblique left-lateral convergence within a mylonite zone locally preserved along the boundary between the two terranes (May, 1990). Regional telescoping along Cretaceous or Paleogene ductile zones may well account for the primary structural geometry between the two crystalline terranes. However, we propose that their *present* juxtaposition in the San Gabriel Mountains resulted from brittle displacements on throughgoing Neogene faults whose dismembered segments now are represented by the "San Jacinto", Icehouse Canyon, and Evey Canyon faults.

If these three faults are Neogene, and once were continuous with other Neogene strike-slip faults in southern California, then their regional counterparts should be nearby and should have a similar relationship to rocks of San Gabriel Mountains-type and Peninsular Ranges-type. One candidate is the Banning fault, which in the San Gorgonio Pass region intervenes between rocks of San Gabriel Mountains-type to the north and rocks of Peninsular Ranges-type to the south. Likewise, in the southeastern San Gabriel Mountains, the "San Jacinto" and Icehouse Canyon faults intervene between rocks of San Gabriel Mountains-type to the north and east and rocks we identify as Peninsular Ranges-type to the south (fig. 3). The structural position occupied by the "San Jacinto" and Icehouse Canyon faults thus is similar to that of the Banning fault (fig. 3, map sheets 1 and 2). We use this relation as a primary basis for our proposal that the Banning, "San Jacinto", and Icehouse Canyon faults once were continuous and shared common movement histories.

We complete the San Gabriel-Banning connection by projecting the Banning-"San Jacinto"-Icehouse Canyon trend westward beyond San Antonio Canyon. A likely candidate for this continuation is the east-oriented north branch of the San Gabriel fault--a structure that has about 22 km of late Miocene right slip (Ehlig, 1973, 1975, 1981) that compares well with 16 to 25 km of late Miocene right slip on the Banning fault in San Gorgonio Pass. Similarities in their movement histories suggest that the faults are related, and we propose that they once formed a single throughgoing right-lateral trend that since has been disrupted by about 25 km of Quaternary right slip on the "San Jacinto fault" and about 3 km of Quaternary left slip on the San Antonio fault. The former has displaced the east end of the Icehouse Canyon fault from the Banning fault; the latter has displaced the west end of the Icehouse Canyon fault from the north branch of the San Gabriel fault (fig. 3).

This scenario provides a connection between the north branch of the San Gabriel fault and the Banning fault but leaves unresolved the connection (if any) between the south branch of the San Gabriel fault and the Banning. Most workers follow Crowell (1975a,b, 1981, 1982) and Ehlig (1975, 1981) who convey 38 km of right slip on the south branch eastward toward the San Andreas or Banning faults by way of connecting faults in the southeastern San Gabriel Mountains (Dibblee, 1968a, fig. 1; Ehlig, 1973, fig. 1 and 1981, fig. 10-2; Crowell, 1975a, fig. 1, 1975c, p. 208-209, 1982a, fig. 1). To these scenarios we add one in which the San Gabriel fault (south branch) traverses the south front of the San Gabriel Mountains, is displaced about 3 km left laterally by the San Antonio fault, and continues east to the "San Jacinto fault" by way of the Stoddard Canyon fault and thence to the Banning fault (fig. 3).

As developed to this point, our model for the San Gabriel-Banning connection accomodates three concerns: (1) it accounts for two of the three Neogene faults in the southeastern San Gabriel Mountains that separate Peninsular Ranges-type rock from San Gabriel Mountains-type rock; (2) it ties together similar right-slip histories on the San Gabriel fault (north branch) and the Banning fault; and (3) it provides a testable hypothesis for a connection between the San Gabriel fault (south branch) and the Banning fault. This model also provides a testable solution for two other problems: the amount of right slip on the San Gabriel fault (south branch) and the regional distribution of the left-lateral Malibu Coast fault zone. We propose that a solution to both problems is provided by the Evey Canyon fault--the third Neogene fault in the southeastern San Gabriel Mountains that juxtaposes rocks of Peninsular Ranges-type and San Gabriel Mountains-type.

Pivotal to this analysis is the regional distribution and tectonic role of the Malibu Coast-Santa Monica-Raymond fault zone--a major left-lateral fault that trends easterly from the California coast to the south-frontal fault zone of the San Gabriel Mountains. Barbat (1958, fig. 2, p. 64) originally suggested that the Santa Monica segment of the zone generated about 13 km of left slip. Subsequently, Yeats (1968), Yerkes and Campbell (1971), Jahns (1973), Campbell and Yerkes (1976), and Truex (1976) presented evidence for 60 to 90 km of left slip on the Malibu Coast-Santa Monica-Raymond trend during the middle Miocene (about 16 Ma to 12 Ma). Based on the premise that a left-lateral fault of this scale must be of regional extent, these workers extended the Malibu Coast-Raymond system eastward through the Cucamonga fault zone (Barbat, 1958, fig. 1; Jahns, 1973, fig. 5; Campbell and Yerkes, 1976, fig. 1) and ultimately through San Gorgonio Pass by way of the Banning fault (Jahns, 1973, fig. 6-9, p. 166).

We accept the premise that the Malibu Coast-Santa Monica-Raymond fault is a major left-lateral structure that should be recognizable east of the frontal-fault zone of the San Gabriel Mountains. However, rather than merge the Malibu Coast system with the frontal fault zone and extend it east through the Cucamonga fault, we suggest that the Malibu

Coast system may have been truncated by the south branch of the San Gabriel fault and displaced right laterally from a cross-fault counterpart located to the east. We propose that the Evey Canyon fault is the displaced continuation of the Malibu Coast-Santa Monica-Raymond trend, which requires that the Evey Canyon is a left-lateral fault that juxtaposed Peninsular Ranges-type rocks against San Gabriel Mountains-type rocks (fig. 3; Matti and others, 1985). The once continuous middle Miocene Malibu Coast-Santa Monica-Raymond-Evey Canyon fault was truncated in late Miocene time by the San Gabriel fault (south branch), which has displaced the southwest end of the Evey Canyon fault about 22 km from the east end of the Raymond fault. This forms the basis for our displacement estimate of 22 km for the south branch, and underlies our conclusion that the San Gabriel fault (north and south branches) has no more than 44 km of right slip (22 km + 22 km).

Our conclusion that the Evey Canyon fault is a left-lateral structure that once was part of the Malibu Coast system has implications for the Icehouse Canyon, "San Jacinto", and Banning faults. The northeast end of the Evey Canyon fault terminates against the north-trending San Antonio fault, a structure that has displaced the north and south branches of the San Gabriel fault about 3 km from their inferred cross-fault counterparts (the Icehouse Canyon and Stoddard Canyon faults, respectively; fig. 3). Oblique convergence between the Evey Canyon and San Antonio faults precludes accurate determination of their geometric relations, and it is likely that left slip on the north-trending San Antonio fault has occurred by reactivation of north-trending segments of the Evey Canyon fault. Despite these complications, we propose that restoration of 3 km of left slip on the San Antonio fault would align the northeast end of the Evey Canyon fault with the Icehouse Canyon fault, which thereby is potentially continuous with the left-lateral Malibu Coast-Evey Canyon trend.

This implication appears to be at odds with our proposal that the Icehouse Canyon fault is a right-lateral component of the San Gabriel-Banning connection--a contradiction that becomes more profound if large left-lateral displacements proposed for the Malibu Coast-Raymond system are projected east along an Evey Canyon-Icehouse Canyon-"San Jacinto" trend that ultimately includes the Banning fault. This apparent contradiction can be resolved in two ways:

First, fault zones established initially by middle Miocene left slip within a throughgoing Malibu Coast-Santa Monica-Raymond-Evey Canyon-Icehouse Canyon-"San Jacinto"-Banning trend could have been reactivated as zones of late Miocene right slip when the Banning-"San Jacinto"-Icehouse Canyon segment of the Malibu Coast system was incorporated into the San Gabriel-Banning system (a concept suggested to us generically by T.H. McCulloh).

Second, May and Walker (1989, p. 1262-1263) suggested that kinematic models for tectonic rotations in southern California (Luyendyk and others, 1980; Hornafius and others, 1986) require that left slip on the Malibu Coast-Raymond system should decrease to the east, thereby eliminating the need to extend large left-lateral displacements throughout the entire length of the Malibu Coast system. May and Walker (1989) adopted our earlier suggestion (Matti and others, 1985) that the Evey Canyon fault is part of the Malibu Coast system, but suggest that large left-lateral displacements (60 to 90 km) proposed for western segments of the Malibu Coast-Evey Canyon system diminish to about 20 km in the southeastern San Gabriel Mountains. By this interpretation, left slip may not be significant on the Icehouse Canyon-"San Jacinto"-Banning segment of the Malibu Coast system, and may not even have extended all the way east on the Banning fault. This would obviate the need to extend large displacements on the Malibu Coast system east through San Gorgonio Pass (Jahns, 1973), and would fit the lack of evidence for Neogene left slip on the Banning fault.

We cannot resolve uncertainties involving the regional distribution of the middle Miocene Malibu Coast system. However, rather than arbitrarily ending the Malibu Coast-Santa Monica-Raymond system at the northeast end of the Evey Canyon fault, we incorporate modest left slip on the Evey Canyon-Icehouse Canyon-Banning segment of the Malibu Coast system. We estimate this left slip to be about 25 km based on our speculation that the Eastern Peninsular Ranges mylonite zone in the southeastern San Gabriel Mountains has been displaced about 25 km from a possible cross-fault counterpart buried beneath Neogene and Quaternary sedimentary rocks between the Santa Monica Mountains and Verdugo Hills.

Summary.--In the southeastern San Gabriel Mountains and San Gorgonio Pass region, several strike-slip faults traverse the boundary zone between rocks of Peninsular Ranges-type and San Gabriel Mountains-type. Our interpretation of movement histories for these faults requires that they are local segments of regionwide strike-slip fault trends that include (1) the middle Miocene Malibu Coast-Santa Monica-Raymond-Evey Canyon-Icehouse Canyon-"San Jacinto"-Banning left-lateral system and (2) the late Miocene San Gabriel-Icehouse Canyon-Stoddard Canyon-"San Jacinto"-Banning right-lateral system. The Malibu Coast-Banning system produced about 25 km of left slip in middle Miocene time (14 to about 12 Ma). In late Miocene time (about 10 Ma), the Malibu Coast-Banning left-lateral system was dismembered and locally reactivated by displacements within the right-lateral San Gabriel-Banning system.

During late Miocene time the San Gabriel-Banning fault formed a single, throughgoing right-lateral structure that was part of the San Andreas transform system. The middle segment of this throughgoing structure, now located in the San Gabriel Mountains, developed two discrete strands that probably formed sequentially. To the northwest, these two strands coalesced to form a single strand (the San Gabriel fault) that traverses the west margin of Ridge Basin; to the southeast, the two strands coalesced to form a single strand (the Banning fault) that traverses the San Bernardino Valley, San Gorgonio Pass, and Salton Trough. Within the southeastern San Gabriel Mountains, remnants of the two San Gabriel-Banning fault strands are represented by the Stoddard Canyon, Icehouse Canyon, and "San Jacinto" faults.

The throughgoing San Gabriel-Banning system generated about 44 km of right-lateral displacement in late Miocene to earliest Pliocene time (10 to 4 or 5 Ma). The south branch of the San Gabriel fault probably is the older fault strand, and we propose that from about 10 Ma to about 7.5 Ma it generated about 22 km of displacement that displaced the Evey Canyon fault from the Raymond fault. This displacement must have extended along the Banning fault, but rocks of this age that would record right-lateral movements from 10 Ma to 8 Ma are not exposed in San Gorgonio Pass. If the San Gabriel-Banning fault gradually was bowed into a convex-west arc during this early history, the

curvature ultimately could have become too extreme to have accommodated efficient right-slip displacements. We propose that this happened about 7.5 m.y. ago, at which time the south branch was abandoned and right slip stepped inboard (east) to the north branch. From about 7.5 Ma to about 4 or 5 Ma the north branch generated 22 km of displacement (Ehlig, 1973, p. 174)--a displacement recorded by upper Miocene sedimentary and volcanic rocks that are traversed by the Banning fault in San Gorgonio Pass. According to this model, total right slip on the combined north and south branches of the San Gabriel-Banning fault is about 44 km--16 km short of the 60 km proposed by Crowell (1982a) and by Ehlig and Crowell (1982). Major right-lateral activity on the throughgoing fault ceased about 4 or 5 m.y. ago (Crowell, 1982a, p. 35, fig. 12) as the San Gabriel-Banning strand was bypassed by the San Andreas system and as strands of the San Andreas fault proper evolved to the east.

COMPRESSIONAL FAULT SYSTEMS

SAN GORGONIO PASS FAULT ZONE

We apply the name San Gorgonio Pass fault zone to a series of Quaternary reverse, thrust, and wrench faults that extends from the Whitewater area westward to the Calimesa area. This system is associated spatially with the Banning fault, but the evolution of the San Gorgonio Pass fault zone has no relationship kinematically to the paleotectonic Banning fault. The following discussion is based on unpublished mapping still in progress.

In map view, the San Gorgonio Pass fault zone has a distinctive zig-zag character caused by repetition of a distinctive fault geometry--an L-shaped fault distribution in which the elongate staff of the L is oriented northwestward and the shorter base of the L eastward to northeastward. The east-oriented segments are reverse and thrust faults, with moderately dipping reverse faults in the west half of the fault zone and shallowly dipping thrust faults in the east half. The northwest-oriented segments appear to be vertical wrench faults having oblique right-lateral displacements. These segments have approximately the same orientation as active right-lateral faults in the region.

On the east, faults of the San Gorgonio Pass zone first appear a few km west of Whitewater River, where the Coachella Valley segment of the Banning fault splays into multiple north-dipping thrust sheets (Morton and others, 1987). Traced westward, faults of the San Gorgonio Pass zone disappear in the Calimesa area--a region where we identify normal faults of the Crafton Hills horst-and-graben complex and where the San Bernardino strand of the San Andreas fault changes to a more northerly strike. These spatial relations between neotectonic fault complexes having three different kinematic styles (right-lateral strike slip, extension, and contraction) suggest that the fault systems are mechanically interelated.

Faults of the San Gorgonio Pass zone all are late Quaternary in age. Some faults in the complex may have been active only in late Pleistocene time; others have been active throughout the late Pleistocene and Holocene and have generated ground ruptures as recently as a few thousand years ago (J.C. Tinsley and J.C. Matti, unpubl. trench data, 1986). Faults with confirmed Holocene displacements have been identified only in the eastern part of the San Gorgonio Pass zone between Beaumont and Whitewater; faults in the western part of the zone between Beaumont and Calimesa appear to have been active only in late Pleistocene time (J.C. Matti and D.M. Morton, unpubl. data). However, future ground ruptures throughout the entire extent of the San Gorgonio Pass fault zone cannot be ruled out.

CUCAMONGA FAULT ZONE

The Cucamonga fault is a zone of Quaternary reverse and thrust faults that separates crystalline rocks of the San Gabriel Mountains from alluviated lowlands of the upper Santa Ana River valley (Morton, 1975a,b, 1976; Morton and Matti, 1987). The pre-Quaternary history of the Cucamonga fault is obscure, but its latest Pleistocene and Holocene history reflects convergence between the Perris block and the San Gabriel Mountains (Morton and Yerkes, 1974; Morton and others, 1982; Morton and Matti, 1987).

Faulting within the Cucamonga fault zone has recurred episodically during Quaternary time. The oldest faults occur within the north part of the fault zone, where some faults cut crystalline basement rock but do not break even the oldest Quaternary alluvial units. Younger faults occur farther south at the mountain front and form conspicuous scarps in young Pleistocene and Holocene alluvial fans (Morton and Matti, 1987). These relations suggest that during late Pleistocene and Holocene time, faulting within the Cucamonga fault zone migrated southward. This southward-younging pattern is complicated by merging of individual strands locally and by apparent merging of all strands in the western part of the fault zone. Latest episodes of strain release may have occurred mainly in the eastern 15 km of the fault zone and not throughout its entire 25-km length. The more complicated fault pattern in the eastern part of the zone may reflect interaction between the Cucamonga and San Jacinto faults. We speculate that northwestward migration of the Perris block by right-lateral strike-slip on the San Jacinto fault during the Quaternary has been taken up partly by reverse and thrust-fault displacements within the Cucamonga fault zone.

EXTENSIONAL FAULT SYSTEMS

NORMAL FAULTS OF THE COACHELLA AND MORONGO VALLEYS

Faults that have normal dip-slip separations occur in the southern Indio Hills and in the northern Coachella Valley. Clark (1984, p. 4-5, map sheet 1) attributed the distinctive zone of normal faults in the southern Indio Hills to uplift northeast of the San Andreas fault, which he in turn related to displacements across the San Andreas. Northeast-oriented faults in the northern Coachella Valley have not been studied; the faults have both north- and south-facing scarps, and break late (but not latest) Quaternary alluvium. Northeast-oriented faults and lineaments in the Morongo Valley area, including the Morongo Valley fault, also appear to have normal dip-slip separations. The kinematic role of normal faults in this region has not been documented.

BEAUMONT PLAIN FAULT ZONE

We apply the name Beaumont Plain fault zone to a series of northwest-trending en-echelon fault scarps that traverse late Quaternary alluvial deposits in the vicinity of Beaumont. Most of the scarps face northeast, but one short scarp segment faces southwest. We have not documented the style or history of faulting that created these scarps; however, they appear to have formed by normal dip-slip displacements and probably represent an extensional strain field. This interpretation is strengthened by closely spaced northeast- and southwest-facing scarps northeast of Beaumont which bound a downdropped block that forms a graben. Similar faults having northwest trends and northeast-facing scarps occur elsewhere in the San Gorgonio Pass region--for example, scarps that have been referred to the modern trace of the San Andreas fault at Burro Flat, and scarps near Oak Glen and Wildwood Canyon. We do not understand the kinematic role of these faults, but they may represent a family of related features formed by regional extension.

CRAFTON HILLS HORST-AND-GRABEN COMPLEX

We apply the name Crafton Hills fault zone to a system of normal dip-slip faults that forms a horst-and-graben complex in the vicinity of Redlands and Yucaipa. These faults bound the west and east flanks of the Crafton Hills, and break late Quaternary alluvium in the valleys of Oak Glen and Wilson Creeks. The faults trend northeast in the vicinity of the Crafton Hills (Matti and others, 1992), but adopt more easterly trends near the San Bernardino strand of the San Andreas fault and south of Redlands (Morton, 1978b). Normal faulting within this zone coincides geographically with a series of conspicuous left steps in the San Bernardino strand, and with the western termination of the San Gorgonio Pass compressional fault system.

The Crafton Hills horst-and-graben complex is a neotectonic structural element that has been active during both late Pleistocene and Holocene time, although not all faults in the zone break Holocene alluvial deposits. The complex represents a zone of extensional faulting in a region where right-lateral and reverse faulting are the most obvious expressions of crustal deformation.

DIP-SLIP FAULTS OF THE SAN BERNARDINO VALLEY AND SAN BERNARDINO MOUNTAINS

The Peters and Tokay Hill faults occur south of the San Bernardino strand of the San Andreas fault in the Devore area southeast of Cajon Pass (Morton and Miller, 1975; Morton and Matti, 1990b). The faults break Holocene deposits and probably have normal dip-slip displacements. This geometry is complicated locally where the Tokay Hill fault intersects the San Bernardino strand of the San Andreas fault: there, the Tokay Hill fault dips southwest and appears to have a reverse dip-slip geometry (relations observed by us in a trench excavated by G. Rasmussen and Associates). Similar faults traverse the southwest-facing escarpment of the western San Bernardino Mountains; they are east-trending, and almost all have north-facing scarps with down-on-the-north displacements (Weldon, 1985b, pl. 12). The Peters and Tokay Hill faults and those in the western part of the San Bernardino Mountains form a family of related dip-slip faults that reflect an extensional strain field.

NEOTECTONIC FRAMEWORK OF THE SOUTH-CENTRAL TRANSVERSE RANGES AND VICINITY

Seismicity, strain, and slip rates

Seismicity

Early studies of seismicity in the vicinity of the south-central Transverse Ranges were published by Dehlinger (1952), Richter and others (1958), Allen and others (1965), Brune and Allen (1967), Cheatum and Combs (1973), Hadley and Combs (1974), Thatcher and others (1975), and Fuis and Lamanuzzi (1978). Recent studies have been conducted by Green (1983), Nicholson and others (1983, 1984a, b, 1986), Williams and others (1984), Corbett and Hearn (1984), Sanders and Kanamori (1984), Webb and Kanamori (1985), Jones (1988), and Jones and others (1988).

Richter and others (1958) evaluated the 1948 Desert Hot Springs earthquake (M_L=6.5), which they attributed to the Coachella Valley segment of the San Andreas fault (their Mission Creek fault). However, epicenters for this earthquake and for associated shocks did not align with the surface trace of the fault but instead formed a lineamint parallel to and several kilometers north-northeast of the trace, and surface ruptures were not reported for the earthquakes. First-motion studies for the 1948 earthquake suggest oblique right-lateral displacement having a thrust component along a fault plane dipping northeast (Allen, 1957, p. 342; Richter and others, 1958). Thus, it is unclear if the 1948 earthquake sequence can be attributed to the Coachella Valley segment.

Allen and others (1965) evaluated the seismicity of the southern California region, including the south-central Transverse Ranges and vicinity, and concluded that although seismicity patterns were consistent with some of the major fault systems, much of the seismicity is diffuse and is not associated with known faults. Brune and Allen (1967) and later workers have emphasized this conclusion with regard to the San Andreas fault system.

Comprehensive analysis of focal mechanisms and hypocentral plots in the south-central Transverse Ranges and vicinity refined the results of earlier studies and offered several new conclusions (Green, 1983; Jones, 1988). (1) Seismicity is not associated with strands of the San Andreas fault (also see Allen and others, 1965; Brune and Allen, 1967; Nicholson and others, 1983). (2) A deep wedge of seismicity in San Gorgonio Pass yields reverse and thrust mechanisms but includes left-lateral and right-lateral mechanisms, and defines the deepest seismicity known from southern California (22 km; also see Fuis and Lamanuzzi, 1978; Nicholson and others, 1983, 1986; Corbett and Hearn, 1984; Webb and Kanamori, 1985). This wedge is bounded on the north by the Mission Creek fault, on the west by the Banning Canyon - Burro Flat segment of the San Bernardino strand of the San Andreas, on the south by the Banning fault, and on the east by a transitional boundary with an area of low seismicity in the northern Coachella Valley. (3) Pure dip-slip mechanisms and oblique dip-slip mechanisms with a left-lateral component

occur in the vicinity of the Crafton Hills horst-and-graben complex (also see Nicholson and others, 1983, 1986), and normal mechanisms occur locally within the San Bernardino valley region (Jones, 1988; also see Webb and Kanamori, 1985, fig. 5a). (4) Left-lateral mechanisms appear to define northeast-oriented seismicity lineaments that traverse the San Bernardino valley region (also see Nicholson and others, 1983, 1986). (5) No seismicity is associated with the Coachella Valley segments of the San Andreas and Banning faults.

In contrast to the San Andreas fault, active seismicity is associated with the trace of the San Jacinto fault, which in the vicinity of the south-central Transeverse Ranges has generated at least three historic earthquakes of magnitude (M_L) 6 or greater. Two of these occurred in the southern San Jacinto Valley (Sanders and Kanamori, 1984, p. 5874-5875, fig. 2; note slight differences in epicentral position compared to Thatcher and others, 1975, fig. 1); the third probably occurred near Loma Linda on either the San Jacinto fault or the nearby Loma Linda fault (Sanders and Kanamori, 1984, p. 5873-5874, fig. 2). Both macro- and microseismicity define relatively quiet and active segments of the fault. For example, rates of microseismicity are relatively high in the southern part of the San Jacinto Valley but are significantly lower in the Reche Canyon area (Brune and Allen, 1967, locs. 13 and 37 of Table 1 and fig. 3; Cheatum and Combs, 1973, p. 5). Green (1983, pl 1) indicates that microseismicity is low along the San Jacinto fault between Reche Canyon and Cajon Pass, but she reported a dense cluster of seismicity presumably associated with the Loma Linda fault 2 km east of the San Jacinto fault near Loma Linda. This cluster is associated with the convex-west bow in the regional strike of the San Jacinto fault. Thatcher and others (1975) used macroseismicity patterns to suggest that a gap in seismic slip occurs on the San Jacinto fault between Reche Canyon and the Cajon Pass region.

Slip rates

San Andreas fault, Coachella Valley segment.--Studies by Keller and others (1982) in the southern Indio Hills indicate that the Coachella Valley segment of the San Andreas fault (their Mission Creek fault) has late Quaternary slip rates of between 10 and 35 mm/year, with a best estimate of 25 to 35 mm/year; this rate presumably applies to the Holocene as well as the late Pleistocene. During late Pleistocene time, this amount of slip probably carried up the Coachella Valley segment and through the San Bernardino Mountains on the Mill Creek fault. However, as discussed below, during Holocene time the 25- to 35-mm rate may have carried no farther northwest than the vicinity of Desert Hot Springs.

San Gorgonio Pass fault zone.--Ongoing studies by the U.S. Geological Survey (J.C. Tinsley and J.C. Matti, unpubl. data) indicate that the strain budget for thrust faults of the San Gorgonio Pass zone may be quite complex. A thrust-fault scarp trenched on the Millard Canyon fan disrupts young alluvial deposits along fault planes that dips north at less than 20°. Preliminary age determinations from detrital charcoal suggest that some of the faulted deposits may be as young as 2,850 to 3,600 yr (^{14}C ages uncorrected). An intense scarp-building period during the early part of this period was followed by a period during which only one scarp-forming event may have occurred in the last 2,850 years. These data suggest that modern seismicity patterns may be spatially and temporally cyclic, with high-strain periods followed by low-strain periods.

San Jacinto fault.---Sharp (1981) indicates a minimum Quaternary long-term slip rate of about 8 to 12 mm/year for the fault in the vicinity of Anza. South of metropolitan San Bernardino, Wesnousky and others (1991; Prentice and others, 1986) determined a minimum slip rate of 1.7 to 3.3 mm/yr for the San Jacinto fault, although their studies did not capture all strands of the San Jacinto zone. Prentice and others (1986) propose that the long-term Quaternary slip rate on the northern San Jacinto fault probably averages about 10 mm/yr. However, Morton and others (1986) discuss San Bernardino Mountains-derived clast populations in Pleistocene deposits of the San Timoteo Badlands that may require accelerated long-term slip on the San Jacinto fault--particularly during geologic intervals when strands of the San Andreas fault in the San Bernardino Mountains region were tied up within the San Gorgonio Pass structural knot.

San Andreas fault, San Bernardino strand.--In the Cajon Pass region the San Bernardino strand has a Holocene slip rate of about 25 mm/year (Weldon and Sieh, 1985). Rasmussen (1982) indicates a similar rate farther southeast in the vicinity of Highland.

The San Bernardino strand southeast of Santa Ana River may have a variable slip-rate history that reflects the complex geologic evolution of the strand. In order to determine long-term slip rates for the fault at its southeast extent, Harden and Matti (1989) examined soil profiles of alluvial units in the Yucaipa area that contain clast populations derived from various distinctive bedrock units that crop out on Yucaipa Ridge. Throughout Holocene and latest Pleistocene time these alluvial-fan units have been displaced right-laterally away from their source areas. Within the limits of uncertainty posed by the soils data and by ambiguities in the displacement paths of the alluvial-fan deposits, Harden and Matti (1989) reached two main conclusions: (1) Holcene slip rates on the San Bernardino strand here approach the 25 mm/yr rates proposed for the fault in the Cajon Pass region (Weldon and Sieh, 1985; McFadden and Weldon, 1987); and (2) late Pleistocene slip rates appear to be considerably lower than Holocene rates, on the order of 6 to 13 mm/yr. These conclusions suggest that long-term slip on the San Bernardino strand has accelerated with time. We believe that this slip-rate scenario is compatible with gradual inception of the San Bernardino strand by reactivation of the abandoned Mission Creek strand starting in late Pleistocene time (discussed above).

Cucamonga fault zone.--The Cucamonga fault zone at Day Canyon in the east-central part of the zone has a minimum convergence rate of about 5 mm/year for the last 13,000 years (J.C. Matti, D.M. Morton, J.C. Tinsley, and L.D. McFadden, unpubl. data). Age control for this determination is based on correlation of pedogenic soils that cap faulted alluvial deposits; the faulted deposits could be younger (but probably not older), in which case the convergence rate would be greater. Matti and coworkers conclude that earthquakes with vertical displacements of about 2 m had an average recurrence of about 625 years. Seismic-moment calculations indicate expectable surface-wave magnitudes (M_S) of 6.9 to 7.2 for fault-rupture lengths of 10 to 25 km.

Strain

Trilateration measurements in the Salton Trough indicate that the Coachella Valley segment of the San Andreas fault is accumulating strain at a rate of about 25 mm/year (Savage and others, 1979, table 3; King and Savage, 1983; Savage, 1983, figs. 2, 3). Line-length measurements by Savage and Prescott (1967) across a doubly braced quadrilateral spanning the San Jacinto fault in the San Jacinto Valley indicate that 25 mm/year of right-lateral shear strain is accumulating across the fault, assuming it is locked to depths of 20 km; this rate contrasts with a minimum long-term Quaternary rate of 8 to 12 mm/year determined by Sharp (1981) from geologic data further to the southeast.

Neotectonic framework

Most of the neotectonic elements in the vicinity of the south-central Transverse Ranges occur within or adjacent to San Gorgonio Pass--a structural knot in the modern San Andreas fault. We propose that many of these fault complexes owe their origin and kinematics to this structural knot.

The San Gorgonio Pass knot lies between the Coachella Valley and Mojave Desert segments of the San Andreas fault. Both segments approach the knot in a straightforward manner, but as Allen (1957, p. 337-339) originally demonstrated, neotectonic strands of these faults cannot be traced as continuous features through the San Gorgonio Pass region. Similar difficulties exist for the Coachella Valley segment of the Banning fault: the regional strike of this strand is aligned with the San Bernardino strand of the San Andreas fault, suggesting a geometric and kinematic relation between the two faults, but Allen (1957) showed that Quaternary thrust and reverse faults in San Gorgonio Pass obscure relations between them. Allen (1957, p. 337) explored five ways that the modern San Andreas might pass through the San Gorgonio Pass knot, of which three are major possibilities:

(1) The aligned San Bernardino strand and Coachella Valley segment of the Banning fault once formed a straight throughgoing trace within the San Gorgonio Pass region, but this trace subsequently has been deflected into a sharp bend that has created the San Gorgonio Pass knot. This interpretation is favored by Dibblee (1968; 1975a, p. 134; 1982, p. 166).

(2) The aligned San Bernardino strand and Coachella Valley segment of the Banning fault may form a straight throughgoing trace within the San Gorgonio Pass region, but this trace is concealed beneath a major thrust sheet of crystalline rock. This interpretation requires that right-slip occurs beneath the thrust plate and that the two strike-slip faults plunge beneath the thrust sheets as they approach San Gorgonio Pass from the northwest and southeast, respectively. Although such a relation can be mapped where the Coachella Valley segment of the Banning fault enters San Gorgonio Pass, similar relations have not been demonstrated for the San Bernardino strand where it would have to plunge southeastward beneath the thrust sheet.

(3) The San Bernardino strand and Coachella Valley segment of the Banning fault may be aligned and may interact kinematically, but the two strands never had a throughgoing connection. Thus, the San Bernardino strand dies out as it approaches San Gorgonio Pass, and neotectonic displacements on the Banning fault have been taken up by compressional convergence in the Pass region. Allen (1957, p. 338-339) favored this interpretation, and we concur.

The fact that none of the neotectonic right-lateral faults of the Coachella Valley can be traced northwestward through the greater San Gorgonio Pass region raises a major question: how is right-slip in the Salton Trough passed through or around the San Bernardino Mountains? We address this question below.

The San Andreas fault system in the vicinity of the central Transverse Ranges: a product of left and right steps in a right-lateral fault zone

The neotectonic setting of the San Gorgonio Pass region owes its origin and kinematics to a bottleneck that gradually evolved in the San Andreas fault during the Pleistocene as the San Bernardino Mountains block was projected across the path of the San Andreas fault and multiple right-lateral strands successively were deformed and abandoned. The geometric effect of these events is apparent from a geologic map of the region: the northwest-oriented trace of the Coachella Valley segment of the San Andreas fault is offset or stepped left about 15 km from the northwest-oriented trace of the Mojave Desert segment (fig. 5). The modern neotectonic framework thus has inherited a bottleneck that must be accommodated in the late Quaternary strain budget of the region.

Any neotectonic model that attempts to distribute strain through or around the San Gorgonio Pass bottleneck must accommodate the following elements: (1) right slip on the Coachella Valley segment of the San Andreas fault falls off as the segment approaches the Transverse Ranges segment; (2) convergence is occurring in San Gorgonio Pass; (3) the San Bernardino valley region is undergoing extension; and (4) right slip on the Mojave Desert segment carries southeastward toward the San Bernardino Mountains segment by way of the San Bernardino strand, but does not carry simply or easily through that segment. To accommodate these elements we propose a speculative model (fig. 6) in which slip is carried around, not through, the Transverse Ranges segment of the San Andreas fault by a complicated series of left and right steps that have created compressional and extensional fault complexes in San Gorgonio Pass and the San Bernardino valley region.

We start with the premise that right-slip occurs on the San Andreas fault in the Coachella Valley but does not carry through the San Bernardino Mountains. We assume that about 25 mm of annual slip occurs on the Coachella Valley segment of the San Andreas between the Salton Sea and the northern Coachella Valley; this figure is consistent with a range of slip values indicated by geologic and geodetic data (Keller and others, 1982; Savage and others, 1979; Savage, 1983). Modern neotectonic slip accounts for the youthful tectonic geomorphology displayed by the San Andreas fault along this segment (Keller and others, 1982; Clark, 1984). However, northwest of Desert Hot Springs, the Coachella Valley segment loses its fresh tectonic geomorphology and our preliminary data suggest that late Quaternary alluvial units have not been displaced significantly by the fault. Farther northwest, the Wilson Creek, Mission Creek, and Mill Creek strands of the San Bernardino Mountains segment are paleotectonic faults that have been abandoned as

throughgoing right-lateral strands of the San Andreas fault. Thus, we conclude that during late Quaternary time, most if not all right slip on the San Andreas fault in the northern Coachella Valley has stepped left onto the Banning fault. This process may account for two features. (1) As slip has been transferred across the gap between the two faults, the youthful Indio Hills have been squeezed into an anticlinal uplift. Thus, some percentage of right-slip on the San Andreas would be converted into compressional strain. (2) A left step between the San Andreas and Banning faults in the northern Coachella Valley may explain the absence of fresh tectonic geomorphology for the Banning fault near its junction with the San Andreas fault in the southern Indio Hills (Keller and others, 1982): youthful slip along this segment of the Banning fault would not be necessary if right slip were transferred to the strand farther to the northwest.

Between the Indio Hills and San Gorgonio Pass, late Quaternary right-slip on the Banning fault is indicated by youthful tectonic geomorphology and by right-lateral displacement of late Pleistocene fluvial gravels 2 or 3 km into the Pass (Sheet 2, F-F', G-G'). Moreover, Allen and Sieh (1983) report 2 mm of annual creep on the fault just east of San Gorgonio Pass. The Holocene history of the Banning fault in the Coachella Valley has not been documented, however, and modern right-slip may step still farther west (left) from the Banning fault onto the Garnet Hill fault. This speculation is based on two features: (1) Several youthful domelike uplifts of Quaternary gravel that occur between the two faults in the vicinity of Whitewater River and Garnet Hill (Allen, 1957, fig. 1 of pl. 6; Dibblee, 1982, p. 166, oblique aerial photograph) may reflect compression within a left-stepping zone; and (2) geomorphic evidence suggests that late Quaternary fluvial gravels in the east part of San Gorgonio Pass may have been displaced right-laterally by the Garnet Hill fault. Whether or not latest right-slip has occurred on the Banning fault or the Garnet Hill fault, neither strand can be traced beyond the eastern San Gorgonio Pass area, and late Quaternary right-slip in the Coachella Valley must have been partly absorbed within the San Gorgonio Pass fault complex.

Although right-slip on the San Andreas fault largely may have been absorbed by convergence within San Gorgonio Pass, some component of slip may step left through San Gorgonio Pass and onto the San Jacinto fault, where it would be added to the 10 mm/year average slip determined by Sharp (1981) for the fault in the Anza area (fig. 6). Local acceleration of slip on the San Jacinto might explain four features of the region. (1) Northwest-trending faults of the Beaumont Plain that appear to have normal dip-slip displacements may reflect extensional fragmentation created as slip steps left to the San Jacinto fault. (2) The San Jacinto Valley is a graben that is rapidly subsiding (Morton, 1977) between right- and left-stepping strands of the San Jacinto fault (Cheatum and Combs, 1973, figs. 2, 4). Rapid subsidence may reflect addition of right-slip acquired from the San Andreas fault. (3) The San Jacinto Valley has been the site of two earthquakes of magnitude (M_L) greater than 6.5 during the last 85 years (Thatcher and others, 1975; Sanders and Kanamori, 1984), and the southern San Jacinto Valley has high rates of microseismicity (Brune and Allen, 1967; Cheatum and Combs, 1973); this may reflect an increased potential for seismic activity in response to locally accelerated slip in the San Jacinto Valley area. (4) The San Jacinto fault in the San Jacinto Valley is accumulating about 25 mm/year of right-lateral shear strain (Savage and Prescott, 1967); this departure from the long-term slip rate determined by Sharp (1981) may reflect local acceleration of strain accumulation due to slip acquired from the San Andreas fault.

The neotectonic framework of the San Bernardino valley region includes several distinctive features whose origin and kinematics may require transfer of slip from the San Jacinto fault back to the San Andreas (fig. 6). (1) The San Bernardino strand of the San Andreas fault appears to die out southeastward toward San Gorgonio Pass; (2) the greater San Bernardino valley region is the site of dip-slip fault complexes like the Crafton Hills horst-and-graben complex and the Peters and Tokay Hill faults, which appear to represent an extensional strain field; (3) south of the San Bernardino valley, the San Jacinto fault has a pronounced convex-west bend which may form an impediment to right-slip; (4) the San Jacinto fault between Reche Canyon and Cajon Pass may represent a seismic-slip gap (Thatcher and others, 1975); (5) Morton and Matti (1987) have shown that the San Jacinto fault in the southeastern San Gabriel Mountains does not rupture latest Quaternary alluvium; the youngest branch of the San Jacinto system in this vicinity appears to be the Glen Helen fault, and even this strand is concealed by youngest alluvial deposits in the Cajon Pass region; and (6) the San Bernardino valley region is traversed by northeast-trending left-lateral seismicity lineaments (Green, 1983; Nicholson and others, 1986) that may define the boundaries of clockwise-rotating blocks (Nicholson and others, 1986). In combination, these features may require a common explanation.

We propose that slip on the San Jacinto fault gradually steps right onto the modern San Andreas fault throughout the San Bernardino valley region (fig. 6). By this interpretation, the San Bernardino valley has moved northwestward away from the San Gorgonio Pass region, and the crust between the two regions is pulling apart. This extension is manifested by faults like those in the Crafton Hills extensional complex. Northwestward movement of the San Bernardino valley has occurred along the San Bernardino strand, which extends as a youthful neotectonic feature southeastward from Cajon Pass to the Crafton Hills-Oak Glen region but may not necessarily continue through San Gorgonio Pass and on into the Coachella Valley to the Banning fault. In the Devore area southeast of Cajon Pass, slip may step right from the San Jacinto fault to the Glen Helen fault, which has scarps and sag ponds in the Devore area, and thence to the San Bernardino strand--thereby creating an extensional strain field that gives rise to normal dip-slip displacements on the Peters and Tokay Hill faults. A right step from the San Jacinto to the Glen Helen may explain a distinctive seismicity lineament between the inferred traces of the two faults beneath the floodplains of Cajon and Lytle Creeks (Green, 1983, fig. 7). Extension created by a regional right step from the San Jacinto to the San Andreas fault may occur throughout the San Bernardino Valley region, and may create high heat flow that accounts for hot springs and subsurface hot-water zones that occur at several locations in the valley region.

Right-stepping transfer of slip and (or) accumulated strain from the San Jacinto to the San Andreas would create a right-lateral shear couple that could generate clockwise block rotations of the type proposed by Nicholson and others (1986). During the period between large earthquakes on either the San Jacinto or San Andreas faults (the interseismic period of Nicholson and others, 1986), accumulated shear strain within the San Bernardino valley region partly could be released by block rotations and extensional faulting; large earthquake

events on the San Andreas and San Jacinto faults would release strain accumulated along the margins of the shear couple. Thus, two styles of seismicity might alternate through time.

We have not documented geometric and kinematic relations between the San Jacinto, San Andreas, and Cucamonga faults in the vicinity of Cajon Pass and the southeastern San Gabriel Mountains. However, one point is clear: at the surface, right-slip on the San Jacinto fault does not pass easily into the San Andreas fault. For example, northwestward migration of the Perris block by right-lateral displacements on the San Jacinto fault partly has been taken up by late Pleistocene and Holocene thrust-fault displacements within the Cucamonga fault zone (Morton and others, 1982; Matti and others, 1982; Morton and Matti, 1987; J. C. Matti, D. M. Morton, J. C. Tinsley, and L. D. McFadden, unpubl. data). Thus, the fault zone represents a zone of convergence between the Peninsular and Transverse Ranges Provinces: to the south, the Perris block and Peninsular Ranges are slipping northwestward along traces of the San Jacinto fault zone; however, this right-lateral migration apparently is impeded by the eastern Transverse Ranges, and the Perris block and alluviated lowlands of the upper Santa Ana River Valley apparently are being thrust beneath the eastern San Gabriel Mountains.

Convergence rates across the Cucamonga fault must be factored into the overall strain budget of the region. Here, the neotectonic San Andreas and San Jacinto faults have late Quaternary slip rates of 25 mm/year and 8 to 12 mm/year, respectively (Weldon and Sieh, 1985; Sharp, 1981). Our studies suggest a minimum convergence rate of 5 mm/year for the Cucamonga fault zone during latest Pleistocene and Holocene time--a rate that could double to 10 mm/year if the faulted alluvial succession proves to be younger than we believe. Thus, if the Cucamonga fault zone represents convergence between the Peninsular and Transverse Ranges Provinces, then half to nearly all of the 8 to 12 mm of annual slip on the San Jacinto fault could have been taken up by latest Pleistocene and Holocene convergence within the Cucamonga fault zone. Such a model would imply that part or all of the slip on the San Jacinto fault has not contributed to slip on the San Andreas during latest Quaternary time. Viewed in this way, the Cucamonga fault may represent a major zone of convergence between large crustal blocks.

By contrast, Weldon (1984, 1985a,b) suggests that, even though the San Jacinto fault zone may not have a surface connection with the San Andreas fault (Morton, 1975b), the 8 to 12 mm of annual slip on the San Jacinto nevertheless feeds into the San Andreas and contributes to slip on that fault. If this interpretation is correct, then the annual 5-mm convergence rate within the Cucamonga fault zone may not reflect wholescale convergence between major crustal blocks of the Peninsular and Transverse Ranges but instead may simply reflect interactions between local small blocks in a region where the San Jacinto and San Andreas faults merge in a complicated manner. This interpretation might also account for the geographically segmented strain-release behavior that appears to have characterized the Cucamonga fault zone during latest Pleistocene and Holocene time (Morton and Matti, in press).

CONCLUSIONS

The vicinity of the south-central Transverse Ranges is traversed by multiple faults of the San Andreas transform system--including the Banning, San Andreas, and San Jacinto faults. After generating 15 to 25 km of right-slip during late Miocene time, the Banning fault was abandoned in early Pliocene time and was succeeded by the San Andreas fault. At the latitude of the Pinto Mountain fault, crustal convergence created a structural knot that led to the evolution of multiple fault strands; these constitute the San Bernardino Mountains segment of the San Andreas. The structural knot evolved gradually during the late Pliocene and Pleistocene, and created a left step in the San Andreas fault as convergence coupled with left-lateral displacements on the Pinto Mountain fault gradually projected the San Bernardino Mountains block across the path of the San Andreas; the multiple right-lateral strands developed sequentially as the fault attempted to maintain a geometrically simple trace through the left-stepping region. The Wilson Creek and Mission Creek faults are the oldest strands, and sequentially generated about 130 km of displacement before the Mission Creek fault was abandoned in the Pleistocene (prior to 0.5 m.y. ago). In late Pleistocene time the Mill Creek fault evolved inboard of the locked-up Mission Creek fault and generated 8 km of displacement before it was abandoned as a throughgoing strand.

The Coachella Valley and Mojave Desert segments of the San Andreas fault are offset about 15 km by the left step in the Transverse Ranges segment. The modern San Andreas fault apparently is responding to this left step by transferring slip from the Coachella Valley segment to the Banning fault and thence into San Gorgonio Pass, where right-slip has been absorbed within the San Gorgonio Pass fault complex. Some component of slip may step farther west to the San Jacinto fault in the San Jacinto Valley. Throughout the San Bernardino valley region, slip steps from the San Jacinto fault back onto the San Bernardino strand of the San Andreas, which creates a regional right-lateral shear couple between the two strike-slip faults and accounts for extensional fault complexes like the Crafton Hills horst-and-graben complex and the Peters and Tokay Hill faults. Thus, the modern neotectonic framework of the south-central Transverse Ranges reflects an integrated regional response to an evolving left step in the San Andreas fault.

Acknowledgements

This report is a revised version of U.S. Geological Survey Open-File Report OFR 85-365. We thank J.C. Crowell, P.L. Ehlig, P. Stone, R.E. Powell, D.C. Ross, R.J. Weldon, M.O. Woodburne, and R.F. Yerkes for reviews of various drafts of that report and its present incarnation. Our studies are funded by the U.S. Geological Survey's National Geologic Mapping Program (GEOMAP and COGEOMAP Components) and National Earthquake Hazards Reduction Program (Regional Geologic Hazards Element).

REFERENCES CITED

Alf, R.M., 1948, A mylonite belt in the southeastern San Gabriel Mountains, California: Geological Society of America Bulletin, v. 69, p. 1101-1120.

Allen, C.R., 1957, San Andreas fault zone in San Gorgonio Pass, southern California: Geological Society of America Bulletin, v. 68, p. 319-350.

-----1968, The tectonic environments of seismically active and inactive areas along the San Andreas fault system, in Dickinson, W.R., and Grantz, Arthur, eds., Proceedings of conference on geologic problems of San Andreas fault system: Stanford University Publications in Geological Sciences, v. XI, p. 70-82.

-----1981, The modern San Andreas fault, in Ernst, W.G., ed., The geotectonic development of California [Rubey Volume I]: Englewood Cliffs, New Jersey, Prentice-Hall, Inc., p. 511-534.

Allen, C.R., and Sieh, K.E., 1983, Creep and strain studies in southern California, in Summaries of technical reports, Earthquake Hazards Reduction Program, v. XVII: U.S. Geological Survey Open-File Report 83-918, p. 199-202.

Allen, C.R., St. Amand, P., Richter, C.F., and Nordquist, J.M., 1965, Relationship between seismicity and geologic structure in the southern California region: Bulletin of the Seismological Society of America, v. 55, no. 4, p. 753-797.

Atwater, Tanya, 1970, Implications of plate tectonics for the Cenozoic tectonic evolution of western North America: Geological Society of America Bulletin, v. 81, p. 3513-3536.

Baird, A.K., Morton, D.M., Baird, K.W., and Woodford, A.O., 1974, Transverse Ranges province: a unique structural-petrochemical belt across the San Andreas fault system: Geological Society of America Bulletin, v. 85, p. 163-174.

Baird, A.K., Baird, K.W., and Welday, E.E., 1979, Batholithic rocks of the northern Peninsular and Transverse Ranges, southern California, in Abbott, P.L., and Todd, V.R., eds., Mesozoic crystalline rocks: Peninsular Ranges batholith and pegmatites, Point Sal Ophiolite: San Diego State University, Department of Geological Sciences, manuscripts and road logs prepared for the Geological Society of America Annual Meeting, p. 111-132.

Barbat, W.F., 1958, The Los Angeles Basin area, California, in Weeks, L.G., ed., Habitat of oil--a symposium: Tulsa, Oklahoma, American Association of Petroleum Geologists, p. 62-77.

Barrows, A.G., 1975, The San Andreas fault zone in the Juniper Hills quadrangle, southern California, in Crowell, J.C., ed., San Andreas fault in southern California: California Division of Mines and Geology Special Report 118, p. 197-202.

Barrows, A.G., 1979, Geology and fault activity of the Valyermo segment of the San Andreas fault zone, Los Angeles County, California: California Division of Mines and Geology Open-File Report 79-1LA, 49 p., scale 1:12,000.

Barrows, A.G., 1980, Geologic map of the San Andreas fault zone and adjoining terrane, Juniper Hills and vicinity, Los Angeles County, California: California Division of Mines and Geology Open-File Report 80-2LA, scale 1:9,600.

Barrows, A.G., 1987, Geology of the San Andreas fault zone and adjoining terrrane, Juniper Hills and vicinity, Los Angeles County, California, in Hester, R.L., and Hallinger, D.E., eds., San Andreas fault-Cajon Pass to Palmdale: Pacific Section, American Association of Petroleum Geologists, Volume and guidebook no. 59, p. 93-157.

Barrows, A.G., Kahle, J.E., and Beeby, D.J., 1976, Geology and fault activity of the Palmdale segment of the San Andreas fault zone, Los Angeles County, California: California Division of Mines and Geology Open-File Report 76-6LA, 30 p., scale 1:12,000.

Barrows, A.G., Kahle, J.E., and Beeby, D.J., 1985, Earthquake hazards and tectonic history of the San Andreas fault zone, Los Angeles County, California: California Division of Mines and Geology Open-File Report 85-10LA, 139 p., scale 1:12,000.

Barrows, A.G., Kahle, J.E., and Beeby, D.J., 1987, Earthquake hazards and tectonic history of the San Andreas fault zone, Los Angeles County, California, in Hester, R.L., and Hallinger, D.E., eds., San Andreas fault-Cajon Pass to Palmdale: Pacific Section, American Association of Petroleum Geologists, Volume and guidebook no. 59, p. 1-92.

Barth, A.P., and Ehlig, P.L., 1988, Geochemistry and petrogenesis of the marginal zone of the Mount Lowe Intrusion, central San Gabriel Mountains, California: Contributions to Mineralogy and Petrology, v. 100, p. 192-204.

Beeby, D.J., 1979, Geology and fault activity of the Lake Hughes segment of the San Andreas fault zone, Los Angeles County, California: California Division of Mines and Geology Open-File Report 79-2LA, 35 P., scale 1:12,000.

Biehler, S., Kovach, R.L., and Allen, C.R., 1964, Geophysical framework of northern end of Gulf of California structural province, in Marine geology of the Gulf of California--a symposium: American Association of Petroleum Geologists Memoir 3, p. 126-143.

Bilham, Roger, and Williams, Patrick, 1985, Sawtooth segmentation and deformation processes on the southern San Andreas fault, California: Geophysical Research Letters, v. 12, no. 9, p. 557-560.

Cameron, C.S., 1981, Geology of the Sugarloaf and Delamar Mountain areas, San Bernardino Mountains,

California: Cambridge, Massachusetts Institute of Technology, Ph.D. Thesis, 399 p.

Campbell, R.H., and Yerkes, R.F., 1971, Cenozoic evolution of the Santa Monica Mountains-Los Angeles basin area: II. Relation to plate tectonics of the northeast Pacific Ocean: Geological society of America Abstracts with Programs, v. 3, no. 2, p. 92.

Campbell, R.H., and Yerkes, R.F., 1976, Cenozoic evolution of the Los Angeles basin area--relation to plate tectonics, in Howell, David G., ed., Aspects of the geologic history of the California Continental borderland: Pacific Section, American Association of Petroleum Geologists, Miscellaneous Publication 24, p. 541-558.

Carman, M.F., Jr., 1964, Geology of the Lockwood Valley area, Kern and Ventura Counties, California: California Division of Mines Special Report 81, 62 p.

Carter, B.A., 1982, Geology and structural setting of the San Gabriel anorthosite-syenite body and adjacent rocks of the western San Gabriel Mountains, Los Angeles County, California, Field trip 5 of Cooper, J.D., Compiler, Geologic excursions in the Transverse Ranges, southern California: Geological Society of America, Cordilleran Section, 78th annual meeting, Anaheim, Calif., Guidebook, p. 1-53.

Cheatum, Craig, and Combs, Jim, 1973, Microearthquake study of the San Jacinto Valley, Riverside County, California, in Kovach, R.L., and Nur, Amos, eds., Proceedings of the Conference on tectonic problems of the San Andreas fault system: Stanford University Publications in Geological Sciences, v. XIII, p. 1-10.

Clark, M.M., 1984, Map showing recently active breaks along the San Andreas Fault and associated faults between Salton Sea and Whitewater River-Mission Creek, California: U.S. Geological Survey Miscellaneous Investigations Map I-1483, scale 1:24,000.

Corbett, E.J., and Hearn, T.M., 1984, The depth of the seismic zone in the Transverse Ranges of southern California: Seismological Society of America, Earthquake Notes, v. 55, no. 1, p. 23.

Crowell, J.C., 1950, Geology of Hungry Valley area, southern California: American Association of Petroleum Geologists Bulletin, v. 34, p. 1623-1646.

-----1952, Probable large lateral displacement on San Gabriel fault, southern California: American Association of Petroleum Geologists Bulletin, v. 36, no. 10, p. 2026-2035.

-----1954a, Strike-slip displacement of the San Gabriel fault, southern California, in Jahns, R.H., ed., Geology of Southern California: California Division of Mines Bulletin, 170, Chapter 4, Contribution 6, p. 49-52.

-----1954b, Geologic map of the Ridge Basin area, California: California Division of Mines Bulletin 170, Map Sheet 7.

-----1962, Displacement along the San Andreas fault, California: Geological Society of America Special Paper 71, 61 p.

-----1974, Sedimentation along the San Andreas fault, California, in Dott, R.H., Shaver, R.H., eds., Modern and Ancient Geosynclinal Sedimentation: Society of Economic Paleontologists and Mineralogists Special Paper 19, p. 292-303.

-----1975a, The San Andreas fault in southern California, in Crowell, J.C., ed., San Andreas fault in southern California: California Division of Mines and Geology Special Report 118, p. 7-27.

-----1975b, The San Gabriel Fault and Ridge Basin, southern California, in Crowell, J.C., ed., San Andreas fault in southern California: California Division of Mines and Geology Special Report 118, p. 208-219.

-----1975c, Geologic sketch of the Orocopia Mountains, southeastern California, in Crowell, J.C., ed., San Andreas Fault in Southern California: California Division of Mines and Geology Special Report 118, p. 99-110.

-----1979, The San Andreas Fault system through time: Geological Society of London Journal, v. 136, p. 293-302.

-----1981, An outline of the tectonic history of southeastern California, in Ernst, W.G., ed., The geotectonic development of California (Rubey Volume I): Englewood Cliffs, New Jersey, Prentice-Hall, Inc., p. 583-600.

-----1982a, The tectonics of Ridge Basin, southern California, in Crowell, J.C., and Link, M.H., eds., Geologic history of Ridge Basin, southern California: Pacific Section, Society of Economic Paleontologists and Mineralogists, Field trip guide and volume, p. 25-42.

-----1982b, Pliocene Hungry Valley formation, Ridge Basin, southern California, in Crowell, J.C., and Link, M.H., eds., Geologic history of Ridge Basin, southern California: Pacific Section, Society of Economic Paleontologists and Mineralogists, Field trip guide and volume, p. 143-150.

Crowell, J.C., and Ramirez, V.R., 1979, Late Cenozoic faults in southeastern California, in Crowell, J.C., and Sylvester, A.G., eds., Tectonics of the juncture between the San Andreas fault system and the Salton Trough, southeastern California: A guidebook for fieldtrips, Geological Society of America Annual Meeting, San Diego, California: Santa Barbara, University of California publication, p. 27-39.

Curray, J.R., and Moore, D.G., 1984, Geologic history of the mouth of the Gulf of California, in Crouch, J.K., and Bachman, S.B., eds., Tectonics and sedimentation along the California margin: Pacific Section, Society of Economic Paleontologists and Mineralogists, v. 38, p. 17-36.

Dehlinger, P., 1952, Shear-wave vibrational directions and related fault movements in southern California earthquakes: Bulletin of the Seismological Society of America, v. 42, p. 155-173.

Demirer, Ali, 1985, The Mill Creek Formation--a strike-slip basin filling in the San Andreas fault zone, San Bernardino County, California: Riverside, University of California, M.S. Thesis, 108 p.

Dibblee, T.W., Jr., 1954, Geology of the Imperial Valley region, California, in Jahns, R.H., ed., Geology of southern California: California Division of Mines Bulletin 170, p. 21-28 and plate 2 of Chapter II.

-----1964a, Geologic map of the San Gorgonio Mountain quadrangle, San Bernardino and Riverside Counties, California: U.S. Geological Survey Miscellaneous Geologic Investigations Map I-431, scale 1:62,500.

-----1964b, Geologic map of the Lucerne Valley quadrangle, San Bernardino County, California: U.S. Geological Survey Miscellaneous Geologic Investigations Map I-426, scale 1:62,500.

-----1967a, Areal geology of the western Mojave Desert, California: U.S. Geological Survey Professional Paper 522, 153 p.

-----1967b, Geologic map of the Morongo Valley quadrangle, San Bernardino County, California: U.S. Geological Survey Miscellaneous Geologic Investigations Map I-517, scale 1:62,5OO.

-----1968a, Displacements on San Andreas fault system in San Gabriel, San Bernardino, and San Jacinto Mountains, southern California, in Dickinson, W.R., and Grantz, Arthur, eds., Proceedings of conference on geologic problems of San Andreas fault system: Stanford University Publications in Geological Sciences, v. XI, p. 269-278.

-----1968b, Evidence of major lateral displacement on the Pinto Mountain fault, southern California: Geological Society of America Special Paper 115, p. 322.

-----1968c, Geologic map of the Twentynine Palms quadrangle, San Gabriel and Riverside Counties, California: U.S. Geological Survey Miscellaneous Geologic Investigations Map I-561, scale 1:62,500.

-----1975a, Late Quaternary uplift of the San Bernardino Mountains on the San Andreas and related faults, in Crowell, J.C., ed., San Andreas fault in southern California: California Division of Mines and Geology Special Report 118, p. 127-135.

-----1975b, Tectonics of the western Mojave Desert near the San Andreas rift, in Crowell, J.C., ed., San Andreas fault in southern California: California Division of Mines and Geology Special Report 118, p. 155-161.

-----1982a, Geology of the San Gabriel Mountains, southern California, in Fife, D.L., and Minch, J.A., eds., Geology and mineral wealth of the California Transverse Ranges: South Coast Geological Society Guidebook no. 10 (Mason Hill volume), p. 131-147.

-----1982b, Geology of the San Bernardino Mountains, southern California, in Fife, D.L., and Minch, J.A., eds., Geology and mineral wealth of the California Transverse Ranges: South Coast Geological Society Guidebook no. 10 (Mason Hill volume), p. 148-169.

Dickinson, W.R., and Snyder, W.S., 1979a, Geometry of triple junctions related to the San Andreas transform: Journal of Geophysical Research, v. 84, no. B2, p. 561-572.

-----1979b, Geometry of subducted slabs related to San Andreas transform: Journal of Geology, v. 87, p. 6O9-627.

Dillon, J.T., 1975, Geology of the Chocolate and Cargo Muchacho Mountains, southeasternmost California: Santa Barbara, University of California, unpublished Ph.D. thesis, 405 p.

Ehlig, P.L., 1968a, Displacement along the San Gabriel fault, San Gabriel Mountains, southern California: Geological Society of America Special Paper 115, p. 55.

-----1968b, Causes of distribution of Pelona, Rand, and Orocopia Schist along the San Andreas and Garlock faults, in Dickinson, W.R., and Grantz, Arthur, eds., Proceedings of conference on geologic problems of San Andreas fault system: Stanford University Publications in Geological Sciences, v. XI, p. 294-305.

-----1973, History, seismicity, and engineering geology of the San Gabriel fault, in Moran, D.E., Slosson, J.E., Stone, R.O., and Yelverton, C.A., eds., Geology, seismicity, and environmental impact: Association of Engineering Geologists Special Publication, p. 247-251.

-----1975, Basement rocks of the San Gabriel Mountains south of the San Andreas fault, southern California, in Crowell, J.C., ed., San Andreas fault in southern California: California Division of Mines and Geology Special Report 118, p. 177-186.

-----1977, Structure of the San Andreas fault zone in San Gorgonio Pass, southern California: Geological Society of America Abstracts with Programs, v. 9., no. 4, p. 416.

-----1981, Origin and tectonic history of the basement terrane of the San Gabriel Mountains, central Transverse Ranges, in Ernst, W.G., ed., The geotectonic development of California (Rubey Volume I): Englewood Cliffs, New Jersey, Prentice-Hall, Inc., p. 253-283.

-----1982, The Vincent thrust: its nature, paleogeographic reconstruction across the San Andreas fault, and bearing on the evolution of the Tranverse Ranges, in Fife, D.L., and Minch, J.A., eds., Geology and mineral wealth of the California Transverse Ranges: South Coast Geological Society Guidebook no. 10 (Mason Hill volume), p. 370-379.

Ehlig, P.L., Ehlert, K.W, and Crowe, B.M., 1975, Offset of the upper Miocene Caliente and Mint Canyon Formations along the San Gabriel and San Andreas faults, in Crowell, J.C., ed., San Andreas fault in southern California: California Division of Mines and Geology Special Report 118, p. 83-92.

Elders, W.A., Rex, R.W., Meidav, Tsvi, Robinson, P.T., and Biehler, Shawn, 1972, Crustal spreading in southern California: Science, v. 178, p. 15-24.

Erskine, B.E., 1985, Mylonitic deformation and associated low-angle faulting in the Santa Rosa mylonite zone, southern California: Berkeley, University of California, unpublished Ph.D. thesis, 247 p.

Farley, Thomas, 1979, Geology of a part of northern San Gorgonio Pass, California: Los Angeles, California State University, unpublished M.S. thesis, 159 p.

Farley, T., and Ehlig, P.L., 1977, Displacement on the Punchbowl fault based on occurrence of "Polka-dot" granite clasts: Geological Society of America Abstracts with Programs, v. 9, no. 4, p. 419.

Frick, C., 1921, Extinct vertebrate faunas of the Badlands of Bautista Creek and San Timeteo Canon, southern California: University of California Publications in Geology, v. 12, no. 5, p. 277-424.

Frizzell, V.A., Jr., Mattinson, J.M., and Matti, J.C., 1986, Distinctive Triassic megaporphyritic monzogranite: evidence for only 160 km offset along the San Andreas fault, southern California: Journal of Geophysical Research, v. 91, no. B14, p. 14,080-14,088.

Fuis, G., and Lamanuzzi, V., 1978, Seismicity of the eastern Transverse Ranges, southern California: EOS, American Geophysical Union Transactions, v. 59, no. 12, p. 1051.

Gibson, R.C., 1964, Geology of a portion of the Mill Creek area, San Bernardino County, California: Riverside, University of California, M.S. thesis, 50 p.

-----1971, Nonmarine turbidites and the San Andreas fault, San Bernardino Mountains, California, in Elders, W.A., ed., Geological excursions in southern California: Riverside, University of California Campus Museum Contributions, no. 1, p. 167-181.

Green, S.M., 1983, Seismotectonic study of the San Andreas, Mission Creek, and Banning fault system: Los Angeles, University of California, unpublished M.S. thesis, 52 p.

Hadley, David, and Kanamori, Hiroo, 1977, Seismic structure of the Transverse Ranges, California: Geological Society of America Bulletin, v. 88, p. 1469-1478.

Hadley, David, and Coombs, Jim, 1974, Microearthquake distribution and mechanisms of faulting in the Fontana-San Bernardino area of southern California: Bulletin of the Seismological Society of America, v. 64, no. 5, p. 1477-1499.

Hadley, D.M., and Smith, S.W., 1973, Two geophysical investigations in the San Bernardino Valley area, California, in Geological Investigations of the San Jacinto fault zone, and aspects of the socio-economic impact of earthquakes in the Riverside-San Bernardino area, California: University of California, Riverside, Campus Museum Contributions, no. 3-September 1973.

Hanks, T.C., Hileman, J.A., and Thatcher, Wayne, 1975, Seismic moments of the larger earthquakes of the southern California region: Geological Society of America Bulletin, v. 86, p. 1131-1139.

Harden, J.W., and Matti, J.C., 1989, Holocene and late Pleistocene slip rates on the San Andreas fault in Yucaipa, California, using displaced alluvial-fan deposits and soil chronology: Geological Society of America Bulletin, v. 101, p. 1107-1117.

Hileman, J.A., Allen, C.R., and Nordquist, J.M., 1973, Seismicity of the southern California region, 1 January 1932 to 31 December 1972: California Institute of Technology Earthquake Research Associates Contribution 2385, 83 p.

Hill, D.P., 1982, Contemporary block tectonics, California and Nevada: Journal of Geophysical Research, v. 87, p. 5433-5450.

Hill, M.L., 1981, San Andreas fault: history of concepts: Geological Society of America Bulletin, v. 92, p. 112-131.

Hill, M.L., and Dibblee, T.W., Jr., 1953, San Andreas, Garlock, and Big Pine faults, California: Geological Society of America Bulletin, v. 64, p. 443-458.

Hill, R.T., 1928, Southern California geology and Los Angeles earthquakes: Los Angeles, Southern California Acadamy of Sciences, 232 p.

Hillenbrand, J. M., 1990, The Potato Sandstone between the Santa Ana River and Badger Canyon, San Bernardino County, southern California: implications for displacement in the San Andreas

fault zone: Riverside, University of California, unpublished M.S thesis, 163 p.

Hsu, K.J., 1955, Granulites and mylonites of the region about Cucamonga and San Antonio Canyons, San Gabriel Mountains, California: University of California Publications in Geological Sciences, v. 30, p. 223-324.

Jahns, R.H., 1954, Geology of the Peninsular Range province, southern California and Baja California, in Jahns, R.H., ed., Geology of southern California, Chapter II, Geology of the natural provinces: California Division of Mines Bulletin 170, p. 29-52.

-----1973, Tectonic evolution of the Transverse Ranges province as related to the San Andreas fault system, in Kovach, R.L., and Nur, Amos, eds., Proceedings of the Conference on tectonic problems of the San Andreas fault system: Stanford University, Publications in Geological Sciences, v. XIII, p. 149-170.

Johnson, C.E., and Hill, D.P., 1982, Seismicity of the Imperial Valley, in The Imperial Valley, California, earthquake of October 15, 1979: U.S. Geological Survey Professional Paper 1254, p. 15-24.

Jones, L.M., 1988, Focal mechanisms and the state of stress on the San Andreas fault in southern California: Journal of Geophysical Research, v. 93, no. B8, p. 8869-8891.

Jones, L.M., Hutton, L.K., Given, D.D., and Allen, C.R., 1988, The north Palm Springs California earthquake sequence of July, 1986: Seismological Society of America Bulletin, v. 76, p. 1830-1837.

Joseph, S.E., Criscione, J.J., Davis, T.E., and Ehlig, P.L., 1982, The Lowe igneous pluton, in Fife, D.L., and Minch, J.A., eds., Geology and mineral wealth of the California Tranverse Ranges: South Coast Geological Society Guidebook no. 10 (Mason Hill volume), p. 307-309.

Kahle, J.E., 1975, Recent fault features and related geology, Leona Valley area, southern California, in Crowell, J.C., ed., San Andreas fault in southern California: California Divison of Mines and Geology Special Report 118, p. 203-207.

-----1979, Geology and fault activity of the San Andreas fault zone between Quail Lake and Three Points, Los Angeles County, California: California Division of Mines and Geology Open-File Report 79-3LA, 42 p., scale 1:12,000.

Kahle, J.E., and Barrows, A.G., 1980, Geology and fault activity of the Three Points and Pine Canyon segments, San Andreas fault zone, Los Angeles County, California: California Division of Mines and Geology Open-File Report 80-13LA, 38 p., scale 1:12,000.

Kahle, J.E., Smith, D.P., and Beeby, D.J., 1975, Geology of the Leona Valley segment of the San Andreas fault zone, Los Angeles County, California: California Division of Mines and Geology Open-File Report 75-2LA, 169 p., 1:6,000.

Keller, E.A., Bonkowski, M.S., Korsch, R.J., and Schlemon, R.J., 1982, Tectonic geomorphology of the San Andreas fault zone in the Southern Indio Hills, Coachella Valley, California: Geological Society of America Bulletin, v. 93, p. 46-56.

King, N.E., and Savage, J.C., 1983, Strain-rate profile across the Elsinore, San Jacinto, and San Andreas faults near Palm Springs, California, 1973-81: Geophysical Research Letters, v. 10, no. 1, p. 55-57.

Lamar, D.L., Merifield, P.M., and Proctor, R.J., 1973, Earthquake recurrence intervals on major faults in southern California, in Moran, D.E., Slosson, J.E., Stone, R.O., and Yelverton, C.A., eds., Geology, seismicity, and environmental impact: Association of Engineering Geologists Special Publication, p. 265-276.

Larson, R.L., 1972, Bathymetry, magnetic anomalies, and plate tectonic history of the mouth of the Gulf of California: Geological Society of America Bulletin, v. 83, p. 3345-3360.

Larson, R.L., Menard, H.W., and Smith, S.M., 1968, Gulf of California: A result of ocean-floor spreading and transform faulting: Science, v. 161, p. 781-784.

Lindh, A.G., 1983, Preliminary assessment of long-term probabilities for large earthquakes along selected fault segments of the San Andreas fault system in California: U.S. Geological Survey Open-File Report 83-63, 15 p.

Lonsdale, Peter, and Lawver, L.A., 1980, Immature plate boundary zones studied with a submersible in the Gulf of California: Geological Society of America Bulletin, Part 1, v. 91, p. 555-569.

Matti, J.C., and Morton, D.M., 1975, Geologic history of the San Timoteo Badlands, southern California: Geological Society of America Abstracts with Programs, v. 7, no. 3, p. 344.

-----1982, Geologic history of the Banning fault zone, southern California: Geological Society of America Abstracts with Programs, v. 14, no. 4, p. 184.

-----1992, Paleogeographic evolution of the San Andreas fault in southern California: a reconstruction based on a new cross-fault correlation, in Powell, R.E., Weldon, R.J., and Matti, J.C., eds., The San Andreas fault system: displacement, palinspastic reconstruction, and geologic evolution: Geological Society of America Memoir 178 (in press).

Matti, J.C., Cox, B.F., Obi, C.M., Powell, R.E., Hinkle, M.E., Griscom, Andrew, and McHugh, E.L., 1982a,

Mineral resource potential map of the Whitewater Wilderness Study Area, Riverside and San Bernardino Counties, California: U.S. Geological Survey Miscellaneous Field Studies Map MF-1478, scale 1:24,000.

Matti, J.C., Tinsley, J.C., McFadden, L.D., and Morton, D.M., 1982b, Holocence faulting history as recorded by alluvial history within the Cucamonga fault zone: a preliminary view, in Tinsley, J.C., McFadden, L.D., and Matti, J.C., eds., Late Quaternary pedogenesis and alluvial chronologies of the Los Angeles and San Gabriel Mountains areas, southern California: Field trip 12, Geological Society of America, Cordilleran Section, 78th annual meeting, Anaheim, California, Guidebook, p. 21-44.

Matti, J.C., Cox, B.F., and Iverson, S.R., 1983a, Mineral resource potential map of the Raywood Flat Roadless Area, San Bernardino and Riverside Counties, California: U.S. Geological Survey Miscellaneous Field Studies Map MF-1563-A, scale 1:62,500.

Matti, J.C., Cox, B.F., Powell, R.E., Oliver, H.W., and Kuizon, Lucia, 1983b, Mineral resource potential map of the Cactus Spring Roadless Area, Riverside County, California: U.S. Geological Survey Miscellaneous Field Studies Map MF-1650-A, scale 1:24,000.

Matti, J.C., Morton, D.M. and Cox, B.F., 1985, Distribution and geologic relations of fault systems in the vicinity of the central Transverse Ranges, southern California: U.S. Geological Survey Open-File Report 85-365, 27 p., scale 1:250,000.

Matti, J.C., Frizzell, V.A., and Mattinson, J.M., 1986, Distinctive Triassic megaporphyritic monzogranite displaced 160±10 km by the San Andreas fault, southern California: a new constraint for palinspastic reconstructions: Geological Society of America Abstracts with Programs, v. 18, no. 2, p. 154.

Matti, J.C., Morton, D.M., Cox, B.F., Carson, S.E., and Yetter, T.J., 1992, Geologic map of the Yucaipa 7.5' quadrangle, California: U.S. Geological Survey Open-File Report 92- , Scale 1:24,000..

May, D.J., and Walker, N.W., 1989, Late Cretaceous juxtaposition of metamorphic terranes in the southeastern San Gabriel Mountains, California: Geological Society of America Bulletin, v. 101, p. 1246-1267.

May, S.R., and Repenning, C.A., 1982a, New evidence for the age of the Old Woman Sandstone, Mojave Desert, California, in Sadler, P.M., and Kooser, M.A. eds., Late Cenozoic stratigraphy and structure of the San Bernardino Mountains, field trip 6 of Cooper, J.D., compiler, Geologic excursions in the Transverse Ranges: Geological Society of America, Cordilleran Section, 78th Annual Meeting, Anaheim, Calif., Volume and Guidebook, p. 93-96.

May, S.R., and Repenning, C.A., 1982b, New evidence for the age of the Mount Eden fauna, southern California: Jounal of Vertebrate Paleontology, v. 2, no. 1, p. 109-113.

McFadden, L.D., 1982, The impacts of temporal and spatial climatic changes on alluvial soils genesis in southern California: Tucson, University of Arizona, Ph.D. thesis, 430 p.

McFadden, L.D., and Weldon, R.J., 1987, Rates and processes of soil development on Quaternary terraces in Cajon Pass, California: Geological Society of America Bulletin, v. 98, p. 280-293

Meisling, K.E., 1984, Neotectonics of the north frontal fault system of the San Bernardino Mountains, southern California: Cajon Pass to Lucerne Valley: Pasadena, California Institute of Technology, unpublished Ph.D. thesis, 394 p.

Meisling, K.E., and Weldon, R.J., 1982, The late-Cenozoic structure and stratigraphy of the western San Bernardino Mountains, in Sadler, P.M., and Kooser, M.A., eds., Late Cenozoic stratigraphy and structure of the San Bernardino Mountains, field trip 6 of Cooper, J.D., compiler, Geologic excursions in the Transverse Ranges, southern California: Geological Society of America, Cordilleran Section, 78th Annual Meeting, Anaheim, Calif., 1982, Volume and Guidebook, p. 75-82.

-----1986, Cenozoic uplift of the San Bernardino Mountains: possible thrusting across the San Andreas fault: Geological Society of America Abstracts with Programs, v. 18, no. 2, p. 157.

-----1989, Late Cenozoic tectonics of the northwestern San Bernardino Mountains, southern California: Geological Society of America Bulletin, v. 101, p. 106-128.

Mezger, LiLi, and Weldon, R.J., 1983, Tectonic implications of the Quaternary history of lower Lytle Creek, southeast San Gabriel Mountains: Geological Society of America Abstracts with Programs, v. 15, no. 5, p. 418.

Miller, F.K., 1979, Geologic map of the San Bernardino North 7.5' quadrangle: U.S. Geological Survey Open-File Report 79-770, scale 1:24,000.

Miller, F.K., and Morton, D.M., 1980, Potassium-Argon geochronology of the eastern Transverse Ranges and southern Mojave Desert, southern California: U.S. Geological Survey Professional Paper 1152, 30 p.

Moore, D.G., 1973, Plate-edge deformation and crustal growth, Gulf of California structural province: Geological Society of America Bulletin, v. 84, p. 1883-19O6.

Moore, D.G., and Buffington, E.C., 1968, Transform faulting and growth of the Gulf of California since the late Pliocene: Science, v. 161, p. 12381241.

Morton, D.M., 1975a, Relations between major faults, eastern San Gabriel Mountains, southern California: Geological Society of America, Abstracts with Programs, v. 7, no. 3, p. 352-353.

-----1975b, Synopsis of the geology of the eastern San Gabriel Mountains, southern California, in Crowell, J.C., ed., San Andreas fault in southern California: California Division of Mines and Geology Special Report 118, p. 17O-176.

-----1976, Geologic map of the Cucamonga fault zone between San Antonio Canyon and Cajon Creek, southern California: U.S. Geological Survey Open-File Report 76-726, scale 1:24,000. -----1977, Surface deformation in part of the San Jacinto Valley, southern California: U.S. Geological Survey Journal of Research, v. 5, no. 1, p. 117-124.

-----1978a, Geologic map of the San Bernardino South 7.5' quadrangle, California: U.S. Geological Survey Open-File Report 78-20, scale 1:24,000.

-----1978b, Geologic map of the Redlands 7.5' quadrangle, California: U.S. Geological Survey Open-File Report 78-21, scale 1:24,OOO.

-----1978c, Geologic map of the Sunnymead 7.5' quadrangle, California: U.S. Geological Survey Open-File Report 78-22, scale 1:24,000.

Morton, D.M., and Matti, J.C., 1987, The Cucamonga fault zone: Geologic setting and Quaternary history, in Morton, D.M., and Yerkes R.F., eds., Recent reverse faulting in the Transverse Ranges, California: U.S. Geological Survey Professional Paper 1339, p. 179-203.

-----1990a, Geologic map of the Cucamonga Peak 7.5' Quadrangle, California: U.S. Geological Survey Open-File Report 90-694, scale 1:24,000.

-----1990b, Geologic map of the Devore 7.5' Quadrangle, California: U.S. Geological Survey Open-File Report 90-695, scale 1:24,000.

-----1992, Slip transfer between the San Andreas and San Jacinto fault zones in the eastern San Gabriel Mountains-San Bernardino basin region, southern California, in Powell, R.E., Weldon, R.J., and Matti, J.C., eds., The San Andreas fault system: displacement, palinspastic reconstruction, and geologic evolution: Geological Society of America Memoir 178 (in press).

Morton, D.M., and Miller, F.K., 1975, Geology of the San Andreas fault zone north of San Bernardino between Cajon Canyon and Santa Ana Wash, in Crowell, J.C., ed., San Andreas fault in southern California: California Division of Mines and Geology Special Report 118, p. 136-146.

Morton, D.M., and Yerkes, R.F., 1974, Spectacular scarps of the frontal fault system, eastern San Gabriel Mountains, southern California: Geological Society of America Abstracts with Programs, v. 6, no. 3, p. 223-224.

Morton, D.M., Cox, B.F., and Matti, J.C , 1980, Geologic map of the San Gorgonio Wilderness: U.S. Geological Survey Miscellaneous Field Studies Map MF-1164-A, scale 1:62,500.

Morton, D.M., Matti, J.C., and Tinsley, J.C., 1982, Quaternary history of the Cucamonga fault zone, southern California: Geological Society of America Abstracts with Programs, v. 14, no. 4, p. 218.

Morton, D.M., Rodriguez, E.A., Obi, C.M., Simpson, R.W., Jr., and Peters, T.J., 1983, Mineral resource potential map of the Cucamonga Roadless Areas, San Bernardino County, California: U.S. Geological Survey Miscellaneous Field Studies Map MF-1646-A, scale 1:31,680.

Morton, D.M., Matti, J.C., Miller, F.K., and Repenning, C.A., 1986, Pleistocene conglomerate from the San Timoteo Badlands, southern California; constraints on strike-slip displacements on the San Andreas faults: Geological Society of America Abstracts with Programs, v. 18, no. 2, p. 161.

Morton, D.M., Matti, J.C., and Tinsley, J.C., 1987, Banning fault, Cottonwood Canyon, San Gorgonio Pass, southern California, in Hill, M.L., ed., Geological Society of America Centennial Field Guide, v. 1, Cordilleran Section, p. 191-192.

Morton, D.M., Campbell, R.H., Jibson, R.W., Wesson, R.L., and Nicholson, C., 1989, Ground fracturing and landsliding produced by the July 8, 1986 North Palm Springs earthquake, in Sadler, P.M., and Morton, D.M., eds., Landslides in a semi-arid environment, with emphasis on the inland valleys of southern California: Publications of the Inland Geological Society, v. 2, p. 183-196.

National Earthquake Prediction Evaluation Council, 1988, Probabilities of large earthquakes occurring in California on the San Andreas fault: U.S. Geological Survey Open-File Report 88-398, 62 p.

Nicholson, C., Williams, P., Leeber, L., and Sykes, L., 1983, San Andreas seismicity and fault tectonics through the eastern Transverse Ranges: EOS, American Geophysical Union Transactions, v. 64, no. 45, p. 768.

Nicholson, C., Seeber, L., Williams, P., and Sykes, L., 1984a, Seismotectonics of the eastern and Transverse Ranges: Block rotations and shallow-angle thrusts: EOS, American Geophysical Union Transaction, v. 65, no. 16, p. 285.

-----1984b, A new paradigm for understanding southern San Andreas fault tectonics: EOS, Transactions of the American Geophysical Union, v. 65, no. , p. 996.

Nicholson, Craig, Seeber, Leonardo, Williams, Patrick, and Sykes, L.R., 1986, Seismicity and fault kinematics through the eastern Transverse Ranges, California: block rotation, strike-slip faulting and low-angle thrusts: Journal of Geophysical Research, v. 91, no. B5, p. 4891-4908.

Nishenko, S.P., and Sykes, L.R., 1982, Probabilities of occurrences of large plate rupturing earthquakes for the San Andreas, San Jacinto, and Imperial faults, California, 1983-2003: American Geophysical Union Transactions, v. 64, no. 18, p. 258.

Noble, L.F., 1926, The San Andreas rift and some other active faults in the desert region of southeastern California: Carnegie Institute of Washington Yearbook No. 25 (1925-1926), p. 415-435.

-----1932, The San Andreas rift in the desert region of southeastern California: Carnegie Institute of Washington Year Book 31, p. 355-363.

-----1933, Excursion to the San Andreas fault and Cajon Pass, in Gale, H.S., ed., southern California: 16th International Geological Congress, Guidebook 15, 68 p.

-----1954a, Geology of the Valyermo Quadrangle and vicinity, California: U.S. Geological Survey Geologic Quadrangle Map GQ-50, scale 1:24,000.

-----1954b, The San Andreas fault zone from Soledad Pass to Cajon Pass, California, in Jahns, R.H., ed., Geology of southern California: California Division of Mines Bulletin 170, p. 37-48, and Plate 5 of chapter IV, scale 1:125,000.

Owens, G.V., 1959, Sedimentary rocks of lower Mill Creek, San Bernardino Mountains, California: Pomona, Pomona College, M.S. thesis,111 p.

Paschall, R.H., and Off, T., 1961, Dip-slip versus strike-slip movement on the San Gabriel fault, southern California: American Association of Petroleum Geologists Bulletin, v. 45, p. 1941-1956.

Peterson, M.S., 1975, Geology of the Coachella fanglomerate, in Crowell, J.C., ed., San Andreas fault in southern California: California Division of Mines and Geology Special Report 118, p. 119-126.

Powell, R.E., 1981, Geology of the crystalline basement complex, eastern Transverse Ranges, southern California: constrainst on regional tectonic interpretation: Pasadena, California Institute of Technology, unpublished Ph.D. thesis, 441 p.

-----1982a, Prebatholithic terranes in the crystalline basement complex of the Transverse Ranges, southern California: Geological Society of America Abstracts with Programs, v. 14, no. 4. p. 225.

-----1982b, Prebatholithic terranes in the crystalline basement of the Transverse Ranges, California: Geological Society of America Abstracts with Programs, Cordilleran Section, 1982, v. 14, no. 4, p. 225.

-----1986, Palinspastic reconstruction of crystalline-rock assemblages in southern California: San Andreas fault as part of an evolving system of late Cenozoic strike-slip faults: Geological Society of America Abstracts with Programs, v. 18, no. 2, p. 172.
Proctor, R.J., 1968, Geology of the Desert Hot Springs-Upper Coachella Valley, Salton Sea, and vicinity: California Division of Mines and Geology, Special Report 94, 5O p.

Prentice, C.S., Weldon, R.J., and Sieh, K.E., 1986, Distribution of slip between the San Andreas and San Jacinto faults near San Bernardino, southern California: Geological Soiciety of America Abstracts with Programs, v. 18, p. 172.

Raleigh, C.B., Sieh, K.E., Sykes, L.R., and Anderson, D.L., 1982, Forecasting southern California earthquakes: Science, v. 217, p. 1097-1104.

Rasmussen, G.S., 1981, San Andreas fault geometry and maximum probable earthquakes in southern California: Geological Society of America Abstracts with Programs, v. 13, no. 2, p. 1O2.

Rasmussen, G.S., 1982, Geologic features and rate of movement along the south branch of the San Andreas fault, San Bernardino, California, in Rasmussen, G.S., ed., Geologic hazards along the San Andreas fault system, San BernardinoHemet-Elsinore, California, field trip 4 of Cooper, J.D., compiler, Neotectonics in southern California: Geological Society of America, Cordilleran Section, 78th Annual Meeting, Anaheim, Calif., Volume and Guidebook, p. 109-114.

Rasmussen, G.S., and Reeder, W.A., 1986, What happens to the real San Andreas fault at Cottonwood Canyon, San Gorgonio Pass, California? in Kooser, M.A., and Reynolds, R.E., eds., Geology around the margins of the eastern San Bernardino Mountains: Publications of the Inland Geological Society, v. 1, p. 57-62.

Richter, C.F., Allen, C.R., and Nordquist, J.M., 1958, The Desert Hot Springs earthquakes and their tectonic environment: Seismological Society of America Bulletin, v. 48, p. 315-337.

Rogers, T.H., Compiler, 1965, Santa Ana sheet of Geologic map of California: California Division of Mines and Geology, scale 1:25O,OOO.

-----1967, San Bernardino sheet of Geologic map of California: California Division of Mines and Geology, scale 1:250,000.

Ross, D.C., 1969, Map showing recently active breaks along the San Andreas fault between Tejon Pass and Cajon Pass, southern California: U.S. Geological Survey Miscellaneous Investigations Map I-553, scale 1:24,000.

Sadler, P.M., 1982a, An introduction to the San Bernardino Mountains as the product of young orogenesis, in Sadler, P.M., and Kooser, M.A., eds., Late Cenozoic stratigraphy and structure of the San Bernardino Mountains, field trip 6 of Cooper, J.D., compiler, Geologic excursions in the Transverse Ranges, southern California: Geological Society of America, Cordilleran Section, 78th Annual Meeting, Anaheim, Calif., 1982, Volume and Guidebook, p. 57-65.

-----1982b, Provenance and structure of late Cenozoic sediments in the northeast San Bernardino Mountains, in Sadler, P.M., and Kooser, M.A., eds., Late Cenozoic stratigraphy and structure of the San Bernardino Mountains, field trip 6 of Cooper, J.D., compiler, Geologic excursions in the Transverse Ranges, southern California: Geological Society of America, Cordilleran Section, 78th Annual Meeting, Anaheim, Calif., 1982, Volume and Guidebook, p. 83-92.

Sadler, P.M., and Demirer, Ali, 1986, Geology of upper Mill Creek and Santa Ana Canyon, southern San Bernardino Mountains, California, field trip 12 of Ehlig, P.L., compiler, Neotectonics and faulting in southern California: Geological Society of America, Cordilleran Section, 82nd Annual Meeting, Los Angeles, California, 1986, Guidebook and Volume, p. 129-140.

Sadler, P.M., and Reeder, W.A., 1983, Upper Cenozoic quartzite-bearing gravels of the San Bernardino Mountains, southern California: recycling and mixing as a result of transpressional uplift, in Anderson, D.W., and Rymer, M.J., eds., Tectonics and sedimentation along faults of the San Andreas system: Pacific Section, Society of Economic Paleontologists and Mineralogists, p. 45-57.

Sanders, C.O., and Kanamori, Hiroo, 1984, A seismotectonic analysis of the Anza seismic gap, San Jacinto fault zone, southern California: Journal of Geophysical Research, v. 89, no. B7, p. 5873-5890.

Savage, J.C., 1983, Strain accumulation in western United States: Annual Reviews of Earth and Planetary Sciences, v. 11, p. 11-43.

Savage, J.C., and Prescott, W.H., 1976, Strain accumulation on the San Jacinto fault near Riverside, California: Seismological Society of America Bulletin, v. 66, no. 5, p. 1749-1754.

Savage, J.C., Prescott, W.H., Lisowski, M., and King, N., 1979, Deformation across the Salton Trough, California, 1973-1977: Journal of Geophysical Research, v. 84, no. B6, p. 3069-3079.

Schwartz, D.P., and Coppersmith, K.J., 1984, Fault behavior and characteristic earthquakes: examples from the Wasatch and San Andreas fault zones: Journal of Geophysical Research, v. 89, no. B7, p. 5681-5698.

Sharp, R.V., 1967, San Jacinto fault zone in the Peninsular Ranges of southern California: Geological Society of America Bulletin, v. 78, p. 705-730.

-----1972, Map showing recently active breaks along the San Jacinto fault zone between the San Bernardino area and Borrego Valley, California: U.S. Geological Survey Miscellaneous Geologic Investigations Map I-675, scale 1:24,000.

-----1979, Some characteristics of the eastern Peninsular Ranges mylonite zone, in Analysis of actual fault zones in bedrock: U.S. Geological Survey Open-File Report 79-1239, p. 258-267.

-----1981, Variable rates of late Quaternary strike slip on the San Jacinto fault zone, southern California: Journal of Geophysical Research, v. 86, no. B3, p. 1754-1762.

-----1982, Tectonic setting of the Imperial Valley region, in The Imperial Valley, California, earthquake of October 15, 1979: U.S. Geological Survey Professional Paper 1254, p. 1-14.

Sieh, K.E., 1978a, Slip along the San Andreas fault associated with the great 1857 earthquake: Seismological Society of America Bulletin, v. 68, no. 5, p. 1421-1448.

-----1978b, Prehistoric large earthquakes produced by slip on the San Andreas fault at Pallet Creek, California: Journal of Geophysical Research, v. 83, no. B8, p. 3907-3939.

-----1981, A review of geological evidence for recurrence times of large earthquakes, in Simpson, D.W., and Richards, P.G., eds., Earthquake prediction--An international review: American Geophysical Union Maurice Ewing Series, no. 4, p. 181-207.

-----1984, Lateral offsets and revised dates of large prehistoric earthquake at Pallett Creek, southern California: Journal of Geophysical Research, v. 89, no. B9, p. 7641-7670.

Sieh, K.E., and Jahns, R.H., 1984, Holocene activity of the San Andreas fault at Wallace Creek, California: Geological Society of America Bulletin, v. 95, p. 883-896.

Smith, D.P., 1977, San Juan-St. Francis fault--hypothesized major middle Tertiary right-lateral fault in central and southern California, California Division of Mines and Geology, Special Report 129, p. 41-50.

Smith, R.E., 1959, Geology of the Mill Creek area, San Bernardino County, California: Los Angeles,

University of California, unpublished M.A. thesis, 95 p.

Stewart, J.H., and Poole, F.G., 1975, Extension of the Cordilleran miogeosynclinal belt to the San Andreas fault, southern California: Geological Society of America Bulletin, v. 86, p. 205-212.

Sykes, L.R., and Seeber, Leonardo, 1982, Great earthquakes and great asperities along the San Andreas fault, southern California: EOS, American Geophysical Union Transactions, v. 63, no. 45, p. 1030.

Sykes, L.R., and Nishenko, S.P., 1984, Probabilities of occurrence of large plate-rupturing earthquakes for the San Andreas, San Jacinto, and Imperial faults, California, 1983-2003: Journal of Geophysical Research, v. 89, no. B7, p. 5905-5927.

Sykes, L.R., and Seeber, Leonardo, 1982, Great earthquakes and great asperities along the San Andreas fault, southern California: EOS, American Geophysical Union Transactions, v. 63, no. 45, p. 1030.

Sykes, L.R., and Seeber, Leonardo, 1985, Great earthquakes and great asperities, San Andreas fault, southern California: Geology, v. 13, no. 12, p. 835-838.

Thatcher, W., Hileman, J.A., and Hanks, T.C., 1975, Seismic slip distribution along the San Jacinto fault zone, Southern California, and its implications: Geological Society of America Bulletin, v. 86, p. 1140 1146.

Truex, J.N., 1976, Santa Monica and Santa Ana Mountains - relation to Oligocene Santa Barbara Basin: American Association of Petroleum Geologists Bulletin, v. 60, p. 65-86

Vaughan, F.E., 1922, Geology of the San Bernardino Mountains north of San Gorgonio Pass: California University Publications in Geological Sciences, v. 13, p. 319-411.

Wallace, R.E., 1949, Structure of a portion of the San Andreas rift in southern California: Geological Society of America Bulletin, v. 60, no. 4, p. 781-806.

Webb, T.H., and Kanamori, Hiroo, 1985, Earthquake focal mechanisms in the eastern Transverse Ranges and San Emigdio Mountains, southern California, and evidence for a regional decollement: Bulletin of the Seismological Society of America, v. 75, no. 3, p. 737-757.

Weldon, R.J., 1983, Climatic control for the formation of terraces in Cajon Creek, southern California: Geological Society of America Abstracts with Programs, v. 15, no. 5, p. 429.

-----1984, Quaternary deformation due to the junction of the San Andreas and San Jacinto faults, southern California: Geological Society of America, Abstracts with Programs, v. 16, no. 6, p., 689.

-----1985a, Implications of the age and distribution of the late Cenozoic stratigraphy in Cajon Pass, southern California, in Reynolds, R.E., compiler, Geological investigations along Interstate 15, Cajon Pass to Manix Lake, California: San Bernardino County Museum Publication, p. 59-68.

-----1985b, The late Cenozoic geology of Cajon Pass; implications for tectonics and sedimentation along the San Andreas fault: Pasadena, California Institute of Technology, unpublished Ph.D. thesis, 382 p.

Weldon, Ray, and Humphreys, Eugene, 1985, A kinematic model of southern California: Tectonics, v. 5, no. 1, p. 33-48.

Weldon, R.J., and Meisling, K.E., 1982, Late Cenozoic tectonics in the western San Bernardino Mountains; Implications for the uplift and offset of the central Transverse Ranges: Geological Society of America Abstracts with Programs, v. 14, no. 4, p. 243-244.

Weldon, R.J., II, and Sieh, K.E., 1985, Holocene rate of slip and tentative recurrence interval for large earthquakes on the San Andreas fault, Cajon Pass, southern California: Geological Society of America Bulletin, v. 96, p. 793-812.

Weldon, R.J., Meisling, K.E., Sieh, K.E., and Allen, C.R., 1981, Neotectonics of the Silverwood Lake area, San Bernardino County: Report to the California Department of Water Resources, 22 p., scale 1:24,000.

Weldon, R.J., Winston, D.S., Kirschvink, J.L., and Burbank, D.W., 1984, Magnetic stratigraphy of the Crowder Formation, Cajon Pass, southern California: Geological Society of America Abstracts with Programs, v. 16, p. 689.

Wesnousky, S.G., Prentice, C.S., and Sieh, K.E., 1991, An offset Holocene stream channel and the rate of slip along the northern reach of the San Jacinto fault zone, San Bernardino Valley, California: Geological Society of America Bulletin, v. 103, p. 700-709.

Wesson, R.L., and Wallace, R.E., 1985, Predicting the next great earthquake in California: Scientific American, v. 252, no. 2, p. 35-43.

West, D.L. 1987, Geology of the Wilson Creek-Mill Creek fault zone--the north flank of the former Mill Creek basin, San Bernardino County, California: Riverside, University of California, unpublished M.S. thesis, 94 p.

Williams, P., Nicholson, C., Seeber, L., and Sykes, L., 1984, Seismicity of the southern San Andreas fault, California: EOS, Transactions of the American Geophysical Union, v. 65, no. , p. 996.

Willingham, R.C., 1971, Basement fault geometries in the San Bernardino Valley and western San Gorgonio Pass area, southern California: Geological Society of America Abstracts with Programs, v. 3, no. 2, p. 217.

-----1981, Gravity anomaly patterns and fault interpretations in the San Bernardino Valley and western San Gorgonio Pass area, southern California, in Brown, A.R., and Ruff, R.W., eds., Geology of the San Jacinto Mountains: Santa Ana, California, South Coast Geological Society, Annual Field trip guidebook, no. 9, p. 164-174.

Woodburne, M.O., 1975, Cenozoic stratigraphy of the Transverse Ranges and adjacent areas, southern California: Geological Society of America Special Paper 162, 91 p.

Woodburne, M.O., and Golz, D.J., 1972, Stratigraphy of the Punchbowl formation, Cajon Valley, southern California: California University, Publications in Geological Sciences, v. 92, 73 p.

Yeats, R.S., 1968a, Rifting and rafting in the southern California borderland, in Dickinson, W.R., and Grantz, Arthur, eds., Proceedings of Conference on Geologic Problems of San Andreas Fault System: Stanford University Publications, Geological Sciences, v. 11, p. 307-322.

Yerkes, R.F., and Campbell, R.H., 1971, Cenozoic evolution of the Santa Monica Mountains-Los Angeles Basin area: I. Constraints on tectonic models: Geological Society of America Abstracts with Programs, v. 3, no. 2, p. 222-223.

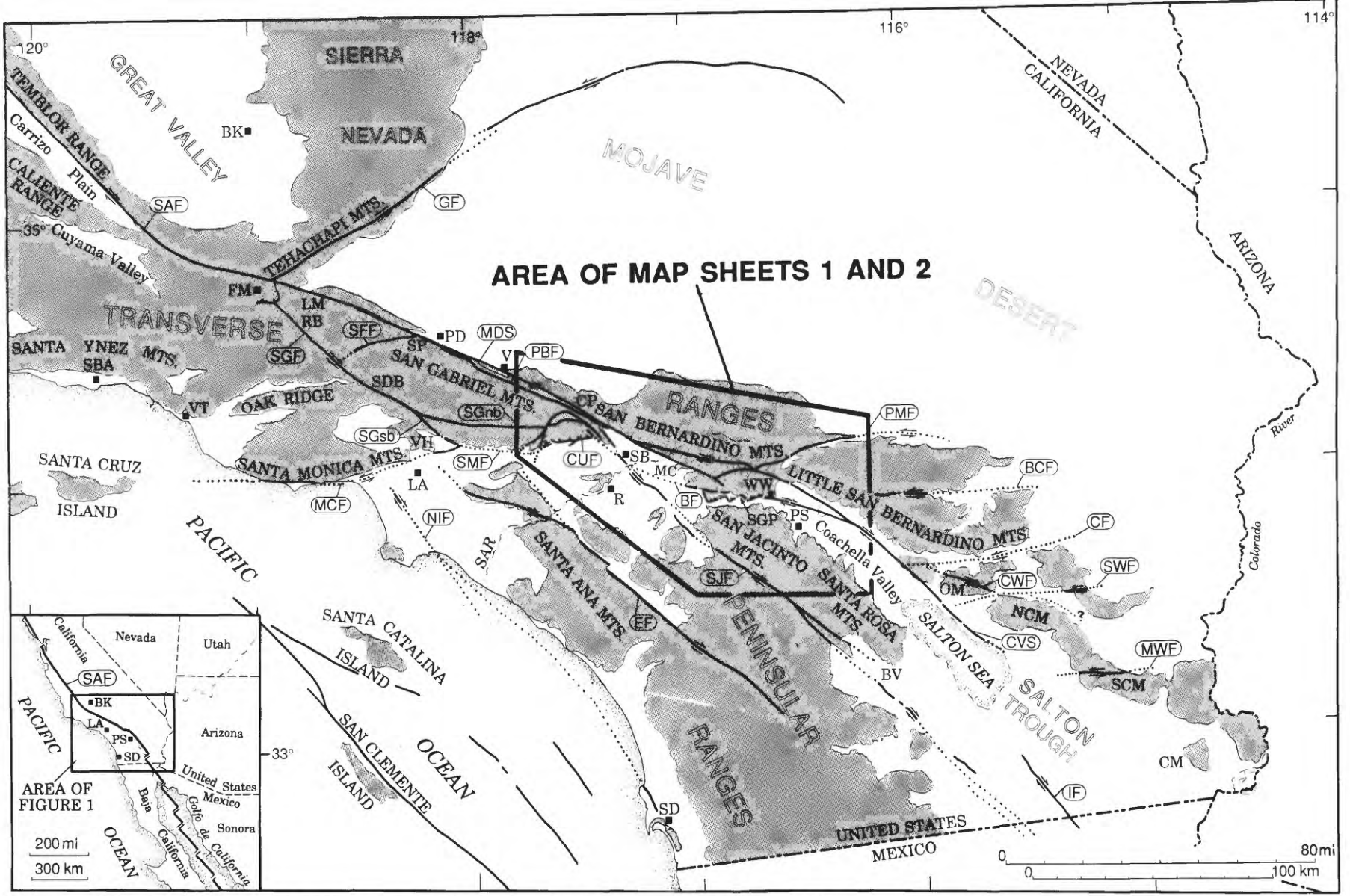

Figure 1.--Index map showing geographic features and faults discussed in this report. BCF, Blue Cut fault; BF, Banning fault; BK, Bakersfield; BV, Borrego Valley region; CF, Chiriaco fault; CM, Cargo Muchacho Mountains; CP, Cajon Pass region; CUF, Cucamonga fault; CVS, Coachella Valley segment, San Andreas fault; CWF, Clemens Well fault; EF, Elsinore fault; FM, Frazier Mountain region; GF, Garlock fault; IF, Imperial fault; LA, Los Angeles; LM, Liebre Mountain; MCF, Malibu Coast-Santa Monica-Raymond fault; MC, Mill Creek; MDS, Mojave Desert segment, San Andreas fault; MWF, Mammoth Wash fault; NCM, northern Chocolate Mountains; NIF, Newport-Inglewood fault; OM, Orocopia Mountains; PBF, Punchbowl fault; PD, Palmdale; PMF, Pinto Mountain fault; R, Riverside; RB, Ridge Basin; SAF, San Andreas fault; SAR, Santa Ana River; SB, San Bernardino; SBA, Santa Barbara; SBM, San Bernardino Mountains; SCM, southern Chocolate Mountains; SD, San Diego; SDB, Soledad Basin; SFF, San Francisquito fault; SGF, San Gabriel fault; SGnb, north branch, San Gabriel fault; SGsb, south branch, San Gabriel fault; SGP, San Gorgonio Pass; SJF, San Jacinto fault; SMF, Sierra Madre fault; SP, Sierra Pelona; SWF, Salton Wash fault; V, Valyermo; VT, Ventura; WW, Whitewater.

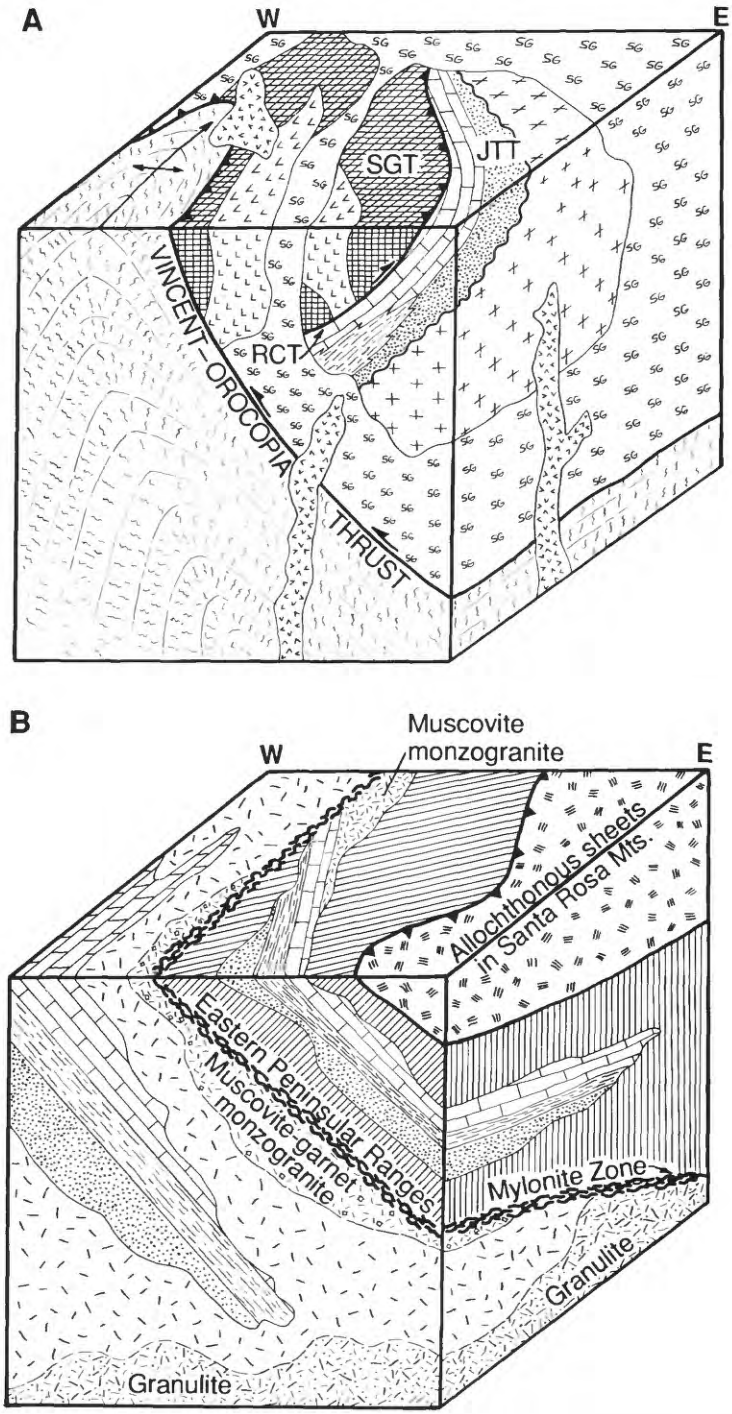

Figure 2.--Block diagrams schematically illustrating relations among major lithologies and structures in rocks of San Gabriel Mountains-type, Peninsular Ranges-type, and San Bernardino Mountains-type. W, west; E, east. (A) Rocks of San Gabriel Mountains-type, including rocks of Powell's (1982a,b) Joshua Tree terrane (JTT) and San Gabriel terrane (SGT) separated by the pre-Cretaceous Red Cloud thrust (RCT). The Joshua Tree terrane includes Proterozoic metaquartzite, pelitic schist and gneiss, and marble resting nonconformably on granitic gneiss; the San Gabriel terrane includes anorthosite and gabbro, syenite-mangerite, and orthogneiss (augen gneiss and retrograded granulite). (B) Rocks of Peninsular Ranges-type, including lower and upper plates of the Eastern Peninsular Ranges mylonite zone of Sharp (1979). In both plates, metasedimentary rocks include metaquartzite, pelitic gneiss and schist, graphitic schist, and marble.

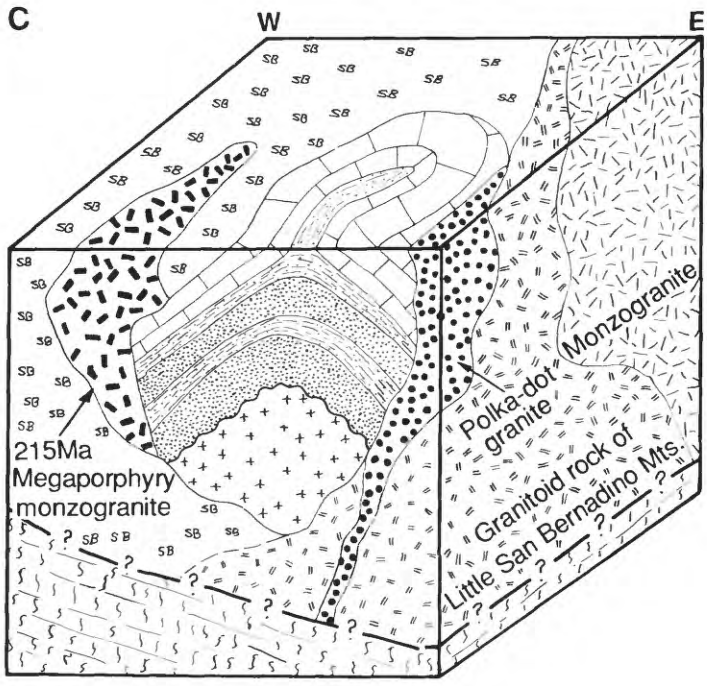

Figure 2 (Continued).--(C) Rocks of San Bernardino Mountains-type. Metasedimentary rocks include metaquartzite, pelitic gneiss and schist, and marble that are comparable to uppermost Proterozoic and Paleozoic rocks of the Cordilleran miogeocline (Stewart and Poole, 1975). SB indicates undifferentiated metasedimentary rocks of San Bernardino Mountains-type.

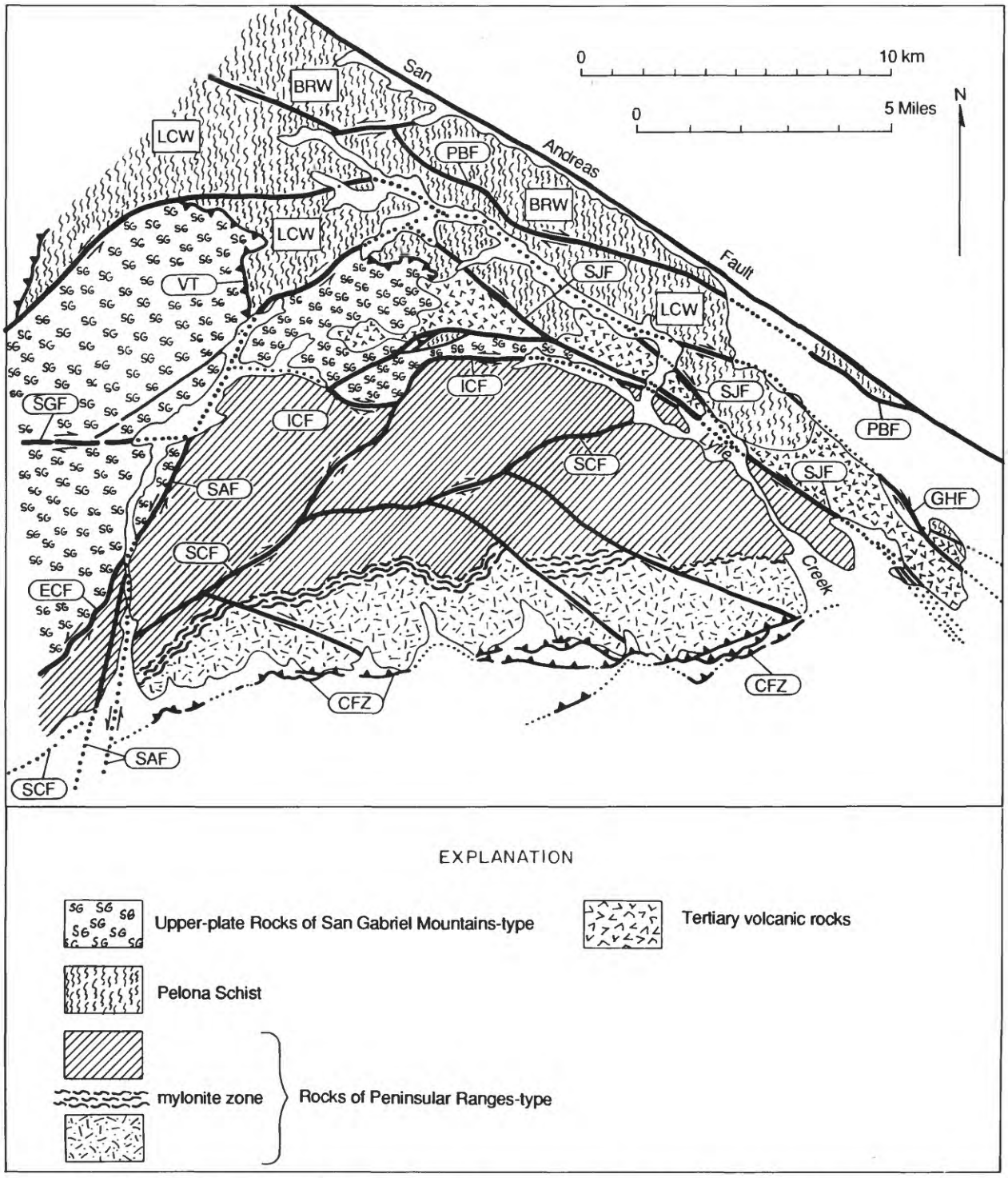

Figure 3.--Distribution, geologic relations, and nomenclature of geologic terranes and Neogene faults in the southeastern San Gabriel Mountains (modified from Morton, 1975a, figs. 1,2). BRW, Blue Ridge Window of Pelona Schist; CFZ, Cucamonga fault zone; ECF, Evey Canyon fault; GHF, Glen Helen fault; ICF, Icehouse Canyon fault; LCW, Lytle Creek window of Pelona Schist; PBF, Punchbowl fault; SAF, San Antonio fault; SCF, Stoddard Canyon fault (includes San Gabriel fault [south branch] west of the San Antonio fault); SGF, San Gabriel fault (north branch); SJF, faults traditionally referred to the San Jacinto fault; VT, Vincent thrust.

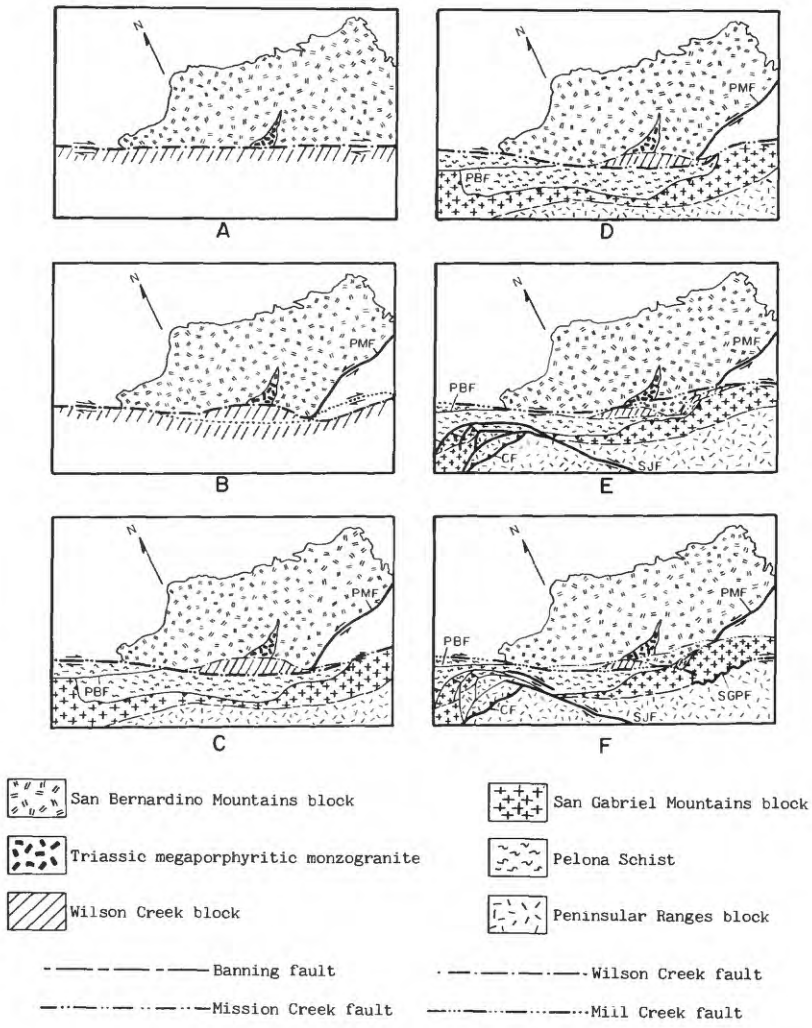

Figure 4.--Schematic diagram summarizing the history of the San Andreas fault system in the vicinity of the central Transverse Ranges. Heavy lines indicate active faults; lighter lines indicate inactive faults. CF, Cucamonga fault; PBF, Punchbowl fault. (A) Approximately 40 km of right slip on the Wilson Creek-Punchbowl strand of the San Andreas fault juxtaposes the Wilson Creek block against the San Bernardino Mountains block. The total geographic extent of the Wilson Creek block and its relations with other terranes to the northwest, west, and southeast are not indicated because they are not known. (B) The Wilson Creek-Punchbowl strand is compressed into a trace that is sinuous regionally, and the strand locks up. Dotted line shows the future trace of the Mission Creek strand of the San Andreas. (C) The Mission Creek strand evolves outboard (west) of the Wilson Creek-Punchbowl strand adjacent to the southeastern San Bernardino Mountains but inboard (east) of the strand to the southeast. This allows the Punchbowl fault to be conveyed northwestward away from its dismembered counterpart--the Wilson Creek fault--that remains stranded against the San Bernardino Mountains. The Mission Creek strand eventually generates about 89 km of right slip that juxtaposes the San Gabriel Mountains block against the Wilson Creek and San Bernardino Mountains blocks. (D) The Mission Creek strand gradually is deformed as the San Bernardino Mountains block is projected across the path of the San Andreas fault by left-slip on the Pinto Mountain fault (PMF). These events create a left step between the Coachella Valley and Mojave Desert segments of the San Andreas fault (see fig. 5). (E) The San Jacinto fault evolves outboard (west) of the locked-up Mission Creek strand, probably about 1.0 to 1.5 m.y. ago; the Mill Creek strand of the San Andreas evolves inboard of the locked-up Mission Creek strand at a later time--perhaps 0.5 m.y. ago . (F) The Mill Creek strand is locked up by continued left slip on the Pinto Mountin fault, leading to the modern neotectonic setting (fig. 6) where slips steps left from the Coachella Valley segment of the San Andreas fault to the Banning fault and thence into the San Gorgonio Pass fault zone (SGPF), where the Peninsular Ranges block is converging with the San Gabriel Mountains block.

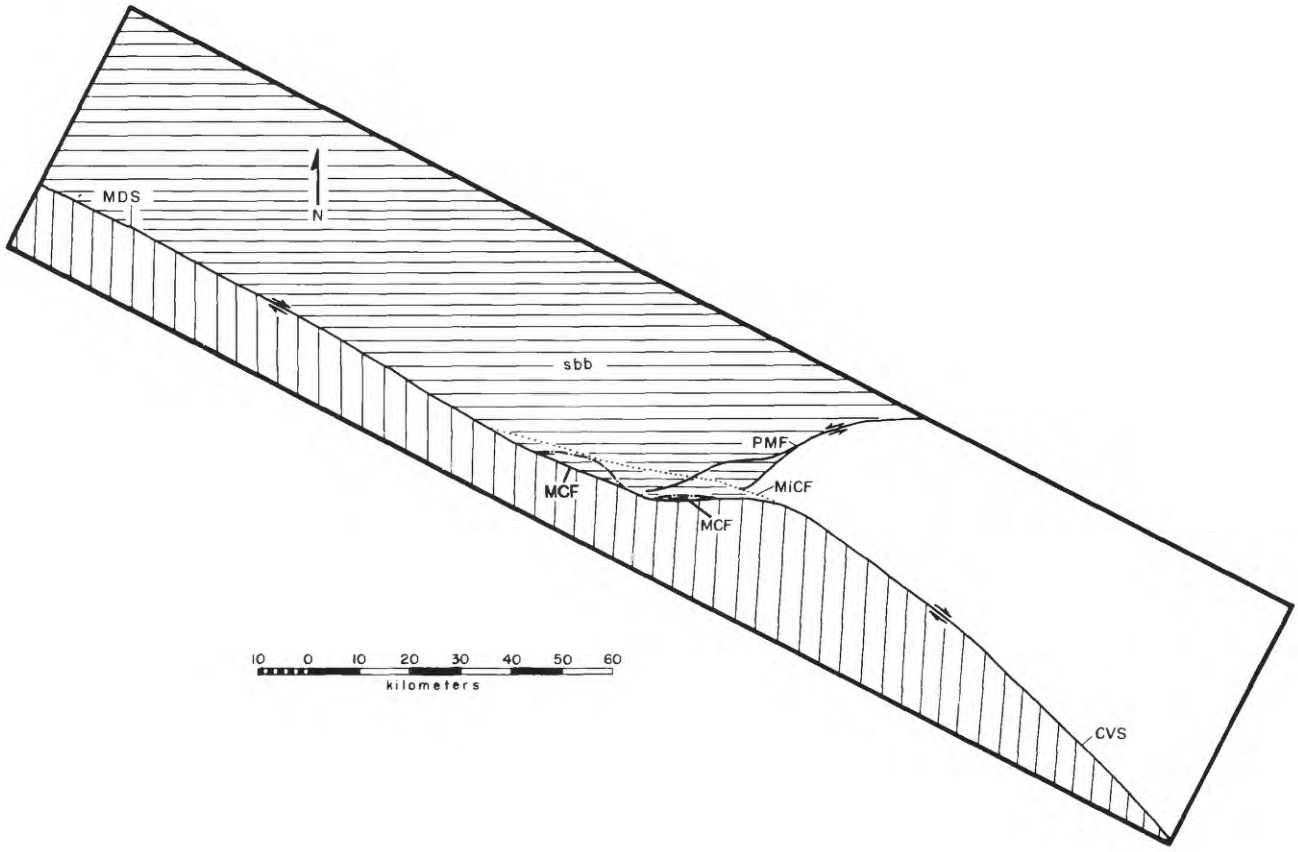

Figure 5.--Diagram illustrating the left step that displaces the Coachella Valley and Mojave Desert segments of the San Andreas fault in the vicinity of San Gorgonio Pass. The diagram represents geologic relations in the Pleistocene, about 750,000 yr ago. The Mission Creek strand of the San Andreas (MCF) has generated all of its right slip, has been abandoned by the San Andreas system, and eventually will be succeeded by the Mill Creek strand (MiCF) that will evolve along the dotted trace and will generate about 8 km of right slip. The San Bernardino Mountains block (sbb) has been projected across the path of the San Andreas fault, accompanied by left-slip on the Pinto Mountain fault (PMF). These events have displaced the Mojave Desert segment (MDS) and Coachella Valley segment (CVS) by about 15 km--the amount of left slip on the Pinto Mountain fault as determined by Dibblee (1968b). Exotic rocks of the Wilson Creek block, originally juxtaposed against the San Bernardino Mountains block by right-slip on the Wilson Creek strand (WCF) of the San Andreas, became attached to the San Bernardino Mountains block once they were bypassed by the Mission Creek strand; since that time, the Wilson Creek and San Bernardino Mountains blocks have behaved as a single unit that has been projected across the path of the San Andreas fault.

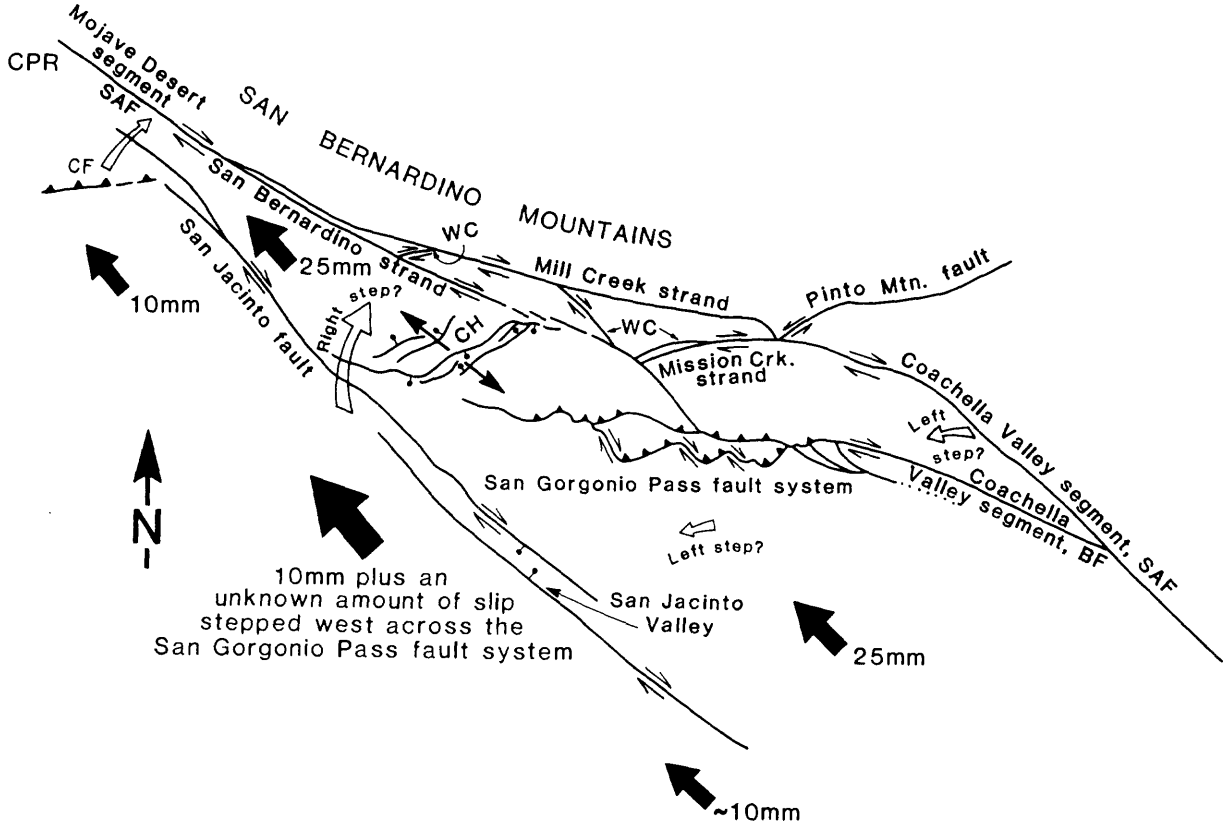

Figure 6.--Schematic diagram illustrating relations between faults and crustal blocks in the vicinity of the south-central Transverse Ranges. Large solid arrows indicate the relative motion of crustal blocks; large hollow arrows indicate lateral transfer of slip. Small solid arrows indicate crustal extension in the Crafton Hills horst-and-graben complex. BF, Banning fault; CF, Cucamonga fault; CH, Crafton Hills; CPR, Cajon Pass region; SAF, San Sandreas fault; WC, Wilson Creek strand, San Andreas fault. Ten millimeters of annual slip on the San Jacinto fault is assumed from data of Sharp (1981).

TABLE 1. NOMENCLATURAL USAGE FOR FAULTS OF THE SAN ANDREAS FAULT SYSTEM

Usage in this Chapter	Previous Usage
	SAN ANDREAS FAULT ZONE
Salton Trough	
Coachella Valley segment, San Andreas fault	North Branch, San Andreas fault (Dibblee, 1954, 1967b, 1975a; Dillon, 1975; Peterson, 1975) Mission Creek fault (Allen, 1957; Farley,1979)
Coachella Valley segment, Banning fault	South Branch, San Andreas fault (Dibblee, 1954, 1968a, 1975a; Dillon, 1975) Banning fault (Allen, 1957)
San Bernardino Mountains	
Wilson Creek strand, San Andreas fault	Wilson Creek fault (Dibblee, 1964, 1982b; Gibson, 1964, 1971; Sadler and Demirer, 1986)
Mission Creek strand, San Andreas fault	Mission Creek fault (Allen, 1957; Ehlig, 1977; Farley, 1979; Matti and others, 1983a, 1985)
Mill Creek strand, San Andreas fault	Mill Creek fault (Allen, 1957; Gibson, 1964, 1971; Ehlig, 1977; Farley, 1979); north branch, San Andreas fault (Dibblee, 1964, 1967b, 1968a, 1975a, 1982b)
San Bernardino strand, San Andreas fault	South Branch, San Andreas fault (Dibblee, 1964, 1968a, 1975a, 1982b)
San Gabriel Mountains–Mojave Desert	
Punchbowl fault	Noble (1953; 1954a, b); Dibblee (1967a, 1968a, 1982a); Ehlig (1975, 1981); Barrows and others (1985, 1987); Barrows (1975, 1987)
Nadeau fault (south branch)	Barrows and others (1985, 1987); Barrows (1987)
Nadeau fault (north branch)	Barrows and others (1985, 1987); Barrows (1987)
Mojave Desert strand	Dibblee (1967a, 1968a, 1982a); "main trace" of Barrows and others (1985, 1987); Barrows (1975, 1987)
Little Rock fault	Barrows and others (1985, 1987); Barrows (1975, 1987)
	SAN GABRIEL FAULT ZONE
Salton Trough through San Bernardino Valley	
Banning fault	Matti and Morton (1982); Matti and others (1985)
San Gabriel Mountains	
San Gabriel fault (south branch)	No consistent or documented usage
Stoddard Canyon fault	Interpreted as a left-lateral fault by Morton (1975a)
San Gabriel fault (north branch)	Ehlig (1973, 1975, 1981, 1982); Dibblee (1968a, 1982a); Crowell (1975a, c; 1981, 1982a)
Icehouse Canyon fault	Evans (1982); Matti and others (1985); May and Walker (1989)
Cajon Pass	
Cajon Valley fault	Dibblee (1967a, 1968a); Woodburne and Golz (1972); Matti and others (1985); Weldon (1986); Meisling and Weldon (1989)
	SAN JACINTO FAULT ZONE
San Jacinto Mountains to San Bernardino Valley	
San Jacinto fault	Sharp (1967); Matti and others (1985)
San Gabriel Mountains	
San Jacinto fault	Morton (1975a); Dibblee (1968a, 1975a, 1982a)
Glen Helen fault	Morton (1975a); Matti and others (1985); Morton and Matti (1987, this volume)
	CLEMENS WELL–FENNER–SAN FRANCISQUITO FAULT ZONE
Orocopia Mountains	
Clemens Well fault	Crowell (1975b); Powell (1981, 1986, this volume)
San Gabriel Mountains	
Fenner fault	Dibblee (1967a, 1968a, 1982a); Powell (1981, 1986, this volume); Ehlig (1975, 1981); Barrows and others (1985, 1987); Barrows (1975, 1987)
Soledad Basin region	
San Francisquito fault	Dibblee (1967a, 1968a, 1982a); Powell (1981,1986, this volume); Ehlig (1975, 1981); Barrows and others (1985, 1987); Barrows (1975, 1987)

From Matti and Morton, 1992

TABLE 2. DOCUMENTATION FOR K/Ar RADIOMETRIC AGE DATES FROM BASALT IN THE PAINTED HILL FORMATION, WHITEWATER AREA*

Sample	K_2O (%)	^{40}Ar (moles/gm)	$^{40}Ar/\Sigma^{40}Ar$ (%)	Age (Ma)
DG-1A	1.133, 1.121	9.813×10^{-12}	60	6.04 ± 0.18
DG-1B	1.095, 1.087	9.341×10^{-12}	66	5.94 ± 0.18

Constants used in age calculation: $\lambda B = 4.963 \times 10^{-10}\ yr^{-1}$
$\lambda_\varepsilon + \lambda_{\varepsilon'} = 0.581 \times 10^{-10}\ yr^{-1}$
$^{40}K/K_{total} = 1.167 \times 10^{-4}$ mole/mole

*A basalt flow in the lower part of the Painted Hill Formation north of the Banning fault has yielded two concordant whole-rock K/Ar age determinations of 6.04 ± 0.18 and 5.94 ±0.18 Ma. The analyses were performed by J. L. Morton at the U.S. Geological Survey. Both samples are fresh, fine-grained basalt with plagioclase phenocrysts as long as 0.5 cm. The whole-rock samples were crushed and sieved, then treated with hydrofluoric and nitric acid to reduce atmospheric argon contamination. Potassium was analyzed by flame photometry; argon was analyzed by standard isotope-dilution procedures, using a 60°, 15.2-cm radius, Neir-type mass spectrometer. The overall analytical uncertainty of the ages is approximately 3 percent and is a combined estimate of the precision of the argon and potassium measurements at 1 standard deviation.

From Matti and Morton, 1992

Geophysical Research Letters

RESEARCH LETTER
10.1029/2020GL088532

Key Points:
- End-member model examines the fewest, but longest, ruptures required by ages of ground-rupturing earthquakes from 31 paleoseismic sites
- Regional clustering emerges, with largest moment release ruptures similar to the historic record with ruptures breaking much of the system
- Ruptures through San Gorgonio Pass are infrequent, and anticorrelated with episodes when fault sections near Cajon Pass are active

Supporting Information:
- Supporting Information S1
- Figure S1
- Figure S2
- Figure S3
- Figure S4
- Table S1
- Table S2

Correspondence to:
K. M. Scharer,
kscharer@usgs.gov

Citation:
Scharer, K. M., & Yule, D. (2020). A Maximum Rupture Model for the Southern San Andreas and San Jacinto Faults, California, Derived From Paleoseismic Earthquake Ages: Observations and Limitations. *Geophysical Research Letters*, *47*, e2020GL088532. https://doi.org/10.1029/2020GL088532

Received 22 APR 2020
Accepted 27 JUN 2020
Accepted article online 8 JUL 2020

©2020. The Authors.
This is an open access article under the terms of the Creative Commons Attribution-NonCommercial-NoDerivs License, which permits use and distribution in any medium, provided the original work is properly cited, the use is non-commercial and no modifications or adaptations are made.

A Maximum Rupture Model for the Southern San Andreas and San Jacinto Faults, California, Derived From Paleoseismic Earthquake Ages: Observations and Limitations

Katherine M. Scharer[1] and **Doug Yule**[2]

[1]Earthquake Science Center, U.S. Geological Survey, Pasadena, CA, USA, [2]Department of Geological Sciences, California State University, Northridge, CA, USA

Abstract Paleoseismic rupture histories provide spatiotemporal models of earthquake moment release needed to test numerical models and lengthen the instrumental catalog. We develop a model of the fewest and thus largest magnitude earthquakes permitted by paleoseismic data for the last 1,500 years on the southern San Andreas and San Jacinto Faults, California, USA. The largest geometric complexity appears to regulate the system: Only two ruptures break the San Gorgonio Pass region, followed by episodes of ruptures that could bridge the northern San Jacinto Fault and the San Andreas Fault. When tested against independent data on slip per event, the model produces comparable values indicating the end-member model does not underpredict rupture rates. Rupture of >85% of the fault length in the historic period between 1800 and 1857 and the subsequent quiescence is similar to epochs of activity in the prehistoric model, suggesting that regional clustering of seismicity could be a trait of the system.

Plain Language Summary Large, damaging earthquakes are rare, so geologic data are essential to supplement the record of earthquakes from seismographs. We use the geologic record to determine the magnitude and timing of past earthquakes on the San Andreas and San Jacinto Faults. A pattern emerges in which the biggest bends and splays control the length of most ruptures. Because the model estimates the largest-possible earthquakes on this system, it is useful as an upper limit on earthquake size used in engineering and earthquake forecasting.

1. Introduction

A single, large magnitude earthquake can devastate a region, but a sequence of significant earthquakes will magnify the social challenges of mitigation, emergency response, and reconstruction. In the historic record of plate boundary regions, large earthquakes occurring in isolation appear rare, whereas there are a number of well-documented examples of regional sequences in which several hundreds of kilometers of a fault system have ruptured in a few earthquakes over multiple decades. Examples on strike-slip faults include the 20th century progression along the North Anatolian Fault in Turkey (Barka et al., 2002) and the cluster of Mw > 7 events along the Kunlun Fault culminating in the 2001 Kokoxili earthquake in Tibet (Xie et al., 2014). The 21st century seismic events on the Sumatra-Andaman Sunda Megathrust provide a classic cascade example from subduction zones (Philibosian & Meltzner, 2020). The causes of rupture sequences on a fault network have been explored in terms of static stress conditions such as Coulomb stress transfer (King et al., 1994), cumulative Coulomb stress transfer (Mildon et al., 2019), heterogeneous prestress (Duan & Oglesby, 2007), elapsed time since previous ruptures (Schwartz et al., 2012), and time-dependent behavior of the lithosphere (Bürgmann & Dresen, 2008), though no single approach has been shown to be a definitive predictor (e.g., Freed, 2005; Harris & Simpson, 1998). Understanding if isolated ruptures, cascades, or clusters typifies large ruptures on a fault system is of interest because it may reveal complex time evolution of stress on faults and fault networks, effects that are not currently incorporated into seismic hazard assessments. There are a few papers that explore lithospheric mechanisms that would produce regional clustering (e.g., Ben-Zion et al., 1999; Scholz, 2010), but additional work is warranted if this is a robust feature of fault networks.

Several studies, from relatively short records for the San Francisco Bay Region in California, USA (Schwartz et al., 2014), moderate length records in the central Italian Apennines (Mildon et al., 2019), and longer

Table 1
Site ID and References for Field Sites Used in Maximum Rupture Model (Figure 1)

Site ID	Site name	Primary and/or date references[a]
An	Annette	Williams et al. (2018)
LY	Las Yeguas	Young et al. (2002)
BF	Bidart Fan	Akçiz et al. (2010)
MP	Mil Potrero	Davis (1983)
FM	Frazier Mountain	Scharer et al. (2017)
3P	Three Points	Rust (2005)
EL	Elizabeth Lake	Bemis et al. (2016)
LR	Littlerock	Pruitt et al. (2009)
PC	Pallett Creek	Sieh et al. (1989); Scharer et al. (2011)
WW	Wrightwood	Biasi et al. (2002); Weldon et al. (2004)
LS	Lost Swamp	Weldon and Sieh (1985)
Pt	Pitman Canyon	Weldon et al. (2013); Seitz et al. (1997)
Ci	City Creek	McGill et al. (2002)
Pl	Plunge Creek	McGill et al. (2002)
Bu	Burro Flats	Yule et al. (2007); Howland (2003); Figure S5
Mi	Millard Canyon	McBurnett (2011); Figure S6
Ca	Cabazon	Ramzan (2012); Wolff (2018); Figure S2
EW	East Whitewater Wash	Cardona (2016)
EA	18th Avenue	Castillo (2019)
TP	Thousand Palms	Fumal et al. (2002)
Pu	Pushawalla Creek	Earth Systems Southwest (2007)
In	Indio	Sieh (1986)
Co	Coachella	Philibosian et al. (2011)
SC	Salt Creek	Seitz and Williams (2008)
Wa	Walnut	Fumal and Kendrick (2008)
Cn	Colton	Kendrick and Fumal (2005)
Qu	Quincy	Onderdonk et al. (2015)
ML	Mystic Lake	Onderdonk et al. (2018)
BC	Blackburn Canyon	Salisbury et al. (2017)
HL	Hog Lake	Rockwell et al. (2015)
CL	Clark Lake	Buga (2012, 2015)
SM	Superstition Mountain	Gurrola and Rockwell (1996)
LC	Lake Cahuila	Rockwell et al. (2018)

[a]95% confidence ranges of ages provided in Table S1.

records on the Dead Sea Fault (Lefevre et al., 2018), suggest periods of relative quiescence alternate with episodes of increased regional activity. Paleoseismic data provide the only empirical data able to push these observations back in time to reveal the spatial-temporal patterns of large earthquakes. Here we examine the fastest moving faults in southern California, the San Andreas Fault (SAF) and the San Jacinto Fault (SJF). Three historic earthquakes ruptured at least 560 km out of a total considered length of 710 km of these faults in less than 60 years in 1800, 1812, and 1857; we ask if this is typical for the system.

We focus on the SAF and SJF, as these faults carry the majority of the plate motion in southern California and have been characterized by a high density of well-developed paleoseismic sites (Table 1; Figure 1). The slip rate along the system varies; in the south, the SAF and SJF are coparallel and exhibit roughly coequal rates of ~12–22 and 10–16 mm/year, respectively (Dawson & Weldon, 2013). Northwest of where the faults join at Cajon Pass, the slip rate increases to a maximum of ~33 mm/year (Dawson & Weldon, 2013). We assembled available paleoearthquake ages from 31 sites spanning 510 km of the southern SAF and 200 km of the SJF and build a rupture history using only these temporal constraints (Table 1). Data sets from the San Gorgonio Pass Fault Zone (SGPFZ) and the region encompassing the junction of the SAF and SJF at Cajon Pass (Figure 1a) provide insight into the regions of greatest fault complexity along this system. The model is designed as an end-member model to explore the longest ruptures (i.e., largest magnitude) that fit the data, yet we find the calculated magnitudes and predicted average slip are compatible with independent estimates. The model suggests episodes of cascades and overlapping events that are broadly consistent with the historic record and can be used to inform earthquake forecasts.

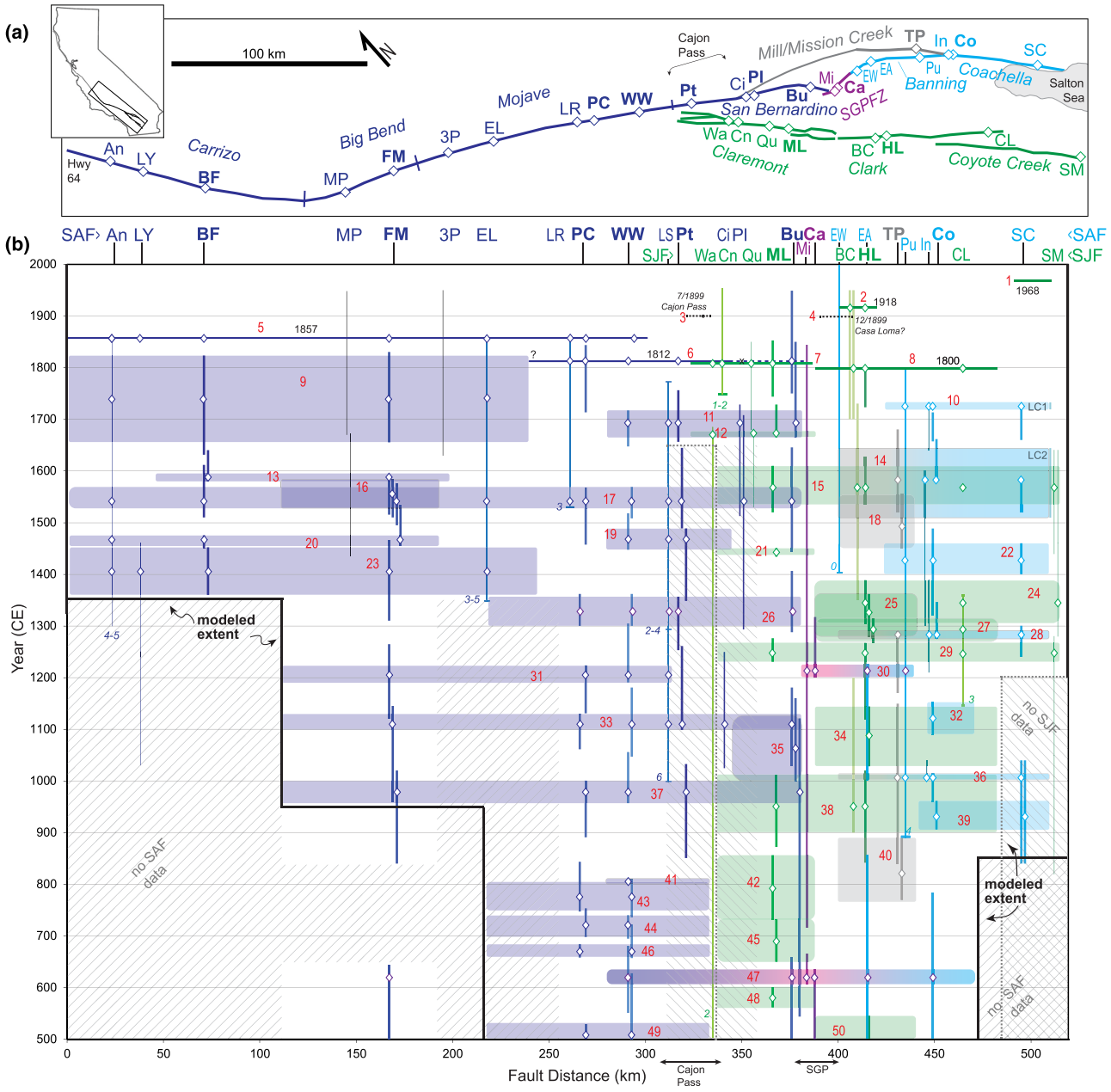

Figure 1. Maximum rupture model for SAF (dark and light blues), SJF (green), SGPFZ (purple), and Mill/Mission Creek (gray). (a) Map with fault section (or strand) and site identification as provided in Table 1; bold indicates sites with high temporal resolution. The Garnet Hill strand is too small to be seen at this scale but would be located under text "EW." (b) Correlation diagram based on 95% confidence range of site earthquake ages (vertical bars, Table S1). A version with SAF and SJF in separate panels is provided in Figure S1. When individual ages are not known, the total number of events is indicated with italic number at base of thin vertical line. Horizontal bands show length of ruptures permitted; height of bands is based on limiting ages of correlated site earthquakes. Red numbers refer to rupture ID (Table S2). Diamonds identify which sites ruptured in each earthquake and are aligned with mean rupture age. Periods with no data are indicated by diagonal hatching; black and dotted gray lines delimit extent of fault length used to calculate scaled moment release for SAF and SJF, respectively.

2. Paleoseismic Data and Model Construction

The rupture model uses ages of ground-rupturing earthquakes from published trenching investigations, Master's Theses, and technical reports (Tables 1 and S1 in the supporting information). Earthquake ages are determined by Bayesian modeling of radiocarbon dates on plant remains in layers that bound the paleo-ground surface of the earthquake (e.g., Lienkaemper & Bronk Ramsey, 2009) and in a few cases other environmental data such as European pollen or tree rings, and historical constraints. The model is a

maximum rupture model (MRM), as it accommodates all paleoseismic ages with the fewest number of ruptures. Rupture length is determined by comparing sites along strike; if site earthquake ages at neighboring sites overlap, the rupture is extended; if not, the rupture conventionally ends halfway between sites. Site records are assumed to be correct and complete. The extents of historic earthquakes since 1800 CE are estimated from written record sources and available geomorphic and paleoseismic observations (Table S1). The ruptures are built from the present back through time. Earthquakes at sites with a known number of events over an interval (rather than specific dates) are included in the youngest-permissible correlations. In the three cases identified in Table S2, correlations are not extended despite apparent temporal overlap, reflecting climatic data that refine event timing beyond the radiocarbon dating (Scharer et al., 2014), early historic information (e.g., Toppozada et al., 2002), or to permit a longer earthquake at an earlier time, consistent with the goal to produce the maximum rupture size permitted. Hereafter, each rupture is indicated with an "R" prefix, for example, R6, and labeled in red in Figure 1. The age of each prehistoric rupture is determined by the overlap of all connected site earthquake ages, that is, strictly limited by the youngest maximum and oldest minimum ages of contributing site earthquakes. Spatial and temporal constraints for each rupture are provided in Table S2.

Alternative rupture histories are possible given the dating and magnitude uncertainty of each site earthquake. At one extreme, if each site earthquake is a single rupture, the model would predict over 120 ~ M6.7 ruptures given the average spacing of 22 km per site, at an average rate of about one per decade. This is an unlikely scenario given the earthquakes in the historic period (1800 CE to present). Previously published work has incorporated other data, such as rupture extent derived from displacement (Biasi & Weldon, 2009) or dynamic modeling through complex geometries such as bends and splays to derive rupture behavior (e.g., Douilly et al., 2020; Lozos et al., 2011). We note that at least 30% of historical earthquakes on strike-slip faults end at no apparent geometric complexity (Biasi & Wesnousky, 2016) and that outside of the SGPFZ, the SAF and SJF strands are relatively smooth and planar. Neither fault trace contains the large >4 km step overs shown to commonly terminate ruptures (e.g., Biasi & Wesnousky, 2016; Lozos et al., 2011). We expect that implementing geometrically based rules would reduce the average magnitudes produced in the MRM and likely lead to broader magnitude distributions given the fault geometry. This paper examines the longest possible ruptures, in search of periods of activity similar to the 1800s.

3. Results

3.1. Maximum Rupture Model

The resultant MRM is composed of 50 ruptures (Figures 1b and S1), ranging in length from 20 to 380 km. Along each major fault branch, there is a visual appearance of periods of activity separated by periods of subregional quiescence. This appearance results from wide age uncertainty of ruptures and is reinforced where potential cascades (e.g., R9-R6) or overlapping sequences (e.g., R17-R16-R13) occur.

Rupture extent, though dictated solely by site location and ages, appears to reflect major structural discontinuities like fault splays and bends. For example, ruptures on the Coachella section are equally likely to connect to either the Mission Creek or Banning strands (three each), whereas two ruptures terminate where the fault splays (Figure 1b). Farther north, data from the Mi, Ca, EW, and EA sites (Figures S2 and S4) in the San Gorgonio Pass region permit only two earthquakes through the complex SGPFZ in the last 1,500 years (R30 and R47), providing robust evidence that the SGPFZ is a strong barrier to rupture. The younger San Gorgonio Pass event (R30), circa 1200 CE, is restricted to the SGPFZ and Banning section of the SAF in the model (Figure 1b). Trenching evidence established that earthquake has at least 4 m of oblique-slip motion (Heermance & Yule, 2017). Given this displacement, the 63 km-long rupture R30 is shorter than would be predicted from standard scaling relations (e.g., Wesnousky, 2008). It is possible that the rupture continued west on fault strands not modeled here; the SGPFZ continues for another 10 km, for example (see Yule & Sieh, 2003, for detailed mapping of this region).

The longest earthquake ruptures (Figure 1b; R17, R33, R37, and R47) involve the SAF north of SGPFZ, where the SAF is smooth and continuous compared to the rest of the model domain. An intermittent barrier in the Mojave section between EL and PC in the last 500 years breaks up some of the ruptures (Bemis et al., 2019), though the barrier could be absent in the preceding 500 years (Figure 1b). Longer records

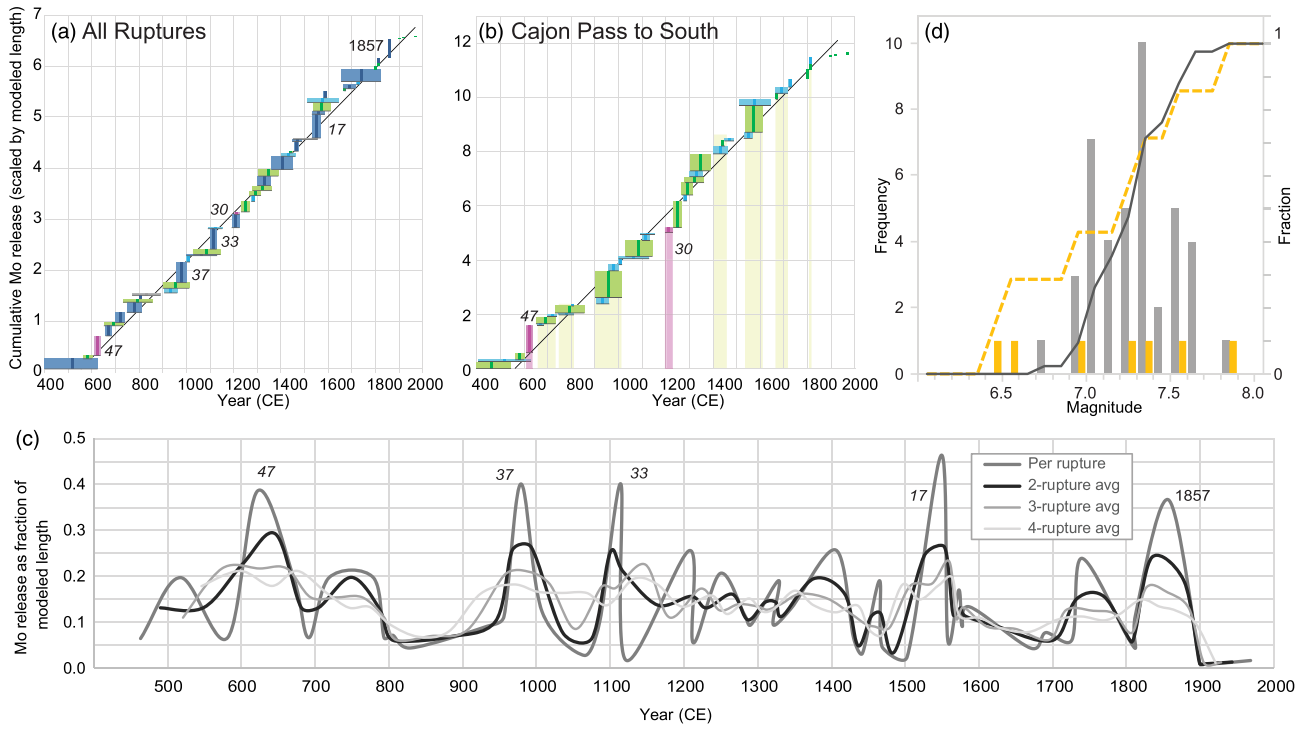

Figure 2. (a) Cumulative moment (Mo) release for all ruptures sorted by mean rupture age. Mo is scaled by modeled length as shown in Figure 1b and color coded by fault section as in Figure 1. Horizontal bars show uncertainty on rupture age (Table S2). Moment release is fairly constant for the region, within 100-year dating uncertainties. The rupture ID of the largest earthquakes are provided. (b) As in (a) but scaled to the southern half of the model domain to show regional behavior of SAF-SJF from Cajon Pass to the south. Cajon Pass sequences (periods highlighted with yellow bars; see text) appear in spates after each rupture through the SGPFZ (pink bars). (c) Variations in moment release over time and smoothed with sliding window of two to four ruptures to reflect uncertainty in sequence of events. Average of one to two ruptures maintains peaks from episodic long ruptures, but variability is reduced when >2 ruptures are averaged. Both (a) and (c) illustrate frequency of ruptures (one per 30 years on average across the domain) but highlight episodes of higher strain release, centered on 650, 975, 1110, 1550, and 1850 CE. (d) Histogram of magnitude of modeled ruptures; orange bars are historic ground-rupturing events, gray bars are prehistoric using scaling from Wesnousky (2008) for the rupture lengths in Figure 1b. Cumulative probability distribution for historic events (orange dashed line) extends to smaller ruptures and has a flatter distribution than prehistoric (black line) below ~M7.2.

from the central Mojave are needed to test this apparent behavioral shift. On the SJF, contemporaneity of a few ruptures at ML, HL, and SM produces large ruptures that span all of the SJF strands (e.g., R15 and R29). Most SFJ ruptures, however, are restricted to only one strand (Figures 1b and S1).

3.2. Moment Release Through Time

We estimate moment magnitude using the empirical relationship for strike slip faults in Wesnousky (2008), where Mw = 5.56 + 0.87*log (length) (Table S2). To examine fault activity through time, we scale rupture length (and thus moment) by the fraction of available model extent to account for the shorter records at the ends of each fault (black line, Figure 1b). Plotted by mean rupture age, moment release is fairly constant through time for the full MRM domain (Figure 2a). However, during two ~100 year-long episodes, 95% of the model domain ruptures in a few earthquakes: R38, R37, and R36 centered on 975 CE and R17, R15, and R14 around 1550 CE. Like the historic record, both episodes include most of the SAF and much of the SJF, and both occur when no earthquakes are recorded in the SGPFZ (Figure 1). Given age uncertainties and the permitted sequence of events, both of these episodes can be preceded and followed by long elapsed periods with no ruptures. The ~975 CE episode occurs after a gap up to 161 years long and can be followed by a lull of up to 130 years (Figure 2c). Similar values (120 and 95 years) bound the 1550 CE episode, permitting a time-dependency associated with the regional clusters. Other peaks in moment release correlate to the SGPFZ event (R47) that connects the Coachella section with the southern or 1857-length ruptures such as R33 (Figure 2c). Only one other gap greater than 100 years is permitted, between the limiting ages of R33 and R30. Such variations are poorly expressed by the mean interval for the MRM (32 years between ruptures anywhere in the system) but may be similar to the current lull since the sequence of ruptures culminating in the 1857 earthquake.

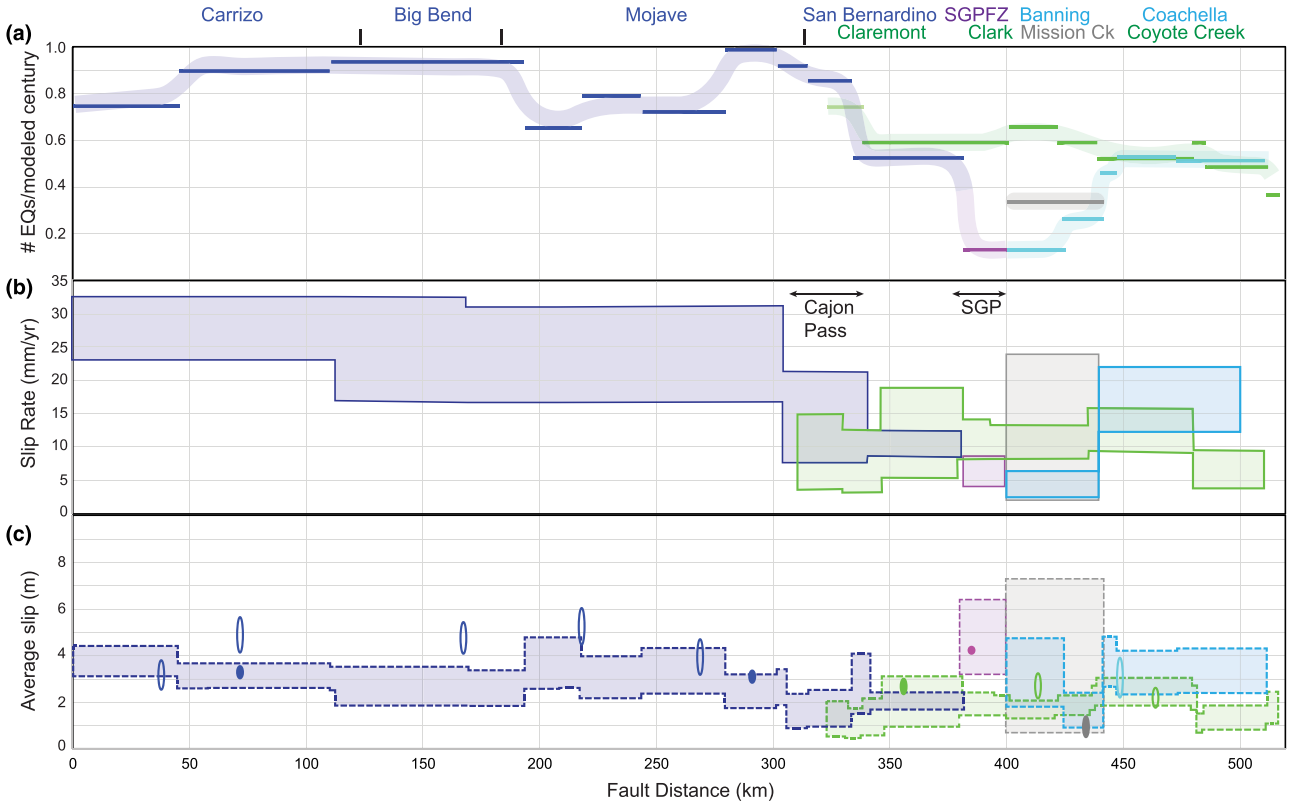

Figure 3. (a) Number of ruptures from the MRM. Colors as in Figure 1. Smooth line connects values through small variations (10–15%) caused by the limits of the modeled domain and regions of overlaps or historic earthquakes. (b) Preferred geologic-geodetic slip rates from (Dawson & Weldon, 2013), updated with rates for SGPFZ, Banning and Mission Creek, and SJF-Claremont (Blisniuk et al., 2013; Gold et al., 2015; Heermance & Yule, 2017; Onderdonk et al., 2015). (c) Average slip determined along length of faults by ratio of slip rate and earthquake rate. For comparison, average slip from geomorphic studies (open ellipses) and dated trenching studies (closed ellipses) are shown (references in text).

Ruptures of the SAF and SJF are shown separately in the MRM, but we recognize that joint rupture from one to the other is possible, amplifying potential impacts in the urban Cajon Pass region (Figure 1a) and the major lifelines that cross it. Lozos (2016) used dynamic rupture models constrained by damage records, for example, to propagate the historic 8 December 1812 SAF earthquake (R6) onto the SJF (R7). In the MRM there are up to six other periods when ruptures on the San Bernardino SAF section and northern SJF section earthquakes temporally overlap. We use the term Cajon Pass sequences to describe these periods, which given age uncertainties could be coeval ruptures (such as proposed for 1812) or clusters (e.g., separate rupture of R6 and R7). It is notable that the MRM produces an intriguing pattern in which ruptures through the SGPFZ (R47 and R30) do not overlap with earthquakes on the northern SJF and thus are not part of plausible Cajon Pass sequences. Rather, in the MRM the ruptures through the SGPFZ alternate with periods of heightened activity around Cajon Pass (Figure 2c).

4. Discussion

4.1. Model Testing

Given the MRM is an end-member model built to produce the fewest (and thus largest) ruptures, how reasonable is the variety of earthquakes, in terms of magnitude and distribution, or compared to other metrics? A simple test is provided by comparing the magnitude distribution of the historic record with the prehistoric MRM (Figure 2d). The two populations show similar range, though events <M6.7 are absent from the prehistoric data (Table S2), as expected given the close average spacing of individual sites and wide age uncertainties promote longer rupture in the model. Over ~70% of both the prehistoric and historic ruptures are greater than M7.2. The MRM produces an average modeled Mw of 7.24 and a maximum

prehistoric Mw of 7.8 (Table S2) for the 50 ruptures shown. If all Cajon Pass sequences are in fact coeval SAF and SJF ruptures, these long ruptures increase the model average to Mw 7.29 with a maximum Mw of 8.0. We consider such a scenario unlikely, as it would require both splays to corupture for 40 km for all seven of these pairs (e.g., R11-R12 and R15-R17), which far exceeds the length of corupture of strike-slip splays documented globally for any individual historic rupture (<15 km; Biasi & Wesnousky, 2017).

To test the MRM in aggregate, we calculate the number of ruptures along each kilometer of fault per modeled century (Figure 3a). The most pronounced changes in rupture rate occur on the SAF at the geometric complexities of Cajon Pass and the SGPFZ. Rates on the SJF are fairly constant along strike. By dividing the rupture rates (Figure 3a) by the slip rates along each section (Figure 3b), we calculate an average slip per rupture that can be compared to independent offset measurements (Figure 3c). Calculated average displacements are 2–4 m for much of the SAF, decreasing to 1–2 m at the San Bernardino section. Average displacement is 1–2 m along the Claremont SJF and increases to 2–3 m on the Clark. Overall, these show strong agreement with available estimates from offset channels and trenching studies available for most of the 1857 stretch, the Clark SJF, and Coachella SAF (Madden et al., 2013; Salisbury et al., 2012; Zielke et al., 2012). Interestingly, the values for the Carrizo SAF are lower than the 5 m average estimated from geomorphic offsets, supporting the observations in Zielke et al. (2015) that some ruptures observed in trench studies are not recorded in the landscape as individual offsets. Predicted slip is high in SGPFZ (4–7 m), consistent with trenching data that estimate >4.2 m in the most recent event (Heermance & Yule, 2017). No geomorphic offsets are available from the Mission Creek strand, though a trenching study suggests an average of 1 m per event (Fumal et al., 2002) that is inconsistent with high long-term slip rates (Blisniuk et al., 2013); additional work on Holocene displacements is warranted to resolve this discrepancy. Taken as a whole, Figure 3c suggests the number of earthquakes at each site is fairly robust, and we are not likely missing earthquakes.

4.2. Comparison With Similar Datasets

At the gross scale, the 1,500 year-long MRM presents a complex pattern of superimposed cycles containing cascades, re-rupture, and large multiasperity ruptures (Philibosian & Meltzner, 2020). At the subregional scale (e.g., Figure 2b), the repetition of periods of activity has similarities to historical earthquake patterns elsewhere. Schwartz et al. (2014) argued for pulses of activity and stress shadows in the San Francisco Bay Area, and more recent dating shows that moderate SAF earthquakes preceded the 1906 rupture (Streig et al., 2020). In the Central Apennines, Mildon et al. (2019) and Verdecchia et al. (2018) consider how postseismic and interseismic stress change modulate periods of activity in the historic period. The record along the Dead Sea Fault, similar in length to the MRM, has no dating uncertainties due to the length of the historic record there, but rupture location and extent are less constrained due to the site spacing (Lefevre et al., 2018). That record also shows periods of rupture cascades and rare multisegment ruptures (as defined by Philibosian & Meltzner, 2020). While statistical approaches will resolve a range of rupture scenarios given the paleoseismic data (e.g., Biasi & Weldon, 2009), the observation of patterns of clustering and quiescence on a global set of continental strike-slip faults suggests a common mechanical cause. Research on the relevant timescales over which such mechanism(s) may operate is needed to properly forecast future behavior.

5. Conclusions

The purpose of the MRM is to determine if the spate of earthquakes that ruptured most of the SAF and SJF in the first half of the 19th century is expressed in the paleoseismic record. We find similar periods of activity are permitted by the MRM, though comparison of the MRM with the rupture lengths and timing of earthquakes in the historic period provides important guidance on the model limits. Since 1800 AD, five ground-rupturing earthquakes are known, and a sixth (R4) is possible (Figure 1). If the 1812 event did rupture the SJF (Lozos, 2016), then most of the modeled SJF length has ruptured in the past 219 years through a mix of moderate earthquakes like the M6.4 Superstition Hills event (R1) and the larger ~M7.3 1800 Clark event (R8; Salisbury et al., 2012). Such patterns could be readily hidden within single long ruptures presented in the MRM (e.g., within R15), which could be split to mirror the historic magnitude distribution (Figure 2d). On the SAF, the historic period includes rerupture of much of the 1812 event (R6) during the 1857 earthquake (R5). This is followed by the current long gap, a pattern that is also exhibited in the MRM in the apparent R17-R13 cluster and the century-long gap preceding R9, and again

for the period from R23 to R17. Thus, the MRM provides some support that the historic period is typical for the SAF, while ruptures of an entire SJF section as shown in the MRM may be uncommon (e.g., Sanders & Magistrale, 1997). The model also reveals that ruptures through the SGPFZ alternate with periods of activity within Cajon Pass. The agreement between independent measurements of slip from geomorphic studies and calculated slip using the rupture rate and slip rates suggests that despite being an end-member model designed to produce the longest possible ruptures, the MRM produces a reasonable set of earthquake magnitudes. The rupture pattern suggests that cascades and overlapping events are common and produce epochs of heightened regional clustering, yet these issues are not addressed in most earthquake scenarios or in preparedness planning.

Data Availability Statements

Data sets for this research are included in the following papers: Akçiz et al. (2010), Bemis et al. (2019), 1. Weldon et al. (2013), Biasi et al. (2002), Buga (2012, 2015), Cardona (2016), Castillo (2019), Davis (1983), Earth Systems Southwest (2007), Fumal and Kendrick (2008), Fumal et al. (2002), Gurrola and Rockwell (1996), Howland (2003), Kendrick and Fumal (2005), McBurnett (2011), McGill et al. (2002), Onderdonk et al. (2015, 2018), Philibosian et al. (2011), Pruitt et al. (2009), Ramzan (2012), Wolff (2018), Rockwell et al. (2015, 2018), Rust (2005), Salisbury et al. (2017), Scharer et al. (2011, 2017), Seitz and Williams (2008), Seitz et al. (1997), Sieh (1986), Sieh et al. (1989), Weldon et al. (2004), Weldon and Sieh (1985), Williams et al. (2018), Young et al. (2002), and Yule et al. (2007).

Acknowledgments

The authors have no real or perceived financial conflicts of interest. Reviews by Belle Philibosian, Tom Rockwell, Katherine Kendrick, and Paolo Galli improved the clarity of the work. Scharer is funded by internal grants by the National Earthquake Hazard Reduction Program, and Yule received funding from the U.S. Geological Survey National Earthquake Hazard Reduction Program (G13AP00013). This research was supported by the Southern California Earthquake Center (Contribution No. 10105). SCEC is funded by NSF Cooperative Agreement EAR-1600087 and USGS Cooperative Agreement G17AC00047. We specifically acknowledge the contributions in the San Gorgonio Pass region by Bryan Castillo, Jose Cardona, Caryn Howland, Paul McBurnett, Shahid Ramzan, and Lisa Wolff to the question of earthquake hazards in southern California.

References

Akçiz, S. O., Ludwig, L. G., Arrowsmith, J. R., & Zielke, O. (2010). Century-long average time intervals between earthquake ruptures of the San Andreas fault in the Carrizo Plain, California. *Geology*, *38*(9), 787–790. https://doi.org/10.1130/G30995.1

Barka, A., Akyüz, H. S., Altunel, E., Sunal, G., Çakir, Z., Dikbas, A., et al. (2002). The surface rupture and slip distribution of the 17 August 1999 İzmit earthquake (M 7.4), North Anatolian Fault. *Bulletin of the Seismological Society of America*, *92*(1), 43–60. https://doi.org/10.1785/0120000841

Bemis, S., Scharer, K., & Dolan, J. R. (2019). Barriers to rupture propagation may be different beneath the surface: Insights from the Elizabeth Lake paleoseismic record. In *Poster Presentation at SCEC Annual Meeting*.

Ben-Zion, Y., Dahmen, K., Lyakhovsky, V., Ertas, D., & Agnon, A. (1999). Self-driven mode switching of earthquake activity on a fault system. *Earth and Planetary Science Letters*, *172*(1–2), 11–21. https://doi.org/10.1016/S0012-821X(99)00187-9

Biasi, G. P., & Weldon, R. J. (2009). San Andreas Fault rupture scenarios from multiple paleoseismic records: Stringing pearls. *Bulletin of the Seismological Society of America*, *99*(2A), 471–498. https://doi.org/10.1785/0120080287

Biasi, G. P., Weldon, R. J., Fumal, T. E., & Seitz, G. G. (2002). Paleoseismic event dating and the conditional probability of large earthquakes on the Southern San Andreas Fault, California. *Bulletin of the Seismological Society of America*, *92*(7), 2761–2781. https://doi.org/10.1785/0120000605

Biasi, G. P., & Wesnousky, S. G. (2016). Steps and gaps in ground ruptures: Empirical bounds on rupture propagation. *Bulletin of the Seismological Society of America*, *106*(3), 1110–1124. https://doi.org/10.1785/0120150175

Biasi, G. P., & Wesnousky, S. G. (2017). Bends and ends of surface rupture. *Bulletin of the Seismological Society of America*, *107*(6), 2543–2560. https://doi.org/10.1785/0120160292

Blisniuk, K., Scharer, K., Sharp, W., Burgmann, R., Rymer, M. J., & Williams, P. L. (2013). New slip rate estimates for the Mission Creek strand of the San Andreas fault zone, abstract T42A-01. In *American Geophysical Union Fall Meeting Abstracts*. San Francisco, CA.

Buga, M. T. (2012). Paleoseismology of the southern Clark Strand of the San Jacinto Fault zone, Southern California (M.S. Thesis). San Diego State University. https://digitallibrary.sdsu.edu/islandora/object/sdsu%3A28007

Buga, M.T. (2015). Paleoseismology of the southern Clark Strand of the San Jacinto Fault Zone, Southern California:, https://www.fugro.com/about-fugro/our-expertise/research-and-development/technical-papers/technical-papers-details/paleoseismology-of-the-southern-clark-strand-of-the-san-jacinto-fault-zone-southern-california (accessed).

Bürgmann, R., & Dresen, G. (2008). Rheology of the lower crust and upper mantle: Evidence from rock mechanics, geodesy, and field observations. *Annual Review of Earth and Planetary Sciences*, *36*(1), 531–567. https://doi.org/10.1146/annurev.earth.36.031207.124326

Cardona, J. (2016). Constraining the most recent surface rupture on the Garnet Hill strand, San Andreas Fault, Coachella Valley, California (M.S. Thesis). California State University, Northridge. Retrieved from http://scholarworks.csun.edu/handle/10211.3/171784

Castillo, J. (2019). Ages of prehistoric earthquakes on the Banning Strand of the San Andreas Fault, near north Palm Springs, Califorina (M.S. Thesis). California State University, San Bernardino. Retrieved from https://scholarworks.lib.csusb.edu/etd/877/

Davis, T. L. (1983). Late Cenozoic structure and tectonic history of the western "Big Bend" of the San Andreas fault and adjacent San Emigdio Mountains (Ph. D. thesis). Santa Barbara, University of California.

Dawson, T. E., & Weldon, R. (2013). Appendix B: Geologic-slip-rate data and geologic deformation model, *U.S. Geological Survey Open-File Report 2013–1165, Uniform California Earthquake Rupture Forecast Version 3 (UCERF3)—The Time-Independent Model*. https://pubs.usgs.gov/of/2013/1165/

Douilly, R., Oglesby, D. D., Cooke, M. L., & Hatch, J. L. (2020). Dynamic models of earthquake rupture along branch faults of the eastern San Gorgonio Pass region in California using complex fault structure. *Geosphere*, *16*(2), 474–489. https://doi.org/10.1130/GES02192.1

Duan, B., & Oglesby, D. D. (2007). Nonuniform prestress from prior earthquakes and the effect on dynamics of branched fault systems. *Journal of Geophysical Research*, *112*, B05308. https://doi.org/10.1029/2006JB004443

Earth Systems Southwest (2007). Earthquake fault hazard evaluation, indio trails, Washington Street: Riverside County (No. GEO #01435).

Freed, A. M. (2005). Earthquake triggering by static, dynamic, and postseismic stress transfer. *Annual Review of Earth and Planetary Sciences*, *33*(1), 335–367. https://doi.org/10.1146/annurev.earth.33.092203.122505

Fumal, T., & Kendrick, K. (2008). Paleoseismic investigations of the Walnut Site on the San Jacinto Fault. Retrieved from https://pubs.usgs.gov/of/2007/1437/o/

Fumal, T. E., Rymer, M. J., & Seitz, G. G. (2002). Timing of large earthquakes since A.D. 800 on the Mission Creek strand of the San Andreas Fault zone at Thousand Palms Oasis, near Palm Springs, California. *Bulletin of the Seismological Society of America*, *92*(7), 2841–2860. https://doi.org/10.1785/0120000609

Gold, P. O., Behr, W. M., Rood, D., Sharp, W. D., Rockwell, T. K., Kendrick, K., & Salin, A. (2015). Holocene geologic slip rate for the Banning strand of the southern San Andreas Fault, southern California. *Journal of Geophysical Research: Solid Earth*, *120*, 5639–5663. https://doi.org/10.1002/2015JB012004

Gurrola, L. D., & Rockwell, T. K. (1996). Timing and slip for prehistoric earthquakes on the Superstition Mountain Fault, Imperial Valley, southern California. *Journal of Geophysical Research*, *101*(B3), 5977–5985. https://doi.org/10.1029/95JB03061

Harris, R. A., & Simpson, R. W. (1998). Suppression of large earthquakes by stress shadows: A comparison of Coulomb and rate-and-state failure. *Journal of Geophysical Research*, *103*, 24,439–24,451. https://doi.org/10.1029/98JB00793

Heermance, R. V., & Yule, J. D. (2017). Holocene slip rates along the San Andreas Fault System in the San Gorgonio Pass and implications for large earthquakes in southern California. *Geophysical Research Letters*, *44*, 5391–5400. https://doi.org/10.1002/2017GL072612

Howland, C. (2003). Determining the depositional age of peat: Implications for dating paleoearthquakes at the Burro Flats Paleoseismic site near Banning, CA (M.S. Thesis). California State University, Northridge.

Kendrick, K., & Fumal, T. (2005). Paleoseismicity of the northern San Jacinto fault, Colton and San Bernardino, southern California; preliminary results. In Geological Society of America Abstracts with Programs, 37, 559.

King, G. C. P., Stein, R. S., & Lin, J. (1994). Static stress changes and the triggering of earthquakes. *Bulletin of the Seismological Society of America*, *84*(3), 935–953.

Lefevre, M., Klinger, Y., Al-Qaryouti, M., Béon, M. L., & Moumani, K. (2018). Slip deficit and temporal clustering along the Dead Sea fault from paleoseismological investigations. *Scientific Reports*, *8*, 4511. https://doi.org/10.1038/s41598-018-22627-9

Lienkaemper, J. J., & Bronk Ramsey, C. (2009). OxCal: Versatile tool for developing paleoearthquake chronologies—A primer. *Seismological Research Letters*, *80*(3), 431–434. https://doi.org/10.1785/gssrl.80.3.431

Lozos, J. C. (2016). A case for historic joint rupture of the San Andreas and San Jacinto faults. *Science Advances*, *2*(3), e1500621. https://doi.org/10.1126/sciadv.1500621

Lozos, J. C., Oglesby, D. D., Duan, B., & Wesnousky, S. G. (2011). The effects of double fault bends on rupture propagation: A geometrical parameter study. *Bulletin of the Seismological Society of America*, *101*(1), 385–398. https://doi.org/10.1785/0120100029

Madden, C., Haddad, D. E., Salisbury, J. B., Zielke, O., & Arrowsmith, J. R. (2013). Appendix R: Compilation of slip-in-the-last-event data and analysis of last event, repeated slip, and average displacement for recent and prehistoric ruptures, *U.S. Geological Survey Open-File Report 2013–1165, Uniform California Earthquake Rupture Forecast Version 3 (UCERF3)—The Time-Independent Model*. https://pubs.usgs.gov/of/2013/1165/

McBurnett, P. (2011). Paleoseismicity of the San Gorgonio Pass fault zone at Millard Canyon: Testing the likelihood of a through-going San Andreas rupture (M.S. Thesis). California State University, Northridge. Retrieved from. http://scholarworks.csun.edu/handle/10211.3/142046

McGill, S., Dergham, S., Barton, K., Berney-Ficklin, T., Grant, D., Hartling, C., et al. (2002). Paleoseismology of the San Andreas Fault at Plunge Creek, near San Bernardino, Southern California. *Bulletin of the Seismological Society of America*, *92*(7), 2803–2840. https://doi.org/10.1785/0120000607

Mildon, Z. K., Roberts, G. P., Walker, J. F., & Toda, S. (2019). Coulomb pre-stress and fault bends are ignored yet vital factors for earthquake triggering and hazard. *Nature Communications*, *10*, 2744. https://doi.org/10.1038/s41467-019-10520-6

Onderdonk, N., McGill, S., & Rockwell, T. (2018). A 3700 yr paleoseismic record from the northern San Jacinto fault and implications for joint rupture of the San Jacinto and San Andreas faults. *Geosphere*, *14*(6), 2447–2468. https://doi.org/10.1130/GES01687.1

Onderdonk, N., McGill, S. F., & Rockwell, T. K. (2015). Short-term variations in slip rate and size of prehistoric earthquakes during the past 2000 years on the northern San Jacinto fault zone, a major plate-boundary structure in southern California. *Lithosphere*, *7*(3), 211–234. https://doi.org/10.1130/L393.1

Philibosian, B., Fumal, T., & Weldon, R. (2011). San Andreas fault earthquake chronology and Lake Cahuilla history at Coachella, California. *Bulletin of the Seismological Society of America*, *101*(1), 13–38. https://doi.org/10.1785/0120100050

Philibosian, B., & Meltzner, A. J. (2020). Segmentation and supercycles: A catalog of earthquake cycle complexities from the Sumatran Sunda Megathrust and other well-studied faults worldwide. *Quaternary Science Reviews*, *241*. https://doi.org/10.1016/j.quascirev.2020.106390

Pruitt, A., Scharer, K., Fumal, T., Weldon, R. J., Gilleland, C., & Sickler, R. (2009). Microgeomorphic reconstruction to determine slip rate on the San Andreas fault near Littlerock, CA. In *2009 SCEC Annual Meeting. Palm Springs, CA*.

Ramzan, S. (2012). Paleoseismic investigation of the San Gorgonio Pass fault zone near Cabazon, California (M.S. Thesis). California State University, Northridge. Retrieved from http://scholarworks.csun.edu/handle/10211.2/1880

Rockwell, T. K., Dawson, T. E., Young Ben-Horin, J., & Seitz, G. (2015). A 21-event, 4,000-year history of surface ruptures in the Anza seismic gap, San Jacinto Fault, and implications for long-term earthquake production on a major plate boundary fault. *Pure and Applied Geophysics*, *172*(5), 1143–1165. https://doi.org/10.1007/s00024-014-0955-z

Rockwell, T. K., Meltzner, A. J., & Haaker, E. C. (2018). Dates of the two most recent surface ruptures on the southernmost San Andreas Fault recalculated by precise dating of Lake Cahuilla dry periods. *Bulletin of the Seismological Society of America*, *108*(5A), 2634–2649. https://doi.org/10.1785/0120170392

Rust, D. (2005). Palaeoseismology in steep terrain: The Big Bend of the San Andreas Fault, Transverse Ranges, California. *Tectonophysics*, *408*(1–4), 193–212.

Salisbury, J. B., Rockwell, T. K., & Buga, M. T. (2017). Paleoseismic evidence for the 21 April 1918 Mw 6.9 surface rupture of the northern Clark Strand of the central San Jacinto Fault, California. *Bulletin of the Seismological Society of America*, *107*(2), 1027–1032. https://doi.org/10.1785/0120160026

Salisbury, J. B., Rockwell, T. K., Middleton, T. J., & Hudnut, K. W. (2012). LiDAR and field observations of slip distribution for the most recent surface ruptures along the central San Jacinto fault. *Bulletin of the Seismological Society of America*, *102*(2), 598–619. https://doi.org/10.1785/0120110068

Sanders, C., & Magistrale, H. (1997). Segmentation of the northern San Jacinto Fault zone, southern California. *Journal of Geophysical Research*, *102*(B12), 27,453–27,467. https://doi.org/10.1029/97JB02377

Scharer, K., Weldon, R., Biasi, G., Streig, A., & Fumal, T. (2017). Ground-rupturing earthquakes on the northern Big Bend of the San Andreas Fault, California, 800 AD to present. *Journal of Geophysical Research: Solid Earth*, *122*, 2193–2218. https://doi.org/10.1002/2016JB013606

Scharer, K. M., Biasi, G. P., & Weldon, R. J. (2011). A reevaluation of the Pallett Creek earthquake chronology based on new AMS radiocarbon dates, San Andreas fault, California. *Journal of Geophysical Research*, *116*, B12111. https://doi.org/10.1029/2010JB008099

Scharer, K., Weldon, R., Streig, A., & Fumal, T. (2014). Paleoearthquakes at Frazier Mountain, California delimit extent and frequency of past San Andreas Fault ruptures along 1857 trace. *Geophysical Research Letters*, *41*(13), 4527–4534.

Scholz, C. H. (2010). Large earthquake triggering, clustering, and the synchronization of faults. *Bulletin of the Seismological Society of America*, *100*(3), 901–909. https://doi.org/10.1785/0120090309

Schwartz, D. P., Haeussler, P. J., Seitz, G. G., & Dawson, T. E. (2012). Why the 2002 Denali fault rupture propagated onto the Totschunda fault: Implications for fault branching and seismic hazards. *Journal of Geophysical Research*, *117*, B11304. https://doi.org/10.1029/2011JB008918

Schwartz, D. P., Lienkaemper, J. J., Hecker, S., Kelson, K. I., Fumal, T. E., Baldwin, J. N., et al. (2014). The earthquake cycle in the San Francisco Bay region: AD 1600–2012. *Bulletin of the Seismological Society of America*, *104*(3), 1299–1328. https://doi.org/10.1785/0120120322

Seitz, G., Weldon, R., & Biasi, G. P. (1997). The Pitman Canyon paleoseismic record: A re-evaluation of southern San Andreas Fault segmentation. *Journal of Geodynamics*, *24*(1-4), 129–138. https://doi.org/10.1016/S0264-3707(96)00042-7

Seitz, G. G., & Williams, P. L. (2008). Establishing the southernmost long-term earthquake record on the San Andreas Fault (SCEC Annual Report No. 08136) Retrieved from https://files.scec.org/s3fs-public/reports/2008/08136_report.pdf

Sieh, K., Stuiver, M., & Brillinger, D. (1989). A more precise chronology of earthquakes produced by the San Andreas Fault in southern California. *Journal of Geophysical Research*, *94*(B1), 603–623. https://doi.org/10.1029/JB094iB01p00603

Sieh, K. E. (1986). Slip rate across the San Andreas fault and prehistoric earthquakes at Indio, California. *Eos, Transactions, American Geophysical Union*, *67*(44), 1200.

Streig, A. R., Weldon, R. J., Biasi, G., Dawson, T. E., Gavin, D. G., & Guilderson, T. P. (2020). New insights into paleoseismic age models on the northern San Andreas Fault: Charcoal inbuilt ages and updated earthquake correlations. *Bulletin of the Seismological Society of America*, *110*(3), 1077–1089. https://doi.org/10.1785/0120190307

Toppozada, T. R., Branum, D. M., Reichle, M. S., & Hallstrom, C. L. (2002). San Andreas fault zone, California: M≥ 5.5 earthquake history. *Bulletin of the Seismological Society of America*, *92*(7), 2555–2601.

Verdecchia, A., Pace, B., Visini, F., Scotti, O., Peruzza, L., & Benedetti, L. (2018). The role of viscoelastic stress transfer in long-term earthquake cascades: Insights after the central Italy 2016–2017 seismic sequence. *Tectonics*, *37*, 3411–3428. https://doi.org/10.1029/2018TC005110

Weldon, R. J., Dawson, T. E., Biasi, G. P., Madden, C., & Streig, A. R. (2013). Appendix G: Paleoseismic sites recurrence database, *U.S. Geological Survey Open-File Report 2013–1165, Uniform California Earthquake Rupture Forecast Version 3 (UCERF3)—The Time-Independent Model*. https://pubs.usgs.gov/of/2013/1165/

Weldon, R. J., Scharer, K., Fumal, T., & Biasi, G. (2004). Wrightwood and the earthquake cycle: What a long recurrence record tells us about how faults work. *GSA Today*, *14*(9), 4–10. https://doi.org/10.1130/1052-5173(2004)014%3C4:WATECW%3E2.0.CO;2

Weldon, R. J., & Sieh, K. E. (1985). Holocene rate of slip and tentative recurrence interval for large earthquakes on the San Andreas fault, Cajon Pass, southern California. *GSA Bulletin*, *96*(6), 793–812. https://doi.org/10.1130/0016-7606(1985)96%3C793:HROSAT%3E2.0.CO;2

Wesnousky, S. G. (2008). Displacement and geometrical characteristics of earthquake surface ruptures: Issues and implications for seismic-hazard analysis and the process of earthquake rupture. *Bulletin of the Seismological Society of America*, *98*(4), 1609–1632. https://doi.org/10.1785/0120070111

Williams, A., Arrowsmith, J. R., Rockwell, T., Akciz, S. O., & Grant Ludwig, L. (2018). Refining the earthquake chronology of the last millennium along the Cholame segment of the San Andreas fault. In *2018 SCEC Annual Meeting*. Palm Springs, CA.

Wolff, L. (2018). 6000-year record of large, infrequent earthquakes on the San Andreas Fault system in San Gorgonio Pass, near Cabezon, California (M.S. Thesis). California State University, Northridge. Retrieved from http://scholarworks.csun.edu/handle/10211.3/207861

Xie, C., Lei, X., Wu, X., & Hu, X. (2014). Short- and long-term earthquake triggering along the strike-slip Kunlun fault, China: Insights gained from the Ms 8.1 Kunlun earthquake and other modern large earthquakes. *Tectonophysics*, *617*, 114–125. https://doi.org/10.1016/j.tecto.2014.01.023

Young, J. J., Arrowsmith, J. R., Colini, L., Grant, L. B., & Gootee, B. (2002). Three-dimensional excavation and recent rupture history along the Cholame segment of the San Andreas fault. *Bulletin of the Seismological Society of America*, *92*(7), 2670–2688. https://doi.org/10.1785/0120000604

Yule, D., & Sieh, K. (2003). Complexities of the San Andreas fault near San Gorgonio Pass: Implications for large earthquakes. *Journal of Geophysical Research*, *108*(B11), 2548. https://doi.org/10.1029/2001JB000451

Yule, J. D., Sieh, K., & Howland, C. (2007). Evidence for large earthquakes on the San Andreas Fault at the Burro Flats paleoseismic site: A.D. 150 to present. *Poster presented at SCEC Annual Meeting, 196*. Palm Springs, CA.

Zielke, O., Arrowsmith, J. R., Grant Ludwig, L., & Akciz, S. O. (2012). High-resolution topography-derived offsets along the 1857 Fort Tejon earthquake rupture trace, San Andreas Fault. *Bulletin of the Seismological Society of America*, *102*(3), 1135–1154. https://doi.org/10.1785/0120110230

Zielke, O., Klinger, Y., & Arrowsmith, J. R. (2015). Fault slip and earthquake recurrence along strike-slip faults—Contributions of high-resolution geomorphic data. *Tectonophysics*, *638*, 43–62. https://doi.org/10.1016/j.tecto.2014.11.004

References From the Supporting Information

Bronk Ramsey, C. (2017). Methods for summarizing radiocarbon datasets. *Radiocarbon*, *59*(6), 1809–1833. https://doi.org/10.1017/RDC.2017.108

Claypole, E. W. (1900). The earthquake at San Jacinto, December 25, 1899. *American Geologist*, *25*, 106–108.

Jacoby, G. C., Sheppard, P. R., & Sieh, K. E. (1988). Irregular recurrence of large earthquakes along the San Andreas fault: Evidence from trees. *Science*, *241*(4862), 196–199. https://doi.org/10.1126/science.241.4862.196

Kirby, M. E., Poulsen, C. J., Lund, S. P., Patterson, W. P., Reidy, L., & Hammond, D. E. (2004). Late Holocene lake level dynamics inferred from magnetic susceptibility and stable oxygen isotope data: Lake Elsinore, southern California (USA). *Journal of Paleolimnology*, *31*(3), 275–293. https://doi.org/10.1023/B:JOPL.0000021710.39800.f6

Reimer, P. J., Bard, E., Bayliss, A., Beck, J. W., Blackwell, P. G., Ramsey, C. B., et al. (2013). IntCal13 and Marine13 radiocarbon age calibration curves 0–50,000 years cal BP. *Radiocarbon*, *55*(4), 1869–1887. https://doi.org/10.2458/azu_js_rc.55.16947

Sharp, R. V., & Clark, M. M. (1972). *Geologic evidence of previous faulting near the 1968 rupture on the Coyote Creek fault, U.S. Geological Survey Professional Paper* (Vol. 787, 131–140). https://pubs.usgs.gov/pp/0787/report.pdf

Toppozada, T. R., Real, C. R., Bezore, S. P., & Parke, D. L. (1981). Preparation of isoseismal maps and summaries of reported effects for pre-1900 California earthquakes. *U.S. Geol. Surv. Open-File Rept. 81–262*.

Townley, S. D., & Allen, M. W. (1939). Descriptive catalog of earthquakes of the Pacific Coast of the United States 1769 to 1928. *Bulletin of the Seismological Society of America*, *29*(1), 1–297.

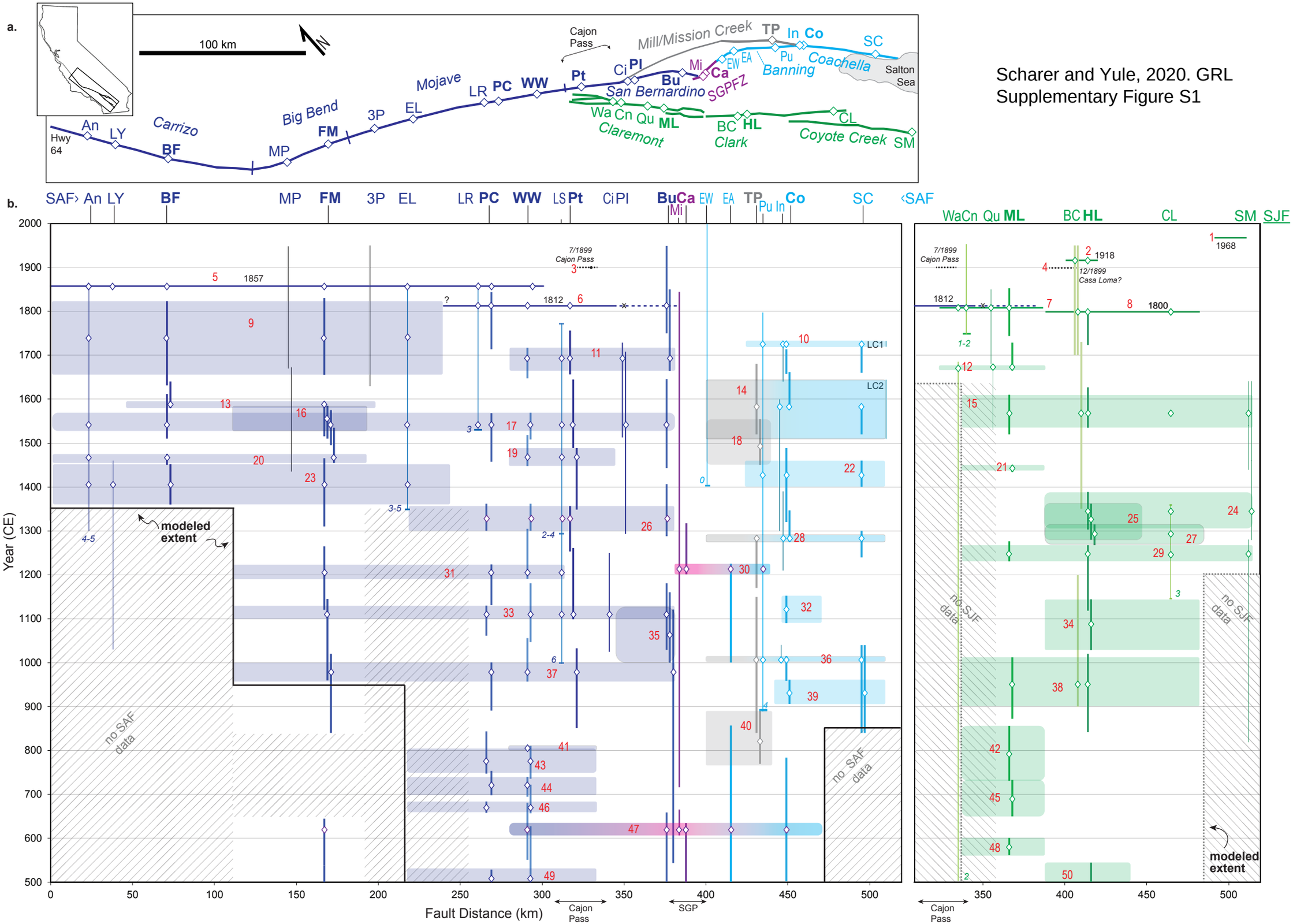
a.
100 km
N
Hwy 64
An
LY
Carrizo
BF
MP
Big Bend
FM
3P
EL
Mojave
LR
PC
WW
Pt
Cajon Pass
Mill/Mission Creek
TP
In
Co
SC
Ci
Pl
Bu
Mi
Ca
EW
EA
Pu
Banning
Coachella
Salton Sea
San Bernardino
SGPFZ
Wa
Cn
Qu
ML
Claremont
BC
HL
Clark
CL
Coyote Creek
SM
Scharer and Yule, 2020. GRL
Supplementary Figure S1
b.
SAF
SJF
Year (CE)
Fault Distance (km)
modeled extent
no SAF data
no SJF data
7/1899 Cajon Pass
12/1899 Casa Loma?
1857
1812
1800
1968
1918
LC1
LC2
Cajon Pass
SGP

AGU PUBLICATIONS

JGR

Journal of Geophysical Research: Solid Earth

RESEARCH ARTICLE
10.1002/2015JB012004

Key Points:
- The Holocene slip rate for the Banning strand of the southern San Andreas fault is 4–5 mm/yr
- This new geologic slip rate is only 25–35% of total southern San Andreas slip, lower than expected
- Slip is not concentrated on the Banning strand; regional earthquake hazard models need expansion

Supporting Information:
- Texts S1–S3, Figures S1–S6, and Tables S1 and S2

Correspondence to:
P. O. Gold,
peter.gold@utexas.edu

Citation:
Gold, P. O., W. M. Behr, D. Rood, W. D. Sharp, T. K. Rockwell, K. Kendrick, and A. Salin (2015), Holocene geologic slip rate for the Banning strand of the southern San Andreas Fault, southern California, *J. Geophys. Res. Solid Earth*, *120*, 5639–5663, doi:10.1002/2015JB012004.

Received 5 MAR 2015
Accepted 11 JUL 2015
Accepted article online 21 JUL 2015
Published online 18 AUG 2015

©2015. American Geophysical Union. All Rights Reserved.

Holocene geologic slip rate for the Banning strand of the southern San Andreas Fault, southern California

Peter O. Gold[1], Whitney M. Behr[1], Dylan Rood[2,3], Warren D. Sharp[4], Thomas K. Rockwell[5], Katherine Kendrick[6], and Aaron Salin[1]

[1]Department of Geological Sciences, University of Texas, Austin, Texas, USA, [2]Department of Earth Science and Engineering, Imperial College London, London, UK, [3]AMS Laboratory, Scottish Universities Environmental Research Centre, Glasgow, UK, [4]Berkeley Geochronology Center, Berkeley, California, USA, [5]Department of Geological Sciences, San Diego State University, San Diego, California, USA, [6]United States Geological Survey, Pasadena, California, USA

Abstract Northwest directed slip from the southern San Andreas Fault is transferred to the Mission Creek, Banning, and Garnet Hill fault strands in the northwestern Coachella Valley. How slip is partitioned between these three faults is critical to southern California seismic hazard estimates but is poorly understood. In this paper, we report the first slip rate measured for the Banning fault strand. We constrain the depositional age of an alluvial fan offset 25 ± 5 m from its source by the Banning strand to between 5.1 ± 0.4 ka (95% confidence interval (CI)) and 6.4 + 3.7/−2.1 ka (95% CI) using U-series dating of pedogenic carbonate clast coatings and ^{10}Be cosmogenic nuclide exposure dating of surface clasts. We calculate a Holocene geologic slip rate for the Banning strand of 3.9 + 2.3/−1.6 mm/yr (median, 95% CI) to 4.9 + 1.0/−0.9 mm/yr (median, 95% CI). This rate represents only 25–35% of the total slip accommodated by this section of the southern San Andreas Fault, suggesting a model in which slip is less concentrated on the Banning strand than previously thought. In rejecting the possibility that the Banning strand is the dominant structure, our results highlight an even greater need for slip rate and paleoseismic measurements along faults in the northwestern Coachella Valley in order to test the validity of current earthquake hazard models. In addition, our comparison of ages measured with U-series and ^{10}Be exposure dating demonstrates the importance of using multiple geochronometers when estimating the depositional age of alluvial landforms.

1. Introduction

The Coachella Valley segment of the southern San Andreas Fault in southern California consists of a system of faults that increase in complexity toward the northwest, from a single right-lateral strand at Bombay Beach (Indio strand) to an intricate network of right-lateral-reverse faults in the San Gorgonio Pass region [*Allen*, 1957; *Matti and Morton*, 1993] (Figure 1). Because the Coachella Valley segment is considered well past its average earthquake recurrence interval [*Fumal et al*., 2002; *Fialko*, 2006; *Weldon et al*., 2005; *Field et al*., 2009; *Philibosian et al*., 2011], an understanding of how these faults interact to accommodate Pacific-North American plate motion and transfer slip to other faults within the San Andreas Fault System is critical to realistically assessing seismic hazard and, more broadly, to understanding the evolution of long-lived strike-slip fault systems over different spatial and temporal scales.

An issue of particular importance in assessing seismic hazard in southern California is the frequency with which large earthquakes generated on the Coachella Valley segment propagate into and through the San Gorgonio Pass region, potentially triggering slip on the San Bernardino segment of the San Andreas Fault and continuing into the Los Angeles Basin. At present, however, there are no constraints on the amount of slip that enters San Gorgonio Pass from the southeast. The closest geologic slip rate measured for the Coachella Valley segment is at Biskra Palms Oasis in the southeastern Indio Hills (Figure 1), about 50 km southeast of San Gorgonio Pass [*Van der Woerd et al*., 2006; *Behr et al*., 2010; *Keller et al*., 1982]. At that latitude, the Indio strand of the Coachella Valley segment splits into three additional primary strands: the Mission Creek, Banning, and Garnet Hill strands. The Mission Creek strand trends northwestward, bounding the northern side of the Indio Hills, across the northern Coachella Valley and into the San Bernardino Mountains where it intersects northeast trending faults within the Eastern Transverse Ranges before continuing west and northwest [*Dibblee*, 1964, 1967; *Matti and Morton*, 1993; *Kendrick et al*., 2015]. Although bluffs south of the

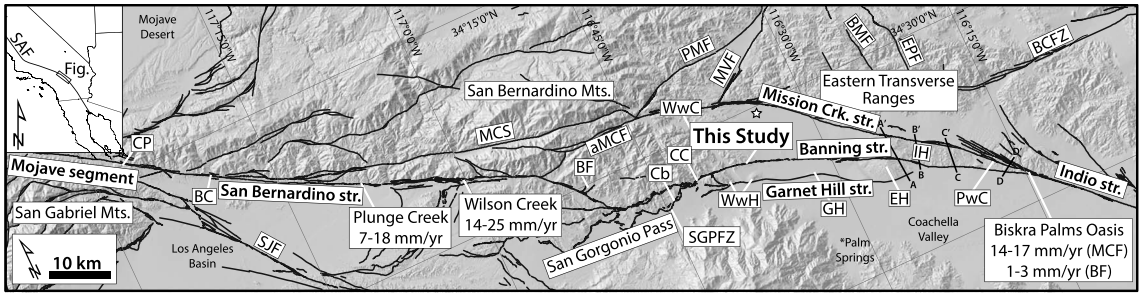

Figure 1. Fault map of the southern San Andreas Fault (SAF) system in the vicinity of San Gorgonio Pass. Late Quaternary fault slip rates have been determined at Plunge Creek [*McGill et al*., 2013] and Wilson Creek [*Harden and Matti*, 1989] along the San Bernardino strand and at Biskra Palms Oasis [*Behr et al*., 2010; *Van der Woerd et al*., 2006; *Keller et al*., 1982] along the Coachella Valley segment, of which the Banning, Mission Creek, Garnet Hill and Indio strands are a part. This study contributes the first slip rate for the Banning strand (Banning str.) at its northwest end. Cross sections A–D illustrating structural deformation within the Indio Hills are presented in Figure 5. Star north of study area indicates the epicenter of the 1986 *M*5.9 North Palm Springs. aMCF: ancestral Mission Creek Fault; BC: Badger Canyon; BCFZ: Blue Cut Fault zone; BF: Burro Flats; BMF: Burnt Mountain Fault; Cb: Cabazon; CC: Cottonwood Canyon; CP: Cajon Pass; EH: Edom Hill; EPF: Eureka Peak Fault; GH: Garnet Hill; IH: Indio Hills; MCS: Mission Creek strand; MVF: Morongo Valley Fault; PMF: Pinto Mountain Fault; PwC: Pushawalla Canyon; SGPFZ: San Gorgonio Pass Fault Zone; SJF: San Jacinto Fault; WwC: Whitewater Canyon; WwH: Whitewater Hills.

town of Desert Hot Springs are related to slip on the Mission Creek strand, geomorphic indicators of recent slip are scarce and it is thought to be inactive over the Holocene farther west [*Matti and Morton*, 1993; *Kendrick et al*., 2015; *Owen et al*., 2014]. The Banning strand continues out of the Indio Hills across Holocene alluvium in the northwestern Coachella Valley subparallel to the Garnet Hill strand where both strands intersect faults of the San Gorgonio Pass Fault zone [*Matti et al*., 1992; *Matti and Morton*, 1993; *Yule and Sieh*, 2003].

At Biskra Palms Oasis, the slip rate on the Mission Creek strand of the fault is 12–22 mm/yr averaged over ~50 kyr, but how slip is partitioned between the primary structures (Banning, Mission Creek, and Garnet Hill strands) to the northwest is entirely unconstrained. In this paper, we investigate this issue by (1) presenting new geomorphic and structural constraints on fault kinematics and slip transfer between the Banning and Mission Creek strands within the Indio Hills and (2) providing the first quantitative estimate of the slip rate for the Banning strand in the northwestern Coachella Valley. We discuss the implications of these new data for seismic hazard and slip partitioning in southern California.

2. Tectonic Setting

The southern San Andreas Fault System displays considerable complexity, and we therefore use the following nomenclature throughout this paper. The terms segment, strand (or fault strand), and splay are used in a hierarchical fashion, with segment representing a regional domain of San Andreas–related fault strands that themselves may be split into two or more fault splays. We refer to the San Andreas Fault Zone southeast and northwest of San Gorgonio Pass as the Coachella Valley segment and San Bernardino strand of the Mojave segment, respectively. We refer to the various strands and splays that compose these segments according to previously used classifications that are cited accordingly.

2.1. Miocene-recent Fault Zone Development

The late Cenozoic development of the southern San Andreas Fault System in the area of the Transverse Ranges is described in detail by *Matti et al*. [1992] and *Matti and Morton* [1993]; we provide a brief summary of their work here. The present-day Banning strand is the reactivated southern section of an ancestral fault system that was abandoned around 5 Ma as the San Andreas Fault system migrated inboard and the ancestral Mission Creek Fault developed as the dominant structure accommodating relative plate motion [*Matti et al*., 1992; *Matti and Morton*, 1993]. During the late Pliocene, the majority of San Andreas Fault slip (~130 km) was concentrated on the Mission Creek Fault, but increasing structural complexity forced its partial abandonment in the late Quaternary, leading to the development of the Mill Creek Fault (Figure 1) [*Kendrick et al*., 2015; *Matti et al*., 1992; *Matti and Morton*, 1993]. The Mill Creek Fault accommodated only ~8 km of slip

before the development of the San Bernardino strand of the Mojave segment, which has been the primary structure accommodating right-lateral slip between Cajon Pass and San Gorgonio Pass since the late Pleistocene [*Matti et al*., 1992; *Matti and Morton*, 1993]. Also in the late Pleistocene, and presumably in response to the continued difficulty of transferring slip though the San Bernardino Mountains, the present-day Banning strand was reactivated across the northern Coachella Valley and has since accommodated 2–3 km of right-lateral slip. The San Bernardino strand and the Banning strand have colinear fault traces, but there is no surface evidence of a throughgoing strike-slip structure traversing the complex San Gorgonio Pass Fault zone [*Matti and Morton*, 1993; *Yule and Sieh*, 2003]. Little is known about the reverse or right-reverse Garnet Hill strand.

This model of Mio-Pliocene northeastward migration of plate boundary slip and late Pleistocene migration of slip back to the southwest is based on sedimentological and structural data from within the San Bernardino Mountains [*Matti et al*., 1992; *Matti and Morton*, 1993]. More recent geologic, geodetic, and seismic data are too sparse to uniquely constrain how slip is presently partitioned between the faults in this area. The *M*5.9 1986 North Palm Springs earthquake main shock and aftershock sequences were interpreted to have been on the Banning strand [*Jones et al*., 1986; *Sharp et al*., 1986], but this depends critically on the Banning and Mission Creek strand dips and their depth of intersection, neither of which are well constrained. GPS measurements of contemporary slip are also too sparse to model the Banning and Mission Creek strands as separate structures [*Meade*, 2005; *Loveless and Meade*, 2011; *Fialko*, 2006; *Spinler et al*., 2010; *Fay and Humphreys*, 2005]. Thus, more detailed geomorphic and structural observations and late Pleistocene-Holocene geologic slip rates are needed to resolve modern-day strain partitioning in this complex zone.

2.2. Quaternary Slip Rates From the Southern San Andreas Fault

Quantitative geologic slip rates for the active fault strands immediately to the north (San Bernardino strand) and south (Mission Creek, Banning, and Garnet Hill strands) of San Gorgonio Pass have been published for only two sites. *McGill et al*. [2013] measured slip rates of 7.0–15.7 mm/yr and 6.3–18.5 mm/yr averaged over 35 ka and 10 ka, respectively, along the San Bernardino strand of the Mojave segment at Plunge Creek from offset fluvial and alluvial features dated using radiocarbon (Figure 1). This rate overlaps with a qualitatively constrained 14–25 mm/yr slip rate for the San Bernardino strand measured from an offset alluvial fan to the southeast at Wilson Creek that was dated to ~14 ka using soil development observations (Figure 1) [*Harden and Matti*, 1989]. A dip-slip rate of 1.0–1.3 mm/yr on a single thrust strand to the southeast within the San Gorgonio Pass Fault zone is lower than the published rates from Plunge Creek but represents a minimum rate through this distributed fault zone [*Yule and Sieh*, 2003]. Two additional, although unpublished, lateral slip rates from within San Gorgonio Pass overlap with the lower bounds on the slip rates measured for the San Bernardino strand at Plunge Creek [*Orozco and Yule*, 2003; *Yule et al*., 2001].

On the Coachella Valley segment, in a revision of early work by *Keller et al*. [1982] and *van der Woerd et al*. [2006], *Behr et al*. [2010] measured an ~50 kyr average slip rate of 12–22 mm/yr (14–17 mm/yr preferred) near Biskra Palms Oasis at the very southern end of the Mission Creek strand where it intersects the Banning and Indio strands (Figure 1). This rate overlaps, within error, with somewhat higher preliminary, unpublished rates from northwest of Biskra Palms near Pushawalla Canyon [*Blisniuk et al*., 2013]. The Biskra Palms slip rate is the only published slip rate for the Mission Creek strand and is considered representative of the total slip rate for the Coachella Valley segment because the relatively poor surface expression of the adjacent Banning strand suggests it accommodates only a minor component of total slip. *Behr et al*. [2010] estimated a slip rate of 1–3 mm/yr for the Banning strand at this locality, consistent with the Mission Creek strand being the immediate recipient of nearly all slip from the Indio strand to the southeast. In the Indio Hills block, multiple splay faults associated with the Mission Creek strand, along with geomorphic and topographic complexities of the Indio Hills landscape, strongly point to significant along-strike variations in slip in this area, as we discuss further in subsequent sections. For this reason, we emphasize that published rates for the Mission Creek and Banning strands should not be projected more than a few kilometers along strike in either direction.

Taken together, the rates from Plunge Creek and Biskra Palms permit interpretations wherein ~50% to 100% of the total slip from the Coachella Valley segment is transferred northwest to the San Bernardino strand. There is little evidence for significant latest Quaternary slip on the ancestral Mission Creek Fault or the Mill Creek strand in the San Bernardino Mountains [*Matti et al*., 1992; *Weldon*, 2010; *Sieh*, 1994; *Kendrick et al*., 2015]. Thus, slip transfer from the southern Mission Creek strand to the Banning and Garnet Hill strands and eventually to the

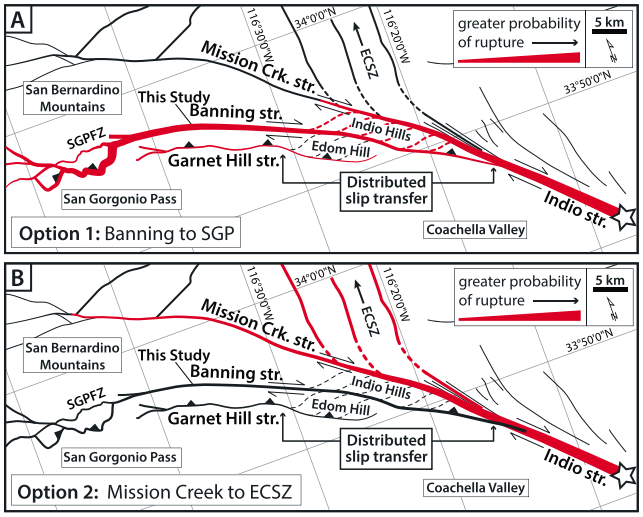

Figure 2. End-member options for slip partitioning and the probable distribution of displacement on the Mission Creek, Banning, and Garnet Hill strands during a future rupture on the Coachella Valley segment of the southern San Andreas Fault. (a) Option 1: Future ruptures are most likely to follow the Banning strand. This option is consistent with a fast (≥15 mm/yr) slip rate at the study location. (b) Option 2: Future ruptures are equally likely to bypass the Banning strand in favor of the Mission Creek strand and eventual transfer of slip to the Eastern California Shear Zone. This option is consistent with a slow (<10 mm/yr) slip rate at our study site. Intermediate scenarios are also possible, including rupture of the Garnet Hill strand with the Banning strand and a more even distribution of slip between all three faults. Distinguishing between these models requires slip rate data for the Banning strand.

San Gorgonio Pass Fault zone must be the primary mechanism by which slip, regardless of the amount, propagates northwest from the Coachella Valley segment to the San Bernardino strand. In the absence of quantitative slip rate data, two end-member rupture scenarios for an earthquake that nucleates on the Indio strand of the Coachella Valley segment may be possible:

1. Rupture may propagate northwest, primarily along the Banning strand (Figure 2a), transferring slip into the San Gorgonio Pass Fault zone and potentially threatening southern California populations, as is considered probable by the Uniform California Earthquake Rupture Forecast Version 3 hazard model [*Field et al.*, 2014, 2015].
2. Rupture may propagate northwest, primarily along the Mission Creek strand (Figure 2b), and transfer slip away from southern California populations via faults in the Eastern Transverse Ranges.

More evenly distributed slip partitioning and multipath rupture scenarios, including slip on the Garnet Hill strand, that lie between these two end-members are also possible. In subsequent sections, we will discuss both qualitative and quantitative constraints on the minimum slip transfer that occurs between these two important fault strands in the northern Coachella Valley, focusing primarily on the geomorphology, structure, and slip rate on the Banning strand.

3. Evidence for Slip Transfer Between the Mission Creek and Banning Strands

3.1. Geomorphic Evidence

We used the B4 lidar data, Google Earth imagery, and field observations to systematically investigate the tectonic geomorphology of the Banning and Mission Creek strands in the northern Coachella Valley (Figures 3 and 4). In the southeast Indio Hills, the Banning and Mission Creek strands diverge about 1 km east of Biskra Palms Oasis (Figure 3a). Along strike to the northwest, the surface trace of the Mission Creek strand is well expressed (Figures 3a and 3e), whereas evidence of displacement along the Banning strand is poorly expressed until just west of Pushawalla Canyon where a prominent fault scarp in late Pleistocene alluvium records several meters of apparently vertical offset (Figures 3a and 3i). Farther to the northwest, evidence of recent faulting along the Banning strand is again scarce until ~2.5 km east of Edom Hill, where it clearly defines a linear surface trace (Figure 3h). Field measurements from along this section yield minimum right-lateral offsets of 2–4 m of small drainages cut through modern sediments (Figure S1 in the supporting information). Farther toward the northwest, the Banning strand can be traced almost without interruption out of the Indio Hills across modern alluvium in the northernmost Coachella Valley (Figure 3g) to the eastern entrance to San Gorgonio Pass. Although the linear trace in Figure 3g is defined primarily by aeolian sand trapped by vegetation lineaments, the Banning strand clearly displaces several late Pleistocene and Holocene alluvial deposits (Figure 3f) before merging with the San Gorgonio Pass Fault zone near Cottonwood Canyon. Both walls of Whitewater Canyon (Figure 1) are also right-laterally displaced by the Banning strand; the actively refreshed eastern wall is deflected ~40 m, providing additional evidence of

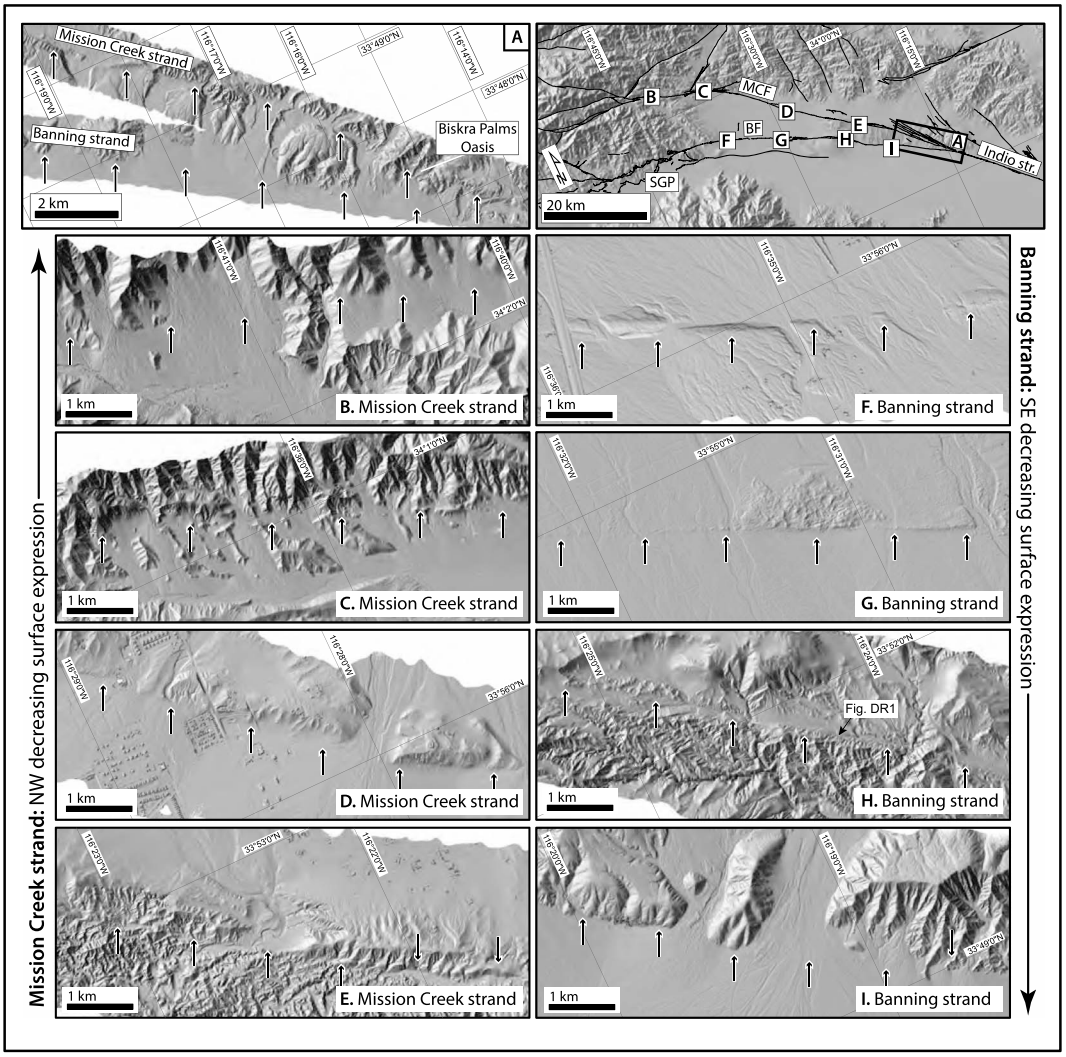

Figure 3. Shaded relief images showing geomorphic evidence of active faulting along sections of the Mission Creek (b–e) and the Banning strand (f–i) from their junction at the south end of the Indio Hills (a) to the San Bernardino Mountains and San Gorgonio Pass to the northwest. Images are derived from B4 airborne lidar; black and white arrows indicate the fault surface traces as observed or inferred by lidar-based observations. Figure locations along each fault are shown on the upper right map. Upper right abbreviations: San Gorgonio Pass (SGP), Mission Creek fault strand (MCF), Banning fault strand (BF), Coachella Valley segment of the southern San Andreas Fault (CV-SAF). The northwest increasing geomorphic expression of the Banning strand is coincident with the northwest decrease in geomorphic expression of the Mission Creek strand, suggesting that the Banning strand is the most active structure by the time both faults exit the Coachella Valley.

recent faulting, whereas the protected western wall is offset several hundred meters, providing evidence of sustained longer-term right lateral slip.

The trace of the Mission Creek strand is most obvious at its southeast end, where it defines a clear linear trace bounding the northern flank of the Indio Hills (Figure 3e), and the fault can be followed northwest through modern alluvium in the Coachella Valley until the town of Desert Hot Springs (Figure 3d). However, farther along strike, offsets of more recent alluvium become scarce and the surface trace of the Mission Creek strand is most clearly defined by shutter ridges and offset bedrock that record the longer-term slip history (Figure 3c). Whereas the northwest section of the Banning strand is clearly resolved in airborne lidar and imagery data (Figure 3f), the opposite is true of the northwest section of the Mission Creek strand, which does not appear to displace late Pleistocene alluvium as it climbs into the San Bernardino Mountains east of its junction with the Mill Creek strand and Pinto Mountain Fault (Figure 3b) [*Matti et al*., 1992; *Kendrick et al*., 2015]. In addition, the gradients in geomorphic expression observed along strike of the Banning and

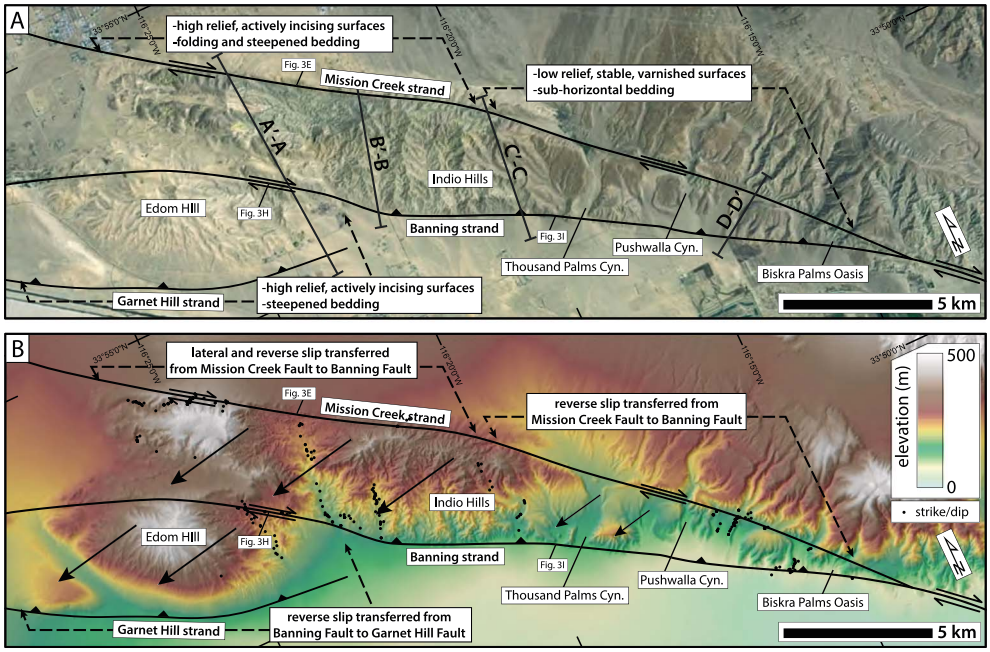

Figure 4. (a) Satellite image and (b) lidar-derived color-shaded relief maps of the Indio Hills. Alluvial sediments between the Mission Creek and Banning strands are relatively undisturbed between Biskra Palms Oasis and Thousand Palms Canyon except immediately adjacent to the faults, suggesting only moderate fault interaction. The abrupt increase in topography, relief, stream incision, and erosion northwest of Thousand Palms Canyon suggests the onset of more significant slip transfer from the Mission Creek to the Banning strand. The uplift of Edom Hill suggests further transfer of slip to the Garnet Hill strand. Structural measurements (black dots) along with existing mapping [*Dibblee*, 2008] were used to construct cross sections A though D (Figure 5), which show deformation and uplift consistent with these geomorphic observations.

Mission Creek strands are mirrored by changes in the amount of offset recorded by small drainages displaced where they cross each fault (Figure S2). Drainage offsets are formed during surface rupturing earthquakes so the ease with which a fault trace can be identified by their presence is primarily a function of how active the fault is (although climate and lithology are also factors). The observed along-strike gradients in drainage offsets and fault expression in the northwestern Coachella Valley imply a northwest increase in fault activity along the Banning strand coincident with an apparent decrease in fault activity along the Mission Creek strand in the same direction.

Larger-scale geomorphic observations in the Indio Hills are also consistent with slip transfer between the Banning and Mission Creek strands. The Indio Hills separate the Banning and Mission Creek strands for roughly 23 km northwest of their divergence near Biskra Palms Oasis (Figure 4). This area of uplifted and deformed fluvial and deltaic sedimentary units is the only significant topography along either fault until the San Bernardino Mountains and is nowhere wider than ~4 km. Immediately northwest of their divergence, the Banning and Mission Creek strands are separated by the alluvial Ocotillo Formation. For the first ~11 km along strike northwest from Biskra Palms Oasis, the Ocotillo Formation is characterized by several low-relief, fluvially planed, well-varnished surfaces separated by large incised drainages (Figure 4). About 1.5 km from Thousand Palms Canyon, the geomorphology of the Indio Hills transitions abruptly into a high-relief landscape defined by densely spaced active modern channels that expose deeper stratigraphic levels of the Ocotillo and underlying Palm Spring Formation. This change in the geomorphic expression of the Indio Hills landscape is compatible with a model in which most of the slip transfer between the Banning and Mission Creek strands occurs within the Indio Hills west of Thousand Palms Canyon (Figure 4).

The gradients in surface expression observed along strike of the Banning and Mission Creek strands and the geomorphic and erosional changes in the Indio Hills are consistent with a model in which slip transfers from Mission Creek strand to the Banning strand in the northwestern Indio Hills. Structural measurements described in the next section provide further evidence that right-lateral slip is transferred to the Banning strand within the western Indio Hills.

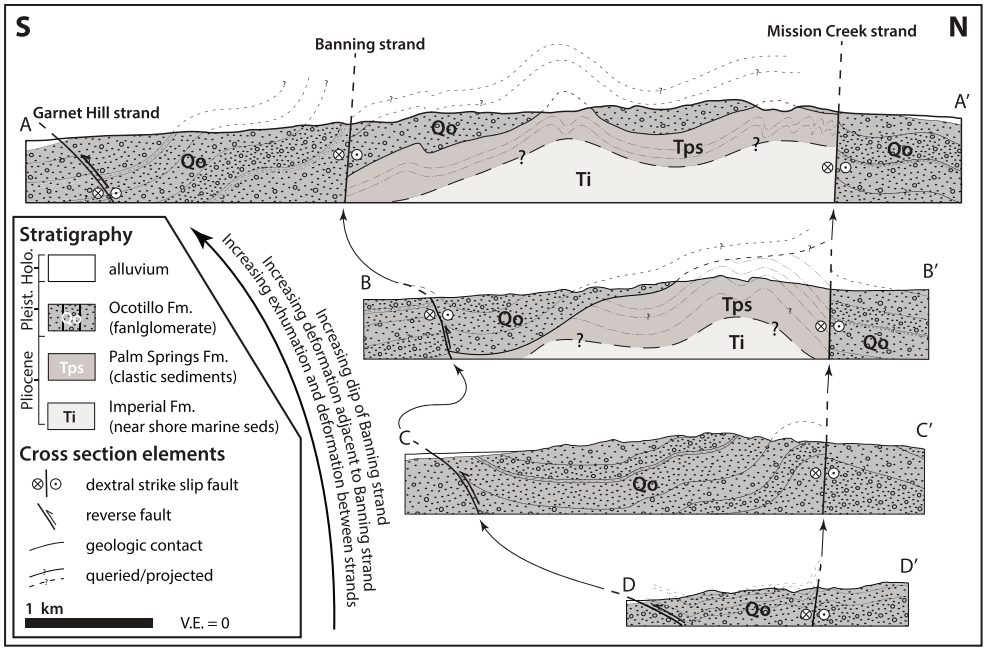

Figure 5. Cross sections traversing the Indio Hills based on structural mapping showing along-strike gradients in fault dip and deformation of the Ocotillo and Palm Springs Formations between the Banning, Mission Creek, and Garnet Hill strands. The northwest increase in exhumation, folding, and topography between the two faults and the increasing dip of the Banning strand provide structural evidence for the transfer of right-lateral slip from the Mission Creek strand to the Banning strand within the Indio Hills. The greater deformation adjacent to the Banning strand shown at the SW edge of A-A′ suggests subsequent transfer of some displacement to the Garnet Hill strand.

3.2. Structural Evidence

New cross sections illustrating the internal structure of the Indio Hills (Figure 5) were constructed by combining existing structural data and geologic mapping [*Dibblee*, 2008] with new structural measurements collected along major N-S trending channels that cross the Indio Hills. The locations of the new structural measurements are shown on Figure 4b and reported in Table S1. The cross sections highlight several relationships critical to understanding strain partitioning and kinematics between fault strands in the Indio Hills. Measurements of fault dips in the Indio Hills indicate that at the surface, the Mission Creek strand dips steeply toward the south and does not vary significantly along strike, whereas the dip of the Banning strand increases from subhorizontal near Biskra Palms Oasis [*Behr et al.*, 2010] to near vertical just east of Edom Hill ~18 km to the northwest. This increase in dip is reflected in a northwestward transition from variably striking isolated fault scarps near Pushawalla and Thousand Palms Canyons to the relatively linear fault scarps east and west of Edom Hill (Figure 3h). Between the two fault strands in the southeast Indio Hills, the Pleistocene Ocotillo Formation is broadly warped, exhibiting open folding, but very little internal deformation (Figure 5, D-D′). Local steepening of the Ocotillo Formation gravel bedding is observed adjacent to both faults but is greater along the Mission Creek strand. By contrast, in the northwest Indio Hills near Edom Hill, the Ocotillo Formation is locally vertically dipping adjacent to the steeply dipping Banning strand on its south side. This deformation coincides spatially with the inception of the reverse- or oblique reverse-slip Garnet Hill strand along the south side of Edom Hill. Additionally, in the northwest Indio Hills, the Ocotillo Formation exhibits more significant, shorter-wavelength folding between the Banning and Mission Creek strands, accommodated by significant bedding-parallel shear along clay-rich intervals (Figure S3). This increased deformation is associated with greater amounts of uplift and erosion as indicated by exhumed exposures of the Pliocene Palm Spring Formation and small slivers of the underlying Imperial Formation. The increased deformation and exhumation are also spatially coincident with the change in drainage patterns and relief discussed in the previous section (Figure 4). The Imperial and Palm Spring Formations are substantially more deformed than the overlying Ocotillo gravels, suggesting deformation between the two faults strands has been ongoing probably since at least the Pliocene.

These along-strike variations in fault dip and deformation patterns indicate that significant slip transfer occurs between the Mission Creek and Banning strands and between the Banning and Garnet Hill strands over both long (Quaternary) and short (Holocene) timescales. It suggests that for a few kilometers toward the northwest of the intersection of the Mission Creek and Banning strands in the southeast Indio Hills, the Mission Creek strand is accommodating the majority of right-lateral motion, whereas the Banning strand is dominantly dip slip. This is consistent with observations from a shallow subsurface trench in which the Palm Spring Formation is thrust over a late Pleistocene alluvial fan complex by the shallowly dipping Banning strand [*Behr et al*., 2010]. As the Banning strand steepens toward the northwest, deformation steps left and is transferred from the Mission Creek strand and right-lateral shear is localized onto the Banning strand. The presence of Edom Hill and the structural and geomorphic relationships observed there suggest that the Banning strand is accommodating primarily right-lateral shear in this area and the Garnet Hill strand accommodates the dip-slip component, effectively mimicking the Banning-Mission Creek relationship seen near Biskra Palms. This pattern of progressive left-stepping of faults to form local restraining bends and associated topography has been described for other closely spaced faults in the Big Bend region of the San Andreas Fault [*Sylvester*, 1999; *Sylvester and Smith*, 1976; *Bilham and Williams*, 1985; *Bürgmann*, 1991]. Evidence for slip transfer between the Mission Creek and Banning strands dies out at the northwest end of the Indio Hills, which can be explained by a northwest decrease in the Mission Creek strand slip rate and the separation of the two faults to distances exceeding 4 km, the maximum distance across which slip can be transferred between subparallel structures [*Elliott et al*., 2009; *Wesnousky*, 2006].

4. The Painted Hill Slip Rate Site

The geomorphologic and structural data discussed in previous sections suggest significant slip transfer between the Mission Creek and Banning strands but do not provide quantitative information as to *how much* slip is concentrated on the Banning strand as it enters San Gorgonio Pass. To investigate this, we use offset measurements and Quaternary geochronology to estimate the slip rate at a newly identified site along the Banning strand near the eastern entrance to San Gorgonio Pass, which we informally refer to as the "Painted Hill" site.

In the southeastern section of San Gorgonio Pass, the 285° trending, steeply dipping Banning strand separates moderately SE dipping Pliocene fanglomerates north of the fault from beheaded late Pleistocene and Holocene alluvial fans south of the fault. At this location (33.942005°N, −116.620846°E), the Banning strand offsets a small alluvial fan, which we refer to as Qfr, from its small (~0.03 km^2) source catchment north of the fault (Figure 6). Previous mapping did not differentiate this small (also ~0.03 km^2 in area) deposit from an older, truncated, and tilted alluvial fan surface (Qoa3s on Figure 6), which it overlies. Dirt roads and windmill foundations constructed along the fault and along the Qfr fan crest have superficially disrupted the fan surface (Figure 6a). Consequently, the elevation contours and the morphology apparent in the hillshaded elevation models near the top of the Qfr fan do not reflect the original fan morphology, but rather topography that has been modified by construction. However, despite anthropogenic modification, the distinctive topographic curvature of the fan allows us to precisely locate its apex, axis, and margins using the B4 lidar data. Shallow bar and swale topography distinguish the western side of Qfr downslope from the fan apex from the texturally smoother eastern side, which is currently downstream of the source catchment and so may have been subject to slight postdepositional modification. Channels incised by less than 10 cm near the top of Qfr deepen to about a meter at its margins and radiate away from the fan apex. The largest clast sizes observed at the fan surface are small boulders, but cobble-sized clasts are most abundant. The clasts are unvarnished, and there is no pavement development on the fan surface.

We excavated a 180 cm deep pit close to the Qfr fan crest near its apex to expose the fan in cross section. Bedding within it is very poorly developed but shows a weak inverse grading, with the largest clasts concentrated in the upper 60 cm. This upper interval is matrix supported, with the matrix consisting primarily of sand and silt. At ~60 cm depth, a higher concentration and weak imbrication of large clasts suggest that this interval may represent the reworked top of an earlier depositional sequence represented by the interval from 60 to 180 cm. This lower interval contains some cobbles but is dominated by sand and large pebbles. As in the upper interval, there is no coherent bedding, but there are anastomosing, lighter-colored, pebble-rich

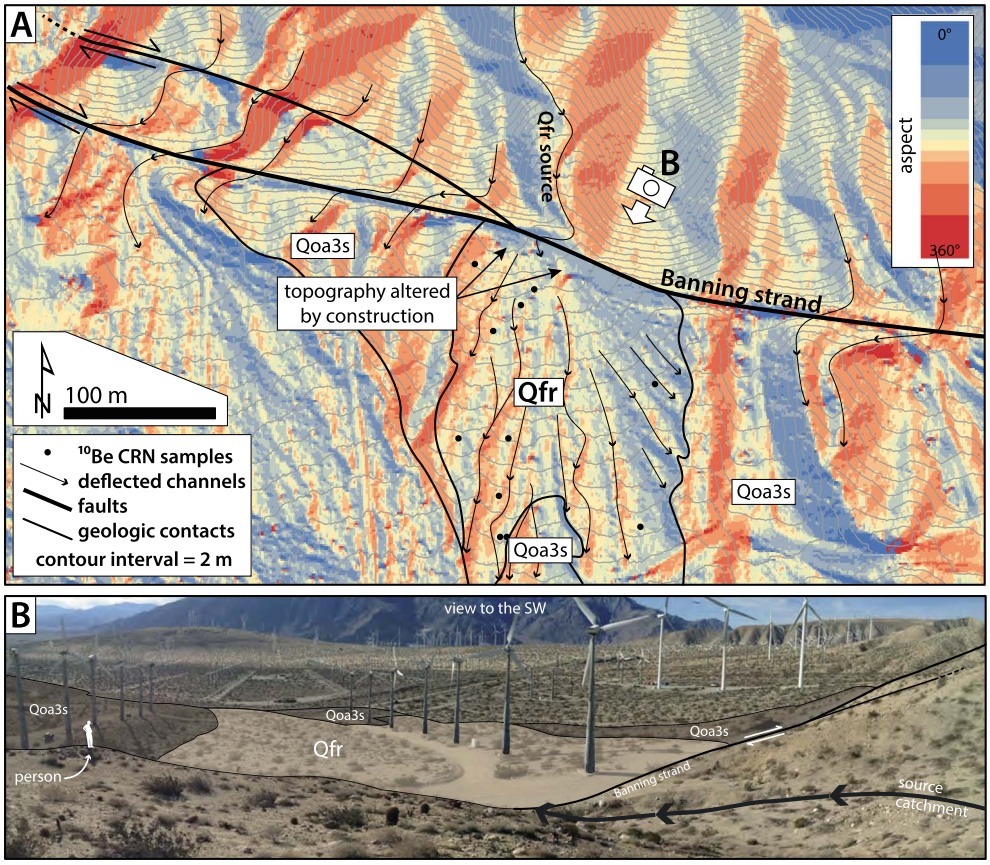

Figure 6. (a) Aspect colored slope shade map of the offset Qfr alluvial fan, which was deposited on top of the older Qoa3s alluvial deposit during no more than two debris flow events. Two meter contours reveal typical alluvial fan curvature. Black dots show sampling locations for U-series and ^{10}Be exposure dating. Offset and deflected to the east and west signify predominantly right-lateral slip along this section of the Banning strand. Topography and fan morphology near the top of Qfr are have been disrupted by construction. (b) Annotated panoramic photograph of the field site looking to the southwest from the vantage shown in Figure 6a.

lenses that are laterally continuous for up to 40 cm. These relationships suggest that the upper ~2 m of Qfr fan consists of one to two stacked debris flow deposits. Soil descriptions are provided in Table 1.

5. Offset Model

The curvature of the Qfr fan surface is most easily visualized with 1 m elevation contours derived from 1 m resolution B4 lidar. Although modification of the fan surface by construction along the axis produces irregularities near the centers of the topographic contours, they can be modeled to reveal the projected apex location and fan axis orientation. We approach this in two ways. First, we model the contours as

Table 1. Soil Descriptions

Horizon	Depth (cm)	Description
Av	0–1.5	Dark brown (10YR 3/3m, 5/3d); Loamy sand to sandy loam texture; moderate, medium platy structure; soft, nonsticky and nonplastic consistence; abrupt, smooth boundary
Bw	1.5–8	Dark yellowish brown (10YR 4/4m, 5/4d); slightly gravelly sandy loam texture; massive breaking to weak, fine subangular blocky structure; soft to loose, nonsticky and nonplastic consistence; no clay films; clear, wavy boundary
Cox	8–23.5	Dark brown to brown (10YR 4/3m, 5/3d); slightly gravelly loamy sand; massive breaking to weak, coarse subangular blocky structure; loose, nonsticky and nonplastic consistence; clear to gradual, wavy boundary
2C	23.5–46	Dark brown to brown (10YR 4/3m, 6/3d); gravelly sand texture; single-grain structure; loose, nonsticky and nonplastic consistence; no $CaCO_3$
2Ck	46–152+	Dark brown to brown (10YR 4/3m, 6/3d); gravelly sand texture; single-grain structure; loose, nonsticky and nonplastic consistence; Stage I $CaCO_3$ with thin dustings to 91 cm depth and thin coatings on clast bottoms from 91 cm to the bottom of the pit

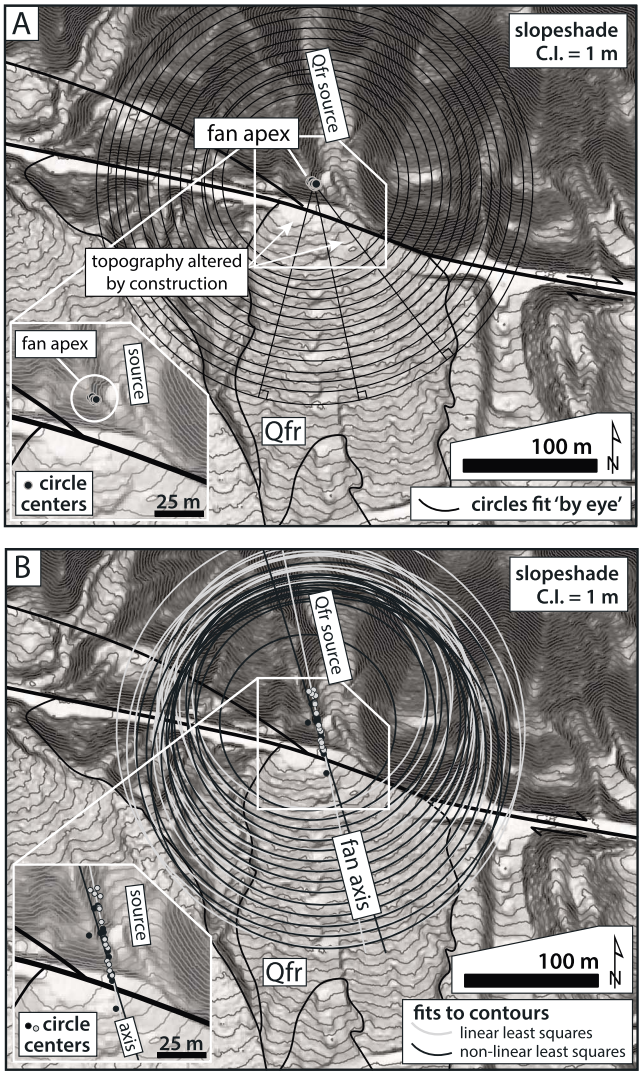

Figure 7. Topography-based methods for approximating the apex (a) and axis (b) of the Qfr fan. The upper four contours reflect topography modified by construction and are excluded from the analysis. In Figure 7a, circles fit visually to 1 m topographic contours. Forcing the circles to be concentric gives an approximation of the location of the fan apex (inset). In Figure 7b, linear and nonlinear least squares circle fits to the contours result in linear distributions of the circle centers that approximate the orientation and along-strike location of the fan axis. The quantitatively constrained fan axis serves as the offset piercing line, which we reconstruct ~25 m from the Qfr source catchment.

approximately concentric circles whose centers of curvature indicate the apex of the fan (Figure 7a) [*Keller et al.*, 2000]. The upper four contours dominantly reflect topography created during road construction and are therefore excluded from the analysis. This qualitative method results in a cluster of circle centers that project the apex of Qfr to a location about 4 m north of the fault and about 30 m from the modern catchment thalweg in a direction parallel to fault strike.

Second, we use the MATLAB function fitcircle to calculate both linear (minimizing algebraic error) and nonlinear (minimizing geometric errors) least squares circle fits to the contours [*Gander et al.*, 1994]. For this analysis, we used ArcGIS and the B4 airborne lidar data to generate 1 m topographic contour lines clipped to limit their coverage to the area of the Qfr fan. We then exported 13 consecutive contours from near the top of Qfr as *xyz* files. We excluded the upper four contour intervals where the topography has been most significantly affected by road and windmill construction as well as the lower several contours where erosion has most altered the fan morphology (Figure 6a). We then use our MATLAB code to fit circles to each *xyz* contour data set and plot the contours, the circles, and the circle centers of curvature (Figure 7b). This quantitative calculation results in two nearly identical distributions of circle centers from the linear and nonlinear fits. Since circles are not forced to be concentric using this method, the circle centers define linear distributions that we interpret to reflect the location and azimuth of the fan axis because they match the location and orientation of both the topographic drainage divide and the fan axis determined visually from the aspect map of the Qfr fan (Figure 6a). As a last step, we calculated a linear least squares fit through both groups of circle centers to provide a linear approximation of the axis. A detailed description of the workflow, the MATLAB code, and a link to the fitcircle download page are provided in the supporting information.

Using this method, we find that the fan axis, which should extend away from the mouth of the modern catchment, is offset from the modern catchment thalweg by 25 m in a direction parallel to fault strike (Figure 8). For our final offset model, we rely on this slightly lower but less qualitatively constrained offset value and we emphasize again that the topography west of this axis that appears to mark the apex of the fan is the product of road construction. Although the current channel thalweg occupies a deeper, narrower incision at the

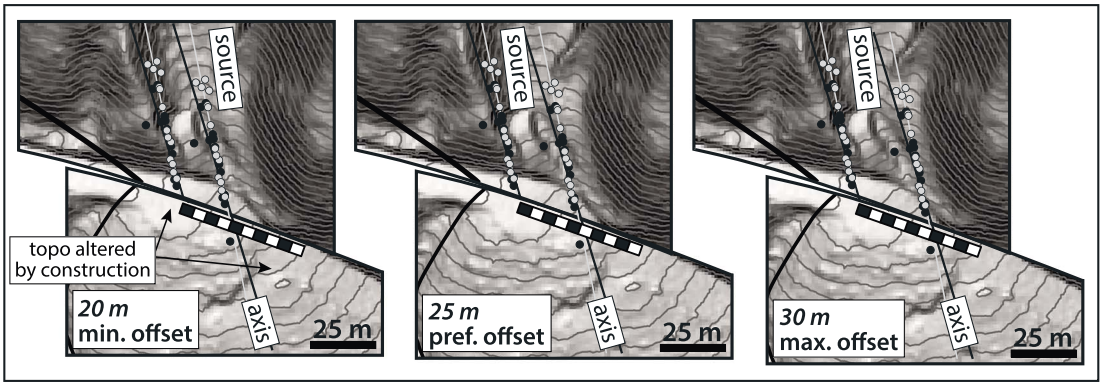

Figure 8. (a) Minimum, (b) preferred, and (c) maximum offsets measured by reconstructing the axis of the Qfr fan to the mouth of its source catchment indicate between 20 and 30 m of right-lateral displacement since deposition. The scale bar along the fault represents 50 m; increments are 5 m. The offset error of ±5 m reflects uncertainty in the location of the catchment thalweg at the time of deposition.

mouth of the catchment where it intersects the fault, this feature likely postdates deposition and westward transport of Qfr along the fault. At the time of deposition, however, the thalweg may have intersected the fault anywhere along the ~10 m wide catchment mouth. To account for this uncertainty, we assign errors of ±5 m to the offset axis measurement. Tools for assigning statistically determined errors to lateral reconstructions of offset features have been successfully implemented for channel-channel offsets [*Zielke and Arrowsmith*, 2012] and could possibly be adapted to catchment-fan offsets such as that analyzed here. However, since the morphology of Qfr adjacent to the fault has been altered by construction, calculating statistically determined errors using these methods is not straightforward. Therefore, the final 25 ± 5 m offset reflects the minimum (20 m), preferred (25 m), and maximum (30 m) measurements (Figure 8), not a 2σ error or a 95% confident interval. Best practices for assigning uncertainty to offset features are still evolving [*Scharer et al*., 2014]; however, we believe ±20% conservatively estimates the combined uncertainties in estimating the thalweg and axis location because it eclipses the uncertainty in the fan axis location due to fault parallel scatter in circle centers and is on par with or exceeds errors assigned to measurements of both historical single-event and older multievent offsets reported in several recent studies in which uncertainties were carefully considered [*Zielke et al*., 2012; *Salisbury et al*., 2012; *Gold et al*., 2013].

6. Geochronology

A variety of quantitative geochronologic techniques are used to estimate depositional ages of Quaternary alluvial deposits including luminescence dating, radiocarbon dating, U-series dating of pedogenic carbonate clast coatings, and cosmogenic exposure dating of surface cobbles, surface boulders, depth profiles, and buried clasts. The complex processes governing the geomorphic history of alluvial deposits are poorly understood but may exert significant control on the formation and retention of the atomic and isotopic concentrations targeted by these commonly employed dating methods. Therefore, interpretations of depositional age from a measured date rely upon major assumptions about geomorphic history, increasing the chances that using a single dating technique could lead to an erroneous interpretation of the age of an alluvial landform. In order to limit the influence that the epistemic uncertainty associated with a single technique might have over an age interpretation, several recent studies have combined multiple geochronologic methods to evaluate the age of the alluvial deposit [*Fletcher et al*., 2010; *Blisniuk et al*., 2012; *Behr et al*., 2010]. We follow these studies by using both cosmogenic exposure dating and U-series dating of pedogenic carbonate.

6.1. ^{10}Be Exposure Dating: Methods

In situ terrestrial cosmogenic nuclide surface exposure dating (hereafter exposure dating) of rocks found at the upper 2 m of the Earth's surface provides a method for quantifying the geomorphic evolution and depositional age of alluvial surfaces over 10^2–10^7 year timescales. This method has been described in detail in several comprehensive reviews but is summarized below in the context of ^{10}Be exposure dating [*Gosse and Phillips*, 2001; *Granger et al*., 2013; *Dunai*, 2010; *Bierman*, 1994; *Lal*, 1991]. Beryllium-10 is produced at the Earth's surface primarily by spallogenic reactions between high-energy secondary cosmic ray-derived

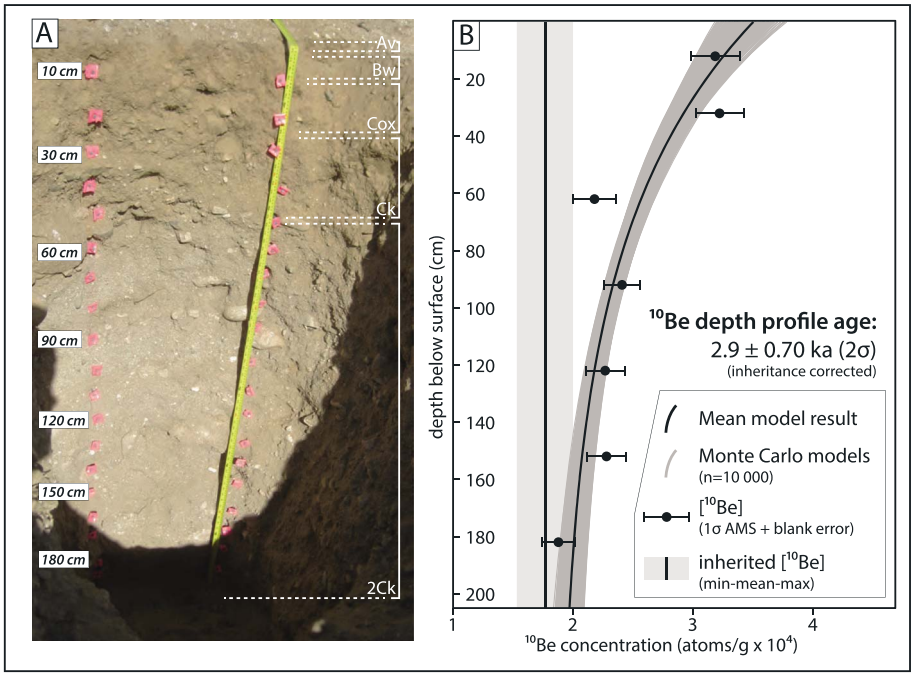

Figure 9. (a) Photograph and soil horizons for the ~2 m deep soil pit excavated near the apex of the Qfr fan. Clasts with pedogenic carbonate coatings measured using U-series dating were taken from depths between 100 and 180 cm. Sediment samples for ^{10}Be depth profile exposure dating are collected at the intervals shown on the photograph. The location of the pit is shown on Figure 5. Full soil descriptions are provided in Table 1. (b) Depth profile modeling results of the seven samples taken from the soil pit shown with 1σ internal uncertainties. The median age with 2σ uncertainty corrected for ~3 kyr of inheritance is significantly younger than both the U-series age and the median cobble age.

particles and oxygen (and to a lesser extent silicon) in quartz. Because ^{10}Be is not produced within minerals in significant quantities by any other means, its concentration in quartz is related to (1) the length of exposure on Earth's surface, (2) the production rate of ^{10}Be at a specific latitude and elevation, and (3) the half-life of ^{10}Be, all of which are known or can be inferred. By measuring the concentration of ^{10}Be in quartz-bearing surface clasts, it is possible to estimate the time since that clast was first exposed to cosmic rays, which, with several assumptions, can be related to depositional age. Additionally, the production of ^{10}Be nuclides by neutron spallation decreases exponentially to near zero at a depth of ~2 m in gravelly sediments. Beryllium-10 concentrations measured in samples composed of the sand-sized fraction or amalgamated clasts collected at different depth intervals from a soil pit excavated into an alluvial deposit can be modeled to provide a surface exposure age as well. This method also measures the average concentration of inherited ^{10}Be nuclides that may have accumulated when the sediments analyzed were exposed at the surface prior to final deposition. Correcting for inheritance in depth profile measurements simply requires subtracting the inherited component from the total nuclide concentration [*Anderson et al*., 1996; *Repka et al*., 1997]. Correcting for inheritance in individual surface clasts is less straightforward and has been approached by measuring the mean age of multiple surface clasts in order to average out differences in inherited nuclide concentrations and the effects of clast erosion, which lowers nuclide concentrations over time [*Repka et al*., 1997]. Measuring ages from clasts currently in the source catchment or channel may provide approximate estimates of clast inheritance [*Owen et al*., 2011; *Blisniuk et al*., 2010], although this latter method assumes no change in rates of erosion and deposition over time. In addition to inherited ^{10}Be concentrations, uncertainties in production rates, shielding, erosion, blank corrections, and analytical error as well as the relationship of an exposure age to a particular geomorphic event all contribute to uncertainties in exposure ages.

6.1.1. Sample Collection, Preparation, and Analysis

We collected samples from two small boulders (intermediate axes ≈ 40 cm), as well as seven cobbles (intermediate axes ≈ 10 cm), and seven depth profile samples from the Qfr surface for ^{10}Be exposure dating (Figures 6a and S4). The boulder and cobble samples were quartz-rich lithologies (quartzite and granite), exhibited minimal evidence of surface weathering, and were collected from stable positions in topographic

Table 2. ^{10}Be Cosmogenic Exposure Dating: Isotopic Data and Results

Sample[a]	Clast Type	Height[b] (cm)	Thickness[c] (cm)	Latitude °N	Longitude °W	Elevation (m)	Production rate (atoms g^{-1} a^{-1}) Spallation[d]	Muon[e]	Density (g/cm^3)	Shielding factor
					Qfr Surface Clast Data					
GDH63	cobble	4	2–4	33.94091	−116.6201	495	5.60	0.212	2.7	0.989
GDH64	cobble	4	2–4	33.94163	−116.62001	504	5.64	0.213	2.7	0.989
GDH65	boulder	15	2–4	33.94224	−116.6211	517	5.70	0.214	2.7	0.989
GDH66	cobble	4	2–4	33.9419	−116.62099	512	5.67	0.213	2.7	0.989
GDH67	boulder	13	2–4	33.94136	−116.6209	503	5.63	0.213	2.7	0.989
GDH68	amalg. peb.	2	2–4	33.94163	−116.62001	514	5.68	0.214	2.7	0.989
GDH84	cobble	4	2–4	33.94086	−116.62095	495	5.60	0.212	2.7	0.989
GDH85	cobble	4	2–4	33.94107	−116.62096	498	5.61	0.212	2.7	0.989
GDH86	cobble	4	2–4	33.94137	−116.6212	502	5.63	0.213	2.7	0.989
GDH87	cobble	4	2–4	33.94211	−116.62074	516	5.69	0.214	2.7	0.989
					Qfr Depth Profile Data					
Qfr10	250–500 μ	−10	4	33.94203	−116.62082	517	-	-	1.8–2.4	0.989
Qfr30	250–500 μ	−30	4	-	-	-	-	-	1.8–2.4	-
Qfr60	250–500 μ	−60	4	-	-	-	-	-	1.8–2.4	-
Qfr90	250–500 μ	−90	4	-	-	-	-	-	1.8–2.4	-
Qfr120	250–500 μ	−120	4	-	-	-	-	-	1.8–2.4	-
Qfr150	250–500 μ	−150	4	-	-	-	-	-	1.8-2.4	-
Qfr180	250–500 μ	−180	4	-	-	-	-	-	1.8–2.4	-

[a]For photographs of each sample, see Figure S4.
[b]Height above Qfr surface.
[c]Approximate thickness of sample removed from clast tops and depth profile intervals.
[d]Time-independent production rate based on *Lal* [1991] and *Stone* [2000]. Value calculated by CRONUS.
[e]Time-independent production rate based on *Heisinger et al.* [2002a, 2002b]. Value calculated by CRONUS.
[f]Atoms of ^{10}Be in blanks (2σ uncertainties include analytical and 1% carrier mass error, combined in quadrature): 1406: 39273.45949 ± 18986.07664; 1407: 15772.98813 ± 5799.391763; 1409: 46484.18427 ± 18147.42554.
[g]SUERC standard: National Institute of Standards and Technology SRM4325, ^{10}Be/Be ratio of 2.79 × 10−11. LLNL-CAMS standard: 07KNSTD3110, ^{10}Be/Be ratio of 2.85 × 10−12 (samples GDH63, 64, 67, and 68 only).
[h]Assuming a ^{10}Be half-life = 1.36 Ma.
[i]Carrier [^{9}Be] = 204 μg/g.
[j]Background corrected.
[k]The 2σ internal uncertainties include analytical (counting statistics), blank, 1% carrier mass, and 2% sample preparation errors, combined in quadrature.
[l]Clast ages calculated using CRONUS v. 2.2.1 [*Balco et al.*, 2008], time-invariant production, reference production rate: 4.49 ± 0.3 atoms/g/yr. Depth profile age calculated using MATLAB GUI of *Hidy et al.* [2010].
[m]The 2σ external uncertainties include previously named errors (footnote k) plus an 8.7% production rate and 1% ^{10}Be decay constant errors, combined in quadrature.

bars. Cobbles make up the majority of the surface clasts that we collected because boulders are scarce on Qfr, and of those present, only two were of the correct lithology and displayed sufficiently minimal weathering. The depth profile samples were collected at 30 cm intervals from a 180 cm deep trench excavated near the Qfr fan apex (Figure 9a). We also collected pebbles (n = ~20) from the western lobe of the Qfr surface, which were combined into an amalgamated pebble sample.

Rock crushing and magnetic separation were performed at UT Austin, and all subsequent steps were carried out at the Scottish Universities Environment Research Centre (SUERC), Scotland, UK. Accelerator mass spectrometer (AMS) measurements were completed at the SUERC AMS Laboratory and at the Lawrence Livermore National Laboratory Center for Accelerator Mass Spectrometry (LLNL-CAMS). Detailed descriptions of the processing techniques, the measurement conditions, and the ^{10}Be concentration calculations are given in the supporting information.

6.1.2. Exposure Age Calculation

We calculated boulder and cobble exposure ages using the CRONUS-Earth online calculator, version 2.2.1 (http://hess.ess.washington.edu) [*Balco et al.*, 2008]. Input parameters for each sample are given in Table S2; input uncertainty in the ^{10}Be concentration includes the 1σ analytical, blank, 1% carrier mass, and 2% sample preparation errors. Given the lack of consensus regarding which time-dependent nuclide production model is most accurate, we present exposure ages calculated using a time-invariant reference production rate of 4.49 ± 0.3 atoms g^{-1} yr^{-1} (sea level and high latitude) based on the scaling models of

Table 2. (continued)

Blank[f]	$^{10}Be/^{9}Be$[g,h] ($\times10^{-14}$)	Error 1σ ± (%)	Sample Wt. (g)	Carrier[i] (g)	[^{10}Be][j] atoms g^{-1} ($x10^4$)	Error[k] 2σ ± atoms g^{-1} ($x10^4$)	Age[l] (ka)	Error[m] 2σ ext. ± (ka)	Error[k] 2σ int. ± (ka)
					Qfr Surface Clast Data				
1407	2.9144	3.9175	13.466	0.9786	2.770	0.286	4.773	0.971	0.492
1407	2.9584	3.3082	11.267	0.9752	3.350	0.312	5.735	1.138	0.534
1406	6.6123	4.1519	15.473	0.9693	5.393	0.542	9.147	1.849	0.922
1406	4.5198	5.7469	13.992	0.9698	3.990	0.540	6.789	1.504	0.922
1409	4.6770	2.8586	14.958	0.9727	3.835	0.307	6.57	1.267	0.528
1407	9.1109	2.2300	22.06	0.9736	5.410	0.337	9.197	1.710	0.574
1406	5.3568	4.5469	17.727	0.9654	3.755	0.414	6.473	1.340	0.714
1406	4.7430	5.0176	19.511	0.9616	2.985	0.361	5.132	1.093	0.62
1406	5.3289	4.5916	13.710	0.9677	4.841	0.537	8.303	1.724	0.924
1406	2.2097	6.9192	17.775	0.9761	1.433	0.261	2.429	0.614	0.442
					Qfr Depth Profile Data				
1406	4.0176	5.2778	15.520	0.9743	3.185	0.409	2.9	0.7	-
1409	5.3847	5.3368	20.651	0.9695	3.221	0.400	-	-	-
1406	3.9339	7.1631	22.136	0.9727	2.179	0.362	-	-	-
1406	4.4082	5.0316	22.661	0.9734	2.408	0.294	-	-	-
1406	3.8502	5.9565	20.767	0.9722	2.268	0.324	-	-	-
1406	3.9339	5.8936	21.152	0.9720	2.279	0.321	-	-	-
1406	3.5154	5.8571	22.649	0.9697	1.878	0.269	-	-	-

Lal [1991] and *Stone* [2000]. Exposure ages calculated simultaneously using variable production rates [*Lal*, 1991; *Stone*, 2000; *Staiger et al*., 2007; *Desilets et al*., 2006; *Desilets and Zreda*, 2003; *Pigati and Lifton*, 2004; *Lifton et al*., 2005; *Dunai*, 2001] are given in the supporting information (Table S3). The external errors given by CRONUS include an 8.7% uncertainty in production rate that is related to scatter in reference production rates determined at the various calibration sites used in the time-invariant production scaling model [*Balco et al*., 2008]. To calculate the total error, we add in quadrature to the external error a 1% uncertainty in the ^{10}Be decay constant, which in this CRONUS version has been updated to $4.998 \pm 0.043 \times 10^{-7}$ yr^{-1} to reflect the most recent ^{10}Be half-life measurements [*Chmeleff et al*., 2010; *Korschinek et al*., 2010].

We calculated the surface exposure age and inheritance from the depth profile samples using the MATLAB graphical user interface (GUI) presented by *Hidy et al*. [2010], which is available online (http://geochronology.earthsciences.dal.ca). Input uncertainty in the ^{10}Be concentration is the 1σ internal error described above and in the supporting information. A complete list of input parameters for the calculations is also given in the supporting information (Figure S6). The resulting uncertainties in exposure age and inheritance do not include error in production rate, so we add in quadrature an additional 8.7% error to match the production rate error used by CRONUS to calculate the external uncertainty in clast ages.

6.2. Beryllium-10 Exposure Dating: Results

Exposure ages from clasts and the depth profile are given in Table 2. Exposure ages from two small boulders, seven cobbles, and a selection of amalgamated pebbles range from 2.4 ka to 9.2 ka (not corrected for inheritance) with individual 2σ total uncertainties of around ±20% (Table 2 and Figures 10 and 11). Modeling the depth profile data (seven depth intervals) using the Monte Carlo simulator presented by *Hidy et al*. [2010] gives an inheritance-corrected age of 2.9 ± 0.70 ka (2σ) and indicates $1.56–2.0 \times 10^4$ atoms/g inherited ^{10}Be, which is equivalent to 3.0 ± 0.25 kyr (1σ internal uncertainty) of prior exposure (Table 2 and Figure 9b).

6.3. Uranium Series Dating of Pedogenic Carbonate: Methods

In arid environments, pedogenic calcium carbonate ($CaCO_3$) laminations form as coatings on the bottom surfaces of clasts in gravelly or pebbly alluvium at subsurface depths of 50–200 cm upon initiation of carbonate accumulation [*Gile et al*., 1966; *Machette*, 1985]. Trace amounts of radiogenic ^{238}U and ^{234}U are incorporated into the pedogenic carbonate as it forms, but poorly soluble Th is not, so ^{238}U-^{234}U-^{230}Th dating (U-series dating) can be used to determine the amount of time since such secondary carbonate formed

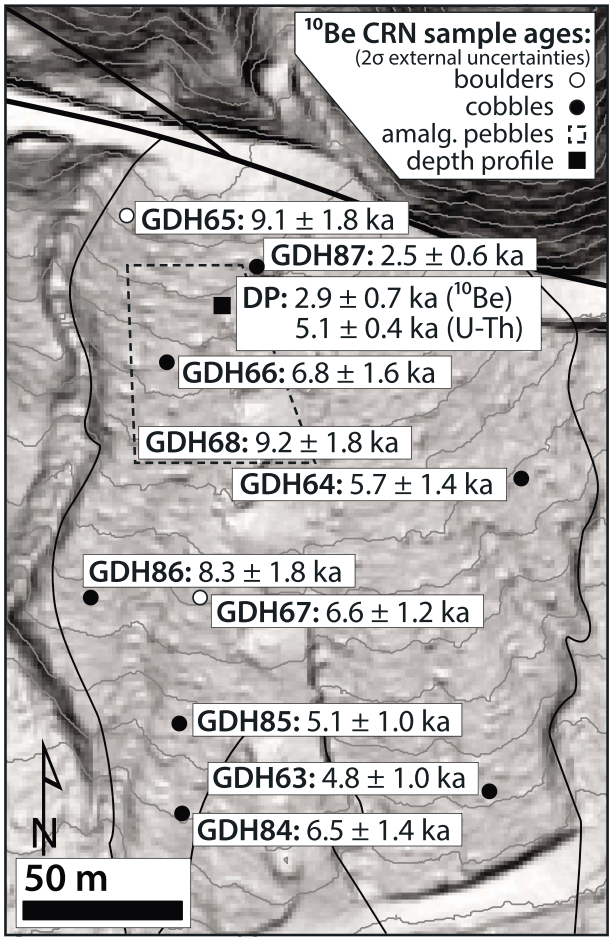

Figure 10. (a) Results of ^{10}Be cosmogenic nuclide exposure dating of clasts and (b) the depth profile from the Qfr fan. Results are given in Table 1. Figure 10a shows shaded relief map of Qfr showing the names, locations, and exposure ages of the seven cobbles, two boulders, and amalgamated pebbles as well as the location of the depth profile and U-series ages (DP). Clast ages are shown with 2σ external uncertainties.

[*Ku et al.*, 1979]. Because carbonate clast coatings form after deposition, U-series dating of pedogenic carbonate provides estimates of the minimum depositional age of an alluvial deposit [*Sharp et al.*, 2003; *Blisniuk and Sharp*, 2003; *Ludwig and Paces*, 2002; *Behr et al.*, 2010; *Fletcher et al.*, 2010; *Blisniuk et al.*, 2012]. In the northwestern Coachella Valley, rainwater and carbonate-bearing aeolian dust [*Reheis et al.*, 1995] are inferred to be the primary sources of calcium (Ca^{2-}) ions for pedogenic carbonate formation because the host fans lack significant concentrations of carbonate rocks and Ca-bearing minerals weather only slowly in the semiarid climate [*Capo and Chadwick*, 1999; *Machette*, 1985]. In soils, carbonate ions (CO_3^{2-}) form from atmospheric and plant-respired CO_2 and from carbon released during plant decomposition. In the region of this study, pedogenic carbonate precipitation on the bottoms of clasts is dominantly a consequence of evapotranspiration, although degassing of CO_2 from water in the soil and temperature-dependent changes in $CaCO_3$ solubility may also induce precipitation [*Gile et al.*, 1966; *Birkland*, 1999; *Machette*, 1985]. Although six stages of carbonate accumulation have been recognized in older (>100 kyr) alluvium [*Gile et al.*, 1966; *Machette*, 1985], the carbonate coatings we analyzed in this study are representative of only the very first stage of carbonate accumulation.

Constraining the minimum depositional age of alluvium using U-series dates on pedogenic carbonate requires consideration of several factors. First, it is important to confirm that the pedogenic carbonate formed in situ, as carbonate formed on clasts prior to final transport and incorporation into the alluvial deposit would lead to an anomalously old estimate of the depositional age. Although turbulent transport processes may largely scrub prior carbonate accumulations from clasts before final deposition, this process may be less effective where transport distances are short, as between the Qfr fan and its source catchment. Second, this dating technique relies upon the measured ^{230}Th/^{238}U ratio, so detrital ^{230}Th incorporated as silicate inclusions must be subtracted using ^{232}Th as an index [*Ludwig and Paces*, 2002]. Third, it is important to verify that the dated carbonate has retained a closed U-series system since formation, which can be assessed by the reproducibility of ages because open U-series systems would cause ages to scatter. Fourth, the lag time between alluvial deposition and formation of datable thicknesses of carbonate is expected to vary with several geologic and environmental factors including climate, parent material, dust input, and surface roughness. However, recent studies suggest that it may be no more than a few hundred to a few thousand years in dusty arid environments such as our study area [*Ludwig and Paces*, 2002; *Blisniuk and Sharp*, 2003; *Sharp et al.*, 2003; *Blisniuk et al.*, 2012]. Even a relatively brief lag time, however, may be significant in the case of Holocene alluvial deposits where it may be a sizable fraction of the depositional age. Accordingly, we interpret the U-series ages of clast coatings as minimum estimates of the age of deposition of the host alluvium.

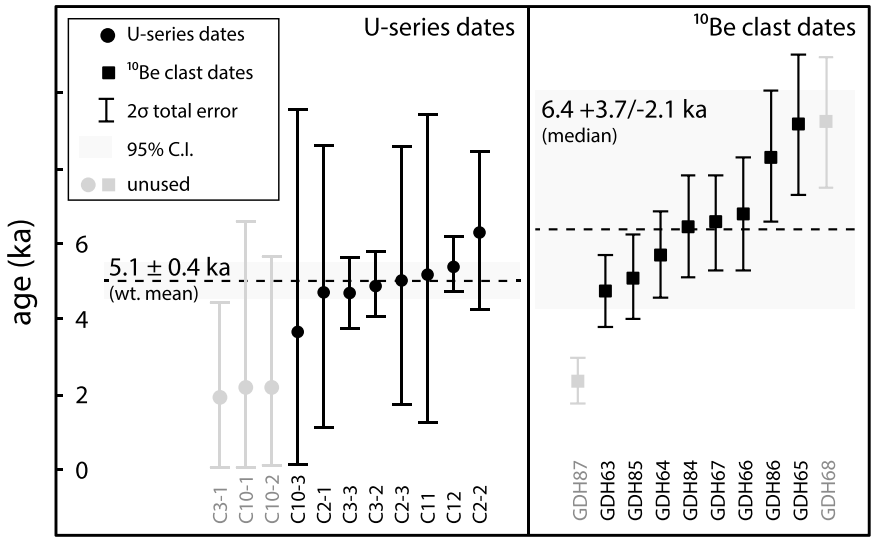

Figure 11. (left) Results of U-series dating of pedogenic carbonate clast coatings from five pebbles and (right) ^{10}Be clast exposure dates for comparison. Individual measurements are shown with 2σ total errors and show significant overlap between the distributions of measurements from both methods. Samples excluded from the weighted mean (U-series) and median (exposure dating) calculations are shown in grey. The mean U series age and median clast exposure age overlap at the 95% confidence level. The mean U-series age provides a minimum depositional age for Qfr.

6.3.1. Sample Collection, Preparation, and Analysis

We collected gravel clasts with carbonate coatings for U-series analysis from the same soil pit sampled for the ^{10}Be depth profile. Carbonate accumulation in this young deposit has not advanced sufficiently to form a visible zone of maximum accumulation, so we selected well-coated clasts from a range of depths between about 100 and 180 cm below the surface. To avoid visibly inherited carbonate, we were careful to collect clasts with carbonate coatings on their bottom surfaces only.

We performed all sample processing and analyses at the Berkeley Geochronology Center. The clasts were cleaned using a soft nylon brush and inspected under a microscope. Clasts free of visible detrital contamination and secondary porosity indicative of partial dissolution were selected. Eleven ~10–20 mg carbonate samples from five clasts were collected by separating the carbonate coatings from the clasts using a finely pointed straight steel probe and transferring each sample to a glass vial. Photographs of each clast prior to sampling and annotated to show the sampled areas are provided in the supporting information (Figure S5). The samples were cleaned in an ultrasonic bath to remove external contaminants, dissolved in 7 N HNO_3 and spiked with a mixture of ^{229}Th, ^{233}U, and ^{236}U before separation of uranium and thorium using anion exchange techniques. The samples were analyzed using a Thermo NEPTUNE multicollector inductively coupled plasma-mass spectrometry. See supporting information for full U-series analytical details. Ages were calculated using the half-lives of *Jaffey et al.* [1971] for ^{238}U, *Holden* [1989] for ^{232}Th, and *Cheng et al.* [2013] for ^{230}Th and ^{234}U. Correction for U and Th from detritus was made assuming detritus with activity ratios of $(^{232}Th/^{238}U) = 1.2 \pm 0.6$, $(^{230}Th/^{238}U) = 1.0 \pm 0.1$, and $(^{234}U/^{238}U) = 1.0 \pm 0.1$, which correspond to average silicate crust in secular equilibrium. Ages and uncertainties were calculated with Isoplot [*Ludwig*, 2009]. Uncertainties of corrected ages include measurement errors and uncertainties associated with the detritus correction. Solutions to the age equation were constrained to finite, positive values and were calculated using Isoplot and 10,000 Monte Carlo trials.

6.4. Uranium Series Dating of Pedogenic Carbonate: Results

Analytical data and ages are given in Table 3, and the dates are plotted in Figure 11. All of the U-series ages agree within uncertainties. We note that scatter of the U-series ages beyond that expected from analytical uncertainties is absent, consistent with closed U-Th systems and the absence of inherited clast coatings. Three relatively precise analyses (those with the smallest corrections for ^{230}Th from detritus) with ages of 4.70 ± 0.92 ka (2σ), 4.87 ± 0.84 ka and 5.40 ± 0.72 ka are in good mutual agreement. Because the youngest dates are likely to be those biased most by relatively late growth of their clast coatings, we adopt the

Table 3. U-Th Pedogenic Carbonate Dating: Isotopic Data and Results

Sample[a]	Sample wt. (mg)	U (ppb)	^{232}Th (ppb)	(^{230}Th/^{232}Th)[b]	(^{232}Th/^{238}U)	2σ ± (%)	(^{230}Th/^{238}U)	2σ ± (%)	(^{234}U/^{238}U)	2σ ± (%)	Uncorrected Age[c] (ka)	Error 2σ (±ka)	Corrected age[d] (ka)	Error[e] 95% CI (+ka)	Error[e] 95% CI (−ka)
C2-1	6.54	1855	568.9	1.236	0.10099	0.27	0.1248	2.92	1.071	12.21	13.5	0.70	4.7	3.9	3.6
C2-2	11.89	1957	377.3	1.817	0.06318	0.10	0.1148	1.06	1.1435	0.76	11.5	0.03	6.4	2.1	2.1
C2-3	16.01	1737	519.1	1.318	0.09797	0.13	0.1291	1.12	1.1485	0.45	13.0	0.05	5.1	3.5	3.3
C3-1	7.88	2361	578.9	1.013	0.08046	0.12	0.0815	1.58	1.1367	1.04	8.10	0.11	1.9	2.5	1.8
C3-2	9.17	2447	184.7	2.811	0.02483	0.20	0.0698	2.20	1.1479	0.92	6.83	0.10	4.90	0.84	0.84
C3-3	10.94	2501	207.4	2.572	0.02714	0.12	0.0698	0.86	1.1446	0.35	6.85	0.02	4.70	0.92	0.91
C10-1	11.34	1735	803.1	0.812	0.15238	0.27	0.1238	4.29	1.1393	1.06	12.5	0.34	2.3	4.3	2.2
C10-2	9.37	1593	532.1	0.948	0.10966	0.12	0.1039	1.92	1.1452	0.33	10.4	0.12	2.2	3.4	2.1
C10-3	11.20	2133	1147	0.936	0.17635	0.13	0.1651	1.15	1.1316	0.28	17.1	0.08	3.7	5.9	3.5
C11	10.19	2289	785.9	1.254	0.11266	0.10	0.1413	1.49	1.1356	0.75	14.4	0.07	5.2	4.2	3.9
C12	14.02	1974	129.4	3.367	0.02146	0.13	0.0722	2.05	1.1458	0.36	7.1	0.06	5.40	0.72	0.71

[a] For photographs of each sample, see Figure S5.
[b] All isotope ratios are activity ratios.
[c] Uncorrected ages are calculated without correction for U and Th from detritus.
[d] Corrected ages are calculated assuming detritus with (^{232}Th/^{238}U) = 1.2 ± 0.6, (^{230}Th/^{238}U) = 1.0 ± 0.1, and (^{234}U/^{238}U) = 1.0 ± 0.1. (^{234}U/^{238}U) initial is back-calculated from measured ratio and corrected age. Decay constants are those of *Jaffey et al.* [1971] for ^{238}U and *Cheng et al.* [2013] for ^{230}Th and ^{234}U.
[e] Corrected ages are constrained to positive, finite values.

weighted mean age of the eight remaining samples, 5.09 ± 0.44 (95% confidence interval (CI); MSWD = 0.57), as our best estimate of the minimum age of the Qfr fan (Figure 11). We emphasize that this measurement simply constrains Qfr deposition to no later than ~5 ka. Interpreting this date as the fan age would require an additional estimate of the time between fan deposition and carbonate accumulation, which is not possible to make with these data.

7. Qfr Fan Age

We use probability distributions to model a composite exposure age for the clasts collected from the Qfr alluvial fan [*Zechar and Frankel*, 2009]. Combining the 10 ^{10}Be exposure ages from surface clasts and using total uncertainties and assuming a Gaussian distribution of individual ages yield a median composite exposure age of 6.4 + 3.9/−4.2 ka (95% CI) (Figure 12a). Sample GDH87, which yielded the youngest individual age, defines a separate peak in the probability density curve and does not overlap with any other samples within 2σ internal uncertainty. For this reason, we consider sample GDH87 to be a statistical outlier that can be excluded from the final age calculation and we interpret its young age to indicate significantly later colluvial deposition, which is consistent with its location near the apex of Qfr.

Sample GDH68, which yielded the oldest exposure age, was measured from an amalgamation of ~20 pebble-sized surface clasts with intermediate axis lengths generally less than ~3 cm. We collected these pebbles from an area within ~50 m from the apex of Qfr. Although GDH68 overlaps in age with the remaining samples, we exclude it from the final age calculation because it is not appropriately compared to the other samples considering the different transport and depositional processes that affect pebble-sized and cobble- to boulder-sized samples. Although samples GDH65 and GDH86 define a distinct shoulder in the probability density curve, they overlap in age with the

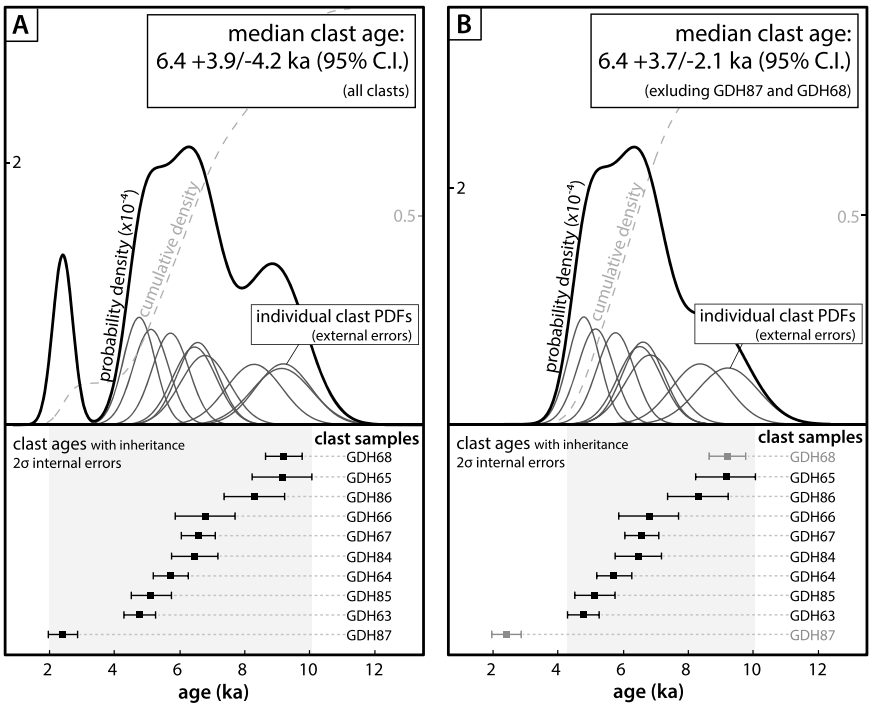

Figure 12. Individual and combined median exposure ages calculated from (a) all clasts and (b) all but two clasts. Upper rows show combined (bold curve) and individual (light curves) clast ages modeled using probability density functions assuming a Gaussian distribution of individual clast ages. The median combined ages are computed using 2σ external uncertainties associated with the individual clast dates. The lower rows compare the clasts dates within 2σ internal uncertainties. Sample GDH87 does not overlap any other sample within internal error, so we excluded it from the final median clast age calculation shown in Figure 12b. We also exclude the amalgamated pebble sample GDH68 since pebbles are subject to different geomorphic processes than larger clast. The final median combined age (Figure 12b) is the same as that calculated with all clasts included (Figure 12a), but with a tighter 95% confidence interval. Because the median clast age overlaps within error of the U-series age, we assume that it effectively averages out differences in inherited ^{10}Be among the clasts and thus provides a reliable constraint on the depositional age of Qfr.

remaining samples within 2σ internal uncertainties, and there is no strong geological argument for their exclusion. Excluding samples GDH87 and GDH68 and combining the eight remaining clast ages and again assuming a Gaussian distribution of individual ages yield the same, though more tightly constrained, median composite exposure age of 6.4 + 3.7/−2.1 ka (95% CI) (Figure 12b).

Median or mean exposure ages calculated by combining multiple surface clasts do not necessarily have any direct relation to the timing of fan deposition because individual clasts may have inherited ^{10}Be (making their apparent ages too old) and/or may have experienced clast erosion or exhumation of the surrounding matrix (making their apparent ages too young). However, we consider using the oldest clast age (GDH65: 9.1 ± 1.8 ka, 2σ total error) as the depositional age for Qfr to be an overly conservative interpretation and no more justifiable than using the youngest age (GDH63: 4.8 ± 1.0 ka, 2σ total error). Taking the ~6.4 ka median exposure age as representative of the depositional age in this context requires the simplifying assumption that these processes balance and cancel each other out [*Repka et al.*, 1997]. However, we find limited evidence for clast erosion or surface exhumation on the Qfr fan, consistent with the expectation that effects of these processes should be minor over the Holocene. For this reason, it is unsurprising that separately, the boulders and cobbles do not define measurably different age distributions, suggesting that ^{10}Be concentration does not depend on clast size at this site, as has been observed on older surfaces elsewhere [*Behr et al.*, 2010]. Therefore, deviations in clast dates away from the true depositional age of Qfr are likely to be dominated by inherited ^{10}Be; thus, the 6.4 ka median clast age is more likely to represent an upper bound on the timing of fan deposition.

This interpretation of the Qfr fan is consistent with the observed relation between the median composite exposure age of 6.4 + 3.7/−2.1 ka and the age of 5.09 ± 0.44 ka from U-series dating of pedogenic carbonate

(Figure 11). As discussed above, we interpret the mean U-series age as a *minimum* estimate of the age of fan deposition for three reasons. First, scatter of the U-series ages is attributable to analytical uncertainty, consistent with closed system behavior and the absence of inherited clast coatings. Second, carbonate accumulation ensues only after fan deposition. Third, we by necessity sampled the whole thickness of the carbonate coatings, so the U-series ages average over the entire interval of carbonate accumulation. We note that the weighted mean U-series age overlaps within uncertainties with the lower bound of the median composite ^{10}Be exposure age (see Figure 11). We interpret such agreement to indicate that the many possible factors discussed above that could confound the ^{10}Be and U-series ages of the Qfr fan are, in fact, not severe in this case.

Both the U-series age and the median clast exposure age are significantly older than the 2.9 ± 0.70 ka (2σ) ^{10}Be exposure age calculated from the depth profile modeling (Figure 9b). Multiple model runs using the *Hidy et al.* [2010] MATLAB script failed to satisfactorily reconcile the inheritance-corrected depth profile age with either the clast exposure or the U-series age without excluding the 10 and 60 cm depth intervals and invoking greater than half a meter of surface lowering, for which we do not see obvious geomorphic evidence. The distribution of ^{10}Be with depth measured in the depth profile can be better reconciled with the other ages by considering nonuniform inherited ^{10}Be or by incremental deposition, although sedimentological evidence suggests at most two debris flow deposits (Figure 9). An additional factor that may have influenced the depth profile age is that we analyzed only the 250–500 μm sand fraction sieved from each sample. This sample size may be more susceptible to contamination by infiltration of younger grains blown in from more actively eroding upwind areas like Whitewater Canyon. It is possible that measuring gravel- and pebble-sized clasts from the same depth intervals would yield an older age more compatible with the U-series and cobble exposure ages. A more in-depth exploration of these apparently discrepant depth profile ages will be presented in a future study, but because the median clast exposure age and U-series carbonate age agree satisfactorily, we favor these ages and not the depth profile age for the slip rate calculation.

8. Slip Rate for the Banning Strand

We determine the best constrained Holocene right-lateral slip rate for the Banning strand of 3.9 + 2.3/−1.6 mm/yr (median, 95% CI) by combining the 6.4 + 3.7/−2.1 ka (95% CI) median combined surface clast age with the 25 ± 5 m, quantitatively determined fan axis offset. This slip rate is modeled using probability distributions that assume a Gaussian uncertainty distribution for the age and a trapezoidal distribution for the offset, which takes into account a preferred offset range of 22–28 m [*Zechar and Frankel*, 2009]. The slip rate uncertainty includes uncertainties in the offset and age measurements but does not account for uncertainties related to the seismic cycle [*Weldon and Sieh*, 1985] of the Banning strand, which are expected to be comparatively small and can be ignored, for two reasons. First, error derived from relating the depositional timing of Qfr to the seismic cycle of the Banning strand is impossible to quantify given the large uncertainty in the age of Qfr relative to the recurrence interval of the Banning strand (probably several hundred years; see section 9 and *Yule et al.* [2001] and *Onderdonk et al.* [2013]), rendering this source of error irrelevant. Second, given our best constrained slip rate of ~4 mm/yr and assuming a several hundred year recurrence interval, slip per event for the Banning fault should not often exceed 3 m. Even if the Banning strand is near the end of an earthquake cycle and the displacement recorded by Qfr is too low by the amount of slip that will be produced in the next rupture, this error would still be well within the ±5 m uncertainty bounds assigned to the 25 m offset and can therefore be ignored as well. We also report a similar maximum slip rate of 4.9 + 1.0/−0.9 mm/yr (median, 95% CI) by combining the 5.1 ± 0.4 ka U-series carbonate minimum age with the offset. The slip rate predicted by the 2.9 ± 0.7 ka (2σ) depth profile age is 8.6 + 3.3/−2.3 mm/yr (median, 95% CI), although we are more confident in the U-series and clast exposure ages, so we do not favor this rate in our discussion of how these new slip rates affect our understanding of seismic hazard and slip partitioning in southern California.

9. Implications for Seismic Hazard and Slip Partitioning

Our preferred Holocene right-lateral geologic slip rate for the Banning strand of 4–5 mm/yr represents only 25–35% of the right-lateral geologic slip rate for the southern Mission Creek strand (14–17 mm/yr) [*Behr et al.*, 2010] and around 20% of the geodetically estimated slip rate for the Indio strand of the Coachella Valley segment of the southern San Andreas Fault (~23–25 mm/yr) [*Becker et al.*, 2005; *Fay and Humphreys*, 2005;

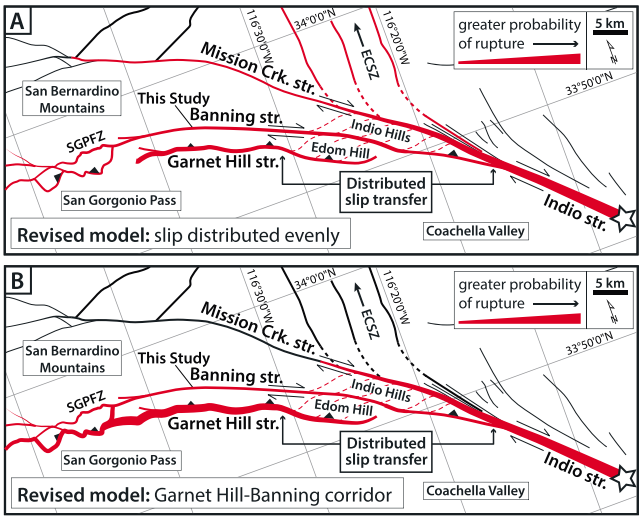

Figure 13. Revised models for how slip may be partitioned between the Mission Creek, Banning, and Garnet Hill strands given the relatively low Banning strand slip rate. (a) Slip is more evenly distributed between all three faults in the northwestern Coachella Valley. In this case, the majority of southern San Andreas Fault slip is still transferred northwest to San Gorgonio Pass via the Banning and Garnet Hill strands, with a smaller proportion transferred to the Eastern California Shear Zone via the Mission Creek strand. (b) Slip is concentrated on the Garnet Hill strand and, to a lesser extent, the Banning strand. In this case, southern San Andreas Fault slip is almost entirely transferred northwest to San Gorgonio Pass.

Fialko, 2006; *Spinler et al*., 2010; *Loveless and Meade*, 2011]. This implies that only about 20–35% of total southern San Andreas Fault slip is transferred northwest into San Gorgonio Pass via the Banning strand. We emphasize, however, that this is a minimum constraint on both the slip rate for the Banning strand and the amount of slip entering San Gorgonio Pass from the southeast.

First, the westward increase in topographic relief in the hanging wall of the Garnet Hill strand (e.g., Garnet Hill and East and West Whitewater Hills; Figure 1) is likely the product of slip transfer away from the Banning strand [*Yule and Sieh*, 2003] that occurs southeast of our slip rate site. Therefore, the 4–5 mm/yr slip rate recorded by the offset Qfr fan may be less than the slip rate of the Banning strand to the southeast. Similarly, if earthquakes propagating northwest along the Banning strand do not frequently rupture through San Gorgonio Pass, it is likely that they terminate near Cottonwood Canyon (Figure 1) where the Banning strand abruptly loses surface expression. Although this location is ~7 km along strike from the Painted Hill slip rate site, it is possible that coseismic offsets of the Qfr fan are at times near the tail ends of the earthquake slip distributions where slip is lower, also leading to a slip rate underestimate. Furthermore, 4–5 mm/yr represents the lateral component of slip only; thus, we could be missing a reverse component. However, we think this is unlikely because although the Banning Fault begins to dip to the north near Whitewater Canyon, offsets and stream deflections adjacent to the Qfr fan indicate right-lateral displacement, and evidence for a reverse component of motion across this part of the Banning strand is ambiguous. Finally, the amount of slip entering San Gorgonio Pass is equal to the total slip summed across the northwest ends of the Banning and Garnet Hills strands. The 4–5 mm/yr minimum Banning strand slip rate represents a minimum constraint on total slip entering San Gorgonio Pass because the slip rate of the Garnet Hill strand has not been determined. Determining how applicable this slip rate is for reaches of the Banning strand to the southeast and knowing what proportion of total slip entering San Gorgonio Pass this slip rate represents will require slip rate measurements from the Garnet Hill strand as well as from elsewhere on the Banning strand.

The primary implication of this relatively low 4–5 mm/yr slip rate for the Banning strand is that slip may be more evenly distributed between the Banning, Garnet Hill, and Mission Creek strands in the northwestern Coachella Valley than was previously thought, as illustrated in Figure 13a. A slip rate of 4–5 mm/yr, or 25–35% of geologically measured slip on the southern San Andreas Fault, is consistent with recent mechanical slip rate models [*Fattaruso et al*., 2014] but is significantly less than has been assumed in seismic hazard models and is inconsistent with it being a dominant structure transferring plate boundary slip to the northwest. This leaves 65–75% (~9–13 mm/yr) of southern San Andreas Fault slip to be taken up by the Mission Creek and/or Garnet Hill strands, or by faults that have not been identified. It is worth considering the possibility that southeast propagating ruptures could contribute to the offset of the Qfr fan without continuing far enough south to contribute offset to the Biskra Palms Oasis slip rate site. If this occurred relatively frequently, the slip rate we have measured would represent an even smaller proportion of southern San Andreas Fault slip. However, it remains unclear to what extent ruptures can actually propagate though San Gorgonio Pass, and given the abrupt northwest termination of the Banning strand and the lack of obvious connectivity between it and the San Gorgonio Pass Fault system, slip from southeast propagating ruptures is unlikely to

have a significant effect on our slip rate measurement. Regardless, the model proposed in Figure 2a, whereby slip is concentrated on the Banning strand, appears to be invalid. Several slip-partitioning models are therefore possible, including that illustrated in Figure 13a, where slip is approximately evenly shared between the Mission Creek, Banning, and Garnet Hill strands. A potential issue with this model is that the surface trace of the Mission Creek strand, although well expressed north of the Indio Hills, is not suggestive of a fault accommodating significant slip northwest of Desert Hot Springs (see section 3.1 and Figure 3), and it does not displace Holocene alluvium higher in San Bernardino Mountains [*Matti and Morton*, 1993; *Kendrick et al*., 2015; *Owen et al*., 2014]. This can be resolved to a certain extent by invoking northward slip transfer from the Mission Creek strand via faults in the Eastern Transverse Ranges (Figure 1) to the Eastern California Shear Zone, which geologic slip rate measurements suggest accommodates 6.2 ± 1.9 mm/yr of right-lateral slip over a 60 km wide shear zone [*Oskin et al*., 2008]. Although the northern ends of the Burnt Mountain and Eureka Peak faults did rupture during the 1992 Landers earthquake, many of the Eastern Transverse Ranges faults are bedrock bounded, making assessments of late Quaternary activity difficult, and it is possible that slip transfer through this region may simply be too distributed to confidently quantify.

An alternative model that places less emphasis on the Mission Creek strand would place much of the slip not accommodated by the Banning strand on the Garnet Hill strand, making this the dominant fault in the northwestern Coachella Valley (Figure 13b). Little is known about the Garnet Hill strand, partly because it is so poorly expressed at the surface. While folding and uplifts along the Garnet Hill strand seem to indicate a reverse-slip component, the topography of Edom Hill to the south and the Whitewater Hills to the north may be related to a complex interaction with the Banning strand, and it remains unclear exactly what relationship Garnet Hill (Figure 1) has to latest Quaternary deformation along the Garnet Hill strand [*Yule and Sieh*, 2003]. If this model (Figure 13b) best represents present-day slip partitioning, then coseismic slip associated with southern San Andreas Fault ruptures may tend to be partitioned between the Garnet Hill and Banning strands, with dominantly right-lateral slip that is initially concentrated on the southeastern Banning strand transitioning to the northwest to right-reverse slip concentrated on the Garnet Hill strand as the strike of both faults rotates to a more transpressive geometry near San Gorgonio Pass. While it is certainly possible that the Garnet Hill strand accommodates a significant lateral slip component as it enters San Gorgonio Pass [*Yule and Sieh*, 2003], this would be somewhat surprising given that there is little evidence along its surface trace, where identifiable, of offset consistent with a fault accommodating ~10 mm/yr.

However, when comparing the well-expressed Banning strand to the less easily identified Garnet Hill strand, it its important to consider the widely varying erosional and depositional processes governing preservation of their surface traces. For example, the Garnet Hill strand is subject to rates of aeolian deposition and volumes of flooding that the Banning strand, although only 2–3 km to the north, is less affected by. Surface evidence of a fast Garnet Hill strand could be rapidly covered or washed away, particularly if it is accommodating dominantly lateral motion. In contrast, several of the late Pleistocene surfaces that so prominently highlight the surface trace of the Banning strand (Figure 3f) may be exaggerated or enhanced by flood erosion along the fault, and the ease with which the linear central reach of the Banning strand (Figure 3g) can be followed may be as much due to sand trapped by vegetation lineaments as to topography related to fault rupture. Therefore, when comparing the Banning and Garnet Hill strands, the better expression of the Banning strand may be misleading. Differences in the geomorphic processes affecting the Banning and Mission Creek strands are less stark; thus, we consider the comparison of their surface expression in section 3.1 (Figure 3) to still be useful. However, given the lack of slip rates for the Mission Creek and Garnet Hill strands, we can say definitively only that slip does not appear to be concentrated on the Banning Fault at its northwest end.

Because 4–5 mm/yr is a relatively small proportion of the total slip accommodated by the southern San Andreas Fault System, an alternative explanation for the strong geomorphic expression of the Banning strand may simply be that it ruptured more recently than the Mission Creek or Garnet Hill strands. Earthquake timing and recurrence measurements northwest of the Banning strand at Burro Flats (Figure 1) along the southeast end of the San Bernardino strand [*Yule et al*., 2001] and to the southeast at Thousand Palms Canyon along the southeast end of the Mission Creek strand [*Fumal et al*., 2002] suggest recurrence timings of 200–300 years with the most recent events on each strand having occurred about 300 years ago (although it is unclear if

these are the same earthquake). It is reasonable to assume that the Banning strand is significantly involved in transferring slip between these two bracketing fault strands, and based on these data, it is probable that it has a recurrence interval of several hundred years, but because no direct measurements of earthquake timing or recurrence have been measured for the Banning strand, its rupture history remains unknown. Slip rates alone cannot reveal anything about rupture timing, so lacking paleoseismic constraints for the Banning strand, the slip rate we have measured cannot be used to determine whether it is the most probable rupture path for the next southern San Andreas Fault earthquake, as current earthquake hazard models suggest. Given the potential pitfalls in relating surface expression to fault activity, especially for the faults in the northwestern Coachella Valley, we believe that since slip rate and earthquake recurrence constraints remain very sparse, designating a preferred slip-partitioning model would be premature. We suggest instead that hazard models should more seriously consider alternative rupture paths, including the possibility that rupture might bypass the Banning and Garnet Hill strands altogether and follow the Mission Creek strand (Figure 2b), that rupture might be directed toward San Gorgonio Pass but be diffusely partitioned between the Garnet Hill and Banning strands (Figure 13b), or that rupture might be distributed on to all three strands (Figure 13a). This new rate does not have significant bearing on the question of if or how often earthquakes rupture through San Gorgonio Pass rather than terminate at its southeastern entrance because in either case it is probable that earthquakes would rupture the patch of the Banning strand where the rate is measured. Put another way, it is probable that the majority of earthquakes that follow the Banning strand but that do not propagate through San Gorgonio Pass terminate northwest of the Painted Hill slip rate site and are therefore still recorded by offset of the Qfr fan. This new slip rate for the Banning strand leads us to conclude that slip is not concentrated on the Banning strand and may be more evenly partitioned between all three faults in the northwestern Coachella Valley or largely concentrated on the Garnet Hill strand. This result underscores the need for paleoseismic measurements of earthquake timing as well as additional slip rate measurements from all the major fault strands in order to adequately assess the hazard associated with northwest propagating earthquake ruptures.

10. Summary

The primary conclusions of this study are as follows.

1. Structural measurements and geomorphic observations suggest that slip is transferred from the Mission Creek strand to the Banning strand in the northwestern Indio Hills, west of Thousand Palms Canyon.
2. The quantitatively constrained Holocene geologic slip rate for the Banning strand is 4–5 mm/yr since ~5.1–6.4 ka. This is a minimum slip rate for the Banning strand, since some slip may be transferred to the Garnet Hill strand before reaching the Painted Hill slip rate site.
3. At least 4–5 mm/yr of slip enters San Gorgonio Pass. This is a minimum because the slip rate for the Garnet Hill strand is unknown.
4. Because 4–5 mm/yr represents only ~25–35% of the total amount of slip accommodated by the Coachella Valley segment of the San Andreas Fault slip must be is less concentrated on the Banning strand than previously thought.
5. The more prominent geomorphic expression of the trace of the Banning strand relative to the Garnet Hill and Mission Creek strands cannot be explained by a faster slip rate and may instead indicate more recent surface rupture or result from other factors favoring geomorphic preservation of the fault trace.
6. Although current seismic hazard models may not be incorrect in assuming that the next southern San Andreas Fault earthquake will rupture the Banning strand, they should consider other scenarios in which the Banning and Garnet Hill strands rupture together or are completely bypassed in favor of the Mission Creek strand or where all three faults rupture together.
7. Because our understanding of the geomorphic processes that contribute to the formation, stabilization, and evolution of alluvial deposits is incomplete, use of multiple complimentary geochronometers may help to reduce the likelihood that erroneous depositional ages will be interpreted from dates that are incorrect because of unknown epistemic uncertainties.
8. Our results emphasize the urgent need to collect a greater number of slip rate measurements and paleoseismic constraints on earthquake timing from the Mission Creek, Banning, and Garnet Hill strands in order to produce better informed hazard estimates for southern California and to improve our understanding of the evolution of this fault system.

Acknowledgments
This project was funded by the southern California Earthquake Center grants 12097 and 13039 and USGS National Earthquake Hazard Reduction Program (NEHRP) grant G14AP00072. The B4 airborne lidar data used in this study are freely available from OpenTopography (opentopography.org), which is supported by the National Science Foundation under awards 1226353 and 1225810. The CRONUS online exposure age calculator is accessible here: http://hess.ess.washington.edu/math/. The MATLAB GUI of *Hidy et al.* [2010] is available here: http://geochronology.earthsciences.dal.ca. The MATLAB code of *Zechar and Frankel* [2009] used to generate the PDFs is available here: ftp://ftp.agu.org/apend/jb/2009jb006325. We thank Jon Matti, Dick Heermance, and two anonymous reviewers for input that greatly improved this report, and we thank Kory Kirchner and Kate Atakturk for help in the field. Southern California Earthquake Center publication 2083.

References

Allen, C. R. (1957), San Andreas Fault zone in San Gorgonio Pass, southern California, *Geol. Soc. Am. Bull.*, *68*, 315, doi:10.1130/0016-7606(1957)68[315:SAFZIS]2.0.CO;2.

Anderson, R. S., J. L. Repka, and G. S. Dick (1996), Explicit treatment of inheritance in dating depositional surfaces using in situ ^{10}Be and ^{26}Al, *Geology*, *24*, 47–51.

Balco, G., J. O. Stone, N. A. Lifton, and T. J. Dunai (2008), A complete and easily accessible means of calculating surface exposure ages or erosion rates from ^{10}Be and ^{26}Al measurements, *Quat. Geochronol.*, *3*, 174–195, doi:10.1016/j.quageo.2007.12.001.

Becker, T. W., J. L. Hardebeck, and G. Anderson (2005), Constraints on fault slip rates of the southern California plate boundary from GPS velocity and stress inversions, *Geophys. J. Int.*, *160*, 634–650, doi:10.1111/j.1365-246X.2004.02528.x.

Behr, W. M., et al. (2010), Uncertainties in slip-rate estimates for the Mission Creek strand of the southern San Andreas fault at Biskra Palms Oasis, southern California, *Geol. Soc. Am. Bull.*, *122*, 1360–1377, doi:10.1130/B30020.1.

Bierman, P. R. (1994), Using in situ produced cosmogenic isotopes to estimate rates of landscape evolution: A review from the geomorphic perspective, *J. Geophys. Res.*, *99*, 13,885–13,896, doi:10.1029/94JB00459.

Bilham, R., and P. Williams (1985), Sawtooth segmentation and deformation processes on the southern San Andreas fault, California, *Geophys. Res. Lett.*, *12*, 557–560, doi:10.1029/GL012i009p00557.

Birkland, P. W. (1999), *Soils and Geomorphology*, Oxford Univ. Press, New York.

Blisniuk, K., T. Rockwell, L. A. Owen, M. Oskin, C. Lippincott, M. W. Caffee, and J. Dortch (2010), Late Quaternary slip rate gradient defined using high-resolution topography and ^{10}Be dating of offset landforms on the southern San Jacinto Fault zone, California, *J. Geophys. Res.*, *115*, B08401, doi:10.1029/2009JB006346.

Blisniuk, K., M. Oskin, K. Fletcher, T. Rockwell, and W. Sharp (2012), Assessing the reliability of U-series and ^{10}Be dating techniques on alluvial fans in the Anza Borrego Desert, California, *Quat. Geochronol.*, *13*, 26–41, doi:10.1016/j.quageo.2012.08.004.

Blisniuk, K., K. M. Scharer, W. D. Sharp, R. Bürgmann, M. J. Rymer, and P. L. Williams (2013), New slip rate estimates for the Mission Creek strand of the San Andreas fault zone, Presentation T42A-01, AGU Fall Meeting.

Blisniuk, P. M., and W. D. Sharp (2003), Rates of late Quaternary normal faulting in central Tibet from U-series dating of pedogenic carbonate in displaced fluvial gravel deposits, *Earth Planet. Sci. Lett.*, *215*, 169–186, doi:10.1016/S0012-821X(03)00374-1.

Bürgmann, R. (1991), Transpression along the southern San Andreas fault, Durmid Hill, California, *Tectonics*, *10*, 1152–1163, doi:10.1029/91TC01443.

Capo, R. C., and O. A. Chadwick (1999), Sources of strontium and calcium in desert soil and calcrete, *Earth Planet. Sci. Lett.*, *170*, 61–72.

Cheng, H., et al. (2013), Improvements in ^{230}Th dating, ^{230}Th and ^{234}U half-life values, and U-Th isotopic measurements by multi-collector inductively coupled plasma mass spectrometry, *Earth Planet. Sci. Lett.*, *371–372*, 82–91, doi:10.1016/j.epsl.2013.04.006.

Chmeleff, J., F. von Blanckenburg, K. Kossert, and D. Jakob (2010), Determination of the ^{10}Be half-life by multicollector ICP-MS and liquid scintillation counting, *Nucl. Inst. Methods Phys. Res. B*, *268*, 192–199, doi:10.1016/j.nimb.2009.09.012.

Desilets, D., and M. Zreda (2003), Spatial and temporal distribution of secondary cosmic-ray nucleon intensities and applications to in situ cosmogenic dating, *Earth Planet. Sci. Lett.*, *206*, 21–42.

Desilets, D., M. Zreda, and T. Prabu (2006), Extended scaling factors for in situ cosmogenic nuclides: new measurements at low latitude, *Earth Planet. Sci. Lett.*, *246*, 265–276, doi:10.1016/j.epsl.2006.03.051.

Dibblee, T. W. (1964), Geologic map of the San Gorgonio Mountain quadrangle, San Bernardino and Riverside Counties, Calif.

Dibblee, T. W. (1967), Geologic map of the Morongo Valley quadrangle, San Bernardino and Riverside Counties, Calif.

Dibblee, T. W. (2008), Geologic map of the Thousand Palms & Lost Horse Mountain 15 minute quadrangles, Riverside County, California, 1:62,500: Dibblee Foundation Map DF-372.

Dunai, T. J. (2001), Influence of secular variation of the geomagnetic field on production rates of in situ produced cosmogenic nuclides, *Earth Planet. Sci. Lett.*, *193*, 197–212.

Dunai, T. J. (2010), *Cosmogenic Nuclides: Principles, Concepts and Applications in the Earth Surface Sciences*, Academic Press, Cambridge.

Elliott, A. J., J. F. Dolan, and D. D. Oglesby (2009), Evidence from coseismic slip gradients for dynamic control on rupture propagation and arrest through stepovers, *J. Geophys. Res.*, *114*, B02313, doi:10.1029/2008JB005969.

Fattaruso, L. A., M. L. Cooke, and R. J. Dorsey (2014), Sensitivity of uplift patterns to dip of the San Andreas fault in the Coachella Valley, California, *Geosphere*, *10*, 1235–1246, doi:10.1130/GES01050.1.

Fay, N. P., and E. D. Humphreys (2005), Fault slip rates, effects of elastic heterogeneity on geodetic data, and the strength of the lower crust in the Salton Trough region, southern California, *J. Geophys. Res.*, *110*, B09401, doi:10.1029/2004JB003548.

Fialko, Y. (2006), Interseismic strain accumulation and the earthquake potential on the southern San Andreas fault system, *Nature*, *441*, 968–971, doi:10.1038/nature04797.

Field, E. H., et al. (2009), Uniform California Earthquake Rupture Forecast, Version 2 (UCERF 2), *Bull. Seismol. Soc. Am.*, *99*, 2053–2107, doi:10.1785/0120080049.

Field, E. H., et al. (2014), Uniform California earthquake rupture forecast, Version 3 (UCERF3)—The time-independent model, *Bull. Seismol. Soc. Am.*, *104*, 1122–1180, doi:10.1785/0120130164.

Field, E. H., et al. (2015), Long-term time-dependent probabilities for the third Uniform California Earthquake Rupture Forecast (UCERF3), *Bull. Seismol. Soc. Am.*, *105*, 511–543, doi:10.1785/0120140093.

Fletcher, K. E. K., W. D. Sharp, K. J. Kendrick, W. M. Behr, K. W. Hudnut, and T. C. Hanks (2010), ^{230}Th/U dating of a late Pleistocene alluvial fan along the southern San Andreas fault, *Geol. Soc. Am. Bull.*, *122*, 1347–1359, doi:10.1130/B30018.1.

Fumal, T. E., R. J. Weldon, G. P. Biasi, T. E. Dawson, G. G. Seitz, W. T. Frost, and D. P. Schwartz (2002), Evidence for large earthquakes on the San Andreas fault at the Wrightwood, California, paleoseismic site: AD 500 to present, *Bull. Seismol. Soc. Am.*, *92*, 2726–2760.

Gander, W., G. H. Golub, and R. Strebel (1994), Least-squares fitting of circles and ellipses, *BIT Numer. Math.*, *34*, 558–578.

Gile, L. H., F. F. Peterson, and R. B. Grossman (1966), Morphological and genetic sequences of carbonate accumulation in desert soils, *Soil Sci.*, *101*, 347–360.

Gold, P. O., M. E. Oskin, A. J. Elliott, A. Hinojosa-Corona, M. H. Taylor, O. Kreylos, and E. Cowgill (2013), Coseismic slip variation assessed from terrestrial lidar scans of the El Mayor-Cucapah surface rupture, *Earth Planet. Sci. Lett.*, *366*, 151–162, doi:10.1016/j.epsl.2013.01.040.

Gosse, J. C., and F. M. Phillips (2001), Terrestrial in situ cosmogenic nuclides: theory and application, *Quat. Sci. Rev.*, *20*, 1475–1560.

Granger, D. E., N. A. Lifton, and J. K. Willenbring (2013), A cosmic trip: 25 years of cosmogenic nuclides in geology, *Geol. Soc. Am. Bull.*, *125*, 1379–1402, doi:10.1130/B30774.1.

Harden, J. W., and J. C. Matti (1989), Holocene and late Pleistocene slip rates on the San Andreas fault in Yucaipa, California, using displaced alluvial-fan deposits and soil chronology, *Geol. Soc. Am. Bull.*, *101*, 1107–1117, doi:10.1130/0016-7606(1989)101<1107:HALPSR>2.3.CO;2.

Hidy, A. J., J. C. Gosse, J. L. Pederson, J. P. Mattern, and R. C. Finkel (2010), A geologically constrained Monte Carlo approach to modeling exposure ages from profiles of cosmogenic nuclides: An example from Lees Ferry, Arizona, *Geochem. Geophys. Geosyst.*, *11*, Q0AA10, doi:10.1029/2010GC003084.

Heisinger, B., D. Lal, A. J. T. Jull, P. Kubik, S. Ivy-Ochs, S. Neumaier, K. Knie, V. Lazarev, and E. Nolte (2002a), Production of selected cosmogenic radionuclides by muons: 1. Fast muons, *Earth Planet. Sci. Lett.*, *200*, 345–355.

Heisinger, B., D. Lal, A. J. T. Jull, P. Kubik, S. Ivy-Ochs, K. Knie, and E. Nolte (2002b), Production of selected cosmogenic radionuclides by muons: 2. Capture of negative muons, *Earth Planet. Sci. Lett.*, *200*(3–4), 357–369.

Holden, N. E. (1989), Total and spontaneous fission half-lives for uranium, plutonium, americium and curium nuclides, *Pure Appl. Chem.*, *61*, 1483–1504.

Jaffey, A. H., K. F. Flynn, L. E. Glendenin, W. T. Bentley, and A. M. Essling (1971), Precision measurement of half-lives and specific activities of U 235 and U 238, *Phys. Rev. C*, *4*, 1889.

Jones, L. M., L. K. Hutton, D. D. Given, and C. R. Allen (1986), The North Palm Springs, California, earthquake sequence of July 1986, *Bull. Seismol. Soc. Am.*, *76*, 1830–1837.

Keller, E. A., M. S. Bonkowski, R. J. Korsch, and R. J. Shlemon (1982), Tectonic geomorphology of the San Andreas fault zone in the southern Indio Hills, Coachella Valley, California, *Geol. Soc. Am. Bull.*, *93*, 46–56, doi:10.1130/0016-7606(1982)93<46:TGOTSA>2.0.CO;2.

Keller, E. A., D. B. Seaver, D. L. Laduzinsky, D. L. Johnson, and T. L. Ku (2000), Tectonic geomorphology of active folding over buried reverse faults, San Emigdio Mountain front, southern San Joaquin Valley, California, *Geol. Soc. Am. Bull.*, *112*, 86–97, doi:10.1130/0016-7606(2000)112<86:TGOAFO>2.0.CO;2.

Kendrick, K. J., J. C. Matti, and S. A. Mahan (2015), Late Quaternary slip history of the Mill Creek strand of the San Andreas fault in San Gorgonio Pass, southern California: The role of a subsidiary left-lateral fault in strand switching, *Geol. Soc. Am. Bull.*, *127*, 1–26, doi:10.1130/B31101.1.

Korschinek, G., et al. (2010), A new value for the half-life of ^{10}Be by heavy-ion elastic recoil detection and liquid scintillation counting, *Nucl. Inst. Methods Phys. Res. B*, *268*, 187–191, doi:10.1016/j.nimb.2009.09.020.

Ku, T.-L., W. B. Bull, S. T. Freeman, and K. G. Knauss (1979), Th230-U234 dating of pedogenic carbonates in gravelly desert soils of Vidal Valley, southeastern California, *Geol. Soc. Am. Bull.*, *90*, 1063–1073.

Lal, D. (1991), Cosmic ray labeling of erosion surfaces: In situ nuclide production rates and erosion models, *Earth Planet. Sci. Lett.*, *104*, 424–439.

Lifton, N. A., J. W. Bieber, J. M. Clem, M. L. Duldig, P. Evenson, J. E. Humble, and R. Pyle (2005), Addressing solar modulation and long-term uncertainties in scaling secondary cosmic rays for in situ cosmogenic nuclide applications, *Earth Planet. Sci. Lett.*, *239*, 140–161, doi:10.1016/j.epsl.2005.07.001.

Loveless, J. P., and B. J. Meade (2011), Stress modulation on the San Andreas fault by interseismic fault system interactions, *Geology*, *39*, 1035–1038, doi:10.1130/G32215.1.

Ludwig, K. R. (2009), *Using Isoplot/Ex, Version 3.72: A Geochronological Toolkit for Microsoft Excel*, *Spec. Publ.*, pp. 1–47, Geochronology Center, Berkeley.

Ludwig, K. R., and J. B. Paces (2002), Uranium-series dating of pedogenic silica and carbonate, Crater Flat, Nevada, *Geochim. Cosmochim. Acta*, *66*, 487–506.

Machette, M. N. (1985), Calcic soils of the southwestern United States, *Geol. Soc. Am. Spec. Pap.*, *203*, 1–22.

Matti, J. C., and D. M. Morton (1993), Paleogeographic evolution of the San Andreas fault in southern California: A reconstruction based on a new cross-fault correlation, in *The San Andreas Fault System: Displacement, Palinspastic Reconstruction, and Geologic Evolution*, vol. 178, edited by R. E. Powell, R. J. Weldon II, and J. C. Matti, pp. 107–159, Geol. Soc. Am., Boulder Colo.

Matti, J. C., D. M. Morton, and B. F. Cox (1992), The San Andreas fault system in the vicinity of the central Transverse Ranges province, southern California, *U.S. Geol. Surv. Open File Rep., 92-354*, 40 p., scale 1:250,000.

McGill, S. F., L. A. Owen, R. J. Weldon, and K. J. Kendrick (2013), Latest Pleistocene and Holocene slip rate for the San Bernardino strand of the San Andreas fault, Plunge Creek, southern California: Implications for strain partitioning within the southern San Andreas fault system for the last 35 k.y, *Geol. Soc. Am. Bull.*, *125*, 48–72, doi:10.1130/B30647.1.

Meade, B. J. (2005), Block models of crustal motion in southern California constrained by GPS measurements, *J. Geophys. Res.*, *110*, B03403, doi:10.1029/2004JB003209.

Onderdonk, N. W., T. K. Rockwell, S. F. McGill, and G. I. Marliyani (2013), Evidence for seven surface ruptures in the past 1600 years on the Claremont fault at mystic lake, Northern San Jacinto Fault Zone, California, *Bull. Seismol. Soc. Am.*, *103*, 519–541, doi:10.1785/0120120060.

Orozco, A., and D. Yule (2003), Late Holocene slip rate for the San Bernardino strand of the San Andreas Fault near Banning, California, *Seismol. Res. Lett.*, *74*, 237.

Oskin, M., L. Perg, E. Shelef, M. Strane, E. Gurney, B. Singer, and X. Zhang (2008), Elevated shear zone loading rate during an earthquake cluster in eastern California, *Geology*, *36*, 507, doi:10.1130/G24814A.1.

Owen, L. A., K. L. Frankel, J. R. Knott, S. Reynhout, R. C. Finkel, J. F. Dolan, and J. Lee (2011), Beryllium-10 terrestrial cosmogenic nuclide surface exposure dating of Quaternary landforms in Death Valley, *Geomorphology*, *125*, 541–557, doi:10.1016/j.geomorph.2010.10.024.

Owen, L. A., S. J. Clemmens, R. C. Finkel, and H. Gray (2014), Late Quaternary alluvial fans at the eastern end of the San Bernardino Mountains, southern California, *Quat. Sci. Rev.*, *87*, 114–134, doi:10.1016/j.quascirev.2014.01.003.

Philibosian, B., T. Fumal, and R. Weldon (2011), San Andreas Fault earthquake chronology and Lake Cahuilla history at Coachella, California, *Bull. Seismol. Soc. Am.*, *101*, 13–38, doi:10.1785/0120100050.

Pigati, J. S., and N. A. Lifton (2004), Geomagnetic effects on time-integrated cosmogenic nuclide production with emphasis on in situ ^{14}C and ^{10}Be, *Earth Planet. Sci. Lett.*, *226*, 193–205, doi:10.1016/j.epsl.2004.07.031.

Reheis, M. C., J. C. Goodmacher, J. W. Harden, L. D. McFadden, T. K. Rockwell, R. R. Shroba, J. M. Sowers, and E. M. Taylor (1995), Quaternary soils and dust deposition in southern Nevada and California, *Geol. Soc. Am. Bull.*, *107*, 1003–1022, doi:10.1130/0016-7606(1995)107<1003:QSADDI>2.3.CO;2.

Repka, J. L., R. S. Anderson, and R. C. Finkel (1997), Cosmogenic dating of fluvial terraces, Fremont River, Utah, *Earth Planet. Sci. Lett.*, *152*, 59–73.

Salisbury, J. B., T. K. Rockwell, T. J. Middleton, and K. W. Hudnut (2012), Lidar and field observations of slip distribution for the most recent surface ruptures along the central San Jacinto Fault, *Bull. Seismol. Soc. Am.*, *102*, 598–619, doi:10.1785/0120110068.

Scharer, K. M., J. B. Salisbury, J. R. Arrowsmith, and T. K. Rockwell (2014), Southern San Andreas Fault evaluation field activity: Approaches to measuring small geomorphic offsets—Challenges and recommendations for active fault studies, *Seismol. Res. Lett.*, *85*, 68–76, doi:10.1785/0220130108.

Sharp, R. V., M. J. Rymer, and D. M. Morton (1986), Trace-fractures on the Banning fault created in association with the 1986 North Palm Springs earthquake, *Bull. Seismol. Soc. Am.*, *76*, 1838–1843.

Sharp, W. D., K. R. Ludwig, O. A. Chadwick, R. Amundson, and L. L. Glaser (2003), Dating fluvial terraces by ^{230}Th/U on pedogenic carbonate, Wind River Basin, Wyoming, *Quat. Res.*, *59*, 139–150, doi:10.1016/S0033-5894(03)00003-6.

Sieh, K. E. (1994), Late Quaternary slip rate of the north branch of the San Andreas fault at City Creek, California, *Geol. Soc. Am. Abstr. Programs*, *2*, 91.

Spinler, J. C., R. A. Bennett, M. L. Anderson, S. F. McGill, S. Hreinsdóttir, and A. McCallister (2010), Present-day strain accumulation and slip rates associated with southern San Andreas and eastern California shear zone faults, *J. Geophys. Res.*, *115*, B11407, doi:10.1029/2010JB007424.

Staiger, J., J. Gosse, R. Toracinta, B. Oglesby, J. Fastook, and J. V. Johnson (2007), Atmospheric scaling of cosmogenic nuclide production: Climate effect, *J. Geophys. Res.*, *112*, B02205, doi:10.1029/2005JB003811.

Stone, J. O. (2000), Air pressure and cosmogenic isotope production, *J. Geophys. Res.*, *105*, 237,53–23,759, doi:10.1029/2000JB900181.

Sylvester, A. G. (1999), Rifting, transpression, and neotectonics in the Central Mecca Hills, Salton Trough, California, in *Field Trip Guidebook for the SEPM Fall Field Trip*, vol. iv, 52 pp., Soc. of Sediment. Geol., Los Angeles, Calif.

Sylvester, A. G., and R. R. Smith (1976), Tectonic transpression and basement-controlled deformation in San Andreas fault zone, Salton Trough, California, *AAPG Bull.*, *60*, 2081–2102.

Van der Woerd, J., Y. Klinger, K. Sieh, P. Tapponnier, F. J. Ryerson, and A.-S. Mériaux (2006), Long-term slip rate of the southern San Andreas Fault from ^{10}Be-^{26}Al surface exposure dating of an offset alluvial fan, *J. Geophys. Res.*, *111*, B04407, doi:10.1029/2004JB003559.

Weldon, R. J., II (2010), Slip rate for the North Branch of the San Andreas fault, San Bernardino Valley: Southern California Earthquake Center, *Ann. Rep.*, pp. 1–5.

Weldon, R. J., and K. E. Sieh (1985), Holocene rate of slip and tentative recurrence interval for large earthquakes on the San Andreas fault, Cajon Pass, southern California, *Geol. Soc. Am. Bull.*, *96*, 793, doi:10.1130/0016-7606(1985)96<793:HROSAT>2.0.CO;2.

Weldon, R. J., T. E. Fumal, G. P. Biasi, and K. M. Scharer (2005), Past and future earthquakes on the San Andreas fault, *Science*, *308*, 966–967.

Wesnousky, S. G. (2006), Predicting the endpoints of earthquake ruptures, *Nature*, *444*, 358–360, doi:10.1038/nature05275.

Yule, D., and K. Sieh (2003), Complexities of the San Andreas fault near San Gorgonio Pass: Implications for large earthquakes, *J. Geophys. Res.*, *108*(B11), 2548, doi:10.1029/2001JB000451.

Yule, D., T. Fumal, and G. G. Seitz (2001), Active tectonics and paleoseismic record of the San Andreas fault, Wrightwood to Indio, Working toward a forecast for the next "Big Event": Geologic excursions in the California deserts and the adjacent transverse ranges.

Zechar, J. D., and K. L. Frankel (2009), Incorporating and reporting uncertainties in fault slip rates, *J. Geophys. Res.*, *114*, B12407, doi:10.1029/2009JB006325.

Zielke, O., and J. R. Arrowsmith (2012), LaDiCaoz and LiDARimager—MATLAB GUIs for lidar data handling and lateral displacement measurement, *Geosphere*, *8*, 206–221, doi:10.1130/GES00686.S1.

Zielke, O., J. R. Arrowsmith, L. Grant Ludwig, and S. O. Akciz (2012), High-resolution topography-derived offsets along the 1857 Fort Tejon earthquake rupture trace, San Andreas fault, *Bull. Seismol. Soc. Am.*, *102*, 1135–1154, doi:10.1785/0120110230.

Late Quaternary slip history of the Mill Creek strand of the San Andreas fault in San Gorgonio Pass, southern California: The role of a subsidiary left-lateral fault in strand switching

K.J. Kendrick[1,†], J.C. Matti[2], and S.A. Mahan[3]
[1]*U.S. Geological Survey, Earthquake Science Center, Pasadena, California 91106, USA*
[2]*U.S. Geological Survey, Geology, Minerals, Energy, and Geophysics Science Center, Tucson, Arizona 85719, USA*
[3]*U.S. Geological Survey, Crustal Geophysics and Geochemistry Science Center, Denver, Colorado 80225, USA*

ABSTRACT

The fault history of the Mill Creek strand of the San Andreas fault (SAF) in the San Gorgonio Pass region, along with the reconstructed geomorphology surrounding this fault strand, reveals the important role of the left-lateral Pinto Mountain fault in the regional fault strand switching. The Mill Creek strand has 7.1–8.7 km total slip. Following this displacement, the Pinto Mountain fault offset the Mill Creek strand 1–1.25 km, as SAF slip transferred to the San Bernardino, Banning, and Garnet Hill strands. An alluvial complex within the Mission Creek watershed can be linked to palinspastic reconstruction of drainage segments to constrain slip history of the Mill Creek strand. We investigated surface remnants through detailed geologic mapping, morphometric and stratigraphic analysis, geochronology, and pedogenic analysis. The degree of soil development constrains the duration of surface stability when correlated to other regional, independently dated pedons. This correlation indicates that the oldest surfaces are significantly older than 500 ka. Luminescence dates of 106 ka and 95 ka from (respectively) 5 and 4 m beneath a younger fan surface are consistent with age estimates based on soil-profile development. Offset of the Mill Creek strand by the Pinto Mountain fault suggests a short-term slip rate of ~10–12.5 mm/yr for the Pinto Mountain fault, and a lower long-term slip rate. Uplift of the Yucaipa Ridge block during the period of Mill Creek strand activity is consistent with thermochronologic modeled uplift estimates.

†E-mail: kendrick@usgs.gov.

INTRODUCTION

Statement of Problem

Accurately evaluating seismic hazard is critical to societies worldwide (e.g., Jordan et al., 2011). A key element to seismic hazard assessment is knowledge of fault system complexity. The distribution and length of active faults in a complex fault system likely affect rupture termination, and thus earthquake magnitude potential (Wesnousky, 2008). Determination of the history, evolution, and timing of most recent movement along fault strands, and thus their activity level, is key to understanding complex fault systems. Continental transform fault systems, such as the North Anatolian, Alpine, and San Andreas faults, represent significant seismic hazard, but vary in their complexity.

The slip history of the San Andreas fault (SAF) becomes increasingly challenging to resolve and also more relevant to hazard analysis when considered in progressively greater spatial detail. At a global scale, the fault is routinely explained as a continental transform fault that simply resolves the motions of the North American and Pacific plates (e.g., Wallace, 1990). At the scale of the state of California, the fault trace is evidently divided into segments with different strike directions and seismic histories (e.g., Jones, 1988; Weldon et al., 2004). It also becomes clear that relative plate motion must be partitioned between the SAF and other right- and left-lateral strike-slip faults. Within the Transverse Ranges of southern California, the trace of the SAF deviates from its general N35°–40°W strike direction, and estimates of the amount of right-lateral slip vary significantly from place to place (Powell, 1993a). Many of these discrepant estimates are reconciled by evidence that the trace of the SAF through the Transverse Ranges is a braid of four successive right-lateral, strike-slip fault strands (Matti et al., 1985; Matti and Morton, 1993).

Why does slip switch from one strand to another in the Transverse Ranges? We present evidence of the role of subsidiary left-lateral faults in the switching process, a view that has broad relevance for the evolution of strike-slip fault systems in general, but must be developed from detailed geologic and geomorphic mapping. Our study focuses on the interaction of the left-lateral Pinto Mountain fault with the SAF where the latter changes strike direction in San Gorgonio Pass (SGP; Fig. 1). The time-space history of the SAF in SGP is critical not only to understanding the modern seismotectonic framework of the southern SAF system, but also to evaluating how various components of that system have interacted since inception of the SAF proper in the Pliocene (ca. 5 Ma). Previous workers have outlined key elements of this time-space history (Allen, 1957; Matti et al., 1985, 1992; Matti and Morton, 1993; Yule and Sieh, 2003), and the modern SAF in the SGP region recently has been the focus of considerable debate among seismologists concerned with fault-rupture scenarios and attendant seismic risk (e.g., Carena et al., 2004; Plesch et al., 2007; Yule, 2009, 2010; Dair and Cooke, 2009; Cooke and Dair, 2011). Despite this recent interest, little is known about the Quaternary slip history of the SAF in the SGP region. We address this issue by investigating the slip history for the Mill Creek strand of the SAF. The response of four drainages to strike-slip offsets between four fault blocks provides crucial evidence of slip history, recorded in the form of wind gaps, underfit drainages, and orphan alluvial deposits. We have remapped the geology, geomorphology, and alluvial stratigraphy of three critical locations along the trace of the Mill Creek strand of the SAF to reconstruct slip history. To place the new evidence in context, we must introduce

GSA Bulletin; May/June 2015; v. 127; no. 5/6; p. 825–849; doi:10.1130/B31101.1; 13 figures; 7 tables; published online 22 January 2015.

For permission to copy, contact editing@geosociety.org
© 2015 Geological Society of America

Downloaded from http://pubs.geoscienceworld.org/gsa/gsabulletin/article-pdf/127/5-6/825/3410110/825.pdf
by USGS Library user

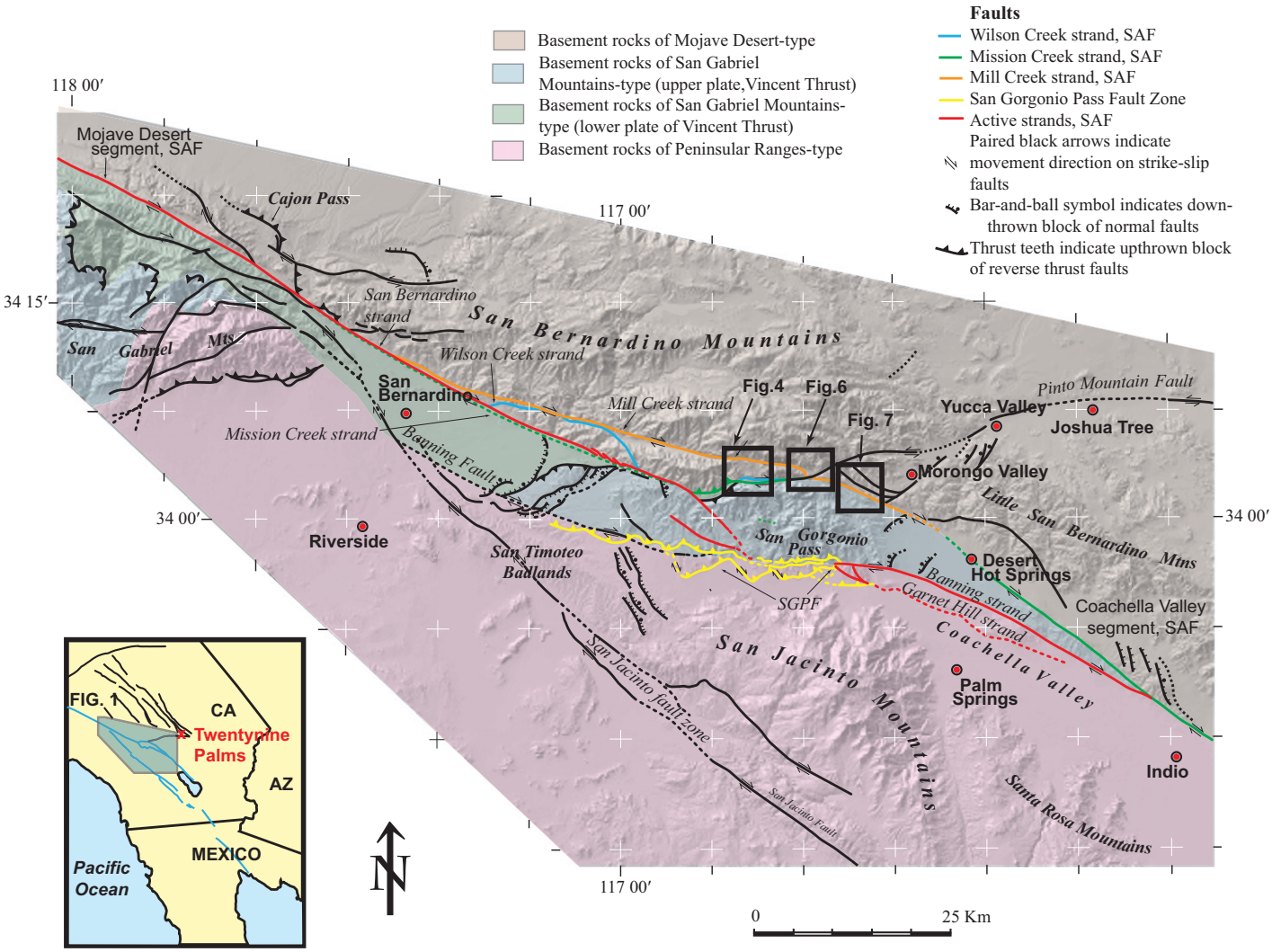

Figure 1. Map showing location of the Raywood Flat, Pinto Mountain fault junction, and Mission Creek study areas (black boxes, west to east, respectively), relative to faults and basement-rock terranes in the region. Faults in red are modern strands of the San Andreas fault (SAF); progressively older strands of the San Andreas fault include the Mill Creek strand (orange), Mission Creek strand (green), and Wilson Creek strand (blue). The San Gorgonio Pass thrust fault is shown in yellow. SGPF—San Gorgonio Pass fault zone; AZ—Arizona; CA—California. Modified from Matti et al. (1982) and Matti and Morton (1993).

the local nomenclature, first for fault segments and strands (below) and then for geomorphic basement blocks and drainages (Table 1).

San Andreas Fault Zone

Following Allen's (1957) pioneering work on the SAF in SGP, later workers (Ehlig, 1977; Farley, 1979; Matti et al., 1982, 1983) recognized that differences among regional crystalline-rock packages could be used to distinguish faults that exhibit major right-slip displacement. These distinctions led to formal recognition of multiple strands of the SAF in the SGP region (Fig. 1; Matti et al., 1985, 1992; Matti and Morton, 1993). These strands developed sequentially (Fig. 2), and represent the full history of Pliocene and Quaternary slip on the SAF in southern California since its inception (Matti and Morton, 1993). In SGP, the Mission Creek strand has not generated dextral slip in late Quaternary time (Matti et al., 1992; Matti and Morton, 1993).

We adopt the fault nomenclature established by Matti et al. (1992) for the SGP region. We refer to faults of the SAF zone as strands (e.g., Mission Creek strand of the SAF; Fig. 1). Because these terms are cumbersome, for convenience we commonly refer to them only by their specific names (e.g., Mill Creek strand); moreover, we use the terms "strand" and "fault" interchangeably, without changing the intrinsic concept that each structure is a strand of the parent SAF. The Wilson Creek strand (Matti et al., 1992) pre-dates the slip history discussed here.

In terms of total dextral slip, the Mission Creek strand is the main SAF strand in southern California. In SGP the Mission Creek strand has ~90 km of dextral slip and juxtaposes previously separated crystalline rocks of San Gabriel Mountains type against distinctly different crystalline rocks of Mojave Desert type (Fig. 1; Matti et al., 1992; Matti and Morton, 1993).

The Mill Creek strand lies north of, and subparallel to, the Mission Creek strand (Fig. 1). Although Dibblee (1968a, 1975, 1982, his "San Andreas fault, north branch") attributed significant dextral slip to the fault, and although this pathway for fault motion through the SGP is often used in geophysical and computer modeling (e.g., Plesch et al., 2007; Spinler et al., 2010), there is no more than ~8–10 km of slip,

Downloaded from http://pubs.geoscienceworld.org/gsa/gsabulletin/article-pdf/127/5-6/825/3410110/825.pdf
by USGS Library user

TABLE 1. DESCRIPTIONS OF STRUCTURAL BLOCKS AND MAJOR DRAINAGES IN THE STUDY AREA

Feature	Description
	Structural blocks
Big Bear structural block	Defined by Spotila et al. (1998). Comprises the broad upland plateau of the San Bernardino Mountains. Separated from the San Gorgonio block to the south by an intermontane lowland that forms the headwaters of the Santa Ana River (Fig. 3). Poorly understood high-angle faults mapped by Sadler (1993) demarcate this lowland from the San Gorgonio block. Other than these faults, the block's structural boundaries and regional extent have not been rigorously defined or documented.
San Gorgonio structural block	Defined by Spotila et al. (1998). Bounded on the south by the Mill Creek strand of the San Andreas fault (SAF), and to the north by the poorly understood high-angle faults mapped by Sadler (1993). Other than these faults, the block's structural boundaries and regional extent have not been rigorously defined or documented.
Cram Peak structural block	Defined by this study, and named for a topographic summit directly west of Mill Creek Canyon. Bound to the north by the Mill Creek strand, to the south by the Mission Creek strand, and separated from the Yucaipa Ridge block to the east by the Ford Canyon fault (Fig. 3). We replace the name "Wilson Creek block" of Spotila et al. (1998, 2001); see text for further explanation.
Yucaipa Ridge structural block	Defined by Spotila et al. (1998), and modified by this study (Fig. 3). Bound to the north and east by the Mill Creek strand, to the south by the Mission Creek strand, and separated from the Cram Peak block to the west by the Ford Canyon fault.
	Major drainages
San Gorgonio River	Integrates a large catchment area in the western San Gorgonio Pass (SGP) region (Fig. 3); headwaters transect both the inactive Mission Creek strand of the SAF and the modern San Bernardino strand.
South Fork Whitewater River	Includes two branches that—in the Raywood Flat area—are incised into older surficial deposits. This modern drainage is underfit to a deeply incised, branched canyon system (Fig. 3). In upper Raywood Flat, these two branches head onto the San Gorgonio block. In lower Raywood Flat, the two branches merge, turn abruptly eastward, and ultimately join the combined North Fork and Middle Fork Whitewater River to form the main Whitewater River. For simplicity, we commonly refer to the forks of the Whitewater River by an abbreviated name (e.g., North Fork).
North Fork Whitewater River	Drains the northeast flank of the San Gorgonio block (Fig. 3). Flows southeastward and joins the Middle Fork Whitewater River in the deep canyon occupied by the Mill Creek fault (Fig. 3). Drainage area of 20.7 km^2, and basin relief of 2025 m.
Hell For Sure Canyon	Parallel to—and just east of—the North Fork drainage (Fig. 3). Drainage area of 12.1 km^2, overall relief of 1770 m. Like North Fork, it joins the Middle Fork Whitewater River in the deep canyon occupied by the Mill Creek fault (Fig. 3).
Mission Creek drainage	Largest in the SGP region north of the SAF (Fig. 3). Heads onto the San Gorgonio and Big Bear blocks. Upstream from the Mill Creek strand of the SAF, occupies a catchment area of approximately 87 km^2. South of this strand, the stream flows through the Mission Creek alluvial complex, and then to the Coachella Valley. There, it joins the San Gorgonio and Whitewater Rivers to form the throughgoing axial drainage that flows into the Salton Trough and thence into the Gulf of California.

displacing a narrow slice of Mojave Desert–type basement (the Yucaipa Ridge block, defined in Table 1) northwestward (Matti et al., 1985, 1992). The Mill Creek strand locally displays fault features that may indicate minor late Quaternary slip; however, these are sparse and discontinuous and their continuity throughout the eastern portal to SGP is difficult to demonstrate. This led Matti et al. (1992; Matti and Morton, 1993) to propose that the Mill Creek Fault has been abandoned by the San Andreas Fault.

The San Bernardino strand of the SAF, northwest of the SGP, and the Banning and Garnet Hill strands to the southeast are modern neotectonic strands of the SAF (Fig. 1). Building on Allen's (1957) findings, Matti et al. (1985, 1992; Matti and Morton, 1993) proposed that relations among dextral faults in SGP have been complicated and obscured by a belt of contractional deformation, mapped as the San Gorgonio Pass fault zone. This fault zone intervenes between the Banning and Garnet Hill strands (to the southeast) and the San Bernardino strand (to the northwest), and has obscured throughgoing relations among the dextral faults (Fig. 1).

Pinto Mountain Fault

The Pinto Mountain fault is a poorly understood, sinistral strike-slip fault that traverses the boundary between the Mojave Desert and Transverse Ranges provinces. Allen (1957, p. 343) noted similarities between the Pinto Mountain and the sinistral Garlock fault of the northern Mojave Desert, but he did not specifically indicate a left-slip origin for the fault. Dibblee (1967, 1968a, 1968b) first recognized that the Pinto Mountain is a significant left-lateral structure. Allen (1957, p. 342) was the first researcher to recognize that the Pinto Mountain fault system extended as far west as the Mission Creek drainage (Fig. 1). The fault is represented by discontinuous scarps and bedrock traces that trend westward from the Twentynine Palms area to our study area in the northern SGP. There is no consensus about the timing of inception, but Quaternary displacements are well documented by deflected drainages, linear scarps, pressure ridges, shutter ridges, closed depressions, and springs (Allen, 1957; Bryant, 2000). The Pinto Mountain fault zone as a whole has a reported maximum displacement of between 16 and 19 km (Dibblee, 1975; Batcheller, 1978; Hopson, 1996), determined from offset Mesozoic and older crystalline bedrock units.

METHODS

We report on the analyses at three locations along the trace of the Mill Creek fault strand. At two locations, Quaternary alluvial deposits are truncated by faulting: upper Raywood Flat on Yucaipa Ridge, and the Mission Creek alluvial complex within the drainage system of Mission Creek (Fig. 1). The third location is the juncture of the Mill Creek, Mission Creek, and Pinto Mountain faults (Fig. 1), where we map structures that may reflect fault interactions. We reconstruct drainage systems through upper Raywood Flat, in order to determine the total slip on the Mill Creek strand of the SAF. Deposits within the Mission Creek alluvial complex, located within the present Mission Creek drainage basin, help to limit the timing of movement of this fault strand.

We mapped the geology of this area at scales of 1:24,000 and larger, mainly using traverse-mapping techniques. From the locality where a map unit or its boundaries were initially identified or defined, we extended those features to other areas through direct outcrop observation and aerial-photographic interpretation. For surficial units, we plotted bounding contacts digitally from rectified and georeferenced 2005-vintage National Agricultural Imagery Program aerial photographs that allow location accuracy equivalent to the accuracy standard for the topographic-contour base.

We subdivide surficial materials according to a map-unit classification being developed cooperatively for southern California by the U.S. Geological Survey and California Geological Survey (see Bedrossian et al., 2012; Matti et al.,

Downloaded from http://pubs.geoscienceworld.org/gsa/gsabulletin/article-pdf/127/5-6/825/3410110/825.pdf
by USGS Library user

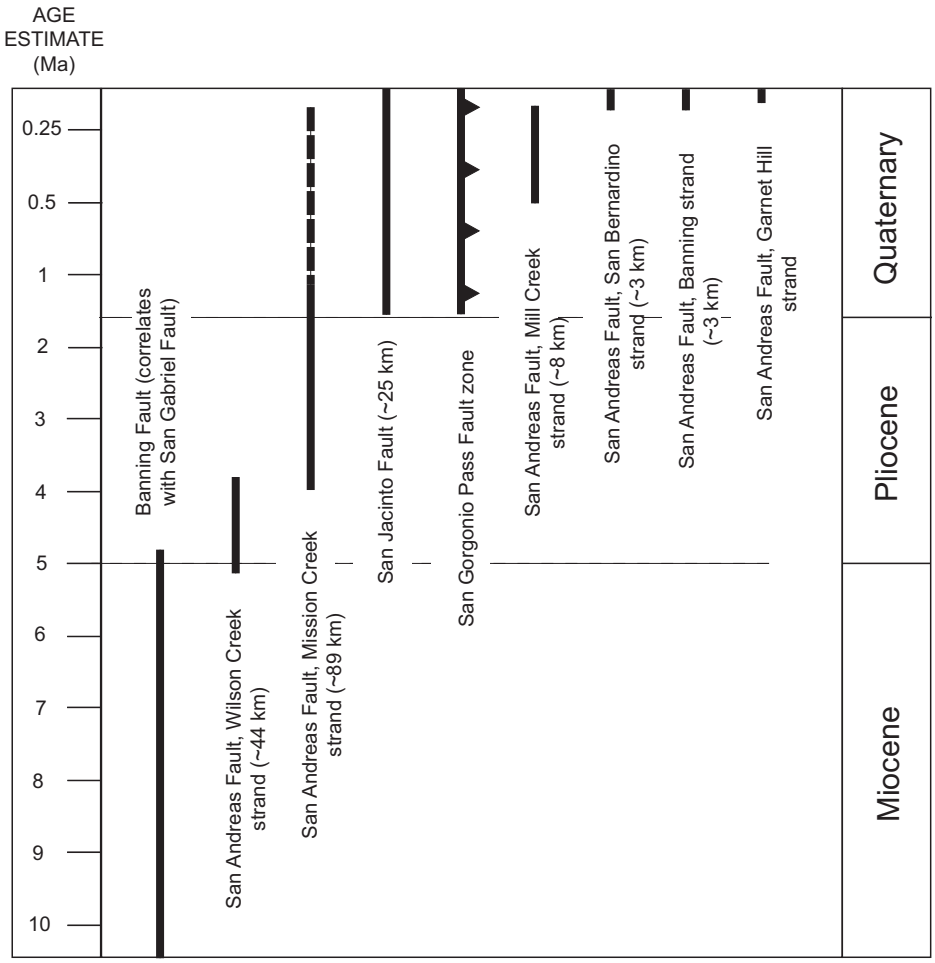

Figure 2. Diagram illustrating displacement history of various faults in the greater San Gorgonio Pass region, showing the timing of displacement (solid vertical lines) and amount of right slip (in parentheses); note change of scale at 1.0 Ma. Timing of displacement is based on general assignment of ages to depositional units, rather than quantitative determination. Dashed line for Mission Creek strand indicates continuation of dextral slip in Coachella Valley when the strand was abandoned in San Gorgonio Pass (solid line; see text for discussion). Adapted from Langenheim et al. (2005, their figure 3) using data published by Matti et al. (1985, 1992) and Matti and Morton (1993).

2013). Because the classification is intended for use throughout a large region, not all map units are found in any one area. For example, in the Mission Creek area we recognize units $Qvof_2$ and $Qvof_3$ even though we don't recognize an older unit $Qvof_1$.

We measured morphometric parameters for the major drainage basins in the region. We constructed stream profiles and analyzed these for discontinuities and knickpoints (for a discussion of methodology, see Wobus et al. [2006]). Within the Mission Creek alluvial complex, we determined morphometric surface texture parameters, including drainage density and post-depositional incision, using a series of lateral profiles constructed from a 10 m digital elevation model. Longitudinal profiles on the surface remnants revealed uplift and tilting.

We described soil development on selected surfaces within the Mission Creek alluvial complex, using established methods (Birkeland, 1999; Schoeneberger et al., 2002). Laboratory analysis on the collected samples included particle size determined by pipette and wet-sieving methods. We determined profile development indices (Harden, 1982) and rubification indices (Torrent et al., 1980) for each of these pedons, as well as for three pedons previously described by McFadden (1982) within this study area.

We sampled for optical luminescence dating from samples collected by hammering a 5 cm interior diameter and 40–50 cm length of PVC tubing into profile walls. We determined luminescence ages on the fine-grained (4–11 μm), polymineral fraction of the inner portion of the sample, using multiple-aliquot techniques (Singhvi et al., 1982; Lang, 1994; Richardson et al., 1997; Forman and Pierson, 2002) with infrared excitation. We isolated and dated the fine-grained silt separate of representative samples using multiple-aliquot techniques.

RESULTS

Mapped Faults in the Study Area

We focus on the SAF in northern SGP, where not only the Mill Creek and Mission Creek faults represent the major part of SAF history but—more importantly—late Quaternary tectonic events set the stage for the modern seismic hazards in the transition zone between the SGP region and the Coachella Valley to the southeast.

Mission Creek and Mill Creek Fault Strands of the SAF

Mission Creek fault. As it approaches SGP from the Coachella Valley (Fig. 1), the Mission Creek fault curves gently westward and follows the deep canyon of the South Fork Whitewater River (Fig. 3). The fault is marked by a zone of crushed and sheared crystalline rock as wide as 200–300 m (Allen, 1957); the zone is locally cut by discrete fault traces and shears that dip northward as shallowly as 45° (Allen, 1957). The crush zone and its discrete fault surfaces continue west to the Raywood Flat area, thence southwest down the canyon of San Gorgonio River (Fig. 3). The contrast in crystalline rocks north and south of the fault suggests that the Mission Creek fault is an important structure: those to the north (Yucaipa Ridge and the main San Bernardino Mountains) are of Mojave Desert type whereas those to the south (southeastern San Bernardino Mountains) are of San Gabriel Mountains type (Fig. 1; Ehlig, 1977; Farley, 1979; Matti et al., 1982, 1983). The fault does not break surficial deposits, estimated to be middle and late Quaternary, that cover the zone throughout its entire reach between Mission Creek and San Gorgonio River (Matti et al., 1983, 1985, 1992); thus the fault is probably older than ca. 500 ka.

Mill Creek fault. For this report we investigated the Mill Creek fault from the Mill Creek Jumpoff (steep, erosional fluvial headscarp) eastward to the Mission Creek study area. Our findings largely confirm those of Allen (1957) and later workers (Farley, 1979; Matti et al., 1983), as discussed in subsequent sections, but add new data and interpretation relevant to the fault's movement history. We document more

Downloaded from http://pubs.geoscienceworld.org/gsa/gsabulletin/article-pdf/127/5-6/825/3410110/825.pdf
by USGS Library user

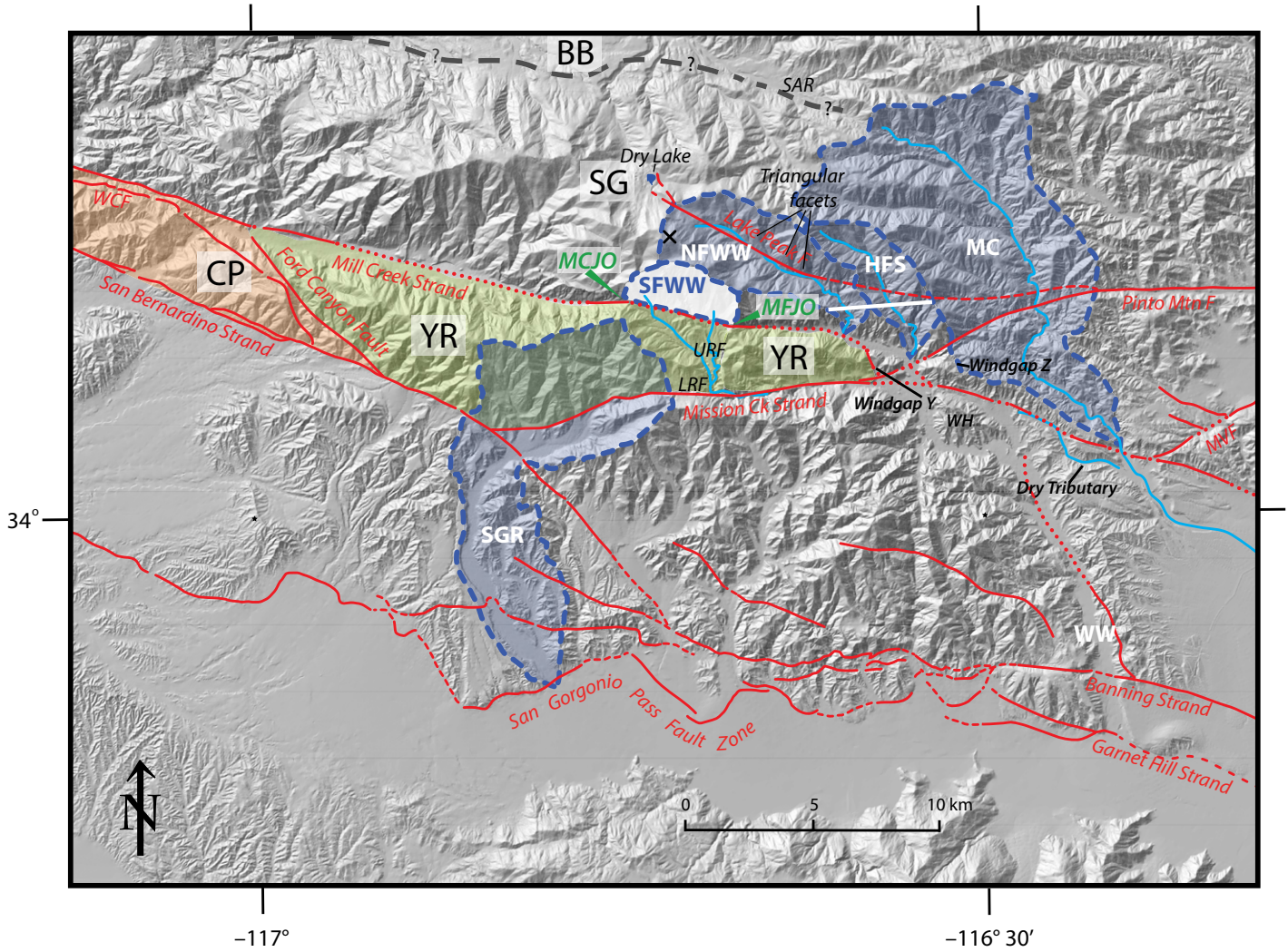

Figure 3. Geomorphic summary of the study area. Structural blocks include Big Bear (BB), San Gorgonio (SG), Yucaipa Ridge (YR), and Cram Peak (CP). Major drainages include North Fork Whitewater River (NFWW), Hell For Sure Canyon (HFS), Whitewater River (WW), and Mission Creek (MC). The headwaters of the South Fork Whitewater (SFWW) and the drainage basin of the San Gorgonio River (SGR) are also delineated. Faults and fault strands are shown in red; WCF—Wilson Creek Fault. The headwaters of the Santa Ana River, which forms the northern boundary of Spotila et al.'s (1998) San Gorgonio block, is indicated (SAR). Dashed gray line suggests the northern boundary of the San Gorgonio block. Black "x" marks San Gorgonio Mountain, the highest peak in southern California. Mill Creek (MCJO) and Middle Fork (MFJO) Jumpoffs are shown with green labels. Locations of wind gaps Y and Z, "dry tributary", Wathier Hill (WH), and upper and lower Raywood Flat (URF and LRF, respectively) are shown with black labels. Location of profile transect across the North Fork and Hell For Sure drainages is shown by a white line. MVF—Morongo Valley fault.

carefully its relation to the Mission Creek strand and, especially, to the sinistral Pinto Mountain fault.

Raywood Flat area. We begin our discussion of the Mill Creek fault at the Mill Creek Jumpoff on the northwest edge of the Raywood Flat area (Figs. 4, 5A). There, a wide zone of crushed and sheared rock separates the Yucaipa Ridge block (on the south) from the San Gorgonio block (to the north). The crush zone is traversed by several discrete faults (red lines in Fig. 5A), but rocks in the crush zone are so sheared and broken that it is difficult to determine which discrete structure coincides with the Mill Creek fault itself. None of the discrete faults appears to displace a thick wedge of colluvial deposits that overlies the crush zone, although steep exposures prevented our direct observation of the contact.

Between the Mill Creek and Middle Fork Jumpoffs, the Mill Creek fault largely is concealed by surficial deposits. Colluvial and debris-fan deposits derived from the San Gorgonio block (Figs. 3, 4) are the most widespread covering deposits in upper Raywood Flat. These deposits are crudely stratified and largely retain colluvial and fan-shaped depositional landforms that smoothly grade to adjacent hillslopes. This pristine morphology suggests that the deposits are relatively young, and we conclude that they are likely to be late Pleistocene and Holocene, based on the lack of incision and our regional surficial correlations. Our mapping (Fig. 4) suggests multiple generations of colluvial and debris-fan deposition, and stratigraphically lower deposits could be considerably older (Table 2).

A down-to-the-north fault scarp locally disrupts the Raywood Flat deposits at the Middle

Downloaded from http://pubs.geoscienceworld.org/gsa/gsabulletin/article-pdf/127/5-6/825/3410110/825.pdf
by USGS Library user

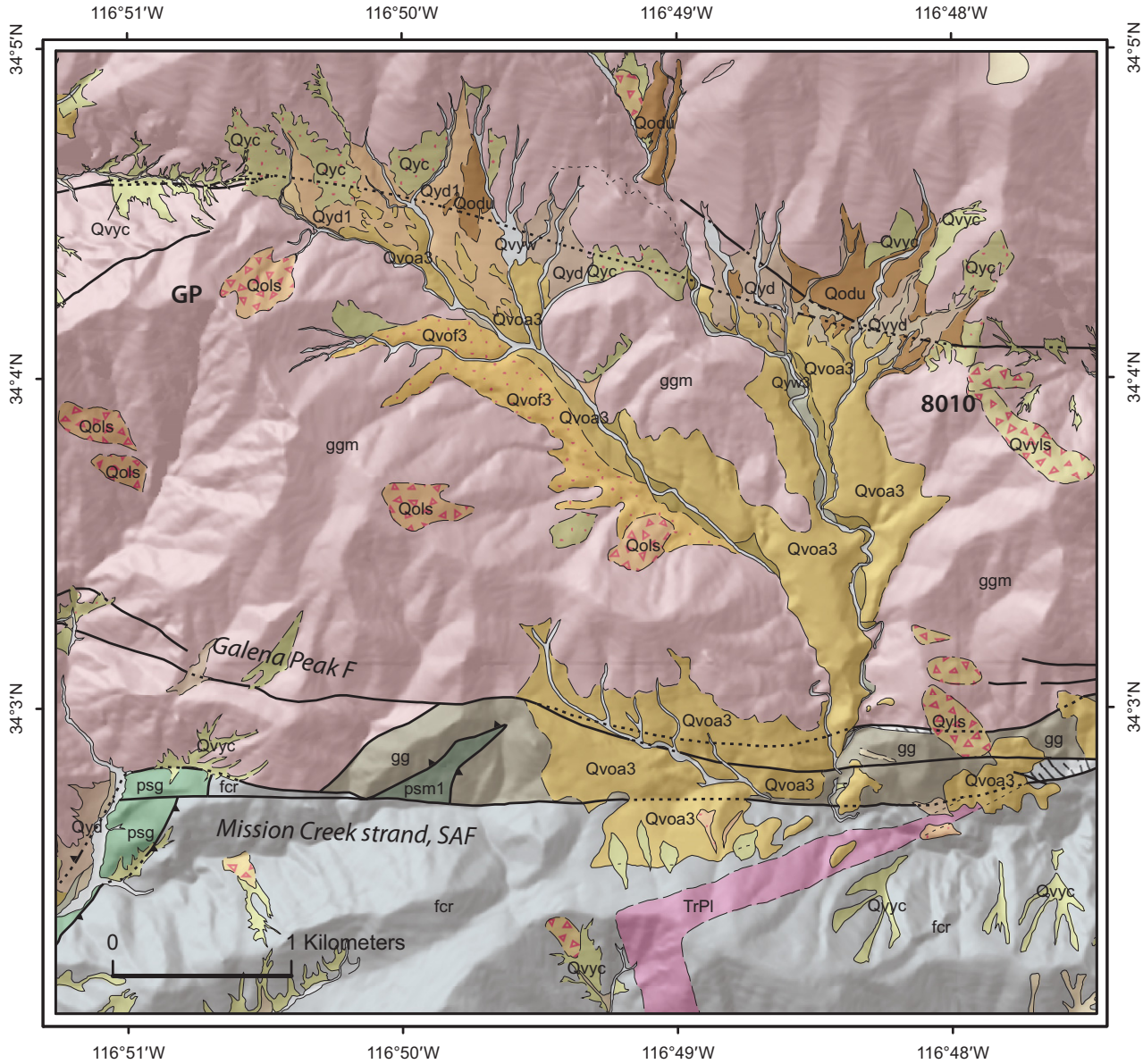

Figure 4. Geology of the upper Raywood Flat study area. Points used to construct the cross-sectional transect for Figure 9 are shown: Galena Peak (GP) and Peak 8010. SAF—San Andreas fault.

Downloaded from http://pubs.geoscienceworld.org/gsa/gsabulletin/article-pdf/127/5-6/825/3410110/825.pdf
by USGS Library user

Fork Jumpoff (Figs. 4, 5B). This scarp traverses the broad zone of crushed and sheared rock exposed in the Middle Fork Jumpoff (Fig. 5B) and clearly displaces late Quaternary colluvial deposits at the headscarp crest. Two or more depositional sequences are present in the colluvium, with the older resting nonconformably on crystalline rocks and the younger overlying the older with slight angular unconformity (Fig. 5B). The older deposits clearly are faulted. The younger deposits also may be faulted, or they may buttress unconformably against the fault scarp and thus post-date fault movements. The interpretation and role of this fault are further explored below.

Raywood Flat to Whitewater forks. Southeast of the Middle Fork Jumpoff, the discrete fault in Figure 5B can be mapped for a short distance in crystalline rocks before it is concealed by young alluvial wash of the Middle Fork Whitewater River (Fig. 6). For several kilometers southeast of this point, the fault's location only can be inferred beneath these young deposits.

At the confluence of the Middle and North Forks (Fig. 6), geologic relations are not obvious. (For simplicity, we commonly refer to the forks of the Whitewater River by an abbreviated name [e.g., North Fork].) Here, the Mill Creek fault is spatially associated with two other important structures: the Mission Creek fault and the sinistral Pinto Mountain fault.

As depicted in Figure 6, we interpret that the Pinto Mountain fault projects westward across the Middle Fork Whitewater River and merges with the Mission Creek fault crush zone. We propose that the Pinto Mountain fault has truncated the Mill Creek fault and offset the severed ends by 1–1.25 km.

Whitewater forks to Mission Creek. Between Whitewater River and Mission Creek, geologic relations are complex. Factors contributing to this complexity are: (1) more than one discrete fault trace potentially is assignable to the SAF; (2) a thick zone of crushed and sheared rock associated with the faults is difficult to attribute to any one of them; and (3) the faults are associated with a thin slice of steeply dipping sedimentary rocks whose questionable stratigraphic assignment bears on which faults are major strands of the SAF zone versus those that play some other structural role.

Clasts contained in the sedimentary unit (marked Tp in Fig. 6) help resolve this complex geology. The unit contains abundant volcanic-rock clasts (basalt, andesite, latitic rock) and gneissose and granitoid clasts that are unlike bedrock known from the San Bernardino Mountains The exotic-clast suite in the sedimentary slice indicates that the fault separating it from crystalline rocks of Mojave Desert type played

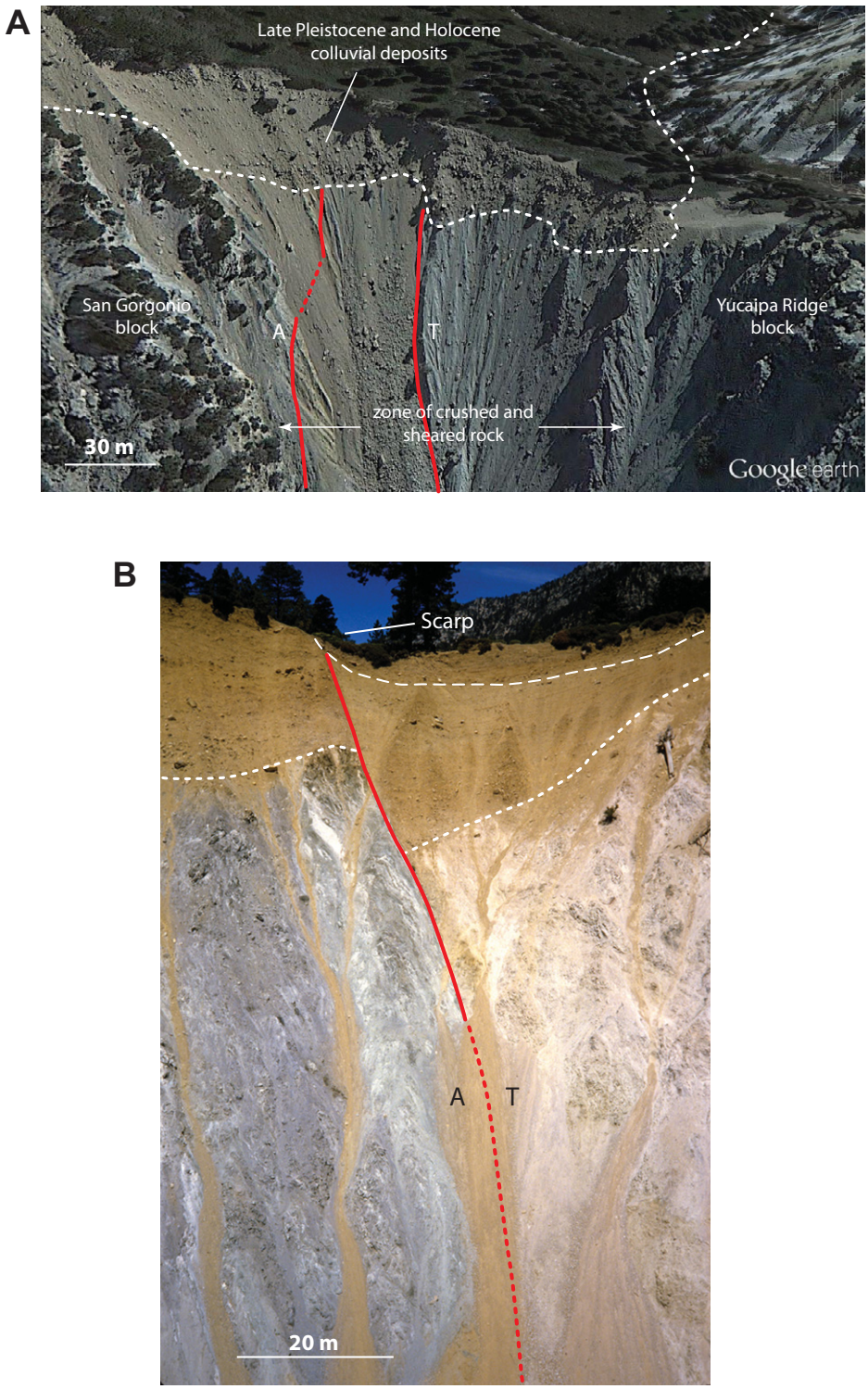

Figure 5. (A) View of Mill Creek Jumpoff, showing a broad zone of crushed and sheared rock. (B) View of Middle Fork Jumpoff, showing contrasting lithologies across the Mill Creek strand. Motion on the Mill Creek strand is indicated by A (away) and T (toward). Scale is approximate only, since these erosional amphitheatres are neither planar nor vertical.

Downloaded from http://pubs.geoscienceworld.org/gsa/gsabulletin/article-pdf/127/5-6/825/3410110/825.pdf
by USGS Library user

TABLE 2. DEPOSITIONAL UNITS IN UPPER RAYWOOD FLAT

Surficial unit	Description
Axial deposits	Dominantly gravelly deposits but include finer-grained materials. Clasts consist mainly of granitoid rocks that are texturally massive to foliated; these range from granodiorite to monzogranite, and include leucocratic muscovite-garnet monzogranite like that mapped by Morton et al. (1980) on the San Gorgonio block. Clasts of migmatitic or gneissic rock are subordinate, and mafic granitoids are rare. Clasts typically range from small boulders to small cobbles; in sandier layers, clasts range from small cobbles to pebbles. Clasts typically are subrounded, but range from rounded to subangular. Depositional fabrics include both clast support and matrix support, indicating fluvial and sediment gravity-flow processes, respectively. Fluvial fabrics are common. The axial deposits are poorly dated, but they appear to be at least a few hundred thousand years old based on the high-standing, deeply dissected character of the deposits, and well-developed argillic B horizons locally preserved on fill surfaces.
Tributary deposits	Deposits of fan-shaped sediment bodies that head onto the Yucaipa Ridge block interfinger with those of the axial drainage, although we infer this mainly from geomorphic relations. Compositionally more heterogeneous than axial deposits. Clast types include granitoid, gneissose, and migmatitic rocks that typify crystalline rocks of the Yucaipa Ridge block.
Colluvial deposits	Coarse to fine detritus deposited on moderate to slight hillslopes and at the base of hillslopes; formed by downslope particle movement under the influence of gravity, intermittently assisted by unconfined water flow (runoff). Depositional textures range from non-bedded or crudely bedded (disorganized mass) to somewhat stratified, reflecting particle response to gravitational transport with ancillary water transport. In base-of-slope settings, colluvium may pass obviously or vaguely into alluvium deposited by streamflow.

a major tectonic role, because no nearby source exists; we interpret this to be the Mission Creek strand. We assign these sedimentary rocks to the Pliocene Painted Hill Formation of Allen (1957) (Fig. 6, our unit Tp).

We discount that the fault bounding the south margin of the sedimentary-rock slice is the Mill Creek fault (Fig. 6), because it cannot be traced throughout the Mission Creek area (Figs. 6, 7A) and because it cannot be linked to the Mill Creek fault farther northwest (Fig. 6). Consequently, we conclude that—in the area directly east of Whitewater River—the Mill Creek strand merges with the Mission Creek strand. The combined Mill Creek–Mission Creek configuration persists for a few kilometers southeast of the footprint of Figure 6, although locally the two strands diverge as in the Mission Creek area (right side of Fig. 7A).

Geologic relations directly northwest of Mission Creek (top left corner of Fig. 7A) indicate the relative timing of most recent fault activity on the Mill Creek and Mission Creek strands. There, a southern fault strand breaks surficial deposits of unit $Qvof_3$ while a northern strand is concealed beneath undifferentiated (but very old) surficial deposits we assign to unit Qvosu; both faults traverse a zone of crushed and sheared crystalline rock pulverized beyond easy identification.

Southeast of the Mission Creek drainage, the zone of crushed crystalline rock and the individual Mill Creek and Mission Creek strands continue southeastward for about a kilometer, until the two strands once again merge into a single discrete trace that we assign to the Mill Creek strand.

Secondary Faults

Galena Peak fault. Where the Mission Creek fault trends westward beneath surficial deposits of lower Raywood Flat, it is flanked a short distance to the north by a degraded, north-facing fault scarp that diagonals westward from the South Fork Whitewater River to the San Gorgonio River drainage basin (Fig. 4). Along the west wall of the South Fork Whitewater River, this fault juxtaposes Raywood Flat surficial deposits against crushed and sheared crystalline rock. Given its occurrence proximal to the Mission Creek crush zone, the fault scarp conceivably could be attributed to the Mission Creek strand, thereby calling into question that fault's antiquity. Indeed, the nomenclature assigned in the Quaternary fault and fold database (U.S. Geological Survey and California Geological Survey, 2006) suggests that this structure is simply a splay of the Mission Creek fault. However, because the scarp (1) cuts across the crush zone rather than paralleling it; (2) has a more northwesterly trend; (3) exhibits only vertical and no obvious lateral offset; and (4) can be mapped trending away from the Mission Creek fault toward Yucaipa Ridge (Fig. 4), Matti et al. (1983, 1985) attributed the scarp to younger tectonism that led to north-facing fault scarps throughout the SGP region. We accept this hypothesis, and apply the name "Galena Peak fault" to the Raywood Flat structure.

Lake Peak fault. In the upper part of the North Fork Whitewater drainage, the parent stream parallels a northwest-trending fault mapped by Dibblee (1964, 1967) and Morton et al. (1980), and named the "San Gorgonio Mountain fault" by Wesnousky (1986). This fault may or may not have played a role in the structural evolution of the San Gorgonio block, so to avoid confusion we refer to it as the "Lake Peak fault," named for a topographic prominence northeast of San Gorgonio Mountain. The fault has been active during the late Quaternary, as evidenced by its displacement of Wisconsin-age glacial deposits to the south of Dry Lake, and by pronounced triangular facets along the North Fork Whitewater River (Fig. 3).

Unnamed faults in Mission Creek drainage area. Two northeast-trending down-to-the-west faults disrupt geomorphic surfaces in Mission Creek, located near the midline of, and in the western part of, surface B_2 (Fig. 7A). Both faults have west-facing scarps that have been significantly modified by weathering and erosion. We have not determined the age and structural role of these faults, although they clearly post-date surface B_2 (Fig. 7B) and appear to be normal-slip structures. The western fault has more obvious geomorphic expression, and this structure may project northeast toward Mission Creek (Fig. 7A) where it may influence the interpretation of longitudinal profiles (discussed below).

Geomorphologic Features

We follow Spotila et al. (1998; Spotila and Sieh, 2000) in their description of the Big Bear and San Gorgonio blocks, as described in Table 1. However, we modify the nomenclature and extent of the Yucaipa Ridge and Wilson Creek structural blocks (Spotila et al., 1998; Spotila and Sieh, 2000) in two ways.

First, we abandon the name "Wilson Creek block" of Spotila et al. (1998, 2001) in favor of the name "Cram Peak block". The name "Wilson Creek block" was introduced by Matti et al. (1985, 1992; Matti and Morton, 1993) for a structural block of crystalline rock and overlying Miocene sedimentary rock bounded by the Wilson Creek and Mission Creek strands of the SAF; thus constrained, the block was emplaced against the San Bernardino Mountains in the early Pliocene by dextral slip on the Wilson Creek strand (Fig. 3). Our use of the name "Cram Peak block" avoids any confusion between the original Pliocene role played by the Wilson Creek block (*sensu* Matti et al., 1985, 1992) and any role the block might subsequently have played in Quaternary time.

Downloaded from http://pubs.geoscienceworld.org/gsa/gsabulletin/article-pdf/127/5-6/825/3410110/825.pdf
by USGS Library user

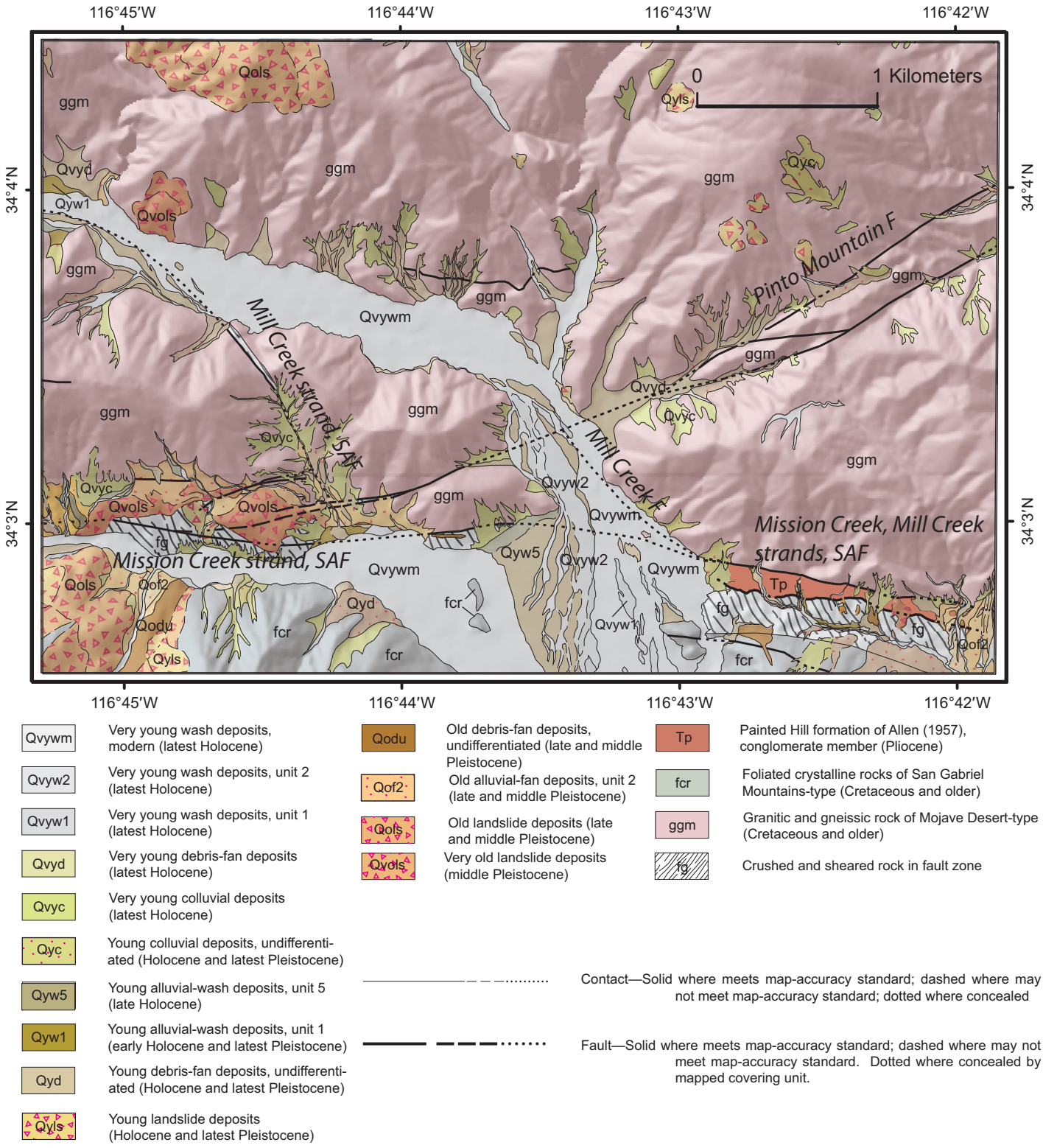

Figure 6. Geologic map of the region of intersection of the Pinto Mountain, Mission Creek, and Mill Creek faults. SAF—San Andreas fault.

Downloaded from http://pubs.geoscienceworld.org/gsa/gsabulletin/article-pdf/127/5-6/825/3410110/825.pdf
by USGS Library user

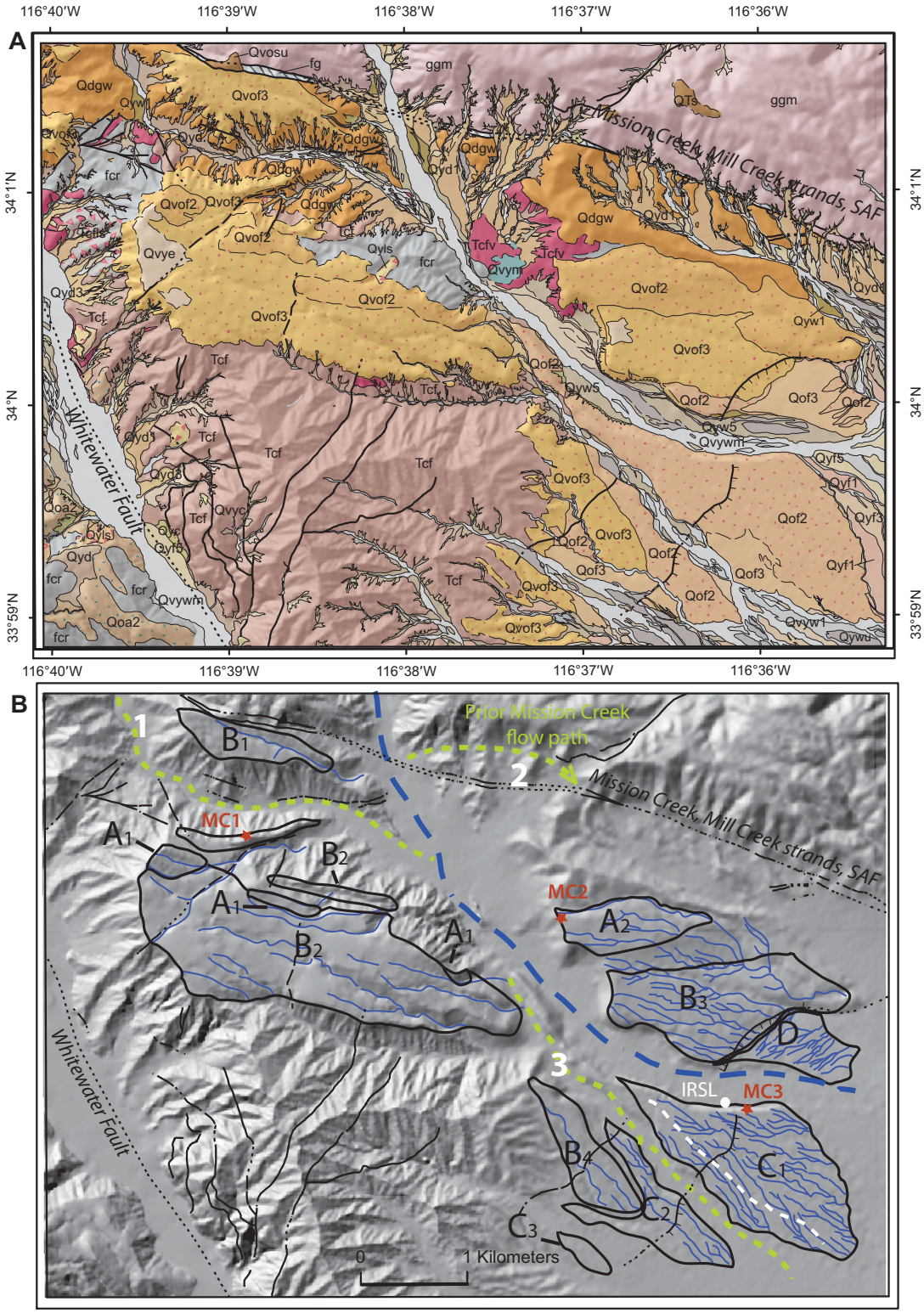

Figure 7 (*legend on following page*). (A) Geology of the region of the Mission Creek alluvial sequence, located downstream from where Mission Creek exits the San Bernardino Mountains. Younger units are progressively incised into older units. Geology modified from Matti et al. (1982, 1983, 1985, 1992) and Matti and Morton (1993). (B) Geomorphic features in the same region of the Mission Creek alluvial complex. Locations for pedons MC1–MC3 (red stars) are shown. Location for pedons described by McFadden (1982) are reported in general terms only. Location for infrared stimulated luminescence (IRSL) samples is shown by a white circle. Prior flow paths of the Mission Creek drainage are shown with green dashed lines, numbered in the order discussed. White dashed line shows the axial crest of the surface C alluvial fan deposit. Blue dashed line represents current flow along Mission Creek. SAF—San Andreas fault.

Downloaded from http://pubs.geoscienceworld.org/gsa/gsabulletin/article-pdf/127/5-6/825/3410110/825.pdf
by USGS Library user

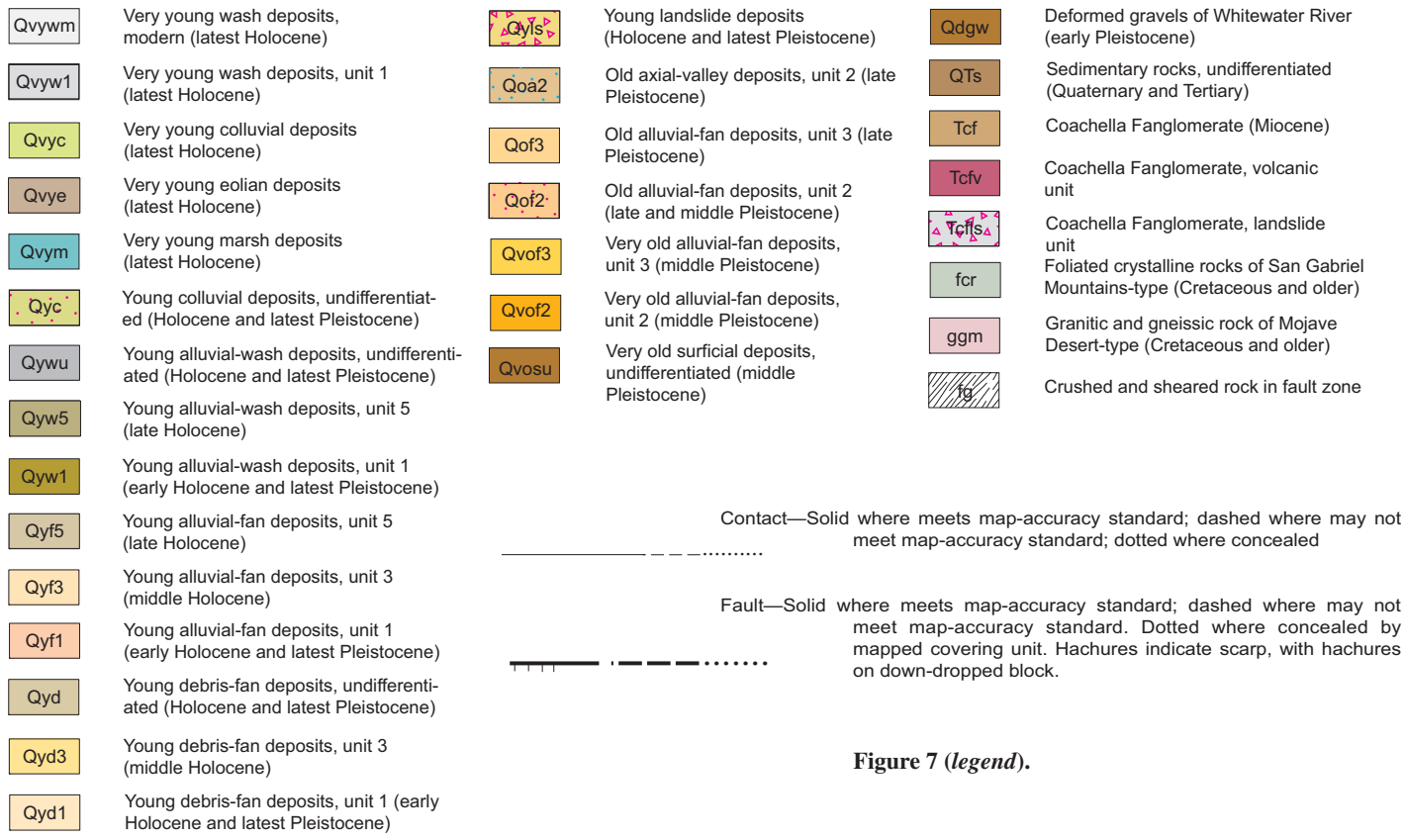

Figure 7 (*legend*).

Second, Spotila et al. (1998, their figure 1) indicated that the Wilson Creek fault separates their Yucaipa Ridge and Wilson Creek blocks, with Quaternary dextral slip on that fault allowing for different uplift histories for the two blocks. However, Matti et al. (1992; Matti and Morton, 1993) indicated that the Wilson Creek fault was active only in the early Pliocene (Fig. 2). Moreover, the fault has no geomorphic expression in the modern landscape, and is truncated by the younger Mission Creek and San Bernardino strands of the SAF at such a high angle that it seems unlikely that the Wilson Creek fault has played any landscape-forming role in the Quaternary. By contrast, a fault that (1) crosses Yucaipa Ridge at its west end; (2) obliquely traverses its southwest margin subparallel to topography; and (3) forms lineaments in the modern landscape more likely is the structure that has controlled Quaternary landscape evolution of blocks associated with Yucaipa Ridge. We refer to this structure as the Ford Canyon fault (Fig. 3), and we propose that it—rather than the Wilson Creek fault—separates the Yucaipa Ridge block from the Cram Peak block to the northwest.

Wind Gaps, Abandoned Stream Courses, and Wathier Hill

Five elevated valleys within the study area help in understanding the slip history of faults in the region and the effect of fault displacements on the evolving landscape. Wind gap Y is a prominent bisecting valley on Yucaipa Ridge (Fig. 3). This valley follows the crush zone of the Mill Creek fault where it exits the canyon of the Middle Fork Whitewater River. It is positioned immediately downstream of the confluence of the North Fork with the Middle Fork. A tributary to the South Fork occupies the lower reach of this valley, although it is underfit to the valley, indicating that it was not the drainage responsible for carving the valley. The upper slope of wind gap Y is ~80 m above the active drainage of the Middle Fork, immediately northwest. The slope of this wind gap is ~45° in the upper reach; recent alluvial and colluvial deposition has effectively decreased the slope in the lower reach. The second elevated valley, wind gap Z, is an isolated valley that is bound to the north by the Pinto Mountain fault and to the south by the combined Mission Creek and Mill Creek fault zones. The upstream side of the wind gap is elevated ~60 m above a tributary to the Middle Fork that follows the trace of the Pinto Mountain fault. The downstream end of this wind gap abuts the combined Mill Creek and Mission Creek fault escarpment. The third elevated valley is a tributary to the Mission Creek drainage. This is a beheaded canyon that parallels the Mill Creek strand in its upper reaches before flowing away from the fault in a convex-to-the-south arc. Like wind gap Y, this canyon contains local flow in the lower reach, which is underfit to the canyon dimensions. We informally refer to this feature as "dry tributary" in this report, for ease of discussion (Fig. 3; flow path 1, Fig. 7B). The fourth drainage flow path of importance is a curved, convex-to-the-north strath surface just to the east of the position where the active Mission Creek crosses the combined Mill Creek and Mission Creek strands of the SAF (flow path 2, Fig. 7B). Finally, a beheaded drainage is located just to the southeast of the active Mission Creek, elevated ~30 m above the active channel (flow path 3, Fig. 7B).

Adjacent to the active course of the Whitewater River is a bedrock high which has been isolated by a complex history of drainage switching and capture, as discussed below. This landform is a lozenge-shaped island hill

Downloaded from http://pubs.geoscienceworld.org/gsa/gsabulletin/article-pdf/127/5-6/825/3410110/825.pdf
by USGS Library user

surrounded by alluvium. At its northwestern end is a location designated Wathier Landing. Although this island hill is an unnamed feature on modern topographic base maps, in this report we will informally refer to this landform as Wathier Hill (Fig. 3).

Quaternary Surficial Deposits

Mission Creek Alluvial Complex

Where Mission Creek emerges from its bedrock canyon and crosses the Mill Creek and Mission Creek strands of the SAF, its incised course bisects nested alluvial deposits (Fig. 7A). The youngest of these is the active wash of Mission Creek that has its headwaters in the San Bernardino Mountains and incises the alluvial complex before flowing into Coachella Valley. The highest-standing alluvial units are the oldest, the most dissected, and associated with strongest soil development; successively lower-elevation units are younger and buttress unconformably against the older units (Fig. 7A; Table 3). This sequence represents pulses of erosional downcutting followed by aggradational backfilling. Each unit is a singular morphostratigraphic entity separable from others in the succession, and each represents a significant volume of alluvial sediment sourced from the large Mission Creek drainage basin. Stratigraphic units in the nested alluvial complex are generally similar lithologically, and have similar clast composition and degree of weathering of these clasts (Tables 4, 5).

Morphology of surfaces in Mission Creek. Geomorphic surfaces have developed on each of the depositional units within the Mission Creek alluvial complex. We designate the surface developed atop the oldest unit, $Qvof_2$, as surface A. We refer to correlative surfaces west and east of Mission Creek wash separately (Fig. 7B): west of the wash, surface A_1 designates surface remnants on the three isolated outcrops of unit $Qvof_2$; east of the wash, surface A_2 refers to an equivalent but more extensive surface.

The surface developed atop unit $Qvof_3$, surface B, is well incised and exhibits ridge-and-ravine morphology, which is particularly pronounced on B_1 and B_2. Incision patterns on B_1, B_2, and B_3 trend roughly east-west, parallel with the narrow depositional corridor we invoke for the accumulation of units $Qvof_2$ and $Qvof_3$; by contrast, incision on surface B_4 trends more southerly, paralleling the south-radiating extent we envision for this sector of the unit $Qvof_3$ fill. In all cases, headward parts of the ridge-and-ravine morphology extend to the edge of each B surface, at which point the erosional grain is truncated by cannibalization associated with later Quaternary processes unrelated to the ridge-and-ravine landscapes. We take this to mean that incision probably was associated

TABLE 3. STRATIGRAPHIC RELATIONS, GEOMORPHIC PROPERTIES, AND PEDOGENESIS OF MAP UNITS OF THE MISSION CREEK ALLUVIAL COMPLEX

Map unit / associated surface designation	Stratigraphic relations	Geomorphic properties	Pedogenic development
Qof_3 / D	Unit accumulated on a strath surface eroded into unit Qof_2 and older units.	Fan-shaped surface at the east margin of the Mission Creek alluvial complex, north of the incised modern wash. The surface associated with this deposit is incised by a dense network of shallow drainages, with gullies heading on the upper portion of the surface.	Soil development associated with this surface shows 7.5YR colors and moderately thick clay films on grains in a 59-cm-thick Bt horizon, underlain by a 14-cm-thick horizon exhibiting stage I carbonate accumulation (Gile et al., 1966).
Qof_2 / C	Unit accumulated on strath surfaces incised into the older units ($Qvof_2$ and $Qvof_3$); paleosols that preserve remnant Bt horizons locally are preserved on these strath surfaces. In the north-facing wall of Mission Creek wash, unit is up to 23 m thick. In the Mission Creek alluvial complex, this unit appears to correlate with localized alluvial fills south of Mission Creek that debouch from canyons eroded into the Miocene Coachella Fanglomerate (Fig. 7).	Represented by a large, well-preserved alluvial-fan landform radiating southeast and south away from the incised modern wash. The apex of the fan points up the incised axial wash of Mission Creek (Fig. 7A). The drainage pattern incised on these surfaces is radial, and the gullies head on the surface, rather than extending beyond the upstream edge.	Pedogenesis associated with these surfaces displays moderately thick clay films and 7.5YR to 5YR hues in a 150-cm-thick Bt horizon.
$Qvof_3$ / B	Unit is commonly > 30 m, and up to 40 m thick. Unit buttresses unconformably against various underlying bedrock units, and also against high ground of unit $Qvof_2$.	Represented to the northwest (upstream) by two elongate, high-standing alluvial bodies west and east of the incised modern Mission Creek wash. Unit appears to have accumulated in a narrow, northwest-southeast–oriented valley flanked to the southwest by Coachella Fanglomerate and crystalline rocks of San Gabriel–Chocolate Mountains type and northeast by crystalline rocks of Mojave Desert type. Downstream, this unit is preserved as remnants of an alluvial fan, where the deposition extended beyond, and was no longer constrained by, the ridge of Coachella Fanglomerate bedrock. This unit is associated with similarly aged deposits shed from canyons incised into Coachella Fanglomerate. Deeply incised ridge-and-ravine morphology is particularly pronounced on surfaces B_1 and B_2. Incision extends beyond the upstream edge of each surface.	Soil development associated with surface B_2 is characterized by strong 5YR colors and thick clay films in a 48-cm-thick Bt horizon. Soil development associated with surface B_3 has 2.5YR colors, abundant thick clay films, and a sandy clay texture.
$Qvof_2$ / A	Unit represents a major fill event up to 25 m thick, although thickness varies locally. Unconformably overlies various older units, including (1) deformed gravels of Whitewater River, (2) Miocene Coachella Fanglomerate, and (3) crystalline bedrock of San Gabriel Mountains and Chocolate Mountains type.	Highest-standing, most dissected unit of the Mission Creek alluvial complex. Unit is represented by a large depositional body east of the incised wash of Mission Creek (surface A_2) and several smaller isolated bodies west of the incised wash (surface A_1; Fig. 7A). The preserved bodies are elongate northwest-southeast subparallel to the Mill Creek and Mission Creek faults. Surface A_1 has a ridge-and-ravine surface morphology (Fig. 7B).	Very well-developed soils are associated with surface A_2. These soils have strong red colors (2.5YR 4/6), thick, abundant clay films, prismatic structure and a 2-m-thick silica-cemented duripan. Duripan is nearly continuous, with much of the soil matrix engulfed in secondary amorphous silica.

Note: Color classification after Munsell Soil Color Chart.

Downloaded from http://pubs.geoscienceworld.org/gsa/gsabulletin/article-pdf/127/5-6/825/3410110/825.pdf
by USGS Library user

TABLE 4. LITHOLOGIC CHARACTERISTICS OF MISSION CREEK ALLUVIAL COMPLEX

Representative lithologic types	(1) Cobble-pebble gravel, (2) sandy cobble-pebble gravel, (3) gravelly sand, (4) cobble-boulder gravel, and (5) slightly gravelly sand (minor).
Bedding characteristics	Most two-dimensional views of stratification suggest that parallel bedding ranging in thickness from medium to very thick; rare three-dimensional views indicate that stratification is lenticular over distances of a few tens of meters to many hundreds of meters. Layer bases are sharp, and commonly are channelate.
Depositional fabrics	Depositional fabrics in gravelly layers range from clast supported to matrix supported. Clast-supported fabrics commonly have imbricated cobbles and pebbles; sandy interlayers are parallel laminated to cross laminated. These materials are fluvial in origin. Matrix-supported fabrics are texturally massive and consist of cobble- and boulder-size clasts surrounded by sandy and pebbly matrix; these materials formed by sediment gravity-flow processes, mainly as subaerial debris flows.
Particle size, sorting, and rounding	Particle textures are quite variable. Particle size ranges from boulders as large as 3 m to sand size; pebble- and cobble-size clasts are dominant, with boulders less common and sand-size particles occurring either as matrix in clast-supported layers, as components of sandy gravel layers, or as sand-rich layers between gravelly layers. Sorting typically is poor, given the extreme range of particle sizes in most layers. Particle rounding is variable, with all rounding classes represented; angular to subangular particles are common, but subrounded to rounded particles occur.

TABLE 5. REPRESENTATIVE CLAST SUITES IN STRATIGRAPHIC UNITS OF THE MISSION CREEK NESTED ALLUVIAL COMPLEX

Clast suite	Representative clast types
Texturally massive to slightly foliated leucocratic granitoid rock	Biotite granodiorite; biotite monzogranite; muscovite monzogranite (rare)
Biotite-quartz-feldspar rock that is strongly foliated to compositionally layered (gneissose) to migmatitic	Biotite-quartz-feldspar gneiss; biotite-quartz-feldspar migmatite; gneissose biotite-quartz-feldspar rock of undetermined origin. Textures vary from distinctly layered to diffusely layered
Fine-grained texturally massive leucocratic plutonic rocks	Aplite; fine-grained leucogranite
Mafic plutonic rocks	Diorite; gabbro
Metasedimentary rocks	Quartzite; calcsilicate rock; white marble; fine-grained pelitic gneiss

with—and triggered by—streamflows that followed trajectories similar to those that deposited unit $Qvof_3$ alluvium.

Geologic age determination—Luminescence. Regionally in southern California, researchers have found that quartz optically stimulated luminescence (OSL) can have poor characteristics, such as low bleachability, low sensitivity, and high thermal transfer, which have hindered its application toward geological research problems (Roder et al., 2012; Lawson et al., 2012; Lawson et al., in press). Further, there is wide variation in the depositional environments, which complicates OSL dating (Rhodes, 2011). While some of the difficulties associated with these settings, such as incomplete zeroing and the effect of bioturbation, can be mitigated using single-grain measurement (Porat and Botha, 2008), the effects of signal contamination are still a concern. Because of this, we sampled feldspar grains using infrared stimulated luminescence (IRSL). The age of unit Qof_2 (Fig. 7A) is determined by two IRSL dates; samples from depths of 4 and 5 m below the surface yielded results of 95 ± 15 ka and 106 ± 15 ka, respectively (Table 6). The dose rates for these sediments showed very high concentrations of Th and K, and it would be expected that the luminescence centers would become rapidly filled, thus these age determinations are considered to be minima.

Geologic age determination—Pedogenic development. Pedogenic development increases as a function of time, and an index quantifying the degree of soil development can be a useful indicator of the age of the associated geomorphic surface (e.g., Harden, 1982). Where soil-forming factors are equivalent, quantified pedogenic development of dated soils can be used to estimate the duration of stability of nearby soil pedons. In the semi-arid region of southern California, iron oxide content increases, and compositionally transforms (e.g., McFadden and Hendricks, 1985), resulting in an increase in soil redness (rubification). Clay content also increases, and pedogenic structure and consistence change in a predictable manner. We use a profile development index (Harden, 1982; Harden and Taylor, 1983), quantification of clay content, and a rubification index (Torrent et al., 1980) to compare soils in the Mission Creek alluvial complex (Table 7) with nearby, dated soil chronosequences at Cajon Pass and San Timoteo Badlands (McFadden and Weldon, 1987; Kendrick and McFadden, 1996; Kendrick et al., 2002).

Surface A is associated with the highest-standing deposit of the Mission Creek alluvial complex, unit $Qvof_2$ (Table 3). A well-developed soil is associated with surface A_2, which includes a 2-m-thick silica-cemented duripan. Using the degree of soil development to estimate an age of this surface is somewhat problematic. The criteria we use to determine approximate ages, based on soils, include a profile development index, a rubification index, and the weighted mean value of clay content, as compared to regional dated soil chronosequences (Table 7). The profile development index (Harden, 1982; Harden and Taylor, 1983) is not designed to be used in soils with a well-cemented duripan, such as is associated with this surface. The duripan imparts a buff or yellow color, rather than the redness that developed prior to cementation, so the rubification index is not useful. Sampling the duripan to extract the clay is problematic, because the clay can only be released by chemical dissolution of the silica cement. So our estimates of age are based only on the pedogenic properties for the horizons above the duripan. This results

TABLE 6. FELDSPAR INFRARED STIMULATED LUMINESCENCE (IRSL) AGES FOR THE MISSION CREEK AREA, SOUTHERN CALIFORNIA

Sample information	Water content (%)*	K (%)†	U (ppm)†	Th (ppm)†	Cosmic dose§ component (Gy/k.y.)	Total dose rate (Gy/k.y.)	Equivalent dose (Gy)	IRSL age (ka)#
USGS-07-114	1 (30)	2.74 ± 0.03	1.77 ± 0.16	19.0 ± 0.41	0.09 ± 0.01	6.17 ± 0.11	>654 ± 100	>106 ± 15
USGS-07-115	1 (33)	2.95 ± 0.02	2.69 ± 0.12	17.9 ± 0.39	0.11 ± 0.01	6.54 ± 0.11	>621 ± 100	>95 ± 15

*Field moisture, with figures in parentheses indicating the complete sample saturation percent. Ages calculated using 35% of total saturation values.
†Analyses obtained using laboratory gamma spectrometry (high-resolution Ge detector).
§Cosmic doses and attenuation with depth were calculated using the methods of Prescott and Hutton (1994). See text for details.
#Feldspar from fine grains of 4 to 11 μm. Exponential fit is used for equivalent dose. Errors are one sigma. Fade tests indicate no correction.

Downloaded from http://pubs.geoscienceworld.org/gsa/gsabulletin/article-pdf/127/5-6/825/3410110/825.pdf
by USGS Library user

TABLE 7. COMPARISON OF SOIL DEVELOPMENT PROPERTIES FROM THIS STUDY TO REGIONAL CHRONOSEQUENCES

Geomorphic surface / pedon ID	Mapping unit	Age range; preferred age (ka)	Profile Development Index, weighted mean#	Rubification index, field description**	Profile clay content, weighted mean (%)	Maximum clay value (%)
Mission Creek*						
Surface A_2 / MC2	$Qvof_3$	–	0.46	11.25	13.24	17.31
Surface B_2 / MC1	Qof_1	–	0.38	6.67	17.95	22.46
Surface B_3 / LDM 43	Qof_1	–	0.28	15	–	–
Surface C_1 / MC3	Qof_2	ca. 106–95; >95	0.31	5	6	19.81
Surface C_1 / LDM 38A	Qof_2	ca. 106–95; >95	0.21	5	–	–
Surface D / LDM 39A	Qof_3	–	0.25	3.34	–	–
San Timoteo Badlands†						
Q1		62–37	0.24	3.75	11.8	18
Q2		94–58	0.31	6	12.1	17
Cajon Pass§						
RW-11	Qoad	67–43; 55	0.24	6	10.47	24.2
RW-14	Qoae	300–700; 500	0.4	11.25	14.58	34.5

*This study; "LDM" soils described by McFadden (1982).
†Data from Kendrick and McFadden (1996) and Kendrick et al. (2002).
§Data from McFadden and Weldon (1987).
#Profile Development Index calculated using soil properties: rubification, structure, dry consistence, clay film (thickness and frequency), and total texture; method after Harden (1982) and Harden and Taylor (1983).
**Hue multiplied by chroma, divided by value; after Torrent et al. (1980).

in a significant underestimation of the age, because the maximum development is actually expressed by the silica cementation, but not in a way that can be quantified by the profile development index. Using this limited part of the pedon, the profile development values and the rubification indices both indicate that surface A_2 is older than 500 ka, as compared to the Cajon Pass chronosequence (McFadden and Weldon, 1987; Table 7). However, the degree of development of the duripan is much greater than that of regional duripans of roughly 500 ka. Such duripans are preserved in surfaces within the San Timoteo Badlands chronosequence (Fig. 1; Kendrick and Graham, 2004), 50 km to the southwest. There the duripan is typified by widely spaced (averaging 50 cm), silica-rich seams, defining the tops of, and draping down the sides of, large prismatic peds (pedogenic structural units). In contrast, the duripan associated with surface A_2 is nearly continuous, with much of the soil matrix engulfed in secondary amorphous silica.

McFadden (1982) described a soil on surface B_3 (Fig. 7B), and classified this soil as S2, indicating that it initiated between 700 ka and 250 ka (pedon LDM 43). We described pedon MC1, located on B_2. McFadden's pedon (LDM 43) appears to be more mature than pedon MC1, even though both are developed on surfaces that are correlative. We attribute this discrepancy to the fact that McFadden's pedon LDM 43 is developed on a broad surface (B_3) that is spatially more extensive than that (B_2) on which pedon MC1 is developed. The latter is a narrow, slightly lower surface remnant located just north of the main B_2 surface. Based on the geomorphology of the latter site, we interpret that this soil has been eroded. For the soils on this surface, the results of comparison to the Cajon Pass chronosequence (McFadden and Weldon, 1987) yields quite different results, depending on the criteria used. In using the weighted mean value of clay content, this soil appears to be older than 500 ka, as compared to Cajon Pass (Table 7). However, using the profile development and rubification indices generally suggests that this soil falls somewhere between the two dated soils at Cajon Pass. The exception to the latter comparison is the rubification index of the LDM 43 pedon; based on this criterion, this soil age estimate would be greater than 500 ka. Because we recognize that the soil described on B_2 is eroded, we weight higher the results of comparison with pedon LDM 43, on B_3, to infer that this soil is older than 500 ka.

Unit Qof_2 (Fig. 7A) was deposited as an alluvial fan incised into the two older alluvial units, $Qvof_2$ and $Qvof_3$; it is inset into and downstream of these older units. Surfaces associated with depositional unit Qof_2 are C_1 through C_3 (Fig. 7B). Two pedons have been described on this surface: LDM 38A by McFadden (1982), and MC3 in this investigation. McFadden (1982) determined that this soil was an S3 in his classification, indicating a broad age of between 250 ka and 70 ka. Correlation of pedogenic properties to those of the Cajon Pass chronosequence (McFadden and Weldon, 1987) indicates that this soil is intermediate to the two dated soil pedons, though much more similar to the younger soil (55 ± 12 ka). When compared to dated soils in San Timoteo Badlands, the soil properties are most similar to those of Q2 (94–58 ka), with the exception of the profile development index value of LDM 38A (Table 7).

The youngest unit considered in this study, unit Qof_3 occupies a fan-shaped area on the north side of the Mission Creek axial wash, where it was deposited on a strath surface eroded into unit Qof_2 (Fig. 7). McFadden (1982) described a soil on the associated surface D and classified the soil as an S4 (pedon LDM 39A), indicating that has an age of between 70 ka and 13 ka. Comparison of the profile development index of this soil to values from the Cajon Pass chronosequence suggests that the soil is younger than 67 ka. This soil is most similar to Q1 in San Timoteo Badlands (62–37 ka; Table 7).

The ages determined by luminescence and by the degree of pedogenic development in our study differ from those recently reported by Owen et al. (2014), which were determined using cosmogenic surface dating of boulders in the Mission Creek alluvial complex. In our view, the ^{10}Be data reported by Owen et al. do not provide a consistent basis for assigning numerical ages to the geomorphic surfaces or their underlying depositional fills. Not only do ages for individual surfaces show considerable variation, but mean ages for the surfaces in some cases are out of sequence relative to their stratigraphic position in the overall alluvial complex. Finally, the ^{10}Be ages in general appear to indicate that the ages of surfaces A through D (their surfaces FM1–FM4) are compressed into a narrow interval of time, despite the clear evidence of progressively increasing morphometric and pedogenic development of these surfaces.

Long profiles of surfaces in the Mission Creek alluvial complex. When projected into a common plane, the profiles of the surfaces in the Mission Creek alluvial complex fall on two distinct trends (Fig. 8): a 10% grade that includes surfaces A and B, and a 5%–6% grade that includes surfaces C and D and the active channel. The downstream side of surface B_2 is

Downloaded from http://pubs.geoscienceworld.org/gsa/gsabulletin/article-pdf/127/5-6/825/3410110/825.pdf
by USGS Library user

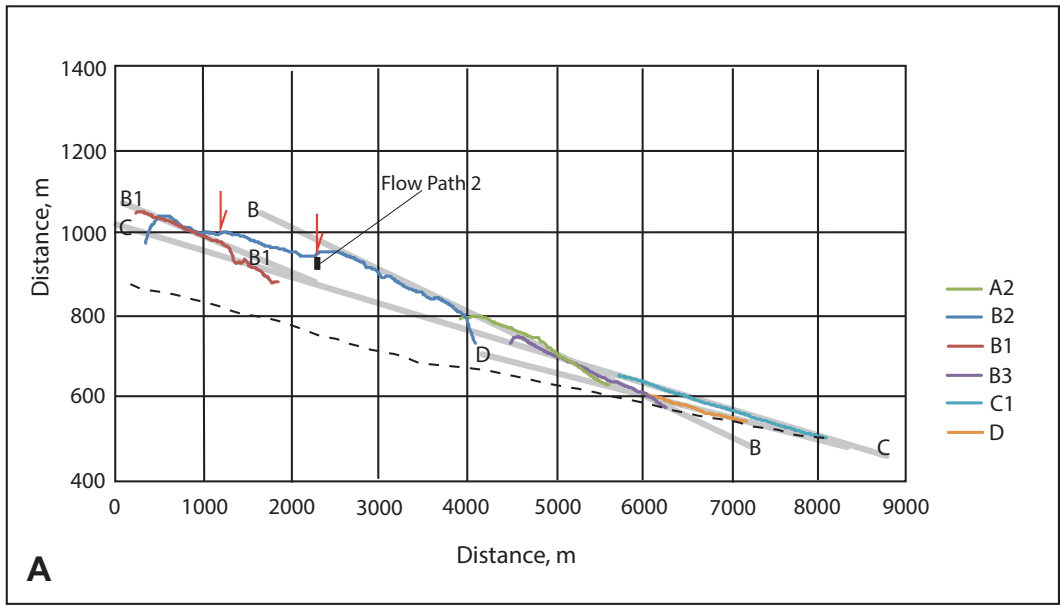

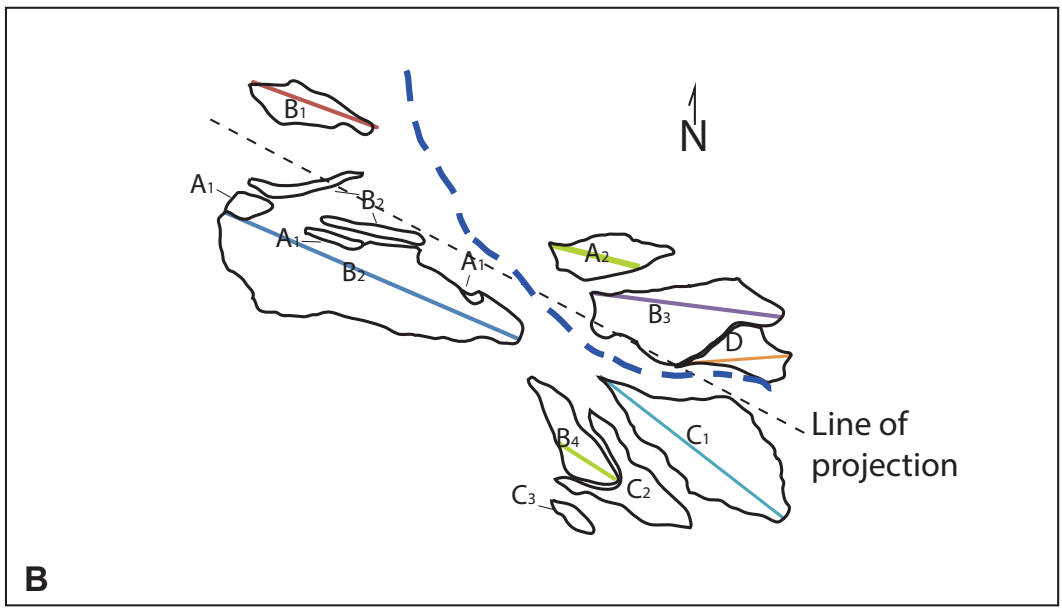

Figure 8. (A) Long profiles of the Mission Creek geomorphic surfaces. Dashed line is the active Mission Creek channel. Black bar is the elevation and location of flow path 2 (see Fig. 7B) at the time of formation. Note that it is significantly above the profile trend of surface C. Individual surfaces are shown in colored lines; gray lines depict overall trends for surfaces B, B_1, C and D. Note that there is a fivefold vertical exaggeration. Red arrows mark locations of unnamed faults where they intersect surface B_2. (B) Map view of surfaces in the Mission Creek Alluvial Complex, showing location of surface profiles shown in A. Blue dashed line is the flow path of the modern Mission Creek. Dashed gray line is the plane into which the profiles are projected in A. It is important to note that the deviation in trend between the slope of a surface and the plane into which the profile is projected will serve to make a slope appear greater.

aligned with surface B_3, further to the southeast. Both of these fall on a trend, shown as B on Figure 8A. Surface A_2 also falls on this trend, although the surface is somewhat irregular. The upper portion of B_2 has been offset and tilted by the unnamed faults that displace this surface (Fig. 7A). The northwestern part of the B_2 surface is parallel to, and at the same elevation as, the B_1 surface. We interpret this to mean that the unnamed fault may have extended far enough to the north to have disrupted and tilted the B_1 surface, although we were not able to directly map the structure this far (Fig. 7A).

Between the deposition and stabilization of surfaces B and C, tilting occurred, as evidenced by the difference in surface grade, elevating the A and B surfaces up to the northwest. The surface remnant of C is only slightly steeper than that of surface D (6% versus 5% grade). Both of these younger surfaces are essentially parallel to the local active stream, indicating that no observable tilt has occurred since the time of their formation. Surface D is elevated ~5 m above the current drainage (Fig. 8). Surfaces C and D and the active channel all grade to the same base level. We interpret the slight flaring upstream among the profiles of these surfaces to indicate erosion in the headwater region, consistent with other geomorphic observations.

Upper Raywood Flat

In plan view, surficial deposits in the Raywood Flat area form a Y-shaped pattern: adjacent to the San Gorgonio block, two alluvial lobes separated by a spur of crystalline rock converge southward into a single lobe that abuts a ridge of San Gabriel Mountains–type rocks before continuing east down the South Fork Whitewater River (Fig. 4). Here, the Raywood Flat alluvial sequence depositionally overlaps the broad crush zone of the Mission Creek fault. By contrast, the two northern alluvial lobes are faulted against the San Gorgonio Mountain block by the Mill Creek fault. Descriptions of the surficial deposits are presented in Table 2.

Downloaded from http://pubs.geoscienceworld.org/gsa/gsabulletin/article-pdf/127/5-6/825/3410110/825.pdf
by USGS Library user

Drainage reconstruction through upper Raywood Flat. The deposits in upper Raywood Flat highlight the bifurcated drainage system that created this intermontane lowland. The branched valleys terminate fairly abruptly in their upstream reach, where they have been beheaded by the trace of the Mill Creek fault. The South Fork, the drainage that currently flows through this intermontane low, is underfit to the canyons. We interpret that upper Raywood Flat preserves the former course of two drainages, which flowed across the Yucaipa Ridge block terrain, prior to disruption by uplift and lateral displacement along the Mill Creek strand. These two drainages joined at the southern end of upper Raywood Flat, then turned abruptly eastward and flowed along the crush zone of the Mission Creek fault (Fig. 4) within the canyon currently occupied by the South Fork.

The North Fork Whitewater and the Hell For Sure drainages, which currently flow to the Whitewater River, likely flowed through and formed upper Raywood Flat prior to slip on the Mill Creek fault. The width of each of these two drainages to the north of the Mill Creek fault matches well with the widths of the drainages in upper Raywood Flat (Fig. 9A). The spacing between these two drainages is slightly more than the spacing of the two valleys in upper Raywood Flat, which would be expected, as they represent the upstream extension of the Y-shaped stream juncture. They are located 7.3–8.5 km to the southeast, respectively. We assign an uncertainty of ±0.2 km to these measurements, resulting in a range of 7.1–8.7 km. Aggradation both from the flanks of Yucaipa Ridge and from the San Gorgonio block has filled upper Raywood Flat, though subsequent downcutting of the South Fork has incised these deposits. Incision has continued in the Hell For Sure and North Fork drainages, as evidenced by the deep, V-shaped valley morphology and lack of high preserved terraces along these drainages.

Reconstructing the long profiles of this restored drainage system indicates that there is ~930 ± 25 m elevation difference between the western drainage in upper Raywood Flat and the North Fork Whitewater River, and 950 ± 25 m between the eastern drainage in Raywood Flat and the Hell For Sure drainage (Fig. 9B). Because incision has continued on the north side, but a complex history of aggradation and subsequent incision has occurred on the south side of Mill Creek fault, we have assigned broad uncertainty to these values. Knickpoints in the Hell For Sure and North Fork drainages upstream from the Mill Creek strand indicate that incision occurred in response to the reorganization of the drainages by lateral slip along the Mill Creek strand, and we use the stream profile above these lowest knickpoints for purposes of reconstruction (Fig. 9B).

Erosion in the headwater region of the South Fork Whitewater drainage. Following the displacement of upper Raywood Flat to its current position, headward extension of the South Fork Whitewater River, which currently occupies this topographic lowland, has led to erosion in the flank of the San Gorgonio block (Fig. 3), on the south side of San Gorgonio Mountain. A reconstruction of paleotopography, accomplished by filling in the dissected portion of the landscape, indicates removal of ~31.5 km^3 of material over an area of 7 km^2 (Fig. 10).

DISCUSSION

Intersection of the Mill Creek and Pinto Mountain Faults

Previous Interpretations

The role of the Pinto Mountain fault in the architecture of the SAF system has been interpreted by various researchers and conveyed through their mapping of the traces of the faults in this region. Allen (1957) mapped a singular fault trace of the Mill Creek strand eastward from the Middle Fork Jumpoff and near the confluence of the Middle and South Forks, and he interpreted that the fault split into three strands, each of which terminated before reaching either the Pinto Mountain fault or the Mission Creek strand (Fig. 11A). By implication, any dextral displacement on the Mill Creek fault would be dispersed into distributed strain. Allen mapped the Pinto Mountain fault across the Middle Fork drainage and into the South Fork drainage. By contrast, Dibblee (1967) interpreted that the Mill Creek fault (his "North Branch, San Andreas Fault") split into two strands: one mapped by Allen that crosses the bedrock of Yucaipa Ridge, the second mapped by Dibblee down the active wash of Middle Fork and thence southeastward to the Mission Creek area and beyond (Fig. 11B). Dibblee (1967, 1968b, 1975) interpreted this strand as a throughgoing structure that *terminates* the sinistral Pinto Mountain fault.

Matti et al. (1982, 1983) adopted Allen's fault framework and mapped the Pinto Mountain fault westward across the Middle Fork drainage and into the wide crush zone of the Middle Fork drainage (Fig. 11C); like Allen, they interpreted the fault crossing bedrock of Yucaipa Ridge as a major (and only) splay of the Mill Creek fault, and extended it completely across the ridge where it appeared to truncate against the Pinto Mountain fault. To connect the Mill Creek fault on Yucaipa Ridge to its counterpart to the southeast in the Mission Creek area, Matti et al. (1982, 1983, 1985, 1992) assumed that sinistral slip on the Pinto Mountain fault had deformed the Mill Creek fault into a bend that disrupted its once-straight continuity between the South Fork and Middle Fork Whitewater River, although the implications of this were not explicitly discussed. In this interpretation, the Mill Creek fault can be viewed as a throughgoing strand of the SAF, rather than as a "dangling" fault that Allen viewed as ending at the southeast end of Yucaipa Ridge.

Findings of This Report

We refine the interpretation by Matti et al. (1982, 1983, 1985, 1992) by suggesting that the Mill Creek fault crush zone, where it crosses the Yucaipa Ridge block, has not merely been deformed by the Pinto Mountain fault but has been truncated and offset from a cross-fault counterpart concealed beneath young alluvial wash of the Middle Fork Whitewater River (Fig. 11D). This interpretation would explain why the Mill Creek strand to the west on the Yucaipa Ridge block does not actually meet the Mission Creek strand.

Implications of the Offset of the Mill Creek Fault by the Pinto Mountain Fault

Configuration of the junction between the Mill Creek and Mission Creek strands. Prior to disruption by the Pinto Mountain fault, the Mill Creek strand ostensibly was a throughgoing structure that splayed northeast away from the older Mission Creek strand, which, by this time, had been long abandoned by the SAF (Matti et al., 1985, 1992; Matti and Morton, 1993). Whether the Mill Creek strand initiated (1) by reactivation of the old Mission Creek trace or (2) by pioneering a closely associated fault within the latter's crush zone, the two strands southeast of the Whitewater River forks would have been closely spaced and would have trended southeasterly. However, west of the Whitewater River, where the Mission Creek fault crush zone gradually adopts a more westerly orientation, the zone would not have been compatible with SAF slip vectors. Accordingly, Matti et al. (1985, 1992) reasoned that, at the confluence of the Whitewater River forks, the Mill Creek strand initiated by stepping to the northeast of the Mission Creek crush zone. This new trace would have been aligned better with SAF slip vectors, as suggested by its regional orientation subparallel to the Coachella Valley and Mojave Desert segments of the SAF (Figs. 1, 2). These regional considerations make sense, but they do not address what the divergence zone between the Mill Creek and Mission Creek strands would have looked like.

Our hypothesis that the Pinto Mountain fault has truncated and sinistrally displaced the Mill

Downloaded from http://pubs.geoscienceworld.org/gsa/gsabulletin/article-pdf/127/5-6/825/3410110/825.pdf
by USGS Library user

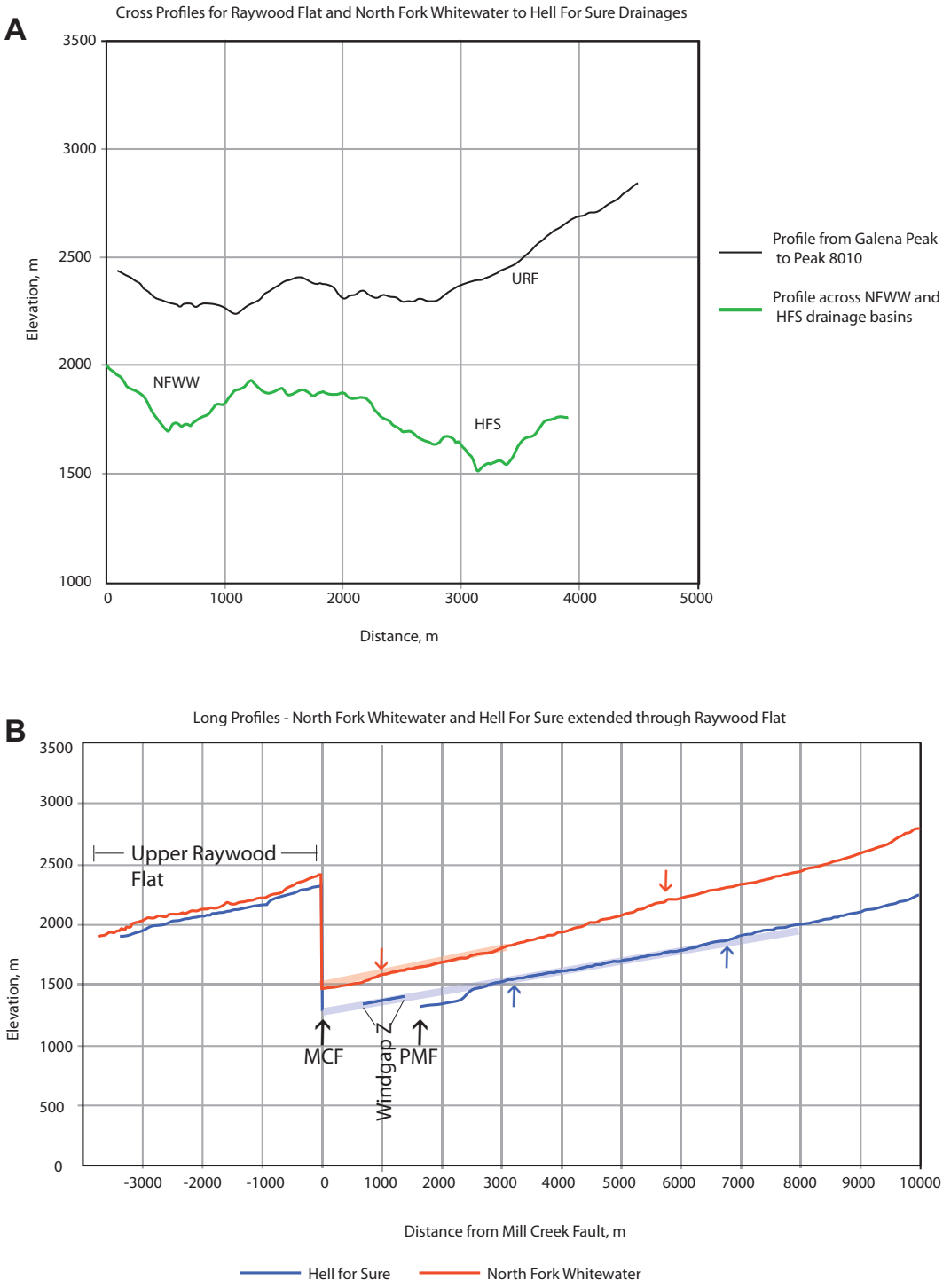

Figure 9. (A) Cross profiles for upper Raywood Flat (URF, black line) and North Fork Whitewater River (NFWW) and Hell For Sure (HFS) canyons (green line). Note that there is a twofold vertical exaggeration. Locations for these profiles are documented on Figures 4 and 3, respectively. (B) Long profiles of Hell For Sure (blue) and North Fork (red) canyons with counterparts in upper Raywood Flat. Note that there is a twofold vertical exaggeration. Note location the of wind gap Z in the profile of Hell For Sure. Locations of Mill Creek Fault (MCF) and Pinto Mountain Fault (PMF) are shown by black arrows. Blue and red arrows indicate the location of knickpoints in Hell For Sure and North Fork Whitewater Canyons, respectively. Thick transparent lines show smoothed drainage profiles of HFS and NFWW. Note that Windgap Z is positioned along the projected profile of HFS; reconstruction of the landscape indicates that this was an integrated drainage system prior to disruption by the Pinto Mountain Fault, as discussed in text.

Creek fault provides insight into this question. When 1–1.25 km of left slip is restored on the Pinto Mountain, the north-trending crush zone at the southeast end of the Yucaipa Ridge block that we (and Matti et al. [1982, 1983]) associate with the Mill Creek fault returns to a position close to the last observed occurrence of the strand southeast of the Middle Fork Whitewater River. There, the Mill Creek and Mission Creek faults either occupy the same trace or are closely spaced. Given this, and given that their separate paths farther west in SGP converge toward this coextensive reach, the point where the two faults originally would have diverged can be constrained to a small area near where the Middle Fork and South Fork Whitewater River currently join. Here, in order to acquire its west-northwest path along the Middle Fork Whitewater River (Fig. 6), the Mill Creek strand would have had to splay northward away from the Mission Creek strand. Restoration of ~1–1.25 km of left slip on the Pinto Mountain fault returns the Mill Creek strand on the Yucaipa Ridge block to a position where its north-trending orientation makes sense. There, at the mouth of the Middle Fork Whitewater River, all that is needed to connect this trace of

Downloaded from http://pubs.geoscienceworld.org/gsa/gsabulletin/article-pdf/127/5-6/825/3410110/825.pdf
by USGS Library user

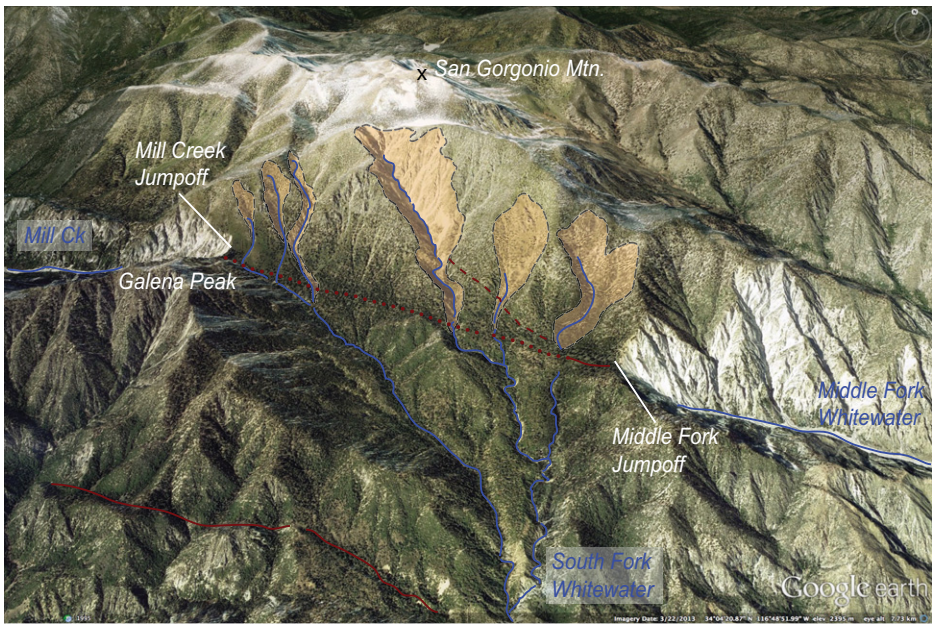

Figure 10. Headwater region of South Fork Whitewater River, showing removal of material (in peach color) by headward erosion onto the San Gorgonio block. View is to the north. Scale is not possible to accurately depict on this oblique view, but, for reference, the distance between the Mill Creek and the Middle Fork Jumpoffs is ~4.2 km. Red lines are partial representation of faults; Mission Creek Fault in the foreground, and Mill Creek Fault in the middle of the figure, dashed across upper Raywood Flat (between Mill Creek and Middle Fork Jumpoffs).

the fault with its counterpart to the southeast is a short concealed segment that we infer between the two bedrock traces. This inferred segment would curve from the last-documented orientation of approximately N80°W to a north-trending orientation as it approached the intersection with the Pinto Mountain fault, in order to efficiently jump the Mill Creek strand eastward to its path up the Middle Fork Whitewater.

Termination of throughgoing slip along the Mill Creek strand of the SAF. Our interpretation of the fault interactions in SGP indicates that there has been no dextral slip on the Mill Creek fault since it was offset by the Pinto Mountain fault. Disruption of the trace of the Mill Creek strand by sinistral displacement along the Pinto Mountain fault can address the following issue which has been puzzling. That is, the Mill Creek strand of the SAF is better aligned with the plate motion than the configuration that is currently carrying the plate motion, along the San Bernardino–Banning and Garnet Hill strands of the SAF, linked by the San Gorgonio Pass fault. Indeed, three-dimensional modeling confirms maximum dextral efficiency during the time of activity of the Mill Creek strand (Cooke and Dair, 2011). Abandonment of this strand requires a shift in stress regime or some other driving force. Offset of this strand by the Pinto Mountain fault effectively explains this conundrum.

Recent sinistral motion on the Pinto Mountain fault. Although the Pinto Mountain fault system is recognized to have late Quaternary activity, as evidenced by morphometry (Bryant, 2000), and paleoseismicity documenting four to five Holocene earthquakes (Cadena et al., 2003, 2004), it is generally considered to be a low-activity fault zone (Bryant, 2000; WGCEP, 2008). However, the available data on this fault zone are extremely limited and are considered inadequate to determine a long-term geologic slip rate (WGCEP, 2008). A significant implication of our mapped solution for the northern SGP regions is that the western end of the Pinto Mountain fault has been more active recently than the Mill Creek strand of the SAF.

One of the reasons that the Pinto Mountain fault is considered to have low activity is the low rate of historical seismicity. Regional seismicity between A.D. 1977 and 1985 indicates that the Pinto Mountain fault was dominantly aseismic during this time interval (Williams et al., 1990). Very limited seismicity occurred along the westernmost extent of the fault, however, and yields focal mechanisms consistent with left-lateral motion along N45°E orientations.

The Pinto Mountain fault did not show evidence of seismogenesis during the Landers earthquake sequence of 1992 (Hauksson et al., 1993). Seismicity patterns during the period 1981–1992 show the dextral motion associated with the Joshua–Big Bear–Landers earthquake sequence in a cross-cutting relation to the east-oriented left-lateral fault plane solutions associated with the eastern Transverse Ranges (Seeber and Armbruster, 1995). However, seismicity to the south of the Pinto Mountain fault was generated by an aftershock sequence that occurred ~3 min after the main shock, and propagated toward the south (Hough et al., 1993), suggesting a break in the seismicity across the Pinto Mountain fault.

Geodetic models demonstrate contrasting slip rates for the Pinto Mountain fault. Meade and Hagar (2005) developed a complex geodetic model of southern California, with 24 fault-bounded blocks. In this model, the Pinto Mountain fault is found to exhibit 9.4 ± 0.9 mm/yr sinistral slip, with a locking depth of 10 km and a simple two-layer rheology model. In an alternate analysis, Spinler et al. (2010) proposed different fault-block scenarios that result in slip rates along the western Pinto Mountain fault ranging from 0.7 ± 0.2 mm/yr dextral to 3.8 ± 0.1 mm/yr sinistral.

Precariously balanced rocks of undetermined age are located just north of the fault between Morongo and Yucca Valleys (Brune et al., 2010). Without age control and a complete understanding of the geomorphic setting and erosional history of these rocks, we cannot know the significance of their presence. Displacements, probably Holocene, have occurred east of these precariously balanced rocks, where discontinuous scarps in Quaternary alluvium occur between the communities of Yucca Valley and Joshua Tree (Fig. 1). However, the stratigraphy and age of the alluvial deposits have not been documented other than by general age estimates based on the development of soil properties and the degree of desert pavement formation (Bryant, 2000; see also the general geologic setting presented by Nishikawa et al. [2003] based on unpublished geologic mapping by J.C. Matti).

In the northern SGP region, information about the Pinto Mountain fault is known mainly from reconnaissance geologic mapping by Dibblee (1967) and Matti et al. (1988), and from groundwater investigations (Bader and Moyle, 1958). In the Morongo Valley area, the fault is concealed by young Quaternary alluvial deposits but forms prominent scarps in older Quaternary deposits that probably are middle or late Pleistocene in age (Matti et al., 1988). Traced westward to the Whitewater River (Fig. 6), the fault forms conspicuous crush zones in crys-

Downloaded from http://pubs.geoscienceworld.org/gsa/gsabulletin/article-pdf/127/5-6/825/3410110/825.pdf
by USGS Library user

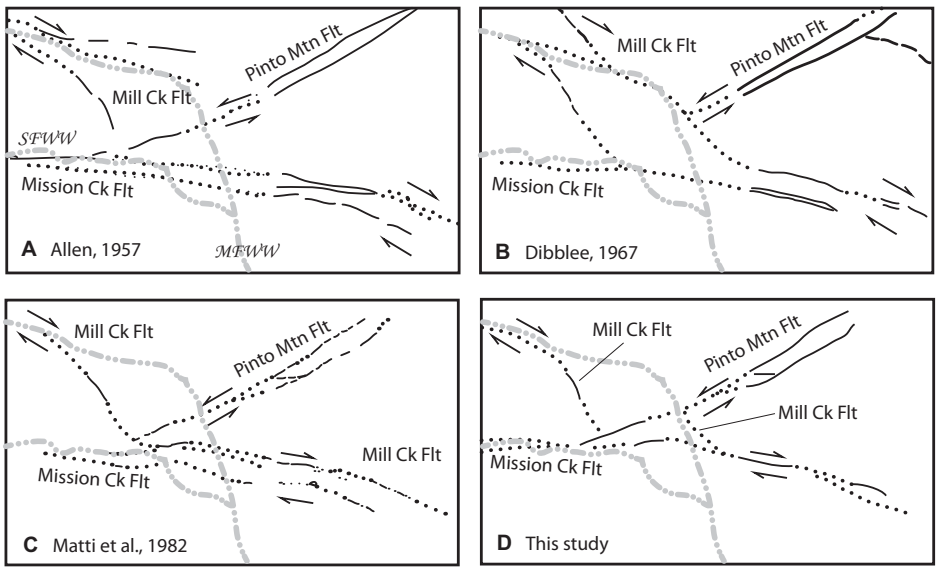

Figure 11. Schematic presentations of different interpretations of the intersection of the Mission Creek, Mill Creek, and Pinto Mountain faults. (A) Allen (1957) mapped the Mill Creek fault splaying into three strands, each of which terminates before reaching either the Pinto Mountain fault or the San Andreas fault (MFWW—Middle Fork Whitewater River; SFWW—South Fork Whitewater River). (B) Dibblee (1967) splayed the Mill Creek fault (his "North Branch, San Andreas fault") into two strands. Dibblee (1967, 1968b, 1975) interpreted one strand as a throughgoing structure that terminates the sinistral Pinto Mountain fault. (C) Matti et al. (1982, 1983, 1985, 1992) assumed that sinistral slip on the Pinto Mountain fault had deformed the Mill Creek fault into a bend. (D) This study. The Mill Creek fault crush zone where it crosses the Yucaipa Ridge block has been truncated and displaced from a cross-fault counterpart concealed beneath young alluvial wash of the Middle Fork Whitewater River (Fig. 6).

talline rocks and locally forms scarps in older Quaternary deposits. Further research is clearly needed to constrain slip rates along the Pinto Mountain fault.

Sinistral slip on the Mission Creek fault. Our reconstruction of the sinistral offset of the Mill Creek strand by the Pinto Mountain fault also has implications for the most recent motion along the Mission Creek fault. In order for left slip on the Pinto Mountain fault to have truncated and offset the Mill Creek fault but not similarly affected the Mission Creek fault, sinistral slip from the Pinto Mountain fault must have fed into the Mission Creek crush zone that trends up the South Fork Whitewater River. We base this interpretation on the fact that the Pinto Mountain fault meets the Mission Creek crush zone at a low oblique angle, suggesting that the two faults physically merge (Figs. 1, 6). This poses kinematic problems comparable to those where other left-lateral strike-slip faults interact with the SAF (e.g., left-lateral faults of the eastern Transverse Ranges; Powell, 1993b; Dickinson, 1997; Langenheim and Powell, 2009). This sinistral motion may help to explain the enigmatic fault scarps in the South Fork drainage, and may continue onto the Galena Peak fault. Sinistral motion along the broad restraining curve that links the Mission Creek and Pinto Mountain fault systems would be expected to resolve as up-to-the-north displacement along faults with this orientation, consistent with what is observed.

Palinspastic Reconstruction of the Pinto Mountain and Mill Creek Faults

Restoring 1–1.25 km of sinistral slip on the Pinto Mountain fault, by aligning the trace of the Mill Creek fault (u-u′ on Fig. 12), rearranges the drainage net of the Mission Creek drainage system. Matches within this drainage system include offsets indicated by w-w′, x- x′, y-y′, and z-z′ (Fig. 12). Prior to the 1.25 km displacement along the Pinto Mountain fault, the Hell For Sure drainage was aligned with wind gap Z (offset v-v′ in Fig. 12; long profile in Fig. 9). The slope and position of the wind gap matches the long profile of the Hell For Sure drainage, above the lowest knickpoint (Fig. 9). We interpret that wind gap Z and the Hell For Sure drainage were part of an integrated drainage prior to slip on the Pinto Mountain fault.

Wind gap Y is located near the juncture of the North Fork and the Middle Fork Whitewater River (Fig. 12). Prior to the displacement along the Pinto Mountain fault, the southeastern end of this wind gap was positioned to flow into the Middle Fork, just above its confluence with the South Fork. This distinctive gap in the ridgeline marks an important element in the landscape. It follows the Mill Creek fault and displays the distinctive wide crush zone associated with this fault strand. This feature may have been formed when the North Fork and Middle Fork flowed through this canyon. It is not clear, however, when this flow occurred or what event caused the flow to be captured toward the Hell For Sure drainage. Uplift of the Yucaipa Ridge block, discussed below, would be expected to affect the slope of this feature. Currently the slope of wind gap Y is significantly higher than that of either the North Fork or the Middle Fork Whitewater River.

Drainage Reconstruction During Intervals of Slip along the Mill Creek Fault

The reconstruction of the drainages across the Mill Creek strand allows us to better understand the fault history of both the Mill Creek strand and the Pinto Mountain fault. Here we present our proposed solution for the complex geometry of the drainages in their present configuration.

Prior to Slip on the Mill Creek Strand

In order to examine the distribution of landforms at different times in the slip history of the Mill Creek strand, we need to first restore the 1–1.25 km of sinistral slip on the Pinto Mountain fault, as discussed above (Fig. 12). Then, to consider the landscape prior to slip along the Mill Creek fault, we restore the maximum indicated by the reconstructed drainage system, ~8.7 km of dextral slip along that fault (Fig. 13A). With this palinspastic reconstruction, upper Raywood Flat was positioned downstream of the North Fork and Hell For Sure drainages. We hypothesize that the North Fork and Hell For Sure drainages flowed through wind gaps Y and Z, respectively, before joining in upper Raywood Flat and flowing down the South Fork drainage. Below upper Raywood Flat, the South Fork flowed eastward along the canyon formed in the crush zone of the Mission Creek fault. Mission Creek was positioned on a path to flow to the west of Wathier Hill (denoted by "w" in Fig. 13H). At the northwestern end of the island, the Mission Creek and all of the tributaries of the Whitewater drainage system joined, resulting in a contributing area of roughly 120 km^2. Flow of the drainage system was confined in a fault-parallel valley that was bound to the north-

Downloaded from http://pubs.geoscienceworld.org/gsa/gsabulletin/article-pdf/127/5-6/825/3410110/825.pdf
by USGS Library user

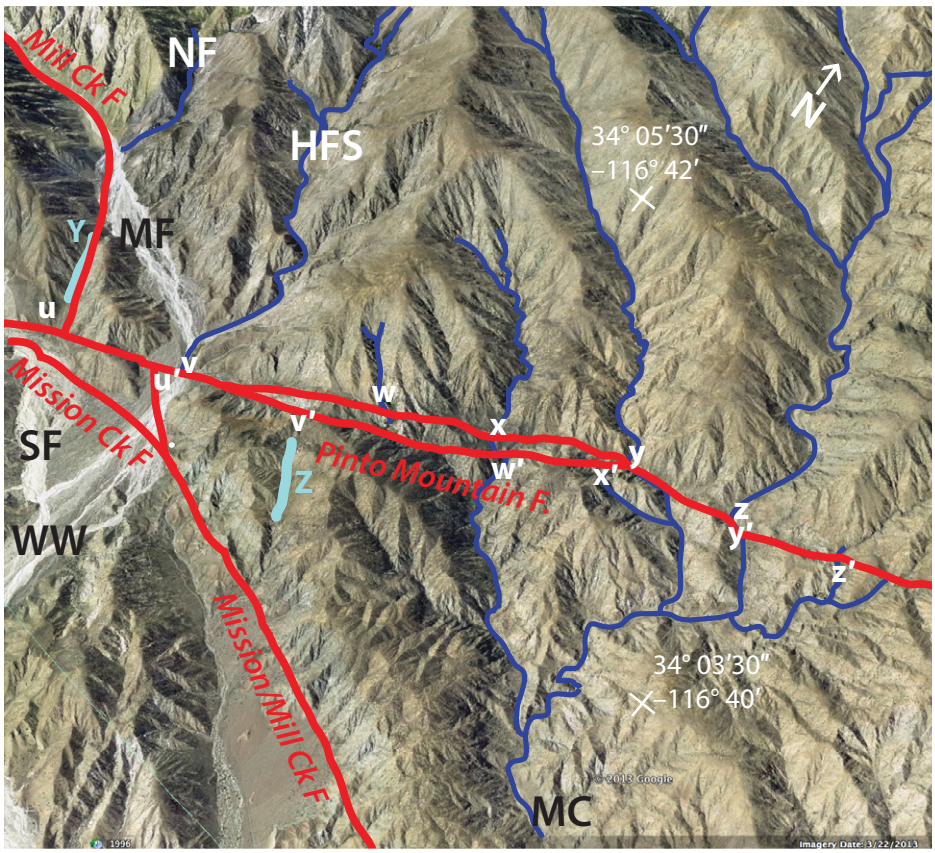

Figure 12. Pinto Mountain fault, showing match points for most recent 1–1.25 km sinistral displacement. Wind gaps Y and Z are shown as light blue lines and labels. Since view is oblique, scale cannot be accurately represented for the entire figure. The distance from u to u′ is 1.25 km; the distance from z to z′ is 1.3 km. Drainages are: North Fork Whitewater River (NF), Hell For Sure Canyon (HFS), Middle Fork Whitewater River (MF), South Fork Whitewater River (SF), Whitewater River (WW), and Mission Creek (MC).

east by the escarpment of the Mission Creek strand, and to the southwest by a high ridgeline of Miocene Coachella Fanglomerate. This linear valley was ~2.5 km wide. Note that in Figures 13A–13B we do not show fluvial flow down the modern Whitewater Canyon. We interpret that the canyon did not exist during this time frame; in its place we infer that the high ground of Miocene Coachella Fanglomerate now forming the east margin of the modern canyon was continuous to its west margin now formed by crystalline rocks of San Gabriel Mountains type.

Initial Displacement of the Mill Creek Strand: 0–3.25 km

The Mill Creek strand became active, and after ~0.75 km of lateral motion, Mission Creek was displaced into a position where flow was blocked by the bedrock that would form the future Wathier Hill. Flow toward the east-southeast around the eastern side of this obstruction helped to form the streamlined morphology of the island hill that is present today, although the drainages were more shallowly etched on the landscape. At the same time, lateral slip along the Mill Creek fault, combined with uplift of the Yucaipa Ridge block (discussed below), separated the upper Raywood Flat region from its headwaters. The North Fork and Hell For Sure drainages were forced to deflect to the east around the rising Yucaipa Ridge block (further discussed below) and establish a flow path along the Mill Creek fault zone. Headward erosion would begin along the Mill Creek fault to the west of the intersection of the North Fork with the fault zone, the initiation of the Middle Fork drainage.

After ~3.25 km of slip on the Mill Creek strand, Mission Creek was positioned to initiate flow down an ancestral Whitewater Canyon (Fig. 13C), by way of flow around the eastern side of Wathier Hill. We interpret that at this time the Whitewater drainage system continued to flow on the west side of Wathier Hill, and the two drainages joined just downstream from the northeastern end of the island. This flow path of the Mission Creek drainage, to the east of Wathier Hill, corresponds to the trace of the Whitewater fault. Fractured rock would have allowed this drainage route to be more readily occupied than a path in the surrounding intact bedrock. During this time interval, drainage that once flowed directly toward Coachella Valley by way of the narrow, linear, intermontane valley, in which units $Qvof_2$ and $Qvof_3$ were deposited, was now captured toward the south and joined with the San Gorgonio River. We would propose that this diversion of the flow of the combined drainages was precipitated by regional uplift and tilting of surfaces A and B in the Mission Creek alluvial complex. Evidence for this uplift and tilting is demonstrated in the long profiles of these surfaces (Fig. 8), and the potential cause will be further discussed below. High terraces are present throughout Whitewater Canyon, which we interpret to have been deposited at this time interval. Dating of these is planned for future research.

Continued Lateral Slip of the Mill Creek Strand: Approximately 4–6 km

After further lateral displacement along the Mill Creek fault, Mission Creek was blocked from easy access to Whitewater Canyon by the high ground just to the west-northwest of our surface B_1, and carved a prominent flow path, referred to as "dry tributary" (flow path 1, Fig. 7B), that is incised into unit $Qvof_3$, isolating surfaces B_1 and B_2 (Figs. 13D, 7B). This marks an important milestone in the evolution of the drainages and the alluvial deposits. At approximately the time represented by 4 km of slip, Mission Creek was separated from the Hell For Sure and the Whitewater tributary drainages, which continued to flow down Whitewater Canyon. Subsequently, deposits within the Mission Creek alluvial complex would reflect flow from the modern Mission Creek catchment area, rather than flow from the combined Mission Creek and Whitewater drainage basin areas. Flow by Mission Creek continued along this dry tributary until ~6 km of displacement along the Mill Creek fault, at which time flow was positioned against the northern edge of surface B_1. We hypothesize that the flow diverted to the east of surface B_1, eroding the fault escarpment along a curved, convex-to-the-northeast path (shown as flow path 2 on Fig. 7B, and positioned on the plot of long profiles in Fig. 8A), before occupying the modern drainage path at the southeastern end of surface B_1 (Fig. 13E).

Termination of Slip along the Mill Creek Fault: Approximately 7.1–8.7 km

After ~8.7 km of slip had occurred along the Mill Creek fault, the Mission Creek drainage

Downloaded from http://pubs.geoscienceworld.org/gsa/gsabulletin/article-pdf/127/5-6/825/3410110/825.pdf
by USGS Library user

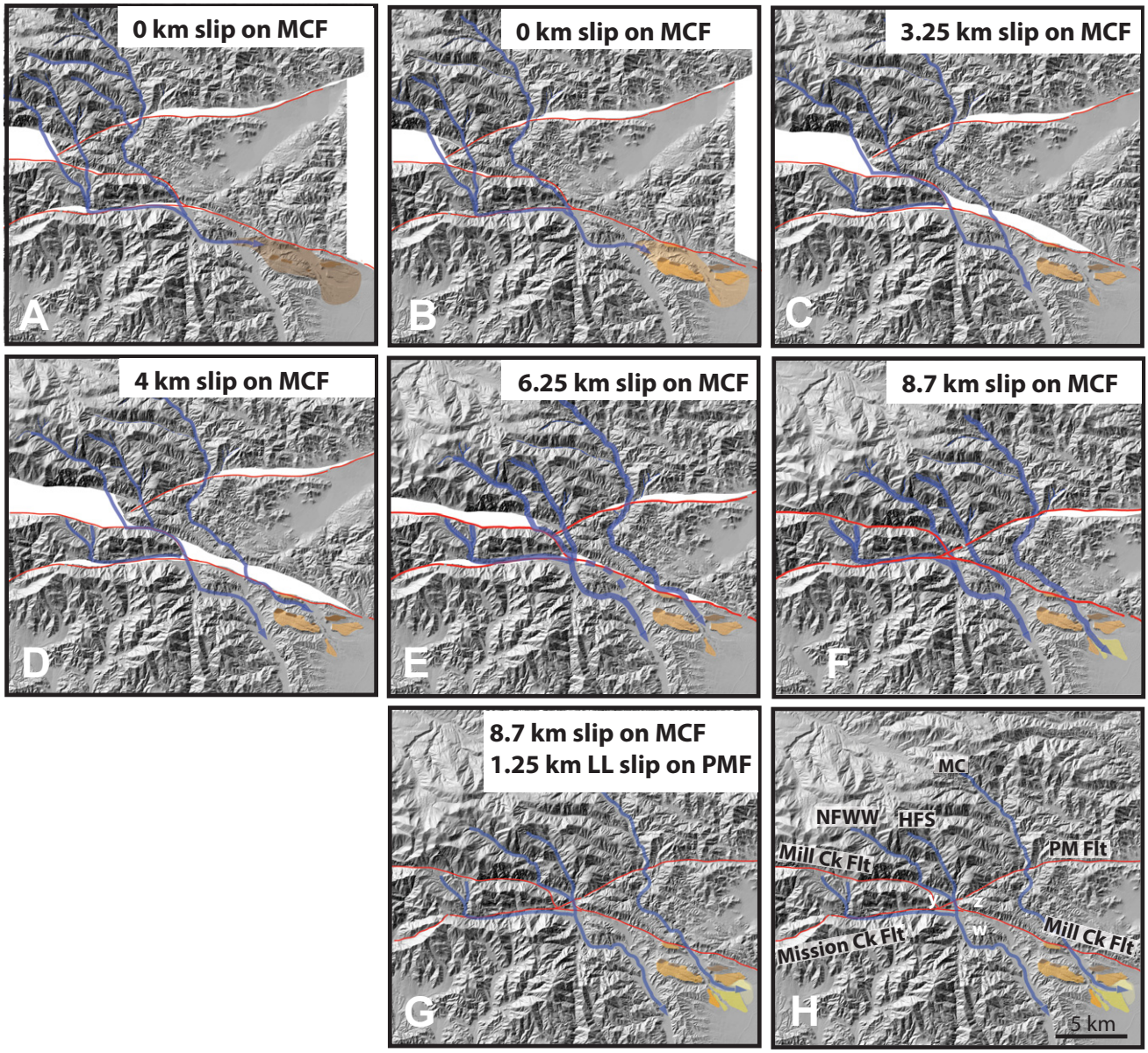

Figure 13. Reconstruction of drainage system disrupted by faulting. Hell For Sure Canyon and North Fork Whitewater River are aligned to flow through upper Raywood Flat. (A) Initial time in reconstruction. 1.25 km of sinistral slip has been restored along the Pinto Mountain fault, and 8.7 km of dextral slip has been restored along the Mill Creek strand. Combined flow from Mission Creek and Whitewater drainages flows along a corridor adjacent to the Mission Creek escarpment of the San Andreas fault. Here we depict deposition of unit $Qvof_2$ (light brown), although we discuss timing options in the text. Dark brown indicates preserved surfaces on this unit. (B) Same position of landscape as in A, with no fault motion along the Mill Creek fault. Deposition of unit $Qvof_3$ is shown (light orange), with preserved surface B remnants (dark orange). Again, timing for this deposition in relation to fault position is discussed in the text. (C) After ~3.25 km slip along the Mill Creek strand, Mission Creek flows along the eastern side of Wathier Hill ("w" in H) and establishes a flow path for the first time along the Whitewater fault, forming the trunk drainage of the Whitewater River. This occurs because uplift of surfaces A and B, in response to a rising landscape, defeats the previous drainage pathway. (D) After ~4 km of slip along the Mill Creek strand, Mission Creek is blocked from further flow down the Whitewater trunk drainage, and is positioned to occupy the course of the "dry tributary". Separation of flow between the Mission Creek and Whitewater catchment areas occurs. (E) After ~6.25 km of slip along the Mill Creek strand, Mission Creek bypasses surface B_1, developed on unit $Qvof_3$, and forms a curved strath surface north of the Mill Creek fault and just east of current drainage (see Fig. 7B for more detail). (F) After slip is complete on the Mill Creek strand (~8.7 km of slip), deposition of unit Qof_2, within the Mission Creek drainage, occurs by way of flow path 3 (see Fig. 7B for detailed view). Hell For Sure continues to flow through wind gap Z and along the eastern side of Wathier Hill. (G) Pinto Mountain Fault left-lateral (LL) slip of between 1–1.25 km offsets the Mill Creek strand (see Figs. 6 and 11), separates Hell For Sure from windgap Z (see Fig. 12), and creates the current landscape. (H) Locations of features, shown on the current landscape. Drainages: Hell For Sure (HFS), North Fork Whitewater (NFWW), and Mission Creek (MC). Faults: Mill Creek, Mission Creek, and Pinto Mountain (PM). w—Wathier Hill; y and z—wind gaps.

Downloaded from http://pubs.geoscienceworld.org/gsa/gsabulletin/article-pdf/127/5-6/825/3410110/825.pdf
by USGS Library user

was flowing down its modern thalweg where it intersects the Mission Creek alluvial complex (Fig. 13F). Hell For Sure, aligned with wind gap Z, was in position to reoccupy the flow path along the eastern side of Wathier Hill. At this time, flow along this course incised into, and beheaded, the dry tributary. We show the North Fork, along with the headward-lengthening Middle Fork, continuing to flow through wind gap Y, and then along the modern course of the Whitewater River. As previously stated, we do not know the cause for abandonment of the stream course through wind gap Y, so we do not know the timing of the capture toward Hell For Sure.

During the above intervals of time, corresponding to the entire range of slip along the Mill Creek fault, we interpret that the Pinto Mountain fault was inactive. We base this interpretation on the lack of complexity at the intersection between the Mill Creek strand and the Pinto Mountain fault. Following the final slip along the Mill Creek strand, the Pinto Mountain fault experienced 1–1.25 km of displacement (Fig. 13G), offsetting the Mill Creek strand, as discussed previously.

Drainage Reconstruction—Implication for Uplift of Structural Blocks

Yucaipa Ridge is characterized by extremely steep slopes and dominated by high-energy deposition, including debris flows and debris avalanches (Morton et al., 2008). Spotila et al. (1998, 2001) proposed that the Yucaipa Ridge has experienced relatively recent, rapid uplift. Very young apatite (U-Th)/He ages and fission-track analysis (Blythe et al., 2002) suggest that the ridgeline has been uplifted 3–4 km. The thermochronologic models suggest that the block experienced very rapid uplift, with rates as high as 7 mm/yr during the interval 1.65–1.25 Ma. Following this rapid uplift, an additional 1–2 km of uplift is proposed during the interval 1.25 Ma to present, although the models do not constrain the temporal distribution of this uplift within this interval of time (Blythe et al., 2002). Data from Spotila et al. (1998, 2001) and their resulting model that the Yucaipa Ridge block has been uplifted ~1 km higher than the San Gorgonio block. The denudation rates that result from this modeled uplift history agree well with the shorter-term denudation rates determined using cosmogenic ^{10}Be concentrations (Binnie et al., 2008).

The reconstruction of drainages proposed in this study allows us to provide further evidence as to the history of uplift of these two blocks. The deep incision of the drainage system of Hell For Sure and North Fork Whitewater through upper Raywood Flat suggests that both the Yucaipa Ridge and San Gorgonio blocks were being actively uplifted. This may have been in response to oblique motion along the Mission Creek strand, as the strand became rotated counterclockwise with respect to the plate motion vector. Following inception of the Mill Creek strand, and lateral displacement and beheading of the upper Raywood Flat drainage system (Figs. 13C–13F), there has been ~975 ± 70 m of uplift on the Yucaipa Ridge block relative to the San Gorgonio block (Fig. 9B). Because the Mill Creek strand forms the structural boundary between these blocks, it is not unexpected that the differential uplift between the Yucaipa Ridge and San Gorgonio blocks occurred during the time of activity of this fault system. We also hypothesize that the uplift of the Yucaipa Ridge block would have affected the surrounding landscape to some extent. Incomplete decoupling between the Yucaipa Ridge block and the terrain to the south and east, separated by the abandoned Mission Creek strand, would be expected to have caused uplift along surrounding terrain as well. We interpret that this is the cause of the increased tilt of surfaces A and B, relative to surfaces C and D and the active channel in the Mission Creek alluvial complex (Fig. 8).

Linkage Between Deposition of the Mission Creek Alluvial Complex and Fault Offset

The alluvial complex in Mission Creek reveals a depositional history that resulted from drainage capture and rearrangement, due to slip along the Mill Creek strand. Here we explore the utility of the age control in constraining the timing of slip along this fault strand.

Depositional History of Units $Qvof_2$ and $Qvof_3$, Mission Creek Alluvial Complex

Deposition of the alluvial complex in Mission Creek began with the emplacement of unit $Qvof_2$. The original extent of unit $Qvof_2$ is not known, but it presumably extended upstream beyond the preserved remnants. Deposition was confined to the fault-parallel valley described above. An extended period of landscape stability occurred following the deposition of unit $Qvof_2$, as indicated by the extremely well-developed duripan in the associated soil profile. Although soils associated with both units $Qvof_2$ and $Qvof_3$ (on surfaces A and B, respectively) are both determined to be older than 500 ka, based on correlation with dated soils, surface A is significantly older than surface B. At some point following deposition of unit $Qvof_2$, the associated surface A was displaced by the pair of unnamed faults (Fig. 7B) discussed previously. Subsequent erosion isolated the surface remnants, designated A_1 in Figure 7B and shown in darker brown on Figure 13A.

Deposition of unit $Qvof_3$ followed this erosional episode, filling in around isolated surface A uplands developed on unit $Qvof_2$. As currently preserved, unit $Qvof_3$ is a more extensive deposit than unit $Qvof_2$, although it is not known to what extent unit $Qvof_2$ was eroded prior to and during the deposition of unit $Qvof_3$. Unit $Qvof_3$ was also deposited in the linear, fault-parallel valley. Extensive incision into these high surfaces associated with units $Qvof_2$ and $Qvof_3$ in the Mission Creek alluvial complex followed, resulting in the prominent east-west–oriented, deeply incised ridge-and-ravine pattern on these surfaces. Uplift and tilting of surfaces A and B occurred prior to subsequent deposition.

A major drainage rearrangement followed the deposition and erosion of units $Qvof_2$ and $Qvof_3$. Flow down the linear valley from the northwest was replaced with a flow path that bisects the valley and the contained deposits. Incision occurred at a high angle to the depositional and erosional texture of surfaces A and B.

In our reconstruction we show the deposition and erosion of units $Qvof_2$ and $Qvof_3$ as occurring prior to the initiation of slip on the Mill Creek strand (Figs. 13A–13B). We propose this timing because the long profiles of the associated surfaces, A and B, are parallel to each other, are nearly congruent, and are tilted the same amount (Fig. 8). Because we attribute the tilting to motion along the Mill Creek strand, we conclude that these deposits preceded this motion.

Depositional History of Units Qof_2 and Qof_3, Mission Creek Alluvial Complex

Following the interval of downcutting and erosion that removed much of units $Qvof_2$ and $Qvof_3$, unit Qof_2 was deposited unconformably as an alluvial fan on a strath surface developed on those older units and on various bedrock units. The apex of the unit Qof_2 fan points toward the upper portion of the deeply incised modern Mission Creek wash that transects the entire nested alluvial complex. This indicates that unit Qof_2 streamflows coursed through the same upper incised wash that currently is occupied by modern Mission Creek streamflows. The longitudinal axial crest of the alluvial fan (associated with surface C) is located near flow path 3 (Fig. 7B), with the deposits symmetrically distributed from that central location, suggesting that this was the route of deposition. Luminescence dating of the deposits, combined with the age estimate of the associated soil, indicates that this unit was deposited by ca. 100 ka. The tributary that deposited unit Qof_2 (flow path 3 in Fig. 7B) was abandoned by capture along the lower portion of the modern stream course (Fig. 13F).

Downloaded from http://pubs.geoscienceworld.org/gsa/gsabulletin/article-pdf/127/5-6/825/3410110/825.pdf
by USGS Library user

The final history of this alluvial complex, as considered in this study, was the emplacement and incision of unit Qof_3 (Fig. 13G).

It is difficult to determine the position of Mission Creek, upstream of the Mill Creek fault, when unit Qof_2 was deposited. It is possible that it occurred at any time during the interval represented by the amount of displacement along the Mill Creek strand (4–8.7 km) shown in Figures 13D–13F, because during those intervals the drainage occupied the same path just south of the Mill Creek fault. We prefer the interpretation that this deposition occurred at the position represented by Figures 13E–13F, when the slip along the Mill Creek strand was complete or nearly complete. We prefer this interpretation for three reasons. First, the long profiles of surfaces C and D parallel the active channel, all graded to a common base level. We interpret this to mean that these surfaces post-date the uplift and tilting of the landscape toward the east, a function of lateral slip along the Mill Creek strand. The slight differences in the slopes of these surfaces (C, D, and the modern wash) can be attributed to erosion in the headwaters. This is in agreement with the erosion that was responsible for isolating wind gap Z, following cessation of motion along the Mill Creek strand and the initiation of motion along the Pinto Mountain fault.

Second, since upper Raywood Flat has been in its current position, following cessation of slip along the Mill Creek strand, headward extension of the South Fork drainage onto the San Gorgonio block has resulted in the erosion of ~31.5 km^2 of material (Fig. 10). We apply an independently determined, long-term erosion rate of 270 ± 28 mm/yr, measured nearby on the San Gorgonio block (Binnie et al., 2008), to determine that ~130–106 k.y. is required to erode this volume. This suggests that slip along the Mill Creek strand was complete by about this time.

Finally, for the Pinto Mountain fault to have offset the Mill Creek strand by 1–1.25 km in the past ~100 k.y. requires a slip rate for the Pinto Mountain fault of ~10–12.5 mm/yr. This is significantly higher than most previously estimated slip rates. If the Mill Creek strand has continued to be active more recently than ca. 100 ka, as would be the case if unit Qof_2 pre-dated final slip on the Mill Creek strand, then slip rate on the Pinto Mountain fault necessarily would be even greater.

Slip Rates

Prior slip-rate estimates for the Pinto Mountain fault range from ~1 to 5 mm/yr, based on inferred ages of offset units (Anderson, 1979; Bird and Rosenstock, 1984; Wesnousky, 1986; Peterson and Wesnousky, 1994), and modern geodetically measured slip rates range up to ~9 mm/yr (Meade and Hagar, 2005). We would propose that the slip rate on the Pinto Mountain fault has been temporally variable. Our study suggests that for a limited time in the recent geologic history, the slip rate on the Pinto Mountain fault was significantly higher than these previous determinations. Between 1 and 1.25 km of slip along the Pinto Mountain fault offset and disrupted the Mill Creek strand following its cessation of slip. If the entire slip amount along the Mill Creek strand was completed by the time of emplacement of deposits associated with surface C_1, with a preferred age estimate of ca. 100 ka, then the slip rate on the Pinto Mountain fault would be ~1 cm/yr for this interval. If the emplacement of surface C_1 occurred prior to complete slip on the Mill Creek strand (e.g., emplaced at time indicated by Fig. 13E rather than that of Fig. 13F), then the slip rate on the Pinto Mountain would be higher. The Pinto Mountain fault seems to have not been active during the time of activity along the Mill Creek strand; had it been, it would have repeatedly offset and complicated the trace of this very linear fault strand. If the Pinto Mountain fault was inactive when the Mill Creek strand was active, then the slip rate, averaged over this much longer time interval, would be quite low.

CONCLUSIONS

This study examines the history of plate motion along the SAF in the complex SGP. It is important to understand this region because the seismic hazard assessment for the greater Los Angeles basin, home to more than 18 million people, depends on how earthquake energy is transmitted through this complex zone (Jones et al., 2008). The SAF system in SGP has experienced a long history of fault strand switching. Evidence of the strand switching history is preserved in the complex fault structure, in the presence of inactive, subparallel fault strands, and in the regional geomorphology, and contrasts with the simpler fault geometries to the north and south of the Transverse Ranges. The Mill Creek strand of the SAF has been active more recently than the Mission Creek strand, and the Pinto Mountain fault has laterally displaced the Mill Creek strand, terminating activity on that strand.

Between 7.1 and 8.7 km of total dextral slip occurred along the Mill Creek strand. Realigning the disrupted Hell For Sure and North Fork drainages with the beheaded South Fork in upper Raywood Flat in turn positions the oldest deposits in the Mission Creek alluvial complex along the flow path for the combined Whitewater River and Mission Creek drainage basins. Palinspastic reconstruction of the Pinto Mountain fault, prior to the most recent 1–1.25 km offset and prior to the complete slip on the Mill Creek fault, allows us to reconstruct Whitewater River flow through two wind gaps. Stepping forward through the offset along the Mill Creek fault explains the formation and positional timing for three additional flow paths that are now either abandoned or occupied by underfit drainages.

Following cessation of slip along the Mill Creek strand, the Pinto Mountain fault offset the trace of the Mill Creek strand by 1–1.25 km. This offset also disrupted drainages within the Mission Creek drainage system, resulting in sinistral offsets along the western section of the Pinto Mountain fault. Offset of the Mill Creek strand explains a puzzling aspect of the history of strand switching in the SGP. Because the Mill Creek strand is the more favorably aligned pathway through the SGP region, it had not previously been clear why SAF motion would step away from this strand onto the more complex path through the San Bernardino, San Gorgonio Pass, Garnet Hill, and Banning fault strands. Disruption by the Pinto Mountain fault provides a significant asperity to throughgoing motion, and may account for the abandonment of the Mill Creek strand.

During the period of activity of the Mill Creek strand, the Yucaipa Ridge block was uplifted 975 ± 70 m relative to the San Gorgonio block. This is determined by the same drainage reconstruction that is used to establish total slip amount along the Mill Creek strand. This calculation agrees well with independently determined uplift amounts based on thermochronologic modeling.

Long profiles of the surfaces in the Mission Creek alluvial complex suggest that the oldest surfaces (A and B) were uplifted and tilted relative to the younger surfaces (C and D) and the modern Mission Creek. We interpret that this tilting resulted from connectivity between this region and the nearby Yucaipa Ridge block, which was actively rising at this time. Because the uplift of Yucaipa Ridge block occurred during the period of slip along the Mill Creek strand, we infer that cessation of slip pre-dated the formation of surface C. The best estimate for the timing of the formation of surface C is ca. 100 ka, determined using IRSL and an age estimate based on the degree of soil development.

After cessation of slip along the Mill Creek fault, the South Fork Whitewater River eroded headward onto the San Gorgonio block. The quantity of material removed as a result of this erosion, combined with an independently determined rate of erosion, suggests that the duration of erosion was between 130 k.y. and 106 k.y.

Downloaded from http://pubs.geoscienceworld.org/gsa/gsabulletin/article-pdf/127/5-6/825/3410110/825.pdf
by USGS Library user

This rough estimate is in general agreement with the timing suggested by the age determination of surface C.

Displacement of the Mill Creek strand by the Pinto Mountain fault suggests that the latter fault has had variable slip rates since initiation of slip on the Mill Creek strand. The Pinto Mountain fault appears to have been quiescent during the time when the Mill Creek fault was active. Our calculated rate of slip ranges from very low values when the 1–1.25 km is integrated over this entire period, to much higher rates of ~10–12.5 mm/yr for the interval ca. 100 ka to present. To the extent that estimates of slip rates guide the prediction of seismic hazard, it is crucial to understand the impact of subsidiary sinistral faults on the strand behavior of the primary dextral faults. Our findings should generalize to other junctions in strike-slip fault systems where a multi-strand main trace changes alignment and is met by the relatively simple trace of a subordinate fault with contrasting slip direction. The subordinate fault is confined to one side of the main trace and the two strike-slip sets do not meet at the conjugate angle predicted by simple Coulomb criteria.

ACKNOWLEDGMENTS

Funding support for this project was from the U.S. Geological Survey Earthquake Hazards, National Cooperative Geologic Mapping, and Mineral Resources Programs. We thank Pete Sadler for many helpful discussions as we developed the ideas in this study. The GIS support of Rachel Alvarez, John Conrad, and Doug Hirschberg is gratefully acknowledged. We thank Doug Yule, Kate Scharer, and Pat McCrory for very helpful early reviews of this manuscript. We thank Jim Evans and Whitney Behr for their formal reviews of this paper. All of these reviews resulted in significant improvement to this paper.

REFERENCES CITED

Allen, C.R., 1957, San Andreas fault zone in San Gorgonio Pass, southern California: Geological Society of America Bulletin, v. 68, p. 315–350, doi:10.1130/0016-7606(1957)68[315:SAFZIS]2.0.CO;2.

Anderson, J.G., 1979, Estimating the seismicity from geologic structure, for seismic risk studies: Bulletin of the Seismological Society of America, v. 69, p. 135–158.

Bader, J.S., and Moyle, W.R., Jr., 1958, Data on water wells and springs in Morongo Valley and vicinity, San Bernardino and Riverside Counties, California: U.S. Geological Survey Open-File Report 58-7, 31 p.

Batcheller, J., III, 1978, Quaternary geology of the Mojave Desert–eastern Transverse Range boundary in the vicinity of Twentynine Palms, California [unpublished M.S. thesis]: Los Angeles, University of California, 157 p.

Bedrossian, T.L., Roffers, P.D., Hayhurst, C.A., Lancaster, J.T., and Short, W.R., 2012, Geologic compilation of surficial deposits in southern California: California Geological Survey Special Report 217 (revised), 21 p., http://www.conservation.ca.gov/cgs/fwgp/Pages/sr217.aspx.

Binnie, S.A., Phillips, W.M., Summerfield, M.A., Fifield, L.K., and Spotila, J.A., 2008, Patterns of denudation through time in the San Bernardino Mountains, California: Implications for early-stage orogenesis: Earth and Planetary Science Letters, v. 276, p. 62–72, doi:10.1016/j.epsl.2008.09.008.

Bird, P., and Rosenstock, R.W., 1984, Kinematics of present crust and mantle flow in southern California: Geological Society of America Bulletin, v. 95, p. 946–957, doi:10.1130/0016-7606(1984)95<946:KOPCAM>2.0.CO;2.

Birkeland, P.W., 1999, Soils and Geomorphology: New York, Oxford University Press, 430 p.

Blythe, A.E., House, M.A., and Spotila, J.A., 2002, Low-temperature thermochronology of the San Gabriel and San Bernardino Mountains, southern California: Constraining structural evolution, *in* Barth, A., ed., Contributions to Crustal Evolution of the Southwestern United States: Geological Society of America Special Paper 365, p. 231–250, doi:10.1130/0-8137-2365-5.231.

Brune, J., Purvance, M., Anooshehpoor, R., Anderson, J., Grant-Ludwig, L., Rood, D., and Kendrick, K., 2010, Possible explanations for discrepancies between precariously balanced rocks and 2008 hazard maps: Seismological Research Letters, v. 81, p. 330.

Bryant, W.A., compiler, 2000, Fault number 118, Pinto Mountain fault zone (includes Morongo Valley fault), *in* Quaternary Fault and Fold Database of the United States: U.S. Geological Survey, http://earthqukes.usgs.gov/regional/qfaults (accessed August 2012).

Cadena, A., Rubin, C., Walls, C., Khatib, F., Rockwell, T., Lindvall, S., and Madden, C., 2003, Paleoseismic investigation on the Pinto Mountain fault at the Oasis of Mara, Mojave Desert, California: Eos (Transactions, American Geophysical Union), v. 84, no. 46, abstract S12B-0392.

Cadena, A., Rubin, C., Rockwell, T., Walls, C., Lindvall, S., Madden, C., Khatib, F., and Owen, L., 2004, Late Quaternary activity of the Pinto Mountain fault at the Oasis of Mara: Implications for the Eastern California shear zone: Geological Society of America Abstracts with Programs, v. 36, no. 5, p. 137.

Carena, S., Suppe, J., and Kao, H., 2004, Lack of continuity of the San Andreas Fault in southern California: Three-dimensional fault models and earthquake scenarios: Journal of Geophysical Research, v. 109, B04313, doi:10.1029/2003JB002643.

Cooke, M.L., and Dair, L.C., 2011, Simulating the recent evolution of the southern big bend of the San Andreas fault, Southern California: Journal of Geophysical Research, v. 116, B04405, doi:10.1029/2010JB007835.

Dair, L.C., and Cooke, M.L., 2009, San Andreas fault geometry through the San Gorgonio Pass, California: Geology, v. 37, p. 119–122, doi:10.1130/G25101A.1.

Dickinson, W.R., 1997, Kinematics of Transrotational Tectonism in the California Transverse Ranges and Its Contribution to Cumulative Slip Along the San Andreas Transform Fault System: Geological Society of America Special Paper 305, 46 p., doi:10.1130/0-8137-2305-1.1.

Dibblee, T.W., Jr., 1964, Geologic map of the San Gorgonio Mountain quadrangle, San Bernardino and Riverside Counties, California: U.S. Geological Survey Miscellaneous Geologic Investigations Map I-431, scale 1:62,500.

Dibblee, T.W., Jr., 1967, Geologic map of the Morongo Valley quadrangle, San Bernardino and Riverside Counties, California: U.S. Geological Survey Miscellaneous Geologic Investigations Map I-517, scale 1:62,500.

Dibblee, T.W., Jr., 1968a, Displacements on San Andreas fault system in San Gabriel, San Bernardino, and San Jacinto Mountains, southern California, *in* Dickinson, W.R., and Grantz, A., eds., Proceedings of Conference on Geologic Problems of San Andreas Fault System: Stanford University Publications in Geological Sciences, v. XI, p. 269–278.

Dibblee, T.W., Jr., 1968b, Evidence of major lateral displacement on the Pinto Mountain fault, southern California, *in* Abstracts of Papers Submitted for Seven Meetings with Which the Society Was Associated: Geological Society of America Special Paper 115, p. 322.

Dibblee, T.W., Jr., 1975, Late Quaternary uplift of the San Bernardino Mountains on the San Andreas and related faults, *in* Crowell, J.C., ed., San Andreas Fault in Southern California: California Division of Mines and Geology Special Report 118, p. 127–135.

Dibblee, T.W., Jr., 1982, Geology of the San Bernardino Mountains, southern California, *in* Fife, D.L., and Minch, J.A., eds., Geology and Mineral Wealth of the California Transverse Ranges: South Coast Geological Society Guidebook 10 (Mason Hill volume), p. 148–169.

Ehlig, P.L., 1977, Structure of the San Andreas fault zone in San Gorgonio Pass, southern California: Geological Society of America Abstracts with Programs, v. 9, no. 4, p. 416.

Farley, T., 1979, Geology of a part of northern San Gorgonio Pass, California [unpublished M.S. thesis]: Los Angeles, California State University, 159 p.

Forman, S.L., and Pierson, J., 2002: Late Pleistocene luminescence chronology of loess deposition in the Missouri and Mississippi river valleys, United States: Paleogeography, Paleoclimatology, Paleoecology, v. 186, p. 25–46, doi:10.1016/S0031-0182(02)00440-6.

Gile, L.H., Peterson, F.F., and Grossman, R.B., 1966, Morphological and genetic sequences of carbonate accumulations in desert soils: Soil Science, v. 101, no. 5, p. 347–360.

Harden, J.W., 1982, A quantitative index of soil development from field descriptions: Examples from a chronosequence in central California: Geoderma, v. 28, p. 1–28, doi:10.1016/0016-7061(82)90037-4.

Harden, J.W., and Taylor, E.M., 1983, A quantitative comparison of soil development in four climatic regimes: Quaternary Research, v. 20, p. 342–359, doi:10.1016/0033-5894(83)90017-0.

Hauksson, E., Jones, L.M., Hutton, K., and Eberhart-Phillips, D., 1993, The 1992 Landers earthquake sequence: Seismological observations: Journal of Geophysical Research, v. 98, p. 19,835–19,858, doi:10.1029/93JB02384.

Hopson, R.F., 1996, The Pinto Mountain fault, Mojave Desert, southern California: Offset documentation and tectonics: Geological Society of America Abstracts with Programs, v. 28, no. 5, p. 76.

Hough, S.E., Mori, J., Sembera, E., Glassmoyer, G., Mueller, C., and Lydeen, S., 1993, Southern surface rupture associated with the 1992 M7.4 Landers Earthquake: Did it all happen during the mainshock?: Geophysical Research Letters, v. 20, p. 2615–2618, doi:10.1029/93GL00666.

Jones, L.M., 1988, Focal mechanisms and the state of stress on the San Andreas Fault in southern California: Journal of Geophysical Research, v. 93, p. 8869–8891, doi:10.1029/JB093iB08p08869.

Jones, L.M., Bernknopf, R., Cox, D., Goltz, J., Hudnut, K., Mileti, D., Perry, S., Ponti, D., Porter, K., Reichle, M., Seligson, H., Shoaf, K., Treiman, J., and Wein, A., 2008, The ShakeOut Scenario: U.S. Geological Survey Open-File Report 2008-1150, 308 p.

Jordan, T.H., Chen, Y.-T., Gasparini, P., Madariaga, R., Main, I., Marzocchi, W., Papadopoulos, G., Sobolev, G., Yamaoka, K., and Zschau, J., 2011, Operational earthquake forecasting: State of knowledge and guidelines for implementation—Final report of the International Commission on Earthquake Forecasting for Civil Protection: Annals of Geophysics, v. 54, p. 315–391.

Kendrick, K.J., and Graham, R.C., 2004, Pedogenic silica accumulation in chronosequence soils, southern California: Soil Science Society of America Journal, v. 68, p. 1295–1303, doi:10.2136/sssaj2004.1295.

Kendrick, K.J., and McFadden, L.D., 1996, Comparison and contrast of processes of soil formation in the San Timoteo Badlands with chronosequences in California: Quaternary Research, v. 46, p. 149–160, doi:10.1006/qres.1996.0055.

Kendrick, K.J., Morton, D.M., Wells, S.G., and Simpson, R.W., 2002, Spatial and temporal deformation along the northern San Jacinto fault, southern California: Implications for slip rates: Bulletin of the Seismological Society of America, v. 92, p. 2782–2802, doi:10.1785/0120000615.

Lang, A., 1994, Infrared stimulated luminescence dating of Holocene reworked silty sediments: Quaternary Science Reviews, v. 13, p. 525–528, doi:10.1016/0277-3791(94)90071-X.

Langenheim, V.E., and Powell, R., 2009, Basin geometry and cumulative offsets in the Eastern Transverse Ranges, southern California: Implications for transrotational deformation along the San Andreas fault system: Geosphere, v. 5, p. 1–22, doi:10.1130/GES00177.1.

Downloaded from http://pubs.geoscienceworld.org/gsa/gsabulletin/article-pdf/127/5-6/825/3410110/825.pdf
by USGS Library user

Langenheim, V.E., Jachens, R.C., Matti, J.C., Morton, D.M., Hauksson, E., and Christensen, A., 2005, Geophysical evidence for wedging in the San Gorgonio Pass structural knot, southern San Andreas Fault zone, southern California: Geological Society of America Bulletin, v. 117, p. 1554–1572; doi:10.1130/B25760.1.

Lawson, M., Roder, B., Stang, D., and Rhodes, E., 2012, OSL and IRSL characteristics of quartz and feldspar from southern California, USA: Radiation Measurements, v. 47, p. 830–836, doi:10.1016/j.radmeas.2012.03.025.

Lawson, M., Daniels, J.T.M., and Rhodes, E., Assessing optically stimulated luminescence (OSL) signal contamination within small aliquots and single grain measurements utilizing the composition test: Quaternary International, doi:10.1016/j.quaint.2014.05.017 (in press).

Matti, J.C., and Morton, D.M., 1993, Paleogeographic evolution of the San Andreas fault in southern California: A reconstruction based on a new cross-fault correlation, *in* Powell, R.E., Weldon, R.J., II, and Matti, J.C., eds., The San Andreas Fault System: Displacement, Palinspastic Reconstruction, and Geologic Evolution: Geological Society of America Memoir 178, p. 107–159, doi:10.1130/MEM178-p107.

Matti, J.C., Cox, B.F., Obi, C.M., Powell, R.E., Hinkle, M.E., Griscom, A., and McHugh, E.L., 1982, Mineral resource potential of the Whitewater Wilderness Study Area, Riverside and San Bernardino Counties, California: U.S. Geological Survey Miscellaneous Field Studies Map MF-1478, scale 1:62,500.

Matti, J.C., Cox, B.F., and Iverson, S.R., 1983, Mineral resource potential map of the Raywood Flat Roadless Areas, San Bernardino and Riverside Counties, California: U.S. Geological Survey Miscellaneous Field Studies Map MF-1563-A, scale 1:62,500.

Matti, J.C., Morton, D.M., and Cox, B.F., 1985, Distribution and geologic relations of fault systems in the vicinity of the central Transverse Ranges, southern California: U.S. Geological Survey Open-File Report 85-365, 27 p., scale 1:250,000.

Matti, J.C., Carson, S.E., Kilburn, J.E., Griscom, A., Kuizon, L., and Prose, D., 1988, Mineral resources of the Morongo Wilderness Study Area (CDCA-218), San Bernardino County, California: U.S. Geological Survey Bulletin 1710-B, 34 p.

Matti, J.C., Morton, D.M., and Cox, B.F., 1992, The San Andreas fault system in the vicinity of the central Transverse Ranges Province, southern California: U.S. Geological Survey Open-File Report 92-354, 40 p., scale 1:250,000.

Matti, J.C., Morton, D.M., and Langenheim, V.E., 2013, Geologic map and digital database of the El Casco 7.5′ quadrangle, Riverside County, California: U.S. Geological Survey Open-File Report 2010-1274, scale 1:24,000, 185 p.

McFadden, L.D., 1982, The impacts of temporal and spatial climatic changes on alluvial soils genesis in southern California [unpublished Ph.D. thesis]: Tucson, University of Arizona, 430 p.

McFadden, L.D., and Hendricks, D.M., 1985, Changes in the content and composition of pedogenic iron oxyhydroxides in a chronosequence of soils in southern California: Quaternary Research, v. 23, p. 189–204, doi:10.1016/0033-5894(85)90028-6.

McFadden, L.D., and Weldon, R.J., 1987, Rates and processes of soil development on Quaternary terraces in Cajon Pass, California: Geological Society of America Bulletin, v. 98, p. 280–293, doi:10.1130/0016-7606(1987)98<280:RAPOSD>2.0.CO;2.

Meade, B.J., and Hagar, B.H., 2005, Block models of crustal motion in southern California constrained by GPS measurements: Journal of Geophysical Research, v. 110, B03403, doi:10.1029/2004JB003209.

Morton, D.M., Cox, B.F., and Matti, J.C., 1980, Geologic map of the San Gorgonio Wilderness: U.S. Geological Survey Miscellaneous Field Studies Map MF-1164-A, scale 1:62,500.

Morton, D.M., Alvarez, R.M., Ruppert, K.R., and Goforth, B., 2008, Contrasting rainfall generated debris flows from adjacent watersheds at Forest Falls, southern California, USA: Geomorphology, v. 96, p. 322–338, doi:10.1016/j.geomorph.2007.03.021.

Nishikawa, T., Densmore, J.N., Martin, P., and Matti, J., 2003, Evaluation of the source and transport of high nitrate concentrations in ground water, Warren Subbasin, California: U.S. Geological Survey Water Resources Investigation Report 03-4009, 133 p.

Owen, L.A., Clemmens, S.J., Finkel, R.C., and Gray, H., 2014, Late Quaternary alluvial fans at the eastern end of the San Bernardino Mountains, Southern California: Quaternary Science Reviews, v. 87, p. 114–134, doi:10.1016/j.quascirev.2014.01.003.

Peterson, M.D., and Wesnousky, S.G., 1994, Fault slip rates and earthquake histories for active faults in southern California: Bulletin of the Seismological Society of America, v. 84, p. 1608–1649.

Plesch, A., Shaw, J.H., Benson, C., Bryant, W.A., Carena, S., Cooke, M., Dolan, J., Fuis, G.S., Gath, E., Grant, L., Hauksson, E., Jordan, T., Kamerling, M., Legg, M., Lindvall, S., Magistrale, H., Nicholson, C., Niemi, N., Oskin, M., Perry, S., Planansky, G., Rockwell, T., Shearer, P., Sorlien, C., Suess, M.P., Suppe, J., Treiman, J., and Yeats, R., 2007, Community fault model for southern California: Bulletin of the Seismological Society of America, v. 97, p. 1793–1802, doi:10.1785/0120050211.

Porat, N., and Botha, G., 2008, The luminescence chronology of dune development on the Maputaland coastal plain, southeast Africa: Quaternary Science Reviews, v. 27, no. 9–10, p. 1024–1046.

Powell, R.E., 1993a, Foreword, *in* Powell, R.E., Weldon, R.J., and Matti, J.C., eds., The San Andreas Fault System: Displacement, Palinspastic Reconstruction, and Geologic Evolution: Geological Society of America Memoir 178, p. vii–xix, doi:10.1130/MEM178-pvii.

Powell, R.E., 1993b, Balanced palinspastic reconstruction of pre–late Cenozoic paleogeology, southern California: Geologic and kinematic constraints on evolution of the San Andreas fault system, *in* Powell, R.E., Weldon, R.J., and Matti, J.C., eds., The San Andreas Fault System: Displacement, Palinspastic Reconstruction, and Geologic Evolution: Geological Society of America Memoir 178, p. 1–106, doi:10.1130/MEM178-p1.

Prescott, J.R., and Hutton, J.T., 1994, Cosmic ray contributions to dose rates for luminescence and ESR dating: Large depths and long-term time variations: Radiation Measurements, v. 23, p. 497–500, doi:10.1016/1350-4487(94)90086-8.

Rhodes, E.J., 2011, Optically stimulated luminescence dating of sediments over the past 200,000 years: Annual Review of Earth and Planetary Sciences, v. 39, p. 461–488, doi:10.1146/annurev-earth-040610-133425.

Richardson, C.A., McDonald, E.V., and Busacca, A.J., 1997, Luminescence dating of loess from the northwest United States: Quaternary Science Reviews, v. 16, p. 403–415, doi:10.1016/S0277-3791(96)00111-4.

Roder, B., Lawson, M., Rhodes, E., Dolan, J., McAuliffe, L., and McGill, S., 2012, Assessing the potential of luminescence dating for fault slip rate studies on the Garlock fault, Mojave Desert, California, USA: Quaternary Geochronology, v. 10, p. 285–290, doi:10.1016/j.quageo.2012.03.013.

Sadler, P.M., 1993, The Santa Ana basin of the central San Bernardino Mountains: Evidence of the timing of uplift and strike slip relative to the San Gabriel Mountains, *in* Powell, R.E., Weldon, R.J., and Matti, J.C., eds., The San Andreas Fault System: Displacement, Palinspastic Reconstruction, and Geologic Evolution: Geological Society of America Memoir 178, p. 307–322, doi:10.1130/MEM178-p307.

Schoeneberger, P.J., Wysocki, D.A., Benham, E.C., and Broderson, W.D., eds., 2002, Field Book for Describing and Sampling Soils, Version 2.0: Lincoln, Nebraska, Natural Resources Conservation Service, National Soil Survey Center, 211 p.

Seeber, L., and Armbruster, J.G., 1995, The San Andreas Fault system through the Transverse Ranges as illuminated by earthquakes: Journal of Geophysical Research, v. 100, p. 8285–8310, doi:10.1029/94JB02939.

Singhvi, A.K., Sharma, Y.P., and Agrawal, D.P., 1982, Thermoluminescence dating of sand dunes in Rajasthan, India: Nature, v. 295, p. 313–315, doi:10.1038/295313a0.

Spinler, J.C., Bennett, R.A., Anderson, M.L., McGill, S.F., Hreinsdóttir, S., and McCallister, A., 2010, Present-day strain accumulation and slip rates associated with southern San Andreas and eastern California shear zone faults: Journal of Geophysical Research, v. 115, B11407, doi:10.1029/2010JB007424.

Spotila, J.A., and Sieh, K.E., 2000, Architecture of transpressional thrust faulting in the San Bernardino Mountains, southern California, from deformation of a deeply weathered surface: Tectonics, v. 19, p. 589–615, doi:10.1029/1999TC001150.

Spotila, J.A., Farley, K.A., and Sieh, K., 1998, Uplift and erosion of the San Bernardino Mountains associated with transpression along the San Andreas fault, California, as constrained by radiogenic helium thermochronometry: Tectonics, v. 17, p. 360–378, doi:10.1029/98TC00378.

Spotila, J.A., Farley, K.A., Yule, J.D., and Reiners, P.W., 2001, Near-field transpressive deformation along the San Andreas fault zone in southern California, based on exhumation constrained by (U-Th)/He dating: Journal of Geophysical Research, v. 106, p. 30,909–30,922, doi:10.1029/2001JB000348.

Torrent, J., Schwertmann, U., and Shulze, D.J., 1980, Iron oxide mineralogy of some soils of two river terrace sequences in Spain: Geoderma, v. 23, p. 191–208, doi:10.1016/0016-7061(80)90002-6.

U.S. Geological Survey and California Geological Survey, 2006, Quaternary fault and fold database for the United States, http//earthquakes.usgs.gov/regional/qfaults/ (accessed 23 October 2014).

Wallace, R.E., 1990, General features, *in* Wallace, R.E., ed., The San Andreas Fault System, California: U.S. Geological Survey Professional Paper 1515, p. 3–12.

Weldon, R.J., Scharer, K., Fumal, T., and Biasi, G., 2004, Wrightwood and the earthquake cycle: What a long recurrence record tells us about how faults work: GSA Today, v. 14, no. 9, p. 4–10, doi:10.1130/1052-5173(2004)014<4:WATECW>2.0.CO;2.

Wesnousky, S.G., 1986, Earthquakes, Quaternary faults, and seismic hazard in California: Journal of Geophysical Research, v. 91, p. 2587–2631, doi:10.1029/JB091iB12p12587.

Wesnousky, S.G., 2008, Displacement and geometrical characteristics of earthquake surface ruptures: Issues and implications for seismic-hazard analysis and the process of earthquake rupture: Bulletin of the Seismological Society of America, v. 98, p. 1609–1632, doi:10.1785/0120070111.

WGCEP (Working Group California Earthquake Probabilities), 2008, The Uniform California Earthquake Rupture Forecast, Version 2 (UCERF 2): U.S. Geological Survey Open-File Report 2007-1437 and California Geological Survey Special Report 203, http://pubs.usgs.gov/of/2007/1437/ (accessed April 2008).

Williams, P.L., Sykes, L.R., Nicholson, C., and Seeber, L., 1990, Seismotectonics of the easternmost Transverse Ranges, California: Relevance for seismic potential of the southern San Andreas Fault: Tectonics, v. 9, p. 185–204, doi:10.1029/TC009i001p00185.

Wobus, C., Whipple, K.X., Kirby, E., Snyder, N., Johnson, J., Spyropolou, K., Crosby, B., and Sheehan, D., 2006, Tectonics from topography: Procedures, promise, and pitfalls, *in* Willett, S.D., Hovius, N., Brandon, M.T., and Fisher, D.M., eds., Tectonics, Climate, and Landscape Evolution: Geological Society of America Special Paper 398, p. 55–74, doi:10.1130/2006.2398(04).

Yule, D., 2009, The enigmatic San Gorgonio Pass: Geology, v. 37, p. 191–192, doi:10.1130/focus022009.1.

Yule, D., 2010, Testing the "shakeout" scenario earthquake in San Gorgonio Pass: Fact or fiction?: Geological Society of America Abstracts with Programs, v. 42, no. 4, p. 69.

Yule, D., and Sieh, K., 2003, Complexities of the San Andreas fault near San Gorgonio Pass: Implications for large earthquakes: Journal of Geophysical Research, v. 108, 2548, doi:10.1029/2001JB000451.

Science Editor: Christian Koeberl
Associate Editor: Enrico Tavarnelli

Manuscript Received 26 March 2014
Revised Manuscript Received 27 August 2014
Manuscript Accepted 14 November 2014

Printed in the USA

Downloaded from http://pubs.geoscienceworld.org/gsa/gsabulletin/article-pdf/127/5-6/825/3410110/825.pdf
by USGS Library user

GEOSPHERE

GEOSPHERE

https://doi.org/10.1130/GES02424.1

14 figures; 2 tables

CORRESPONDENCE: kendrick@usgs.gov

CITATION: Kendrick, K.J., Matti, J.C., and Barth, N.C., 2022, Geologic and geomorphic evidence for multi-phase history of strands of the San Andreas fault through the San Gorgonio Pass structural knot, southern California: Geosphere, https://doi.org/10.1130/GES02424.1.

Science Editor: Andrea Hampel
Guest Associate Editor: Michele Cooke

Received 25 February 2021
Revision received 30 September 2021
Accepted 29 November 2021

Published online 18 February 2022

GOLD OPEN ACCESS

THE GEOLOGICAL SOCIETY OF AMERICA®

This paper is published under the terms of the CC-BY-NC license.

© 2022 The Authors

Geologic and geomorphic evidence for multi-phase history of strands of the San Andreas fault through the San Gorgonio Pass structural knot, southern California

Katherine J. Kendrick[1,*], Jonathan C. Matti[2,*], and Nicolas C. Barth[3,*]

[1]U.S. Geological Survey, 525 South Wilson Avenue, Pasadena, California 91106, USA
[2]U.S. Geological Survey, 520 North Park Avenue, Tucson, Arizona 85719, USA
[3]University of California, Riverside, 900 University Avenue, Riverside, California 92521, USA

ABSTRACT

The San Gorgonio Pass region of southern California is a locus of extensive Quaternary deformation within a multi-strand section of the San Andreas fault zone. The geomorphology of the San Gorgonio Pass region reflects the complicated history of geologic events in the formation of this structurally complex region. We define fault-bounded blocks in San Gorgonio Pass and focus on two that are characterized by extensive crystalline bedrock outcrops with similar bedrock lithologies. These two blocks are separated by the San Bernardino strand of the San Andreas fault. Morphometric variables, including local relief, slope, slope distribution, and surface roughness, consistently demonstrate distinctions between the bedrock upland regions of the two blocks. Geologic observations of the region highlight differences in Quaternary units within the two blocks, reflective of the differing surficial processes active in each block. Within the Kitching Peak block, the morphology highlights a lineament that we informally name the Lion Canyon lineament. This boundary more clearly differentiates the two regions, as compared to the mapped San Bernardino strand, and may represent the previously active strand or bounding structure in this section. The distinction in morphology and surficial processes leads to our interpretation that the Kitching Peak and Pisgah Peak blocks have experienced different uplift histories. This further leads to the conclusion that the San Bernardino strand, broadly defined, has been integrated, at some point in the past, with the Banning strand, allowing for through-going rupture along the fault system. This connectivity may have occurred along the Burro Flats section of the San Bernardino strand or the Lion Canyon lineament. The fault connection along the mapped trace of the San Bernardino strand is not currently evident at the surface, however, suggesting that the integration has been disrupted. We propose this is due to intervals of N-S compression in the region, manifest as slip along the San Gorgonio Pass fault zone and other regional faults. We present evidence for lateral displacement along the San Bernardino and Banning strands of the San Andreas fault, discuss the implications of these displacements, and propose a sequence of fault activity, including multiple phases of activity along the San Bernardino and Banning strand pathway to account for the structural complexity and lack of surficial fault continuity.

*E-mail: kendrick@usgs.gov; jmatti@usgs.gov; nic.barth@ucr.edu

INTRODUCTION

The San Andreas fault (SAF) zone is uniquely complex through the San Gorgonio Pass region (SGPr) (Fig. 1) and, despite numerous investigations, remains incompletely understood. This complexity, demonstrated by multiple subparallel fault strands, bends, kinks, or offsets of individual fault strands, along with an orientation that is rotated in a counterclockwise sense relative to the overall strike of the fault system, led to previous descriptions of this region as a "structural knot" (Matti et al., 1992a). Allen (1957) recognized this complexity and questioned the continuity of faulting through the SGPr, citing the apparent absence of large displacements and the lack of youthful tectonic geomorphology associated with the most likely path of the modern SAF. Many of the questions posed by Allen (1957) persist, in spite of numerous investigations designed to better understand this enigmatic region. Among the questions remaining are how the SAF resolves itself through the SGPr, and whether there is a pathway for fault rupture to propagate through the SGPr, or if instead, this region serves as a barrier to rupture along the SAF initiating from the southeast or northwest. Additionally, it is important to know both the three-dimensional geometry and the kinematic evolution of the SAF through the region in order to fully characterize the earthquake hazards of the system.

Principal geologic structures within the SGPr landscape (Fig. 1) include (1) strands of the SAF zone, including the Mission Creek, Mill Creek, San Bernardino, Gandy Ranch, Banning, and Garnet Hill strands, that have been active at different intervals in the recent geologic past (Matti et al., 1992a; Matti and Morton, 1993; Kendrick et al., 2015); (2) the transpressive San Gorgonio Pass fault zone (SGPFZ); (3) the Crafton Hills fault complex; and (4) the Whitewater fault (nomenclatural usage for all of these faults follows Matti et al., 1985, 1992a, 2003; Kendrick et al., 2015). Throughout this study, we will refer to the strands of the SAF simply as strands without designating that they are strands of the

Downloaded from http://pubs.geoscienceworld.org/gsa/geosphere/article-pdf/doi/10.1130/GES02424.1/5548351/ges02424.pdf
by USGS Library user

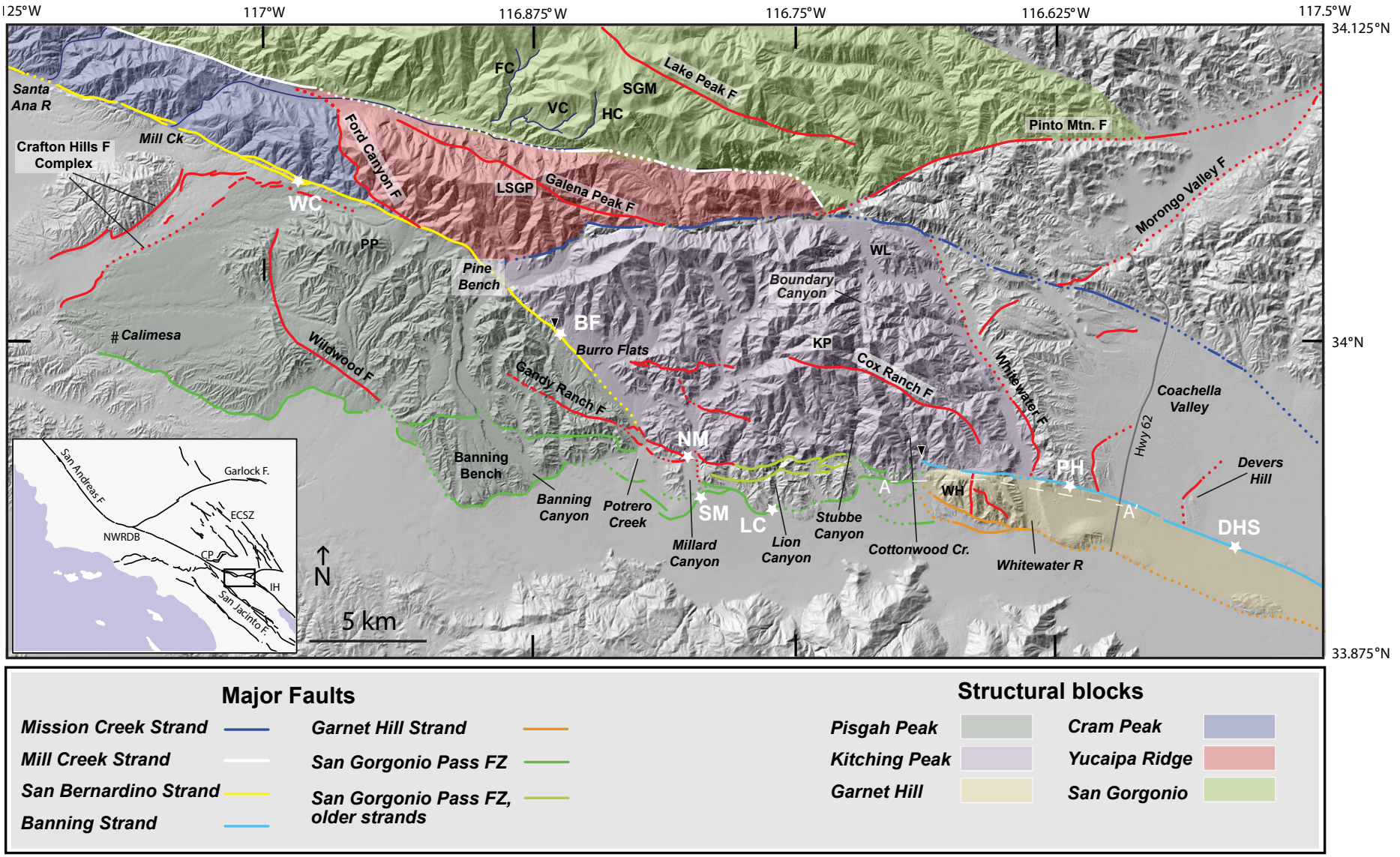

Figure 1. Shaded relief of San Gorgonio Pass region, showing location of faults, structural blocks, paleoseismic and slip rate sites, and notable landscape features. Major fault strands of the San Andreas fault are colored; additional regional faults are shown in red. Abbreviations of paleoseismic and slip rate study sites (white text with white stars) are Burro Flats (BF), Desert Hot Springs (DHS), Lion Canyon (LC), Northern Millard (NM), Painted Hills (PH), Southern Millard (SM), and Wilson Creek (WC). Other abbreviations include Falls Creek (FC), High Creek (HC), Vivian Creek (VC), Kitching Peak (KP), Little San Gorgonio Peak (LSGP), Pisgah Peak (PP), San Gorgonio Mountain (SGM), Wathier Landing (WL), and Whitewater Hill (WH). Inset shows location of the study area (rectangle), the location of the northwestern part of the restraining double bend (NWRDB), Cajon Pass (CP), the Indio Hills (IH), and regional faults, including the eastern California shear zone (ECSZ). Dashed white line indicates the cross section in Figure 11A.

Downloaded from http://pubs.geoscienceworld.org/gsa/geosphere/article-pdf/doi/10.1130/GES02424.1/5548351/ges02424.pdf
by USGS Library user

SAF at each mention. Matti et al. (1992a) proposed that these SAF strands formed sequentially, with each new pathway produced in response to the increasingly complex deformation and offset of older strands.

Evidence for the most recent slip is located along faults, including, from west to east, the dextral San Bernardino strand, the transpressive SGPFZ, and the transpressive Garnet Hill and dextral Banning strands (Fig. 1); all of these faults are characterized by youthful primary fault features indicating Holocene activity (Matti et al., 1992a; Yule and Sieh, 2003). At the surface, the transpressive SGPFZ seems to link the Banning and the Garnet Hill strands to the southeast and the San Bernardino strand to the northwest.

In spite of clear evidence of recent faulting along these faults, there is a gap in the surface expression of through-going late Quaternary rupture between the Burro Flats section of the San Bernardino strand and the SGPFZ (shown by the dotted yellow line on Fig. 1). Some studies have interpreted that the active trace of the SAF terminates just south of Burro Flats (Allen, 1957; Matti et al., 1985, 1992a; Matti and Morton, 1993), whereas other researchers have cited some limited evidence for a continuation of the active SAF (Yule and Sieh, 2003) through this gap. Yule and Sieh (2003) noted subtle pressure ridges and hanging valleys along the western margin of Potrero Creek. They interpreted that these features indicate the San Bernardino strand continues southeastward from Burro Flats. Yule and Sieh (2003) acknowledge, however, that the observed features are subtle and, thus, must indicate a diminished rate of slip, as compared to that measured along the SAF to the northwest.

STATEMENT OF PROBLEM

The SGPr is critical to understanding the seismic potential of the SAF, which depends on the connectivity of the fault strands, and the ability for earthquake rupture to propagate through the structural complexity found there. This region recently has been the focus of considerable debate among geoscientists concerned with fault-rupture scenarios and attendant seismic risk (e.g., Carena et al., 2004; Plesch et al., 2007; Dair and Cooke, 2009; Yule, 2009, 2010; Cooke and Dair, 2011; Heermance and Yule, 2017; Fosdick and Blisniuk, 2018; Douilly et al., 2020). For example, the scenario earthquake presented to the public and frequently cited (Jones et al., 2008; Perry et al., 2008; Treiman et al., 2008) highlights a tremendous seismic hazard to the heavily populated Los Angeles Basin when SAF rupture originating from the southeast, near the Salton Sea, continues through the SGPr unhindered. If rupture were to be arrested or significantly slowed at the SGPr, the resulting seismic energy within the Los Angeles Basin would be much lower, but other regions could be more severely impacted.

This study explores the fault linkage and kinematic evolution of the SGPr as well as how the landscape is affected by slip along the San Bernardino, Banning, and Garnet Hill strands. We first present our mapping of faults in the study area. We define discrete tectonic blocks in the area, building on and modifying the work of Spotila and colleagues (Spotila et al., 1998, 2001; Spotila and Sieh, 2000). Morphometric analysis is presented that confirms that the terrains on either side of the San Bernardino strand in the vicinity of Burro Flats have experienced different uplift histories, suggesting that through-going faulting has separated these terrains during some interval in their history, and we discuss the implications for this fault strand continuity. Finally, we present observations of offset geologic units and landforms along the San Bernardino and Banning strands, estimate displacement and age of some of these features, and discuss the implications of this to fault strand switching in the SGPr.

METHODS

In this study, we used geologic observations and geomorphic mapping and analysis, combined with soil description and correlation, to better constrain the fault activity along SAF strands in the SGPr. We made geologic and geomorphic observations of the study area at scales of 1:24,000 and larger, mainly using traverse-mapping techniques. From the locality where a map unit or its boundaries were initially identified or defined, we extended those features to other areas through direct outcrop observation and aerial photographic interpretation. For surficial units, we plotted bounding contacts digitally from rectified and georeferenced 2005-vintage National Agriculture Imagery Program (NAIP) aerial stereo pairs that allow location accuracy equivalent to or better than the accuracy standard for the topographic-contour base. Landslide deposits were defined based on morphologic characteristics observed on topographic maps, aerial photos, and imagery. For a calculation of landslide areal percent of each block, each landslide area was attributed to its source block.

Many high-resolution (~1 m) airborne light detection and ranging (lidar) data sets are available within the SGPr and were used to examine geomorphic features in detail. Because the lidar spatial coverage is not complete in the region, we used 10-m digital elevation models (DEMs) to assess the elevation and slope distribution in the morphometric analyses to avoid bias. To compare the landscapes within each structural block, we define a subsection area that delineates the extent of the bedrock highlands. For morphometric analyses within these subsections, we have also removed the areal extent of mapped landslides. We measured local relief and the standard deviation of slope using a 100-m-radius circular area centered on each pixel. We mapped the drainage net within the selected terrain using flow-path tools (ArcMap v. 10) and confirmed it using aerial photography.

Soil pedons were described using the definitions and abbreviations of Birkeland (1999) and the Soil Survey Staff (1951). The degree of soil development was characterized using indices of Torrent et al. (1980), Harden (1982), and Harden and Taylor (1983) and was compared to regional, dated soil chronosequences (McFadden and Weldon, 1987; Kendrick and McFadden, 1996; Kendrick et al., 2002).

Downloaded from http://pubs.geoscienceworld.org/gsa/geosphere/article-pdf/doi/10.1130/GES02424.1/5548351/ges02424.pdf
by USGS Library user

RESULTS

Regional Fault Distribution

Here we report on our mapping of the faults critical to understanding the recent activity of the San Bernardino and Banning strands of the SAF.

San Bernardino Strand

The San Bernardino strand extends over 60 km along the base of the San Bernardino Mountains from Cajon Pass southeast to the vicinity of Banning Canyon, in the SGPr (Fig. 1). About halfway between the Santa Ana River and Mill Creek (Figs. 1 and 2), the structural configuration of the San Bernardino strand becomes progressively more complex to the southeast (Matti et al., 1992a; this study), with multiple anastomosing fault strands replacing a single strand. At Pine Bench (Fig. 1), the mapped trace of the strand bends to a more southerly strike, from ~290° to the west of Pine Bench, to ~325° to the east of Pine Bench. From there, the San Bernardino strand traverses Burro Flats (Yule et al., 2001; Yule and Sieh, 2003; Yule and Spotila, 2010) and presumably passes into the Potrero Creek drainage (Fig. 2). Because of the fault's unique northwest strike along this reach, we refer to it as the Burro Flats section of the San Bernardino strand.

The San Bernardino strand continues through the southern part of Burro Flats and demonstrates clear youthful morphology as it crosses the Burnt Canyon landslide breccia, first identified and described by Allen (1957). Just southeast of this deposit (Fig. 3) is a northeast-facing topographic step in youthful alluvial deposits of Potrero Creek. This scarp-like feature (Fig. 3, inset) is most prominent in visualizations of the 2007 Earthscope lidar (Bevis et al., 2017) and appears to be fault-controlled because (1) it is on-trend with the last documented trace of the San Bernardino strand directly to the northwest with a consistent up-to-the-southwest vertical separation; (2) the two alluvial surfaces it separates have similar surface texture, including spacing and depth and orientation of fluvial channels suggesting identical or similar ages; and (3) there is an ~35° obliquity between the fluvial channels on both sides of the topographic step (165°) and the orientation of the step (130°), which makes a purely fluvial origin for the scarp less convincing. Assuming a vertical fault, this scarp indicates an ~1.5 m up-to-the-southwest throw and an unknown horizontal offset. The scarp is most clearly expressed along an ~300 m length but appears to extend up to 1300 m.

Southeast of this scarp, for ~3 km, we see no convincing tectonic geomorphology, either in the 2007 Earthscope lidar imagery or in 1930- and 1952-vintage aerial photographs or 1975 low-sun-angle aerial photographs flown for the U.S. Geological Survey by I.K. Curtis. We note, however, that the expected position of the fault is within youthful fluvial sediments of Potrero Creek, and the primary fault features could well have been removed or covered by recent fluvial processes. In Figure 3, we show the inferred trace of the San Bernardino strand as dotted where concealed, which is also how it was depicted by Yule and Sieh (2003). On the eastern side of the canyon containing Potrero Creek, near the mouth, is a fault segment that is aligned with the Burro Flats section farther to the north (labeled in Fig. 3). This could be a continuation of the San Bernardino strand, or might be part of the Gandy Ranch strand, discussed below.

Gandy Ranch Strand

The Gandy Ranch fault was named and described by Allen (1957); it extends from Millard Canyon west to Hathaway Creek (Figs. 1 and 3). This fault was recognized as having active fault morphology and recent lateral displacements (Allen, 1957). Yule and Sieh (2003) included the fault in their kinematic model for the SAF through the SGPr; we agree with this interpretation and hereafter refer to the fault as a strand of the SAF.

Between Millard Canyon and Hathaway Creek, crystalline rocks of San Gabriel Mountains–type (as defined by Matti et al., 1985, 1992a) locally are traversed by zones of crushed rock having one or more discrete fault planes. These are best observed between Millard Canyon and Potrero Creek, where both Allen (1957) and Yule and Sieh (2003) associate the bedrock traces with the Gandy Ranch strand. Locally though, some zones of crushed rock could coincide with the toes of large landslide blocks. The Gandy Ranch strand also can be observed in crystalline rocks at the head of an unnamed tributary that extends northwest from the mouth of Potrero Creek (Fig. 3). Our mapping here confirms observations made originally by Allen (1957): the fault is localized along a narrow zone of crushed crystalline rock. This crush zone projects westward into the Hathaway Creek drainage, where the fault dextrally offsets bedrock ridgelines by as much as ~125 m.

Pivotal to interpreting the spatial extent of the Gandy Ranch strand are tectonogeomorphic features developed in young Quaternary alluvial deposits, particularly between Potrero Creek and Millard Canyon. We begin with the easternmost occurrence of the Gandy Ranch strand in Millard Canyon, where previous workers recognize prominent scarps traversing Holocene alluvium in the canyon narrows (Fig. 3). The scarps were discussed by Yule and Sieh (2003) and were trenched by McBurnett (2011; location NM on Fig. 1). Ages for Holocene sediment are provided by McBurnett (2011), Heermance et al. (2014, 2015), Desjarlais (2018), and Heermance and Yule (2017).

West of Millard Canyon, tectonostratigraphic relations among Quaternary surficial materials are not as obvious. Along this reach, localized Holocene debris-fan deposits heading into crystalline rocks of San Gabriel Mountains–type have prograded southward onto the broad Potrero Creek fan head. Our examination of B4 lidar (bare-earth rendering of Bevis et al., 2017) at this location identified discontinuous geomorphic features that we interpret as fault scarps (Fig. 3). These features project northwestward toward Potrero Creek, where they are associated with a conspicuous area of warped ground, characterized by gently folded and uplifted surfaces, in the vicinity of the Potrero Creek narrows (Fig. 3). Allen (1957) observed springs associated with this area, and in vintage aerial photographs as recent as 1975, the zone is populated with abundant cottonwood trees and other vegetation.

Downloaded from http://pubs.geoscienceworld.org/gsa/geosphere/article-pdf/doi/10.1130/GES02424.1/5548351/ges02424.pdf
by USGS Library user

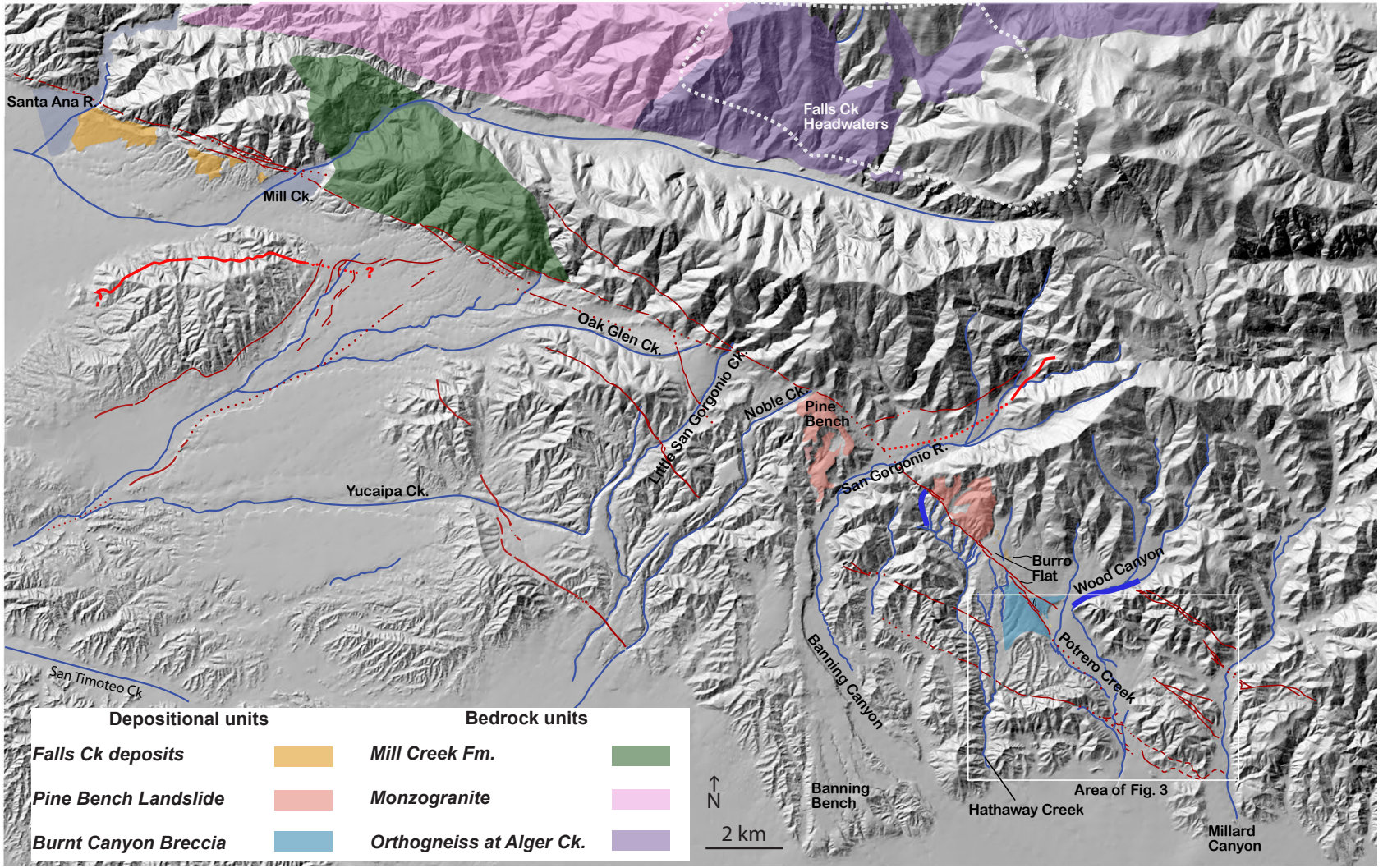

Figure 2. Shaded-relief topographic map of the San Bernardino strand within the San Gorgonio Pass region (SGPr), showing selected geologic units. Bedrock units include the Miocene Mill Creek Formation of Gibson (1964, 1971), Triassic Monzogranite of Manzanita Springs (described by Morton et al., 1980; Matti et al., 2003), and the Orthogneiss of Alger Creek, possibly Proterozoic in age (described by Matti et al., 1992b, 2003, 2015). Faults are displayed as red lines and labeled on Figure 1. The Vincent thrust fault is indicated by the thicker, bright red line. Major drainages are shown as blue lines; the depositional area of Santa Ana River and Mill Creek are shown in light-blue shading. The headwaters of the Falls Creek drainage system are shown by a dashed white line. The heavy blue line highlights Wood Canyon and the beheaded Hathaway Creek. Area of Figure 3 is shown by white box.

Downloaded from http://pubs.geoscienceworld.org/gsa/geosphere/article-pdf/doi/10.1130/GES02424.1/5548351/ges02424.pdf
by USGS Library user

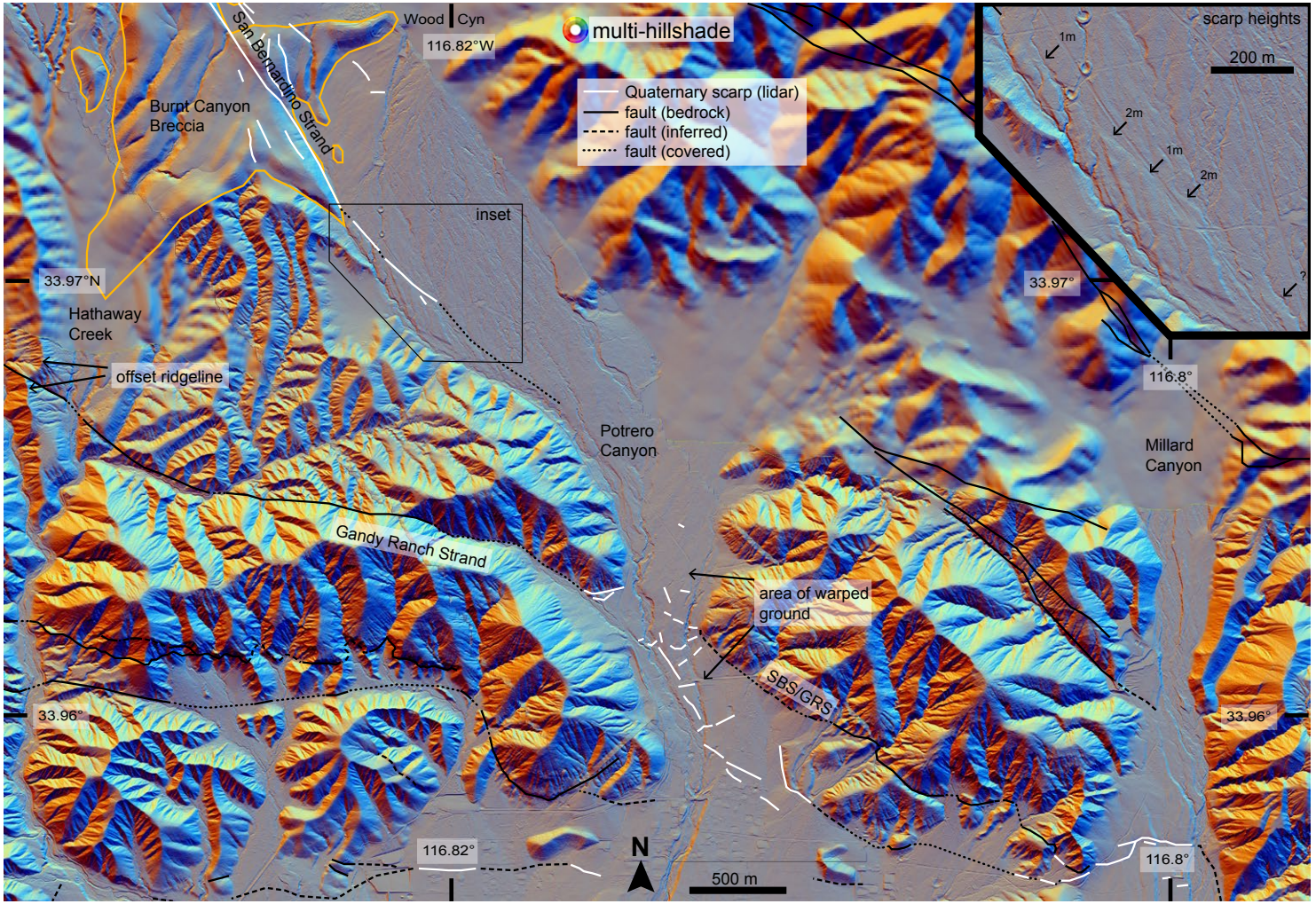

Figure 3. Multi-hillshade relief map of the intersection region of the San Bernardino and Gandy Ranch strands. See Figure 2 for location. Slope aspects indicated by color; index above legend. Quaternary scarps are shown by white lines and may be formed as a result of tectonic or fluvial processes, as discussed in text, including the scarps highlighted by the black arrows within the inset region, and the area of warped ground that is located within the Potrero Creek narrows (lower, central portion of figure).

Downloaded from http://pubs.geoscienceworld.org/gsa/geosphere/article-pdf/doi/10.1130/GES02424.1/5548351/ges02424.pdf
by USGS Library user

We have not examined this area on the ground due to access limitations. However, various imagery sets (1930, 1938, 1952, 1975, 2005 NAIP, and B4 lidar) show that the warped ground is traversed by several west-northwest to west-trending discontinuous scarps, some obvious but others subtle. We interpret these scarps as faults and conclude that the zone of warped ground has resulted from contraction in an area where the Gandy Ranch and San Bernardino strands converge. The disruption is a broad monoclinal step in the topography, ~14 m down to the south, over a distance of 500 m.

We have no direct evidence for the age of surficial deposits in the warped-ground footprint, nor do we have ages for tectonogeomorphic features (fault scarps and folding) that deform them. The surficial materials can be subdivided into two kinds: (1) those old enough to have been deformed within the warped-ground complex and (2) those incised into the complex and postdate deformation that produced it. The older deposits have upper surfaces the geomorphic traits of which are similar to those on deposits upstream and downstream from the warped-ground area, and the deposits themselves appear to be stratigraphically continuous with those upstream and downstream. We interpret the latter as mainly Holocene in age and conclude that this deformation is Holocene (and probably older).

We interpret that the warped-ground footprint bears on the distribution of the Gandy Ranch and San Bernardino strands of the SAF, which in turn, inform the latest Quaternary record of dextral slip on the SAF zone in the SGPr. The San Bernardino strand presumably approaches the warped-ground area from the northwest and (as discussed above) displays no primary fault features in youthful alluvial deposits of the Potrero Creek lowland (Figs. 2 and 3). Scarps in the warped ground trend west and northwest, an orientation similar to—but not identical with—the west-northwest trend of the Gandy Ranch strand in the Hathaway Creek drainage. Given the apparent absence of primary fault features associated with the San Bernardino strand directly to the northwest, we conclude that scarps in the Potrero Creek narrows were formed by fault ruptures on the Gandy Ranch strand. This interpretation is supported by scarps between Potrero Creek and Millard Canyon. It is consistent with Allen's (1957) conclusion that scarps in the Millard Canyon narrows are a southeastern continuation of his Gandy Ranch strand. Yule and Sieh (2003) propose that the San Bernardino strand (Burro Flats section) merges here with the Gandy Ranch strand and therefore contributes to ground-surface deformation ("subtle pressure ridges"). We cannot rule out this hypothesis, given that geometric and kinematic relations here no doubt are complex.

San Gorgonio Pass Fault Zone

Smith (1979) first applied the name "San Gorgonio Pass Fault" to a scarp in the eastern SGPr. Matti et al. (1985) independently applied the name "San Gorgonio Pass Fault zone" (SGPFZ) more regionally to a collection of Quaternary reverse, thrust, and dextral tear faults that extends from the Whitewater area westward to the Calimesa area (Fig. 1) with diminishing displacement and geomorphic expression. Smith's (1979) "San Gorgonio Pass Fault" is part of that regional fault complex. The fault system has a distinctive zig-zag expression caused by repetition of a characteristic serially partitioned fault geometry (e.g., Norris and Cooper, 2007)—an L-shaped fault segment with the longer section oriented northwestward and exhibiting dextral lateral slip and the shorter section oriented northeastward and contractional in nature (Matti et al., 1985, 1992b).

All faults of the SGPFZ have been active in late Quaternary time. Some faults in the complex may have been active only in the Pleistocene; others have been active throughout the late Pleistocene and Holocene and have generated ground ruptures as recently as a few hundred years ago (Smith, 1979; Matti et al., 1985, 1992a; Treiman, 1995; Ramzan, 2012; Wolff et al., 2013, Wolff, 2018). We separate the SGPFZ into an eastern section and a western section, with a crustal fault boundary (not a tear fault) near Banning Canyon (Fig. 1). We base this boundary on differences in characteristics between the two sections. The eastern section is structurally more complex than the western section, having multiple thrust-fault strands that together represent a long period of Quaternary contractional deformation; it is not clear whether older strands recognizable in the eastern section are present in the western section. There are longer and more clearly pronounced faults at the surface in the eastern section. Finally, there is abundant evidence for Holocene activity in the eastern section, but in the western section, this evidence is equivocal west of the Banning Bench.

Banning Strand

The Banning strand of the SAF extends from the Indio Hills across the Coachella Valley to the eastern edge of the SGPr. To the east of the SGPr, in the vicinity of Devers Hill (Fig. 1), the trace of the Banning strand can be distinguished by a subparallel series of north- and south-facing scarps. At Devers Hill and to the southeast, the scarps face to the south; just northwest of Devers Hill, they face north. In the transition zone between these two sections, a right step occurs between two en echelon fault strands. Just southeast of State Highway 62 (Fig. 1), scarps associated with the Banning strand again face south; continuing northwest across the highway, the strand is marked by local scarps and is dotted-where-concealed beneath late Quaternary deposits of various ages.

Where it crosses Whitewater River, the Banning strand is marked by a prominent vegetation lineation. To the west of Whitewater River, the Banning strand forms the northern edge of Whitewater Hill[1], and the fault dips ~45°N. Just to the west of Whitewater Hill, the strand is characterized by dextrally

[1]In this report, we refer to landmarks in the Whitewater River area as they were originally labeled on the U.S. Geological Survey (USGS) 1944 1:62,500 topographic map, with Whitewater Hill to the west and Beacon Hill to the east; these designations also matched the benchmark labels on each peak. Unfortunately, beginning in 1955, and due perhaps to a cartographic error, all U.S. Geological Survey (USGS) topographic quadrangle maps for the 7.5′ Whitewater and Desert Hot Springs quadrangles apply the name "Whitewater Hill" to the smaller, *eastern* landform, leaving the large *western* landform unnamed. Dating from Allen's (1957) pioneering work, most workers in the SGPr have referred to the western feature as "Whitewater Hill," ignoring formal USGS naming protocols. To avoid confusion, we also apply that name to the western dome-shaped uplift.

Downloaded from http://pubs.geoscienceworld.org/gsa/geosphere/article-pdf/doi/10.1130/GES02424.1/5548351/ges02424.pdf
by USGS Library user

offset ridges and drainages. The Banning strand is not observable farther to the west, where it intersects the SGPFZ.

Garnet Hill Strand

The Garnet Hill strand was named "Garnet Hill Fault" by Proctor (1968) who deduced its existence in the northern Coachella Valley mainly on the basis of gravity data. Langenheim et al. (2005) refined this geophysical diagnosis by associating the Garnet Hill strand in the northern Coachella Valley with an alignment of magnetic lows and thicker basin fill. The fault is also defined by steps in groundwater levels (Tyley, 1974). Proctor's geologic map denotes the fault using a dotted-where-concealed trace. We concur: throughout most of its extent in the northern Coachella Valley, we do not observe primary fault features (scarps and/or lineaments) that would constrain the location of the fault.

In the eastern SGPr, Allen (1957) does not use the name "Garnet Hill Fault." Along the southern base of Whitewater Hill, however, he mapped two faults that Matti et al. (1985, 1992a; Matti and Morton, 1993) associated with the Garnet Hill strand—an interpretation refined by Yule and Sieh (2003) and Huerta (2017). Although mapping interpretations in this area differ in detail, all agree that the Garnet Hill strand lies along the south flank of Whitewater Hill and projects northwestward toward the Cottonwood Creek area. There, each investigator offers a different interpretation of structural relations. In our usage, we associate with the SAF those geologic structures having high-angle dips and predominantly dextral slip; in contrast, we associate with the SGPFZ those geologic structures having low-angle dips and predominantly thrust and/or reverse slip. Using these criteria, the Banning and Garnet Hill strands are high-angle dextral faults that approach the SGPr from the southeast and gradually transition into shallowly north-dipping contractional structures that we associate with the SGPFZ—mainly west of Cottonwood Canyon. Our Figures 1 and 4 illustrate how we interpret geologic relations between the Garnet Hill strand and the SGPFZ.

Pinto Mountain Fault System

The Pinto Mountain fault was named by Hill (1928), and early researchers noted that the intersection of the Pinto Mountain fault with the SAF resembled the intersection between the sinistral Garlock fault with the SAF to the northwest (Hill and Dibblee, 1953; Allen, 1957). Dibblee (1968a, 1968b) first documented that the Pinto Mountain fault is a left-slip structure, proposing that the fault in the Morongo Valley area has as much as 9.7 km of sinistral slip displacing Quaternary sedimentary materials containing quartzite and basalt clasts from recognizable bedrock sources in the San Bernardino Mountains. Subsequently, offset crystalline bedrock units of Mesozoic age and older have been cited as evidence for total left slip on the Pinto Mountain fault of 16 to19 km (Dibblee, 1975, 1992; Bacheller, 1978; Powell, 1993; Hopson, 1996). The range of geologic offsets is confirmed by geophysical observations of magnetic anomalies displaced along the fault as well as the length of narrow pull-apart basins between left steps in the fault trace (Langenheim and Powell, 2009).

In the western portion of the Pinto Mountain fault system, a major strand branches southward from the main fault in a northeast orientation (Dibblee, 1968b). Proctor (1968) named this southern branch the "Morongo Valley Fault" and noted sinistral displacements along the strand. In addition to sinistral slip, the fault has generated significant up-on-the-south displacement that has formed the north-facing bedrock escarpment bounding the south margin of Morongo Valley (Fig. 5). The Morongo Valley, between these two major strands of the fault system, has been interpreted as a pull-apart basin formed by sinistral slip along both of these faults combined with dextral slip on the SAF (Dibblee, 1982; Hopson 2012).

Kendrick et al. (2015) mapped the intersection of the Pinto Mountain fault and the Mill Creek strand and noted the latter was offset between 1–1.25 km by the former. This same amount of slip restores displaced streams in the Mission Creek drainage (Kendrick et al., 2015, their figure 12). We build on these observations by noting that the eroded mountain front of the San Bernardino Mountains, on the northwest side of Morongo Valley, is similarly offset by approximately this amount (Fig. 5). We interpret the morphology of the mountain front to indicate that this most recent slip along the Pinto Mountain fault has either reactivated a long-dormant strand within the system or has pioneered a new strand. Previous researchers have suggested that the Pinto Mountain fault was responsible for the ~15 km left bend in the Mission Creek strand (Matti et al., 1985, 1992a). Restoring the 7.1–8.7 km of slip along the Mill Creek strand (Kendrick et al., 2015), which is co-located with the trace of the Mission Creek strand to the south of the juncture with the Pinto Mountain fault, positions the Morongo fault, the southern splay of the fault zone, adjacent to the left bend in the Mission Creek strand. We interpret that the Morongo fault carried much of the total fault displacement, measured to the east of the juncture of the Morongo and Pinto Mountain faults. This interpretation is revisited below when we propose a model of fault activity for the region.

Whitewater Fault

Allen (1957) applied the name "Whitewater Fault" to a north-trending structure that occurs along the east wall of Whitewater Canyon. Allen does not discuss the fault, but his geologic map shows it extending for ~3.3 km (~2 mi) from the Banning strand of the SAF north to where the fault enters the modern wash of Whitewater River. From that point, Allen (1957) does not speculate about the fault's northward continuation. At its south end, Allen indicates that the Whitewater fault is terminated by the Banning strand.

Peterson (1975) reexamined structural and stratigraphic relations associated with Allen's (1957) Whitewater fault and reported that the fault dips 60° to 80° to the east, displays both normal and reverse separations, and juxtaposes the Miocene Coachella Fanglomerate against rocks of the basement complex and Quaternary alluvium. He noted that the fault zone is usually marked by up to 2 m of basement gouge.

Downloaded from http://pubs.geoscienceworld.org/gsa/geosphere/article-pdf/doi/10.1130/GES02424.1/5548351/ges02424.pdf
by USGS Library user

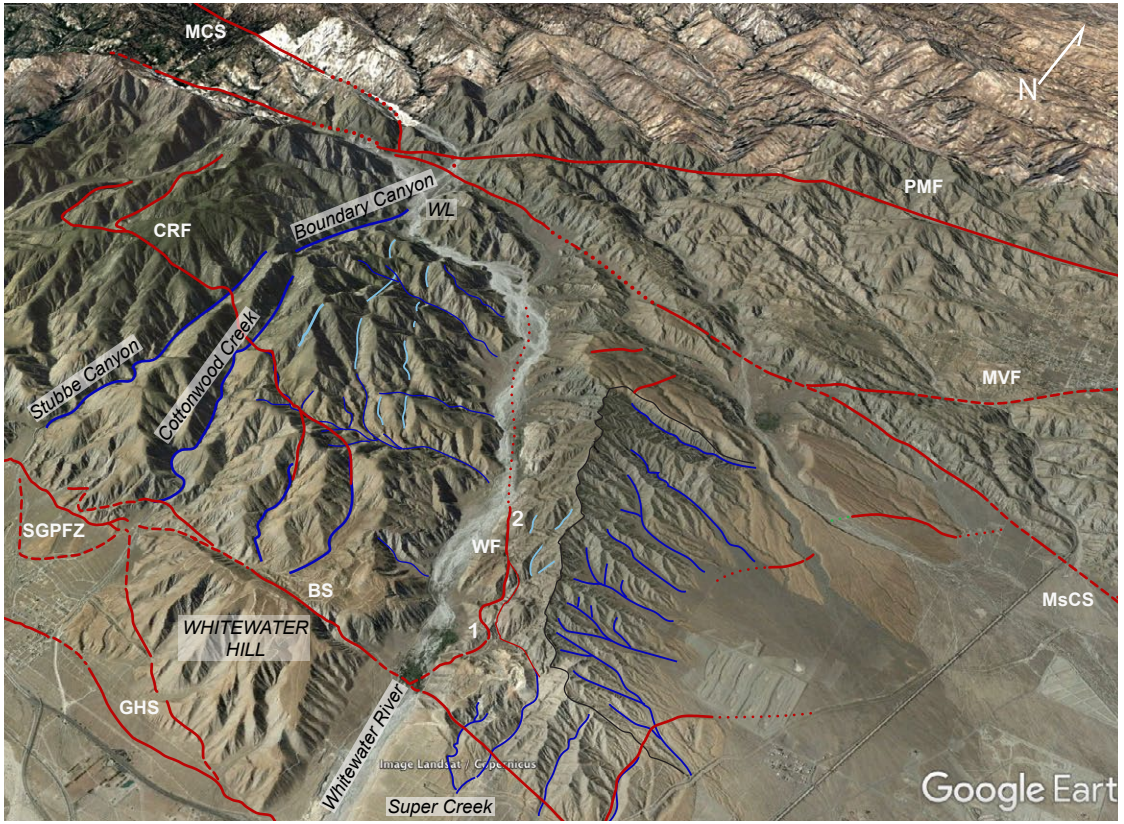

Figure 4. Oblique view of the Whitewater River system, showing faults (red lines) and stream captures. Light-blue lines show geomorphic features interpreted as ancient drainage systems that predate the incised drainage of the current Whitewater River. Active drainages are shown as dark-blue lines. Faults and fault strands are abbreviated as Banning strand (BS), Cox Ranch fault (CRF), Garnet Hill strand (GHS), Mill Creek strand (MCS), Mission Creek strand (MsCS), Morongo Valley fault (MVF), Pinto Mountain fault (PMF), San Gorgonio Pass fault zone (SGPFZ), and Whitewater fault (WF). Wathier Landing is labeled as WL. Sites 1 and 2 indicate locations where the dips of shears within the crush zone of Whitewater fault have been measured (35° to 65° to the east and 38° to 84° to the east, respectively).

Our interpretation of the Whitewater fault differs somewhat from that of either previous investigator, in that we use different criteria for distinguishing this fault from older faults. As a result, our mapping of the Whitewater fault is positioned slightly to the west of the fault mapped by Allen (1957) in the southern section of the fault. This southern portion of the fault (Fig. 4) is marked by scarps in Pleistocene alluvial deposits and by a zone of sheared and crushed crystalline rocks. Shears within this crush zone dip between 65° and 35° to the east, with motion up on the east (site 1 on Fig. 4). Farther to the north, the fault dips between 38° and 84° to the east (site 2 on Fig. 4).

Designation of Structural Blocks

In this study, we define three structural blocks (Fig. 1), approximately within the bounds of the Morongo block defined by Spotila et al. (1998, 2001).

Kitching Peak Block

We apply the name "Kitching Peak block" to the eastern part of the "Morongo block" of Spotila et al. (1998, 2001). The name derives from a summit located centrally within the block's footprint (Fig. 1). The majority of the block is underlain by crystalline rocks of San Gabriel/Chocolate Mountains–type (bedrock nomenclature after Matti et al., 1983, 1985, 1992a; Matti and Morton, 1993). The rocks are characterized by pervasively layered fabrics and structures that range from textural foliation through gneissose compositional layering. Some rocks clearly are plutonic in origin and typically are granodioritic to tonalitic in composition; monzogranite is rare. Other rocks are metamorphic in origin and range from layered gneiss to augen gneiss; these rocks also are granodioritic to tonalitic, although locally mafic components are dioritic to amphibolitic. Pegmatite dikes and layers are common in some areas. The rocks locally are highly fractured and sheared, and they weather readily into colluvial slopes and cones.

Downloaded from http://pubs.geoscienceworld.org/gsa/geosphere/article-pdf/doi/10.1130/GES02424.1/5548351/ges02424.pdf
by USGS Library user

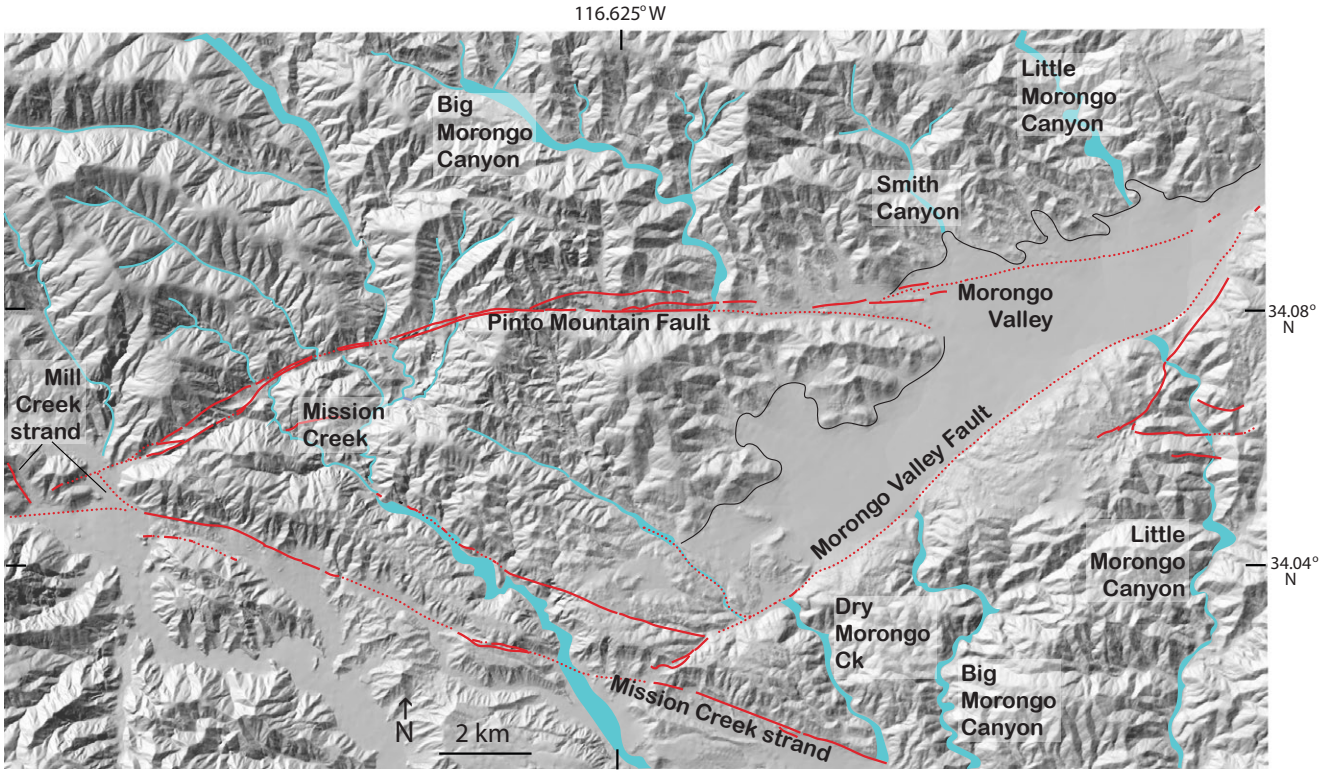

Figure 5. Shaded-relief elevation map of the Pinto Mountain fault system, including the Pinto Mountain and Morongo Valley faults. Faults are shown by red lines, solid where well located, dashed where inferred, and dotted where concealed. Major drainages are shown in blue. The thin black line delineates the mountain front of the southeastern edge of the San Bernardino Mountains.

Boundaries for the Kitching Peak block differ structurally and geomorphically throughout their extent (Fig. 1). To the west, the block is bounded by the Burro Flats section of the San Bernardino strand, and the contrast between the low-standing landscape of Burro Flats and the high-standing Kitching Peak terrain is dramatic. To the north, the Kitching Peak block is separated from the Yucaipa Ridge block by the Mission Creek strand of the SAF. To the south, the Kitching Peak block is bounded by thrust and reverse faults of the SGPFZ that carry crystalline rocks of the block over late Cenozoic sedimentary rocks in foothills to the south. The Banning strand marks the block's southeastern boundary. The eastern boundary of the Kitching Peak block is defined as the Whitewater fault. The northern extent of the Whitewater fault is unknown, but here we extend it to intersect the Mission Creek strand, and we map it as concealed beneath the alluvium along Whitewater River and to the east of the hill associated with Wathier Landing (Fig. 1).

Pisgah Peak Block

We apply the name "Pisgah Peak block" to the western part of the "Morongo block" of Spotila et al. (1998, 2001). The name derives from a summit located at the north part of the block's footprint (Fig. 1). The Pisgah Peak block is underlain by foliated crystalline rocks of San Gabriel Mountains–type that are lithologically and structurally similar to those in the Kitching Peak block (described above).

The Pisgah Peak block is bounded to the east by the Burro Flats section of the San Bernardino strand and to the south by the SGPFZ (Fig. 1). Together, the Mission Creek and San Bernardino strands form a compound structural boundary that separates the Pisgah Peak block on the north side from the Yucaipa Ridge and Cram Peak blocks (Fig. 1). A western boundary for the Pisgah Peak block is open to interpretation. We note that the boundary zone coincides with the westward transition from contractional structures of the SGPFZ (Matti et

Downloaded from http://pubs.geoscienceworld.org/gsa/geosphere/article-pdf/doi/10.1130/GES02424.1/5548351/ges02424.pdf
by USGS Library user

al., 2015) to extensional structures of the Crafton Hills fault complex (Figs. 1 and 2). Logically, this tectonic transition marks the western boundary of the Pisgah Peak block. Unfortunately, faults that might define a western boundary for the block have not been recognized at the surface, although groundwater investigations and gravity surveys (summarized by Mendez et al., 2016) recognize groundwater barriers in the eastern part of the Yucaipa lowland that may coincide with faults that do not daylight. Acknowledging these uncertainties, we propose that the western boundary of the Pisgah Peak block coincides with the eastern margin of the Yucaipa alluvial lowland (Fig. 1).

Garnet Hill Block

We apply the name "Garnet Hill block" to the landscape between the Banning and Garnet Hill strands of the SAF; the name derives from the isolated outlier of late Cenozoic sedimentary rocks that occur at Garnet Hill (Fig. 1). This landscape is distinguished by two features: (1) high-standing, dome-shaped structural uplifts that expose late Cenozoic sedimentary deposits (some as young as middle Pleistocene) and (2) low-lying areas of late Quaternary surficial materials that either buttress against the domal uplifts or issue from canyons and arroyos that are aggressively eroding into the uplifts. In either case, the tectonic geomorphology of the Garnet Hill block is the most recent and obvious example in the SGPr of the interplay between tectonism and attendant landscape response.

Geomorphology of Kitching Peak and Pisgah Peak Blocks

Our primary interest is to compare the geomorphology of the Pisgah Peak and the Kitching Peak blocks in order to evaluate the continuity of the San Bernardino strand to the south of Burro Flats. Here we present geomorphic variables of the bedrock and the mapped distribution of Quaternary deposits for each of the two blocks (Figs. 6–8).

We compare the elevation distribution of the Kitching Peak and Pisgah Peak blocks (Fig. 6A). The overall relief of the Pisgah Peak block is lower, with elevations ranging from 673–1675 m, as compared to Kitching Peak block elevations, which range from 500–2415 m. The Kitching Peak block has high elevations along its northern boundary, especially adjacent to lower Raywood Flats on the Yucaipa Ridge block, as well as at Kitching Peak, decreasing to the east, south, and west from this high. High elevations within the Pisgah Peak block, while lower than those in the Kitching Peak block, are also concentrated at the northern edge, along the boundary with the Yucaipa Ridge block, and decrease to the south. The hypsometry of the two areas is nearly identical, as indicated by the hypsometric integral (Table 1) and the normalized plot of hypsometry (inset, Fig. 6A); we suggest this is likely a function of sampling similar bedrock types across large regions.

A comparison of the areal extent of landslides shows that the Kitching Peak block hosts numerous landslide deposits, whereas landslide deposits are largely lacking in the Pisgah Peak block (Fig. 8; Table 1). Approximately 15.9% of the area represented by the bedrock upland region of the Kitching Peak block is covered by landslide deposits, as compared to ~3% of the Pisgah Peak block area. Within the Pisgah Peak block are landslide deposits (Pine Bench and Burnt Canyon) that originated on the Kitching Peak block and are therefore not included in the areal total for the Pisgah Peak block.

Local relief (Fig. 6B), measured for a radius of 100 m for each pixel, shows many of the same features as does the elevation plot. This measure also highlights, within the Kitching Peak block, a zone of high local relief that extends approximately N-S, located just to the east of Kitching Peak, as well as high local relief extending east of that feature toward Whitewater River. This is a region that is also characterized by many drainage net irregularities and recent stream captures, discussed in the following section. To the north of Whitewater Hill is a region that is both low in elevation and low in local relief and slope. The southwest portion of the Kitching Peak block is also characterized by low elevation and low relief and slope measurements (Figs. 6A and 7A).

The distribution of the standard deviation of slope in each of these blocks also shows that the Pisgah Peak block is morphologically distinct from the Kitching Peak block (Fig. 7B). This metric is a useful measure of surface roughness (Grohmann et al., 2011) and highlights the variability of the shorter slopes within the drainage net of the Pisgah Peak block, in contrast with that of the Kitching Peak block. The characteristics of the elevation distribution as well as of the standard deviation of slope of the southwesternmost portion of the Kitching Peak block seems to be more similar to the Pisgah Peak block, suggesting that the boundary between these blocks may have followed a different fault system prior to the most recent fault configuration, discussed further below. Drainage density, the length of drainages as a function of area, is quite similar between the bedrock regions of the two blocks beyond an accumulation threshold of 100 m^2 (Fig. 8B; Table 1).

The Pisgah Peak block is characterized by thick Pleistocene through earliest Holocene accumulations of sediment in the canyons, including, from west to east, along Little San Gorgonio River, Noble Creek, and San Gorgonio River (for locations, see Fig. 1). Incision into the Banning Bench by the San Gorgonio River provides a three-dimensional view of the volume of sediment accumulation, where exposed thickness of the deposit associated with the Banning Bench ranges from ~15 to >30 m. These canyons and the associated deposits divide the bedrock upland region of the block. In contrast, the Kitching Peak block is largely lacking such sedimentary accumulations. The sedimentary deposits that are present are located along the edges of the block, particularly in the Burro Flats region, and, to a lesser extent, along the eastern side of the crystalline bedrock.

Displacements along the San Bernardino, Garnet Hill, and Banning Strands of the SAF and San Gorgonio Pass Fault Zone

To understand the history of slip along the San Bernardino and Banning strands of the SAF, as well as of the SGPFZ, we describe displacements along these faults that are indicated by our mapping.

Downloaded from http://pubs.geoscienceworld.org/gsa/geosphere/article-pdf/doi/10.1130/GES02424.1/5548351/ges02424.pdf
by USGS Library user

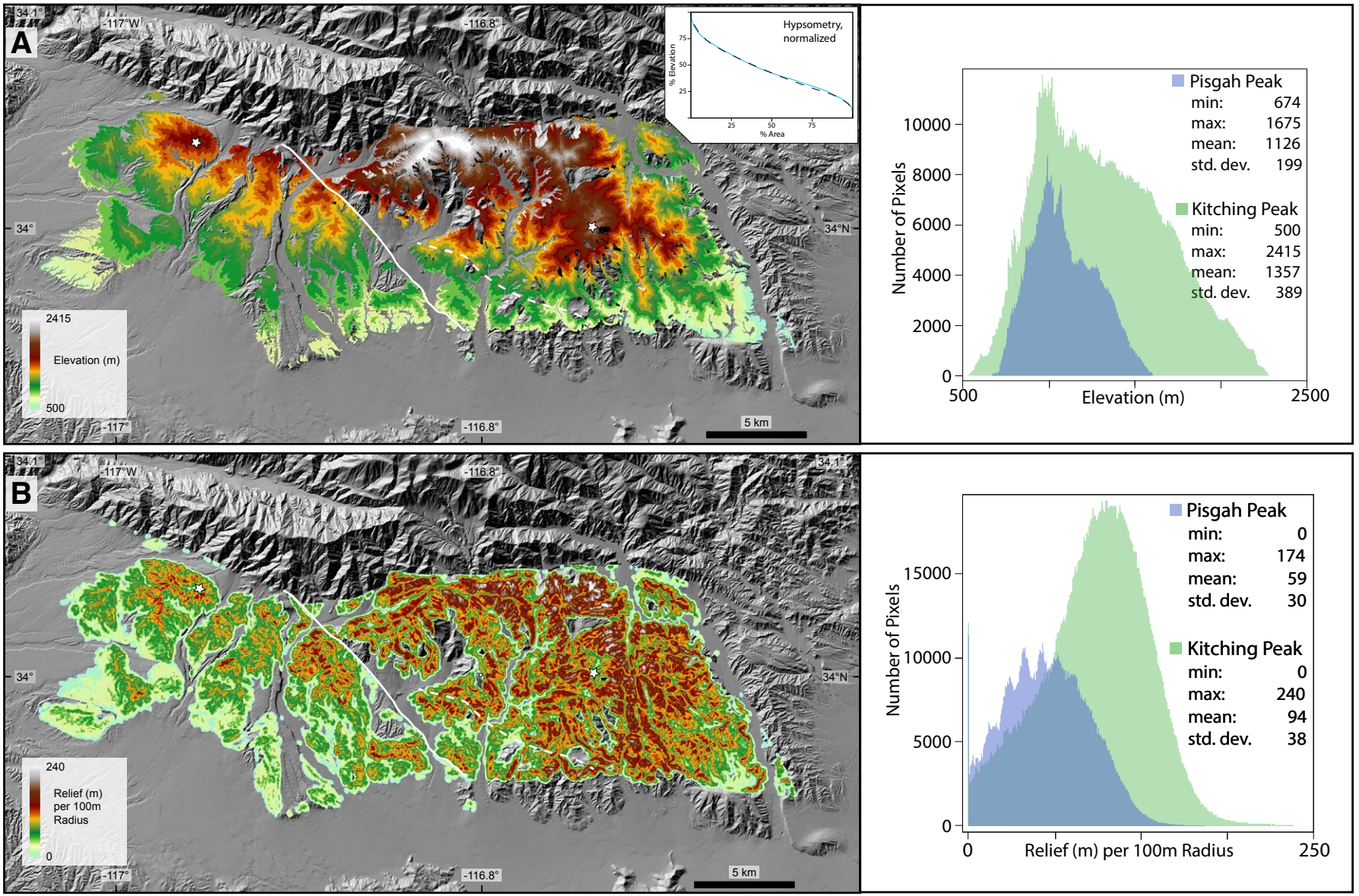

Figure 6. Elevation and relief of the Kitching Peak and Pisgah Peak blocks, using 10 m digital elevation models. Area measured is the upland bedrock portion of each block, the areal extent of landslide deposits removed, as depicted in this figure. White stars are locations of Pisgah Peak (west) and Kitching Peak (east). White line is the division between the two blocks. Dashed white line highlights the southwestern portion of the Kitching Peak block. (A) Elevation, averaged for each pixel. Inset shows the normalized hypsometry with the Pisgah Peak block shown as a solid blue line and the Kitching Peak block as a dashed line. (B) Local area relief (elevation range over each 100 m radius region). Values from both figures are plotted to the right.

Downloaded from http://pubs.geoscienceworld.org/gsa/geosphere/article-pdf/doi/10.1130/GES02424.1/5548351/ges02424.pdf
by USGS Library user

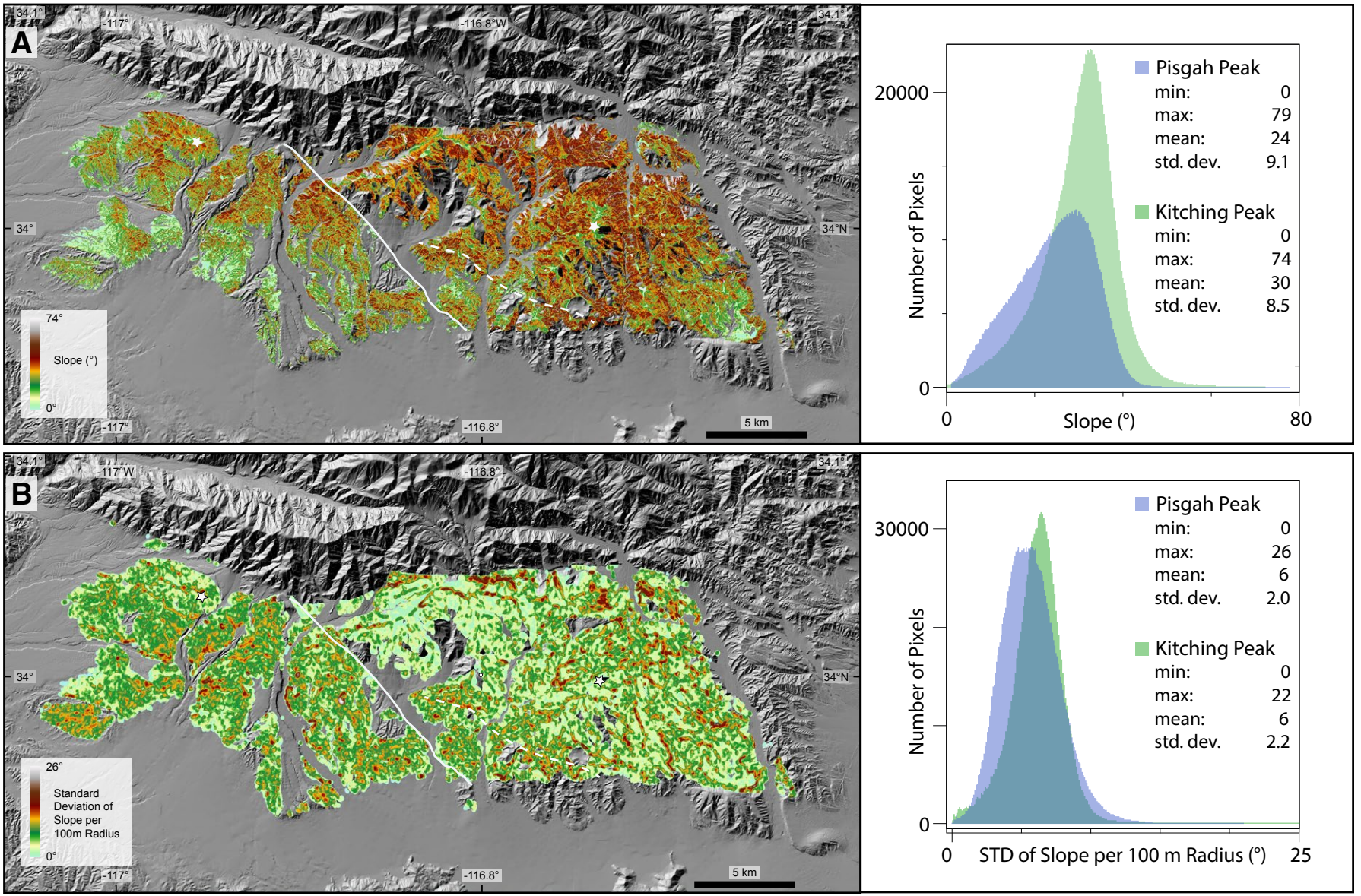

Figure 7. Slope measurements of the Kitching Peak and Pisgah Peak blocks. White stars are locations of Pisgah Peak (west) and Kitching Peak (east). White line is the division between the two blocks. Dashed white line highlights the southwestern portion of the Kitching Peak block. (A) Slope value for each 10 m pixel. (B) Standard deviation of slope within circular areas, 100 m radius, centered on each pixel.

Downloaded from http://pubs.geoscienceworld.org/gsa/geosphere/article-pdf/doi/10.1130/GES02424.1/5548351/ges02424.pdf
by USGS Library user

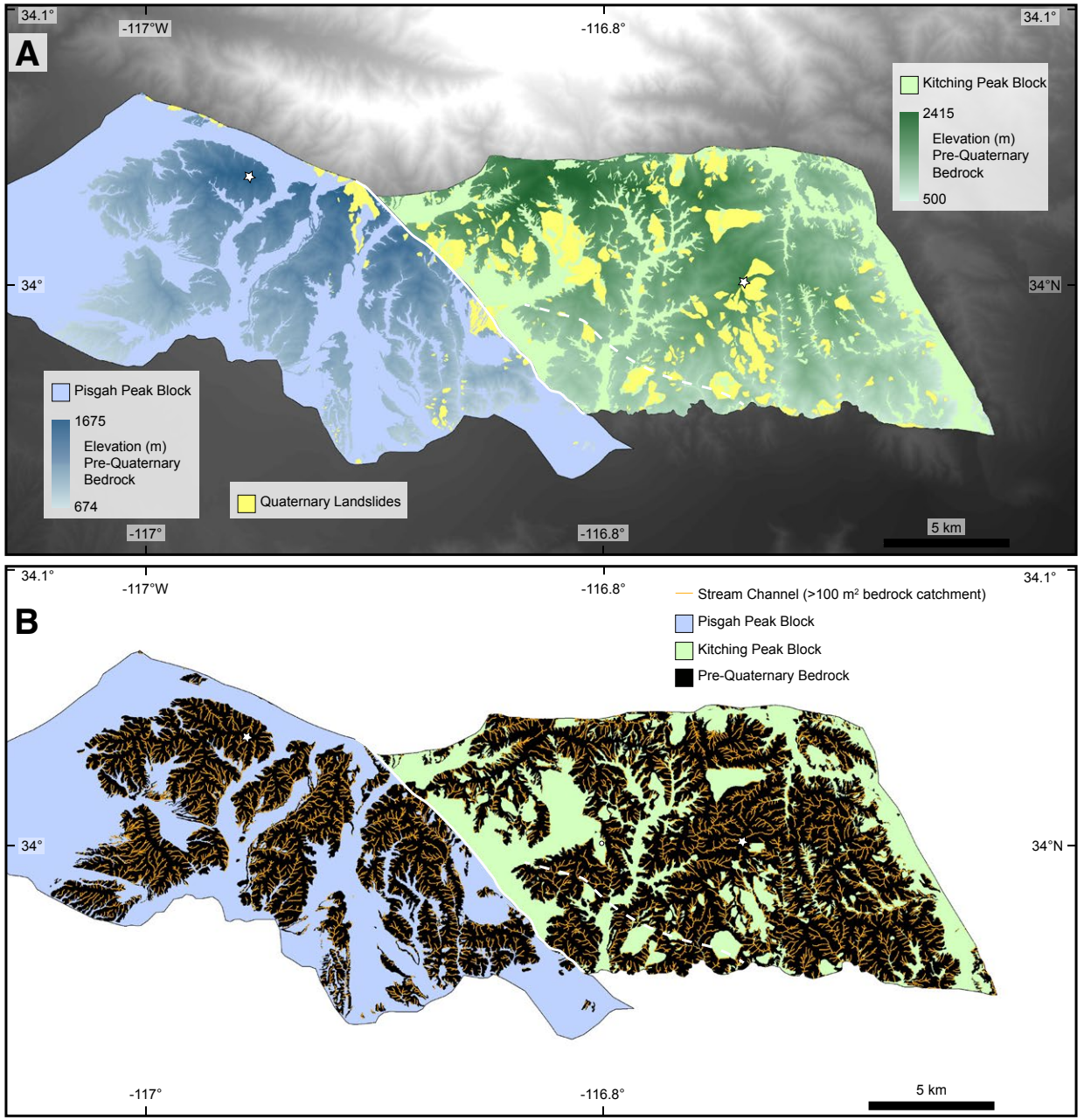

Figure 8. Landslide distribution and drainage net for the Pisgah Peak and Kitching Peak blocks. White stars are locations of Pisgah Peak (west) and Kitching Peak (east). White line is the division between the two blocks. Dashed white line highlights the southwestern portion of the Kitching Peak block. (A) Distribution of mapped landslides (yellow) in the study area. Upland bedrock regions of both blocks are shown with shaded elevation; green for Kitching Peak block and blue for Pisgah Peak block. (B) Drainage net (orange) shown for the same upland bedrock regions as above (shown in black). Drainage net constructed using 100 m² catchment area for 10 m digital elevation model, using flow path tools (ArcGIS v. 10).

Downloaded from http://pubs.geoscienceworld.org/gsa/geosphere/article-pdf/doi/10.1130/GES02424.1/5548351/ges02424.pdf
by USGS Library user

TABLE 1. MORPHOLOGY OF THE KITCHING PEAK AND PISGAH PEAK BLOCKS

	Pisgah Peak Block (PPB)	Kitching Peak Block (KPB)	Southwestern Kitching Peak Block (SWKP)	PPB + SWKP	KP - SWKP
Area of granitic bedrock (km^2)	84.0	123.1	12.4	96.4	110.7
Area of granitic bedrock + landslides (km^2)*	85.3	147.6	14.1	99.4	133.5
Area of landslides (km^2)*	1.3	24.5	1.7	3.0	22.8
Landslides as a function of bedrock area (%)	1.5	16.6	12.1	3.0	17.1
Elevation, minimum (m)	673	500	726	674	500
Elevation, maximum (m)	1675	2415	1353	1675	2415
Elevation, mean (m)	1126	1358	993	1109	1399
Elevation, std. dev. (m)	199	389	108	195	388
Relief, 100, minimum (m)	0	0	0	0	0
Relief, 100, maximum (m)	174	240	198	240	198
Relief, 100, mean (m)	59	94	74	61	95
Relief, 100, std. dev. (m)	30	38	35	31	38
Slope, min (degrees)	0	0	0	0	0
Slope, max (degrees)	79	74	63	79	74
Slope, mean (degrees)	24	30	27	25	31
Slope, std. dev. (degrees)	9	8	9	9	8
Drainage density, 100 m^2 threshold	5.2	5.1	4.7	5.2	5.1
Hypsometric integral	0.447	0.443	0.422	0.430	0.464

*In all instances, landslide deposits are assigned based on their source area block provenance, including Pine Bench and Burnt Canyon Breccia landslide deposits to the Kitching Peak block (totaling 2.1 km^2).

Very Old Alluvial Deposits Northwest of Mill Creek Canyon

At the northwest end of our study area, Matti and colleagues (Matti et al., 1985, 1992a, 1992b, 2003; Matti and Morton, 1993) describe deposits adjacent to the San Bernardino strand, between the Santa Ana River and Mill Creek; these deposits provide an estimate of displacement along the San Bernardino strand (Figs. 2 and 9). These deposits contain clasts that, taken together, are unique and characteristic of those in the Mill Creek drainage system, including Triassic porphyritic monzogranite, the orthogneiss of Alger Creek, and those derived from the Mill Creek Formation. Matti et al. (2003) mapped beds within the unit as dipping up to 65°SW and interpret the unit to represent alluvial fan deposits that were originally adjacent to the canyon mouth of Mill Creek. This previous study suggested that 2–3 km of dextral slip has occurred on the San Bernardino strand since the deposition of this unit. This reconstruction aligned the center of the deposit, and associated landform, with the mouth of the present-day Mill Creek Canyon.

Here we refine and modify this palinspastic and paleogeographic scenario. First, we propose that the stream system that delivered sediment to the displaced alluvial deposits was a broad catchment area on the north side of the modern Mill Creek, centered approximately on Falls Creek (Figs. 1 and 2). This drainage, which we informally name the Falls Creek drainage system, contains the unique rock types that are present in the deposits along the fault. Allen (1957) observed that "rapid erosion of [Mill Creek] canyon has left the valleys of Falls, Vivian, and High creeks hanging 1000 feet above the floor of the main canyon." By implication, the modern floor of Mill Creek once was at an elevation where Falls Creek, High Creek, and Vivian Creek and other tributaries to the west could combine to form a trunk drainage that then coursed downstream and through the narrows at the range front—the current mouth of Mill Creek Canyon. The elevation of Falls, Vivian, and High creeks illuminates the most recent capture by the headward erosion of the modern Mill Creek; the western portion of this original drainage basin has had more time to adjust to the deep incision and lengthening of Mill Creek. The deposition of the unit adjacent to the San Bernardino strand, hereafter called Falls Creek deposits, precedes motion along the Mill Creek strand, based on the degree of soil development and comparison with soils associated with deposits that constrain the timing of slip on that strand (Kendrick et al., 2015); for further discussion, see the "Proposed Long-Term History of San Gorgonio Pass Region" section. Prior to motion along the Mill Creek strand, with the associated elongation of the drainage along that fault, this Falls Creek drainage system, with the associated catchment region, was directly across the Mission Creek strand fault escarpment from the deposits. The modern Mill Creek replaced the ancestral drainage system when tectonic uplift caused excavation of the modern Mill Creek Canyon and headward erosion of Mill Creek along the crush zone of the Mill Creek strand to the dramatic headwaters of the Mill Creek Jumpoff (Kendrick et al., 2015; see their fig. 5A). These events left the Vivian, Falls, and High Creek tributaries hanging above the modern floor of Mill Creek Canyon.

Downloaded from http://pubs.geoscienceworld.org/gsa/geosphere/article-pdf/doi/10.1130/GES02424.1/5548351/ges02424.pdf
by USGS Library user

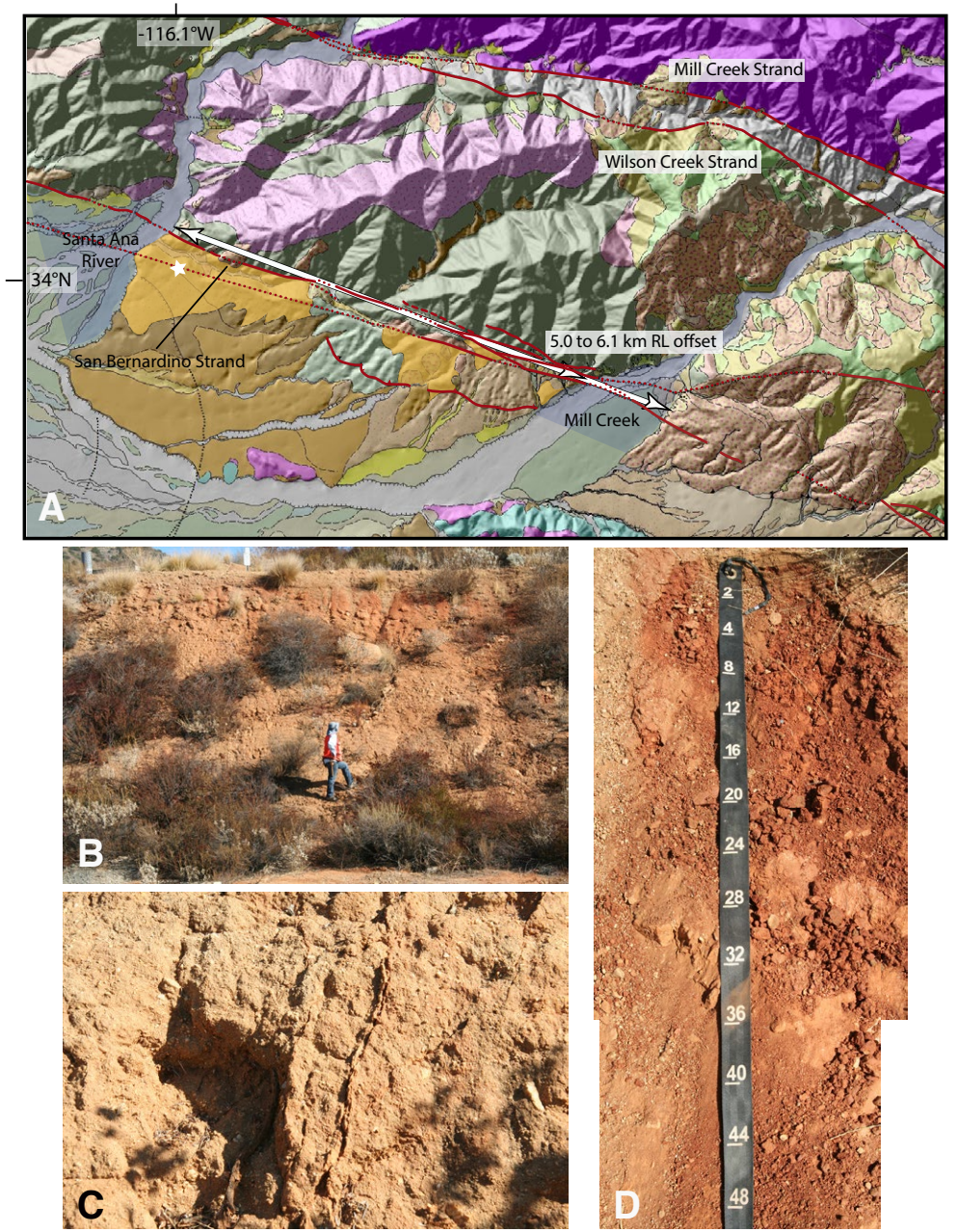

Figure 9. (A) Mapped deposits derived from Falls Creek headwaters, in orange. Arrows show displacement reconstructions, using the western edge of the preserved deposits and the entire width of the canyon mouth. White star indicates location of soil profile described (VC01; Table 2). (B) Photo of soil profile developed in the Falls Creek deposits. (C) Pedogenic silica cementation along fractures in the soil profile; pedogenic silica is also present as grain-to-grain cementation within the soil. (D) Upper part of soil profile associated with this unit.

Downloaded from http://pubs.geoscienceworld.org/gsa/geosphere/article-pdf/doi/10.1130/GES02424.1/5548351/ges02424.pdf
by USGS Library user

In a second modification to the previous fault displacement model (Matti et al., 2003), we propose that dextral displacement of this unit could be as much as 6.1 km, using as a piercing point gravelly and sandy sediment exposed on the incised east wall of the Santa Ana River (Fig. 9A) and considering the entire width of the canyon mouth as a potential source area. The sedimentary sequence in the offset deposit is >40–50 m thick and contains most of the clast types transported down the ancestral Falls Creek Canyon; hence, the sequence could well have accumulated directly down-gradient from the canyon mouth—again, depending on the radial orientation of streamflows associated with the alluvial-fan landform. Based on this model, we interpret that the deposit is time-transgressive, with the western part deposited prior to the eastern portion. Importantly, although the 6.1 km offset is the maximum indicated by the present configuration, the NW extent of the deposit has been eroded by the modern Santa Ana River. The degree of soil development associated with the western part of this deposit (Fig. 2) indicates an estimated age greater than 500 ka (Figs. 9B–9D; VC01 in Table 2), based on comparison with regional, dated surfaces (McFadden and Weldon, 1987; Kendrick et al., 2002). This soil contains abundant secondary pedogenic silica, present in seams and sheets throughout the pedon, as well as in grain-to-grain cementation. The degree of development of this soil pedon indicates that it was stable either prior to the initiation of slip along the Mill Creek strand (Kendrick et al., 2015) or early in the history of slip along that strand. Restoring the displacement on the Mill Creek strand positions the Falls Creek headwaters to be nearly adjacent to the mouth of the drainage system, as discussed further below.

Pine Bench Landslide

At Pine Bench, ~1–2 km northwest of Banning Canyon and the San Gorgonio River (Figs. 1, 2, and 10A), Matti et al. (1983, 1992a) mapped an extensive landslide deposit that caps ~2 km^2 of the Pine Bench landscape. This depositional unit constitutes a large body of crushed and shattered crystalline rock (Figs. 10B–10D). These rocks are highly deformed rocks of the San Gabriel/Chocolate Mountains–type and were not derived from the Mojave Desert–type rocks of Yucaipa Ridge directly to the north. Although it is not possible to unequivocally argue for a cross-fault match for this deposit, we propose that a truncated landslide on the north side of the San Bernardino strand, just northwest of Burro Flats, has a similar dimension as that of the Pine Bench landslide; we interpret that this is the cross-fault source (Fig. 10A). Restoring ~4–4.9 km dextral slip and 90–230 m vertical, up on the southwest, on the San Bernardino strand aligns these landslide deposits. We do not have age control of this feature.

Whitewater Hill Deposits

Whitewater Hill, to the west of Whitewater River, is a distinctive dome-shaped geomorphic feature bound on the north by the Banning strand and on the south by the Garnet Hill strand. The preserved surface of Whitewater Hill is associated with very strong soil development and the key to our geologic and stratigraphic interpretations. Observationally, the soil is strongly rubified (2.5YR hues) and has an associated duripan that extends to a depth of several meters (Figs. 11E and 11F). A shallow soil pit (depth limited to 117 cm) shows that the profile is stripped, a characteristic shared by many old soils in the region, and that numerous clay films are present, up to the designation of thick clay films (soil description nomenclature after Birkeland, 1999; Soil Survey Staff, 1951) on ped faces. We noted silica cementation present at a depth of 71 cm in the soil pit, but the limited depth of the pit prevented us from describing the full soil profile. Pedogenic processes associated with duripan formation created a very hard and resistant soil profile that accounts for extremely steep slopes.

Whitewater Hill is undergoing aggressive erosion by south-flowing streams the canyons of which expose a succession of gravelly and sandy alluvial sediment that is at least 230 m thick. Allen (1957) originally grouped all these sediments into his Cabezon Fanglomerate—a Pleistocene unit that was defined by Vaughan (1922) and crops out in the foothills of the central and eastern SGPr. We prefer a distinct nomenclature, to recognize the unique clast assemblage within these deposits that is not present in the Cabezon Formation, as described to the west. Clasts observed in the basal unit of this succession include (1) sedimentary and volcanic clasts derived from the Miocene Coachella Fanglomerate; (2) saussuritized porphyritic quartz monzonite; (3) foliated and texturally massive rocks of the Mojave Desert–type; (4) mafic tonalite rock, foliated granodiorite, and piedmontite-bearing felsic rock of the San Gabriel Mountains–type; (5) quartz biotite gneiss of Mojave Desert–type; and (6) pegmatite. These clasts suggest a source similar to that sampled by the modern Whitewater River (Matti et al., 1985, 1992a).

We classify the Whitewater Hill succession as depicted in Figure 11A. Like Huerta (2017), we recognize two units: a lower unit that we assign to Qvof1 and an upper unit defined as Qvof2 (Figs. 11E and 11F). The degree of soil development associated with the upper unit, described above, is comparable to a similar duripan developed on alluvial deposits in the Mission Creek alluvial complex that Kendrick et al. (2015, their pedon MC-2) assign to their unit Qvof2.

The sedimentary succession underlying Whitewater Hill is important because it provides evidence for the amount and timing of late Quaternary dextral slip on the Banning strand of the SAF in the SGPr. In addition to the clast compositions, reconnaissance paleocurrent measurements (streamflow toward the south, southeast, and rarely southwest) are consistent with a northern source for these deposits. Clast counts and paleocurrent measurements by Huerta (2017) generally reinforce this interpretation, although Huerta reports some southwest-oriented paleocurrent directions. To accommodate these data, Matti et al. (1985, 1992a) and Matti and Morton (1993) proposed that the Banning strand of the SAF has displaced the Whitewater Hill sequence 2–3 km from its original depositional position downstream from the ancestral Whitewater River to its current position west of the modern Whitewater River. Huerta (2017) proposed a similar offset of 1.5–2.7 km to realign the central portion of this landform with Whitewater River. In the following Discussion section, we

Downloaded from http://pubs.geoscienceworld.org/gsa/geosphere/article-pdf/doi/10.1130/GES02424.1/5548351/ges02424.pdf
by USGS Library user

TABLE 2. SOIL DESCRIPTIONS

Profile horizon	Depth (cm)	Dry color[a]	Moist color[a]	Clay film color[a]	Texture[b]	Structure[c]	Consistency[d] Dry; Wet	Clay films[e]
Pedon WW01; Buried soil at Whitewater River riser site; 33°56.203′ 116°38.199′ Weighted-Mean Soil Development Index: 21.20; Rubification Index: 3.75[f]								
B1	0–45	10YR4/4	10YR3/3	—	SL	2 m sbk	vh–eh; so, po	—
	Cobble to boulder clasts ~ 70%; mafic clasts very weathered.							
B2	45–118	7.5YR5/6 to 4/6	7.5YR5/4	—	LS	Hard to determine; see notes	eh; so, po	2 n po, pf; grain coatings
	Grain-supported horizon; dominantly granule to small cobble; ~3 cm average; Si cementation, interstitial matrix strongly adhered to clasts.							
B3	118–183	7.5YR6/4	7.5YR5/3	—	LS	Hard to determine	vh; so, po	1 n pf
	Clast supported							
B4/Cox	183–301	10YR6/4	7.5YR5/3	—	LS	2 m sbk	h; so, po	1 very few n on clasts
	Clast supported; granule to boulder.							
Pedon WW02; Surface soil at Whitewater River riser site; 33°56.203′ 116°38.199′ Weighted-Mean Soil Development Index: 27.12; Rubification Index: 6.67[f]								
B1	0–16	7.5YR5/6	7.5YR4/4	5YR4/4	SL	2 m sbk	sh–h; ss, po	v1 k pf; v1 mk pf, po; 1 n pf, po
	Clasts are almost completely grussified.							
B2	16–72	7.5YR4/6 pf; 5YR4/4 sieved	5YR4/4	5YR3/4	L	2 m sbk	sh; s, ps	1 k pf, 1 mk pf
	Clasts are almost completely grussified.							
B3	72–124	7.5YR6/6 pf 7.5YR5/6 sieve	7.5YR5/3	—	SL	m, 1 m sbk	sh–vh*; vss, po	1 n pf and on clasts
	Variable consistency; h–vh on small peds; sh–h on large peds.							
C	124–171	10YR5/4	10YR5/4	—	LS	1 m sbk	loose to soft; so, po	—
	Described to the base of the pit.							
Pedon VC01; Vivian Creek deposits; 34°5.9251′ 117°6.056′ Weighted-Mean Soil Development Index: 50.64; Rubification Index: 11.25[f]								
B1	0–21	2.5YR4/5–4/6	2.5YR4/6	—	CL–C	3 m sbk, 3 f abk	h–vh; vs, p	2 k pf, po; 3 mk pf, po
					Clasts very weathered			
B2	21–45	2.5YR4/4	2.5YR4/6	2.5YR4/4	CL	3 m sbk, 3 f abk	h–vh; s, ps	1 k pf, 2 mk pf, po
	Smaller peds are extremely hard.							
B3	45–110	5YR4/4	5YR4/4	—	L+	2 m sbk	vh; s, ps	1 mk pf, 1 n pf
	Boulder/cobble stone line at top of horizon; description of interstitial.							
BC	110–166	5YR5/6	5YR4/4	—	L	2 m sbk	eh; ss, ps	1 mk pf, 1 n pf
	BC extends into lower horizon, which is dominated by Si cementation in sheets and along ped faces; this cementation extends approximately 25 feet to base of artificial cut.							
Whitewater Hill site; 33.9482712°, 116.681832°; Described to only 117 cm **Weighted-Mean Soil Development Index: 40.31; Rubification Index: 11.25[f]**								
B1	0–8	10YR4/4	10YR4/4	—	L	3 m pl	—	—
B2	8–18	7.5YR4/4	5YR4/4	2.5YR4/6	L	2 m sbk	h; ss, ps	1 mk pf, po; 2 n pf
B3	18–36	5YR4/6	5YR4/6	2.5YR4/6	L to SiL	3 m abk	vh; s, ps	2 n pf
B4	36–71	5YR5/6	5YR5/6	—	SL	2 f–m abk	vh; s, ps	2 n pf, 1 mk pf, v1 k pf
B5	71–117	5YR7/8, 5YR6/6	7.5YR4/6	—	co SL	m, 3 m abk	h; s, ps	—
	Silica cementation							

Note: Soil pedons described using nomenclature of Birkeland (1999) and Soil Survey Staff (1951).

[a]Munsell Soil Color Chart.

[b]In this soil, not all abbreviations are used, but they are listed here to show the range of possible values in a soil profile. S—sand; LS—loamy sand; SL—sandy loam; SiL—silty loam; L—loam; SCL—sandy clay loam; SC—sandy clay; CL—clay loam; C—clay; co—coarse; g—gravelly; vg—very gravelly.

[c]Grade: 1—weak; 2—moderate; 3—strong. Size: f—fine; m—medium; co—coarse. Type: m—massive; sg—single grain; sbk—subangular blocky; abk—angular blocky; pl—platy.

[d]l—loose; s—soft; sh—slightly hard; mh—moderately hard; h—hard; vh—very hard; eh—extremely hard; so—not sticky; vss—very slightly sticky; ss—slightly sticky; s—sticky; vs—very sticky; po—not plastic; vsp—very slightly plastic; sp—slightly plastic; p—moderately plastic; vp—very plastic.

[e]Frequency: v1—very few; 1—few; 2—common; 3—many; 4—very many. Thickness: vn—very thin; n—thin; mk—moderately thick; k—thick. Location: pf—ped face; po—pores; br—bridges between grains; gr—grains.

[f]Weighted-mean soil development index, multiplied by 100, after the methods described in Harden (1982) and Harden and Taylor (1983); Rubification Index after the methods described in Torrent et al. (1980).

Downloaded from http://pubs.geoscienceworld.org/gsa/geosphere/article-pdf/doi/10.1130/GES02424.1/5548351/ges02424.pdf
by USGS Library user

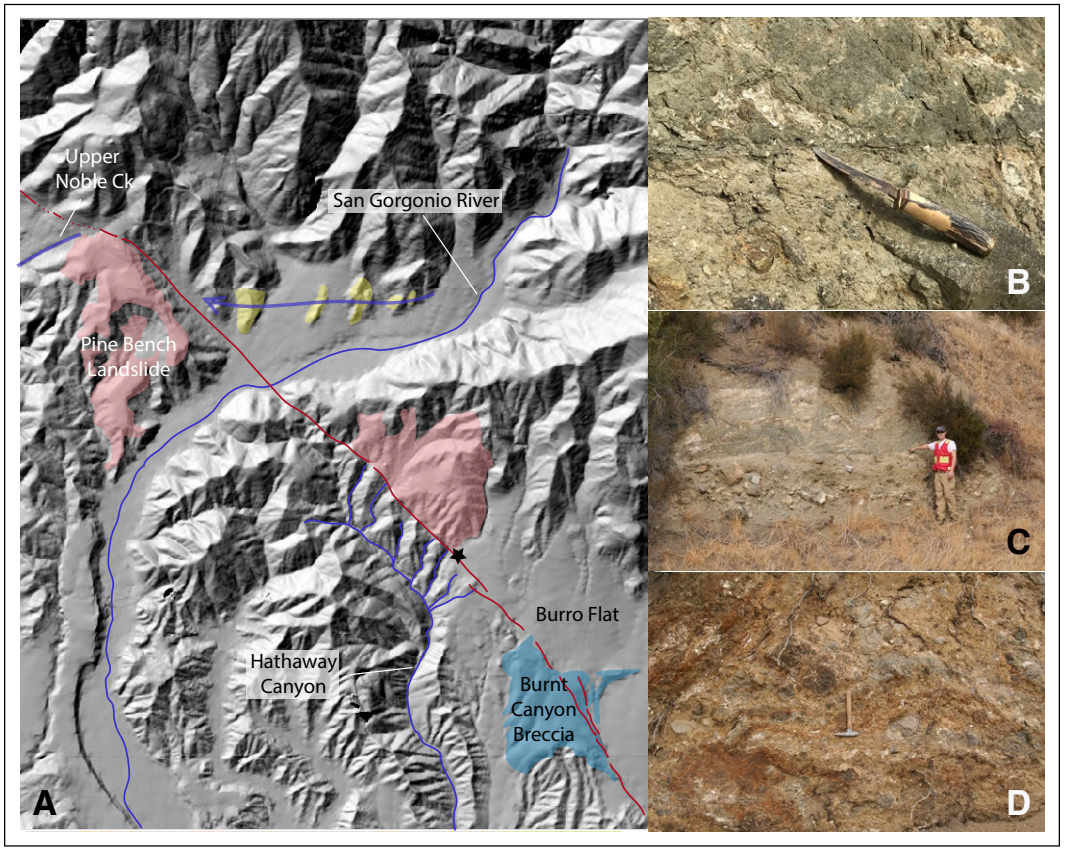

Figure 10. (A) Pine Bench landslide (pink), Burnt Canyon Breccia (blue), and unnamed deposit and terrace surface (yellow). Lower portion of the landslide forms the Pine Bench landform. The unnamed deposits likely represent a former flow path (indicated by blue arrow) of the San Gorgonio River, as it flowed down Noble Creek prior to the most recent slip along the San Bernardino strand. (B and C) Two views of the contact between the landslide deposit and the underlying unit at Pine Bench. (D) The landslide deposits, showing entrained boulders and matrix.

will present various models to constrain minimum and maximum offset of the geomorphic feature and associated deposits, as well as justification for our preferred option.

Two prominent soil profiles are present on the eastern embankment of Whitewater River (Hofmann et al., 2017, 2019; Fig. 11B). The surface soil is rubified, with 7.5YR colors in the maximum B horizons and 5YR clay film colors, and has very few to few clay films on ped faces and in pores. In the maximum B horizons, the clasts are nearly completely grussified, and there is no duripan associated with this soil (pedon WW01; Table 2). The buried soil is characterized by 7.5YR colors in the maximum B horizon, thin, scarce clay films, and less weathered clasts than within the surface soil (WW02; Table 2). This buried soil profile also lacks the duripan that is present in the soil pedon associated with Whitewater Hill. These results suggest that a direct correlation cannot be made between either of these two soils and the soil developed on Whitewater Hill.

DISCUSSION

Elevation, total relief, local relief, and slope metrics all differ significantly between the Kitching Peak and Pisgah Peak blocks. In addition, the distribution of landslide and fluvial deposits indicates that these two blocks have had differing uplift histories and continue to experience different dominant surficial processes. Landslide deposits are abundant on the Kitching Peak block, which is also characterized by longer, steeper slopes, indicated by the elevation, local relief, and slope measurements (Figs. 6 and 7). Thick sedimentary packages of Quaternary alluvium are located along drainages that divide the bedrock uplands of the Pisgah Peak block but are absent on the Kitching Peak block. This pattern suggests that, because of either the amount or recency of uplift, or both, sediments generated from the bedrock uplands of the Kitching Peak block are transported beyond the boundaries of the terrain, rather than being stored along canyons within the block. Alternatively, the equivalently aged

Downloaded from http://pubs.geoscienceworld.org/gsa/geosphere/article-pdf/doi/10.1130/GES02424.1/5548351/ges02424.pdf
by USGS Library user

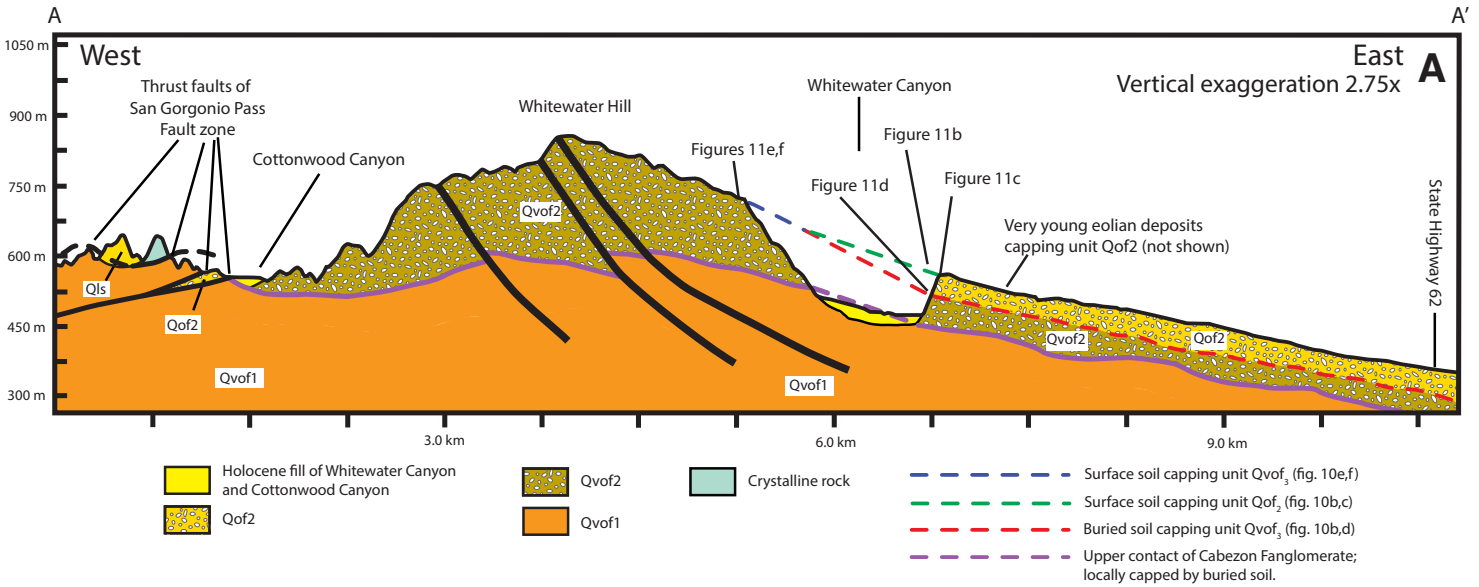

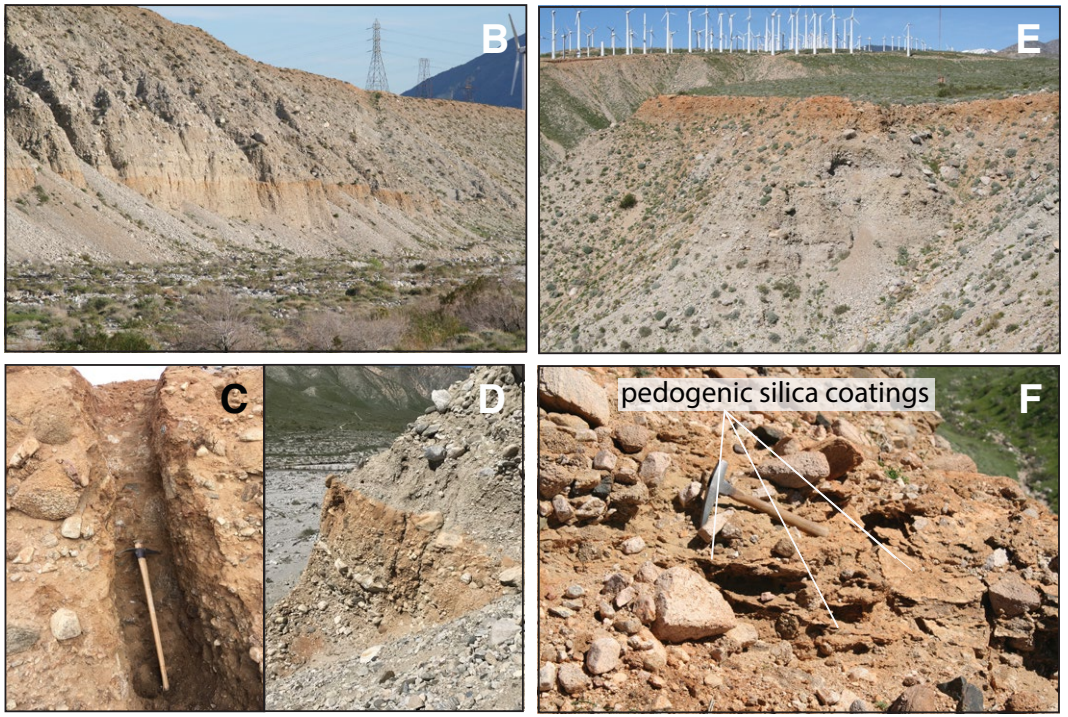

Figure 11. Whitewater Hill units and soil profiles. (A) Schematic cross section, approximately E-W, based on our mapping and pedogenic descriptions; location shown on Figure 1. See text for description and discussion. (B) View ESE across the Whitewater Canyon, showing the surface and buried soils. (C) Upper soil profile. (D) Buried soil profile. (E) Surface soil associated with Whitewater Hill. (F) Pedogenic silica forms sheets and undulating surfaces through the soils associated with Whitewater Hill.

Downloaded from http://pubs.geoscienceworld.org/gsa/geosphere/article-pdf/doi/10.1130/GES02424.1/5548351/ges02424.pdf
by USGS Library user

deposits within the Kitching Peak block boundaries may have been present in the past but were stripped by erosion during recent uplift. In contrast to the Pisgah Peak block, the Kitching Peak block is characterized by numerous stream captures, discussed further in subsequent sections.

Morphometric variables of these two blocks provide evidence that the SAF bisects the landscape to the southeast of Pine Bench; the Kitching Peak and Pisgah Peak blocks have experienced different uplift histories, likely over an extended period of time. The Pisgah Peak block is a landscape that has experienced either lower uplift rate or prolonged stability and increased maturity. We can use the morphometric contrasts between the Kitching Peak and Pisgah Peak blocks to infer that at some point in the past, the SAF system was well integrated, and that slip transferred between the San Bernardino and the Banning strands.

Integration of Geomorphologic and Geologic Data

In spite of the evidence for different uplift histories for the two blocks, evidence for the bounding fault between the Pisgah Peak and Kitching Peak blocks is discontinuous at the surface. The San Bernardino strand cannot be unequivocally mapped to connect with the SGPFZ, as discussed above. One possibility for this lack of continuity may be that slip is stepping across to the Gandy Ranch strand (Yule and Sieh, 2003), to the south of the Burro Flats section. This fault has evidence of recent faulting, including scarps and small offsets. According to our mapping, this fault is the northernmost fault in the fault study of the Millard Canyon area (McBurnett, 2011; Heermance and Yule, 2017). In spite of this youthful activity, the Gandy Ranch strand lacks evidence for long-term fault offset and cannot be traced farther to the west than Banning Canyon. Another possibility is that the evidence for youthful faulting along the San Bernardino strand has been removed by fluvial activity along Potrero Creek. A short, inferred fault fragment, labeled SBS/GRS on Figure 3, has a similar strike and is approximately aligned to the San Bernardino strand where we map it to the northwest. This fault section might represent an active part of the San Bernardino strand. It might alternatively be a part of the Gandy Ranch strand, or be reactivated by recent activity on the Gandy Ranch strand.

The lack of strong geomorphic evidence for sustained, youthful faulting along the San Bernardino strand south of the Burro Flats region (Allen, 1957; Matti et al., 1985, 1992a; Matti and Morton, 1993) might be explained by one of two scenarios. One possibility is that the SAF is actively re-establishing a through-going trace following disruption of a previously active strand and the accompanying obliteration of surface expression by young fluvial processes and deposits, as mentioned above. In this scenario, the young fault trace has been lengthening and extending toward the SE from the approximate location of Pine Bench. This hypothesis follows from the model presented by Matti et al. (1992a) of the establishment of the San Bernardino–Banning–Garnet Hill route for plate-boundary slip following the disruption of, and termination of, significant slip along the Mill Creek strand. This scenario can explain why the fault segment to the south of Burro Flats lacks the tectonic geomorphology associated with a major fault system. This lack of evidence for faulting would be a result of the recency of formation; this segment would have experienced only a limited number of ground-rupturing earthquakes, and a strong, well-defined geomorphologic expression of the fault is therefore absent.

The distinct difference in morphology between the Pisgah Peak and Kitching Peak blocks suggests an alternative scenario. The differences in the landscapes on either side of the projection of the San Bernardino strand suggest that these blocks have experienced differing uplift histories over a long interval of time. This would be explained if the San Bernardino strand was well-integrated with the then-active SAF in the northern Coachella Valley at some time in the past, permitting through-going rupture along the SAF through the SGPr, and varying uplift between the two blocks as a result. In this case, more recent disruption has complicated and obscured the connectivity between the structures. This disruption might be compressional movement along the SGPFZ, as proposed by Matti et al. (1985, 1992a), or some other structural disruption to through-going slip. The eastern section of the SGPFZ, the section that demonstrates current fault slip, spans the region of the projected juncture of the San Bernardino strand with this fault, as discussed above. This is similar to the results presented by Fattaruso et al. (2016) using Boundary Element Method models to explore the fault network changes. They find a similar uplift of the Kitching Peak block and down-dropping of the Pisgah Peak block when the San Bernardino strand is active and connected with the SAF strands to the SE.

A third option would be a combination of these two models. There may have been a long-active fault connection along the path of the San Bernardino–Banning–Garnet Hill strands in the SGPr, but the Burro Flats section, with its discontinuity, might represent a newly active portion of the fault system.

An intriguing aspect of the morphologic analysis is the apparent lineament that separates the southwest portion of the Kitching Peak block from the remainder of the block (Figs. 6, 7, and 12). The measure of standard deviation of slope, calculated over a 100 m radius for each 10 m pixel, yields a fairly sharp delineation (the northernmost dashed line on Fig. 12). The elevation range by pixel (Fig. 6A) also indicates a broad step in topography at this location. A second lineament is present roughly parallel to the first and is marked by short, disconnected segments of faults mapped in bedrock (Allen, 1957; Yule and Sieh, 2003; this study) and multiple large landslide deposits. The southern lineament bounds the southern edge of an unusual geomorphic landform. This landform, a circular closed depression that lies to the northeast of Lion Canyon, might represent a southward-oriented headwater region blocked by lateral translation of an elevated terrain (a shutter ridge) or have a purely landslide origin. For purposes of discussion, we refer to this unnamed landform as Hidden Flat, after a nearby benchmark. The northern of the two lineaments seems to fall along the northern edge of this closed depression, is covered by a large landslide (Fig. 12A), and has a fault mapped by Allen (1957) and Yule and Sieh (2003) along some of the reach. The projection of this lineament to the northwest might have continued along the northeastern edge of Burro Flats, and its presence could help to explain the shape of this intermontane valley. This region, in the southwest portion of the Kitching Peak block, shares morphometric similarities

Downloaded from http://pubs.geoscienceworld.org/gsa/geosphere/article-pdf/doi/10.1130/GES02424.1/5548351/ges02424.pdf
by USGS Library user

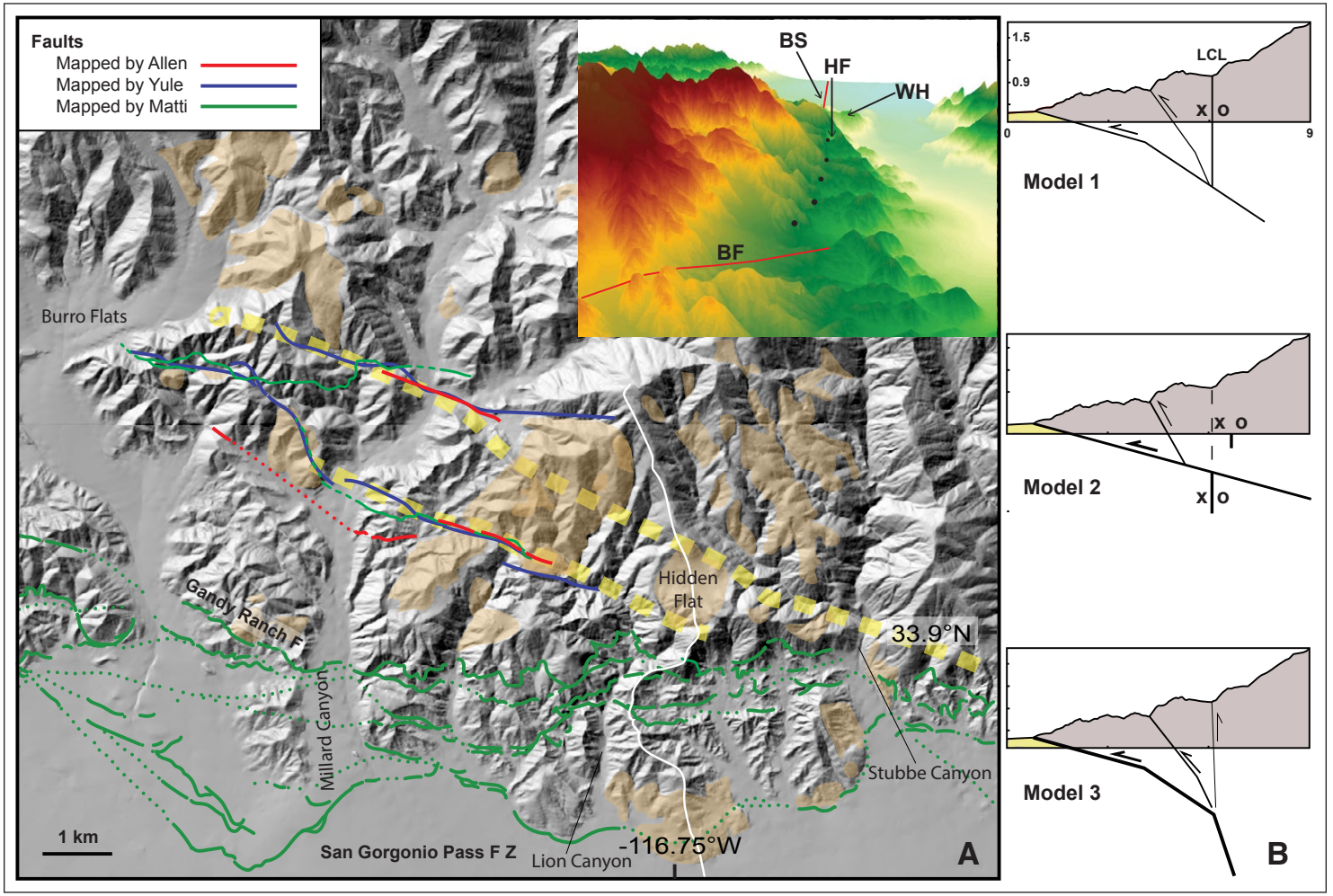

Figure 12. (A) Overlay of morphometric lineaments, defined here as the Lion Canyon lineament zone (yellow dashed lines) with mapped faults and landslide deposits (tan polygons) on shaded-relief topographic base. Faults mapped by Allen (1957), Yule (Yule and Sieh, 2003), and this study. Landslide deposits are mapped as a part of this study. Inset shows an Arc-GIS oblique view of the Lion Canyon lineament zone with 3× vertical exaggeration. The view is ~090° above latitude 33.99°, longitude –116.99° with eye elevation of ~10 km. Elevation is depicted using a standard Arc-stretched color ramp with low of 130 m and high of 3506 m. Abbreviations: BS—Banning strand, BF—Burro Flats, HF—Hidden Flat, and WH—Whitewater Hill. Dots show Lion Canyon lineament zone (LCL) position. (B) Three models to explain the presence of the Lion Canyon lineament zone (LCL). Topographic profile for the models is shown by white line in Figure 12A, looking west. Model 1 assumes that the lineament is caused by right-lateral, strike-slip faulting along a previously active strand of the San Andreas fault (SAF). Model 2 proposes that the lineament is caused by gravitational collapse above footwall sediments above the active SAF. In this case, faulting does not extend to the surface. Model 3 proposes that this lineation is an abandoned thrust fault that once defined the range front but has been uplifted and rotated as a result of lower-angle, younger thrust faults forming basinward from this older thrust fault.

Downloaded from http://pubs.geoscienceworld.org/gsa/geosphere/article-pdf/doi/10.1130/GES02424.1/5548351/ges02424.pdf
by USGS Library user

with the Pisgah Peak block. This suggests that a bounding structure in the past may have followed one or both of these lineaments. We informally refer to this zone as the Lion Canyon lineament zone, named for a canyon central to its trace. This zone is within a region where we lack the land access to make bedrock observations. Considering this limitation, we envision three alternative models that could explain this lineament (Fig. 12B).

Model 1 asserts that this is a previously active fault zone but acknowledges that the evidence for this fault zone is not robust, particularly toward the east. The fault traces within this lineament zone, as mapped by this study and previous researchers (Allen, 1957; Yule and Sieh, 2003), are discontinuous, but have been verified by field checking (D. Yule, 2019, written commun.). The lineament zone is partially obscured by landslides (Fig. 12A), and our reconstruction, described below, would have had fault slip occurring on this section prior to initiation of slip along the Mill Creek strand, with no recent activity; both of these factors account for the lack of clear fault morphology. This zone is within a region where we lack the access necessary to check our interpretation.

An alternative interpretation of this lineament zone is that it is a manifestation of an active footwall structure (Model 2). In their N-S cross section, Langenheim et al. (2005; their Figure 7) interpret that the presence of a wedge of low-density materials beneath the SGPFZ best matches their magnetic and gravity data. This low-density material is bound to the north by the subvertical Banning strand, which is present in the footwall of the SGPFZ, and does not extend to the surface. The broad Lion Canyon lineament zone then might reflect a brittle fabric or damage zone that has developed above this footwall structure, perhaps enhanced by the contrast in material properties of the emplaced sediments adjacent to the crystalline bedrock at depth. A shallowing of SGPFZ fault could be associated with overthrusting of the basin sediments and be a contributing factor. This lineation zone is aligned with a projected connection between the San Bernardino strand, just north of Burro Flats, and the Banning strand where it is last clearly defined (shown as small black triangles on Fig. 1). This connection at depth would represent an active high-angle fault and offers an alternative explanation for the lack of surficial connection through the SGPr.

A third model to explain the presence of this lineament would be that it represents an abandoned thrust strand (Model 3). The Lion Canyon lineament would be the former position of a range-front thrust that is now uplifted and back-rotated by the development of more outward and active thrust faults. An argument in favor of either Model 2 or Model 3 is that the lineament zone lacks preserved fault offsets in the geomorphology.

For purposes of comparison, we reevaluated the geomorphic variables, using this Lion Canyon lineament zone as a boundary to the south of Burro Flats (Table 1; dashed line shown on Figs. 6–8). This southwest portion of the Kitching Peak block (SWKP) is characterized by numerous landslides, similar to that observed in the Kitching Peak block as a whole. Including the area within Pisgah Peak slightly reduces the distinction between the two blocks for this variable. Including the SWKP in the Pisgah Peak block slightly increases the difference between blocks for elevation mean and standard deviation but has a negligible effect on other geomorphic differences (Table 1).

Implications for Fault Activity

To better address the alternate explanations for the continuation of the San Bernardino strand south of Burro Flats, we focus on what is known about recent fault activity on the San Bernardino, Gandy Ranch, and Banning strands, as well as the SGPFZ. We then turn to the evidence provided in the offsets along these strands, presented above, and explore the implications for timing of activity of these strands.

Recent Fault Activity

The Wilson Creek slip-rate site is to the west of the SGPr (WC; Fig. 1). There, Harden and Matti (1989) described alluvial fan displacements and estimated the age of the surfaces using the degree of soil development. The alluvial fans contained distinctive clasts of the Potato Sandstone, transported along Wilson Creek. The preferred slip rates at this site are 14–25 mm/yr for the past 14 k.y., 22–34 mm/yr for the past 30 k.y., and 12–16 mm/yr for the past 65 k.y., or 90 ka.

At the northwestern corner of Burro Flats (Figs. 1 and 2), Yule and others conducted paleoseismic and slip-rate studies of the San Bernardino strand and associated secondary splays (BF; Fig. 1; Yule and Sieh, 2001; Yule et al., 2001; Yule and Sieh, 2003; Orozco, 2004; Yule, 2009, 2010; Yule and Spotila, 2010). They report fault dips of 75°SW and five paleoearthquakes in the past ~1500 years. Orozco (2004) reported slip rates ranging from 4.0 ± 1.5–6.0 ± 5.0 mm/yr over the past 4.0–4.3 k.y.

Along the Gandy Ranch strand, Heermance and Yule (2017) report a slip rate of ~1.2 mm/yr for the past 5.7 k.y. and 3.7 mm/yr for the past ~1.3 k.y. on what they refer to as the northern fault (NM; Fig. 1). They estimate the amount of slip by combining vertical separation and an assumed regional stress vector to calculate lateral slip. They combine this slip determination with ^{10}Be dating of the vertically separated terrace surfaces. These researchers estimate the number of earthquakes by assuming a vertical displacement of 1 m per event.

In the same study, along the SGPFZ, Heermance and Yule (2017) report slip rates of between 3.2 and 4.2 mm/yr, over the past 1.3–5.7 k.y., respectively (SM; Fig. 1). These slip-rate sites are along the fault they refer to as the southern fault in their study. The estimation of slip rates at this location is based on the same criteria as are applied to the Gandy Ranch strand—using a similar regional stress vector combined with vertical separation. Just to the east of Millard Canyon, at Lion Canyon (LC; Fig. 1), also along the SGPFZ, paleoseismic investigations have recorded the most recent earthquake to have occurred between 0.6–0.8 ka (Ramzan, 2012; Wolff, 2018), along with three to four previous earthquakes over the past ~6 k.y. (Wolff, 2018).

In the Painted Hills region, east of Whitewater River, Gold et al. (2015) constrained the age of an offset alluvial fan using U-series dating of pedogenic carbonates and ^{10}Be cosmogenic nuclide exposure dating of surface clasts (PH; Fig. 1). They used this age along with the displaced fan apex to conclude a Holocene slip rate for the Banning strand of 3.9 +2.3/–1.6 mm/yr

Downloaded from http://pubs.geoscienceworld.org/gsa/geosphere/article-pdf/doi/10.1130/GES02424.1/5548351/ges02424.pdf
by USGS Library user

to 4.9 +1.0/–0.9 mm/yr. Paleoseismic investigations along the Banning strand in Desert Hot Springs, to the east of the Painted Hills site, documented five paleoearthquakes that occurred in the past ~3 k.y. and eight paleoearthquakes in the past 7.1–5.7 k.y. (Castillo, 2019; DHS; Fig. 1).

Older History of the San Bernardino Strand and Lion Canyon Lineament Zone

To the northwest of Burro Flats, a maximum measured slip of 6.1 km is required to restore the deposits adjacent to the mouth of present-day Mill Creek Canyon to their source in the Falls Creek headwaters (Figs. 1 and 9). We hypothesize that this canyon mouth is a long-lived landscape feature, previously associated with the Falls Creek drainage system, as discussed above. The displacement might be larger than this measurement, though, because the NW extent of these deposits is adjacent to the Santa Ana River, and any deposits farther to the north would have been removed by erosion along this stream course. The displacement might also have been less than this measurement, if the landform emplaced was an alluvial fan with flow to the northwest along the fault strand; we lack the paleocurrent measurements to address this uncertainty. The soil development associated with this deposit indicates that these deposits have been stable for more than ~500 k.y. (VC01; Table 2). A consequent interpretation stemming from this restoration is that the headwater region of the San Gorgonio River was aligned with the Oak Glen/Live Oak drainage system, and flowed toward the Santa Ana River by way of the San Timoteo drainage system (Fig. 2). At the same time, the downstream portion of what is now the San Gorgonio River had its headwaters in the catchment of Wood Canyon (Fig. 2). This amount of slip, as much as 6.1 km, represents the total cumulative slip observed on this fault strand within the SGPr. Although the displacement of the Vincent thrust fault (shown by thick red lines on Fig. 2) cannot be measured with any accuracy, given the distances over which it is concealed by youthful sediments, the 6.1 km of restored slip on the San Bernardino strand better matches an approximation of that slip than the previously proposed 2–3 km (Matti et al., 2003).

A slightly lower amount of slip, ~4–4.9 km, restores the lower portion of the Pine Bench landslide to its probable origin, discussed above (Figs. 2 and 10). The same amount of slip aligns the northwesternmost beheaded drainage of Hathaway Canyon with the eastern edge of Wood Canyon catchment area (Fig. 2); subsequent beheaded tributary drainages to the southeast are likely to have been occupied sequentially. Each of these smaller beheaded channels was likely occupied for a relatively short interval; this would result in a size differential between these and the continuously occupied Wood Canyon headwater drainage. The headwaters of the San Gorgonio River would also have sequentially occupied drainages to the east of the Oak Glen/Live Oak drainage system (Fig. 2), including Little San Gorgonio Creek (~4.6 km offset) and Noble Creek (~2.5 km offset). The downstream portion of Millard Canyon would have aligned with Hidden Flat and was likely a much smaller drainage prior to the capture of the upper reach of the canyon.

Within Burro Flats is the Burnt Canyon Breccia of Allen (1957; Figs. 2 and 10), which he recognized as a body of fractured and crushed crystalline rock and rock rubble. He hypothesized that it was sourced from one of the tributaries to Wood Canyon, labeled Burnt Canyon on older topographic maps. We refine this interpretation by proposing that the "Burnt Canyon" unit probably was emplaced as a long-runout rock avalanche deposit (sturzstrom) that coursed down Wood Canyon and came to rest in the Burro Flats area (Figs. 2 and 10). The deposit buttresses against both crystalline rocks as well as tilted sedimentary deposits of Burro Flats and locally overlies alluvial deposits we assign to unit Qvof3 (Allen's [1957] "Heights Fanglomerate"). Since its deposition, the rock avalanche deposit has been displaced by the San Bernardino strand. Thus, the mapped distribution of the Burnt Canyon Breccia (Fig. 3) does not represent its original paleogeographic configuration. Although there is clear indication of recent faulting, how much displacement might have occurred along the San Bernardino strand here is not apparent, since the original extent of the landslide deposit cannot be determined, and reliable piercing lines are lacking.

We prefer the interpretation that the two larger offsets described above occurred on a fault system that stepped across to the Lion Canyon lineament zone, rather than continuing southeast along the Burro Flats section of the San Bernardino strand. The Lion Canyon lineament zone is on strike with SAF strands to the NW and SE, including the San Bernardino strand NW of Pine Bench and the Garnet Hill strand to the SE. The most recent movement, displaying youthful tectonic geomorphology and offsetting the Burnt Canyon Breccia, occurs along the Burro Flats section of the San Bernardino strand. Regardless of the fault system that carried the slip, it is significant that the San Bernardino strand, broadly defined, has had a much longer history than previously recognized.

Older History of the Banning Strand

Along the Banning strand, the displacement of Whitewater Hill and the associated deposits, from a position to receive clasts sourced from the Whitewater River headwaters to its current position, poses several conundrums, which we here describe and address with alternate models of slip. One question is in understanding the nature of the deposits. The depositional units that comprise Whitewater Hill might have been sourced from a central apex, forming an alluvial fan. This would require that the Banning strand defined the edge of landscape that was high to the north, so that the location of the strand served as a transition from canyon to unconfined drainage. A further consideration is that, in order for Whitewater Hill to be the remnant of a single alluvial fan, the axial drainage would need to be entrenched, and the landform able to be displaced without reworking of the deposits.

An alternative interpretation is that these deposits were emplaced by a stream system that flowed across the landscape without forming an alluvial fan. This would be expected if there were not an escarpment associated with the Banning strand at the time of deposition. We prefer this model because the observed reconnaissance paleocurrent measurements in our mapping

Downloaded from http://pubs.geoscienceworld.org/gsa/geosphere/article-pdf/doi/10.1130/GES02424.1/5548351/ges02424.pdf
by USGS Library user

demonstrate that the streams flowed primarily to the south-southeast and south, rather than in a radial pattern. A consequence of this streamflow model is that the deposits are time-transgressive, with the western deposits emplaced first. A second consequence, though, is that the easternmost stratigraphy of the Whitewater Hill is only displaced ~750 m from the Whitewater River at its intersection with the Banning strand. Farther to the south, near the intersection with the Garnet Hill strand, the deposits are located within 200 m of the active Whitewater River. It is difficult to conceive that this deposit, which is associated with a very strongly developed duripan, indicating stability for more than ~500 k.y., and has subsequently been uplifted and deformed, has experienced so little displacement along the Banning strand. This leads us to a second consideration—that the source of these deposits might not have been Whitewater River as we currently define it.

We propose a model that utilizes flow down a former drainage of Whitewater River, flowing along the ancestral Super Creek to emplace the units (Fig. 13). This former drainage would access the lithologies (associated with the current Whitewater River) that are present in the deposits associated with Whitewater Hill. Restoring 5.5 km of slip on the Banning strand positions the western portion of the Whitewater Hill to receive deposits on its western margin by way of a drainage that is higher in the landscape than the currently active drainage system. Note that at this time, Whitewater Hill was not an elevated landform. This drainage is defined by, from north to south, the upper portion of Whitewater River, wind gaps in the landscape to the southeast of the upper Whitewater River (also shown in Fig. 4), and Super Creek (Fig. 13A). After ~2.5 km of motion along the Banning strand, restoring 3 km, the easternmost portion of the current Whitewater Hill was positioned to receive deposits from Super Creek (Fig. 13B). Following this time interval, Whitewater Hill was laterally moved away from the active drainage, the surface associated with these deposits began to stabilize, and a soil began to form. Uplift and compression along the north-dipping Garnet Hill strand began after a lengthy period of soil development, and the Whitewater Hill was folded and uplifted (Fig. 13C). The soil profile is deformed, as well as the deposits, indicating that the soil was already well developed when the folding began. After ~3.5 km of slip had occurred along the Banning strand, Super Creek continued to deposit on the eastern flank of the fold, resulting in the buried soil that today is observable in the eastern wall of Whitewater River (Figs. 11B–11D). Following this deposition, and with continued uplift and deformation of the Garnet Hill block, Super Creek became incised between the Banning and Garnet Hill strands, just to the west of the current path of lower Whitewater River. Eastward tilting of the Kitching Peak block, as described in Kendrick et al. (2015), results in initiation and development of eastward-flowing streams. These are shown in this step of development (Fig. 13C) but may have originated earlier.

By the time that ~4.7 km of displacement had occurred along the Banning strand (Fig. 13D), alignment of a terrace surface on the eastern flank of Whitewater Hill with the crush zone of the Whitewater fault and the upstream portion of the modern Whitewater River permits the integration of drainage along the current drainage course. Super Creek continues to flow, although with a diminished headwater region. The last ~450 m of displacement along the Banning strand have separated the upper and lower portions of the ancestral Super Creek drainage (Fig. 13E). The truncated upper portion of Super Creek now exits the mountain front to the east of the main channel, and forms a small alluvial fan, with a distributed drainage pattern, before finally connecting to the lower portion of Super Creek as a tributary. The lower portion of the original Super Creek has extended across the mountain front by headward erosion. Continued headward growth and capture of the drainages flowing eastward into Coachella Valley has impinged farther onto the upstream portion of Super Creek. This last interval of slip also displaces the incised edge of the Whitewater Canyon, resulting in a preserved terrace with a width of up to ~200 m. Increased incision into the canyon of Whitewater River leads to tributary growth and drainage captures on the west flank of the river, on the uplifting flank of the Kitching Peak block (Figs. 4 and 13E). Tributaries to the east of Whitewater River further disrupted and captured sections of Super Creek, leading to the discontinuous preservations of the drainage system observed today.

Punctuated Slip Activity

The discussion above suggests that the San Bernardino and Banning strands have experienced a punctuated history of slip, with very old deposits displaced on these strands from the source rock types by ~5–6 km. The long history of slip is also indicated by the very different morphologies of the Kitching Peak and Pisgah Peak blocks. A younger history is also present on these strands, as evidenced by the paleoseismic record and the displacement of younger landforms, discussed above. Indications that this slip history is punctuated instead of continuous include the discontinuity of the mapped active fault trace, the lack of intermediate offsets, both temporally and spatially, and the lack of long-term evidence of faulting on secondary strands and sections that are now active (i.e., Gandy Ranch strand and Burro Flats section of the San Bernardino strand).

These observations are not the only indication that there may be punctuated activity and strand switching in the SGPr. Kendrick et al. (2015) proposed that the Mill Creek strand of the SAF has been displaced by 1–1.25 km of left-lateral slip along the Pinto Mountain fault. Matti et al. (1985, 1992a) proposed that the 15 km left bend in the Mission Creek strand was caused by left-lateral slip on the Pinto Mountain fault, though we would modify that hypothesis and suggest, as discussed above, that it was left-lateral slip along the Morongo Valley fault, specifically, that offset the Mission Creek strand. Summed, these offsets approximate the cumulative slip of 16–19 km reported for the Pinto Mountain fault system (Dibblee, 1975; Bacheller, 1978) and the 16 km offset of geophysical features at the western end of the Pinto Mountain fault system (Langenheim and Powell, 2009). These displacements of SAF strands during two separate intervals along faults of the Pinto Mountain fault zone suggest alternating intervals of northwest dextral slip with northeast-oriented sinistral slip, likely associated with increased compression across the SGPr as a whole.

Alternating periods of activity between the eastern California shear zone and sections of the SAF system on a multi-millennial scale were noted by

Downloaded from http://pubs.geoscienceworld.org/gsa/geosphere/article-pdf/doi/10.1130/GES02424.1/5548351/ges02424.pdf
by USGS Library user

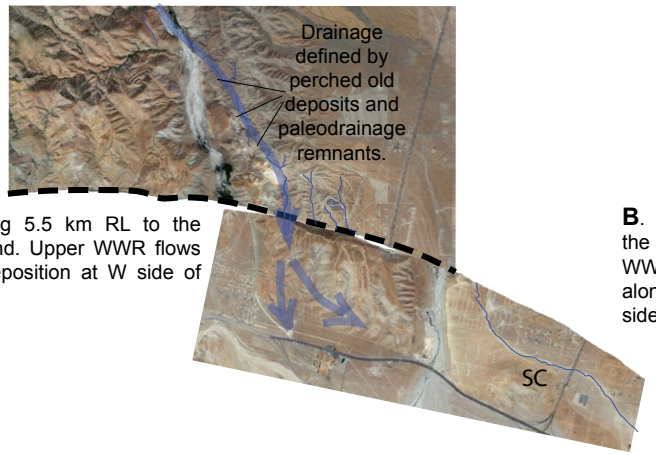

A. Restoring 5.5 km RL to the Banning strand. Upper WWR flows along SC; deposition at W side of WH.

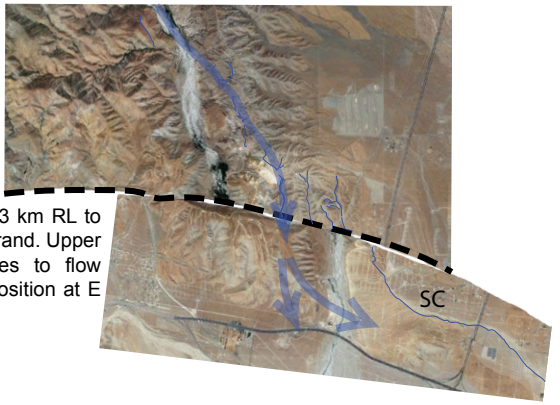

B. Restoring 3 km RL to the Banning strand. Upper WWR continues to flow along SC; deposition at E side of WH.

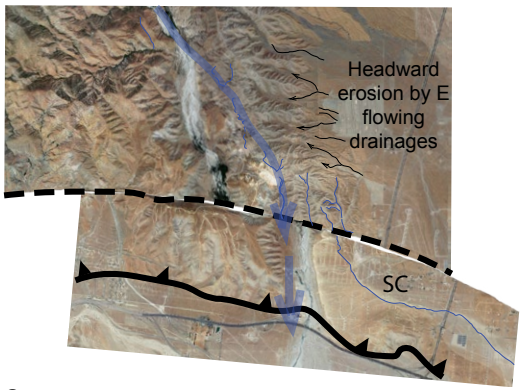

C. Restoring 2.2 km RL to the Banning strand. Uplift and folding of Garnet Hill block, including WH, by motion along the Garnet Hill strand. Upper WWR continues to flow along SC; lower portion is incised as an antecedent drainage with the uplift of WH, positioned just west of current WWR drainage.

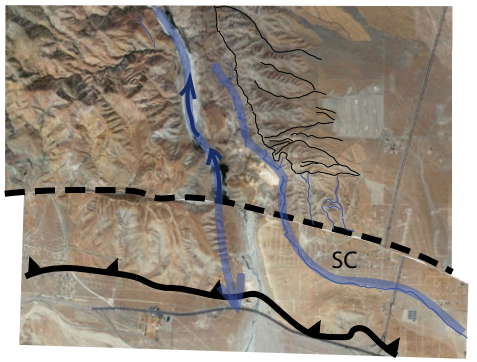

D. Restoring 0.45 km RL to the Banning strand. Capture of upper WWR by headward erosion of lower incised drainage section. Modern SC is established to the south of Banning strand.

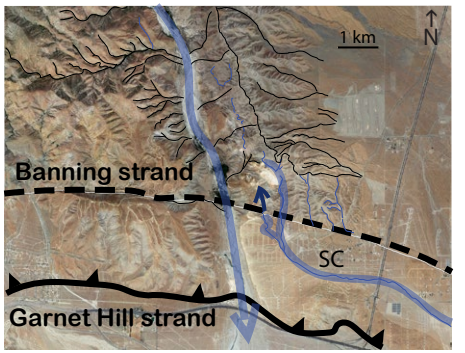

E. Current position. Incision of WWR along modern channel and development of tributaries. Previous SC headwaters displaced from lower SC. Headward erosion from lower SC forms modern headwaters; the previous, beheaded upper SC connects to lower SC via distributed flow.

Figure 13. Deposition of units associated with Whitewater Hill by the Super Creek drainage system. See text for more discussion and description. Abbreviations in figure include Super Creek (SC) and Whitewater River (WWR). (A) The western side of Whitewater Hill is in position to receive sediments from the Super Creek drainage system. (B) The eastern portion of Whitewater Hill is positioned to receive deposits from Super Creek. (C) The surface of Whitewater Hill is stabilized, and soil begins to develop. Uplift and folding of this surface and associated soil begin, as a result of slip on the Garnet Hill strand. Deposits from Super Creek are emplaced on the flank of Whitewater Hill on the Garnet Hill block. (D) The upper portion of the current Whitewater River is aligned with a preserved terrace on the flank of the Whitewater Hill. The modern course of the Whitewater River can be established via headward erosion from the incised lower reach of Super Creek. Drainages that flow east toward Coachella Valley on the eastern flank of the Kitching Peak block begin to capture portions of the Super Creek catchment area. These drainages also caused beheading of drainages east of Super Creek, north of the Banning strand. (E) The upper and lower portions of the modern Super Creek are separated. The beheaded lower Super Creek has expanded across the Banning strand by headward erosion and lengthening. The original upper portion of Super Creek forms a small alluvial fan where it crosses the Banning strand and flows to the named Super Creek as a tributary stream. This last 450 m of slip along the Banning strand has left a terrace on the west side of Whitewater River as the modern course of the drainage is established. Whitewater River has been incised, and the associated tributaries have disrupted perched ancient drainages to the west and the ancient Super Creek drainage to the east of the river, leaving only knickpoints, wind gaps, and canyon fragments to indicate the location of these drainages.

Downloaded from http://pubs.geoscienceworld.org/gsa/geosphere/article-pdf/doi/10.1130/GES02424.1/5548351/ges02424.pdf
by USGS Library user

Dolan et al. (2007) and attributed to the development of the eastern California shear zone as an active part of the plate boundary. Similarly, the evolution of a complex fault system may be the driving force to the alternating intervals of slip we observe in the SGPr, between right-lateral slip along NW-trending faults and N-S compression and left-lateral slip on NE-trending faults. Ingersoll and Coffey (2017) propose that the double left restraining bend within the southern SAF, with the SGPr as the southeastern of the pair, is a function of the interaction between the rigid Peninsular Range and Sierra Nevada batholiths, and the response of less rigid blocks moving through these restraining bends. Based on the geologic and geomorphic evidence presented in this study, we propose that the SGPr is currently in a stage of N-S compression, with much of the plate motion stepping off of the SAF onto secondary fault systems, including the San Jacinto fault and eastern California shear zone. This model has implications for establishing regional hazard based on proposed scenario earthquakes.

Proposed Long-Term History of San Gorgonio Pass Region

We propose a model to explain the geologic and geomorphic observations we have made of the SGPr. We use as criteria the cumulative slip along various faults and SAF strands and the youthfulness of tectonic features along faults. In this model, we seek to explain the presence of low-density units present below the Kitching Peak block, based on gravity measurements (Langenheim et al., 2005), and to reconcile recent findings by Fosdick and Blisniuk (2018) that demonstrate provenance for the oldest deposits in the Mission Creek alluvial complex included sources in the Little San Bernardino Mountains.

In the presentation of this model, we hold the San Gorgonio block, including San Gorgonio Mountain, fixed, with the other blocks allowed to move (Fig. 14). By necessity, we make further subdivisions in our block configuration. We include the Morongo Valley fault, Pinto Mountain fault, and Lion Canyon lineament zone as block boundaries.

Mission Creek Strand Is Dominant and Through-Going (Fig. 14B)

Our first snapshot of the model reconstructs the landscape at the end of activity on the Mission Creek strand. The Mission Creek strand has a long history with ~90 km of cumulative right-lateral slip (Matti et al., 1992a; Matti and Morton, 1993). At this point in time, we assume that no other faults are active or have significant offset, and the segments of the Mission Creek strand are aligned

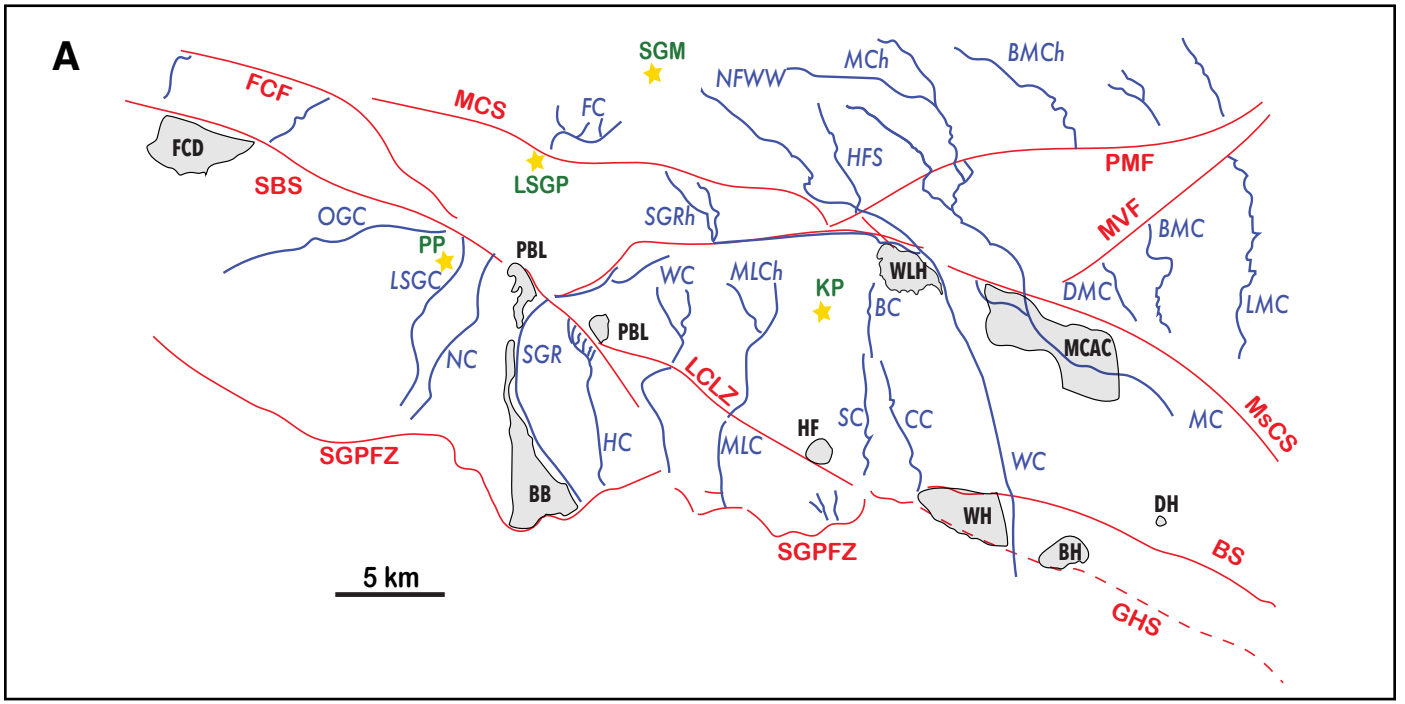

Figure 14. Reconstruction of the geologic and geomorphic history of the San Gorgonio Pass region (SGPr). (A) Current configuration, with key to features in lower panels. Abbreviations and symbols used as follows. Faults (red lines, red labels): BS—Banning strand; FCF—Ford Canyon fault; GHS—Garnet Hill strand; LCLZ—Lion Canyon lineament zone; MCS—Mill Creek strand; MsCS—Mission Creek strand; MVF—Moreno Valley fault; PMF—Pinto Mountain fault; SBS—San Bernardino strand; SGPFZ—San Gorgonio Pass fault zone. Geomorphic features (shaded, bold black labels): BB—Banning Bench; BH—Beacon Hill; DH—Devers Hill; FCD—Falls Creek deposits; HF—Hidden Flat; MCAC—Mission Creek alluvial complex; WFH—Wathier Flat Hill; WH—Whitewater Hill. Peaks (yellow stars, green labels): KP—Kitching Peak; LSGP—Little San Gorgonio Peak; PP—Pisgah Peak; SGM—San Gorgonio Mountain; drainages and canyons (blue linework, blue italicized labels): BC—Boundary Canyon; BMC—Big Morongo Canyon; BMCh—Big Morongo Canyon headwaters; CC—Cottonwood Creek; DMC—Dry Morongo Creek; FC—Falls Creek; HC—Hathaway Canyon; HFS—Hell For Sure Canyon; LMC—Little Morongo Canyon; LSGC—Little San Gorgonio Creek; MC—Mission Creek; MCh—Mission Creek headwaters; MCC—Mill Creek Canyon; MLC—Millard Canyon; MLCh—Millard Canyon headwaters; NC—Noble Creek; NFWW—North Fork Whitewater Creek; OGC—Oak Glen Creek; SC—Stubbe Canyon; SGR—San Gorgonio River; SGRh—San Gorgonio River headwaters. In panels B through J, uplift is shown with hachured lines, active faults and major drainages are shown in bold, and geomorphic features are shown in darker shading when the associated deposits are actively being emplaced. (*Continued on following page.*)

Downloaded from http://pubs.geoscienceworld.org/gsa/geosphere/article-pdf/doi/10.1130/GES02424.1/5548351/ges02424.pdf
by USGS Library user

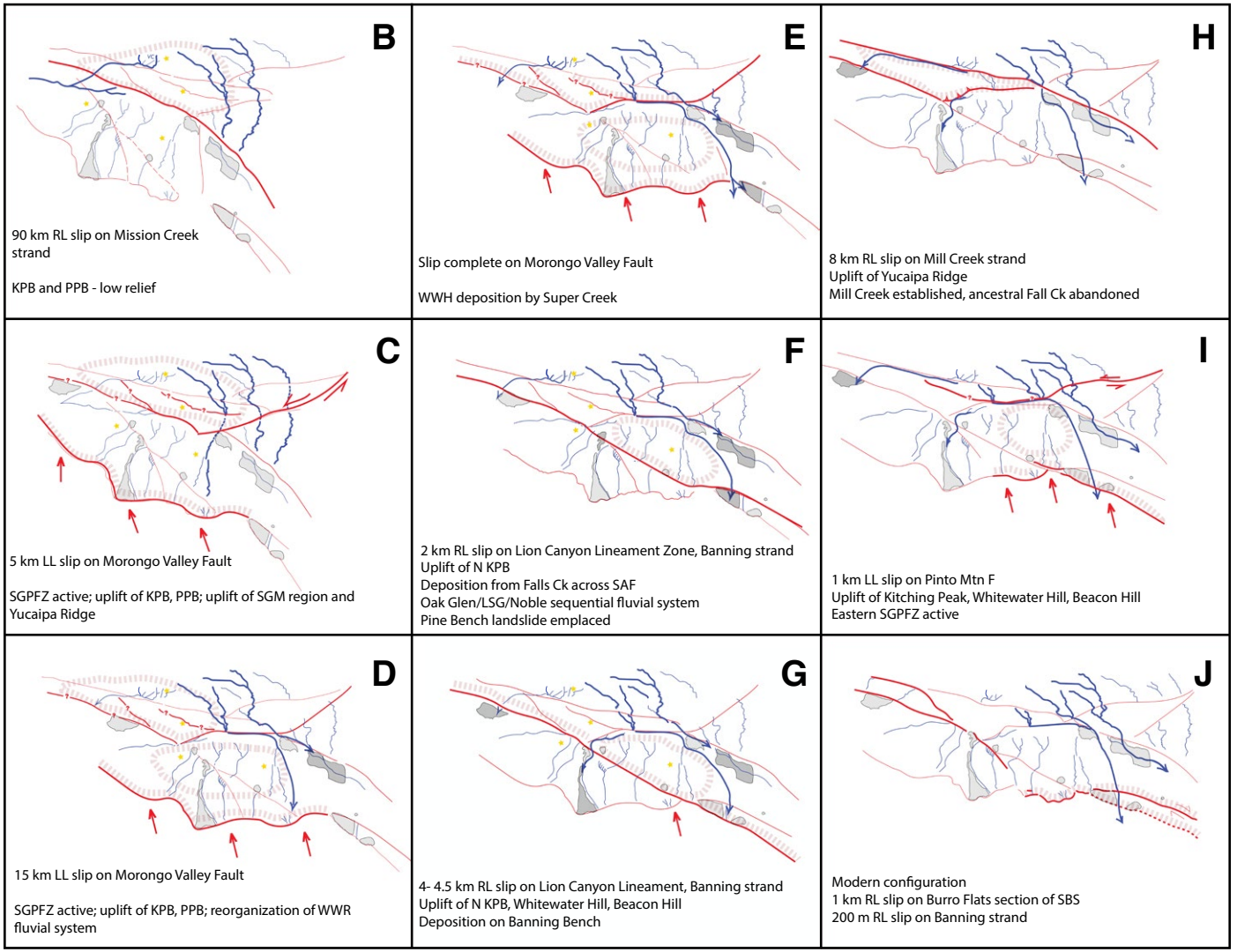

Figure 14 (*continued*). (B) In tHe starting model, the Mission Creek strand is the dominant strand of the San Andreas fault and has just finished carrying ~90 km of slip. (C) At this point, the Mission Creek strand is disrupted and abandoned. Approximately 5 km sinistral slip has occurred along the Morongo Valley fault, which might be resolved as uplift along the NW section of Mission Creek strand, Ford Canyon fault, and/or Galena Peak fault. SGPFZ is initiated. (D) The Mission Creek strand is displaced by ~15 km sinistral slip on the Morongo Valley fault. Uplift continues as a result of compressive motion on the SGPFZ. Flow down Boundary Canyon to Stubbe Canyon or Cottonwood Creek is disrupted. Hell For Sure and North Fork drainages combine and flow down ancient drainages to east of Boundary Canyon. Mission Creek headwaters flow down the valley defined by the Mission Creek strand, depositing the oldest units in the Mission Creek alluvial complex. (E) Slip along the Morongo Valley fault is complete. Deposition of units associated with Whitewater Hill by flow from Whitewater River headwaters by way of Super Creek is initiated. (F) Approximately 2 km dextral slip occurs along the San Bernardino strand, the Lion Canyon lineament zone, and the Banning strand. Falls Creek flows through mouth of present Mill Creek, across the escarpment of the inactive Mission Creek strand, and deposits alluvium. Pine Bench landslide is emplaced at this step. Deposition continues in the Mission Creek alluvial complex and at the location of Whitewater Hill. During the lateral slip along the San Bernardino strand, the headwaters of the San Gorgonio River flow down Oak Glen Creek, Little San Gorgonio Creek, and Noble Creek, sequentially. (G) Dextral slip has continued along the San Bernardino strand, the Lion Canyon lineament zone, and the Banning strand; at this stage ~4–4.5 km of slip has accumulated along this fault system. During this last part of the dextral slip along this fault system the headwaters of Wood Creek sequentially occupied the beheaded tributaries of Hathaway Creek. Compressional motion now occurs along the Garnet Hill strand and the Lion Canyon lineament zone, resulting in the uplift of Whitewater and Beacon Hills, and the northern portion of the Kitching Peak block. Flow of the Hell For Sure and North Fork Whitewater Rivers now courses down the location of the current upper canyon of Whitewater River, although positioned much higher in the landscape, before continuing to flow down Super Creek. Remnants of the Super Creek drainage are also shown on Figure 4 (pale-blue lines to the east of the modern Whitewater River). Mission Creek headwaters continue to deposit the oldest units in the Mission Creek alluvial complex. The headwaters of San Gorgonio River are deflected around the lower part of the Pine Bench landslide and established flow along the modern course of San Gorgonio River, in Banning Canyon. The deposits associated with Banning Bench begin to be emplaced. (H) Following this compression along the Lion Canyon lineament zone and Garnet Hill strand, ~8 km of dextral slip occurs along the Mill Creek strand. Mission Creek headwaters flow down modern drainage course and deposit youngest units in the Mission Creek alluvial complex. Falls Creek drainage lengthens with displacement; modern Mill Creek is formed by headward erosion within the fault zone; Falls, Vivian, and High Creek headwaters are bypassed resulting in hanging valleys. (I) At this time, we model compression along SGPFZ, ~1–1.25 km sinistral slip along Pinto Mountain fault, and displacement of the Mill Creek strand. Uplift of the Kitching Peak Block occurs along SGPFZ and emplacement of low-density material under this block continues. Uplift of Whitewater Hill along Garnet Hill strand continues. (J) Current configuration, highlighting faults that demonstrate active slip. A minor amount of dextral slip, perhaps up to 1 km, has occurred on Burro Flat section of San Bernardino strand. Approximately 500 m of dextral slip occurs on the Banning strand, resulting in the formation of the terrace on the east side of Whitewater Hill. Transpressive slip occurs along portions of the SGPFZ; evidence of this recent slip is observed in trench sites in Millard Canyon and Lion Canyon (Ramzan, 2012; Heermance and Yule, 2017; Wolff, 2018).

Downloaded from http://pubs.geoscienceworld.org/gsa/geosphere/article-pdf/doi/10.1130/GES02424.1/5548351/ges02424.pdf
by USGS Library user

in a NW-striking system with a gentle convex to the NE curve. Based on our reconstruction, the overall strike of the Mission Creek strand through the SGPr is ~305°. The curve to the fault trace in our reconstruction likely indicates the initiation of disruption to through-going slip. At this time, the drainage systems Hell For Sure and North Fork Whitewater are combining and flowing down Big Morongo Canyon, and the headwaters of Mission Creek are flowing down Little Morongo Canyon. The headwaters of San Gorgonio River flow down Potato Canyon (current path of Oak Glen Creek) to San Timoteo Canyon, ultimately joining the Santa Ana River. Flow from the Wood Canyon headwater region is along Banning Canyon, the current path of San Gorgonio River. Although we lack age control, previous studies have suggested that this phase of activity occurred prior to initiation of slip along the San Jacinto fault. Studies have suggested that the San Jacinto fault inception was ca. 1.1 Ma (Janecke et al., 2011), 1.2 Ma (Matti and Morton, 1993), and less than 1.5 Ma (Morton and Matti, 1993). This latter estimate used several approaches, including age control of the uppermost San Timoteo Beds. Subsequent findings by Albright (1999) refine that age to less than 0.78 Ma. We agree with the model that the San Jacinto fault formed in response to development of the left bend along the Mission Creek strand of the SAF in SGPr; these age estimates provide a reasonable estimate of the time frame for our model at this stage and the subsequent stage.

Disruption of Mission Creek Strand Begins: Morongo Valley Fault Active (Fig. 14C)

During this interval, the Morongo Valley fault, part of the Pinto Mountain fault system, becomes active. Left-lateral displacement along this fault disrupts the trace of the Mission Creek strand. The faults are responding to an episode of compression; we envision this as the impingement of the rigid Peninsular Range batholith on the Little San Bernardino Mountains and San Bernardino Mountains, sequentially, after the model proposed by Ingersoll and Coffey (2017). Fattaruso et al. (2016) alternatively propose that this disruption of the Mission Creek strand is created by E-W extension on the West Salton detachment fault. In both models, the Pinto Mountain fault system, including the Morongo Valley fault are passive. This displacement of the Mission Creek strand is also manifest as uplift along the strand west of the fault intersection; uplift of the Yucaipa Ridge and San Gorgonio blocks is occurring. The Galena Peak and Ford Canyon faults might also be active at this time, accommodating some of the uplift generated from this left-lateral movement. We also propose that compressional movement along the SGPFZ is initiated at this time.

After ~7 km of left-lateral motion along the Morongo Valley fault, Hell For Sure and North Fork Whitewater flow southward down Boundary Canyon and either Stubbe Canyon or Cottonwood Creek; Mission Creek is aligned to flow down Big Morongo Canyon; and drainage from the headwaters of Big Morongo Canyon is flowing down Little Morongo Canyon (depicted in Fig. 14C).

After continued left-lateral displacement on the Morongo Valley fault, compression along the SGPFZ, and uplift of the Kitching Peak block, flow from the Hell For Sure and North Fork Whitewater might abandon Boundary Canyon in favor of a drainage system farther east; evidence of this old drainage remains in a series of perched landscape fragments, wind gaps, and knickpoints (Fig. 4).

Completion of Slip on the Morongo Valley Fault (Figs. 14D and 14E)

At this step, the Mission Creek strand has been offset left laterally ~15 km by the Morongo Valley fault. With completion of slip along the Morongo Valley fault, and completion of the initial compressional phase in the SGPr, there has been enough uplift of the Kitching Peak block and wedging of low-density material below the SGPFZ (Langenheim et al., 2005) to further divert flow from Hell For Sure and North Fork Whitewater drainages.

We interpret that tilting initiates at this interval in time, in response to the uplift described, and continues through much of the history of the region. This tilting of the Kitching Peak block and the adjacent terrain to the east is indicated by the uplift of the oldest surfaces in the Mission Creek alluvial complex (Kendrick et al., 2015) and east-flowing drainages east of the modern Whitewater River, discussed above. Within the bounds of the Kitching Peak block, three samples were collected and apatite (U/Th)/He ages were measured by Spotila and others (Spotila et al., 2001, 2002). Spotila et al. (2002) attributed the resulting pattern of exhumation to doming, as per Yule and Sieh (2003), but an alternate explanation for the apparent eastward decrease in exhumation is east-directed tilting of the Kitching Peak block.

At this time, flow from the headwater region of Whitewater drainage system, Hell For Sure and North Fork Whitewater, follows the existing Mission Creek strand fault zone, either because it contains easily erodible material, or because the Kitching Peak block is actually uplifted along this bounding fault resulting in differential movement between Kitching Peak and Yucaipa Ridge blocks. The drainage then follows the route along the southern edge of the hill associated with Wathier Landing before flowing down a drainage system to the east of Boundary Canyon (Fig. 14D). At some point, this drainage links with the (current) headwaters of Super Creek, and deposition begins at the location of the western edge of deposits associated with Whitewater Hill (Figs. 13A and 14E).

At this time, Mission Creek drainage is now flowing down the axis of the Mission Creek alluvial fan complex and depositing the older two units (Kendrick et al., 2015). In their analysis of detrital zircon U/Pb geochronology and clast compositions, Fosdick and Blisniuk (2018) propose that these older deposits were sourced from both Mission Creek headwaters and the Little San Bernardino Mountains, and not from the headwaters of modern Whitewater River. Allowing the Hell For Sure and North Fork Whitewater rivers to flow down Boundary Canyon and other ancestral drainages to the east of Boundary Canyon results in a reconstruction consistent with this finding. Both Big Morongo and Little Morongo creeks were positioned to have contributed clasts to the oldest units in the Mission Creek alluvial complex, providing the source from the Little San Bernardino Mountains. During the interval represented by

Downloaded from http://pubs.geoscienceworld.org/gsa/geosphere/article-pdf/doi/10.1130/GES02424.1/5548351/ges02424.pdf
by USGS Library user

Figures 14C–14E, we envision that the dextral slip along the SAF in Coachella Valley is stepping around the SGPr, either onto the San Jacinto fault or onto the eastern California shear zone. The degree of soil development associated with the deposits in Mission Creek alluvial complex indicates that this deposition occurred before ca. 0.5 Ma.

Integration of Slip along the Banning Strand, Lion Canyon Lineament Zone, and San Bernardino Strand (Fig. 14F)

At this point in time, ~2 km right-lateral cumulative slip has occurred along the Banning and San Bernardino strands. We propose that these faults were linked by a structure that was located along the Lion Canyon lineament zone, defined by the morphologic boundary, as described and proposed above. This is consistent with our Model 1 (Fig. 12B), although the reconstruction could be accomplished instead with motion along the Burro Flats section of the San Bernardino strand.

During this interval, Mission Creek continues to deposit older units in the Mission Creek alluvial complex. Hell For Sure and North Fork Whitewater drainages continue to flow down the same route as in the previous developmental interval; the central portion of Whitewater Hill is adjacent to Super Creek and receives deposits from this ancient drainage (also shown in Fig. 13B).

The Pine Bench landslide is emplaced then bisected by the San Bernardino strand and begins to be displaced. Falls Creek deposits are beginning to be separated from the headwater source and canyon mouth. San Gorgonio River headwaters are positioned to flow down Little San Gorgonio Creek; before the next interval, it will subsequently occupy Noble Creek. Drainage from Wood Canyon flows along Hathaway Creek; subsequent motion causes beheading of Hathaway Creek in favor of succeeding tributaries to the east of the main channel. The degree of soil development associated with the deposits at Whitewater Hill and the Falls Creek deposits indicates an age estimate for this step at greater than 0.5 Ma.

Disruption of Right-Lateral Slip on the SAF Strands (Fig. 14G)

After ~4.5–5 km of slip has occurred on the San Bernardino strand, Lion Canyon lineament zone, and Banning strand, through-going slip seems to again be interrupted by a compressional episode. This results in further uplift of the Kitching Peak block and continued emplacement of the low-density material beneath Kitching Peak (Langenheim et al., 2005).

We propose that compressional motion along the Garnet Hill strand occurs at this time, uplifting the Whitewater Hill. Compression also occurs along the SGPFZ. Alignment at this point favors the establishment of the Whitewater drainage along the modern trace, following the Whitewater fault gouge zone. This shift, combined with uplift along the Garnet Hill strand, causes the Whitewater River to incise into the Super Creek fan deposits.

Flow from the headwaters of Big Morongo is coursed through Dry Morongo Canyon, and aligned to incise into the Mission Creek alluvial complex, along the future path of the Mission Creek drainage. Flow from the headwaters of the San Gorgonio River previously flowed sequentially down the Oak Glen Creek, Little San Gorgonio River, and Noble Creek and is now deflected by the Pine Bench landslide deposit and flows down Banning Canyon, depositing the units associated with the Banning Bench.

Slip Begins on Mill Creek Strand (Fig. 14H)

Right-lateral slip initiates on the Mill Creek strand. After ~4 km of right-lateral motion has occurred along this strand, Mission Creek occupies its modern flow path (Fig. 14H), Whitewater River is located along the current path, and incision of Whitewater Canyon is continuing. This incision leads to stream captures to the west of the modern drainage, on the flank of the uplifting Kitching Peak block. The slope of the oldest surfaces in the Mission Creek alluvial complex (Kendrick et al., 2015) as well as the establishment of east-trending drainages to the south of the alluvial complex indicate tilting at this time. These east-trending drainages, also discussed in the previous section, have captured some of the catchment of the ancestral Super Creek drainage system. Tributaries of the Whitewater River have also disrupted Super Creek drainage by capture.

Completion of Right-Lateral Slip on the Mill Creek Strand: Initiation of the Pinto Mountain Fault (Fig. 14I)

This interval marks the completion of cumulative slip of 7.1–8.7 km along the Mill Creek strand, indicated by offset drainages (Kendrick et al., 2015). Based on luminescence dating, Kendrick et al. (2015) suggest this slip concluded at ca. 100 ka. Blisniuk et al. (2021) concluded that the high rate of slip they propose for the Coachella Valley continues into the SGPr, with the combined Mill Creek and Mission Creek strands carrying the majority of the recent SAF slip. We uphold the analyses and conclusion of Kendrick et al. (2015) that there is little evidence for recent activity and no evidence for a rapid rate of slip for these strands of the fault. Slip observed along the Mission Creek and Mill Creek strands to the SE of SGPr could be stepping off onto other faults such as the eastern California shear zone.

Subsequent to this right-lateral slip on the Mill Creek strand, and represented in this interval, the Mill Creek strand is left-laterally offset 1–1.25 km by the Pinto Mountain fault. We propose that this left-lateral slip feeds into the existing NW-striking faults to the west and is resolved in further uplift of the Yucaipa Ridge and San Gorgonio blocks; slip might also step off onto the Ford Canyon and Galena Peak faults.

As with the previous interval in which the Pinto Mountain fault system was active, we propose that this interval is also accompanied by regional N-S

Downloaded from http://pubs.geoscienceworld.org/gsa/geosphere/article-pdf/doi/10.1130/GES02424.1/5548351/ges02424.pdf
by USGS Library user

compression, including along the eastern portion of the SGPFZ and the Garnet Hill strand. This compression would result in further uplift of the Kitching Peak block and would also contribute to obscuring the fault connection between the Lion Canyon lineament zone and the Banning strand. In addition, the uplift of the Kitching Peak block has resulted in numerous landslides; several of these obscure the trace of the Lion Canyon lineament zone.

Most Recent Phase of Right-Lateral Slip (Fig. 14J)

This interval represents our knowledge of the currently active faults and fault sections, based on mapping of displaced late Holocene units and results from paleoseismic and slip-rate investigations (summarized above). The Burro Flats section of the SBS is initiated; right-lateral slip continues on the San Bernardino and Banning strands, and likely on the Garnet Hill strand. We interpret this phase as re-establishing a pathway for strike-slip motion, following disruption by a compressive interval. An unresolved question is why the active faulting would shift from a structure aligned with the far-field strike of the SAF to the northwest and southeast (the Lion Canyon lineament zone) to a fault segment (the Burro Flats section) that strikes more southerly. We note, however, that the orientation of the Burro Flats section is subparallel with the mapped tear faults of the SGPFZ. This stage, as well as the most recent left-lateral slip along the Pinto Mountain fault, would have occurred in the past 100 k.y., based on the timing of completion of slip along the Mill Creek strand.

Linkage between San Bernardino and Banning Strands

We consider the implications to our proposed model of fault activity if the lineaments along our Lion Canyon lineament zone instead represent the surface expression of a blind, high-angle structure in the footwall of the SGPFZ, as discussed previously. In this alternate configuration, this structure would link the San Bernardino and Banning strands through the SGPr at depth, beneath the hanging wall of the SGPFZ. The position of the Lion Canyon lineament zone is in agreement with the geophysical data (Langenheim et al., 2005) and is approximately aligned with the San Bernardino and Banning strands. In our proposed model, the Lion Canyon lineament zone is active during the interval represented by Figures 14F and 14G. If, during this time, slip was occurring at depth along this structure, then we would expect that the surface manifestation of this slip would be quite distributed between oblique slip on the SGPFZ and on the numerous discontinuous faults in the SGPr, (e.g., Gandy Ranch strand). This dispersal of surface slip would be occurring between the northern edge of Burro Flats, to the northwest, and the mouth of Cottonwood Creek, to the southeast (indicated by black triangles on Fig. 1). This would not impact the displacements and reconstructions we have discussed at the Falls Creek deposits, Pine Bench Landslide, or Whitewater Hill, as all of these sites are beyond the bounds of this obscured portion of the fault system.

CONCLUSIONS

One of the primary questions facing the southern California earthquake hazards community is whether or not slip is able to transfer through the SGPr (e.g., Jones et al., 2008). This is critical to evaluate the magnitude and impact of large earthquakes on the SAF zone. Research indicates that in the SGPr, the San Bernardino, Banning, and Garnet Hill strands of the SAF, and the SGPFZ, sometimes referred to as the southern faults in the SGPr, are the active faults that transfer slip through the SGPr (e.g., Yule and Sieh, 2003). Geologic observations, however, reveal a discontinuity between active faults at the surface. The San Bernardino strand does not unequivocally continue as far south as the SGPFZ; at best, there is very subtle evidence, not suggestive of large or frequent ground rupture.

In this study, we have addressed the difficulty in mapping a throughgoing, active fault system within the SGPr, the southeastern component of the double restraining bend of the southern SAF. We demonstrate that the geomorphology of the SGPr indicates that the two blocks separated by the San Bernardino strand have morphologies distinct from each other. We interpret these differences to indicate that the two blocks, the Kitching Peak and Pisgah Peak blocks, have experienced different uplift histories. From this interpretation, we propose that a bounding structure, either the San Bernardino strand along the Burro Flats section or our hypothesized Lion Canyon lineament zone, has been actively transferring slip during a prior interval of uplift. We have used mapping to document the areal extent of landslides and late Quaternary deposits that show the differences in surface processes operating in each terrain.

We describe two duripans located within our study area. These soil profiles, along with the soil associated on the oldest deposit in the Mission Creek alluvial complex (Kendrick et al., 2015), represent the oldest preserved remnants of the Quaternary landscape in the SGPr and help us to constrain fault activity. We define offsets along the San Bernardino and Banning strands and use these displacements, clast provenance, and age estimates based on the degree of soil development to propose a sequence of slip along the faults in the SGPr during the late Quaternary. We propose that the Morongo Valley fault, part of the Pinto Mountain fault system, rather than the Pinto Mountain fault, was responsible for the displacement of the Mission Creek strand.

We propose that flow from the headwaters of Whitewater River and Mission Creek once coursed along Big Morongo and Little Morongo canyons, which became incised with uplift of the San Bernardino Mountains along the Morongo Valley fault. After some motion along the left-lateral Morongo Valley fault, flow from the headwaters of Whitewater River shifted. We propose an alternate model of this flow, modified slightly from previous work (Kendrick et al., 2015) to explain the presence of Boundary Canyon, its alignment with Cottonwood and Stubbe canyons, and ancestral drainage remnants between Boundary Canyon and the modern Whitewater River. We propose that one of these ancestral drainages, Super Creek, was responsible for the emplacement of deposits associated with Whitewater Hill.

Downloaded from http://pubs.geoscienceworld.org/gsa/geosphere/article-pdf/doi/10.1130/GES02424.1/5548351/ges02424.pdf
by USGS Library user

We conclude that there have been two phases of activity along the southern set of faults through the SGPr, including San Bernardino strand, Lion Canyon lineament zone, and Banning and Garnet Hill strands. We define two segments of the SGPFZ that differ in tectonic geomorphology and propose that this reflects differing fault history. We consider the possible interpretation that the Lion Canyon lineament zone is instead the surface manifestation of a high-angle strand of the SAF in the footwall of the SGPFZ or an abandoned range-front thrust fault. Our reconstruction model suggests that there have been alternating intervals of compression and strike-slip plate boundary motion. We interpret that this is an outgrowth of the continued tightening of the double restraining bend along the southern SAF.

ACKNOWLEDGMENTS

We appreciate helpful reviews of earlier drafts of this manuscript by Peter Sadler, Victoria Langenheim, Keith Knudsen, Nate Onderdonk, Lisa Grant Ludwig, and Michele Cooke. Support for this study was provided by the Earthquake Hazards and the National Cooperative Geologic Mapping Programs of the U.S. Geological Survey. Any use of trade, firm, or product names is for descriptive purposes only and does not imply endorsement by the U.S. Government.

REFERENCES CITED

Albright, L.B., III, 1999, Magnetostratigraphy and biochronology of the San Timoteo Badlands, southern California, with implications for local Pliocene–Pleistocene tectonic and depositional patterns: Geological Society of America Bulletin, v. 111, no. 9, p. 1265–1293, https://doi.org/10.1130/0016-7606(1999)111<1265:MABOTS>2.3.CO;2.

Allen, C.R., 1957, San Andreas fault zone in San Gorgonio Pass, southern California: Geological Society of America Bulletin, v. 68, p. 315–350, https://doi.org/10.1130/0016-7606(1957)68[315:SAFZIS]2.0.CO;2.

Bacheller, J., III, 1978, Quaternary geology of the Mojave Desert-eastern Transverse Ranges boundary in the vicinity of Twentynine Palms, California [M.S. thesis]: Los Angeles, University of California, 157 p., scale 1:24,000.

Bevis, M.G., Hudnut, K.W., Sanchez, R.D., Toth, C.K., Grejner-Brzezinska, D.A., Kendrick, E.C., Caccamise, D.J., Raleigh, D., Zhou, H., Shan, S., Shindle, W.M., Yong, A.K., Harvey, J.C., Borsa, A.A., Ayoub, F., Shrestha, R.L., Carter, W.E., Sartori, M.P., Phillips, D.A., Coloma, F., and DeLong, S.B., 2017, Classified point cloud and gridded elevation data from the 2005 B4 Lidar Project, southern California, USA: U.S. Geological Survey data release (https://www.sciencebase.gov/catalog/item/get/5887eb35e4b05ccb964a6742).

Birkeland, P.W., 1999, Soils and Geomorphology: New York, Oxford University Press.

Blisniuk, K., Scharer, K., Sharp, W.D., Burgmann, R., Amos, C., Rymer, M., 2021, A revised position for the primary strand of the Pleistocene–Holocene San Andreas fault in southern California: Science Advances, v. 7, https://doi.org/10.1126/sciadv.aaz5691.

Carena, S., Suppe, J., and Kao, H., 2004, Lack of continuity of the San Andreas Fault in southern California: Three-dimensional fault models and earthquake scenarios: Journal of Geophysical Research, v. 109, 17 p., https://doi.org/10.1029/2003JB002643.

Castillo, B.A., 2019, Ages of prehistoric earthquakes on the Banning Strand of the San Andreas Fault, near North Palm Springs, California [M.S. thesis]: Northridge, California State University, 84 p.

Cooke, M.L., and Dair, L.C., 2011, Simulating the recent evolution of the southern big bend of the San Andreas fault, southern California: Journal of Geophysical Research, v. 116, B04405, https://doi.org/10.1029/2010JB007835.

Dair, L.C., and Cooke, M.L., 2009, San Andreas fault geometry through the San Gorgonio Pass, California: Geology, v. 37, no. 2, p. 119–122, https://doi.org/10.1130/G25101A.1.

Desjarlais, I.C., 2018, Constraining long term slip rates along the San Andreas Fault System using B4 LiDAR and cosmogenic beryllium-10 dating methods at Millard Canyon, San Gorgonio Pass, California [M.S. thesis]: Northridge, California State University, 69 p.

Dibblee, T.W., Jr., 1968a, Displacements on San Andreas fault system in San Gabriel, San Bernardino, and San Jacinto Mountains, southern California, *in* Proceedings of conference on geologic problems of San Andreas fault system: Stanford University Publications, Geological Sciences, v. XI, p. 269–278.

Dibblee, T.W., Jr., 1968b, Evidence of major lateral displacement on the Pinto Mountain fault, southern California: Geological Society of America Special Paper 115, 322 p.

Dibblee, T.W., Jr., 1975, Late Quaternary uplift of the San Bernardino Mountains on the San Andreas and related faults, *in* San Andreas Fault in Southern California: California Division of Mines and Geology Special Report 118, p. 127–135.

Dibblee, T.W., Jr., 1982, Geology of the San Bernardino Mountains, southern California, *in* Geology and Mineral Wealth of the California Transverse Ranges: South Coast Geological Society Guidebook no. 10 (Mason Hill volume), p. 148–169.

Dibblee, T.W., Jr., 1992, Geology and inferred tectonics of the Pinto Mountain fault, eastern Transverse Ranges, California, *in* Richard, S.M., ed., Deformation Associated with the Neogene Eastern California Shear Zone, Southwestern Arizona and Southeastern California: San Bernardino County Museum Special Publication 92–1, p. 28–31.

Dolan, J.F., Bowman, D.D., and Sammis, C.G., 2007, Long-range and long-term fault interactions in Southern California: Geology, v. 35, no. 9, p. 855–858, https://doi.org/10.1130/G23789A.1.

Douilly, R., Oglesby, D.D., Cooke, M.L., and Hatch, J.L., 2020, Dynamic models of earthquake rupture along branch faults of the eastern San Gorgonio Pass region in California using complex fault structure: Geosphere, v. 16, no. 2, p. 474–489, https://doi.org/10.1130/GES02192.1.

Fattaruso, L.A., Cooke, M.L., Dorsey, R.J., and Housen, B.A., 2016, Response of deformation patterns to reorganization of the southern San Andreas fault system since ca. 1.5 Ma: Tectonophysics, https://doi.org/10.1016/j.tecto.2016.05.035.

Fosdick, J.C., and Blisniuk, K.D., 2018, Sedimentary signals of recent faulting along an old strand of the San Andreas Fault: Scientific Reports, v. 8, p. 12132, https://doi.org/10.1038/s41598-018-30622-3.

Gibson, R.C., 1964, Geology of a portion of the Mill Creek area, San Bernardino County, California [M.S. thesis]: Riverside, University of California, 50 p.

Gibson, R.C., 1971, Nonmarine turbidites and the San Andreas fault, San Bernardino Mountains, California, *in* Elders, W.A., ed., Geological Excursions in Southern California: Riverside, University of California Campus Museum Contributions, no. 1, p. 167–181.

Gold, P.O., Behr, W.M., Rood, D., Sharp, W.D., Rockwell, T.K., Kendrick, K., and Salin, A., 2015, Holocene geologic slip rate for the Banning strand of the southern San Andreas Fault, southern California: Journal of Geophysical Research, Solid Earth, v. 120, 25 p. https://doi.org/10.1002/2015JB012004.

Grohmann, C.H., Smith, M.J., and Riccomini, C., 2011, Multi-scale Analysis of Topographic Surface Roughness in the Midland Valley, Scotland: IEEE Transactions on Geoscience and Remote Sensing, v. 49, p. 1200–1213, https://doi.org/10.1109/TGRS.2010.2053546.

Harden, J.W., 1982, A quantitative index of soil development from field descriptions: Examples from a chronosequence in central California: Geoderma, v. 28, p. 1–28, https://doi.org/10.1016/0016-7061(82)90037-4.

Harden, J.W., and Matti, J.C., 1989, Holocene and late Pleistocene slip rates on the San Andreas fault in Yucaipa, California, using displaced alluvial-fan deposits and soil chronology: Geological Society of America Bulletin, v. 101, p. 1107–1117, https://doi.org/10.1130/0016-7606(1989)101<1107:HALPSR>2.3.CO;2.

Harden, J.W., and Taylor, E.M., 1983, A quantitative comparison of soil development in four climatic regimes: Quaternary Research, v. 20, p. 342–359, https://doi.org/10.1016/0033-5894(83)90017-0.

Heermance, R.V., and Yule, D., 2017, Holocene slip rates along the San Andreas Fault System in the San Gorgonio Pass and implications for large earthquakes in southern California: Geophysical Research Letters, v. 44, p. 5391–5400, https://doi.org/10.1002/2017GL072612.

Heermance, R.V., Kendrick, K.J., Dejarlais, I., Yule, D., McBurnett, P., and Ramzan, S., 2014, Geochronology of surfaces within the San Gorgonio Pass from radiocarbon, in-situ cosmogenic nuclides, and pedogenesis: Implications for climate and tectonics since the mid–late Pleistocene: Southern California Earthquake Center 2014 Annual Meeting: Proceedings, v. XXIV, p. 148, http://files.scec.org/s3fs-public/SCEC2014Proceedings.pdf.

Heermance, R.V., Yule, D., and Desjarlais, I., 2015, Evidence for trans-San Gorgonio Pass earthquakes based on Holocene slip rates along the San Andreas Fault System at Millard Canyon: Southern California Earthquake Center 2015 Annual Meeting: Proceedings, v. XXV, p. 153, http://files.scec.org/s3fs-public/SCEC2015Proceedings.pdf.

Downloaded from http://pubs.geoscienceworld.org/gsa/geosphere/article-pdf/doi/10.1130/GES02424.1/5548351/ges02424.pdf
by USGS Library user

Hill, M.L., and Dibblee, T.W., 1953, San Andreas, Garlock, and Big Pine faults, California: A study of the character, history, and tectonic significance of their displacements: Geological Society of America Bulletin, v. 64, p. 443–458, https://doi.org/10.1130/0016-7606(1953)64[443:SAGABP]2.0.CO;2.

Hill, R.T., 1928, Southern California geology and Los Angeles earthquakes: Los Angeles, Southern California Academy of Sciences, 232 p.

Hofmann, F., McPhillips, D., Kendrick, K., and Farley, K., 2017, The potential of fine-grained pedogenic iron-oxides for cosmogenic ^{3}He dating: Geological Society of America Abstracts with Programs, v. 49, no. 6, https://doi.org/10.1130/abs/2017AM-307549.

Hofmann, F., McPhillips, D., Kendrick, K.J., and Farley, K.A., 2019, Utilizing Pedogenic Iron-oxides for Cosmogenic ^{3}He Geochronology of Soils: San Francisco, California, Abstract GC13A-08 presented at 2019 Fall Meeting, American Geophysical Union, 9–13 December.

Hopson, R.F., 1996, The Pinto Mountain Fault, Mojave Desert, Southern California; offset documentation and tectonics: Geological Society of America Abstracts with Programs, v. 28, no. 5, p. 76.

Hopson, R.F., 2012, The origin of Morongo Valley, an extensional basin in the eastern Transverse Ranges, southern California, *in* Palms to Pines: Geological and Historical Excursions through the Palm Springs Region, Riverside County, California: Road Logs and Papers: San Diego Geological Society and South Coast Geological Society, v. 39, p. 87–93.

Huerta, B.E., 2017, Structure and Geomorphology of West Whitewater Hill, a compressive stepover between the Banning and Garnet Hill Strands of the San Andreas Fault, Whitewater, CA [M.S. thesis]: Northridge, California State University, 64 p.

Ingersoll, R.V., and Coffey, K.T., 2017, Transrotation induced by crustal blocks moving through restraining double bends, with southern California examples: The Journal of Geology, v. 125, p. 551–559, https://doi.org/10.1086/692654.

Janecke, S.U., Dorsey, R.J., Forand, D., Steely, A.N., Kirby, S.M., Lutz, A.T., Housen, B.A., Belgarde, B., Langenheim, V.E., and Rittenour, T.M., 2011, High Geologic Slip Rates since Early Pleistocene Initiation of the San Jacinto and San Felipe Fault Zones in the San Andreas Fault System: Southern California, USA: Geological Society of America Special Paper 475, 48 p., https://doi.org/10.1130/2010.2475.

Jones, L.M., Bernknopf, R., Cox, D., Goltz, J., Hudnut, K., Mileti, D., Perry, S., Ponti, D., Porter, K., Reichle, M., Seligson, H., Shoaf, K., Treiman, J., and Wein, A., 2008, The ShakeOut scenario: U.S. Geological Survey Open-File Report 2008-1150, 308 p.

Kendrick, K.J., and McFadden, L.D., 1996, Comparison and contrast of processes of soil formation in the San Timoteo Badlands with chronosequences in California: Quaternary Research, v. 46, p. 149–160, https://doi.org/10.1006/qres.1996.0055.

Kendrick, K.J., Morton, D.M., Wells, S.G., and Simpson, R.W., 2002, Spatial and Temporal Deformation along the Northern San Jacinto Fault, Southern California: Implications for Slip Rates: Seismological Society of America Bulletin, v. 92, no. 7, p. 2782–2802, https://doi.org/10.1785/0120000615.

Kendrick, K.J., Matti, J.C., and Mahan, S.A., 2015, Late Quaternary slip history of the Mill Creek strand of the San Andreas fault in San Gorgonio Pass, southern California: The role of a subsidiary left-lateral fault in strand switching: Geological Society of America Bulletin, v. 127, no. 5–6, p. 825–849, https://doi.org/10.1130/B31101.1.

Langenheim, V.E., and Powell, R.E., 2009, Basin geometry and cumulative offsets in the Eastern Transverse Ranges, southern California: Implications for transrotational deformation along the San Andreas fault system: Geosphere, v. 5, p. 1–22, https://doi.org/10.1130/GES00177.1.

Langenheim, V.E., Jachens, R.C., Matti, J.C., Morton, D.M., Hauksson, E., and Christensen, A., 2005, Geophysical evidence for wedging in the San Gorgonio Pass structural knot, southern San Andreas Fault zone, southern California: Geological Society of America Bulletin, v. 117, p. 1554–1572, https://doi.org/10.1130/B25760.1.

Matti, J.C., and Morton, D.M., 1993, Paleogeographic evolution of the San Andreas fault in southern California: A reconstruction based on a new cross-fault correlation, *in* Powell, R.E., Weldon, R.J., II, and Matti, J.C., eds., The San Andreas Fault System: Displacement, Palinspastic Reconstruction, and Geologic Evolution: Geological Society of America Memoir 178, p. 107–159, https://doi.org/10.1130/MEM178-p107.

Matti, J.C., Cox, B.F., and Iverson, S.R., 1983, Mineral resource potential map of the Raywood Flat Roadless Area, San Bernardino and Riverside Counties, California: U.S. Geological Survey Miscellaneous Field Studies Map MF-1563-A, scale 1:62,500.

Matti, J.C., Morton, D.M., and Cox, B.F., 1985, Distribution and geologic relations of fault systems in the vicinity of the central Transverse Ranges, southern California: U.S. Geological Survey Open-File Report 85-365, 27 p., scale 1:250,000.

Matti, J.C., Morton, D.M., and Cox, B.F., 1992a, The San Andreas fault system in the vicinity of the central Transverse Ranges Province, southern California: U.S. Geological Survey Open-File Report 92-354, 40 p., scale 1:250,000.

Matti, J.C., Morton, D.M., Cox, B.F., Carson, S.E., and Yetter, T.J., 1992b, Geologic map of the Yucaipa 7.5′ quadrangle, California: U.S. Geological Survey Open-File Report 92-446, 14 p., scale 1:24,000.

Matti, J.C., Morton, D.M., Cox, B.F., Carson, S.E., and Yetter, T.J., 2003, Geologic map and digital database of the Yucaipa 7.5′ quadrangle, San Bernardino and Riverside Counties, California, version 1.0: U.S. Geological Survey Open-File Report 03-301, scale 1:24,000.

Matti, J.C., Morton, D.M., and Langenheim, V.E., 2015, Geologic and geophysical maps of the El Casco 7.5′ quadrangle, Riverside County, southern California, with accompanying geologic-map database, U.S. Geological Survey Open-File Report 2010-1274, 141 p., 3 sheets, scale 1:24,000, https://doi.org/10.3133/ofr20101274.

McBurnett, P., 2011, Paleoseismicity of the San Gorgonio Pass Fault Zone at Millard Canyon: Testing the likelihood of a through-going San Andreas rupture [M.S. thesis]: Northridge, California State University, 76 p.

McFadden, L.D., and Weldon, R.J., 1987, Rates and processes of soil development on Quaternary terraces in Cajon Pass, California: Geological Society of America Bulletin, v. 98, p. 280–293, https://doi.org/10.1130/0016-7606(1987)98<280:RAPOSD>2.0.CO;2.

Mendez, G.O., Langenheim, V.E., Morita, A., and Danskin, W.R., 2016, Geologic structure of the Yucaipa area inferred from gravity data, San Bernardino and Riverside Counties, California: U.S. Geological Survey Open-File Report 2016-1127, 22 p., https://doi.org/10.3133/ofr20161127.

Morton, D.M., and Matti, J.C., 1993, Extension and contraction within an evolving divergent strike-slip fault complex: The San Andreas and San Jacinto fault zones at their convergence in southern California, *in* Powell, R.E., Weldon, R.J., II, and Matti, J.C., eds., The San Andreas Fault System: Displacement, Palinspastic Reconstruction, and Geologic Evolution: Geological Society of America Memoir 178, p. 217–230, https://doi.org/10.1130/MEM178-p217.

Morton, D.M., Cox, B.F., and Matti, J.C., 1980, Geologic map of the San Gorgonio Wilderness: U.S. Geological Survey Miscellaneous Field Studies Map MF-1164-A, scale 1:62,500.

Norris, R.J., and Cooper, A.F., 2007, The Alpine Fault, New Zealand: Surface Geology and Field Relationships, *in* Okaya, D., Stern, T., and Davey, F., eds., A Continental Plate Boundary: Tectonics at South Island, New Zealand: American Geophysical Union, Geophysical Monograph Series, v. 175, https://doi.org/10.1029/175GM09.

Orozco, A., 2004, Offset of a mid-Holocene alluvial fan near Banning, CA; constraints on the slip rate of the San Bernardino Strand of the San Andreas Fault [M.S. thesis]: Northridge, California State University, 56 p.

Perry, S., Cox, D., Jones, L., Bernknopf, R., Goltz, J., Hudnut, K., Mileti, D., Ponti, D., Porter, K., Reichle, M., Seligson, H., Shoaf, K., Treiman, J., and Wein, A., 2008, The ShakeOut Earthquake Scenario: A story that southern Californians are writing: U.S. Geological Survey Circular 1324 and California Geological Survey Special Report 207, 16 p., https://doi.org/10.3133/cir1324.

Peterson, M.S., 1975, Geology of the Coachella fanglomerate, *in* San Andreas fault in southern California: California Division of Mines and Geology Special Report 118, p. 119–126.

Plesch, A., Shaw, J.H., Benson, C., Bryant, W.A., Carena, S., Cooke, M., Dolan, J., Fuis, G.S., Gath, E., Grant, L., Hauksson, E., Jordan, T., Kamerling, M., Legg, M., Lindvall, S., Magistrale, H., Nicholson, C., Niemi, N., Oskin, M., Perry, S., Planansky, G., Rockwell, T., Shearer, P., Sorlien, C., Suess, M.P., Suppe, J., Treiman, J., and Yeats, R., 2007, Community Fault Model for Southern California: Bulletin of the Seismological Society of America, v. 97, p. 1793–1802, https://doi.org/10.1785/0120050211.

Powell, R.E., 1993, Balanced palinspastic reconstruction of pre-Late Cenozoic paleogeology, southern California: geologic and kinematic constraints on evolution of the San Andreas fault system, *in* Powell, R.E., Weldon, R.J., II, and Matti, J.C., eds., The San Andreas Fault System: Displacement, Palinspastic Reconstruction, and Geologic Evolution: Geological Society of America Memoir 178, 106 p., https://doi.org/10.1130/MEM178-p1.

Proctor, R.J., 1968, Geology of the Desert Hot Springs-Upper Coachella Valley, Salton Sea, and vicinity: California Division of Mines and Geology, Special Report 94, 50 p.

Ramzan, S., 2012, Paleoseismic investigation of the San Gorgonio Pass Fault zone near Cabazon, California [M.S. thesis]: Northridge, California State University, 63 p.

Smith, D.P., 1979, The San Gorgonio Pass Fault: California Division of Mines and Geology, Fault Evaluation Report FER-87, 7 p.

Soil Survey Staff, 1951, Soil survey manual: Washington D.C., USDA Agricultural Handbook 18, U.S. Government Printing Office.

Downloaded from http://pubs.geoscienceworld.org/gsa/geosphere/article-pdf/doi/10.1130/GES02424.1/5548351/ges02424.pdf
by USGS Library user

Spotila, J.A., and Sieh, K.E., 2000, Architecture of transpressional thrust faulting in the San Bernardino Mountains, southern California, from deformation of a deeply weathered surface: Tectonics, v. 19, p. 589–615, https://doi.org/10.1029/1999TC001150.

Spotila, J.A., Farley, K.A., and Sieh, K.E., 1998, Uplift and erosion of the San Bernardino Mountains associated with transpression along the San Andreas fault, California, as constrained by radiogenic helium thermochronometry: Tectonics, v. 17, p. 360–378, https://doi.org/10.1029/98TC00378.

Spotila, J.A., Farley, K.A., Yule, J.D., and Reiners, P.W., 2001, Near-field transpressive deformation along the San Andreas fault zone in southern California, based on exhumation constrained by (U-Th)/He dating: Journal of Geophysical Research, v. 106, p. 30,909–30,922, https://doi.org/10.1029/2001JB000348.

Spotila, J.A., House, M.A., Blythe, A.E., Niemi, N.A., and Bank, G.C., 2002, Controls on the erosion and geomorphic evolution of the San Bernardino and San Gabriel Mountains, southern California, *in* Barth, A., ed., Contributions to Crustal Evolution of the Southwestern United States: Geological Society of America Special Paper 365, p. 205–230, https://doi.org/10.1130/0-8137-2365-5.205.

Torrent, J., Schwertmann, U., and Shulze, D.J., 1980, Iron oxide mineralogy of some soils of two river terrace sequences in Spain: Geoderma, v. 23, p. 191–208, https://doi.org/10.1016/0016-7061(80)90002-6.

Treiman, J., Real, C.R., Wilson, R.I., Silva, M.A., Pridmore, C.L., McCrink, T.P., Loyd, R.C., and Reichle, M.S., 2008, ShakeOut Scenario Appendix E: Fault rupture impacts at areas of lifeline concentration: Appendix E of Jones, L.M., The ShakeOut Scenario: U.S. Geological Survey Open-File Report 2008-1150, and California Geological Survey Preliminary Report 25E, 26 p., http://pubs.usgs.gov/of/2008/1150/appendixes/of2008-1150_appendix_e.pdf.

Treiman, J.A., 1995, The San Gorgonio Pass, Banning and related faults, Riverside County, California (Supplement #1): California Division of Mines and Geology, Fault Evaluation Report FER-235, 11 p.

Tyley, S., 1974, Analog model study of the ground-water basin of the upper Coachella Valley, California: United States Geological Survey, Water-Supply Paper 2027, 77 p.

Vaughan, F.E., 1922, Geology of the San Bernardino Mountains north of San Gorgonio Pass: California University Publications in Geological Sciences, v. 13, p. 319–411.

Wolff, L., 2018, A 6000-year record of large, infrequent earthquakes on the San Andreas Fault System in San Gorgonio Pass, near Cabezon, California [M.S. thesis]: Northridge, California State University, 97 p.

Wolff, L., Yule, D., Scharer, K., Witkosky, R., Desjarlais, I., and Huerta, B., 2013, Evidence for five paleoearthquakes on the San Gorgonio Pass Fault Zone in the last 6000 years: Southern California Earthquake Center 2013 Annual Meeting: Proceedings, v. XXIIII, p. 156, http://files.scec.org/s3fs-public/SCEC2013Proceedings.pdf.

Yule, D., 2009, The enigmatic San Gorgonio Pass: Geology, v. 37, p. 191–192, https://doi.org/10.1130/focus022009.1.

Yule, D., 2010, Testing the "shakeout" scenario earthquake in San Gorgonio Pass: Fact or fiction?: Geological Society of America Abstracts with Programs, v. 42, p. 69.

Yule, D., and Sieh, K., 2001, The paleoseismic record at Burro Flats: Evidence for a 300-year average recurrence for large earthquakes on the San Andreas fault in San Gorgonio Pass, southern California: Geological Society of America Abstracts with Programs, v. 33, no. 3, p. A31.

Yule, D., and Sieh, K., 2003, Complexities of the San Andreas fault near San Gorgonio Pass: Implications for large earthquakes: Journal of Geophysical Research, v. 108, 23 p., https://doi.org/10.1029/2001JB000451.

Yule, D., and Spotila, J., 2010, Quaternary geology of the San Bernardino Mountains and their tectonic margins, *in* Geologic Excursions in California and Nevada: Tectonics, Stratigraphy and Hydrogeology: Pacific Section, SEPM (Society for Sedimentary Geology) Book, v. 108, p. 273–322.

Yule, D., Fumal, T., McGill, S., and Seitz, G., 2001, Active tectonics and paleoseismic record of the San Andreas fault, Wrightwood to Indio: Working toward a forecast for the next 'Big Event', *in* Geologic Excursions in the California Deserts and Adjacent Transverse Ranges: Los Angeles, California, Pacific Section, Society of Economic Paleontologists and Mineralogists, p. 91–126.

Downloaded from http://pubs.geoscienceworld.org/gsa/geosphere/article-pdf/doi/10.1130/GES02424.1/5548351/ges02424.pdf
by USGS Library user

WHAT HAPPENS TO THE REAL SAN ANDREAS FAULT AT COTTONWOOD CANYON, SAN GORGONIO PASS, CALIFORNIA?

Gary S. Rasmussen
Gary S. Rasmussen & Associates, Inc.
1811 Commercenter W.
San Bernardino, CA 92408

Wessly A. Reeder
Gary S. Rasmussen & Associates, Inc.
1811 Commercenter W.
San Bernardino, CA 92408

INTRODUCTION

The San Andreas fault has been difficult to trace through the San Gorgonio Pass, despite numerous efforts to precisely define its location and style of movement. In this paper we have attempted to provide an alternate explanation for the fault through the San Gorgonio Pass. At this time, our field work has been primarily confined to the terrain between Millard Canyon and Cottonwood Canyon, the easternmost portion of the area where the fault is most elusive. In describing the geologic features of the San Andreas fault from Burro Flats to Cottonwood Canyon, the convention of describing the fault from north to south has been followed. The fault itself and most of the structural features associated with it, however, were created by forces imposed from south to north as the oceanic plate collided with the continental plate.

This paper is the result of several years of observations of the fault in this area. It is based on time and effort unrelated to any outside funding. The increasing pressure of development in the upper Coachella Valley is resulting in many more site specific geologic studies that rely on the published literature. The interaction of man with geologic forces makes it mandatory that we more completely understand the geologic facts prior to modifying or building on the natural terrain.

The purpose of this paper is to offer a possible explanation for most, if not all of the puzzling aspects related to where and what is the real San Andreas fault between Burro Flats and Cottonwood Canyon.

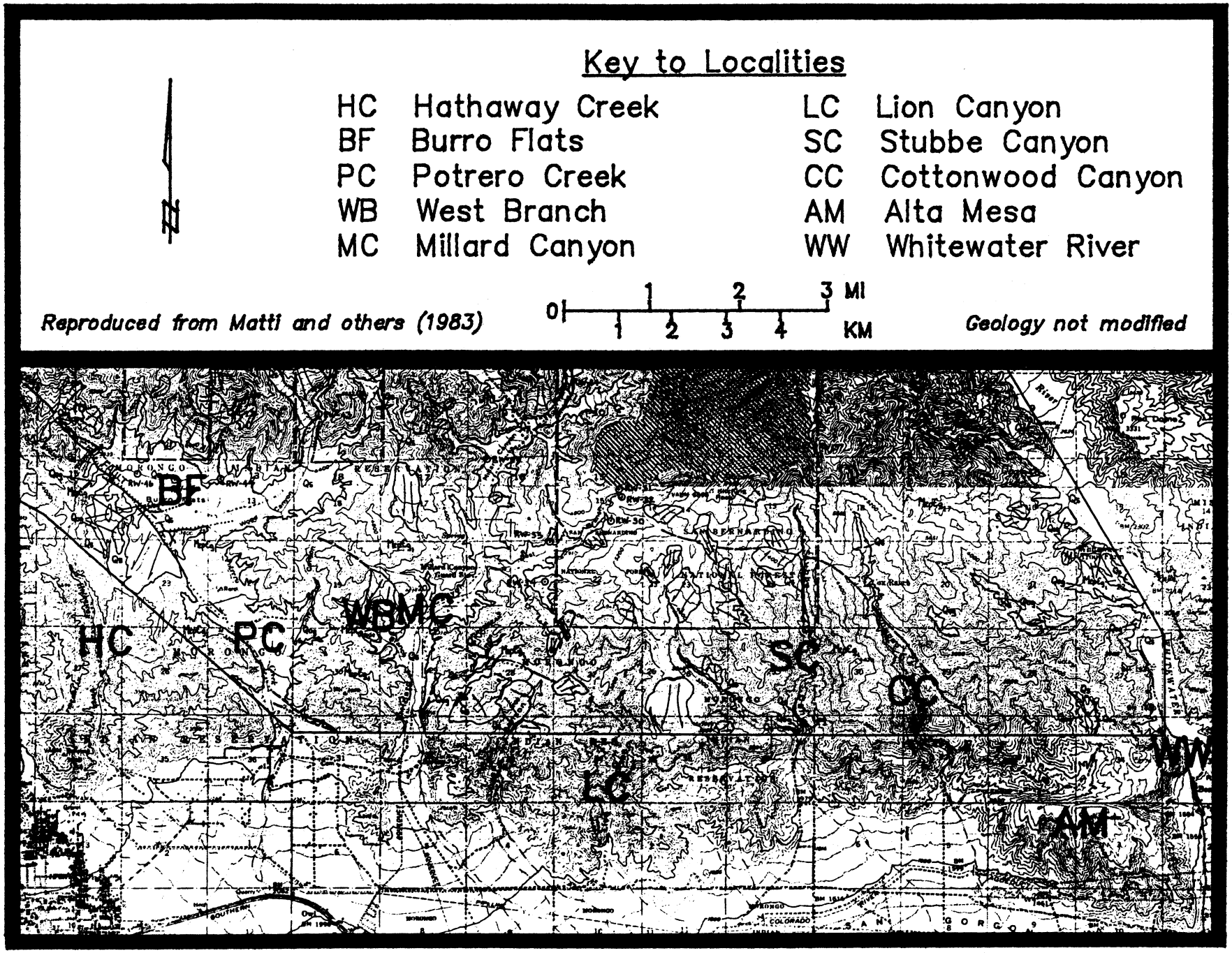

Figure 1. Location Map.

HISTORICAL PERSPECTIVE

The existence, location, type of movement, amount of movement, degree of activity, and terminology of the San Andreas fault through the San Gorgonio Pass has been controversial since it was first mapped by Fairbanks in 1908. The main reason geologists working in the area cannot agree on what actually constitutes the San Andreas fault in this area is its lack of well defined geomorphic expression. Fairbanks, in describing the fault from the northwest as it enters San Gorgonio Pass states that Potato Canyon, northwest of San Gorgonio Pass was "the last of the longitudinal depressions of any size marking the line of the rift" (in Lawson, and others, 1908). He indicated the lack of rift topography in the pass area was due to rapid erosion caused by "recent disturbances".

Vaughn (1922) succeeded in tracing the San Andreas fault intermittently through San Gorgonio Pass. He states "The physiographic expression can be readily followed along Potato Canon to Oak Glen and thence a mile east of Pine Bench. Here the trace of the fault is lost from sight for nearly two miles, but is again seen on the north side of the valley at the heads of Hathaway and Potrero Canons and along the West Branch of Millard Canon. Crossing Millard Canon, it is again lost until about two miles west of Stubby Canon, where definite displacement can be seen. From Stubby Canon eastward to Cottonwood Canon the position of the San Andreas fault cannot be exactly determined."

Allen (1957) has probably conducted the most extensive mapping in the area with the specific purpose of documenting the fault location and character. He concluded that "the surface break that has been called the San Andreas fault is dying out in the vicinity of Burro Flat. This conclusion implies, of course, that displacement on the fault in this area has not been large." Allen favors the hypothesis that the nature of the fault changes from a strike-slip fault to one of major thrusting along the Banning fault from east of Potrero Canyon to west of Cottonwood Canyon. His main reasons for this seem to be an apparent change in strike of the San Andreas fault through Burro Flats together with fault plane solutions indicating that first motion along historic earthquakes east of Potrero Canyon have been predominately thrusting.

Most workers since Allen's 1957 paper have accepted his hypothesis that the San Andreas fault is characterized primarily by thrusting between Potrero Canyon and Cottonwood Canyon. The most recent mapping in the area was that

of Matti and others (1985). One of the most important contributions of their mapping with respect to faulting in the area was their recognition of large and abundant landslides.

CONTROVERSY

Most geologists working in the area have agreed that the San Andreas fault is not well defined in San Gorgonio Pass. The major factors contributing to the lack of recognition of a single, through-going San Andreas fault in this area seem to be: 1) lack of rift topography from Burro Flats to Cottonwood Canyon; 2) lack of streams exhibiting right-lateral offset; 3) apparent change in strike of the fault in the general area; 4) first motion indicators of historic earthquakes that suggest thrust motion rather than strike-slip motion; 5) the fact that no great earthquakes are known to have occurred along this reach of the fault; and 6) a general lack of geomorphic fault expression in young materials between Burro Flats and Cottonwood Canyon.

FAULT SETTING

San Andreas Fault

Any discussion of the San Andreas fault through San Gorgonio Pass becomes difficult to follow because of the fault's history of sequential evolution and abandonment (Matti and others, 1985). The various old and new strands have been referred to in different names by different papers. For our discussion, the San Andreas fault will be considered to be the fault as expressed to Burro Flats, then continuing along nearly the same strike to the southeast and exposed intermittently as described by Vaughn (1922) to Cottonwood Canyon, then southeast to where it merges with the Mission Creek fault. Most other work refers to the San Andreas fault in this area as that portion of the fault shown as buried from Burro Flats to its juncture with the Banning fault at Potrero Canyon, considerably farther south than where the San Andreas fault is suggested in this paper.

The fault which is considered by us to be the Banning fault includes others (Allen, 1957; Dibblee, 1964, 1982; Matti and others, 1982, 1985) Banning fault from Potrero Canyon to Cottonwood Canyon. Most geologic maps of the Banning fault in this reach show it as a thrust fault. Fault segments are usually characterized by consistent geometries and styles of motion (Rasmussen, 1981). Therefore, the term Banning

fault should only refer to that fault segment from near Redlands Heights east to Cottonwood Canyon. Along this reach it is consistently a high angle reverse fault, except immediately west of Cottonwood Canyon. Immediately west of Cottonwood Canyon it appears to be completely covered by massive landslides, whose toes are currently exposed in dissected drainages. From Cottonwood Canyon to the southeast, the Banning fault of others is the same as that described as the San Andreas fault in this paper. Dibblee (1964) refers to this segment as the south branch of the San Andreas fault.

The main trace of the San Andreas fault can be easily observed in both the field and on stereoscopic aerial photographs from Point Arena (north of San Francisco) to Burro Flats (western San Gorgonio Pass area). There are only a few places over this long distance where the fault is not distinct, and these places are relatively short; usually less than 1/2 mile. However, no one has successfully traced the San Andreas fault from Burro Flats to Alta Mesa (hill east of Cottonwood Canyon and west of Whitewater Canyon, referred to as Whitewater Hill by Allen).

Vaughn (1922) noted several locations where he thought the fault existed in this reach, as described earlier. Most others have tended to change the fault strike at Burro Flats and bend it sharply to the south, where it must once again bend sharply to the east and merge with the Banning fault. However, what Allen shows as the main fault scarp through Burro Flats may actually be erosional in origin. Offset drainages, together with changes in drainage gradients and a weak lineament on aerial photographs evident across part of Potrero Canyon suggest that the fault may not change strike at Burro Flats. In addition, the landslide-debris flow deposit (Burnt Canyon Breccia of Allen, 1957) crosses the fault and tends to obscure the geomorphic expression of faulting that existed prior to the latest debris flow. Observation of the aerial photographs suggests that there have been multiple episodes of debris flows at Burro Flats. Southeast of Cottonwood Canyon the fault, commonly referred to as the Banning fault, is again obvious from the north side of Alta Mesa to the north end of the Salton Sea. Near Indio, the San Andreas fault (Banning fault of others) merges with the Mission Creek fault.

Based on recent work by Reeder and Rasmussen (1986) and that of Clark (1984), the term San Andreas fault will be used to describe the Banning fault from Cottonwood Canyon to Indio. The Banning fault should be used to describe the Banning fault (south of the San Andreas fault) from the Redlands Heights-Calimesa area to Cottonwood Canyon, where it is either offset by the San Andreas fault or merges with

it. The San Andreas fault system in this area can simplistically be considered to consist of the Mill Creek fault, the Mission Creek fault, the San Andreas fault and the Banning fault. Based on detailed observations of these faults in San Gorgonio Pass, it is apparent that the major motion on the San Andreas fault has transferred between these major fault traces at different times. Matti and others (1985) provide an excellent discussion of modern and ancestral branches of the San Andreas fault in this region. The interaction of the east-west trending Pinto Mountain fault and its parallel, less well known faults has probably had a major influence on which of the three strands of the San Andreas fault system has been the "master" fault for any given time period. For purposes of this paper, the term San Andreas fault is used to refer to the fault trace that exhibits the most evidence for Holocene movement that is relatively continuous, either as a continuous fault or an en echelon feature.

The San Andreas fault (Banning fault of others) from Alta Mesa to the Indio Hills can be easily followed by the abundant vegetation growing along the fault, numerous fault scarps, springs, deflected drainages, and offset sedimentary surfaces. The fault is exposed in the canyon wall of Whitewater River and is dipping steeply to the north. Along the north side of Alta Mesa, the fault is partially obscured by landslides that have failed towards the north. However, the fault maintains a relatively consistent strike obliquely to the northwest along the north side of the nearly east-west trending drainage of Alta Mesa, to the spring and dense vegetation in the bottom of Cottonwood Canyon. Most previous workers have tried to curve the fault more to the south along the drainage bounding the north side of Alta Mesa (Allen, 1957; Dibblee, 1964, 1975; and Matti and others, 1982, 1985). However, there is evidence in the form of offset drainages, offset ridges, a strong lineament on the aerial photographs, and aligned saddles that the fault continues in a straight line to the spring in Cottonwood Canyon. The real problem of continuing the fault along this strike is that there suddenly is no evidence of the fault's existence on the west side of Cottonwood Canyon.

Banning Fault

The Banning fault is an ancestral trace of the San Andreas fault from at least the Redlands Heights area east to Potrero Canyon (Allen, 1957, Morton, 1978, Matti and others 1982, 1985). In nearly all areas west of Potrero Canyon where it is exposed, the Banning fault dips steeply to the north and is characterized by reverse movement. Allen suggested that the Banning fault continues to the west from

the Redlands Heights area to the San Jacinto fault and may be an offset trace of one of the Transverse Range faults in the San Gabriel Mountains. From San Gorgonio Canyon east to Cottonwood Canyon, Allen (1957) and most workers since then consider the Banning fault to be the modern trace of the San Andreas fault. Between Potrero Canyon and Cottonwood Canyon it has been mapped as a major thrust fault as opposed to a strike-slip fault. It merges with or is truncated by the San Andreas fault in the vicinity of Cottonwood Canyon.

Mission Creek Fault

The most recent work along the Mission Creek fault suggests that it merges with the Pinto Mountain fault west of the south fork of Whitewater River and is a major east-west fault south of the Mill Creek fault (Ehlig, 1977; Farley, 1979; Matti and others, 1985). Southeast from Whitewater River, the fault intermittently forms the southern margin of the mountain front of the Little San Bernardino Mountains and forms conspicuous scarps east of State Highway 62. From the base of the Little San Bernardino Mountains northwest of Desert Hot Springs to its merging with the San Andreas fault north of Indio, it is well defined by fault scarps and vegetational lineaments (Reeder and Rasmussen, 1986). Based on detailed trenching near Whitewater River and observation of aerial photographs, it appears that this fault has not been active since Late Pleistocene time from the Whitewater River to State Highway No. 62 (Rasmussen, 1977). It is obvious in the area immediately east of Whitewater River that at one time a great amount of movement took place along the Mission Creek fault, well into mid-Pleistocene time.

The strike of the Mission Creek fault takes a 10 degree bend just northwest of Desert Hot Springs and then continues along a relatively consistent strike through Desert Hot Springs to its merging with the San Andreas fault north of Indio. Recent trenching indicates the fault may not be active (at least in the past 6000 years) north of Mission Lakes Boulevard (Reeder and Rasmussen, 1986). Trenching approximately 3 kilometers to the southeast of that location however, found abundant evidence of recent activity (Rasmussen, 1977). Therefore, the Mission Creek fault is only active for a short distance and appears to be the dying out expression of the San Andreas fault as the Holocene trace curves to the west toward Alta Mesa.

SAN ANDREAS FAULT AT COTTONWOOD CANYON

The San Andreas fault along the north side of Alta Mesa forms a nearly continuous, straight line. It is buried in places by small landslides failing off the north face of Alta Mesa. However, its trace is indicative of a high angle fault, as evidenced by its straight path across irregular topography. It continues this straight trace northwest to the spring in Cottonwood Canyon as previously discussed. Many geologists show a buried trace of the fault within the slightly arcuate drainage north of Alta Mesa (Allen, 1957; Dibblee, 1970, 1975; Matti and others 1982, 1985). The only apparent reason for doing this is that it makes it easier to merge it with the Banning fault west of Cottonwood Canyon, south of the spring. Connecting these faults by dotted lines tends to reinforce the idea that the nearly vertical strike-slip San Andreas fault suddenly becomes a flat thrust fault within less than 1 mile.

A trench was recently excavated immediately west of Cottonwood Canyon, south of the spring. This trench was placed across the projection of the flat-lying plane of what has been mapped as the Banning fault based on exposures along the south and east flank of the hill. A nearly horizontal slip surface was encountered at a depth of 1.2 meters below the alluvial surface. This plane is the same plane described as the Banning fault just south of the trench. However, observation of this plane, together with the continuation of this plane exposed within incised drainages immediately to the south and southwest, revealed tensional features commonly associated with landslides. In fact, this plane dips to the south in some exposures (Allen, 1957).

The continuation of this flat-lying plane north of the dotted trace of the fault mapped by others north of Alta Mesa suggests that if it merges with the San Andreas fault, it would have to do so at Cottonwood Springs. However, the geomorphic expression of the San Andreas fault at Cottonwood Springs suggests that it is still a high angle fault with strike-slip indicators of movement. Therefore, in order for the Banning thrust fault, as mapped by others, to merge with the San Andreas fault, it would have to change from a flat thrust fault to a high angle strike-slip fault within 400 meters. Considering the amount of strain and amount of movement that has to take place along this fault, such an abrupt change in character over this short of a distance is unlikely given the mechanics of the materials involved.

Normally, a sudden change in strike or character of a fault is related to an intersecting fault. There are no

intersecting faults in the vicinity of Cottonwood Canyon that would cause such a drastic change in fault character.

The Banning fault west of the area of controversy is a steeply dipping reverse fault and is exposed in many places with this type of geometry. West of Potrero Canyon it is an inactive fault, described as an ancestral San Andreas fault (Allen, 1957; Matti and others, 1982, 1985). It does not offset Late Pleistocene sediments to the west. It does not seem reasonable that the high angle, strike-slip fault characteristic of the San Andreas fault southeast of Cottonwood Canyon and northwest of Burro Flats, would abruptly change to a nearly flat thrust for such a short distance along the older Banning fault. Right-lateral strike-slip movement is evident at both Burro Flats and at Cottonwood Canyon. Given the forces involved with plate tectonics and the inconsistency and high degree of fracturing of the rocks within the segment between Burro Flats and Cottonwood Canyon, it is much more reasonable to continue the fault beneath the massive landslides than to change the character of the San Andreas fault. Even where the Pinto Mountain fault intersects the San Andreas fault near Pine Bench, it does not significantly change the San Andreas fault except to affect the strike.

Detailed observation of the terrain between Stubbe Canyon and Cottonwood Canyon, in the field, in trenches, and on stereoscopic aerial photographs revealed abundant evidence of very recent and on-going landsliding. At Cottonwood Springs, numerous landslides were observed on the aerial photographs and in the field. A small landslide (more than one hundred meters by approximately 300 meters) has failed to the east into Cottonwood Canyon. At least two larger landslides have failed north into Cottonwood Canyon north of the springs. In fact, the abrupt bend in Cottonwood Canyon north of the springs, from a north-south flowing drainage to an east-west flowing drainage, may have been caused by a massive landslide that failed to the northeast.

A geologic reconnaissance along the projected trace of the San Andreas fault from Stubbe Canyon to Cottonwood Canyon failed to find any in-place material that was not part of a landslide. Within this small area, the landslides numbered within the hundreds. In nearly all cases where similar landslide terrain has been observed, there has been at least one or more megalandslides which underlie and delimit the landslide terrain. Subsequently many smaller landslides develop due to the fracturing and increased infiltration of water. The larger slides can move as relatively intact blocks, which may have continuity of structure above the slide plane.

At least two megalandslides with dimensions of the order of 1.5 kilometers by 1.6 kilometers have been identified within massive granitic rocks within the Rim Forest and Running Springs area of the San Bernardino Mountains (Rasmussen, 1978, 1982). The metamorphic and igneous rocks between Millard Canyon and Cottonwood Canyon are less massive than those in the Rim Forest and Running Springs area. Nearly continuous, massive landslides were observed on the aerial photographs between these canyons and abundant, very active landslides between Millard Canyon and Cottonwood Canyon were evident in the field. The "Dry Lake" west of Stubbe Canyon described by Allen is a combination of a large landslide and faulting along the true trace of the San Andreas fault (Rasmussen, personal observation; Matti and others, 1982, 1985).

Numerous closed depressions and basins, on both a small and large scale, exist within this area. Some of the landslides have dammed drainages and have resulted in deposition of more than 30 meters of sediments west of Cottonwood Canyon. Drainage patterns between Millard Canyon and Cottonwood Canyon are characteristic of landsliding on both a normal and mega-scale.

Based on the abundant evidence for large-scale landsliding in the area where the San Andreas fault would project from Millard Canyon to Cottonwood Canyon, the windows of fault exposed within a few deeply incised drainages (Vaughn 1922; Allen 1957; and Matti and others, 1985), what appear to be fault related landslide scarps, a few offset drainages and ridges within the deeper incised drainages, and the fact that the San Andreas fault is very difficult to see where it has been overridden by landsliding (Yucaipa Ridge east of Mill Creek); it appears that the San Andreas fault may indeed continue in a nearly straight line between Burro Flats and Cottonwood Springs in a consistent high-angle strike-slip configuration. The lack of distinct geomorphic expression of faulting can be attributed to the existence of large landslides with literally thousands of smaller landslides, which have overridden the fault. The large degree of void spaces in landslides resulting from fracturing during initial movement allows a much greater amount of fault movement beneath the slide and therefore results in much less geomorphic expression than that which would be observed in a normally deposited, intact sediment or rock. Large landslides crossing the San Andreas fault between Mill Creek and Oak Glen attest to the ability of landslides to obscure surficial expressions of faulting. The recognition of pervasive landsliding in an area where active faulting is being sought is considered to be critical when attempting to delineate faulting.

CONCLUSIONS

Based on observation of fault features within landslides in similar terrain, it appears that much of the real San Andreas fault between Millard Canyon and Cottonwood Canyon may be obscured by landsliding on both a small and extremely large scale.

Landslides are very effective in obscuring rapidly moving faults and many landslides evident where one would expect the San Andreas fault to be in San Gorgonio Pass exhibited evidence of very recent movement. Good examples of other areas where the fault has been obscured or partially obscured exist along the south flank of Yucaipa Ridge, between Mill Creek and Pine Bench.

The alignment of the Kitching Peak earthquake swarm (Richter, and others, 1958) parallels the "projected trace" of the true San Andreas fault and not that of the Banning fault. This suggests a through going tectonic feature at the location indicated in this paper for the San Andreas fault. Fault plane solutions from small earthquakes can usually be interpreted for more than one type of fault geometry. If the earthquake motion records are precise enough in this area, a reevaluation of them should be made to see if a high-angle, strike-slip motion parallel to our suggested San Andreas fault might not make a suitable fault plane solution.

There appears to be little change in strike of the San Andreas fault through San Gorgonio Pass, other than at Pine Bench where it is intersected by the Pinto Mountain fault. The main trace of the San Andreas fault at Burro Flats does not appear to follow the southwesterly most ridge as suggested by Allen (1957), and Matti and others (1985), but based on small scarps, offset drainages, and drainage gradient changes continues along its trend across the ridge formed by the Burnt Canyon Breccia and across Potrero Canyon.

The San Andreas fault between Burro Flats and Cottonwood Canyon is obscured in most places by massive landsliding, but is marked by a few offset drainages, offset ridges, and in some windows incised deeply into the landslides.

We suggest that some of the mapped traces of the Banning fault between Stubbe and Cottonwood Canyons, which exhibit unusually shallow dips, may in many cases be the toe of megalandslides that have been exposed by uplift and erosion. In some of these, the source of the megalandslide may have been displaced significantly by movement

along the San Andreas fault. Allen maps one of these large landslide remnants along the front of the mountains. The true Banning fault is likely to have a dip of 60 degrees or greater as is characteristic of it throughout the remainder of its reach.

Although field work to this date is limited, the evidence stated in this paper strongly suggests that the San Andreas fault through San Gorgonio Pass is a continuous feature located north of the "Banning thrust fault" and that it is not drastically different with respect to geometry or components of movement than from the San Andreas fault to the southeast or northwest.

REFERENCES CITED

Allen, C.R., 1957, San Andreas fault zone in San Gorgonio Pass,southern California: Geological Society of America Bulletin, v.68, no. 3, p. 315-350.

Clark, M. M., 1984, Map showing recently active breaks along the San Andreas fault and associated faults between Salton Sea and Whitewater River-Mission Creek, California: U.S. Geological Survey Miscellaneous Investigations Map I-1483, scale 1:24,000.

Cox, B.F., Matti, J.C., Oliver, H.W., and Zilka, N.T., 1983, Mineral resource potential map of the San Gorgonio Wilderness, San Bernardino County, California: U.S. Geological Survey Miscellaneous Field Studies Map MF-1161-C, scale 1:62,500.

Dibblee, T.W., Jr., 1964, Geologic map of the San Gorgonio Mountain quadrangle, San Bernardino and Riverside Counties, California: U.S. Geological Survey Miscellaneous Geologic Investigations Map I-431, scale 1:62,500.

Dibblee, T.W., Jr., 1975, Late Quaternary uplift of the San Bernardino Mountains on the San Andreas and related faults, in Crowell, J.C., ed., San Andreas fault in southern California, a guide to San Andreas fault from Mexico to Carrizo Plain: California Division of Mines and Geology Special Report 118, p. 127-135.

Dibblee, T.W., Jr., 1982, Geology of the San Bernardino Mountains, southern California, in Fife, D.L., and Minch, J.A., eds., Geology and mineral wealth of the California Transverse Ranges: South Coast Geological Society, Annual Symposium and Guidebook Number 10 (Mason Hill volume), p. 148-169.

Ehlig, P.L., 1977, Structure of the San Andreas fault zone in San Gorgonio Pass, southern California: Geological Society of America Abstracts with Programs, v. 9, no. 4, p. 516.

Farley, Thomas, 1979, Geology of a part of northern San Gorgonio Pass, California: California State University, Los Angeles unpublished M.S. thesis, 159 p.

Lawson, A.C., and others, 1908, The California earthquake of April 18, 1906: Carnegie Institute Publication 87, v. 1, 451p.

Matti, J.C., and Morton, D.M., 1982, Geologic history of the Banning fault zone, southern California: Geological Society of America Abstracts with Programs, v. 14, no. 4, p. 184.

Matti, J.C., Cox, B.F., Obi, C.M., Powell, R.E., Hinkle, M.E., Griscom, Andrew, and McHugh, E.L., 1982, Mineral resource potential map of the Whitewater Wilderness Study Area, Riverside and San Bernardino Counties, California: U.S. Geological Survey Miscellaneous Field Studies Map MF-1478, scale 1:24,000.

Matti, J.C., Cox, B.F., and Iverson, S.R., 1983, Mineral resource potential map of the Raywood Flat Roadless Area, San Bernardino and Riverside Counties, California: U.S. Geological Survey Miscellaneous Field Studies Map MF 1563-A, scale 1:62,500.

Matti, J.C., Morton, D.M., and Cox, B.F., 1985, Distribution and geologic relations of fault systems in the vicinity of the Central Transverse Ranges, southern California: U.S. Geological Survey Open File Report 85-365, 27 p., scale 1:24,000.

Morton, D.M., 1978, Geologic map of the Redlands 7.5' quadrangle, San Bernardino and Riverside Counties, California: U.S. Geological Survey Open-File report 78-21, scale 1:24,000.

Morton, D.M., Cox, B.F., and Matti, J.C., 1980, Geologic map of the San Gorgonio Mountain Wilderness: U.S. Geological Survey Miscellaneous Field Studies Map MF-1164-A, scale 1:62,500.

Rasmussen, G.S., 1981, San Andreas fault geometry and maximum probable earthquakes in southern California: Geological Society of America Abstracts with Programs, v. 13, no. 2, p. 102.

Rasmussen, G.S., 1982, Geologic features and rate of movement along the south branch of the San Andreas fault, San Bernardino, California, in Rasmussen, G.S., ed., Geologic hazards along the San Andreas fault system, San Bernardino-Hemet-Chino, California, field trip no. 4 of Cooper, J.D., compiler, Neotectonics in southern California: Geological Society of America, Cordilleran Section, 78th Annual Meeting, Volume and Guidebook, p. 109-114.

Rasmussen, G.S. and Associates, Inc., August 16, 1977, Engineering Geology Investigation, Lots 14-17, Pierson Boulevard, West of Palm Drive, Desert Hot Springs, California, Project No. 1230.

Rasmussen, G.S. and Associates, Inc., August 9, 1977, Engineering geology investigation of Alquist-Priolo Special

Studies Zones portions of Parcel Maps 3303 and 3304, Portions of Sections 31 and 33, T1S, R3E, SBB&M, san Bernardino County, California, Project Number 1136, 30 p.

Rasmussen, G.S. and Associates, Inc., June 29, 1978, Landslide affecting sewage lift station, south of Apache Trail and Blackfoot Trail West, Rimforest, California, Project Number 1323, 13 p.

Rasmussen, G.S. and Associates, Inc., September 30, 1982, Preliminary engineering geology evaluation of slope instability, John Duckworth residence, Running Springs, California, Project Number 1475.

Reeder, W.A. and Rasmussen, G.S., 1986, Character and Holocene activity of the Mission Creek fault in the vicinity of Desert Hot Springs, Riverside County, California (this volume).

Richter, C.F., 1958, Elementary Seismology: W.H. Freeman and Company, 768 p.

Vaughn, F.E., 1922, Geology of the San Bernardino Mountains north of San Gorgonio Pass: California University Publications in Geological Sciences, v. 13, p. 319-411.

CHARACTER AND HOLOCENE ACTIVITY OF THE MISSION CREEK FAULT IN THE VICINITY OF DESERT HOT SPRINGS, RIVERSIDE COUNTY, CALIFORNIA

Wessly A. Reeder
Gary S. Rasmussen & Associates, Inc.
1811 Commercenter W.
San Bernardino, CA 92408

Gary S. Rasmussen
Gary S. Rasmussen & Associates, Inc.
1811 Commercenter W.
San Bernardino, CA 92408

INTRODUCTION

The Mission Creek fault is a major branch of the San Andreas fault that obliquely traverses a series of coalescing Quaternary alluvial fans through the community of Desert Hot Springs in the Coachella Valley. The near surface trace of the Mission Creek fault is readily apparent as a distinct vegetational lineament, accented by modified fault scarps visible on aerial photographs flown prior to major development of Desert Hot Springs. The Mission Creek fault is generally referred to as the north branch of the San Andreas fault in the Coachella Valley and the Banning fault is referred to as the south branch. The Mission Creek and Banning faults apparently merge southeast of Desert Hot Springs in the Indio Hills.

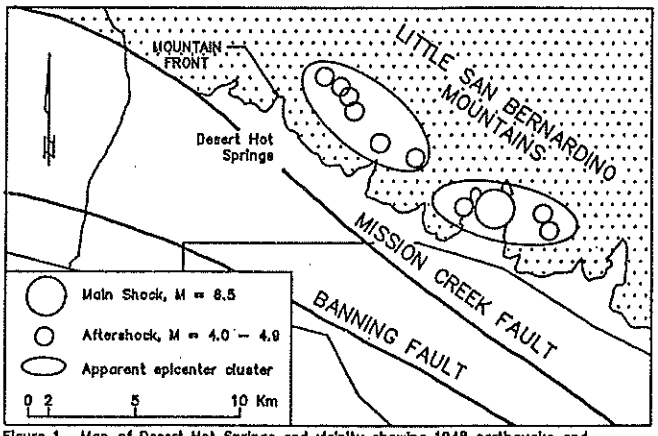

Figure 1. Map of Desert Hot Springs and vicinity showing 1948 earthquake and its aftershocks recorded between Dec. 1, 1948 and Dec. 1, 1957, modified from Richter and others (1958).

1948 DESERT HOT SPRINGS EARTHQUAKE

On December 4, 1948, a moderately large earthquake, estimated at Richter magnitude 6.5, occurred in the foothills of the Little San Bernardino Mountains, just east-southeast of Desert Hot Springs. The epicenter of this earthquake was located approximately 5 kilometers northeast of the Mission Creek fault as mapped by Proctor (1968), Dibblee (1982) and Clark (1984). Following the main shock, numerous aftershocks occurred (up to Richter magnitude 4.9) which continued for a period of approximately 10 years. Nearly all of these aftershocks were also located northeast of the mapped fault trace (Fig. 1). No evidence for any surface fault rupture was observed following the earthquake.

Richter and others (1958, page 332) attribute the apparent "displacement" of epicenters from the mapped fault trace to a northeast dipping fault plane which they calculated could be no steeper than 65 degrees. Based on an analysis of first motion data, they indicate that movement on the Mission Creek fault was oblique, being a combination of thrust slip and right-lateral slip.

A principal reason why Richter and others (1958) assumed that the 1948 earthquake occurred on the Mission Creek fault was the fact that aftershock epicenters were apparently aligned parallel to the trend of the Mission Creek fault. However, a plot of the earthquake epicenters greater than Richter magnitude 4.0 reveals two epicenter clusters: a northwestern cluster located northeast of Desert Hot Springs and a southeastern cluster located east-southeast of Desert Hot Springs. The southeast cluster includes the main shock. The alignment of the northwest cluster of events trends approximately N50°W and the alignment of the southeast cluster trends approximately N75-80°W. The alignments of both of these seismic clusters reflects the general change in trend of the mountain front. The mapped trace of the Mission Creek fault exhibits no corresponding change in strike.

Subsequent to the Richter and others (1958) analysis of the character of the Mission Creek fault, numerous trenching investigations across the Mission Creek fault have been completed in the Desert Hot Springs area in conformance with Alquist-Priolo Special Studies Zone requirements and are on file with the City of Desert Hot Springs and the County of Riverside. Typically, these investigations have revealed high-angle faulting with a relatively consistent strike. Review of trench logs indicates that the main fault is often bounded on the northeast and southwest by lower angle, apparent normal faulting with minor offsets which is often typical of strike-slip faulting as observed in trench walls. No evidence for reverse movement is evident on the trench logs. The Mission Creek fault, as indicated by the numerous trenches across its trace in the vicinity of Desert Hot Springs, seems to be characterized by strike-slip movement with very little reverse or oblique movement. It is structurally unlikely that the Mission Creek fault becomes a lower angle oblique fault at depth without any expression of reverse movement at the surface.

Apparent fault "scarps" occur in the Desert Hot Springs area which suggest a vertical component of movement. However, many of these scarps can be explained by topographically low areas right-laterally displaced along the Mission Creek fault and juxtaposed against topographically high areas. In addition, apparent fault scarps that are coincident with vegetation lineaments are often the result of denudation by both wind and water along the non-vegetated margin and aeolian deposition of sands and silts along the vegetated margin.

Rather than readily assuming that the 1948 Desert Hot Springs earthquake occurred along the Mission Creek fault at depth, it is just as reasonable to assume that it occurred along any one of the many potentially active faults in the foothills of the Little San Bernardino Mountains including the Morongo Reverse fault, Dillion Shear Zone or other related faults. Detailed geologic mapping and evaluation of fault activity is needed to better assess the role that these faults play in the neotectonic setting of the region.

HOLOCENE SEISMICITY

Trench logs documenting numerous subsurface investigations across the Mission Creek fault in the Desert Hot Springs area indicate fault rupture to within a few feet of the ground surface (Rasmussen, August 16, 1977; November 21, 1977; January 30, 1978; January 15, 1979; January 18, 1979; April 17, 1979; September 28, 1984). Most of the upper sediments observed in the trenches were considered to be less than 2,000 years in age, primarily based on surface geomorphology (current depositional environments) and soil development. Although recurrence intervals have not, as yet, been established for the Mission Creek fault in Desert Hot Springs, fault rupture to within a few feet of the ground surface, together with the young geomorphic expression of faulting, suggests that recurrence intervals are probably less than 500 years.

The Mission Creek fault can be observed on early aerial photographs as a semi-continuous lineament through Desert Hot Springs to a point just northwest of Desert Hot Springs. Northwest of this point to the mountain front of the Little San Bernardino Mountains near the mouth of White House Canyon, the Mission Creek fault is mapped as a buried fault trace (Proctor, 1968; Dibblee, 1982).

A recent subsurface investigation across the projection of the lineament did not encounter faulting within 6 meters of the original ground surface (Rasmussen, January 23, 1986). A zone of abundant near vertical, calcium carbonate-filled fractures and possible slight warping of the sediments was observed in the deep trench. This zone occurs along the northwest projection of the aerial photograph lineament. Most of the filled fractures were found to trend parallel to the trend of the Mission Creek fault. The coincidence of increasingly closely spaced, calcium carbonate-filled fractures together with their well defined alignment with the known fault location to the southeast is strong evidence that the buried trace of the Mission Creek fault exists at this location.

The age of the unruptured alluvial materials at a depth of 6 meters was not known with certainty. However, based on weathering of specific clast lithologies, induration, abundance of secondary calcium carbonate and the presence of three buried paleosols, we estimate the age of these materials to be at least 6,000 years and perhaps as old as 9,000 years.

If the state of activity of the Mission Creek fault were uniform along the fault, primary fault rupture should have been encountered, in at least one of the recently excavated trenches northwest of Desert Hot Springs (Rasmussen, January 23, 1986; Leighton, June 29, 1978; Southern California Soil & Testing, December 2, 1985). Due to the fact that the sediments are probably much older than 2,000 years and may be as old as 9,000 years in the deepest trench, the fault should have been obvious. Since fault rupture was not encountered and the surface expression of faulting appears to become less and less distinct northwest of Desert Hot Springs, it appears that Holocene activity along the Mission Creek fault decreases towards the northwest.

A subsurface investigation conducted near the juncture of the Mission Creek and Pinto Mountain fault zones (Rasmussen, August 9, 1977) revealed no evidence of Holocene activity of the Mission Creek fault at that location. This suggests that the Mission Creek fault may be inactive (not having experienced surface fault rupture during Holocene time) northwest of Desert Hot Springs.

The Mission Creek fault exhibits a relatively consistent strike (approximately N45°W) through Desert Hot Springs to White House Canyon. Northwest of White House Canyon the fault is coincident with the mountain front of the Little San Bernardino Mountains and exhibits a different strike, which varies from that to the southeast by approximately 10 degrees.

A bend in the surface trace of the Mission Creek fault apparently occurs in order to accommodate the change in strike, if the fault represents a continuous structure. The change in strike of the Mission Creek fault suggests that at least two distinct fault segments exist in this area. Each segment is probably characterized by a separate fault geometry and separate earthquake history (Rasmussen, 1981).

SUMMARY

Subsurface investigations across the trace of the Mission Creek fault in Desert Hot Springs during the past 10 years suggest that the Mission Creek fault is characterized by strike-slip movement. No evidence of significant reverse movement has been documented. These studies reveal that the Mission Creek fault is relatively steeply inclined at the surface, which is in contrast to the maximum dip of 65° as proposed by Richter and others (1958, page 332). Based on this, we suggest that the 1948 Desert Hot Springs earthquake may not necessarily have occurred on the Mission Creek fault but may have occurred on any one of several, possibly related faults, within the Little San Bernardino Mountains.

The San Andreas fault is characterized along portions of its reach by fault segments which may exhibit different fault geometries and have different earthquake histories (Rasmussen, 1981). Preliminary data suggest that two such segments exist in the Desert Hot Springs area and a third along the Banning fault. The junction or boundary of the two fault segments in the Desert Hot Springs area occurs just northwest of Desert Hot Springs in the vicinity of White House Canyon.

The evidence further suggests that the Mission Creek fault is not an active feature northwest of White House Canyon. The Mission Creek fault northwest of Desert Hot Springs apparently no longer represents the main trace of the San Andreas fault in this region. Its abandonment may have

been the result of left-lateral movement along the Morongo and Pinto Mountain faults and right-lateral movement along the south branch of the San Andreas fault in San Gorgonio Pass (Rasmussen and Reeder, 1986).

REFERENCES CITED

Clark, M.M., 1984, Map showing recently active breaks along the San Andreas fault and associated faults between Salton Sea and Whitewater River-Mission Creek, California: U.S. Geological Survey Miscellaneous Investigations Series, Map I-1483, Scale 1:24,000.

Dibblee, T.W., Jr., 1982, Geologic Map of the Palm Springs (15-minute) Quadrangle, California: South Coast Geological Society, Scale: 1:62,500.

Leighton & Associates, Incorporated, June 29, 1978, Geologic and Seismic Investigation of 160-Acre Parcel (NW 1/4, Section 25, T2S, R4E), Southeast of the Intersection of Mission Lakes Boulevard and Little Morongo Road, Desert Hot Springs, County of Riverside, California, Project No. 678031-02.

Proctor, R.J., 1968, Geology of the Desert Hot Springs, Upper Coachella Valley area, California: California Division of Mines and Geology Special Report 94.

Rasmussen, Gary S., April 1981, San Andreas fault geometry and maximum probable earthquakes in southern California: in Abstracts with programs, Cordilleran Section, Geological Society of America, 77th Annual Meeting, v. 13, no. 2, p. 102.

Rasmussen, Gary S. & Associates, Inc., August 9, 1977, Engineering Geology Investigation, Portions of Parcel Maps 3303 and 3304, Sections 31 and 33, T1S, R3E, San Bernardino County, California, Project No. 1136.

Rasmussen, Gary S. & Associates, Inc., August 16, 1977, Engineerinng Geology Investigation, Lots 14-17, Pierson Boulevard, West of Palm Drive, Desert Hot Springs, California, Project No. 1230.

Rasmussen, Gary S. & Associates, Inc., November 21, 1977, Engineering Geology Investigation, 40-Acre Parcel, NW Corner, 19th Avenue and Palm View, Desert Hot Springs, California, Project No. 1255.

Rasmussen, Gary S. & Associates, Inc., January 30, 1978, Enginneering Geology Investigation, 190-Acre Parcel, Two Bunch Palms, Desert Hot Springs, California, Project No. 1256-2.

Rasmussen, Gary S. & Associates, Inc., January 15, 1979, Subsurface Engineering Geology Investigation, 2 1/2-Acre Site South of Dillon Road and West of Corkhill Road, Desert Hot Springs, California, Project No. 1412-2.

Rasmussen, Gary S. & Associates, Inc., January 18, 1979, Engineering Geology Investigation, 100-Acre Parcel, North of Dillon Road, East of Long Canyon Road, Desert Hot Springs, California, Project No. 1430.

Rasmussen, Gary S. & Associates, Inc., April 17, 1979, Engineering Geology Investigation, 30-Acre Parcel, Dillon Road, 1,341 Feet West of Corkhill Road, Desert Hot Springs, California, Project No. 1473.

Rasmussen, Gary S. & Associates, Inc., September 28, 1984, Engineering Geology Investigation of Lots 1, 2, 48 and 49, Block D, Tract 3, Immediately Southwest of the Intersection of Palm Drive and Acoma Avenue, Desert Hot Springs, California, Project No. 2066.

Rasmussen, Gary S. & Associates, Inc., January 23, 1986, Subsurface Engineering Geology Investigation of Tract 21107, NW 1/4 of Section 25, T2S, R4E, SBB&M, Desert Hot Springs, California, Project No. 2222.1.

Rasmussen, G.S., and Reeder, W.A., 1986, What Happens to the Real San Andreas Fault at Cottonwood Canyon: San Gorgonio Pass, California? (This Volume).

Richter, C.F., Allen, C.R., and Nordquist, J.M., 1958, The Desert Hot Springs earthquakes and their tectonic environment: Seismological Society of America Bulletin, v. 48, p. 315-337.

Southern California Soil & Testing, Incorporated, December 2, 1985, Report of Alquist-Priolo Geotechnical Study for Tract 21107, Northwest 1/4, Section 25, T2S, R4E, SBB&M, Riverside County, California, Project No. 8531095, Report No. 2.

Complexities of the San Andreas fault near San Gorgonio Pass: Implications for large earthquakes

Doug Yule[1] and Kerry Sieh

Seismological Laboratory, California Institute of Technology, Pasadena, California, USA

Received 13 February 2001; revised 30 December 2002; accepted 27 February 2003; published 29 November 2003.

[1] Geologic relationships and patterns of crustal seismicity constrain the three-dimensional geometry of the active portions of San Andreas fault zone near San Gorgonio Pass, southern California. Within a 20-km-wide contractional stepover between two segments of the fault zone, the San Bernardino and Coachella Valley segments, folds, and dextral-reverse and dextral-normal faults form an east-west belt of active structures. The dominant active structure within the stepover is the San Gorgonio Pass-Garnet Hill faults, a dextral-reverse fault system that dips moderately northward. Within the hanging wall block of the San Gorgonio Pass-Garnet Hill fault system are subsidiary active dextral and dextral-normal faults. These faults relate in complex but understandable ways to the strike-slip faults that bound the stepover. The pattern of crustal seismicity beneath these structures includes a 5–8 km high east-west striking step in the base of crustal seismicity, which corresponds to the downdip limit of rupture of the 1986 North Palm Springs earthquake. We infer that this step has been produced by slip on the linked San Gorgonio Pass-Garnet Hill-Coachella Valley Banning (SGP-GH-CVB) fault. This association enables us to construct a structure contour map of the fault plane. The large step in the base of seismicity downdip from the SGP-GH-CVB fault system probably reflects a several kilometers offset of the midcrustal brittle-plastic transition. (U/Th)/He thermochronometry supports our interpretation that this south-under-north thickening of the crust has created the region's 3 km of topographic relief. We conclude that future large earthquakes generated along the San Andreas fault in this region will have a multiplicity of mostly specifiable sources having dimensions of 1–20 km. Two tasks in seismic hazard evaluation may now be attempted with greater confidence: first, the construction of synthetic seismograms that make useful predictions of ground shaking, and second, theoretical investigations of the role of this complexity in retarding the propagation of future seismic ruptures. *INDEX TERMS:* 8102 Tectonophysics: Continental contractional orogenic belts; 8105 Tectonophysics: Continental margins and sedimentary basins (1212); 8107 Tectonophysics: Continental neotectonics; 8110 Tectonophysics: Continental tectonics—general (0905); 8115 Tectonophysics: Core processes (1507); 8124 Tectonophysics: Earth's interior—composition and state (1212); *KEYWORDS:* San Andreas fault zone, San Gorgonio Pass, neotectonics, three-dimensional fault geometry, transpression, fault interaction

Citation: Yule, D., and K. Sieh, Complexities of the San Andreas fault near San Gorgonio Pass: Implications for large earthquakes, *J. Geophys. Res.*, *108*(B11), 2548, doi:10.1029/2001JB000451, 2003.

1. Introduction

[2] Discontinuities of crustal dimension are rare along the 1100-km length of the San Andreas fault (Figure 1, inset). This scarcity of large structural irregularities may, in fact, encourage lengthy seismic ruptures like the 360- and 420-km-long events of 1857 and 1906 [*Sieh*, 1978], since geometrical complexities appear to play a critical role in impeding rupture propagation [for example, *Barka and Kadinsky-Cade*, 1988; *Harris and Day*, 1993; *Wesnousky and Jones*, 1994; *Rice and Ben-Zion*, 1996; *Sieh and Natawidjaja*, 2000]. The largest irregularity in the San Andreas fault occurs in southern California, in the vicinity of San Gorgonio Pass (Figure 1). Here at a contractional left step [*Matti et al.*, 1985, 1992a; *Matti and Morton*, 1993], the surface trace of the San Andreas fault disaggregates into a family of irregular and discontinuous faults [*Allen*, 1957; *Dibblee*, 1968, 1982; *Hill*, 1982; *Matti et al.*, 1985, 1992a; *Matti and Morton*, 1993].

[3] The exceptional complexity of the San Andreas fault zone in the region of San Gorgonio Pass, southern California, presents a formidable challenge to forecasting the source characteristics of future earthquakes there. Recent earthquakes in structurally complex regions provide two general insights, however. First, the nearly synchronous failure of several faults can lead to unusually complex earthquakes. The complex Spitak, Armenia, earthquake of

[1]Now at Department of Geological Sciences, California State University, Northridge, California, USA.

Copyright 2003 by the American Geophysical Union.
0148-0227/03/2001JB000451$09.00

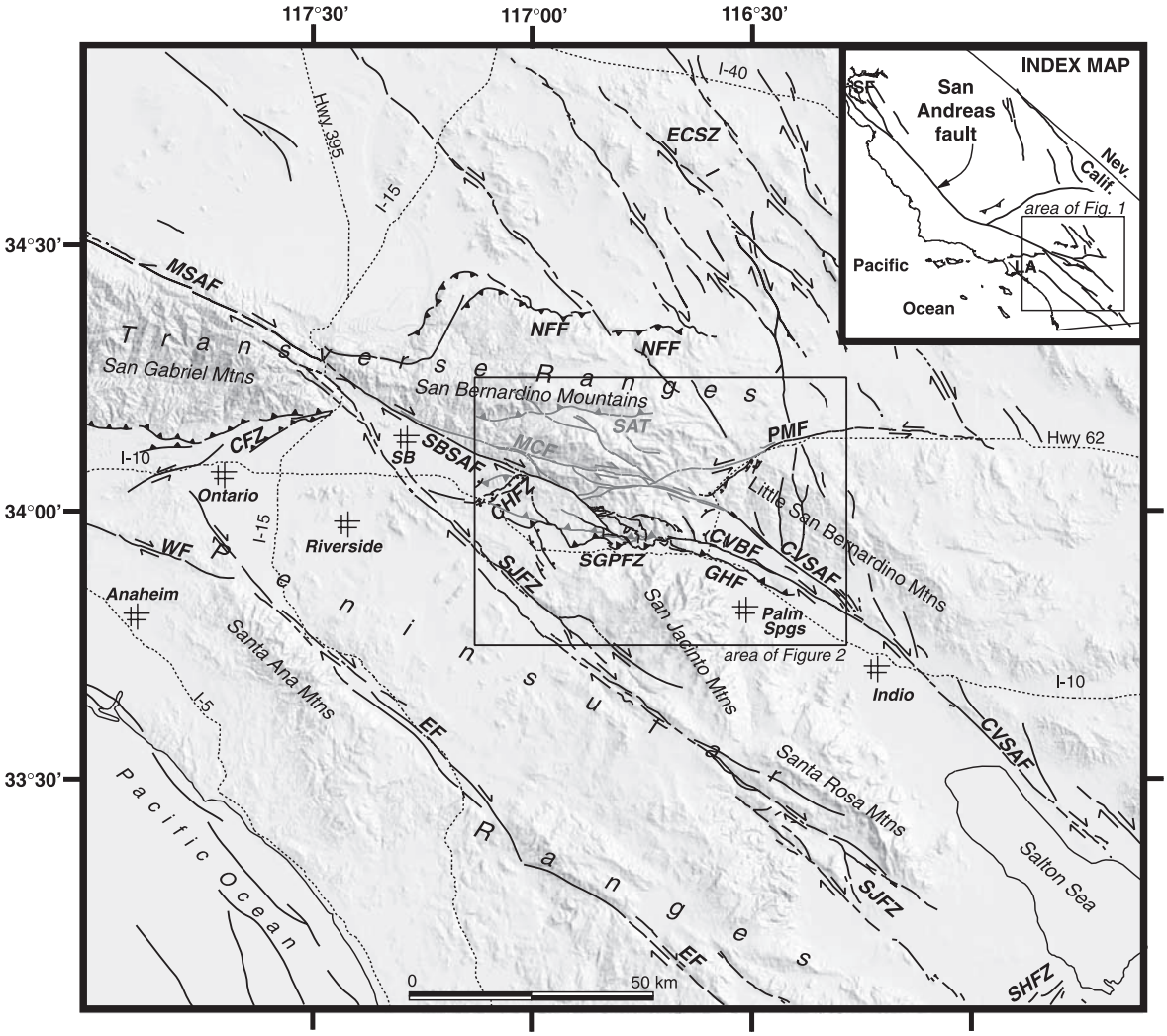

Figure 1. Shaded topographic relief map of the eastern Transverse Ranges and northern Peninsular Ranges, southern California, showing Holocene faults in black. Late Pleistocene faults in the vicinity of San Gorgonio Pass, considered inactive, in gray. Abbreviations: CFZ, Cucamonga fault zone; CHFZ, Crafton Hills fault zone; CVBF, Coachella Valley segment Banning fault; CVSAF, Coachella Valley segment, San Andreas fault; EF, Elsinore fault; ECSZ, eastern California shear zone; GHF, Garnet Hill fault; MCF, Mill Creek fault; MSAF, Mojave segment, San Andreas fault; NFF, north frontal fault; PMF, Pinto Mountain fault; SAT, Santa Ana thrust; SBSAF, San Bernardino strand, San Andreas fault; SGPFZ, San Gorgonio Pass fault zone; SHFZ, Superstition Hills fault zone; SJFZ, San Jacinto fault zone; and WF, Whittier fault; SB, San Bernardino; LA, Los Angeles; SF, San Francisco.

1988, for example, was caused by sequential rupture of adjacent strike-slip, thrust, and blind thrust faults [*Cisternas et al.*, 1989]. The complicated Landers, California, earthquake of 1992 was also produced by sequential rupture of several strike-slip faults [*Sieh et al.*, 1993; *Wald and Heaton*, 1994]. Second, relatively simple faults within structurally complex regions may be unrecognized prior to failure in destructive earthquakes. The source of the 1989 *M*7.1 Loma Prieta earthquake, for example, was a simple but hidden, moderately dipping, dextral-reverse fault beneath a large contractional jog in the San Andreas fault in the southern San Francisco Bay region [*Lisowski et al.*, 1990; *Marshall et al.*, 1991; *Anderson*, 1994]. Likewise, the dip and dextral-reverse sense of slip on a portion of the San Andreas fault zone north of Palm Springs was underappreciated until the occurrence of a moderate earthquake in 1986 [*Hartzell*, 1989; *Jones et al.*, 1986].

[4] Some basis exists therefore for speculation that past and future ruptures of the San Andreas fault through the San Gorgonio Pass region have been and will be complex and surprising. In addition, some have speculated that the structural complexity will impede or terminate rupture [for example, *Sykes and Seeber*, 1985].

[5] But beyond these broad, general expectations, what can we say about the past and future behavior of the fault zone? In this paper, we attempt to gain a more specific understanding of the San Andreas fault's seismic potential through new geologic mapping and a kinematic analysis of the active

structures. We integrate these data with upper crustal seismicity [*Jones et al.*, 1986; *Seeber and Armbruster*, 1995; *Magistrale and Sanders*, 1996] and present a plausible three-dimensional configuration of the brittle crust through the San Gorgonio Pass stepover. Our model, modified from that of *Matti et al.* [1985, 1992a] and *Matti and Morton* [1993], depicts the San Gorgonio Pass region as a south-under-north restraining ''bend'' in the San Andreas fault zone, with dextral-oblique strain broadly distributed on a family of faults and folds. This integrated view of the available geologic and geophysical data provides a basis for our construction of realistic seismic source models.

2. Overview of Active Structures

[6] *Vaughan* [1922] first showed the general distribution of rock units in the area, but did not recognize that many of the contacts are faults. *Noble* [1926, 1932] observed that the San Andreas splays into several branches in this region. *Allen* [1957] mapped most of the important faults and added critical details about sedimentary history. Particularly important were his recognition of the Banning fault and demonstration of its dextral-reverse character. *Matti et al.* [1985, 1992a] and *Matti and Morton* [1993] produced synoptic maps of active structures within the region and emphasized the significance of the contractional left stepover in the San Andreas fault and the major role currently being played by the active dextral-reverse San Gorgonio Pass fault (SGPF) system.

[7] We have modified the earlier mapping of the stepover region, paying particular attention to determination of which structures are active and which are not. Active structures possess one or more of the following characteristics: fault scarps in Holocene alluvium or steep scarps in older units, deflected drainages, offset ridgelines, and deformed late Quaternary surfaces. Inactive structures do not meet any or most of these criteria. By these criteria, we find that some faults have both active and inactive segments. Except where noted, we adopt the nomenclature of *Matti et al.* [1985, 1992a] and *Matti and Morton* [1993] for the primary faults and of *Allen* [1957] for the secondary structures.

[8] Figure 2 provides a synoptic view of the active structures that comprise the San Gorgonio Pass stepover region, superimposed on topography. We define the San Gorgonio Pass stepover as a 20-km-wide left stepover between the right-lateral strike-slip San Bernardino and Coachella Valley strands of the San Andreas fault (Figure 2). Other faults in the region act to transfer slip across the stepover. The right-oblique, San Gorgonio Pass thrust and Garnet Hill reverse faults bound the stepover on the south; the SGPF system extends westward beyond the stepover (Figure 2a). A system of right-oblique normal faults dominates the active structures within the hanging wall block of the stepover. Active local and regional scale folds are also important within the region (Figure 2b). Slip transfer in the stepover region is addressed in later sections. Below, we describe in general each of these active folds and fault zones by class, and then focus in detail on two small areas to illustrate the nature of the structures more fully.

2.1. Bounding Right-Lateral Strike-Slip Faults

[9] The ''San Bernardino strand, San Andreas fault'' bounds the San Gorgonio stepover on the west. Northwest of the stepover region, near Yucaipa (Figure 2a), it displays clear geomorphic and stratigraphic evidence of recent strike-slip movement [for example, see *Harden and Matti*, 1989]. Here (U-Th)/He thermochronometry appears to show that the fault's steep SSW-facing escarpment (Figure 2a) formed about 1.5 Ma ago [*Spotila et al.*, 1998]. Both large and small landforms diminish in their geomorphic expression southeastward from Yucaipa, along the western flank of the stepover. At San Gorgonio Canyon the fault experiences a pronounced southward bend, breaks into discontinuous right-stepping segments, and may die out southeast of Burro Flats [*Matti et al.*, 1985, 1992a; *Matti and Morton*, 1993] where its geomorphic expression is obscure (Figures 2a and 3a). However, subtle pressure ridges and hanging valleys along the southwest edge of Potrero Canyon suggest that the fault continues and merges with the Gandy Ranch fault (Figures 2a and 3a). The broadly linear trace of the fault between San Gorgonio and Potrero Canyons suggests that its dip is steep, but surface exposures are poor, so this has not been verified by direct measurement. A recent excavation at Burro Flats does, however, show the fault dipping 75° southwest [*Yule et al.*, 2001].

[10] The ''Coachella Valley segments of the Banning (CVB) and San Andreas (CVSA) faults'' diverge from one another and bend toward the west as they approach the San Gorgonio Pass stepover from the southeast. The active trace of the CVB fault merges with the SGPF at Cottonwood Canyon, and the active trace of the CVSA fault appears to end at Hwy 62 [*Matti et al.*, 1985, 1992a, Figure 2a]. The CVSA fault bifurcates into the Mill Creek and Mission Creek faults northwest of Hwy 62, but evidence for Holocene offset on these structures is equivocal. Farther to the southeast the CVSA faults exhibit clear Holocene scarps, laterally offset landforms, deformed adjacent young alluvial surfaces, and vegetation alignments [*Allen*, 1957; *Keller et al.*, 1982; *Clark*, 1984], and the CVB displays these features all the way into San Gorgonio Pass.

2.2. Right-Oblique Contractional Structures

[11] Right-oblique contractional structures skirt the southern boundary of the San Gorgonio Pass stepover. These constitute the San Gorgonio Pass and Garnet Hill faults (Figures 2a and 3).

[12] The ''San Gorgonio Pass fault'' exhibits an irregular sawtooth shape. Generally, east to northeast-trending thrust faults alternate with northwest-trending tears [*Matti et al.*, 1985, 1992a; *Matti and Morton*, 1993] (Figures 2a and 3a). West of Deep Canyon (Figure 3a), the fault trace is well defined by small scarps in late Holocene alluvium. Three lobes of deformed Pleistocene alluvium east of Deep Canyon indicate that the underlying fault has a scalloped geometry (Figure 3a). But the amplitude of the scalloping is uncertain, due to erosion or burial of the fault trace in the two large intervening canyons. Scarps in late Holocene alluvium occur only very locally, principally in locations that are sheltered from the rapid deposition and erosion that occurs at the mouths of major canyons.

[13] Traces of the ''Banning fault'' appear to be inactive along most of the fault's length, with the exception of one segment at Millard Canyon (Figure 3). A scarp in late Holocene alluvium across the valley floor and offset of late Quaternary fluvial gravels demonstrate its activity there. But

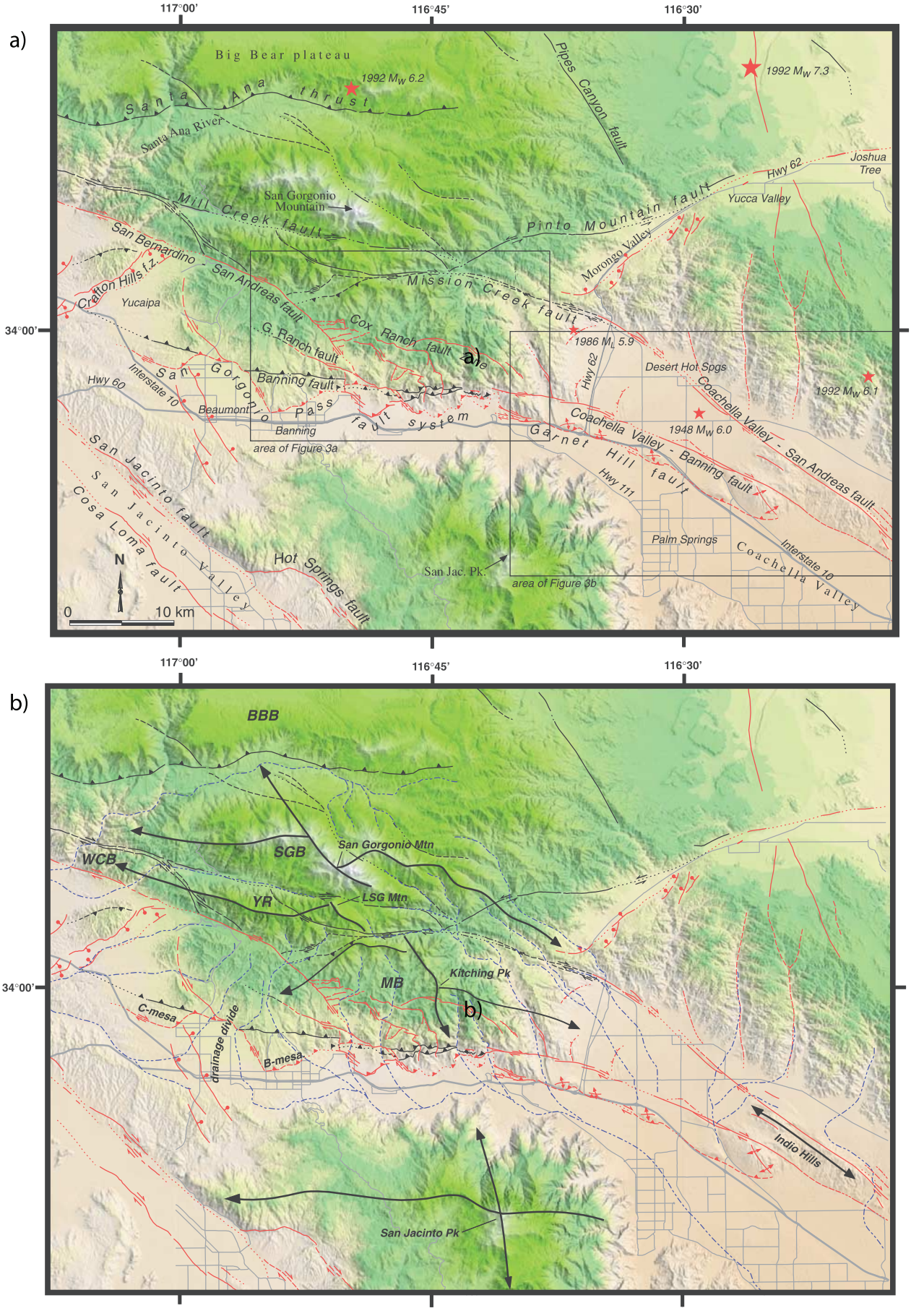
a)
117°00'
116°45'
116°30'
34°00'
Big Bear plateau
Santa Ana thrust
1992 Mw 6.2
1992 Mw 7.3
Santa Ana River
Pipes Canyon fault
Joshua Tree
Hwy 62
Yucca Valley
San Gorgonio Mountain
Mill Creek fault
Pinto Mountain fault
Morongo Valley
San Bernardino - San Andreas fault
Crafton Hills fz.
Yucaipa
Mission Creek fault
Cox Ranch fault
G. Ranch fault
1986 ML 5.9
Desert Hot Spgs
Hwy 60
Interstate 10
San Gorgonio Pass fault system
Banning fault
Beaumont
Banning
area of Figure 3a
Coachella Valley - San Andreas fault
1948 Mw 6.0
1992 Mw 6.1
Garnet Hill fault
Hwy 111
Coachella Valley - Banning fault
San Jacinto fault
San Jacinto Valley
Cosa Loma fault
Palm Springs
Interstate 10
Coachella Valley
Hot Springs fault
San Jac. Pk.
area of Figure 3b
N
0
10 km
b)
BBB
SGB
WCB
YR
San Gorgonio Mtn
LSG Mtn
MB
Kitching Pk
C-mesa
drainage divide
B-mesa
Indio Hills
San Jacinto Pk

the absence of geomorphic or stratigraphic evidence of young offsets in the next canyon to the east (Deep Canyon) suggests that slip transfers to another structure between Millard and Deep Canyons.

[14] The active portion of the "Gandy Ranch fault" is marked by up-on-the-north, west-northwest trending scarps in young alluvium at the mouth of Potrero Canyon (Figure 3). The fault also places crystalline rocks over late Quaternary gravels between Potrero and Millard Canyons. The Gandy Ranch fault appears to merge with the active segment of the Banning fault.

[15] The "Garnet Hill fault" consists of a series of left-stepping, northwest-trending right-lateral faults with active folds at each stepover. Amplitudes and axial trends define two types of folds. Those at the eastern and western ends of the fault, marked by Edom Hill and West Whitewater Hill, show about 400 m of relief and north- to northwest-trending axes (Figure 3b). These larger folds at the end of the fault are manifestations of the transfer of slip from the Coachella Valley strand of the Banning fault onto the Garnet Hill fault. Folds at stepovers along the fault, marked by Garnet Hill, "Hugo" Hill, and East Whitewater Hill are much smaller. They show only 30–200 m of relief and east-trending axes. These smaller folds result from contractional, en echelon stepovers in the fault trace. The discontinuous geometry of the Garnet Hill fault and the small size of these folds suggest that cumulative slip is too low to have led yet to integration of the fault into a single strand.

2.3. Right-Oblique Normal Faults

[16] *Allen* [1957] applied the name "Cox Ranch fault" to a 10-km fault segment cutting crystalline basement rocks to the north of the SGPF (Figures 2a and 3a). We group this fault with a series of similar, unnamed faults mapped by *Allen* [1957] and by ourselves, and refer to them as the "Cox Ranch fault zone." These arcuate structures strike predominantly west-northwest to east-west with the exception of a few short north-south striking faults. They offset ridgelines and show faceted surfaces and slickensides, but do not show obvious scarps where they cross Holocene alluvium. This is an indication that rates of slip on these structures are small, relative to the other structures in the region.

[17] These structures show variable orientations and offsets. For example, the Cox Ranch fault and a subparallel set of discontinuous faults to the south and southwest show dextral-normal ridgeline offsets (Figures 3a and 4). In contrast, faults in and near Burro Flats comprise an asymmetric, intramontane graben with both down-to-the-north and down-to-the-south, primarily dip-slip displacements (Figures 3a and 5). North-trending faults about a kilometer east of Millard Canyon define another intramontane graben (Figure 3a). Estimates of displacement across individual faults, based on offset ridges, range from tens of meters to 250 m of dextral offset and tens of meters to 100 meters of vertical offset. Cumulative offset across the Cox Ranch fault system, since inception of the current topography, equals 250–500 m of dextral offset and 150–250 m of normal (down-to-the-south) offset.

2.4. Normal Faults

[18] A series of discontinuous and overlapping, northeast-trending scarps with down-to-the-northwest displacement bound the southeastern margin of the Morongo Valley [*Matti et al.*, 1985, 1992a] (Figure 2a). Quaternary displacement on the "Morongo Valley fault" has therefore produced an intermontane valley that separates the San Bernardino and Little San Bernardino Mountains. In the northwestern Coachella Valley, similar northeast-trending late Quaternary scarps occur between the Coachella Valley segments of the San Andreas and Banning faults (Figure 3b). These scarps show northwest-down or northwest-up displacement, consistent with northwest-directed transtension in the greater Coachella Valley region [*Matti and Morton*, 1993].

3. Selected Details of Active Structures

[19] Having completed an overview of the active structures of the San Gorgonio Pass region, we will now focus on two localities where the geologic relationships are particularly illustrative of active neotectonic deformation. First, we consider young deformation near the mouth of Millard Canyon (Figure 3a). The relationship between thrust segments and lateral tears of the SGPF zone in this area is particularly important. Also, our mapping places important constraints on the relationship of the SGP fault zone to the dextral-slip faults that form the western edge of the San Gorgonio Pass stepover. Next, we examine young deformation near the mouths of Cottonwood and Whitewater Canyons (Figure 3a). Here also the relationship between strike-slip faults and thrust faults is particularly interesting and relevant.

3.1. Millard Canyon

[20] Figure 6 is a geologic map of the region around the mouth of Millard Canyon. Active faults (Holocene) appear in

Figure 2. (opposite) Synoptic view of the structures of the San Gorgonio Pass region (modified from *Matti et al.*, 1985, 1992a, 1992b and *Matti and Morton*, 1993), superimposed on topography. Both the Holocene (red) and late Pleistocene (black) structures between San Gorgonio and San Jacinto peaks show important relationships to the landforms of the San Bernardino Mountains. (a) Red stars indicate epicenters of significant earthquakes. Boxes show areas covered by Figures 3a and 3b. (b) Heavy dark lines with arrows marking large drainage divide approximate broad, regional flexures associated with crustal shortening at and near the stepover. Arrows point in direction of plunge. Dashed blue lines are streams and rivers that drain the south flank of the San Bernardino Mountains. Note that streams are deflected to the west and east of the central topographic highs, specifically San Gorgonio Mountain, Little San Gorgonio Mountain (LSG Mtn), and Kitching Peak. Streams draining the southwest flank of the Little San Bernardino Mountains are deflected to the northwest and southeast around the Indio Hills. Crustal blocks include: BBB, Big Bear block; SGB, San Gorgonio block; YR, Yucaipa Ridge; WCB, Wilson Creek block; and MB, Morongo block. Beaumont mesa (B-mesa) and Calimesa (C-mesa) are back-tilted late Pleistocene alluvial surfaces in the hanging wall of the SGPF system. Topographic base is shaded relief of a composite DEM image (10-m resolution) constructed from USGS 7.5′ quadrangle maps.

red and inactive faults (non-Holocene) appear in black. The principal "inactive" structures are strands of the east-west trending Banning fault. East of Millard Canyon, the northern strand places Cretaceous to pre-Cambrian crystalline rocks over Plio-Pleistocene sediments. The southern strands position Pliocene (Painted Hill and Hathaway Formations) sediments over late Pleistocene alluvial sands and gravels (Cabezon Formation). These traces merge into a solitary trace west of Millard Canyon. Although the black strands of the Banning fault were active after deposition of late Pleistocene

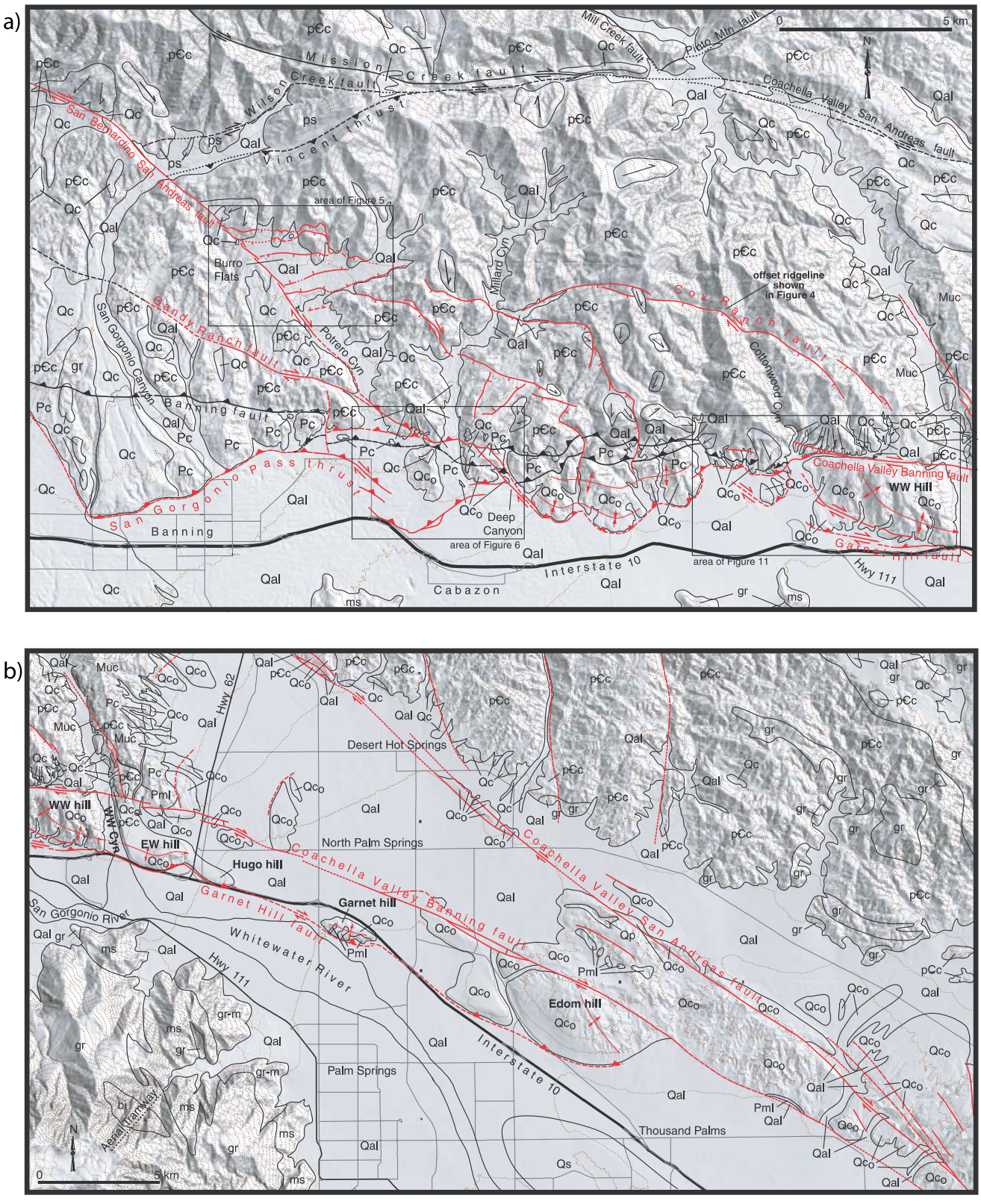

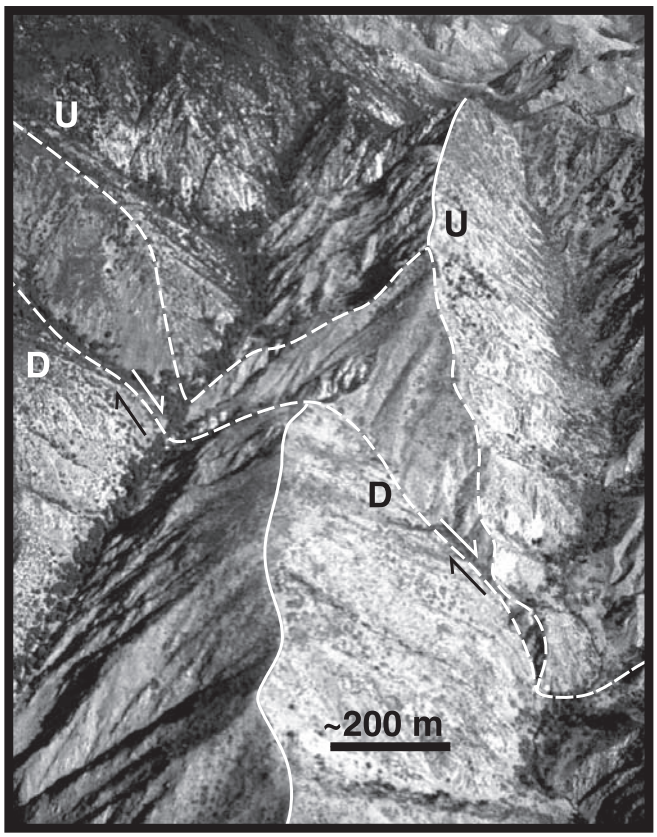

Figure 4. Oblique aerial view of scarp at an offset ridgeline along the Cox Ranch fault. Arrows indicate displacement. Up and downthrown sides are designated by U and D, respectively. View is northward from the ridgeline divide between Cottonwood and Stubbe Canyons. Trace of ridgeline shows ~200 m of dextral separation and ~100 m of vertical separation. See Figure 3a for location.

alluvial sands and gravels, an utter lack of geomorphic expression demonstrates that these strands are not currently active.

3.1.1. Banning Fault

[21] A 3-km-long segment of the northern strand of the Banning fault is, however, currently active at Millard Canyon (red portion in Figure 6). This section of the fault displays a 5-m-high scarp in Qf_3 (Qf, faulted alluvium; Qu, unfaulted alluvium), and a 2.5-m-high scarp in Qf_2 (Figure 7). Radiocarbon analysis of detrital charcoal within Qf_{1-2} indicates that it was deposited between about 2850 and 3600 radiocarbon years BP [J. C. Tinsley and J. C. Matti, in *Matti et al.*, 1992a, p. 26]. The base of the terrace riser that separates these two fluvial surfaces appears to be offset right-laterally about 4.5 m (Figure 8). Thus the dextral component of offset across the fault (1.3–1.6 mm/yr) appears to be about 80% greater than the vertical component (0.7–0.9 mm/yr).

[22] This active portion of the Banning fault also offsets the late Pleistocene heights fanglomerate several hundred meters. On the eastern wall of the canyon, the fault trace rises from the canyon floor at a dip of about 45° and juxtaposes crystalline rocks over the fanglomerate (Figures 6 and 9). Halfway up the canyon wall, the fault rolls over to a nearly horizontal dip and rides over the surface of the Heights fanglomerate.

[23] The age of this fluvial deposit (Qh) of Millard Canyon is poorly constrained. A deep reddish orange, clayey soil more than a meter thick atop the unit suggests that it is older than about 10^5 years, and the excellent preservation of remnants of its depositional surface suggests that it must be much less than 10^6 years old. Just east of the eastern wall of Millard Canyon, the Heights fanglomerate is plastered against an older eastern wall of the canyon, and this buttress unconformity is offset obliquely (Figure 6, inset). The base of the Heights buttress unconformity is exposed in six outcrops north of the fault and in two outcrops south of the fault. These allow us to constrain post-Heights offset of the Banning fault. Vertical offset is 140 ± 15 m, and dextral offset is 375 ± 75 m. The ratio of horizontal and vertical offset derived from these data is somewhat greater than that derived from the younger scarp on the valley floor. Nonetheless, both observations show that strike-slip offset exceeds dip-slip offset on this active section of the Banning fault. The post-Heights slip vector is about 480 m directed S59°E, nearly parallel to the strike of the San Bernardino strand of the San Andreas fault (Figure 2). Assuming an oldest plausible age of 100,000 years for the Heights surface, this strand of the fault zone accommodates a minimum of about 5 mm/yr of the

Figure 3. (opposite) Generalized geologic maps of (a) the central San Gorgonio Pass region and (b) the northern Coachella Valley superposed on topography. Late Pleistocene structural features, considered inactive, are black. Holocene structural features are red and include right-lateral, reverse, and normal-dextral faults (arrows, teeth, and ticks, respectively; teeth and ticks are in hanging wall of thrust and normal faults, respectively), and folds (hinge line, perpendicular arrows points in dip direction of limbs; parallel arrow points in plunge direction of fold). Rock units: Qal, Holocene alluvium; Qc, early Holocene and late Pleistocene alluvium, typically uplifted, back-tilted, and/or highly dissected; Qc_0, moderately deformed Late Pleistocene alluvium, including but not limited to the Cabezon Formation; Pc, strongly deformed Pliocene nonmarine deposits; Pml, lower Pliocene marine deposits of the Imperial Formation, exposed east of Whitewater Cyn; Muc, upper Miocene nonmarine deposits; gr, Mesozoic granitic rocks; bi, basic intrusive rock; ms, metasedimentary rocks; gr-m, granitic migmatite; pCc, undivided Cretaceous to pre-Cambrian igneous and metamorphic complex. Boxes show areas covered by Figures 5, 6, and 11. Contour interval = 100 m. Topographic base is shaded relief of a composite DEM (10-m resolution) constructed from USGS 7.5′ quadrangle maps [geology modified from *Allen*, 1957; *Dibblee*, 1964; 1970; *Matti et al.*, 1985, 1992a, 1992b; *Matti and Morton*, 1993, and J. C. Matti and D. M. Morton, 1991, unpublished mapping, Cabazon and Whitewater 7.5′ quadrangles].

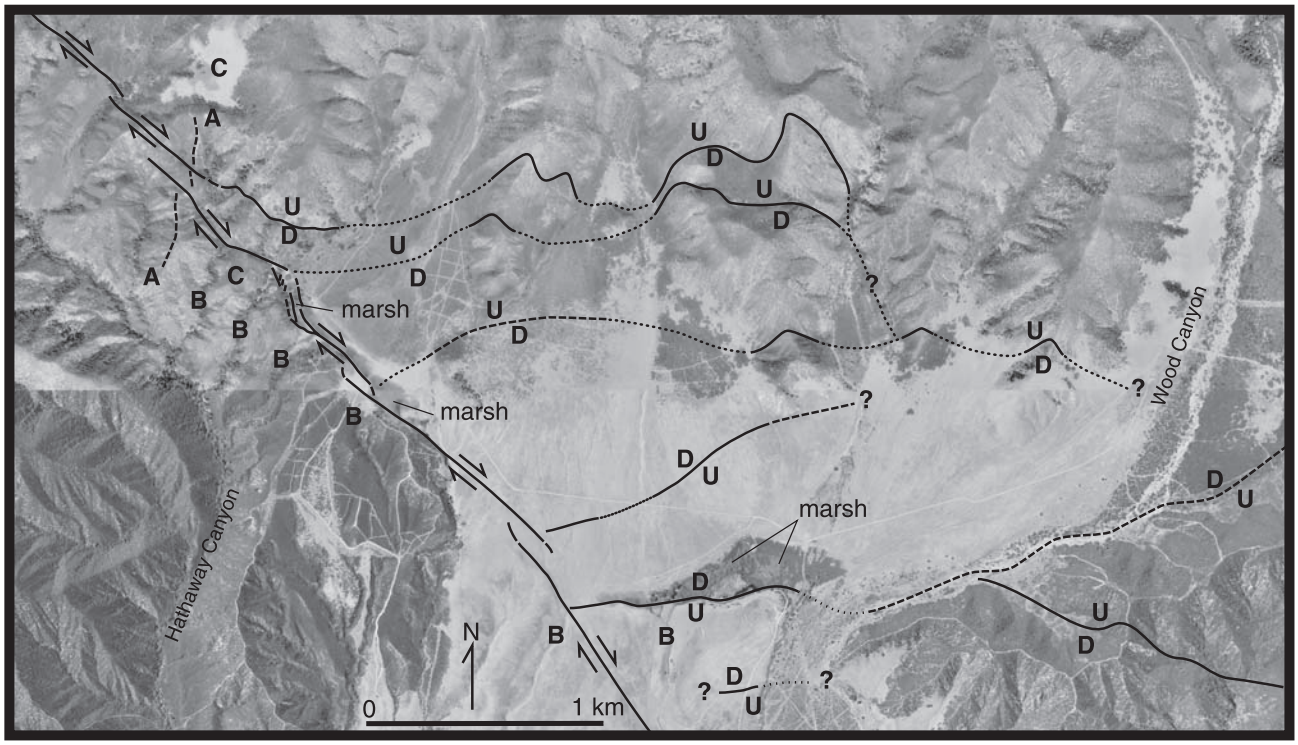

Figure 5. Orthophoto mosaic of the Burro Flats region showing the geomorphic expression of active structural features (see Figure 3a for location). The San Bernardino strand of the San Andreas fault crosses from upper left to middle bottom in a series of right-stepping segments. Marshes occur at some stepovers. Geomorphic features of the fault include A, a right-lateral offset ridgeline; B, beheaded stream channels; and C, uplifted and faulted alluvial surfaces (Qc of Figure 3a). The E-W striking fault segments are both down- and up-to-the-south strands of the western end of the Cox Ranch fault system and have produced the intermontane valley of Burro Flats. North- and south-facing scarps are locally preserved in Holocene alluvium. South-facing faceted slopes in crystalline bedrock characterize the northern strands. One of the southern strands acts as a barrier to groundwater forming the large marsh in the lower center of the photograph.

21–28 mm/yr [*Weldon and Sieh*, 1985] or of the 12–16 mm/yr [*Harden and Matti*, 1989] (0–90 ka best estimate) of dextral slip rate across the SAF zone near Cajon Pass and Yucaipa, 75 and 25 km to the northwest, respectively.

[24] Youthful offsets of the Heights fanglomerate are absent immediately east and west of this active segment of the Banning fault. To the east, slip may transfer off the Banning fault and onto faults at the mountain front via northwest-striking active faults. The total offset on these structures must, however, be no more than a few hundred meters, because separations of traces of the inactive Banning fault and on the axis of an anticline in the Pliocene Hathaway Fm are of this order (Figure 6). Northwest of Millard Canyon, slip appears to transfer off the Banning fault and onto the Gandy Ranch fault at a small right stepover where the two faults overlap between Millard and Potrero Canyons (Figures 3a and 6). Similarly, diminishing northwestward expression of the Gandy Ranch fault coupled with increasing northwestward expression of the San Bernardino strand of the San Andreas fault suggests that slip is transferred at a 2-km-wide right stepover between Potrero and San Gorgonio Canyons (Figure 3a). This right-stepping pattern can therefore explain how slip is transferred, via the Gandy Ranch and Banning faults, between the San Bernardino strand of the San Andreas fault and the SGPF zone (see below).

3.1.2. San Gorogonio Pass Fault Zone

[25] The SGPF zone forms a prominent northeast-trending scarp across the alluvial fan of Millard Canyon. Across Qf_1 the scarp is about 1.5-m high (Figure 10). In the western wall of the modern arroyo, the fault is well exposed in Qf_1 gravel and sand. Here it is a thrust fault zone that dips 24° northward in alluvial sand and gravel. The match of sand and gravel layers across the fault planes demonstrates that slip on the fault zone is nearly pure dip slip. Using the radiocarbon age of detrital charcoal contained within Qf_{1-2}, 2850–3600 radiocarbon years BP [J. C. Tinsley and J. C. Matti in *Matti et al.*, 1992a, p. 26], yields a minimum slip rate of 1.0–1.3 mm/yr and a horizontal contraction rate of about 0.9–1.2 mm/yr.

[26] The Qf_3 surface of Millard Canyon displays a scarp of about 3 m across the SGPF (Figure 10). Its age, however, is not well constrained. An older surface (Qf_4 on Figures 6 and 10) is offset about 12.5 m. This scarp must be a monoclinal flexure, rather than a fault scarp, because a small fluvial terrace riser traverses the scarp from the hanging wall block to the footwall block (hachured line in Qf_4 in Figure 6). The age

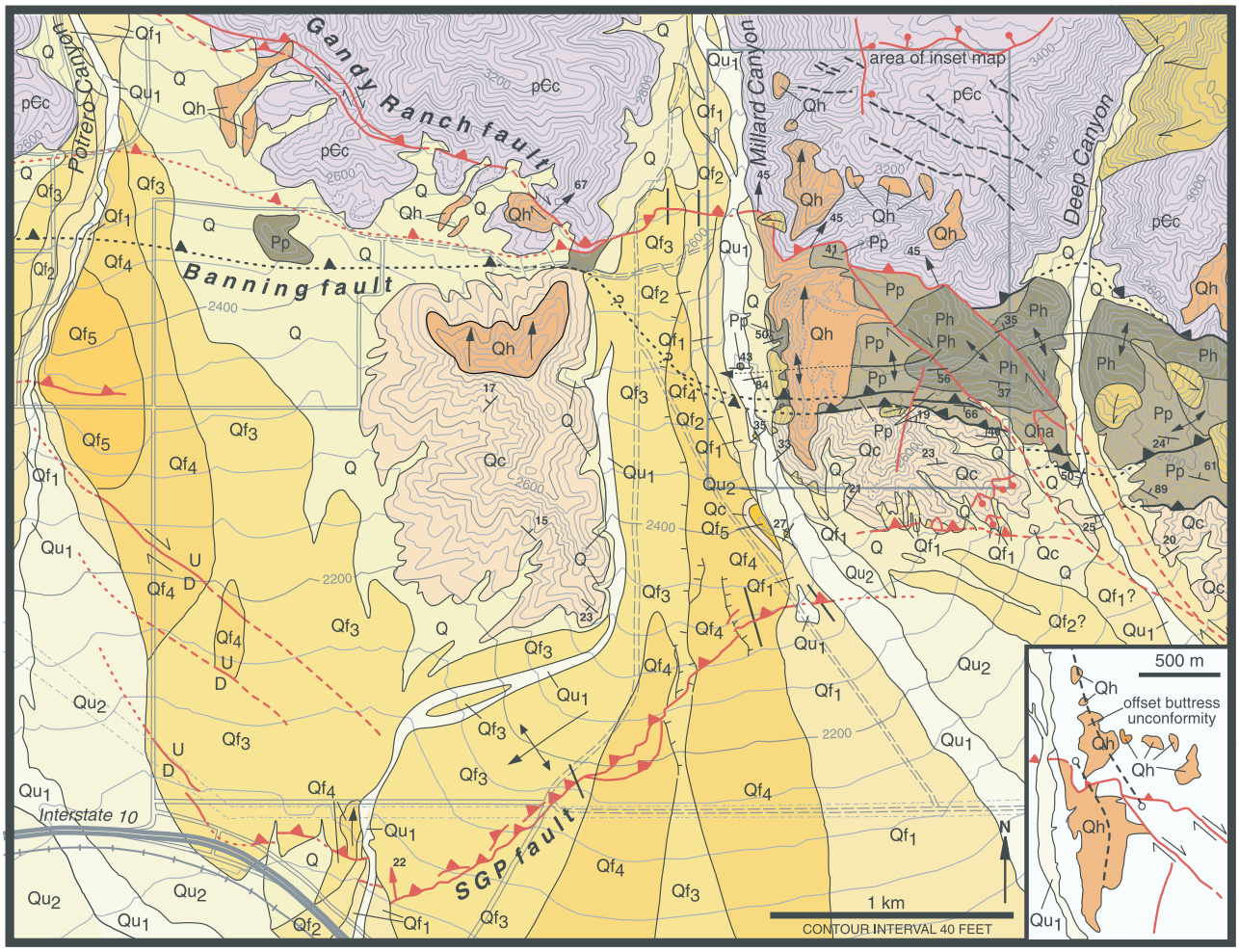

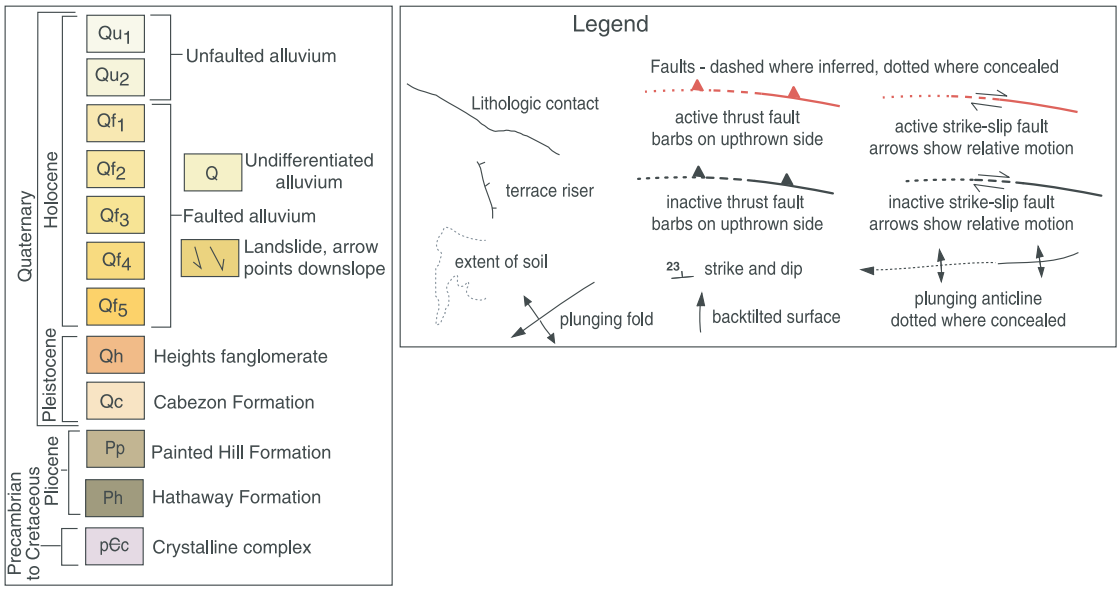

Figure 6. Geologic map of the Millard Canyon area (See Figure 3a for location). The San Gorgonio Pass and Banning fault zones consist of multiple, subparallel fault strands, some clearly active and others probably inactive. Scarps in Holocene alluvium are the clearest evidence for activity. Faults without preserved Holocene scarps or geomorphic evidence of recent slip are considered inactive. The San Bernardino strand, San Andreas fault merges with the SGPF zone just east of Millard Canyon. Black lines across the scarps in Millard Canyon represent surveyed profiles shown in Figures 7 and 10. The offset terrace riser, depicted on Figure 8, was surveyed between the two lines of profile shown across the northern scarp.

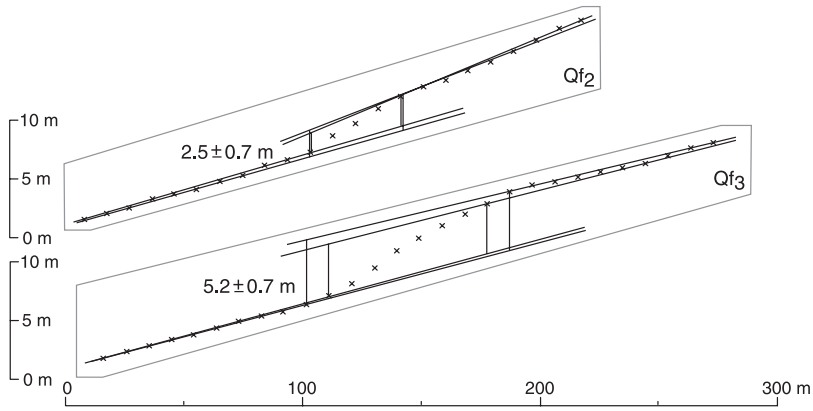

Figure 7. Cross-sectional view of surveyed profiles across the active segment of the Banning fault in Millard Canyon (see Figure 6 for locations of profiles). This scarp is 5.2 ± 0.7 m high in unit Qf_3 and 2.5 ± 0.7 m high in unit Qf_2. Vertical offsets were calculated taking the average of four measurements at the base and at the top of the scarp (see profiles). See text for discussion of slip-rate estimates based on these offsets.

of Qf_4 is also poorly known, but the poor degree of soil development suggests that it is no older than latest Pleistocene. We can estimate a shortening rate for the Qf_4 surface by assuming a latest Pleistocene age (<13,000 years) and a fault propagation fold geometry for the monocline, a reasonable assumption given that a 24° north-dipping thrust is exposed about 400 m to the east in the Qf_1/Qu_1 terrace riser of Millard Creek. Thirteen meters of vertical offset would be consistent with a rate of slip >2.5 mm/yr and a north-south shortening of >2.2 mm/yr.

[27] On the Millard Canyon fan, the scarp of the SGPF does not continue northeastward beyond the modern arroyo. However, another trace of the fault runs eastward along the mountain front a couple of hundred meters to the north (Figure 6). In addition to producing a 40-m-high scarp in the Quaternary Cabezon Fm and topped by the Heights fanglomerate (Figures 6 and 9), this fault has produced meter-high scarps in small Qf_1 alluvial fans at the mountain front. Small normal faults upslope on the hanging wall block indicate that the dip of this thrust fault shallows upward in the shallow subsurface. The trace of this thrust fault disappears eastward under the very young alluvium of Deep Canyon. Here it probably connects with a southeast-striking tear fault that connects with the next thrust segment of the fault zone to the east (Figures 3a and 6).

[28] The southwestern termination of the principal trace of the SGPF on the Millard Canyon fan is near the freeway (Figure 6). Just north of the freeway, the fault zone curves toward the west and then northwestward away from the freeway. Scarps that defined this transition from southwest to northwest strikes were mapped before their destruction by construction of a large retail complex there, begun in the early 1990s. The dips of the northwest-striking structures, on the fan of Potrero Canyon are unknown. We accept the interpretation of *Matti et al.* [1985, 1992a] and *Matti and Morton* [1993] that these structures comprise a tear fault that connects thrust faults west of Potrero Canyon with those of Millard Canyon. If this is correct, their dips are probably steeply northeastward or near vertical, since only a nearly vertical tear fault could share a slip vector with the thrust fault of Millard Canyon.

3.2. Cottonwood Canyon

[29] Figure 3 shows that a major change in the style of active faulting occurs at Cottonwood Canyon. To the west, thrust faults dominate the pattern of active deformation. East of the canyon, strike-slip motions are dominant. The nature of these two systems and their interaction are critical for understanding the behavior of the San Andreas fault zone through San Gorgonio Pass.

3.2.1. East of Cottonwood Canyon

[30] The dextral-slip Coachella Valley strand of the Banning fault and the dextral-oblique Garnet Hill fault are the most prominent faults between Cottonwood and Whitewater Canyons (Figure 11). Between these two active faults is Whitewater Hill, the geomorphic manifestation of an active anticline in the Pleistocene Cabezon fanglomerate.

[31] Between Cottonwood and Whitewater Canyons, the Coachella strand of the Banning fault separates crystalline rocks from the Cabezon Fm across a deep east-west-trending fosse. The linearity of the fault trace suggests that slip on the fault is primarily dextral. Additional support for the dominance of strike-slip is the source of the Cabezon gravels; clast types indicate that the gravels derive from north of the Mission Creek fault, by way of an ancestral Whitewater River [*Allen*, 1957; *Matti et al.*, 1985, 1992a; *Matti and Morton*, 1993]. The position of Whitewater-derived Cabezon gravels at Cottonwood Canyon requires about 4 km of dextral slip (the distance from Whitewater to Cottonwood Canyons) on the Coachella Valley strand of the Banning fault, assuming that deposition occurred in front of the present Whitewater Canyon. Paleocurrent indicators led *Matti et al.* [1985, 1992a] and *Matti and Morton* [1993] to propose about 2–3 km of dextral slip here.

[32] Small dextrally offset gravel shutter ridges along the Coachella Valley strand of the Banning fault (near A on Figure 11) demonstrate that the most recent several meters of dislocation across the fault also have been right-lateral.

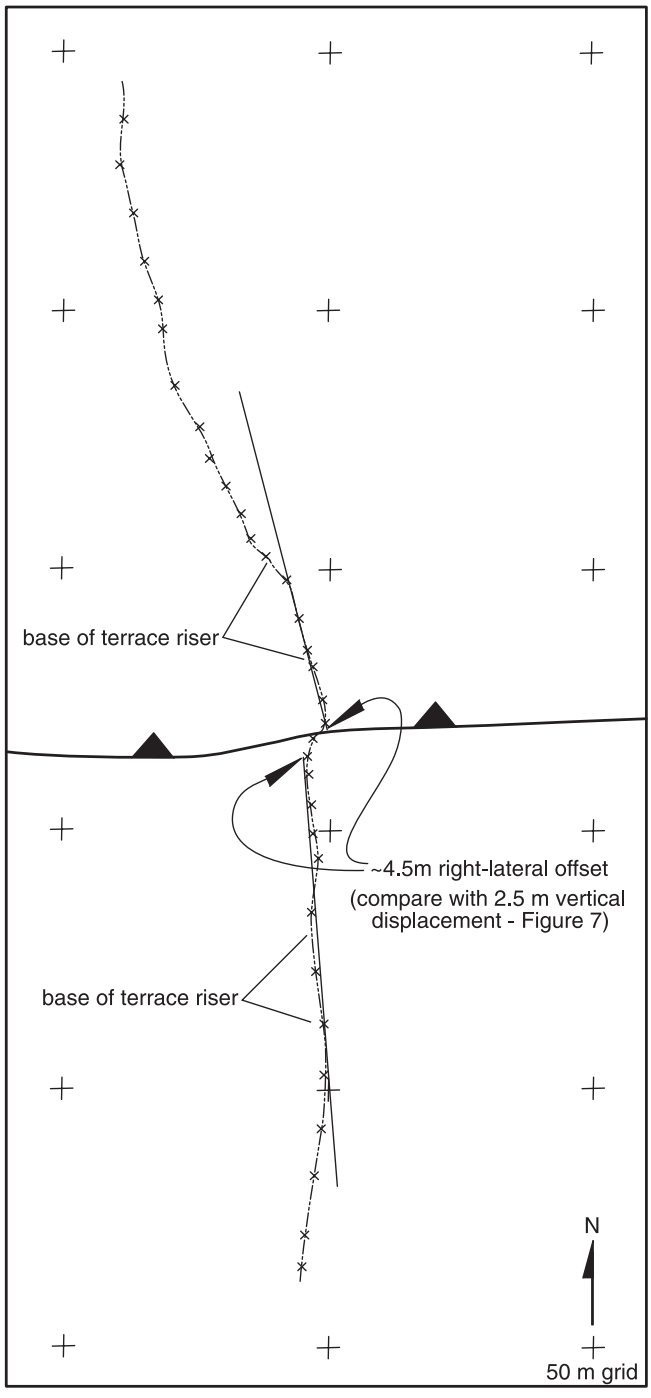

Figure 8. Map view of survey along the base of a terrace riser between Qf_2 and Qf_3 where it shows a right-lateral offset of about 4.5 m across the active segment of the Banning fault. This is about 80% greater than the vertical component (2.5 m), somewhat less than the vertical/lateral ratio of the offset of a buttress unconformity in the late Pleistocene Heights fanglomerate, exposed in the east wall of Millard Canyon (Figure 6, inset map; see text for details).

Dextral deflections of channels cut into bedrock (near B on Figure 11) also indicate a predominance of recent dextral slip. These small, young landforms near A and B also suggest that the rate of dextral slip diminishes westward along this reach of the Coachella Valley strand of the Banning fault. Contrary to expectations, the most pronounced small offsets are in rugged terrain, near A, rather than in the more gentle terrain near B. One would expect rapid erosion and burial in front of the steep, small, gravelly channels eroded into the 130-m-high gravelly escarpment at A. Less erosion and burial would be likely in the gentler terrain at B. A higher slip rate, and hence a substantially more rapid rate of creation of small tectonic landforms near A than near B, is the best explanation for this anomaly. The Coachella Valley strand of the Banning fault ends as an active strike-slip fault at Cottonwood Canyon. Although the faulted bedrock contact continues west across the canyon, the fault on the west side shows no evidence of recent activity and is a thrust fault.

[33] A depositional surface with a deep-red soil, indicative of $\geq$100,000 years of exposure, caps the fluvial Cabezon deposits of Whitewater Hill. This surface has an anticlinal shape (Figure 11). Moderate dips in the underlying deposits define this anticlinal warp as well. The deposits are more deformed than the surface, so the anticline was growing during, as well as after, deposition of the sediments, and the soil has formed on an erosional surface. A group of northwest-trending dip-slip faults cut the deposits and the old surface. Their orientation suggests that they are normal faults. The faults define a minor system of graben and horst, which are evidence for extension across the east flank of the anticline [e.g., *Yeats*, 1986]. If we assume that the surface is $\geq$100,000-years old, based on the extreme development of the capping soil, a 4-km (maximum) offset of the deposit would have accrued at an average rate of 40 mm/yr or less. This is not a very tight constraint on the slip rate of the Coachella Valley strand of the Banning fault here, but it does suggest that the rate of slip is high, on the order of centimeters rather than millimeters per year.

[34] The Garnet Hill fault bounds the southern flank of the Whitewater Hill anticline. It has two traces, one along the flank of the steep southern slope of the anticline, and another in the young alluvium farther south [*Matti et al.*, 1992a; *Matti and Morton*, 1993; *Morton et al.*, 1987]. The subtle scarp in young alluvium is only a meter or so high and its orientation, about N75°W, suggests that the scarp is the result of oblique motion on a dextral thrust fault, north over south. There is strong geomorphic evidence that slip on the other fault, at the base of the anticline, is a combination of dextral and reverse. Most of the large drainages crossed by this structure have distinct, large shutter ridges at their mouths. The stream channels deflect right-laterally around these ridges. By the Rule of V's, the trace geometry of the fault indicates a steep to moderate dip northward, under the anticline.

[35] Neither of the two traces of the Garnet Hill fault continues across the young fan deposits of Cottonwood Canyon. Thus the relationship of these faults to the active thrust faults west of the canyon is obscure.

3.2.2. West of Cottonwood Canyon

[36] Active reverse faults dominate the neotectonic landscape west of Cottonwood Canyon (Figure 11). Small scarps in young alluvium, the clearest direct evidence of the latest event or events, appear only along a short segment of the mountain front (near C in Figure 11).

[37] Elsewhere youthful scarps have presumably been either buried or eroded. However, many old alluvial surfa-

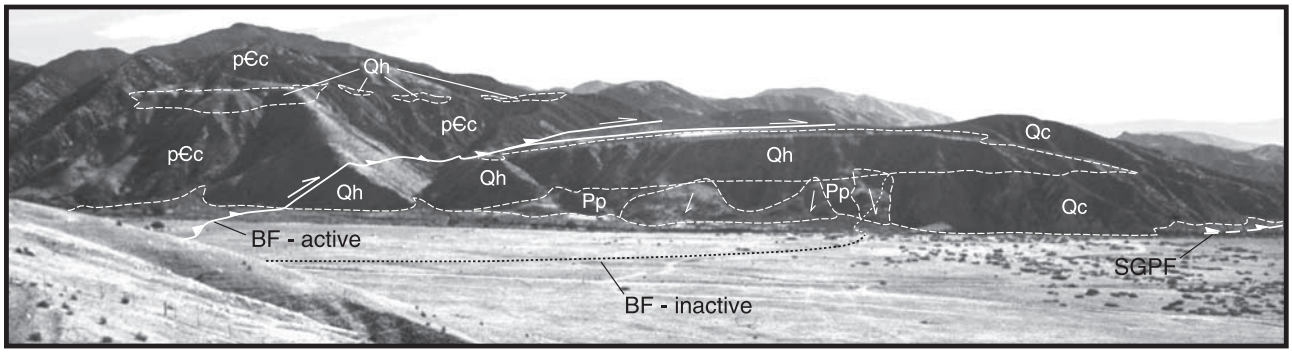

Figure 9. Tiled photographs of the east wall of Millard Canyon. An abandoned alluvial surface on the top of the late Pleistocene Heights fanglomerate (Qh) has been uplifted about 85 and 170 m across the San Gorgonio Pass and Banning faults, respectively, above the Holocene alluvial surface in the foreground (see text, Figures 6, 8, and 10). The inactive strand of the Banning fault thrusts Pliocene rocks (Pp) over the Cabezon Formation (Qc) in the middle of the photo. Rock unit symbols are as shown in Figure 6.

ces along the mountain front project well above neighboring active alluvial fans. This is clear evidence for uplift on faults at and near the mountain front. For example, a few hundred meters south of the mountain front (near D in Figure 11) a broad active channel separates an old alluvial surface into two remnant terraces. Young alluvium laps onto both remnants on their northern edges and onto the eastern flank of the eastern remnant. A stream has eroded the western flank of the western remnant. The southeastern edges of both terrace remnants are also eroded, but that erosion is not due to stream erosion. Uplift of the terraces along a northeast-southwest-striking fault is a more viable interpretation. The orientation of this scarp supports the interpretation that the causative fault is a reverse fault that dips northwest, toward the mountains.

[38] Other alluvial terraces along the mountain front between Stubbe and Cottonwood Canyons belie the presence of another thrust fault, structurally above the one just described (between E and F on Figure 11) [*Morton et al.*, 1987; *Sieh and Matti*, 1992; *Matti and Morton*, 1993]. The trace of this fault is buried beneath young alluvium along most of its length; but it must follow the irregular shape of the mountain front, because the triangular facets of the mountain front cannot be due to stream erosion parallel to the mountain front. For the same reason, uplift of the lobate, alluvial terrace west of the mouth of Stubbe Canyon (Figures 3a and 11) must also be related to slip on an arcuate active thrust fault that circumscribes that lobe of the mountain front.

[39] A large rotational landslide obscures the geologic relationships of the slopes immediately west of Cottonwood Canyon (Figures 11 and 12) [*Morton et al.*, 1987]. The headscarp and lateral margins of this slide are readily apparent and leave no doubt that the feature is of nontectonic origin. A small sector on the western flank of the slide slumped again in 1993. The high degree of preservation of the landslide suggests that it is no more than a few thousand years old. The toe of the landslide partially overrides a paleochannel cut into crystalline bedrock and old alluvium (near G on Figure 11, and Figure 12). This

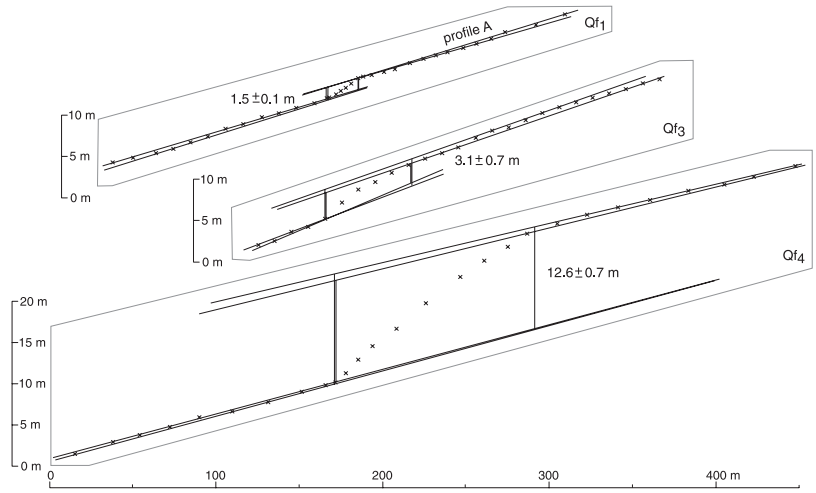

Figure 10. Cross-sectional view of surveyed profiles across the SGPF in Millard Canyon (see Figure 6 for locations of profiles). Vertical offsets were calculated as described for Figure 7. See text for discussion of slip-rate estimates based on these offsets.

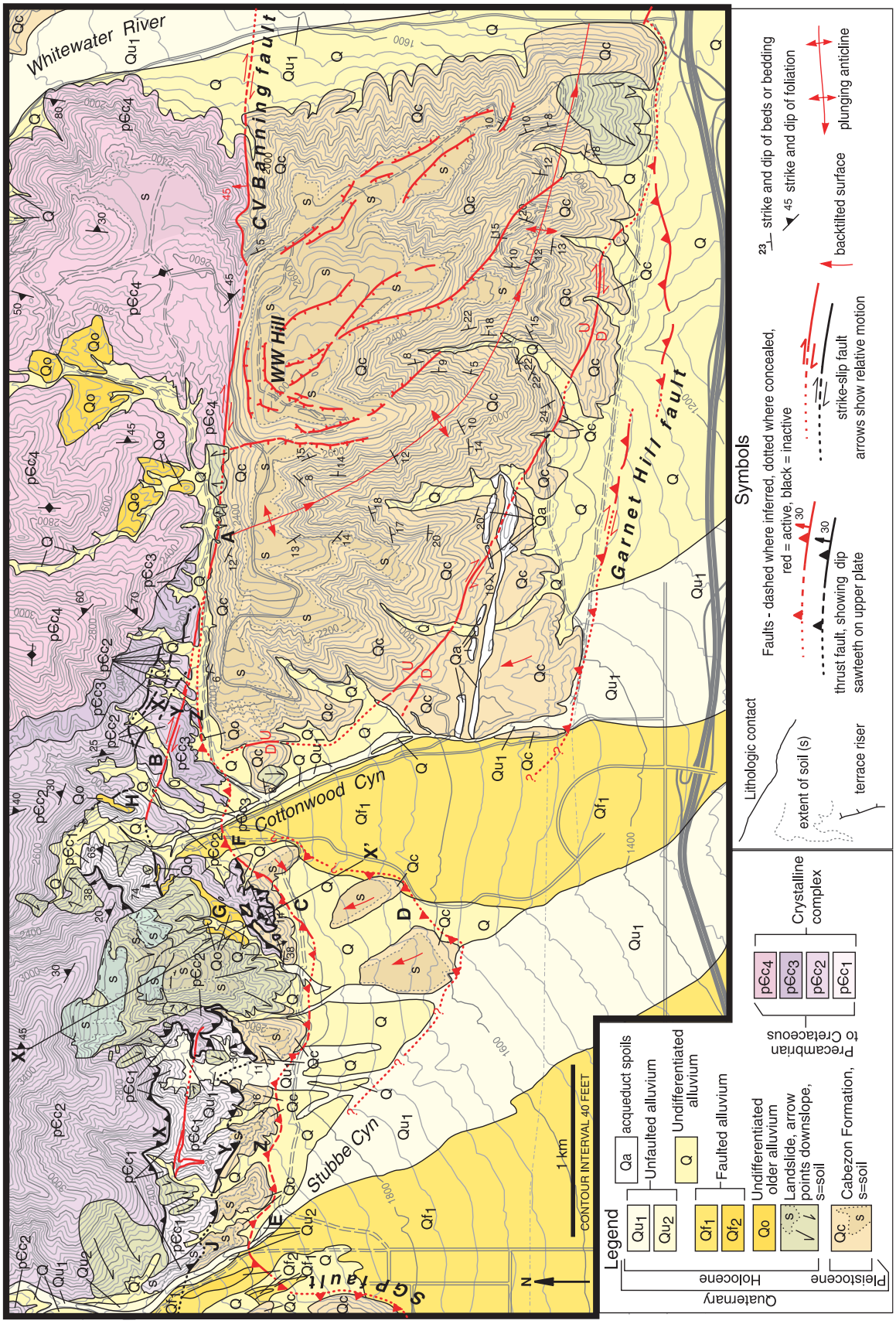

Figure 11. Geologic map of the Cottonwood Canyon area [portions modified from *Matti et al.*, 1992a; *Sieh and Matti*, 1992; *Matti and Morton*, 1993; *Morton et al.*, 1987; R. Wolf, unpublished mapping] shows the convergence of predominantly right-lateral faults (east of the canyon) with predominantly reverse-slip active faults (west of the canyon). See Figure 3a for the location of the map. Figure 12 is taken along line of cross section X-X'.

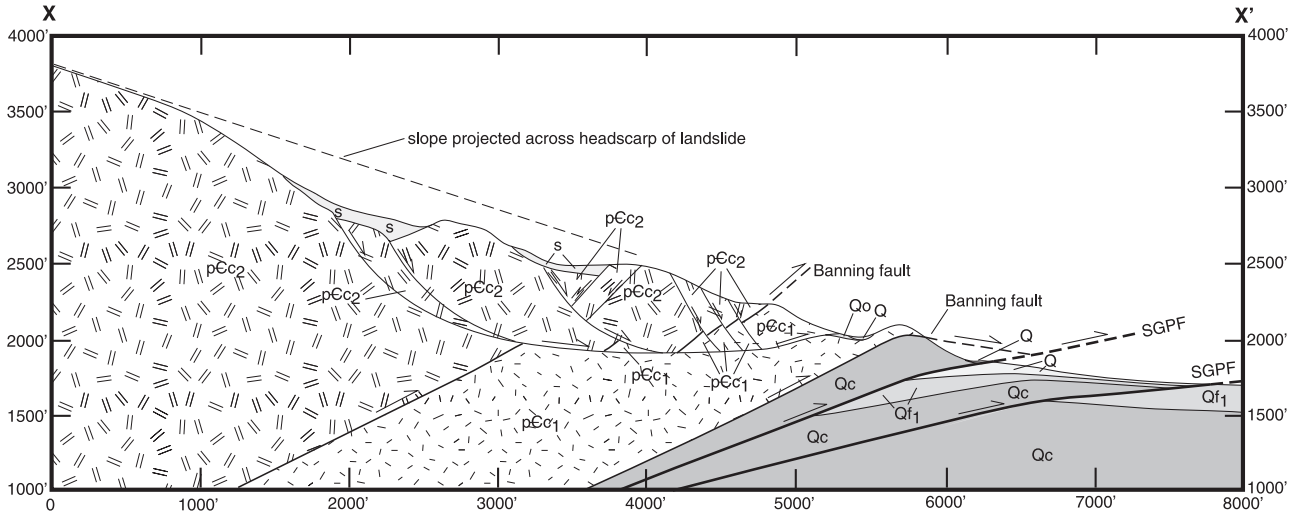

Figure 12. Geologic cross section along line X-X' (location shown in Figure 11). Note the two active fault strands of the San Gorgonio Pass fault (SGPF), dipping shallowly to the north. Strands of the Banning fault thrust Cretaceous to Precambrian crystalline rocks (pCc_1 and pCc_2) over late Pleistocene Cabezon Formation (Qc) but are considered inactive. The landslide in the hanging wall shows a clear headscarp and lateral margins.

relationship is clear at the eastern end of the buried channel, in an exposure on the west wall of Cottonwood Canyon. This channel appears to have served as a conduit for Cottonwood creek prior to its burial by the slide and prior to a few tens of meters of incision by Cottonwood creek. The outlet of the buried channel (at the mountain front) aligns with the broad channel that bisects the old alluvial deposits at D (J. Treiman, oral communication, 1992). These channels were probably contiguous when active, but uplift of the mountain front has led to deposition of younger alluvium between them, completely burying the old channel immediately downstream from the mountain front.

[40] Numerous older, inactive thrust faults crop out north of the active mountain front [*Morton et al.*, 1987; *Sieh and Matti*, 1992; *Matti and Morton*, 1993]. We show the obvious ones (those mappable by virtue of their juxtaposition of crystalline basement units over one another and over older alluvial deposits) (Figures 11 and 12). The lack of geomorphic expression indicates that none of these shallow-dipping structures is active. In addition, unbroken old alluvium or old surfaces bury some, or fensters have been cut through them. All but the northernmost of these inactive faults override old alluvium and alluvial surfaces and have thus been active in the late Pleistocene. Their contiguity with the Coachella Valley strand of the Banning fault at Cottonwood Canyon suggests that they were active when dextral slip on the Coachella Valley strand of the Banning fault transformed into thrust faulting at Cottonwood Canyon.

3.2.3. Connections

[41] Geologic relationships near the mouth of Cottonwood Canyon place important constraints on the interactions between faults west and east of the canyon. An interpretation of these relationships must precede our discussion of a tectonic concept for the region.

[42] The Coachella Valley strand of the Banning fault splays into three traces as it approaches Cottonwood Canyon from the east (X, Y, and Z on Figure 11). The two northernmost traces (X and Y on Figure 11) connect across the canyon with steep to gently dipping inactive strands of the Banning fault. The northernmost inactive strand is buried by the large landslide on the west wall of the canyon and by a thin alluvial gravel high on the east wall (H on Figure 11). It emerges west of the landslide as an inactive thrust fault within crystalline basement rocks. The southernmost inactive fault connects across Cottonwood Canyon with the strand of the Coachella Valley strand that has the clearest geomorphic evidence for dextral slip (B on Figure 11). West of the large landslide, this thrust fault places crystalline basement rocks over an alluvial terrace remnant. On the east side of Stubbe Canyon, this fault is overlain by a younger fluvial terrace remnant and soil (J on Figure 11). The current inactivity of both of these thrust faults is consistent with the observation that dextral slip on the Coachella Valley strand of the Banning fault dies out westward as it approaches Cottonwood Canyon [*Allen*, 1957; *Matti et al.*, 1985, 1992a]. The subtle geomorphic evidence for dextral slip on the Coachella Valley strand just east of Cottonwood Canyon (A on Figure 11) is consistent with activity on the thrust fault in the not too distant past, say 10^4–10^5 years ago.

[43] The presence of Whitewater Hill anticline, between the Garnet Hill fault and the Coachella Valley strand of the Banning fault, implies a transfer of dextral slip from the latter fault onto the former [*Matti et al.*, 1985, 1992a]. Geomorphic evidence for westward diminishment of dextral slip on the Coachella Valley strand is clear. This diminishment may be translated into shortening across the anticline and increased slip westward on the Garnet Hill system. In addition, dextral slip may be translated to the north via transtension onto the oblique dextral-normal Cox Ranch

fault zone. Regardless of the details of this transfer, all of the slip on the Coachella Valley segment ceases by Cottonwood Canyon; and so, these other structures must absorb the slip [*Matti et al.*, 1985, 1992a].

[44] The geomorphic expression of the Garnet Hill fault shows no sign of diminishing as it approaches Cottonwood Canyon from the east. The geomorphic expression of the active thrust faults at and in front of the range shows no signs of diminishing as they approach the canyon mouth from the west. We suspect, therefore, that these two fault zones are contiguous beneath the young alluvium of Cottonwood Canyon. Much of the dextral slip on the Garnet Hill fault could be transformed into reverse slip on the thrust faults of the SGPF zone, as *Matti et al.* [1985, 1992a] originally proposed.

4. Regional Folds and Blocks

[45] Flexure of fault-bounded crustal strips accommodates a significant component of the strain in the San Gorgonio Pass stepover region [*Dibblee*, 1975]. The regional warping has northwest-trending axes in the southern San Bernardino Mountains and a west-trending axis in the northern San Jacinto Mountains (Figure 2b). Evidence of regional scale flexures includes anomalously high topography, gross geomorphology, deformed late Quaternary sediments, and (U-Th)/He thermochronologic data. Below, we consider each of several large blocks, separately.

4.1. Morongo Block

[46] The Morongo block is characterized by a central topographic high at Kitching Peak, which rises about 1–1.5 km above low-lying areas to the west and east (Figure 2b). South flowing drainages of the upper San Gorgonio and Whitewater Rivers deflect toward the west and east, respectively, around this topographic high. Kitching Peak is also surrounded by outliers and outcrop belts of late Pleistocene deposits (Figure 3a). Miocene to middle Pliocene strata to the east of Whitewater River dip 20°E to NE on average. These observations can be explained by a northwest-trending arch of late Quaternary age with limbs gently plunging to the east and west from the central topographic high of the Morongo block. (U-Th)/He samples are being analyzed to help constrain the geometry of this structure [*Spotila et al.*, 2001].

4.2. Yucaipa Ridge

[47] Yucaipa Ridge is a rugged, elongate ridge bounded by the San Bernardino strand of the San Andreas fault and the Mill Creek fault. The ridgeline elevation increases steadily from ~1.5 to 3 km toward the east-southeast (Figure 2b) [*Spotila et al.*, 1998]. A ridgeline profile is therefore similar to the profile of the western flank of the Morongo block. Apatite (U-Th)/He cooling ages indicate that the Yucaipa Ridge block experienced >3 km of Quaternary denudation about 1.5 myr ago [*Spotila et al.*, 1998, 2001]. We suggest that more recent uplift, westward tilting, and erosion may have attended broad uplift of the region.

4.3. San Gorgonio Mountain Block

[48] The San Gorgonio Mountain block; [*Dibblee*, 1975, 1982; *Sadler and Reeder*, 1983] is also characterized by a central topographic high of ~1–1.5 km higher than regions to the west and east (Figure 2b). Apatite (U-Th)/He cooling ages obtained from the western flank of the block suggest that post-Miocene ~5° westward and ~10° northward tilts have occurred [*Spotila et al.*, 1998]. This tilt closely parallels the topographic gradient of the western flank of San Gorgonio Mountain. Though no cooling ages have been obtained from the eastern flank, we suspect that cooling ages will show eastward and northward tilting. Northward tilt of the block is also shown by ~25° north dips of Mio-Pliocene Santa Ana sandstone beds at Barton Flats [*Dibblee*, 1964; *Sadler et al.*, 1993]. The San Gorgonio Mountain block therefore appears to be a broad northwest-southeast-plunging arch.

4.4. San Jacinto Mountains Block

[49] The northern end of the San Jacinto Mountains block exhibits a topographic bulge centered on San Jacinto Peak. Relief to the south and west is about 1 km and to the north and east is over 3 km. Southeast-northwest-trending profiles across the arch define a west-plunging topographic arch (Figure 2b). (U-Th)/He apatite cooling ages [*Wolf et al.*, 1997] loosely define thermochrons that show flexure that mimics the broad topographic arch (see discussion below). Hornblende barometry and (U-Th)/He apatite cooling ages also document a modest westward tilt about a N-S tilt-axis of the San Jacinto block, roughly parallel to the topographic profile [*Ague and Brandon*, 1992; *Wolf et al.*, 1997]. The age of this structure, constrained by apatite cooling, is post-40 Ma, but may be quite young.

5. Relevant Observations of Seismicity

[50] Recorded seismicity in the region of the Pass is important for interpreting the neotectonic behavior of the San Andreas fault system there. Rather than relying on structural modeling to extrapolate surface traces of active faults farther into the crust, we use crustal seismicity as a guide. In this section, we present relevant information about the depth of seismicity and we summarize previous work on the source parameters of small to moderate earthquakes.

5.1. Base of Seismicity

[51] The pattern of crustal seismicity in this region plays a crucial role in our interpretation of its earthquake geology. A key observation is that maximum hypocentral depths of small earthquakes beneath San Gorgonio Pass and the southern San Bernardino Mountains are anomalously deep. Whereas most of southern California experiences maximum focal depths between 10 and 15 km, this region has hypocentral depths as great as 20 km.

[52] The geographic pattern of the base of seismicity must relate to the present-day tectonics of the region. *Magistrale and Sanders* [1996] demonstrated that the deepest hypocenters cluster beneath the stepover of the San Andreas fault zone near San Gorgonio Pass. They also showed that the base of seismicity drops precipitously from 13 km or so on the north, to 20 km on the south along an east-west plane beneath the fault zone. They argued that this abrupt drop represents a sharp juxtaposition of the brittle-ductile transition for feldspar-dominated rocks of the Peninsular ranges, south of the abrupt drop, against the transition for quartz-

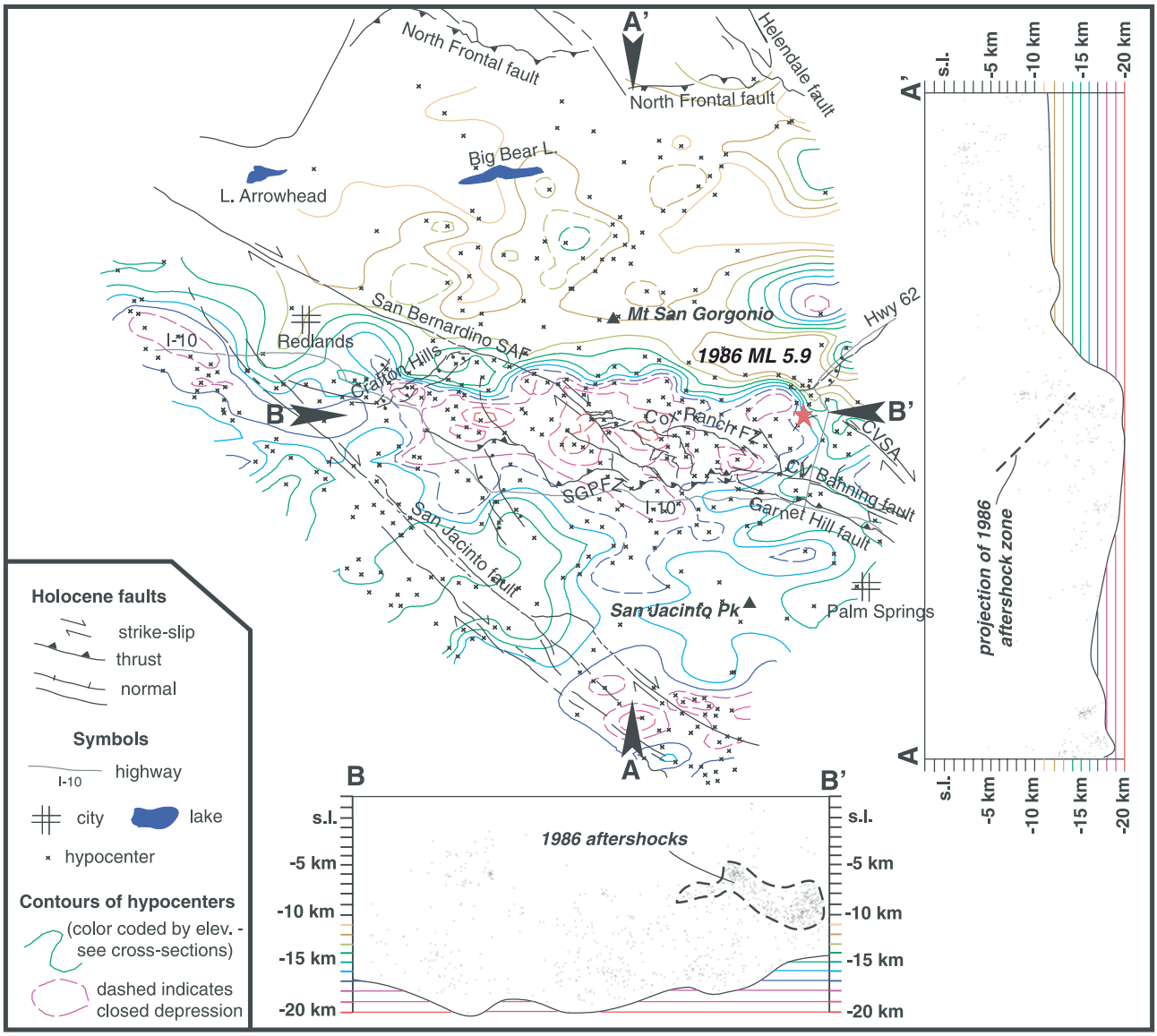

Figure 13. Contours on the base of seismicity in the SGP region show a distinct east-west-trending vertical step, 6–7 km high. The deepest hypocenters, one selected for each 3–5 km^2 area, are contoured at a 1-km interval. Hypocenters were supplied by Magistrale for the years 1981–1993. The seismicity step separates regions of anomalously deep and shallow limits of seismicity, to the south and north, respectively. Vertical cross sections A-A' and B-B' show the base of seismicity and hypocenters taken from a 5-km-wide vertical slice and projected onto the plane of cross section. The 1986 North Palm Springs aftershock sequence [*Hartzell*, 1989; *Nicholson*, 1996] intersects B-B' in a nearly horizontal plane. We use the 1986 rupture plane, as illuminated by aftershocks, to carry the San Gorgonio Pass-Garnet Hill fault system to depth (see text for further details). The along strike projection of this rupture plane is shown in A-A'.

dominated rocks of the San Bernardino Mountains, to the north. We argue below that this is not the primary reason for the drop. But first, let us describe the geometry of the base of seismicity in more detail than did *Magistrale and Sanders* [1996] and explain its geologic associations.

[53] Figure 13 is a map of the base of seismicity with the traces of active faults superimposed. We used a catalog of earthquakes supplied by Magistrale for the years 1981–1993 from the work of *Magistrale and Sanders* [1996]. Cross section A-A' shows the change in-depth of seismicity along a vertical plane, 5-km wide, perpendicular to the east-west step. This shows that the step in seismicity is about 5–8 km high. It also shows that the southern flank of the trough formed by the base of the seismicity dips very gently northward from about San Jacinto Peak. Cross section B-B' shows the change in-depth along a plane parallel to and within the trough of deepest seismicity. Comparison of the geographic extent of the trough with topography (Figure 2) shows that the trough is precisely coincident with the eastern and western flanks of the southern San Bernardino

Mountains. Furthermore, the dimensions of the trough match the dimensions of the hanging wall block of the SGPF (Figure 13). This suggests a common cause of the seismicity trough, the topography, and active faulting in San Gorgonio Pass. Another fundamental observation of *Magistrale and Sanders* [1996] is clear from the map: the San Bernardino strand of the San Andreas fault does not appear to offset the seismicity step.

5.2. Focal Mechanisms of Background Seismicity

[54] The focal mechanisms of background earthquakes within the region of deep crustal seismicity also must bear on the active tectonics of the region. *Nicholson et al.* [1986] and *Seeber and Armbruster* [1995] analyzed hundreds of events beneath the San Andreas fault zone here. *Nicholson et al.* [1986] draw a distinction between shallow and deep seismicity; above about 10 km, oblique left slip in combination with both normal and reverse faulting predominates, and below 10 km strike-slip and less common low angle thrust faulting predominates. *Nicholson et al.* [1986] attributes the change in microearthquake focal mechanism with depth to the presence of a regional detachment [also see *Hadley and Kanamori*, 1977]; a set of small, upper crustal blocks currently rotating under a regional right-lateral shear system decoupled from a wedge-shaped region of the lower crust experiencing pervasive north-south shortening and east-west extension. *Seeber and Armbruster* [1995] envision shortening accommodated by north-dipping thrust faults, primarily the SGPF in the upper crust and a San Gorgonio Pass detachment at depth; extension is accommodated by dextral strike slip on the San Andreas, a throughgoing feature beneath the SGPF. A scarcity of hypocenters above 5-km depth makes connecting faults at depth with surface faults problematic. Furthermore, both studies caution that the great majority of microearthquakes occur off the primary structures, and that the pattern indicated from microseismicity, collected over a relatively short time period (10–20 year), might not characterize the primary active tectonic features of the Pass region.

5.3. The 1986 North Palm Springs Earthquake

[55] Studies of the M_L5.9 North Palm Springs earthquake and aftershock sequence show another critical relationship between the seismicity step and certain active faults of the stepover. The focal mechanism and aftershock zone determined by *Jones et al.* [1986] show that the source of the earthquake was a 50°-NE-dipping, N60°W-striking fault. The short-period mechanism shows that slip was purely right-lateral, but an analysis of long-period waves [*Hartzell*, 1989] indicates that slip during most of the rupture was highly oblique, with significant components of reverse, as well as dextral slip. The ratio of dextral to reverse slip was between 1:1 and 2:1.

[56] Regardless of the slip vector, the fault plane projects updip to the trace of either the Coachella Valley segment of the Banning fault or the trace of the Garnet Hill fault [*Jones et al.*, 1986]. The oblique-slip motion of the 1986 rupture is compatible with the sense of slip of the Garnet Hill fault at the surface, with the uplifted Pleistocene gravels of east and west Whitewater Hill (Figure 3b) an indication of the dip-slip component in its hanging wall. It is inconsistent with the geometry and sense of slip on the Coachella Valley strand of the Banning fault at the surface, which is subvertical east of Whitewater Canyon [*Allen*, 1957] and nearly pure strike slip. We interpret the more steeply dipping Coachella Valley strand to reside in the hanging wall of a more gently dipping fault whose surface expression is the Garnet Hill fault. We therefore conclude that the 1986 earthquake ruptured a single fault plane that bifurcates into the Garnet Hill and Coachella Valley strand of the Banning fault above about 5-km depth, the upper limit of the aftershocks.

5.4. The 1948 Desert Hot Springs Earthquake

[57] Another important earthquake for our analysis is the M_W6.0 Desert Hot Springs earthquake. *Nicholson*'s [1996] seismographic comparison of the 1948 and 1986 earthquakes shows that the earlier earthquake involved rupture of a fault plane immediately southeast of the 1986 rupture. The strike of the plane is slightly more northerly than the 1986 rupture (N55°W), the dip is slightly steeper (60°–70°), and the slip vector has a much smaller component of reverse slip (a rake of only bout 10°). These parameters are consistent with rupture of either the Coachella strand of the Banning fault or the Garnet Hill fault, southeast of the 1986 rupture. Along this reach, even the Garnet Hill fault displays only local geomorphic evidence of vertical slip, associated with small en echelon stepovers inferred for the fault trace.

6. Kinematic Concept

[58] We are now prepared to attempt a synthesis of the data we have presented above. Our analysis of active faults and folds, augmented by seismicity, provides a basis for constructing a three-dimensional model of active deformation. Later, we discuss the impact of our three-dimensional crustal model on plausible sources for future and past large earthquakes in the region.

[59] Recent explanations of the active tectonics of the San Andreas fault zone in the region of San Gorgonio Pass have differed substantially. Two of these recent proposals involve the concealment of a more-or-less straight and contiguous San Andreas fault zone through the region. *Rasmussen and Reeder* [1986] suggest, on the basis of geomorphologic evidence, that the San Andreas fault continues as a simple strike-slip fault beneath the region, obscured at the surface by a very large landslide complex (Figure 14a). *Seeber and Armbruster* [1995] believe that the SGPF is an active thrust fault, but from the alignment of about 20 strike-slip focal mechanisms, conclude that it conceals the principal active structure, which is a simple, throughgoing strike-slip fault at depth (Figure 14b). A third interpretation, synthesized by *Matti et al.* [1985, 1992a], *Matti and Morton* [1993], and *Morton and Matti* [1993], and supported by *Magistrale and Sanders* [1996], envisions a left-stepping zone of convergence with a discontinuous system of strike-slip and thrust faults that transfers dextral slip through the region. Our mapping and analysis refutes the first two models and substantiates the third. We propose the geometry and senses of slip illustrated in Figure 14c.

6.1. Landslide Hypothesis

[60] The landslide hypothesis [*Rasmussen and Reeder*, 1986] is not consistent with the geometry and sense of slip

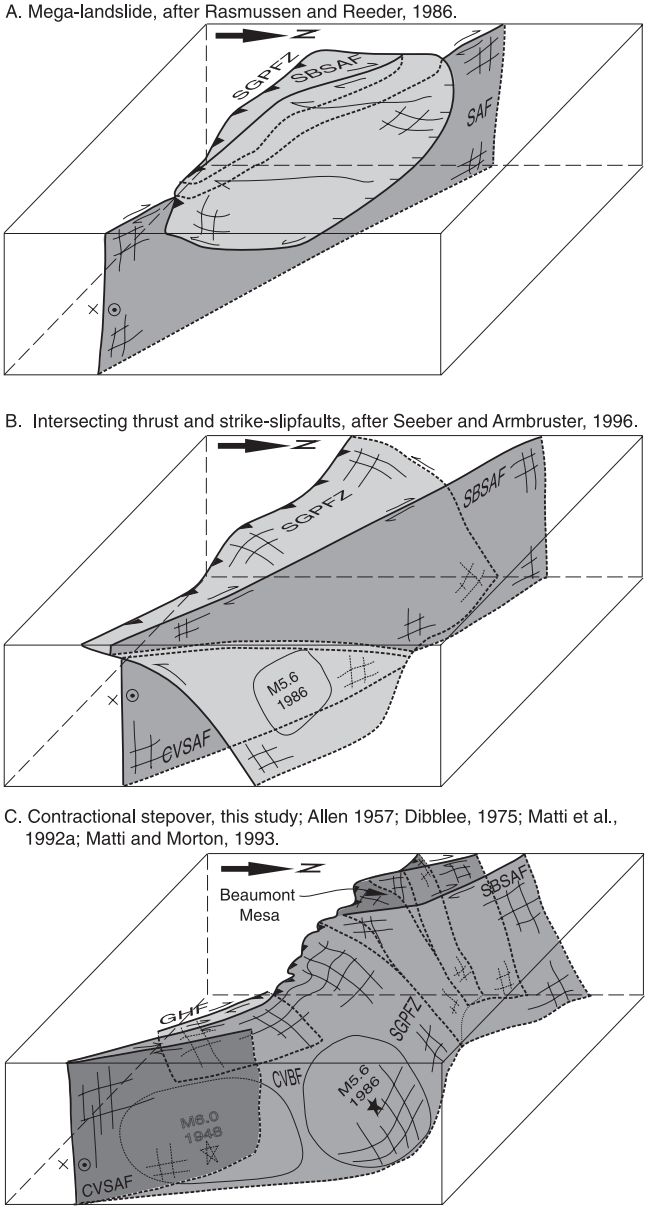

Figure 14. Three block diagrams illustrate three alternative kinematic models for the active faults of the San Gorgonio Pass region. (a) In this mega-landslide model [*Rasmussen and Reeder*, 1986] a large landslide overrides and obscures the vertical plane of the San Andreas fault. (b) In this thrust-flap model [Figure 3c of *Seeber and Armbruster*, 1995] a south-vergent thrust fault offsets the vertical, strike-slip plane of the San Andreas fault. (c) In the fault-bend-fold model [modified from *Allen*, 1957; *Dibblee*, 1968, 1975, 1982; *Matti et al.*, 1985, 1992a; *Matti and Morton*, 1993], which we advocate, vertical to moderately dipping strike-slip planes cut the hanging wall block of the SGP thrust fault on the west and approach the thrust fault on the east. Only the latter model fits the data we have presented in this paper. Dashed lines indicate features in the background. Abbreviations include SGPFZ, San Gorgonio Pass fault zone; SBSAF, San Bernardino strand, San Andreas fault; SAF, San Andreas fault; CVSAF, Coachella strand, San Andreas fault; and CVBF, Coachella Valley strand, San Andreas fault.

on the active features of the region. One of its serious deficiencies is the lack of a credible headscarp in the southern San Bernardino Mountains. The most obvious candidate for a headscarp would be the Cox Ranch fault zone, since this structure does have a significant component of normal dip slip and traverses the entire stepover region. But the en echelon geometry of the Cox Ranch fault zone and its clear dextral component of motion are inconsistent with a landslide origin. Slip on the western third of the Cox Ranch fault zone would, for example, need to be left-lateral if it were the headscarp of a large landslide that had the dextral-slip faults in Potrero Canyon as its western margin and the San Gorgonio Pass thrust as its toe (Figure 3a). Furthermore, this portion of the SGPF west of Potrero Canyon has no extensional structures to the north that would support the hypothesis that it is the toe of a large landslide (Figure 2). A similar lack of candidate headscarps (and the large component of dextral slip) leads to rejection of the Garnet Hill fault zone as the toe of a massive landslide. Although it is true that the mountainous region north of the Pass is rife with landslides (Figure 3a), none of these is large enough to claim the thrust faults as their toe.

6.2. Thrust-Flap Hypothesis

[61] *Seeber and Armbruster*'s [1995] hypothesis is based upon the existence of about 20 hypocenters with strike-slip mechanisms beneath the region, at depths of 11–22 km. On the west, these hypocenters are coincident with the 5–8 km high step in the base of seismicity; on the east, they are several kilometers south of the step. These hypocenters align approximately N70°W between the San Bernardino strand of the San Andreas fault and the Coachella Valley strand of the Banning fault, though in detail this trend deviates from the N45°W trend of the San Andreas strand at its southern extent in Potrero Canyon (Figure 3a).

[62] The principal flaw in a thrust-flap hypothesis is that it predicts the existence of decapitated remains of steeply dipping strands of the San Andreas fault within the thrust flap (as illustrated in Figure 14b). Our mapping precludes the existence of structures that could be interpreted as such. The only candidates are the dormant strands of the Banning fault (Figures 2 and 3a), a set of thrust faults whose geometry and kinematics identifies them as precursors to the SGPF, not the San Andreas fault. This does not mean that a handful of strike-slip mechanisms do not form an east-west alignment beneath the region. But the aligned events do not appear to illuminate a major strike-slip structure there. The use of just a handful of selected small earthquakes to characterize a major neotectonic element of the San Gorgonio stepover, the 20 hypocenters constitute a small fraction of the strike-slip mechanisms beneath the region [Figure 4 of *Seeber and Armbruster*, 1995], is analogous to using a handful of bricks in the wall of a building to characterize the wall. In this case, we find no reason to believe that these few bricks are representative of a major active structure.

6.3. Transpressional Stepover Hypothesis

[63] *Allen* [1957] proposed, as one of five possible models, that the San Bernardino and Coachella Valley strands of the San Andreas fault do not connect but transfer slip via thrust faulting in the San Gorgonio Pass region.

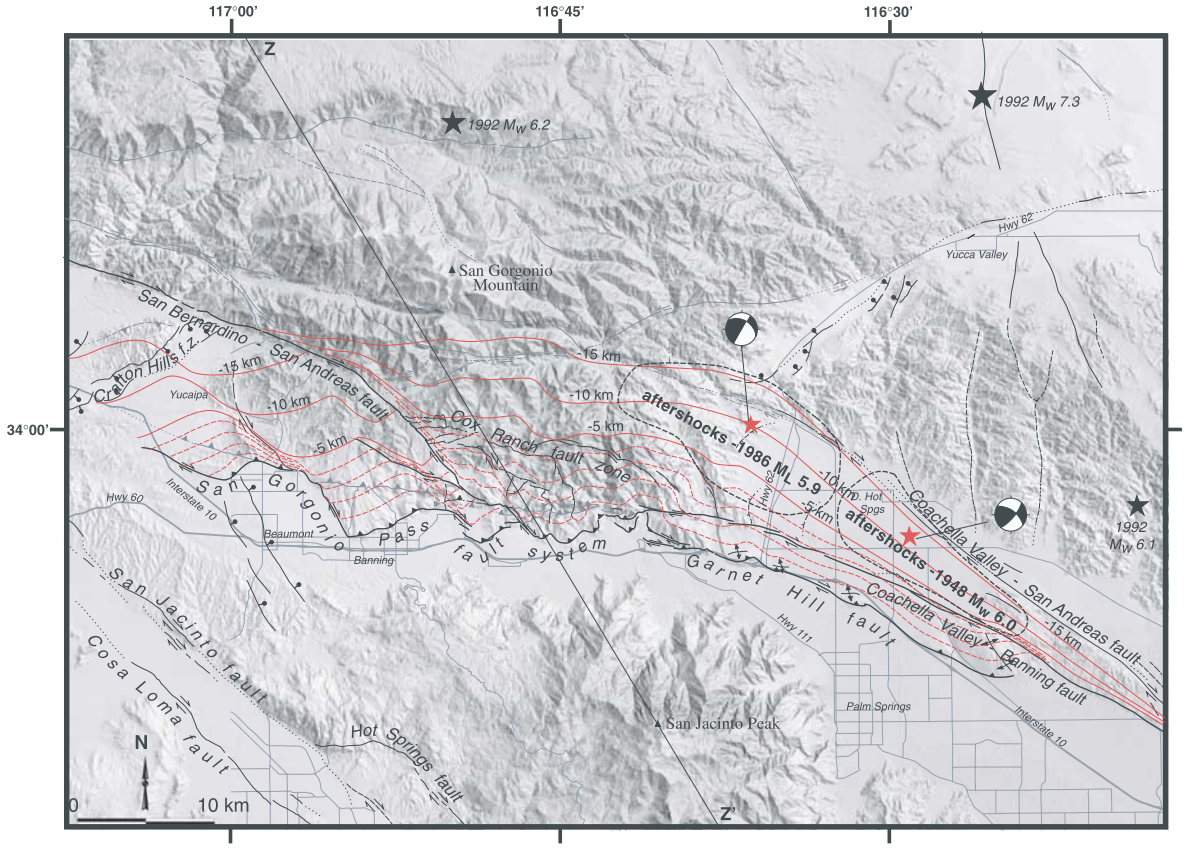

Figure 15. Structural contour map of the primary fault systems of the San Gorgonio Pass region. These structural contours on the active elements of the San Andreas and San Gorgonio Pass fault zones are constrained by geologic mapping, regional seismicity, and the aftershocks of the 1986 M_L5.9 North Palm Springs and the M_w6.0 1948 Desert Hot Springs earthquakes (dashed outlines). In this interpretation, the San Bernardino strand of the fault is a tear fault in the hanging wall block of the San Gorgonio Pass fault system. The moderately dipping Garnet Hill and more steeply dipping Coachella Valley Banning fault strands merge at depth and merge with the San Gorgonio Pass fault system from the east.

Dibblee [1968, 1975, 1982] modified another model of *Allen* [1957] describing how the San Bernardino strand, Coachella Valley strand, and Banning fault once formed a throughgoing trace within the Pass region that was subsequently deflected into a sharp transpressive bend. *Matti et al.* [1985, 1992a] and *Matti and Morton* [1993] cite evidence that indicates slip dies out on the San Bernardino and Coachella Valley strands as they approach the San Gorgonio Pass region from the northwest and southeast, respectively. They view the San Gorgonio Pass region as a structural knot whereby slip is transferred around the knot via the Coachella Valley Banning fault, SGPF system, Crafton Hills fault system, and San Jacinto faults.

[64] Together, geologic and seismographic data support an interpretation whereby the dominant structure of the Pass region is a wide, complex, transcrustal oblique-slip fault system, bounded on the south by the San Gorgonio Pass-Garnet Hill fault zones. We propose that slip on these, the other active structures of the Pass region (Figures 2 and 15), and perhaps, significant rotations between them, account for about half, if not more, of the 20–25 mm/yr of dextral slip measured across the San Andreas fault zone outside of the stepover region [*Weldon and Sieh*, 1985; *Harden and Matti*, 1989; *van der Woerd et al.*, 2001].

[65] A structural contour map of the southern boundary of these fault systems (Figure 15) illustrates in three dimensions our concept of the principal, active crustal structure of the San Gorgonio Pass region and the data upon which it is based. We adopt the time-space model of *Matti and Morton* [1993] and infer that the geometry for active structures shown in Figure 15 has evolved in the last 125,000 years or so. The geologic architecture of the region centers on the north-dipping, dextral-reverse San Gorgonio Pass-Garnet Hill fault zone. We show the Garnet Hill fault and the Coachella Valley, Banning fault merging at a depth to form a single fault plane below about 5 km. We believe that the aftershock zones from 1986 and 1948, shown as patches on this fault at depths between about 5 and 15 km, illuminate this ''master fault'' at depth that bends to the west to become the SGPF zone. Figure 15 shows the San Bernardino strand of the San Andreas fault as a large tear fault in its the hanging wall. The SGPF zone continues to the west, transferring a component of slip to the northern San Jacinto fault and back to the San Bernardino strand via the Crafton Hills fault zone [see Figure 6 of *Matti et al.*, 1992a]. The San Gorgonio Pass-Garnet Hill fault zone therefore is the locus of south-under-north thrusting created by the oblique collision of the northeastern corner of the Peninsular Ranges

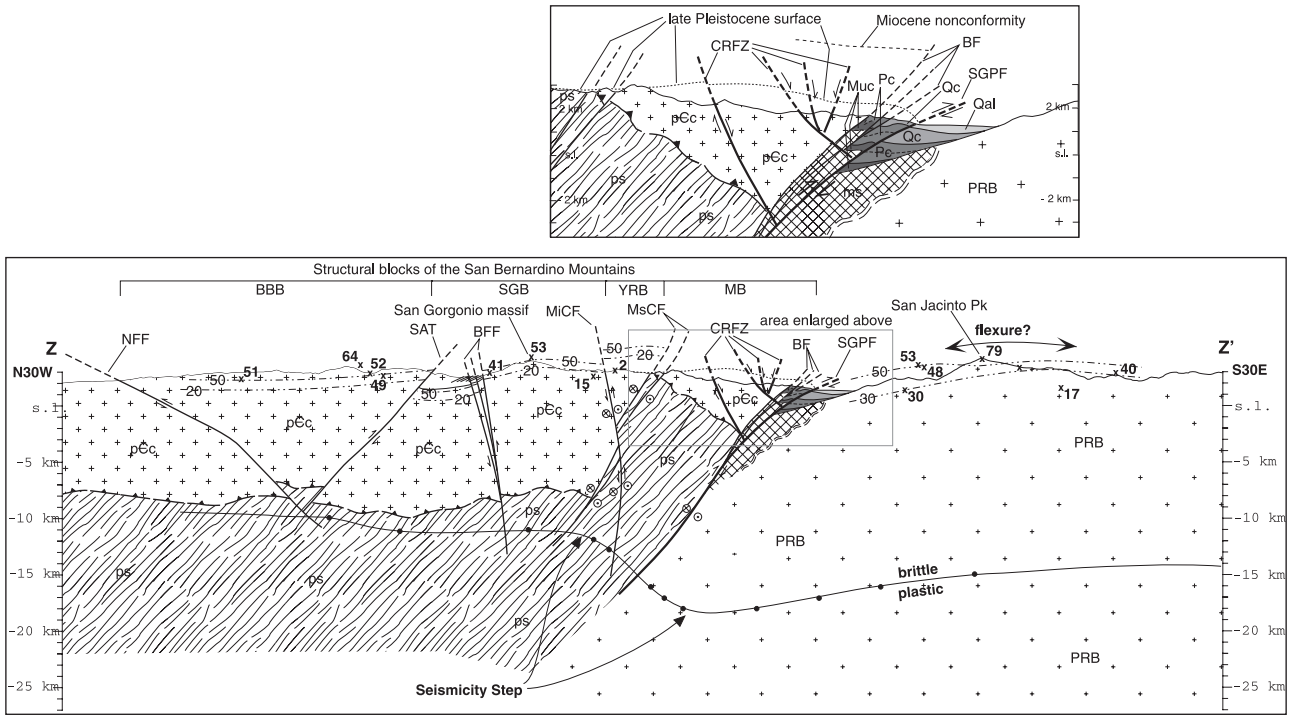

Figure 16. Interpretive regional cross section that is consistent with surface geologic observations and regional seismicity. See Figure 15 for line of cross section. Faults are projected downward based on surface dips, taken from *Allen* [1957], *Dibblee* [1982], *Matti et al.* [1985], and this study. Basement units are juxtaposed by strike slip on the Mission Creek fault and the ancestral Banning-San Gabriel fault [*Matti and Morton*, 1993]. The Pelona schist occupies the deepest structural level in the eastern Transverse Ranges suggesting that it comprises the deep crust beneath the granitic upper crust of the San Bernardino Mountains [*Matti and Morton*, 1993]. Exposures of the Pelona schist to the north of Burro Flats beneath the Vincent thrust (Figure 3a) indicate that it comprises much of the crust between the San Gorgonio Pass and Wilson Creek faults. The Banning and San Gorgonio Pass faults represent an in-sequence fold and thrust belt that has accommodated Quaternary south-under-north convergence between the San Bernardino and San Jacinto Mountains. Dashed-dotted parallel lines are the 20 and 50 Ma and the 30 and 50 Ma helium isochrons interpreted for the San Bernardino Mountains [*Spotila et al.*, 1998] and the San Jacinto Mountains [*Wolf et al.*, 1997]. Helium data, bold 'x' and number, projected perpendicular to cross sections. The He isochrons are elevated and depressed to the north and south of the San Gorgonio Pass fault, consistent with south-under-north convergence and associated regional warping (Figure 2a). Abbreviations of structural blocks as shown in Figure 2b; rock unit abbreviation as in Figure 3. Fault abbreviations: NFF, North Frontal fault; SAT, Santa Ana thrust; BFF, Barton Flats fault; MiCF, Mill Creek fault; MsCF, Mission Creek fault; CRFZ, Cox Ranch fault zone; BF, Banning fault; SGPFZ, San Gorgonio Pass fault.

(San Jacinto Mountains) with the eastern Transverse Ranges (San Bernardino Mountains). Below, we explain how we constructed this structure contour map.

6.4. Extrapolation of the 1986 Rupture Plane

[66] We have argued that the characteristics of the 1986 rupture are consistent with the Garnet Hill fault being the source of the 1986 North Palm Springs earthquake. The geographic coincidence of the 1986 fault rupture and the step in deepest seismicity (A-A', Figure 13) suggest to us that the Garnet Hill fault is responsible for the step in seismicity. Since the Garnet Hill fault appears to transform into the San Gorgonio Pass fault at Cottonwood Canyon, slip on the latter fault may also be responsible for the step in seismicity. Using the rupture plane defined by the 1986 main shock and aftershocks as a starting point, we have drawn structural contours for the entire San Gorgonio Pass-Garnet Hill fault system so that the fault planes extend downward from the surface to the middle of the step in seismicity (15-km depth) (Figure 15).

[67] The contours updip from the 1986 rupture represent the fault plane between the 1986 rupture plane and the surface trace of the Garnet Hill fault. Southeast of the 1986 rupture plane, the closer spacing of the contours and their more southerly trend are consistent with *Nicholson*'s [1996] mechanism for the 1948 earthquake and with the surface strike of the Garnet Hill fault. (To keep the figure uncluttered, contours of the Coachella Valley strand of the Banning fault do not appear in Figure 15. We envision this steeper strike-slip fault wholly within the hanging wall block of the Garnet Hill fault (Figure 14c).)

[68] Farther west, between the surface trace of SGPF zone and the seismicity step, the contours show a fault plane that steepens gradually from about 30° dips near the surface to

Table 1. Plausible Moment Magnitudes for Major Active Faults and Fault Systems

Name	Surface Area, km^2	d,[a] m	Moment,[b] Nm	M_W
Cox Ranch fault zone[c]	20 × 7 = 140	2.0	8.4×10^{18}	6.6
Coachella Valley Banning-Garnet Hill faults[d]	CVB, 45 × 17 = 765; GHF, 30 × 5 = 150; total area = 915	3.5	9.6×10^{19}	7.3
San Gorgonio Pass fault[e]	55 × 22 = 1210	4.0	1.5×10^{20}	7.4
San Bernardino SAF[f]	80 × 15 = 1200	4.0	1.4×10^{20}	7.4
Coachella Valley SAF[g]	115 × 15 = 1725	4.0	2.1×10^{20}	7.5
SGP-GH-CVB	total area = 2125	4.5	2.9×10^{20}	7.6
CVSAF-CVBF-GHF	total area = 2640	5.0	4.0×10^{20}	7.7
All faults	total area = 5190	5.0	9.3×10^{20}	7.9

[a]Average surface displacement.
[b]We assume a shear modulus of 3×10^{10} Nm^{-2}.
[c]This includes all sections of the fault system.
[d]This assumes that the western end of the CVB is at Cottonwood Canyon and that the CVB and GH faults merge at a depth of about 5 km.
[e]This assumes the active portion extends from Calimesa to Cottonwood Canyon.
[f]This includes the active portion of the Gandy Ranch and Banning faults, near Millard Canyon.
[g]This assumes the active portion extends from the Salton Sea to Highway 62.

about 60° dips at about 15 km. This convex-upward geometry in the fault plane is consistent with minor extension within the hanging wall block along the Cox Ranch fault zone (Figure 2a), and with the broad fold in the Morongo block (Figure 2b). First-order irregularities in the strike of the seismicity step (Figure 13) suggest the existence of a few bends in the plane of the SGPF at the seismicity step.

[69] The biggest challenge in creating a structure contour map of the fault zone is the sharp transition from oblique slip to thrust faulting that *Morton et al.* [1987], *Matti and Morton* [1993], and we have mapped at Cottonwood Canyon. To be consistent with this markedly abrupt change in surficial expression of faulting, we have chosen to bend the structure contours sharply at Cottonwood Canyon. We have drawn the down-plunge projection of this bend as a broad warp pointing toward the aftershock region of the 1986 earthquake (dashed outline, Figure 15). If correct, this would predict that the rake of the 1986 slip vector changes from relatively more oblique to relatively more strike slip from west to east, respectively. Whether first motion solutions of the aftershocks reflect this change is not known.

7. Tests of the Concept

[70] The three-dimensional geometry that we propose for the San Andreas fault zone through the San Gorgonio Pass stepover has implications for the geologic history of the region. If the San Gorgonio Pass-Garnet Hill fault were to have formed the entire 5–8 km high seismicity step as an offset, total uplift across the faults would have to equal 5–8 km. This is inconsistent with the geologic history of these faults. Total slip across the Garnet Hill and SGPFs is almost certainly too small and their history too short [*Matti and Morton*, 1993] to account for the entire 5–8 km high step in seismicity. Furthermore, these faults have not been active long enough to have accrued such large offsets, even if they were to have carried the entire 25 mm/yr of the entire San Andreas fault zone during their short lifetimes. Near-surface vertical offsets across these two faults are probably no more than about 1 km, and they have probably not been active for more than a 125,000 years or so [*Matti and Morton*, 1993].

[71] To create the entire seismic step by offset on reverse faults, the currently inactive reverse faults farther north would need to be called upon. Figure 16 consists of a cross section across the faults, the seismicity step, and related structures. It shows that vertical offset across the entire system of faults could be as great as about 3–5 km, about 50–75% of what would be needed to account for the step in seismicity. We estimated this vertical offset by projecting the Miocene nonconformity, dipping about 15°–20° toward the east in the Whitewater Canyon area [*Allen*, 1957], westward to the line of cross section (Figure 16). Much if not all of the slip on these faults occurred after deposition of the late Pliocene Painted Hill Formation, and perhaps as recently as after the deposition of the late Pleistocene Cabezon Formation.

[72] We do not consider the apparent shortfall in the vertical offset near the surface across the San Gorgonio and Banning faults to be a flaw in the model. Rather, as *Magistrale and Sanders* [1996] concluded, a rheological difference in basement rocktypes at depth can explain the remainder of the step in seismicity, with relatively weak quartz-rich crust on the north (Pelona schist) and relatively strong feldspar-rich rocks on the south (Peninsular Ranges batholith). A combination of vertical offset and rheologic differences across the SGPF can therefore account for the 5–8 km seismicity step (Figure 13). Furthermore, we show Pelona schist at a depth of 8–10 km beneath the San Bernardino Mountains (to the north of the Mill Creek fault). This not only explains the unusually shallow seismicity there [*Magistrale and Sanders*, 1996], but might represent the detachment surface proposed by *Hadley and Kanamori* [1977] and *Nicholson et al.* [1986] for this depth in the San Gorgonio Pass region.

8. Implications for Future Ruptures

[73] We have proposed a structural model, modified from the work of *Allen* [1957], *Matti et al.* [1992a], and *Matti and Morton* [1993], that involves a gradual northwestward transformation of the San Andreas fault from a near-vertical strike-slip fault (in the southeastern Coachella Valley) into a shallow-dipping, oblique-reverse fault (along the southern margin of the San Bernardino Mountains). In contrast, the

joint between the near-vertical strike-slip San Bernardino strand of the fault and the oblique-reverse segment is abrupt. What are the implications of this structural model for future large earthquakes there?

[74] First, it defines a plausible geometry for future earthquake sources. This is a critical initial step in modeling the seismic energy released by rupture of the various fault planes. Table 1 shows the area of the active fault planes we have mapped and extrapolated to depth. Average displacements are approximate and depend on poorly constrained slip rates. In addition, our model provides crude characterization of the slip vectors we would expect on the various seismic sources.

[75] Second, it provides a better basis for quantitative modeling of dynamic rupture propagation through the fault zone in this region. Can ruptures propagate through, or is this a ''knot'' as suggested by *Sykes and Seeber* [1985]. A rupture of some or all of the faults in the pass region would likely produce rupture delays at stepovers, similar to those observed during the Landers quake [*Wald and Heaton*, 1994].

[76] Third, it provides a starting point for analysis of the partitioning of 20–25 mm/yr through the region on the various faults, by rotations, and by folding. Slip-rate studies can test hypotheses implicit in our model, such as the transfer of slip off the Coachella Valley strand of the Banning fault and onto the Garnet Hill fault. Individual ruptures must sum to create the cumulative neotectonic motions. But once slip and rotation rates are known, we can construct scenario events for this section of the fault zone that will include the lesser normal-oblique faults and folds.

[77] Fourth, our structural model provides a context in which to understand paleoseismic data, which could be one of the arbiters of whether or not the several faults move in conjunction or separately. Does the structurally complex San Gorgonio Pass region block or inhibit throughgoing rupture [*Sykes and Seeber*, 1985]? Paleoseismic data permit the correlation of certain events reported from sites between Pallett Creek on the northwest and Indio on the southeast, over a distance of about 200 km [*Sieh and Jahns*, 1984; *Sieh et al.*, 1989; *Seitz et al.*, 1997; *Fumal et al.*, 1993; *Yule et al.*, 2001]. This suggests that the San Andreas fault system in San Gorgonio Pass might rupture in relatively infrequent large (*M*8) earthquakes from the Coachella Valley to the Mojave Desert, contradictory to the concept of a restraining bend acting as an impediment to throughgoing rupture.

[78] **Acknowledgments.** Our work in San Gorgonio Pass began in the late 1980s and early 1990s as a series of mapping exercises for undergraduate and graduate students. Later work was supported by the Southern California Earthquake Center (SCEC). SCEC is funded by NSF Cooperative Agreement EAR-8920136, USGS Cooperative Agreements 14-08-0001-A0899 and 1434-HQ-97AG01718. A portion of our work was also funded through SCEC by Pacific Gas and Electric. Thorough and constructive critiques were provided by *Journal of Geophysical Research* reviewers Jon Matti and Harold Magistrale. Early drafts benefited from reviews and conversations with Andrew Meigs, Jim Spotila, Anke Friederich, Yann Klinger, Jing Liu, and an initial GIS compilation of our data by Tony Soeller. We appreciate the cooperation and support of the Morongo Band of Mission Indians. Harold Magistrale generously provided hypocentral locations for microearthquakes in the San Gorgonio Pass region for the years 1981–1993. Jon Matti and Doug Morton kindly provided copies of unpublished geologic maps of the Cabazon and Whitewater 7.5' quadrangles. We are grateful to Richmond Wolf for providing us with his preliminary geologic maps of the Whitewater Hill-Garnet Hill region. Arnie N. Clyde enthusiastically provided field assistance. This is SCEC contribution no. 709 and Caltech Seismological Laboratory contribution no. 8981.

References

Ague, J., and M. Brandon, Tilt and northward offset of Cordilleran batholiths resolved using igneous barometry, *Nature*, *360*, 146–149, 1992.

Allen, C., San Andreas fault zone in San Gorgonio Pass, southern California, *Geol. Soc. Am. Bull.*, *68*, 315–350, 1957.

Anderson, R., Evolution of the Santa Cruz Mountains, California, through tectonic growth and geomorphic decay, *J. Geophys. Res.*, *99*, 20,161–20,180, 1994.

Barka, A., and K. Kadinsky-Cade, Strike-slip fault geometry in Turkey and its influence on earthquake activity, *Tectonics*, *7*, 663–684, 1988.

Cisternas, A., et al., The Spitak (Armenia) earthquake of 7 December 1988: Field observations, seismology, and tectonics, *Nature*, *339*, 675–679, 1989.

Clark, M., Map showing recently active breaks along the San Andreas fault and associated faults between the Salton Sea and Whitewater River-Mission Creek, California, *Misc. Geol. Invest. Map, I-1483*, U.S. Geol. Surv., Boulder, Colo., 1984.

Dibblee, T., Geologic map of the San Gorgonio Mountain 15′ quadrangle, San Bernardino and Riverside counties, scale 1:62,500, *Misc. Geol. Invest. Map, I-517*, U. S. Geol. Surv., Boulder, Colo., 1964.

Dibblee, T., Displacements on San Andreas fault system in San Gabriel, San Bernardino, and San Jacinto Mountains, southern California, in *Proceedings of Conference on Geologic Problems of San Andreas Fault System*, edited by W. R. Dickinson and A. Grantz, pp. 260–278, Stanford Univ. Press, Stanford, Calif., 1968.

Dibblee, T., Regional geologic map of San Andreas and related faults in eastern San Gabriel Mountains, San Bernardino Mountains, western San Jacinto Mountains and vicinity, Los Angeles, San Bernardino, and Riverside counties, California, *Open File Map*, U. S. Geol. Surv., Boulder, Colo., 1970.

Dibblee, T., Late quaternary uplift of the San Bernardino Mountains on the San Andreas and related faults, *Spec. Rep. Calif. Div. Mines Geol.*, *118*, 127–135, 1975.

Dibblee, T., Geology of the San Bernardino Mountains, southern California, in *Geology and Mineral Wealth of the California Transverse Ranges*, *South Coast Geol. Soc. Guideb.*, vol. 10 (Mason Hill volume), edited by D. L. Fife and J. A. Minch, pp. 148–169, South Coast Geol. Soc., Santa Ana, Calif., 1982.

Fumal, T., S. Pezzopane, I. R. Weldon, and D. Schwartz, A 100-year average recurrence interval for the San Andreas fault at Wrightwood, California, *Science*, *259*, 199–203, 1993.

Hadley, D., and H. Kanamori, Seismic structure of the Transverse Ranges, California, *Geol. Soc. Am. Bull.*, *88*, 1469–1478, 1977.

Harden, J., and J. Matti, Holocene and late Pleistocene slip rates on the San Andreas fault in Yucaipa, California, using displaced alluvial-fan deposits and soil chronology, *Geol. Soc. Am. Bull.*, *101*, 1107–1117, 1989.

Harris, R., and S. Day, Dynamics of fault interaction: Parallel strike-slip faults, *J. Geophys. Res.*, *98*, 4461–4472, 1993.

Hartzell, S., Comparison of seismic waveform inversion results for the rupture history of a finite fault: Application to the 1986 North Palm Springs, California, earthquake, *J. Geophys. Res.*, *94*, 7515–7534, 1989.

Hill, M., Anomalous trends of the San Andreas fault in the Transverse Ranges, California, in *Geology and Mineral Wealth of the California Transverse Ranges*, edited by D. L. Fife and J. A. Minch pp. 367–369, South Coast Geol. Soc., Santa Ana, Calif., 1982.

Jones, L., L. Hutton, D. Given, and C. Allen, The North Palm Springs, California, earthquake sequence of July 1986, *Bull. Seismol. Soc. Am.*, *76*, 1830–1837, 1986.

Keller, E., M. Bonkowski, R. Korsch, and R. Shiemon, Tectonic geomorphology of the San Andreas fault zone in the southern Indio Hills, Coachella Valley, California, *Geol. Soc. Am. Bull.*, *93*, 46–56, 1982.

Lisowski, M., W. Prescott, J. Savage, and M. Johnston, Geodetic estimate of coseismic slip during the 1989 Loma Prieta, California, earthquake, *Geophys. Res. Lett.*, *17*, 1437–1440, 1990.

Magistrale, H., and C. Sanders, Evidence from precise earthquake hypocenters for segmentation of the San Andreas fault in San Gorgonio Pass, *J. Geophys. Res.*, *101*, 3031–3041, 1996.

Marshall, G., R. Stein, and W. Thatcher, Faulting geometry and slip from co-seismic elevation changes: The 18 October 1989, Loma Prieta, California, earthquake, *Bull. Seismol. Soc. Am.*, *81*, 1660–1693, 1991.

Matti, J., and D. Morton, Paleogeographic evolution of the San Andreas fault in southern California: A reconstruction based on a new cross-fault correlation, *Geol. Soc. Am. Mem.*, *178*, 107–159, 1993.

Matti, J., D. Morton, and B. Cox, Distribution and geologic relations of fault systems in the vicinity of the central Transverse Ranges, southern

California, *U.S. Geol. Surv. Open File Rep. 85-365*, scale 1:25,0000, 27 pp., U.S. Geol. Surv., Reston, Va., 1985.

Matti, J., D. Morton, and B. Cox, The San Andreas fault system in the vicinity of the central Transverse Ranges province, southern California, *U.S. Geol. Surv. Open File Rep., 92-354*, 40 pp., U.S. Geol. Surv., Reston, Va., 1992a.

Matti, J., D. Morton, B. Cox, S. Carson, and T. Yetter, Geologic map of the Yucaipa 7.5′ quadrangle, California, *U.S. Geol. Surv. Open File Rep., 85-446*, 14 pp., U.S. Geol. Surv., Reston, Va., 1992b.

Morton, D., J. Matti, and J. Tinsley, Banning fault, Cottonwood canyon, San Gorgonio pass, southern California, in *Cordilleran Section of the Geological Society of America*, edited by M. Hill, pp. 191–192, Geol. Soc. of Am., Boulder, Colo., 1987.

Morton, D. M., and J. C. Matti, Extension and contraction within an evolving divergent strike-slip fault complex: The San Andreas and San Jacinto fault zones at their convergence in southern California, *Geol. Soc. Am. Mem.*, *178*, 217–230, 1993.

Nicholson, C., Seismic behavior of the southern San Andreas Fault Zone in the Northern Coachella Valley, California: Comparison of the 1948 and 1986 earthquake sequences, *Bull. Seismol. Soc. Am.*, *86*, 1331–1349, 1996.

Nicholson, C., L. Seeber, P. Williams, and L. R. Sykes, Seismicity and fault kinematics through the eastern Transverse Ranges, California: Block rotation, strike-slip faulting and shallow-angle thrusts, *J. Geophys. Res.*, *91*, 4891–4908, 1986.

Noble, L. F., The San Andreas rift and some other active faults in the desert region of southeastern California, *Year Book Carnegie Inst. Washington*, *25*, 415–435, 1926.

Noble, L. F., The San Andreas rift in the desert region of southeastern California, *Year Book Carnegie Inst. Washington*, *31*, 355–363, 1932.

Rasmussen, G., and W. Reeder, What happens to the real San Andreas fault at Cottonwood canyon, San Gorgonio pass, California?, in *Geology Around the Margins of the Eastern San Bernardino Mountains*, edited by M. A. Kooser and R. E. Reynolds, pp. 157–162, Inland Geol. Soc., Redlands, Calif., 1986.

Rice, J., and Y. Ben-Zion, Slip complexity in earthquake fault models, *Proc. Natl. Acad. Sci. U. S. A.*, *93*, 3811–3818, 1996.

Sadler, P. M., and W. A. Reeder, Upper Cenozoic, quartzite-bearing gravels of the San Bernardino Mountains, southern California; recycling and mixing as a result of transpressional uplift, in *Tectonics and Sedimentation Along Faults of the San Andreas System*, edited by D. W. Anderson and M. J. Rymer, pp. 45–57, Pac. Sect., Soc. of Econ. Paleontol. and Min., Los Angeles, Calif., 1983.

Sadler, P. M., A. Demirer, D. West, and J. M. Hillenbrand, The Mill Creek basin, the Potato sandstone, and fault strands in the San Andreas fault south of the San Bernardino Mountains, *Geol. Soc. Am. Mem.*, *178*, 289–306, 1993.

Seeber, L., and J. Armbruster, The San Andreas fault system through the Transverse Ranges as illuminated by earthquakes, *J. Geophys. Res.*, *100*, 8285–8310, 1995.

Seitz, G., R. Weldon, and G. P. Biasi, The Pitman Canyon paleoseismic record: A re-evaluation of southern San Andreas fault segmentation, *J. Geodyn.*, *24*, 129–138, 1997.

Sieh, K., Slip along the San Andreas fault associated with the great 1857 earthquake, *Seismol. Soc. Am. Bull.*, *68*, 1421–1428, 1978.

Sieh, K., and R. H. Jahns, Holocene activity of the San Andreas Fault at Wallace Creek, California, *Geol. Soc. Am. Bull.*, *95*, 883–896, 1984.

Sieh, K., and J. C. Matti, The San Andreas fault system between Palm Springs and Palmdale, southern California: Field trip guidebook, in *Earthquake Geology San Andreas Fault System Palm Springs to Palmdale*, pp. 1–12, Assoc. of Eng. Geol., South. Calif. Sec., 1992.

Sieh, K., and D. Natawidjaja, Neotectonics of the Sumatran fault, Indonesia, *J. Geophys. Res.*, *105*, 28,295–28,326, 2000.

Sieh, K., M. Stuiver, and D. Brillinger, A more precise chronology of earthquakes produced by the San Andreas fault in southern California, *J. Geophys. Res.*, *94*, 603–623, 1989.

Sieh, K., et al., Near-field investigations of the Landers earthquake sequence, April to July 1992, *Science*, *260*, 171–176, 1993.

Spotila, J., K. Farley, and K. Sieh, Uplift and erosion of the San Bernardino Mountains associated with transpression along the San Andreas fault, California, as constrained by radiogenic helium thermochronometry, *Tectonics*, *17*, 360–378, 1998.

Spotila, J., K. Farley, D. Yule, and P. Reiners, Near-field transpressive deformation along the San Andreas fault zone in southern California, based on exhumation constrained by (U-Th)/He dating, *J. Geophys. Res.*, *106*, 30,909–30,922, 2001.

Sykes, L., and L. Seeber, Great earthquakes and great asperities, San Andreas fault, southern California, *Geology*, *13*, 835–838, 1985.

van der Woerd, J., Y. Klinger, K. Sieh, P. Tapponier, and F. Reyerson, First long-term slip-rate along the San Andreas fault based on 10-Be-26Al surface exposure dating: The Biskra Palms site, 22 mm/yr for the last 30,000 years, *Eos Trans. AGU*, *82*(47), Fall Meet. Suppl., F934, 2001.

Vaughan, F., Geology of the San Bernardino Mountains north of San Gorgonio Pass, *Univ. Calif. Dept. Geol. Sci. Bull.*, *13*, 319–411, 1922.

Wald, D., and T. Heaton, Spatial and Temporal Distribution of Slip for the 1992 Landers, California, Earthquake, *Seismol. Soc. Am. Bull.*, *84*, 668–691, 1994.

Weldon, R., and K. Sieh, Holocene rate of slip and tentative recurrence interval for large earthquakes on the San Andreas fault, Cajon Pass, southern California, *Geol. Soc. Am. Bull.*, *96*, 793–812, 1985.

Wesnousky, S., and C. Jones, Oblique slip, slip partitioning, spatial and temporal changes in the regional stress field, and the relative strength of active faults in the Basin And Range, western United States, *Geology*, *22*, 1031–1034, 1994.

Wolf, R., K. Farley, and L. Silver, Assessment of (U-Th)/He thermochronometry: The low-temperature history of the San Jacinto Mountains, California, *Geology*, *25*, 65–68, 1997.

Yeats, R., Active faults related to folding, in *Active Tectonics*, edited by R. Wallace, pp. 63–79, Natl. Acad. Press, Washington, D. C., 1986.

Yule, J., T. Fumal, S. McGill, and G. Seitz, Active tectonics and paleoseismic record of the San Andreas fault, Wrightwood to Indio: Working toward a forecast for the next "Big Event," in *Geologic Excursions in the California Deserts and Adjacent Transverse Ranges*, edited by G. Dunne and J. Cooper, pp. 91–126, Pac. Sect., Soc. of Econ. Paleontol. and Min., Los Angeles, Calif., 2001.

K. Sieh, Seismological Laboratory, California Institute of Technology, Pasadena, CA 91125, USA.

D. Yule, Department of Geological Sciences, California State University, Northridge, CA 91330-8266, USA. (j.d.yule@csun.edu)

The enigmatic San Gorgonio Pass

Doug Yule
Department of Geological Sciences, California State University, Northridge, 18111 Nordhoff Street, Northridge, California 91330-8266, USA

The largest discontinuity along the San Andreas fault occurs in the San Gorgonio Pass (SGP) region of Southern California. Here, the San Bernardino and Coachella Valley strands (from the northwest and southeast, respectively) disaggregate into a family of irregular and discontinuous right-lateral, reverse, thrust, and oblique-normal faults (Fig. 1) (Allen, 1957; Matti et al., 1985; Matti and Morton, 1993; Yule and Sieh, 2003; Langenheim et al., 2005). Seismological studies also show that crustal deformation here is diffuse and distributed primarily on strike-slip and thrust faults at depths of ~5–20 km (Jones et al., 1986; Seeber and Armbruster, 1995; Magistrale and Sanders, 1996; Hauksson, 2000; Carena et al., 2004). Deformation along the San Andreas fault zone in the SGP region is therefore broadly distributed, in contrast to regions to the north and south where deformation is restricted to a much narrower zone.

Interpretations of the surface and subsurface data have produced competing three-dimensional (3-D) kinematic models for the SGP region. All models include a combination of thrust and strike-slip faulting. Based on their analysis of aligned nodal planes and slip vectors, Seeber and Armbruster (1995) proposed that a throughgoing, near-vertical strike-slip fault exists at depth beneath the active SGP thrust. In this model, the thrust has "beheaded" the active San Andreas fault in the upper 5 km of the crust. A second model envisions the San Andreas fault zone as a complex system of strike-slip and north-dipping thrust faults that transfer dextral-oblique slip through the SGP region (Matti and Morton, 1993; Magistrale and Sanders, 1996; Yule and Sieh, 2003; Carena et al., 2004). A third model is based on the analysis of gravity and aeromagnetic data that identify a buried magnetic source beneath the SGP. Langenheim et al. (2005) interpreted this to be a block of San Gabriel and/or Mojave/San Bernardino Mountains basement. In this model, a thrust-bounded wedge of Peninsular Ranges basement has been inserted beneath the Banning and SGP thrust faults and above the buried magnetic block.

Several researchers have used a relatively simple, vertical fault geometry to model the kinematics of the San Andreas fault in the SGP (Meade and Hager, 2005; Olsen et al., 2006; Smith and Sandwell, 2006). The choice to oversimplify the crustal structure at SGP relates to the limits of computing capacity and the difficulty in using dipping fault grids. Dair and Cooke (2009, p. 119 in this issue of *Geology*) have taken advantage of an ever-increasing computing capacity and the relatively new Southern California Earthquake Center Community Fault Model (CFM) (Plesch et al., 2007) to compare vertical versus dipping fault models in the SGP. By applying a 3-D numerical model to vertical and north-dipping scenarios, Dair and Cooke found that the dipping model provides a better match to the available strike-slip and uplift data for the San Andreas fault and southern San Bernardino Mountains. This innovative result implies that, at least in the case of SGP, an oversimplified fault model introduces systemic errors and yields flawed results. Given this result, it is intriguing to consider how model results may change in other regions where oversimplified fault geometries have been used.

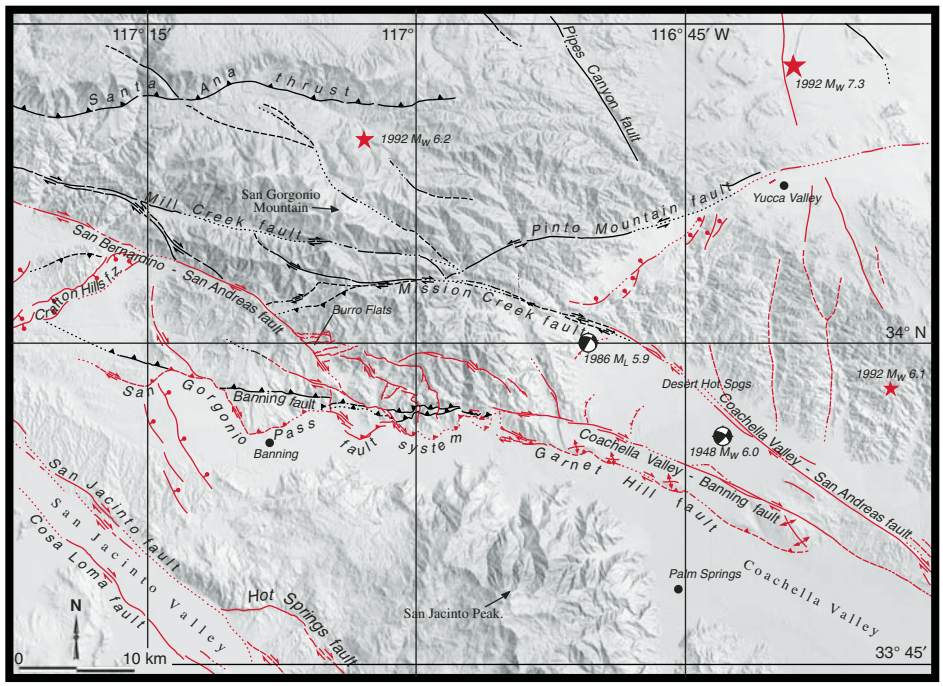

Figure 1. Shaded-relief topographic map of San Gorgonio Pass (SGP) region. Traces of active faults shown in red, inactive faults shown in black. Mapping from Allen (1957), Matti et al. (1985), and Yule and Sieh (2003). Beach-balls show epicenter and oblique slip during earthquakes on the north-dipping San Gorgonio Pass–Garnet Hill fault system at depth. Stars show epicenters of other earthquakes on faults outside of SGP.

All of the available data indicate that San Andreas fault slip decreases to a minimum of 5–10 mm/yr at the SGP, from 24 ± 3.5 mm/yr at Cajon Pass on the northwest and 12–22 mm/yr at Indio on the southeast (Weldon and Sieh, 1985; Yule and Sieh, 2003; Meade and Hager, 2005; Dair and Cooke, 2009; W. Behr, 2008, personal commun.). Even Dair and Cooke's vertical fault model reveals this trend. As they discuss, this decrease in slip can be explained by slip transfer to the west onto the San Jacinto fault zone and to the east onto the Eastern California Shear Zone. However, the geologic slip rates reported for SGP come from single fault strands, and therefore provide a minimum estimate. The broad zone of deformation defined by the active faults in Figure 1 suggests that an as yet undetermined amount of dextral slip is partitioned onto a number of structures in the SGP. It is conceivable that an additional 50% of dextral slip (3–5 mm/yr) could be carried by secondary structures (folds and faults) in SGP, increasing the total slip rate to 8–15 mm/yr. If correct, this overlaps with slip rates obtained from both the vertical and the dipping model of Dair and Cooke (2009). This point does not diminish their findings, but illustrates the need to continue this work as well as geologic slip-rate studies. For example, it would be interesting to take Dair and Cooke's study a step further and analyze a

© 2009 The Geological Society of America. For permission to copy, contact Copyright Permissions, GSA, or editing@geosociety.org.

Downloaded from http://pubs.geoscienceworld.org/gsa/geology/article-pdf/37/2/191/3941948/i0091-7613-37-2-191.pdf
by 13598

dipping fault model that incorporates all of the active faults in the SGP region (Fig. 1).

One overarching objective of the research in the SGP region is to answer a long-standing question: is a throughgoing San Andreas rupture possible? A definitive answer to this question has fundamental implications for forecasting the earthquake hazard in the Los Angeles region. If "yes," the region can expect relatively infrequent but very large earthquakes (~M_w 7.8) that rupture through SGP and simultaneously involve the Coachella Valley, San Bernardino, and the Mojave segments. If "no," the region can expect more frequent large earthquakes (~M_w 7) that separately rupture on either side of SGP. The available paleoseismic data show 5–6 rupture events since ca. A.D. 800 in the Mojave, SGP, and Coachella Valley regions that overlap in age by 50–100 yr (e.g., Weldon et al., 2004). Though these 5–6 events may record simultaneous very large throughgoing paleoearthquakes, it is equally possible that they represent separate, "smaller" events that were limited to either side of SGP but occurred within a 50–100 yr period.

"The Great Southern California ShakeOut," an emergency response and preparedness exercise held on 13 November 2008 (Jones et al., 2008), underscores the need for a definitive answer to the "is it possible" question above. Early in 2007, ~25 geoscientists met to decide upon a scenario earthquake for this exercise. A consensus view emerged to use a M_w 7.8 scenario earthquake on the San Andreas fault that initiates at the Salton Sea, ruptures through SGP, and ends in the central Mojave Desert. This worst-case scenario was used because the paleoseismic data cannot rule out the possibility that this type of an earthquake can occur, and many believed that it is better to prepare for a larger, more damaging earthquake. An alternative, though minority, opinion was held by some who argued in favor of a smaller scenario earthquake with limits at SGP, based on the hypothesis that the structural complexity of the SGP region forms a barrier against throughgoing rupture (Sykes and Seeber, 1985; Carena et al., 2004; Langenheim et al., 2005).

Evaluating the role that discontinuities like the SGP region play in arresting fault rupture remains a fundamental issue in earthquake science. Recent progress in this area includes analyses of historical earthquakes for which maps and coseismic slip distributions are known (Wesnousky, 2008). This novel approach shows that ruptures tend to end at >3–4 km steps (seen in map view), whereas they tend to continue through smaller geometric steps. It is intriguing to consider using this method to evaluate scenario earthquakes. For example, by studying the available active fault maps (e.g., CFM), one could test whether or not scenario ruptures violate the 3-4 km limit set by historical data, either by rupturing across a >3-4 km step or by stopping at a < 3-4 km step. At SGP, though disconnected, the active faults shown in Figure 1 reveal no step larger than 3 km. Assuming that slip occurs on all active structures in the SGP, the Wesnousky (2008) model therefore supports the M_w 7.8 ShakeOut scenario of a San Andreas fault earthquake rupturing through the SGP.

REFERENCES CITED

Allen, C.R., 1957, San Andreas fault zone in San Gorgonio Pass, Southern California: Geological Society of America Bulletin, v. 68, p. 315–350, doi: 10.1130/0016-7606(1957)68[315:SAFZIS]2.0.CO;2.

Carena, S., Suppe, J., and Kao, H., 2004, Lack of continuity of the San Andreas fault in Southern California: Three-dimensional fault models and earthquake scenarios: Journal of Geophysical Research, v. 109, B04313, doi: 10.1029/2003JB002643.

Dair, L., and Cooke, M.L., 2009, San Andreas fault geometry through the San Gorgonio Pass, California: Geology, v. 37, p. 119-122, doi: 10.1130/G25101A.1.

Hauksson, E., 2000, Crustal structure and seismicity distribution adjacent to the Pacific and North America plate boundary in Southern California: Journal of Geophysical Research, v. 105, p. 13,875–13,903, doi: 10.1029/2000JB900016.

Jones, L., Hutton, Given D., and Allen C., 1986, The North Palm Springs, California, earthquake sequence of July 1986: Seismological Society America Bulletin, v. 76, p. 1830–1837.

Jones, L.M., Bernknopf, R., Cox, D., Goltz, J., Hudnut, K., Mileti, D., Perry, S., Ponti, D., Porter, K., Reichle, M., Seligson, H., Shoaf, K., Treiman, J., and Wein, A., 2008, The ShakeOut Scenario: U.S. Geological Survey Open File Report 2008–1150, California Geological Survey Preliminary Report 25, version 1.0, 312 p.

Langenheim, V.E., Jachens, R.C., Matti, J.C., Hauksson, E., Morton, D.M., and Christensen, A., 2005, Geophysical evidence for wedging in the San Gorgonio Pass structural knot, southern San Andreas fault zone, Southern California: Geological Society of America Bulletin, v. 117, p. 1554–1572, doi: 10.1130/B25760.1.

Magistrale, H., and Sanders, C., 1996, Evidence from precise earthquake hypocenters for segmentation of the San Andreas fault in San Gorgonio Pass: Journal of Geophysical Research, v. 101, p. 3031–3041, doi: 10.1029/95JB03447.

Matti, J.C., and Morton, D.M., 1993, Paleogeographic evolution of the San Andreas fault in Southern California: A reconstruction based on a new cross-fault correlation, *in* Powell, R.E., Weldon, R.E., II, and Matti, J.C., eds., The San Andreas fault system: Displacement, palinspastic reconstruction, and geologic evolution: Geological Society of America Memoir 178, p. 107–159.

Matti, J.C., Morton, D.M., and Cox, B.F., 1985, Distribution and geologic relations of fault systems in the vicinity of the central Transverse Ranges, Southern California: U.S. Geological Survey Open-File Report 85–365, 23 p.

Meade, B.J., and Hager, B.H., 2005, Block models of crustal motion in Southern California constrained by GPS measurements: Journal of Geophysical Research, v. 110, B03403, doi: 10.1029/2004JB003209.

Olsen, K.B., Day, S.M., Minster, J.B., Cui, Y., Chourasia, A., Faerman, M., Moore, R., Maechling, P., and Jordan, T., 2006, Strong shaking in Los Angeles expected from southern San Andreas earthquake: Geophysical Research Letters, v. 33, L07305, doi: 10.1029/2005GL025472.

Plesch, A., Shaw, J.H., Benson, C., Bryant, W.A., Carena, S., Cooke, M., Dolan, J., Fuis, G., Garth, E., Grant, L., Hauksson, E., Jordon, T., Kamerling, M., Legg, M., Lindvall, S., Magistrale, H., Nicholson, C., Niemi, N., Oskin, M., Perry, S., Planansky, G., Rockwell, T., Shearer, P., Sorlien, C., Suss, M.P., Suppe, J., Treiman, J., and Yeats, R., 2007, Community fault model (CFM) for Southern California: Bulletin of the Seismological Society of America, v. 97, p. 1793–1802, doi: 10.1785/0120050211.

Seeber, L., and Armbruster, J.G., 1995, The San Andreas fault system through the Transverse Ranges as illuminated by earthquakes: Journal of Geophysical Research, v. 100, B5, p. 8285–8310, doi: 10.1029/94JB02939.

Smith, B.R., and Sandwell, D.T., 2006, A model of the earthquake cycle along the San Andreas Fault System for the last 1000 years: Journal of Geophysical Research, v. 111, B01405, doi: 10.1029/2005JB003703.

Sykes, L.R., and Seeber, L., 1985, Great earthquakes and great asperities, San Andreas fault, Southern California: Geology, v. 13, p. 835–838, doi: 10.1130/0091-7613(1985)13<835:GEAGAS>2.0.CO;2.

Weldon, R.J., and Sieh, K., 1985, Holocene rate of slip and tentative recurrence interval for large earthquakes on the San Andreas fault, Cajon Pass, Southern California: Geological Society of America Bulletin, v. 96, p. 793–812, doi: 10.1130/0016-7606(1985)96<793:HROSAT>2.0.CO;2.

Weldon, R.J., Scharer, K., Fumal, T., and Biasi, G., 2004, Wrightwood and the earthquake cycle: What a long recurrence record tells us about how faults work: GSA Today, v. 14, no. 9, doi: 10.1130/1052-5173(2004)014<4:WATECW>2.0.CO;2.

Wesnousky, S.G., 2008, Displacement and geometrical characteristics of earthquake surface ruptures: Issues and implications for seismic-hazard analysis and the process of earthquake rupture: Bulletin of the Seismological Society of America, v. 98, p. 1609–1632, doi: 10.1785/0120070111.

Yule, D., and Sieh, K., 2003, Complexities of the San Andreas fault near San Gorgonio Pass: Implications for large earthquakes: Journal of Geophysical Research, v. 108, ETG 9–1–9–23, doi: 10.1029/2001JB000451.

Printed in USA

Downloaded from http://pubs.geoscienceworld.org/gsa/geology/article-pdf/37/2/191/3941948/i0091-7613-37-2-191.pdf
by 13598

DAY 2 PAPERS

Quaternary Science Reviews 282 (2022) 107456

Contents lists available at ScienceDirect

Quaternary Science Reviews

journal homepage: www.elsevier.com/locate/quascirev

The late Holocene history of Lake Cahuilla: Two thousand years of repeated fillings within the Salton Trough, Imperial Valley, California

Thomas K. Rockwell [a, *], Aron J. Meltzner [b, c], Erik C. Haaker [d], Danielle Madugo [e]

[a] Dept. Geological Sciences, San Diego State University, San Diego, CA, 92182, USA
[b] Earth Observatory of Singapore, Nanyang Technological University, 639798, Singapore
[c] Asian School of the Environment, Nanyang Technological University, 639798, Singapore
[d] G3Soilworks, Inc., 350 Fischer Avenue, Costa Mesa, CA, 92626, USA
[e] Garrick Institute for the Risk Sciences, University of California Los Angeles, Engineering VI, Phase 1, 404 Westwood Plaza, Los Angeles, CA, 90095, USA

ARTICLE INFO

Article history:
Received 11 November 2021
Received in revised form
26 February 2022
Accepted 6 March 2022
Available online xxx

Handling Editor: Dr I Hendy

Keywords:
Lake Cahuilla
Lake chronology
Radiocarbon
Paleoseismology
Archaeology

ABSTRACT

To constrain the timing of the past seven lake highstands in the Salton Trough, we compiled 423 radiocarbon dates, of which 284 are reliable and have good stratigraphic control, from paleoseismic and archeological sites in the basin. We developed two OxCal models that assume most charcoal, wood, seeds, and twigs recovered from organic mats at or near the shoreline are derived from material that grew within the lake footprint, and therefore date a dry period between lakes. Charcoal samples collected from lacustrine clastic strata may have also been derived from fires burned during a dry period. As an initial constraint, we assume that samples older than those in earlier lake deposits have age inheritance. Assuming the dates are accurately described by their respective 2σ uncertainties, we ran all dates that would run in a preliminary OxCal model, and then removed those with a poor agreement index as defined in OxCal. From this, of the 423 total dates in the compilation, 151 dates are used in the base model and 149 dates are used in an alternative model, with the differences in the models resulting from choices of whether to include or exclude specific dates that may or may not be representative of a particular dry period between lakes. Where the two models agree, the results are robust, but where the models differ, any differences are taken as uncertainty in the lake ages. Historical accounts and a high-resolution paleohydrologic reconstruction allow us to refine some lake ages.

The age windows for the past seven Lake Cahuilla highstands are 1731–1733 CE (Lake A), 1618–1636 CE (Lake B), 1486–1503 CE (Lake C), 1118–1165 or 1192–1241 CE (Lake D), 1007–1070 CE (Lake E), 930–966 CE (Lake F), and 612–5 BCE (Lake G). These ages represent the maximum allowable ranges during which a lake may have filled the basin up to the +13 m highstand elevation; the basin may have been dry for significant portions of each time window, though the lake filling and desiccation episodes may have extended beyond the stated highstand age range for each lake. If the paleohydrologic constraints are ignored, some of the lakes may have initiated earlier, by up to three decades. Additional dates would be needed to further bracket the ages of the earlier lakes. Notably, 120 of the original 284 reliable dates were rejected because they clearly violate stratigraphic ordering, implying that more than 40% of all radiocarbon dates in the Salton Basin exhibit statistically significant age inheritance.
© 2022 The Author(s). Published by Elsevier Ltd. This is an open access article under the CC BY license (http://creativecommons.org/licenses/by/4.0/).

1. Introduction

Lake Cahuilla was a freshwater lake that filled the Salton Trough in southeastern California many times during the Holocene, up to the sill elevation at ~13 m above sea level (Sykes, 1937; Wilke, 1978; Waters, 1983; Philibosian et al., 2011). Each filling of Lake Cahuilla followed an avulsion of the Colorado River (Waters, 1983; Li et al., 2008), away from its usual southerly course to the Gulf of California, with flow instead directed west and north along the Alamo and New Rivers (Fig. 1). Six filling episodes resulting in full lakes have been recognized in the past ~1100 years, all of them from before written history in the Salton Basin, although there are oral Indigenous American accounts that record the latest filling (Modesto and

* Corresponding author.
E-mail addresses: trockwell@sdsu.edu (T.K. Rockwell), meltzner@ntu.edu.sg (A.J. Meltzner), ehaaker@g3soilworks.com (E.C. Haaker), daniellemadugo@gmail.com (D. Madugo).

https://doi.org/10.1016/j.quascirev.2022.107456
0277-3791/© 2022 The Author(s). Published by Elsevier Ltd. This is an open access article under the CC BY license (http://creativecommons.org/licenses/by/4.0/).

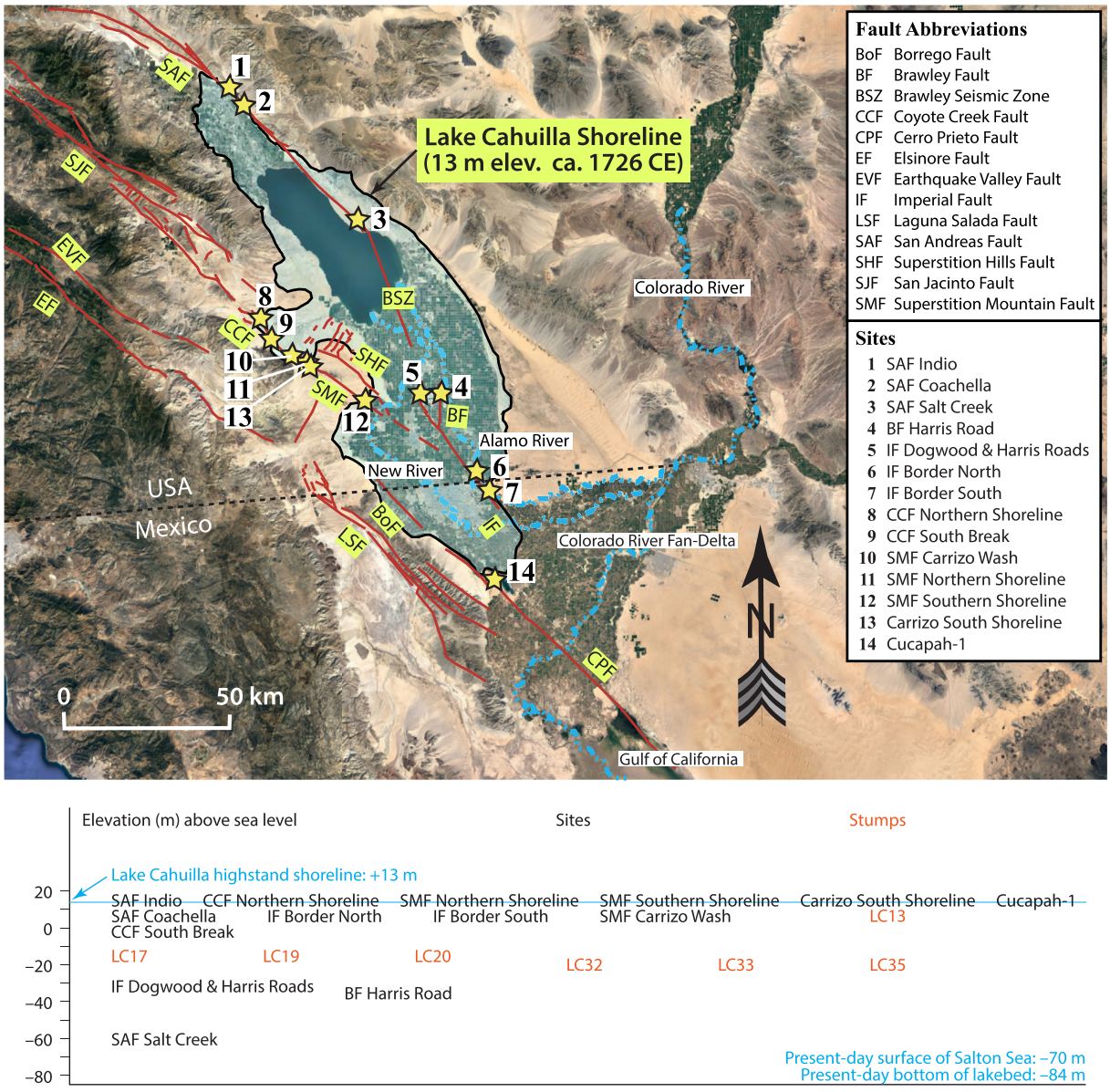

Fig. 1. *Top:* Map of the shoreline and inundation zone of Lake Cahuilla, outlined in black. Colorado River channels (including the Alamo and New Rivers) are marked as light blue dash-dotted lines. Faults (in red) are adapted from Fletcher et al. (2014), Rockwell et al. (2015), and U.S. Geological Survey and California Geological Survey (2020). Referenced sites are indicated by stars, with site names listed to the right. Stratigraphic descriptions and context of radiocarbon samples for sites 2 and 4–13 are provided in Supplementary Text S1 and Supplementary Figs. S1–S20 and were compiled from the following. Site 2: Philibosian et al. (2011); Site 4: Meltzner et al. (2006); Site 5: Meltzner (2006), Rockwell et al. (2011); Site 6: Jerrett (2015), Wessel (2015); Site 7: Thomas and Rockwell (1996); Site 8: Pollard and Rockwell (1995); Site 9: Orgil (2001); Site 10: Ragona, 2003, Verdugo (2004); Site 11: Gurrola and Rockwell (1996); Site 12: Faneros (2005); Site 13: White (2017). For Site 1 see Sieh (1986) and Sieh and Williams (1990); for Site 3 see Williams (1989) and Sieh and Williams (1990). Details for Site 14 are in Supplementary Table S1. *Bottom:* Sites (black text) arranged by elevation, along with the Lake Cahuilla highstand shoreline and lake bottom (blue text). Also shown are elevations of the mesquite stumps used in our model (red text; Rockwell et al., 2018). All elevations given relative to present mean sea level. (For interpretation of the references to colour in this figure legend, the reader is referred to the Web version of this article.)

Mount, 1980). The lake almost filled from an avulsion of the main channel in 1905 CE (Ross, 2020), which resulted in two years of flooding into the Salton depression; the Salton Sea is a remnant of that flooding episode (Cory, 1913; Sykes, 1937) and persists due to irrigation run-off and leakage from unlined canals.

Resolving the precise timing of these past lakes is important from several perspectives. For one, the shorelines of the lakes were occupied by the Cahuilla and Kumeyaay Indigenous Americans (Laylander, 1997, and references therein), so a precise lake chronology provides a temporal framework to interpret past occupation events. Archeological sites are also found below the highstand shoreline of Lake Cahuilla, and the precise lake timing is relevant for these occupations as well.

Another motivation is that the lake paleo-shoreline crosses several major faults of the southern San Andreas fault system, which means that the lake sediments are an archive of the rupture history of much of the southern San Andreas system (Rockwell et al., 2018). Many of the faults have been studied at paleoseismic sites developed in the lacustrine deposits, but precise dating of the past earthquakes has been hampered in many of these studies by age inheritance in detrital charcoal. That is, the radiocarbon date on a piece of detrital charcoal dates to the time of wood growth and death and not the timing of the lake or deposit that hosts the charcoal. Further, most charcoal samples collected from lake

deposits must have originated either from outside the lake or from wood that grew in the lake footprint prior to inundation, as most wood does not grow under water, and wood does not burn underwater; these different possible origins lead to potentially clashing implications for each sample as they can pre-date or be equivalent to the age of any lake. Rockwell et al. (2018) avoided this ambiguity by dating in situ stumps that had been drowned by the most recent two highstands of the lake, but no in situ stumps have been found to date the earlier late Holocene lakes.

A precise lake chronology would allow a sequencing of earthquakes that overcomes the chronological limitations at individual sites, particularly sites where most samples have significant age inheritance. Paleoseismic records have been documented at sites that range from at or near the shoreline (+13 m: Sieh, 1986; Gurrola and Rockwell, 1996; Philibosian et al., 2011) to as low as 60 m below sea level (Sieh and Williams, 1990; Williams and Seitz, 2005, 2006; Rockwell et al., 2011), or imaged below the lake bottom (Brothers et al., 2009, 2011), and all sites have exposed multiple late Holocene lake phases.

Other applications of a precise lake chronology include studies of the Colorado River delta, an extensive fan delta system that is now host to extensive agriculture both north and south of the international border, as well as Baja California's capital and largest city, Mexicali. Knowing when water flowed north into the Salton Trough versus south to the Gulf provides information on the architecture of the delta.

The timing of the most recent Lake Cahuilla highstand ("Lake A″) has been well constrained by Rockwell et al. (2018) at CE 1726 ± 7 (2σ), based primarily on paired dates from in situ stumps that grew within the Lake Cahuilla footprint during the dry period prior to the most recent highstand, combined with early historical accounts. The timing of the penultimate lake highstand ("Lake B″) was moderately constrained at CE 1577 ± 67 (2σ), based on the aforementioned dates and a small selection of additional samples recovered from within Lake B and earlier deposits (Rockwell et al., 2018).

In this study, we build upon the model developed for the past two full lake inundations by Rockwell et al. (2018) by compiling and analyzing 423 radiocarbon dates from sites within the Lake Cahuilla footprint (Fig. 1; Supplementary Table S1). From this database, we develop a base model of the ages of lakes and intervening dry periods that is consistent with the data from the various sites within the lake. Using OxCal (Bronk Ramsey, 2008, 2009a) and the most recent radiocarbon calibration curve (IntCal20; Reimer et al., 2020), we extend the model back to include the past seven Lake Cahuilla highstands. In addition, we reorganize the structure of the OxCal model of Rockwell et al. (2018) to refine the ages of the past two highstands. We compare this model to the paleoclimate record of the Colorado Plateau region and inferred Colorado River flow (Meko et al., 2007; Robeson et al., 2020), which is the source region for >90% of the water that filled the various lake episodes (Rockwell et al., 2018). We then discuss how eliminating or adding a few dates, which may be outliers, affects the stability of the base model.

2. Prior work

2.1. Lake Cahuilla reconstructions: early efforts

Prior work to establish the chronology of lake highstands was undertaken by Wilke (1978), Waters (1983), Gurrola and Rockwell (1996), and Philibosian et al. (2011). Wilke (1978) focused on the late prehistoric human ecology at Lake Cahuilla. He applied ^{14}C dating on various cultural elements to establish that water had been in the basin, possibly intermittently, since about 900 CE, although all of his dates have large uncertainties of 100–200 years and are thus of limited use. Waters (1983) focused specifically on the history of highstands of Lake Cahuilla, but identified only four highstand episodes in the past 2 ka, and again, had large uncertainties associated with his ^{14}C dates. Gurrola and Rockwell (1996) worked at a site where the Superstition Mountain fault crosses the shoreline. They recognized 5 or 6 highstands and applied higher resolution ^{14}C dating to establish a chronology of these lakes. Philibosian et al. (2011), in contrast, recognized evidence for up to seven lakes at the Coachella paleoseismic site located at a few meters below the shoreline, although their lowest potential lake sequence had limited exposure, and therefore its interpretation is equivocal (Supplementary Text S1). They applied much higher resolution ^{14}C dates than in most prior work and we use most of these in our study. Nonetheless, each of these earlier studies was based on the limited number of dates available to the authors of those studies; there is significant room for improvement of the chronology from each of these earlier studies, which could be obtained by combining dates collected in recent decades from all the sites within the basin.

2.2. Stump dates and ages of the past two lakes

The most recent effort to refine the Lake Cahuilla chronology was undertaken by Rockwell et al. (2018), who dated stumps drowned by the past two lake inundations. Based on their new dates and analysis of historical constraints, they place the timing of the most recent full lake (Lake A) at CE 1726 ± 7 (2σ). This age accounts for three things: the stump ages that force the timing of the highstand into the 18th century; the written accounts by Kino that indicate that the Colorado River was flowing to the Gulf of California as late as 1706; and the lack of description of water in the basin when Anza's expedition traversed the region in 1774. The penultimate lake (Lake B) had a larger uncertainty of CE 1577 ± 67 (2σ) for two reasons: first, the age was based only on radiocarbon data with no historical constraints; and second, there is a bimodal probability distribution or double peak in the calibration curve for that time period, which tends to inhibit a narrow calibrated age window. Rockwell et al. (2018) did not attempt to refine the age estimates for any lakes prior to Lake B. In this paper, we build upon the work of Rockwell et al. (2018) by adding additional dates from Lake B strata, plus many more from older stratigraphy, spanning five older lakes (Lakes C, D, E, F, and G) (Table 1).

3. Methods

3.1. Depositional environments for radiocarbon samples

Apart from stumps in growth position, which will be discussed in the next section, samples were collected from one of seven depositional environments, each of which has specific implications for the interpretation.

Samples recovered from within laminated or thinly bedded silty and clayey units, interpreted as lacustrine deposits, are derived either from the desert floor below the shoreline (and incorporated into the lake strata during flooding of the basin) or from outside the lake. In Table 1, samples collected from lake strata are indicated as "La".

Some localities describe sediments interpreted as delta deposits, indicated in Table 1 as "De", which represent deposition during flooding of the Salton depression (e.g., Jerrett, 2015; Wessel, 2015). These strata are typically dominated by silt and sandy silt and are

Table 1
Sample details and stratigraphic context for modeled radiocarbon dates.

Lab Code *	Lab Sample #	Sample Name	Stratigraphic Unit	Depositional Environment **	Material	^{14}C age yr	± yr	Model 1 ***	Model 2 ***	OxCal Function	Site	Ref ****	Elevation m *****
Maximum age of dry period after Lake A (includes dates from post-Lake A desiccation)													
CAMS-LLNL	90755	BFH-C-25	130	Bu	charcoal	65	40	Include	Include	After	Brawley Harris Rd	M06	−36.5
CAMS-LLNL	90753	BFH-C-33	154–156	Fl or De	charcoal	70	40	Include	Include	After	Brawley Harris Rd	M06	−36.5
CAMS-LLNL	90756	BFH-C-30	130	Bu	charcoal	70	40	Include	Include	After	Brawley Harris Rd	M06	−36.5
CAMS-LLNL	90754	BFH-C-24	130	Bu	charcoal	80	30	Include	Include	After	Brawley Harris Rd	M06	−36.5
CAMS-LLNL	97476	SMF-S18	Q1	Fl	charcoal	85	40	Include	Include	After	SMF South Shoreline	F05	13
CAMS-LLNL	90752	BFH-C-29	156	Fl or De	charcoal	105	40	Include	Include	After	Brawley Harris Rd	M06	−36.5
CAMS-LLNL	97484	SMF-S38	Q1	Fl	charcoal	130	40	Include	Include	After	SMF South Shoreline	F05	13
		2382001-1	200	Ae	charcoal	230	50	Include	Include	After	SMF Carrizo Wash	R03	8
Maximum age of Lake A (burns from sites at the shoreline; wood could be derived from above or at shoreline)													
Beta	78082	CCF-T1-C3		Sh	charcoal	0	80	Include	Include	After	CCF North Shoreline	P95	13
Beta	37907	RIV-1182a		Cu	charcoal	50	60	Include	Include	After	RIV-1182	L97a	12.2
Beta	37906	RIV-1182b		Cu	charcoal	80	50	Include	Include	After	RIV-1182	L97a	12.2
Beta	57861	RIV-1349a		Cu	charcoal	80	70	Include	Include	After	RIV-1349	L97c	12.2
Beta	57860	RIV-1349b		Cu	charcoal	110	80	Include	Include	After	RIV-1349	L97c	12.2
Beta	37904	RIV-3682a			charcoal	210	50	Include	Include	After	RIV-3682	L97d	12.2
		IMP-5296		Cu	charcoal	220	70	Include	Include	After	IMP-5296	L97b	12.2
Beta	37911	RIV-3144a			charcoal	300	50	Include	Include	After	RIV-3144	L97a	12.2
Beta	37902	RIV-3682b			charcoal	320	60	Include	Include	After	RIV-3682	L97d	12.2
Beta	57863	RIV-1331		Cu	charcoal	320	90	Include	Include	After	RIV-1331	L97c	12.2
Dry period before Lake A or Maximum age of Lake A													
CAMS-LLNL	125189	Nb1m57A-b-hum	1La	La	humic	−5	30	Include	Include	Phase	SAF Coachella	P11	9
CAMS-LLNL	97478	SMF-S21	Q2	Sh	organic mat	80	40	Include	Include	Phase	SMF South Shoreline	F05	13
UCIAMS	157516	CSS-1P-twig		Sh	charcoalized twig in org. mat	90	40	Include	Include	Phase	Carrizo South Shoreline	W17	13
UCIAMS	35630	Nb1m22A-c	1Lb	La	charcoal	105	20	Include	Include	Phase	SAF Coachella	P11	9
UCIAMS	35404	Nb1m45A-c	1S	Ae (or Sh)	charcoal	125	20	Include	Include	Phase	SAF Coachella	P11	9
UCIAMS	47182	IFD-T2-C61a	240 (?)	Fl or La	charcoal	130	15	Include	Include	Phase	Imperial Dogwood Rd	R11	−32
UCIAMS	157512	CSS-1P-2w		Sh	wood from organic mat	145	15	Include	Include	Phase	Carrizo South Shoreline	W17	13
UCIAMS	157518	CSS-8P-1		Sh	charcoal from organic mat	150	20	Include	Include	Phase	Carrizo South Shoreline	W17	13
UCIAMS	55811	IFD-T2-C61b	240 (?)	Fl or La	charcoal	155	20	Include	Include	Phase	Imperial Dogwood Rd	R11	−32
QL	4647	C28	P1	Sh	bulk date on organic mat	159	14	Include	Include	Phase	SMF North Shoreline	G96	13
UCIAMS	157522	CSS-9P-1		Sh	charcoal from organic mat	160	60	Include	Include	Phase	Carrizo South Shoreline	W17	13
UCIAMS	35405	Nb1m51A-c	1S	Ae (or Sh)	charcoal	175	15	Include	Include	Phase	SAF Coachella	P11	9
QL	4648	C47	P1	Sh	bulk date on organic mat	177	14	Include	Include	Phase	SMF North Shoreline	G96	13
UCIAMS	157513	CSS-1P-2c		Sh	charcoal from organic mat	180	20	Include	Include	Phase	Carrizo South Shoreline	W17	13
UCIAMS	157520	CSS-8P-3		Sh	charcoal from organic mat	180	20	Include	Include	Phase	Carrizo South Shoreline	W17	13
UCIAMS	157521	CSS-8P-4		Sh	charcoal from organic mat	180	25	Include	Include	Phase	Carrizo South Shoreline	W17	13
QL	4649	C18	P2	Sh	bulk date on organic mat	190	90	Include	Include	Phase	SMF North Shoreline	G96	13
QL	643	CAH-80-4		La	organic mat	192	50	Include	Include	Phase	SAF Indio	S90	13
UCIAMS	157519	CSS-8P-2		Sh	charcoal from organic mat	195	20	Include	Include	Phase	Carrizo South Shoreline	W17	13
CAMS-LLNL	125108	Nb1m57A-b-AAA	1La	La	AAA	200	35	Include	Include	Phase	SAF Coachella	P11	9
UCIAMS	35408	Sb1m44A-c	1S	Ae (or Sh)	charcoal	210	15	Include	Include	Phase	SAF Coachella	P11	9
UCIAMS	157515	CSS-1P-3c		Sh	charcoal from organic mat	220	25	Include	Include	Phase	Carrizo South Shoreline	W17	13

Table 1 (*continued*)

Lab Code *	Lab Sample #	Sample Name	Stratigraphic Unit	Depositional Environment **	Material	^{14}C age yr	± yr	Model 1 ***	Model 2 ***	OxCal Function	Site	Ref ****	Elevation m *****
UCIAMS	157517	CSS-1P-seeds		Sh	seeds from organic mat	230	25	Include	Include	Phase	Carrizo South Shoreline	W17	13
QL	4654	P2b	P2	Sh	bulk date on organic mat	230	40	Include	Include	Phase	SMF North Shoreline	G96	13
QL	642	CAH-80-3		La	organic mat	231	45	Include	Include	Phase	SAF Indio	S90	13
AA	33526	SB 14C-117	C1	La	charcoal	235	60	Include	Include	Phase	CCF South Break	O01	−4
AA	33524	SB 14C-107	C1	La	charcoal	250	55	Include	Include	Phase	CCF South Break	O01	−4
UCIAMS	155645	IFBT2-127	220–270	Fl or De	charcoal	255	15	Include	Include	Phase	Imperial Border North	J15	8
CAMS-LLNL	125109	Nb1m57A-c	1La	La	charcoal	260	40	Include	Include	Phase	SAF Coachella	P11	9
UCIAMS	157523	CSS-9P-2		Sh	charcoal from organic mat	265	25	Include	Include	Phase	Carrizo South Shoreline	W17	13
UCIAMS	155637	IFBT1-47	200	La	charcoal	275	20	Include	Include	Phase	Imperial Border North	W15	8
UCIAMS	157525	CSS-6		Sh	charcoal	280	25	Include	Include	Phase	Carrizo South Shoreline	W17	13
UCIAMS	157524	CSS-3		Sh	charcoal	290	20	Include	Include	Phase	Carrizo South Shoreline	W17	13
UCIAMS	155649	IFBT2-141	220	De	charcoal	310	15	Include	Include	Phase	Imperial Border North	J15	8
AA	33525	SB 14C-115	C1	La	charcoal	350	55	Include	Include	Phase	CCF South Break	O01	−4
UCIAMS	111439	LC32 outer		–	in situ stump below Lake A	70	20	Include	Include	Sequence		H12	−20
UCIAMS	111438	LC32 inner		–	in situ stump below Lake A	215	20	Include	Include	Sequence		H12	−20
UCIAMS	111435	LC17 outer		–	in situ stump below Lake A	115	20	Include	Include	Sequence		H12	−16
UCIAMS	101759	LC17 inner		–	in situ stump below Lake A	130	15	Include	Include	Sequence		H12	−16
UCIAMS	111436	LC19 outer		–	in situ stump below Lake A	115	20	Include	Include	Sequence		H12	−15
UCIAMS	101761	LC19 inner		–	in situ stump below Lake A	205	15	Include	Include	Sequence		H12	−15
UCIAMS	111441	LC33 outer		–	in situ stump below Lake A	125	20	Include	Include	Sequence		H12	−20
UCIAMS	111440	LC33 inner		–	in situ stump below Lake A	125	20	Include	Include	Sequence		H12	−20
UCIAMS	111443	LC35 outer		–	in situ stump below Lake A	125	20	Include	Include	Sequence		H12	−20
UCIAMS	111442	LC35 inner		–	in situ stump below Lake A	205	15	Include	Include	Sequence		H12	−20
UCIAMS	111437	LC20 outer		–	in situ stump below Lake A	155	20	Include	Include	Sequence		H12	−15
UCIAMS	101762	LC20 inner		–	in situ stump below Lake A	160	15	Include	Include	Sequence		H12	−15
UCIAMS	111434	LC13 outer		–	in situ stump below Lake A	180	20	Include	Include	Sequence		H12	8
UCIAMS	101757	LC13 inner		–	in situ stump below Lake A	180	15	Include	Include	Sequence		H12	8
Dry period before Lake B or Maximum age of Lake B													
UCIAMS	155639	IFBT2-109	361	De	charcoal	230	170	Include	Include	Phase	Imperial Border North	J15	8
UCIAMS	35427	Sb3m45A-c	2Ld	La	charcoal	310	15	Include	Include	Phase	SAF Coachella	P11	9
QL	4651	C25b	P3	Sh	charcoal from organic mat	310	40	Include	Include	Phase	SMF North Shoreline	G96	13
UCIAMS	48820	IFD-T2-C67	306	La	charcoal	320	15	Include	Include	Phase	Imperial Dogwood Rd	R11	−32
UCIAMS	155615	IFBT1-15	355	De	charcoal	330	15	Include	Include	Phase	Imperial Border North	W15	8
UCIAMS	35412	Sb2m10A-c	2Ld	La	charcoal	335	15	Include	Include	Phase	SAF Coachella	P11	9
UCIAMS	35426	Sb3m44A-c	2Ld	La	charcoal	335	20	Include	Include	Phase	SAF Coachella	P11	9
UCIAMS	183592	SB 3DIII-23B	C3	–	in situ bush below Lake B	350	15	Include	Include	Phase	CCF South Break	O01	−4
CAMS-LLNL	73117	SB 3DIII-23A	C3	–	in situ bush below Lake B	350	40	Include	Include	Phase	CCF South Break	O01	−4
UCIAMS	35413	Sb2m10B-c	2Ld	La	charcoal	360	25	Include	Include	Phase	SAF Coachella	P11	9
UCIAMS	35428	Sb3m48A-c	2Ld	La	charcoal	380	15	Include	Include	Phase	SAF Coachella	P11	9
CAMS-LLNL	128364	Sb2m26A-c	2Lb	La	charcoal	385	35	Include	Include	Phase	SAF Coachella	P11	9
CAMS-LLNL	97482	SMF-S29	Q3	Sh	charcoal	395	40	Include	Include	Phase	SMF South Shoreline	F05	13
CAMS-LLNL	128363	Nb2m36A-c	2Lb	La	charcoal	400	30	Include	Include	Phase	SAF Coachella	P11	9

(*continued on next page*)

Table 1 (*continued*)

Lab Code *	Lab Sample #	Sample Name	Stratigraphic Unit	Depositional Environment **	Material	^{14}C age yr	± yr	Model 1 ***	Model 2 ***	OxCal Function	Site	Ref ****	Elevation m *****
QL	4650	C20 (1)	D	Fl	charcoal	450	70	Include	Include	Phase	SMF North Shoreline	G96	13
Dry period before Lake C or Maximum age of Lake C													
CAMS-LLNL	75451	SB 3DIII-40 /wd	D	Ae or De	wood	380	50	Include	Include	Phase	CCF South Break	O01	−4
UCIAMS	47204	IFD-T2-C36	342	La	charcoal	380	15	Include	Include	Phase	Imperial Dogwood Rd	R11	−32
AA	11063	C21a	F1	La	charcoal	387	55	Include	Include	Phase	SMF North Shoreline	G96	13
CAMS-LLNL	128362	Sb3m59A-c	3L	La	charcoal	435	35	Include	Include	Phase	SAF Coachella	P11	9
CAMS-LLNL	75462	SB 3DIII-40 /hu	D	Ae or De	humic	460	60	Include	Include	Phase	CCF South Break	O01	−4
UCIAMS	35449	T2-Sb2-3-c	3L	La	charcoal	530	15	Include	Include	Phase	SAF Coachella	P11	9
CAMS-LLNL	125190	Nb2m30A-b-hum	3L	La	humic	545	40	Include	Include	Phase	SAF Coachella	P11	9
UCIAMS	35448	T2-Sb2-2-c	3L	La	charcoal	580	15	Include	Include	Phase	SAF Coachella	P11	9
CAMS-LLNL	125110	Nb2m30A-b-AAA	3L	La	AAA	585	30	Include	Include	Phase	SAF Coachella	P11	9
UCIAMS	47190	IFD-T2-C47	356	La	charcoal	605	15	Include	Include	Phase	Imperial Dogwood Rd	R11	−32
UCIAMS	35629	T2-Sb2-9-c	3L	La	charcoal	605	20	Include	Include	Phase	SAF Coachella	P11	9
UCIAMS	35454	T2-Sb2-17-c	3L	La	charcoal	610	15	Include	Include	Phase	SAF Coachella	P11	9
UCIAMS	47194	IFD-T2-C11	349–354	La	charcoal	610	15	Include	Include	Phase	Imperial Dogwood Rd	R11	−32
CAMS-LLNL	128264	Nb3m41A-b-hum	4Sc	La	humic	610	30	Include	Include	Phase	SAF Coachella	P11	9
CAMS-LLNL	97481	SMF-S28	Q4	La	organic mat	610	40	Include	Include	Phase	SMF South Shoreline	F05	13
AA	9493	C14	G3	Fl	charcoal	615	60	Include	Include	Phase	SMF North Shoreline	G96	13
UCIAMS	48828	IFD-T5-C80	348–358	La	charcoal	615	15	Include	Include	Phase	Imperial Dogwood Rd	R11	−32
UCIAMS	48829	IFD-T5-C84	348–358	La	charcoal	625	15	Include	Include	Phase	Imperial Dogwood Rd	R11	−32
UCIAMS	47189	IFD-T2-C45	354/356	La	charcoal	625	15	Include	Include	Phase	Imperial Dogwood Rd	R11	−32
UCIAMS	47192	IFD-T2-C20	342/344	La	charcoal	630	15	Include	Include	Phase	Imperial Dogwood Rd	R11	−32
UCIAMS	48827	IFD-T5-C79	348–358	La	charcoal	630	15	Include	Include	Phase	Imperial Dogwood Rd	R11	−32
UCIAMS	47191	IFD-T2-C21	336	La	charcoal	640	15	Include	Include	Phase	Imperial Dogwood Rd	R11	−32
UCIAMS	88837	IFD-T9-C320	358/361	La	charcoal	640	30	Include	Include	Phase	Imperial Dogwood Rd	R11	−32
AA	11062	C20 (2)	F1	La	charcoal	643	60	Include	Include	Phase	SMF North Shoreline	G96	13
CAMS-LLNL	128352	Nb3m41A-b-AAA	4Sc	La	AAA	645	30	Include	Include	Phase	SAF Coachella	P11	9
UCIAMS	47187	IFD-T2-C44	342/344	La	charcoal	655	15	Include	Include	Phase	Imperial Dogwood Rd	R11	−32
UCIAMS	47188	IFD-T2-C49	346	La	charcoal	655	15	Include	Include	Phase	Imperial Dogwood Rd	R11	−32
UCIAMS	88833	IFD-T3-C180	360–385 (?)	La	charcoal	660	25	Include	Include	Phase	Imperial Dogwood Rd	R11	−32
CAMS-LLNL	128265	Nb2m44A-b-AAA	3L	La	AAA	665	30	Include	Include	Phase	SAF Coachella	P11	9
CAMS-LLNL	128353	Nb2m44A-b-hum	3L	La	humic	700	30	Include	Include	Phase	SAF Coachella	P11	9
AA	9492	C9	G3	Fl	charcoal	700	55	Include	Include	Phase	SMF North Shoreline	G96	13
CAMS-LLNL	125111	Nb3m20A-b-AAA	4Se	La	AAA	700	30	Include	Include	Phase	SAF Coachella	P11	9
CAMS-LLNL	125191	Nb3m20A-b-hum	4Se	La	humic	705	35	Include	Include	Phase	SAF Coachella	P11	9
CAMS-LLNL	128356	Nb4m28B-c	4Sf	Fl	charcoal	815	35	Include	Include	Phase	SAF Coachella	P11	9
AA	9490	C21b	F1	La	charcoal	905	60	Include	Include	Phase	SMF North Shoreline	G96	13
UCIAMS	35422	Sb3m4B-b-hum	4Sg	Fl	humic	915	15	Include	Not Dry?	Phase	SAF Coachella	P11	9
UCIAMS	35450	T2-Sb2-4-c	4S	Fl or La	charcoal	930	15	Include	Not Dry?	Phase	SAF Coachella	P11	9

Table 1 (*continued*)

Lab Code *	Lab Sample #	Sample Name	Stratigraphic Unit	Depositional Environment **	Material	^{14}C age yr	± yr	Model 1 ***	Model 2 ***	OxCal Function	Site	Ref ****	Elevation m *****
Dry period before Lake D or Maximum age of Lake D													
UCIAMS	35444	Sb4m26A-c	4La	La	charcoal	890	15	Poor Fit	Include	Phase	SAF Coachella	P11	9
UCIAMS	35628	Sb3m49A-b-hum	5S	De or La	humic	910	20	Include	Include	Phase	SAF Coachella	P11	9
UCIAMS	35429	Sb3m49A-b-AAA	5S	De or La	AAA	915	20	Include	Include	Phase	SAF Coachella	P11	9
CAMS-LLNL	128261	Nb5m28B-b-AAA	5S	De or La	AAA	935	30	Include	Include	Phase	SAF Coachella	P11	9
UCIAMS	35451	T2-Sb2-6-c	4L	La	charcoal	945	15	Include	Include	Phase	SAF Coachella	P11	9
CAMS-LLNL	128262	Nb5m28B-b-hum	5S	De or La	humic	955	30	Include	Include	Phase	SAF Coachella	P11	9
UCIAMS	35446	Sb4m27B-c	4La	La	charcoal	960	15	Include	Include	Phase	SAF Coachella	P11	9
CAMS-LLNL	128256	T2-Sb2-1-b-AAA	5Sa	De or La	AAA	960	30	Include	Include	Phase	SAF Coachella	P11	9
CAMS-LLNL	125218	Sb4m49B-b-hum	5S	De or La	humic	965	30	Include	Include	Phase	SAF Coachella	P11	9
UCIAMS	35445	Sb4m27A-c	4La	La	charcoal	980	15	Include	Include	Phase	SAF Coachella	P11	9
CAMS-LLNL	73111	3012	161	La	charcoal	980	30	Include	Include	Phase	SMF Carrizo Wash	R03	8
CAMS-LLNL	128351	Nb3m65B-b-AAA	5S	De or La	AAA	985	30	Include	Include	Phase	SAF Coachella	P11	9
CAMS-LLNL	128263	Nb3m65B-b-hum	5S	De or La	humic	995	35	Include	Include	Phase	SAF Coachella	P11	9
CAMS-LLNL	125217	Sb4m49B-b-AAA	5S	De or La	AAA	1030	35	Poor Fit	Include	Phase	SAF Coachella	P11	9
Dry period before Lake E or Maximum age of Lake E													
UCIAMS	90991	IFD-T4-C412	420 ddd–f	La	charcoal	845	15	Poor Fit	Not Dry?	Phase	Imperial Dogwood Rd	R11	−32
CAMS-LLNL	128361	Sb3m7A-c	5Ld	La	charcoal	955	30	Include	Not Dry?	Phase	SAF Coachella	P11	9
UCIAMS	75459	IFD-T2-C140	390	Bl	charcoal	1010	20	Include	Include	Phase	Imperial Dogwood Rd	R11	−32
UCIAMS	35424	Sb3m11A-c	5Ld	La	charcoal	1075	15	Include	Include	Phase	SAF Coachella	P11	9
UCIAMS	35420	Sb3m3B-c	5Ld	La	charcoal	1095	20	Include	Include	Phase	SAF Coachella	P11	9
CAMS-LLNL	128040	T9-103	160	La	charcoal	1100	30	Include	Include	Phase	SMF Carrizo Wash	This	8
UCIAMS	35419	Sb3m3A-c	5Ld	La	charcoal	1150	15	Include	Include	Phase	SAF Coachella	P11	9
Dry period before Lake F or Maximum age of Lake F													
UCIAMS	35416	Sb3m0B-c	6La SW	La	charcoal	1080	15	Include	Include	Phase	SAF Coachella	P11	9
UCIAMS	35417	Sb3m1B-c	6La SW	La	charcoal	1105	15	Include	Include	Phase	SAF Coachella	P11	9
UCIAMS	35407	Nb4m13B-c	6La SW	La	charcoal	1125	20	Include	Include	Phase	SAF Coachella	P11	9
CAMS-LLNL	73106	3001b	156	La	charcoal	1160	40	Include	Include	Phase	SMF Carrizo Wash	R03	8
CAMS-LLNL	128355	Nb4m13A-c	6Lb SW	La	charcoal	1185	30	Include	Include	Phase	SAF Coachella	P11	9
CAMS-LLNL	128359	Sb4m14A-c	7S SW	Fl	charcoal	1185	30	Include	Include	Phase	SAF Coachella	P11	9
		662001-1	157b	De or La	charcoal	1710	50	Include	Include	Phase	SMF Carrizo Wash	R03	8
UCIAMS	90988	IFD-T4-C406b	550–560 (?)	De or La or Bl	charcoal	1965	15	Include	Include	Phase	Imperial Dogwood Rd	R11	−32
UCIAMS	90985	IFD-T4-C398	501/510	La	charcoal	2035	15	Include	Include	Phase	Imperial Dogwood Rd	R11	−32
UCIAMS	90987	IFD-T4-C404	550–560 (?)	De or La or Bl	charcoal	2100	90	Include	Include	Phase	Imperial Dogwood Rd	R11	−32
UCIAMS	75461	IFD-T3-C159	501/510 FF	La (FF)	charcoal	2230	20	Include	Not Dry?	Phase	Imperial Dogwood Rd	R11	−32
UCIAMS	88835	IFD-T3-C200	500–501	La	charcoal	2275	25	Include	Not Dry?	Phase	Imperial Dogwood Rd	R11	−32
UCIAMS	90989	IFD-T4-C407	550–560 (?)	De or La or Bl	charcoal	2280	15	Poor Fit	Not Dry?	Phase	Imperial Dogwood Rd	R11	−32
UCIAMS	90557	IFD-T4-C362	503	Bl	charcoal	2330	15	Poor Fit	Not Dry?	Phase	Imperial Dogwood Rd	R11	−32
UCIAMS	75462	IFD-T1-C163	580	La	charcoal	2345	20	Poor Fit	Not Dry?	Phase	Imperial Dogwood Rd	R11	−32
UCIAMS	88836	IFD-T3-C204	480	Bl	charcoal	2355	35	Poor Fit	Not Dry?	Phase	Imperial Dogwood Rd	R11	−32
Dry period before Lake G or Maximum age of Lake G													
UCIAMS	90984	IFD-T4-C394b	600	La	charcoal	2115	15	Poor Fit	Include	Phase	Imperial Dogwood Rd	R11	−32

(*continued on next page*)

Table 1 (*continued*)

Lab Code *	Lab Sample #	Sample Name	Stratigraphic Unit	Depositional Environment **	Material	^{14}C age yr	± yr	Model 1 ***	Model 2 ***	OxCal Function	Site	Ref ****	Elevation m *****
UCIAMS	90983	IFD-T4-C390	600	La	charcoal	2190	110	Include	Include	Phase	Imperial Dogwood Rd	R11	−32
UCIAMS	90986	IFD-T4-C402	600	La	charcoal	2550	45	Include	Include	Phase	Imperial Dogwood Rd	R11	−32

* **Lab codes:** AA: NSF—Arizona AMS Facility at University of Arizona, Beta: Beta Analytic, CAMS-LLNL: Center for AMS at Lawrence Livermore National Lab, La Jolla: Scripps (now University of California San Diego), QL: Quaternary Isotope Lab (now University of Washington), TO: University of Toronto, UCIAMS: Keck—Carbon Cycle AMS Facility at University of California Irvine, UCLA: University of California Los Angeles, UCR: University of California Riverside, UGa: University of Georgia, Umich: University of Michigan.
** **Depositional environment abbreviations:** Ae: Aeolian, Bl: Sand blow, Bu: Burn horizon, Cu: Cultural, De: Deltaic, Fl: Fluvial, La: Lacustrine, Sh: Shoreline berm.
*** **Explanation of terms for Model 1 & 2 columns:** "Include": Date included in model. "Poor Fit": Date excluded a posteriori because the agreement index in OxCal was below 60%. "Not Dry?": Date excluded a priori in Model 2 as possibly coinciding with a lake highstand, as it does not cluster with other dates in the same lake package.
**** **References:** F05: Faneros (2005), G96: Gurrola and Rockwell (1996), H12: Haaker (2012), J15: Jerrett (2015), L97a: Arkush (1990) in Laylander (1997), L97b: Schaefer (1987) in Laylander (1997), L97c: Schaefer and Pallette (1993) in Laylander (1997), L97d: Yohe (1990) in Laylander (1997), M06: Meltzner et al. (2006), O01: Orgil (2001), P11: Philibosian et al. (2011), P95: Pollard and Rockwell (1995), R03: Ragona (2003), R11: Rockwell et al. (2011), S90: Sieh and Williams (1990), This: This paper, W15: Wessel (2015), W17: White (2017).
***** **All elevations given relative to present mean sea level.**

quite distinctive from the clay strata that are interpreted to represent deeper water deposition. Where overlain by clayey lake strata, the deltaic deposits are interpreted to be essentially the same age as the overlying lacustrine deposits as they likely represent the filling phase of the same lake.

Sediments interpreted as fluvial in origin, "Fl" in Table 1, are present between lake deposits at some localities (Gurrola and Rockwell, 1996; Faneros, 2005; Meltzner et al., 2006; Philibosian et al., 2011; Rockwell et al., 2011; Jerrett, 2015), and these demonstrably indicate a separation of one lake from another in that they must represent a "dry period" between lakes, or at least some lowering of the lake during a dry period. Samples from these deposits date a dry period prior to the overlying lake, but because of inheritance of older, sometimes reworked charcoal, they can be substantially older than the overlying lake strata.

Possible aeolian deposits, indicated "Ae", are found at a few sites (Orgil, 2001; Ragona, 2003; Philibosian et al., 2011), and they would indicate subaerial deposition, and therefore a lack of lake water. Samples recovered from these deposits give a maximum age for the overlying lake strata.

A few dates are on samples recovered from in situ surface burns at elevations below the highstand shoreline of Lake Cahuilla (Meltzner et al., 2006) and are indicated "Bu" in Table 1. These surfaces must represent a period of no water at the site.

Samples recovered from shoreline berm deposits ("Sh" in Table 1; e.g., Gurrola and Rockwell, 1996; Faneros, 2005; Philibosian et al., 2011; White, 2017) may be as young as the lake itself, although detrital charcoal still provides maximum ages (terminus post quem) for a lake. Eight of the dates in our model from shoreline berms are cultural and associated with an archeological site ("Cu" in Table 1). Some of these lend confirmation towards a post-1700 date for the most recent filling of Lake Cahuilla.

A number of the dated samples in our compilation originate from organic mats. The organic mats range from millimeters to a centimeter in thickness, and they were found exclusively at sites at an elevation between +9 m and +13 m, at or within 0.5 km of the highstand shoreline. These organic layers typically have sharp upper and lower contacts and are commonly interbedded with beach berm deposits. They are interpreted as the organic detritus that floated or was washed to the shoreline during inundation (Gurrola and Rockwell, 1996). Organic mats such as these rarely survive prolonged exposure, so their preservation in the sedimentary record is most readily explained if they were quickly buried by deltaic or littoral deposits in one or more storms in the same year. Fig. 2 compares an organic mat at the Gurrola and Rockwell (1996) site with the organic detritus that accumulated along the shore of nearby Laguna Salada during its filling in 1984, which we interpret as an analogous event: the material is strikingly similar in composition, and the organic detritus at Laguna Salada was subsequently buried by berm deposits produced by wind-driven waves.

3.2. Radiocarbon constraints: dated materials

Several types of organic materials have been collected and dated at the various sites around the basin. The most common are detrital charcoal; organic mat deposits or components therein (including humic acid dates); wood (including one humic acid date on a sample of wood); dead stumps in growth position buried by lake deposits; fish bone; and shell.

Many aspects of radiocarbon dating must be considered carefully in order to precisely and accurately determine the chronology of Lake Cahuilla. For charcoal, the "old wood problem" is well-recognized in archeological and paleoseismological studies (Blong and Gillespie, 1978; Schiffer, 1986; Erlandson and Rockwell, 1987; Gavin, 2001), as radiocarbon dates determine the time of wood growth and death, which for most vascular plants is the same year. As there must be some time lag between annual wood growth, the burning of the wood, and its transport and deposition, all radiocarbon dates on detrital charcoal have some age inheritance relative to the sediments that contain them. In the arid Salton Trough, this inheritance problem may be particularly noteworthy: the valley bottom below the shoreline of Lake Cahuilla is unlikely to burn in wildfires, as the vegetation density is low (Anderson et al., 2022; Monitoring Trends in Burn Severity MTBS, 2022). In contrast, there is abundant dry wood scattered across the basin floor, including above the shoreline, that may have been dead for a long time. The Cahuilla and Kumeyaay tribes needed wood for cooking fires (Aschmann, 1959; Weide, 1974; Wilke, 1978; Laylander, 1997), and the dry wood on the basin floor could have been easily utilized for this purpose; this may be the most common source of charcoal in our study area.

Many of the charcoal samples collected from sites at or below the highstand shoreline were observed as distributed or rare pieces within lacustrine and deltaic strata. The wood that burned to produce the charcoal would not have grown underwater, except for some woody vegetation that may have grown at the shoreline, and this raises an additional question: was the charcoal introduced from outside the lake footprint, or did it grow on the desert floor during dry periods and then get incorporated into the lake deposits during the inundation and lake phases? At the Imperial fault site at Dogwood Road, 16 km from the highstand shoreline, some charcoal

Fig. 2. The organic mat layers at the Northern Shoreline Site (upper right; Gurrola and Rockwell, 1996) are composed of charcoal and carbonized twigs, leaves, grass blades, and seeds. They are strikingly similar in composition to the organic detritus resulting from the 1984 flooding of Laguna Salada; the left photo shows an accumulation of organic detritus at the Laguna Salada shoreline that was subsequently buried by berm deposits produced by wind-driven waves. Based on the similarity between the deposits, we infer the organic mat deposits in Lake Cahuilla were also formed during inundation events. In the vertical trench exposure (upper right), the yellow-and-blue flagged nails define a stratigraphic contact; the dark organic mat below the nails is ~1 cm thick, and the field of view is roughly 20–25 cm wide. (For interpretation of the references to colour in this figure legend, the reader is referred to the Web version of this article.)

was found in clusters with as many as 30–50 pieces in a single bedded lacustrine stratum within a small, <1 m area (Rockwell et al., 2011). Such a dense cluster of charcoal is unlikely to have accumulated in a non-channelized deposit if the individual pieces had each floated in from beyond the distant shoreline; the wood is more likely to have grown and been burned nearby during a preceding dry period.

The organic mats are composed of organic detritus, including detrital charcoal, carbonized or charred twigs, carbonized seeds, wood, and carbonized leaves and grass fragments. Accelerator mass spectrometry (AMS) dating of different components extracted from individual organic mats has yielded suites of ages, each of which generally clusters about a common age, but which may have some components that are significantly older. The cluster of ages implies that most of the material likely grew within the lake footprint during the dry interval immediately prior to inundation, though a small fraction of the material may have grown during an earlier dry period or may have come in from beyond the lake shoreline when the lake was full.

Some of the dates on the organic layers are bulk dates where the entire stratum was dated. These fall into two categories: material with pretreatment limited to acid-only washing (described in Table 1 as "organic mats") versus bulk dates, also on organic mats, where the sample was washed in acid, alkali, and then more acid (referred to as "AAA" in Table 1). In our model, we treat the organic mat and AAA dates similarly. Because organic bulk dates contain a suite of materials that may span the preceding dry period, they represent not only a maximum age (terminus post quem) for the overlying lake deposits, but multiple organic bulk dates from the same horizon may help map out the extent of the preceding dry period. However, as there is little data on the preservation potential for organic material from early in a long dry period, the organic bulk dates may not map out the entirety of the preceding dry period. Additionally, as the organic bulk dates may contain still older charcoal, care must be taken to avoid overinterpreting individual, particularly isolated dates. Consequently, all of these organic bulk dates are expected to be older than the overlying lake stratum itself, but many dates will have only the inheritance that is residual from some portion of the immediately preceding dry phase.

Some dates were run on wood. Most of these are from the in situ mesquite stumps dated by Rockwell et al. (2018). These stumps were surrounded by coppice dunes that were covered in gastropod shells (*Physa humerosa*) from at least one lake inundation. The trees necessarily grew during some dry period prior to the most recent Lake Cahuilla highstand, and based on the ages of these stumps (some date to ~1700 CE or later) it is clear they are too young to have grown prior to the penultimate lake, so they must date the dry interval immediately prior to the most recent highstand.

In each case, the stump was sawed from its base and collected in its entirety, and the innermost and outermost 2–3 rings were sampled separately for radiocarbon dating (Rockwell et al., 2018). The respective dates from the inner and outer samples from each stump were paired together and nested in a sequence in the age model; growth rings were assumed to be annual, and the number of rings between the paired inner and outer samples was estimated and included in the age model as an additional constraint.

Composite charcoal dates (samples with multiple fragments of charcoal that are derived from different-aged pieces) are not used in the OxCal models that we present below, because an average of two detrital charcoal ages from different dry periods may not itself date a dry period. Additionally, we do not include fish bone and shell in our analysis because of the poorly constrained and potentially different radiocarbon reservoir corrections (R) that would be required to compare the various samples in the same model.

3.3. Summary of stratigraphic sites used in this study

Radiocarbon data from paleoseismic sites with constraints on lake stratigraphy (Sieh and Williams, 1990; Pollard and Rockwell, 1995; Gurrola and Rockwell, 1996; Thomas and Rockwell, 1996; Orgil, 2001; Ragona, 2003; Verdugo, 2004; Faneros, 2005; Meltzner et al., 2006; Philibosian et al., 2011; Rockwell et al., 2011; Jerrett, 2015; Wessel, 2015), a shoreline site (White, 2017), several archeological sites (Laylander, 1997), and scattered mesquite stumps (Haaker, 2012; Rockwell et al., 2018) have been compiled and considered in this analysis (Supplementary Table S1). Only some of the sites are previously published, but all unpublished dates are contained in MS theses at San Diego State University (SDSU) or in accessible technical reports, and a summary of the stratigraphic context of each date is provided in Supplementary Text S1 and Supplementary Figs. S1–S20. A brief overview of each site is provided here for context; see the supplementary material for a more complete description as well as a stratigraphic column for each site.

3.3.1 San Andreas fault sites

Three paleoseismic sites have been developed along the southernmost section of the San Andreas fault at or below the highstand shoreline of Lake Cahuilla: the Indio, Coachella, and Salt Creek sites. The Indio (Sieh, 1986) and Salt Creek (Williams, 1989) sites were never formally published so the radiocarbon dates published in abstract form are of limited use. However, some data are presented by Sieh and Williams (1990). The Coachella site (Philibosian et al., 2011) has a rich record of lakes and dates and provides the best chronologic and stratigraphic data from the northeastern margin of Lake Cahuilla.

3.3.2 Imperial and Brawley fault sites

Four sites have been studied along the Imperial and Brawley faults that yielded useful age data: the Brawley site at Harris Road (Meltzner et al., 2006), the Imperial site at Dogwood Road (Rockwell et al., 2011), and the northern (Jerrett, 2015; Wessel, 2015) and southern Imperial Border sites (Thomas and Rockwell, 1996).

3.3.3 San Jacinto fault sites

Five paleoseismic sites have been developed along strands of the southern San Jacinto fault that provide useful stratigraphic and age information for Lake Cahuilla: the Superstition Mountain Fault (SMF) South Shoreline (Faneros, 2005); SMF North Shoreline (Gurrola and Rockwell, 1996); Carrizo Wash (Ragona, 2003; Verdugo, 2004); Coyote Creek Fault (CCF) South Break (Orgil, 2001); and CCF Middle Break Northern Shoreline (Pollard and Rockwell, 1995) sites.

3.3.4 Other sites

Limited radiocarbon data are summarized from other sites, including the Carrizo South Shoreline site (White, 2017), which lies ~2 km east of the Gurrola and Rockwell (1996) site, and from a study of dead stumps that were inundated by the last Cahuilla highstand (Haaker, 2012; Rockwell et al., 2018).

3.3.5 Archeological sites

A number of data are also compiled from archeological sources that document periods of occupation at the shoreline during a lake highstand (Schaefer, 1987; Arkush, 1990; Yohe, 1990; Schaefer and Pallette, 1993; Laylander, 1997).

3.4. The base OxCal model (Model 1)

Of the 423 radiocarbon dates compiled for this assessment, 127 samples (black samples in Supplementary Table S1) were excluded a priori either because (1) a sample yielded a modern date, was assessed by the original authors to be a root, was collected from artificial fill, or had uncertain stratigraphic context; (2) a date was not ^{13}C corrected; or (3) there was an irregularity in date reporting. We also removed 12 samples (gray samples in Supplementary Table S1) that were collected from below a local unconformity where the specific lake associated with the sample could not be independently correlated. The remaining 284 samples have good stratigraphic control.

Next, we removed 120 samples (red samples in Supplementary Table S1) where the calibrated dates were older than the calibrated dates of two or more samples from underlying lakes (with fewer than 20 years of overlap between the respective 2σ probability density functions). Here we imposed a requirement that at least two samples from underlying lakes must be younger in order to remove a sample, to avoid potentially biasing the model by a single young outlier in an underlying lake. The 120 samples that were removed at this stage are interpreted as having age inheritance and therefore not representing the dry period immediately preceding the lake package they were found in. Notably, more than 40% of all stratigraphically well-defined dates (120 of 284) are out of sequence and clearly older than a stratigraphically lower lake, demonstrating significant age inheritance beyond the calibrated age uncertainty.

The reduced set of dates contains 164 stratigraphically consistent radiocarbon dates from sites within the Lake Cahuilla footprint or at the +13 m highstand shoreline (Supplementary Table S1). Of these dates, 10 were found at the +13 m shoreline and have cultural context: nine from archeological sites (Laylander, 1997) and one from a paleoseismic site (Pollard and Rockwell, 1995). All 10 dates provide information on the timing of an Indigenous American occupation and therefore a maximum age (terminus post quem) for the most recent lake highstand. An additional 154 samples were collected for geological studies and comprise detrital charcoal; wood; organic matter in condensed organic mats that include seeds, charcoal, charred twigs, wood, and leaves, most of which likely grew within the lake footprint during dry conditions and were drowned by the lake infilling; in situ stumps that also grew during dry conditions and were presumably drowned by the lake infilling; and humic acid dates on wood samples or other organic matter. These geological sites have the advantage of placing dates into a stratigraphic context where the samples can be related to a particular lake or inter-lake period.

We attempted to run an OxCal model with these 164 dates, grouping the samples in Phases according to the specific dry period they are inferred to have grown in, with the cultural samples from the shoreline providing only a maximum age constraint on the most recent highstand shoreline. However, a problem arose with one sample (Sb3m2A-c) that has a mean calibrated age ~600 years younger than any other sample at the same stratigraphic position and ~700 years younger than multiple samples that were stratigraphically higher: this sample caused the OxCal model to fail, i.e., OxCal yielded a “NULL distribution” error. After removing sample Sb3m2A-c, which we speculate was a root and treat as an outlier, we reattempted the OxCal model. This time, the model ran successfully (“Model 1: Initial Run” in Supplementary Text S2), but 12 dates yielded poor agreement indices (roughly equivalent to χ^2 test failure at 5%; Bronk Ramsey, 1995, 2009b). In our base model (Model 1) we assume the dates with poor agreement indices represent additional outliers. We thus removed the inferred outliers and reran the model with the remaining 151 dates, resulting in

a final base model ("Model 1: Final Version" in Supplementary Text S2; "Model 1" in Supplementary Table S1; Supplementary Fig. S21). In an alternative model (Model 2), discussed next, we will revisit the assumption that the dates with poor agreement indices are necessarily all outliers.

3.5. An alternative OxCal model (Model 2)

As discussed above, we assumed that each date with a poor agreement index in the initial run of Model 1 is an outlier and therefore does not represent the dry period immediately preceding the lake package the sample was found in. However, if OxCal encounters a conflict between dates in two sequential Phases (in two different lake packages) and the two Phases are not sampled evenly, the sampling bias may lead OxCal to prefer the dates in the more densely sampled lake, at the expense of the more sparsely sampled lake. In particular, the seventh lake back (Lake G) was exposed at only a few sites, in most cases below an unconformity, and only three useful dates that are definitively from this lake episode have so far been obtained at any site in the basin (Supplementary Table S1). In Model 1, our rule of using at least two dates from Lake G to determine which dates in Lake F are "too old" results in the inclusion of six dates in Lake F that are older than the youngest date in Lake G. OxCal flags the oldest four dates from Lake F and, importantly, also the youngest date from Lake G for having poor agreement (Supplementary Fig. S21), and those five dates are thus excluded from the final version of Model 1.

In order to test the sensitivity of the OxCal model to the sparse sampling from Lake G, we consider an alternative OxCal model (Model 2) in which all three Lake G dates are assumed to be robust, and we remove the six oldest dates from Lake F a priori (orange samples in Supplementary Table S1; purple dates on Supplementary Fig. S22).

At this stage, we also consider that there may be isolated samples that came in from above the lake shoreline and do not necessarily date a dry period between lakes. We bear in mind that samples that grew within the footprint of Lake Cahuilla would have ages that cluster during the various dry periods between lakes, but samples that grew above the Lake Cahuilla highstand shoreline should have ages that are randomly distributed with respect to the precise Lake Cahuilla chronology. To identify samples that are (slightly) more likely to date a period when the lake was full, we searched for isolated dates at either the young end or the old end of a dry period that do not cluster with other dates from within that package. Aside from sample Sb3m2A-c, which would not run in the OxCal model regardless, we identify two such cases: two dates at the old end of the dry period before Lake C and two dates at the young end of the dry period before Lake E.

In total, in Model 2 we removed 10 dates a priori from the 164 stratigraphically consistent radiocarbon dates discussed in the previous section (orange samples in Supplementary Table S1; purple dates on Supplementary Fig. S22), and additionally we again exclude sample Sb3m2A-c. We ran the OxCal model with the remaining dates ("Model 2: Initial Run" in Supplementary Text S2), but four dates still yielded poor agreement indices. We then removed these four dates and reran the model with the remaining 149 dates, resulting in a final alternative model ("Model 2: Final Version" in Supplementary Text S2; "Model 2" in Supplementary Table S1; Supplementary Fig. S22).

4. Results

4.1. The base OxCal model (Model 1)

Fig. 3 and Supplementary Fig. S21 show an OxCal plot of 295 of the 296 radiocarbon dates for which there is some stratigraphic control, including those samples collected from below a stratigraphic unconformity, but they do not plot the 127 black dates in Supplementary Table S1 (excluded for reasons mentioned earlier) nor the one pre-Holocene date (~40 ka). The near-vertical light brown band encompasses the dates used in the base model, with the individual date probability density functions (PDFs) shown in green, yellow, red and gray. PDFs of dates shown in red represent the dates that violate the stratigraphic ordering, being older than dates from underlying lakes; none of the red dates are used in the base model. The gray dates were collected from below local unconformities and do not necessarily provide age information for the dry period immediately preceding a lake; none of the gray dates are used in the base model. The dates in yellow represent one date that would not run in OxCal and additional dates with poor agreement indices that were excluded from the final base model; we omitted the yellow dates as outliers. Only those dates in green were included in the final model.

Supplementary Figs. S23 and S24 show the "multiple" plots from OxCal for the initial and final runs of Model 1, before and after removing outliers, respectively. Fig. 4a summarizes these results, showing the PDFs for the lake ages from the final run of Model 1. Note that for Lake A, the timing of the beginning and end of the lake highstand are estimated separately, but because the timing of the beginning and end are indistinguishable, we simply combine them as the timing of the highstand itself. The modeled OxCal ages for the lake highstands are 1720–1738 CE (Lake A), 1587–1636 CE (Lake B), 1459–1503 CE (Lake C), 1116–1165 CE (Lake D), 1009–1070 CE (Lake E), 907–966 CE (Lake F), and 612–241 BCE (Lake G). It is important to note that these ages represent the maximum allowable ranges when a lake may have filled the basin up to the highstand elevation: water was not necessarily in the basin for the entirety of each range. Additionally, using the desiccation rate range of 1.52–2.05 m/yr and the filling model of Rockwell et al. (2018), the Colorado River avulsion that initiated the filling may have occurred up to 13–20 years earlier and desiccation may have continued up to 47–64 years later than the respective highstand ranges (green trapezoids, Fig. 4c).

4.2. The alternative OxCal model (Model 2)

Similarly to Supplementary Fig. S21 for Model 1, Supplementary Fig. S22 shows an OxCal plot of the 295 radiocarbon dates for Model 2. The main difference in Model 2 is that 10 PDFs appear in purple, indicating that they were excluded a priori in Model 2, either to test the sensitivity of the OxCal model to the sparse sampling from Lake G or to test its sensitivity to isolated samples that may have come in from above the lake shoreline and do not necessarily date a dry period between lakes. A consequence of excluding these 10 samples a priori is that three dates that had been flagged as outliers in Model 1 now have good agreement with the model, and so have switched from yellow in Model 1 to green in Model 2. Fig. 5 highlights the differences between Models 1 and 2.

Supplementary Figs. S25 and S26 show the "multiple" plots from OxCal for the initial and final runs of Model 2, before and after removing outliers, respectively. Fig. 4b summarizes these results, showing the PDFs for the lake ages from the final run of Model 2, in comparison with those from Model 1. The Model 2 lake highstand possible timings are 1720–1735 CE (Lake A), 1587–1636 CE (Lake B), 1459–1503 CE (Lake C), 1151–1241 CE (Lake D), 995–1042 CE (Lake E), 906–966 CE (Lake F), and 166–5 BCE (Lake G). The biggest differences from Model 1 to Model 2 are in the possible timings of Lakes D, E, and G (Fig. 4a and b). Again, using the desiccation rates and filling model of Rockwell et al. (2018), the Colorado River avulsion that initiated the filling may have occurred up to 13–20

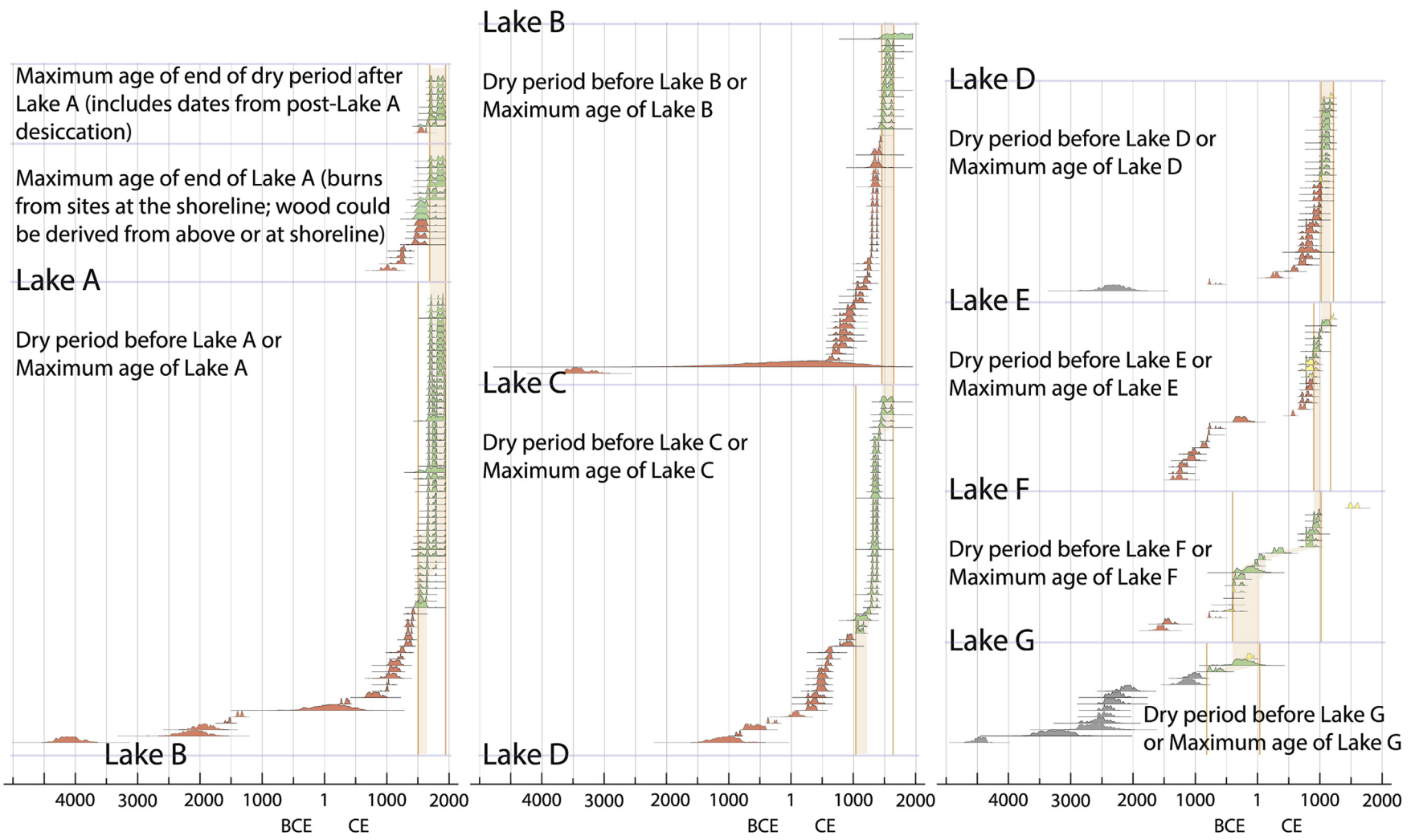

Fig. 3. Plot of all 295 Holocene dates with stratigraphic control, organized by lake and then by relative radiocarbon age; roots and dates from artificial fill are not included. The light brown subvertical bar represents an age bound for consistency: dates that fall to the left of the brown band are considered to have some inherited age; those to the right are likely outliers. The probability density functions (PDFs) shown in green are those that are used in the base model. The PDFs in yellow represent one date that would not run in OxCal and additional dates with poor agreement indices that were excluded from the final base model. The red PDFs are interpreted to have some age inheritance, and the gray PDFs are from samples below a local unconformity. The yellow, red, and gray dates are not used in the base model. See Table 1 and Supplementary Fig. S21 for details. (For interpretation of the references to colour in this figure legend, the reader is referred to the Web version of this article.)

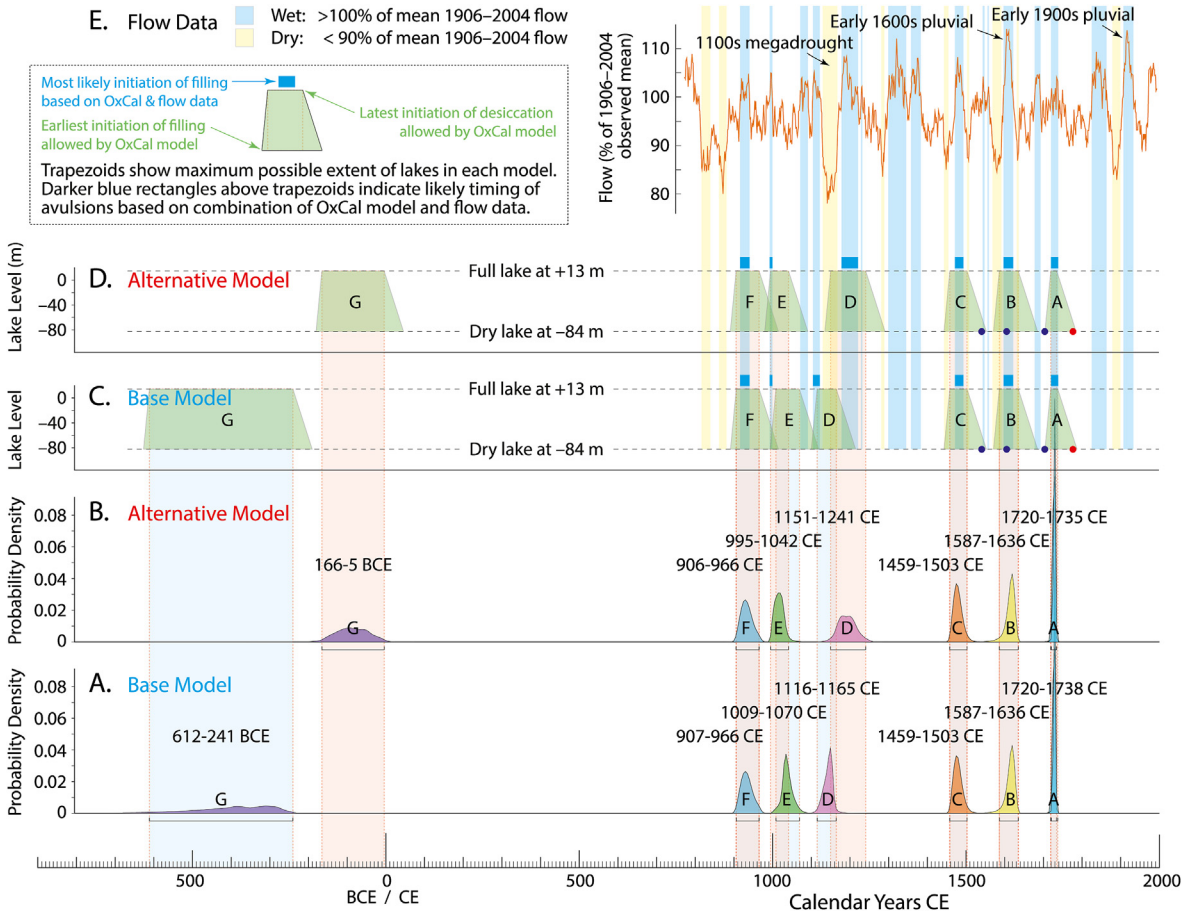

Fig. 4. The base and alternative OxCal models (Models 1 and 2) for Lake Cahuilla highstands compared with a streamflow reconstruction for the upper Colorado River. Probability density functions (PDFs), taken from the OxCal output, are shown for the timing of each lake highstand for the (a) base and (b) alternative models. In each case, these PDFs illustrate the maximum possible extent of the highstand and may overestimate its duration. Differences between the models result from the inclusion or exclusion of specific dates that may or may not be representative of a particular inter-lake dry period. Where the base and alternative models agree, the results are considered robust, but where the models differ, those differences are indicative of real uncertainty in the lake ages. Trapezoids in (c) for the base model and in (d) for the alternative model schematically extend the highstand windows from OxCal (a and b, respectively) to allow 13–20 years for the lake to fill and 47–64 years for it to completely desiccate. The trapezoids are then compared to (e) upper Colorado River flow, shown as a 25-yr moving average and expressed as a % of 1906–2004 mean flow (18.53×10^9 m^3; from Meko et al., 2007, and bias-corrected using quantile mapping by Robeson et al., 2020). The dark blue rectangles immediately above the trapezoids indicate the likely timing of Colorado River avulsions, as determined from the overlap of wet periods in (e) with the portion of each lake between the earliest possible initiation of filling and the end of the highstand, i.e., between the lower left and upper right corners of each trapezoid in (c) and (d). Purple dots in (c) and (d) designate the timing of historical observations that the Colorado River was flowing southward into the Gulf of California (Rockwell et al., 2018); of particular interest is the 1605 observation of Oñate, which would require either that Lake B had already completed filling and had begun desiccating before 1605 or that Lake B began filling only after 1605. The red dot in (c) and (d) marks Anza's visit in 1774, when no water was found in the basin; this requires that Lake A began desiccating no later than 1733 (Rockwell et al., 2018). For Lake A, both the beginning-of-lake and end-of-lake PDFs are retained, but they nearly overlap. Note also that the 1905–1907 flooding of the basin occurred at the onset of the "early 1900s pluvial" of Robeson et al. (2020), which led Ross (2020) to argue that this likely would have completely filled the basin to +13 m had the Colorado River not been redirected back to the Gulf of California by engineers. (For interpretation of the references to colour in this figure legend, the reader is referred to the Web version of this article.)

years earlier and desiccation may have continued up to 47–64 years later than the respective highstand ranges (Fig. 4d).

4.3. Refinement of end of Lake A based on historical accounts

Both the base model and the alternative model suggest a slightly longer window for Lake A compared to the model of Rockwell et al. (2018), 1720–1738 and 1720–1735, respectively, compared to 1719–1733. Rockwell et al. (2018) trimmed their Lake A age on the argument that Lake Cahuilla had mostly or completely desiccated by the time of Anza's visit in 1774, when Anza's party did not report finding water in the Salton Basin. Using plausible desiccation rates, they estimated that the lake must have begun desiccating by the early 1730s in order to be consistent with the historical observations. Following the logic of Rockwell et al. (2018), we also trim the end of the Lake A highstand to 1733 CE.

5. Discussion

5.1. Model comparison and implications of model divergence

The age estimates from the base model and the alternative model generally agree with one another for both Lakes A and B, but as the ages for these two lakes were also estimated previously by Rockwell et al. (2018), it is interesting to compare these new results to those from the earlier study. For Lake A, if historical accounts (Anza's observations in 1774) are considered as noted in the previous section, our new results here agree with those of Rockwell et al. (2018). For Lake B, Rockwell et al. (2018) estimated a comparatively imprecise range of 1509–1644 CE. With the new dates we have added in this paper, we refine the age of the Lake B highstand to sometime in the interval 1587–1636 CE. This new estimate falls entirely within the range estimated by Rockwell et al.

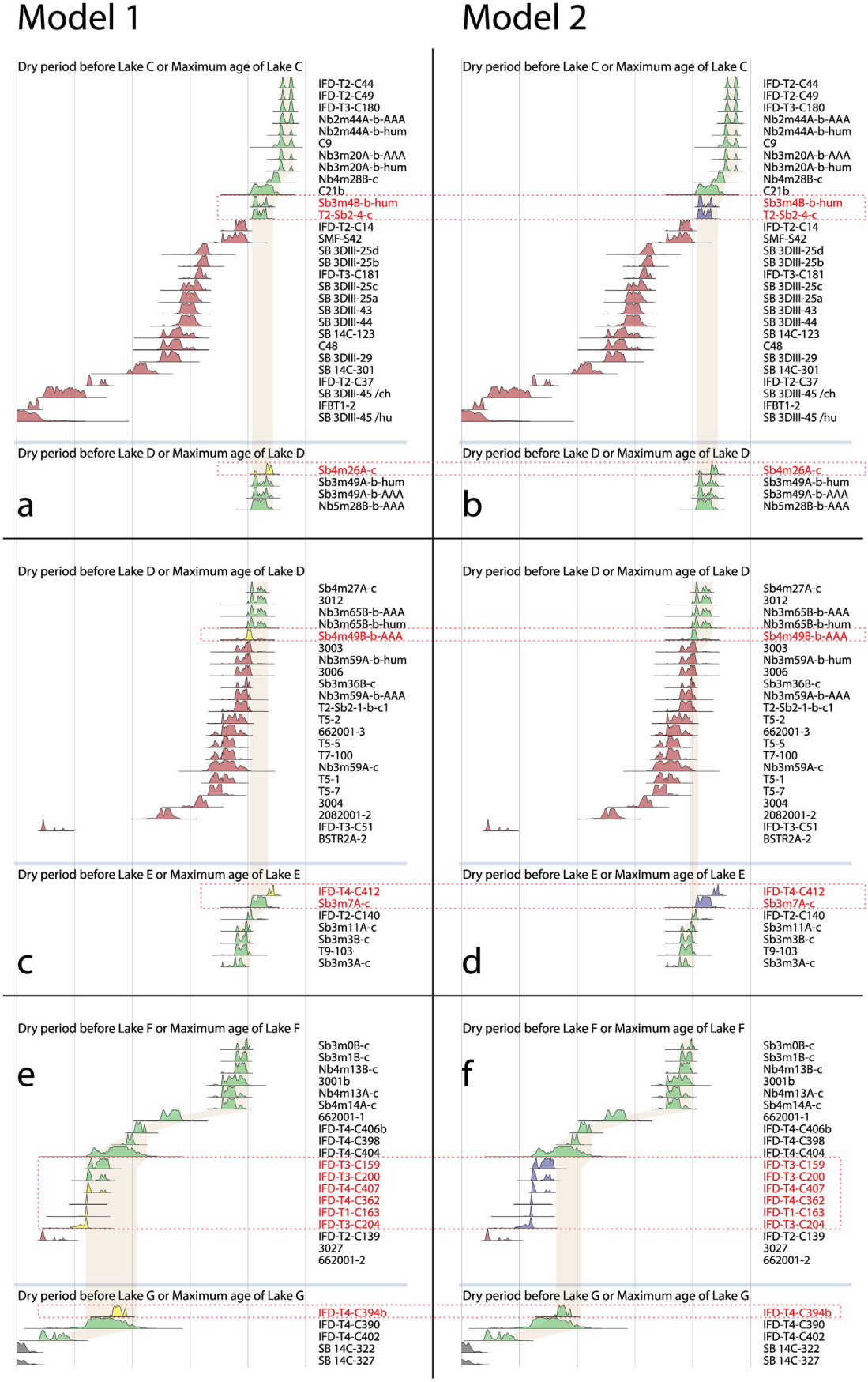
Model 1
Model 2
Dry period before Lake C or Maximum age of Lake C
IFD-T2-C44
IFD-T2-C49
IFD-T3-C180
Nb2m44A-b-AAA
Nb2m44A-b-hum
C9
Nb3m20A-b-AAA
Nb3m20A-b-hum
Nb4m28B-c
C21b
Sb3m4B-b-hum
T2-Sb2-4-c
IFD-T2-C14
SMF-S42
SB 3DIII-25d
SB 3DIII-25b
IFD-T3-C181
SB 3DIII-25c
SB 3DIII-25a
SB 3DIII-43
SB 3DIII-44
SB 14C-123
C48
SB 3DIII-29
SB 14C-301
IFD-T2-C37
SB 3DIII-45 /ch
IFBT1-2
SB 3DIII-45 /hu
Dry period before Lake D or Maximum age of Lake D
Sb4m26A-c
Sb3m49A-b-hum
Sb3m49A-b-AAA
Nb5m28B-b-AAA
a
b
Dry period before Lake D or Maximum age of Lake D
Sb4m27A-c
3012
Nb3m65B-b-AAA
Nb3m65B-b-hum
Sb4m49B-b-AAA
3003
Nb3m59A-b-hum
3006
Sb3m36B-c
Nb3m59A-b-AAA
T2-Sb2-1-b-c1
T5-2
662001-3
T5-5
T7-100
Nb3m59A-c
T5-1
T5-7
3004
2082001-2
IFD-T3-C51
BSTR2A-2
Dry period before Lake E or Maximum age of Lake E
IFD-T4-C412
Sb3m7A-c
IFD-T2-C140
Sb3m11A-c
Sb3m3B-c
T9-103
Sb3m3A-c
c
d
Dry period before Lake F or Maximum age of Lake F
Sb3m0B-c
Sb3m1B-c
Nb4m13B-c
3001b
Nb4m13A-c
Sb4m14A-c
662001-1
IFD-T4-C406b
IFD-T4-C398
IFD-T4-C404
IFD-T3-C159
IFD-T3-C200
IFD-T4-C407
IFD-T4-C362
IFD-T1-C163
IFD-T3-C204
IFD-T2-C139
3027
662001-2
e
f
Dry period before Lake G or Maximum age of Lake G
IFD-T4-C394b
IFD-T4-C390
IFD-T4-C402
SB 14C-322
SB 14C-327

(2018). Nevertheless, the primary reason that the newly-added dates push the onset of Lake B forward by nearly eight decades is because of a double peak at this time in the radiocarbon calibration curve, with the Bayesian trimming algorithm in OxCal now favoring the younger intercept in the calibration curve. In reality, the radiocarbon data cannot strictly distinguish which peak or intercept is correct, so some of the broader age range reported for Lake B by Rockwell et al. (2018) may still be valid.

Going back beyond Lake B, the only significant differences between the base and alternative models are in the possible timings of Lakes D, E, and G. This should not be surprising, considering that those are the lakes most affected by the changes highlighted in Fig. 5. In Model 1 the youngest date in the dry period before Lake D (Sb4m26A-c) was removed a posteriori as an outlier (Fig. 5a), but in Model 2 the a priori removal of the two oldest dates in the dry period before Lake C (Sb3m4B-b-hum and T2-Sb2-4-c) results in the inclusion of Sb4m26A-c, which was not flagged as an outlier in Model 2 (Fig. 5b). The upshot of these changes is a push in the mean age of Lake D forward in time by five decades (Fig. 4a and b and Supplementary Figs. S24 and S26), coupled with an overall broadening of the PDF for Lake D. Similarly, in Model 1 the oldest date in the dry period before Lake D (Sb4m49B-b-AAA) was removed a posteriori as an outlier (Fig. 5c), but in Model 2 the a priori removal of the two youngest dates in the dry period before Lake E (IFD-T4-C412 and Sb3m7A-c) results in the inclusion of Sb4m49B-b-AAA, which was not flagged as an outlier in Model 2 (Fig. 5d). The consequence of these changes is a push in the mean age of Lake E backward in time by two decades (Fig. 4a and b and Supplementary Figs. S24 and S26).

Focusing on Lake G, removing the youngest sample in the preceding dry period has a profound effect on the age of Lake G. In Model 1 the youngest date in the dry period before Lake G (IFD-T4-C394b) was removed a posteriori as an outlier (Fig. 5e), but in Model 2 the a priori removal of the six oldest dates in the dry period before Lake F results in the inclusion of IFD-T4-C394b, which was not flagged as an outlier in Model 2 (Fig. 5f). The result of these changes is a push in the mean age of Lake G forward in time by three centuries (Fig. 4a and b and Supplementary Figs. S24 and S26), coupled with an overall narrowing of the PDF for Lake G.

Reflecting on the differences between the base and alternative models, because we cannot know without additional information whether the assumptions underpinning the alternative model are more defensible than those incorporated into the base model, any differences between the two models should be considered a reflection of the true uncertainty in the lake ages. In particular, the instability in the modeled age for Lake G reveals that additional age constraints on Lake G are still critically needed. For the more recent lakes, in the next section we will explore whether high-resolution paleohydrologic reconstructions can provide additional insight into the likely timing of each lake filling.

5.2. Comparison to streamflow reconstruction and a preferred Lake Cahuilla model

A common hypothesis is that the filling phases of Lake Cahuilla initiate during wet periods in the Colorado River basin and Colorado Plateau, as an avulsion of the Colorado River would be more likely during a period of high discharge (Waters, 1983; Slingerland and Smith, 2004). In an attempt to test this hypothesis, we compare the lake chronology with rainfall estimates based on tree-ring data from the upper Colorado River drainage basin (Meko et al., 2007; Robeson et al., 2020). The Robeson et al. (2020) study applied quantile mapping to correct biases in the historical rainfall and tree ring data of Meko et al. (2007) to refine the upper Colorado River flow for the past 1200+ years (Fig. 4e). This comparison is shown in Fig. 4.

In this comparison, it is important to remember that although a northward avulsion is more likely to occur during flood conditions in a wet year, the base-level changes involved would favor rapid headward-cutting and enlargement of the channel in the alluvial terrain, as observed in 1905–1907, and the entire flow of the Colorado River would eventually be captured (Waters, 1983), even if an extended and severe drought immediately followed the flood that initially triggered the avulsion. In other words, even if an avulsion is more likely to occur during a wet period, much of the lake filling and the entirety of the highstand are no more likely to occur during a wet period than during a dry period.

While there are more high discharge events in the upper Colorado River flow reconstruction (Robeson et al., 2020) than there are lakes in the Salton Basin, we can look to (approximate) overlap between the two (Fig. 4) to propose discrete intervals that are more likely to have triggered the lake filling. The middle of the window for the Lake F highstand corresponds to a period of elevated river flow (blue rectangles above Lake F trapezoids in Fig. 4c and d) and, if this is when Lake F actually began filling, it would agree with the notion that lake fillings should initiate during wet periods. In the base model, the Lake E highstand post-dates a brief wet period at ~1000 CE (Fig. 4c), while the alternative model moves the timing of Lake E back by two decades (Fig. 4d); considering the 13–20 years required to fill Lake Cahuilla (Rockwell et al., 2018), the avulsion may have indeed occurred during the period of high flow at ~1000 CE (blue rectangles above Lake E trapezoids in Fig. 4c and d). The base model places most of Lake D in the longest drought of the past millennium, though Lake D may have initiated filling during the preceding wet period at ~1110 CE (blue rectangle above Lake D trapezoid in Fig. 4c); alternatively, Model 2 shifts the middle of Lake D forward into an extended wet period at ~1200 CE, which would be another likely candidate for the timing of the avulsion that led to Lake D (blue rectangle above Lake D trapezoid in Fig. 4d). For Lake D, we cannot strictly distinguish between these two possibilities with data presently available, though the later wet interval (1179–1221 CE) is arguably a more likely candidate for the avulsion that led to the filling of Lake D, as it was the longer and wetter interval (Fig. 4e). The ages of Lakes A, B, and C all overlap with wet periods (blue rectangles above Lakes A, B, and C trapezoids in Fig. 4c and d), consistent with avulsions of the Colorado River northward into the Salton Basin occurring during periods of elevated rainfall and river flow.

As stated in the previous section, because we cannot know whether the alternative model is more defensible than the base

Fig. 5. Changes from the base model (Model 1; a, c, e) to the alternative model (Model 2; b, d, f), as indicated by the dashed boxes. The main difference in Model 2 is that ten PDFs appear in purple, indicating that they were excluded a priori in Model 2, either to test the sensitivity of the OxCal model to the sparse sampling from Lake G or to test its sensitivity to isolated samples that do not necessarily date a dry period between lakes. In Model 1 the youngest date in the dry period before Lake D (Sb4m26A-c) was removed a posteriori as an outlier (a), but in Model 2 the a priori removal of the two oldest dates in the dry period before Lake C (Sb3m4B-b-hum and T2-Sb2-4-c) results in the inclusion of Sb4m26A-c, which was not flagged as an outlier in Model 2 (b). Similarly, in Model 1 the oldest date in the dry period before Lake D (Sb4m49B-b-AAA) was removed a posteriori as an outlier (c), but in Model 2 the a priori removal of the two youngest dates in the dry period before Lake E (IFD-T4-C412 and Sb3m7A-c) results in the inclusion of Sb4m49B-b-AAA, which was not flagged as an outlier in Model 2 (d). Finally, in Model 1 the youngest date in the dry period before Lake G (IFD-T4-C394b) was removed a posteriori as an outlier (e), but in Model 2 the a priori removal of the six oldest dates in the dry period before Lake F results in the inclusion of IFD-T4-C394b, which was not flagged as an outlier in Model 2 (f). The effects of these changes are seen in Fig. 4. See Supplementary Figs. S21–S26 and Supplementary Table S1 for full details of each model. (For interpretation of the references to colour in this figure legend, the reader is referred to the Web version of this article.)

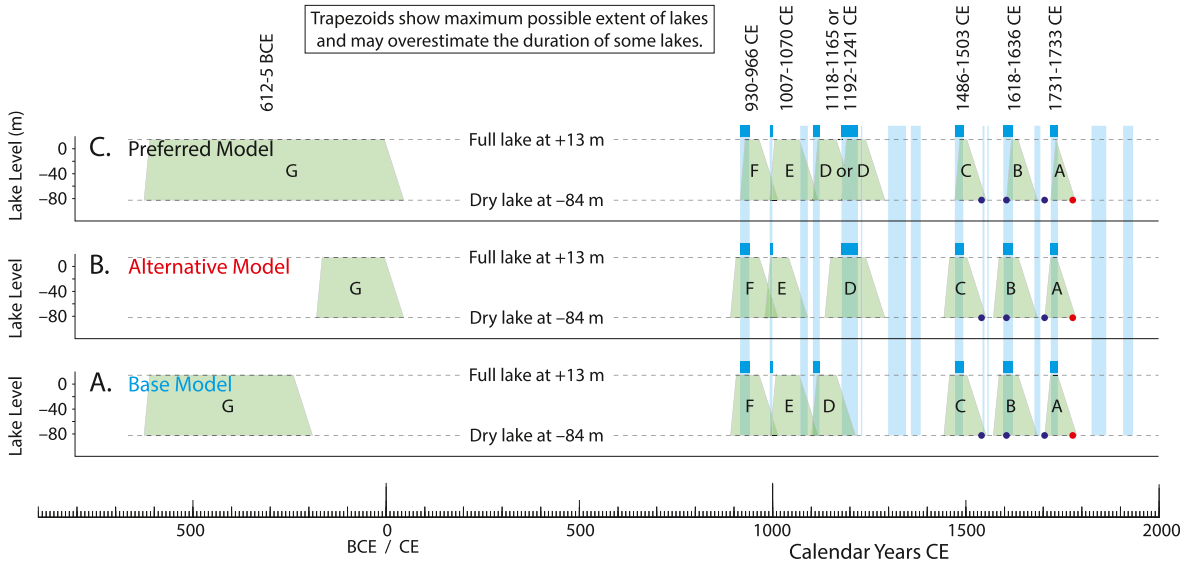

Fig. 6. Preferred Lake Cahuilla chronology. Initially, for each lake highstand, the full range of possible dates is considered, allowing for uncertainties in either (a) the base model or (b) the alternative model. In (c), the preferred model, the full range of possible dates is then trimmed based on historical observations and a streamflow reconstruction. This trimming includes delaying the onset of each lake so that the earliest possible initiating of filling (lower left corner of each trapezoid) aligns with the beginning of the wet period (left side of the corresponding blue rectangle). Trapezoids show maximum possible extent of lakes; the actual timing and extent of a given lake could be anywhere within the respective trapezoid. The years shown above the trapezoids in (c) represent the maximum allowable window for each lake highstand. Symbology follows from Fig. 4. (For interpretation of the references to colour in this figure legend, the reader is referred to the Web version of this article.)

model, any differences between the two models should be considered indicative of real uncertainty in the lake ages. Our preferred model age for each lake should therefore span the respective uncertainties from the base and alternative models. Additionally, if we wish to consider the streamflow reconstruction as a guide to potential timings of northward avulsions of the Colorado River that are more plausible, then we would not expect any lake to begin filling earlier than the blue rectangles above the respective trapezoids in Fig. 4c and d. In our preferred model (Fig. 6c), we combine the uncertainties for each lake from the base and alternative models (Fig. 6a–b, respectively), but we delay the onset of each lake so that the earliest possible initiating of filling (lower left corner of each trapezoid) corresponds to the onset of the wet period (left side of the corresponding blue rectangle).

For Lakes A, B, C, and F the preferred model closely resembles the base and alternative models, but for Lakes E and G the possible window for each lake is expanded relative to the corresponding extent in the base or alternative models individually. For Lake D, two plausible windows emerge, depending upon whether the lake began filling during the wet period around 1110 CE or during the longer wet period around 1200 CE (Fig. 6). The two possible windows in the preferred model for Lake D, and the broader possible ranges for Lakes E and G, result from ambiguity over the validity of the assumptions underpinning the alternative model. These broader windows do not imply that those lakes were necessarily longer-lived than other lakes, but it suggests that additional dates are needed to better constrain the timing of those lakes.

The base and alternative models suggest the Lake B highstand most likely occurred sometime between 1587 and 1636 CE (Fig. 4). Considering the 13–20 years required to fill Lake Cahuilla (Rockwell et al., 2018), this implies that the filling started between 1567 and 1623 CE. Additional information comes from the historical observations of Oñate and Escobar, who described the Colorado River flowing to the Gulf of California in 1605 (purple dot in Lake B in Fig. 4c and d; Rockwell et al., 2018). These details collectively suggest one of two scenarios: either Lake B filled mostly in the late 16th century and the Colorado River had reverted to southward flow into the Gulf of California by 1605, or the avulsion leading to Lake B occurred only after 1605. A comparison to the streamflow reconstruction (Fig. 4) reveals that in the former scenario, the Lake B filling would have necessarily initiated during an extended dry period in the late 16th century. In contrast, in the latter scenario, the filling would have initiated during the "early 1600s pluvial" of Robeson et al. (2020). Based on the streamflow reconstruction and historical data, we consider a post-1605 avulsion to be more likely, which implies that a full Lake B could not have occurred earlier than 1618. This tightens the age of the Lake B highstand in the preferred model to between 1618 and 1636 CE (Fig. 6c).

For Lake A, Anza's inability to find water during treks across the Salton Basin in 1774–1776 suggests that Lake A must have begun desiccating no later than ~1733 CE (Rockwell et al., 2018). As discussed by Rockwell et al. (2018), the filling of Lake A may have initiated during several comparatively wet years beginning in ~1718; if so, the Lake A highstand may have lasted only a few years (Fig. 6c).

It is notable that Ross (2020) argues that the avulsion that occurred in 1905, and which resulted in the Salton Sea, was a natural event and would have occurred separately from human interventions. This avulsion also occurred during a wet period in the Colorado River basin, termed the "early 1900s pluvial" by Robeson et al. (2020), and followed several years of low rainfall. As rainfall remained high for the following two decades, Ross (2020) argues that without human intervention, it is possible that the basin could have filled once again.

The above notwithstanding, it is important to emphasize that, unlike most lakes, Lake Cahuilla is not necessarily high during long wet periods and low during long dry periods. This occurs because the timing of avulsions of the Colorado River is likely controlled by single floods in individual wet years, but the beginning of the highstand would necessarily lag behind the avulsion by 13–20 years and may extend into a drought. To illustrate the uniqueness of the paleohydrologic setting of Lake Cahuilla, we note that a number of pluvial lakes filled basins within the Mojave Desert in the late Pleistocene, but these lakes gradually receded and transitioned to

playa conditions as the climate became more arid in the early Holocene. In some locations, such as at Soda Lake, wetland conditions briefly returned at the time of the Medieval Climate Anomaly and Little Ice Age, but otherwise the past 9 ka have been generally dry (Honke et al., 2019). In contrast, conditions in the Salton Basin have changed rapidly and frequently, with six unique lake fillings and desiccations alone between the 10th and 18th centuries CE.

Given the dynamics of Lake Cahuilla paleohydrology, we do not expect a correlation between regional paleoclimate and the timing of Lake Cahuilla highstands, beyond the potential correlation between Colorado River streamflow, Colorado River avulsions, and the initiation of filling of Lake Cahuilla. Additionally, climate histories have not necessarily been consistent across the region. For instance, Meko et al. (2007) identified the extended drought in the upper Colorado River Basin in the mid-1100s which coincided with dry conditions in the Great Basin, but they concluded that it did not coincide with droughts elsewhere in the American West.

Finally, the comparison of the OxCal models with the streamflow reconstruction reveals that some significant wet periods are clearly not associated with lake highstands, such as the two extended periods of high rainfall between 1300 and 1400 CE, between Lakes D and C (Fig. 4). While this conclusion seems inescapable, we note that water does spill into the basin from time to time, more frequently than full avulsions. For instance, water was observed flowing into the Salton Basin historically in 1840, 1842 or 1849 (accounts differ), 1852, 1859, 1862, 1867, 1884, and 1891 (Orcutt, 1891; Barrows, 1900; Cory, 1913, pp. 1228, 1247; Sykes, 1914, p. 19; MacDougal, 1915, pp. 234–235), though none of these instances led to a full Lake Cahuilla.

Although in our preferred model we delayed the onset of each lake so that the earliest possible initiation of filling aligns with the beginning of the corresponding wet period, these shifts in the lake timings were no more than a few decades in any case (compare Figs. 4 and 6): the beginning of the Lake B highstand was pushed forward by 31 years; the beginning of the Lake C highstand was pushed forward by 27 years; and the beginning of the Lake F highstand was pushed forward by 23–24 years; for other lakes, the shift was 12 years or less.

5.3. Highstand elevation for each lake

Deposits from Lakes A, B, and C are observed and dated at multiple +13 m shoreline sites (Supplementary Table S1), but Lakes D, E, and F left unambiguous, conformable deposits only at sites at 8–9 m above sea level (e.g., Coachella and Carrizo Wash) or lower. Of Lakes D, E, and F, two of them left deposits at +13 m at the SMF Northern Shoreline site, but it is unclear which two they are, and it is unclear whether evidence for the third lake was simply cut out by fluvial erosion or if one of the lakes did not quite make it up to +13 m (Supplementary Text S1 §3.5; Supplementary Fig. S19). In any case, at least five of the past six lakes must have reached the +13 m shoreline. So far, unambiguous, conformable deposits from a seventh lake (Lake G) have been found and dated only at the Imperial fault site at −32 m, although deposits from this lake are likely observed below local unconformities at sites much higher in the basin, perhaps up to 13 m above sea level (Supplementary Text S1; Supplementary Figs. S8, S9, S20; Supplementary Table S1).

Based on the evidence, it is likely that all seven lakes reached at least +9 m, and at least five of the lakes, including with certainty the past three, reached +13 m. It is unlikely that any lake rose higher than +13 m, as this is the modern elevation of the sill of the Colorado River delta, i.e., the minimum crest altitude of the delta at Cerro Prieto (Waters, 1983). Once the lake reached this level, any additional input into Lake Cahuilla would be balanced by southward overflow across the delta into the Gulf of California.

5.4. Evidence for the completeness of desiccations between highstands

To get at the question of whether there was complete desiccation between each highstand, we consider how many discrete lakes are observed at sites at different elevations in the basin, but we must also consider the possibility for a partial filling of the basin that is seen only at the lower-elevation sites. There is compelling evidence from sites at or near the shoreline for six lake highstands (A–F) in the past 1100 years. Many of these sites also record an earlier lake highstand (G) that is capped by a pronounced oxidation horizon or soil, suggesting there was a long gap in deposition between Lakes F and G; however, the only useful dating constraints on Lake G come from lower in the basin (Table 1). Rockwell et al. (2011) document all seven of these lakes at the Dogwood paleoseismic site, so we know that each of the lakes desiccated to at least −32 m elevation. Using the desiccation rate range of 1.52–2.05 m/yr (Rockwell et al., 2018), this 45 m drop in water level would have required 22–30 years. Further, there is evidence at the Salt Creek paleoseismic site, which lies at −60 m, for the presence of at least five and possibly as many as seven discrete lakes, but not necessarily with intervening dry periods, in the past 1100 years (Williams and Seitz, 2005), although the presence of root casts between some lakes does indicate desiccation down to at least −60 m. A seventh lake in the past 1100 years could have resulted from a partial filling of the basin, as occurred in 1905–1907 when the Salton Sea formed: the water reached the Salt Creek site in that filling and flooded Salt Creek up to −59.6 m (Sieh and Williams, 1990). If all six of the Lake Cahuilla highstands in the past 1100 years desiccated to as low as −60 m, this 73 m drop in lake level would have required at least 48–67 years between successive highstands, using the desiccation rates and filling model of Rockwell et al. (2018). This could be consistent with the preferred model (Fig. 6c), as long as Lake F began desiccating by 940–959 CE. Wood growth within the lake footprint may not only span the entire period between successive highstands, but it would start in different locations once the lake level dropped below a site's elevation and would continue until that elevation was re-inundated.

5.5. Archeological and seismological considerations

The more precise timing of past lakes helps to refine, and perhaps even resolve, a number of research problems. For one, this new chronology will permit a more robust comparison between archaeology or imprecisely dated oral traditions with more accurately dated historical information. Our models constrain when the Indigenous Americans occupied shoreline sites for fishing, versus when lake-bottom farming occurred (Wilke, 1978). Arrangement of fish traps at various elevations below the highstand shoreline indicate that they seasonally rebuilt new traps to account for the drawdown of the lake (Phukan et al., 2019) until the water became too saline, resulting in major fish die-offs (Wilke, 1978). Historical accounts record that the Indigenous Cahuilla farmed the lakebed southeast of Palm Springs during the contact period (Blake, 1915), and that there was an oral tradition of fishing the lake in the past.

Additionally, many paleoseismic studies have been completed around the lake basin, from sites at the highstand shoreline (Sieh, 1986; Sieh and Williams, 1990; Pollard and Rockwell, 1995; Gurrola and Rockwell, 1996; Faneros, 2005) to other sites close to or above sea level (Thomas and Rockwell, 1996; Orgil, 2001; Ragona, 2003; Philibosian et al., 2011; Jerrett, 2015; Wessel, 2015), to sites well below sea level (Williams, 1989; Sieh and Williams, 1990; Meltzner et al., 2006; Rockwell et al., 2011). Many of these have limited radiocarbon control, but all reference the timing of earthquakes relative to various Lake Cahuilla highstands. The ages of the

interpreted earthquakes recorded at these various sites can be recalculated with these new lake age data such that large earthquakes in the southern San Andreas system can be sequenced to test whether rupture patterns of triggering emerge.

5.6. Age inheritance in radiocarbon dates

As noted previously, 120 of the 284 stratigraphically well-defined dates in our compilation (42%) are out of sequence and clearly older than a stratigraphically lower lake, demonstrating significant age inheritance beyond the calibrated age uncertainty; some samples date thousands of years older than the inferred sediment age. This number (120 of 284) is likely an undercount, as dates with some overlap with the bulk of the younger ages for each lake were retained, yet these may nonetheless have some degree of inheritance. Considered another way, at flatter parts of the radiocarbon calibration curve, high-precision dates with an age inheritance of ~150 years could easily have been missed in our count, but the same amount of age inheritance would have been obvious (and statistically significant) at a steeper part of the calibration curve.

Furthermore, the in situ mesquite stumps capped by Lake A deposits provide robust evidence that the lakebed was dry and that Lake A did not fill until sometime after 1705 CE. Nevertheless, 21 of the 51 radiocarbon samples within deltaic, lacustrine, or shoreline deposits associated with Lake A (41%) are necessarily older than 1705 CE, i.e., none of those samples' age PDFs overlap with 1705 CE at 95% confidence. Notably, eight of these samples (16%) are too old by > 600 years, and five of these samples (10%) are too old by > 1000 years.

Collectively, these observations imply that statistically significant age inheritance should be expected in more than 40% of all radiocarbon samples in the Salton Basin, with the inherited age (the difference between the sample age and the age of the sediment it is collected from) exceeding 1000 years ~10% of the time.

Nonetheless, it is also remarkable that for each of Lakes A, B, and C, at least 15 dates from sites scattered around the basin give indistinguishable and reliable ages for the dry period immediately preceding the respective lake (Fig. 3). As we have shown, the age clustering can be used to overcome the age inheritance problem, as long as rational, defensible age models are constructed with those clustered radiocarbon dates.

6. Conclusions

To constrain the timing of the past seven lake highstands in the Salton Trough, we compiled 423 radiocarbon dates, of which 284 are reliable and have good stratigraphic control. We developed two models in OxCal, a base model and an alternative model, which use 151 and 149 of the dates, respectively, after discarding dates that are out of sequence (indicating age inheritance) or that were flagged by OxCal for having poor agreement. Notably, 120 of the 284 reliable dates were rejected because they clearly violated stratigraphic ordering, implying that more than 40% of all radiocarbon dates in the Salton Basin exhibit statistically significant age inheritance.

The radiocarbon dates and Bayesian modeling in OxCal cannot by themselves distinguish between the base and alternative models (Fig. 4); the differences in the models result from choices of whether to include or exclude specific dates that may or may not be representative of a particular dry period. Where the base and alternative models are similar, the results can be considered robust, but where the models differ, any differences between the two models should be considered a reflection of the true uncertainty in the lake ages. Consideration of historical accounts and a high-resolution paleohydrologic reconstruction allows us to trim the ages of Lakes A and B, and the paleohydrologic reconstruction also provides insight into the most likely intervals during which earlier lakes may have initiated filling.

The preferred model age windows for the past seven Lake Cahuilla highstands are 1731–1733 CE (Lake A), 1618–1636 CE (Lake B), 1486–1503 CE (Lake C), 1118–1165 or 1192–1241 CE (Lake D), 1007–1070 CE (Lake E), 930–966 CE (Lake F), and 612–5 BCE (Lake G). These ages represent the maximum allowable ranges during which a lake may have filled the basin up to the +13 m highstand elevation; the basin may have been dry for a significant portion of each time window. Additionally, the Colorado River avulsion that initiated each filling likely occurred 13–20 years prior to the beginning of the respective highstand, and a complete desiccation would have required at least 47 years after the end of the highstand (Rockwell et al., 2018); the lake filling and desiccation episodes may have extended beyond the aforementioned highstand age range for each lake. If the paleohydrologic constraints are ignored, some of the lakes may have initiated earlier, by up to three decades.

Author Contributions

Thomas K. Rockwell: Conceptualization, Methodology, Formal analysis, Investigation, Writing – original draft, Writing – review & editing, Visualization, **Aron J. Meltzner:** Methodology, Formal analysis, Investigation, Data curation, Writing – original draft, Writing – review & editing, Visualization, **Erik C. Haaker**: Methodology, Investigation, Writing – review & editing, **Danielle Madugo**: Investigation, Writing – review & editing

Declaration of competing interest

The authors declare that they have no known competing financial interests or personal relationships that could have appeared to influence the work reported in this paper.

Acknowledgements

We thank the many researchers who have worked on Lake Cahuilla and with whom we have had numerous discussions over the years, including but not limited to Jerry Schaefer, Belle Philibosian, Ray Weldon, Kate Scharer, Kerry Sieh, Gordon Seitz, and Pat Williams. We thank Kate Scharer, Pat Williams, and an anonymous reviewer for thoughtful, constructive feedback on an early version, which substantially improved the manuscript. We also thank Glenn Biasi and Joanne Lim for insight, suggestions, and assistance with probabilistic calculations. This research was supported by the Southern California Earthquake Center (SCEC Contribution # 10218). SCEC is funded by NSF Cooperative Agreement EAR-1600087 & USGS Cooperative Agreement G17AC00047. This research was also funded by the National Research Foundation Singapore and the Singapore Ministry of Education under the Research Centres of Excellence initiative. This is Earth Observatory of Singapore Contribution Number 318.

Appendix A. Supplementary data

Supplementary data to this article can be found online at https://doi.org/10.1016/j.quascirev.2022.107456.

References

Anderson, L., Zentner, E., Nagy, V., Hagan, C., Thompson, R., Kidwell, K., Salinas, H., 2022. California Wildfire History Map. Capital Public Radio. https://projects.capradio.org/california-fire-history/.

Arkush, B.S., 1990. Archaeological Investigations at CA-RIV-1182, CA-RIV-3143, CA-RIV-3144, CA-RIV-3868, and CA-RIV-3882, Tentative Tract 25429, La Quinta,

Central Riverside County, California. Archaeological Research Unit, University of California, Riverside.
Aschmann, H., 1959. The evolution of a wild landscape and its persistence in Southern California. Ann. Assoc. Am. Geogr. 49 (No. 3, Part 2), 34–56. https://www.jstor.org/stable/2561246.
Barrows, D.P., 1900. The Colorado Desert. Natl. Geogr. Mag. 11, 337–351.
Blake, W.P., 1915. Sketch of the region at the head of the Gulf of California. In: Cory, H.T. (Ed.), The Imperial Valley and the Salton Sink. J.J. Newbegin, San Francisco, California, pp. 1–35. https://archive.org/details/imperialvalleya00blakgoog.
Blong, R., Gillespie, R., 1978. Fluvially transported charcoal gives erroneous ^{14}C ages for recent deposits. Nature 271, 739–741. https://doi.org/10.1038/271739a0.
Bronk Ramsey, C., 1995. Radiocarbon calibration and analysis of stratigraphy: the OxCal program. Radiocarbon 37, 425–430. https://doi.org/10.1017/S0033822200030903.
Bronk Ramsey, C., 2008. Deposition models for chronological records. Quat. Sci. Rev. 27, 42–60. https://doi.org/10.1016/j.quascirev.2007.01.019.
Bronk Ramsey, C., 2009a. Bayesian analysis of radiocarbon dates. Radiocarbon 51, 337–360. https://doi.org/10.1017/S0033822200033865.
Bronk Ramsey, C., 2009b. Dealing with outliers and offsets in radiocarbon dating. Radiocarbon 51, 1023–1045. https://doi.org/10.1017/S0033822200034093.
Brothers, D.S., Driscoll, N.W., Kent, G.M., Harding, A.J., Babcock, J.M., Baskin, R.L., 2009. Tectonic evolution of the Salton Sea inferred from seismic reflection data. Nat. Geosci. 2, 581–584. https://doi.org/10.1038/ngeo590.
Brothers, D., Kilb, D., Luttrell, K., Driscoll, N., Kent, G., 2011. Loading of the San Andreas fault by flood-induced rupture of faults beneath the Salton Sea. Nat. Geosci. 4, 486–492. https://doi.org/10.1038/ngeo1184.
Cory, H.T., 1913. Irrigation and river control in the Colorado River delta. Trans. Am. Soc. Civ. Eng. 76, 1204–1453 paper no. 1270. https://doi.org/10.1061/TACEAT.0002448. Reprinted in Cory, H.T., 1915. The Imperial Valley and the Salton Sink, J.J. Newbegin, San Francisco, California, 452 pp. https://archive.org/details/imperialvalleya00blakgoog.
Erlandson, J.M., Rockwell, T.K., 1987. Radiocarbon reversals and stratigraphic discontinuities: the effects of natural formation processes on coastal California archeological sites. In: Nash, D.T., Petraglia, M.D. (Eds.), Natural Formation Processes and the Archaeological Record. British Archaeological Reports International Series 352, pp. 51–73.
Faneros, G.A., 2005. Structure and Neotectonics of the Superstition Mountain Fault, Imperial County, California. MS Thesis. San Diego State University. http://hdl.handle.net/20.500.11929/sdsu:26237.
Fletcher, J.M., Teran, O.J., Rockwell, T.K., Oskin, M.E., Hudnut, K.W., Mueller, K.J., Spelz, R.M., Akciz, S.O., Masana, E., Faneros, G., Fielding, E.J., Leprince, S., Morelan, A.E., Stock, J., Lynch, D.K., Elliott, A.J., Gold, P., Liu-Zeng, J., González-Ortega, A., Hinojosa-Corona, A., González-García, J., 2014. Assembly of a large earthquake from a complex fault system: surface rupture kinematics of the 4 April 2010 El Mayor–Cucapah (Mexico) M_w 7.2 earthquake. Geosphere 10, 797–827. https://doi.org/10.1130/GES00933.1.
Gavin, D., 2001. Estimation of inbuilt age in radiocarbon ages of soil charcoal for fire history studies. Radiocarbon 43, 27–44. https://doi.org/10.1017/S003382220003160X.
Gurrola, L.D., Rockwell, T.K., 1996. Timing and slip for prehistoric earthquakes on the Superstition Mountain fault, Imperial Valley, southern California. J. Geophys. Res. 101, 5977–5985. https://doi.org/10.1029/95JB03061.
Haaker, E.C., 2012. Moving towards a More Complete Late Holocene Chronology of Ancient Lake Cahuilla. BS Thesis. San Diego State University.
Honke, J.S., Pigati, J.S., Wilson, J., Bright, J., Goldstein, H.L., Skipp, G.L., Reheis, M.C., Havens, J.C., 2019. Late Quaternary paleohydrology of desert wetlands and pluvial lakes in the Soda Lake basin, central Mojave Desert, California (USA). Quat. Sci. Rev. 216, 89–106. https://doi.org/10.1016/j.quascirev.2019.05.021.
Jerrett, A.S., 2015. Paleoseismology of the Imperial Fault at the US–Mexico Border and Correlation of Regional Lake Stratigraphy through Analysis of Oxygen/Carbon Isotope Data. MS Thesis. San Diego State University. http://hdl.handle.net/20.500.11929/sdsu:1764.
Laylander, D., 1997. The last days of Lake Cahuilla: the Elmore site. Pacific Coast Archaeological Society Quarterly 33, 1–138. http://www.pcas.org/V3312.htm.
Li, H.-C., You, C.-F., Ku, T.-L., Xu, X.-M., Buchheim, H.P., Wan, N.-J., Wang, R.-M., Shen, M.-L., 2008. Isotopic and geochemical evidence of palaeoclimate changes in Salton Basin, California, during the past 20 kyr: 2. $^{87}Sr/^{86}Sr$ ratio in lake tufa as an indicator of connection between Colorado River and Salton Basin. Palaeogeogr. Palaeoclimatol. Palaeoecol. 259, 198–212. https://doi.org/10.1016/j.palaeo.2007.10.007.
MacDougal, D.T., 1915. The Salton Sea. Am. J. Sci. (4th series) 39, 231–250. https://doi.org/10.2475/ajs.s4-39.231.231.
Meko, D., Woodhouse, C.A., Baisan, C.A., Knight, T., Lukas, J.J., Hughes, M.K., Salzer, M.W., 2007. Medieval drought in the upper Colorado River basin. Geophys. Res. Lett. 34, L10705. https://doi.org/10.1029/2007GL029988.
Meltzner, A.J., 2006. Characterization of the Long-Term Behavior of the Imperial and Brawley Faults, Imperial Valley, California. MS Thesis. San Diego State University. http://hdl.handle.net/20.500.11929/sdsu:26314.
Meltzner, A.J., Rockwell, T.K., Owen, L.A., 2006. Recent and long-term behavior of the Brawley fault zone, Imperial Valley, California: an escalation in slip rate? Bull. Seismol. Soc. Am. 96, 2304–2328. https://doi.org/10.1785/0120050233.
Modesto, R., Mount, G., 1980. Not for Innocent Ears: Spiritual Traditions of a Desert Cahuilla Medicine Woman. Sweetlight Books, Arcata, California, p. 120.
Monitoring Trends in Burn Severity (MTBS), 2022. Interactive Viewer. United States Department of Agriculture (Forest Service) / U.S. Geological Survey. https://mtbs.gov/viewer/.
Orcutt, C.R., 1891. A visit to Lake Maquata. The West American Scientist 7, 158–164. https://archive.org/details/westamericanscie759orcut.
Orgil, A., 2001. Three-dimensional Paleoseismic Investigation on the South Break of the Coyote Creek Fault, Southern California. MS Thesis. San Diego State University. http://hdl.handle.net/20.500.11929/sdsu:26337.
Philibosian, B., Fumal, T., Weldon, R., 2011. San Andreas fault earthquake chronology and Lake Cahuilla history at Coachella, California. Bull. Seismol. Soc. Am. 101, 13–38. https://doi.org/10.1785/0120100050.
Phukan, A., Braje, T.J., Rockwell, T.K., Ullah, I., 2019. Shorelines in the desert: mapping fish trap features along the southwest coast of ancient Lake Cahuilla, California. Advances in Archaeological Practice 7, 325–336. https://doi.org/10.1017/aap.2019.31.
Pollard, W.J., Rockwell, T.K., 1995. Late Holocene slip rate for the Coyote Creek fault, Imperial County, California. Abstr. Progr. Geol. Soc. Am. 27 (5), 72.
Ragona, D., 2003. A High-Resolution Paleoseismic Study in the Southern San Jacinto Fault Zone, Imperial County, California. MS Thesis. San Diego State University. http://hdl.handle.net/20.500.11929/sdsu:28066.
Reimer, P., Austin, W., Bard, E., Bayliss, A., Blackwell, P., Bronk Ramsey, C., Butzin, M., Cheng, H., Edwards, R., Friedrich, M., Grootes, P., Guilderson, T., Hajdas, I., Heaton, T., Hogg, A., Hughen, K., Kromer, B., Manning, S., Muscheler, R., Palmer, J., Pearson, C., van der Plicht, J., Reimer, R., Richards, D., Scott, E., Southon, J., Turney, C., Wacker, L., Adolphi, F., Büntgen, U., Capano, M., Fahrni, S., Fogtmann-Schulz, A., Friedrich, R., Köhler, P., Kudsk, S., Miyake, F., Olsen, J., Reinig, F., Sakamoto, M., Sookdeo, A., Talamo, S., 2020. The IntCal20 Northern Hemisphere radiocarbon age calibration curve (0–55 cal kBP). Radiocarbon 62, 725–757. https://doi.org/10.1017/RDC.2020.41.
Robeson, S.M., Maxwell, J.T., Ficklin, D.L., 2020. Bias correction of paleoclimatic reconstructions: a new look at 1,200+ years of Upper Colorado River flow. Geophys. Res. Lett. 47, e2019GL086689. https://doi.org/10.1029/2019GL086689.
Rockwell, T.K., Meltzner, A., Tsang, R., 2011. A Long Record of Earthquakes with Timing and Displacements for the Imperial Fault: a Test of Earthquake Recurrence Models. Final Technical Report. U.S. Geological Survey, 28 pp.
Rockwell, T.K., Fletcher, J.M., Teran, O.J., Hernandez, A.P., Mueller, K.J., Salisbury, J.B., Akciz, S.O., Štěpančíková, P., 2015. Reassessment of the 1892 Laguna Salada earthquake: fault kinematics and rupture patterns. Bull. Seismol. Soc. Am. 105, 2885–2893. https://doi.org/10.1785/0120140274.
Rockwell, T.K., Meltzner, A.J., Haaker, E.C., 2018. Dates of the two most recent surface ruptures on the southernmost San Andreas Fault recalculated by precise dating of Lake Cahuilla dry periods. Bull. Seismol. Soc. Am. 108, 2634–2649. https://doi.org/10.1785/0120170392.
Ross, J.E., 2020. Formation of California's Salton Sea in 1905–07 was not "accidental". In: Miller, D.M. (Ed.), Changing Facies: the 2020 Desert Symposium Field Guide and Proceedings. Desert Symposium, Inc., Zzyzx, CA, pp. 217–230. http://www.desertsymposium.org/History.html.
Schaefer, J., 1987. The Ormesa-IID Transmission Line and Ormesa Geothermal Pipeline Network Cultural Resources Survey and Testing Program, East Mesa, Imperial County, California. Mooney-Levine and Associates, San Diego, California.
Schaefer, J., Pallette, D., 1993. Archaeological Investigations of Two Lake Cahuilla Sites in the Toro Canyon Area, Riverside County, California. Brian F. Mooney Associates, San Diego, California.
Schiffer, M.B., 1986. Radiocarbon dating and the "old wood" problem: the case of the Hohokam chronology. J. Archaeol. Sci. 13, 13–30. https://doi.org/10.1016/0305-4403(86)90024-5.
Sieh, K.E., 1986. Slip rate across the San Andreas and prehistoric earthquakes at Indio, California. Eos Trans. Am. Geophys. Union 67, 1200.
Sieh, K.E., Williams, P.L., 1990. Behavior of the southernmost San Andreas fault during the past 300 years. J. Geophys. Res. 95, 6629–6645. https://doi.org/10.1029/JB095iB05p06629.
Slingerland, R., Smith, N.D., 2004. River avulsions and their deposits. Annu. Rev. Earth Planet. Sci. 32, 257–285. https://doi.org/10.1146/annurev.earth.32.101802.120201.
Sykes, G., 1914. Geographical features of the Cahuilla Basin. In: MacDougal, D.T. (Ed.), The Salton Sea: a Study of the Geography, the Geology, the Floristics, and the Ecology of a Desert Basin. Carnegie Institution of Washington, Washington, D.C., pp. 13–20. https://archive.org/details/saltonseastudyof00macduoft. https://archive.org/details/cu31924002078065
Sykes, G., 1937. The Colorado Delta. Carnegie Institution of Washington Publication 460 and American Geographical Society Special Publication 19, Washington, D.C. https://catalog.hathitrust.org/Record/001631435.
Thomas, A.P., Rockwell, T.K., 1996. A 300- to 550-year history of slip on the Imperial fault near the U.S.–Mexico border: missing slip at the Imperial fault bottleneck. J. Geophys. Res. 101, 5987–5997. https://doi.org/10.1029/95JB01547.
U.S. Geological Survey and California Geological Survey, 2020. Quaternary Fault and Fold Database of the United States. Updated 2 September 2020. https://www.usgs.gov/natural-hazards/earthquake-hazards/faults.
Verdugo, D., 2004. Further Resolution of Past Earthquake Surface Ruptures at Carrizo Wash, Southern San Jacinto Fault, Imperial Valley, California: the Devil is in the Deposits. BS Thesis. San Diego State University. http://hdl.handle.net/20.500.11929/sdsu:30450.
Waters, M.R., 1983. Late Holocene lacustrine chronology and archaeology of ancient Lake Cahuilla, California. Quat. Res. 19, 373–387. https://doi.org/10.1016/0033-5894(83)90042-X.

Weide, D.L., 1974. Regional environmental history of the Yuha Desert region. In: Weide, M.L., Barker, J.P., Lawton, H.W., Weide, D.L., Wilke, P.J. (Eds.), Background to Prehistory of the Yuha Desert Region. Report for U.S. Department of Interior, Bureau of Land Management, California Desert Planning Program, pp. 4–15. https://doi.org/10.6067/XCV8X34WNH.

Wessel, K.N., 2015. 500 Year Rupture History of the Imperial Fault at the International Border through Analysis of Faulted Lake Cahuilla Sediments, Carbon-14 Data, and Climate Data. MS Thesis. San Diego State University. http://hdl.handle.net/20.500.11929/sdsu:1832.

Wilke, P.J., 1978. Late Prehistoric Human Ecology at Lake Cahuilla, Coachella Valley, California. Contributions of the University of California Archaeological Research Facility. Department of Anthropology, University of California Berkeley, No. 38, 168 pp. https://escholarship.org/uc/item/8367m039.

Williams, P.L., 1989. Aspects of the Earthquake Geology and Seismotectonics of the Southern San Andreas and Related Faults, Southern California. Ph.D. Thesis. Columbia University, New York, New York.

Williams, P., Seitz, G., 2005. Development of Earthquake Slip and Age Constraints, Southernmost San Andreas Fault, California. Final Technical Report. USDI/USGS Awards 04HQGR0003 and 04HQGR0012, 6 pp.

Williams, P., Seitz, G., 2006. New insights to earthquake behavior of the southernmost San Andreas fault. Seismol. Res. Lett. 77, 270. https://doi.org/10.1785/gssrl.77.2.160.

White, E.M., 2017. Determining Radiocarbon Reservoir Corrections for Freshwater Mollusks from Ancient Lake Cahuilla, Imperial County, California. MS Thesis. San Diego State University. http://hdl.handle.net/20.500.11929/sdsu:21608.

Yohe II, R.M., 1990. Archaeological Investigations at Five Sites Located at One Eleven La Quinta Center in the City of La Quinta, Central Riverside County, California. Archaeological Research Unit, University of California, Riverside.

Bulletin of the Seismological Society of America, Vol. 108, No. 5A, pp. 2634–2649, October 2018, doi: 10.1785/0120170392

Dates of the Two Most Recent Surface Ruptures on the Southernmost San Andreas Fault Recalculated by Precise Dating of Lake Cahuilla Dry Periods

by Thomas K. Rockwell, Aron J. Meltzner,* and Erik C. Haaker

Abstract The past two southernmost San Andreas fault (SAF) ruptures occurred when ancient Lake Cahuilla was full, based on faulted lake sediment relationships and extensive liquefaction at sites near the shoreline. The times of the past two southern SAF ruptures have been reevaluated with new radiocarbon data on *in situ* stumps that grew between the past three Lake Cahuilla highstands, which, when taken in combination with historical accounts and modeling of the time to fill and desiccate the lake, provide more precise and accurate ages for the past two SAF earthquakes. The ^{14}C dates on inner and outer rings combined with historical observations show that the dry period prior to the last lake ended after 1706 C.E., leaving a narrow window of less than 25 yrs to fill and begin desiccating the most recent lake, and that the penultimate lake began dropping from a highstand around 1640 C.E. or earlier. Our analysis shows that the most recent earthquake occurred about 1726 ± 7 C.E., whereas the timing of the penultimate event is slightly older at 1577 ± 67 C.E. (both at 2σ). These new dates, when combined with previous age estimates of earlier southern SAF events, suggest more regular recurrence of surface-rupturing events, with an average interval of about 180 yrs, but leave the open interval at nearly 300 yrs.

Introduction

Assessment of earthquake hazard from fast-moving faults using time-dependent forecast models is critically dependent on knowing the timing of the most recent large earthquake (Gomberg *et al.*, 2005; Petersen *et al.*, 2007; Field *et al.*, 2015). This is particularly true for the southern San Andreas fault (SAF), where the published average recurrence interval for the past millennium is on the order of 116–221 yrs, with a best estimate of 180 yrs (Philibosian *et al.*, 2011), whereas the last large surface rupture has been estimated to have occurred 330–340 yrs ago (Sieh, 1986; Sieh and Williams, 1990; Fumal *et al.*, 2002; Philibosian *et al.*, 2011). All of these studies used radiocarbon dating to resolve the timing of past earthquakes, but the radiocarbon calibration curve for the time period after about 1680 C.E. fluctuates about a horizontal axis, resulting in multiple age intercepts and discrete, broad ranges for predicted earthquake ages. The historical record has been used to trim these dates, but the historical observations are sparse, allowing for substantial uncertainty in the timing of the most recent large southern SAF earthquake.

The southern SAF crosses the shoreline and lake deposits of ancient Lake Cahuilla (Fig. 1), a freshwater lake that covered much of the Salton trough, up to its sill elevation of 13 m above sea level, at least six times in the past 1000–1200 yrs (Waters, 1983; Gurrola and Rockwell, 1996; Philibosian *et al.*, 2011). The two most recent southern SAF surface ruptures are interpreted to have occurred during the two most recent highstands of Lake Cahuilla, based on the presence of extensive liquefaction, plastic slumping, and soft-sediment deformation of lake deposits in association with upward termination of fault splays and accumulation of growth strata (Sieh, 1986; Sieh and Williams, 1990; Philibosian *et al.*, 2011).

The timings of these past earthquakes are based, in part, on radiocarbon dates on detrital charcoal recovered from the lake sediments. Because wood in this region neither grows under water nor burns in the water, most of the detrital charcoal is either derived from outside the lake basin or represents wood growth below the lake shoreline during a dry period between lakes. Consequently, the published dates of large SAF earthquakes almost certainly are older than the actual dates of the events because they do not account for the inherited age of the wood, which includes the time between plant growth and death, the burning of the wood, and the transport and burial of the charcoal in the lake sediments.

*Also at Asian School of the Environment, Nanyang Technological University, 50 Nanyang Avenue, Singapore 639798, Singapore.

Downloaded from https://pubs.geoscienceworld.org/ssa/bssa/article-pdf/108/5A/2634/4345479/bssa-2017392.1.pdf
by 13598
on 30 September 2018

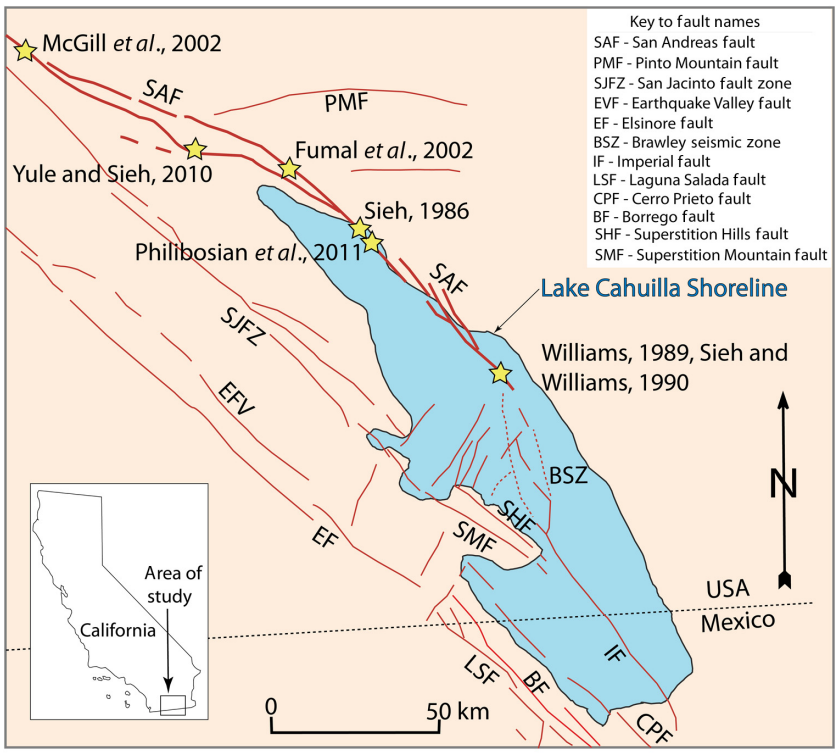

Figure 1. Map of the southern San Andreas fault (SAF) system showing paleoseismic sites (stars) on the SAF above, at, and below the shoreline of Lake Cahuilla that is shown at +13 m elevation. The color version of this figure is available only in the electronic edition.

To better date the past two southern SAF earthquakes, we apply a new approach to date the lake sediments that display evidence of faulting. We dated the dry interval between the past two lake highstands by collecting several dead mesquite stumps that were inundated by the most recent lake (lake A), and we add dates from one stump (SB 3DIII-23; Orgil, 2001) from below the penultimate lake (lake B). We also add radiocarbon ages obtained on two particularly young detrital charcoal samples associated with the filling of lake B and inferred to be derived from wood that grew and burned during the preceding dry period, between lakes B and C. The first sample (C25b/P3; Gurrola and Rockwell, 1996) was extracted from a shoreline peat-like organic layer, whereas the second (IFD-T2-C67; Rockwell *et al.*, 2011) was embedded within the penultimate lake-filling sequence at a site at −32 m elevation. These new data place tight constraints on when there was no water at various elevations within the basin. Finally, we add radiocarbon ages from young detrital charcoal samples embedded within the lake B deposits at a site at the shoreline (Philibosian *et al.*, 2011); these samples provide a maximum age on when lake B began to recede. We then combine these data with modeling of the time required to completely fill and desiccate a lake based on reasonable rates of discharge from the Colorado River and estimates of local and regional desiccation rates that we combine with the historical observations to more precisely date the most recent two lake stands that together improve both the accuracy and precision of the ages of the two most recent large southern SAF earthquakes.

Collection and Dating of *In Situ* Stumps

Stumps of dead mesquite (*Prosopis* sp., probably *P. glandulosa*) that were inundated by the most recent highstand of Lake Cahuilla are recognized in two ways. Some are now buried by lacustrine sediments, and we exposed them in trenches or by hand digging around the remnant tops of the bushes to expose the entire buried bush (Fig. 2a) (Haaker, 2012). More commonly, stumps were found in areas of little or no sedimentation from the last lake and exhibited coppice dunes around their bases. The coppice dunes appear to have been washed by water and are covered in gastropod shells (*Physa humerosa*; Fig. 2b).

In each case, we collected the entire stump by sawing it from its base, and we cut cross sections though it is in the lab. From the cross section with the most complete set of rings, we sampled the innermost and outermost 2–3 rings for radiocarbon dating. The wood samples were pretreated with the standard acid–base–acid rinses and dated at the Center for Accelerator Mass Spectrometry facility at University of California Irvine. For our age model, we assumed the growth rings were annual, and we counted the number of rings between the samples to provide an estimate of the expected number of years between the paired dates, allowing for reasonable uncertainties (Table 1).

In most cases, the core of the stump had been eaten away by termites, so the older part of the age range for these stumps is missing. We attempt to account for this by estimating the number of missing rings based on how much of the core is gone (Table 1). For the missing core of each stump, we used the documented growth rate of *P. glandulosa* for young trees with ample water supply of 4 cm/decade (Ansley *et al.*, 2010). We assumed that the initial growth of the mesquite likely initiated with the drawdown of Lake Cahuilla and that the mesquite taproot could keep up with the drawdown, initially maintaining rapid growth, although the mesquite could have started growing at any time after recession, which we also account for in our model. We hypothesize that the reason that most of the mesquite samples we collected had the heartwood eaten by termites is that the initial wood growth was from the early period of rapid growth and was likely softer than the outer rings, as is common in trees that formed after the water table dropped sufficiently to slow

Downloaded from https://pubs.geoscienceworld.org/ssa/bssa/article-pdf/108/5A/2634/4345479/bssa-2017392.1.pdf
by 13598
on 30 September 2018

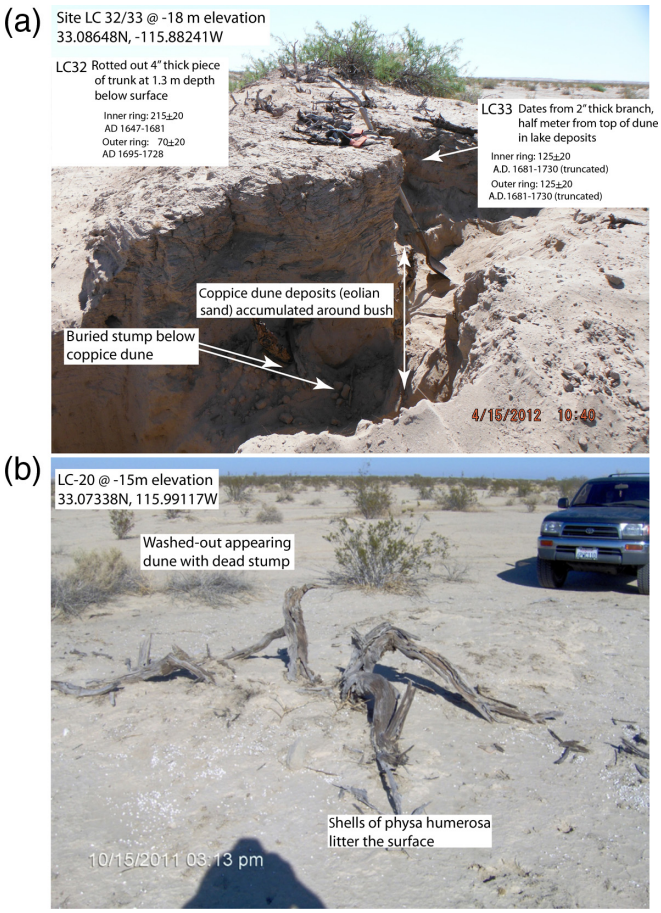

Figure 2. (a) Coppice dune with a thin capping of fine-grained sediments interpreted as lacustrine in origin. The mesquite is rooted in eolian sand near the base of the pit. (b) Dead mesquite bush surrounded by a small coppice dune with gastropod shells (*Physa humerosa*) scatted around and on the dune deposits, indicating that this bush was inundated by Lake Cahuilla (from Haaker, 2012). The color version of this figure is available only in the electronic edition.

growth. Using this model, there is probably no more than a decade or two of missing wood in any of the stumps that we dated. We note, however, that this assumption is

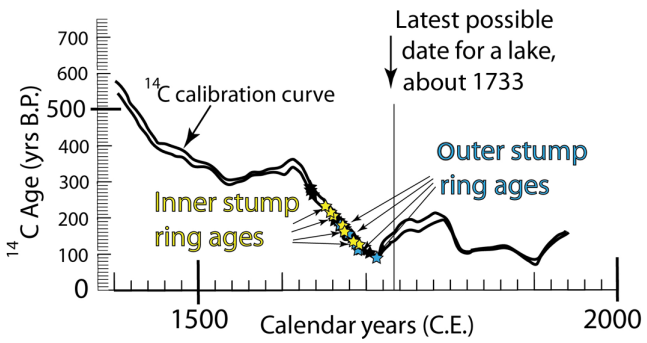

Figure 3. Inner and outer stump ages plotted on the ^{14}C calibration curve (Reimer *et al.*, 2013). Only the earliest descending part of the curve is consistent with the historical record. The color version of this figure is available only in the electronic edition.

conservative, because it avoids biasing the age of the penultimate lake. An alternative assumption that the growth rate of the stumps was more uniform throughout the lifetime of the tree would imply more missing rings in the core of each stump and would necessarily push the age of the penultimate lake farther back in time.

Dating Results

The results of dating the inner and outer rings of the drowned mesquite bushes appear in Table 2. All of the stumps that were drowned by lake A yielded dates of 1650 C.E. or younger, although the inferred missing rings could push the initiation of wood growth back a decade or two earlier. For all of these stumps, the outer rings yielded younger ^{14}C ages than the inner rings, which require that the bushes grew during a descending period on the ^{14}C calibration curve (Reimer *et al.*, 2013). The only descending periods during the past 400 yrs are for the calendar periods of about 1620–1700, 1790–1815, and 1860–1900 (Fig. 3), and only the earliest of these is consistent with the historical record, as discussed below. The apparent lack of wood growth at any

Table 1
Mesquite Stump Samples from between the Two Most Recent Lake Cahuilla Highstands

Stump Name	Latitude (°N)	Longitude (°E)	Elevation (m.a.s.l.)	Years to Fill Lake after Drowning Stump*	Years (Rings) between Inner and Outer Samples†	Missing Years (Rings) before Inner Sample‡	Years to Desiccate Full Lake down to Stump Elevation§	Total Number of Years before Inner Sample‖
LC13	33.00240	−115.95739	8	2.5 ± 0.4	21.5 ± 5.5	0.5 ± 0.3	2.9 ± 0.2	3.4 ± 0.4
LC17	33.05792	−115.97720	−14	9.5 ± 1.2	21.5 ± 5.5	8.0 ± 2.2	15.5 ± 1.1	23.5 ± 2.5
LC19	33.07330	−115.99456	−12	9.0 ± 1.2	34.3 ± 8.8	2.0 ± 0.7	14.3 ± 1.1	16.3 ± 1.3
LC20	33.07338	−115.99117	−15	9.7 ± 1.3	12.5 ± 3.3	10.0 ± 2.7	16.0 ± 1.2	26.0 ± 2.9
LC32	33.08648	−115.88241	−18	10.4 ± 1.3	62.5 ± 15.9	15.0 ± 6.3	17.8 ± 1.3	32.8 ± 6.4
LC33	33.08648	−115.88241	−18	10.4 ± 1.3	7.0 ± 2.1	22.0 ± 6.3	17.8 ± 1.3	39.8 ± 6.4

All uncertainties given at 1σ significance.
*Based on our model. See Figure 5.
†Based on our counting estimate.
‡Based on missing wood in the center of the stump.
§Based on a net desiccation rate of 1.52–2.05 m/yr.
‖The sum of the number of missing rings before the inner sample and the number of years to desiccate a full lake down to the stump elevation.

Downloaded from https://pubs.geoscienceworld.org/ssa/bssa/article-pdf/108/5A/2634/4345479/bssa-2017392.1.pdf
by 13598
on 30 September 2018

Table 2
Radiocarbon Dates Used in the OxCal Model

Sample*	Lab ID Number	$\delta^{13}C$ (‰)	Conventional ^{14}C Age (yr B.P.)	Calibrated Date Range (C.E.)†	Source
LC13-outer	UCI 111434	−23.3 ± 0.1	180 ± 20	1664–1685 1731–1808 1927–1950‡	Not previously published
LC13-inner	UCI 101757		180 ± 15	1666–1683 1734–1784 1795–1806 1930–1950‡	Not previously published
LC17-outer	UCI 111435	−23.6 ± 0.1	115 ± 20	1683–1735 1805–1895 1903–1931	Not previously published
LC17-inner	UCI 101759		130 ± 15	1681–1710 1717–1739 1750–1762 1802–1890 1909–1938	Not previously published
LC19-outer	UCI 111436	−22.5 ± 0.1	115 ± 20	1683–1735 1805–1895 1903–1931	Not previously published
LC19-inner	UCI 101761		205 ± 15	1654–1680 1764–1801 1939–1950‡	Not previously published
LC20-outer	UCI 111437	−24.3 ± 0.1	155 ± 20	1668–1696 1725–1782 1797–1815 1835–1877 1917–1949	Not previously published
LC20-inner	UCI 101762		160 ± 15	1668–1691 1728–1781 1797–1811 1920–1947	Not previously published
LC32-outer	UCI 111439	−23.7 ± 0.1	70 ± 20	1695–1726 1813–1838 1842–1853 1868–1918	Not previously published
LC32-inner	UCI 111438	−24.4 ± 0.1	215 ± 20	1647–1680 1763–1801 1938–1950‡	Not previously published
LC33-outer	UCI 111441	−24.5 ± 0.1	125 ± 20	1681–1739 1750–1762 1802–1893 1906–1938	Not previously published
LC33-inner	UCI 111440	−24.0 ± 0.1	125 ± 20	1681–1739 1750–1762 1802–1893 1906–1938	Not previously published
Sb3m45A-c	UCI 35427		310 ± 15	1516–1595 1618–1644	Philibosian *et al.* (2011)
Sb2m10A-c	UCI 35412		335 ± 15	1486–1532 1538–1604 1607–1635	Philibosian *et al.* (2011)
Sb3m44A-c	UCI 35426		335 ± 20	1484–1637	Philibosian *et al.* (2011)
Sb2m10B-c	UCI 35413		360 ± 25	1452–1527 1553–1633	Philibosian *et al.* (2011)
Sb3m48A-c	UCI 35428		380 ± 15	1449–1515 1598–1617	Philibosian *et al.* (2011)
C25b (P3)	QL4651		310 ± 40	1473–1653	Gurrola and Rockwell (1996)
IFD-T2-C67	UCI 48820	−27.6 ± 0.1	320 ± 15	1496–1506 1512–1601 1616–1642	Rockwell *et al.* (2011)

(*continued*)

Downloaded from https://pubs.geoscienceworld.org/ssa/bssa/article-pdf/108/5A/2634/4345479/bssa-2017392.1.pdf
by 13598
on 30 September 2018

Table 2 (*Continued*)

Sample*	Lab ID Number	$\delta^{13}C$ (‰)	Conventional ^{14}C Age (yr B.P.)	Calibrated Date Range (C.E.)†	Source
SB 3DIII-23B			350 ± 15	1470–1525 1557–1632	Orgil (2001)
SB 3DIII-23A			350 ± 40	1456–1637	Orgil (2001)

*Samples LC-13 through LC-33 are stump ages, and their elevations are listed in Table 1. The other dates are on detrital charcoal, and elevations are provided in the cited references. All results have been corrected for isotopic fractionation, and conventional radiocarbon ages are reported following the conventions of Stuiver and Polach (1977).

†Calibrated date ranges are 2σ ranges from Calib rev. 7.1.0 (Stuiver and Reimer, 1993).

‡These ranges are suspect due to impingement on the end of the calibration data set.

site prior to 1630–1650 C.E. suggests that all the sites were under water until shortly before that time.

Two dates on the older stump below lake B calibrate to between 1470 and 1525 C.E. or between 1557 and 1632 C.E. (Table 2), with two intercept peaks due to the calibration curve. The ^{14}C date on detrital charcoal from the Rockwell *et al.* (2011) Dogwood site at −32 m (sample IFD-T2-C67 in Table 2) may be slightly younger, calibrating to between 1496 and 1506 C.E., between 1512 and 1601 C.E., or between 1616 and 1642 C.E. The actual date of wood growth in these cases would have been during a dry period between fillings of Lake Cahuilla. The youngest date on detrital charcoal within the lake B deposits at the +13 m shoreline (sample Sb3m45A-c in Table 2) calibrates to between 1516 and 1595 C.E. or between 1618 and 1644 C.E. This provides a maximum constraint on the age of the end of the lake B highstand, when lake B began to recede.

Rates of Lake Filling and Desiccation

The range of possible dates for the timings of the most recent Lake Cahuilla highstands must account for both the amount of time required to fill the basin and the time required for its desiccation. To estimate these values, a number of input parameters must be considered: the volumetric capacity of the Salton trough below various topographic contours, from the bottom of the Lake Cahuilla at ∼84.2 m below sea level to its highstand elevation ∼13 m above sea level; the average rates of Colorado River discharge entering the basin over a given period; and the average rates of evaporation. Estimates of Salton trough capacity required a digital elevation model, available above the present elevation of the Salton Sea, and bathymetric data below that. Colorado River discharge and evaporation rates were evaluated from historical and proxy data.

The fill volumes above the present level of the Salton Sea (70.28 m below sea level) were estimated using 1 arcsec (∼30 m horizontal resolution) elevation data for the Salton trough (National Elevation Dataset; U.S. Geological Survey, 2017 ,2016 ,2013a) that are based on the North American Vertical Datum of 1988 (NAVD 88). Using Global Mapper GIS software by Blue Marble Geographics, the volumetric capacity was calculated at 1 m increments from the −70 m elevation contour to the +13 m shoreline elevation. Below the surface of the Salton Sea, fill volumes were obtained from surface elevation–capacity data derived from Global-Positioning-System-based bathymetric surveys reported relative to the National Geodetic Vertical Datum of 1929 (NGVD 29; Ferrari and Weghorst, 1997). These two data sets were combined by applying an orthometric height correction of +0.7 m to the bathymetric survey data to adjust contour elevations relative to the NAVD 88 reference datum. The combined elevation–capacity data for the Salton trough (summarized in the inset table in Fig. 4) were used to generate a sixth-order polynomial line of best fit and regression equation (Fig. 4) in Microsoft Excel 2010. Using the regression equation, lake volumes calculated as a function of surface elevation agree closely with the combined surface elevation–capacity data, with an R^2-value of 0.9999984 and a root mean square error (rmse) of 87.528×10^6 m^3 (< 0.04% of total lake capacity). Our lake model is based on this regression equation that we used to approximate lake volume as a function of surface elevation.

For filling the lake, the Colorado River would have been the primary source of water for Lake Cahuilla. Other sources of water entering the basin would have included direct precipitation, surface runoff from lesser streams and canyons, and groundwater inflow. We assume that inflows from direct precipitation, groundwater seepage, and all other channels are insignificant compared with annual flows of the Colorado River and recognize that any additional inflows from such sources would likely be offset by evaporative losses, losses resulting from surface water infiltration, and groundwater recharge during the initial stages of lake filling. For example, using a precipitation value of 6.4 cm/yr from Weide (1974) and a surface area of 5.4455×10^9 m^2, we estimate the average annual volume of rainfall into a full Lake Cahuilla to be 0.349×10^9 m^3; combined estimates of annual inflow from the Whitewater River, Salt Creek, and San Felipe Creek for the years 1961–1962 (Hely *et al.*, 1966) range between 57.99 thousand acre-feet (0.072×10^9 m^3) and 74.38 thousand acre-feet (0.092×10^9 m^3), with greater than 92%–93% of these combined flows derived from the Whitewater River. Combining these estimates of direct precipitation and surface runoff from lesser streams and canyons, we estimate a net inflow of 0.441×10^9 m^3, which is an order of magnitude less than estimated rates of volumetric evaporation at the present level of the Salton Sea, −70 m, and approximately 2 orders of magnitude less than at the highstand elevation of Lake

Downloaded from https://pubs.geoscienceworld.org/ssa/bssa/article-pdf/108/5A/2634/4345479/bssa-2017392.1.pdf
by 13598
on 30 September 2018

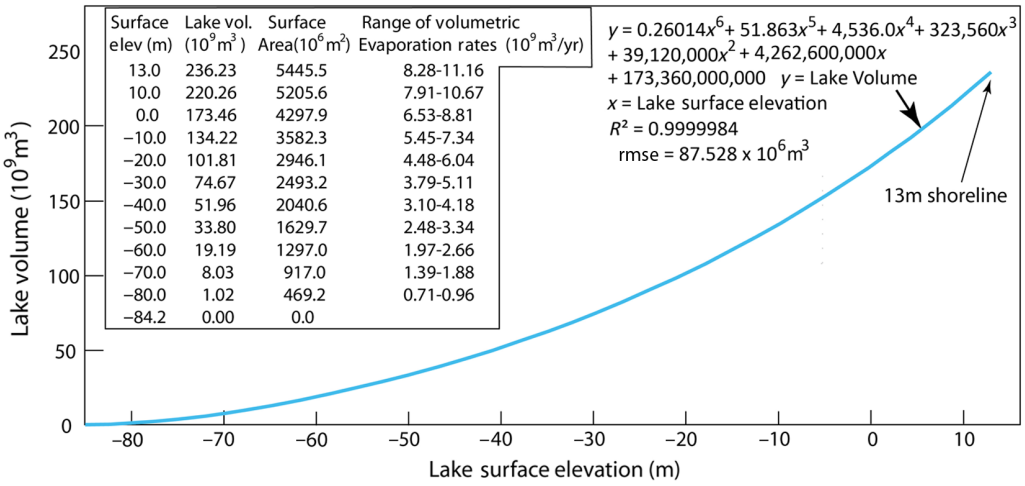

Figure 4. Plot of lake volume as a function of lake-surface elevation. Inset table shows lake volume versus surface area with the range of volumetric evaporation rates. In our model, we assumed that Lake Cahuilla filled up to +13 m, based on the sill elevation (Sieh and Williams, 1990). However, given the resolution of the digital elevation model, we cannot independently resolve the elevation of the sill of the basin to better than a few meters. The color version of this figure is available only in the electronic edition.

Cahuilla at +13 m (inset table, Fig. 4). Furthermore, we recognize that, as the lake expanded northward and southward into the Coachella and Mexicali valleys, some additional capacity for water storage would have been afforded by the presence of coarse-grained alluvial deposits along the basin's margins and delta distributary deposits near the apex of the ancestral Colorado River Delta (Van de Kamp, 1973). We assume that this additional capacity would also serve to offset inflows from precipitation and surface runoff, and we therefore use average annual rates of Colorado River discharge as the sole source of water for Lake Cahuilla in our calculations.

Weide (1974) estimated an annual rate of discharge for the Colorado River of 16.96 million acre-feet (20.92×10^9 m^3), based on normal flow conditions, averaged over the years 1902–1916. This is similar to the estimate of Wilke (1978, pp. 36–39) of 16.3 million acre-feet (20.11×10^9 m^3), based on Colorado River flow data over the longer period 1896–1966 at Lee's Ferry, Arizona, upstream of major dams, combined with estimates of discharge from tributaries downstream of Lee's Ferry. To better assess the temporal variability of Colorado River discharge, we supplemented those studies with our own analyses of historical stream flow statistics for (1) the Colorado River near Yuma, Arizona, for 1906–1963 C.E. (32°43′45″ N, 114°37′15″ W, NAD27, Gage datum 102.86 ft above NGVD 29 sea level; U.S. Geological Survey, 2017b); and (2) a combination of historical stream flow data from the Colorado River at Lee's Ferry, Arizona, for 1906–2004 (Woodhouse *et al.*, 2006a,b, c; Meko *et al.*, 2007; stream flow data were obtained from TreeFlow, an online database of stream flow reconstructions from tree rings—see Data and Resources) from the Gila River near Solomon, Arizona, for 1915–2006 (Meko and Hirschboeck, 2008; stream flow data were obtained from TreeFlow, see Data and Resources) and from tributaries of the Gila including the Salt River, the Verde River, and Tonto Creek for 1914–2004 (Meko and Hirschboeck, 2008; stream flow data were obtained from TreeFlow, see Data and Resources). Combining annual flow data for Lee's Ferry and the Gila River tributaries and comparing those values with flow statistics for the Colorado River near Yuma for the years 1906–1930, we note a relatively strong and positive linear correlation between the two data sets ($R^2 = 0.6816$; rmse $= 3.527 \times 10^9$ m^3). In contrast, we note that the two data sets diverge after 1930, with significant declines at Yuma, presumably due to anthropogenic modifications to the Colorado River upstream (e.g., construction of Hoover Dam, Parker Dam, and Imperial Dam, 1931–1938). For the purposes of utilizing longer records of annual stream flow that are less encumbered by the effects of anthropogenic modification, we used the combined flow data for Lee's Ferry and the Gila River tributaries as the basis of our model, along with estimates of normal flow conditions by Weide (1974).

We therefore adopt the Weide (1974) estimate of Colorado River discharge over the period 1902–1916 as our preferred rate, but we allow for the possibility that, during wetter periods, the discharge was higher. Based on our evaluation of the combined annual stream flow data (see table in Fig. 5), we assign a maximum plausible rate of 23.54×10^9 m^3/yr, based on an 11-yr running average over the period 1906–1995; the wettest 11-yr period was 1912–1922, assuming a Gila River contribution of 2% relative to the observed flows at Lee's Ferry for 1912–1914. We also assign a historical (1906–1995) mean of 19.19×10^9 m^3/yr, neglecting Gila River contributions for the years 1906–1914, which we take as a lower bound on annual discharge in our model. A summary table of combined historical stream flow statistics for 6-, 11-, 16-, and 23-yr running averages is included in Figure 5 for reference.

The other key parameter necessary to calculate the filling time of Lake Cahuilla is the evaporation rate of lake

Downloaded from https://pubs.geoscienceworld.org/ssa/bssa/article-pdf/108/5A/2634/4345479/bssa-2017392.1.pdf
by 13598
on 30 September 2018

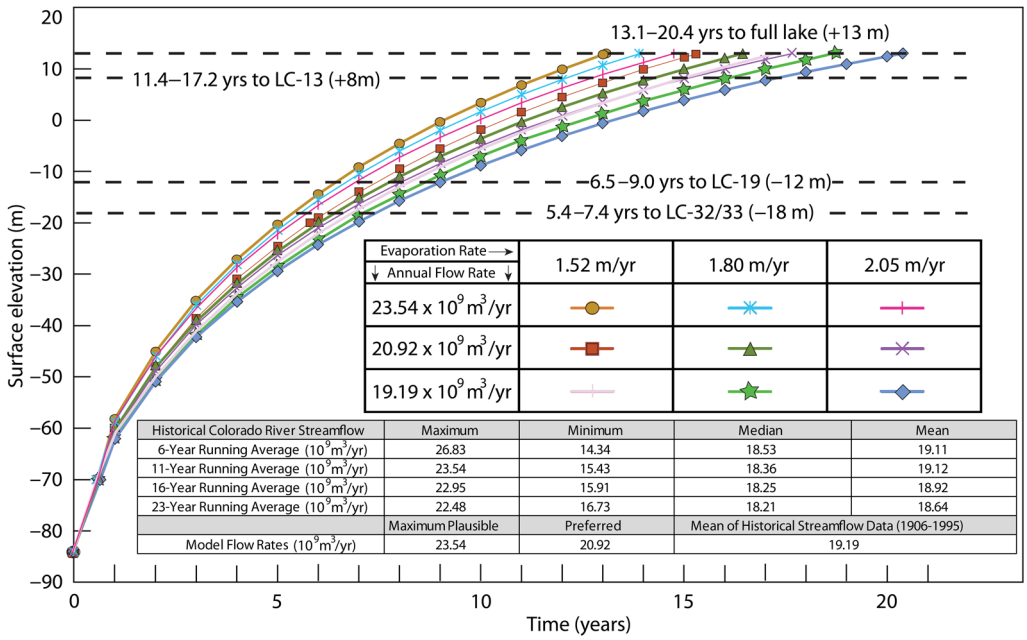

Figure 5. Lake filling model results and estimated ranges of historical Colorado River stream flow (1906–2004 C.E.). Surface elevations reported relative to mean sea level (as defined by North American Vertical Datum 1988). Historical ranges of Colorado River stream flow derived from combined annual flow rates observed on the Colorado River at Lee's Ferry (Woodhouse *et al.*, 2006a,b,c; Meko *et al.*, 2007), on the Gila River near Solomon, on the Salt River, on the Verde River, and at Tonto Creek (Meko and Hirschboeck, 2008). Our preferred Colorado River stream flow is that determined by Weide (1974), as discussed in the Rates of Lake Filling and Desiccation section. The color version of this figure is available only in the electronic edition.

water. Evaporation rates for the desiccation of Lake Cahuilla have been variously estimated at 1.52–1.55 m/yr (Sieh and Williams, 1990) to 1.8 m/yr (Wilke, 1978, p. 38). A faster evaporation rate was directly measured from a water surface in a tank in Calexico from 1904 to 1906 with an average annual rate of 2.05 m/yr (Blake, 1915, p. 21), although over those 3 yrs alone the evaporation ranged from 1.6 to 2.6 m/yr. An even faster evaporation rate of ~2.08 m/yr is estimated for the Salton Sea on the U.S. Weather Bureau's *Evaporation Maps for the United States* (Kohler *et al.*, 1959, plate 2; Meyers and Nordenson, 1962, plate 3; Hely and Peck, 1964, plate 2). However, as Hely *et al.* (1966, pp. C18–C19) note, the evaporation rates shown on the *Evaporation Maps for the United States* should be approximately correct for evaporation from small bodies of fresh water; the larger effective diameter of the Salton Sea (and Lake Cahuilla) would increase the humidity of the air moving across the water surface, thereby decreasing the evaporation rate from that predicted by Kohler *et al.* (1959), Meyers and Nordenson (1962), and Hely and Peck (1964). In light of the aforementioned estimates, we adopt 1.52, 1.80, and 2.05 m/yr as plausible evaporation rates in our model.

Hydrologic Modeling and Time Required to Fill Lake Cahuilla

Using the input parameters described above, we developed a hydrologic model for estimating the time required to partially fill Lake Cahuilla to the elevations of our dated stump samples and to completely fill it to the +13 m shoreline. The sixth-order polynomial regression equation generated from the 1 m elevation–capacity data for the Salton trough $Q_{net} = f(H_{eq})$ was used to convert lake volumes (Q_{net}) to equivalent lake-surface elevations (H_{eq}). Complete capture of annual Colorado River discharge (Q_{in}) was assumed constant for each year and added to the net volume of lake water (Q_{net}) from the previous year; this yielded the initial volume of lake water ($Q_{initial}$) for each year, prior to evaporation. Starting with an empty basin ($Q_{net} = 0$, $H_{eq} = -84.2$ m), water entering the basin each year (Q_{in}) would result in an initial lake volume ($Q_{initial}$), causing the surface elevation of the lake (H_{eq}) to rise to an initial surface elevation ($H_{initial}$); values of $Q_{initial}$ were converted to values of $H_{initial}$ ($Q_{initial} \rightarrow H_{initial}$) by linear interpolation of the regression equation calculated at 0.1 m increments of equivalent surface elevation. After the value of $H_{initial}$ was determined, evaporation would lower the surface of the lake linearly by an amount equal to the average annual evaporation rate (ΔH_{evap}), assumed to be constant for each year, resulting in the final surface elevation of the lake at the end of each model year. To repeat the calculation for the following year, values of H_{eq} were converted back to equivalent lake volumes using the regression equation $Q_{net} = f(H_{eq})$. This process was repeated for subsequent years until H_{eq} for the final year equaled or exceeded the 13 m shoreline elevation. To approximate the amount of time (t) required to fill the lake completely ($H_{eq} = +13$ m) and partially fill it to the elevations of our stump samples (H_{eq} = stump elevation),

Downloaded from https://pubs.geoscienceworld.org/ssa/bssa/article-pdf/108/5A/2634/4345479/bssa-2017392.1.pdf
by 13598
on 30 September 2018

we used linear interpolation to approximate the value of t as a function of H_{eq} between model years bracketing the desired value of H_{eq}. A total of nine simulations were run using annual Colorado River discharge rates of 23.54×10^9, 20.92×10^9, and 19.19×10^9 m^3 in combination with annual evaporation rates of 1.52, 1.80, and 2.05 m/yr. The results of our hydrologic modeling are summarized in Figure 5.

The results of the model suggest it would have taken between 13.1 and 20.4 yrs to completely fill Lake Cahuilla, and using our "preferred" discharge rate (20.92×10^9 m^3), we provide a best estimate of 15.3–17.7 yrs. It would take only 5.4–7.4 yrs to fill the basin to the elevation of our lowest dated stump (LC-32/33) at approximately −18 m. If the previous lake had not fully desiccated, less time would have been required.

Historical Constraints

Several early Spanish explorers made expeditions to the mouth of the Colorado River, starting with Francisco de Ulloa in 1539 (Bancroft, 1884, pp. 78–81; Wagner, 1929, pp. 19–20 and 307) and Hernando de Alarcón in 1540 (Bancroft, 1884, pp. 90–93; Hammond and Rey, 1940, pp. 124–155). This continued 65 yrs later with Don Juan de Oñate and Father Francisco de Escobar in 1605 (Bolton, 1916, pp. 268–280; Bolton, 1919a) and then 95 yrs after that with a series of expeditions by Father Eusebio Francisco Kino between 1700 and 1706 (Venegas, 1759, Vol. 1, pp. 300–311; Bolton, 1919b, Vol. 1, pp. 246–256, 312–320, 340–345, and Vol. 2, pp. 205–214). Finally, Father Juan de Ugarte reached the mouth of the Colorado River in 1721 (Venegas, 1759, Vol. 2, pp. 46–62), as did Father Ferdinand Konščak (Fernando Consag) in 1746 (Venegas, 1759, Vol. 2, pp. 308–353). Details are in Appendix A, and locations mentioned here in the Historical Constraints section are shown in Figure A1. None of these explorers reached the Salton trough, but in 1540, 1605, and 1700–1706, their accounts indicate that the Colorado River was flowing to the Gulf of California at those times.

Another European explorer, Jacobo Sedelmayer (Jocobo Sedelmair), made a number of overland expeditions to the Gila and Colorado Rivers between 1744 and 1750 (Venegas, 1759, Vol. 2, pp. 181–211; Bancroft, 1884, pp. 536–543; Dunne, 1955). It appears that the only time during which Sedelmair followed the Colorado for any significant distance downstream of its confluence with the Gila River was in 1750, when he reached a point west of the sand dunes of the Gran Desierto de Altar that he subsequently crossed (Dunne, 1955, pp. 69–72). Sedelmair's journey along the Colorado River almost to the Gulf of California suggests the river was, once again, flowing southward to the Gulf. However, an unusual story related to Sedelmair in 1748 suggests that the Colorado River flowed, at least partially or intermittently, into the Salton trough. Sedelmair recounts a story told to him by Yuma Indians, while he was stationed just east of the confluence of the Colorado and Gila Rivers: "Here they informed me that if one crossed the Colorado and traveled northwest for two days one would touch once again the banks of the same river" (Dunne, 1955, p. 60). Later, Bancroft (1884, pp. 541–543) discusses a letter written in 1751 to the king of Spain, in which Captain Fernando Sanchez Salvador "advances the theory that the Colorado before reaching the gulf throws off a branch to the westward, which flows into the Pacific between Monterey and Point Concepcion." Although the details of a river reaching the Pacific are clearly impossible, the theory was likely based on the reports of the natives, and it suggests that, at least in what was then recent memory, the Colorado River had flowed, in part, into the Salton trough. And although Kino had visited with the same tribes at the same location in 1700, 1701, and again in 1702, no stories emerged during any of Kino's visits of a westward distributary of the Colorado River.

A series of expeditions between 1771 and 1776 unequivocally demonstrate the absence of a lake in the Salton trough at that time. In 1771, although Father Francisco Garcés was confused about his location at the time, he followed the Colorado River from its confluence with the Gila southward to the head of tidewater, near Heintzelman's Point (Bolton, 1917, pp. 322–325). From there, Garcés traveled northwestward, reaching a point about three leagues east of present-day Yuha Well; at that point, he was forced to turn around because he was out of water and had lost hope of finding water farther along (Bolton, 1917, pp. 325–328; Bolton, 1930, Vol. 1, pp. 45–47 and opposite p. 120, and Vol. 2, pp. 337–338).

Starting in 1774, Juan Bautista de Anza, Father Francisco Garcés, Father Pedro Font, and Juan Díaz continued to explore the region, searching for a land route to the west coast. On 10–11 March and 7–8 May 1774 (Bolton, 1930, Vol. 2, pp. 81–85, 113–114, 194–197, 228, 280–281, 296, 338–341) and again on 13–18 December 1775 and 7–8 May 1776 (Bolton, 1930, Vol. 3, pp. 56–62, 172–174, 195, 229–230, 295–296, and Vol. 4, pp. 129–140, 478–481), Anza and his party camped at a site they named San Sebastián, on San Felipe Creek near its confluence with Carrizo Wash, at an elevation of −40 to −35 m, near 33.099° N, 115.925° W. On 8 May 1774, both Anza and Díaz wrote in their diaries about looking for watering holes to the east or southeast of San Sebastián (Bolton, 1930, Vol. 2, pp. 114, 228, 296); exactly 2 yrs later, on 8 May 1776, Anza and Font described searching once again for a watering hole in that vicinity (Bolton, 1930, Vol. 3, pp. 173–174, 296, and Vol. 4, pp. 479–481), and this time they made it to Kane Spring, at 33.110° N, 115.836° W and −43 m. Despite their efforts, Font stated definitively on 8 May 1776 that the water at Kane Spring was "all the water we found" until they reached some wells at Pozo Salobre del Carrizal, where Font found "the water as red as if it had vermilion [and] very salty" (Bolton, 1930, Vol. 4, p. 481; see also, Vol. 3, p. 174). Bolton places the Pozo Salobre del Carrizal site on the old Paredones River, south of Cocopah in Baja California; Cocopah (Estación Cucapah) is present-day Ejido Tamaulipas, at 32.550° N, 115.232° W, and in the early twentieth century the Paredones

Downloaded from https://pubs.geoscienceworld.org/ssa/bssa/article-pdf/108/5A/2634/4345479/bssa-2017392.1.pdf
by 13598
on 30 September 2018

River was 5–10 km south of that point (Bolton, 1930, Vol. 1, opposite p. 120; see also Cory, 1915, p. 1219). No mention is ever made in any of the diaries of finding a body of water of any size in the center of the Salton trough, indicating that the most recent lake (lake A) must have desiccated completely or nearly completely by 1774. Furthermore, in his diary on 10 March 1774, Díaz described the diet of the natives who lived near the San Sebastián site, and it included mesquite beans (Bolton, 1930, Vol. 2, p. 280); if mature mesquite trees were growing at −35 m in 1774, the lake must have desiccated to below that elevation many years before then.

We use the historical accounts to place constraints on when the Colorado River was flowing to the Gulf, in which case we interpret that the lake was not in a filling phase. We also use Anza's traverse of the region as a hard constraint as to when the lake was mostly or completely dry, which limits how recently a complete filling could have occurred.

Climate Proxy Data

The stump ages (Table 2) require that the most recent Lake Cahuilla (lake A) must have filled around or after the beginning of the eighteenth century, and if we account for the time required to desiccate the lake from +13 m to −84.2 m, then historical accounts limit the filling of the most recent Lake Cahuilla to the early eighteenth century or earlier. We are therefore particularly interested in rainfall on the Colorado River catchment area in the early eighteenth century. Climate proxy records from the lower and upper Colorado River basin reveal decadal variations in rainfall. Precipitation on the lower Colorado River basin averaged 30.0 cm/yr over 1902–1916; the period 1707–1717 was drier, with precipitation averaging 26.3 cm/yr, whereas 1718–1727 was wetter, with precipitation averaging 33.8 cm/yr (Salzer and Kipfmueller, 2005a,b). For the upper Colorado River, annual flows at Lee's Ferry were reconstructed from tree rings (Woodhouse *et al.*, 2006a,b,c; Meko *et al.*, 2007; stream flow data were obtained from TreeFlow,see Data and Resources). The period 1902–1916 saw an average annual flow at Lee's Ferry of 19.4×10^9 m^3/yr, whereas 1707–1717 was drier, with an average flow of 17.5×10^9 m^3/yr, and 1718–1727 was wetter, with an average flow of 20.9×10^9 m^3/yr. These paleoclimate reconstructions consistently show that the Colorado River catchment area was ∼10% drier in 1707–1717, and ∼10% wetter in 1718–1727, relative to the 1902–1916 baseline. This implies that, depending on the exact timing of the most recent filling of Lake Cahuilla, it may have been possible to trim a year or so off the time required to fill the lake, but at other times it might have required an extra year. In any case, if the most recent lake did not begin filling until after Kino's final visit in 1706, the full lake highstand is not likely to have occurred until after 1721 C.E. or perhaps a year or two earlier if there was already some water in the basin in 1706; if the most recent lake did not begin filling until 1718 C.E., the full lake highstand is not likely to have occurred until after 1731 C.E. or perhaps a year or two earlier if there was already some water in the basin. Although it seems reasonable to infer that an avulsion of the Colorado River would be more likely during the wet period from 1718 to 1727 than during the dry period from 1707 to 1717, we do not impose this as a prior constraint in our model.

As stated previously, desiccation rates for evaporation of Lake Cahuilla are estimated at 1.52–2.05 m/yr (Blake, 1915, p. 21; Wilke, 1978, p. 38; Sieh and Williams, 1990), implying that between 47 and 64 yrs is required for full desiccation from +13 to −84.2 m. If the Cahuilla basin had completely desiccated by 1774, then the lake would have had to start drying up between 1710 and 1727. However, if some saline water was still resident in the basin in 1774, then the date of avulsion of the Colorado River back into the Gulf of California (and the onset of desiccation) could be advanced by several years. Alternatively, if the faster, historically documented evaporation rate from Lake Mead is applied (2.18 m/yr; Hely *et al.*, 1966, p. C18), then a slightly later date of 1731 is allowable for the end of lake A at +13 m. In any case, the historical constraints provided by Kino's and Anza's visits, along with the limits on the filling and desiccation rates, provide strong bounds on the timing of filling and desiccation of lake A and therefore on the timing of the most recent large SAF earthquake.

Chronological Modeling and Final Ages

We constructed an OxCal model (Bronk Ramsey, 2008; Fig. 6 and Fig. A2) that incorporates four sets of constraints. Working backward in time, we impose a historical prior of 1730 ± 3 C.E. (2σ) that represents the last date at which Lake Cahuilla could have been full (at +13 m elevation) if it had mostly or completely desiccated by the time of Anza's visit in 1774. The second set of constraints comes from the dated mesquite (*Prosopis* sp.) stumps that were growing in the footprint of Lake Cahuilla but which, we infer, were drowned by the last filling of the lake; these date the dry period between lakes A and B. The third set of constraints consists of five samples from the lake B shoreline deposits that provide a maximum limit on the age of the end of the lake B highstand. The oldest set consists of four additional radiocarbon dates that date the dry period prior to lake B (Fig. 6).

For each of the stumps that were killed by the filling of lake A, we ran radiocarbon dates on both the outermost and the innermost preserved growth rings (Fig. 3), and we visually counted the number of rings separating the outermost and innermost preserved rings (Table 1). Because the central core of some of the stumps was missing, presumably eaten by termites, we also crudely estimated (with appropriately large uncertainties) the number of years of growth that were missing from the center of the stump, based on the growth rate of mesquite (Ansley *et al.*, 2010; Table 1). To overcome the complication that the various stumps grew at different elevations and therefore could have begun growing at different times, we estimated the number of years that it

Downloaded from https://pubs.geoscienceworld.org/ssa/bssa/article-pdf/108/5A/2634/4345479/bssa-2017392.1.pdf
by 13598
on 30 September 2018

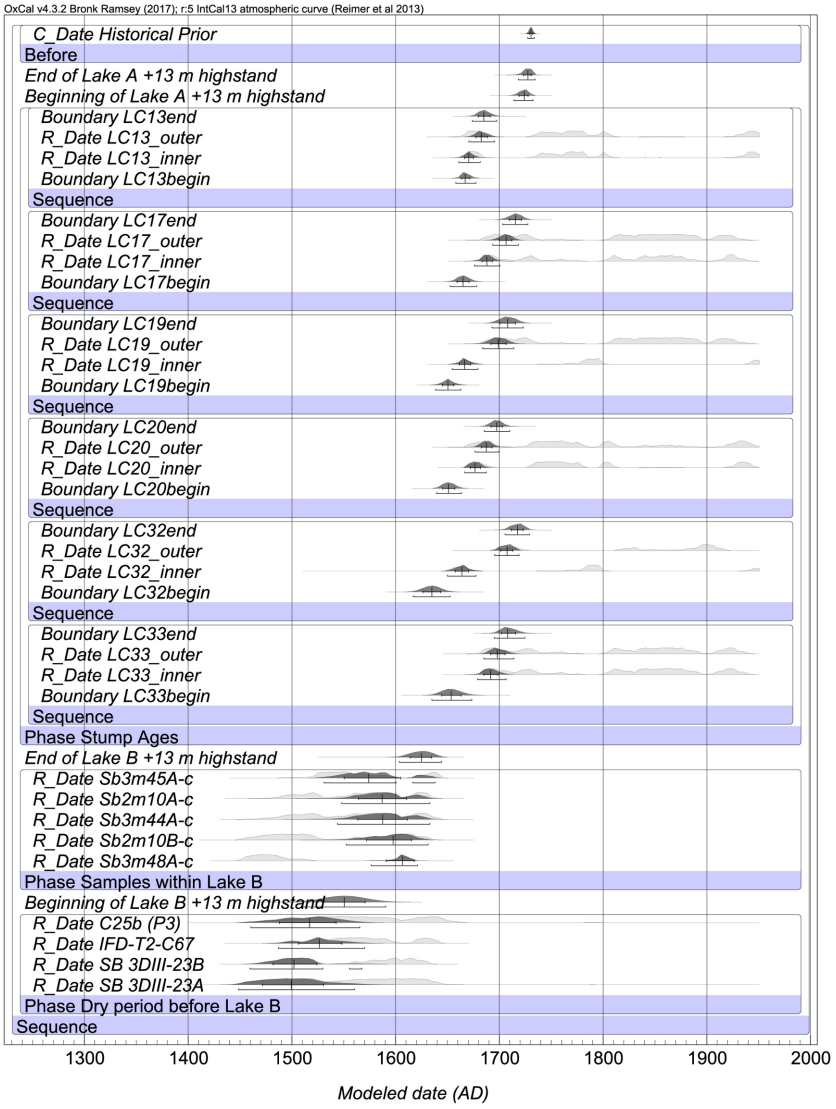

Figure 6. OxCal model of stump ages and detrital ^{14}C dates that constrain the timing of the past two lake stands and, therefore, the dates of the two most recent large southern SAF earthquakes. The color version of this figure is available only in the electronic edition.

would have taken for lake B to drop from its highstand elevation of +13 m down to the elevation of each stump. Lastly, we used the elevation of each stump to estimate the number of years it would have taken for lake A to complete its filling up to +13 m after it drowned the respective stump.

In OxCal, for each stump, we ordered the inner and outer dates as a Sequence(), and we used the Interval() function to impose, with appropriate uncertainties: (1) the number of growth rings separating the two dated samples, (2) the amount of growth inferred to be missing from the center of the stump, (3) the amount of time estimated for the lake to fall from its highstand elevation to the elevation of the stump, and (4) the amount of time estimated for the lake to complete its filling after drowning the stump. Imposition (1) forces the model to limit the posterior probability distribution to reasonable segments of the radiocarbon calibration curve (the dry period between lakes A and B must have occurred during a descending part of the calibration curve); impositions (2) and (3) force the model to extend the dry period between lakes A and B back an appropriate amount of time; and imposition (4) forces the model to allow an appropriate amount of time for lake A to fill. Because of the way the nested OxCal model is constructed, the results should not be biased if a stump did not begin growing immediately after lake B receded below its elevation or if a stump died from other causes before lake A rose to the stump's elevation.

The oldest set of radiocarbon constraints includes two dates from a mesquite stump inferred to have been drowned by the filling of lake B (Orgil, 2001): a date from a shoreline peat inferred to comprise material that had grown within the Lake Cahuilla footprint prior to the filling of lake B (Gurrola and Rockwell, 1996), and a date from charcoal at the base of the filling sequence of lake B at a site at −32 m elevation (Rockwell *et al.*, 2011). The wood being dated in each of these four cases necessarily grew prior to lake B, and therefore these samples provide a maximum age of the lake B filling event; however, because the radiocarbon calibration curve is essentially flat at that time (Fig. 3), this maximum age may overestimate the true age of the filling event by many decades, possibly even by a century.

To these we add dates from five particularly young samples embedded within lake B deposits at a site at the shoreline (Philibosian *et al.*, 2011); these samples constrain the maximum age of the end of the lake B highstand, but because these samples may have grown above the +13 m shoreline, we caution that we have no *a priori* reason to assume they grew during a lake stand versus during a dry interlude. Unfortunately, these samples also grew during a flat part of the radiocarbon calibration curve, leaving ambiguity in the interpretation. If at least some of these lake B shoreline samples have no more than a few decades of inherited age, then the samples' true ages, and the age of the lake B deposits, must fall near the younger end of the samples' probability density functions, as indicated in Figure 6. If, however, all of the lake B shoreline samples have more than a few decades of inherited age, then the samples' true ages may fall near the older end of their probability density functions; the OxCal results for Phase("Samples within Lake B") may not be valid, and the modeled age of the end of the lake B highstand may

Downloaded from https://pubs.geoscienceworld.org/ssa/bssa/article-pdf/108/5A/2634/4345479/bssa-2017392.1.pdf
by 13598
on 30 September 2018

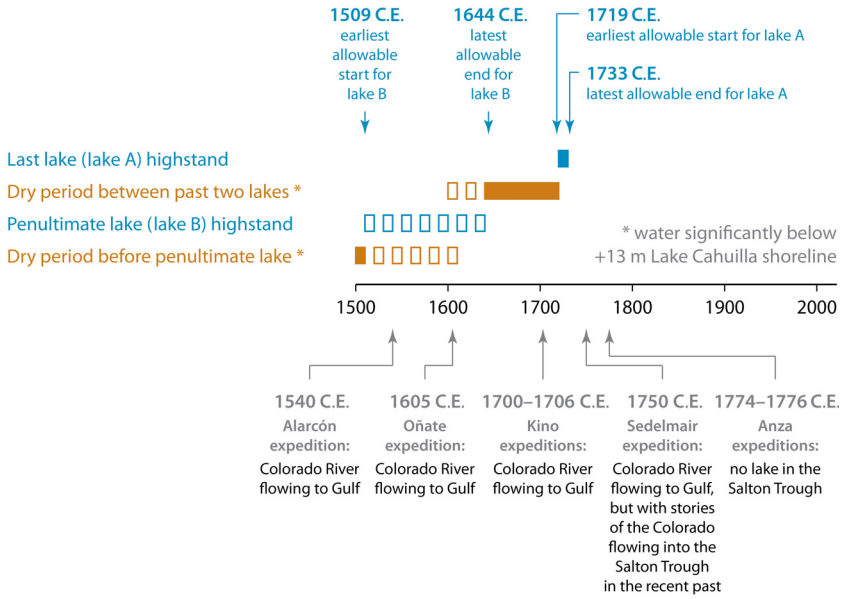

Figure 7. Timeline showing possible timings of the two most recent highstands of Lake Cahuilla and the intervening dry period. Solid bars denote periods of high confidence for the timing of the event; open bars indicate possible timing for the event. There is considerable uncertainty in the date range of lake B because of the double hump in the radiocarbon calibration curve. The color version of this figure is available only in the electronic edition.

underestimate the true age by many decades, possibly even by a century. In spite of the aforementioned complications, we can robustly conclude that the lake B highstand began no earlier than 1550 ± 40 C.E. (2σ) and ended no later than 1624 ± 20 C.E. (2σ). The actual timing of lake B could be anywhere in that interval, and the duration of the lake B highstand is not tightly constrained by these data (Fig. 7).

The OxCal model suggests that the lake A highstand occurred sometime between 1723 ± 9 and 1726 ± 8 C.E. (2σ). This is driven primarily by the ages of the LC17 and LC32 stump samples. This is consistent with the argument that lake A did not begin filling until after Kino's final visit in 1706, even though that information is not included in the model as a prior. If we now add the constraints (discussed previously) from Kino's observation that the Colorado River was still flowing southward in 1706 and from Anza's inability to find water during the treks across the basin in 1774–1776, then the earliest the lake A highstand could have begun is ~1719 C.E., and the latest it could have ended is ~1733 C.E. (Fig. 7). This leaves 1719–1733 C.E. as the maximum allowable time span for the lake A highstand, although it may have lasted only a year or two during that period. We place the highstand at 1726 ± 7 C.E.

Discussion and Conclusions

The two most recent surface-rupturing earthquakes on the southern SAF in Coachella Valley occurred when Lake Cahuilla was full, or nearly so. Sieh (1986) and Sieh and Williams (1990) reported from a shoreline site at Indio that the most recent earthquake (MRE) occurred when the lake was full, because the rupture broke up through shoreline berm sediments and was capped by topset beds associated with the most recent lake. Similarly, Philibosian *et al.* (2011) reported that the MRE produced slumping at the Coachella site that they interpreted could only have happened if the site was saturated, or nearly so. They also report that the rupture is capped by fine, well-sorted eolian sand that we reinterpret as recessional shoreline sand. These two observations are consistent with each other and argue that the MRE occurred between about 1719 and 1733 C.E., or about 1726 ± 7 (2σ). This moves forward in time the MRE on the southernmost SAF by 30–50 yrs, because prior studies placed the event at about 1680 (Sieh, 1986) to 1690 C.E. (Philibosian *et al.*, 2011).

The penultimate event at the Coachella site produced massive liquefaction that again requires the presence of water, and upward fault terminations occur in the lake B sediments (Philibosian *et al.*, 2011). After the liquefaction, additional lake deposits accumulated, which suggests that the earthquake occurred sometime during the middle of lake B, so we place a 1509–1644 C.E. age range for that earthquake, which we simplify to 1577 ± 67 C.E. (2σ). Philibosian *et al.* (2011) dated this event to between 1588 and 1662, so the timing of the penultimate event is shifted older by a several decades.

These new dates for the timing of the two MREs on the southernmost SAF even out the distribution of event ages by expanding the time between the two events to about 150 yrs, and they decrease the open interval to just under 300 yrs. Using the dates of earlier events in Philibosian *et al.* (2011), the average recurrence interval remains at about 180 yrs. Thus, by all accounts, the southern SAF is probably late in the earthquake cycle because it has now accumulated on the order of 6 m of elastic strain and potential slip (Fialko, 2006) that is more than inferred for the 1857 M_w 7.8 Ft. Tejon earthquake (Zielke *et al.*, 2010).

Data and Resources

All radiocarbon data and site elevation data used in this article were collected by the authors or appropriately cited. The websites https://www.ncdc.noaa.gov/paleo-search/study/6387, http://www.treeflow.info/content/colorado-r-lees-ferry-az-meko, http://www.treeflow.info/content/gila-river-near-solomon-az, and http://www.treeflow.info/content/salt-river-verde-river-tonto-creek-az (last accessed June 2018). All other data sources are cited.

Downloaded from https://pubs.geoscienceworld.org/ssa/bssa/article-pdf/108/5A/2634/4345479/bssa-2017392.1.pdf
by 13598
on 30 September 2018

Acknowledgments

The authors thank the reviewers (Neta Wechsler and anonymous) for improving the presentation of this article. This work was supported by the Southern California Earthquake Center (SCEC) Grant Numbers 12170 and 14049. This research was also supported by the National Research Foundation Singapore and the Singapore Ministry of Education under the Research Centres of Excellence initiative. This is SCEC Contribution Number 7970 and Earth Observatory of Singapore Contribution Number 179.

References

Ansley, R. J., M. Mirik, and M. J. Castellano (2010). Structural biomass partitioning in regrowth and undisturbed mesquite (Prosopis glandulosa): Implications for bioenergy uses, *GCB Bioenergy* **2,** 26–36, doi: 10.1111/j.1757-1707.2010.01036.x.

Bancroft, H. H. (1884). *History of the North Mexican States*, Vol. 1, A.L. Bancroft & Company, San Francisco, California, 1531–1800.

Blake, W. P. (1915). Sketch of the region at the head of the Gulf of California, in *The Imperial Valley and the Salton Sink*, H. T. Cory (Editor), John J. Newbegin, San Francisco, California, 1–35.

Bolton, H. E. (1916). *Spanish Exploration in the Southwest*, Charles Scribner's Sons, New York, New York, 1542–1706.

Bolton, H. E. (1917). The early explorations of Father Garcés on the Pacific slope, in *The Pacific Ocean in History*, H. M. Stephens and H. E. Bolton (Editors), Macmillan Company, New York, New York, 317–330.

Bolton, H. E. (1919a). Father Escobar's relation of the Oñate expedition to California, *Catholic Hist. Rev.* **5,** 19–41.

Bolton, H. E. (1919b). *Kino's Historical Memoir of Pimería Alta*, 2 Vols., Arthur H. Clark Company, Cleveland, Ohio.

Bolton, H. E. (1930). *Anza's California Expeditions*, 5 Vols., University of California Press, Berkeley, California.

Bronk Ramsey, C. (2008). Deposition models for chronological records, *Quaternary Sci. Rev.* **27,** 42–60, doi: 10.1016/j.quascirev.2007.01.019.

Cory, H. T. (1915). *The Imperial Valley and the Salton Sink*, John J. Newbegin, San Francisco, California.

Dunne, P. M. (1955). *Jacobo Sedelmayr: Missionary, Frontiersman, Explorer in Arizona and Sonora*, Arizona Pioneers' Historical Society, Tucson, Arizona.

Ferrari, R. L., and P. Weghorst (1997). *Salton Sea 1995 Hydrographic GPS Survey*, U.S. Department of the Interior, Bureau of Reclamation, 24 pp.

Fialko, Y. (2006). Interseismic strain accumulation and the earthquake potential on the southern San Andreas fault system, *Nature* **441,** 968–971.

Field, E. H., G. P. Biasi, P. Bird, T. E. Dawson, K. R. Felzer, D. D. Jackson, K. M. Johnson, T. H. Jordan, C. Madden, A. J. Michael, et al. (2015). Long-term time-dependent probabilities for the third Uniform California Earthquake Rupture Forecast (UCERF3), *Bull. Seismol. Soc. Am.* **105,** 511–543, doi: 10.1785/0120140093.

Fumal, T. E., M. J. Rymer, and G. G. Seitz (2002). Timing of large earthquakes since A.D. 800 on the Mission Creek strand of the San Andreas fault zone at Thousand Palms Oasis, near Palm Springs, California, *Bull. Seismol. Soc. Am.* **92,** 2841–2860, doi: 10.1785/0120000609.

Gomberg, J., M. E. Belardinelli, M. Cocco, and P. Reasenberg (2005). Time-dependent earthquake probabilities, *J. Geophys. Res.* **110,** no. B05S04, doi: 10.1029/2004JB003405.

Gurrola, L. D., and T. K. Rockwell (1996). Timing and slip for prehistoric earthquakes on the Superstition Mountain fault, Imperial Valley, southern California, *J. Geophys. Res.* **101,** 5977–5985, doi: 10.1029/95JB03061.

Haaker, E. C. (2012). Moving towards a more complete Late Holocene chronology of ancient Lake Cahuilla, *B.S. Thesis*, San Diego State University, San Diego, California, 19 pp.

Hammond, G. P., and A. Rey (1940). *Narratives of the Coronado Expedition, 1540–1542*, University of New Mexico Press, Albuquerque, New Mexico, 413 pp.

Hely, A. G., and E. L. Peck (1964). Precipitation, runoff, and water loss in the Lower Colorado River–Salton Sea area, *U.S. Geol. Surv. Profess. Pap. 486-B*, available at https://pubs.usgs.gov/pp/0486b/ (last accessed June 2018).

Hely, A. G., G. H. Hughes, and B. Irelan (1966). Hydrologic regimen of Salton Sea, California, *U.S. Geol. Surv. Profess. Pap. 486-C*, available at https://pubs.usgs.gov/pp/0486c/ (last accessed June 2018).

Kohler, M. A., T. J. Nordenson, and D. R. Baker (1959). Evaporation maps for the United States, *U.S. Weather Bur. Tech. Pap. 37*.

Meko, D. M., and K. K. Hirschboeck (2008). The current drought in context: A tree-ring based evaluation of water supply variability for the Salt–Verde River basin, *Final Report*, available at http://www.treeflow.info/sites/default/files/SRP-II-Final-Final-Report-08-08-08.pdf (last accessed June 2018).

Meko, D. M., C. A. Woodhouse, C. A. Baisan, T. Knight, J. J. Lukas, M. K. Hughes, and M. W. Salzer (2007). Medieval drought in the upper Colorado River basin, *Geophys. Res. Lett.* **34,** L10705, doi: 10.1029/2007GL029988.

Meyers, J. S., and T. J. Nordenson (1962). Evaporation from the 17 Western States, *U.S. Geol. Surv. Profess. Pap. 272-D*, available at https://pubs.usgs.gov/pp/0272d/ (last accessed June 2018).

Orgil, A. (2001). Three-dimensional paleoseismic investigation on the south break of the Coyote Creek fault, southern California, *M.S. Thesis*, San Diego State University, San Diego, California, 85 pp.

Petersen, M. D., T. Cao, K. W. Campbell, and A. D. Frankel (2007). Time-independent and time-dependent seismic hazard assessment for the State of California: Uniform California Earthquake Rupture Forecast Model 1.0. *Seismol. Res. Lett.* **78,** 99–109, doi: 10.1785/gssrl.78.1.99.

Philibosian, B., T. Fumal, and R. Weldon (2011). San Andreas fault earthquake chronology and Lake Cahuilla history at Coachella, California, *Bull. Seismol. Soc. Am.* **101,** 13–38, doi: 10.1785/0120100050.

Reimer, P. J., E. Bard, A. Bayliss, J. W. Beck, P. G. Blackwell, C. Bronk Ramsey, C. E. Buck, H. Cheng, R. L. Edwards, M. Friedrich, et al. (2013). IntCal13 and Marine13 radiocarbon age calibration curves 0-50,000 years cal BP, *Radiocarbon* **55,** 1869–1887, doi: 10.2458/azu_js_rc.55.16947.

Rockwell, T. K., A. Meltzner, and R. Tsang (2011). A long record of earthquakes with timing and displacements for the Imperial fault: A test of earthquake recurrence models, *Final Technical Report, U.S. Geological Survey*, 28 pp.

Salzer, M. W., and K. F. Kipfmueller (2005a). Reconstructed temperature and precipitation on a millennial timescale from tree-rings in the southern Colorado Plateau, U.S.A, *Clim. Change* **70,** 465–487, doi: 10.1007/s10584-005-5922-3 (last accessed June 2018).

Salzer, M. W., and K. F. Kipfmueller (2005b). *Southern Colorado Plateau Temperature and Precipitation Reconstructions*, IGBP PAGES/World Data Center for Paleoclimatology, Data Contribution Series Number 2005-066, NOAA/NCDC Paleoclimatology Program, Boulder, Colorado, available at ftp://ftp.ncdc.noaa.gov/pub/data/paleo/treering/reconstructions/northamerica/usa/colorado-plateau2005.txt.

Sedelmair, J. (1750). Entrada a la nacion de los yumas gentiles por el mes de Octubre y Noviembre del año de 1749, in *Documentos para la Historia de México*, F. García Figueroa (Editor) (1856), quarta série (4th series), tomo I, Vol. 1, Vicente García Torres, Mexico City, 18–25 (in Spanish).

Sieh, K. E. (1986). Slip rate across the San Andreas and prehistoric earthquakes at Indio, California, *Eos Trans. AGU* **67,** 1200.

Sieh, K. E., and P. L. Williams (1990). Behavior of the southernmost San Andreas fault during the past 300 years, *J. Geophys. Res.* **95,** 6629–6645, doi: 10.1029/JB095iB05p06629.

Stuiver, M., and H. A. Polach (1977). Discussion: Reporting of ^{14}C data, *Radiocarbon* **19,** 355–363, doi: 10.1017/S0033822200003672.

Stuiver, M., and P. J. Reimer (1993). Extended ^{14}C data base and revised CALIB 3.0 ^{14}C age calibration program, *Radiocarbon* **35,** 215–230, doi: 10.1017/S0033822200013904.

United States Hydrographic Office (1918). *Mexico and Central American Pilot (Pacific Coast) from the United States to Colombia including*

Downloaded from https://pubs.geoscienceworld.org/ssa/bssa/article-pdf/108/5A/2634/4345479/bssa-2017392.1.pdf
by 13598
on 30 September 2018

the Gulfs of California and Panama, Fifth Ed., Government Printing Office, Washington, D.C.

U.S. Geological Survey (2013). USGS NED 1 arc-second n34w116 1 x 1 degree ArcGrid, available at https://www.sciencebase.gov/catalog/item/581d26e1e4b08da350d5cd86 (last accessed June 2018).

U.S. Geological Survey (2016). USGS NED 1 arc-second n34w117 1 x 1 degree ArcGrid (last accessed June 2018).

U.S. Geological Survey (2017a). USGS NED 1 arc-second n33w116 1 x 1 degree ArcGrid, available at https://www.sciencebase.gov/catalog/item/581d25eee4b08da350d5b3ea (last accessed June 2018).

U.S. Geological Survey (2017b). USGS surface-water annual statistics for the nation: USGS 09521000 Colorado River at Yuma, AZ, available at https://waterdata.usgs.gov/nwis/annual?search_site_no=09521000&format=sites_selection_links (last accessed June 2018).

Van de Kamp, P. C. (1973). Holocene continental sedimentation in the Salton Basin, California: A reconnaissance, *Geol. Soc. Am. Bull.* **84,** 827–848, doi: 10.1130/0016-7606(1973)84<827:HCSITS>2.0.CO;2.

Venegas, M. (1757). Noticia de la California, y de su Conquista Temporal, y Espiritual hasta el Tiempo Presente, 3 Vols., *La Imprenta de la Viuda de Manuel Fernández, y del Supremo Consejo de la Inquisicion, Madrid* (in Spanish).

Venegas, M. (1759). *A Natural and Civil History of California*, 2 Vols., James Rivington and James Fletcher, London, United Kingdom.

Wagner, H. R. (1929). *Spanish Voyages to the Northwest Coast of America in the Sixteenth Century*, California Historical Society, San Francisco, California, 571 pp.

Waters, M. R. (1983). Late Holocene lacustrine chronology and archaeology of ancient Lake Cahuilla, California, *Quaternary Res.* **19,** 373–387, doi: 10.1016/0033-5894(83)90042-X.

Weide, D. L. (1974). Regional environmental history of the Yuha Desert region, in *Background to Prehistory of the Yuha Desert Region*, M. L. Weide, J. P. Barker, H. W. Lawton, D. L. Weide, and P. J. Wilke (Editors), Report for U.S. Department of Interior, Bureau of Land Management, California Desert Planning Program, 4–15, doi: 10.6067/XCV8X34WNH.

Wilke, P. J. (1978). Late prehistoric human ecology at Lake Cahuilla, Coachella Valley, California, *Contributions of the University of California Archaeological Research Facility*, Department of Anthropology, University of California Berkeley, No. 38, 168 pp., available at https://escholarship.org/uc/item/8367m039 (last accessed June 2018).

Woodhouse, C. A., S. T. Gray, and D. M. Meko (2006a). Updated streamflow reconstructions for the Upper Colorado River basin, *Water Resour. Res.* **42,** no. W05415, doi: 10.1029/2005WR004455.

Woodhouse, C. A., S.T. Gray, and D. M. Meko (2006b). *Updated Streamflow Reconstructions for the Upper Colorado River Basin*, IGBP PAGES/World Data Center for Paleoclimatology, Data Contribution Series Number 2006-050, NOAA/NCDC Paleoclimatology Program, Boulder, Colorado, available at https://www.ncdc.noaa.gov/paleo-search/study/6352 (last accessed June 2018).

Woodhouse, C. A., S. T. Gray, and D. M. Meko (2006c). Colorado R. at Lees Ferry, AZ, available at http://www.treeflow.info/content/colorado-r-lees-ferry-az (last accessed June 2018).

Zielke, O., J. R. Arrowsmith, L. Grant Ludwig, and S. O. Akciz (2010). Slip in the 1857 and earlier large earthquakes along the Carrizo Plain, San Andreas fault, *Science* **327,** 1119–1122, doi: 10.1126/science.1182781.

Appendix A

Summary of Observations of the Colorado River Delta up to 1750 C.E. and the OxCal Model Used in Our Analysis

Figure A1 shows site locations. Figure A2 shows the OxCal model used in this study. A summary of historical observations follows, below.

In September 1539, Ulloa sailed up the Gulf of California to the Colorado River Delta. Ulloa got about as far north

Figure A1. Location of site names used in the Historical Constraints section. The inset shows the location of stumps of dead mesquite that grew between lakes A and B and were inundated by Lake A. The color version of this figure is available only in the electronic edition.

Downloaded from https://pubs.geoscienceworld.org/ssa/bssa/article-pdf/108/5A/2634/4345479/bssa-2017392.1.pdf
by 13598
on 30 September 2018

as present-day Montague Island, at the southern edge of the Delta, but that was not northward enough to determine whether the full Colorado River was flowing southward into the Gulf. He described the sea there as "reddish and turned to mud," as if the Colorado River was actively dumping sediment nearby, yet the channels he attempted to navigate were entirely tidal and were left dry at low tide (Ulloa, in Wagner, 1929, p. 20). This was no different from conditions there in the nineteenth and twentieth centuries, where a tidal range approaching 10 m creates strong currents and a tidal bore exceeding 1 m during spring tides (United States Hydrographic Office, 1918, pp. 155–157). In the end, Ulloa abandoned his northward journey near Montague Island because his boats could not go further.

In 1540, Alarcón sailed up the Gulf of California, in an attempt to extend Ulloa's exploration northward. By August, Alarcón reached the shoals where Ulloa had turned back, but Alarcón pushed onward. Eventually, with much difficulty, his crew "found a mighty river with such a furious current that [they] could scarcely sail against it" (Alarcón, in Hammond and Rey, 1940, pp. 125–126). Determining the upstream extent of Alarcón's journey has been an elusive task ever since; Alarcón described reaching "some very high mountains among which the river flowed in a narrow canyon" (Alarcón, in Hammond and Rey, 1940, p. 153), which would imply he had passed the confluence of the Gila and Colorado Rivers above present-day Yuma, but other estimates suggest a shorter upstream traverse (Alarcón, in Hammond and Rey, 1940, p. 154; Pedro de Castañeda, in Hammond and Rey, 1940, p. 211; Bancroft, 1884, p. 93). Regardless, it is clear that in 1540 the Colorado River had strong currents to the Gulf of California, indicating that Lake Cahuilla was not filling at that time.

In 1604 and 1605, Oñate and Escobar explored overland westward from New Mexico, following the Bill Williams River to the Colorado River at present-day Lake Havasu; from there, they followed the Colorado River downstream past the Gila River (Bolton, 1919a, pp. 27–32). Below the confluence with the Gila River, Escobar estimated that the river continued 20 leagues (~110 km) to the sea and that "the river bottom appeared wider [and] the river has some branches which all the year carry water" (Escobar, in Bolton, 1919a, pp. 32–33). They reached the Cocapa settlement that "extends to the sea, or to the place reached by the salt water, which enters the river from the sea some four or five leagues" (Escobar, in Bolton, 1919a, p. 33) before continuing to Montague Island and the Gulf of California (Bolton, 1916, pp. 276–278; Bolton, 1919a, pp. 34–35). In January 1605, as in 1540, the Colorado River was clearly flowing to the Gulf of California.

In 1687, Kino founded Mission Nuestra Señora de los Dolores in what is now the inland parts of Sonora, Mexico, south of Nogales; he continued to live there for the next 24 yrs, until his death. In 1700, Kino explored the Gila River valley westward to its confluence with the Colorado River. He climbed two hills just east of the confluence (likely in the Gila Mountains), from which he could see that "the two rivers, below the confluence, ran united about ten leagues to the west, and then, turning southward, about twenty leagues farther on emptied into the head of the Sea of California" (Kino, in Bolton, 1919b, Vol. 1, pp. 249, 253). He also saw "a large stretch of country in California" (Kino, in Bolton, 1919b, Vol. 1, p. 253), but it is unclear whether he would have climbed high enough to be able to see a full Lake Cahuilla, had it existed at the time. Nonetheless, Kino made no notes of reports or descriptions of a lake in the Salton trough.

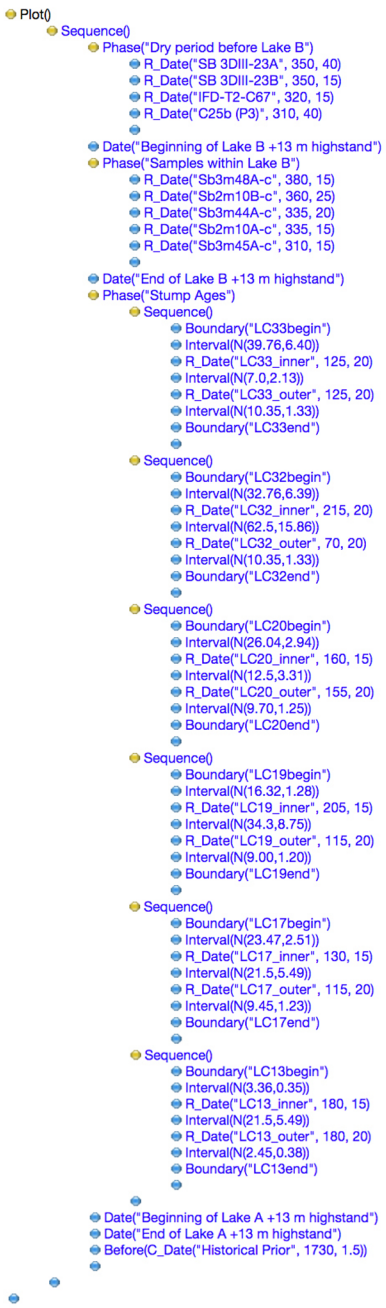

Figure A2. OxCal model used to calculate the ages of lakes A and B. The color version of this figure is available only in the electronic edition.

Downloaded from https://pubs.geoscienceworld.org/ssa/bssa/article-pdf/108/5A/2634/4345479/bssa-2017392.1.pdf
by 13598
on 30 September 2018

In 1701, Kino returned to the confluence of the Gila and Colorado Rivers and continued onward, following the river more than 18 leagues (~100 km) toward the Gulf of California. There, Kino crossed the river on a raft, and he described the river as "very large volumed" and "about two hundred *varas* [~170 m] wide," noting that people "did not touch the bottom except at the two banks" (Kino, in Bolton, 1919b, Vol. 1, p. 316). The next year, Kino returned to the Colorado River near where it "empties into the head of the Sea of California." There, he again described the river as "very large volumed and very wide" and difficult to cross (Kino, in Bolton, 1919b, Vol. 1, pp. 341–344).

In 1706, Fray Manuel de Oyuela traveled with Kino and climbed the highest of the Pinacate Peaks. From there, Oyuela could see as far as the Gulf of California, and he described "the very large volumed Rio Colorado which enters into the sea" at the head of the Gulf (Oyuela, in Bolton, 1919b, Vol. 2, p. 212). During all of Kino's visits to the Colorado Delta, from 1700 to 1706, it is clear that the Colorado River was flowing to the Gulf of California.

One driving question of Kino's expeditions was determining whether California was a peninsula or an island. At one point in 1702, Kino acknowledges in his diary that there were reports of a body of water northwest of the Colorado Delta, but he summarily dismisses those reports as describing the Pacific Ocean: "if some hostile and obstinate persons should maintain that some Quiquima Indians say that farther west the sea still extends to the northwest, these Quiquima speak of the other sea, on the opposite coast, and not of this our Sea of California …" (Kino, in Bolton, 1919b, Vol. 1, p. 354). Thus, it is possible that some water may have been present in the Salton trough between 1700 and 1706, but the Colorado River was clearly flowing into the Gulf at that time.

In 1721, Ugarte sailed up the Gulf of California to the mouth of the Colorado River but, like Ulloa 182 yrs earlier, was unable to pass through the shoals, where there were strong, tidally driven currents (Venegas, 1759, Vol. 2, pp. 56–58). Ugarte proceeded to Montague Island, where he observed that the river "ejected into the sea grass, leaves, weeds, trunks of trees, burnt logs, the timbers of cottages and the like" (Venegas, 1759, Vol. 2, p. 59). While this would be consistent with a full-flowing Colorado River emptying into the Gulf, Ugarte also noted that "on the two preceding nights the weather had been very tempestuous with thunders and lightnings and violent rains, which had occasioned the two inundations they had observed in the river" (Venegas, 1759, Vol. 2, p. 59). Our assessment, therefore, is that the evidence is inconclusive as to whether the full Colorado River was flowing to the Gulf in 1721.

In 1746, Consag sailed up the Gulf of California to the mouth of the Colorado River, where he described similar challenges with the tides as the previous explorers; he reached Montague Island but was unable to travel much further upstream due to strong tidal currents (Consag, in Venegas, 1759, Vol. 2, pp. 342–349). Meanwhile, Consag's crew explored limited distances overland by foot: they spent a day and a half looking for drinking water near a place they called San Buenaventura (~10 km north of present-day San Felipe, Baja California; see map of Consag, in original Spanish text of Venegas, 1757, Vol. 3, after p. 194), and they briefly explored the land near Montague Island (Consag, in Venegas, 1759, Vol. 2, pp. 346, 348). Again, the evidence is inconclusive as to whether the full Colorado River was flowing to the Gulf of California in 1746. Furthermore, it appears Consag did not reach a place where he could have seen a lake in the Salton trough, had it existed at the time.

Father Sedelmair explored the region of the Gila and Colorado Rivers on several expeditions between 1744 and 1750. In 1744, he explored both rivers upstream of their confluence but did not explore downstream (Venegas, 1759, Vol. 2, pp. 181–185; Bancroft, 1884, pp. 536–537; Sedelmair, in Dunne, 1955, pp. 15–53). Sedelmair returned to the region in October and November 1748, although he oddly reported the dates of that trip as being in October and November 1749; regardless, he explored only a short distance downstream of the confluence of the Colorado and Gila Rivers (Sedelmair, 1750; Venegas, 1759, Vol. 2, pp. 209–210; Bancroft, 1884, p. 540; Dunne, 1955, pp. 55–66). Finally, in 1750, Sedelmair went farther downstream, to a point west of the sand dunes of the Gran Desierto de Altar, apparently almost reaching the Gulf of California (Bancroft, 1884, pp. 540–541; Dunne, 1955, pp. 67–75).

Appendix B

Online Access to Historical Accounts

Some historical accounts consulted in this study are available online:

Sedelmair (1750):
https://books.google.com/books?id=HJgEAAAAQAAJ
http://cdigital.dgb.uanl.mx/la/1080023894_C/1080023894_T1/1080023894_MA.PDF
http://cdigital.dgb.uanl.mx/la/1080023894_C/1080023894_T1/1080023894_03.pdf

Venegas (1757):
Volume 1: https://archive.org/details/cihm_18688
Volume 2: https://archive.org/details/cihm_18689
Volume 3: https://archive.org/details/cihm_18690
All: https://catalog.hathitrust.org/Record/100258713

Venegas (1759):
Volume 1: https://archive.org/details/naturalcivilhist01vene
Volume 2: https://archive.org/details/naturalcivilhist02vene
All: https://catalog.hathitrust.org/Record/100268375

Bancroft (1884):
https://archive.org/details/thenorthmexivol115bancmiss
https://archive.org/details/worksofhuberthow15bancrich

Downloaded from https://pubs.geoscienceworld.org/ssa/bssa/article-pdf/108/5A/2634/4345479/bssa-2017392.1.pdf
by 13598
on 30 September 2018

https://archive.org/details/historynorthmex02nemogoog
https://archive.org/details/historynorthmex03nemogoog
https://archive.org/details/annalsofspanishn01oakhrich

Blake (1915):
https://archive.org/details/imperialvalleya00blakgoog

Cory (1915):
https://archive.org/details/imperialvalleya00blakgoog

Bolton (1916):
https://archive.org/details/spanishexplorati00bolt
https://archive.org/details/spanishexplorat03boltgoog

Bolton (1917):
https://archive.org/details/pacificoceaninhi00panaiala
https://archive.org/details/pacificoceaninhi00panauoft

Bolton (1919a):
http://www.jstor.org/stable/25011616
https://archive.org/details/fatherescobarsre00boltrich

Bolton (1919b):
Volume 1: https://archive.org/details/kinoshistoricalm00kino
Volume 2: https://archive.org/details/kinoshistoricalm02kinouoft

Bolton (1930):
Volume 1: https://archive.org/details/anzascaliforniae01bolt
Volume 2: https://archive.org/details/anzascaliforniae02bolt
Volume 3: https://archive.org/details/anzascaliforniae03bolt
Volume 4: https://archive.org/details/anzascaliforniae04bolt
Volume 5: https://archive.org/details/anzascaliforniae05bolt

Dunne (1955):
https://catalog.hathitrust.org/Record/001652279

United States Hydrographic Office (1918):
https://archive.org/details/mexicoandcentra00offigoog

Kohler *et al.* (1959):
https://catalog.hathitrust.org/Record/101740906
http://www.nws.noaa.gov/oh/hdsc/Technical_papers/TP37.pdf

All websites were last accessed on June 2018.

Department of Geological Sciences
San Diego State University
San Diego, California 92182
trockwell@mail.sdsu.edu
(T.K.R.)

Earth Observatory of Singapore
Nanyang Technological University
50 Nanyang Avenue
Singapore 639798
Singapore
meltzner@ntu.edu.sg
(A.J.M.)

G3SoilWorks, Inc.
350 Fischer Avenue Front
Costa Mesa, California 92626
ehaaker@g3soilworks.com
(E.C.H.)

Manuscript received 28 December 2017;
Published Online 17 July 2018

Downloaded from https://pubs.geoscienceworld.org/ssa/bssa/article-pdf/108/5A/2634/4345479/bssa-2017392.1.pdf
by 13598
on 30 September 2018

Estimating slip distribution along the southernmost ~80 km of the San Andreas Fault by examining tectonically offset features

***William C. Buckley[1], Patrick L. Williams[2], Thomas K. Rockwell[1], and Allen M. Gontz[3]**

[1]Department of Geological Sciences, San Diego State University, 5500 Campanile Drive, San Diego, California 92182

[2]Patrick Williams & Associates, P.O. Box 1437, Alpine, California 91903

[3]Department of Civil and Environmental Engineering, Clarkson University, 8 Clarkson Avenue, Potsdam, New York, 13699

ABSTRACT

We measured tectonically offset geomorphic features along approximately 80 km of the southernmost San Andreas Fault (sSAF) between Bombay Beach and Indio Hills in the Salton Trough to obtain a better estimate for slip distribution and slip-per-event for the past several large, surface rupturing earthquakes along this segment of the fault. In addition to gathering aerial imagery from previously published B4 light detection and ranging (LiDAR) and uncrewed aerial vehicle (UAV) imagery, we constructed new high-resolution orthomosaics and digital surface models (DSMs) generated from Structure-from-Motion-Multiview Stereo (SfM-MVS) techniques from UAV imagery at multiple localities along the San Andreas fault in the Salton Trough region of California, which include areas at Durmid Hill, Salt Creek, Ferrum, Mecca Hills, and Indio Hills. The aerial imagery, along with field mapping, were used to identify and measure a total of 146 offset features with lateral displacement measurements ranging between 2 to 23 m. Investigation of offset features suggests that the last several large, surface rupturing events produced average displacements of 3.1-4.4 m per event, with lower overall lateral slip values where multiple fault strands are present. Offset features displaying less than ~1 m of lateral displacement were not considered in our study as these features likely reflect modern creep and triggered slip events, which post-date the most recent surface rupturing event in ca 1726 AD.

INTRODUCTION

The southernmost San Andreas Fault (sSAF), extending from approximately Bombay Beach to Banning Pass in the Salton Trough (Fig. 1), has been the focus of several notable paleoseismic studies in the Coachella Valley and Salt Creek regions (Sieh and Williams, 1990; Fumal et al., 2002; Philibosian et al., 2011; Rockwell et al., 2018; Castillo et al., 2021), but information on displacement in the paleo-events is much more limited. Some displacement information was included in UCERF3 (Field et al., 2014; Field et al., 2015), and two recent studies in and near the Mecca Hills provide local information on displacement for the past few ruptures (Dingler et al., 2016; Blanton et al., 2020), but information on the distribution of slip in the past several earthquakes has not been constructed for the length of the southern SAF in the Salton Trough. In this paper, we present new information of the amount of displacement

that has occurred in the past few large surface rupturing earthquakes from Bombay Beach northward to the Indio Hills based on offset geomorphic markers (Fig. 1). This work builds on the previous studies in the Mecca Hills area (Blanton et al., 2020; Dingler et al., 2016) that suggest that the MRE produced 2.6 to 3.1 m of lateral displacement. We flew Uncrewed Aerial Vehicles (UAVs) to capture high-resolution imagery from which we produced Digital Surface Models (DSMs) and orthomosaics with millimeter to centimeter-scale precision. We used these maps as a base for field work to resolve displacement on 146 offset features between the Indio Hills and Bombay Beach. We combine these new results with field measurements taken by one of the coauthors (Williams) 10-15 years ago to construct slip distribution for the past several earthquakes on the sSAF.

A complicating factor in estimating displacement in past earthquakes from geomorphic offset features is that the sSAF creeps in its upper 2-3 km at a rate of about 3 mm/yr (Lindsey et al., 2014; Sieh and Williams, 1990), resulting in additional uncertainty in slip measurements (Blanton et al., 2020). As the majority of the fault is locked below the creeping zone, we believe that the creep is best interpreted as extended afterslip. If correct, then the additional slip from creep needs to be added to that which occurred co-seismically. The problem lies in not knowing the age of individual geomorphic features, such as small rills, channel margins, apex ridges, and alluvial bars, relative to the age of the displacement events. Some creep may have accrued prior to a large earthquake if a particular feature was formed decades to a century prior to the earthquake. In this case, the offset may reflect both displacement from the earthquake and its associated afterslip as well as some displacement that may be attributed to the previous earthquake. In contrast, if a rill or other piercing line formed immediately prior to the earthquake, then the measured displacement may be smaller than the previous case. This could result in both larger uncertainty in estimating displacement in past events as well as an apparent variability in displacement laterally along the fault.

Blanton et al. (2020) showed that small displacements of about 20-23 and 50-51 cm are likely the result of incision during past hurricane and tropical storm strikes in 1939 and 1858, respectively. They also document that smaller storms that produced 3-6 cm of rain during the course of their study did not produce new incisions that would be used to measure displacement. This indicates that it is the very-large tropical storms that form during strong El Nino events that are likely to "reset" the landscape and produce geomorphic features that can be used to measure displacement in future earthquakes. Although the frequency of such events is not known, the historical record suggests that they occur about once per century. For the section of fault south of the Indio Hills, which has the shortest recurrence interval, the 3 mm/yr of creep in combination with the frequency of major storms imparts an uncertainty in slip estimation on the order of 30-50 cm.

Paleoseismic data, when combined with slip per event data, can be used as a cross check to test slip data against the fault slip rate as measured by geologic and geodetic methods. Paleoseismic studies conducted in Coachella Valley revealed a

range of average recurrence intervals for surface-rupturing earthquakes in the past millennia; with about 180 years south of the Indio Hills (Philibosian et al., 2011, although that includes the current long open interval) to as much as 380-640 years north of the Indio Hills (Castillo et al., 2021). The most recent surface rupturing event south of the Indio Hills occurred around 1726 CE (Rockwell et al., 2018) which leaves a possibly atypically long 300-year open interval since the last large sSAF earthquake. To the north of Indio Hills, the most recent event is dated at 950 to 730 calibrated years BP, much earlier than to the south. We combine our new displacement data with paleoseismic records to verify a substantial set of displacement observations against known slip rate data.

REGIONAL SETTING

Geologic background

The Salton Trough is located in the Imperial and Coachella Valleys of southeastern, California, as well as the Mexicali Valley and Colorado River Delta in Mexico. The Salton Trough is a large, active tectonic pull-apart basin formed by the interaction of the SAF system and the northernmost portion of the East Pacific Rise known as the Gulf of California Rift Zone (GCRZ) (Fuis and Mooney, 1990). The SAF and GCRZ both terminate in close proximity to the Salton Sea, near the Brawley Seismic Zone, which connects the SAF with the Imperial Fault Zone (IFZ) to the south. As a result of this interaction, the Salton Trough has been subsiding; however, sedimentary deposits have filled the trough as quickly as it has been subsiding and in some areas the sediment has accumulated up to approximately 6,000 m in thickness as it subsides, indicating long-term subsidence of ~1 mm/yr (Younker et al., 1981).

Regional mapping indicates that the Salton Trough is underlain by Holocene-aged surficial deposits and Pliocene-Pleistocene-aged sedimentary bedrock units (Brothers et al., 2009). The surficial sediments consist of alluvial sand and gravel, deltaic and lacustrine silt and clay, as well as sand and gravelly bar deposits along the shoreline of ancient Lake Cahuilla and from a two-year flooding event between 1905 and 1907 CE (Ross, 2020) that resulted from a breached canal derived from spring flooding on the Colorado River, which consequently created the modern-day Salton Sea. The sedimentary bedrock units include the Palm Spring Formation (Tp), which consists of pink-gray laminated sandstone with interbedded clays and fossil hardwoods, and the Borrego Formation (Tbo), which consists of tan-gray lacustrine fossiliferous claystone.

Ancient Lake Cahuilla

During the late Holocene the Salton Trough experienced repeated filling and desiccation events as a result of cyclic diversions of the Colorado River (Waters, 1983; Rockwell et al., 2022). Filling events were caused when the Colorado River, which usually discharges into the Gulf of Mexico, changed course and discharged to the west and north via the Alamo and New Rivers (Rockwell et al., 2022). This change in course would inundate much of the Salton Trough and create a freshwater lake known as Lake Cahuilla, which had a highstand shoreline elevation of ~13 m above sea level. Stratigraphic analyses have revealed evidence for six filling episodes in the past ~1,100 years, with the most recent lake event ending by 1733 CE (Sieh and Williams,

1990; Philibosian et al., 2011; Rockwell et al., 2018; Rockwell et al., 2022). Paleo-shorelines of Lake Cahuilla indicate that this body of freshwater covered much of the sSAF system which indicates that the lake sediments locally record timing of the southernmost sSAF rupture history (Rockwell et al., 2018).

METHODS

Study Sites

We divided ~80 km of the sSAF into five different sections based on where geomorphic features displaying strike-slip evidence are best preserved and most pervasive along the fault (Fig. 1). These sections are in isolated and relatively undisturbed areas where human development is sparse and geomorphic features are well—preserved. To generate slip distribution for the past several surface-rupturing events in each of these sections, we compiled displacement measurements using various piercing points depending on the feature, which included thalwegs of small channels, channel wall margins, and apex ridges. Areas between sections comprise regions where offset features along the fault are buried by young alluvium, are not well-preserved, or have been impacted by recent structural and agricultural developments. Consequently, these sections were deemed unsuitable for our study.

Data Collection

We utilized published geomorphic offset measurements from the southern and northern reaches of the Mecca Hills (Blanton et al., 2020) along with published imagery datasets from UAV and LiDAR surveys (Bunds et al., 2021; Bevis and Hudnut, 2006, respectively). We used the imagery datasets along with Google Earth imagery to determine areas with well-preserved geomorphic features, which were then assessed in the field. Four areas along the fault that are accessible with an off-road vehicle and exhibited well-preserved offset features were selected to collect new, high-resolution imagery. UAV and Real-Time Kinematic (RTK) surveys were conducted at each of these sites and field measurements were obtained by using a standard metric tape measure to quantify displacement for these offset features.

Ground control points (GCPs) were strategically placed on the ground surface along either side of the main fault trace within the survey parameters prior to conducting UAV surveys. These GCPs are placed on benchmarks, or known points on the ground, and can be used to geo-reference imagery with greater accuracy. The total number of GCPs used was determined based on the approximate survey coverage area (Table 1) and ranged from a total of four to nine GCPs. New benchmarks for GCP placement were established for each new survey and locations of each GCP were collected using an EMLID Reach RS RTK GPS (EMLID, 2022), where base and rover stations were setup in RTK mode with a correction link over Long Range (Lo-Ra) radio. During GPS data collection, the fix status was used to provide centimeter-scale precision between the approximate positioning of the rover to the base station.

Imagery from our new surveys was collected using a DJI Phantom 4 Pro UAV system equipped with a GoPro camera (Table 1). All flights were conducted using an automated flight mapping application, DroneDeploy, which was operated on a smart phone. Flight parameters were

established in DroneDeploy prior to each flight to ensure adequate overlap for Structure-from-Motion-Multiview-Stereo (SfM-MVS) processing techniques and efficient coverage over the areas of interest. Most flight missions were conducted during peak sun hours (11am to 1pm) where shadow coverage is minimal. One flight mission was conducted between 10am and 3pm due to a larger coverage area (Table 1; Fig. 2); however, this did not produce significant shadow effects on the imagery. The altitude above ground level (AGL) for each flight mission was determined from the takeoff point and the UAV system did not adjust to changes in topography during flight missions. As a result, some portions of the flight are closer or farther from the ground surface depending on local relief. Changes in local relief for flight missions south of Mecca Hills were relatively insignificant as these locations have gentle or gradually sloping terrain as they are below the shoreline of Lake Cahuilla. The flight mission at Biskra Palms experienced more significant change in local relief as the sSAF in this area is located along the southwestern front of Indio Hills; however, imagery was not negatively impacted. Imagery from published SfM and LiDAR datasets (Bunds et al., 2021; Bevis and Hudnut, 2006, respectively) obtained from the OpenTopography online database were utilized for all other sections of our study area. The SfM dataset from Bunds et al. (2021) covers an area of approximately 40 km^2 from Bombay Beach at the southern terminus of the sSAF to Painted Canyon in the middle of Mecca Hills. DSMs generated from this dataset provide high-resolution imagery with 10 cm/pixel resolution. The LiDAR data from Bevis and Hudnut (2006) covers an extensive area of approximately 1,906 km^2 from Bombay Beach at the southern terminus of the sSAF up to Central California near Coalinga. DSMs generated in this dataset provide imagery with 1 m/pixel resolution, a resolution that allowed examination of larger-scale offsets but smaller-scale features with less than ~5 m of lateral displacement could not be measured with sufficient accuracy. Because the new UAV missions were flown at low altitudes (30 m), resolution was obtained at the decimeter-scale.

After imagery collection, offset features were measured in the field with a standard metric tape measure, where the distance between displaced channel margins or channel thalwegs were used as piercing points to project displacement along strike of the fault (Fig. 3).

Uncertainty and quality ratings for each offset were estimated similarly to the methodology of Blanton et al. (2020), where the amount of uncertainty was dependent on the width of the feature and how well the feature was preserved in the imagery and in the field (i.e., feature quality). Quality ratings were categorized as excellent, good, fair, or poor (Table 2) based on feature quality, preservation, level of erosion, and angle of the feature to the strike of the fault. Best-fit reconstructions were created for features to quantify displacement and were coupled with minimum and maximum reconstructions to quantify the asymmetric uncertainties for each feature. Features that appeared to be geomorphically offset (ie., channel deflections or meanders) but were not located along the main surficial expression of the fault were determined to be non-tectonic features.

Data Processing

After the new imagery was collected, individual images for each flight mission were examined to ensure quality before processing. Images that were sky-dominated or blurry were manually removed from the datasets and all remaining images were imported into Agisoft Metashape Pro (Agisoft LLC, 2020) to produce geo-referenced models including dense point clouds, Digital Surface Models (DSMs) and orthomosaics. Individual photographs were orthorectified for topographic distortions and were projected into a real-world coordinate system (World Geodetic System 1984 UTM Zone 11N) to generate the orthomosaics. The processing parameters in Agisoft were set to 'high' for both photo alignment and dense point cloud generation in order to produce high-resolution DSMs and orthomosaics. Setting the processing parameters of the imagery on 'high' allowed for offset features to be observed and measured at the decimeter scale, allowing DSMs to be generated at 1.41 to 1.87 cm/pixel resolution and orthomosaics at 8.2 mm to 1.68 cm/pixel resolution (Table 1). This was deemed to be adequate in terms of product quality and it significantly decreased the amount of time and computational power needed for processing compared to setting the processing parameters on 'highest'. Once DSMs and orthomosaics were generated, they were exported as GeoTIFF files and imported into ArcGIS Pro for additional processing and analysis. Processing in Agisoft was not necessary for published imagery from the UAV and LiDAR datasets because DSMs were already generated and made available for public use on the OpenTopography online database. Instead, the datasets were exported directly from the database and imported into ArcGIS Pro for additional processing and analysis.

As with most methods, processing UAV-based imagery comes with uncertainty. The UAV's internal GPS system has a vertical and horizontal uncertainty of ± 0.5 m and ± 1.5 m, respectively (DJI, 2022) and consequently our georeferenced imagery provides accuracy equal to the UAV system. GCPs used in this study were of equal dimension to those used in Blanton et al. (2020) and measure 26 x 26 cm in area and 29 cm diagonally across. Using these known parameters, they were found to have less than 2.5 cm uncertainty, on average, for relative object accuracy in location. The uncertainty value reflected in the DSMs and orthomosaic imagery we generated are well within the uncertainty ranges of our offset measurements, which range between 0.20 and 4.63 m.

Analysis and Interpretation

To enhance visualization of ground surface features, DSMs were imported into ArcGIS Pro to create a variety of maps including hillshade, slope, and contour maps. Hillshade maps were generated using 'multidirectional' settings as opposed to 'traditional' settings, as multidirectional hillshade maps appeared to enhance visualization more efficiently than traditional maps. Contour maps were generated with 10 cm, 50 cm, and 1 m contour intervals, depending on local relief near each offset. Contour maps with 10 cm intervals were generally used for offset features along the northeastern shoreline of the Salton Sea as local relief along the fault in these areas experience minimal variability. Contour maps with 50 cm and 1 m intervals were generally used for offset

features located north of the Salton Sea as these areas have more complex local relief along the fault as it leaves the basin and runs through the Mecca and Indio Hills.

All offset features were located using orthomosaic maps exported from Agisoft and hillshade, slope, and contour maps generated in ArcGIS Pro (Figs. S1-S4) and can be found in the electronic supplement to this paper. Field measurements were then verified using imagery by exporting the maps as JPEG files and importing them into Adobe Photoshop, where each feature was reconstructed to their inferred original configuration by slicing maps along the fault trace, placing each side of the fault into separate layers, and slid, or reconstructed, along the fault until piercing points of the offset feature were realigned. Channel thalwegs were used as piercing points for channels with clearly defined thalwegs (Fig. 3) and channel wall margins were used as piercing points for wider channels where thalwegs were not as obvious or may have migrated within the broader channel. The files were then imported into Adobe Illustrator, where interpretations were created for original and reconstructed maps. To further verify field and reconstructed measurements, we also used the Google Earth Pro application along with the MATLAB graphical user interface (GUI) LaDiCaoz to assess displacement values for offset features (Zielke and Arrowsmith, 2012). Methods used to measure offset features in Google Earth Pro were similar to the methods used in the UAV imagery. Fault traces along the sSAF were mapped out and all offset locations with their respective piercing points were verified. The distance between piercing points for each feature was quantified using Google Earth's ruler tool, where the distance between piercing points was measured along strike of the fault. Methods used to measure offset features in LaDiCaoz were the same as the geomorphic methods used in the field and in manual reconstructions of imagery. DSMs were imported into LaDiCaoz to create hillshade maps. Piercing points of each offset along the strike of the fault were defined, and optimal displacement values were generated using goodness-of-fit statistical analyses. Backslipped (reconstructed) models were then autonomously generated based on the optimal displacement values. To further evaluate the accuracy of each method, we plotted each type of measurement against corresponding field measurements to observe any patterns such as strong linear (1:1) correlations, which would suggest a high precision between methods, or where one method was consistently higher or lower than other measurements.

Offset measurements were then divided into separate groups based on similar offset values to assess slip-per-event, with the slip-per-event for each of our sections calculated independently. We interpreted slip in each event by identifying the maximum offset values in each group and calculating the difference in maximum displacement.

After measurements were grouped into probable events, Gaussian distribution analyses were performed in Microsoft Excel with the normal distribution function as a means to evaluate patterns in measured offset data, with data near the mean value having a more frequent occurrence (higher probability) than data further from the mean value. We used our offset measurements along with the average offset amount in each of our interpreted

events as parameters in the analyses. Measurements that were on the border between two events were only used in the event that they were grouped in as probable. The resulting peaks in the distribution indicate the most probable measurement values of cumulative slip in sequential paleoearthquakes. We chose this method as we know that some measurements have some displacement from pre-event creep whereas other may reflect only co-seismic slip (e.g. Blanton et al, 2020).

Using our assessment of slip-per-event along with Gaussian distribution analyses can provide insight into the average displacements that occur during large earthquakes along the sSAF and test whether the fault fails with "characteristic" displacement (Schwartz and Coppersmith, 1984) or in a more random nature (Weldon et al., 2005).

RESULTS

A total of 146 geomorphic features were measured along approximately 80 km of the sSAF at Durmid Hill, Salt Creek, Ferrum, Mecca Hills, and Indio Hills. Most offsets ranged between 2 and 23 m and were particularly abundant at Salt Creek, Mecca Hills, and Indio Hills, which yielded 12, 52, and 45 offset features, respectively. Geomorphic offset features were not as abundant in other sections due to a combination of the presence of young, active alluvium in some areas that buried the surficial expressions of the sSAF. Most of these data-poor areas are located below the highstand shoreline of ancient Lake Cahuilla (~13 m above sea level; Philibosian et al., 2011) and as such, have been subjected to multiple filling and desiccation events during repeated lake cycles (Rockwell et al., 2022). Areas where young, active alluvium does not bury the surficial expressions of the sSAF exhibit relatively young geomorphic features that show evidence of preservation through the past 2 to 3 lake cycles.

Most offset features used for this study were located along a single main strand of the fault, with a few being located where the fault is divided into multiple strands. More complicated fault areas typically preserve lower overall lateral displacement values. Furthermore, some features were located along what appeared to be inactive strands of the fault or where no fault evidence was detected (Fig. 4). These features were not included in our Gaussian distribution analysis as these features represent areas that no longer produce slip or where the apparent offset was not clearly associated with the fault and was therefore suspect. Offset locations along with orthomosaics, hillshade, slope, and contour maps are shown with examples from each of our five studied sections (Figs. 5 thru 9), to highlight each method of measurement. Specific locations of offset features (Figs. S5 thru S63) along with detailed reconstructions of those not shown in Figs. 5 to 9 can be found in the electronic supplement to this paper. To assess the accuracy for each measurement method, linear correlations were made between DSM-derived measurements (digital) and field measurements of offset features (Fig. 10). On average, our digital measurements correlated well with each other along with field measurements, with some variability. Hillshade and contour map measurements were roughly equal to field measurements, slope map and LaDiCaoz measurements were roughly equal to hillshade map measurements, and hillshade and contour

map measurements were roughly equal to orthomosaic measurements, with some features measuring slightly greater or less than the other methods. Overall, all methods of measurement show relatively strong linear relationships with some variability that fits into the range of measurement uncertainty. Measurements generated from contour maps and LaDiCaoz are considered to be the most accurate methods as contour maps have elevation data derived from DSMs, which produce clearly defined thalwegs and channel walls that aid in eliminating measurement bias, and LaDiCaoz relies on goodness-of-fit statistical analyses to realign geomorphic offset features. A Pearson's Correlation Coefficient was then calculated and applied for each correlation (Fig. 10) to quantify the strength of relationships between correlations.

Distribution of offset features along the fault strike show some degree of lateral variability (Fig. 11) with lower overall measured offset values where multiple strands are present. Patterns observed in slip distribution along the fault were used to separate clusters of offset features with similar displacement values, and Gaussian distributions were performed to assess the probability of slip-per-event for the past six paleoearthquakes. Analyses from Gaussian distributions reveal six peaks in offset clusters at 3.10, 6.15, 9.4, 13.35, 17.65, 22.1 m, respectively. From these observations, we infer displacement per event to have been about 3.1, 3.05, 3.25, 3.93, 4.30, and 4.44 m (Fig. 12) in respective chronological order starting with the MRE. This provides an average value of 3.68 m per event. Distributions for the most recent four events form well-defined peaks, while peaks for older events were poorly defined. Older events correlate to larger-scale offset features, which produce larger uncertainties and are not as abundant as smaller-scale features. Consequently, these features provide relatively sparse data that is broadly distributed, and this results in poorly-defined peaks in the Gaussian distribution analyses.

It should be noted that there were certain sections along the fault where DSM data were analyzed but for which new field measurements were not obtained. In the Indio Hills, field measurements were not obtained within the boundaries of the Coachella Valley Preserve and Pushawalla Palms because of temporary access restrictions. Lastly, offset features in Coachella, located between the Mecca and Indio Hills, have either been entirely removed due to recent anthropogenic development or are located in areas where public access is not readily permitted. Consequently, field measurements were not obtained in these areas. Areas that were not accessible for field measurements in our study were instead assessed using digital imagery and past field measurements obtained by one of our coauthors (Williams) approximately 10-15 years ago. Those data are presented in the supplement to this paper (Figs. S38 thru S63).

DISCUSSION

Understanding the seismic history along the sSAF is critical to develop accurate seismic hazard assessments to estimate the probability and magnitude of future events. Using offset geomorphic markers to estimate displacement in past earthquakes has proven to be an effective method (Zielke and Arrowsmith, 2012; Salisbury et al., 2012; Dingler et al., 2016;

Blanton et al., 2020); however, estimating displacement in past earthquakes has its challenges. The phenomenon of creep and triggered slip can produce displacement independently from co-seismic slip events, making them complex variables when resolving displacement from offset geomorphic features. Creep along the sSAF is occurring in its upper 2-3 km at a rate of approximately 3 mm/yr (Lindsey et al., 2014; Sieh and Williams, 1990). Blanton et al. (2020) investigated this phenomenon and showed that the uncertainty in observed offsets is the result of creep that occurs before and after co-seismic offset and should be on the order of 45-60 cm for the sSAF. This level of uncertainty is assumed to be on the same order of magnitude as offset measurement errors, which suggests that slip in an event can be underestimated or overestimated as a result of the 45-60 cm of creep related uncertainty.

Triggered slip was first documented on the southernmost San Andreas fault following the Borrego Mountain earthquake in 1968 (Allen et al., 1972), where 10-25 mm of slip was measured as a result of the shaking. Since then, this phenomenon has been documented along the sSAF resulting from earthquakes such as the 1987 Superstition Hills, 1992 Landers, 1999 Hector Mine, 2010 El Mayor-Cucapah, and 2017 Chiapas earthquakes (Rymer, 2000; Rymer et al., 2002; Wei et al., 2011; Tymofyeyeva et al., 2019). One notable study from Tymofyeyeva et al. (2019) used geodetic and geologic observations to find evidence of triggered slip from the 2017 Mw 8.2 Chiapas earthquake in Mexico, which occurred ~3,000 km away from the sSAF. Evidence of up to 12 mm of triggered slip was found to have occurred along ~40 km of the sSAF from Bombay Beach to Mecca Hills and resulted in a series of cyclic creep events along the sSAF, where slip was observed in mere minutes after nucleation and continued on for more than a year. In the long term, creep is interpreted to integrate intermittent triggered slip between large earthquake events and as such, triggered slip can be integrated with creep (Blanton et al., 2020). Although creep and triggered slip add complexity when resolving displacement, offset features displaying less than ~1 m of lateral displacement were not considered in our study as these features likely reflect modern creep and triggered slip events, which post-date the most recent surface rupturing event around ca 1726 AD (Rockwell et al., 2018). Meter-scale offset features such as those observed in this study are interpreted to be the result of a combination of creep and triggered slip coupled with co-seismic slip from past earthquakes (Blanton et al., 2020). Eliminating the inclusion of decimeter-scale offset features helped to resolve past displacement events along the sSAF with minimal uncertainty. We believe that it is a useful and reasonable assumption to group interseismic creep with the prior segment rupture. This assumption simplifies interpretation of the geomorphic offset record, and we believe it is unlikely that any of the preserved offsets exaggerate prehistoric coseismic displacement.

Our results show that slip distribution varies along strike of the fault, and average slip-per-event estimates range between 3.1 to 4.4 m of lateral displacement per event for the past six large surface rupturing earthquakes – yielding an average of 3.68 m of displacement per event. Average

displacement estimates for the past four earthquakes, in which data are most abundant, range between 3.1 to 3.93 m of lateral displacement per event – yielding an average of ~3.33 m of displacement per event. These estimates agree well with other studies along the sSAF (Blanton et al., 2020; Dingler et al., 2016). Using the ~3.33 m of average displacement from the past four events and applying the 180-year average recurrence interval (Philibosian et al., 2011) yields a slip rate along the sSAF of about 18.5 mm/yr, which agrees well with previous studies (Behr et al., 2010; Lindsey et al., 2014). Another way to assess the rate is to use the ages of past events from paleoseismology and assume that the four events recognized from offset geomorphic features corresponds to the past four paleoseismic events determined by Philibosian et al. (2011) (Coa1, Coa2, Coa3/4 and Coa5, respectively) but corrected for the age of ancient Lake Cahuilla ("Lake") by Rockwell et al. (2022). The events Coa3 and Coa4 were reinterpreted as a single event by Rockwell et al. (2022) as they occurred during the rising stages of Lake C. Coa5 occurred during Lake D, which is dated to 1192-1241 CE. Using the displacement of the past four events at 13.3+1.4/-2.1 m and the time since the first event as 1225+/-25 CE, or about 800 years, yields a slip rate of 16.6 mm/yr but with a longer than average open window which should slightly reduce the inferred rate. Both rate estimates fall within the 16-18 mm/yr range of published rates.

The displacement estimates revealed in the Gaussian distribution analysis align well for the past four large, surface rupturing events resulting in peak displacements of 3.10, 3.05, 3.25, and 3.93 m, respectively. Peaks for older events are not well resolved, likely because the data for these events is too sparse to discern peak displacements or because the displacement amounts for these older events are different from the four most recent events. Older events displaying larger displacement are subjected to the greatest amount of uncertainty compared to smaller, more recent offsets. This is in part due to the lack of abundance for large-scale offsets as these features have been subjected to more erosion and stream capture, particularly for features located below the highstand shoreline of ancient Lake Cahuilla, which may have removed evidence produced by older events. Furthermore, there may also be fewer large offsets because arid climates such as the Salton Trough tend to preserve smaller-scale offsets due to increased channel density (Reitman et al., 2022).

On average, past large earthquake events along the sSAF to the south of the Indio Hills occurred every ~180 years (Philibosian et al., 2011; shorter if the open interval is considered) and occurred between every 380-640 years to the north of the Indio Hills (Castillo et al., 2021). This implies that not all large ruptures occurring south of or within the Indio Hills continue to rupture north along the Banning fault. This would also account for the lower slip rate determined for the Banning fault north of highway 62 (Gold et al., 2015), which also suggests a lower amount of slip per event, as suggested by Castillo et al. (2021).

The latest significant rupture of the sSAF occurred around 1726 CE (Rockwell et al., 2018) which indicates an open interval of about 300 years. This long open interval between earthquakes has led to speculation that the sSAF is due for a relatively large surface rupturing event. Brothers et al.

(2011) notes that although it is commonly believed that the fault is ~100 years overdue for a large earthquake event, this might not be the case due to the absence of rapid stress loading induced by cyclic flooding events from Lake Cahuilla which may be contributing to the prolonged seismic quiescence. Whether this holds to be true or not, substantial dextral elastic loading has accumulated during the present unusually long open interval. Observed strain rates from geodetic evidence along the sSAF suggest that the fault has accumulated a slip deficit during this recent seismic quiescence of up to 5.5-7.0 m, if slip rates are relatively constant over the past several sSAF seismic cycles (Fialko, 2006), which is comparable to past co-seismic offsets recorded along the fault to the north (Zielke et al., 2010). This leads to further speculation on how the accumulated slip deficit will be distributed – will the fault release all accumulated slip in one large earthquake or two smaller events with displacement similar to the past four ruptures (i.e. “characteristic slip”)? If the potential slip accumulated across the fault during the current 300-yearquiescent period is related to the absence of lake loading, it is plausible that the fault is stronger in dry conditions (Brothers et al., 2011; Hill et al., 2020) and could release the entire amount of inferred accumulated slip in a single event. Hill et al. (2020) explain that as pore pressures decrease, the underlying bedrock becomes stronger; however, the degree to which it gets stronger is relevant to tectonically driven slip rates. If this holds true and slip rates along the sSAF have remained constant in the recent geologic past, the next large event could produce lateral displacement on the order of 4.8-5.4 m based on 300 years of accumulation at 16-18 mm/yr. We note that if rupture displacement magnitude plays a role in how often the sSAF propagates through San Gorgonio Pass, and if 5 m or greater displacement occurs in the next earthquake, it is reasonable to assume that the next event may extend beyond the confines of the Salton Trough (or vice versa).

Observationally based time- and slip-predictable models of earthquake occurrence have been invoked to estimate the size of future earthquakes based on the lapse time since the most recent event, or the timing of future earthquakes based on the amount of slip in the most recent event along with the loading rate (Shimazaki and Nakata, 1980). The time-predictable model states that an earthquake will only occur when the stress relieved in the prior earthquake has been re-accumulated whereas the slip- predictable model states that all the stress accumulated since the prior earthquake is released in the next event (Rubinstein et al., 2012) which implies that greater time intervals between two events produce earthquakes of greater size. In these models the basic assumption is that the general characteristics that regulate fault strength have not changed significantly. However, in the case of the sSAF, this is likely not the case because of the fluctuating lake levels (Luttrell et al., 2007; Hill et al., 2020). Similarly, the characteristic earthquake model (Schwartz and Coppersmith, 1984) may not apply because of the changes in fundamental fault properties. Hence, the speculation that the southernmost San Andreas fault is “overdue” may be a misnomer and should probably be left as an unknown until time-dependent offset or slip rate may be developed to evaluate whether a dry lake may delay rupture.

An earthquake causing 5-6 m of displacement along the sSAF could have devastating effects on the population of southern California (Fig. 1) as the fault also crosses all of the major highway systems coming in and out of southern California leading to the east, all of the water supply lines going into Los Angeles from the Colorado River, most of the water supply lines going into San Diego, and a majority of the water canals used for irrigation in the Salton Trough. More notably, if a large earthquake occurs along the sSAF and produces a rupture that propagates through San Gorgonio Pass, it has the potential to cause significant damage in Los Angeles and the surrounding areas due to focusing and basin effects (Olsen et al., 2006). Earthquake scenario models where nucleation occurs along the southern terminus of the sSAF and travels northward show that if the rupture propagates past San Gorgonio Pass, it can travel through the San Bernardino, Chino, San Gabriel, and Los Angeles basins (Olsen et al., 2006), regions that can trap seismic energy and channel it into the Los Angeles region. If all ~5 m of slip is released along the sSAF in the next event, the rupture may propagate northward into the densely populated Los Angeles region, producing what is believed to be the "worst-case scenario" for a large San Andreas earthquake.

CONCLUSION

We identified and measured 146 tectonically offset geomorphic features along the southernmost ~80 km of the San Andreas fault between Bombay Beach and Indio Hills by obtaining imagery datasets from previously published LiDAR and SfM surveys, along with very-high-resolution SfM imagery we obtained from new UAV surveys during this study. From these observations, we derive the slip distribution and slip-per-event for the past six large, surface rupturing earthquakes. Most offsets observed in this study exhibit displacements ranging from 2 to 23 m and provide evidence for displacement for the past six earthquake events. Slip measurements derived from this study were used in a Gaussian analyses, which reveal six peak cumulative displacements of 3.1, 6.15, 9.4, 13.35, 17.65, 22.1 m, respectively, in which we infer average slip-per-event for the past six earthquakes to have been 3.1, 3.05, 3.25, 3.93, 4.30, and 4.44 m in respective chronological order starting with the MRE. The most recent four events with smaller, well-preserved offsets provide distributions which form well-defined peaks; however, older events with large-scale offsets are not as well resolved, which is partly due to the lack of data for these larger features as they have been exposed to more stream capture and erosion through time which may have removed evidence produced by older events, particularly for offset features located below the highstand shoreline of ancient Lake Cahuilla. Consequently, we determined a range for slip rate by first using the average displacement from the past four events (~3.33 m) along with the 180-year average recurrence interval to derive a slip rate of approximately 18.5 mm/yr. Next, we used the cumulative displacement of the past four events (~13.3 m) and the time since the occurrence of the 4th paleoseismic event (~800 years) to derive a slip rate of approximately 16.6 mm/yr. This provides an estimated range for slip rate between 16.6-18.5 mm/yr along the sSAF, which is comparable to other published geologic slip rates in the region. Given this slip rate, coupled with published paleoseismic earthquake ages, an average recurrence interval of 180 years,

and our current 300-year open interval between large events, the sSAF may have accumulated a slip deficit on the order of 4.8-5.4 m. However, if the largest feature used in this study, with a displacement of approximately 23 m, represents slip in the past 6 events, and has occurred after CE 950 (1,070 years), then a rate of 21.5 mm/yr is inferred. Earlier events were more closely spaced in time, and the 180-year recurrence interval includes the current open interval along the sSAF. The actual inter-event recurrence interval may be shorter. In any case, this leads to speculation on if the accumulated slip will be released in one or two events, the latter of which assumes displacement comparable to the previous four events. Some studies suggest that the sSAF is "overdue" for an earthquake given the current seismic quiescence; however, it is possible that the lack of lake loading from ancient Lake Cahuilla is playing a role in the delayed interval since the MRE. It is conceivable that the fault is stronger in dry conditions and if true, an earthquake nucleating along the sSAF could release all accumulated slip in the next large event. If this is the case, it is possible that the sSAF will produce large enough displacement to cause a rupture to propagate northward out of the limits of the Salton Trough, through San Gorgonio Pass, and possibly beyond, which could channel seismic energy into the Los Angeles basin and surrounding regions. Such an event could produce what some have speculated to be the "big one" (greatest damage cost) for an earthquake along the San Andreas fault.

DECLARATION OF COMPETING INTERESTS

The authors declare no competing interests.

DATA AND RESOURCES

Imagery from existing LiDAR and Structure-from-Motion surveys used in this research came from published sources listed in the references. New imagery collected during this research has been uploaded to OpenTopography for free public access, where links to each new dataset can be found at the end of this section.

The electronic supplement to this paper presents the offsets and reconstructions of all new interpreted offsets along the southernmost ~80 km of the San Andreas fault from Bombay Beach northwest into the Indio Hills along with new aerial imagery collected during this study.

New OpenTopography Imagery:

Durmid Hill Imagery:

https://portal.opentopography.org/dataspace/dataset?opentopoID=OTDS.062022.32611.1

Salt Creek Imagery:
https://portal.opentopography.org/datasetMetadata?otCollectionID=OT.072022.32611.1

Ferrum Imagery:

https://portal.opentopography.org/datasetMetadata?otCollectionID=OT.062022.32611.1

Biskra Palms Imagery:

https://portal.opentopography.org/dataspace/dataset?opentopoID=OTDS.062022.4326.1

ACKNOWLEDGEMENTS

This research was supported and funded by the USGS Earthquake Hazards

Program (Award No. G21AP10005, Rockwell and Gontz). We appreciate the field support of Lauren Booth, Faith Burkett, and Zoe Morgan for their assistance with UAS and RTK GPS surveys for this research. We thank Red Jeep Tours by Desert Adventures for access along their private roads near Biskra Palms. We also thank Eagle Mountain Mining and Railroad for access along their property at Ferrum. Finally, we thank Anonymous for their comprehensive reviews which greatly enhanced this paper.

References Cited

Agisoft LLC (2020). Agisoft Metashape User Manual: Professional Edition, Version 1.6, 1-172, accessed 20th Jan 2022.

Allen, C.R., Wyss, M., Brune, J.N., Granz, A., and Wallace, R.E. (1972). Displacements on the Imperial, Superstition Hills, and San Andreas faults triggered by the Borrego Mountain earthquake, in the Borrego Mountain earthquake of April 9, 1968: U.S. Geol. Surv. Prof. Pap. 787, 87-104.

Behr, W.M., Rood, D.H., Fletcher, K.E., Guzman, N., Finkel, R., Hanks, T.C., Hudnut, K.W., Kendrick, K.J., Platt, J.P., Sharp, W.D., Weldon, R.J., and Yule, J.D. (2010). Uncertainties in slip-rate estimates for the Mission Creek strand of the southern San Andreas fault at Biskra Palms Oasis, southern California, Bulletin of the Geological Society of America, **122**, Issue 9-10, 1360-1377, doi: 10.1130/B30020.1.

Bevis, M. and Hudnut, K. (2006). B4 Lidar Project: Airborne Laser Swath Mapping (ALSM) survey of the San Andreas Fault (SAF) system of central and southern California, including the Banning segment of the SAF and the San Jacinto fault system. National Center for Airborne Laser Mapping (NCALM), U.S. Geological Survey, the Ohio State University, and the Southern California Integrated GPS Project. Distributed by OpenTopography, doi: https://doi.org/10.5066/F7TQ5ZQ6.

Blanton, C.M., Rockwell, T.K., Gontz, A.M., and Kelly, J.T. (2020). Refining the spatial and temporal signatures of creep and co-seismic slip along the southern San Andreas Fault using very high resolution UAS imagery and SfM-derived topography, Coachella Valley, California: Elsevier, Geomorphology, **357**, 107064, doi: https://doi.org/10.1016/j.geomorph.2020.107064.

Brothers, D., Driscoll, N.W., Kent, G.M., Harding, A.J., Babcock, J.M., and Baskin, R.L. (2009). Tectonic evolution of the Salton Sea inferred from seismic reflection data: Nature Geoscience, **2**, 581–584, https://doi.org/10.1038/ngeo590.

Brothers, D., Kilb, D., Luttrell, K., Driscoll, N., and Kent, G. (2011). Loading of the San Andreas fault by flood-induced rupture of faults beneath the Salton Sea: Nature Geoscience, **4**, 486–492, https://doi.org/10.1038/ngeo1184.

Bunds, M., Scott, C., Whitney, B., and Lee, V.J.C. (2021). New SfM data over the Southern San Andreas Fault, CA, distributed by OpenTopography, doi: https://opentopography.org/news/new-sfm-data-over-southern-san-andreas-fault-ca.

Castillo, B.A., McGill, S.F., Scharer, K.M., Yule, D., McPhillips, D., McNeil, J., Saha, S., Brown, N.D., and Moon, S. (2021). Prehistoric earthquakes on the Banning strand of the San Andreas fault, North Palm Springs, California, Geosphere, **17**, no. 3, 685-710, https://doi.org/10.1130/GES02237.1.

Dingler, J., Driscoll, N., Seitz, G., and Kent, G. (2016). New quantitative constraints on Holocene slip rate and surface displacement along the southern San Andreas fault in the Mecca Hills using ground based terrestrial laser scanning: in Anderson

R. Anderson, and H. Ferriz (Eds.), Applied Geology in California: Association of Environmental and Engineering Geologists Special Publication, **26** (2016), 809-832.

DJI (2022). Phantom 4 Pro Specs, https://www.dji.com/phantom-4-pro/info#specs, accessed 10th Jan 2022.

EMLID (2022). Reach RS+ (EMLID), https://emlid.com/reachrs/, accessed 10th Jan 2022.

Fialko, Y. (2006). Interseismic strain accumulation and the earthquake potential on the southern San Andreas fault system, Nature, **441**, 968-971, doi: 10.1038/nature04797.

Field, E.H., and 2014 Working Group on California Earthquake Probabilities (2015). UCERF3: A New Earthquake Forecast for California's Complex Fault System: U.S. Geological Survey Fact Sheet 2015–3009, 1-6, http://dx.doi.org/10.3133/fs20153009.

Field, E.H., Arrowsmith, J.R., Biasi, G.P., Bird, P., Dawson, T.E., Felzer, K.R., Jackson, D.D., Johnson, K.M., Jordan, T.H., Madden, C., Michael, A.J., Milner, K.R., Page, M.T., Parsons, T., Powers, P.M., Shaw, B.E., Thatcher, W.R., Weldon, R.J., and Zeng, Y. (2014). Uniform California Earthquake Rupture Forecast, Version 3 (UCERF3)—The time-independent model: Bulletin of the Seismological Society of America, **104**, 1122–1180, https://doi .org/10.1785/0120130164.

Fuis, G.S. and Mooney, W.D. (1990). Lithospheric structure and tectonics from seismic-refraction and other data, The San Andreas Fault System, California (textbook): U.S. Geological Survey Professional Paper 1515, 207-236.

Fumal, T.E. (2002). Timing of Large Earthquakes since A.D. 800 on the Mission Creek Strand of the San Andreas Fault Zone at Thousand Palms Oasis, near Palm Springs, California: Bulletin of the Seismological Society of America, **92**, 2841-2860, doi: 10.1785/0120000609.

Gold, P.O., Behr, W.M., Rood, D., Sharp, W.D., Rockwell, T.K., Kendrick, K., and Salin, A. (2015). Holocene geologic slip rate for the Banning strand of the southern San Andreas Fault, southern California, Journal of Geophysical Research: Solid Earth, **120**, Issue 8, 5639-5663, doi:10.1002/2015JB012004.

Lindsey, E.O., Fialko, Y., Bock, Y., Sandwell, D.T., and Bilham, R. (2014). Localized and distributed creep along the southern San Andreas Fault, Journal of Geophysical Research: Solid Earth, 7909-7922, doi: 10.1002/2014JB011275.

Luttrell, K., Sandwell, D., Smith-Konter, B., Bills, B., and Bock, Y. (2007). Modulation of the earthquake cycle at the southern San Andreas fault by lake loading, Journal of Geophysical Research, **112**, B08411, 1-15, doi:10.1029/2006JB004752.

Olsen, K.B., Day, S.M., Minster, J.B., Cui, Y., Chourasia, A., Faerman, M., Moore, R., Maechling, P., and Jordan, T. (2006). Strong shaking in Los Angeles expected from southern San Andreas earthquake: Geophysical Research Letters, **33**, L07305, https://doi.org /10.1029/2005GL025472.

Philibosian, B., Fumal, T., and Weldon, R. (2011). San Andreas Fault Earthquake Chronology and Lake Cahuilla History at Coachella, California: Bulletin of the Seismological Society of America, **101**, 13–38, doi:10.1785/0120100050.

Reitman, N.G., Klinger, Y., Briggs, R.W., and Gold, R.D. (2022). Climatic influence on the expression of strike-slip faulting: Geology, 1-5, https://doi.org/10.1130/G50393.1.

Rockwell, T.K., Meltzner, A.J., and Haaker, E.C. (2018). Dates of the Two Most Recent Surface Ruptures on the Southernmost San Andreas Fault Recalculated by Precise Dating of Lake Cahuilla Dry Periods Dates of the Two Most Recent Surface Ruptures on the Southernmost SAF Recalculated: Bulletin of the Seismological Society of America, **108**, 2634–2649, doi:10.1785/0120170392.

Rockwell. T.K., Meltzner, A.J., Haaker, E.C., and Madugo, D. (2022). The late Holocene history of Lake Cahuilla: Two thousand years of Repeated fillings within the Salton Trough, Imperial Valley, California, Quaternary Science Reviews, **282**, 107456, https://doi.org/10/1016/j.quascirev.2022.107456.

Ross, J.E. (2020). Formation of California's Salton Sea in 1905-1907 was not "accidental". In: Miller, D.M. (Ed.), Changing Facies: the 2020 Desert Symposium Field Guide and Proceedings, Desert Symposium, Inc., Zzyzx, CA, 217-230, http://www.desertsymposium.org/History.html.

Rymer, M.J. (2000). Triggered surface slips in the Coachella Valley area associated with the 1992 Joshua Tree and Landers, California, earthquakes, Bull. Seismol. Soc. Am. **90**, 832-848, https://doi.org/10.1785/0119980130.

Rymer, M.J., Boatwright, J., Seekins, L.C., Yule, J.D., and Liu, J. (2002). Triggered surface slips in the Salton Trough associated with the 1999 Hector Mine, California, earthquake, Bull. Seismol. Soc. Am. **92**, 1300-1317, https://doi.org/10.1785/0120000935.

Salisbury, J.B., Rockwell, T.K., Middleton, T.J., and Hudnut, K.W. (2012). LiDAR and Field Observations of Slip Distribution for the Most Recent Surface Ruptures along the Central San Jacinto Fault, Bulletin of the Seismological Society of America, **102**, no. 2, 598-619, doi: 10.1785/0120110068.

Salisbury, J.B., Haddad, D.E., Rockwell, T., Arrowsmith, J.R., Madugo, C., Zielke, O., and Scharer, K. (2015). Validation of meter-scale surface faulting offset measurements from high-resolution topographic data, Geosphere **11**, 1884-1901, https://doi.org/10/1130/GES01197.1.

Schwartz, D.P. and Coppersmith, K.J. (1984). Fault Behavior and Characteristic Earthquakes: Examples from the Wasatch and San Andreas Fault Zones, Journal of Geophysical Research, **89**, No. B7, 5681-5698, doi:10.1029/JB089iB07p05681.

Shimazaki, K. and Nakata, T. (1980). Time-predictable recurrence model for large earthquakes, Geophysical Research Letters, **7**, Issue 4, 279-282, doi:10.1029/GL007i004p00279.

Sieh, K.E., and Williams, P.L. (1990). Behavior of the southernmost San Andreas Fault during the past 300 years: Journal of Geophysical Research: Solid Earth, **95**, 6629–6645, doi:10.1029/JB095iB05p06629.

Tymofyeyeva, E., Fialko, Y., Jiang, J., Xu, X., Sandwell, D., Bilham, R., Rockwell, T., Blanton, C., Burkett, F., Gontz, A., and Moafipoor, S. (2019). Slow slip event on the southern San Andreas Fault triggered by the 2017 Mw 8.2 Chiapas (Mexico) earthquake, J. Geophys. Res. Solid Earth **124**, https://doi.org/10.1029/2018JB016765.

U.S. Geological Survey and California Geological Survey, Quaternary fault and fold database for the United States, accessed January 2022, at https://www.usgs.gov/natural-hazards/earthquake-hazards/faults.

Waters, M.R. (1983). Late Holocene lacustrine chronology and archaeology of ancient Lake Cahuilla, California, Quat. Res. **19**, 373-387, https://doi.org/10.1016/0033-5894.

Wei, M., Sandwell, D., Fialko, Y., and Billah, R. (2011). Slip on faults in the Imperial Valley triggered by the 4 April 2010 Mw 7.2 El Major-Cucapah earthquake revealed by InSAR, Geophys. Res. Lett. **38** (1), 1-6, L01308, https://doi.org/10.1029/2010GL045235.

Weldon, R.J., Fumal, T.E., Biasi, G.P., and Scharer, K.M. (2005). Past and future earthquakes on the San Andreas fault, Science, **308**, 966-967.

Younker, L.W., Kasameyer, P.W., and Tewhey, J.D. (1981). Geological, geophysical, and thermal characteristics of the Salton Sea geothermal field, California, Journal of Volcanology and Geothermal Research, 1-74.

Zielke, O., Arrowsmith, R.J., Ludwig, L.G., and Akciz, S.O. (2010). Slip in the 1857 and Earlier Large Earthquakes Along the Carrizo Plain, San Andreas Fault, Science, **327**, 1119-1122, doi: 10.1126/science.1182781.

Zielke, O. and Arrowsmith, R.J. (2012). LaDiCaoz and LiDARimager – MATLAB GUIs for LiDAR data handling and lateral displacement measurement, Geosphere, **8**, no. 1, 206-221, doi: 10.1130/GES00686.1.

TABLES

Table 1. A) (top) UAV Flight Parameters and B) (bottom) UAV Camera Specifications of the 4 new flights performed during this study. Altitude above ground level (AGL) is based on takeoff location. UAV = uncrewed aerial vehicle; GSD = ground sampling distance.

A	**UAV Flight Parameters**					
Flight	**Height AGL (m)**	**Date of Flight**	**UAV**	**Total Coverage Area (m^2)**	**Speed (m/s)**	**GSD (cm/pix)**
Durmid Hill	30	10/29/2020	DJI P4P	428,000	5	1
Ferrum	30	2/23/2021	DJI P4P	717,000	5	1
Salt Creek	30	11/21 & 12/28/2021	DJI P4P	338,000	5	1
Biskra Palms	30	12/29/2021	DJI P4P	128,000	5	1

B	**UAV Camera Specifications**				
Flight	**Camera Model**	**Resolution**	**Focal Length**	**Pixel Size**	**Sensor Width**
Durmid Hill	FC6310	4864x3648	8.8mm	2.41µm x 2.41µm	13.2mm
Ferrum	FC6310	4864x3648	8.8mm	2.41µm x 2.41µm	13.2mm
Salt Creek	FC6310	4864x3648	8.8mm	2.41µm x 2.41µm	13.2mm
Biskra Palms	FC6310	4864x3648	8.8mm	2.41µm x 2.41µm	13.2mm

Table 2. Offset measurements coupled with their respective uncertainties along ~80 km of the sSAF from Bombay Beach to Indio Hills. Minimum and maximum displacement values (uncertainties) were assessed for most features depending on factors such as feature quality, erosion, and angle of projected piercing points to the strike of the fault. Quality ratings were assigned as excellent, good, fair, or poor. T = thalweg, SE CW = southeast channel wall, NW CW = northwest channel wall, BH-C = beheaded channel, GE = Google Earth, Ortho = orthomosaic, Min/Max = new minimum and maximum uncertainty measurements produced in this study, Williams = Pat Williams' field measurements, Williams Min/Max = minimum and maximum uncertainty measurements obtained from Pat Williams, Average = average displacement value from all measurements.

sSAF Offset Master List																			
Name	Site	GPS Location	Distance along fault (km)	Quality Rating	Feature Type	Google Earth (m)	Ortho (m)	Hillshade (m)	Slope (m)	Contour (m)	Field (m)	LaDiCaoz (m)	Min (m)	Max (m)	Williams (m)	Williams Min (m)	Williams Max (m)	Average (m)	Fault Strand
sSAF-1	Durmid Hill	33.3911677, -115.7604411	5.32	Excellent	T	11.39	N/A	11.19	11.20	11.24	10.93	N/A	10.10	12.40	N/A	N/A	N/A	11.19	Main
sSAF-2	Durmid Hill	33.4015008, -115.7790416	7.4	Excellent	T	11.05	N/A	10.62	10.70	10.58	10.24	N/A	9.40	11.80	N/A	N/A	N/A	10.64	Main
sSAF-3	Durmid Hill	33.4030709, -115.7814668	7.68	Fair	SE CW	5.58	N/A	5.42	5.41	5.40	5.53	N/A	4.90	6.70	N/A	N/A	N/A	5.47	Main
sSAF-4	Durmid Hill	33.4103791, -115.7922758	9	Excellent	T	6.69	N/A	6.75	6.78	6.79	6.70	6.80	6.20	7.40	N/A	N/A	N/A	6.75	Minor
sSAF-5	Durmid Hill	33.4104506, -115.7923858	9	Excellent	BH-C	6.69	N/A	6.75	6.78	6.79	6.86	6.80	6.20	7.40	N/A	N/A	N/A	6.78	Multiple
sSAF-6	Durmid Hill	33.4104665, -115.7922670	9	Poor	BH-C	3.74	N/A	3.68	3.67	3.63	3.28	N/A	3.20	4.50	N/A	N/A	N/A	3.60	Multiple
sSAF-7	Durmid Hill	33.4143044, -115.7978758	9.65	Excellent	T	3.64	N/A	3.68	3.65	3.62	3.94	N/A	3.10	4.40	3.50	3.30	4.50	3.67	Main
sSAF-8	Durmid Hill	33.4158879, -115.8002845	9.93	Excellent	T	6.56	6.49	6.09	6.12	6.10	6.60	N/A	5.70	7.80	6.50	5.90	7.40	6.35	Main
sSAF-9	Durmid Hill	33.4299834, -115.8193247	12.3	Excellent	NW CW	12.53	N/A	12.42	12.45	12.62	11.70	N/A	10.30	13.20	12.55	11.00	13.50	12.38	Main
sSAF-10	Durmid Hill	33.4310865, -115.8209294	12.5	Fair	T	7.39	N/A	7.19	7.20	7.22	7.62	N/A	6.00	8.10	N/A	N/A	N/A	7.32	Main
sSAF-11	Durmid Hill	33.4362735, -115.8279458	13.36	Excellent	SE CW	9.13	N/A	9.25	9.23	9.19	9.09	N/A	8.70	10.90	9.00	8.00	10.00	9.15	Main
sSAF-12	Salt Creek	33.4383366, -115.8309005	13.72	Good	T	4.19	N/A	3.89	4.11	4.43	4.24	N/A	3.60	5.10	4.00	3.00	5.00	4.14	Main
sSAF-13	Salt Creek	33.4436464, -115.8366745	14.52	Excellent	T	3.78	3.58	3.76	3.71	3.68	3.66	3.70	3.30	4.30	3.90	3.60	4.40	3.72	Multiple
sSAF-14	Salt Creek	33.4439222, -115.8370470	14.57	Excellent	T	3.80	3.78	4.00	4.08	4.10	4.01	3.90	3.20	4.70	3.50	2.50	4.50	3.90	Multiple
sSAF-15	Salt Creek	33.4441250, -115.8373821	14.61	Fair	BH-C	16.65	17.28	17.72	17.60	17.50	N/A	N/A	16.50	19.10	N/A	N/A	N/A	17.35	Main
sSAF-16	Salt Creek	33.4445025, -115.8377445	14.66	Excellent	SE CW	12.12	12.48	12.40	12.38	12.52	N/A	12.50	11.40	13.60	12.00	10.20	13.80	12.34	Main
sSAF-17	Salt Creek	33.4445025, -115.8377445	14.66	Excellent	BH-C	17.09	16.98	17.16	16.76	17.02	N/A	17.50	15.50	17.80	16.00	14.50	17.50	16.93	Main
sSAF-18	Salt Creek	33.4482990, -115.8430715	15.31	Excellent	T	2.48	N/A	2.58	2.48	2.62	N/A	2.40	2.00	3.00	N/A	N/A	N/A	2.51	Main
sSAF-19	Salt Creek	33.4482990, -115.8430716	15.36	Excellent	T	2.45	N/A	2.58	2.48	2.62	N/A	2.40	2.00	3.00	N/A	N/A	N/A	2.51	Main
sSAF-20	Salt Creek	33.4482990, -115.8430717	15.68	Excellent	T	2.45	N/A	2.58	2.48	2.62	N/A	2.40	2.00	3.00	N/A	N/A	N/A	2.51	Main

sSAF-21	Salt Creek	33.4482990, -115.8430718	16.21	Excellent	T	2.45	N/A	2.58	2.48	2.62	N/A	2.40	2.00	3.00	N/A	N/A	N/A	2.51	Main
sSAF-22	Salt Creek	33.4482990, -115.8430719	16.33	Excellent	T	2.45	N/A	2.58	2.48	2.62	N/A	2.40	2.00	3.00	N/A	N/A	N/A	2.51	Main
sSAF-23	Salt Creek	33.4485574, -115.8434874	16.48	Excellent	BH-C	9.28	9.38	9.44	9.44	9.46	10.70	8.60	8.50	10.20	9.30	8.30	10.30	9.45	Main
sSAF-24	Ferrum	33.4505033, -115.8459946	16.49	Excellent	SE CW	4.23	N/A	4.40	4.42	4.38	4.34	4.60	4.00	4.80	4.25	3.95	4.55	4.37	Main
sSAF-25	Ferrum	33.4505033, -115.8459946	16.49	Excellent	SE CW	4.20	N/A	4.40	4.42	4.38	N/A	4.60	4.00	4.80	N/A	N/A	N/A	4.40	Main
sSAF-26	Ferrum	33.4535323, -115.8504314	17.04	Excellent	SE CW	3.40	N/A	3.48	3.39	3.21	3.05	N/A	2.60	3.40	N/A	N/A	N/A	3.31	Main
sSAF-27	Ferrum	33.4542959, -115.8513038	17.06	Fair	SE CW	3.01	N/A	2.55	2.53	2.30	2.32	N/A	1.70	2.80	N/A	N/A	N/A	2.54	Main
sSAF-28	Ferrum	33.4555517, -115.8522273	17.37	Good	SE CW	2.80	N/A	1.33	1.15	1.44	N/A	N/A	1.00	2.00	N/A	N/A	N/A	1.68	Minor
sSAF-29	Ferrum	33.4556, -115.8520	18.57	Good	SE CW	3.71	N/A	3.56	3.58	3.80	N/A	N/A	2.80	4.00	N/A	N/A	N/A	3.66	Minor
sSAF-30	Ferrum	33.4594002, -115.8563058	18.61	Excellent	SE CW	5.77	5.92	5.88	5.82	5.91	5.38	5.10	5.50	6.80	N/A	N/A	N/A	5.68	Multiple
sSAF-31	Ferrum	33.4592735, -115.8560647	18.58	Excellent	T	5.78	5.92	5.88	5.82	5.91	3.76	N/A	5.50	6.80	N/A	N/A	N/A	5.51	Multiple
sSAF-32	Ferrum	33.4615216, -115.8583188	20.91	Excellent	T	6.84	7.11	7.00	6.89	6.98	6.62	7.10	6.20	7.60	7.00	5.50	7.80	6.94	Main
sSAF-33	Ferrum	33.468136, -115.868521	21.87	Good	T	2.52	N/A	2.50	2.46	2.48	N/A	2.60	1.60	2.80	N/A	N/A	N/A	2.51	Main
sSAF-34	Ferrum	33.468171, -115.868583	22.25	Good	T	2.65	N/A	2.50	2.46	2.48	N/A	2.70	1.60	2.80	N/A	N/A	N/A	2.56	Main
sSAF-35	Ferrum	33.468327, -115.868780	22.31	Good	T	2.10	N/A	2.50	2.46	2.48	N/A	2.60	1.60	2.80	N/A	N/A	N/A	2.43	Main
sSAF-36	Ferrum	33.481870, -115.887515	22.67	Good	T	3.16	N/A	3.62	3.52	3.69	N/A	N/A	3.00	4.30	N/A	N/A	N/A	3.50	Main
sSAF-37	Ferrum	33.488110, -115.894493	22.94	Good	NW CW	2.81	N/A	2.74	2.73	2.78	3.00	N/A	2.10	3.40	N/A	N/A	N/A	2.81	Main
sSAF-38	Ferrum	33.490568, -115.897373	22.96	Fair	T	2.70	N/A	3.19	3.14	3.00	N/A	3.20	2.70	3.40	N/A	N/A	N/A	3.05	Main
sSAF-39	Ferrum	33.491198, -115.897309	22.97	Good	T	2.74	N/A	3.38	3.20	3.32	2.72	3.20	2.40	3.70	N/A	N/A	N/A	3.09	Minor
sSAF-40	Ferrum	33.493453, -115.900360	23.04	Good	BH-C	3.28	N/A	3.43	3.42	3.40	N/A	N/A	3.00	3.70	N/A	N/A	N/A	3.38	Main
sSAF-41	Mecca Hills	33.570947, -115.979608	34	Poor	T	7.75	8.12	8.16	7.15	7.09	6.09	N/A	N/A	N/A	7.60	7.20	8.60	7.42	Main
sSAF-42	Mecca Hills	33.571044, -115.979804	34.02	Fair	T	5.04	5.56	5.46	5.31	5.36	5.05	N/A	N/A	N/A	N/A	N/A	N/A	5.30	Main
sSAF-43	Mecca Hills	33.571187, -115.979962	34.04	Poor	T	2.62	2.70	2.46	N/A	2.45	2.65	N/A	N/A	N/A	N/A	N/A	N/A	2.58	Main
sSAF-44	Mecca Hills	33.571280, -115.979984	34.05	Good	SE CW	3.12	3.16	3.14	3.30	3.24	3.20	N/A	3.00	3.80	3.60	3.30	3.90	3.25	Main
sSAF-45	Mecca Hills	33.571280, -115.979984	34.05	Fair	T	8.41	8.49	8.42	8.24	8.58	9.75	N/A	N/A	N/A	8.60	6.60	10.60	8.64	Main
sSAF-46	Mecca Hills	33.571528, -115.980288	34.09	Fair	T	N/A	4.96	4.80	4.63	5.00	5.10	N/A	4.30	5.80	N/A	N/A	N/A	4.90	Main
sSAF-47	Mecca Hills	33.571578, -115.980337	34.1	Fair	SE CW	N/A	2.58	2.94	2.62	3.04	3.10	N/A	2.60	3.65	N/A	N/A	N/A	2.86	Main
sSAF-48	Mecca Hills	33.571578, -115.980337	34.1	Fair	T	N/A	7.33	7.26	7.05	7.10	7.10	N/A	N/A	N/A	N/A	N/A	N/A	7.17	Main
sSAF-49	Mecca Hills	33.571644, -115.980419	34.11	Fair	T	N/A	7.44	7.48	7.58	7.57	7.20	N/A	6.40	8.10	N/A	N/A	N/A	7.45	Main
sSAF-50	Mecca Hills	33.571644, -115.980419	34.11	Fair	T	N/A	14.62	14.98	14.53	14.85	14.70	N/A	N/A	N/A	N/A	N/A	N/A	14.74	Main

sSAF-51	Mecca Hills	33.571691, -115.980476	34.12	Fair	T	N/A	5.15	5.11	5.08	5.30	5.40	N/A	5.00	5.90	N/A	N/A	N/A	5.21	Main
sSAF-52	Mecca Hills	33.571910, -115.980710	34.15	Fair	T	N/A	4.70	4.44	4.79	4.98	4.60	N/A	N/A	N/A	N/A	N/A	N/A	4.70	Main
sSAF-53	Mecca Hills	33.571910, -115.980710	34.15	Fair	T	N/A	5.12	4.89	5.01	5.19	5.20	N/A	4.40	4.90	N/A	N/A	N/A	5.08	Main
sSAF-54	Mecca Hills	33.571910, -115.980710	34.15	Good	T	N/A	12.15	12.47	12.20	12.65	12.40	N/A	12.40	14.35	N/A	N/A	N/A	12.37	Main
sSAF-55	Mecca Hills	33.571910, -115.980710	34.15	Good	T	N/A	13.74	13.60	13.80	14.00	12.70	N/A	N/A	N/A	N/A	N/A	N/A	13.57	Main
sSAF-56	Mecca Hills	33.572312, -115.981214	34.21	Excellent	SE CW	N/A	3.62	3.33	3.51	3.25	4.15	N/A	3.00	4.25	N/A	N/A	N/A	3.57	Main
sSAF-57	Mecca Hills	33.613475, -116.032921	40.88	Excellent	SE CW	4.99	N/A	4.61	4.49	4.69	4.65	N/A	4.10	5.50	5.00	4.50	6.00	4.74	Main
sSAF-58	Mecca Hills	33.6138, -116.0333	40.93	Excellent	SE CW	6.93	N/A	N/A	N/A	N/A	N/A	N/A	N/A	N/A	6.75	5.40	8.40	6.84	Main
sSAF-59	Mecca Hills	33.613952, -116.033598	40.96	Excellent	SE CW	3.16	N/A	2.62	2.60	2.70	3.25	2.80	1.70	3.00	3.00	1.90	4.10	2.88	Main
sSAF-60	Mecca Hills	33.614114, -116.033825	40.99	Excellent	T	N/A	N/A	N/A	N/A	N/A	2.51	N/A	N/A	N/A	2.60	2.40	2.80	2.56	Main
sSAF-61	Mecca Hills	33.614247, -116.033987	41.01	Excellent	T	3.15	N/A	2.62	2.60	2.70	2.31	2.20	2.30	3.00	3.00	2.40	3.60	2.65	Main
sSAF-62	Mecca Hills	33.614957, -116.034982	41.01	Excellent	T	8.00	N/A	7.70	7.75	7.72	8.10	7.30	7.00	9.40	8.10	6.70	9.60	7.81	Main
sSAF-63	Mecca Hills	33.614957, -116.034982	41.01	Good	BH-C	14.20	N/A	13.50	13.60	13.80	N/A	14.30	13.20	15.60	15.00	14.00	17.00	14.07	Main
sSAF-64	Mecca Hills	33.616971, -116.037705	41.13	Excellent	T	3.50	N/A	4.00	4.18	4.12	4.19	3.90	3.40	4.40	3.80	3.00	4.80	3.96	Main
sSAF-65	Mecca Hills	33.617373, -116.038313	41.47	Excellent	SE CW	21.80	N/A	22.05	22.40	22.50	22.60	22.80	19.00	24.60	22.00	20.50	25.50	22.31	Main
sSAF-66	Mecca Hills	33.6182, -116.0395	41.54	Excellent	T	N/A	N/A	N/A	N/A	N/A	N/A	N/A	N/A	N/A	2.70	N/A	N/A	2.70	Main
sSAF-67	Mecca Hills	33.6183, -116.0397	41.68	Excellent	SE CW	13.82	N/A	N/A	N/A	N/A	N/A	N/A	N/A	N/A	13.70	N/A	N/A	13.76	Main
sSAF-68	Mecca Hills	33.6195, -116.0414	41.71	Good	SE CW	5.10	N/A	N/A	N/A	N/A	N/A	N/A	N/A	N/A	5.30	4.30	5.80	5.20	Main
sSAF-69	Mecca Hills	33.6460, -116.0761	41.91	Poor	SE CW	7.01	N/A	N/A	N/A	N/A	N/A	N/A	N/A	N/A	N/A	N/A	N/A	7.01	Main
sSAF-70	Mecca Hills	33.647192, -116.077815	46.31	Excellent	T	N/A	N/A	N/A	N/A	N/A	N/A	N/A	N/A	N/A	3.40	2.60	3.80	3.40	Main
sSAF-71	Mecca Hills	33.647037, -116.077659	46.5	Fair	T	N/A	5.97	6.00	6.01	5.94	6.00	N/A	5.20	6.40	6.30	5.30	6.50	6.04	Main
sSAF-72	Mecca Hills	33.647037, -116.077659	46.5	Fair	T	N/A	13.10	13.25	13.26	13.42	13.15	N/A	N/A	N/A	12.70	12.20	13.20	13.15	Main
sSAF-73	Mecca Hills	33.647310, -116.078020	46.52	Excellent	T	10.23	10.35	10.38	10.60	11.00	10.00	N/A	9.80	11.10	N/A	N/A	N/A	10.43	Main
sSAF-74	Mecca Hills	33.647833, -116.078657	46.54	Excellent	SE CW	8.24	8.58	8.80	8.52	7.66	8.30	N/A	7.10	9.60	N/A	N/A	N/A	8.35	Main
sSAF-75	Mecca Hills	33.648431, -116.079370	46.62	Poor	NW CW	21.50	21.79	21.00	20.70	21.00	22.00	N/A	16.70	24.00	N/A	N/A	N/A	21.33	Main
sSAF-76	Mecca Hills	33.649527, -116.080764	46.71	Fair	T	N/A	3.40	3.30	3.46	3.48	3.38	N/A	N/A	N/A	3.50	2.70	4.50	3.42	Main
sSAF-77	Mecca Hills	33.6503, -116.0816	46.89	Good	NW CW	N/A	N/A	12.95	12.74	12.66	N/A	N/A	N/A	N/A	11.50	10.00	12.50	12.46	Main
sSAF-78	Mecca Hills	33.650555, -116.082039	47.01	Excellent	SE CW	N/A	N/A	4.22	4.16	4.33	N/A	N/A	N/A	N/A	3.50	3.00	4.50	4.05	Main
sSAF-79	Mecca Hills	33.650555, -116.082039	47.01	Excellent	SE CW	7.11	6.50	6.10	6.90	6.75	5.50	N/A	N/A	N/A	7.00	6.00	7.50	6.55	Main
sSAF-80	Mecca Hills	33.650555, -116.082039	47.01	Good	SE CW	10.32	N/A	9.86	9.65	9.80	N/A	N/A	N/A	N/A	9.20	8.20	9.70	9.77	Main

sSAF-81	Mecca Hills	33.650555, -116.082039	47.01	Fair	SE CW	13.62	N/A	13.48	13.41	13.77	N/A	N/A	N/A	N/A	13.00	12.00	13.80	13.46	Main
sSAF-82	Mecca Hills	33.650555, -116.082039	47.01	Fair	SE CW	17.59	N/A	17.02	16.89	16.96	N/A	N/A	N/A	N/A	17.50	N/A	N/A	17.19	Main
sSAF-83	Mecca Hills	33.650968, -116.082509	47.06	Fair	T	2.80	3.00	3.10	3.30	3.40	2.80	N/A	2.40	3.30	N/A	N/A	N/A	3.07	Main
sSAF-84	Mecca Hills	33.650945, -116.082528	47.12	Poor	NW CW	12.50	15.20	15.13	15.70	15.39	12.50	N/A	N/A	N/A	N/A	N/A	N/A	14.40	Main
sSAF-85	Mecca Hills	33.650945, -116.082528	47.12	Poor	SE CW	17.10	17.70	17.60	17.07	17.00	17.10	N/A	N/A	N/A	N/A	N/A	N/A	17.26	Main
sSAF-86	Mecca Hills	33.6514, -116.0828	47.17	Fair	BH-C	N/A	N/A	N/A	N/A	N/A	N/A	N/A	N/A	N/A	13.00	N/A	N/A	13.00	Main
sSAF-87	Mecca Hills	33.651520, -116.083243	47.21	Poor	T	N/A	3.02	2.95	3.00	3.03	N/A	N/A	N/A	N/A	N/A	N/A	N/A	3.00	Main
sSAF-88	Mecca Hills	33.651520, -116.083243	47.21	Poor	T	6.07	6.05	6.36	6.40	6.20	6.00	N/A	5.00	6.40	N/A	N/A	N/A	6.18	Main
sSAF-89	Mecca Hills	33.651745, -116.083533	47.24	Good	SE CW	5.55	5.40	5.60	5.58	5.50	5.52	N/A	4.50	6.30	N/A	N/A	N/A	5.53	2 strands
sSAF-90	Mecca Hills	33.6518, -116.0833	47.25	Excellent	T	14.43	N/A	14.51	14.69	14.60	N/A	N/A	N/A	N/A	N/A	N/A	N/A	14.56	2 strands
sSAF-91	Mecca Hills	33.652515, -116.084456	47.36	Good	T	9.45	9.70	9.65	9.79	9.52	9.50	N/A	7.80	10.10	N/A	N/A	N/A	9.60	Main
sSAF-92	Mecca Hills	33.652515, -116.084456	47.36	Good	SE CW	N/A	8.10	8.00	8.17	8.08	8.50	N/A	N/A	N/A	N/A	N/A	N/A	8.17	Main
sSAF-93	Indio Hills	33.6667, -116.0993	49.47	Good	T	8.42	N/A	N/A	N/A	N/A	N/A	N/A	N/A	N/A	8.50	7.50	9.50	8.46	Main
sSAF-94	Indio Hills	33.6727, -116.1061	50.38	Good	T	2.89	N/A	N/A	N/A	N/A	N/A	N/A	N/A	N/A	3.00	2.00	4.00	2.95	Main
sSAF-95	Indio Hills	33.673630, -116.107169	50.56	Excellent	SE CW	3.03	N/A	N/A	N/A	N/A	N/A	N/A	N/A	N/A	3.10	2.60	4.10	3.07	Main
sSAF-96	Indio Hills	33.673630, -116.107169	50.56	Excellent	SE CW	5.37	N/A	N/A	N/A	N/A	N/A	N/A	N/A	N/A	6.20	5.20	7.20	5.79	Main
sSAF-97	Indio Hills	33.673630, -116.107169	50.56	Good	SE CW	9.27	N/A	N/A	N/A	N/A	N/A	N/A	N/A	N/A	10.00	9.20	10.80	9.64	Main
sSAF-98	Indio Hills	33.673630, -116.107169	50.56	Good	SE CW	13.61	N/A	N/A	N/A	N/A	N/A	N/A	N/A	N/A	13.20	12.20	13.70	13.41	Main
sSAF-99	Indio Hills	33.7450, -116.1921	61.72	Good	T	N/A	N/A	N/A	N/A	N/A	N/A	N/A	N/A	N/A	3.00	N/A	N/A	3.00	Main
sSAF-100	Indio Hills	33.7450, -116.1921	61.72	Good	T	N/A	N/A	N/A	N/A	N/A	N/A	N/A	N/A	N/A	3.50	N/A	N/A	3.50	Main
sSAF-101	Indio Hills	33.7453, -116.1924	61.76	Good	BH-C	N/A	N/A	N/A	N/A	N/A	N/A	N/A	N/A	N/A	6.00	N/A	N/A	6.00	Main
sSAF-102	Indio Hills	33.7463, -116.1936	61.92	Good	T	N/A	N/A	N/A	N/A	N/A	N/A	N/A	N/A	N/A	3.50	N/A	N/A	3.50	Main
sSAF-103	Indio Hills	33.7463, -116.1936	61.92	Good	BH-C	N/A	N/A	N/A	N/A	N/A	N/A	N/A	N/A	N/A	10.00	N/A	N/A	10.00	Main
sSAF-104	Indio Hills	33.7638, -116.2155	64.72	Good	T	N/A	N/A	N/A	N/A	N/A	N/A	N/A	N/A	N/A	3.30	N/A	N/A	3.30	Main
sSAF-105	Indio Hills	33.7638, -116.2155	64.72	Good	BH-C	N/A	N/A	N/A	N/A	N/A	N/A	N/A	N/A	N/A	6.00	N/A	N/A	6.00	Main
sSAF-106	Indio Hills	33.768652, -116.222348	65.55	Fair	T	N/A	N/A	3.62	3.65	3.40	3.69	N/A	N/A	N/A	N/A	N/A	N/A	3.59	Main
sSAF-107	Indio Hills	33.768738, -116.222449	65.57	Fair	T	3.43	N/A	3.62	3.65	3.40	3.60	N/A	N/A	N/A	3.50	N/A	N/A	3.53	Main
sSAF-108	Indio Hills	33.768888, -116.222666	65.58	Fair	T	3.33	N/A	3.62	3.65	3.40	N/A	N/A	N/A	N/A	N/A	N/A	N/A	3.50	Main
sSAF-109	Indio Hills	33.769139, -116.222871	65.63	Good	SE CW	1.56	1.54	1.62	1.64	1.60	1.76	N/A	0.50	1.70	N/A	N/A	N/A	1.62	Main
sSAF-110	Indio Hills	33.769191, -116.222931	65.64	Good	T	N/A	1.54	1.62	1.64	1.60	1.54	N/A	0.80	1.90	N/A	N/A	N/A	1.59	Main

sSAF-111	Indio Hills	33.769364, -116.223095	65.66	Excellent	T	1.57	1.54	1.62	1.64	1.60	1.64	N/A	0.80	1.90	N/A	N/A	N/A	1.60	Main
sSAF-112	Indio Hills	33.769584, -116.223331	65.69	Good	T	1.59	1.54	1.62	1.64	1.60	1.55	N/A	0.80	1.90	N/A	N/A	N/A	1.59	Main
sSAF-113	Indio Hills	33.7701, -116.2239	65.77	Good	BH-C	N/A	N/A	N/A	N/A	N/A	7.88	N/A	N/A	N/A	8.00	N/A	N/A	7.94	Main
sSAF-114	Indio Hills	33.770284, -116.224129	65.8	Good	SE CW	5.00	4.53	4.49	4.55	4.50	4.27	4.30	3.40	4.80	4.50	N/A	N/A	4.52	Main
sSAF-115	Indio Hills	33.772643, -116.227389	66.2	Excellent	ridge	20.67	20.32	20.50	20.40	20.20	23.63	22.90	N/A	N/A	24.50	N/A	N/A	21.64	Main
sSAF-116	Indio Hills	33.772853, -116.227668	66.23	Excellent	T	9.27	9.42	9.28	9.50	9.40	8.86	N/A	8.40	10.40	N/A	N/A	N/A	9.29	Main
sSAF-117	Indio Hills	33.772929, -116.227796	66.25	Excellent	T	9.20	9.42	9.28	9.50	9.40	8.97	9.10	8.40	10.40	N/A	N/A	N/A	9.27	Main
sSAF-118	Indio Hills	33.813782, -116.273986	71.67	Fair	NW CW	3.38	N/A	N/A	N/A	N/A	N/A	N/A	N/A	N/A	3.10	N/A	N/A	3.24	Multiple
sSAF-119	Indio Hills	33.8091, -116.2692	71.85	Good	T	N/A	N/A	N/A	N/A	N/A	N/A	N/A	N/A	N/A	3.80	N/A	N/A	3.80	Multiple
sSAF-120	Indio Hills	33.8139, -116.2743	72.55	Excellent	T	N/A	N/A	N/A	N/A	N/A	N/A	N/A	N/A	N/A	3.60	N/A	N/A	3.60	Multiple
sSAF-121	Indio Hills	33.8171, -116.2779	73.05	Excellent	T	N/A	N/A	N/A	N/A	N/A	N/A	N/A	N/A	N/A	3.50	N/A	N/A	3.50	Multiple
sSAF-122	Indio Hills	33.8270, -116.2940	74.94	Excellent	T	N/A	N/A	N/A	N/A	N/A	N/A	N/A	N/A	N/A	3.70	N/A	N/A	3.70	Multiple
sSAF-123	Indio Hills	33.8270, -116.2940	74.94	Excellent	BH-C	N/A	N/A	N/A	N/A	N/A	N/A	N/A	N/A	N/A	8.00	N/A	N/A	8.00	Multiple
sSAF-124	Indio Hills	33.8270, -116.2940	74.94	Poor	BH-C	N/A	N/A	N/A	N/A	N/A	N/A	N/A	N/A	N/A	16.50	N/A	N/A	16.50	Multiple
sSAF-125	Indio Hills	33.8270, -116.2940	74.94	Poor	BH-C	N/A	N/A	N/A	N/A	N/A	N/A	N/A	N/A	N/A	24.50	N/A	N/A	24.50	Multiple
sSAF-126	Indio Hills	33.8299, -116.2980	75.42	Fair	SE CW	12.76	N/A	12.16	12.50	13.01	11.46	N/A	N/A	N/A	N/A	N/A	N/A	12.38	Multiple
sSAF-127	Indio Hills	33.8299, -116.2980	75.42	Fair	SE CW	N/A	N/A	N/A	N/A	N/A	4.17	N/A	N/A	N/A	4.10	N/A	N/A	4.14	Multiple
sSAF-128	Indio Hills	33.8302, -116.2984	75.47	Good	T	N/A	N/A	N/A	N/A	N/A	N/A	N/A	N/A	N/A	3.30	N/A	N/A	3.30	Multiple
sSAF-129	Indio Hills	33.8302, -116.2984	75.47	Good	BH-C	N/A	N/A	N/A	N/A	N/A	N/A	N/A	N/A	N/A	10.00	N/A	N/A	10.00	Multiple
sSAF-130	Indio Hills	33.8348, -116.3061	76.35	Fair	BH-C	N/A	N/A	N/A	N/A	N/A	3.15	N/A	N/A	N/A	N/A	N/A	N/A	3.15	Main
sSAF-131	Indio Hills	33.8368, -116.3086	76.68	Excellent	SE CW	7.14	N/A	N/A	N/A	N/A	N/A	N/A	N/A	N/A	7.00	N/A	N/A	7.07	Main
sSAF-132	Indio Hills	33.8368, -116.3086	76.68	Excellent	SE CW	11.64	N/A	N/A	N/A	N/A	N/A	N/A	N/A	N/A	14.50	N/A	N/A	13.07	Main
sSAF-133	Indio Hills	33.8430, -116.3159	77.64	Good	T	3.77	N/A	N/A	N/A	N/A	N/A	N/A	N/A	N/A	4.00	N/A	N/A	3.89	Main
sSAF-134	Indio Hills	33.8430, -116.3159	77.64	Good	BH-C	N/A	N/A	N/A	N/A	N/A	N/A	N/A	N/A	N/A	7.60	N/A	N/A	7.60	Main
sSAF-135	Indio Hills	33.8430, -116.3159	77.64	Good	BH-C	N/A	N/A	N/A	N/A	N/A	N/A	N/A	N/A	N/A	10.70	N/A	N/A	10.70	Main
sSAF-136	Indio Hills	33.8430, -116.3159	77.64	Good	BH-C	N/A	N/A	N/A	N/A	N/A	N/A	N/A	N/A	N/A	14.50	N/A	N/A	14.50	Main
sSAF-137	Indio Hills	33.8430, -116.3159	77.64	Good	BH-C	N/A	N/A	N/A	N/A	N/A	N/A	N/A	N/A	N/A	19.00	N/A	N/A	19.00	Main
sSAF-138	Indio Hills	33.8430, -116.3159	77.64	Good	BH-C	N/A	N/A	N/A	N/A	N/A	N/A	N/A	N/A	N/A	23.00	N/A	N/A	23.00	Main
sSAF-139	Indio Hills	33.8430, -116.3159	77.64	Good	BH-C	N/A	N/A	N/A	N/A	N/A	N/A	N/A	N/A	N/A	26.00	N/A	N/A	26.00	Main
sSAF-140	Indio Hills	33.8434, -116.3166	77.72	Excellent	T	N/A	N/A	N/A	N/A	N/A	N/A	N/A	N/A	N/A	3.80	N/A	N/A	3.80	Main

sSAF-141	Indio Hills	33.8434, -116.3166	77.72	Excellent	BH-C	N/A	N/A	N/A	N/A	N/A	N/A	N/A	N/A	N/A	7.40	N/A	N/A	7.40	Main
sSAF-142	Indio Hills	33.8434, -116.3166	77.72	Excellent	BH-C	N/A	N/A	N/A	N/A	N/A	N/A	N/A	N/A	N/A	10.50	N/A	N/A	10.50	Main
sSAF-143	Indio Hills	33.8434, -116.3166	77.72	Excellent	BH-C	N/A	N/A	N/A	N/A	N/A	N/A	N/A	N/A	N/A	14.50	N/A	N/A	14.50	Main
sSAF-144	Indio Hills	33.8434, -116.3166	77.72	Excellent	BH-C	N/A	N/A	N/A	N/A	N/A	N/A	N/A	N/A	N/A	19.00	N/A	N/A	19.00	Main
sSAF-145	Indio Hills	33.8434, -116.3166	77.72	Excellent	BH-C	N/A	N/A	N/A	N/A	N/A	N/A	N/A	N/A	N/A	25.50	N/A	N/A	25.50	Main
sSAF-146	Indio Hills	33.8434, -116.3166	77.72	Excellent	BH-C	N/A	N/A	N/A	N/A	N/A	N/A	N/A	N/A	N/A	28.00	N/A	N/A	28.00	Main

FIGURES

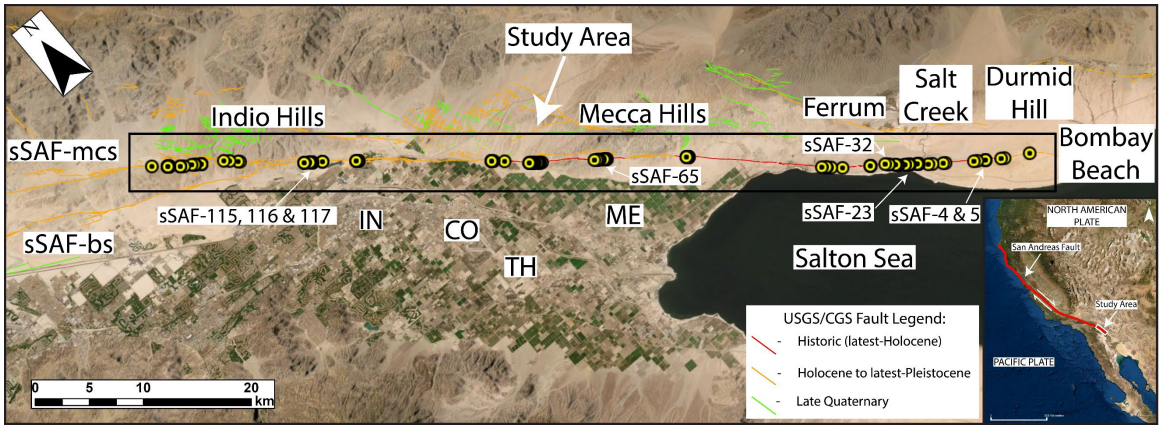

Figure 1. Satellite image of the central-to-northern Salton Trough with the study area shown in the black box. Figure shows ~80 km of the southernmost San Andreas Fault (sSAF), regional Quaternary faults colored by age (USGS and CGS, 2022), and lateral offset locations used in this study (yellow circles). Offset locations used in Figs. 5 through 9 are labeled with their respective numbering. Abbreviations: IN - Indio, CO - Coachella, TH - Thermal, ME - Mecca, SAF-mcs and bs – southernmost San Andreas Fault mission creek and banning strands. Inset figure (lower right) exhibits a map of North America in relation to our study site with the location of the San Andreas Fault (SAF) shown in red between the boundary of the North American and Pacific Plates.

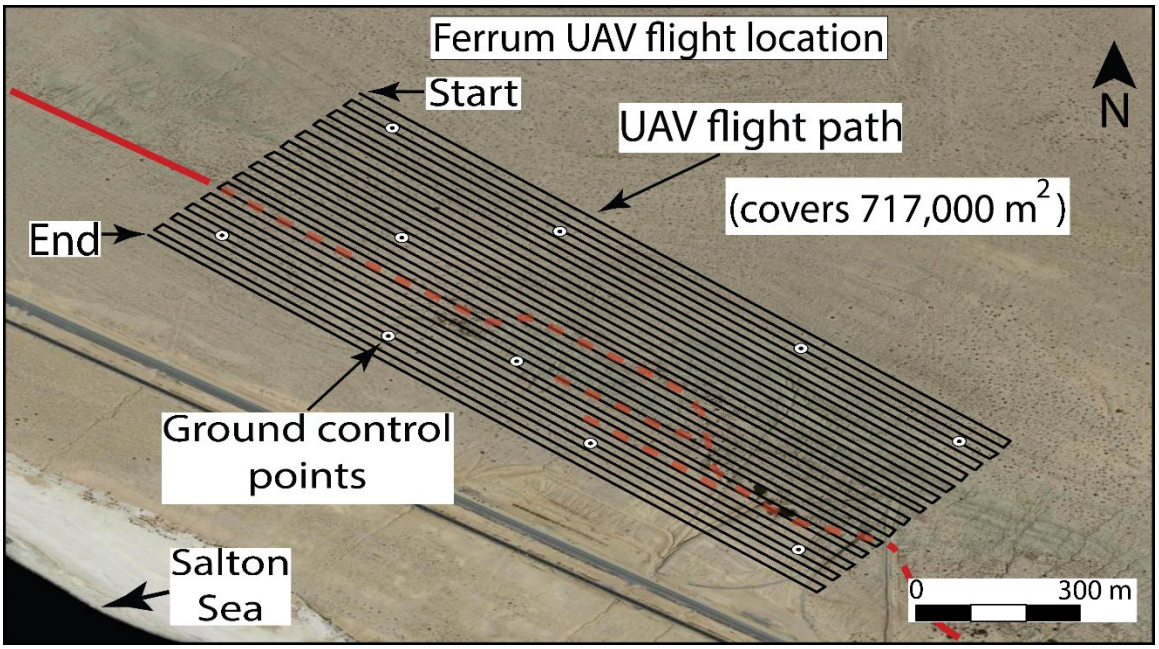

Figure 2. UAV flight path for one of our surveys located in Ferrum along the northeastern shoreline of the modern-day Salton Sea where the sSAF (red lines) exhibits a double releasing bend. The UAV was flown at an altitude of 30 m above ground level from takeoff point and covered an area of approximately 717,000 m^2. Data derived from this flight produced DSMs and orthomosaics with millimeter to centimeter-scale accuracy.

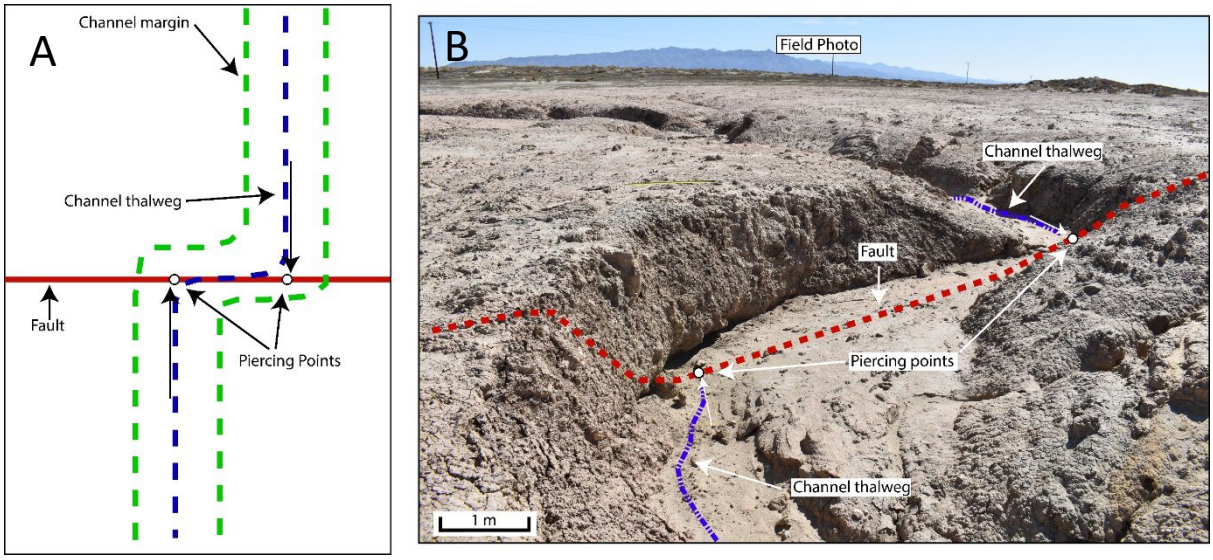

Figure 3. A) Schematic diagram on measuring the displacement a generalized offset channel by using channel thalwegs as piercing points. Geomorphic features such as channel thalwegs are projected into the fault trace to be used as piercing points to resolve displacement. The resulting displacement represents the distance along the fault between the piercing points. Slip vectors on either side of the fault display dextral motion. B) Field photo using the method shown in A. A, modified from Salisbury et al. (2015) and Blanton et al. (2020).

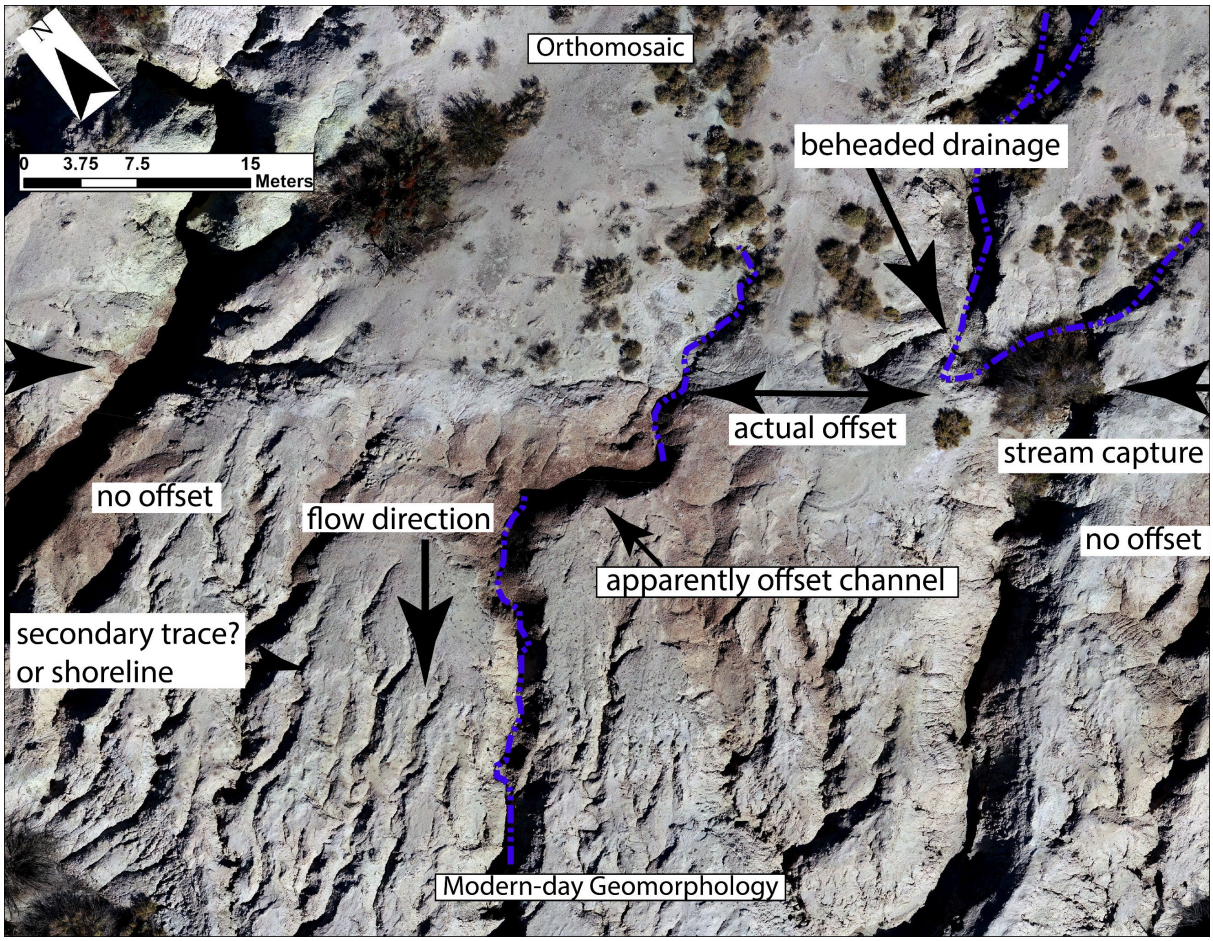

Figure 4. Fault geomorphology of a site near Salt Creek where the main fault is clearly delineated with a scarp and change in bedrock, with ponded alluvium to the NE. The channel in the right side of the figure is interpreted to represent capture by another rill. The channel headwaters are interpreted to be offset from the central channel by about 17 m, which now realigns across the fault. The apparently offset channel does not align with the fault and is interpreted as a meander because channels to the left and right show no deflection at the distance from the main fault. The larger channel on the left of the figure is realigned since the last highstand of lake Cahuilla or has formed since. This deflected channel is not used in our analysis.

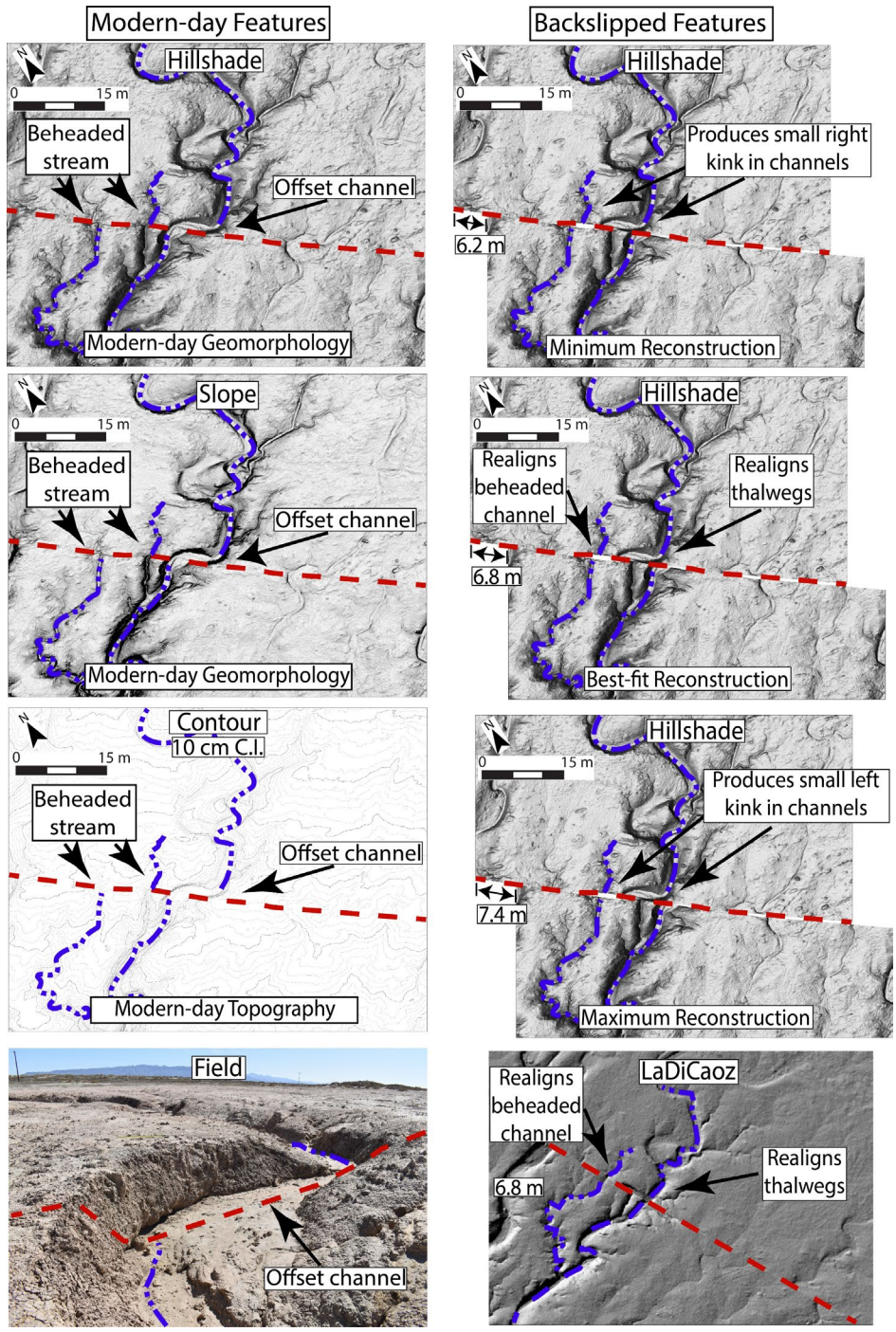

Figure 5. The series of images on the left-hand side, from top to bottom, consist of modern-day geomorphology and topography of a hillshade surface map, slope surface map, contour surface map, and field photograph of offset features sSAF-4 & 5 which display an offset and beheaded channel, respectively. Dashed red lines represent the surficial fault trace and dashed blue lines represent channel thalwegs. The series of images on the right-hand side, from top to bottom, consist of backslipped offsets with minimum, best-fit, and maximum displacement values produced with a hillshade surface map, and a backslipped hillshade surface map model generated in LaDiCaoz.

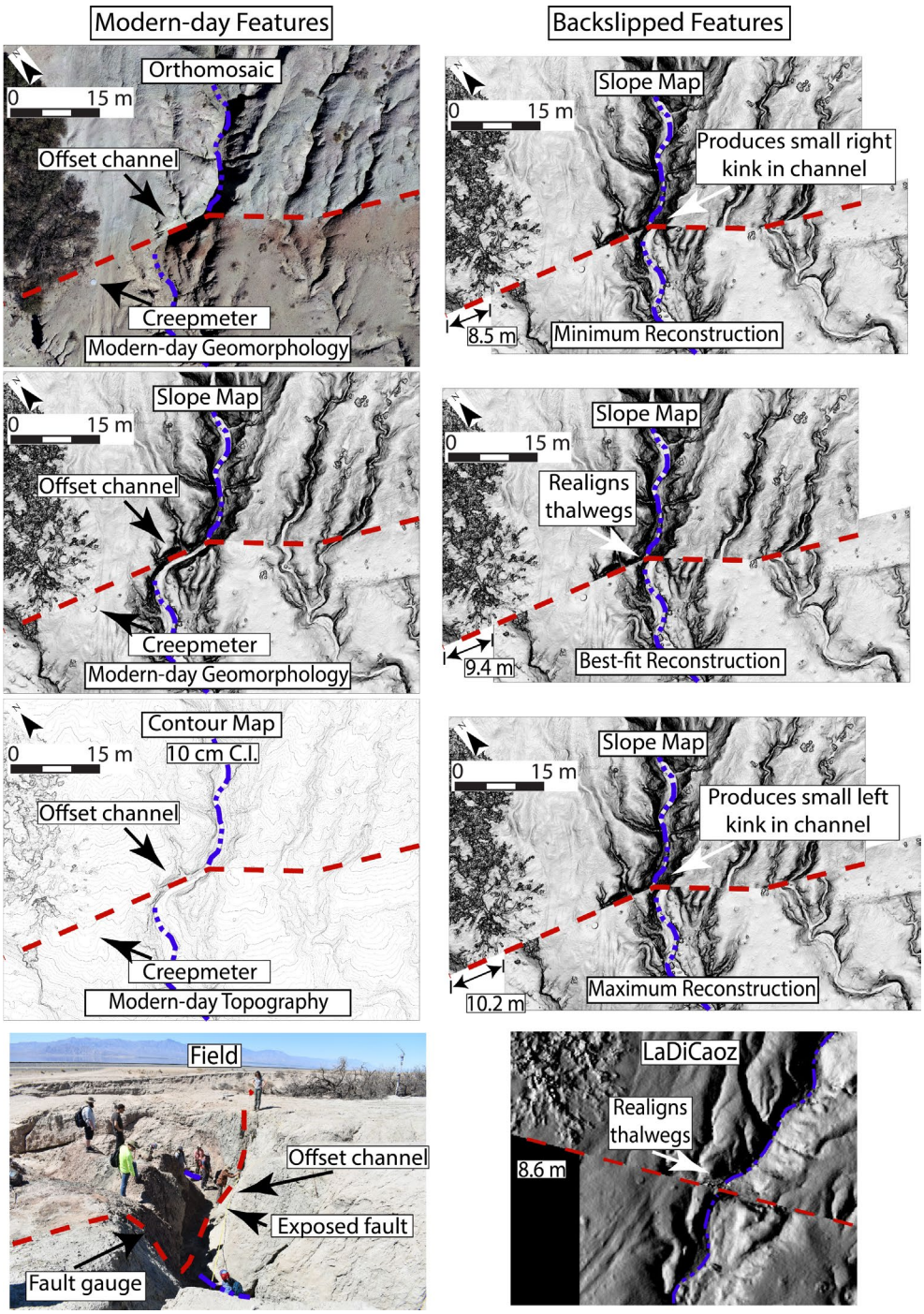

Figure 6. The series of images on the left-hand side, from top to bottom, consist of modern-day geomorphology and topography of an orthomosaic surface map, slope surface map, contour surface map, and field photograph of offset feature sSAF-23 which displays an offset channel. Dashed red lines represent the surficial fault trace and dashed blue lines represent channel thalwegs. The series of images on the right-hand side, from top to bottom, consist of a backslipped offset with minimum, best-fit, and maximum displacement values produced with a slope surface map, and a backslipped hillshade surface map model generated in LaDiCaoz.

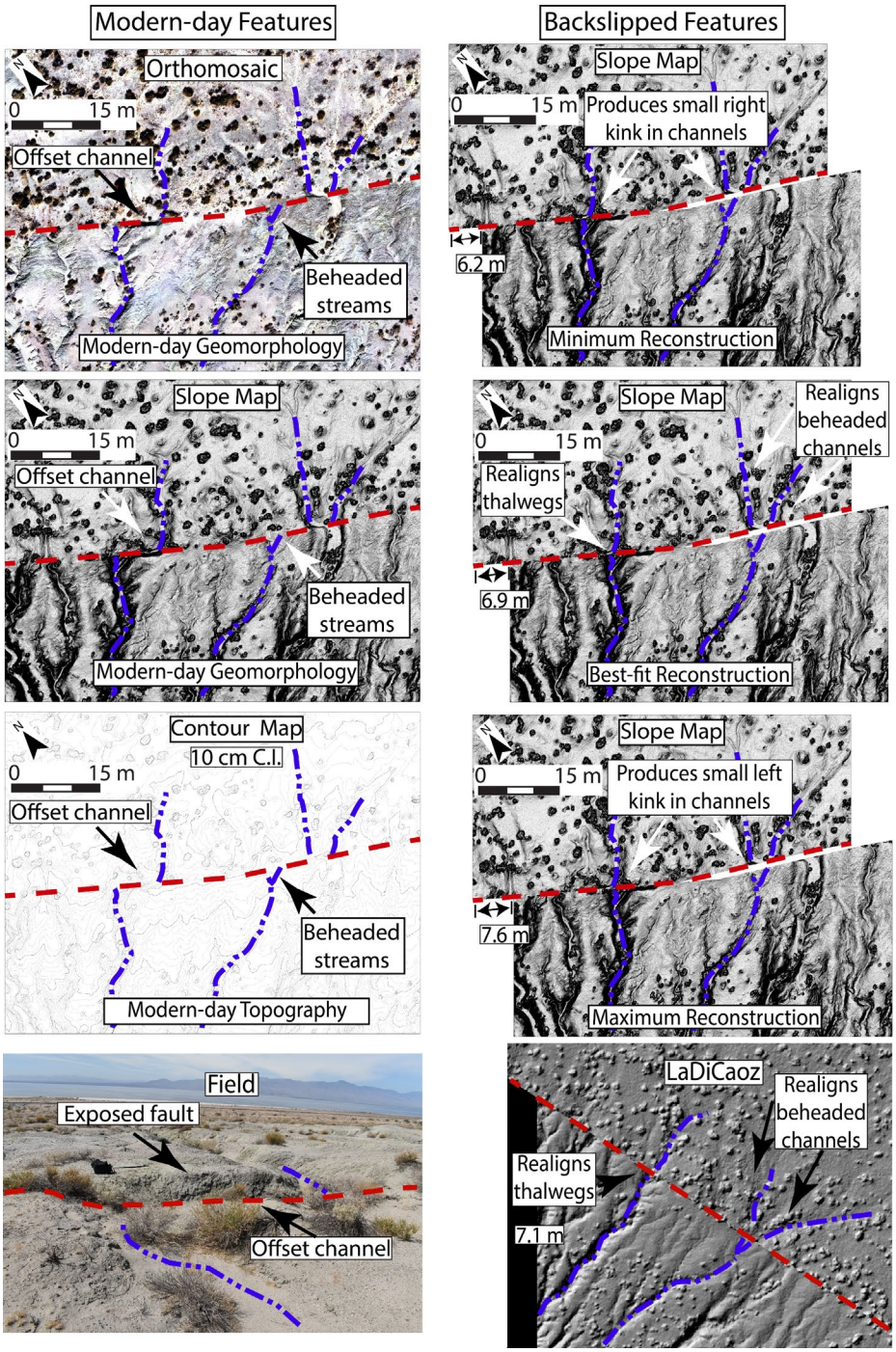

Figure 7. The series of images on the left-hand side, from top to bottom, consist of modern-day geomorphology and topography of an orthomosaic surface map, slope surface map, contour surface map, and field photograph of offset feature sSAF-32 which displays an offset and beheaded channel. Dashed red lines represent the surficial fault trace and dashed blue lines represent channel thalwegs. The series of images on the right-hand side, from top to bottom, consist of backslipped offsets with minimum, best-fit, and maximum displacement values produced with a slope surface map, and a backslipped hillshade surface map model generated in LaDiCaoz.

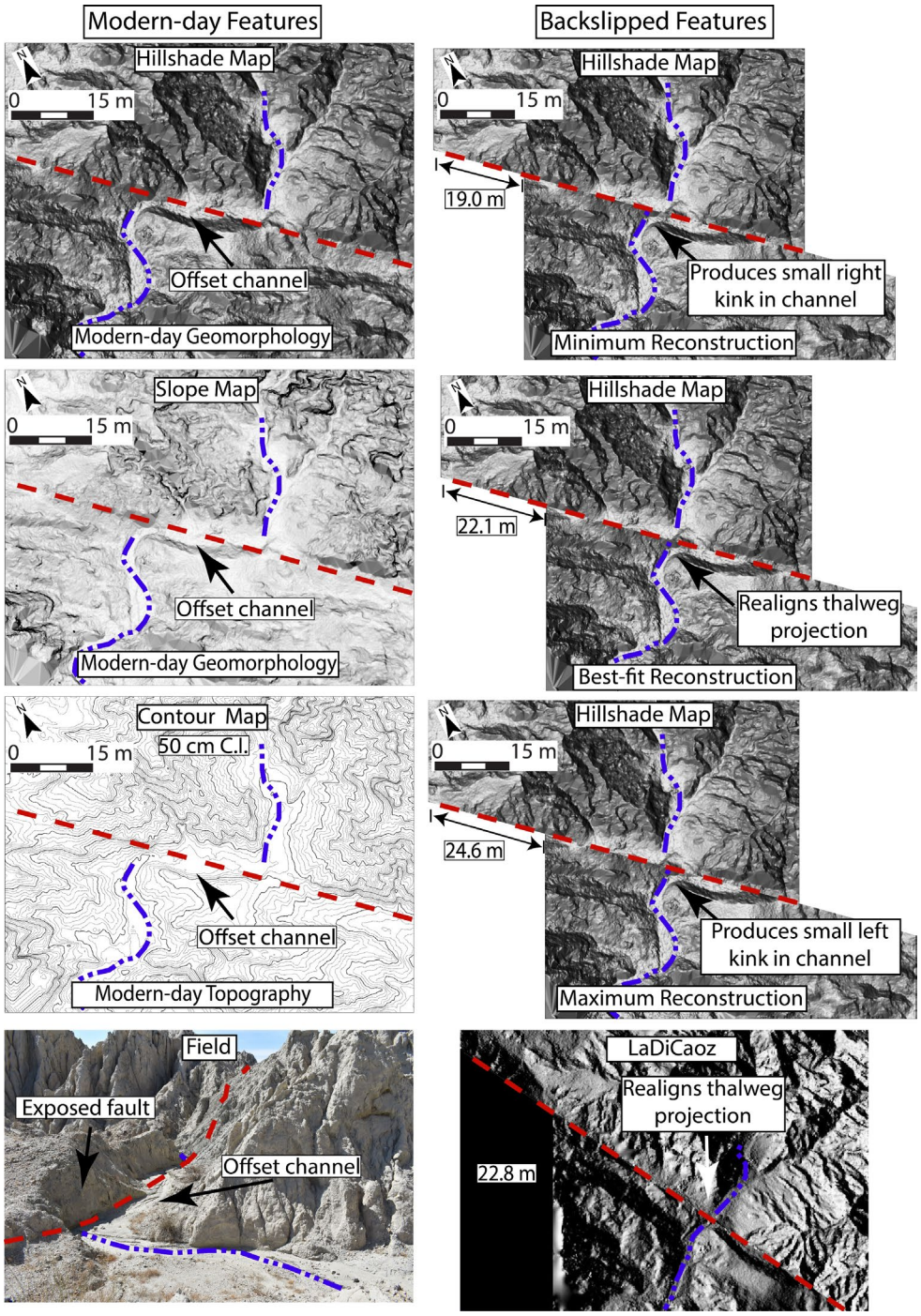

Figure 8. The series of images on the left-hand side, from top to bottom, consist of modern-day geomorphology and topography of a hillshade surface map, slope surface map, contour surface map, and field photograph of offset feature sSAF-65 which displays an offset channel. Dashed red lines represent the surficial fault trace and dashed blue lines represent channel thalwegs. The series of images on the right-hand side, from top to bottom, consist of a backslipped offset with minimum, best-fit, and maximum displacement values produced with a hillshade surface map, and a backslipped hillshade surface map model generated in LaDiCaoz.

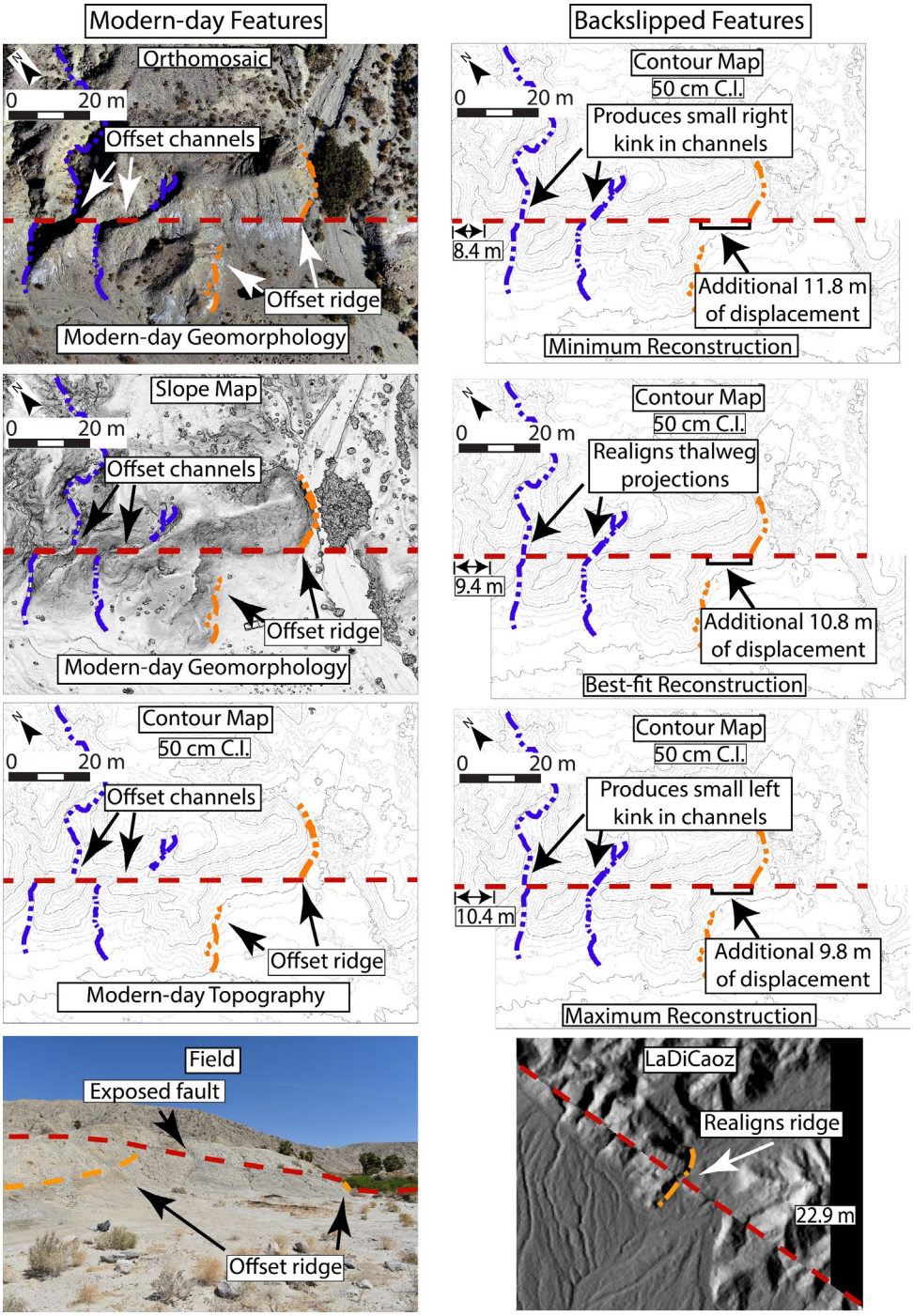

Figure 9. The series of images on the left-hand side, from top to bottom, consist of modern-day geomorphology and topography of an orthomosaic surface map, slope surface map, contour surface map, and field photograph of offset features sSAF-115, 116, & 117 which display an offset ridge and offset channels, respectively. Dashed red lines represent the surficial fault trace and dashed blue lines represent channel thalwegs. The series of images on the right-hand side, from top to bottom, consist of a backslipped offsets with minimum, best-fit, and maximum displacement values produced with a contour surface map, and a backslipped hillshade surface map model of sSAF-117 generated in LaDiCaoz.

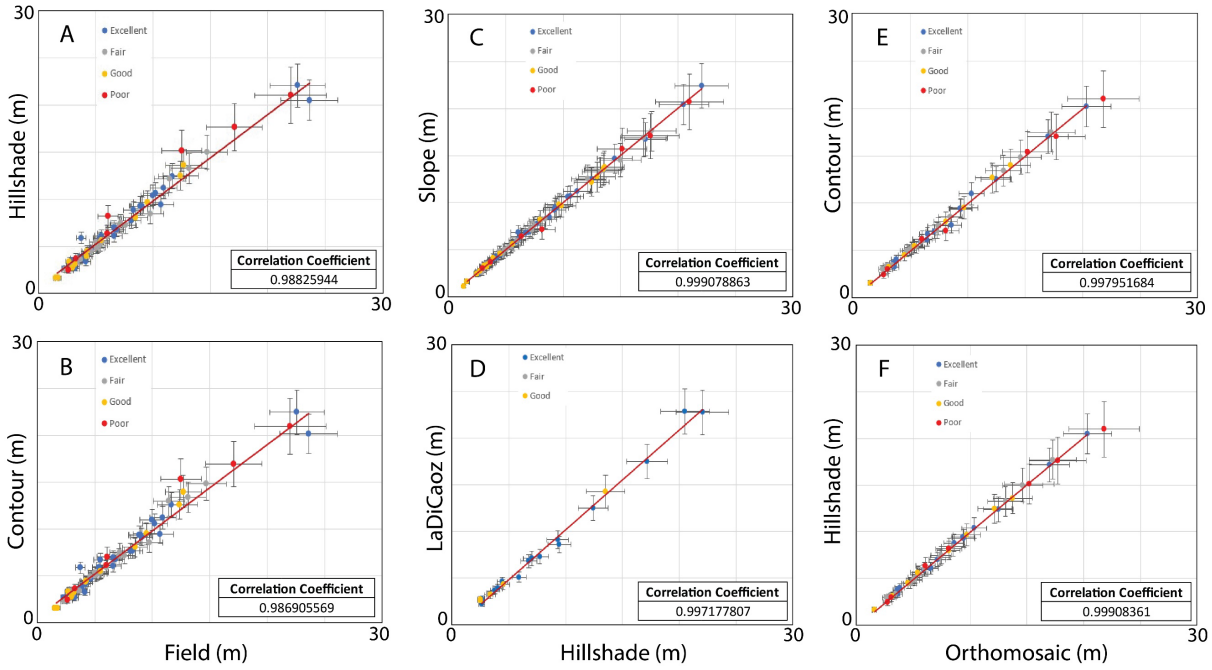

Figure 10. Linear correlations of the various measurement methods applied for offset features along the sSAF. Panels A and B correlate field measurements (x-axis) with hillshade and contour measurements (y-axis), respectively; Panels C and D correlate hillshade measurements (x-axis) with slope and LaDiCaoz measurements (y-axis), respectively; and Panels E and F correlate orthomosaic measurements (x-axis) with contour and hillshade measurements (y-axis), respectively. Only features with where both methods of measurements were used in each correlation and uncertainty values of 10-14% were assigned to each measurement based on the mean uncertainty values of features in each respective quality rating. The solid red line represents a 1:1 line, which exhibits a strong linear relationship between all measurement methods, with some variability. A Pearson's Correlation Coefficient was calculated and applied for each correlation. All methods exhibit a very high correlation of approximately 0.986 or greater.

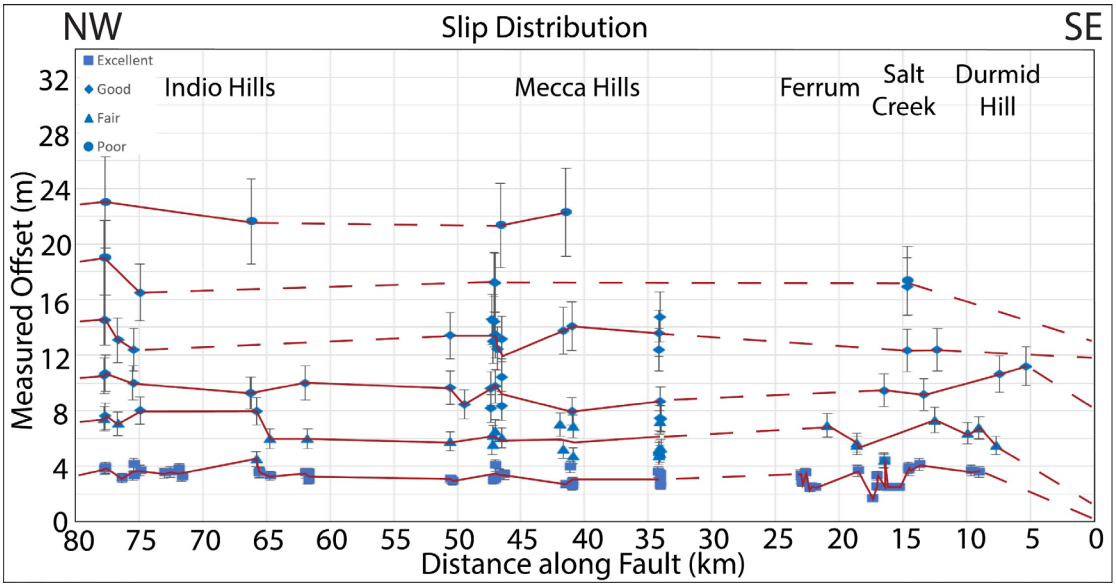

Figure 11. Distribution of offset features exhibiting lateral variability along ~80 km of the sSAF from Durmid Hill (right) to Indio Hills (left). Measured offset for each feature is represented on the y-axis and distance along the fault is represented on the x-axis. Data points represent displacement measurements from offset features ranging from excellent, good, fair, and poor quality and trendlines (red) represent average values for slip-per-event. Uncertainty values of 10-14% were assigned to each measurement based on the mean uncertainty values of features in each respective quality rating.

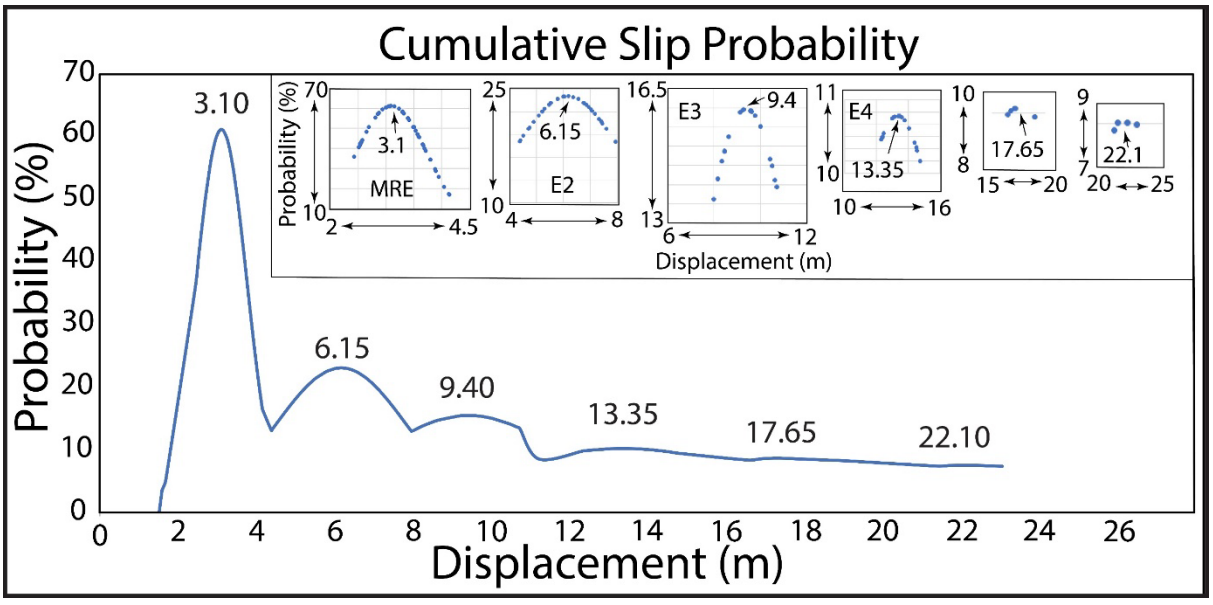

Figure 12. Gaussian distribution for average offset measurements used in analysis of co-seismic offsets. Six peaks shown in the data represent the probability of cumulative displacement for each consecutive event beginning with the MRE (left-most peak). Probability is represented on the y-axis and cumulative displacement is represented on the x-axis. Inset figures exhibit individual data point curves for each respective peak.

Geomorphology 357 (2020) 107064

Contents lists available at ScienceDirect

Geomorphology

journal homepage: www.elsevier.com/locate/geomorph

Refining the spatial and temporal signatures of creep and co-seismic slip along the southern San Andreas Fault using very high resolution UAS imagery and SfM-derived topography, Coachella Valley, California

Chelsea M. Blanton [a,b,*], Thomas K. Rockwell [a], Allen Gontz [a], Joshua T. Kelly [a,c]

[a] Department of Geological Sciences, San Diego State University, San Diego, CA, 92182, USA
[b] Lettis Consultants International, Inc., 27441 Tourney Road, Suite 220 Valencia, CA 91355, USA
[c] Institute of Geophysics and Planetary Physics, Scripps Institution of Oceanography, University of California San Diego, 9500 Gilman Drive, La Jolla, CA 92093, USA

ARTICLE INFO

Article history:
Received 21 July 2019
Received in revised form 28 January 2020
Accepted 31 January 2020
Available online 13 February 2020

Keywords:
Paleoseismology
Tectonic geomorphology
El Niño Southern Oscillation (ENSO)
Photogrammetry

ABSTRACT

The current interseismic period for an event on the Coachella Valley segment of the San Andreas Fault (SAF) is ~300 years, much greater than the best-estimated average recurrence interval of ~180 years, prompting questions regarding earthquake recurrence and fault behavior. Digital Surface Models (DSMs) generated using Structure-from-Motion-Multiview Stereo (SfM-MVS) techniques on unmanned aerial systems (UAS) imagery and very-high resolution UAS orthomosaics were used to identify and measure fault-related offsets of small geomorphic features and develop a model of late Holocene slip-per-event for the southern SAF (sSAF) in the Coachella Valley. We aim to better constrain slip estimates from recent earthquakes along the sSAF and combine new slip data with ages of past earthquakes from paleoseismic studies to understand earthquake recurrence. Slip-per-event for paleoearthquakes, which ruptured this segment of the sSAF, and the relationship between co-seismic slip events, creep or afterslip, and triggered slip were evaluated. Examination of offsets suggests that five (5) large, surface rupturing events produced average displacements of 2.6–3.1 m per event. Gaussian distribution analysis revealed small-scale offset clusters that we attribute to climate-modulated channel incision across the fault and subsequent creep. These offset clusters support a creep rate of ~3 mm/yr in the Mecca Hills averaged over the past ~160 years.

© 2020 Elsevier B.V. All rights reserved.

1. Introduction

1.1. Earthquake recurrence

The Coachella Valley segment of the San Andreas Fault (SAF) in the Salton Trough (Fig. 1) has been the subject of many paleoseismic studies (e.g. Fumal, 2002; Philibosian et al., 2011; Rockwell et al., 2018; Sieh and Williams, 1990). Average recurrence intervals for paleoearthquakes rupturing the Coachella Valley range from 116 to 240 years with a best estimate of 180 years (Philibosian et al., 2011), leaving the current open interval of ~300 years curiously long. Rockwell et al. (2018) re-evaluated the timing of the most recent and penultimate events on the southern San Andreas Fault (sSAF), supporting an average recurrence interval of about 180 years, but this average recurrence interval is biased by the open interval of about 300 years. The current approximately 300-year-long period of quiescence could be a deviation from the normal behavior of shorter intervals and more frequent events, or it could reflect a lower rate of elastic loading (van der Woerd et al., 2006). The extended period of dormancy has led some to speculate that an abnormally large amount of elastic strain has accumulated along the sSAF segment (Fialko, 2006; Philibosian et al., 2011), which provokes questions concerning earthquake recurrence models. If the average interseismic period is 180 years and the current open interval is ~300 years, is it possible that earthquakes follow a quasi-periodic recurrence model with a relatively high coefficient of variation? Is it more likely that this long open interval is producing a buildup of elastic strain energy that will result in an unusually large (infrequent) earthquake in terms of magnitude-frequency distributions? This is a complex relationship that warrants further exploration.

1.2. Creep rate

The sSAF in the Coachella Valley is known to creep at rates that vary between 1 and 4 mm/yr (Bilham, 2019; Lindsey et al., 2014; Sieh and Williams, 1990). Sieh and Williams (1990) calculated an average creep rate of 3.4 ± 0.7 mm/yr at Indio for the past 300 years and a creep rate of only 1.9 ± 0.2 mm/yr for an ~81 year period from ~1906 to 1987 at Salt Creek (Fig. 1). Creep rates near Indio and the Salton Sea have

* Corresponding author at: Lettis Consultants International, Inc., 27441 Tourney Road, Suite 220 Valencia, CA 91355, USA.
E-mail address: blanton@lettisci.com (C.M. Blanton).

https://doi.org/10.1016/j.geomorph.2020.107064
0169-555X/© 2020 Elsevier B.V. All rights reserved.

persisted for at least the past three centuries, suggesting that this is a long-term characteristic of the Coachella Valley segment of the SAF (Sieh and Williams, 1990). Estimated creep rates from Envisat interferometric synthetic aperture radar (InSAR) observations agree with these estimates and imply a pattern of fluctuating localized and distributed creep along the sSAF (Lindsey et al., 2014). Creep was found to be highly localized in the Mecca Hills (Lindsey et al., 2014), with a local creep rate of about 3 mm/yr. Additional corroboration of these rates comes from values based on slip from 2003 to 2007 recorded at creepmeters on the SAF in southern California, which show localized creep rates in the Coachella Valley are 2 ± 1 mm/yr (Bilham, 2019) for that short period of time.

1.3. Triggered slip

Triggered slip resulting from activity on other fault segments has resulted in measurable displacement in the central Salton Trough at least eight times in the past ~50 years (Rymer et al., 2011). Most notably, triggered slip associated with the **M**6.5 1968 Borrego Mountain, **M**6.6 1979 Imperial Valley, **M**6 1986 North Palm Springs, **M**7.3 1992 Landers, **M**7.1 1999 Hector Mine, and **M**7.2 2010 El Mayor-Cucapah earthquakes (Fig. 1) have been documented along this reach of the SAF (Allen et al., 1972; Clark, 1984; Williams et al., 1988; Rymer, 2000; Rymer et al., 2002; Rymer et al., 2011; Wei et al., 2011). Lateral slip of 10–25 mm was measured on the sSAF as a result of the 1968 Borrego Mountain earthquake (Allen et al., 1972). Clark (1984) documented cracks with up to 5 mm width following the 1979 Imperial Valley earthquake. In the Mecca Hills, surface cracks appeared with maximum dextral displacement of 2–3 mm as a response to the 1986 North Palm Springs earthquake (Williams et al., 1988). Measured slip associated with the 1992 Landers earthquake in the Coachella Valley was 1–6 mm (Rymer, 2000). The 1999 Hector Mine earthquake produced 1–13 mm of dextral slip along the southern San Andreas, Superstition Hills, and Imperial faults (Rymer et al., 2002). Additionally, slip due to the 2010 El Mayor-Cucapah earthquake was measured to be about 3.5 mm at the Salt Creek creepmeter and 3.2 mm at the Ferrum creepmeter (Rymer et al., 2011; Fig. 1). Data from InSAR, field measurements, and creepmeters in a study by Wei et al. (2011) yielded an even larger slip triggered by the main shock of the 2010 El Mayor-Cucapah earthquake, with the SAF in the Mecca Hills experiencing up to about 45 mm of horizontal displacement. More recently, the sSAF experienced a sequence of creep events as a response to the 2017 Chiapas earthquake (Tymofyeyeva et al., 2019). Long-term creep is assumed to incorporate episodic triggered slip during interseismic periods, so triggered slip is considered part of the creep rate. The previously noted slip from past earthquakes results in as much as ~100 mm of triggered slip in the Salton Trough. Consequently, we recognize that approximately 49% to 97% of the observed creep along the sSAF is the result of triggered slip based on the InSAR creep rate of 3 ± 1 mm/yr (or 65% based on a 3 mm/yr creep rate) over the past 50-year period. This percentage is likely only a minimum value because every event which produced measurable lateral slip may not have been observed and thus, recorded.

1.4. Geomorphic indicators of slip: rill formation

We use small geomorphic features to measure recent fault offsets as a means for collecting slip data. Offsets as small as 1 to 2 m for the most

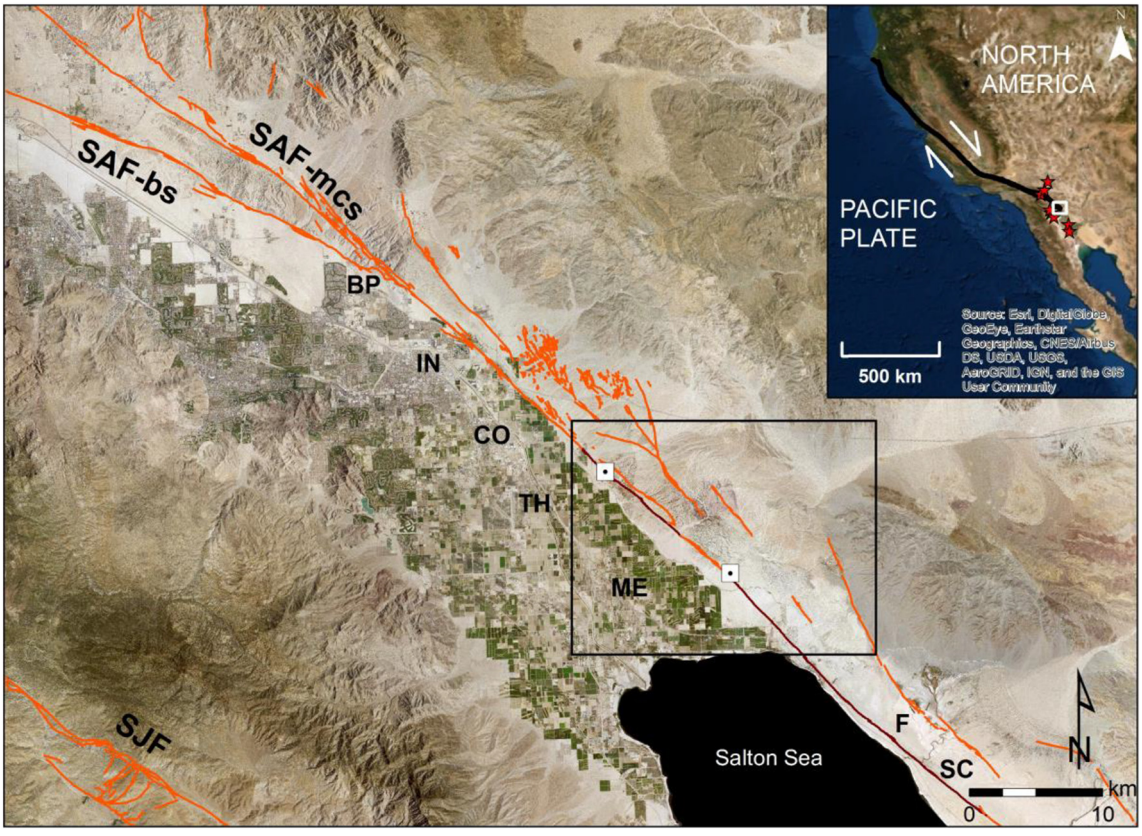

Fig. 1. Map of site locations with sites represented by squares. The black box denotes the extent of the geologic map in Fig. 2. The top right inset map displays the regional area of interest along the Coachella Valley segment in southern California, the southernmost segment of the San Andreas Fault. Stars represent the epicenters of previous earthquakes in 1942, 1954, 1968, 1979, 1986, 1992, 1999, and 2010. The Open Pit Mine is the site to the northwest and Box Canyon is ~12 km southeast from the mine. The faults presented here are historically active (dark solid line) and latest Quaternary (light solid line) from the U.S. Geological Survey and California Geological Survey fault and fold database for the United States (USGS and CGS, 2018). Abbreviations: SAF-mcs – Mission Creek strand of the San Andreas Fault, SAF-bs – Banning strand of the San Andreas Fault, SJF – San Jacinto fault, BP – Biskra Palms, IN – Indio, CO – Coachella, TH – Thermal, ME – Mecca Hills, F – Ferrum, SC – Salt Creek.
Source imagery: NAIP 2016.

recent earthquake are expected, with larger offsets for earlier events. In coastal central California, El Niño-Southern Oscillation (ENSO) events are associated with unusually high precipitation within approximately 100 km of the coast (Cayan et al., 1999). Extreme precipitation associated with these climatic events periodically affect the Mecca Hills and form recognizable geomorphic features, such as channels and rills. As the sSAF in the Coachella Valley is known to creep (Bilham, 2019; Lindsey et al., 2014; Sieh and Williams, 1990), we will also investigate potential offsets less than 1 m that may have formed following rill formation. Significant precipitation events would have incised rills and channels across the fault, producing small offsets as the fault crept, so it is imperative that we are able to collect slip measurements at this resolution and finer. Channels offset along faults are used as markers to measure displacements in consecutive earthquakes and to deduce earthquake recurrence based, in part, on the assumption that channels form more frequently than they are offset by earthquakes (Ludwig et al., 2010). This supposed high occurrence of large precipitation events would suggest that there are discrete, notable events that occur at decadal scales that are expected to produce geomorphic signals. Our evaluation of historic, extreme precipitation events in the Coachella Valley, and their relationship to ENSO events, will be an integral part of our discussion concerning the spatial and temporal signatures of creep in our study areas along the sSAF.

1.5. Photo-based 3D reconstruction

Structure-from-Motion (SfM) methods enable the reconstruction of 3D geometries from a collection of overlapping 2D photographs at a range of scales. Traditional photogrammetric methods require the 3D location and pose of the camera or the 3D location of many ground control points (GCPs). SfM solves this problem with automatic identification of matching features in multiple images, so that photos from many angles and distances can be used with no prior knowledge of locations (Nissen et al., 2016; Westoby et al., 2012). SfM generates a 3D geometry (sparse point cloud) from a set of photographs, and the Multi-View Stereo (MVS) process produces a dense point cloud used to derive digital surface models (DSMs) and orthoimagery. Unmanned Aircraft System (UAS)-based approaches permit the collection of imagery with mm- to cm-scale resolution, depending on camera parameters and distance above ground (Table 1), compared to 10–50 cm/pixel resolution with manned aircraft and upwards of 30 m for satellites (Bemis et al., 2014), resulting in very-high resolution orthoimagery and DSMs. UAS flights at altitudes of 30–40 m produced very-high resolution orthoimagery of ~10 mm/pixel in a study by Bemis et al. (2014) using UAS-based SfM-MVS as a mapping tool for structural geology and paleoseismology. Other studies utilizing SfM achieved sub-meter to decimeter resolution (Javernick et al., 2014; Westoby et al., 2012). In addition to photo-based 3D reconstruction, airborne LiDAR has been used to study geomorphic offset features with success (Zielke et al., 2010). However, in a study comparing the SfM-constructed topography of a site along the SAF with the B4 airborne LiDAR survey, the SfM-DEM (3-cm resolution) revealed geomorphic offsets that were not clearly imaged with LiDAR due to its lower resolution of 0.5 m and pixelated appearance. (Johnson et al., 2014). They presented one of the first inquiries of SfM as a means for mapping fault zone topography in areas of sparse vegetation at two fault sites in southern California and concluded that SfM methodologies more effectively captured subtle geomorphic offsets due to paleoearthquakes. Furthermore, Bemis et al. (2014) recommend UAS-based photogrammetry as a mapping tool for neotectonics applications, particularly as a means for identifying and measuring offset geomorphic features following major surface-rupturing events.

1.6. Earthquake recurrence models

A large earthquake on the sSAF could have disastrous effects on the population of southern California (Fig. 1); thus, understanding the past behavior of this fault is critical to estimating the likelihood and size of a near-future event. Our goal is to understand whether there is a relationship between the timing of large earthquakes and the amount of displacement that occurs in each event. Is there a correlation between the amount of time since an earthquake and the amount of slip that occurs in the next event, evidence for a slip-predictable earthquake model? Can the size of future earthquakes be forecasted by resolving slip and timing of past events? We explore these questions by evaluating earthquake recurrence models. Schwartz and Coppersmith (1984) suggest a characteristic earthquake model to explain the behavior of the Wasatch and San Andreas faults. Decades later, Weldon et al. (2004), investigated the relationship between recurrence interval and displacement at sites near Wrightwood, California, and found no support for slip-predictability and insufficient evidence to suggest time-predictability. We will test if the slip-predictable earthquake recurrence model characterizes earthquake behavior at our sites by developing a model of slip-per-event from young geomorphic offsets.

2. Regional setting

2.1. Geologic background

The Mecca Hills are located within Coachella Valley in the Salton Trough of southern California, southeast of Indio and northwest of Salt Creek (Fig. 1). They are composed of pre-Cenozoic crystalline and schistose basement rocks overlain by late Cenozoic and Quaternary nonmarine sedimentary rocks, locally covered by a thin layer of late Quaternary alluvial deposits (Sylvester and Smith, 1976; Fig. 2). Localized uplift has occurred as a result of transpressional deformation associated

Table 1
A) Flight parameters and B) Camera details of the 9 flights evaluated for this study. Altitude or height above ground level (AGL) is from takeoff. UAS = unmanned aerial system, GSD = ground sampling distance.

A) Flight parameters

Flight	Height AGL (m)	Date of flight(s)	UAS	Total coverage area (m^2)	Speed (m/s)	GSD (mm/pix)
Box Canyon 1–4	30	2/23/2018	M600 Pro[a]	92,100	Unknown	7.38
Open Pit Mine 1	30	5/23/2018	DJI P4P	34,500	3	9.25
Open Pit Mine 2	25	5/23/2018	DJI P4P	43,500	3	7.71
Open Pit Mine 4	30	10/6/2018	DJI P4P	39,000	3	9.25
Open Pit Mine 5	30	10/6/2018	DJI P4P	50,200	3	9.25
Open Pit Mine 6	25	10/7/2018	DJI P4P	30,700	3	7.71

B) Camera details

Site	Camera model	Resolution	Focal length	Pixel size	Sensor width
Box Canyon	ILCE-6000	6000 × 4000	16 mm	4 × 4 μm	23.6 mm
Open Pit Mine	FC6310	4864 × 3648	8.8 mm	2.61 × 2.61 μm	13.2 mm

[a] The M600 Pro equipment was on loan from Geodetics Inc., San Diego, along with their pilot, who conducted all flight operations involving the M600.

with late Quaternary motion on the SAF (Sylvester and Damte, 1999). The Mecca Hills are cut by three major faults: the San Andreas, Painted Canyon and Skeleton Canyon faults (Sylvester and Damte, 1999; Fig. 2). The Coachella Valley segment of the SAF splits into the Mission Creek and Banning strands (Fig. 1) northwest of Interstate 10, where it crosses the fault (Fattaruso et al., 2014). This segment is characterized by northwest-trending high-angle faults dipping 60°–70° to the northeast (Fattaruso et al., 2014) and west-northwest trending, locally overturned en-echelon folds (Sylvester and Smith, 1976). At Painted Canyon the active trace of the SAF splits into multiple strands, which coalesce back to the principal strand near Box Canyon (Fig. 2). Additionally, the active main trace of the SAF is marked by many classical geomorphic features indicative of strike-slip faulting, including deflected and beheaded stream channels, side-hill benches, shutter ridges, sag depressions, and fault scarps (Rymer, 2000; Shifflett et al., 2002; van der Woerd et al., 2006; Behr et al., 2010).

2.2. Study sites

The first site is near Mecca, California, in Box Canyon approximately 1 km southeast of Box Canyon Road and about 0.5 km northwest of the Coachella Canal (Figs. 1 and 2). Dingler et al. (2016) collected a comprehensive 3D dataset using terrestrial laser scanning, and Shifflett et al. (2002) measured gully offsets and identified an offset Native American "fire ring" at this location. Our second site is near Thermal, California and is <0.5 km southeast of Thermal Canyon within the property of an open pit mine operated by West Coast Sand and Gravel, Inc. (Figs. 1 and 2). The mine is approximately 12 km northwest of Box Canyon. Going forward, site one will be called Box Canyon and site two will be referred to as the Open Pit Mine. Both sites have many defendable offset features and were chosen because Box Canyon is directly southeast of where the active trace of the SAF potentially splays into multiple strands, whereas the Open Pit Mine is northwest of where most or all slip has converged back onto the main strand of the SAF, so offset geomorphic features are more likely to represent slip in past earthquakes.

3. Approaches and methods

3.1. Data collection

Initial work consisted of locating sites via Google Earth imagery with clearly observable rill features in the landscape, which could then be assessed in the field. Nine fault sections were evaluated during site visits and those areas that exhibited steep slopes, well-preserved geomorphic offsets, and accessibility with an off-road vehicle were selected for survey. Real-Time Kinematic (RTK) GPS and UAS surveys were conducted at each site, as were collection of field measurements of offset rills and channels with a standard metric tape measure.

At Box Canyon, ground control points (GCPs) were placed at four corners of the area of interest prior to the UAS surveys. GCPs are points on the ground surface of known location used to geo-reference imagery. Two additional GCPs were manually added later using GPS coordinates extracted from WorldView-2 satellite imagery for the central points of two archeological stone rings, approximately 1.5 and 2 m in diameter. The stone ring GCPs help to diminish warping effects during Digital Surface Model (DSM) generation. The geolocation accuracy of WorldView-2 is reported to be 3.5 m in the horizontal axis and 3.6 m in the vertical (DigitalGlobe, 2018), although these values are significantly improved

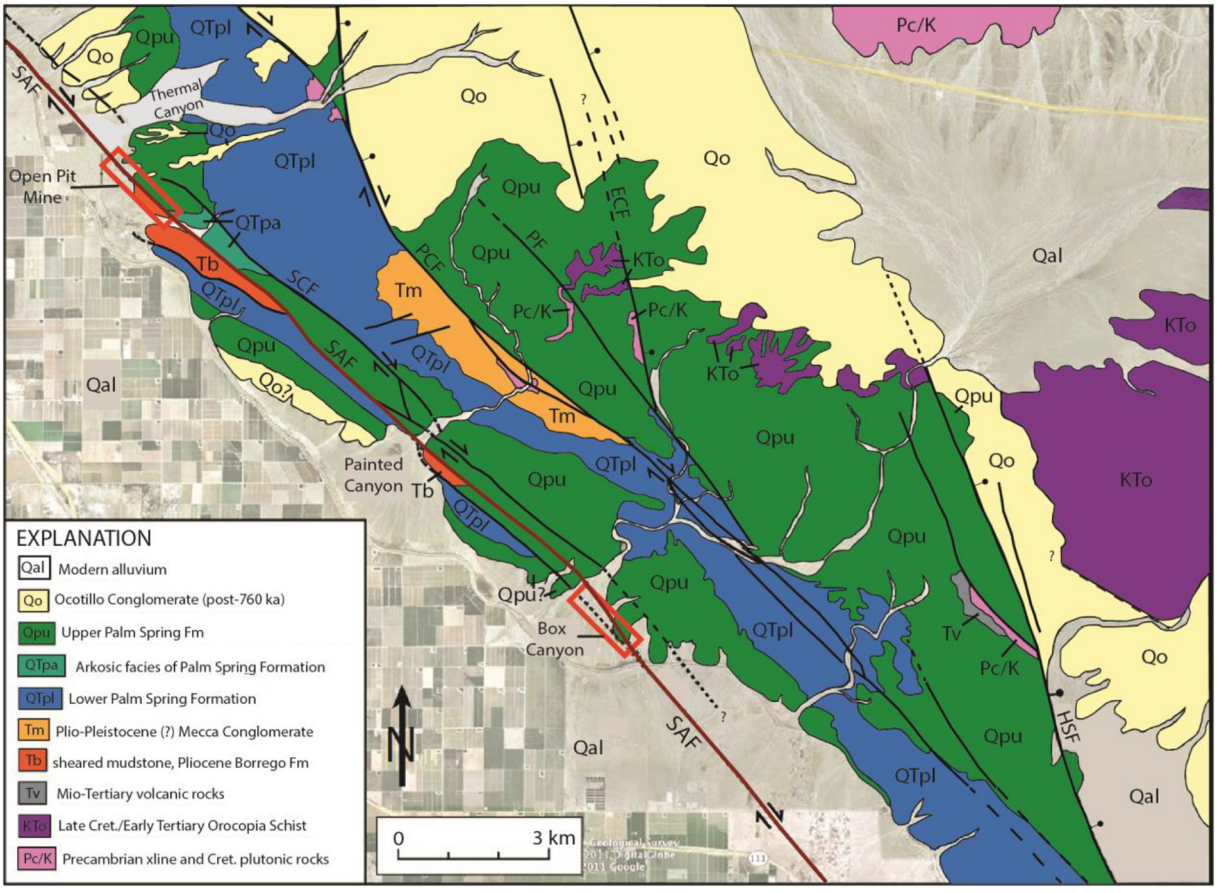

Fig. 2. Regional geology of the Mecca Hills. Abbreviations: ECF—Eagle Canyon fault; HSF—Hidden Springs fault; PCF—Painted Canyon fault; PF—Platform fault; SAF—San Andreas Fault (red); SCF—Skeleton Canyon fault. Rectangles indicate the surveyed fault sections in this study at the Open Pit Mine and Box Canyon. (For interpretation of the references to color in this figure legend, the reader is referred to the web version of this article.)
Modified from Fattaruso et al. (2014).

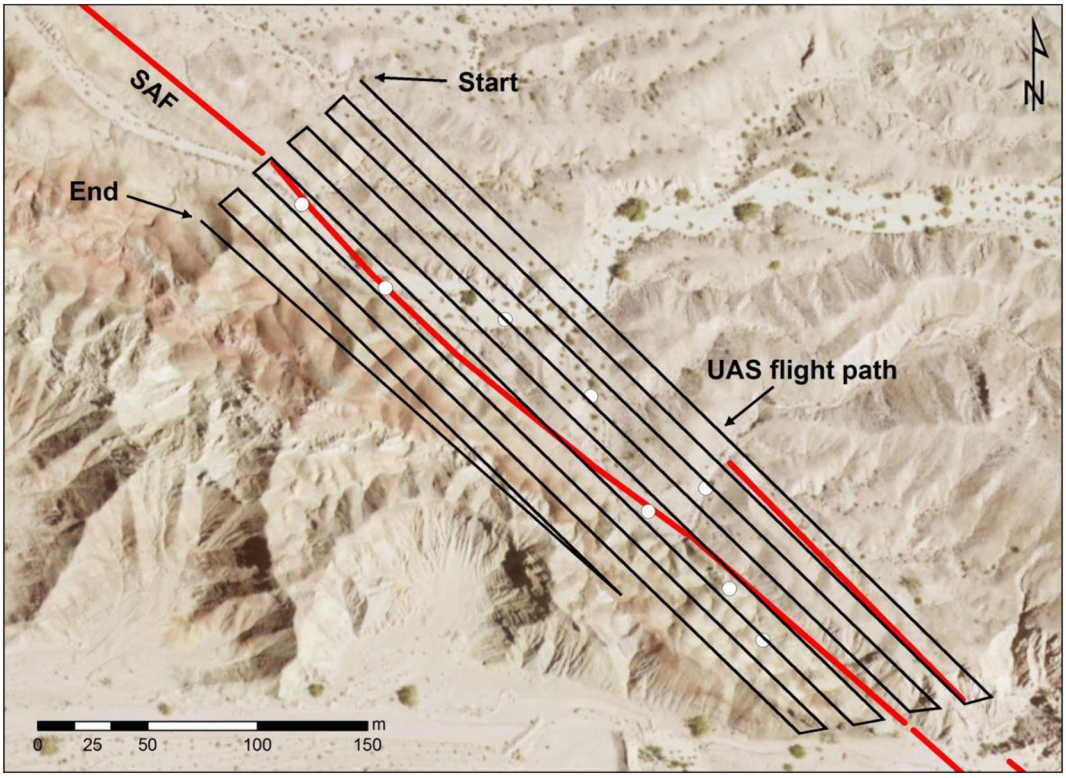

Fig. 3. Flight path for the second flight in the Open Pit Mine flown at 25 m above ground level (AGL) at takeoff with a coverage area of 43,500 m^2. Flight parameters provided in Table 1A. White circles are ground control point (GCP) locations used to increase the accuracy of camera positions. SAF – San Andreas Fault; UAS – unmanned aerial system.
Source imagery: NAIP 2016.

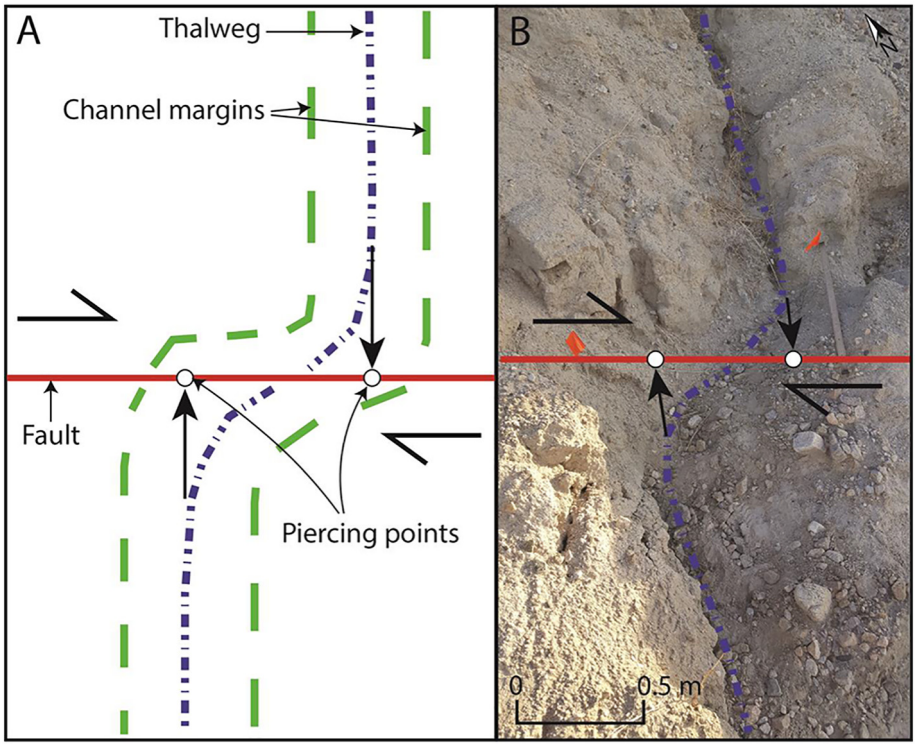

Fig. 4. A) Map view of a generalized offset channel schematic measuring the displacement of the channel thalwegs. Landform elements are projected to the fault trace and the points where the projected elements intersect the fault are inferred to be the piercing points. The estimated offset is the horizontal distance along the fault trace between the piercing points. The measurement projections (black arrows linking the thalwegs to the fault trace) in the schematic represent the ideal measurement. Slip vectors show dextral sense of motion. B) Field photograph and measurement using the method shown in A.
A, modified from Salisbury et al. (2015).

Table 2a
Box Canyon measurements and their associated uncertainty including the feature measured. An uncertainty of 10–30% has been assigned to each measurement, depending on erosion and feature quality. For quality rating (Q rating) 1–4 correspond to poor, fair, good, or excellent features. SE CM – southeast channel margin, NW CM – northwest channel margin, T – channel thalweg, Ortho – orthomosaic, HS – hillshade, Recon – best-estimated reconstruction.

Site	GPS location	Q rating	Field	±	Feature	Ortho	±	HS 315	±	Slope	±	Contour	±	HS 135	±	Recon	±	1 or 2 strands
BC_17	−115.981214 33.572312	4	4.15	0.62	SE CM	3.62	0.54	3.33	0.50	3.51	0.53	3.25	0.49	3.66	0.55	3.80	0.38	1
BC_15	−115.980710 33.571910	3	4.60	0.46	T	4.70	0.47	4.44	0.44	4.79	0.48	4.98	0.50	4.90	0.49	4.70	0.47	1
BC_15a	−115.980710 33.571910	3	5.20	0.52	T	5.12	0.51	4.89	0.49	5.01	0.50	5.19	0.52	4.92	0.49	4.70	0.47	1
BC_15b	−115.980710 33.571910	2	12.40	1.24	T	12.15	1.22	12.47	1.25	12.20	1.22	12.65	1.27	12.56	1.26	13.50	1.35	1
BC_15c	−115.980710 33.571910	2	12.70	1.27	T	13.74	1.37	13.60	1.36	13.80	1.38	14.00	1.40	13.46	1.35	13.50	1.35	1
BC_13	−115.980476 33.571691	3	5.40	0.54	T	5.15	0.52	5.11	0.51	5.08	0.51	5.30	0.53	5.04	0.50	5.40	0.54	1
BC_12	−115.980419 33.571644	3	7.20	0.72	T	7.44	0.74	7.48	0.75	7.58	0.76	7.57	0.76	7.65	0.77	7.30	1.10	2
BC_12a	−115.980419 33.571644	3	14.70	1.47	T	14.62	1.46	14.98	1.50	14.53	1.45	14.85	1.49	15.30	1.53	14.70	1.47	2
BC_11	−115.980337 33.571578	3	3.10	0.47	SE CM	2.58	0.39	2.94	0.44	2.62	0.39	3.04	0.46	3.00	0.45	3.00	0.45	2
BC_11a	−115.980337 33.571578	3	7.10	1.00	T	7.33	1.00	7.26	1.00	7.05	1.00	7.10	1.00	7.01	1.00	7.40	1.11	2
BC_09	−115.980288 33.571528	3	5.10	0.51	T	4.96	0.50	4.80	0.48	4.63	0.46	5.00	0.50	5.13	0.51	5.20	0.78	2
BC_07	−115.979984 33.571280	2	9.75	1.46	T	8.49	1.27	8.42	1.26	8.24	1.24	8.58	1.29	8.53	1.28	11.60	1.16	2
BC_07a	−115.979984 33.571280	3	3.20	0.32	SE CM	3.16	0.32	3.14	0.31	3.30	0.33	3.24	0.32	3.20	0.32	3.40	0.51	2
BC_01	−115.979969 33.571268	3	0.23	0.07	T	0.29	0.09	0.36	0.11	0.33	0.10	0.25	0.08	0.36	0.11	–	–	2
BC_00	−115.979926 33.571225	2	2.00	0.20	T	2.06	0.21	2.10	0.21	1.96	0.20	2.17	0.22	2.11	0.21	2.50	0.63	2
BC_06	−115.979810 33.571137	1	0.53	0.08	T	0.61	0.09	0.74	0.11	0.67	0.10	0.55	0.08	0.78	0.12	0.51	0.10	2
BC_05	−115.979781 33.571114	2	0.65	0.10	SE CM	0.54	0.08	0.63	0.09	0.73	0.11	0.51	0.08	0.54	0.08	0.50	0.10	2
BC_05a	−115.979781 33.571114	2	0.52	0.08	NW CM	0.56	0.08	0.60	0.09	0.64	0.10	0.68	0.10	0.58	0.09	–	–	2
BC_04	−115.979608 33.570947	1	7.90	1.00	T	8.12	1.00	8.16	1.00	7.15	1.00	7.09	1.00	7.69	1.00	6.05	0.61	2
BC_16	−115.979546 33.570881	2	0.50	0.08	NW CM	0.67	0.10	0.64	0.10	0.66	0.10	0.48	0.07	–	–	–	–	2
BC_02	−115.979472 33.570822	1	0.50	0.08	T	0.39	0.06	0.41	0.06	0.35	0.05	0.58	0.09	0.30	0.05	0.52	0.16	2
BC_02a	−115.979472 33.570822	1	0.41	0.06	SE CM	0.43	0.06	0.39	0.06	0.36	0.05	0.47	0.07	–	–	–	–	2
BC_03[a]	−115.979804 33.571044	2	5.05	0.51	T	5.56	0.56	5.46	0.55	5.31	0.53	5.36	0.54	5.54	0.55	6.40	0.64	2
BC_08[a]	−115.979962 33.571187	1	2.65	0.27	T	2.70	0.27	2.46	0.25	–	–	2.45	0.25	2.40	0.24	–	–	2

[a] Offsets BC_03 and BC_08 are on a local second strand of the fault, not the main trace. BC_12a represents maximum slip and is used to estimate slip rate at Box Canyon.

in North America with RMS errors reaching 1.8 m in X and 1.6 m in Y (Cheng and Chaapel, 2010). As such, GCPs derived from WorldView-2 imagery are suitable for improving DSM generation. For the Open Pit Mine, GCPs were placed along the fault on either side of the fault trace to ensure highest accuracy along the fault (Fig. 3). GPS data were collected with an EMLID Reach RS RTK GPS (EMLID, 2020) for each GCP. Rover and base stations were setup in RTK mode with a correction link over Lo-Ra (Long Range) radio. The average single position base setup method was implemented to obtain base station coordinates with approximately 2.5 m position accuracy, which is sufficient for this study as absolute accuracy is not required, only relative accuracy. The fix status was used during survey point collection, which provides cm-level precision between the relative positions of the rover to the base station. For all base setup methods, the relative position of the rover will be cm-precise while using the fix status to collect GCPs; however, the actual accuracy will be determined by the accuracy of the base station position. Therefore, methods with longer observation times, 15 min to 4 h compared to 5 min, were deemed unnecessary.

Approximately 300,000 m^2 of UAS imagery, consisting of over 3200 images, was collected coverings ~3 km of the sSAF with continuous fault sections of ~1.7 km at the Open Pit Mine and ~1.3 km at Box Canyon (Fig. 2) with an average swath width of 95 m. Two UASs were utilized

Table 2b
Open Pit Mine, flights 4 and 5, measurements and their associated uncertainty including the feature measured. An uncertainty of 10–30% has been assigned to each measurement, depending on erosion and feature quality. For quality rating (Q rating) 1–4 correspond to poor, fair, good, or excellent features. SE CM – southeast channel margin, NW CM – northwest channel margin, T – channel thalweg, Ortho – orthomosaic, HS – hillshade, Recon – best-estimated reconstruction.

Site	GPS location	Q rating	Field	±	Feature	Ortho	±	HS 315	±	Slope	±	Contour	±	HS 135	±	Recon	±	1 or 2 strands
MH_OPM5_01	−116.084961 33.652976	1	0.52	0.08	T	–	–	–	–	–	–	–	–	–	–	–	–	1
MH_OPM5_01a	−116.084961 33.652976	1	0.46	0.07	NW CM	–	–	–	–	–	–	–	–	–	–	–	–	1
MH_OPM5_02	−116.084888 33.652923	1	0.15	0.05	NW CM	–	–	0.14	0.04	–	–	0.15	0.05	0.17	0.05	–	–	1
MH_OPM5_02a	−116.084888 33.652923	1	0.17	0.05	SE CM	–	–	0.15	0.05	–	–	0.16	0.05	0.17	0.05	–	–	1
MH_OPM5_03	−116.084456 33.652515	3	9.50	0.95	T	9.70	0.97	9.65	0.97	9.76	0.98	9.52	0.95	9.90	0.99	9.10	1.37	1
MH_OPM5_03a	−116.084456 33.652515	3	8.00	0.80	SE CM	8.10	0.81	8.00	0.80	8.17	0.82	8.08	0.81	8.40	0.84	–	–	1
MH_OPM5_04	−116.084210 33.652274	2	0.53	0.08	T	0.50	0.08	0.51	0.08	0.48	0.07	0.45	0.07	0.59	0.09	–	–	1
MH_OPM5_05	−116.084017 33.652146	3	0.60	0.09	T	0.61	0.09	0.56	0.08	0.56	0.08	0.55	0.08	0.61	0.09	–	–	1
MH_OPM5_06	−116.084002 33.652161	3	0.55	0.08	T	0.55	0.08	0.56	0.08	0.51	0.08	0.55	0.08	0.61	0.09	–	–	1
MH_OPM5_06a	−116.084002 33.652161	3	0.61	0.09	SE CM	0.59	0.09	0.56	0.08	0.58	0.09	0.62	0.09	0.67	0.10	–	–	1
MH_OPM5_07	−116.083887 33.652046	2	0.40	0.06	SE CM	0.47	0.07	0.47	0.07	0.40	0.06	0.42	0.06	0.52	0.08	–	–	1
MH_OPM5_07a	−116.083887 33.652046	2	0.55	0.08	T	0.62	0.09	0.85	0.13	0.66	0.10	0.50	0.08	0.87	0.13	–	–	1
MH_OPM5_08	−116.083867 33.652024	3	0.56	0.08	T	0.55	0.08	0.60	0.09	–	–	0.60	0.09	0.63	0.09	–	–	1
MH_OPM5_09	−116.083766 33.651952	2	0.51	0.08	T	0.51	0.08	0.54	0.08	0.56	0.08	0.50	0.08	0.57	0.09	–	–	1
MH_OPM5_10	−116.083735 33.651930	2	0.57	0.09	T	0.56	0.08	0.60	0.09	0.53	0.08	0.55	0.08	0.57	0.09	–	–	1
MH_OPM5_11	−116.083533 33.651745	3	5.52	0.55	SE CM	5.40	0.54	5.60	0.56	5.58	0.56	5.50	0.55	6.00	0.60	5.65	0.85	1
MH_OPM5_12	−116.083456 33.651677	1	0.86	0.13	T	0.88	0.13	0.89	0.13	0.83	0.12	0.85	0.13	0.84	0.13	–	–	1
MH_OPM5_13	−116.083356 33.651613	2	0.49	0.07	T	0.52	0.08	0.47	0.07	0.55	0.08	0.50	0.08	0.61	0.09	–	–	1
MH_OPM5_14	−116.083265 33.651544	3	0.38	0.06	SE CM	0.39	0.06	0.43	0.06	0.40	0.06	0.43	0.06	0.49	0.07	–	–	1
MH_OPM5_15a	−116.083243 33.651520	1	–	–	T	3.02	0.45	2.95	0.44	3.00	0.45	3.03	0.45	3.15	0.47	2.65	0.53	1
MH_OPM5_15b	−116.083243 33.651520	1	6.00	0.60	T	6.05	0.61	6.36	0.64	6.40	0.64	6.20	0.62	6.48	0.65	5.80	0.87	1
MH_OPM4_01a	−116.082528 33.650945	1	12.50	2.00	NW CM	15.20	2.00	15.13	2.00	15.70	2.00	15.39	2.00	15.42	2.00	–	–	1
MH_OPM4_01b	−116.082528 33.650945	1	17.10	2.00	SE CM	17.70	2.00	17.60	2.00	17.07	2.00	17.00	2.00	17.10	2.00	21.70	2.17	1
MH_OPM4_02	−116.082509 33.650968	3	2.80	0.42	T	3.00	0.45	3.10	0.47	3.30	0.50	3.40	0.51	3.51	0.53	2.85	0.43	1
MH_OPM4_03	−116.082039 33.650555	4	5.50	0.55	T	6.50	0.65	6.10	0.61	6.90	0.69	6.75	0.68	7.19	0.72	6.50	0.98	1

Table 2c
Open Pit Mine, flights 1 and 2, measurements and their uncertainty including the feature measured. An uncertainty of 10–30% has been assigned to each measurement, depending on erosion and feature quality. For quality rating (Q rating) 1–4 correspond to poor, fair, good, or excellent features. SE CM – southeast channel margin, NW CM – northwest channel margin, T – channel thalweg, Ortho – orthomosaic, HS – hillshade, Recon – best-estimated reconstruction. MH_OPM2_09 is used to estimate slip rate at the Open Pit Mine.

Site	GPS location	Q rating	Field	±	Feature	Ortho	±	HS 315	±	Slope	±	Contour	±	HS 135	±	Recon	±	1 or 2 strands
MH_OPM1_00	−116.081143 33.649813	2	0.25	0.08	T	0.30	0.09	0.33	0.10	0.35	0.11	0.28	0.08	–	–	–	–	1
MH_OPM1_01	−116.080764 33.649527	3	3.38	0.34	T	3.40	0.34	3.30	0.33	3.46	0.35	3.48	0.35	3.40	0.34	4.05	0.41	1
MH_OPM1_02	−116.079977 33.648890	3	0.44	0.07	T	0.51	0.08	0.55	0.08	0.53	0.08	0.50	0.08	0.49	0.07	–	–	1
MH_OPM1_03	−116.079952 33.648873	2	0.50	0.08	T	0.57	0.09	0.51	0.08	0.49	0.07	0.40	0.06	0.55	0.08	–	–	1
MH_OPM1_04	−116.079825 33.648758	1	0.17	0.05	T	0.16	0.05	0.15	0.05	–	–	0.15	0.05	–	–	–	–	1
MH_OPM1_05	−116.079811 33.648741	1	0.22	0.07	T	0.22	0.07	0.35	0.11	0.32	0.10	0.19	0.06	0.32	0.10	–	–	1
MH_OPM1_06	−116.079669 33.648648	3	0.24	0.07	T	0.33	0.10	0.33	0.10	0.29	0.09	0.22	0.07	0.32	0.10	–	–	1
MH_OPM1_06a	−116.079669 33.648648	2	0.68	0.10	T	0.52	0.08	0.68	0.10	0.66	0.10	0.65	0.10	0.67	0.10	–	–	1
MH_OPM2_01	−116.079370 33.648431	1	22.00	3.30	NW CM	21.79	3.27	21.00	3.15	20.70	3.11	21.00	3.15	21.90	3.29	19.70	2.96	1
MH_OPM2_02	−116.079010 33.648128	4	–	–	SE CM	85.60	8.56	86.00	8.60	84.80	8.48	86.70	8.67	88.10	8.81	84.00	8.40	1
MH_OPM2_03	−116.078657 33.647833	4	8.50	0.85	SE CM	8.58	0.86	8.80	0.88	8.52	0.85	7.66	0.77	8.42	0.84	8.10	0.81	1
MH_OPM2_04	−116.078341 33.647564	1	0.17	0.05	SE CM	0.26	0.08	0.25	0.08	0.28	0.08	0.20	0.06	0.36	0.11	–	–	1
MH_OPM2_04a	−116.078341 33.647564	1	0.22	0.07	gravel edge	0.26	0.08	–	–	–	–	–	–	–	–	–	–	1
MH_OPM2_05	−116.078157 33.647403	3	0.45	0.07	T	0.46	0.07	0.53	0.08	0.49	0.07	0.48	0.07	0.54	0.08	–	–	1
MH_OPM2_06	−116.078085 33.647357	2	0.24	0.07	T	0.22	0.07	0.20	0.06	0.23	0.07	0.25	0.08	0.21	0.06	0.17	0.07	1
MH_OPM2_07	−116.078020 33.647310	4	10.00	1.00	T	10.35	1.04	10.38	1.04	10.60	1.06	11.00	1.10	11.40	1.14	10.40	1.04	1
MH_OPM2_08	−116.077969 33.647280	2	0.54	0.08	T	0.52	0.08	0.57	0.09	0.56	0.08	0.53	0.08	0.60	0.09	0.60	0.18	1
MH_OPM2_09	−116.077659 33.647037	3	13.15	1.32	T	13.10	1.31	13.25	1.33	13.26	1.33	13.42	1.34	13.40	1.34	12.10	1.21	1
MH_OPM2_09a	−116.077659 33.647037	3	6.00	0.60	T	5.97	0.60	6.00	0.60	6.01	0.60	5.94	0.59	6.09	0.61	5.80	0.58	1
MH_OPM2_12	−116.077611 33.647009	3	1.78	0.18	SE CM	1.86	0.19	1.92	0.19	1.64	0.16	1.29	0.13	2.02	0.20	1.30	0.13	1
MH_OPM2_12a	−116.077611 33.647009	3	2.16	0.22	T	2.13	0.21	2.08	0.21	2.05	0.21	2.07	0.21	2.25	0.23	–	–	1
MH_OPM2_13	−116.077557 33.646973	2	2.15	0.22	T	2.52	0.25	2.60	0.26	2.00	0.20	3.22	0.32	2.97	0.30	1.95	0.39	1
MH_OPM2_14	−116.077287 33.646782	2	0.55	0.08	T	0.63	0.09	0.61	0.09	0.63	0.09	0.67	0.10	0.66	0.10	0.53	0.16	1
MH_OPM2_15	−116.076884 33.646465	2	0.42	0.06	T	0.55	0.08	0.51	0.08	0.57	0.09	0.64	0.10	0.60	0.09	0.47	0.14	1
MH_OPM2_16	−116.076723 33.646352	4	2.08	0.21	T	2.00	0.20	2.04	0.20	2.10	0.21	2.20	0.22	2.07	0.21	1.75	0.26	1
MH_OPM2_17	−116.076453 33.646119	3	0.32	0.05	NW CM	0.40	0.06	0.33	0.05	0.30	0.05	0.41	0.06	0.46	0.07	0.25	0.08	1

in flight missions to collect imagery, a DJI Matrice 600 Pro and DJI Phantom 4 Pro (Table 1A and B). Matrice 600 flights, equipped with a Sony A600 camera, were conducted using an automated flight mapping application, Maps Made Easy (MME, 2020), on an iPad, while automated flight mapping application, Drone Deploy, was operated on a smart phone for Phantom flights. All automated UAS surveys, nine in total

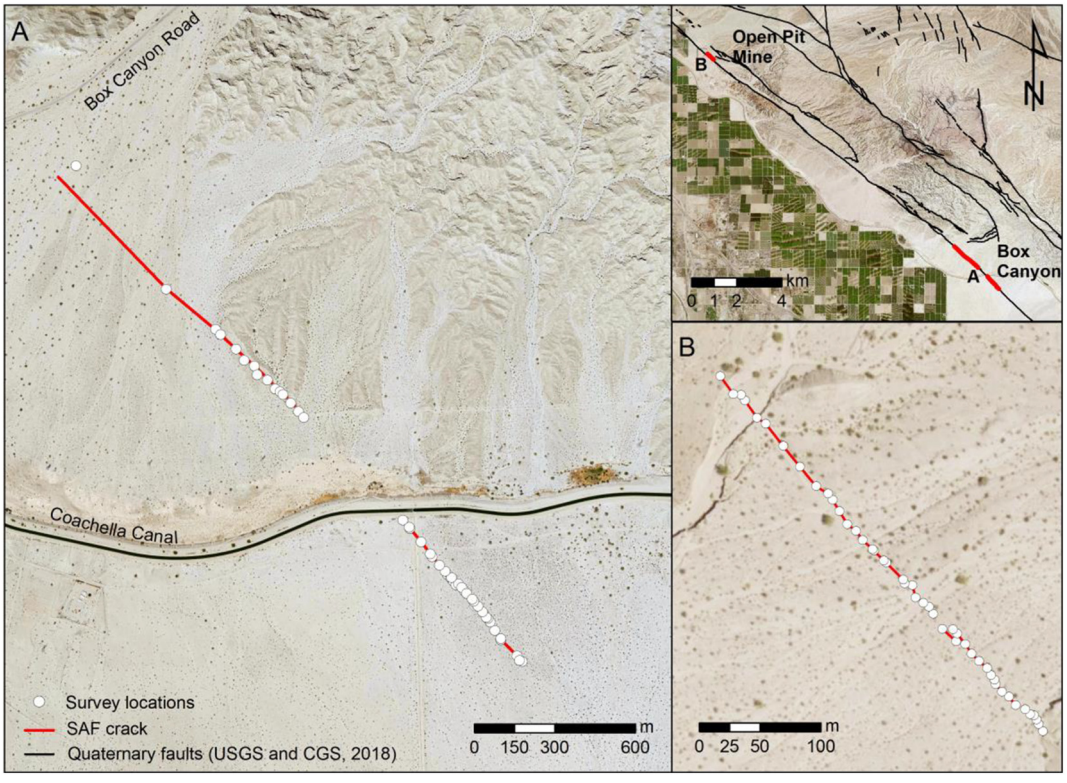

Fig. 5. Detailed map of the ground rupture (en echelon cracking) from a creep episode along the San Andreas Fault (SAF). Top right – inset map showing the extent of the ruptures at Box Canyon and the Open Pit Mine (light solid lines) superimposed on Quaternary faults (dark solid lines). A) Cracking previously noted on February 23, 2018 (Tymofyeyeva et al., 2019) in Box Canyon with lateral displacement as much as 24 mm. B) Cracking of an approximately 300-meter section at the Open Pit Mine observed on October 6, 2018 before the October 12, 2018 rain event washed away evidence of the surface rupture. Lateral displacement was on the order of a few mm. We surveyed the location of the ground rupture with a Samsung Galaxy S6 running US Topo Maps Pro with an accuracy of ±2–4 m.
Source imagery: NAIP 2016.

(Table 1A, B), were flown over the area of interest during peak sun hours (11 am to 1 pm) to diminish shadow effects. The altitude above ground level (AGL) is determined from the takeoff point. The UAS did not automatically adjust to the local topography, so the UAS may be much closer to or further from ground level for portions of the flight depending on local relief. It was necessary to increase the altitude of several flights, so the UAS would not encounter obstacles at any point throughout the flight.

Displaced channels and rills are abundant along the ~1.7 km continuous fault segment at the Open Pit Mine and along ~250 m of the ~1.3 km segment in Box Canyon. After UAS and RTK-GPS surveys were conducted at each site, offset features were measured along the fault with a steel tape measure, using the distance between displaced channel thalwegs or channel margins as piercing points where these features were projected into the fault (Fig. 4). Uncertainty was estimated for each offset depending on the width of the measured feature and how well the feature was preserved in the field. An offset quality rating of poor, fair, good, or excellent was also assigned to each feature (Tables 2a–2c) based on quality, preservation, and erosion level of the feature. Cracking due to lateral creep along the sSAF at Box Canyon

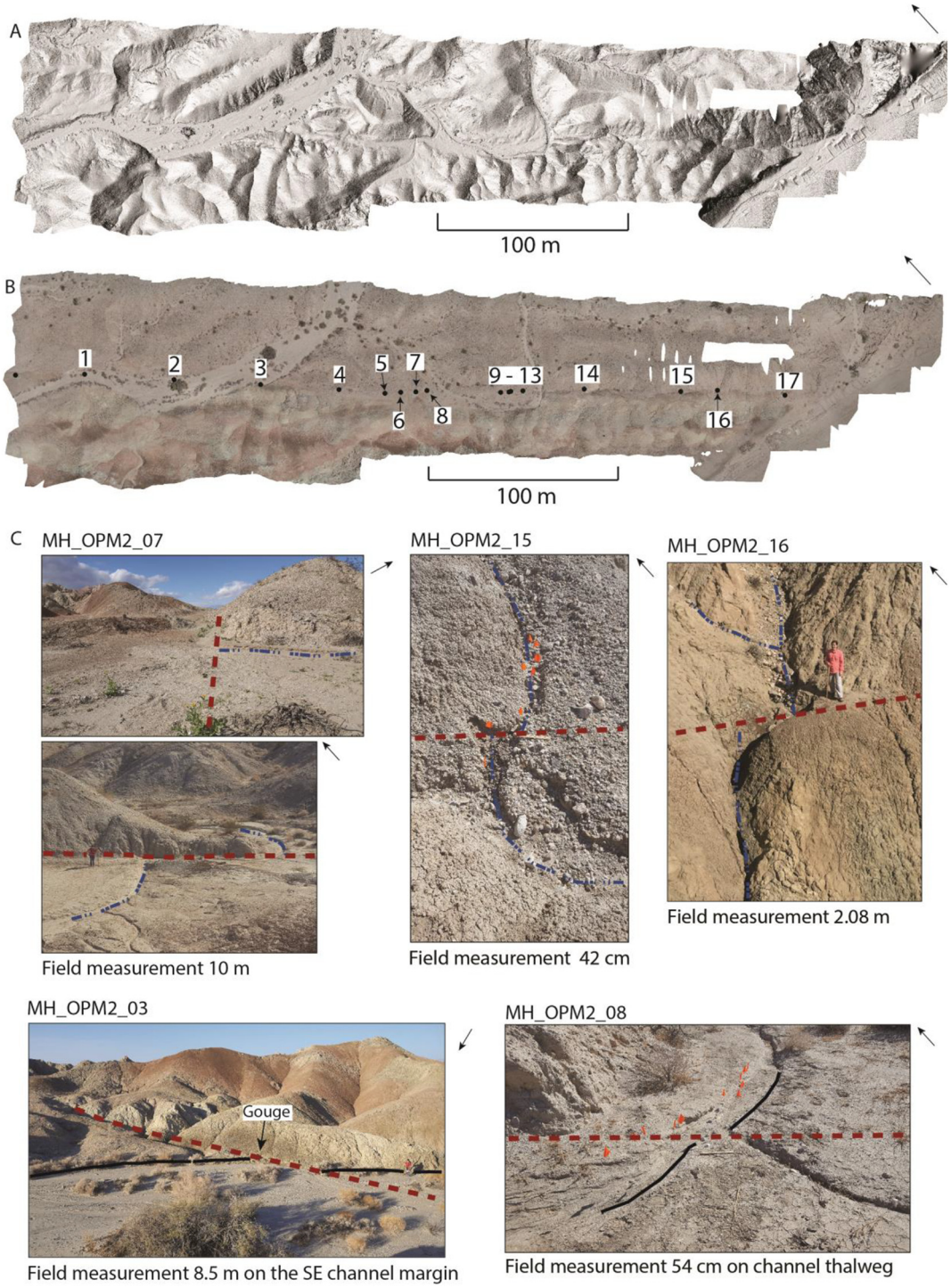

Fig. 6. Open Pit Mine, flight 2 (OPM2). Hillshade (A) and orthomosaic (B) products for the flight. Black circles on the orthomosaic represent offset locations and values are the site numbers. Site numbers correspond to Tables 2b and 2c. C) Field measurements from OPM2. Solid lines are channel margins and dashed-dotted lines are channel thalwegs. The surface trace of the San Andreas Fault is shown as a thick, dashed line.

(Tymofyeyeva et al., 2019) and more recently at the Open Pit Mine (Fig. 5) provided confirmation for the precise location of the main trace of the fault, and assisted in differentiating deflected and offset features from other non-tectonic erosional features at Box Canyon. If a possible geomorphic offset did not coincide with the surface expression of the crack, the feature was categorized as non-tectonic or associated with the double-stranded section in the Box Canyon study area. Additional GPS data were collected to document this cracking using the US Topo Maps application, with an accuracy of approximately 3 ± 1 m, on a smart phone.

3.2. Image processing

Following image collection, dark, blurry, and sky-dominated images were manually removed from the photoset and the remaining geotagged images were imported into Agisoft PhotoScan Professional (Agisoft LLC, 2018) to generate georeferenced dense point clouds, DSMs, and orthomosaics for each area (Figs. 6 and 7). Orthomosaics are generated by orthorectifying individual photographs for topographic distortions and projecting them into a real-world coordinate system (World Geodetic System 1984 UTM Zone 11N). The DSMs and orthomosaics were

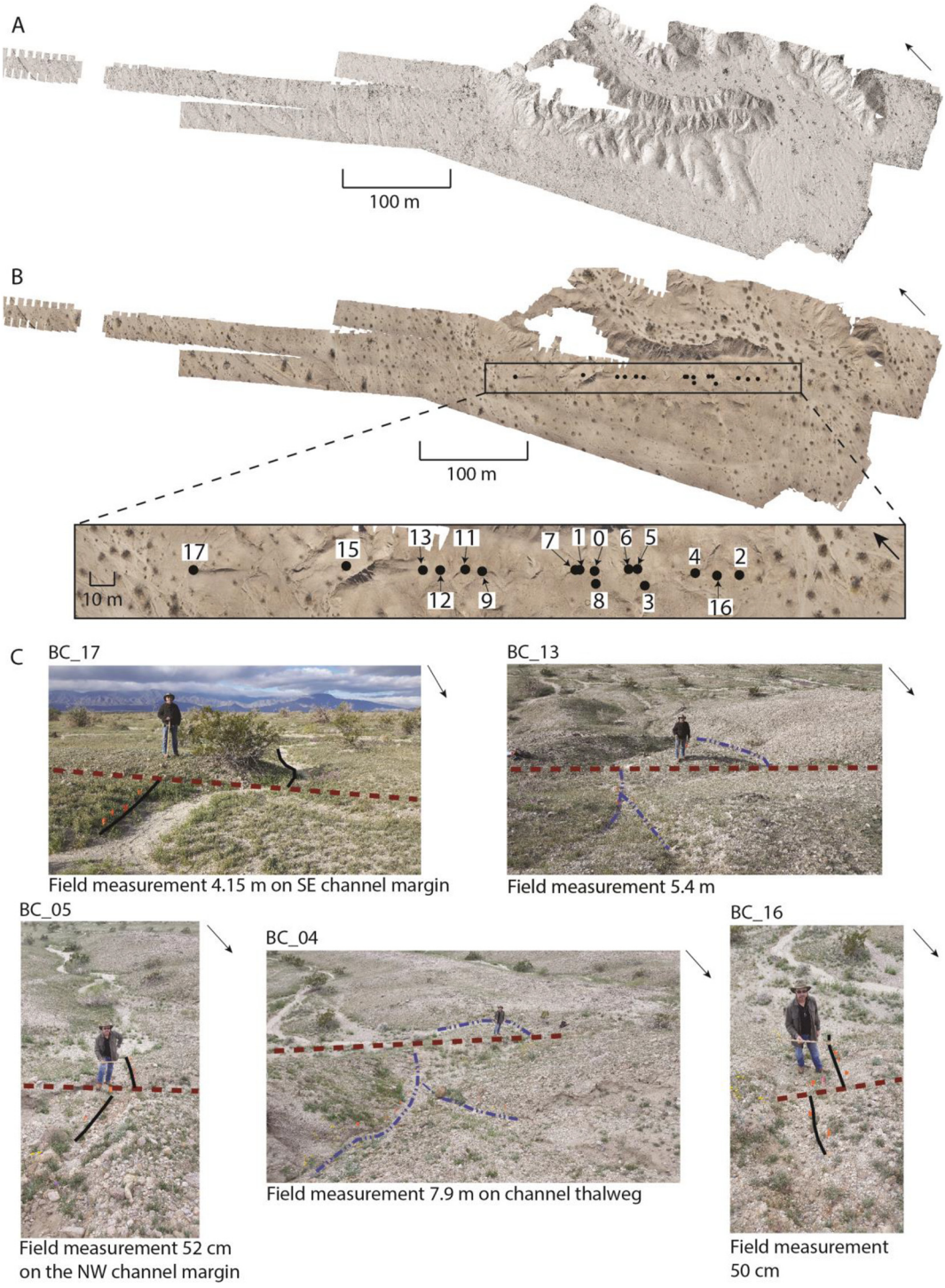

Fig. 7. Box Canyon (BC) flights 1–4. Hillshade (A) and orthomosaic (B) products for the flights. Black circles on the orthomosaic represent offset locations and values are the site numbers. Site numbers correspond to Table 2a. C) Field measurements from BC. Solid lines are channel margins and dashed-dotted lines are channel thalwegs. The surface trace of the San Andreas Fault is shown as a thick, dashed line.

exported as GeoTIFFs for further processing and analysis in ArcGIS. Each flight's Agisoft processing parameters were set to high for photo alignment accuracy and high for dense point cloud quality. We determined that processing on 'high' was adequate to observe decimeter-scale offsets and this setting decreased processing time and computational power dramatically over the highest setting, generating DSMs with 0.98–1.72 cm/pixel resolution (Table S1 in supplemental data).

Processing of UAS imagery has its own inherent complications. The imagery is processed using a set of GCPs, so there is absolute uncertainty in position of the GCPs. The UAS's GPS is accurate to ±0.5 m vertically and ± 1.5 m horizontally (DJI, 2019a; DJI, 2019b), so our imagery has a geolocation accuracy equal to that of the UAS. This is not expected to contribute significantly to error in our measurements. To evaluate overall uncertainty, the dimensions

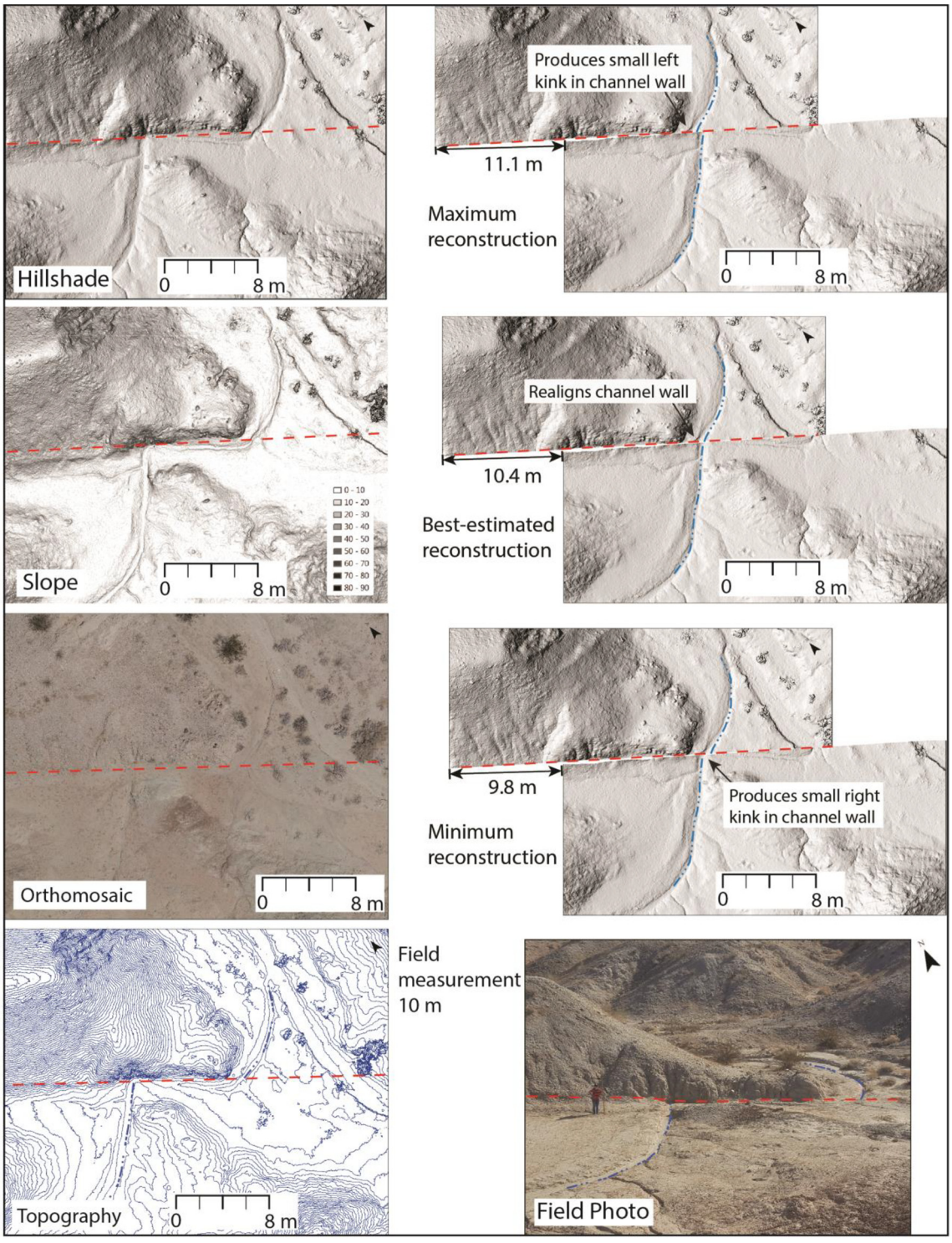

Fig. 8. The series of images on the left, from top to bottom, are the hillshade surface map, slope surface map, orthomosaic, and contour map of the offset feature MH_OPM2_07. The degree of slope is shown by a color ramp that represents flat surfaces as white, shallow slopes as light gray, moderate slopes as dark gray, and steep slopes as black. Dashed-dotted lines represent the channel thalweg and dashed lines depict the surface trace of the San Andreas Fault. The series of images on the right show, from top to bottom, maximum, best- estimated, and minimum offset reconstructions, produced with the hillshade map, and a field photograph of the offset.

of the GCPs, 26 × 26 cm and 29 cm diagonally, were measured after processing in ArcGIS using their known perimeters, from which they were found to have <2.5 cm uncertainty on average for relative object accuracy. This uncertainty value likely reflects the average distortion or error for individual features in the final exported DSMs and orthomosaics and is within the uncertainty of our offset measurements.

3.3. Interpretation and analysis

We imported the DSMs into ArcGIS to derive hillshade, slope, and contour map datasets, which enhanced visualization of ground surface features. To test the sensitivity of hillshade quality to sunlight parameters, we generated two hillshade maps; one at an azimuth of 315° or illumination source from the NW and another with an azimuth of

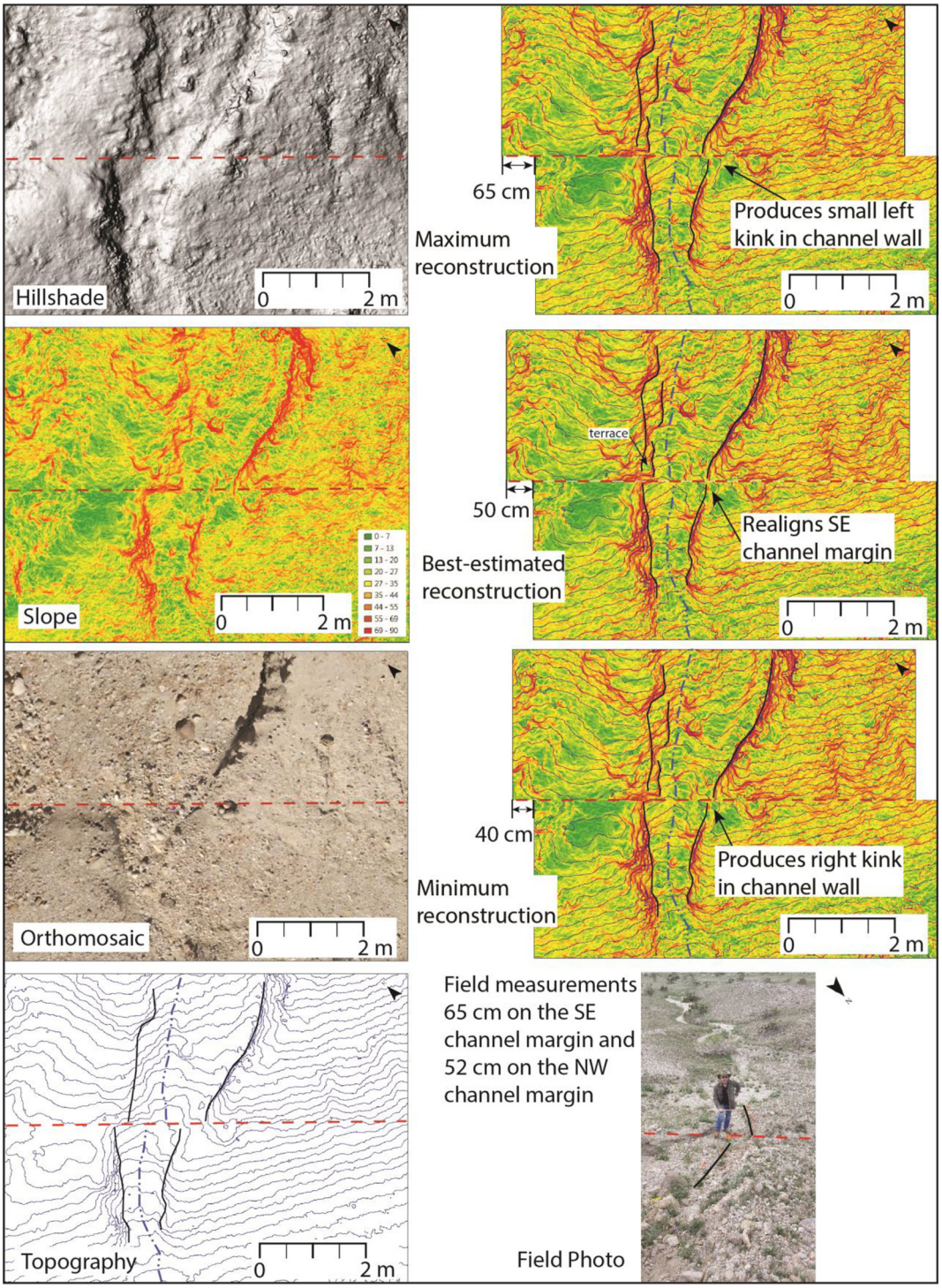

Fig. 9. The series of images on the left, from top to bottom, are the hillshade surface map, slope surface map, orthomosaic, and contour map of the offset feature BC_05. The degree of slope is shown by a color ramp that represents flat surfaces as green, shallow slopes as yellow, moderate slopes as light to dark orange and steep slopes as red. Blue dashed-dotted lines represent the channel thalweg, black solid lines show channel margins, and red dashed lines depict the surface trace of the San Andreas Fault. The series of images on the right show, from top to bottom, maximum, best- estimated, and minimum offset reconstructions, produced with the slope map, and a field photograph of the offset. (For interpretation of the references to color in this figure legend, the reader is referred to the web version of this article.)

135° or illumination source from the SE, both with an altitude of 55°. The hillshade at 315° best represented offset features (Figs. 6A and 7A); however, the hillshade at 135° is also interpreted (Tables 2a–2c). Moving forward, these surface maps will be referred to as hillshade 315 and hillshade 135. To highlight small-scale offset features, we generated contour maps with 1 m, 10 cm, and 5 cm intervals (Figs. 8 and 9).

We located offset features along the fault trace on the hillshade, slope, contour, and orthomosaic (exported from Agisoft) products in ArcGIS (Figs. 6–9, Tables 2a–2c). To verify field measurements >1 m, we transferred hillshade and slope surface rasters to Adobe Photoshop as JPEGs and reconstructed offset features to their inferred original configuration by cutting along the fault trace, placing the divided products in separate layers, and reconstructing (sliding) these layers along the fault until the offset feature was realigned (Figs. 8 and 9). The maximum and minimum reconstructions served a secondary purpose of providing an approximate uncertainty value to the offset measurement.

A comparison of field measurements to digital measurements made using Agisoft (orthomosaic) and ArcGIS products (hillshade, slope, and contour maps) was conducted to understand the accuracy, precision, and uncertainty as it relates to each method (Fig. 10). To evaluate this, we plotted each type of measurement against its corresponding field measurement to observe any patterns, such as consistently higher or lower values in one measurement method, or strong linear (1:1) correlations, which would suggest a high precision between methods.

A Gaussian distribution analysis was performed in Microsoft Excel with the normal distribution function for each type of measurement, separately for the Open Pit Mine and Box Canyon (Fig. 11), using offset measurements and their uncertainty as our parameters. A Gaussian distribution (or normal distribution) is a continuous probability function that represents data symmetrically about the mean (or peak), and describes how the values of a variable are distributed. We use Gaussian distribution analysis as a means to evaluate patterns in measured offset values, with data near the mean more frequent in occurrence than data farther from the mean. The peaks in the distribution indicate the offset magnitudes of the most probable measurement values of cumulative slip in successive paleoearthquakes.

To assess slip-per-event, offset measurements (Tables 2a–2c) were divided into groups based on similar offset values (see Table S2 in supplement), with Box Canyon and the Open Pit Mine slip-per-event calculated separately. Maximum offset values of each group were identified, with the difference in the maximum displacement of each group interpreted to represent slip in each event. The average slip-per-event for each interpreted earthquake is based on the method established in Rockwell and Pinault (1986) and assumes that each group represents a separate event.

4. Results

A total of 60 geomorphic features were measured at Box Canyon and Open Pit Mine, 15 of which had multiple measurements, for a total of 75 measurements. Most offsets are between 0.15 and 25 m, with one offset measurement of 85 m. The Open Pit Mine yielded a higher number of offsets resulting in 51 measurements, with 24 measurements at Box Canyon (Tables 2a–2c). En echelon cracking was observed on October 6, 2018 from a creep episode for an approximately 300-meter section of the SAF at the Open Pit Mine (Fig. 5) before a major rain event on October 12, 2018 washed away evidence of the ground rupture. Lateral displacement was on the order of a few mm. Previously noted cracking in Box Canyon was mapped on February 23, 2018 (Tymofyeyeva et al., 2019), and was visible along the entire ~1.3 km surveyed section along the sSAF (Fig. 5).

All offsets measured were located on the main strand of the sSAF except for two offset measurements on the scale of a meter at Box Canyon (Table 2a). Due to the suggested high degree of localization of primary slip zones in large earthquakes (Rockwell and Ben-Zion, 2007) where most slip is accommodated in very narrow zones on the primary strand

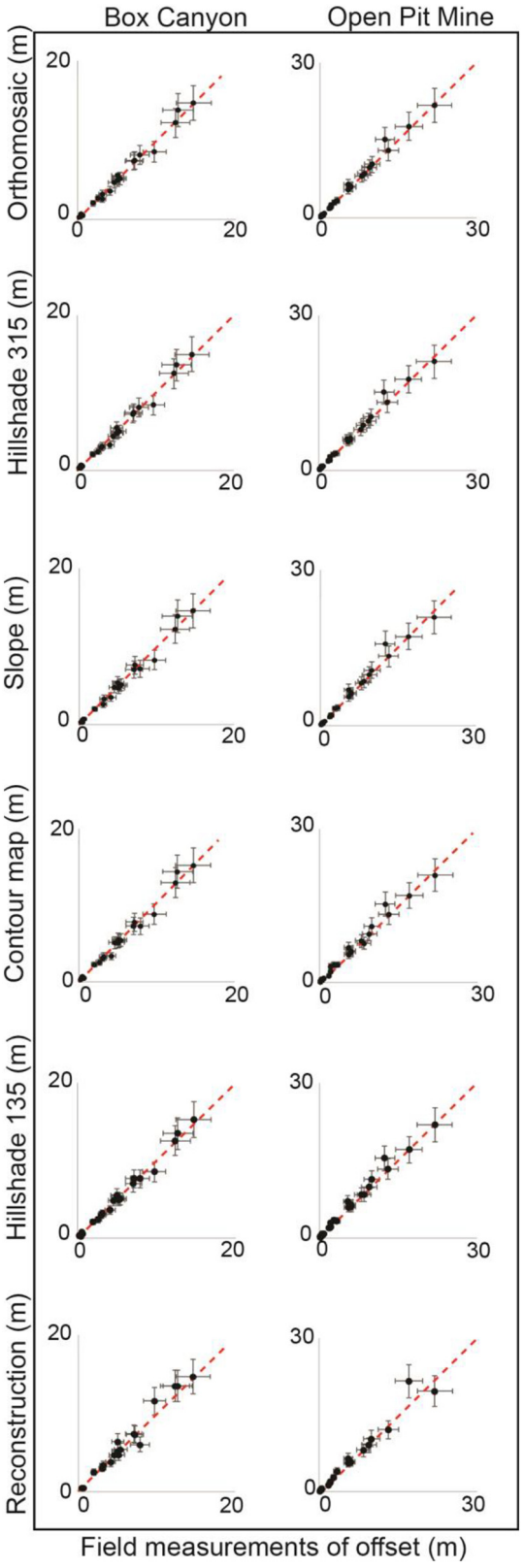

Fig. 10. Linear correlations of the various surface map extrapolated measurements (y-axis) compared to measurements collected in the field (x-axis) at Box Canyon and the Open Pit Mine. All measurements are assigned a 15% error and only offsets discernible in both methods were used in each comparison. The black dashed line is a 1:1 line and illustrates the strong linear relationship between measurement methods.

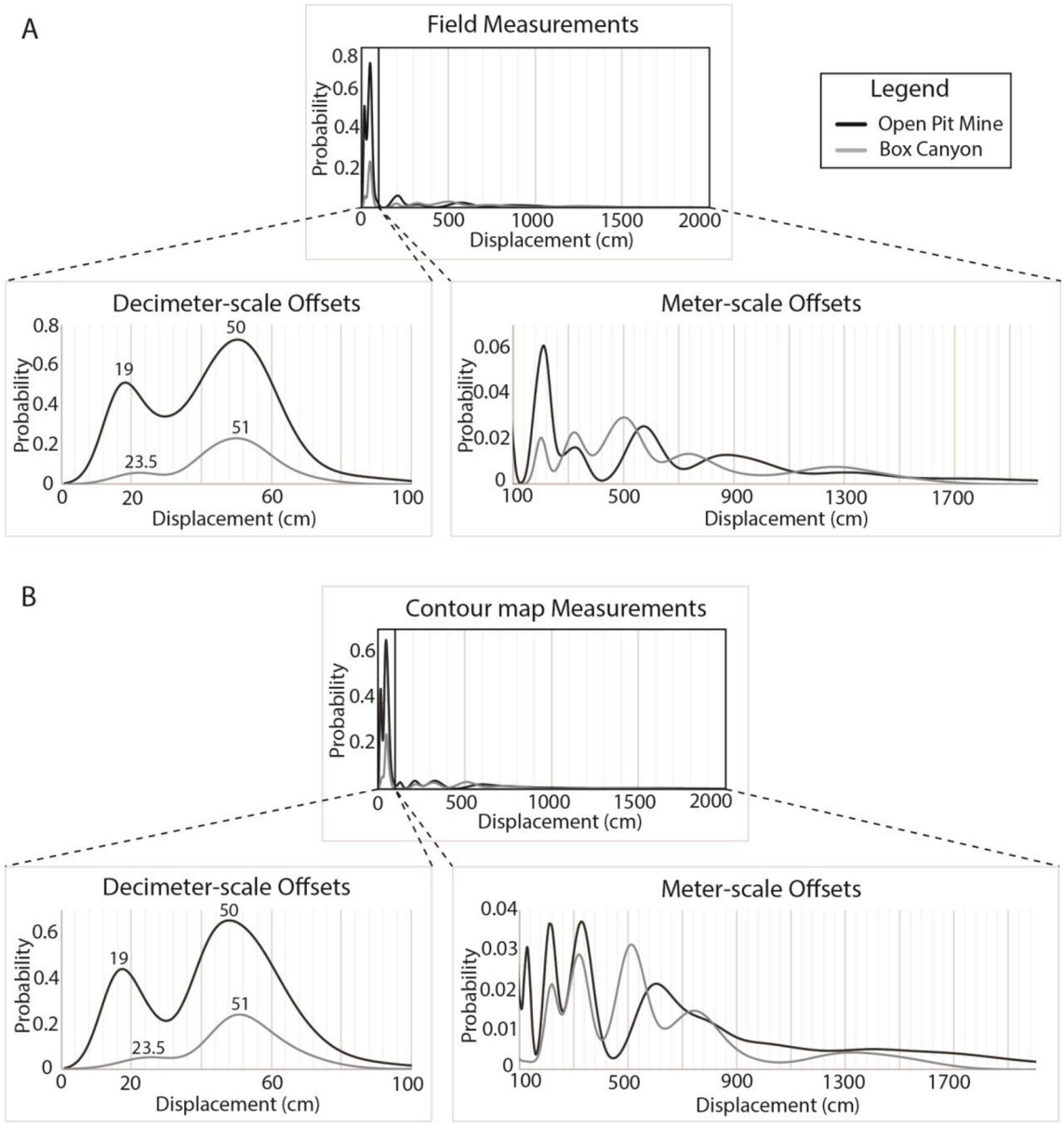

Fig. 11. Gaussian distributions at Box Canyon (gray) and the Open Pit Mine (black) for (A) field measurements and (B) topography measurements used in the analysis of co-seismic and creep-related offsets. Meter-scale and decimeter-scale offsets are expanded for better visualization. Plotted values are the Gaussian distribution peaks for decimeter-scale offsets. Meter-scale offset peaks do not agree well, so the original offset values (Tables 2a–2c) are used to determine slip-per-event; however, the observed peaks are used to develop probable earthquake models.

of large faults, we did not include these offset measurements in our Gaussian distribution analysis. The previously described cracking allowed us to precisely locate the main trace of the fault and no cracking was observed near our two secondary fault measurements. Therefore, the secondary fault is likely inactive or accommodates less slip than the main strand and, as such, offsets measured on this strand would not be suitable to use in our analysis.

Hillshade 315 coverages, orthomosaics, and offset locations are shown for Open Pit Mine, flight 2 and Box Canyon with several offset examples (Figs. 6 and 7). An offset example for each of these sites is provided to illustrate each type of measurement, including hillshade 315, slope, orthomosaic, contour map, and best-estimated reconstruction in addition to field measurements (Figs. 8 and 9). Detailed offset location information (Figs. S4–S6) and all other documented offsets (Figs. S7–S66) can be found in the supplement.

Linear correlations of digital measurements and field measurements were performed to assess the accuracy of each technique (Fig. 10), with only offsets discernible in both methods used in the comparison. On average, the best-estimated reconstruction measurements are slightly greater than those measured in the field. Hillshade 135 measurements are about equal to or slightly greater than those measured in the field. All other measurement methods were not consistently greater or less than field measurements on average, so the various measurement methods reveal a strong linear relationship overall. As contour maps are based directly on the elevation of the DSMs, measurements extrapolated from them are considered the most accurate and when used in conjunction with field measurements, are susceptible to the least amount of bias as the thalwegs of offset geomorphic features are clearly represented by the topography.

Based on the Gaussian distributions for the Open Pit Mine and Box Canyon (Figs. S1 and S2 in the supplement), cluster values are generally in agreement for each method for meter-scale and decimeter-scale offsets at the Open Pit Mine. Offset data for Box Canyon results in misalignment of cluster values for decimeter-scale offsets between different

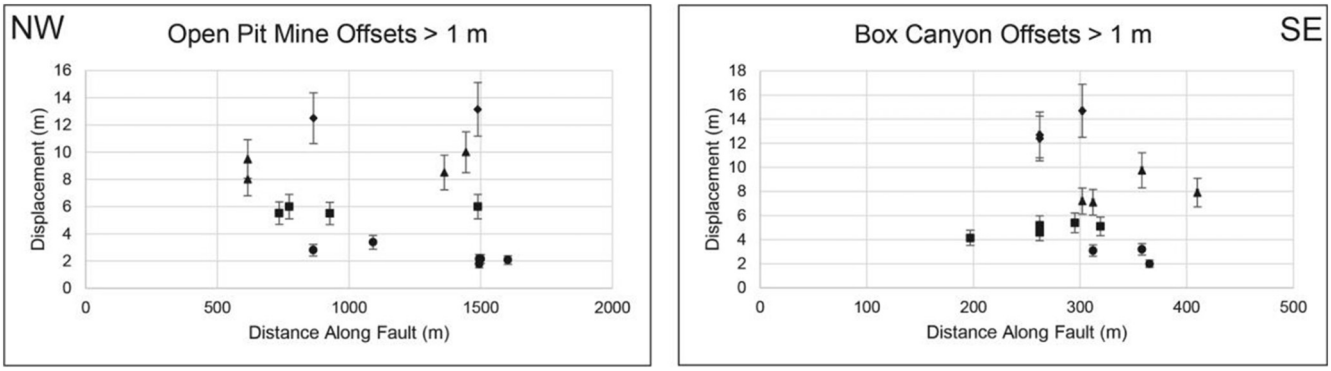

Fig. 12. Lateral distribution of offset features >1 m, illustrating the lateral variability of slip along the fault for an ~1 km distance at the Open Pit Mine and a ~200 m section of fault at Box Canyon. Offsets are symbolized based on the event they are assigned according to the 4-peak model. Circles – E1, boxes – E2, triangles – E3, diamonds – E4. An uncertainty of 15% is applied. Lateral distribution of offset features <1 m can be found in the supplement.

methods, but meter-scale offsets agree well. Furthermore, a reconstruction was not completed for every offset feature at the Open Pit Mine and Box Canyon, so the best-estimated reconstruction curve at each site has significant separation from the general curve trend because this method (best-estimated reconstruction) has approximately 50% of the measurement density in comparison to all other methods. Gaussian distribution analysis reveals offset clusters at about 20 and 50 cm in the field and contour measurements at both the Open Pit Mine and Box Canyon (Fig. 11). As the offsets increase in size, and therefore uncertainty, the data becomes more broadly distributed. In comparing Box Canyon to the Open Pit Mine, meter-scale offset data is well aligned for the first two peaks in the Gaussian distributions; however, older peaks are not well aligned. This may suggest varying amounts of slip for earlier events between the two sites; however, erosion and channel modification could account for these variabilities as well. An additional peak at about 130 cm in the Open Pit Mine contour data is the result of one measurement and is therefore not included in the paleoseismic interpretation. We also find that the distribution of offset measurements along fault strike shows some degree of lateral variability (Fig. 12).

5. Discussion

5.1. Sources of error and limitations of the data

In addition to errors inherited from SfM processing, as discussed in Section 3.2, UAS imagery products and field measurements are both susceptible to errors that affect accuracy and lead to differences in results when comparing methods. In the field, measurements can vary depending on whether the geomorphic offset is measured along the average regional strike of the fault, verified with a compass, or whether the measurement was taken at the local fault strike. This is because the chosen strike of the fault that offset features are projected to impacts the measured slip. According to Rockwell and Klinger (2013), this is not likely a large contributing factor to the error associated with field measurements, but can be up to 20% locally. We don't expect this to have a significant effect on our offset measurements. Measurement error also occurs when offset features are not aligned well, or have a high degree of curvature or sinuosity, resulting in the features being incorrectly projected into the fault. A projection such as this may not account for the overall sinuosity of the channel and might only reflect the shape of the feature close to the fault (Salisbury et al., 2015). This is probably a moderate source of error for field measurements and overestimation or underestimation should be expected depending on how channels are projected into the fault. Additionally, channel modification over time is unpredictable and introduces additional uncertainty to measurements. Scharer et al. (2014) assess many of these challenges associated with measuring small geomorphic offsets. To incorporate uncertainty, an error percentage of 10–30% is included on a case-by-case basis for all collected measurements in this study, with sub-meter and poor-quality rating offset features having the largest relative uncertainty.

When generating hillshades, user error can produce results that don't adequately enhance features, depending on the selected azimuth and altitude parameters. For example, hillshades with variable sunlight azimuths can overemphasize shadows in undesirable areas, portray the topography differently, and yield measurably different results when estimating lateral displacement. To address this, researchers should test shaded relief maps at many different azimuths and altitudes to ensure the final hillshade best illustrates the data. Slight differences between the two measurement techniques (field and ArcGIS) could also be due to selection of different piercing points for the same feature (Fig. 4). Uncertainty and potential interpretation bias are minimized by using the contour map measurements, based on elevation data of the DSM, and field measurements, rather than hillshade or slope products in the final analysis of creep and paleoseismicity.

5.2. Creep, major precipitation events, and climate-modulated channel incision

Decimeter-scale offsets are interpreted to be the result of creep and triggered slip along the sSAF since the last earthquake in 1726 ± 7 years (Rockwell et al., 2018). Gaussian distributions of offset measurement data indicate that sub-meter offsets cluster around 20 and 50 cm at both sites (Fig. 11). Assuming the long-term creep rates at both locations are similar as implied by the similar cluster values, the clusters suggest two simultaneous incision events at both sites likely caused by extreme precipitation events. It is probable that the two sites have similar creep rates in order to have produced similar decimeter-scale offset values. Large precipitation events could have incised new rills and channels across the fault, generating small offsets as the fault crept (Fig. 13). Offsets cluster at 23.5 ± 1.5 cm and 51.0 ± 1 cm at Box Canyon and 19.0 ± 1 cm and 50.0 ± 2 cm at the Open Pit Mine in our Gaussian distributions (Fig. 11). Although the Gaussian distribution shows one peak at 19.0 cm at the Open Pit Mine, this peak may potentially be the average of two separate incision events, based on our measurement data (Tables 2b and 2c), which reveal average offsets of 16.5 ± 0.5 cm ($n = 4$) and 23.5 ± 0.5 cm ($n = 5$). Using the average creep rate of 3 ± 0.2 mm/yr determined from InSAR for sites in the Mecca Hills (Lindsey et al., 2014), these offsets suggest that incision events occurred about 50–61 (~55), 69–89 (~78) and 150–185 (~167) years before present (BP), or slightly before, assuming that there may have been some time lag between when the incision occurred (Fig. 14) and the next creep or triggered slip event producing displacement along the fault. 'Present' refers to the year of data collection, 2018, and applies to all usage of BP.

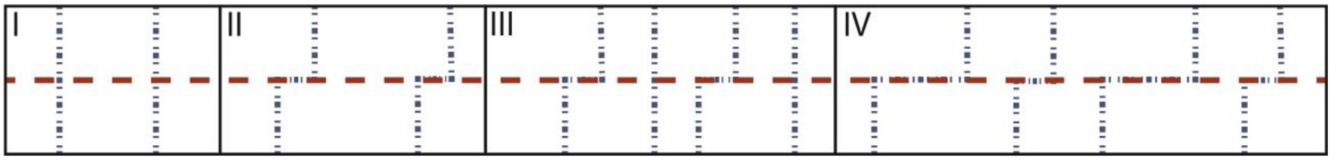

Fig. 13. Series of events illustrating how two incision events following the penultimate event could result in two peak displacement values for the most recent event (MRE). The dashed line shows the location of the San Andreas Fault and the dashed-dotted lines illustrate channel thalwegs. Panel I represents an incision event which incises new channels (C1) across the fault. Panel II shows subsequent creep producing small offsets in C1. Panel III shows another incision event incising new channels (C2) across the fault. Panel IV demonstrations co-seismic slip from the MRE as well as the prior creep, which results in offset in both sets of channels (C1 and C2), with C1 having greater displacement than C2. This figure corresponds to incision event model A in Fig. 15.

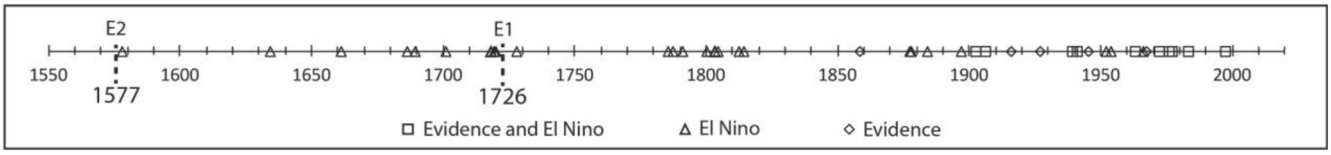

Fig. 14. Timeline of recent and historical major precipitation events and El Niño events. Boxes indicate years with documented evidence of extreme precipitation in southern California and an El Niño event. Triangles represent probable El Niño years with no known evidence of a precipitation event (undocumented). Diamonds show years with documented major precipitation events (>2.5 cm); however, not during an El Niño year. The earthquake dates plotted on the timeline (~1577 and ~1726) are the two most recent earthquake dates determined by Rockwell et al. (2018).
Data is compiled from the National Weather Service (2017), NOAA (2019), and Garcia-Herrera et al. (2008).

The 23.5 ± 1.5 cm clustered offsets suggest an incision age of sometime between 69 and 89 years BP. A 1939 tropical storm sequence is the best candidate for a potential incision event from the historic record during this period (Fig. 14). The greatest documented rainfall event in the northern Salton Trough occurred in 1939 when the "Lash of St. Francis" came onshore at San Pedro near Long Beach and produced 17.8 cm of rainfall in 3 h at Indio, leaving the eastern Coachella Valley under 0.6 m of water (National Weather Service, 2017). This storm followed the remnants of a hurricane, which travelled northeast across Baja California, causing extensive damage in Mecca as well as flooding up to 0.9 m in Thermal (Fig. 1). The Long Beach tropical storm occurred during a strong El Niño year (National Weather Service, 2017). If this storm marks the incision event recording the 23.5 cm offsets, then the implied creep rate is 3 mm/yr for the 79 years since 1939, identical to that estimated for the Mecca Hills with InSAR (Lindsey et al., 2014).

At 3 ± 0.2 mm/yr, the incision time estimated from the 16.5 ± 0.5 cm offsets is about 50–60 years, or ~55 years BP. On September 18, 1963, northeastward moving Tropical Storm Jennifer-Katherine made landfall in northern Baja California with rainfall of up to 16.5 cm in the mountains of southern California and 4.8 cm in Indio (National Weather Service, 2017). More prominently, in 1976 Tropical Storm Kathleen crossed the Baja California Peninsula and passed directly over the Salton Trough. Flooding resulting from this major storm catastrophically damaged the town of Ocotillo, washed out 400 m of Interstate 8, and destroyed a 20-meter bridge (The Telegraph-Herald, 1976). The 1963 storm took place during a moderate El Niño year, while the 1976 storm occurred during the strong El Niño of 1976–1977 (National Weather Service, 2017), and the 1976 storm was a much more catastrophic event with closer proximity to Mecca and Thermal. If the 1976 storm caused the most recent incision that records the ~16.5 cm of displacement, then the inferred creep rate for the past 42 years is slightly higher, about 4 mm/yr, which is still within the range of published uncertainties. One possible explanation for a higher creep rate is that there have been more earthquakes in the Salton Trough region that are known to have caused triggered slip in the past 50 years (1979, 1986, 1992, 1999, 2010) than in the prior 50 years: 1968 Borrego Mountain earthquake, with other moderately large earthquakes in 1942, Fish Creek Mountains earthquake, and 1954, the Arroyo Salada earthquake in the San Filipe Hills (SCEDC, 2017; Fig. 1). As previously discussed in Section 1.3, a considerable amount of the observed creep appears to result from triggered slip events; therefore, regional earthquake frequency may modulate the short-term creep rate.

Finally, the 50.0 ± 2 cm offsets suggest a date of incision in the 150–185-year timeframe at 3 ± 0.2 mm/yr, or somewhat younger if a slightly higher creep rate is considered. Notably, a category 1 hurricane, the "San Diego Hurricane" struck San Diego in 1858 (Fig. 14), bringing with it severe winds up to 120 km/h and heavy rains. Corals from the tropical Pacific indicate that 1858 was a warmer year than 1857 or 1859 (Chenoweth and Landsea, 2004), suggesting a likely El Niño phase. Rainfall in the Salton Trough is not recorded for this event, but a similar storm during the 1997–1998 El Niño, category 1 Hurricane Nora, travelled across northern Baja California and produced 30.4 cm of rainfall in the mountains of western Arizona (Waters, 1997). It is inferred that the San Diego Hurricane likely had a similar effect on the Salton Trough region that Hurricane Nora had on Arizona, as it struck farther north. This hurricane is the likely incision-causing storm for the observed 50.0 cm offsets. If correct, then the long-term 160-year creep rate is estimated at 3.2 mm/yr, within uncertainty from the 79-year creep rate or short-term geodetic rate, and comparable to the 300-year creep rate documented at Indio (Sieh and Williams, 1990).

An incision event would result from major precipitation in the desert climate of the Coachella Valley, which is rare. As precipitation is uncommon in this region, it is important to investigate past major precipitation events and their relationship to the El Niño phenomenon. In a study of ENSO-driven torrential rainfall events in the southern Atacama Desert in Chile, Ortega et al. (2019) found that most of the extreme rainfall events occurred during El Niño years. During El Niño periods, sea surface temperatures are elevated along the western coasts of the United States and Mexico, which makes tropical storms stronger and assists in their northern migration (Chenoweth and Landsea, 2004). Thus, it follows that extreme climatic events resulting in rainfall in the Mecca Hills may be the result of elevated sea-surface temperatures during El Niño years. Using data compiled from the National Weather Service (2017), SCEDC (2017), NOAA (2019), and a chronology of El Niño events conducted by Garcia-Herrera et al. (2008), we constructed a record of known major precipitation events in southern California with historical evidence and both known and probable El Niño years that may have resulted in enough rainfall to cause rill incision in the desert regions of southern California (Fig. 14). According to these data, the aforementioned notable storms in 1939 and 1976 occurred during strong El Niño years and the storm of 1858 was likely an El Niño year as well.

To evaluate a potential incision-causing storm, it is important to understand the kind of event needed to remove geomorphic features that

recorded past slip and creep and incise new rills and channels. Since the collection of UAS imagery (Table 1A), there have been two notable precipitation events in the Coachella Valley: October 12, 2018 and February 14, 2019 during the 2018–2019 El Niño period. From observations on October 13, 2018 at the Open Pit Mine and on February 5, 2018 in the Open Pit Mine and Box Canyon, although there was evidence of flow from the rainfall events, it was not significant enough to cause new rill formation or to reset the geomorphology. The February 14, 2019 rain event produced a greater amount of rainfall than the October event, with 2.5 cm of precipitation in one day recorded at the Thermal airport weather station. In comparison, the same weather station recorded 5.3 cm of total precipitation during the almost four-month period between October 1, 2018 and February 14, 2019, according to preliminary data from the National Weather Service Climate Report (2019). From inspections at both sites on March 5, 2019, we concluded that the geomorphology was not significantly altered by the major precipitation event on February 14 because previously measured offset features were still intact and new rills and channels along the fault were not apparent. Due to our observation that precipitation events of 2.5 cm and less did not have a substantial effect on the overall geomorphology, it is likely that only extreme rainfall events much >2.5 cm cause incision and the development of new rills and channels. The amount of rainfall due to a hurricane or tropical storm intensified by El Niño conditions may be the ideal scenario to produce adequate rainfall to result in incision events in the Mecca Hills. Therefore, it may take a hurricane sized-event, hurricane remnant, or strong tropical storm to engender incision that would be recorded by subsequent creep and earthquakes along the sSAF.

5.3. Which came first: earthquake or hurricane?

The El Niño phenomenon has been documented since the 1500s and rainfall-induced incision has undoubtedly been occurring throughout that time. A list of probable El Niño dates was compiled (Garcia-Herrera et al., 2008), which includes years both before and after the most recent surface rupturing event (MRE) in 1726 ± 7 years (Fig. 14). Therefore, it is pertinent to ask which came first: earthquake or hurricane? If the incision occurred after the earthquake, newly incised channels and rills would be offset as subsequent creep occurred along the fault, and the resulting small-scale features would be solely from creep. If an incision event preceded the earthquake, any co-seismic slip would add to the accumulated creep displacement; thus, newly incised channels and rills would record creep since the incision event and co-seismic slip as a result of the earthquake, making it difficult to distinguish creep and coseismic slip. It is also possible that multiple incision events occurred prior to an earthquake that could also record pre-earthquake creep. This is a factor which likely further confuses the resulting slip distribution in slip-per-event studies and requires further investigation. As the average recurrence interval for the past 1000 years is on the order of 150–200 years (Philibosian et al., 2011), the resulting uncertainty in how much of the observed offsets are the result of creep versus co-seismic offset should only be on the order of 45–60 cm. This is assuming a creep rate of ~3 mm/yr during the interseismic period and is the same order of magnitude as offset measurement errors. The implication of miscalculating a slip event by 45–60 cm is that this could result in an overestimation or underestimation of earthquake magnitude.

5.4. Paleoseismic interpretation

Meter-scale offsets are interpreted as the result of a combination of creep and triggered slip coupled with co-seismic slip from the past one to several earthquakes. In comparing the displacement signals resulting from Gaussian distribution analyses at Box Canyon and the Open Pit Mine, meter-scale offset data is well aligned for the first two peaks at approximately 2.2 m and 3.4 m (Fig. 11). However, older peaks are not well aligned, which suggests varying amounts of slip for earlier events between the two sites or that the data are too sparse to discern all peaks. An additional peak at about 1.3 m in the Open Pit Mine contour Gaussian distribution (Fig. 11) is the result of one measurement and is therefore not included in the paleoseismic interpretation because it does not show up anywhere else in the data. It can be explained simply as a deflection or the result of rill capture plus additional displacement from creep. Uncertainty is greatest for the largest offset features and least for smaller scale features, which explains the narrower peaks in the Gaussian distributions for smaller meter-scale offsets. Older offset features with greater displacements are less abundant than more recent offsets resulting from younger earthquakes because erosion, stream capture, and realignment of channels removes evidence of older offsets. Furthermore, as the southeast section of the SAF at Box Canyon transitions from single-stranded to double-stranded locally, total slip was almost certainly not measured across the entire zone of faulting. Measurements along the main trace of the double-stranded section that exhibited triggered slip in 2018, as evidenced by en echelon cracking (Fig. 5), reflect only minimum estimates of slip in past earthquakes. As the offsets increase in size, and therefore uncertainty, the data become more broadly distributed as shown by broader peaks. Intrinsic variability and measurement uncertainty in this study undoubtedly have a significant effect on the cumulative distribution of lateral offsets and result in a muted signal in offsets with larger displacement and uncertainty (Weldon et al., 1996). Therefore, an older event may not be as apparent in the data. For example, two offset measurements of about 17.0 and 22.0 m at the Open Pit Mine (Tables 2b and 2c) show no signal in the Gaussian distribution (Fig. 11), likely because of their relatively large uncertainty.

Mapping of surface ruptures after large earthquakes has been found to show variability in lateral displacement along strike (Fletcher et al., 2014; Rockwell et al., 2002; Rockwell and Klinger, 2013; Teran et al., 2015; Treiman et al., 2002; this study, Fig. 12), with average values much lower than the peak displacements. However, it is the peak displacements that likely better represent displacement at depth (Fletcher et al., 2014). This issue is discussed further below, but the implications are that the actual displacements in each earthquake are probably best represented by the larger values in the offset clusters.

In classical models, afterslip and interseismic creep are components of the same process, such that a shallow velocity-strengthening layer partly impedes co-seismic slip, and the resulting slip deficit is stabilized aseismically. In this scenario, afterslip rates are highest immediately following an earthquake, then gradually decay to “steady-state” interseismic rates or creep rates (e.g. Kaneko et al., 2013). However, more complex scenarios involving dynamic weakening can preclude a co-seismic slip deficit, or even result in a surplus of slip in a shallow crust. In this case, surface creep immediately after an earthquake may be suppressed, and resume later in the interseismic phase. Either way, the average creep rate late in the interseismic cycle should match predictions of a simple model where a shallow creeping fault section slips freely in response to interseismic loading (Fialko, Y., personal comm., 05/14/2019). Generally, creep following each event is interpreted to reflect afterslip as a result of the surface catching up with slip at depth, in other words, long-term afterslip from the prior earthquake. Still, it should be recognized that a certain amount of creep during the interseismic period likely reflects loading leading up to the next earthquake and thus, this slip would be assigned to the following event. The key issue is resolving how much interseismic creep is afterslip and attributable to the previous earthquake, versus how much is due to seismic loading and attributable to the next earthquake. Essentially, the creep adds “noise” to the displacement signal resolved from offset rills and channels, and with the average recurrence interval on the order of 150–200 years, this results in additional uncertainty of 45–60 cm when estimating the actual amount of displacement associated with a specific past earthquake.

Two different groupings were applied to evaluate the offset data, a 5-peak model and a 4-peak model, based on the resulting peaks in our Gaussian distributions (Fig. 11). The 5-peak model interprets an earthquake for each peak of the Gaussian distribution (except for the 1.3 m peak), while the 4-peak model argues that the first two peaks may represent slip in only the MRE due to either a bimodal displacement behavior (as described in Weldon et al., 1996) or multiple incision events that allowed creep to accrue and be recorded between earthquakes. Each model is discussed next, along with its attendant implications for slip rate and slip-per-event.

In the 5-peak model, each Gaussian peak is interpreted to represent the average cumulative slip along the fault section associated with past earthquakes, with five peaks representing five earthquakes, whereas, the 4-peak model represents four earthquakes. The maximum displacement is represented by the largest displacement values in each cluster (Table S2). Maximum displacement values were used to estimate slip-per-event and slip rate as these are likely more representative of slip at depth. In addition, the oldest (earliest) peak suggests a displacement that is more than twice the average value of the first four peaks (three for the 4-event model) and may actually represent the occurrence of two displacement events if there were no significant storms between earthquakes to cause an incision event, and hence, a mechanism to measure displacement. Therefore, two additional sub-models are evaluated where the 5-peak model represents 6 events and the 4-peak model represents 5 events. The slip-per-event and slip rates for these models are detailed in Table 3A–D.

There are two plausible scenarios that support the 4-peak model, assuming the first two peaks represent a bimodal distribution of displacement in the MRE. This bimodal behavior is suggested because the first two peaks are very close together and a double peak could be the result of (1) lateral variability along the fault rupture (Fig. 12) or (2) incision and rill formation following the penultimate event and preceding the MRE (Figs. 13 and 14).

Rills typically form along faults where there is topographic relief that is either present from juxtaposition of higher and lower topography or a result of transpression and transtension along the fault. If some rills formed along a section that then experienced maximum displacement for the ensuing event, whereas others formed across the fault where lower displacement occurred, this could result in a double slip peak for the earthquake, as documented by Weldon et al. (1996), or a broader distribution of displacements. One would expect that if enough closely-spaced observations are made along the fault, then this would resolve as a single broad peak, but as it has been nearly 300 years since the MRE on the southernmost SAF (Rockwell et al., 2018), the number of remnant offset rills is likely considerably less than if the rupture had been visited immediately after the earthquake. As the first two peaks are approximately 1.2 m apart (Fig. 11), it is reasonable to consider models that explain these peaks as the result of a single event.

In one model, the Weldon et al. (1996) findings are invoked where slip variability along the fault during an earthquake can result in two, closely-spaced slip peaks that represent the largest and smallest offsets along a reach of fault for one rupture. In a study of the 1940 Imperial Valley earthquake on the Imperial fault, Rockwell and Klinger (2013) observed considerable variation of lateral displacement along strike within relatively short sections of the rupture, with offset variability on the order of 1–2 m. These measurements were based on offset crop rows spaced only meters apart, so they likely reflect true variability, rather than near-field measurement uncertainty or inability to see the total strain field. Similarly, Rockwell et al. (2002) observed lateral slip variations on groves of planted poplar trees spaced several meters apart along the 1999 Izmit, Turkey earthquake (M7.4) surface rupture, with differences as much as 30% or more. Displacement from the 1999 Hector Mine earthquake, which was mapped in detail immediately after the earthquake, displayed local variations in slip measurements of 30–40% (Treiman et al., 2002). In each of these and many other field studies undertaken after large strike-slip earthquakes, lateral variability has almost always been recognized. It is assumed that these differences even out after multiple earthquake ruptures, which could then result in broader peaks for earlier events.

In the second model, it is inferred that two incision events occurred between the MRE and the penultimate earthquake ruptures, with one soon after the penultimate event and another preceding the MRE, resulting in incised rills and small channels (let's call these channels C1) across the fault (Fig. 13, panel I). Subsequent creep is then recorded by C1 (Fig. 13, panel II). Next, there is another incision event which again forms new rills and channels (C2) across the fault (Fig. 13, panel III). Co-seismic slip from the MRE and creep during the interseismic period that follows will be recorded on C2, but also on C1 (Fig. 13, panel IV), resulting in a double peak in displacement values. The double incision model (Fig. 15) can be tested with offset measurements using the largest values for each peak (see Tables S2-A and S2-B in supplement), which are interpreted to be more representative of slip at

Table 3
Estimated slip-per-events and average slip-per-events for the past 4 to 6 events on the sSAF at the Open Pit Mine and Box Canyon, slip rates, and years since the previous event, which are calculated from event dates for the most recent surface-rupturing event (MRE) and penultimate event from Rockwell et al. (2018), and successively older median earthquake dates from Philibosian et al. (2011). Note that we are using the best estimated ages and do not incorporate uncertainty in calculating the years since the previous event. Event 1 is the MRE and Event 6 is the earliest earthquake. A) Data for the last 5 earthquakes on the sSAF according to the 5-peak model. B) Data for the last 6 earthquakes on the sSAF according to the 5-peak model. C) Data for the last 4 earthquakes on the sSAF according to the 4-peak model. D) Data for the last 5 earthquakes on the sSAF according to the 4-peak model. This is our preferred model of interpretation. All slip-per-event and slip rate data are produced from field and contour map measurement data.

Event	Open Pit Mine slip (m)	Box Canyon slip (m)	Years since the previous event (years)
A) 5-peak model with 5 events			
Event 1	2.2–2.8	2.5–2.7	149
Event 2	0.6–1.3	0.6–0.8	157
Event 3	2.6–3.3	2.1–2.2	120
Event 4	2.8–4.0	3.2–4.4	160
Event 5	3.2–5.9	5.0–6.3	150
Average slip-per-event	2.6–3.1	2.9–3.0	–
Slip rate	13.5–19.8 mm/yr	15.1–18.6 mm/yr	–
B) 5-peak model with 6 events			
Event 1	2.2–2.8	2.5–2.7	149
Event 2	0.6–1.3	0.6–0.8	157
Event 3	2.6–3.3	2.1–2.2	120
Event 4	2.8–4.0	3.2–4.4	160
Event 5	2.5–3.9	3.0–4.1	150
Event 6	0.7–2	2.0–2.2	60
Average slip-per-event	2.2–2.6	2.4–2.5	–
Slip rate	11.6–16.9 mm/yr	12.6–15.8 mm/yr	–
C) 4-peak model with 4 events			
Event 1	3.4–3.5	3.2–3.3	149
Event 2	2.6–3.3	2.1–2.2	157
Event 3	2.8–4.0	3.2–4.4	120
Event 4	3.2–5.9	5.0–6.3	160
Average slip-per-event	3.3–3.9	3.7	–
Slip rate	16.6–24.2 mm/yr	18.4–22.8 mm/yr	–
D) 4-peak model with 5 events			
Event 1	3.4–3.5	3.2–3.3	149
Event 2	2.6–3.3	2.1–2.2	157
Event 3	2.8–4.0	3.2–4.4	120
Event 4	2.5–3.9	3.0–4.1	160
Event 5	0.7–2.0	2.0–2.2	150
Average slip-per-event	2.6–3.1	2.9–3.0	–
Slip rate	13.5–19.8 mm/yr	14.8–18.6 mm/yr	–

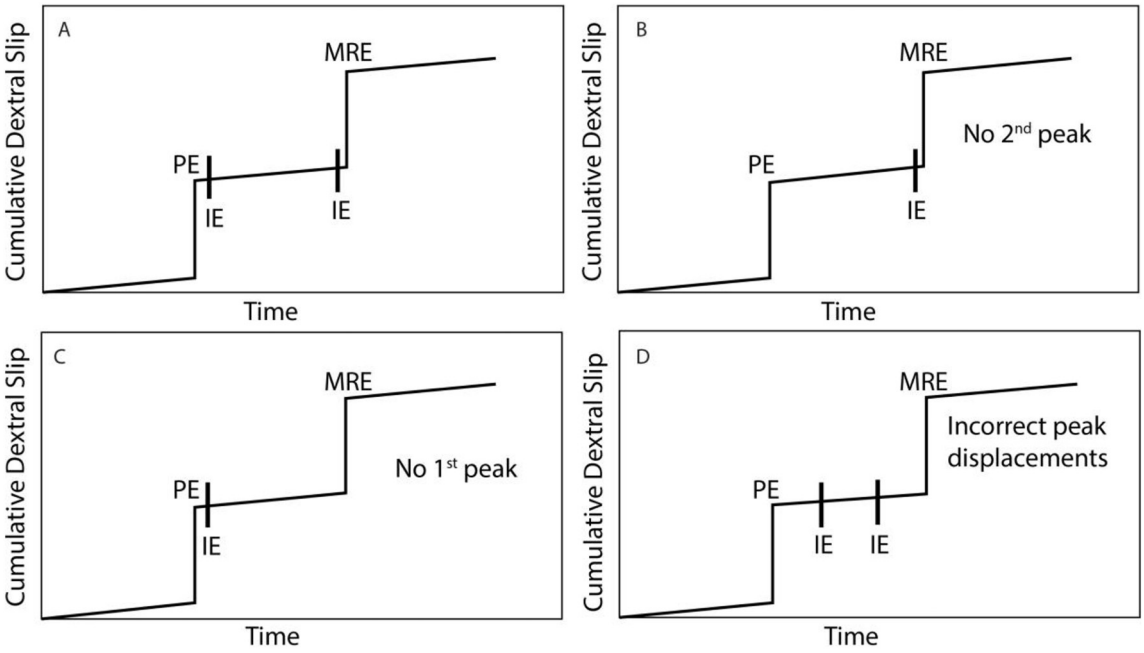

Fig. 15. Incision event models showing how double peaks with our displacements could be generated by at least two incision events following the penultimate event (PE), but not one incision event, and assuming these two peaks are representative of bimodal behavior of the most recent event (MRE). A) Two incision events, one soon after the PE and another soon before the MRE, which results in two peaks in our displacement data. B) One incision event soon before the MRE, which results in only one smaller peak and lacks a larger peak. C) One incision event soon after the PE, resulting in only one larger peak and lacking a smaller peak. D) Two incision events some time after the PE and before the MRE. Although this model produces a double peak in displacement data, it does not yield the displacements that we observe in our data, as there is insufficient time for creep to accumulate between incision events. A series of events illustrating incision event model A is provided in Fig. 13.

depth, and assuming a creep rate of ~3 mm/yr for the ~150–200 year period between the penultimate event and the MRE (based on recalculated ages from Rockwell et al., 2018). For Box Canyon, this amounts to 2.7 m of coseismic slip plus 0.4–0.6 m of creep, totaling ~3.1–3.3 m, which is comparable to the 3.2 m second peak in the Gaussian distribution (Fig. 11). Similarly, at the Open Pit Mine, the largest offset values in the first cluster are about 2.8 m; and adding the 0.4–0.6 m of creep yields 3.2–3.4 m, which compares well to the 3.2–3.4 m slip values recorded in the second peak of the Gaussian distribution (Fig. 11). From this model, the difference in observed displacements between the first two peaks at both sites can be explained by creep that accrued between the penultimate and most recent events. The timing of these two incision events can be slightly variable; but would need to have occurred soon after the penultimate event and soon before the MRE to produce the peaks seen in the displacement data. There could have been more than two incision events, but at least two are necessary to fit the model and produce two peaks, as only one incision event does not produce a second peak (Fig. 15). It is also important to note, especially for earlier events where this phenomenon may not be easily recognizable, that creep following an incision event soon after the penultimate event (afterslip) would be attributable to co-seismic slip from that event; whereas creep following an incision event soon before the MRE (aseismic creep due to loading) would likely be interpreted as co-seismic slip from that earthquake. Therefore, co-seismic slip could be overestimated or underestimated due to the contribution from creep, which would affect the estimated slip-per-event and paleoearthquake magnitudes.

The 5-peak and 4-peak models result in different estimates for slip rate, assuming the timing of past earthquakes is well-resolved from published paleoseismic studies. To compare inferred average slip rates derived from the data to longer-term rates established for the sSAF (Behr et al., 2010; van der Woerd et al., 2006), event dates for the MRE and penultimate event from Rockwell et al. (2018), and successively older median earthquake dates from Philibosian et al. (2011) were applied (Table 3A–D). Estimated slip rates include components of creep, triggered offset, and co-seismic offset, not accounting for lateral variations in displacement (Fig. 12) and excluding off-fault deformation. In the 5-peak-5-event model, event Coa5 from Philibosian et al. (2011) at about 1140 CE is applied, which results in slip rates of 15.1–18.6 mm/yr and 13.5–19.8 mm/yr for the Box Canyon and Open Pit Mine sections, respectively. The 4-peak-4-event model assumes that event 4 corresponds to Coa4 from Philibosian et al. (2011) at ~1300 CE, which yields inferred slip rates of 18.4–22.8 mm/yr and 16.6–24.2 mm/yr at Box Canyon and the Open Pit Mine, respectively. Slip rates are calculated based on the maximum slip measurement (with uncertainty), which also produces a peak in the Gaussian distribution, and the earliest event date (Rockwell et al., 2018; Philibosian et al., 2011). At Box Canyon, site BC_12a has the greatest measured slip, so it is used to calculate the estimated slip rate, while MH_OPM2_09, is used to calculate estimated slip rate at the Open Pit Mine. Two larger measurements of 17.1 m and 22.0 m at the Open Pit Mine did not produce peaks in the Gaussian distribution, so they are not included in the slip rate estimation (Tables 2a–2c). Based on the two closely spaced peaks in the Gaussian slip signals, discussed previously, the 4-peak model is the preferred model of interpretation. Large variations in inferred slip-per-event in both of these models (Table 3A and C) is a direct result of the 11–15 m peak, which is ~5–6 m larger than the previous 7–10 m peak (Table S2). A possible explanation is that the last peak in both the 5-peak and 4-peak models is a consequence of two earthquakes rather than one, which could result if there was a 150–200 year period between earthquakes with no major incision events to record slip from an additional earthquake. If this is the case, then the last peak is the result of 6 earthquakes in the 5-peak model, and 5 earthquakes in the 4-peak model, which drops the inferred slip rates to 12.6–15.8 mm/yr and 11.6–16.9 mm/yr for Box Canyon and the Open Pit Mine, respectively for the 5-peak model. Similarly, the 4-peak model yields slip rates of 14.8–18.6 mm/yr and 13.5–19.8 mm/yr for Box Canyon and the Open Pit Mine, respectively, when 5 events are applied. In summary, we have four models: two 5-peak models representing five and six earthquakes and two 4-peak models representative of four and five

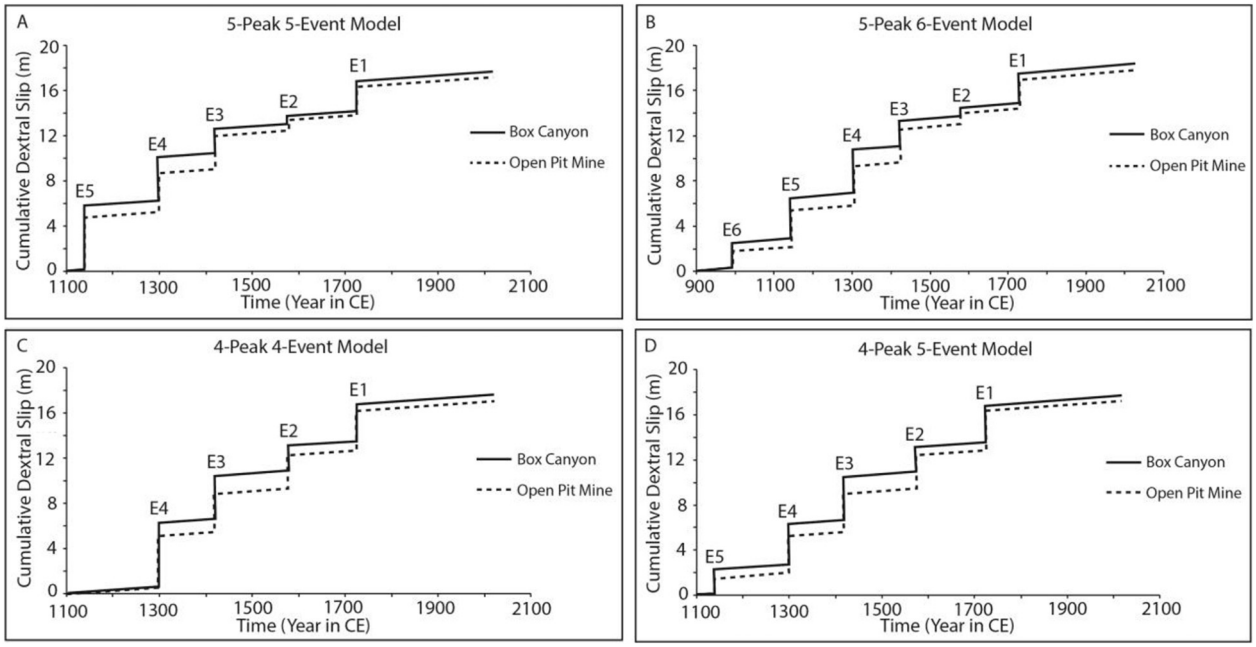

Fig. 16. Time series diagrams of the cumulative dextral slip over time at Box Canyon and the Open Pit Mine for the (A) 5-Peak 5-Event, (B) 5-Peak 6-Event, (C) 4-Peak 4-Event, and (D) 4-Peak 5-Event models. E1–E6 refer to estimated earthquake ages according to paleoseismic studies (Philibosian et al., 2011; Rockwell et al., 2018). Slip distances are from the slip-per-event data in this study based on offset measurements, provided in Table 3A–D. Creep is assumed at a rate of 3 mm/yr (Lindsey et al., 2014). The 4-peak-5-event model is our preferred interpretation.

earthquakes (Table 3A–D, Fig. 16). The 4-peak-5-event model is our preferred scenario of interpretation, and the inferred slip rate agrees well with the published geologic and geodetic rates, as discussed below.

The 4-peak-5-event model yields an average slip-per-event at the Open Pit Mine and Box Canyon in the range of 2.6–3.1 m, with each event fairly characteristic in size, within uncertainty. As the time between events are quite similar for the past six earthquakes (Table 3), within uncertainty, with the exception of the current open interval of ~300 years, this is expected. If slip events of similar size (characteristic earthquakes) are expected in the Mecca Hills region, two earthquakes may be required to accommodate the accumulated elastic strain. If not, the sSAF may experience a single, much larger earthquake with as much as 5–6 m of displacement to release the past 300-year period of strain accumulation. The presented interpretations cannot definitively answer questions regarding future earthquake timing or magnitude of the sSAF in the Coachella Valley. However, slip-per-event for the paleoearthquakes appears somewhat characteristic with similar inter-event periods, which may indicate the sSAF behaves in a slip-predictable manner.

Our preferred model results in slip rates of 13.5–19.8 mm/yr, with the Open Pit Mine having a larger uncertainty, or range of potential slip rates, than Box Canyon. Behr et al. (2010) resolved the slip rate for the Mission Creek fault at Biskra Palms as 12–22 mm/yr, with a preferred estimate of ~14–17 mm/yr. Similarly, van der Woerd et al. (2006) resolved a rate of 15.9 ± 3.4 mm/yr for the same fault section as Behr et al. (2010), yielding essentially the same results. These rates are indistinguishable from the 4-peak-5-event model with a slip rate of 16.7 ± 3.2 mm/yr, which also coincides with Dingler et al.'s (2016) slip rate estimate of 16–21 mm/yr at Box Canyon. The 5-peak-6-event model significantly underestimates the slip rate, whereas the 4-peak-4 event model significantly overestimates the rate. This provides additional support of the 4-peak-5-event model as the preferred model, although the 5-peak-5-event model is still allowable based on the inferred slip rate (Table 3).

Neither the geologic slip rates nor rates estimated here include far-field slip or off-fault deformation because the measurements were collected only along the main trace of the sSAF and do not account for slip on nearby faults or warping and folding. These rates are a minimum and should be lower than the geodetic rate of 17–19 mm/yr (Lindsey and Fialko, 2013), obtained from modeling a 60° NE dip on the SAF, and certainly lower than earlier geodetic modeling (Fialko, 2006) that assumed a vertical SAF and which derived a higher rate of 25 ± 3 mm/yr.

Displacement estimates of the 4-peak-5-event model suggest the MRE produced 3.2–3.5 m of dextral slip at the Open Pit Mine and Box Canyon, with maximum displacement at Box Canyon of 3.3 m. This displacement is slightly less than the purported 3.75 m of slip attributed to the MRE by Dingler et al. (2016), which occupies the same section of fault at Box Canyon. However, they estimated displacement across the entire fault zone along the double-stranded section, whereas we consider displacement solely along the main trace of the SAF.

6. Conclusions

We acquired a very-high-resolution SfM topographic dataset to interpret fault-related offsets along the sSAF in order to analyze creep behavior and derive slip estimates and slip-per-event for recent earthquakes that ruptured this fault segment. Gaussian (normal) distributions of our collected offset measurements reveal clusters of small offsets of similar size at two sites along the Coachella Valley segment of the sSAF. We infer these clusters to be a product of creep following multiple incision events potentially caused by major storms in 1858, 1939, and tentatively 1976. These small-scale offsets suggest similar creep rates of 3 ± 0.2 mm/yr, with a higher creep rate, ~4 mm/yr, since the most recent incision event. As the Salton Trough has experienced a higher incidence of earthquakes in the past 50 years, we suggest that regional earthquake frequency modulates the short-term creep rate. Through a comparison of rainfall events to El Niño periods, we find that not only were extreme rain events closely related to El Niño conditions, but also that it likely takes a hurricane sized-event or strong tropical storm to incise rills and channels that would be recorded by movement along the sSAF. Slip-per-event for the paleoearthquakes appears somewhat characteristic with similar inter-event periods, which could be indicative of a correlation of time between large earthquakes to amount of slip that occurs in the next event, lending support

to the slip-predictable earthquake recurrence model. Although the current ~300-year open interval has accumulated a large amount of elastic strain, it is not clear that this will result in an unusually large earthquake or whether this strain will be released in multiple earthquakes. The interpreted slip distribution from our preferred model of late Holocene slip-per-event suggests our sites in the Mecca Hills both experienced large events with an average of 2.6–3.1 m of displacement per event for the past five earthquakes, although displacement was not identical at each site. An estimated slip rate of 16.7 ± 3.2 mm/yr derived from this model is comparable to geologic slip rates.

Declaration of competing interest

The authors declare that they have no known competing financial interests or personal relationships that could have appeared to influence the work reported in this paper.

Acknowledgements

This research was supported by the Southern California Earthquake Center (Grant No. 18038, Contribution No. 9088, Rockwell). SCEC is funded by NSF Cooperative Agreement EAR-1600087 and USGS Cooperative Agreement G17AC00047. This work was also supported in part by the Geological Society of America in the form of a graduate student research grant. We appreciate the field support of Faith Burkett and Madison Burvant, who without which this project would not have been possible. We thank Geodetics, Inc. for use of their field equipment and assistance with UAS and RTK GPS surveys. We are grateful to West Coast Sand and Gravel Inc. for access to their open pit mine. Finally, we thank Sean Bemis and Anonymous for their thorough reviews which greatly improved this paper.

Appendix A. Supplementary data

Supplementary data to this article can be found online at https://doi.org/10.1016/j.geomorph.2020.107064.

References

Agisoft LLC, 2018. Agisoft PhotoScan User Manual: Professional Edition, Version 1.4. , pp. 1–127. https://www.agisoft.com/pdf/photoscan-pro_1_4_en.pdf, Accessed date: 1 October 2018.

Allen, C.R., Wyss, M., Brune, J.N., Granz, A., Wallace, R.E., 1972. Displacements on the Imperial, Superstition Hills, and San Andreas faults triggered by the Borrego Mountain earthquake, in the Borrego Mountain earthquake of April 9, 1968: U.S. Geol. Surv. Prof. Pap. 787, 87–104.

Behr, W.M., et al., 2010. Uncertainties in slip-rate estimates for the Mission Creek strand of the southern San Andreas fault at Biskra Palms Oasis, southern California. Geol. Soc. Am. Bull. 122, 1360–1377. https://doi.org/10.1130/B30020.1.

Bemis, S.P., Micklethwaite, S., Turner, D., James, M.R., Akciz, S., Thiele, S.T., Bangash, H.A., 2014. Ground-based and UAV-based photogrammetry: a multi-scale, high-resolution mapping tool for structural geology and paleoseismology. J. Struct. Geol. 69, 163–178. https://doi.org/10.1016/j.jsg.2014.10.007.

Bilham, R., 2019. Continued Measurement of Fault Creep in the San Francisco Bay Area, and Continued Measurement of Creep and Long-Baseline Deformation in Southern and Northern California. https://www.researchgate.net/publication/237549679.

Cayan, D., Redmond, K., Riddle, L., 1999. ENSO and hydrologic extremes in the Western United States. J. Clim. 12, 2881–2893. https://doi.org/10.1175/1520-0442(1999)012<2881:EAHEIT>2.0.CO;2.

Cheng, P., Chaapel, C., 2010. Pan-sharpening and geometric correction of WorldView-2 satellite. GeoInformatics 3, 16–21.

Chenoweth, M., Landsea, C., 2004. The San Diego Hurricane of 2 October 1858. Bull. Am. Meteorol. Soc. 85, 1689–1698. https://doi.org/10.1175/BAMS-85-11-1689.

Clark, M.M., 1984. Map showing recently active breaks along the San Andreas Fault and associated faults between Salton Sea and Whitewater River - Mission Creek, California. U.S. Geological Survey Miscellaneous Investigations Series Map I-1483 (2 sheets, scale 1:24,000).

DigitalGlobe, 2018. Accuracy of WorldView products. https://dg-cms-uploads-production.s3.amazonaws.com/uploads/document/file/38/DG_ACCURACY_WP_V3.pdf, Accessed date: 1 November 2019.

Dingler, J., Driscoll, N., Seitz, G., Kent, G., 2016. New quantitative constraints on Holocene slip rate and surface displacement along the southern San Andreas fault in the Mecca Hills using ground based terrestrial laser scanning: in Anderson. In: Anderson, R., Ferriz, H. (Eds.), Applied Geology in California: Association of Environmental and Engineering Geologists Special Publication. vol. 26, pp. 809–832.

DJI, 2019a. Phantom 4 Pro Specs. https://www.dji.com/phantom-4-pro/info#specs, Accessed date: 1 October 2019.

DJI, 2019b. Matrice 600 Pro Specs. https://www.dji.com/matrice600-pro/info, Accessed date: 1 December 2019.

EMLID, 2020. Reach RS+ (EMLID). https://emlid.com/reachrs/, Accessed date: 20 January 2020.

Fattaruso, L.A., Cooke, M.L., Dorsey, R.J., 2014. Sensitivity of uplift patterns to dip of the San Andreas fault in the Coachella Valley, California. Geosphere 10 (6), 1235–1246. https://doi.org/10.1130/GES01050.1.

Fialko, Y., 2006. Interseismic strain accumulation and the earthquake potential on the southern San Andreas fault system. Nature 441, 968–971. https://doi.org/10.1038/nature04797.

Fialko, Y., personal comm., 05/14/2019.

Fletcher, et al., 2014. Assembly of a large earthquake from a complex fault system: surface rupture kinematics of the 4 April 2010 El Mayor–Cucapah (Mexico) Mw 7.2 earthquake. Geosphere 10 (3), 1–31. https://doi.org/10.1130/GES00933.1.

Fumal, T.E., 2002. Timing of large earthquakes since A.D. 800 on the Mission Creek Strand of the San Andreas Fault Zone at Thousand Palms Oasis, near Palm Springs, California. Bull. Seismol. Soc. Am. 92, 2841–2860. https://doi.org/10.1785/0120000609.

Garcia-Herrera, R., Barriopedro, D., Hernández, E., Diaz, H.F., Garcia, R.R., Prieto, M. R., Moyano, R., 2008. A chronology of El Niño events from primary documentary sources in northern Peru. J. Clim. 21, 1948–1962. https://doi.org/10.1175/2007JCLI1830.1.

Javernick, L., Brasington, J., Caruso, B., 2014. Modeling the topography of shallow braided rivers using structure-from-motion photogrammetry. Geomorphology 213, 166–182. https://doi.org/10.1016/j.geomorph.2014.01.006.

Johnson, K., Nissen, E., Saripalli, S., Arrowsmith, J.R., McGarey, P., Scharer, K., Williams, P., Blisniuk, K., 2014. Rapid mapping of ultrafine fault zone topography with structure from motion. Geosphere 10, 969–986. https://doi.org/10.1130/GES01017.1.

Kaneko, Y., Fialko, Y., Sandwell, D.T., Tong, X., Furuya, M., 2013. Interseismic deformation and creep along the central section of the North Anatolian Fault (Turkey): InSAR observations and implications for rate-and-state friction properties. J. Geophys. Res. Solid Earth 118, 316–331. https://doi.org/10.1029/2012JB009661.

Lindsey, E.O., Fialko, Y., 2013. Geodetic slip rates in the southern San Andreas Fault system: effects of elastic heterogeneity and fault geometry. J. Geophys. Res. Solid Earth 118, 689–697.

Lindsey, E.O., Fialko, Y., Bock, Y., Sandwell, D.T., Bilham, R., 2014. Localized and distributed creep along the southern San Andreas Fault. J. Geophys. Res. Solid Earth 119, 7909–7922. https://doi.org/10.1002/2014JB011275.

Ludwig, L.G., Akciz, S., Noriega, G., Zielke, O., Arrowsmith, R., 2010. Climate-modulated channel incision and rupture history of the San Andreas Fault in the Carrizo Plain. Science 327 (5969), 1117–1119. https://doi.org/10.1126/science.1182837.

Maps Made Easy (MME), 2020. https://www.mapsmadeeasy.com/, Accessed date: 20 January 2020.

National Agriculture Imagery Program (NAIP), 2016. U.S. Department of Agriculture's Farm Service Agency. https://doi.org/10.5066/F7QN651G.

National Weather Service, 2017. A History of Significant Weather Events in Southern California. , pp. 1–152. https://www.weather.gov/media/sgx/documents/weatherhistory.pdf (accessed December 2018).

National Weather Service Climate Report, 2019. Thermal Airport California Climate Summary for 14 February 2019. https://w2.weather.gov/climate/index.php?wfo=sgx (accessed April 2019).

Nissen, E., Arrowsmith, R., Crosby, C., 2016. GSA: introduction to structure from motion (SfM) photogrammetry for earth science research and education short course. Article ID: 859. http://kb.unavco.org/kb/article/2016-gsa-introduction-to-structure-from-motion-sfm-photogrammetry-for-earth-science-research-and-education-short-course-859.html.

NOAA Earth System Research Laboratory, 2019. Physical Sciences Division, 2019, El Niño Southern Oscillation (ENSO). https://www.esrl.noaa.gov/psd/enso/climaterisks/years/top24enso.html (accessed March 2019).

Ortega, C., Easton, G.V., Rojas, M., Rutllant, J., Muñoz, P., Lange, C.B., Pantoja, S., Dezileau, L., Ortlieb, L., 2019. Extreme ENSO-driven torrential rainfalls at the southern edge of the Atacama Desert during the Late Holocene and their projection into the 21th Century. Global and Planetary Change 175, 226–237.

Philibosian, B., Fumal, T., Weldon, R., 2011. San Andreas Fault earthquake chronology and Lake Cahuilla history at Coachella, California. Bull. Seismol. Soc. Am. 101, 13–38. https://doi.org/10.1785/0120100050.

Rockwell, T., Lindvall, S., Dawson, T., Langridge, R., Lettis, W., Klinger, Y., 2002. Lateral offsets on surveyed cultural features resulting from the 1999 İzmit and Düzce Earthquakes, Turkey. Bull. Seismol. Soc. Am. 92, 79–94.

Rockwell, T.K., Ben-Zion, Y., 2007. High localization of primary slip zones in large earthquakes from paleoseismic trenches: observations and implications for earthquake physics. J. Geophys. Res. Solid Earth 112 (10), 1–12. https://doi.org/10.1029/2006JB004764.

Rockwell, T.K., Klinger, Y., 2013. Surface rupture and slip distribution of the 1940 Imperial Valley Earthquake, Imperial Fault, Southern California: implications for rupture segmentation and dynamics. Bull. Seismol. Soc. Am. 103, 629–640. https://doi.org/10.1785/0120120192.

Rockwell, T.K., Pinault, C.T., 1986. Holocene slip events of the southern Elsinore fault, Coyote Mountains, southern California. In: Ehlig, P. (Ed.), Neotectonics and Faulting in Southern California: Geological Society of American Guidebook for the Cordilleran Section Meeting in Los Angeles, pp. 193–196.

Rockwell, T.K., Meltzner, A.J., Haaker, E.C., 2018. Dates of the two most recent surface ruptures on the southernmost San Andreas Fault recalculated by precise dating of Lake

Cahuilla dry periods dates of the two most recent surface ruptures on the southernmost SAF recalculated. Bull. Seismol. Soc. Am. 108, 2634–2649. https://doi.org/10.1785/0120170392.

Rymer, M.J., 2000. Triggered surface slips in the Coachella Valley area associated with the 1992 Joshua Tree and Landers, California, earthquakes. Bull. Seismol. Soc. Am. 90, 832–848. https://doi.org/10.1785/0119980130.

Rymer, M.J., Boatwright, J., Seekins, L.C., Yule, J.D., Liu, J., 2002. Triggered surface slips in the Salton Trough associated with the 1999 Hector Mine, California, earthquake. Bull. Seismol. Soc. Am. 92, 1300–1317. https://doi.org/10.1785/0120000935.

Rymer, M.J., Treiman, J.A., Kendrick, K.J., Lienkaemper, J.J., Weldon, R.J., Bilham, R., Wei, M., Fielding, E.J., Hernandez, J.L., Olson, B.P.E., Irvine, P.J., Knepprath, N., Sickler, R.R., Tong, X., Siem, M.E., 2011. Triggered surface slips in southern California associated with the 2010 El Mayor-Cucapah, Baja California, Mexico, earthquake. U.S. Geological Survey Open-File Report 2010–1333 and California Geological Survey Special Report 221, p. 62.

Salisbury, J.B., Haddad, D.E., Rockwell, T., Arrowsmith, J.R., Madugo, C., Zielke, O., Scharer, K., 2015. Validation of meter-scale surface faulting offset measurements from high-resolution topographic data. Geosphere 11, 1884–1901. https://doi.org/10.1130/GES01197.1.

Scharer, K.M., Salisbury, J.B., Arrowsmith, J.R., Rockwell, T.K., 2014. Southern San Andreas Fault evaluation field activity: approaches to measuring small geomorphic offsets–challenges and recommendations for active fault studies. Seismol. Res. Lett. 85, 68–76. https://doi.org/10.1785/0220130108.

Schwartz, D.P., Coppersmith, K.J., 1984. Fault behaviour and characteristic earthquakes: examples from the Wasatch and San Andreas fault zones. J. Geophys. Res. 89, 5681.

Shifflett, H., Gray, M.G., Grannell, R., Ingram, B.L., 2002. New evidence on the slip rate, renewal time, and late Holocene surface displacement, southernmost San Andreas fault, Mecca Hills, California. Bull. Seismol. Soc. Am. 92, 2861–2877. https://doi.org/10.1785/0120000601.

Sieh, K.E., Williams, P.L., 1990. Behavior of the southernmost San Andreas Fault during the past 300 years. J. Geophys. Res. Solid Earth 95, 6629–6645. https://doi.org/10.1029/JB095iB05p06629.

Southern California Earthquake Data Center (SCEDC) at the California Institute of Technology, 2017. Significant earthquakes and faults: chronological earthquake index. https://scedc.caltech.edu/significant/chron-index.html, Accessed date: 1 May 2019.

Sylvester, A.G., Smith, R.R., 1976. Tectonic transpression and basement-controlled deformation in San Andreas Fault Zone, Salton Trough, California. Am. Assoc. Pet. Geol. Bull. 60, 2081–2102.

Sylvester, S.G., Damte, A., 1999. Geology of the Central Mecca Hills, in Sylvester, A.G. (field trip leader), Rifting, Transpression, and Neotectonics in the Central Mecca Hills, Salton Trough, California: SEPM Society for Sedimentary Geology Fall Field Trip Guidebook. 1999 pp. 18–25.

Teran, O.J., Fletcher, J.M., Oskin, M.E., Rockwell, T.K., Hudnut, K.W., Spelz, R.M., Akciz, S.O., Hernandez-Flores, A.P., Morelan, A.E., 2015. Geologic and structural controls on rupture zone fabric: a field-based study of the 2010 Mw 7.2 El Mayor–Cucapah earthquake surface rupture. Geosphere 11 (3), 899–920. https://doi.org/10.1130/GES01078.1.

The Telegraph-Herald, Tropical storm winding down, Dubuque, Iowa, September 12, 1976, https://news.google.com/newspapers?id=f_ZQAAAAIBAJ&sjid=kcEMAAAAIBAJ&pg=5235,1578906&dq=hurricane+kathleen+ocotillo&hl=en (accessed May 2019).

Treiman, J.A., Kendrick, K.J., Bryant, W.A., Rockwell, T.K., McGill, S.F., 2002. Primary surface rupture associated with the Mw 7.1 16 October 1999 Hector Mine Earthquake, San Bernardino County, California. Bull. Seismol. Soc. Am. 92 (4), 1171–1191. https://doi.org/10.1785/0120000923.

Tymofyeyeva, E., Fialko, Y., Jiang, J., Xu, X., Sandwell, D., Bilham, R., Rockwell, T., Blanton, C., Burkett, F., Gontz, A., Moafipoor, S., 2019. Slow slip event on the southern San Andreas Fault triggered by the 2017 Mw 8.2 Chiapas (Mexico) earthquake. J. Geophys. Res. Solid Earth 124. https://doi.org/10.1029/2018JB016765.

U.S. Geological Survey and California Geological Survey (CGS), 2018. Quaternary Fault and Fold Database for the United States. from USGS web site. http://earthquake.usgs.gov/regional/qfaults/, Accessed date: 8 January 2018.

Waters, Stephen D., 1997. Flood control District of Maricopa County, Tropical Storm Nora report. https://web.archive.org/web/20010223010517/http://156.42.96.39/alert/nora/nora_rpt.html, Accessed date: 1 May 2019.

Wei, M., Sandwell, D., Fialko, Y., Billah, R., 2011. Slip on faults in the Imperial Valley triggered by the 4 April 2010 Mw 7.2 El Major-Cucapah earthquake revealed by InSAR. Geophys. Res. Lett. 38 (1), 1–6 L01308. https://doi.org/10.1029/2010GL045235.

Weldon, R., McCalpin, J., Rockwell, T.K., 1996. Chapter 6: paleoseismology of strike-slip tectonic environments. International Geophysics. vol. 95, pp. 421–496. https://doi.org/10.1016/S0074-6142(09)95006-9.

Weldon, R.J., Scharer, K.M., Fumal, T.E., Biasi, G.P., 2004. Wrightwood and the earthquake cycle: What a long recurrence record tells us about how faults work. GSA Today 14, 12–16.

Westoby, M.J., Brasington, J., Glasser, N.F., Hambrey, M.J., Reynolds, J.M., 2012. 'Structure-from-Motion' photogrammetry: a low-cost, effective tool for geoscience applications. Geomorphology 179, 300–314. https://doi.org/10.1016/j.geomorph.2012.08.021.

Williams, P.L., McGill, S.F., Sieh, K.E., Allen, C.R., Louie, J.N., 1988. Triggered slip along the San Andreas fault after the 8 July 1986 North Palm Springs earthquake. Bull. Seismol. Soc. Am. 78 (3), 1112–1122.

van der Woerd, J., Klinger, Y., Sieh, K., Tapponnier, P., Ryerson, F.J., Mériaux, A.S., 2006. Long-term slip rate of the southern San Andreas Fault from ^{10}Be-^{26}Al surface exposure dating of an offset alluvial fan. J. Geophys. Res. 111 (B4). https://doi.org/10.1029/2004JB003559.

Zielke, O., Arrowsmith, J.R., Ludwig, L.G., Akciz, S.O., 2010. Slip in the 1857 and earlier large earthquakes along the Carrizo Plain, San Andreas Fault. Science 327, 1119–1122. https://doi.org/10.1126/science.1182781.

Bulletin of the Seismological Society of America, Vol. 101, No. 1, pp. 13–38, February 2011, doi: 10.1785/0120100050

San Andreas Fault Earthquake Chronology and Lake Cahuilla History at Coachella, California

by Belle Philibosian, Thomas Fumal, and Ray Weldon

Abstract The southernmost ~100 km of the San Andreas fault has not ruptured historically. It is imperative to determine its rupture history to better predict its future behavior. This paleoseismic investigation in Coachella, California, establishes a chronology of at least five and up to seven major earthquakes during the past ~1100 yr. This chronology yields a range of average recurrence intervals between 116 and 221 yr, depending on assumptions, with a best-estimate average recurrence interval of 180 yr. The most recent earthquake occurred c.1690, more than 300 yr ago, suggesting that this stretch of the fault has accumulated a large amount of tectonic stress and is likely to rupture in the near future, assuming the fault follows a stress renewal model. This study also establishes the timing of the past 5–6 highstands of ancient Lake Cahuilla since A.D. 800. We found that earthquakes do not tend to occur at any particular stage in the lake cycle.

Introduction

The Coachella Valley section of the San Andreas fault (SAF), between San Gorgonio Pass and the Imperial Valley, is the only noncreeping portion of the 1300-km-long fault that has not ruptured in a major earthquake during historical time (Fig. 1). For this reason, the hazard potential and likely timing of its next earthquake are poorly constrained in comparison to other sections of the fault, since these parameters must be determined solely from paleoseismology. Paleoseismic analysis of the southernmost SAF is particularly important because a rupture on this fault segment has the potential to severely damage the adjacent Los Angeles metropolitan area, particularly if the rupture propagates northward through the San Gorgonio Pass (Olsen *et al.*, 2006). In addition, rupture history is key to resolving important issues in fault behavior such as periodicity, segmentation, and characteristic versus random rupture behavior (discussed in Weldon *et al.*, 2004). Toward these ends, we have constructed an earthquake chronology for the past ~1200 yr for the southernmost SAF based on a new paleoseismic investigation conducted in the city of Coachella, California.

To date, there have been three other paleoseismic investigations on the SAF south of the San Gorgonio Pass (Fig. 1c), two of which have yet to be completely published. Sieh (1986) reported four earthquakes since A.D. 1000 from an investigation in the city of Indio, only a few kilometers northwest of the Coachella site. An ongoing investigation at Salt Creek, 45 km to the southeast of the Coachella site, includes evidence for six earthquakes since A.D. 800 (Williams, 2009), but specific dates for these have not yet been published. To date, the best record of Coachella Valley earthquakes comes from an extensive investigation 20 km to the northwest of the Coachella site at the Thousand Palms oasis, where Fumal, Rymer, and Seitz (2002) described evidence for five earthquakes since A.D. 800. However, in that region there are at least two active strands of the fault (Banning and Mission Creek), and only the Mission Creek strand passes through the Thousand Palms site. The Mission Creek strand gradually dies out to the northwest, with slip becoming concentrated on the Banning strand. While the Mission Creek strand has a slip rate between 12 and 22 mm/yr at the Biskra Palms site, which is located in the junction zone between the two strands (Behr *et al.*, 2010), its slip rate at the Thousand Palms site is only a few millimeters per year (Fumal, Rymer, and Seitz, 2002), with the Banning strand likely accommodating the majority of the slip. The two strands probably move in concert, but it is possible that the Thousand Palms site record is missing earthquakes that produced surface rupture only on the Banning strand. The Coachella site, located to the southeast in the region where the SAF is singly stranded, does not suffer from this source of ambiguity.

The most recent earthquake recorded at the Indio site has been dated to approximately A.D. 1680 (Sieh, 1986), more than 300 yr ago. This is significantly longer than most estimates of average recurrence interval of on other segments of the fault, which range from ~100 to 250 yr (e.g., Sieh *et al.*, 1989; Weldon *et al.*, 2004; Weldon *et al.*, 2005; Kelson *et al.*, 2006; Goldfinger *et al.*, 2008; Akciz *et al.*, 2009). This open interval is about as long as the longest interval between earthquakes estimated by Sieh (1986) at the Indio site, and longer than any of the estimated interseismic intervals at the Thousand Palms site (Fumal, Rymer, and Seitz, 2002).

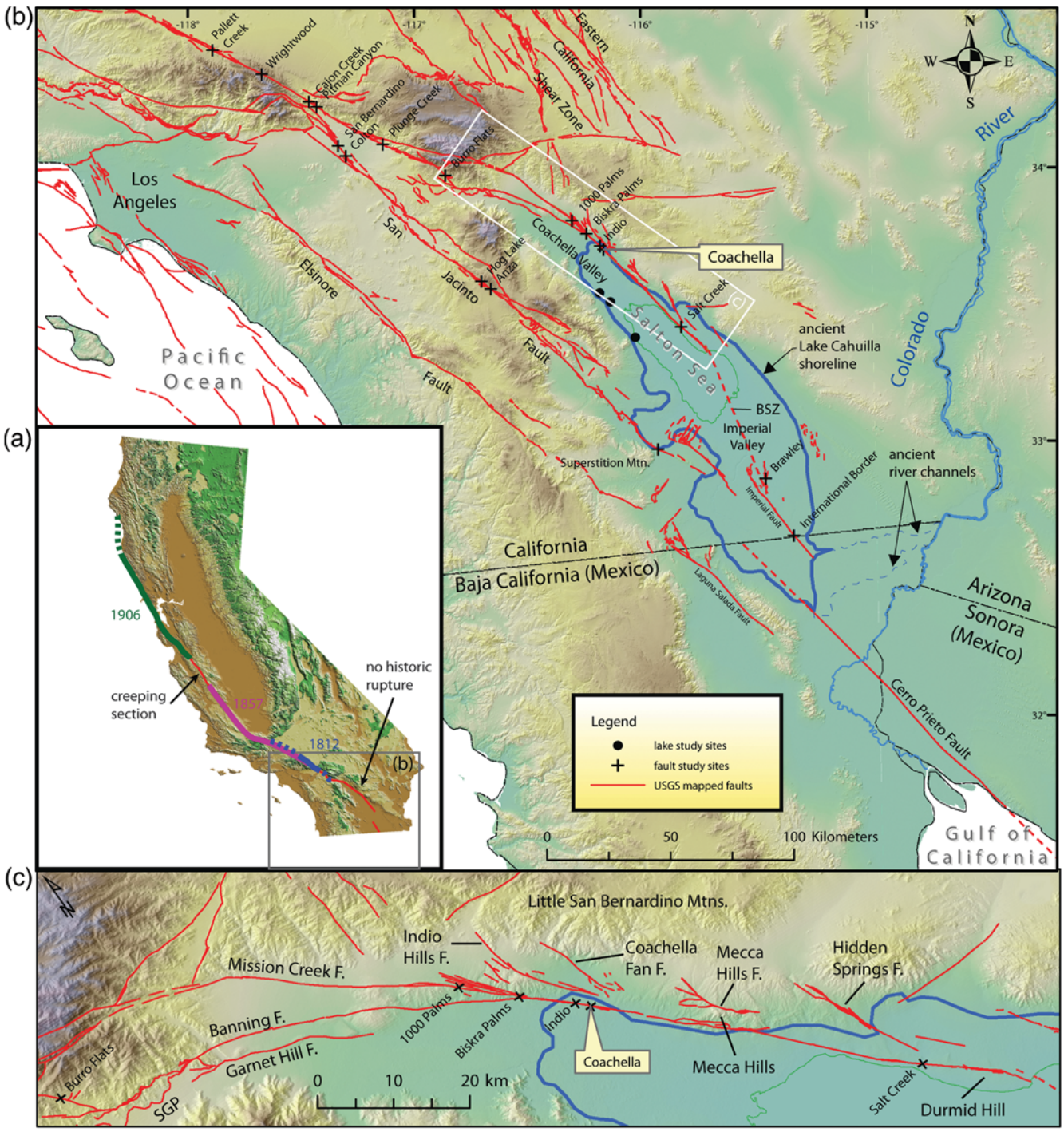

Figure 1. (a) Shaded relief map of California showing large historic ruptures of the San Andreas Fault. (b) Shaded relief map of southern California showing known Quaternary faults (from U.S. Geological Survey and California Geological Survey, 2006), major fault study sites, ancient Lake Cahuilla shoreline (heavy blue line), lake study sites (from Waters, 1983), and ancient alternate channels of the Colorado River which periodically filled the lake in the past. Only faults that are extensions of the San Andreas fault system are shown in Mexico. BSZ: Brawley seismic zone. (c) Shaded relief map showing the Coachella Valley section of the SAF, and associated nearby faults. SGP: San Gorgonio Pass.

This long period of quiescence has led many to suspect that an unusually large amount of elastic strain has built up along the southern San Andreas segment, and thus it is likely to produce a large to great (M_w 7–8) earthquake in the near future (Working Group on California Earthquake Probabilities, 2008).

The Coachella Paleoseismic Site

The Coachella site lies just southwest of the junction of Dillon Road and Avenue 44 in the city of Coachella. It is one of the few as yet undeveloped pieces of land on a stretch of the fault that is attractive for paleoseismology because slip

is concentrated on a single strand, whereas the structure diverges into several strands and becomes increasingly complex to the northwest toward San Gorgonio Pass (U.S. Geological Survey and California Geological Survey, 2006). The site lies at ~9 m elevation, just below the 12-m-high shoreline of the ancient Lake Cahuilla, which has intermittently filled by natural diversion of the Colorado River over the past several thousand years (e.g., Van de Kamp, 1973; Waters, 1983). While this site is one of the best-preserved stretches of the fault in the vicinity, there have been many anthropogenic alterations to the natural landscape. Now largely obliterated in this area, the ancient highstand shoreline can easily be identified ~0.5 km north of the site on stereo aerial photographs of the region taken in 1939 (Fig. 2a), marked by an elevated beach berm and vegetated dunes. The Indio Canyon wash (which drains alluvial fans exiting the Little San Bernardino Mountaing to the north) passes through the site and is prominent in this photograph. However, when the Coachella Canal was constructed in the 1940s the wash outflow was permanently routed through flood control structures into Wasteway Number 3 to the west (Fig. 2b). The trace of the SAF is also easily identifiable in both the 1939 and 1951 photos as a sharp color and/or vegetation contrast. Because of extensive agriculture and other development, the surface trace is no longer easily identifiable in most of the area covered by these photographs (Fig. 2c). Also, the diversion of ground and surface water by flood control structures has led to a loss of vegetation, which has made the surface trace less prominent even in places where it has not been directly disturbed. However, small scarps up to 50 cm in height along with a marked contrast in vegetation density were still preserved at the minimally disturbed Coachella site. High-resolution topographic data from the B4 LiDAR (Light Detection and Ranging) dataset, collected in 2004 (Bevis *et al.*, 2006), show these and other features in detail (Fig. 3).

During an extensive Alquist-Priolo investigation on this property in March–April 2006, we were granted permission to use the trenches for a more detailed paleoseismic analysis. Though our analysis of this site was limited by time constraints and by lack of control over the excavation locations and procedures, this was a rare opportunity to work in very long, deep trenches excavated across the SAF trace within lacustrine and alluvial deposits. Three trenches trending N40°E, approximately perpendicular to the fault, were excavated across the entire property (locations shown in Fig. 3). The trenches were 7–8 meters deep and benched at ~1.5 m depth intervals, making the riser walls ~10 m apart at the top and ~2 m apart at the bottom (Fig. 4). The western most trench did not cross the main fault, with only minor faulting apparent at its northeastern end and essentially no deformation over the 400-m length of trench to the southwest. The easternmost trench revealed two fairly simple fault zones ~75 m apart, with no other deformation or offset visible along the 200-m length of the trench. Because datable material was rare and extensive erosion between lacustrine

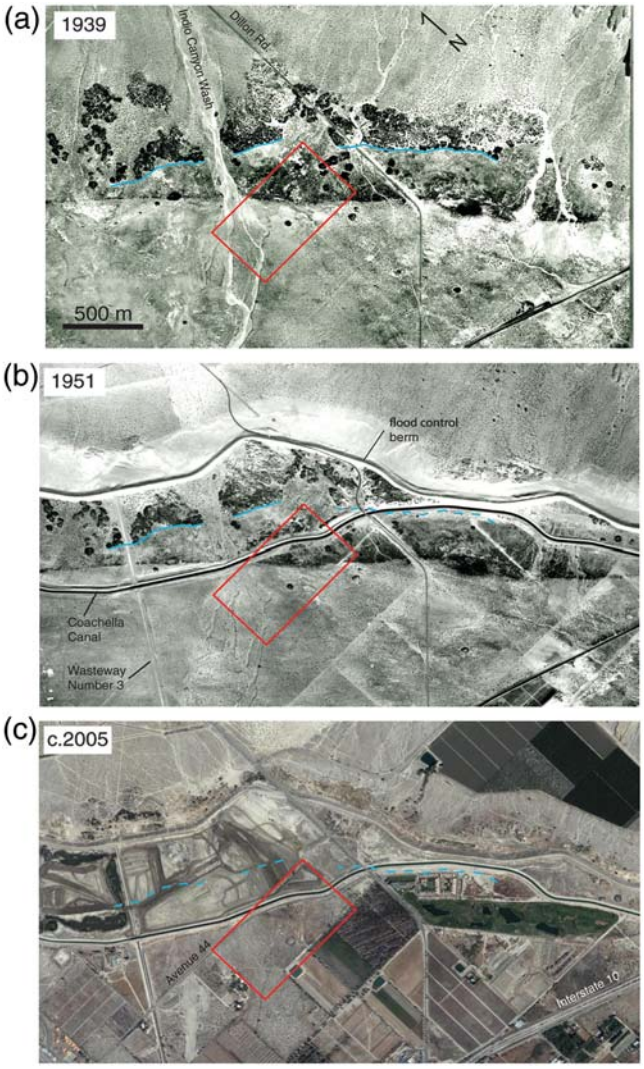

Figure 2. Historical aerial views of the study area. Ancient Lake Cahuilla highstand shoreline is outlined in blue and the Coachella site (area shown in Fig. 3) in red. The SAF trace is visible as a striking vegetation lineament in the two earlier photographs, but is preserved only at the Coachella site in the modern photograph. (a),(b) Photos courtesy of Sladden Engineering; (c) photo from Google Earth.

intervals makes the stratigraphic section incomplete, this trench was less than ideal for paleoseismic analysis. We photographed the walls of the eastern trench but did not analyze them in detail. The focus of our work was a detailed analysis of the three fault zones exposed in the central trench, where a largely complete stratigraphic section is preserved within a fault-bounded depression containing plentiful datable material. We found no significant deformation along the trench walls that extended for 250 m to the southwest of the logged section, only widely spaced fractures with little to no apparent vertical displacement. Exposure to the northeast of the 70-m logged section was limited by Avenue 44 and the Coachella Canal, so it is possible that there are additional minor fault strands in that direction, but none are obvious on the 1939 aerial photo (Fig. 2a). Overall, we are confident

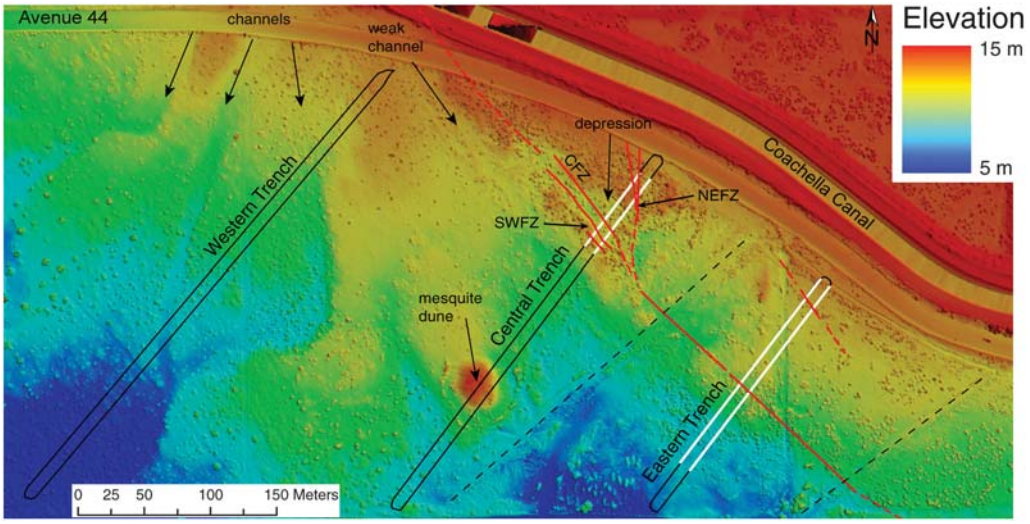

Figure 3. LiDAR topography (from the B4 project) of the study site. Trenches excavated for the 2006 Alquist–Priolo study are outlined in black. We photo-documented the trench walls marked in white. Walls in the central trench were analyzed in detail; in the eastern trench only the areas in the immediate vicinity of the two fault zones were analyzed in detail. Faults are mapped based on geomorphology/vegetation and trench exposures, including locations based on two earlier trenches excavated by Sladden Engineering in 2004 (Sladden Engineering, personal commun., 2006). The spoils from these earlier trenches can be seen in the LiDAR topography and are marked by dashed black lines. The now-blocked-off channels of Indio Canyon wash are visible at the left, as well as a weak channel along the fault scarp that was most likely the source of the thick channel deposit (unit 7S southwest) present at the southwest end of the logged portion of the central trench. The structural depression between the fault traces can be seen as a topographic low near the northeast end of the central trench. SWFZ: southwest fault zone, CFZ: central fault zone, NEFZ: northeast fault zone.

that our study encompasses all the major strands of the fault at this location.

We laid a 1 by 0.5 m string grid over a 70-m-long section of the central trench, covering each of the 5 bench risers on each wall. Each grid rectangle was individually photographed, and the ~1600 photographs were assembled into mosaics for each wall (Philibosian *et al.*, 2009). This area is unusually rich in datable materials, including organic soil and/or burn horizons (which theoretically provide *in situ* carbon-14 dates), plentiful detrital charcoal, and several types of freshwater shells from Lake Cahuilla.

Figure 4. View looking southwest along the central trench. Note that the fault is a highly effective groundwater barrier: the water table is about 6 m below the surface northeast of the central fault zone, which crosses the trench where the people are standing, but the trench is dry to the southwest. The benched excavation revealed a total vertical exposure of ~7 m.

Stratigraphy

The strata visible in the trench wall exposures alternate between fine-grained, often laminar deposits of Lake Cahuilla and subaerial fluvial and aeolian deposits that accumulated during periods when the lake receded below the elevation of the site. The exposed sediments are unlithified and composed largely of quartz and feldspar grains; fine-grained sediments are almost universally highly micaceous. Because this site is just a few meters below the highstand shoreline of the lake, lacustrine deposits represent periods of time when the lake basin was almost completely full (limited by the 12-meter-elevation sill separating the Salton Trough from regions draining to the Gulf of California). Thus, subaerial intervals do not necessarily imply that the entire lake basin desiccated, only that the influx from the Colorado River ceased for a time. The exposures revealed deposits from at least five lake highstands with intervening subaerial deposits. Figure 5 shows a generalized stratigraphic section for the Coachella site with descriptions of each unit. Each lacustrine unit is interpreted to be the product of a single lake highstand, while subunits represent variations in sediment delivery or other secondary environmental factors. The lacustrine-subaerial cycles are numbered in order of increasing stratigraphic depth with the letters S and L indicating subaerial and lacustrine layers, respectively.

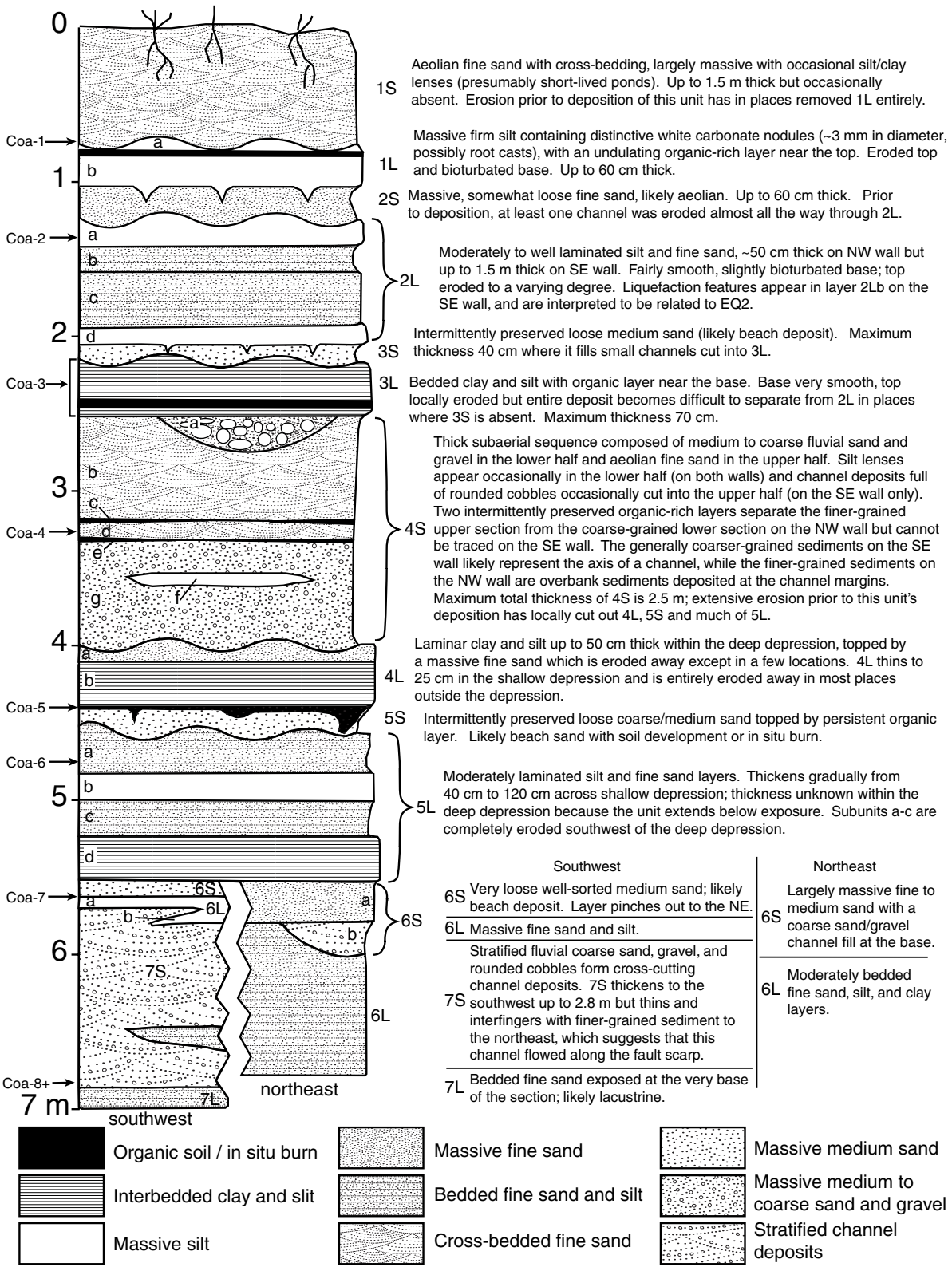

Figure 5. Generalized stratigraphic section of central trench exposures. Unit thickness is averaged over all logged exposures, excluding highly eroded areas. L and S indicate lacustrine and subaerial sediment, respectively. Wavy lines represent erosional contacts. Units below 5L are exposed only at the northeast and southwest ends of the logged exposures outside the structural depression, making correlation questionable, so separate stratigraphic sections are shown for each end. Numbered earthquake horizons (prefaced with Coa-) are indicated on the left side of the column.

Thicknesses of units shown in this section represent the average over the logged exposures (excluding areas where units were clearly substantially eroded). Variations from the average are large and the full range of unit thickness is noted in the description. Both the lacustrine and subaerial deposits commonly thicken across the depression-bounding faults, becoming 2 to 3 times thicker within the depression. This depression provides the most complete section without obvious hiatuses in deposition or major removal of section by erosion. In contrast, outside the depression, several of the lacustrine units are thinned or entirely removed by erosion. The high-resolution stratigraphy preserved within the depression includes many subunits that cannot be discerned outside the depression. These depression-filling deposits preserve the best expression of individual earthquake horizons.

Lacustrine deposits are identified by cohesive, often thinly bedded layers of well-sorted fine sand, silt, and clay. Ripple marks are present near the bases of some lacustrine units, likely reflecting lake transgression. It is generally believed that all lakes during this period initially rose to the same 12-meter level, controlled by the stable height of the sill formed by the Colorado River delta (e.g., Waters, 1983). Therefore, when the lake was at highstand, the depositional surface at this site would have been at a minimum of 3 meters depth, and even deeper for older units when less sediment had accumulated, meaning that the lacustrine deposition would not have been interrupted by very small fluctuations in lake level or shoreline processes such as wave action. The lower contacts of lacustrine units are generally smooth, though locally bioturbated (most likely by Lake Cahuilla mollusks). Internal erosional contacts never occur within a single lake unit. These fine-grained, well-bedded lacustrine sediments were additionally identifiable based on their tendency to retain moisture, causing them to appear considerably darker than the dry subaerial units and to precipitate a crust of salt crystals in a matter of hours as the exposed trench walls dried.

Subaerial deposits at this site include both aeolian and fluvial sediments. Aeolian deposits are characterized by loose, massive, locally cross-bedded, well-sorted fine sand and silt, while fluvial deposits consist of loose, thickly bedded, moderately to poorly sorted medium to coarse sand, pebbles, and rounded cobbles. The lower contacts of subaerial units are generally erosional contacts, often including channels carved into the underlying lacustrine units. Internal erosional contacts are common in the subaerial units, in contrast to the lacustrine units. Rip-up clasts and local mud cracks further support the identification of these deposits as subaerial. The fluvial deposits likely came from Indio Canyon wash. Sediment lobes and fluvial channels associated with this drainage remain visible in the topography (see Fig. 3). Influx from the wash likely produced a high local rate of sedimentation at this site (averaging ~5 mm/yr based on the dates obtained and presented in the following text). A few layers composed of very loose, massive, well-sorted medium sand are likely beach deposits (3S, 5S, and 6S southwest on Fig. 5). This interpretation is supported by their location as relatively thin intervals between lacustrine deposits.

Layer thickness and facies vary tremendously even over distances of a few meters, making lateral correlation of some units challenging. (Unfortunately, no fault-parallel trenches were available for this study). The uppermost units (1S and 1L) are sufficiently undeformed and intact so that we may confidently correlate them across the trench. We are also fairly confident in our cross-trench correlations of the lower units (numbered 4 and 5), because the trench walls were only ~2 m apart at the base. However, the intermediate units (numbered 2 and 3) are at levels where the trench was 7–8 m wide and are displaced substantially across faults, so cross-trench correlations (especially of individual subunits within a lake deposit) are not completely certain. In some cases, subunits that appear on one wall are entirely absent on the opposite wall, or change substantially in character over the intervening distance to be unrecognizable. Units below 5L are exposed only at the northeast and southwest ends of the logged exposures, outside the depositional depression. Substantial differences in the character of these deposits make correlation questionable across the depression so separate sections are shown for the southwest and northeast areas. The age of these deposits (discussed in the following text) coupled with slip rate estimates of at least 1 cm/yr (van der Woerd *et al.*, 2006; Behr *et al.*, 2010) implies that they have been laterally offset across the fault by tens of meters, juxtaposing sediments that potentially correlate in time but were formed in substantially different local environments. Unfortunately, the northeast section was almost entirely devoid of datable material, so correlation between the two basal sections by means of age control is not possible.

Fault Structure

Figure 6 presents summary logs of both walls of the central trench showing the geometry of the sedimentary deposits and fault zone structure. The three fault zones exposed in the central trench form a structural depression with reverse separation at its margins. The central and southwestern fault zones, striking approximately N40°W, bound the deepest ~10-m-wide portion of the depression, in which units are as much as three times thicker than corresponding units outside the depression to the southwest. While all faults are dominantly strike-slip, the down-dropping of the block between the faults clearly created considerable accommodation space for additional sediment, suggesting a transtensional pull-apart basin. The slight right-step of the fault trace visible in the 1939 aerial photo (Fig. 2a) also suggests a transtensional environment. However, both bounding faults dip 50°–60° away from the depression and thus have minor reverse vertical separation rather than the expected normal vertical separation. These faults are inferred to reverse their

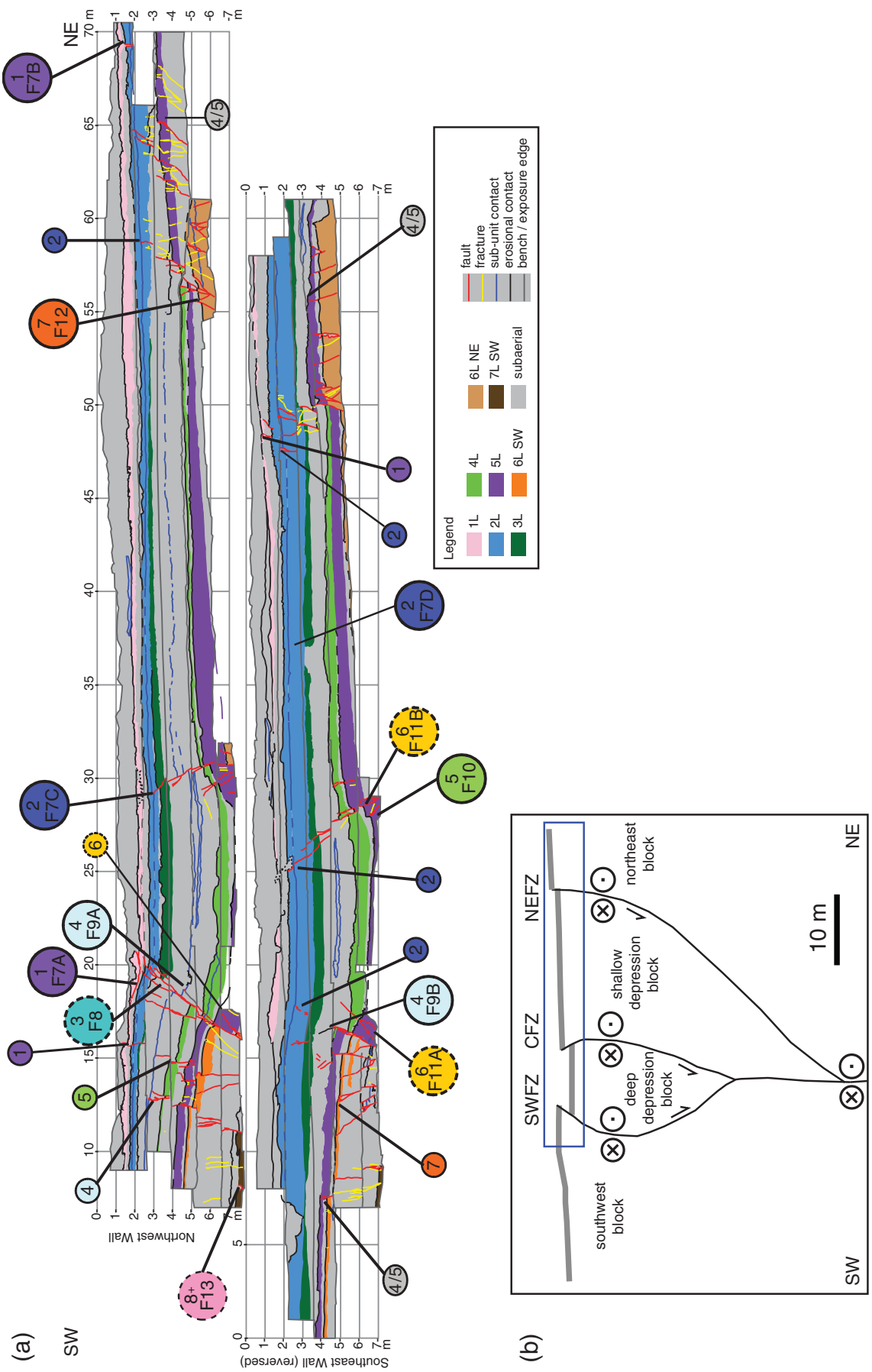

Figure 6. (a) Summary logs of the central trench showing the geometry of the sedimentary deposits and fault zone structure. View looking northwest; southeast wall has been reversed. Numbered circles show locations of earthquake evidence and Figures 7–13. (b) Schematic representation (looking northwest) of the inferred subsurface tulip structure. Box outlined in blue shows area exposed in the trench wall. The southwest, central, and northeast fault zones exposed in the central trench are abbreviated SWFZ, CFZ, and NEFZ, respectively. The overall downward surface slope from northeast to southwest is the regional gradient and is not related to local fault structure.

dip direction at depth to form a tulip structure (Naylor *et al.*, 1986; Sylvester, 1988) as shown in Figure 6b.

Northeast of the central fault zone, the depression shallows gradually for about 30 m (represented by the gradual thinning of deposits) until it is truncated against the complex northeastern fault zone, which strikes approximately northward, far from perpendicular to the trench walls (see Fig. 3). This fault zone dips very steeply to the west. The consistent east-side-up separations suggest that this strand has a normal component. Sediments are thinner and more substantially eroded in the hanging wall of this fault zone outside the depression. The strike of this fault zone suggests that it may connect to another strand of the SAF farther northeast (which, if it exists, would now be covered by Avenue 44 or the Coachella Canal), or even may be related to slip transfer off the main SAF to the Indio Hills fault, a nearby subparallel structure that bounds the Indio Hills on the northeast (see Fig. 1c). Unfortunately, the trace of this northward-striking strand is not clearly visible on the aerial photographs.

There is a notable difference between the southwest fault zone on the northwest and southeast walls. On the northwest wall, the southwest fault zone (SWFZ) appears to be the most active of the three, with two major strands breaking the three most recent lake deposits and larger apparent separation of units. However, on the southeast wall the youngest layer faulted by the SWFZ is 4S, with only minor fractures breaking the 2L and 3L lake deposits and none at all breaking the youngest lake deposit, though 2L and 3L do appear to be monoclinally folded. This suggests that this strand may be dying out to the southeast, which is somewhat surprising given that the southwestern strand would be expected to dominate southeast of a transtensional stepover. In contrast, the central and northeast fault zones appear relatively similar from wall to wall.

Earthquake Evidence

Evidence for past earthquakes at the Coachella site includes upward terminations of major fault strands that vertically separate lower units, sediment-draped scarps, filled fissures, liquefaction-related sedimentary structures, unit thickness and facies changes across faults, growth strata, and downward increase of vertical separation of units. We identify layers or contacts between layers that preserve multiple event indicators as probable earthquake horizons (i.e., were at the ground surface when an earthquake occurred). While subaerial ground ruptures generally disrupt the surface sufficiently so that the earthquake horizon is clear, sublacustrine earthquake horizons can be more subtle (e.g., Pezzopane and Weldon, 1993; Langridge *et al.*, 2000). At the Coachella site, it is sometimes the case that a fault offsets the bottom but not the top of a massive layer, either because sedimentation was continuous before and after the earthquake, or because the surface manifestation of faulting was obliterated by water action or plastic deformation. In such cases, the earthquake horizon cannot be determined more precisely than being within a certain layer. Even in cases where precise contacts between faulted and unfaulted strata can be identified, these contacts are usually not traceable over long lateral distances and thus may not correspond to the contacts used to delineate the major stratigraphic units. Therefore, most earthquakes are identified as having occurred during the deposition of a particular unit or subunit, rather than at a contact.

Because this segment of the fault is known to creep aseismically (Sieh and Williams, 1990; Lyons and Sandwell, 2003) at a rate of several millimeters per year, it is likely that in the centuries following an earthquake, some fractures continue to propagate upward into sediments deposited after the earthquake. This phenomenon could potentially lead to misidentification of paleocreep as a paleoearthquake. However, only one fault strand at the Coachella site continues all the way to the surface through the modern dune deposits (see Fig. 7a), most likely a result of the ~1 m of creep (estimated at the nearby Indio site) since the most recent earthquake (Sieh and Williams, 1990). This and other observations (Rymer *et al.*, 2002 and references therein) suggest that aseismic creep in this region usually occurs on a single fault strand or very narrow zone, so multiple fault strands that terminate at the same sedimentary layer are strong evidence for a seismic event even on a fault that occasionally creeps at the surface. We do not consider a single upward termination of a fault to be sufficient evidence of an earthquake horizon, because fault splays do not always rupture to the surface even in seismic events (McCalpin *et al.*, 2009 and references therein). Minor fractures that decrease downward and frequently do not reach the bottom of the trench are not considered meaningful event evidence either, because they likely form due to very local stresses and do not connect to the main fault. For these reasons, we require multiple pieces of spatially separated evidence in order to identify a particular layer as an earthquake horizon. We count fault terminations separately on each wall, because the walls are sufficiently far apart to allow strands to merge or diverge in the intervening space.

Central Trench Earthquake Evidence

There is excellent evidence exposed on the walls of the central trench for five earthquakes and some evidence for three additional earthquakes (see Fig. 6a). These potential earthquake horizons are given the prefix Coa- for Coachella and are numbered in order of increasing stratigraphic depth. There is a variety of evidence types for Coa-1, -2, -4, -5, and -7 at multiple locations, so we infer these five events to be probable earthquakes. Evidence for Coa-3, -6, and -8+ is less direct and more limited in spatial distribution, so these are evaluated as possible earthquakes. Earthquake evidence is described in the following text and summarized in Table 1. We employ a system similar to that used by Scharer *et al.* (2007) to rank each piece of evidence from 1 to 4 based on quality. High-quality evidence can only be explained

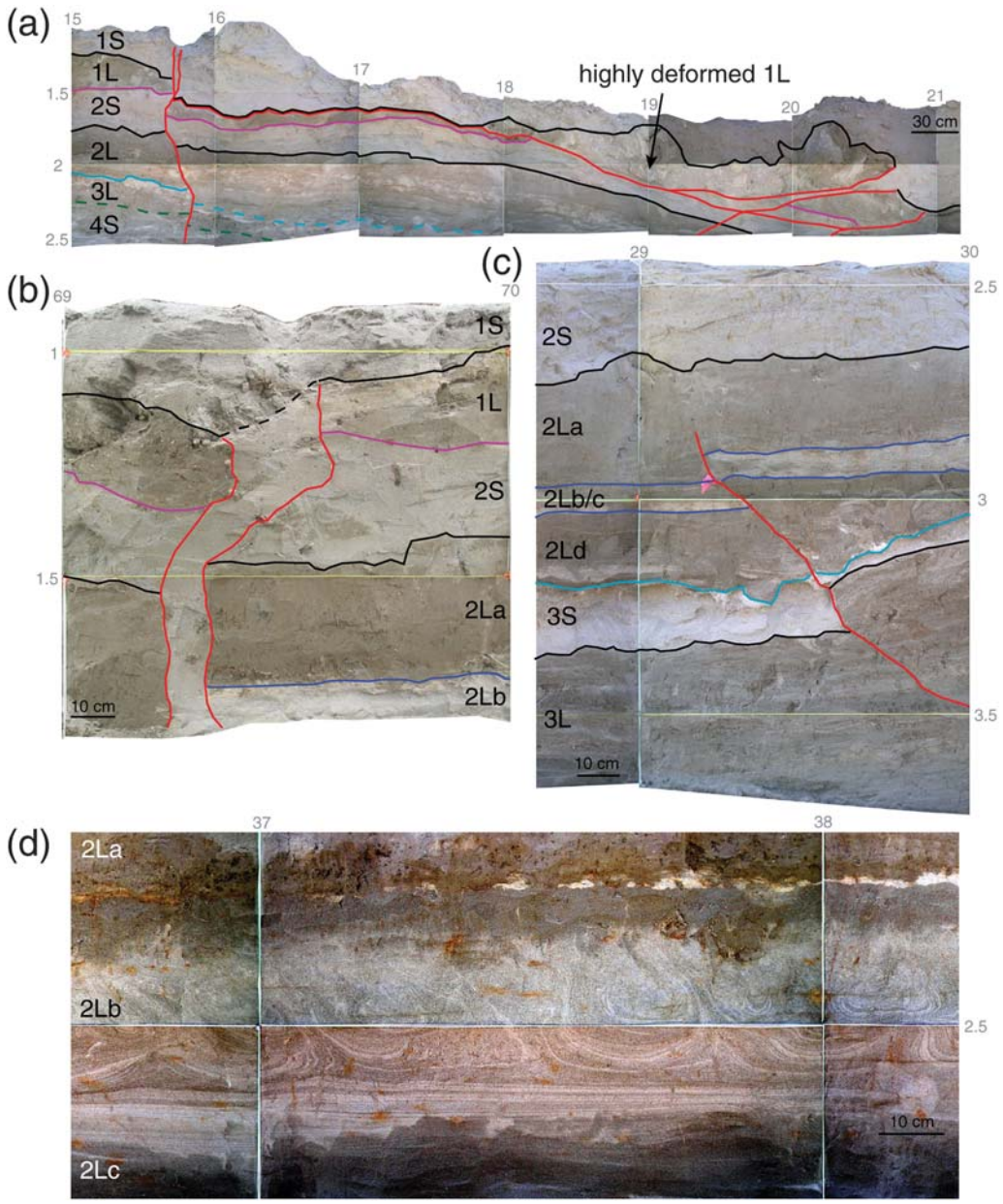

Figure 7. (a–b) Evidence for the most recent earthquake, Coa-1. (a) Northwest wall, riser 1, meters 15–21 showing the slump deposit in unit 1L. The vertical fault at the left also may have broken during Coa-1, but the fractures that extend into unit 1S must be due to more recent aseismic creep. (b) Northwest wall, riser 1, meters 69–70 showing a fissure breaking units 1L and 2L filled with subaerial material. (c–d) Evidence for Coa-2. (c) Northwest wall, riser 2, meters 29–30 showing substantial offset of 3L, 3S, and lower lake 2 subunits and the undeformed top of unit 2L. (d) Southeast wall, riser 2, meters 37–38 (reversed) showing liquefaction features in unit 2Lb.

by an earthquake, and unambiguously delineates the earthquake horizon. Upward terminations are rated 1 or 2 depending on the magnitude of the separation near the tip, because those with large separations that end abruptly are more indicative of a surface rupture (marking a true earthquake horizon) than those which express tapering separation. Liquefaction features and abrupt thickness change of units are generally ranked 3, because they are strong evidence for an earthquake but do not mark the earthquake horizon precisely. Features such as sediment slumps, fissures, and fault terminations associated with clear deformation contrasts are ranked 4, because they must be associated with earthquakes and mark earthquake horizons definitively. To be accepted as a probable earthquake, there must be at least one piece of evidence ranked 4, or the total rank must be greater than 8. The best pieces of evidence are shown in Figures 7–13; others are marked on Figure 6a and can be found on the complete trench logs in Philibosian *et al.* (2009). It is also important to note that earthquake evidence which could be due to more than one of the listed earthquakes is not included in the table and descriptions (e.g., faults that terminate at local unconformities where significant

Table 1
Ranked Evidence for Paleoearthquakes

Earthquake	Description	Rank	Wall	Riser	Meters	Figure
Coa-1	Soft-sediment detachment slump	4	NW	1	15–20	7a
	2 fault terminations	2	NW	1	19–20	7a
	Fault termination and fissure	4	NW	1	69	7b
	2 fault terminations	1	SE	1	48–50	–
	Total (probable)	11				
Coa-2	Fault termination	1	NW	2	58	–
	2 fault terminations	1	NW	2	64	–
	Fault termination	2	SE	2	47	–
	2 fault terminations	1	SE	2	49	–
	Fault termination	2	NW	2	29	7c
	Fault termination	1	SE	2	25	–
	Fault termination	1	SE	2	15	–
	Fault termination	1	SE	2	17	–
	Liquefaction features	3	SE	2	35–42	7d
	Total (probable)	13				
Coa-3	Thickness change of unit 3L	3	NW	1–3	18–21	8; 6a
	Total (possible)	3				
Coa-4	Fault termination and draped scarp	3	NW	3	18	9a
	2 fault terminations	2	NW	2	12–13	–
	Fault termination and possible colluvial wedge	3	SE	3	16–18	9b
	Total (probable)	8				
Coa-5	Fault termination and deformation contrast	4	SE	5	27	10
	Fault termination, draped scarp	3	NW	3	13–15	–
	Total (probable due to rank 4 evidence)	7				
Coa-6	Possible fault terminations	1	SE	4	50–52	–
	Possible fault terminations	1	SE	5	16	11a
	Possible fault termination	1	NW	5	16–17	–
	Possible fault termination	1	NW	5	31	–
	Possible colluvial wedge	3	SE	4–5	28–29	11b
	Total (possible)	7				
Coa-7	Fault termination	1	SE	4	10	–
	Fault termination	1	SE	4	12	–
	Fault termination	1	SE	4	13	–
	Fault termination	2	NW	4	55	12
	Broad thickening of unit 5L	3	both	4	30–50	6a
	Total (probable)	8				
Coa-8+	Fissure	3	NW	5	8	13
	Total (possible)	3				

amounts of section have been removed by erosion, such as those labeled 4/5 on Fig. 6a).

Coa-1. An earthquake probably occurred in the very latest stages of deposition of unit 1L, perhaps when the shoreline was located in the vicinity of this site (having already receded from the 12 m highstand). The best evidence for this earthquake is a slump deposit, formed when the upper half of the latest lake deposit slid northeastward along a detachment (Fig. 7a). Given the very gentle slope of the deposit, it seems highly likely that this deformation was seismically driven. The highly ductile nature of the deformation indicates that it must have occurred while the sediments were water-saturated, but the lack of subsequent lacustrine deposition indicates that the lake level must have dropped below this site very soon after the earthquake occurred. The toe of the slump also overrides some sand that appears to be aeolian, suggesting that the adjacent land surface was dry. Two strands of the SWFZ terminate below this slump (meters 19–20), while another continues all the way to the surface through unit 1S (meter 15), the latter likely a result of subsequent interseismic creep. In the northeast fault zone (northwest wall), faulting offsets the latest lake deposit, forming a fissure that is filled, at least in part, by the overlying sand (Fig. 7b). On the opposite wall, two fault strands offset the latest lake but are truncated by the overlying erosional unconformity. All these features are best explained if an earthquake occurred in a near-shore environment.

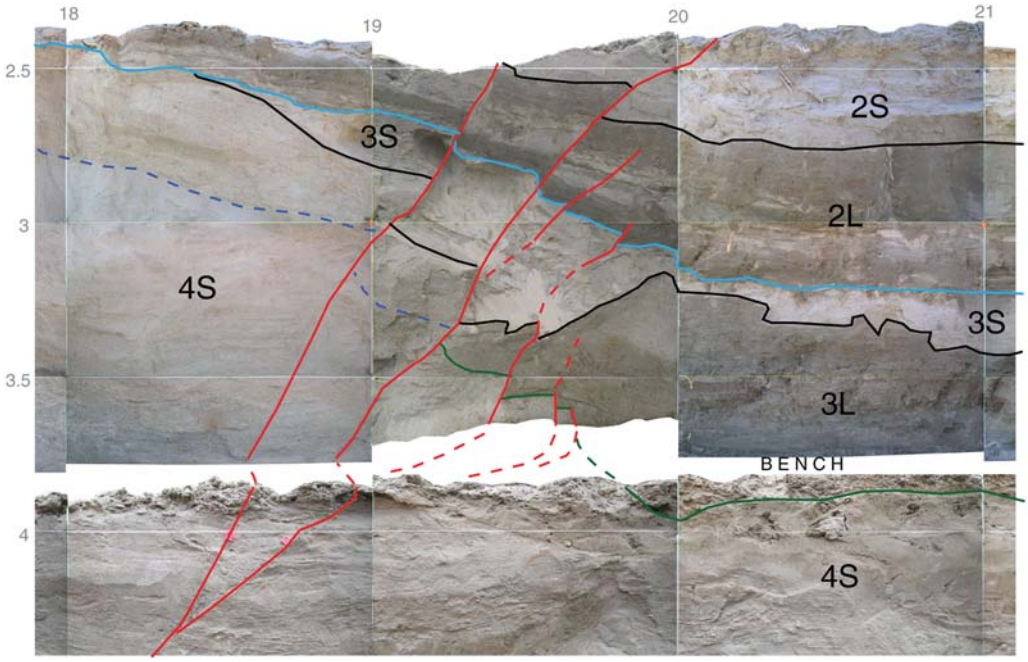

Figure 8. Evidence for Coa-3. Northwest wall, risers 2–3, meters 18–21 showing that unit 3L appears to pinch out and is not preserved on the upthrown side of the fault (the dashed blue line marks an internal contact within 4S). The top of unit 4S is vertically offset more than 2 m, while unit 2L is offset only ~75 cm and does not significantly change thickness. This suggests that an earthquake during the deposition of 3L produced accommodation space, causing 3L to form a significantly thicker deposit in the depression. The two minor fault strands that appear to terminate within 3L near the center of this view may be related to this earthquake. However, it is clear that the top of 4S (which 3L was deposited upon) was not a flat, smooth surface, so it may be possible to explain the evidence via erosional topography and lateral offset during the later earthquakes Coa-1 and 2. Based on this evidence Coa-3 is evaluated as a possible (rather than probable) earthquake.

Coa-2. An earthquake probably occurred during the deposition of the upper part of unit 2L. Six fault strands in the northeast fault zone, two fault strands in the central fault zone, and two fractures in the SWFZ terminate in layer 2La, leaving the upper surface of the lake deposit unfaulted. The locations of these terminations are given in Table 1; the best example is shown in Figure 7c. This earthquake must have occurred shortly before a drying phase of the lake, perhaps preceding desiccation of the site by a few decades. On the southeast wall of the trench, sandy layers within the second youngest lake deposits (layer 2Lb) form swooping flame structures, almost certainly a result of liquefaction (Fig. 7d). Because the layers must have been water-saturated and close to the ground surface (but confined) for this type of deformation to occur, this was most likely caused by an earthquake that occurred during the later stages of 2L deposition, consistent with the upward termination evidence.

Coa-3. An earthquake may have occurred during the deposition of unit 3L, though the exact earthquake horizon is unclear. On the northwest wall, unit 3L gradually thickens southwestward from meter 54 to meter 20 (see Fig. 6a), at which point it appears to pinch out against unit 4S just northeast of the main SWFZ. There are some minor fault strands that appear to terminate within unit 3L near this feature (Fig. 8). On the southwest side of this fault zone, unit 3L is very thin or absent, whereas unit 2L above maintains a significant thickness on both sides of the fault zone (see Fig. 6a). The gradually tapering thickness of 3L could have been produced by the sediments of 3L accumulating in accommodation space produced by a recent fault offset. There are no other recognized fault strands that terminate within unit 3L, so it may be possible to explain the evidence for Coa-3 nontectonically via erosional topography and lateral offset (during Coa-1 and -2) of layers with heterogeneous thickness. The elevation of the top of unit 4S varies considerably along the strike of the fault (on opposing walls), indicating that there was significant erosional topography on this surface prior to the deposition of unit 3L. Therefore, Coa-3 is classified as a possible earthquake because the evidence for it is less direct.

Coa-4. An earthquake probably occurred when unit 4Sd, near the middle of the thick subaerial deposit 4S, was at the ground surface. Three fault strands in the SWFZ terminate in this unit. A set of laminar sand beds overlie the terminus of one fault and pinch out, suggesting that this sediment filled in a low area adjacent to a scarp (Fig. 9a). This earthquake horizon is bracketed between two thin organic layers within layer 4S, the lower one (4Se) faulted and the upper one (4Sc) undisturbed. Additionally, there is a zone of very loose and disorganized sediment in the upper half of layer 4S where it encounters the SWFZ on the southeast wall (Fig. 9b). The bench riser wall below exposes a fault with ~70 cm of reverse separation on unit 4L, suggesting that the zone of loose sediment may be a colluvial wedge related to the

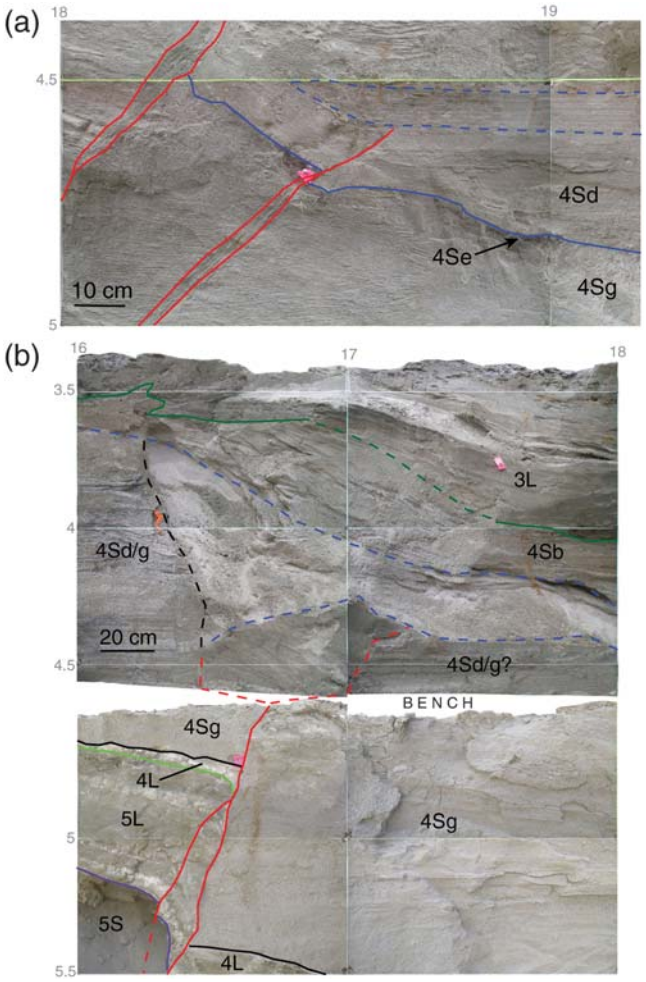

Figure 9. Evidence for Coa-4. (a) Northwest wall, riser 3, meters 18–19 showing a fault termination within unit 4S draped by a set of fine laminar beds (outlined by dashed blue lines), which appear to pinch against a paleoscarp. (b) Southeast wall, risers 3–4, meters 16–18 (reversed) showing probable collapse scarp (dashed black line) and colluvial wedge of loose sand (between dashed blue lines) in unit 4S above a fault that offsets the base of 4S by 70 cm.

collapse of an overhanging scarp. This scenario places the earthquake horizon about halfway up the wall, above which the upper part of 4S and 3L drape over the scarp and wedge. However, it is also possible that the wedge of loose sediment was formed by the cutting and filling of a channel that eroded away the upper part of the fault, in which case the original earthquake horizon is not preserved. In either case the fault terminates within unit 4S.

Coa-5. An earthquake probably occurred when the organic-rich soil developed at the top of the subaerial unit 5S was at the ground surface. Near the base of the section exposed in the central fault zone, unit 5S and the organic soil are strongly folded and unconformably overlain by undeformed beds of unit 4L (Fig. 10). This earthquake probably created the topographic depression that was then filled by the thick sequence of lake sediments that make up unit

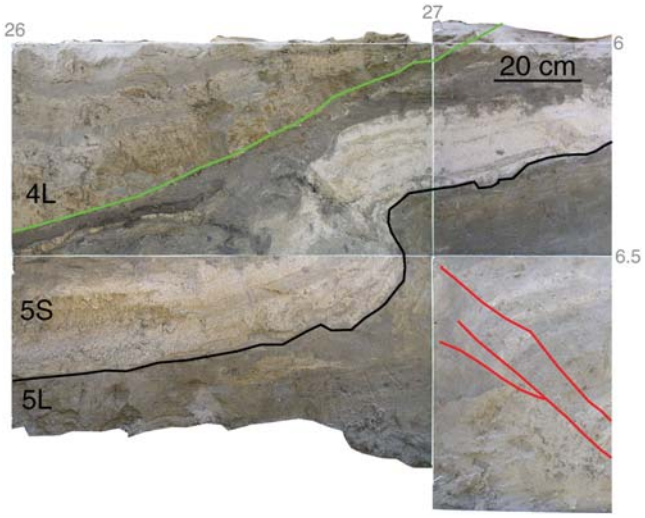

Figure 10. Evidence for Coa-5. Southeast wall, riser 5, meters 26–27 (reversed) showing folded and offset units 5S and 5L unconformably overlain by the undeformed clay and silt layers of unit 4L.

4L; these deposits thin dramatically at the edges of the deep depression. The base of unit 4L also drapes a small scarp at a fault terminus in the SWFZ.

Coa-6. There is some evidence that an earthquake occurred during deposition of unit 5L, though much of this evidence may actually be related to Coa-5. Several minor fault strands seem to terminate within the unit, but the positions of the excavation benches, disruption of bedding in the fault zones, and the obliquity of the faults to the exposed surface make it difficult to determine exactly how high these faults propagate. For instance, fault strands in the SWFZ shown in Figure 11a clearly offset the base of 5L by 20 cm, but it is difficult to determine whether the bioturbated contact between 5L and 5S is offset. Along the same trend is a fault that offsets 4L by 2 cm, but it is unclear how this fault connects to those below (if at all). The upper fault may simply be a later, unconnected minor fracture. There are similarly ambiguous fault terminations exposed in three other locations (see Table 1). There is also a possible colluvial wedge composed of sediment from 5L in the central fault zone (Fig. 11b). At least part of the wedge appears to be overlain by 5S, suggesting that the wedge formed prior to Coa-5 that deforms 5S. Bioturbation of 5S and later faulting make it unclear whether 5S is also deformed as part of the wedge, so it is conceivable that the wedge formed during Coa-5. If Coa-6 is not a true earthquake, most of the evidence for it should instead be attributed to Coa-5, considerably increasing the confidence rank of the later earthquake.

Coa-7. An earthquake probably occurred when the subaerial unit 6S was at the ground surface. Three fault strands in the southwest zone cut the base of the loose beach sand (layer 6S southwest) but do not extend into 5L. The beach

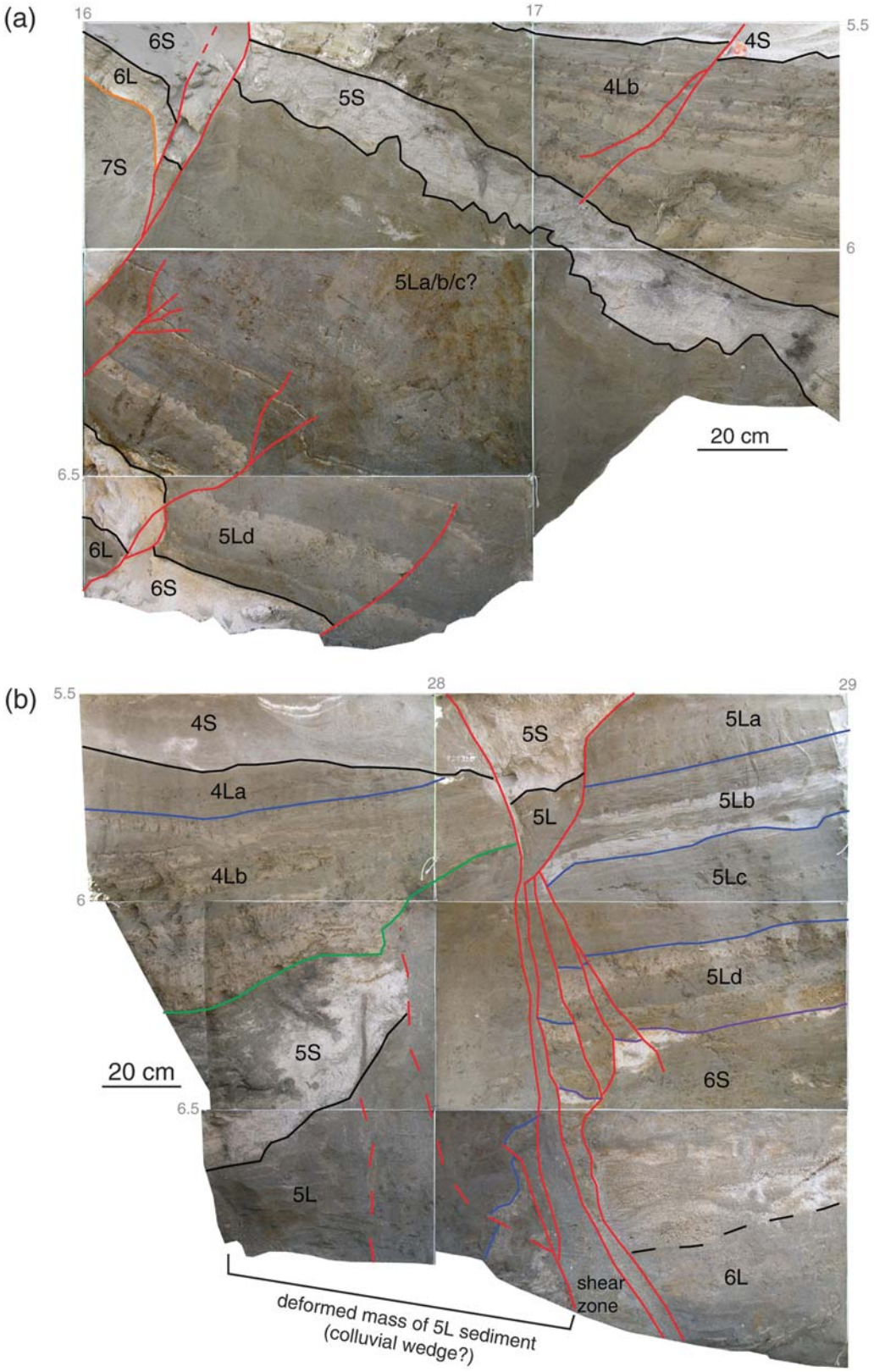

Figure 11. Evidence for Coa-6. (a) Southeast wall, risers 4–5, meters 16–17 (reversed) showing possible fault terminations within unit 5L. (b) Southeast wall, risers 4–5, meter 28–29 (reversed) showing possible colluvial wedge of material from unit 5L, suggesting scarp formation during deposition of 5L. 5S appears to overlie the lower part of the wedge, but it is absent over the highest part of the wedge.

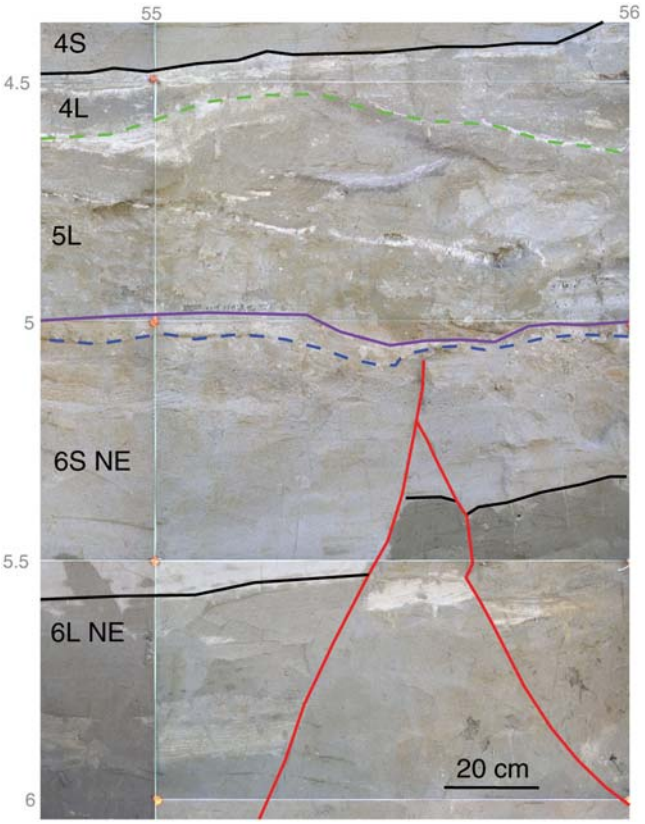

Figure 12. Evidence for Coa-7. Northwest wall, riser 4, meters 55–56 showing faults displacing units 6L NE and 6S NE, but not the upper sand layer of 6S nor the base of 5L.

sand is absent in the northeast fault zone, but one fault strand terminates in the fine-grained subaerial unit below 5L (Fig. 12). Further supporting Coa-7, unit 5L thickens from 40 cm to 120 cm over the 30 m width of the shallow depression (see Fig. 6). It is below the trench floor in the 10-m-wide deep depression, but is presumably thickened to an even greater extent there. This thickening may reflect down-dropping of the depression block prior to Lake 5 deposition.

Coa-8+. An earthquake may have occurred during the early stages of deposition of the thick fluvial unit 7S. A fissure at the very base of the trench exposure cut through unit 7L southwest and the very lowest part of 7S southwest and filled with sand from 7S southwest (Fig. 13). This feature is ranked 3 rather than 4 because it was difficult to see whether there was a fault at the root of the fissure. It is possible that one or more other earthquakes occurred between this event and Coa-7, because there appears to have been substantial erosion between the deposition of units 7L southwest and 7S southwest. Deposits of this age were not exposed in the structural depression, and due to the thickness of overlying deposits could be meters below the base of the exposure.

Eastern Trench Earthquake Evidence

The structure and stratigraphy exposed in the 200-meter-long eastern trench were dramatically different from those in the central trench. In the eastern trench, two fault zones were exposed: (1) the main fault zone that underlies the surface

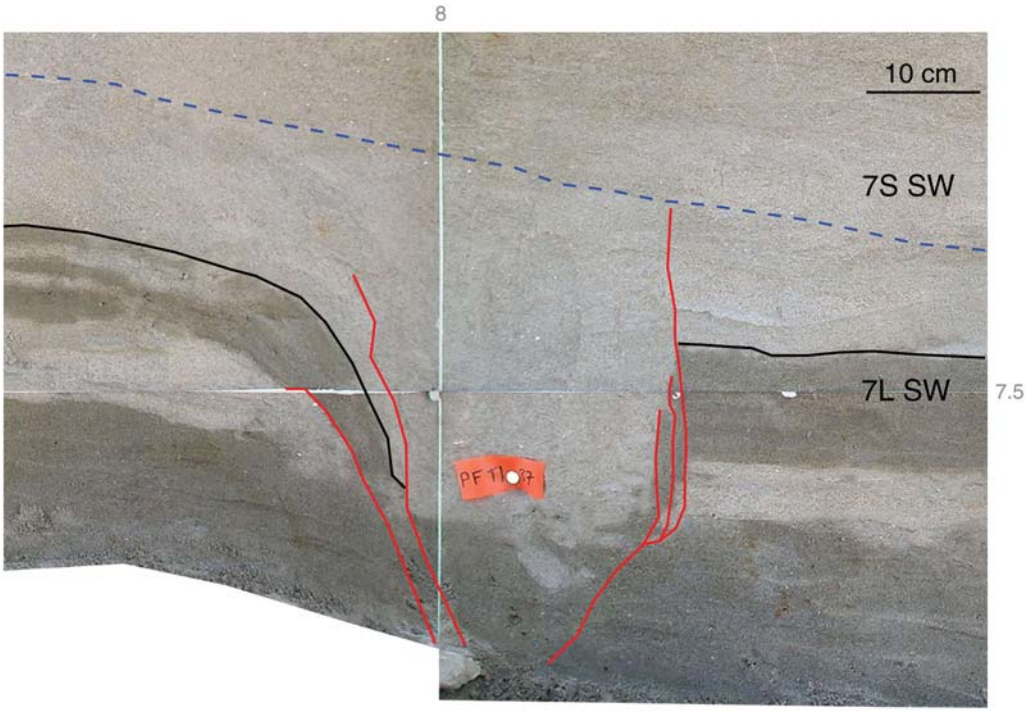

Figure 13. Evidence for Coa-8+. Northwest wall, riser 5, meter 8 showing a fissure in unit 7L southwest filled with sand from unit 7S southwest above. Only the lowermost part of 7S is faulted. Orange tag shows the location of sample Nb5m8A-sh1.

scarp and vegetation lineament and is along strike from the southwest and central fault zones exposed in the central trench, and (2) an apparently minor fault zone near the northeast end of the trench (see Fig. 3). The extensive erosion between lacustrine intervals made it difficult to correlate the stratigraphy between the trenches and to precisely identify earthquake horizons. Because no fault-parallel trenches were available for study, it was necessary to rely on radiocarbon ages to guide our correlations of stratigraphic units between the trenches; carbon samples were unfortunately relatively scarce in the eastern trench exposures. An organic layer associated with the youngest lake in the exposed section (in the vicinity of the minor northern fault zone) yields a date of 390 ± 35 ^{14}C-yr B.P., suggesting that deposits from the most recent lake have been entirely removed or were never deposited at that location. If our correlation is correct, there is some evidence for Coa-3, -4, and -5 (Philibosian *et al.*, 2009), but due to the correlation uncertainties this evidence does not provide much additional confidence in our earthquake chronology.

Radiocarbon Dating

We obtained 82 radiocarbon dates from 61 samples, 49 from the central trench and 12 from the eastern trench (Table 2). See Philibosian *et al.* (2009) for exact sample locations. Sediment blocks containing organic layers were collected at 15 of these locations, while detrital charcoal and/or lacustrine mollusk shells were collected at the others. To isolate the carbon, each organic layer was dissected to remove potentially younger roots and as much nonorganic sediment as possible. The carbon from these organic-rich layers is in the form of black, amorphous, spongy clumps. With essentially none of the material's original structure preserved, it is difficult to determine whether it is decomposed plant matter or burnt material from a local fire. In some places these layers had a ruddy tinge, indicating oxidation of sediment that is often observed following a fire, so we infer that these layers are probably burn horizons.

We applied chemical treatments to the charcoal and soil samples prior to dating them via accelerator mass spectrometry (AMS) carbon-14 analysis. Charcoal samples were given the standard acid-alkali-acid (AAA) chemical pretreatment to remove atmospheric carbon and humic acids. For each sample of the organic-rich layers, humic acid dissolved in the first base wash solution was precipitated and dated separately from the AAA fraction. Humic acid, being soluble in base, is usually discarded in the AAA process because it may be leached from more modern material and transported through groundwater. However, if the organic material is decomposed plant matter, the humic acid may be derived from *in situ* plant matter and thus has the potential to provide a more accurate date than an AAA-treated sample, which may contain older detrital charcoal (Scharer *et al.*, 2007). Following pretreatment, combustion to CO_2, and precipitation as graphite, the samples were dated at the Center for Accelerator Mass Spectrometry (CAMS) facility at Lawrence Livermore National Laboratory (LLNL) or at the Keck Carbon Cycle Accelerator Mass Spectrometry (KCCAMS) Laboratory at the University of California at Irvine. Dates in carbon-14 years before present (B.P.) were obtained from the $^{14}C/^{12}C$ ratio and corrected for isotopic fractionation using the $^{13}C/^{12}C$ ratio.

In a few cases we extracted charcoal and/or shells from block samples and dated those in addition to the AAA and humic fractions from the organic sediment. Both charcoal and a shell from location Nb4m44A were dated, and a lone shell was dated at location Nb5m8A because no charcoal was present. Where both occur, the shell ages are between 400 and 800 yr older than the charcoal and/or organic sediment ages from the same sample location, indicating that past waters of Lake Cahuilla contained a significant reservoir of old carbon. We found no macrofossils other than roots, which are likely young throughout the section because roots from an old organic sediment sample (AAA date of 960 ± 30 B.P.) yielded a modern age.

Earthquake Chronology Determination Using OxCal

We used the OxCal v. 4.1 program (Bronk Ramsey, 2009) to convert ^{14}C yr B.P. into calendar years B.C./A.D. based on the history of atmospheric ^{14}C concentration, using the IntCal04 calibration curve (Reimer *et al.*, 2004). The OxCal program convolves the uncertainties, producing a probability density function (PDF) for each date. We applied additional stratigraphic constraints to trim the PDFs: samples from the same stratigraphic layer are grouped as Phases in OxCal in which no internal stratigraphic constraints are applied, and the known stratigraphic relationships between samples and groups of samples were enforced by an ordered Sequence. Earthquake ages are determined in OxCal by calculating PDFs that are statistically consistent with the radiocarbon age PDFs, using the Date functionality.

Because of fluctuations in atmospheric ^{14}C concentration since the dawn of the industrial revolution, measurements of <200 ^{14}C-yr B.P. generally match multiple calendar date ranges. Thus, it is prudent to consider historical observations in order to better constrain the ages of the youngest deposits. Early expeditions through the region by Europeans provide useful historical constraints on the timing of the two most recent fillings of Lake Cahuilla (summarized in Lippincott, 2007). The first European expedition to pass through the Salton Trough was that of Anza in 1774. Records from this journey make no mention of a lake, but it is possible that a relatively small saline lake (unworthy of mention) may have been present at the time. Frequent subsequent expeditions and the eventual settlement of the region preclude the possibility that Lake Cahuilla filled after 1774. It has been estimated that once cut off from Colorado River input, Lake Cahuilla would require 60 yr to desiccate entirely (Waters, 1983; Sieh and Williams, 1990), so in order for it to have been dry by the time of the Anza expedition a full lake

Table 2
Ages of Carbon Samples in Stratigraphic Order

Sample Name*†	^{14}C age	±	Layer‡§	
Central Trench Samples				
Nb1m45A-c	125	20	1S	–
Nb1m51A-c	175	15	1S	–
Sb1m44A-c	210	15	1S	–
Nb1m57A-b-hum	*Modern*	–	*1La*	*X*
Nb1m57A-b-AAA	*200*	*35*	*1La*	–
Nb1m57A-c	*260*	*40*	*1La*	–
Nb1m22A-c	105	20	1Lb	X2
Sb2m26B-c	545	20	2S	X
Sb1m55A-c	590	15	2S	X
Sb2m34A-c	645	25	2S	X
Nb2m51A-c	485	15	2La	X1
Sb2m26C-c	520	20	2La	X1
Sb1m52A-c	715	20	2La	X
Sb2m26A-c	385	35	2Lb	X2
Nb2m36A-c	400	30	2Lb	X2
Sb3m45A-c	310	15	2Ld	–
Sb2m10A-c	335	15	2Ld	–
Sb3m44A-c	335	20	2Ld	–
Sb2m10B-c	360	25	2Ld	–
Sb3m48A-c	380	15	2Ld	–
Sb2m4A-c	670	15	2Ld	X
Sb3m59A-c	435	35	3L	–
Nb2m30A-b-hum	**545**	**40**	**3L**	**–**
Nb2m30A-b-AAA	**585**	**30**	**3L**	**–**
Nb2m44A-b-AAA	*665*	*30*	*3L*	–
Nb2m44A-b-hum	*700*	*30*	*3L*	*X1*
Nb3m41A-b-hum	**610**	**30**	**4Sc**	**–**
Nb3m41A-b-AAA	**645**	**30**	**4Sc**	**–**
Nb3m20A-b-AAA	*700*	*30*	*4Se*	–
Nb3m20A-b-hum	*705*	*35*	*4Se*	–
Nb4m28B-c	815	35	4Sf	–
Sb3m4B-b-hum	915	15	4Sg	X2
Sb4m26A-c	890	15	4La	–
Sb4m27B-c	960	15	4La	–
Sb4m27A-c	980	15	4La	X1
Sb3m36B-c	1075	15	4La	X
Sb3m49A-b-hum	**910**	**20**	**5S**	**–**
Sb3m49A-b-AAA	**915**	**20**	**5S**	**–**
Nb5m28B-b-AAA	*935*	*30*	*5S*	–
Nb5m28B-b-hum	*955*	*30*	*5S*	–
Sb4m49B-b-hum	**965**	**30**	**5S**	**–**
Sb4m49B-b-AAA	**1030**	**35**	**5S**	**–**
Nb3m65B-b-AAA	*985*	*30*	*5S*	–
Nb3m65B-b-hum	*995*	*35*	*5S*	–
Nb3m59A-b-hum	**1065**	**40**	**5S**	**–**
Nb3m59A-b-AAA	**1095**	**35**	**5S**	**X1**
Nb3m59A-c	**1230**	**80**	**5S**	**X**
Nb4m44A-c	*1185*	*40*	*5Lc*	*X1*
Nb4m44A-sh1	*1550*	*30*	*5Lc*	*X*
Sb3m7A-c	955	30	5Ld	X2
Sb3m11A-c	1075	15	5Ld	–
Sb3m3B-c	1095	20	5Ld	–
Sb3m3A-c	1150	–	–	–
Sb3m4A-c	1290	20	5Ld	X
Sb4m59A-c	2885	30	6Sa NE	X
Sb3m2A-c	365	25	6La SW	X
Sb3m0B-c	1080	15	6La SW	–
Sb3m1B-c	1105	15	6La SW	–
Nb4m13B-c	1125	20	6La SW	–
Nb4m13A-c	1185	30	6Lb SW	–
Sb4m14A-c	1185	30	7S SW	–
Nb5m8A-sh1	2975	30	7L SW	–
Eastern Trench Samples				
Main Fault Zone				
T2-Sb2-3-c	530	15	3L	–
T2-Sb2-2-c	580	15	3L	–
T2-Sb2-9-c	605	20	3L	–
T2-Sb2-17-c	610	15	3L	–
T2-Sb2-4-c	930	15	4S	–
T2-Sb2-6-c	945	15	4L	–
T2-Sb2-1-b-r	**Modern**	**–**	**5Sa**	**–**
T2-Sb2-1-b-AAA	**960**	**30**	**5Sa**	**–**
T2-Sb2-1-b-c1	**1105**	**40**	**5Sa**	**–**
T2-Sb2-1-b-sh2	**1575**	**30**	**5Sa**	**–**
T2-Sb2-1-b-sh3	**1695**	**35**	**5Sa**	**–**
T2-Sb2-1-b-sh1	**1725**	**45**	**5Sa**	**–**
T2-Sb2-8-c	1020	15	5Sb	–
T2-Sb2-7-c	1165	15	5Sc	–
T2-Sb3-1-b-hum	*1550*	*30*	*6.5L?*	–
T2-Sb3-1-b-AAA	*1570*	*35*	*6.5L?*	–
Northeastern (Secondary) Fault Zone				
T2-Sb1-1-b-hum	**390**	**35**	**2L?**	**–**
T2-Sb1-1-b-AAA	**450**	**30**	**2L?**	**–**
T2-Sb2-14-b-AAA	*1080*	*30*	*5L?*	–
T2-Sb2-14-b-hum	*1115*	*30*	*5L?*	–

*Sample nomenclature designates northwest or southeast wall, bench riser number (1 is at the top), and meter number (from the southwest end of the logged exposures). The final capital letter is used to distinguish between multiple samples in a given wall-riser-meter. In the eastern trench, samples are numbered sequentially on each bench riser. The last part of the sample name denotes the sample type:

b-AAA: bulk sediment AAA fraction
b-hum: bulk sediment humic acid
c: charcoal
r: roots
sh1: clam shell
sh2: helmet shell
sh3: turritella shell

†Each bold or italicized group of dates was obtained from different portions of the same sample.

‡Samples followed by X were judged to be stratigraphically inconsistent and were excluded from the final analysis; X numbers indicate the OxCal model refinement step at which the sample was removed.

§Question marks indicate that the layer assignment is uncertain.

must have begun to evaporate by 1715 at the latest. If a small saline lake was present, desiccation may have begun a few years later, but Father Kino's earlier expedition established that the Colorado River was flowing into the Gulf of California in 1702 (Lippincott, 2007). It is possible that the river was briefly diverted back into the Salton Trough after Kino's expedition, but the most likely explanation is that the most recent Colorado River input to the lake was prior to A.D. 1702. Earlier expeditions (discussed in the following text) may provide additional information, but were not used to constrain the carbon-14 dates. Our OxCal model includes a historical razor at A.D. 1710 within the layer 1S phase, adding a conservative estimate of the time it would have taken for the lake level to drop from the 12-meter-

elevation shoreline past the Coachella site (more likely only a few years based on estimated evaporation rates of 1–2 m/yr). Because the most recent earthquake probably occurred before the lake receded from this location, this historical razor places a pre-1710 bound on the age of Coa-1 as well as all the sample ages below layer 1S.

Because correlations of deposits between the two trenches can only be made based on radiocarbon age, only samples from the central trench were used in the OxCal model to determine the ages of paleoearthquakes. Figure 14 shows the 62 dates from the central trench grouped by source layer (excluding the modern ages and the much older shell ages). Clearly some of these detrital charcoal samples are well above the age-depth trend and thus are much older than the layers in which they were deposited. One sample (Sb3m2A-c) is so young compared with many other samples that it must have been contaminated by younger carbon, either by groundwater or during the sample pretreatment process, or been mixed into the older layer through bioturbation. The modern humic acid age (Nb1m57A-b-hum), the Nb4m44A shell age, the inconsistently young charcoal age, and nine inconsistently old detrital charcoal ages were excluded from the initial OxCal analysis.

OxCal calculates several indices that represent how well the model fits the data. For each date, the individual agreement index represents the likelihood of obtaining that measurement assuming the model is correct. The model agreement index represents the likelihood that the model is true given all of the data, and the convergence integral represents how well the Monte Carlo analysis has represented the full range of possible models. In general, the agreement indices should be $>60\%$ and the convergence integral $>95\%$ for the model to be acceptable. All models were run until the convergence integral reached 95%, so we can be confident that the model space was adequately explored in all cases. The initial model, containing 50 dates, had so many samples with low individual agreement indices that the model agreement index was 0%. We twice refined this model, removing two additional samples that appeared inconsistently young and nine that were inconsistently old. (See Philibosian, 2007 for the initial and intermediate OxCal models.) Ultimately, about 40% of the dates (1 shell, 4 possibly contaminated or bioturbated samples, and 18 detrital samples) were determined to be inconsistent with the model. The percentage of stratigraphically consistent dates compares favorably with many other recent paleoseismic sites, dated largely by detrital material, where it has often been necessary to exclude more than half of the sample dates (e.g., Fumal, Rymer, and Seitz, 2002).

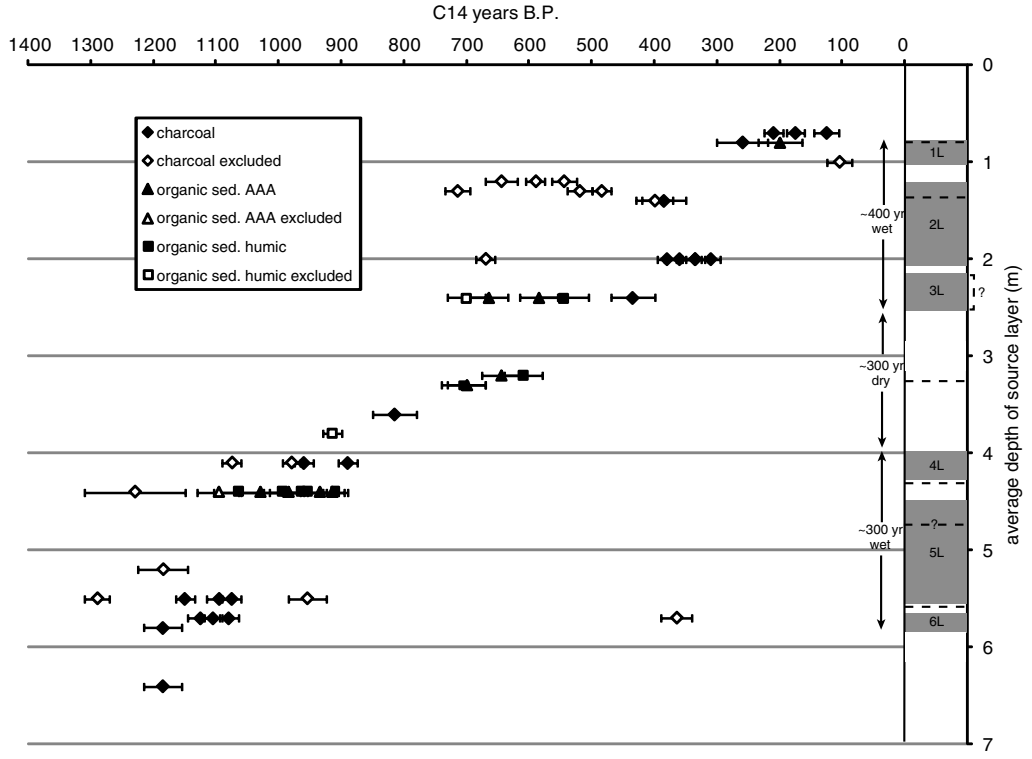

Figure 14. Stratigraphic and age distribution of dated samples from the central trench (excluding modern-aged samples and shells). Samples are plotted using the average depth of their source layer (according to the generalized stratigraphic column shown in Fig. 5). Lacustrine intervals are indicated by gray bars and earthquake horizons by heavy dashed lines. Note that while there are six distinct lacustrine intervals, they appear to be grouped into two longer mostly wet time periods during which the lake basin probably did not desiccate completely. Samples with empty symbols were excluded from the final OxCal model due to stratigraphic inconsistency once converted to calendar years.

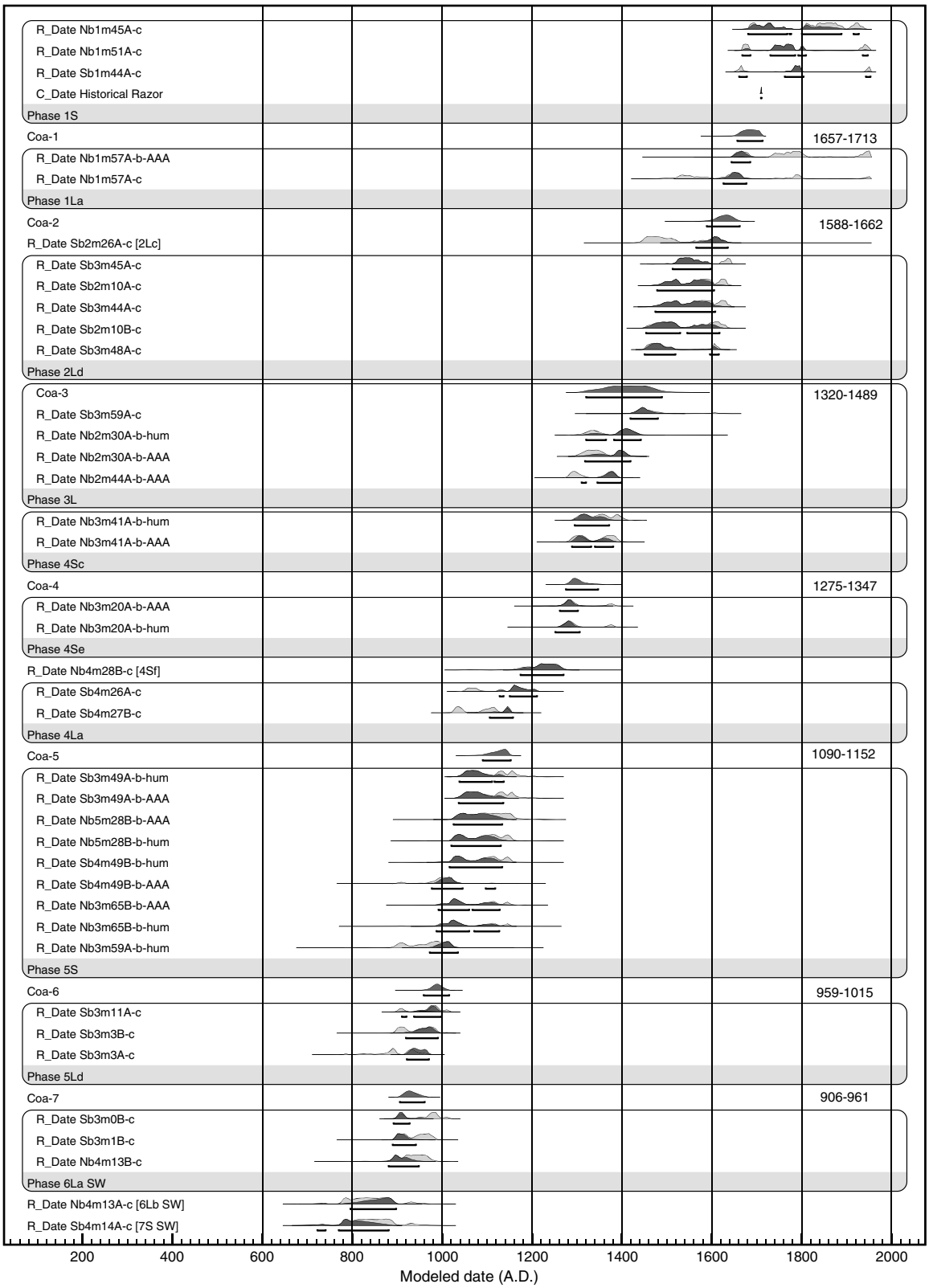

Figure 15. Final OxCal model for the central trench ages showing calibrated age distributions (open curves) and ordering-constrained distributions (shaded) with 95.4% confidence intervals (horizontal brackets). All samples have agreement indices $> 70\%$ and the model agreement index is 104%. The modeled age interval (in calendar years A.D.) for each earthquake is shown at right.

Table 3
Best Estimates (to the Nearest Decade) and 95% Confidence Ranges of Earthquake Dates*

Earthquake	Year	95% Confidence Range
Coa-1	1690	1657–1713
Coa-2	1630	1588–1662
Coa-3 (poss.)	1420	1320–1489
Coa-4	1300	1275–1347
Coa-5	1140	1090–1152
Coa-6 (poss.)	990	959–1015
Coa-7	930	906–961
Coa-8+ (poss.)	–	1090 B.C.–A.D. 784

*Dates are in calendar years A.D. unless otherwise specified.

The final model has an agreement index of 104% with individual agreement indices > 70% for all samples (Fig. 15). Based on this model, we infer that five probable and two possible earthquakes expressed in the Coachella exposures occurred after A.D. 800, in the time intervals A.D. 906–961, 959–1015 (possible), 1090–1152, 1275–1347, 1320–1489 (possible), 1588–1662, and 1657–1713 (Table 3, Fig. 16). The PDF for the poorly bracketed eighth event is essentially flat within its large interval (see fig. 23 of Philibosian, 2007), so no best estimate is given. Because the evidence for this earthquake is a fissure in layer 7L southwest filled with likely subaerial material related to the early stages of deposition of 7S southwest, the earthquake probably occurred toward the more recent end of the interval between 1095 B.C. and A.D. 784. The shell that provides the early bound on the date of this event is most likely reworked from unit 7L southwest, and due to the reservoir effect is probably hundreds of years younger than its radiocarbon age suggests.

Average earthquake recurrence intervals are often calculated by dividing the average single-earthquake displacement by the fault slip rate. However, neither of these parameters is well-characterized for this section of the SAF (see Fumal, Rymer, and Seitz, 2002; Fialko, 2006; van der Woerd *et al.*, 2006; Behr *et al.*, 2010), so the only reliable way to calculate recurrence interval is via paleoseismological earthquake chronologies such as ours. Our estimated average earthquake recurrence interval varies depending on the calculation method (Table 4). Using only the closed earthquake intervals in the chronology, the average recurrence interval can be calculated to lie between 116 and 202 yr, depending on the number of earthquakes. However, the current ~300-yr open interval is longer than most of the closed intervals, and its inclusion in the calculations raises the calculated range to 150–221 yr. Without the open interval, the calculated average recurrence interval is almost certainly biased short, so the latter range is probably closer to the true mean. Including the open interval, assuming that there have been six earthquakes, and using the best-estimate age of Coa-7, the best-estimate average recurrence interval is 180 yr.

Comparison with Other Sites and Implications for Rupture Extent and Magnitude

Figure 17 compares the Coachella earthquake chronology with other paleoseismic sites on the southern San Andreas fault at Indio (Sieh, 1986); Thousand Palms Oasis (TP: Fumal, Rymer, and Seitz, 2002); Burro Flats (BF: Yule and Sieh, 2001; Yule, personal commun., 2004; Yule *et al.*, 2006); Plunge Creek (PlC: McGill *et al.*, 2002); Pitman Canyon (PiC: Seitz *et al.*, 1997); Wrightwood (WW: Biasi *et al.*, 2002; Fumal, Weldon, *et al.*, 2002; Weldon *et al.*, 2002; Weldon *et al.*, 2004); and Pallett Creek (PaC: Sieh *et al.*, 1989; Salyards *et al.*, 1992; Biasi *et al.*, 2002). Locations of these sites are shown on Figure 1b. Coa-1, Coa-3, and Coa-4 correlate reasonably well with the three most recent earthquakes at both Thousand Palms and Indio. (It should be noted that

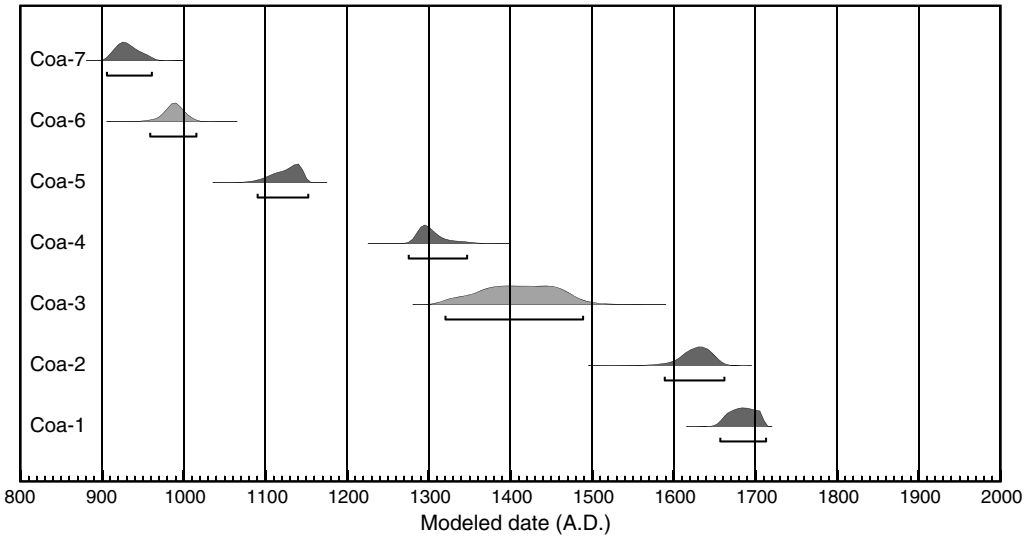

Figure 16. Probability density functions (PDFs) for the seven earthquakes recorded at the Coachella site. Probable earthquakes have darkly shaded PDFs while possible earthquakes are lightly shaded. Brackets below PDFs show 95.4% confidence intervals. Note that the current interseismic interval appears anomalously long.

Table 4
95% Confidence Ranges of Mean Earthquake Recurrence Intervals

Recurrence Intervals	Including Open Interval	Without Open Interval
5-earthquake scenario	210–221 yr	174–202 yr
7-earthquake scenario	150–158 yr	116–135 yr

similar historical constraints were applied to the most recent event at all three sites, so the several estimations of its age are not independent). However, Coa-2 does not correlate well with any of the earthquakes recorded at either Thousand Palms or Indio. The Thousand Palms site is located on the Mission Creek strand of the SAF. It is thought that in the vicinity of this site slip is being transferred from the Mission Creek strand to the Banning fault and indeed, slip-per-event at the Thousand Palms site is small, averaging only about 50 cm (Fumal, Rymer, and Seitz, 2002). Thus, it would not be surprising that an earthquake rupture might be absent or poorly manifested and preserved at that site. Also, detailed results have not been published for the Indio site, so it is not possible to evaluate either the completeness of the stratigraphic record or quality of the earthquake evidence there. Thus, it is possible that three earthquakes occurred since A.D. 1400, but evidence for Coa-2 was not preserved at Thousand Palms or Indio. Alternatively, Coa-2 could represent the tail end of a relatively short southerly rupture that did not extend as far north as Indio. We also cannot entirely rule out the possibility that some faults that ruptured during earlier earthquakes propagated only partway to the surface during the most recent earthquake (Coa-1), leaving misleading evidence for an intervening earthquake (Coa-2) that never actually occurred. However, to the best of our ability to interpret the evidence, Coa-1 occurred within a century of Coa-2.

The correlation of Coa-5, -6, and -7 with the other chronologies is less certain. The stated uncertainty in the date of TP-4 is very large and that for Indio-4 is probably much

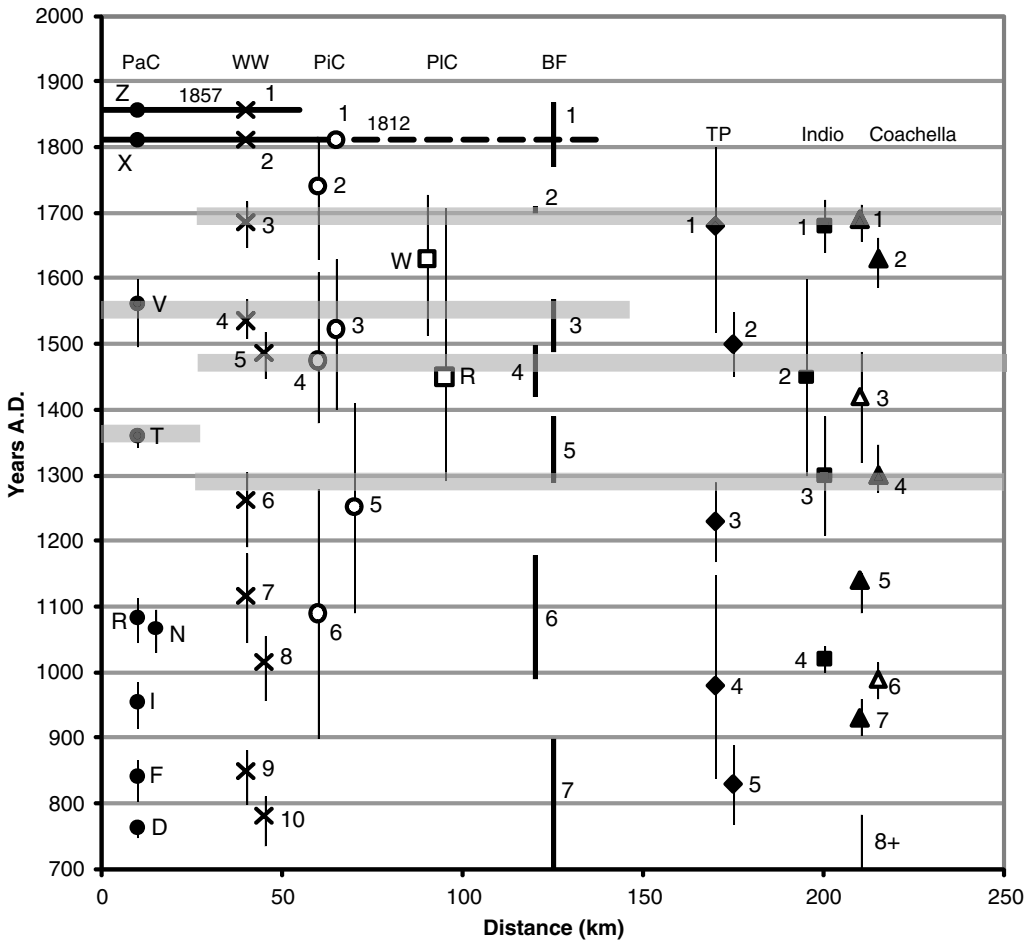

Figure 17. Earthquake chronologies from paleoseismic sites on the southern San Andreas Fault. The possible earthquakes Coa-3 and Coa-6 are shown by empty triangles. Rupture extents of the historical 1857 and 1812 earthquakes are shown by horizontal black bars. Gray bars show possible correlations between sites, delineating separate Coachella Valley and Mojave section ruptures. Site abbreviations: PaC: Pallett Creek, WW: Wrightwood, PiC: Pitman Canyon, PlC: Plunge Creek, BF: Burro Flats, TP: Thousand Palms. (Note that only age brackets, without best estimates, are available for the Burro Flats site). Sources for site chronologies are listed in the text.

smaller than stratigraphic bracketing of the event actually permits. These events could correlate with any of Coa-5, -6 or -7 at Coachella, but it seems most likely that they correlate with Coa-5, because there is an older fifth earthquake at Thousand Palms that may correlate with Coa-6 or -7. (The Indio record does not extend farther back in time than A.D. 1000). Alternatively, if TP-4 and Indio-4 correlate with Coa-6 or -7, this means Coa-5 was not recorded at either of those sites, and TP-5 was not recorded at Indio or Coachella (reasonable because it is older than the continuous section exposed at both sites). For reasons noted previously, the paleoseismic records at the Thousand Palms and Indio site may not be complete and this may account for the discrepancies in the chronologies among the sites. Importantly, all three sites are consistent with 5–7 earthquakes occurring since A.D. 800. Preliminary results from the Salt Creek site are also in agreement (Williams, 2009).

It is of particular scientific and social interest to determine the rupture length of past earthquakes on the Coachella Valley section of the SAF, because this touches on the fault segmentation issue and is related to estimating the damage potential of a future earthquake. The three Coachella Valley sites' similar histories suggest that the Coachella Valley section of the fault is usually part of a single rupture. To estimate rupture extent, we can compare the Coachella Valley chronology with those obtained at more distant sites. Earthquakes at each of the northern sites (WW-3, PiC-2, PlC-W, and BF-2) likely correlate with the most recent (late 1600s) event in the Coachella Valley. However, no event of a similar age appears in the Pallett Creek record, so it seems fair to conclude that the earthquake that occurred in ~A.D. 1690 probably ruptured the 150 kilometers of fault between Coachella and Wrightwood, but did not propagate farther northwest. The penultimate (mid-1400s) Coachella Valley rupture (manifested as Coa-3, Indio-2, and TP-2) potentially correlates with BF-4, PiC-4, and WW-5, but there is again no corresponding Pallett Creek earthquake. PaC-V does likely correlate with WW-4, PiC-3, and BF-3, suggesting that an early 1500s earthquake reruptured the fault between Wrightwood and Burro Flats, but did not extend into the Coachella Valley. (PlC-R could correlate with either the northern or the southern rupture; the Plunge Creek record is almost certainly incomplete). The third (c. 1300) Coachella Valley rupture (Coa-4, Indio-3, and TP-3) similarly potentially correlates with BF-5, PiC-5, and WW-6, but not with any Pallett Creek earthquake. These potential correlations are delineated by gray bars on Figure 17. The earlier parts of the records are more difficult to interpret in terms of regional correlations due to the lack of a clear consensus among the Coachella Valley sites.

These chronologies suggest that the Coachella Valley section of the SAF does not usually rupture with the Mojave–Carrizo Plain section. The stretch of the fault between Wrightwood and Burro Flats appears to be a transition zone that sometimes (but not necessarily always) ruptures along with the Coachella Valley or Mojave sections of the fault. While the data could be explained by a random rupture model, the good agreement between likely Coachella Valley events with Wrightwood, Pitman Canyon, and Burro Flats events (and absence of agreement with Pallett Creek events) lends support to the characteristic model. It is interesting to note that while the Coachella Valley segment ruptures separately from the Mojave–Carrizo Plain segment, there appears to be a broad transition zone between the two rather than an abrupt segment boundary, with Coachella Valley events occasionally propagating through (or starting north of) the structurally complex San Gorgonio Pass. Therefore, evidence presented here suggests that the structural knot may not pose a significant barrier to through-going rupture, and a 500- to 600-km-long rupture of the entire southern SAF is not entirely out of the question.

An additional point of interest is that the penultimate earthquake on the Imperial fault (which last ruptured completely in 1940, with rerupture of the northern section occurring in 1979) appears to have occurred during the most recent lake highstand (Thomas and Rockwell, 1996). Though available age control is far from adequate to determine the relative timing of the penultimate Imperial fault rupture and the most recent Coachella Valley SAF rupture (Coa-1), the brief duration of the most recent lake suggests that they occurred within ~50 yr of each other. It seems likely that the events were related: one earthquake could have triggered the other via stress changes, similar to the suspected triggering of the 1999 Hector Mine earthquake by the Landers earthquake 7 yr earlier (e.g., Felzer *et al.*, 2002; Kilb, 2003). Alternatively, the southernmost San Andreas fault and the Imperial fault could have ruptured in a single earthquake, though this seems somewhat unlikely given the transtensional structural complexities in the intervening Brawley seismic zone (see Fig. 1b).

Lake Chronologies

Our investigations at the Coachella site were focused on developing a paleoearthquake chronology, but our stratigraphic observations and extensive radiocarbon dating provide important data regarding the history of Lake Cahuilla. We obtain approximate dates and durations of lacustrine intervals by projecting the thickness of the lake sediment through the date-constrained sedimentation rate (Fig. 18). Note that these are durations at the 9-meter elevation mark; sites located at lower elevation are expected to record longer durations, and those at the 12-m highstand shoreline would be slightly shorter. The bottom of the basin, at an elevation of ~85 m below sea level, could have lacustrine deposition for a few decades before the lake reached the 12 m highstand, and for ~60 yr after the lake began to desiccate (Waters, 1983; Sieh and Williams, 1990). The only previously published lake sequence, from sites located at sea level (Waters, 1983; see Fig. 1b) is shown at the top of Figure 18 and is very different from the Coachella chronology. These differences cannot simply be attributed to the 9-meter difference in

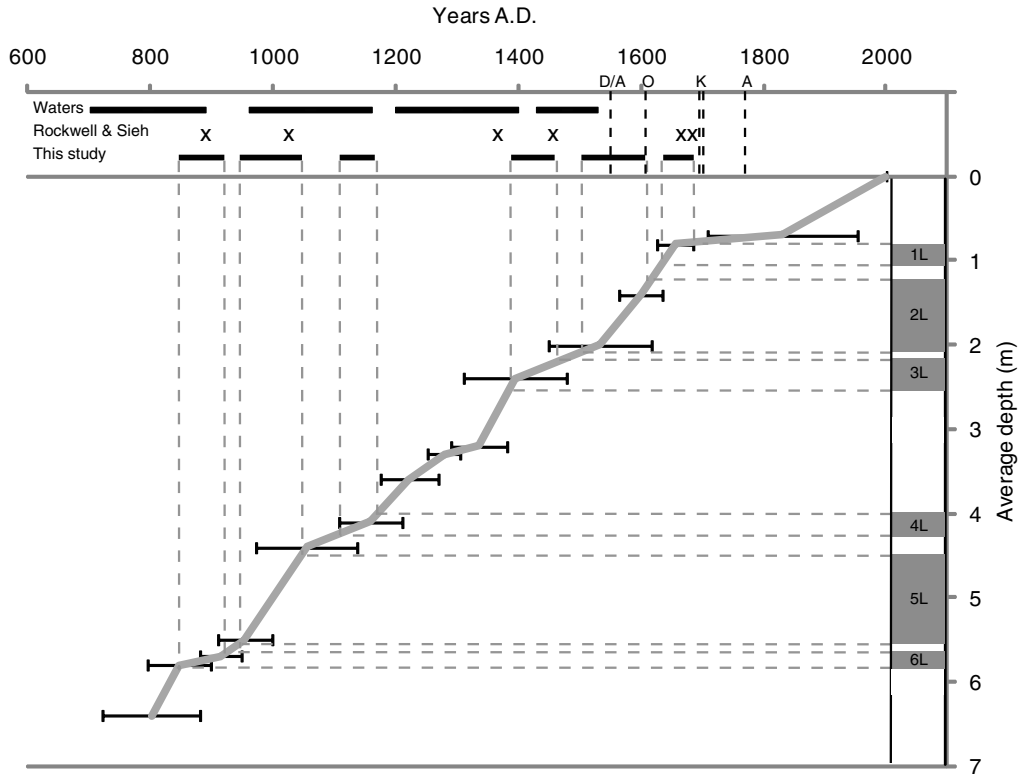

Figure 18. Approximate lake highstand chronology at the Coachella site and comparison to other Lake Cahuilla chronologies. The full 95% confidence range of the modeled ages of samples from each layer is plotted against average depth of the source layer. Lacustrine periods are projected from the depth axis to the time axis using the best-fit instantaneous sedimentation rate (heavy gray line). The resultant chronology has six distinct highstands, but these are grouped into two "mostly wet" periods. The intervals of subaerial deposition within the mostly wet periods were probably not long enough for the lake to desiccate completely. Lake durations from Waters (1983) and ages of deposits immediately preceding lake highstands from Rockwell and Sieh (1994) are shown above the new Coachella lake chronology. Dates of early expeditions to the region from Lippincott (2007) are shown by vertical dashed black lines; D/A: Díaz/Alarcón, O: Oñate, K: Kino, A: Anza.

elevation. However, this early study relied on relatively few carbon dates, most of which were shells (susceptible to the aforementioned old-carbon reservoir effect). The Coachella lake sequence, obtained using a larger date population and modern dating methods, is almost certainly more accurate.

Preliminary data from the Salt Creek site, located at −60 m elevation, support the interpretation that there have been 5–6 lake-filling events during the past 1200 yr (Williams, 2009), suggesting that periods of desiccation were usually long enough for Lake Cahuilla to shrink to the size of the Salton Sea. The complete lake chronology for the Indio site (located at the paleoshoreline) has never been published (Sieh, personal commun., 2006). However, ages of subaerial samples immediately below lacustrine transgressions from the Indio site and other shoreline sites have been published in abstract form and represent times shortly prior to lake highstand (Rockwell and Sieh, 1994). These dates (shown by an X in Fig. 18) are potentially consistent with the Coachella lake chronology, given the dating uncertainties. Incomplete and less well-dated lake chronologies have been reported from the Superstition Mountain (Gurrola and Rockwell, 1996), International Border (Thomas and Rockwell, 1996), and Brawley (Meltzner *et al.*, 2006) paleoseismic sites (see locations on Fig. 1b), at the 12-m highstand shoreline, 9 m elevation, and −37 m, respectively. While none of these chronologies has sufficient stratigraphic resolution or age control to make a useful comparison with the Coachella lake chronology, they are generally consistent with this chronology. All three studies suggest that the most recent lake highstand occurred during the late 1600s, and that the penultimate lake filled during the mid- to late-1400s. Additionally, a recent study of the deep basin stratigraphy below the Salton Sea is generally consistent with our nearshore stratigraphy, supporting the hypothesis that the basin did not desiccate completely between the most recent three highstands (Brothers, 2009).

There is no lake in Waters' (1983) sequence that corresponds with the most recent lake found at Indio and Coachella, but his sequence may be shifted backward in time due to the shell reservoir effect, and/or the thin deposits of the most recent lake may have been eroded away at his sites as they were in the eastern trench at the Coachella site. Waters (1983) argued that Lake Cahuilla could not have filled after A.D. 1540 based on expeditions made by Spanish explorers up the Colorado River to the settlement that is now Yuma, Arizona. These expeditions were led by Díaz and

Alarcón in 1540, Oñate in 1604–1605, Kino in 1700–1702, and Anza in 1774 (Lippincott, 2007; see Fig. 18). However, the expeditions prior to 1774 documented only the course of the river; travelers would not necessarily have noticed whether a lake was present in the Salton Trough if it was disconnected from the river, because the extremely flat terrain in the vicinity of the river makes it impossible to see over the horizon into the Salton Trough. Explorers of the 1605 Oñate and 1702 Kino expeditions were told by local American Indians about a lake to the north, but none went to investigate (Lippincott, 2007). Because it is estimated that the lake would require only 10–20 yr to fill completely if the entire flow of the Colorado River was diverted (Waters, 1983), the lake could easily have filled during both the 1540–1604 and 1605–1700 time intervals but then disconnected from the river before the next expedition arrived. According to the approximate lake chronology shown in Figure 18, the Oñate and Kino expeditions traveled during periods when the lake was not receiving river influx. The Díaz and Alarcón expeditions of 1540 are the most difficult to reconcile with our lake chronology, as this year falls in the middle of the estimated duration of the second youngest lake. The lake would require a substantial influx (perhaps 50% of the Colorado River flow) to sustain its 12 m elevation, but it is not impossible that the Colorado delta fed both the lake and the ocean for a period of time. If the explorers' observations truly indicate that the lake was disconnected from the river in 1540, the most likely explanation is that the second youngest lake filled after 1540, and the older detrital charcoal sample ages are too old to accurately represent the age of deposition.

Lake Triggering

Seismicity exhibits seasonal cycles in some regions, illustrating that the seemingly minor weight of accumulated rainwater or snow can trigger or inhibit fault failure (e.g., Heki, 2003; Bollinger *et al.*, 2007). The filling of large artificial reservoirs commonly triggers seismicity (Simpson *et al.*, 1988; Gupta, 2002), and the filling and emptying of pluvial Lake Bonneville has been cited as a possible cause for Holocene slip rate variations on several Great Basin normal faults (Hetzel and Hampel, 2005). The presence of soft-sediment deformation at the Coachella site indicates that the most recent earthquake occurred just after the last highstand of the lake, demonstrating correlation if not causation. In light of the assessment that there were at least five major ruptures of the southernmost SAF during the ~800 yr between A.D. 900 and 1700, the past 300 + yr of quiescence appears even more anomalous, leading to the hypothesis that the higher frequency of earthquakes in the past may have been linked to stress changes due to the repeated filling and emptying of Lake Cahuilla.

The lake is believed to have filled via the Rio Paredones–New River and Alamo River, former distributary channels of the Colorado River delta (Van de Kamp, 1973). The diversion of the river would have occurred near the apex of the delta (located near the intersection of the California, Arizona, and Mexico borders), from which point a minor alteration in course could send the meandering river into the Salton Trough (see Fig. 1b). However, once diverted into the Salton Trough, it is unlikely that the river would change course back toward the ocean until the lake was full, due to the favorable base level of the Trough in comparison to the Gulf of California (an effect demonstrated by the inadvertent filling of the Salton Sea in the early twentieth century). Thus, the filling of the lake is inferred to have always occurred quite rapidly and could have produced abrupt stress changes. After the lake filled, the level could be maintained for significant periods of time while any excess water spilled over the 12-meter-elevation sill separating the Salton Trough from the Gulf of California. During highstands, the lake would have covered much of the SAF trace from the Coachella Valley southward, at depths up to 90 m. Once the river diverted back into its normal path to the ocean and ceased to feed the lake, the lake would recede due to desiccation, becoming completely dry after ~60 yr (Waters, 1983), a more gradual stress change perhaps less likely to induce an earthquake.

For the vertical SAF, the filling of Lake Cahuilla would have three potential effects on fault stress: the weight of the water would increase the normal stress on the fault plane (inhibiting failure), the pore pressure would increase (promoting failure), and flexure of the earth's crust near the edges of the lake due to viscoelastic deformation would have produced local horizontal compression and extension (inhibiting or promoting failure depending on the location of the fault relative to the crust's inflection points). These effects would then be reversed when the lake emptied. Based on observed isostatic rebound since the desiccation of the most recent lake, Luttrell *et al.* (2007) modeled the stress changes that would have been produced by Lake Cahuilla and concluded that the maximum Coulomb stress changes could have been on the order of 1 MPa (but perhaps were much smaller). While this is an order of magnitude lower than the stress relieved by a typical earthquake, the lake cycle could conceivably have increased the Coulomb stress enough to trigger an earthquake if the SAF was already close to failure, or it could have decreased the stress enough to delay fault rupture. On the parts of the fault submerged by the lake, after a filling event the likelihood of fault rupture would have immediately increased due to pore pressure effects but then gradually decreased over many decades or even hundreds of years due to the viscoelastic effect. The emptying of the lake would have produced equal and opposite effects.

Luttrell *et al.* (2007) calculate Coulomb stress curves over time based on Waters' (1983) lake chronology, which (as discussed previously) is not consistent with modern carbon-14 dating, and compare this with the Thousand Palms earthquake chronology (Fumal, Rymer, and Seitz, 2002). Notwithstanding the possible errors in Waters' chronology, this combination of an earthquake record and a lake record from two spatially separated sites, correlated only via radiometric dating, is not a very reliable determination of the

relative timing of earthquakes and lakes. The relative timing we deduce from the stratigraphy at the Coachella site is independent of any errors in carbon dating or correlation of units between distant sites, and thus provides a better test of the lake-triggering model.

For our results, the earthquakes do not tend to occur at any particular stage in the lake cycle. Coa-1 occurred as the lake was beginning to recede from highstand, Coa-2 and Coa-6 (if the latter is a real earthquake) occurred toward the later end of lake highstands, Coa-4 occurred in the middle of a long subaerial interval, Coa-5 and Coa-7 occurred shortly prior to lake highstands, and the exact earthquake horizon of Coa-3 (if a real earthquake) is uncertain. According to the model put forth by Luttrell *et al.* (2007), the most likely time for triggered earthquakes would be shortly after a lake filled, but none of the earthquakes in the Coachella chronology definitively occurred in such a circumstance. It is possible that a more precise model of the stress history based on the Coachella lake chronology would reveal correlations with time-delayed stress changes related to the viscoelastic affect, but the Coachella record argues against immediate triggering of earthquakes by lake receding or filling.

The only potential relationship that can be observed in the earthquake-lake history is that at least four out of the seven earthquakes occurred shortly prior to a time when the lake either receded or filled. Because it would take a decade or more for the lake to fill up to the level of the Coachella site and a few years to drop from the 12-m high shoreline, it could be argued that these earthquakes were triggered by the early stages of the filling and desiccation processes. However, given that even the maximum possible stress change is small, the even lesser changes in stress that would have occurred early in the filling or emptying processes are highly unlikely to have triggered earthquakes. A more likely possibility is that, rather than the lake cycle triggering earthquakes, earthquakes have triggered shifts in the course of the Colorado River that led to the filling or emptying of Lake Cahuilla. This hypothesis also explains the similarity between the frequencies of earthquakes and lakes, and is consistent with the observation that most of the earthquakes in the Coachella record appear to have preceded a lake-filling or receding event. While the precise mechanisms by which the river was diverted are not known, the very low relief, young unconsolidated sediments, and meandering riverbed of the Colorado River delta could permit seismically induced liquefaction and lateral spreading of the river bank sufficient to divert the river.

Conclusions

The Coachella paleoseismic site study provides evidence for 5–7 earthquakes since A.D. 900. The average recurrence interval is 116–135 yr (probable and possible events) or 174–202 yr (probable events only). If the current open interval of ~320 yr is included, these estimates increase to 150–158 yr and 210–221 yr. However, no matter which of these estimates is most accurate, the current interseismic interval is significantly longer than the average and is approaching the length of the longest observed ~340-yr interval (present between Coa-2 and Coa-4, if Coa-3 did not occur). If all seven of the proposed earthquakes did occur, the current open interval is significantly longer than any of the observed intervals. There can be little doubt that major or great earthquakes rupture the southernmost SAF on average every ~200 yr; therefore the current 300-yr open interval indicates a high probability of rupture in the near future.

The Coachella site has also provided the most complete well-dated stratigraphy recording the history of ancient Lake Cahuilla. There have been 5–6 highstands of the lake since A.D. 800. The similarity of the lake frequency and the earthquake frequency, as well as the correlation in time between the most recent lake and the most recent earthquake, suggests a connection between the two. While earthquakes have not consistently occurred during any particular stage in the lake cycle, future modeling with our more accurate lake chronology may reveal that the earthquake record expresses some effects of lacustrine stress. However, given that many of the earthquakes recorded at the Coachella site appear to have shortly preceded a filling or receding of the lake, it is more likely that the earthquakes trigger changes in lake level rather than the reverse.

Data and Resources

All data used in this paper came from published sources listed in the references.

Acknowledgments

This research was funded by USGS NEHRP grant #07HQGR0019, USGS grant #06HQAG0143, and internal funding from the University of Oregon. Belle Philibosian was supported by a National Science Foundation Graduate Research Fellowship. We are extremely grateful to Rilington Communities for granting access to their property and to Matt Cohrt and Doug Cook of Sladden Engineering for accommodating our study. We would like to thank Katherine Kendrick, Kate Scharer, Sean Bemis, Reed Burgette, Beth Wisely, Nissa Morton, and Mike O'Bleness for their invaluable assistance in the field; Malcolm Britton, Lorna Crider, Tyler Claycomb, and Sarah Hunt for assistance with image processing; and Ken Hudnut of USGS for assistance with funding acquisition and LiDAR data. For assistance with carbon dating, we thank Michaele Kashgarian and Paula Zermeno of the Center for Acceleration Mass Spectrometry at Lawrence Livermore National Laboratory, Douglas Kennett and Brian Culleton of the Coastal Archaeology and Human Ecology Laboratory at the University of Oregon, and John Southon of the Keck Carbon Cycle Accelerator Mass Spectrometry Laboratory at the University of California, Irvine. This paper was greatly improved thanks to thoughtful reviews by Katherine Kendrick, Rob Langridge, Tom Rockwell, and Pat Williams.

References

Akciz, S. O., L. G. Ludwig, and J. R. Arrowsmith (2009). Revised dates of large earthquakes along the Carrizo section of the San Andreas fault, California, since A.D. 1310 ± 30, *J. Geophys. Res.* **114,** B01313, doi 10.1029/2007JB005285.

Behr, W. M., D. H. Rood, K. E. Fletcher, N. Guzman, R. Finkel, T. C. Hanks, K. W. Hudnut, K. J. Kendrick, J. P. Platt, W. D. Sharp, R. J. Weldon,

and J. D. Yule (2010). Uncertainties in slip-rate estimates for the Mission Creek strand of the southern San Andreas fault at Biskra Palms Oasis, southern California, *GSA Bull.* **122,** 1360–1377.

Bevis, M., K. Hudnut, D. Brzezinska, R. Sanchez, and C. Toth (2006). The B4 LiDAR survey of the southern San Andreas and San Jacinto faults, *Seismol. Res. Lett.* **77,** 311.

Biasi, G. P., R. J. Weldon, T. E. Fumal, and G. G. Seitz (2002). Paleoseismic event dating and the conditional probability of large earthquakes on the southern San Andreas fault, California, *Bull. Seismol. Soc. Am.* **92,** 2761–2781.

Bollinger, L., F. Perrier, J.-P. Avouac, S. Sapkota, U. Gautam, and D. R. Tiwari (2007). Seasonal modulation of seismicity in the Himalaya of Nepal, *Geophys. Res. Lett.* **34,** L08304, doi 10.1029/2006GL029192.

Bronk Ramsey, C. (2009). Bayesian analysis of radiocarbon dates, *Radiocarbon* **51,** 337–360.

Brothers, D. S. (2009). New insights into deformation along the North America-Pacific plate boundary from Lake Tahoe, Salton Sea and southern Baja California, *Ph.D. Thesis*, University of California, San Diego, San Diego, California.

Felzer, K. R., T. W. Becker, R. E. Abercrombie, G. Ekström, and J. R. Rice (2002). Triggering of the 1999 M_w 7.1 Hector Mine earthquake by aftershocks of the 1992 M_w 7.3 Landers earthquake, *J. Geophys. Res.* **107,** 2190, doi 10.1029/2001JB000911.

Fialko, Y. (2006). Interseismic strain accumulation and the earthquake potential on the southern San Andreas fault system, *Nature* **441,** 968–971.

Fumal, T. E., M. J. Rymer, and G. G. Seitz (2002). Timing of large earthquakes since A.D. 800 on the Mission Creek strand of the San Andreas fault zone at Thousand Palms Oasis, near Palm Springs, California, *Bull. Seismol. Soc. Am.* **92,** 2841–2860.

Fumal, T. E., R. J. Weldon, G. P. Biasi, T. E. Dawson, G. G. Seitz, W. T. Frost, and D. P. Schwartz (2002). Evidence for large earthquakes on the San Andreas fault at the Wrightwood, California, paleoseismic site: A.D. 500 to present, *Bull. Seismol. Soc. Am.* **92,** 2726–2760.

Goldfinger, C., K. Grijalva, R. Bürgmann, A. E. Morey, J. E. Johnson, C. H. Nelson, J. Gutiérrez-Pastor, A. Ericsson, E. Karabanov, J. D. Chaytor, J. Patton, and E. Gràcia (2008). Late Holocene rupture of the northern San Andreas fault and possible stress linkage to the Cascadia subduction zone, *Bull. Seismol. Soc. Am.* **98,** 861–889.

Gupta, H. K. (2002). A review of recent studies of triggered earthquakes by artificial water reservoirs with special emphasis on earthquakes in Koyna, India, *Earth-Science Reviews* **58,** 279–310.

Gurrola, L. D., and T. K. Rockwell (1996). Timing and slip for prehistoric earthquakes on the Superstition Mountain fault, Imperial Valley, southern California, *J. Geophys. Res.* **101,** 5977–5985.

Heki, K. (2003). Snow load and seasonal variation of earthquake occurrence in Japan, *Earth Planet. Sci. Lett.* **207,** 159–164.

Hetzel, R., and A. Hampel (2005). Slip rate variations on normal faults during glacial-interglacial changes in surface loads, *Nature* **435,** 81–84.

Kelson, K., A. Streig, R. Koehler, and K. Kang (2006). Timing of late Holocene paleoearthquakes on the northern San Andreas fault at the Fort Ross Orchard site, Sonoma County, California, *Bull. Seismol. Soc. Am.* **96,** 1012–1028.

Kilb, D. (2003). A strong correlation between induced peak dynamic Coulomb stress change from the 1992 *M* 7.3 Landers, California, earthquake and the hypocenter of the 1999 *M* 7.1 Hector Mine, California, earthquake, *J. Geophys. Res.* **108,** 2012, doi 10.1029/2001JB000678.

Langridge, R. M., R. J. Weldon II, J. C. Moya, and G. Suárez (2000). Paleoseismology of the 1912 Acambay earthquake and the Acambay–Tixmadeje fault; Trans-Mexican volcanic belt, *J. Geophys. Res.* **105,** 3019–3037.

Lippincott, C. K. (2007). Testing the application and precision of optically stimulated luminescence on dating lacustrine shorelines in the Imperial Valley, southern California, *Master's Thesis*, San Diego State University, San Diego, California.

Luttrell, K., D. T. Sandwell, B. Smith-Konter, B. Bills, and Y. Bock (2007). Modulation of the earthquake cycle at the southern San Andreas fault by lake loading, *J. Geophys. Res.* **112,** B08411, doi 10.1029/2006JB004752.

Lyons, S., and D. T. Sandwell (2003). Fault creep along the southern San Andreas from interferometric synthetic aperture radar, permanent scatterers, and stacking, *J. Geophys. Res.* **108,** 2047, doi 10.1029/2002JB001831.

McCalpin, J. P., T. K. Rockwell, and R. J. Weldon (2009). Stratigraphic indicators of paleoearthquakes, in *Paleoseismology*, J. P. McCalpin (Editor), Elsevier, London, UK, 473–479.

McGill, S., S. Dergham, K. Barton, T. Berney-Ficklin, D. Grant, C. Hartling, K. Hobart, R. Minnich, M. Rodriguez, E. Runnerstrom, J. Russell, K. Schmoker, M. Stumfall, J. Townsend, and J. Williams (2002). Paleoseismology of the San Andreas fault at Plunge Creek, near San Bernardino, southern California, *Bull. Seismol. Soc. Am.* **92,** 2803–2840.

Meltzner, A. J., T. K. Rockwell, and L. A. Owen (2006). Recent and long-term behavior of the Brawley fault zone, Imperial Valley, California: An escalation in slip rate?, *Bull. Seismol. Soc. Am.* **96,** 2304–2328.

Naylor, M. A., G. Mandl, and C. H. K. Sijpesteijn (1986). Fault geometries in basement-induced wrench faulting under different initial stress states, *J. Struct. Geol.* **8,** 737–752.

Olsen, K. B., S. M. Day, J. B. Minster, Y. Cui, A. Chourasia, M. Faerman, R. Moore, P. Maechling, and T. Jordan (2006). Strong shaking in Los Angeles expected from southern San Andreas earthquake, *Geophys. Res. Lett.* **33,** L07305, doi 10.1029/2005GL025472.

Pezzopane, S. K., and R. J. Weldon II (1993). Tectonic role of active faulting in central Oregon, *Tectonics* **12,** 1140–1169.

Philibosian, B. (2007). Paleoseismology of the Southern San Andreas Fault at Coachella, California, *Master's Thesis*, University of Oregon, Eugene, Oregon.

Philibosian, B., T. E. Fumal, R. J. Weldon, K. J. Kendrick, K. M. Scharer, S. P. Bemis, R. J. Burgette, and B. A. Wisely (2009). Photomosaics and logs of trenches on the San Andreas Fault near Coachella, California, in *U.S. Geol. Surv. Open-File Rept. 2009-1039*.

Reimer, P., M. Baillie, E. Bard, A. Bayliss, J. Beck, C. Bertrand, P. Blackwell, C. Buck, G. Burr, K. Cutler, P. Damon, R. Edwards, R. Fairbanks, M. Friedrich, T. Guilderson, A. Hogg, K. Hughen, B. Kromer, G. McCormac, S. Manning, C. B. Ramsey, R. Reimer, S. Remmele, J. Southon, M. Stuiver, S. Talamo, F. Taylor, J. v. d. Plicht, and C. Weyhenmeyer (2004). IntCal04 terrestrial radiocarbon age calibration, 0–26 cal kyr BP, *Radiocarbon* **46,** 1029–1058.

Rockwell, T. K., and K. E. Sieh (1994). Correlation of large earthquakes using regional lacustrine stratigraphy, examples from the Salton Trough, California, *Abstr. Programs Geol. Soc. Am.* **26,** 239.

Rymer, M. J., J. Boatwright, L. C. Seekins, J. D. Yule, and J. Liu (2002). Triggered surface slips in the Salton Trough associated with the 1999 Hector Mine, California, earthquake, *Bull. Seismol. Soc. Am.* **92,** 1300–1317.

Salyards, S. L., K. E. Sieh, and J. L. Kirschvink (1992). Paleomagnetic measurements of nonbrittle deformation across the San Andreas fault at Pallett Creek, *J. Geophys. Res.* **97,** 12,457–12,470.

Scharer, K., R. Weldon, T. Fumal, and G. Biasi (2007). Paleo-earthquakes on the southern San Andreas fault, Wrightwood, California, 3000 to 1500 B.C., *Bull. Seismol. Soc. Am.* **97,** 1054–1093.

Seitz, G. G., R. J. Weldon II, and G. P. Biasi (1997). The Pitman Canyon paleoseismic record: A re-evaluation of southern San Andreas fault segmentation, *J. Geodyn.* **24,** 129–138.

Sieh, K. E. (1986). Slip rate across the San Andreas fault and prehistoric earthquakes at Indio, California, *Eos Trans. AGU* **67,** 1200, Abstract T1222C-1201.

Sieh, K. E., and P. L. Williams (1990). Behavior of the southernmost San Andreas fault during the past 300 years, *J. Geophys. Res.* **95,** 6629–6645.

Sieh, K. E., M. Stuiver, and D. Brillinger (1989). A more precise chronology of earthquakes produced by the San Andreas fault in southern California, *J. Geophys. Res.* **94,** 603–623.

Simpson, D. W., W. S. Leith, and C. H. Scholz (1988). Two types of reservoir-induced seismicity, *Bull. Seismol. Soc. Am.* **78,** 2025–2040.

Sylvester, A. G. (1988). Strike-slip faults, *Geol. Soc. Am. Bull.* **100,** 1666–1703.

Thomas, A. P., and T. K. Rockwell (1996). A 300- to 550-year history of slip on the Imperial fault near the U.S.–Mexico border; Missing slip at the Imperial fault bottleneck, *J. Geophys. Res.* **101,** 5987–5997.

U.S. Geological Survey and California Geological Survey (2006). Quaternary fault and fold database for the United States, accessed April 2006, from USGS web site: http://earthquakes.usgs.gov/regional/qfaults/.

Van de Kamp, P. C. (1973). Holocene continental sedimentation in the Salton Basin, California, a reconnaissance, *Geol. Soc. Am. Bull.* **84,** 827–848.

van der Woerd, J., Y. Klinger, K. Sieh, P. Tapponnier, F. J. Ryerson, and A.-S. Meriaux (2006). Long-term slip rate of the southern San Andreas fault from 10Be-26Al surface exposure dating of an offset alluvial fan, *J. Geophys. Res.* **111,** B04407, doi 10.1029/2004JB003559.

Waters, M. R. (1983). Late Holocene lacustrine chronology and archaeology of ancient Lake Cahuilla, California, *Quaternary Research* **19,** 373–387.

Weldon, R. J., T. E. Fumal, T. J. Powers, S. K. Pezzopane, K. M. Scharer, and J. C. Hamilton (2002). Structure and earthquake offsets on the San Andreas fault at the Wrightwood, California, paleoseismic site, *Bull. Seismol. Soc. Am.* **92,** 2704–2725.

Weldon, R. J., K. M. Scharer, T. E. Fumal, and G. P. Biasi (2004). Wrightwood and the earthquake cycle: What a long recurrence record tells us about how faults work, *GSA Today* **14,** 4–10.

Weldon, R. J., T. E. Fumal, G. P. Biasi, and K. M. Scharer (2005). Past and future earthquakes on the San Andreas fault, *Science* **308,** 966–967.

Williams, P. (2009). Paleoseismic displacement history: Coachella Valley segment, San Andreas fault, presented a *2009 SCEC Annual Meeting*.

Working Group on California Earthquake Probabilities (2008). The Uniform California Earthquake Rupture Forecast, Version 2 (UCERF 2), in *U.S. Geol. Surv. Open-File Rept. 2007-1437 and California Geological Survey Special Report 203*.

Yule, D., and K. Sieh (2001). The paleoseismic record at Burro Flats: Evidence for a 300-year average recurrence for large earthquakes on the San Andreas fault in San Gorgonio Pass, southern California, *Abstr. Programs Geol. Soc. Am.* **33,** 31.

Yule, J. D., S. J. Maloney, and L. S. Cummings (2006). Using pollen to constrain the age of the youngest rupture of the San Andreas fault at San Gorgonio Pass, *Seismol. Res. Lett.* **77,** 245.

Division of Geological and Planetary Sciences
California Institute of Technology
M/C 100-23, Caltech
Pasadena, California 91125
belle@gps.caltech.edu
(B.P.)

U.S. Geological Survey
MS 377, 345 Middlefield Rd.
Menlo Park, California 94025
tfumal@usgs.gov
(T.F.)

Department of Geological Sciences
University of Oregon
Eugene, Oregon 97403
(R.W.)

Manuscript received 5 March 2010

Research Paper

THEMED ISSUE: Seismotectonics of the San Andreas Fault System in the San Gorgonio Pass Region

GEOSPHERE

GEOSPHERE, v. 17, no. 3

https://doi.org/10.1130/GES02237.1

13 figures; 7 tables; 1 plate; 1 supplemental file

CORRESPONDENCE: bryan.castillo@csusb.edu

CITATION: Castillo, B.A., McGill, S.F., Scharer, K.M., Yule, D., McPhillips, D., McNeil, J., Saha, S., Brown, N.D., and Moon, S., 2021, Prehistoric earthquakes on the Banning strand of the San Andreas fault, North Palm Springs, California: Geosphere, v. 17, no. 3, p. 685–710, https://doi.org/10.1130/GES02237.1.

Science Editor: Andrea Hampel
Associate Editor: Craig H. Jones

Received 27 January 2020
Revision received 19 August 2020
Accepted 23 February 2021

Published online 6 May 2021

GOLD OPEN ACCESS

THE GEOLOGICAL SOCIETY OF AMERICA®

This paper is published under the terms of the CC-BY-NC license.

© 2021 The Authors

Prehistoric earthquakes on the Banning strand of the San Andreas fault, North Palm Springs, California

Bryan A. Castillo[1], Sally F. McGill[1], Katherine M. Scharer[2], Doug Yule[3], Devin McPhillips[2], James McNeil[3], Sourav Saha[4], Nathan D. Brown[4,*], and Seulgi Moon[4]

[1]Department of Geological Sciences, California State University, San Bernardino, California 92407, USA
[2]Earthquake Science Center, U.S. Geological Survey, Pasadena, California 91106, USA
[3]Department of Geological Sciences, California State University, Northridge, California 91330, USA
[4]Department of Earth, Planetary, and Space Sciences, University of California, Los Angeles, California 90095, USA

ABSTRACT

We studied a paleoseismic trench excavated in 2017 across the Banning strand of the San Andreas fault and herein provide the first detailed record of ground-breaking earthquakes on this important fault in Southern California. The trench exposed an ~40-m-wide fault zone cutting through alluvial sand, gravel, silt, and clay deposits. We evaluated the paleoseismic record using a new metric that combines event indicator quality and stratigraphic uncertainty. The most recent paleoearthquake occurred between 950 and 730 calibrated years B.P. (cal yr B.P.), potentially contemporaneous with the last rupture of the San Gorgonio Pass fault zone. We interpret five surface-rupturing earthquakes since 3.3–2.5 ka and eight earthquakes since 7.1–5.7 ka. It is possible that additional events have occurred but were not recognized, especially in the deeper (older) section of the stratigraphy, which was not fully exposed across the fault zone. We calculated an average recurrence interval of 380–640 yr based on four complete earthquake cycles between earthquakes 1 and 5. The average recurrence interval is thus slightly less than the elapsed time since the most recent event on the Banning strand. The average recurrence interval on the Banning strand is thus intermediate between longer intervals published for the San Gorgonio Pass fault zone (~1600 yr) and shorter intervals on both the Mission Creek strand of the San Andreas fault (~215 yr) and the Coachella section (~125 yr) of the San Andreas fault.

INTRODUCTION

The San Andreas fault is the longest fault (~1300 km) and has the highest slip rate of all faults in California. The northern section of the fault ruptured in 1906, and the south-central section ruptured in 1857. Only the southernmost section of the San Andreas fault has not ruptured during the historical record.

The Banning strand of the San Andreas fault is located within a complex portion of the southernmost section of the San Andreas fault zone (Fig. 1). Within the San Gorgonio Pass region, the fault bends to a west-northwest orientation, resulting in a complex zone of transpressional faults (Yule and Sieh, 2003). In addition, faults diverge northward from the southernmost section of the San Andreas fault toward the Eastern California shear zone (Fig. 1). This geometry triggers many questions about the southernmost section of the San Andreas fault system, such as: (1) How is plate-boundary slip accommodated within this region? (2) How have earthquake ruptures in this region made use of the various fault strands within this complex region?

The geometry of the southernmost San Andreas fault becomes more complex from southeast to northwest; the Coachella section is a single strand, but it splits as it approaches the San Bernardino Mountains (Fig. 1). Near Indio, California, the Banning strand diverges from the Mission Creek strand, and farther to the northwest, the Garnet Hill strand deviates from the Banning strand. In the San Gorgonio Pass region, the southernmost San Andreas fault comprises an intricate network of right-lateral, oblique thrust and reverse faults known as the San Gorgonio Pass fault zone (Allen, 1957; Matti et al., 1985; Matti and Morton, 1993; Yule and Sieh, 2003), which connects in turn with the San Bernardino strand of the southernmost San Andreas fault. None of the strands southeast of the San Bernardino section has ruptured in a major earthquake during the historical period, with the exception of the 1986 North Palm Springs earthquake of M_w 6.0, which produced minor fracturing, as discussed below. The Mill Creek strand, which diverges from the Mission Creek strand within the San Gorgonio Pass region, also connects to the San Bernardino strand, but its recency of motion is less clear (cf. Kendrick et al., 2015; Fosdick and Blisniuk, 2018). Given this complexity and limited slip rate data, it is has long been debated whether earthquake ruptures on the southernmost San Andreas fault have propagated through the faults within the San Gorgonio Pass region (Allen, 1957; Yule and Sieh, 2003).

The distribution of slip among various strands of the southernmost San Andreas fault is poorly known. The southeastern portion of the Mission Creek strand seems to accommodate the majority of the slip: The slip rate is 12–22 mm/yr (14–17 mm/yr preferred) at Biskra Palms (Fig. 1; Behr et al., 2010; Fletcher et al., 2010) and is 21.6 ± 2 mm/yr at Pushawalla Canyon (Blisniuk et al., 2021). The slip rate of the Banning strand has been proposed to be 2–6 mm/yr in the Indio Hills (Scharer et al., 2016), and it has been measured

*Present address: Department of Earth and Planetary Science, University of California, Berkeley, California 94709, USA

Downloaded from http://pubs.geoscienceworld.org/gsa/geosphere/article-pdf/17/3/685/5319464/685.pdf
by 19162

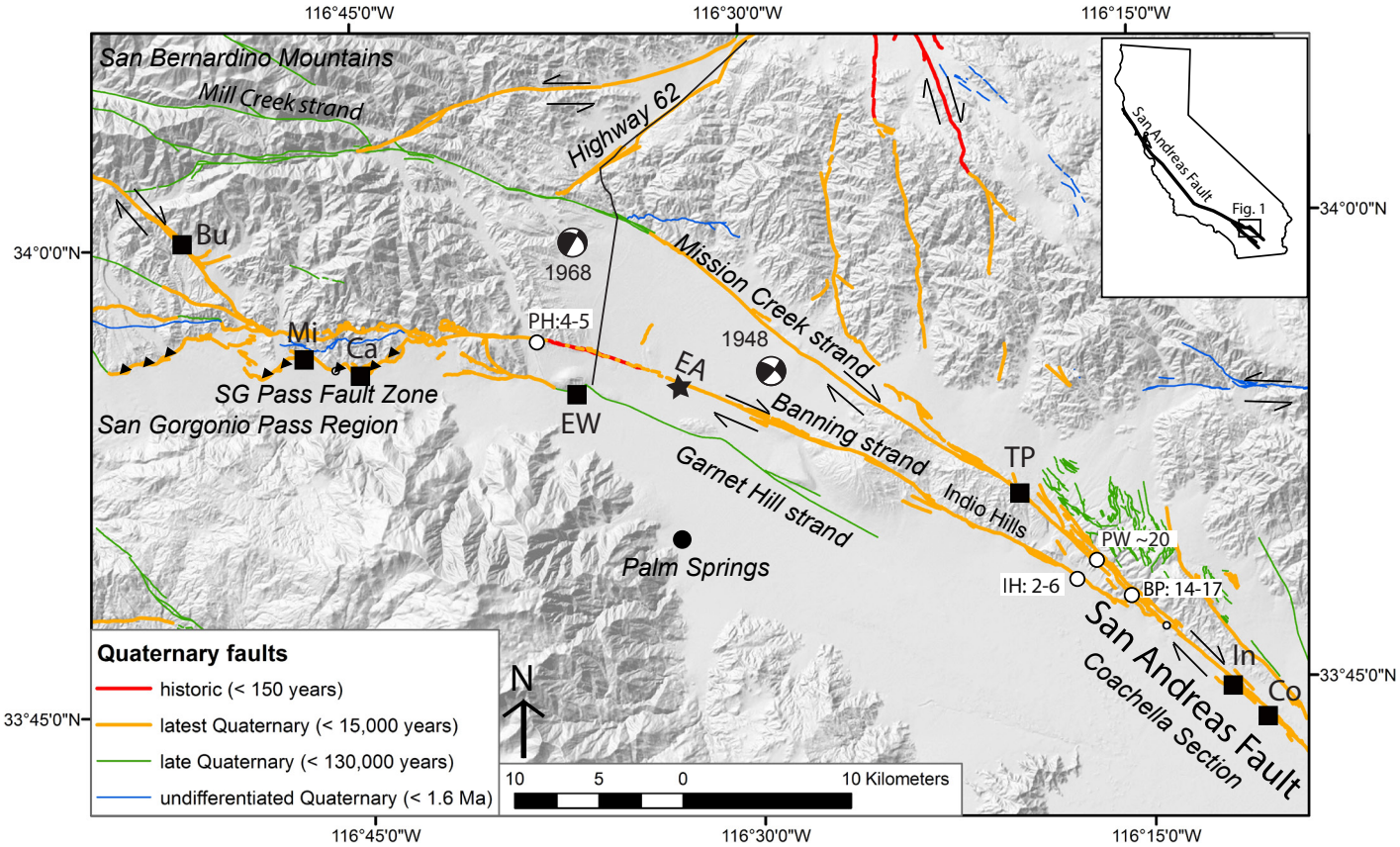

Figure 1. Quaternary fault map of the greater San Gorgonio (SG) Pass region in Southern California. Black star shows the location of the 18th Avenue paleoseismic site (EA) on the Banning strand of the southernmost San Andreas fault. Black squares mark the locations of other paleoseismic sites mentioned in the text (Co—Coachella [Philibosian et al., 2011]; In—Indio [Sieh and Williams, 1990]; TP—Thousand Palms [Fumal et al., 2002]; EW—East Whitewater site on the Garnet Hill strand [Cardona, 2016]; Ca—Cabazon [Scharer et al., 2013, abs.; Wolff and Yule, 2014, abs.]; Mi—Millard Canyon [Heermance and Yule, 2017]; Bu—Burro Flats [Yule et al., 2006]). White circles represents slip rate sites mentioned in the text (PH—Painted Hills [Gold et al., 2015]; IH—Indio Hills [Blisniuk et al., 2021]; PW—Pushawalla [Blisniuk et al., 2021]; BP—Biskra Palms [Behr et al., 2010; Fletcher et al., 2010]). Quaternary fault locations and recency of movement are from U.S. Geological Survey and California Geological Survey (2018).

at 2–6 (4–6 preferred) mm/yr at Painted Hills, near Whitewater (Gold et al., 2015). No slip rate estimates are available for the Garnet Hill fault, but it is thought to be an active right-lateral fault based on the presence of uplifted late Quaternary deposits along a series of left-stepovers (Yule and Sieh, 2003; Cardona, 2016).

Although the Mission Creek strand appears to have the highest slip rate of the fault strands in the Coachella Valley, Holocene slip on this fault strand is not established more than a few kilometers northwest of Highway 62 (Fig. 1), and late Quaternary activity on the continuation of this strand is debated (e.g., Kendrick et al., 2015; Fosdick and Blisniuk, 2018). Instead, slip on the Mission Creek strand has been proposed to transfer northward to the Eastern California shear zone (Nur et al., 1993; Rymer, 1997; Gold et al., 2015), as also suggested by modeling of geodetic data (Meade and Hager, 2005; McCaffrey, 2005; Spinler et al., 2010; McGill et al., 2015).

To better characterize the seismic behavior of the southernmost section of the San Andreas fault, the temporal behavior of these six faults (the Mission Creek, Mill Creek, Banning, Garnet Hill and San Bernardino strands, and the San Gorgonio Pass fault zone) must be examined, including the rate of

Downloaded from http://pubs.geoscienceworld.org/gsa/geosphere/article-pdf/17/3/685/5319464/685.pdf
by 19162

ground-rupturing prehistoric earthquakes. This paper contributes the first detailed record of dates of prehistoric earthquakes on the Banning strand.

Two significant historical earthquakes have occurred near the Banning strand of the San Andreas fault: the 1986 M_w 6.0 North Palm Springs earthquake and the 1948 M_w 6.3 Desert Hot Springs earthquake. Aftershocks of the 1986 event define a nearly planar surface that strikes N60–70°W, is ~15 km in length, dips northeast, and projects to the surface near the Banning strand trace (Nicholson, 1996). The first-motion focal mechanism for the main shock indicates essentially pure right-lateral slip (Nicholson, 1996). Aftershocks of the 1948 event define a plane that strikes N55°W, dips steeply 60° to 70°NE, is ~15 km long, and projects to the surface near the trace of the Banning strand near the northern end of the Indio Hills (Nicholson, 1996). This event was also predominantly right lateral in slip based on focal mechanisms (Nicholson, 1996). From this seismicity, Nicholson (1996) proposed that the Banning strand is nonvertical, is likely segmented according to fault dip as well as fault strike, and was the primary source of both of these recent, moderate-sized earthquakes in the Coachella Valley. A steeper northeastern dip for the Banning strand was modeled from seismic refraction and reflection lines (Fuis et al., 2017).

The 1986 earthquake triggered up to 9 mm of right-lateral slip 44–86 km southeast of the epicenter along the southernmost San Andreas fault (Sharp et al., 1986; Williams et al., 1988). It also produced some ground cracking on the Banning strand between Whitewater River and Highway 62 (Fig. 1), but this was considered to be caused by strong shaking rather than actual surface rupture (Sharp et al., 1986). The 1948 earthquake was very similar to the 1986 earthquake in that they were both initiated at depth, propagated bilaterally, and did not break the surface (Nicholson, 1996).

We report here: (1) the evidence and ages for eight recent paleoearthquakes on the Banning strand; (2) the average recurrence interval between earthquakes on this strand; and (3) a comparison of the timing of paleoearthquakes on the Banning strand with those on the San Gorgonio Pass fault zone and Mission Creek strand of the San Andreas fault.

SITE DESCRIPTION

Petra Geosciences excavated a paleoseismic trench on the Banning strand at 18th Avenue, North Palm Springs, California (33.9172°N, 116.538°W). The purpose of the trench was to determine the precise location of Holocene fault strands for the development of the site as required by the Alquist-Priolo Act of 1972. The lead consultant on the trench invited us to conduct a more detailed paleoseismic study on the open trench. The four-tier, benched trench was ~250 m long, ~8 m deep, ~9 m wide at the bottom and ~22 m wide at the ground surface. Most of this study focused on the northern end of the trench (Fig. 2), where an ~40-m-wide fault zone was exposed in interbedded boulder, cobble, gravel, sand, silt, and clay deposits. The trench was excavated into the floodplain of Mission Creek, an ~5-km-wide, broad alluviated surface that slopes gently to the south (Fig. 2, inset).

We observed recent faulting in the northernmost 40 m section of the trench. Five fault strands at the north end of the trench exhibited down-to-the-south faulting, whereas the eight to nine prominent fault strands farther south exhibited down-to-the-north separation (Fig. 3; Plate 1). The fault geometries and thickened section between them are consistent with a pull-apart basin, which likely formed as a result of a small right step in the Banning strand that is evident in publicly available light detection and ranging (lidar) data (Fig. 2; Bevis and Hudnut, 2005; Bevis et al., 2005). The trench configuration produced an asymmetrical exposure of the pull-apart basin because the trench is deepest at the south side of the fault zone and thus reveals older section and more vertical separation across faults. Unfortunately, a fiber-optic line prevented us from extending or deepening the northern end to look for similar relationships there. Although additional secondary faults may exist farther north than at the area excavated, we infer that the exposed pull-apart basin (from about 8 to 28 m) represents the main fault zone because the faults bounding it had the largest vertical displacements (Fig. 3; Plate 1) and the strongest facies changes across these faults (Plate 1), suggesting large strike-slip displacements.

Within the pull-apart basin, 1- to 20-cm-thick layers of very fine sand, silt, and clay were interbedded with coarse sand to granule layers up to 1 m thick. The fine-grained layers were thickest near the center of the pull-apart basin and thinned away from the center. Most of the fine-grained layers either pinched out or gradually became coarse grained within 16–18 m from the center of the basin. A few fine-grained layers extended all the way to the southern end of the section of the trench that was logged (~38–40 m from the center of the basin).

South of the fault zone, the trench was dominated by coarse sand and gravel units ~10–30 cm thick; fine-grained layers were absent, and a few layers contained boulders up to 0.5 m in diameter. Overall, the stratigraphy showed distinct and abrupt contacts between layers and consistent lateral continuity along the trench wall. Locally, and often near fault terminations, upper contacts were scoured and overlain by younger deposits. Our ability to follow contacts through the fault zone was locally restricted by two factors: (1) In places, the vertical separation (and presumably large lateral separation) produced strong changes in the texture of units across the fault zones, and (2) the width of the trench, 9 m at the base and 22 m at the ground surface, made the detailed correlation of strata between the west and east walls of the trench impossible, except for a few prominent layers.

METHODS

Field Work

Both the east and west walls of the trench had four vertical tiers ~1.5 m high separated by three horizontal benches (each ~1.5 m in width). We photographed the entire fault zone and used Structure-from-Motion photogrammetric techniques to produce a scaled photomosaic (Plate 1) that we used to log the trench (Fig. 3). Absolute reference frame and scale were determined with a

Downloaded from http://pubs.geoscienceworld.org/gsa/geosphere/article-pdf/17/3/685/5319464/685.pdf
by 19162

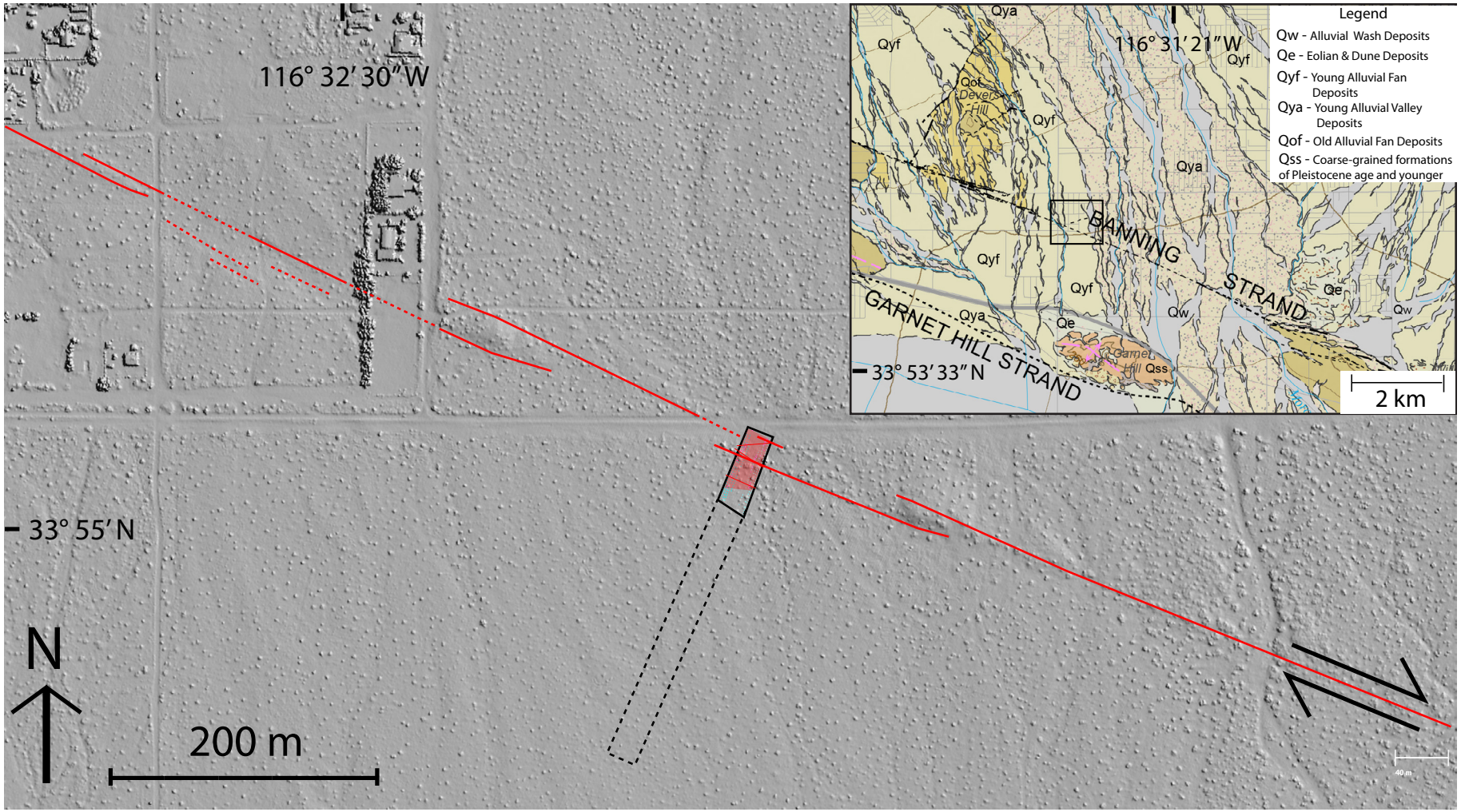

Figure 2. Light detection and ranging (lidar) hillshade image of the Banning strand (Bevis and Hudnut, 2005; Bevis et al., 2005). Fault traces (red lines) based on lidar and historical imagery show alternating steps, with left steps consistent with small pop-up structures. Black solid line shows extent of trench shown in Figure 3 and Plate 1. Within the trench, right-stepping faults are consistent with a pull-apart structure. Red polygon outlines extent of faulting observed in trench. No faults were observed in southern ~160 m of trench (black dashed line). Inset map shows setting of the site on alluvial fans and southward-draining channels (Lancaster et al., 2012).

Downloaded from http://pubs.geoscienceworld.org/gsa/geosphere/article-pdf/17/3/685/5319464/685.pdf
by 19162

Plate 1: 18th Ave Paleoseismic Site Trench Mosaics

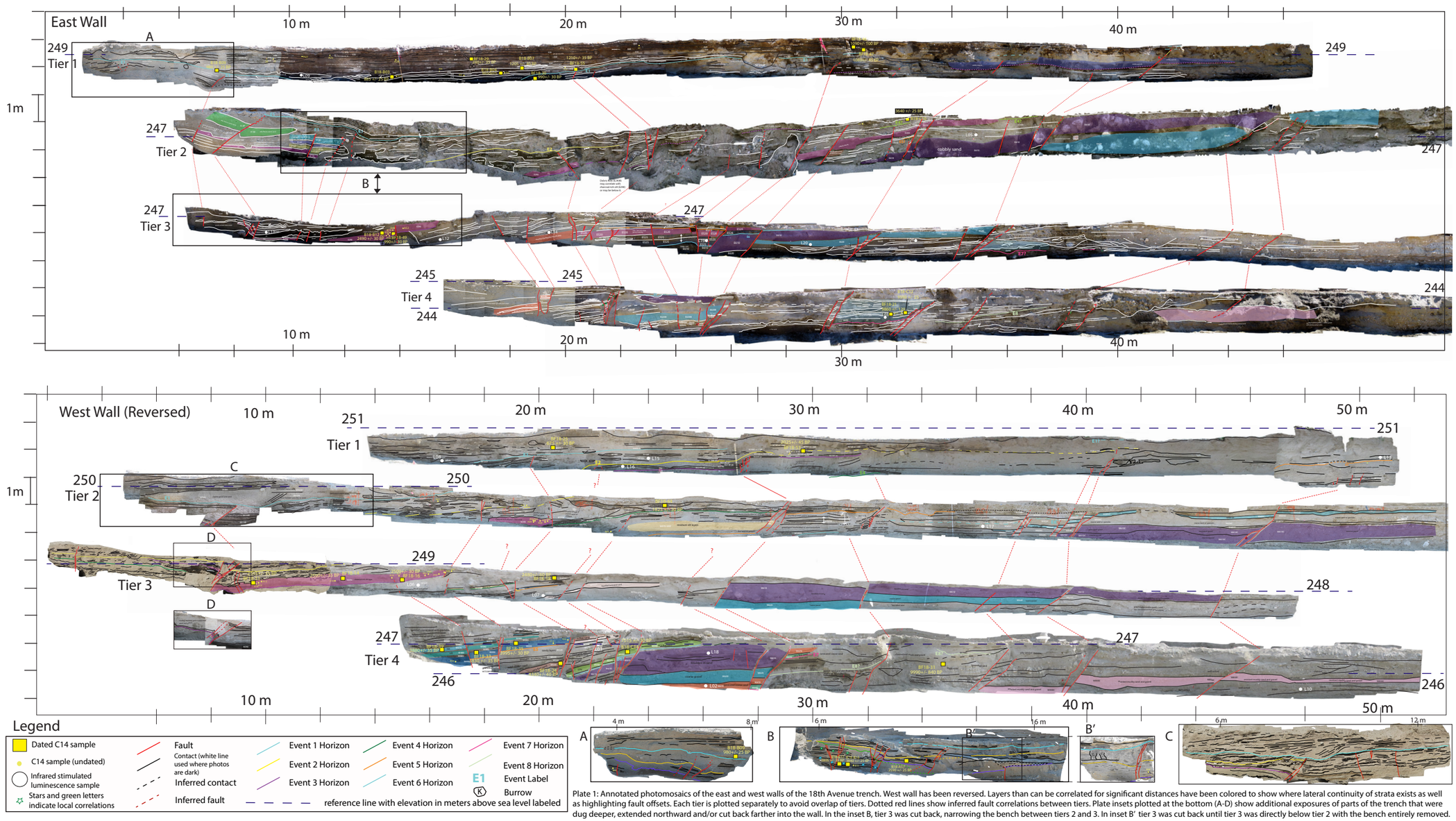

Plate 1: Annotated photomosaics of the east and west walls of the 18th Avenue trench. West wall has been reversed. Layers than can be correlated for significant distances have been colored to show where lateral continuity of strata exists as well as highlighting fault offsets. Each tier is plotted separately to avoid overlap of tiers. Dotted red lines show inferred fault correlations between tiers. Plate insets plotted at the bottom (A-D) show additional exposures of parts of the trench that were dug deeper, extended northward and/or cut back farther into the wall. In the inset B, tier 3 was cut back, narrowing the bench between tiers 2 and 3. In inset B′ tier 3 was cut back until tier 3 was directly below tier 2 with the bench entirely removed.

Plate 1. 18th Avenue paleoseismic site trench mosaics. IRSL—infrared stimulated luminescence.

To access Plate 1 at full size, please visit https://doi.org/10.1130/GEOS.S.14098595.

Downloaded from http://pubs.geoscienceworld.org/gsa/geosphere/article-pdf/17/3/685/5319464/685.pdf
by 19162

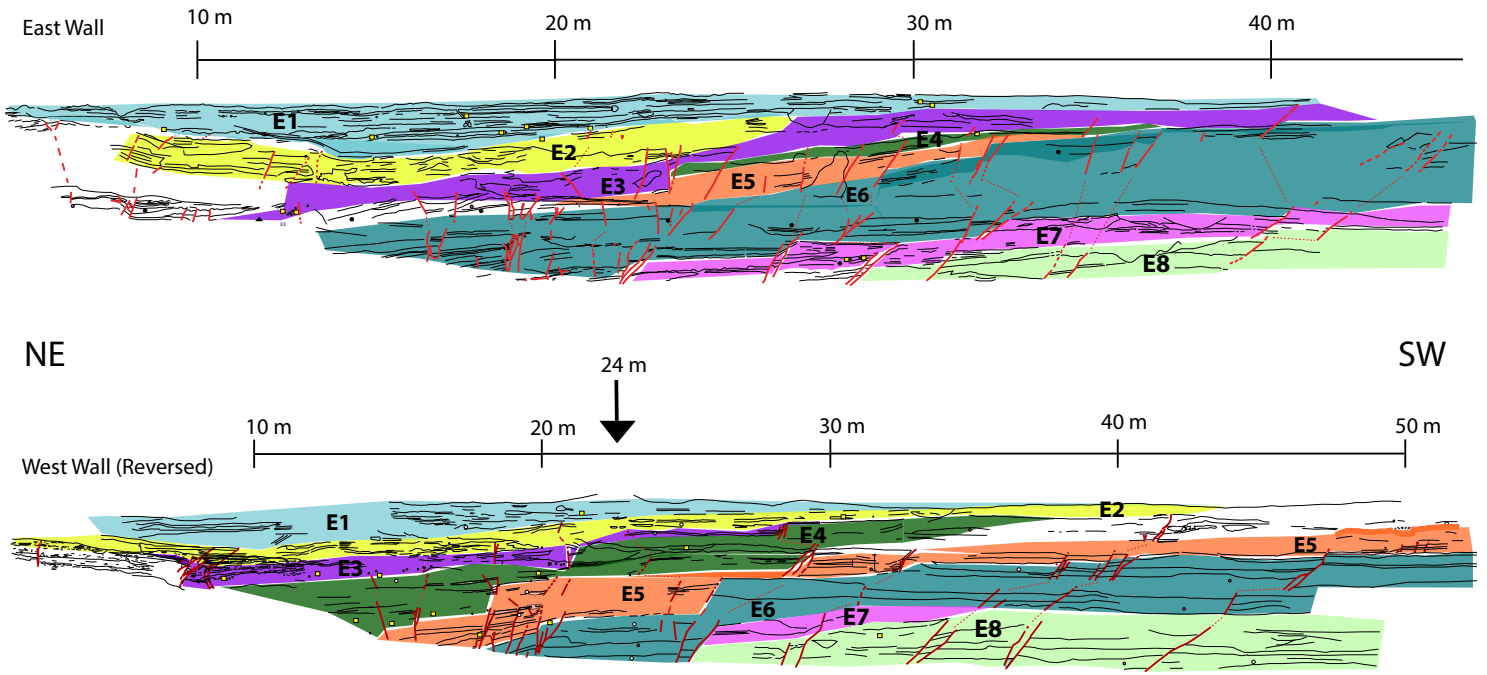

Figure 3. Simplified trench diagram to highlight thickness changes and extent of sedimentary packages associated with each earthquake. Each color illustrates the sedimentary packages between two event horizons. For example, the event 1 horizon is at the base of the light blue package labeled "E1." Benched walls are projected onto a single plane, causing some overlap and omission of units. Red subvertical lines are faults. Dashed thick red lines mark inferred faults in the trench wall. Dashed thin red lines show how faults connect across benches. Small symbols are sample locations, and black lines illustrate contacts between sedimentary layers. Arrow on meter 24 on the west wall locates the type section used to construct the stratigraphic age control column; no vertical exaggeration. E1–E8—earthquake events 1–8.

total station survey of a grid of nails placed ~2 m apart along the top and base of each tier. The photomosaic provided a base for logging of stratigraphic layers and faulting in the field. The final orthomosaic (Plate 1) was rectified using the surveyed nails as control points.

Dating

Thirty-three samples of charcoal, typically collected from fine-grained layers, were radiocarbon dated at the Center for Accelerator Mass Spectrometry at Lawrence Livermore National Laboratory to constrain the ages of the prehistoric earthquake horizons. We used the online software OxCal (Bronk Ramsey, 2009) with the IntCal 13 calibration curve (Reimer et al., 2013) to calibrate radiocarbon measurements. The results are listed in Table 1.

In total, 17 samples were collected and dated using post-infrared infrared stimulated luminescence protocol (p-IR IRSL; Buylaert et al., 2009) at the University of California–Los Angeles Luminescence Laboratory. The equivalent dose (D_e) values for individual grains were measured using a modified single-aliquot regenerative (SAR) dose protocol (Wintle and Murray, 2006) and synthesized into sample D_e values using conventional age models (Galbraith et al., 1999). Post-IR $IRSL_{225}$ ages were obtained by dividing D_e by the geologic dose rate on the DRAC 1.2 online calculator (Durcan et al., 2015). The mean age ± 1σ uncertainty are reported for all luminescence ages (Table 2). Details of the luminescence dating methods used are provided in the Supplemental Material.[1]

Recognition of Earthquake Horizons

A central challenge in paleoseismic investigations is to identify horizons that were at the ground surface when (prehistoric) earthquakes ruptured the fault. Upward termination of fault strands is a common type of evidence for an earthquake horizon. However, upward termination of fault strands alone

Supplementary Information for Castillo et al. (2020): Prehistoric earthquakes on the Banning strand of the San Andreas Fault, https://doi.org/10.1130/GES02237.1

This supplement provides details of the luminescence dating methods and results, as well as details about each indicator for each paleoseismic event in the 18th Avenue trench.

DETAILS OF THE LUMINESCENCE DATING METHOD AND RESULTS

K-feldspar grains of 175–200 µm diameter were isolated from the sedimentary samples under dim amber LED light conditions. Subsamples were wet-sieved and separated by density with lithium metatungstate (ρ <2.565 g/cm^3; Rhodes, 2015). Luminescence measurements were carried out using a TL-DA-20 Risø automated reader equipped with a single-grain IR laser (830 nm, at 90% of 150 mW; Bøtter-Jensen et al., 2003) and a $^{90}Sr/^{90}Y$ beta source. Emissions were detected using a photomultiplier tube with the IRSL signal passing through a Schott BG3- BG39 filter combination. Samples were mounted on aluminum single-grain discs with 100 holes. The gamma dose-rate was measured in situ using a calibrated, portable NaI gamma spectrometer, except for one sample (L11).

The U and Th concentrations were measured with inductively-coupled plasma mass spectrometry (ICP-MS), and the K concentration was measured using inductively-coupled plasma optical emission spectrometry (ICP-OES). These values were used to calculate the total beta dose rate contribution using the conversion factors of Liritzis et

[1]Supplemental Material. Details of luminescence methods and results, and table of event indicators. Please visit https://doi.org/10.1130/GEOS.S.14098589 to access the supplemental material, and contact editing@geosociety.org with any questions.

Downloaded from http://pubs.geoscienceworld.org/gsa/geosphere/article-pdf/17/3/685/5319464/685.pdf
by 19162

TABLE 1. RADIOCARBON DATES FOR 18TH AVENUE TRENCH SAMPLES

CAMS no.*	Original sample name	Simplified sample name	$\delta^{13}C$† (‰)	Fraction modern§	$\delta^{14}C$§ (‰)	^{14}C age§ (yr B.P.)	Calibrated ages (B.C./A.D.)			Calibrated ages (yr B.P.)		Sample location	Tier	Meter
							From	To	%	From	To			
176783	BF18-46	A46	–25	0.8731 ± 0.0105	–126.9 ± 10.5	1090 ± 100	693	1155	95.4	1257	795	East wall	1	29.2
176781	BF18-29	A29	–25	0.9708 ± 0.0038	–29.2 ± 3.8	240 ± 35	1522	—	95.4	428	—	East wall	1	17.3
176782	BF18-47	A47	–25	0.8741 ± 0.0046	–125.9 ± 4.6	1080 ± 45	779	1030	95.4	1171	920	East wall	1	29.5
177821	B18-B09	B09	–21.3	0.8853 ± 0.0026	–114.7 ± 2.6	980 ± 25	996	1154	95.4	954	796	East wall	1	9
177818	B18-B07	B07	–24.2	0.8606 ± 0.0038	–139.4 ± 3.8	1205 ± 40	688	945	95.4	1262	1005	East wall	1	19
177819	B18-B03	B03	–22.5	0.8956 ± 0.0026	–104.4 ± 2.6	885 ± 25	1045	1218	95.4	905	732	East wall	1	15
177820	B18-B04	B04	–25.7	1.0921 ± 0.0032	92.1 ± 3.2	>Modern ± N.A.#	1896	1904	95.4	54	46	East wall	1	18
176784	BF18-55	A55	–25	0.8602 ± 0.0033	–139.8 ± 3.3	1210 ± 35	689	938	95.4	1261	1012	East wall	1	20.4
176785	BF18-25	A25	–25.5	0.9201 ± 0.0027	–79.9 ± 2.7	670 ± 25	1276	1390	95.4	674	560	West wall	1	20.5
176786	BF18-30	A30	–24.2	0.8832 ± 0.0027	–116.8 ± 2.7	1000 ± 25	987	1149	95.4	963	801	East wall	1	19.3
176787	BF18-53	A53	–25	0.7773 ± 0.0043	–222.7 ± 4.3	2025 ± 45	–165	66	95.4	2115	1884	West wall	1	29
176788	BF18-11	A11	–22.7	0.7258 ± 0.0024	–274.2 ± 2.4	2575 ± 30	–811	–569	95.4	2761	2519	West wall	3	9.8
176789	BF18-14	A14	–24.0	0.7238 ± 0.0024	–276.2 ± 2.4	2595 ± 30	–825	–599	95.4	2775	2549	West wall	3	13
176790	BF18-49	A49	–24.2	0.7265 ± 0.0025	–273.5 ± 2.5	2565 ± 30	–806	–556	95.5	2756	2506	East wall	3	14.5
176791	BF18-16	A16	–25.4	0.7328 ± 0.0022	–267.2 ± 2.2	2495 ± 25	–773	–540	95.4	2723	2490	West wall	3	15
177825	B18-B12	B12	–23.9	0.7334 ± 0.0023	–266.6 ± 2.3	2490 ± 30	–781	–511	95.4	2731	2461	East wall	3	14
176792	BF18-44	A44	–22.6	0.7948 ± 0.0021	–205.2 ± 2.1	1845 ± 25	87	238	95.4	1863	1712	West wall	2	23.5
177826	B18-C10	C10	–25.0	0.6357 ± 0.0020	–364.3 ± 2.0	3640 ± 25	–2130	–1926	95.4	4080	3876	East wall	2	32.5
176793	BF18-18	A20	–25	0.7341 ± 0.0051	–265.9 ± 5.1	2480 ± 60	–777	–416	95.4	2727	2366	West wall	3	20
176794	BF18-39	A39	–25	0.6170 ± 0.0026	–383.0 ± 2.6	3880 ± 35	–2469	–2212	95.4	4419	4162	West wall	4	16
177829	BF18-33	A33	–25	0.6207 ± 0.0025	–379.3 ± 2.5	3830 ± 35	–2457	–2150	95.4	4407	4100	West wall	4	18
177830	BF18-35	A35	–20.6	0.6082 ± 0.0019	–391.8 ± 1.9	3995 ± 30	–2576	–2467	95.4	4526	4417	West wall	4	19.5
177849	BF 18-24	A24	–25	0.5826 ± 0.0027	–417.4 ± 2.7	4340 ± 40	–3086	–2890	95.4	5036	4840	West wall	4	20.5
177833	B18-C14	C14	–24.0	0.4176 ± 0.0016	–582.4 ± 1.6	7015 ± 30	–5987	–5840	95.4	7937	7790	West wall	4	23
176795	BF18-21	A21	–25	0.2932 ± 0.0040	–706.8 ± 4.0	9860 ± 120	–9859	–8855	95.4	11,809	10,805	East wall	4	31
177834	B18-C12	C12	–22.7	0.3030 ± 0.0009	–697.0 ± 0.9	9590 ± 25	–9151	–8823	95.4	11,101	10,773	East wall	4	32.5
176796	BF18-31	A31	–25	0.2885 ± 0.0299	–711.5 ± 29.9	9990 ± 840	–11,810	–7519	95.4	13,760	9469	West wall	4	34
177822	B18-B18	B18	–25	0.7723 ± 0.0049	–227.7 ± 4.9	2080 ± 60	–352	55	95.4	2302	1895	East wall	2	12
177823	B18-C01	C01	–26.7	0.7833 ± 0.0023	–216.7 ± 2.3	1960 ± 25	–38	115	95.4	1988	1835	East wall	1–2	N.A.#
177824	BF18-57	A57	–21.9	0.7244 ± 0.0021	–275.6 ± 2.1	2590 ± 25	–811	–767	95.4	2761	2717	East wall	3	10
177827	B18-B11	B11	–23.7	0.6371 ± 0.0022	–362.9 ± 2.2	3620 ± 30	–2118	–1984	95.4	4068	3934	East wall	3B	14.5
177828	B18-B10	B10	–25	0.6381 ± 0.0026	–361.9 ± 2.6	3610 ± 35	–2120	–1885	95.4	4070	3835	East wall	3B	14.5
177831	B18-B16	B16	–22.0	0.6201 ± 0.0019	–379.9 ± 1.9	3840 ± 25	–2456	–2203	95.4	4406	4153	East wall	3	7
177832	B18-B17	B17	–25	0.6226 ± 0.0026	–377.4 ± 2.6	3805 ± 35	–2435	–2136	95.4	4385	4086	East Wall	3	7

Note: Samples from 18th Avenue paleoseismic trench, North Palm Springs, California (33.9172°N, 116.538°W). Sample preparation backgrounds have been subtracted based on measurements of samples of ^{14}C-free coal. Backgrounds were scaled relative to sample size. Error is large on 176796 in part due to the age of sample (nearly two half lives), even though the target was 110 µg C.

*CAMS—Center for Accelerator Mass Spectrometry sample number. CAMS 176783 and 176795 were <30 µg C samples.

†$\delta^{13}C$ values are the assumed values according to Stuiver and Polach (1977) when given without decimal places. Values measured for the material itself are given with a single decimal place.

§Radiocarbon concentration is given as fraction modern, $\delta^{14}C$, and conventional radiocarbon age. The quoted age is in radiocarbon years before present using the Libby half life of 5568 yr and following the conventions of Stuiver and Polach (1977).

#N.A.—not available.

Downloaded from http://pubs.geoscienceworld.org/gsa/geosphere/article-pdf/17/3/685/5319464/685.pdf
by 19162

TABLE 2. DOSE-RATE INFORMATION AND POST-IR IRSL AGES FOR 18TH AVENUE TRENCH SAMPLES

Lab code	Field code	Unit	Depth (m)	K* (%)	Th* (ppm)	U* (ppm)	Measured gamma dose rate† (Gy/k.y.)	Total dose rate (Gy/k.y.)	Equivalent dose (Gy)	Post-IR IRSL age§,# (ka)
J1284	L01 (BF17-01)	W570	3.8	2.8	19.2	3.28	1.993 ± 0.004	6.011 ± 0.26	21.69 ± 2.2	3.61 ± 0.4
J1285	L02 (BF17-02)	W670	4.9	2.7	18.1	2.56	1.897 ± 0.004	5.466 ± 0.23	29.29 ± 2.15	5.36 ± 0.45
J1286	L03 (BF17-03)	E690	5.1	2.7	16.3	2.65	1.709 ± 0.004	5.037 ± 0.213	31.82 ± 1.16	6.32 ± 0.35
J1287	L04 (BF17-04)	E630	3.5	2.8	15.9	2.57	1.944 ± 0.005	5.487 ± 0.229	28.31 ± 3.6	5.16 ± 0.69
J1288	L05 (BF17-05)	E510	2.6	2.7	21.6	2.78	2.458 ± 0.005	6.372 ± 0.265	31.93 ± 1.76	5.01 ± 0.35
J1289	L06 (BF17-06)	W320	2.9	2.7	17.3	2.46	1.925 ± 0.004	5.69 ± 0.243	13.12 ± 1.78	2.31 ± 0.33
J1290	L07 (BF17-07)	W540C	3.2	2.8	18.7	2.97	1.931 ± 0.004	5.899 ± 0.255	17.19 ± 1.71	2.91 ± 0.32
J1291	L08 (BF17-08)	W82B	0.8	2.7	18.5	2.44	1.891 ± 0.004	5.702 ± 0.242	4.04 ± 0.69	0.71 ± 0.13
J1292	L09 (BF17-09)	E40	0.8	2.9	15.1	2.51	1.716 ± 0.004	5.074 ± 0.214	4.29 ± 0.51	0.85 ± 0.11
J1293	L10 (BF17-10)	W860	6	2.6	19.3	2.46	1.946 ± 0.004	5.542 ± 0.234	39.00 ± 3.12	7.04 ± 0.64
J1294	L11 (BF17-11)	E260	3	2.8	13.8	2.02	N/A ± N/A**	5.212 ± 0.233	9.84 ± 0.57	1.89 ± 0.14
J1394	L15 (BF17-15)	W150E	0.8	2.5	16.1	2.17	1.922 ± 0.005	4.879 ± 0.199	6.59 ± 1.03	1.35 ± 0.22
J1395	L16 (BF17-16)	W220E	1.3	2.8	18.3	2.91	1.874 ± 0.004	5.904 ± 0.256	9.82 ± 1.18	1.66 ± 0.21
J1396	L17 (BF17-17)	W602C	2.4	2.3	16.9	2.73	2.004 ± 0.005	5.517 ± 0.228	28.37 ± 2.84	5.14 ± 0.56
J1397	L18 (BF17-18)	W610	4	2.5	16.3	2.09	1.971 ± 0.005	5.054 ± 0.206	28.74 ± 3.04	5.69 ± 0.64
J1398	L19 (BF17-19)	E525	3.6	2.5	17.5	2.71	2.111 ± 0.005	5.084 ± 0.208	20.55 ± 2.78	4.04 ± 0.57
J1399	L20 (BF17-20)	E620	3.7	2.4	17.4	2.71	1.89 ± 0.005	5.297 ± 0.219	26.03 ± 2.94	4.91 ± 0.59

Location: 33.9174°E, 116.5389°W, 247 m above sea level.

Note: Grain size used was 175–200 µm. Radionuclide conversion factor is after Liritzis et al. (2013); α attenuation factor is after Brennan et al. (1991); β attenuation factor is after Guerin et al. (2012). Internal K contents were 12.5% ± 0.5% after Huntley and Baril (1997). Cosmic dose rates followed Prescott and Hutton (1994). Post-IR IRSL—post-infrared infrared stimulated luminescence.

*U, Th, and K contents were derived via inductively coupled plasma–optical emission spectrometry (ICP-OES) with relative uncertainties of 5%.

†Gamma dose rate derived from in situ gamma spectrometry.

§Ages were calculated in DRAC calculator (Durcan et al., 2015).

#No fading was observed. Errors are reported as 1σ.

**N.A.—not available.

does not always provide a reliable indicator of the stratigraphic position of an earthquake horizon because fault strands with small displacements may not necessarily have ruptured all the way to the ground surface at the time of an event (e.g., Bonilla and Lienkaemper, 1991). Earthquake horizons are considered more reliable if a sedimentary response to the displacement is preserved (e.g., Scharer et al., 2017; Onderdonk et al., 2018). For example, when a graben or uphill-facing fault scarp is formed, it may create a closed depression where water will pond and deposit fine-grained material in the depression. In this configuration, the fault scarp may be preserved and buried by the fine-grained sediments, which generally thin and pinch out at the edges of the depression that formed as a result of vertical separation at the surface. Thus, both the fault strand and the subsequent depositional record provide more robust evidence of the paleoearthquake horizon than simple upward termination alone.

At the 18th Avenue trench, most of the exposed fault strands accommodate a component of down-to-the-north displacement. Given the southward slope of the floodplain of Mission Creek, down-to-the-north displacement on individual fault strands created uphill-facing scarps and ponding of fine-grained sediments. Thinning of fine-grained layers across the scarps that filled fault-bounded depressions provided strong evidence for some of the earthquake horizons at the site.

Event Indicator Quality Ranking

At the 18th Avenue trench, we found evidence for eight paleoearthquake horizons with varying quality. To compare the strength of evidence for the different events, we used a ranking scale to classify each of the indicators based on the quality of structural and sedimentological evidence used to identify the stratigraphic level that was at the ground surface at the time of the event. Each event indicator was given a quality rank on a scale of 0 to 5, with higher numbers representing more reliable evidence (Table 3). Table 3 was developed based on a table previously published in Scharer et al. (2017), with several modifications that tailored the criteria to the 18th Avenue trench. Because of unique considerations related to local geology and fault zone architecture, there are always a certain number of site-specific decisions/adjustments that must be made.

Downloaded from http://pubs.geoscienceworld.org/gsa/geosphere/article-pdf/17/3/685/5319464/685.pdf
by 19162

TABLE 3. DESCRIPTION OF EVENT INDICATORS AND ASSOCIATED QUALITY RANKING

Quality	Description
0	Fault tip where upward termination is not distinct due to unclear stratigraphy, resulting in uncertainty as to the event during which this fault slipped, with no preferred event horizon among the possibilities. Fault tip has distinct upward termination, but the event with which it is associated remains unclear because the fault terminates upward at a scoured contact that erodes though one or more event horizons.
1	Fault has minor offset (<5 cm), even if the upward termination is distinct. Fault has moderate offset but indistinct upward termination, allowing multiple interpretations for the event horizon during which this fault slipped. Nonetheless, there is reason to prefer association of this indicator with one of these event horizons over the others. Minor or gradual thickness changes occur across fault that could simply reflect depositional gradients rather than filling of earthquake-produced depression. Folding amplitude is small, and thickness change above horizon of folding is moderate, but stratigraphic location of the lowest unfolded layers is indistinct enough to allow for multiple interpretations for the event horizon during which this folding occurred. Nonetheless, there is reason to prefer one of these event horizons over the others. Possible fissure is observed that could alternatively be interpreted as shear of a massive layer disrupted by multiple fault strands.
2	Fault has moderate offset (≥5 cm) and indistinct upward termination, but the indicator can still be clearly associated with one event horizon. Folding amplitude is small, and thickness change above horizon of folding is moderate.
3	Fault tip has distinct upward termination and moderate offset (≥5 cm). Folding and thickness changes in layers above folding horizon are substantial (~20 cm), but folding horizon has no clearly causative fault, and (or) the horizon of folding is difficult to discern. Possible fissure is observed for which the fill material does not clearly postdate the inferred event horizon, and both walls of the fissure are faults that have reruptured in a younger event.
4	Fault tip is associated with a colluvial wedge or layer thickness changes that reflect modification or erosion of scarp. Possible fissures are observed for which the fill material does not clearly postdate the inferred event horizon, but at least one wall of the fissure is a fault with a distinct upward termination, which has not reruptured in a younger event. Broad warping and large thickness changes in the layer above the folding horizon indicate rapid filling of a depression closely related to the fault that moved to provide accommodation space.
5	Fissures are clearly filled with material that postdates the inferred event horizon. Folding and growth strata occur in which it is clear that the topography was rapidly filled by a single sedimentation event, and event horizon has a causal fault.

Note: Table is modified from Scharer et al. (2017) to reflect the depositional characteristics of the 18th Avenue site.

First, it is common for faults that slipped with minor displacement to terminate upward at different stratigraphic levels because some of the strands did not rupture all the way to the surface (Bonilla and Lienkaemper, 1991; Weldon et al., 2002). Because of this, Scharer et al. (2017) made a distinction between faults with minor offset versus faults with moderate offset, with the latter being viewed as more likely to have ruptured to the ground surface, thus meriting a higher quality ranking. We chose to classify faults as having "moderate" offset if there was ≥5 cm of vertical separation, or if the correlation of units across the fault was uncertain due to textural changes, indicating that the lateral slip was reasonably large. Previous studies have documented rupture with up to 20 cm of vertical separation that terminated at different stratigraphic levels during the same prehistoric earthquake (e.g., Weldon et al., 2002; Bonilla and Lienkaemper, 1991). In other studies, earthquakes with displacement of only a few millimeters or less have ruptured to the ground surface (e.g., McGill and Rubin, 1999). Our selection of 5 cm to define "moderate" offset falls between these values.

Second, we adjusted the ranking to take into account the effects of uncertainties in stratigraphic correlation that made attribution of an indicator to a specific horizon challenging. Specifically, in cases where the upward termination of a fault was not distinct, and there were multiple horizons that could reasonably be associated with the upward termination, we assigned a quality ranking of 0. If the upward termination was indistinct or unclear, but there was an unfaulted unit that was distinguishable below the next higher earthquake horizon, we assigned a quality ranking of 1 for minor offset and 2 for moderate offset, because this was clearly an event distinct from the next younger event, even if the precise location of the earthquake horizon could not be determined. It is worth noting that our treatment of upward fault terminations was designed to produce a minimum number of paleoearthquakes. In other words, in cases where a fault terminated below the stratigraphic level of a known earthquake horizon elsewhere in the trench, and if there were no unfaulted layers precluding the fault from extending up to the earthquake horizon, we assumed that the fault did extend up to the previously recognized earthquake horizon.

Third, Scharer et al. (2017) made a distinction between folding and thickness changes that are "small" versus those that are "substantial," with the latter being viewed as more likely to have resulted from coseismic deformation of the ground surface, thus meriting a higher quality ranking. We specified thickness changes of 20 cm or more to be "substantial," thus justifying a ranking of 3 if a causative fault was not clearly identifiable or 4 if a causative fault was identifiable. Our selection of 20 cm reflected our subjective judgement based on observations in unfaulted portions of the trench where thickness changes and undulations in contacts smaller than this may have resulted from nontectonic causes in some cases.

Stratigraphic Correlation Rankings

Uncertainties in stratigraphic correlation at the 18th Avenue trench led to difficulty in tracing the event horizons along the trench and between the two

Downloaded from http://pubs.geoscienceworld.org/gsa/geosphere/article-pdf/17/3/685/5319464/685.pdf
by 19162

walls, thus producing additional uncertainty in the event recognition. Because of the broad width of the trench, only four distinctive layers could be confidently correlated between the east and west walls. Even along the same wall of the trench and in the absence of faulting, lateral facies changes, local channel scour, and areas of poor stratigraphy made it challenging to trace some stratigraphic units over long distances (>10 m). Most strata could be clearly correlated across faults with minor offset, but stratigraphic correlation was more difficult across a few of the faults with larger amounts of offset.

To address the uncertainty in our stratigraphic correlation of event indicators, we created a stratigraphic correlation ranking table (Table 4). This correlation ranking table required a "type locale" to be defined for each individual event. We selected the type locale from among the best-ranked event indicators for that specific event (i.e., where the event horizon could be narrowly assigned within a stratigraphic package) and located where it was possible to correlate layers at the type locale with other event indicators. The relative stratigraphic position of each event horizon was traced along the trench wall (i.e., within a particular stratigraphic package) from the type section to the other indicators that occurred at that stratigraphic level. A stratigraphic correlation rating between 1 and 5 was assigned based on the continuity of the package. A rating of 5 means an event indicator could be easily followed all the way to the type section, confirming it was located at the same stratigraphic level as the event horizon at the type section. A rating of 1 means that the correlation was uncertain enough to create ambiguity as to the event horizon to which this indicator should be associated. This situation could result from pinch out of marker beds, mismatch or changes in character of units across faults or along section, position of benches, or presence of bioturbated zones. It is worth noting that we attempted to assign each event indicator to an event that also had other indicators, rather than treating each indicator that had an uncertain correlation as a potential independent event. Our method, therefore, was biased toward producing the minimal number of events necessary to explain the observations.

TABLE 4. DESCRIPTION OF STRATIGRAPHIC CORRELATION RANKINGS

Quality	Description
1	Stratigraphic correlation of one or more event horizons is uncertain enough to create ambiguity as to the event with which this indicator should be associated.
2	The stratigraphic level of the indicator cannot be physically traced all the way to the type locale because it crosses one or more faults, benches are areas of poor stratigraphy, leading to a relatively high level of uncertainty, including the possibility that the indicator could correlate with an event other than the proposed event.
3	The stratigraphic level of the indicator cannot be physically traced all the way to the type locale because it crosses a fault, a bench, or an area of poor stratigraphy. The correlation of strata is somewhat uncertain, but correlation with the proposed event is much more likely than correlation with any other recognized event. This rating may be applied to an indicator on the opposite wall from the type locale for the event, as long as it is not far above or below one of the three layers that have been correlated between the walls (units E/W 290, E/W 610, or E/W 850).
4	The stratigraphic level of the indicator cannot be physically traced all the way to the type locale because it crosses a fault, a bench, or an area of poor stratigraphy, but the correlation of strata is fairly certain. This rating may also be applied to an indicator on the opposite wall from type locale for this event, as long as it is not far above or below one of the three layers that have been correlated between the walls (units E/W 290, E/W 610, or E/W 850).
5	The stratigraphic level of the indicator can be **physically traced** all the way to the type locale, with no uncertainty in correlation of strata across any faults located between the indicator and the type locale. This can only be true for indicators that are on the same wall as the type locale for event.

Characterizing the Likelihood of Each Event

We qualified the likelihood of a paleoearthquake at each stratigraphic horizon based on the quality and the number of individual event indicators. Following the example of Scharer et al. (2017), we used the terms "probable," "likely," and "very likely" to denote horizons with increasing probability of representing a paleoearthquake horizon. Also, like Scharer et al. (2017), we used the label "probable" when the number and quality of event indicators suggested at least a 50% likelihood of a surface-rupturing event at that horizon. At this site, we considered events that had three or more indicators with at least one having a quality rating of 2 or higher to be probable earthquakes. Those with one or two indicators with quality rankings of 3 or higher were considered likely or very likely, respectively (Table 5). Horizons with isolated, weak evidence that did not meet these criteria were not given an event number. As noted above, our treatment of upward fault terminations and our approach to correlating earthquake indicators were both designed to produce the minimum number of events. It is quite possible that additional events occurred that were not identified due to these approaches. It is also possible that multiple events occurred at any of the identified horizons if no sedimentation occurred between events.

TABLE 5. CRITERIA FOR CHARACTERIZING THE LIKELIHOOD OF EVENTS

Likelihood	Description
Probable	Three or more individual event indicators with at least one having a quality ranking of 2. No indicator has a quality rank higher than 2.
Likely	At least one event indictor with a quality rank of 3 or higher. Must have 3–5 individual event indicators with at least a rank of 1.
Very likely	Two or more event indicators with a rank of 3 or higher.

SITE STRATIGRAPHY

The orthorectified, georeferenced, and annotated photomosaics for the west and east walls of the trench are shown in Plate 1. A simplified representation

Downloaded from http://pubs.geoscienceworld.org/gsa/geosphere/article-pdf/17/3/685/5319464/685.pdf
by 19162

of the contacts and faults extracted from Plate 1 is shown in Figure 3. Within Plate 1, strata that could be traced were assigned unit numbers, with unit numbers increasing with stratigraphic depth.

Four correlatable units were used to anchor the stratigraphic numbering of units between the trench walls. The uppermost unit is unit 290, which is a 30-cm-thick silt layer with a distinct thin, brown clay at its base. This unit contains more charcoal fragments than any other unit within the trench. The next lower anchor unit is unit 610. On the east wall, this unit is distinguished by the presence of many large boulders (~0.5 m diameter) within a 0.5- to 1-m-thick layer of coarse sand with pebbles and granules. Boulders this large are not present within any other unit. On the west wall, this unit is sandier, and the boulders are smaller (~0.25 m), but it is still the coarsest unit on the west wall, and it is a similar depth below the surface. Immediately below unit 610, there is unit 620, which is composed of coarse sand, pebbles, and small boulders (~0.25 m diameter) on the west wall and pebbly gravel on the east wall. These two units are separated by a sharp contact. The lowest unit is unit 850, a muddy sand and gravel bed with a sharp upper contact. The unit is brownish in color compared to overlying units, which are grayer in color.

All units on the west wall have a "W" prefix before the unit number, and those on the east wall have an "E" prefix. Unit numbers between 0 and 99 were assigned to strata above the E1 horizon, numbers between 100 and 199 were assigned to strata between the E1 and E2 horizons, and so on. Except for units 290, 610, 620, and 850, it was impossible to correlate units between the two walls. Thus, units that have the same number but a different prefix (E vs. W) should not be interpreted as correlating at all across the trench, nor should units with a lower number on one wall necessarily be assumed to be younger than a unit with a higher number on the opposite wall. Uncertainties in correlation of the event horizons were addressed through the correlation ranking system described above (Table 4).

Some unit labels also include a suffix letter after the unit number. In regions where a layer could be traced or correlated with certainty, the suffix letter is the same. In cases where there was some uncertainty in the correlation of the layer across a fault, bench, or region of poor stratigraphy, a different suffix letter was used on each side of the feature interrupting the ability to continuously trace the layer. For example, unit W110A is a very fine sand layer that crosses a fault at meter 8 on tier 2 of the west wall (Plate 1). The plate shows a possible correlation of unit W110 across this fault, but because the correlation is not confirmed by other layers offset with a similar sense and amount, we call this unit W110B on the opposite side of this fault. Similarly, at meter 12 on tier 2 on the west wall, we make a proposed, but uncertain correlation of this unit across an area of poor stratigraphy, so the unit is labeled W110C.

EARTHQUAKE HORIZONS

A complete listing and description of all evidence for each event, including event quality and stratigraphic correlation ratings, may be found in Table S1 in the Supplemental Material. Figure 4 summarizes these data by illustrating the number of indicators for each event, as well as their quality and stratigraphic correlation rankings. The following sections explain key pieces of event evidence in detail. When referring to event indicators, we abbreviate their location by providing the meter number followed by the wall on which the event indicator is located and the tier number in parentheses; e.g., m36W (tier 1) refers to tier 1 on the west wall at meter 36. As will be shown below, applying Table 5, we distinguished one very likely event (E1), four likely events, and three probable events.

E1. *Very Likely.* The most recent paleoearthquake at the 18th Avenue paleoseismic site has 16 event indicators. There are three pieces of evidence with a

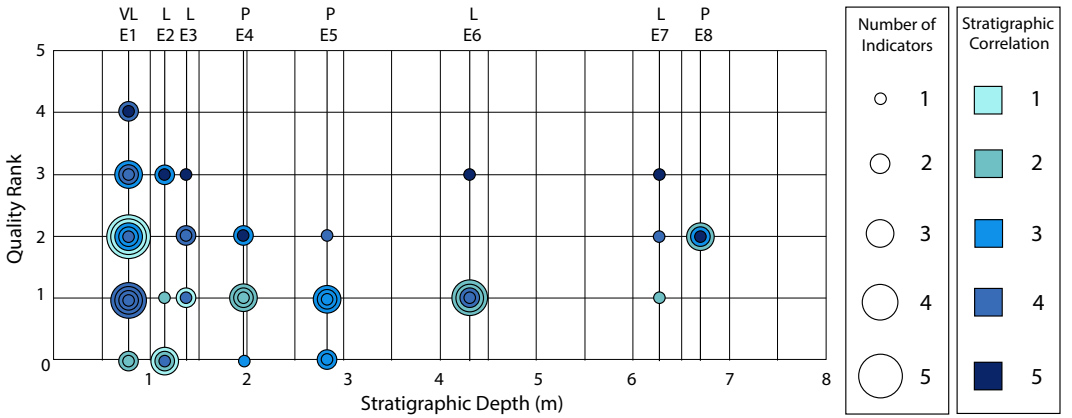

Figure 4. Summary of event indicators. Eight paleoearthquake horizons were identified in the 18th Avenue trench. Events are arranged according to stratigraphic depth on the horizontal axis. Vertical axis indicates quality ranking of each indicator, with higher numbers indicating better quality. The diameter of the symbol is scaled by the number of indicators in each rank. For example, earthquake horizon E1 has five individual event indicators with a rank of 2, producing a symbol diameter of 5. Color of symbols represents the stratigraphic correlation ranking of each event indicator. Indicators with a darker color can be correlated to the type section of the event with greater certainty. For example, of the five rank 2 event indicators for E1, one has a correlation strength of 4, two have a correlation strength of 3, and two have a correlation strength of 1. VL, L, and P indicate the event ranking of very likely, likely, and probable.

Downloaded from http://pubs.geoscienceworld.org/gsa/geosphere/article-pdf/17/3/685/5319464/685.pdf
by 19162

ranking of 3 and two with a ranking of 4 (Plate 1; Table S1), all of which involve sharp upward termination of faults with more than 5 cm of vertical separation and/or stratigraphic units that thin and pinch out against a scarp or folding horizon. An event indicator with a rank 3 is shown in Figure 5A. Two of these five strong pieces of evidence were on the west wall, and three were on the east wall. On each wall, the stratigraphic horizon associated with the strongest evidence for E1 could be traced with moderate to high certainty along the length of the trench. Although it was impossible to physically correlate individual layers in this stratigraphic range between the two walls due to the configuration of the excavation, the sediment packages were similar on both walls (discontinuous 2- to 10-cm-thick layers of coarse sand with granules, fine sand, and silt). Given the similarity in the style of deformation and units both deformed by and postdating the deformation, we infer that the paleoearthquake closest to the present-day ground surface is the same on both walls. There were also 11 lower-rated indicators. Four were faults that terminated upward at the E1 horizon but that had very small amounts of vertical separation,

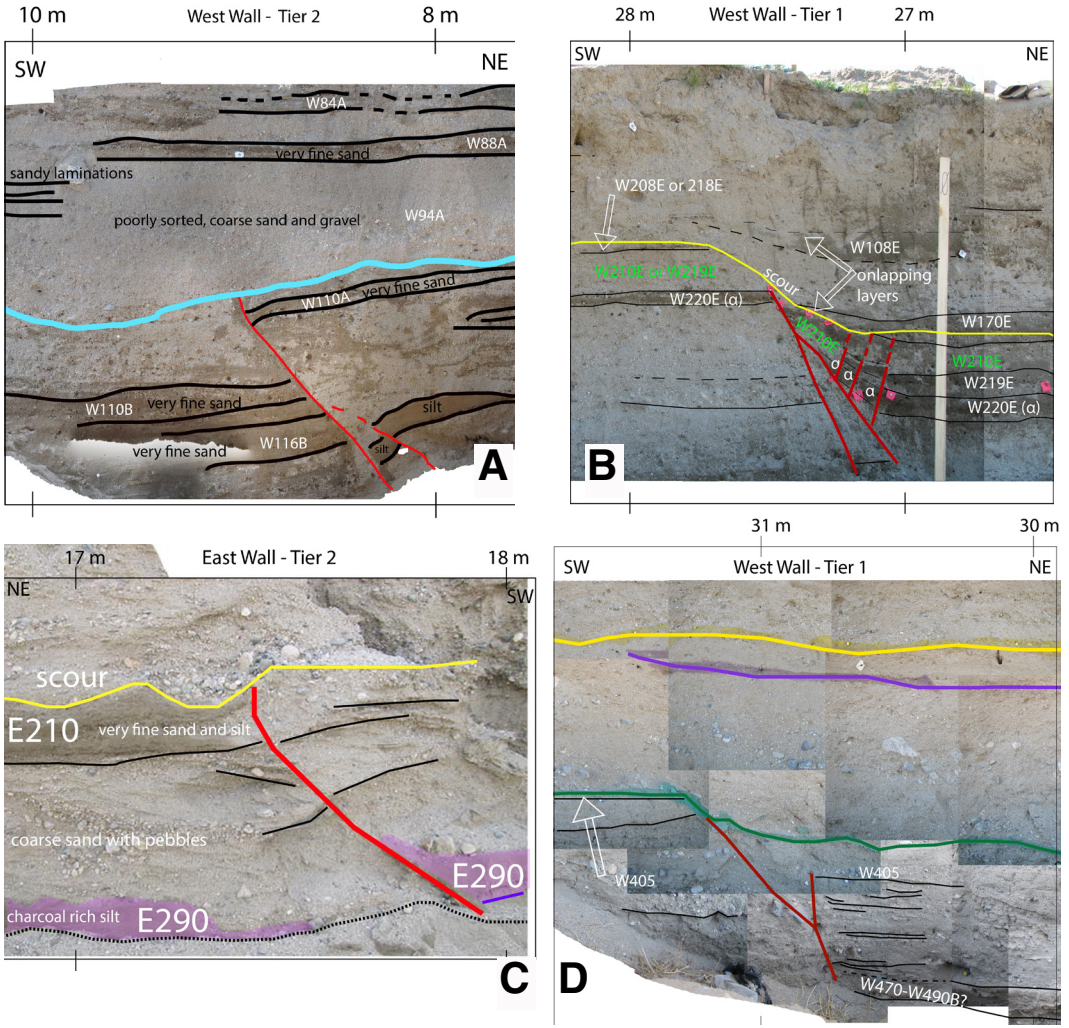

Figure 5. (A) Faulting evidence for event E1 at 8–10 m on tier 2 of the west wall. A fault terminates sharply at the base of an erosive contact (colored light blue). This fault displays at least moderate offset due to one of the following reasons: (1) There is a very fine sand layer that is visible on both sides of the fault and is labeled as W110A and W110B. If this layer is in fact the same layer, then there is at least 40 cm of vertical separation. (2) Alternatively, if layer W110A is not the same as layer W110B, then correlation of layers across the fault is difficult and suggests a large amount of lateral offset. A similar relationship is observed at this stratigraphic interval on the east wall. (B) Event 2 type locale at 26–28 m on tier 1 of the west wall. Series of faults terminate upward at the base of the yellow contact (E2 horizon). The nature of the yellow contact indicates that it is an erosional contact showing scour of the ground surface after deposition of W210E, followed by onlap of W170E and younger strata. This feature has a quality rank of 3. The labels "α" mark the locations of faulted pieces of layer W220E across the fault zone. (C) Exposures of an indicator for E2 on tier 2 of east wall. Here, mismatch of units across the fault indicates lateral separation when E210 was at (or below) the surface. The fault terminates at the base of an erosive contact (yellow line). This indicator has a quality rank of 3. Purple line shows E3 horizon for context. Dotted line delineates the base of the exposure and is not a geologic contact. (D) Type locale for event 4, at 30–32 m on tier 1 of the west wall. Lower part of figure includes photos from a hand-dug, deeper extension of tier 1 that are not included in Plate 1. Green line spray painted on trench wall (and drafted on the photomosaic) highlights the E4 horizon. A fault vertically separates layer W405 and is truncated by an erosional contact (green horizon) that marks the base of a sandy channel and the E4 horizon. The yellow and purple lines represent earthquake horizons E2 and E3, respectively.

Downloaded from http://pubs.geoscienceworld.org/gsa/geosphere/article-pdf/17/3/685/5319464/685.pdf
by 19162

and seven were faults that terminated 8–40 cm below the E1 horizon but that were assumed to have slipped during E1 because of the lack of any unfaulted stratigraphy that would preclude that interpretation (Table S1). It is possible that these seven faults that terminated 8–40 cm below the E1 horizon could represent one or more additional earthquakes between events 1 and 2, but we think it is more likely that they slipped during E1 and that the faults cannot be traced higher due to poor stratigraphy.

E2. *Likely.* There are six indicators for this event, including two with quality rank 3, one with rank 1, and three with rank 0 (Fig. 4). The type locale for this event has a quality ranking of 3 and is located at m28w (tier 1) (Fig. 5B). At that location, layer W220E is vertically separated ~40 cm across a zone of four faults. Layers W170E through W108E onlap across an erosive contact that appears to cap the faults. Alternate logging interpreted layer W170E as offset (correlating with W208E or W218E). While the stratigraphic units involved are not sufficiently distinct to determine which interpretation is correct, the event horizon in the alternate interpretation would definitely be below layer W108E, which thins and pinches out over the scarp. Given the location of samples that constrain the age of this event, the uncertainty in the exact paleo–ground surface does not impact the age estimate for the event. However, this uncertainty could allow for multiple events in the vicinity of the E2 horizon.

Another indicator for E2 is found at m17E (tier 2), where a fault terminates at the base of a gravel deposit (Fig. 5C). This fault has moderate vertical separation (12 cm), and layer E290 has been clearly offset. The fault can be traced to the base of a scour below which layer E210 is truncated by the fault. Layer E210 cannot be seen on the southwest side of the fault, suggesting at least moderate lateral offset. Because the earthquake horizon is represented by a scoured surface, it is possible that multiple events occurred at this horizon. This event indicator has a quality ranking of 3 but is on the opposite wall of the trench from the type locale, so we cannot say with certainty that these two indicators formed in the same earthquake. However, they are both located stratigraphically below E1 and above layer 290 (the base of which is the E3 horizon), which we consider to be correlated with certainty between the two walls, so this event indicator is given a stratigraphic correlation rank of 3.

Additional supporting evidence for E2 includes three event indicators that are found on the west wall (two with quality rank 1 and one with quality rank 0). At m7W (tier 3), there are distinct upward terminations of two faults with minor offset (rank 1). At m22W (tier 3), there are two faults with indistinct upward termini and minor offset (Plate 1). Both of these faults terminate at a stratigraphic level that is lower than E1, although the precise level of the event horizon is poorly constrained, and the fault cannot be traced downward to tier 2. Last, there is an event indicator with quality rank 0 that is found at m14E (tier 3). Here, there is a fault with moderate offset of layer E290 that stops at the bench level in between tiers 2 and 3. The exact location of the termination is unknown, but the termination lies stratigraphically above the event 3 horizon and below the event 1 horizon, suggesting it slipped during E2. The imprecise location of the E2 horizon at several indicators as well as uncertainty in correlations of indicators allow for the possibility for additional events between E1 and E3.

E3. *Likely.* There are six event indicators for E3, with ranks between 3 and 1. The strongest evidence for E3 (type locale) is the pinch out of a ≤40-cm-thick silt layer W290 on the west wall (between 8 and 20 m), centered within the main fault zone and underlying a ≤30-cm-thick package of laminated silty sand with gravel lenses. This ≤30-cm-thick package of laminated silty sand with gravel lenses thins to the north and south, and the underlying silt layer (W290) is absent from the remaining wedge-shaped section at meter 7 (Plate 1). We interpret this silt layer to have been deposited within a graben that formed during E3, resulting in a thick tabular layer of silt (W290) in the center of the graben and silty sand layers that later filled the depression and onlapped across the margins (layer W290 is at the base of the purple package in Fig. 3). Although the north end of the trench was not deep enough to reveal the faults that created this graben, it is clear on the west wall that a graben formed within the main fault zone (between 8 and 18 m) during E2. Thus, it is reasonable to infer that a graben may also have formed here during E3. Based on the stratigraphic evidence, we rank this event indicator with a quality rating of 3.

A similar charcoal-rich silt layer is also observed on the east wall at a similar stratigraphic level, so we correlate it with layer W290. On the east wall, layer E290 can be seen as far south as meter 20. Farther south, layer E290B is interpreted as a possible southward continuation of layer E290, but layer E290B is coarser and more poorly sorted than E290. We suspect that layer E290 thins and pinches out in the vicinity of meter 20, but this is obscured by the incision of a small gully into the trench wall that formed after excavation. Because of the uncertainty as to whether layer E290 pinches out near meter 20 or continues southward as layer E290B, we assign a quality rating of 1 for thickness changes in layer E290.

Three other event indicators associated with E3 are located on the east wall. First, at m18E and m19E (tier 3), there are two faults with significant lateral offset (indicated by the strong mismatch of layers across the faults) that are visible to the top of tier 3 but not visible in tier 2 (Plate 1). Layer E290 lies at the base of tier 2 and is unfaulted over the fault at 19 m, so this fault probably ruptured during E3, and we give this event indicator a quality ranking of 2. The event indicator at m18E (tier 3) has a quality ranking of 2 because layer E290 lies at the bench level and is not exposed over this fault at the base of tier 2. Last, at m27E (tier 2), a fault with minor displacement is capped by layer E290B, which is at the approximate stratigraphic level of layer E290 (and E3). We give this indicator a quality ranking of 1 because the fault has minor (<5 cm) displacement. The stratigraphic correlation ranking for this indicator is 1 (see Table S1). Overall, we rank E3 as *likely* because the evidence depends on our interpretation that the thickness changes in W290 at the type locale are a product of ground deformation, yet the potentially causative faults all extend higher than layer E290.

E4. *Probable.* There are six event indicators for E4, including two with rank 2, two with rank 1, and two with rank 0. The strongest evidence is found at m32W (tier 1) (type locale; Fig. 5D), where a fault produces moderate vertical separation of layer W405. This fault is truncated by an erosional contact (spray-painted green in Fig. 5D), which forms the base of a cobbly sand deposit

Downloaded from http://pubs.geoscienceworld.org/gsa/geosphere/article-pdf/17/3/685/5319464/685.pdf
by 19162

that is unfaulted. The quality ranking is only 2 because it is not clear if the units on the southwest side of the fault were eroded or if the deposit is conformable there. This potentially raises questions as to whether the scoured surface represents the same stratigraphic horizon on both sides of the fault, or whether the fault could have ruptured higher than this scour surface. In either case, there is at least one event at this scoured horizon.

At m23W (tier 2), there is a fault with ~6 cm of vertical separation (moderate offset) that is capped by layer W390, which appears to be unfaulted (Plate 1). The contact at the base of W390 is sharp directly above the fault, but it lacks clear continuity on both sides of the fault, so we assign a quality rating of 2 instead of 3. The event indicators at m32W (tier 1) and m23W (tier 2) are both on the west wall, but they are separated by ~9 m laterally and a bench. Our correlation of stratigraphic units suggests that these two indicators are at the same stratigraphic level. We assign a stratigraphic correlation rating of 3 to this indicator.

At m22W (tier 3), there is a fault with moderate offset of layer W555C. The fault could be capped by layer W470C, near the top of tier 3, or it could continue onto the base of tier 2, and be capped by W390C. In the latter interpretation, this fault would have slipped in E4. In the former interpretation, this fault would have slipped in an earthquake between events 4 and 5. Due to the significant uncertainty in the location of the upward termination of the fault, we assign it a quality ranking of 0.

At m32E and m36E (tier 2), there are two faults that terminate upward with minor vertical separation (quality ranking 1). We cannot be certain that these faults slipped in the same event as E4 on the west wall, but this would be the simplest interpretation and is compatible with the relative stratigraphic position of this feature. Last, at m24E (tier 3), there is a fault with minor offset originally mapped as being capped by unit E480, but it may extend upward and correlate with a fault in tier 2, which could be E3 or possibly even E4. Thus, it has a quality ranking of 1. Overall, E4 is considered a *probable* earthquake because all of the indicators are upward terminations with less than 10 cm of separation, and we do not observe stratigraphic evidence of significant vertical ground deformation (e.g., pinch out of units across grabens).

E5. *Probable.* There are six indicators for this event, including one with rank 3, three with rank 1, and two with rank 0. The best evidence and type locale can be found at m50W (tier 1), where we observe four faults with minor vertical separation of layer W590D that are all capped by the unfaulted layer W490D (Fig. 6A). Total vertical separation across the zone is ~10 cm. Therefore, we assign this moderate offset rank 3. The faults may terminate at or up to 20 cm below layer W490D. The 20 cm interval within which the earthquake horizon lies is bracketed by radiocarbon samples A18 and A24, as well as by luminescence samples L13 and L07. Because there are no dated samples from within this 20 cm interval, the uncertainty in the exact event horizon does not affect the event age.

At m26E (tier 3), three faults with minor offset downdrop a debris-flow deposit (E520) into a small graben that is capped by the unfaulted clayey silt layer E490 (Fig. 6B). We give each of these faults a quality ranking of 1. At m23E

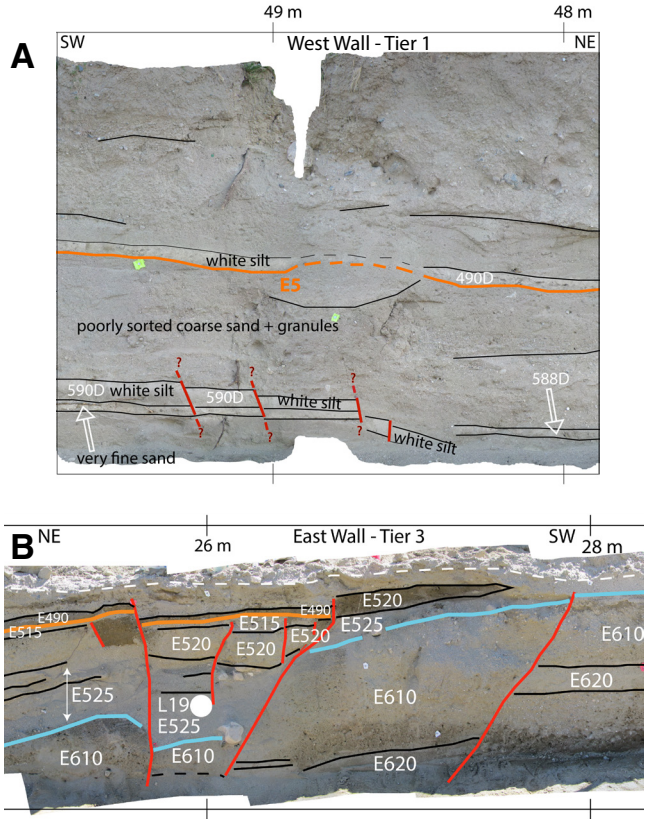

Figure 6. (A) Type locale for event 5, at 48–50 m on tier 1 of the west wall. Four faults (red lines) offset unit 590D but do not appear to offset unit 490D above. The top of the image is the ground surface. (B) Indicators for events 5 and 6 (orange and blue lines, respectively) at 21–27 m on tier 3 of the east wall. Several minor faults slipped in E5 and are capped by an unfaulted layer E490. (Southwest of the fault at meter 27, the event 5 horizon is faulted up into tier 2.) Event 6 is illuminated by layers E520 and E525, which triple in thickness to the northeast (left), suggesting they were deposited within a depression that formed when E610 was at the ground surface. White dashed line marks top of tier 3. White circle represents location of luminescence sample L19.

(tier 3), we also observe a fracture in layer E520 that may connect downward to a fault (quality rank 0) (Fig. 6B). These indicators from the east wall are all clearly capped by the same horizon (E490). At m32E (tier 2), there is a fault splay with unknown but likely very minor offset that is capped by layer E440, assigned a quality ranking of 0. Because E490 pinches out before reaching this location, E440 likely represents the first sediment deposited after E5, and this fault splay likely slipped in E5. Correlation of evidence for E5 between the two

Downloaded from http://pubs.geoscienceworld.org/gsa/geosphere/article-pdf/17/3/685/5319464/685.pdf
by 19162

walls is uncertain, but this represents the simplest interpretation. We qualify E5 as probable because all of the event indicators are upward terminations, and no unit thickness changes can be clearly followed above the terminations.

E6. *Likely.* There are five indicators for E6. There is one event indicator with a rank of 3 and four additional event indicators with a rank of 1. The type locale is located at m22–27E (tier 3). Here, the thickness of layers E520 and E525 decreases from 60 cm at 23 m down to 20 cm at 26 m (Fig. 6B). We interpret these layers as part of a postearthquake depositional sequence that filled a closed depression that was formed during E6, similar in character to basin formation in the youngest events. The large and rapid changes in unit thicknesses indicate filling of a depression, so we give it a quality ranking of 3. The earthquake horizon is interpreted to be at the top of layer E610, which is a thick, bouldery debris-flow deposit that has no noticeable thickness change across this region of the trench.

On the west wall, unit W610 consists of boulders within moderately well-sorted coarse sand. We interpret this layer to be the continuation of debris-flow deposit E610, on the opposite wall of the trench. At m23W (tier 4), two faults produce minor vertical separation within layer W610 and are capped by unfaulted layer W590 (Plate 1), and they are given a quality ranking of 1. Farther south on the west wall, we tentatively correlate the thick clay layer W590 with silt layers W590B, W590C, and W590D, which is the most laterally continuous silt layer to the south. At m38W and m39W (tier 2), we observe two faults that have produced minor vertical separation (~2 cm) of layer W604C and are capped by unfaulted layer W590C. If our correlation of layer W590 with W590C is correct, then these two faults provide additional indicators (quality rank 1) for E6. However, it is also possible that layer W590 at 23 m correlates with layer W604C (at 36–50 m). If this alternate correlation is correct, then the two minor faults at 38 and 39 m would be indicators for an event between events 5 and 6.

E7. *Likely.* There are three event indicators for E7, one with rank 3, one with rank 2, and one with rank 1. The strongest evidence can be seen at the type locale at m32E (tier 4). Here, we observe an 80-cm-thick package of very fine sand, silt, and clay (E670–E690) that thins to 10–15 cm (E690) as it approaches a fault at m34E (Fig. 7); we give a quality rank of 3 due to the substantial thickness change observed here. The causative fault (at 34–36 m) has reruptured in a younger earthquake.

The quality rank 2 indicator can be seen at m36E (tier 3) (Fig. 7). Here, we observe a fault with 5 cm of vertical separation in the upper part of tier 4 (pebble layer E710), capped by an unfaulted fine sand layer (E690) at the base of tier 3. Because the fault and the capping layer are not visible on the same tier, this event indicator is given a quality ranking of 2 instead of 3. Correlation of units between 32 and 36 m on the east wall is clear enough that we are confident that these two indicators represent the same earthquake horizon. The indicator at m36E (tier 3) has thus been assigned a stratigraphic correlation ranking of 4 with respect to the type locale at 32 m.

The rank 1 indicator can be seen at m28W (tier 4), where layer W690 thins to the south and pinches out (Plate 1). The causative fault is likely the fault at

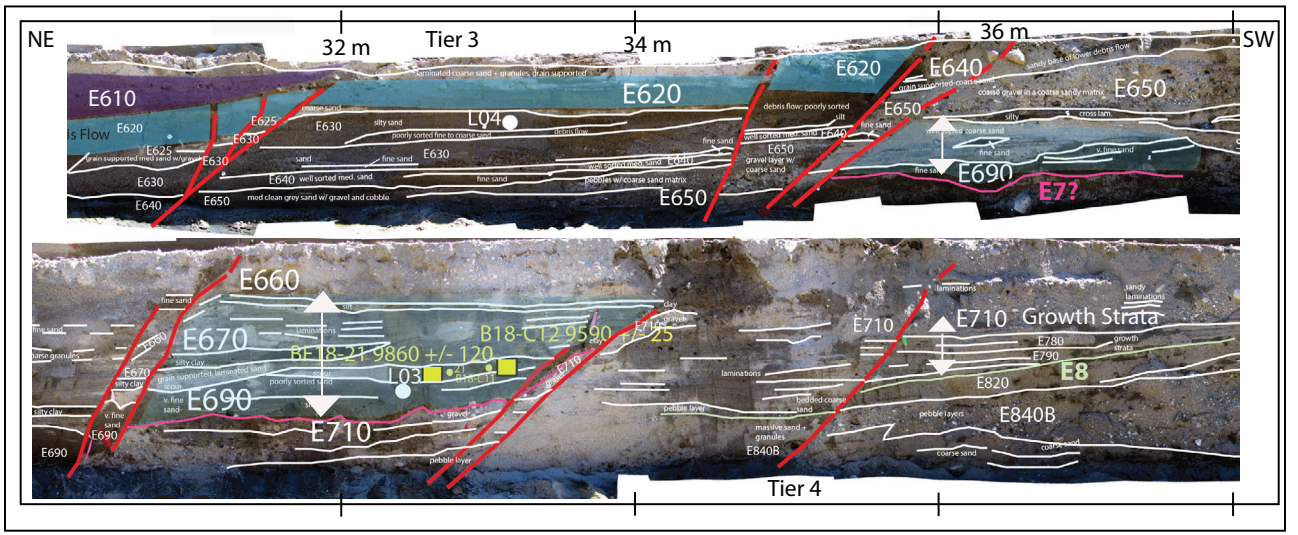

Figure 7. Event 7 and 8 evidence showing type locale for event 7 at 34 m on tiers 3 and 4 of the east wall. Layers E670–E690 (shaded pale blue) thin to the southwest as they approach the fault at m34E. An indicator for event 8 at 36 m on tier 4 is shown in the lower photomosaic. Layers E780–E790 thin to the south, filling a depression formed when layer E820 was tilted during event 8.

Downloaded from http://pubs.geoscienceworld.org/gsa/geosphere/article-pdf/17/3/685/5319464/685.pdf
by 19162

28 m. Although we observe moderate thickness change, which suggests filling of a closed depression, layer W690 is only exposed over a short distance (~2 m), so the full extent of the closed depression is not visible. Therefore, we assign a quality ranking of 1. It is not clear whether layer W690 is the same as layer E690 on the opposite wall of the trench, but it is clear that on both the east and west walls, there is evidence for two events (events E7 and E8) between layers 610 and 850, both of which can be correlated between the two walls of the trench with a high degree of confidence.

Overall, E7 is considered *likely* because the mismatch of unit thickness at the type locale (Fig. 7) occurs across a fault and may be the product of later lateral motion (the fault strand extends almost to the surface and last ruptured in E1) rather than local graben formation and filling.

E8. *Probable.* There are three event indicators (all rank 2) for the oldest event horizon observed at this paleoseismic trench site. Two event indicators with a quality rank of 2 are located at m31W and m36W (tier 4), with the latter being the type locale. At m31W, there is a fault with moderate vertical separation (22 cm) of layer W815-W815B, which is then capped by a layer of fine sand (layer W790) (Plate 1). The basal contact of layer W790 is sharp directly above the fault, but it lacks clear definition to the north; therefore, we assign a quality rating of 2 rather than 3. At the 36 m location (type locale), we observe a fine sand layer (W790C) that thins to the south and pinches out against a fault at 36 m. We infer that layer W790 filled a depression that formed during E8. Only a small section of the pinching layer W790 is visible just below bench level. Therefore, we assign a quality ranking of 2 rather than 3. We tentatively correlate layer W790 with W790B and W790C, which would imply that these two event indicators were caused by the same event. However, is it possible that W790B correlates with W815B instead of with W790, and that W790 has no correlative unit south of the fault strand at 32 m, so we assign a correlation ranking of 3. In addition, it is not clear whether layer W790 is the same as layer E790 on the opposite wall of the trench. Nonetheless, it is clear that on both the east and west walls, there is evidence for two events (events 7 and 8) below layer 610 and above layer 850, and both units 610 and 850 can be correlated between the two walls of the trench with a relatively high degree of confidence.

At m36E (tier 4), layers E780 and E790 thin and pinch out to the south, and we infer these layers represent growth strata filling in a depression produced by an earthquake (Fig. 7). Movement on the fault at 38 m may have caused the depression in which these growth strata were deposited. Although the thickness changes are moderate, the fault at 38 m is not clearly linked to the growth strata, leading to quality rank of 2 for this event indicator.

PALEOEARTHQUAKE AGES

Radiocarbon and Luminescence Dating

Layer ages were obtained from 34 radiocarbon-dated detrital charcoal samples and 17 sediment samples dated using post-IR IRSL techniques (Tables 1 and 2). All dates are plotted in Figure 8 as a function of stratigraphic depth measured at m24W down to layer W620, and then at m34 for layers older than W620 (Fig. 3). These sections were selected because they are within a wide, fault-bounded block with clear stratigraphy and are close to the area where layers are thickest. On Figure 8, all samples from the east wall, and samples from the west wall that are not from the type section are shown with vertical error bars that indicate the uncertainties in the stratigraphic positions of these samples relative to the type section.

The stratigraphic thickness of 9 m exposed in the trench was deposited within the past ~7000 yr, indicating an average depositional rate of ~0.13 cm/yr. Based on the youngest samples at each depth, the sedimentation rate appears to have been relatively constant across the section, yet it could have been variable from unit to unit given the relatively sparse dating. The longest possible depositional hiatus can be no more than the 1–1.5 k.y. interval between samples L01 and L17 (~4–5 m depth). There is no clear indication of a hiatus at this time, and a hiatus this long is only possible if deposition stopped immediately after the layer containing L17 formed, and the overlying 1 m of sediment between sample L01 and L17 was deposited very rapidly. Based on texture and bedding, the layers between these two samples could have been deposited in a few depositional events. Episodes of rapid sedimentation may have also occurred, such as between samples L17/L18 and L20/L04/L02, which all have nearly the same age within the 1σ uncertainties, despite spanning ~1.5 m of stratigraphic depth. This depth range is dominated by the two thickest units in the trench, the boulder units 610 and 620, which were likely deposited very rapidly, potentially during the course of one or a few storms. The presence of scouring within some areas (e.g., Figs. 5A, 5B, and 5C) suggests that parts of the record are locally missing.

Paleoearthquake Model Ages

We used OxCal (Bronk Ramsey, 2009) to estimate the earthquake ages. OxCal uses Bayesian statistics to model posterior ages for paleoearthquakes based on all chronological constraints such as relative stratigraphic position and layer groups. Dates from the same layer, or from layers that we infer correlate with each other, were modeled using the "Phase" command such that relative stratigraphic position within the layer group was not applied (Bronk Ramsey, 2009).

The range of ages for several intervals shown in Figure 8 presents a challenge for constructing a straightforward age model. For example, samples A44 and C10 at 2 m stratigraphic depth have ages that differ by 2000 yr, as do samples A18 and A39 at 2.75 m stratigraphic depth. Many studies have shown that it is common for detrital charcoal samples to be older than the age of the layer from which they were collected by an amount that depends on the length of time between when the plant material stopped growing and when the sample was deposited in the location from which it was collected (e.g., Philibosian et al., 2011; McGill et al., 2002; Fumal et al., 2002). Aside from

Downloaded from http://pubs.geoscienceworld.org/gsa/geosphere/article-pdf/17/3/685/5319464/685.pdf
by 19162

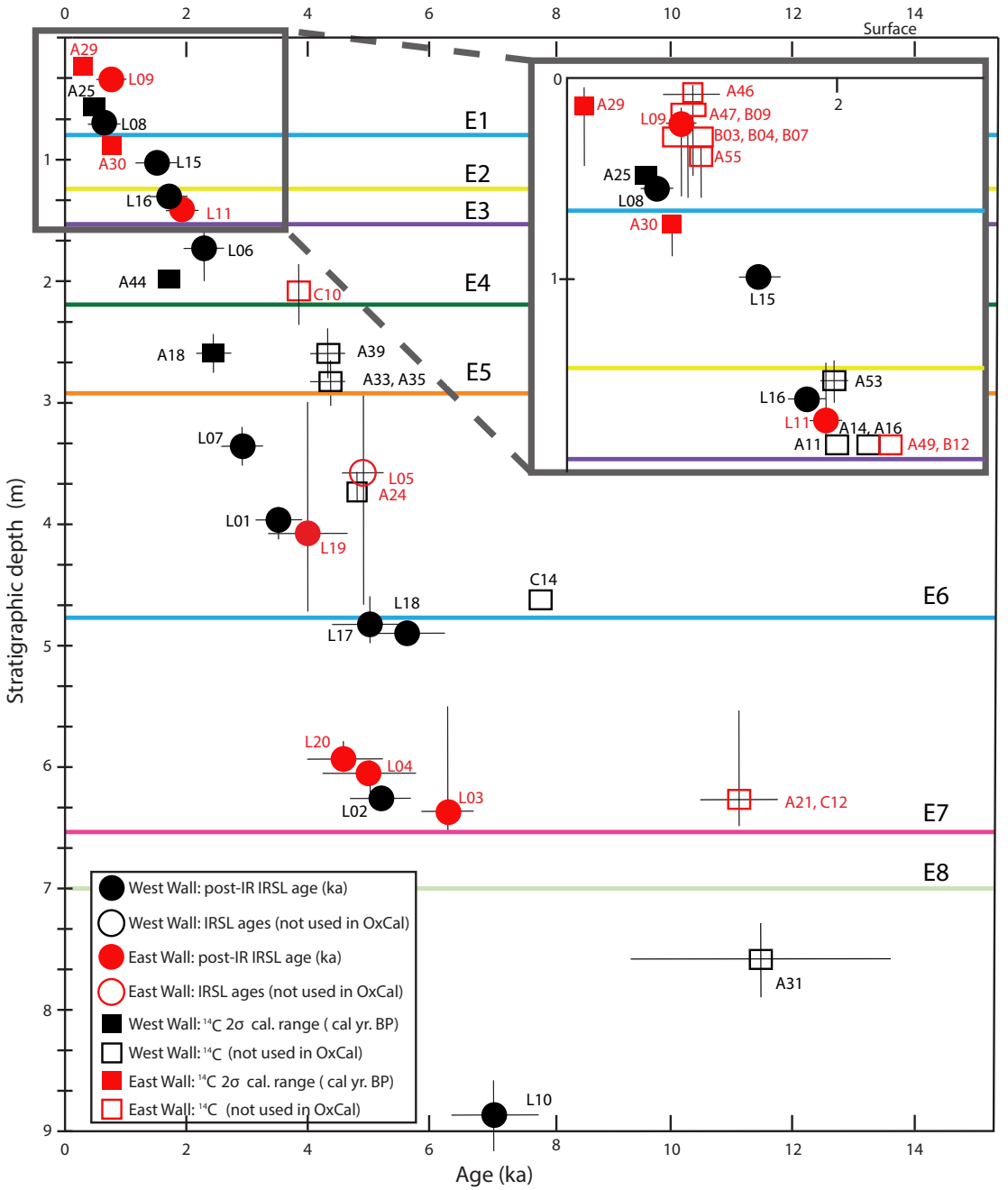

Figure 8. Calibrated radiocarbon and post-infrared infrared stimulated luminescence (post-IR IRSL) ages as a function of stratigraphic depth. Stratigraphic depth was measured on the west wall at 24 m from the surface to the base of unit 620 (see Plate 1) and at 34 m from the base of layer 620 to the base of the trench. Vertical error bars show uncertainties in correlating sample locations from the east wall or from other fault blocks on the west wall with the type section. Solid symbols show ages that were included in our preferred OxCal model; open symbols show samples excluded from that model. Inset shows all ages from the upper 1.6 m.

Downloaded from http://pubs.geoscienceworld.org/gsa/geosphere/article-pdf/17/3/685/5319464/685.pdf
by 19162

contamination of the sample, the only way for charcoal to underestimate the depositional age of a layer is if it was a root or was brought into the section by bioturbation. We were careful in the field to avoid collecting roots or any charcoal samples from obvious filled burrows or areas lacking clear stratigraphy, which could potentially be bioturbated zones, and we reviewed photographs of the sample locations to evaluate the potential for unrecognized bioturbation at each sample location. To construct our preferred age model, we therefore omitted any charcoal samples with dates that were older than other charcoal or luminescence samples from the same layer or lower layers. In Figure 8, dated samples that were included in our preferred age model are plotted with filled symbols, and those that were excluded are plotted with open symbols.

In total, 29 out of 34 radiocarbon dates were omitted from our preferred age model, which thus relied heavily on the IRSL ages to constrain the timing of past earthquakes. The omission of this many radiocarbon samples is supported by previous studies that have shown wide ranges of radiocarbon ages for charcoal samples from the same layer (e.g., McGill et al., 2002; Fumal et al., 2002; Philibosian et al., 2011). In the 18th Avenue trench, we also collected multiple samples from the same depths that have mean radiocarbon ages separated by as much as 2000 yr (e.g., samples A44 and C10 at ~2 m depth and A18 and A39 at ~2.6 m depth), suggesting that detrital lag times can be at least 2000 yr long on the Mission Creek fan. Fumal et al. (2002) also found lag times of up to ~600–1000 yr for charcoal samples from the same layer at a site on the Mission Creek strand at the Thousand Palms site, located ~20 km to the east, and that site, like the 18th Avenue trench, also has a large source catchment.

One IRSL sample from the east wall (L05) was also excluded from our preferred age model because it was older than most other samples at that stratigraphic depth, and it had large uncertainty in its stratigraphic depth relative to the type section on the west wall. The results of the preferred OxCal model are shown in Figure 9 and Table 6.

While it is common practice in paleoseismic studies to omit charcoal samples that are older than other charcoal samples from the same or underlying layers (McGill et al., 2002; Fumal et al., 2002; Philibosian et al., 2011), a factor that may be of concern in this study is that we also omitted charcoal samples that were older than luminescence samples from the same or underlying layers, resulting in an almost exclusive reliance on the IRSL ages. Therefore, we also created an alternate model that took a different approach based on the observation that the 2000 yr lag was based on only two radiocarbon samples. In contrast to the preferred model, the alternate model (Fig. A1) starts with the assumptions that those samples (A44 and A18) were contaminated by younger material (which can occur during sample collection and preparation), and that radiocarbon samples C10 and A39 were accurate. Samples A44 and A18 were thus removed from the OxCal model, along with sample A31, because it was much older than the five IRSL samples near the base of the section, which we assume are correct based on their reproducibility. To achieve an OxCal agreement index >50%, samples L16, L06, L07, and L01 were also removed because they were notably younger than both radiocarbon and IRSL samples in the same phase. Given that the IRSL signal measured for these samples is observed not to fade through time (Fig. A2), the only reasonable explanation for an apparent IRSL age that is too young is postdepositional mixing. Considering that it is unlikely that postdepositional mixing of grains would systematically shift ages in a way that is stratigraphically consistent, these were not removed in the preferred model. However, this alternative model has some advantage of retaining more of the original radiocarbon data, as it used 20 of the original 34 radiocarbon and 13 of 17 IRSL samples. In comparison to the preferred model, this approach produced much older earthquake ages for E2–E6 (Fig. 10; Table 6). Although both models are feasible, we chose the preferred model because it is common for detrital carbon samples to be older than true depositional ages, and the fading tests (Fig. A2) indicated that the IRSL samples are unlikely to be biased too young.

DISCUSSION

Recurrence Intervals

As shown in Figure 4, the overall number of observations and quality rank of event indicators decrease with depth. There are several reasons why the evidence for older events is weaker than that for the younger events. First, the older strata are only exposed within a small portion of the fault zone. Second, evidence for older events has been overprinted by younger earthquakes, making interpretation more difficult. Stratigraphic correlation of event indicators to their respective type locales was also a major challenge in this trench at all stratigraphic levels, but it was compounded for older events due to increased difficulty in correlating layers across faults in which the cumulative lateral offset in multiple events was large.

The earthquake record at the site includes evidence for five events in the upper 3 m, which occurred in the past 2.4–3.3 k.y. (age range for E5). The mean recurrence interval for these five events on the Banning strand is 490 yr (95% range 390–600 yr). The individual intervals between each of these five events are very similar to the mean (Fig. 10). As noted above, we cannot rule out the possibility that additional earthquakes may have occurred and not been recognized. If the alternate age model is correct, ages for E2 through E6 are 600–1800 yr older than in the preferred model, producing a mean recurrence interval of 940 yr, i.e., nearly twice as long as that in the preferred model (Fig. 10).

Only three events are recognized in the lower 6 m, during a 2.4–4.7 k.y. period between events E5 and E8 (Table 6). This suggests that either we are missing events in the lower section, or the recurrence pattern at the 18th Avenue site is variable. We cannot rule out either possibility. However, it is likely that the older part of the earthquake record at this site is incomplete due to limited exposure in which to make observations of the older stratigraphy. Specifically, the trench does not expose stratigraphy older than E3 north of m16, nor does it expose stratigraphy older than E5 north of m20. Faults with large

Downloaded from http://pubs.geoscienceworld.org/gsa/geosphere/article-pdf/17/3/685/5319464/685.pdf
by 19162

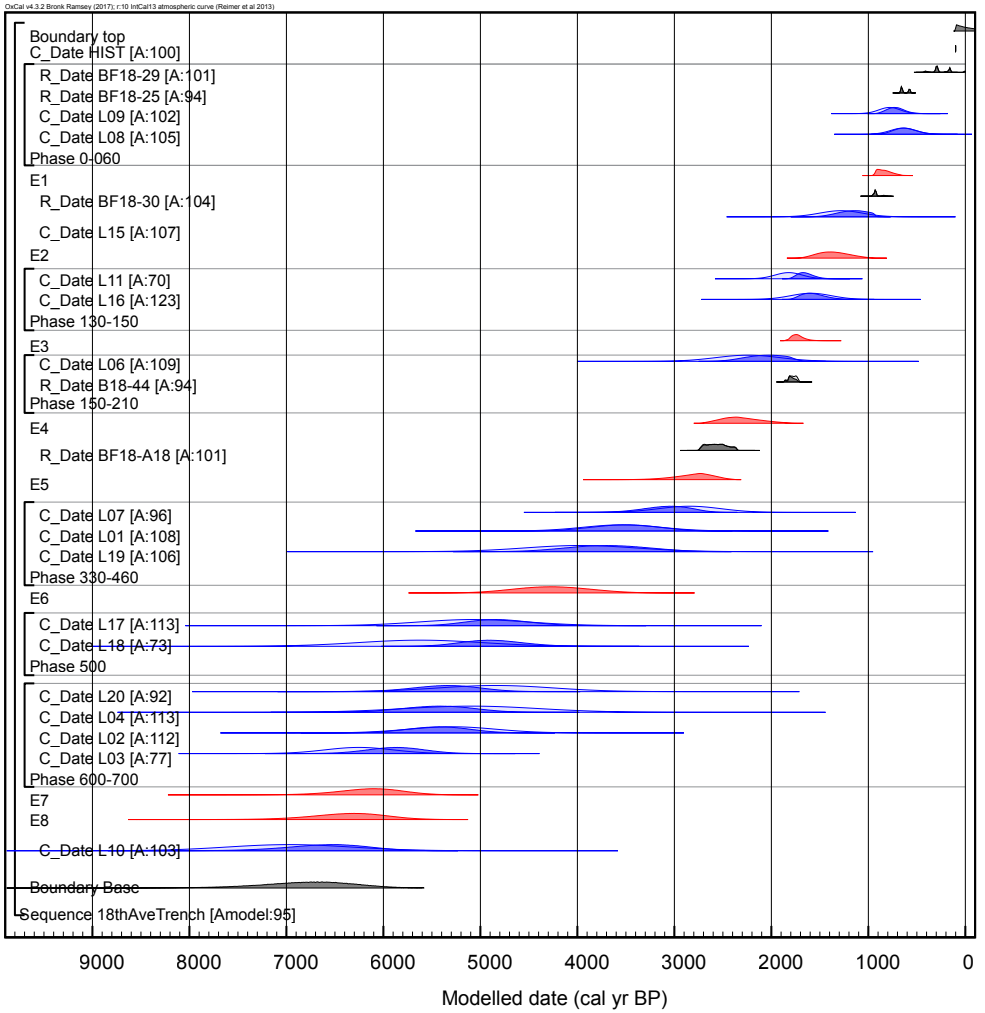

Figure 9. OxCal model used to estimate earthquake ages. Ages are plotted as a function of stratigraphic position; blue shapes are post-infrared infrared stimulated luminescence (IRSL) ages, gray shapes are radiocarbon ages, and red shapes are resultant earthquake ages. Brackets indicate samples from same phase (samples from same layer or from layers for which relative stratigraphic position cannot be differentiated). In the Bayesian approach used within OxCal, the ages of samples above and below a given sample are used to reweight the probability density function for that sample so as to yield a set of ages that are stratigraphically consistent with each other as well as being consistent with the a priori (measured) ages of each sample. Pale color shows prior probability density functions (PDFs) obtained for the ages of individual samples. Opaque colors are the posterior PDFs for each sample. This model assumes that charcoal samples provide a maximum age. The model also assumes that IRSL minimum age model methods have correctly estimated the depositional age of the sediment. To achieve an agreement index of >60% (Lienkaemper and Bronk Ramsey, 2009), 29 radiocarbon samples that were older than stratigraphically lower IRSL or radiocarbon samples were removed. An alternate model that retained more radiocarbon ages is provided in the Appendix (Figs. A1 and A2).

vertical separations are present in the trench north of m20, yet we had no way to investigate paleoearthquakes older than E5 on these faults. In addition, if there was a 1–1.5-k.y.-long hiatus between the deposition of samples L17 and L01, as permitted in the dating, it is possible that we missed the detection of events during this period.

If the full record of up to eight earthquakes is complete, the average recurrence interval during the past ~7000 yr would be ~790 yr (95% range 680–910 yr; Table 7). If the alternate age model is correct, the average recurrence interval for all eight events would be 770 yr (95% range 680–870 yr; Table 7).

Comparison to Other Paleoseismic Sites

The mean recurrence interval between the past five surface-rupturing earthquakes at the 18th Avenue site is 490 yr (95% range 390–600 yr), which is longer than it is for the three sites on the Coachella section and Mission Creek strand (116–300 yr; Philibosian et al., 2011; Sieh and Williams, 1990; Fumal et al., 2002) and shorter than or overlaps with the measured recurrence intervals at the Cabazon trench site on the San Gorgonio Pass fault zone (two intervals between three paleoseismic events have been identified: ~450 and ~1600 yr;

Downloaded from http://pubs.geoscienceworld.org/gsa/geosphere/article-pdf/17/3/685/5319464/685.pdf
by 19162

TABLE 6. EARTHQUAKE AGES AT 18TH AVENUE PALEOSEISMIC SITE

	Preferred model (calibrated yr B.P.)			Alternate model (calibrated yr B.P.)		
	Mean	95% range		Mean	95% range	
E1	830	945	690	830	945	690
E2	1360	1650	1050	1985	2085	1900
E3	1730	1850	1590	3325	3865	2760
E4	2315	2665	1930	3920	3965	3880
E5	2805	3225	2430	4595	4815	4425
E6	4260	5000	3505	5080	5360	4860
E7	6150	6840	5490	6080	6675	5510
E8	6375	7175	5620	6245	6930	5595

Wolff, 2018; Scharer and Yule, 2020). Thus, earthquakes at the 18th Avenue site on the Banning strand occur less frequently than those on the Coachella section and Mission Creek strand but more frequently than those on the San Gorgonio Pass fault zone.

Figure 11 shows the ages of paleoearthquakes at the 18th Avenue site in comparison with prehistoric earthquakes at other sites on the southernmost San Andreas fault. One of the most interesting features shown in Figure 11 is that the age of the two most recent paleoearthquakes at the Cabazon site and 18th Avenue site are contemporaneous. To illustrate how such observations can be modeled as ruptures, we provide two possible rupture histories for the southernmost San Andreas fault near San Gorgonio Pass (Figs. 11B and 11C). Both models are consistent with the dates of paleoearthquakes on the southern San Andreas fault, but they show different correlations that could reflect different geometric segmentation; many other scenarios are possible given the input data (Scharer and Yule, 2020). The first scenario (Fig. 11B) shows an event ca. 1200 CE that connects contemporaneous earthquake ages at Millard Canyon (Mi1), Cabazon (Ca1), and 18th Avenue (E1). Because no earthquakes at Burro Flats (Bu) or Coachella (Co) overlap in age with the limits of Ca1 and E1, this rupture was confined to the San Gorgonio Pass fault zone and Banning strand. This is also consistent with no rupture observed in the past 600 yr at the East Whitewater site on the Garnet Hill strand (Cardona, 2016). The second scenario shows an alternative that separates this rupture into two earthquakes between ca. 1100 and 1300 CE. In Figure 11C, E1 and Co5 are connected for a rupture along the Banning strand and Coachella section, followed by a rupture that is centered in San Gorgonio Pass fault zone, connecting Mi1 and Ca1. Although the San Gorgonio Pass fault zone rupture is relatively short, it could have continued onto other mapped faults in the region; for example, the San Gorgonio Pass fault zone extends for another 40 km to the west (Fig. 11; Yule and Sieh, 2003).

In contrast to the more segmented ruptures ca. 1200 CE, it is possible that the entire model domain in Figure 11 ruptured at 600 CE, as ages permit a San Bernardino–San Gorgonio Pass fault zone–Banning–Coachella rupture, potentially similar to the "Shakeout scenario" (Jones et al. 2008). Scharer and Yule

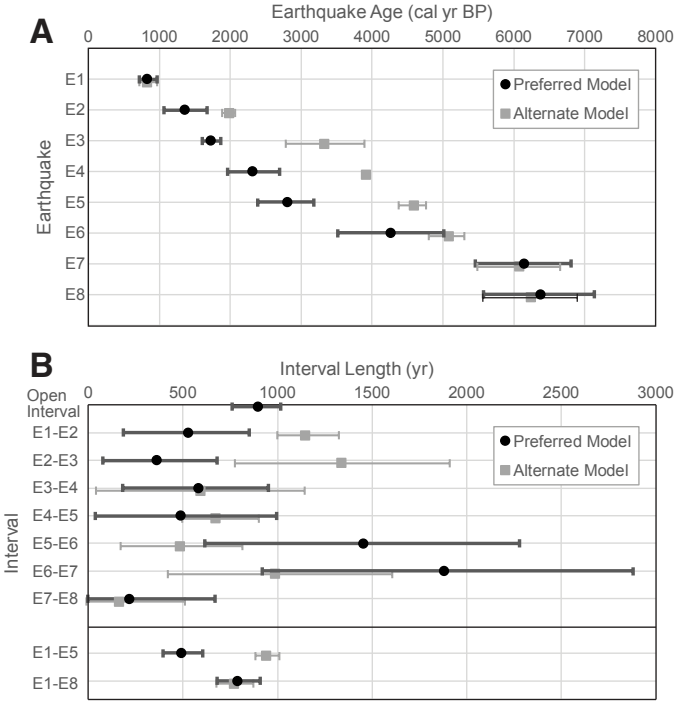

Figure 10. Comparison of preferred and alternate earthquake ages (A) and intervals (B). The preferred model omits 29 of the radiocarbon ages, assuming they reflect significant inheritance due to long transport times. It also assumes that the minimum age model accurately resolved the depositional age of the infrared stimulated luminescence (IRSL) samples. The alternate model (Fig. A1) omits five radiocarbon samples, assuming they were affected by young contamination. The alternate model retains more ages overall and produces older ages for E2 through E5.

TABLE 7. EARTHQUAKE INTERVALS AT 18TH AVENUE PALEOSEISMIC SITE

	Preferred model (yr)			Alternate model (yr)		
	Mean	95% range (calibrated yr B.P.)		Mean	95% range (calibrated yr B.P.)	
Open interval	900	1015	760	830	945	690
E1–E2	530	185	850	1150	1000	1325
E2–E3	365	75	680	1340	775	1910
E3–E4	585	180	950	595	40	1145
E4–E5	490	35	995	675	495	900
E5–E6	1455	615	2280	485	170	815
E6–E7	1885	920	2880	990	420	1605
E7–E8	220	–5	670	165	–10	510
E1–E5	493	393	605	941	884	1010
E1–E8	791	680	909	771	678	872

Downloaded from http://pubs.geoscienceworld.org/gsa/geosphere/article-pdf/17/3/685/5319464/685.pdf
by 19162

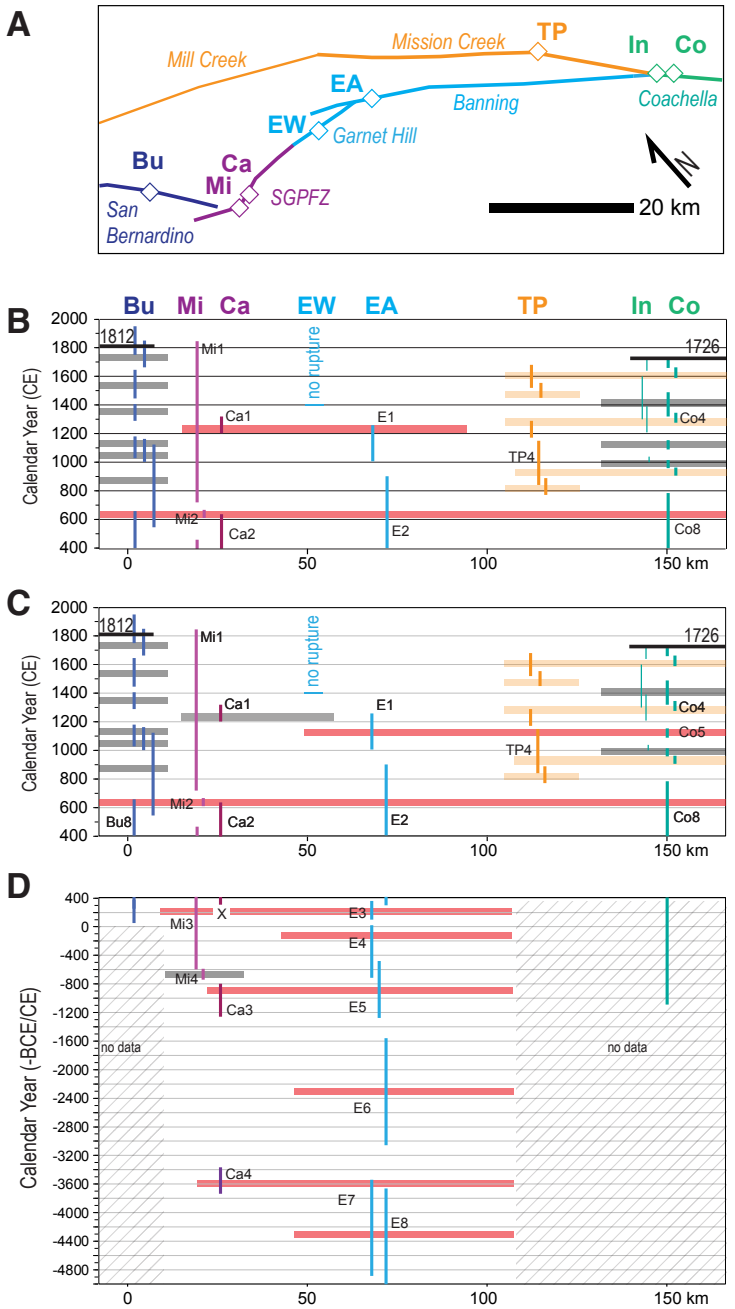

Figure 11. (A) Map showing paleoseismic sites along the southernmost section of the San Andreas fault in the Coachella Valley and San Gorgonio Pass region. Site abbreviations and references are as in Figure 1. SGPFZ—San Gorgonio Pass fault zone. (B–C) Example paleoseismic rupture histories for this region during the past 1600 yr. Vertical bars are earthquake ages from each site (95% range), where select events are labeled with their site abbreviations followed by the event number (e.g., Mi1 is event 1 at Millard Canyon). Events from the 18th Avenue site are labeled E1, E2, etc. Horizontal bars are possible ruptures that are consistent with the ages. Black lines represent historic 1812 (Toppozada et al., 2002) and early historic ca. 1726 (Rockwell et al., 2018) ruptures. Red ruptures connect events at 18th Avenue on the Banning strand with other sections of fault; orange ruptures connect Mission Creek strand to Coachella section but do not rupture the Banning strand at the 18th Avenue site. Gray horizontal bars mark ruptures restricted to a single section within the scope of this diagram. Ends of ruptures are schematic, generally guided by location of geometric complexity (e.g., splay, bend). Age ranges for the ruptures are not shown but can be wide given the ages of the contributing sites (see Scharer and Yule, 2020). (D) Rupture history for older section (note change in scale). Only the Cabazon site extends as long as the 18th Avenue site but has only four known events in that period.

(2020) showed that this rupture had the potential to extend onto the Mojave section of the San Andreas fault. As shown here, this single through-going rupture at 600 CE would have been at least 150 km long, equivalent to M 7.5 or greater using regression equations in Wesnousky (2008). It is worth noting that the event at 600 CE could also be modeled as separate ruptures. Only the two most recent paleoearthquakes at the 18th Avenue site occurred within the time period represented by the Burro Flats record. Although the most recent event at the 18th Avenue site may correlate with Mi1 and Ca1 on the San Gorgonio Pass fault zone, there is no record of an earthquake at this time on the San Bernardino strand at Burro Flats. The 600 CE event is the only Banning strand event that could potentially correlate with an earthquake on the San Bernardino strand within the past 1600 yr, assuming all the paleoseismic records are complete.

A general observation is that in the past 1600 yr, there have been eight earthquakes each at the Burro Flats (San Bernardino strand) and Coachella (Coachella section) paleoseismic sites, while there have only been two at the 18th Avenue site on the Banning strand and at the Cabazon site on the San Gorgonio Pass fault zone, and five on the Mission Creek strand at Thousand Palms. The more frequent earthquakes outside of the sites along the Banning strand and the San Gorgonio Pass fault zone contrast with the fewer earthquakes at those locations and control potential rupture histories in the area. Interestingly, a maximum of two earthquakes connecting the Coachella and northern Banning strands is permitted in the past 1600 yr. This requires that six ruptures on the Coachella section either terminated on the southern Banning strand, extended onto the Mission Creek strand, or ended at the splay (see also Scharer and Yule, 2020). These data generally support the dynamic rupture models of Douilly et al. (2020), which found that rupture on the Banning strand was less likely to occur given the geometry of the fault splay. Only the most recent earthquake at the 18th Avenue site occurred during the period observed at the Thousand Palms site on the Mission Creek strand, and it may have occurred at the same time as TP4 (Figs. 11B and 11C), allowing the

Downloaded from http://pubs.geoscienceworld.org/gsa/geosphere/article-pdf/17/3/685/5319464/685.pdf
by 19162

possibility of rupture jumping from the Mission Creek to the Banning strand, as seen in some dynamic rupture model configurations (Douilly et al., 2020).

Prior to 400 CE, paleoearthquake data from nearby sites are sparse (Fig. 11D); only the Cabazon site has a record as long as the 18th Avenue site (Fig. 11D). In this time period, two ruptures connecting 18th Avenue and Cabazon are permitted, ca. 3600 BCE and 1000 BCE. While the E3 and Mi3 ruptures were contemporaneous, there is no correlative event at Cabazon if Ca2 ruptured with Mi2, as indicated. Wolff (2018) noted that missing events were likely at Cabazon, which is shown with an X on the speculative rupture ca. 200 CE that would span the Banning and San Gorgonio Pass fault zone.

Implications for Average Slip per Earthquake

The Banning strand of the San Andreas fault has a Holocene slip rate of 2.3–6.2 mm/yr (Gold et al., 2015), based on a fan offset at the Painted Hills site, ~8 km northwest of the 18th Avenue site (Fig. 1). Given the elapsed time since the most recent event (945–690 calibrated years B.P. or cal yr B.P.) and the slip rate at Painted Hill, we calculated that the fault could produce slip of 1.6–5.9 m in the next earthquake, using a slip-predictable model, and assuming a relatively constant strain release. Using the average recurrence interval of 390–610 yr between events E1 and E5 and the slip rate, we estimated that the average slip in these past five events was 1–4 m. These estimates of average slip per earthquake are simple because they do not include uncertainties related to variability in strain release, and they assume on-fault displacement is comparable at each location. Alternatively, as the fan age at Painted Hill overlaps with the section dated at 18th Avenue, we can infer that the fan has experienced 6–8 earthquakes if all the ruptures spanned the distance between both sites. This would produce an average slip per event of 2.5–5 m for the northern Banning strand, assuming the 18th Avenue site record is complete. We note that this range is similar to that predicted from the accrued slip since the most recent event, which may indicate the trench record is complete, or nearly so.

CONCLUSIONS

The 18th Avenue site provides the first dated paleoseismic record constructed on the Banning strand of the southernmost section of the San Andreas fault. This 7000-yr-long record can now be compared to paleoseismic records on the neighboring strands that make up the complex network of faults in the southern section of the San Andreas fault. Eight horizons contained evidence of paleoearthquakes based on sedimentological responses to deformation and fault terminations at or below each horizon. These earthquakes were qualified based on the record of deformation and our ability to correlate across this wide trench; E1 is considered very likely; E2, E3, E6, and E7 are considered likely; and E4, E5, and E8 are considered probable. Based on the stratigraphy, dating uncertainties, and physical limits of the trench exposure, the likelihood of missed events is greatest in the older parts of the section, below E5. The most recent event occurred 945–690 cal yr B.P. The open interval is longer than the average interval between events E1–E5 (390–600 yr), but it is shorter than the interval between events E5 and E6 and between events E6 and E7. The longer average interval for the entire section (680–910 yr for events E1–E8) may indicate temporal variations in the rate of strain release on the Banning strand, or it may indicate missing events in the older section of the trench. In the past 1600 yr, eight paleoearthquakes are documented at both the Burro Flats and Coachella sites, five are documented on the Mission Creek strand at Thousand Palms, and only two are documented on the Banning strand and San Gorgonio Pass fault zone. Given the earthquake ages, a maximum of two earthquakes connecting the Coachella and northern Banning strands is permitted in the past 1600 yr, and only one of these events (ca. 600 CE) could have potentially ruptured onto the San Bernardino strand as well. The interpretation of fewer earthquakes on the Banning strand is consistent with its lower slip rate compared to other sections of the southernmost San Andreas fault and would translate to average slip per event of ~1–5 m.

APPENDIX: EARTHQUAKE CHRONOLOGY USING AN ALTERNATIVE AGE MODEL

Figure A1 shows the radiocarbon and luminescence samples used in the alternate age model, and Figure A2 shows the OxCal model for those samples.

ACKNOWLEDGMENTS

This research was funded by U.S. Geological Survey (USGS) National Earthquake Hazards Reduction Program grants G18AP00040 and G18AP00041, and internal funding from California State University–San Bernardino (CSUSB) and the USGS. We are extremely grateful to John Rogers for granting access to work on his property and Alan Pace from Petra Geosciences for accommodating our study. We want to thank all the students from CSUSB and California State University–Northridge who assisted with the hard labor. Reviews by Belle Philobosian, Ray Weldon, Peter Gold, and C.H. Jones improved the clarity of the manuscript. The views and conclusions contained in this document are those of the authors and should not be interpreted as necessarily representing the official policies, either expressed or implied, of the U.S. government. Any use of trade, firm, or product names is for descriptive purposes only and does not imply endorsement by the U.S. government.

REFERENCES CITED

Allen, C.R., 1957, San Andreas fault zone in San Gorgonio Pass, Southern California: Geological Society of America Bulletin, v. 68, p. 315–350, https://doi.org/10.1130/0016-7606(1957)68[315:SAFZIS]2.0.CO;2.

Behr, W.M., Rood, D.H., Fletcher, K.E., Guzman, N., Finkel, R., Hanks, T.C., Hudnut, K.W., Kendrick, K.J., Platt, J.P., Sharp, W.D., Weldon, R.J., and Yule, J.D., 2010, Uncertainties in slip-rate estimates for the Mission Creek strand of the southern San Andreas fault at Biskra Palms Oasis, Southern California: Geological Society of America Bulletin, v. 122, p. 1360–1377, https://doi.org/10.1130/B30020.1.

Bevis, M., and Hudnut, K., 2005, B4 Lidar Project: Airborne Laser Swath Mapping (ALSM) Survey of the San Andreas Fault (SAF) System of Central and Southern California, Including the Banning Segment of the SAF and the San Jacinto Fault System: National Center for Airborne Laser Mapping (NCALM), U.S. Geological Survey, the Ohio State University, and the Southern California Integrated GPS Project, distributed by OpenTopography, https://doi.org/10.5066/F7TQ5ZQ6.

Bevis, M., Hudnut, K., Sanchez, R., Toth, C., Grejner-Brzezinska, D., Kendrick, E., Caccamise, D., Raleigh, D., Zhou, H., Shan, S., Shindle, W., Yong, A., Harvey, J., Borsa, A., Ayoub, F., Shrestha,

Downloaded from http://pubs.geoscienceworld.org/gsa/geosphere/article-pdf/17/3/685/5319464/685.pdf
by 19162

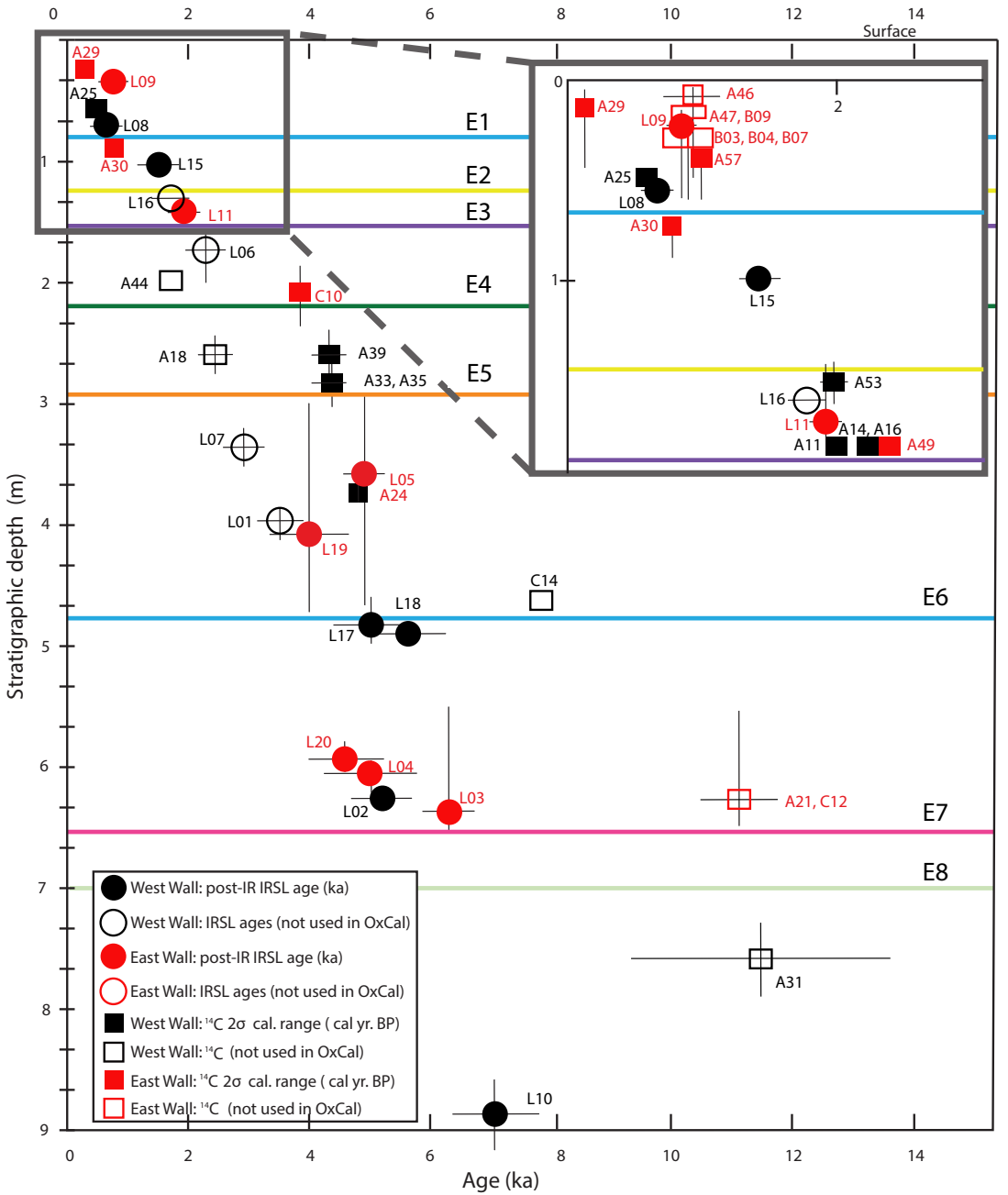

Figure A1. Calibrated radiocarbon and post-infrared infrared stimulated luminescence (post-IR IRSL) ages as a function of stratigraphic depth used in the alternate age model (Fig. A2). Stratigraphic depth was measured on the west wall at 24 m (for layers 20–620) and at 34 m (for layers 620–850). Vertical error bars show uncertainties in correlating sample locations with the type section, and horizontal bars are 2σ errors. Solid symbols show ages that were included in the alternate OxCal model; open symbols show samples excluded from that model.

Downloaded from http://pubs.geoscienceworld.org/gsa/geosphere/article-pdf/17/3/685/5319464/685.pdf
by 19162

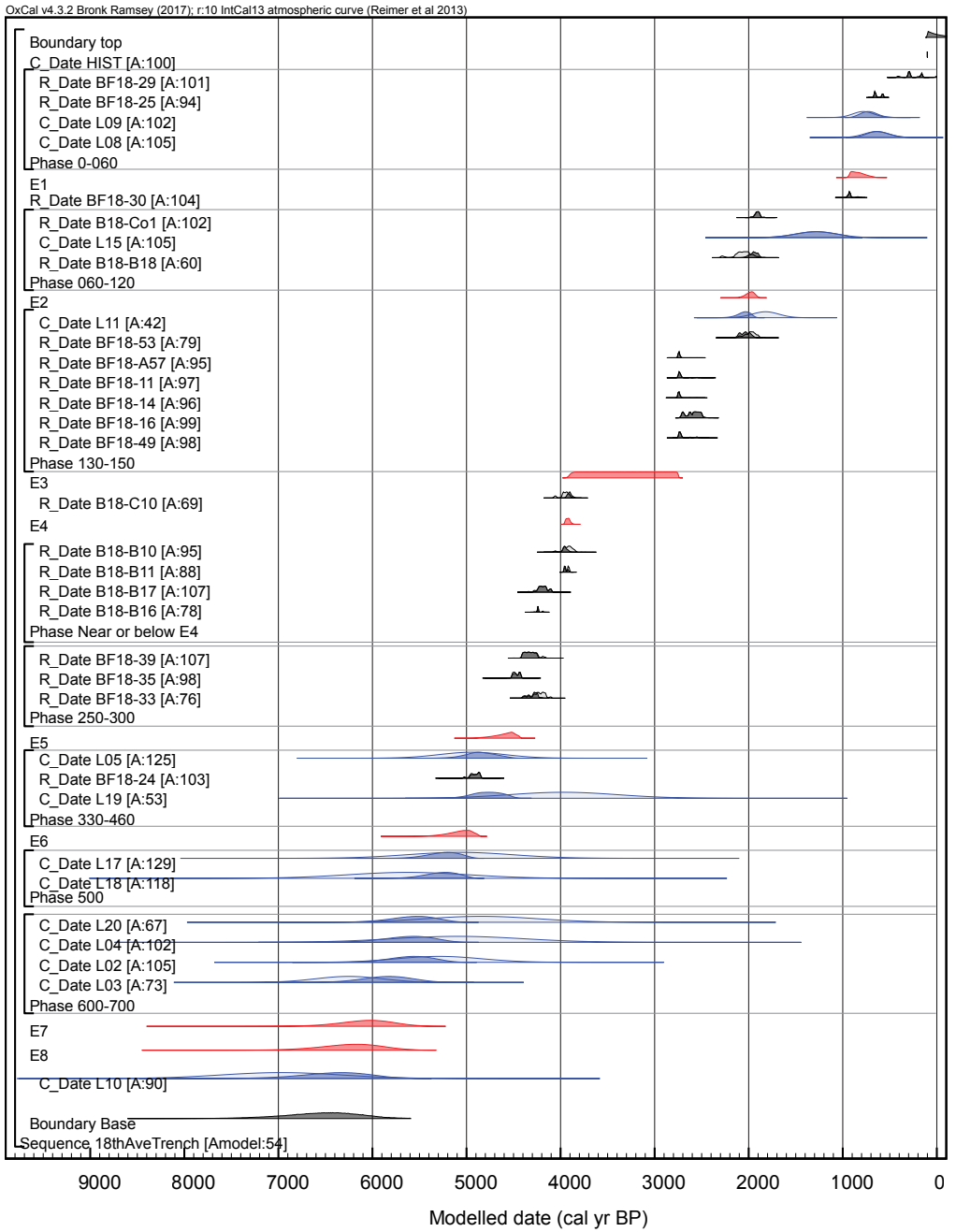

Figure A2. Alternate OxCal model used to estimate earthquake ages, using samples shown in Figure A1. Ages are plotted as a function of stratigraphic position; blue shapes are infrared stimulated luminescence (IRSL) ages, gray shapes are radiocarbon ages, and red shapes are resultant earthquake ages. Brackets indicate samples from the same phase (samples from the same layer or from layers for which the relative stratigraphic position cannot be differentiated). Pale color shows prior probability density functions (PDFs) obtained for the ages of individual samples. Opaque colors are the posterior PDFs for each sample. In this model, we assumed that two samples (A44 and A18) were contaminated by younger material because they are the only radiocarbon samples that produced a 2000 yr spread in layer ages (Fig. 8). These samples were removed first, followed by A31, assuming that the six IRSL samples at the base of the section are correct. To achieve an agreement index >50%, samples L16, L06, L07, and L01 were removed because they are notably younger than both radiocarbon and IRSL samples in the same phase. This model retained 20 of the original radiocarbon and 13 IRSL samples. In comparison to the preferred model, this approach produced much older earthquake ages for E2–E6 (Fig. 10).

Downloaded from http://pubs.geoscienceworld.org/gsa/geosphere/article-pdf/17/3/685/5319464/685.pdf
by 19162

R., Carter, B., Sartori, M., Phillips, D., and Coloma, F., 2005, The B4 project: scanning the San Andreas and San Jacinto fault zones: Abstract H34B-01 presented at 2005 Fall Meeting, AGU, San Francisco, California, December.

Blisniuk, K., Scharer, K., Sharp, W.D., Burgmann, R., Amos, C., and Rymer, M., 2021, A revised position for the primary strand of the Pleistocene-Holocene San Andreas fault in southern California: Science Advances, v. 7, 14 p.

Bonilla, M.G., and Lienkaemper, J.J., 1991, Factors Affecting the Recognition of Faults Exposed in Exploratory Trenches: U.S. Geological Survey Bulletin 1947, 54 p., https://doi.org/10.3133/b1947.

Bøtter-Jensen, L., Andersen, C., Duller, G., and Murray, A., 2003, Developments in radiation, stimulation and observation facilities in luminescence measurements: Radiation Measurements, v. 37, p. 535–541, https://doi.org/10.1016/S1350-4487(03)00020-9.

Brennan, B.J., Lyons, R.G., and Phillips, S.W., 1991, Attenuation of alpha particle track dose for spherical grains: International Journal of Radiation Applications and Instrumentation, Part D, Nuclear Tracks and Radiation Measurements, v. 18, p. 249–253, https://doi.org/10.1016/1359-0189(91)90119-3.

Bronk Ramsey, C., 2009, Bayesian analysis of radiocarbon dates: Radiocarbon, v. 51, p. 337–360, https://doi.org/10.1017/S0033822200033865.

Bronk Ramsey, C., 2017, Methods for summarizing radiocarbon datasets: Radiocarbon, v. 59, p. 1809–1833, https://doi.org/10.1017/RDC.2017.108.

Buylaert, J., Murray, A., Thomsen, K., and Jain, M., 2009, Testing the potential of an elevated temperature IRSL signal from K-feldspar: Radiation Measurements, v. 44, p. 560–565, https://doi.org/10.1016/j.radmeas.2009.02.007.

Cardona, J., 2016, Constraining the Most Recent Surface Rupture on the Garnet Hill Strand, San Andreas Fault, Coachella Valley, California [Master's thesis]: Northridge, California, California State University, 79 p.

Douilly, R., Oglesby, D.D., Cooke, M.L., and Hatch, J.L., 2020, Dynamic models of earthquake rupture along branch faults of the eastern San Gorgonio Pass region in California using complex fault structure: Geosphere, v. 16, no. 2, p. 474–489, https://doi.org/10.1130/GES02192.1.

Durcan, J.A., King, G.E., and Duller, G.A.T., 2015, DRAC: Dose Rate and Age Calculator for trapped charge dating: Quaternary Geochronology, v. 28, p. 54–61, https://doi.org/10.1016/j.quageo.2015.03.012.

Fletcher, K.E.K., Sharp, W.D., Kendrick, K.J., Behr, W.M., Hudnut, K.W., and Hanks, T.C., 2010, ^{230}Th/U dating of a late Pleistocene alluvial fan along the southern San Andreas fault: Geological Society of America Bulletin, v. 122, p. 1347–1359, https://doi.org/10.1130/B30018.1.

Fosdick, J.C., and Blisniuk, K., 2018, Sedimentary signals of recent faulting along an old strand of the San Andreas fault, USA: Scientific Reports, v. 8, p. 12132, https://doi.org/10.1038/s41598-018-30622-3.

Fuis, G.S., Klaus, B., Goldman, M.R., Ryberg, T., and Langenheim, V.E., 2017, Subsurface geometry of the San Andreas fault in Southern California: Results from the Salton Seismic Imaging Project (SSIP) and strong ground motion expectation: Bulletin of the Seismological Society of America, v. 107, no. 4, p. 1642–1662, https://doi.org/10.1785/0120160309.

Fumal, T.E., Rymer, M.J., and Seitz, G.G., 2002, Timing of large earthquakes since A.D. 800 on the Mission Creek strand of the San Andreas fault zone at Thousand Palms Oasis, near Palm Springs, California: Bulletin of the Seismological Society of America, v. 92, no. 7, p. 2841–2860, https://doi.org/10.1785/0120000609.

Galbraith, R.F., Roberts, R.G., Laslett, G.M., Yoshida, H., and Olley, J.M., 1999, Optical dating of single and multiple grains of quartz from Jinmium rock shelter, northern Australia: Part I. Experimental design and statistical models: Archaeometry, v. 41, p. 339–364, https://doi.org/10.1111/j.1475-4754.1999.tb00987.x.

Gold, P.O., Behr, W.M., Rood, D., Kendrick, K., Rockwell, T.K., and Sharp, W.D., 2015, Holocene geologic slip rate for the Banning strand of the southern San Andreas fault near San Gorgonio Pass: Journal of Geophysical Research–Solid Earth, v. 120, no. 8, p. 5639–5663, https://doi.org/10.1002/2015JB012004.

Guerin, G., Mercier, N., Nathan, R., Adamiec, C., and Lefrais, Y., 2012, On the use of the infinite matrix assumption and associated concepts: A critical review: Radiation Measurements, v. 47, p. 778–785, https://doi.org/10.1016/j.radmeas.2012.04.004.

Heermance, R.V., and Yule, J.D., 2017, Holocene slip rates along the San Andreas fault system in the San Gorgonio Pass and implications for large earthquakes in Southern California: Geophysical Research Letters, v. 44, no. 11, p. 5391–5400, https://doi.org/10.1002/2017GL072612.

Huntley, D.J., and Baril, M.R., 1997, The K content of the K-feldspars being measured in optical dating or in thermoluminescence dating: Ancient TL, v. 15, p. 11–13.

Huntley, D.J., and Lamothe, M., 2001, Ubiquity of anomalous fading in K-feldspars and the measurement and correction for it in optical dating: Canadian Journal of Earth Sciences, v. 38, p. 1093–1106, https://doi.org/10.1139/e01-013.

Jones, L.M., Bernknopf, R., Cox, D., Goltz, J., Hudnut, K., Mileti, D., Perry, S., Ponti, D., Porter, K., Reichle, M., Seligson, H., Shoaf, K., Treiman, J., and Wein, A., 2008, The ShakeOut Scenario: U.S. Geological Survey Open-File Report 2008–1150 and California Geological Survey Preliminary Report 25, 312 p., http://pubs.usgs.gov/of/2008/1150.

Kendrick, K.J., Matti, J.C., and Mahan, S.A., 2015, Late Quaternary slip history of the Mill Creek strand of the San Andreas fault in San Gorgonio Pass, Southern California: The role of a subsidiary left-lateral fault in strand switching: Geological Society of America Bulletin, v. 127, no. 5–6, p. 825–849, https://doi.org/10.1130/B31101.1.

Kreutzer, S., Schmidt, C., Fuchs, M., Dietze, M., Fischer, M., and Fuchs, M., 2012, Introducing an R package for luminescence dating analysis: Ancient TL, v. 30, p. 1–8.

Lancaster, J.T., Hayhurst, C.A., and Bedrossian, T.L., compilers, 2012, Preliminary Geologic Map of Quaternary Superficial Deposits in Southern California Palm Springs 30′ × 60′ Quadrangle: California Geological Survey Special Report 217, Plate 24, scale 1:100,000.

Lienkaemper, J.J., and Bronk Ramsey, C., 2009, OxCal: Versatile tool for developing paleoearthquake chronologies; a primer: Seismological Research Letters, v. 80, no. 3, p. 431–434, https://doi.org/10.1785/gssrl.80.3.431.

Liritzis, I., Stamoulis, K., Papachristodoulou, C., and Ioannides, K., 2013, A re-evaluation of radiation dose rate conversion factors: Mediterranean Archaeology and Archaeometry, v. 13, p. 1–15.

Matti, J.C., and Morton, D.M., 1993, Paleogeographic evolution of the San Andreas fault in southern California: A reconstruction based on a new cross-fault correlation, *in* Powell, R.E., Weldon, R.E., II, and Matti, J.C., eds., The San Andreas Fault System: Displacement, Palinspastic Reconstruction, and Geologic Evolution: Geological Society of America Memoir 178, p. 107–160, https://doi.org/10.1130/MEM178-p107.

Matti, J.C., Morton, D.M., and Cox, B.F., 1985, Distribution and Geologic Relations of Fault Systems in the Vicinity of the Central Transverse Ranges, Southern California: U.S. Geological Survey Open-File Report 85-365, 27 p., scale 1:250,000.

McCaffrey, R., 2005, Block kinematics of the Pacific–North America plate boundary in the southwestern United States from inversion of GPS, seismological, and geologic data: Journal of Geophysical Research, v. 110, B07401, https://doi.org/10.1029/2004JB003307.

McGill, S.F., and Rubin, C.M., 1999, Surficial slip distribution on the central Emerson fault during the June 28, 1992, Landers earthquake, California: Journal of Geophysical Research, v. 104, p. 4811–4833, https://doi.org/10.1029/98JB01556.

McGill, S.F., Dergham, S., Barton, K., Berney-Ficklin, T., Grant, D., Hartling, C., Hobart, K., Minnich, R., Rodriguez, M., Runnerstorm, E., Russell, J., Schmoker, K., Stumfall, M., Townsend, J., and Williams, J., 2002, Paleoseismology of the San Andreas fault at Plunge Creek, near San Bernardino, southern California: Bulletin of the Seismological Society of America, v. 92, p. 2803–2840, https://doi.org/10.1785/0120000607.

McGill, S.F., Spinler, J.C., McGill, J.D., Bennett, R.A., Floyd, M., Fryxell, J.E., and Funning, G.J., 2015, Kinematic modeling of fault slip rates using new geodetic velocities from a transect across the Pacific–North America plate boundary through the San Bernardino Mountains, California: Journal of Geophysical Research, v. 120, p. 2772–2793, https://doi.org/10.1002/2014JB011459.

Meade, B.J., and Hager, B.H., 2005, Block models of crustal motion in southern California constrained by GPS measurements: Journal of Geophysical Research, v. 110, B03403, https://doi.org/10.1029/2004JB003209.

Nicholson, C., 1996, Seismic behavior of the southern San Andreas fault zone in the northern Coachella Valley, California: Comparison of the 1948 and 1986 earthquake sequences: Bulletin of the Seismological Society of America, v. 86, no. 5, p. 1331–1349.

Nur, A., Ron, H., and Beroza, G.C., 1993, The nature of the Landers-Mojave earthquake line: Science, v. 261, no. 5118, p. 201–203, https://doi.org/10.1126/science.261.5118.201.

Onderdonk, N., McGill, S., and Rockwell, T., 2018, A 3700 yr paleoseismic record from the northern San Jacinto fault and implications for joint rupture of the San Jacinto and San Andreas faults: Geosphere, v. 14, p. 2447–2468, https://doi.org/10.1130/GES01687.1.

Philibosian, B., Fumal, T.E., and Weldon, R.J., 2011, San Andreas fault earthquake chronology and Lake Cahuilla history at Coachella, California: Bulletin of the Seismological Society of America, v. 101, no. 1, p. 13–38, https://doi.org/10.1785/0120100050.

Downloaded from http://pubs.geoscienceworld.org/gsa/geosphere/article-pdf/17/3/685/5319464/685.pdf
by 19162

Prescott, J.R., and Hutton, J.T., 1994, Cosmic ray contributions to dose rates for luminescence and ESR dating: Large depths and long-term time variations: Radiation Measurements, v. 23, p. 497–500, https://doi.org/10.1016/1350-4487(94)90086-8.

Reimer, P.J., Bard, E., Bayliss, A., Beck, J.W., Blackwell, P.G., Ramsey, C.B., Buck, C.E., Cheng, H., Edwards, R.L., Friedrich, M., Grootes, P.M., Guilderson, T.P., Haflidason, H., Hajdas, I., et al., 2013, IntCal13 and Marine13 radiocarbon age calibration curves 0–50,000 years cal BP: Radiocarbon, v. 55, p. 1869–1887, https://doi.org/10.2458/azu_js_rc.55.16947.

Rhodes, E., 2015, Dating sediments using potassium feldspar single-grain IRSL: Initial methodological considerations: Quaternary International, v. 362, p. 14–22, https://doi.org/10.1016/j.quaint.2014.12.012.

Rockwell, T.K., Meltzner, A.J., and Haaker, E.C., 2018, Dates of the two most recent surface ruptures on the southernmost San Andreas fault recalculated by precise dating of Lake Cahuilla dry periods: Bulletin of the Seismological Society of America, v. 108, p. 2634–2649, https://doi.org/10.1785/0120170392.

Rymer, M.J., 1997, Structural link between the San Andreas fault and the Eastern California shear zone, Coachella Valley and Little San Bernardino Mountains, Southern California: Geological Society of America Abstracts with Programs, v. 29, no. 5, p. 61–62.

Scharer, K.M., and Yule, D., 2020, A maximum rupture model for the southern San Andreas and San Jacinto faults, California, derived from paleoseismic earthquake ages: Observations and limitations: Geophysical Research Letters, v. 47, no. 15, e2020GL088532, https://doi.org/10.1029/2020GL088532.

Scharer, K., Blisniuk, K., Sharp, W., and Mudd, S.M., 2016, Slip transfer and the growth of the Indio and Edom Hills, southern San Andreas fault: Geological Society of America Abstracts with Programs, v. 48, no. 4, abstract 14-3, https://doi.org/10.1130/abs/2016CD-274217.

Scharer, K.R., Weldon, I.I., Biasi, G., Streig, A., and Fumal, T., 2017, Ground-rupturing earthquakes on the northern Big Bend of the San Andreas fault, California, 800 A.D. to present: Journal of Geophysical Research–Solid Earth, v. 122, p. 2193–2218, https://doi.org/10.1002/2016JB013606.

Schielein, P., and Lomax, J., 2013, The effect of fluvial environments on sediment bleaching and Holocene luminescence ages—A case study from the German alpine foreland: Geochronometria, v. 40, p. 283–293, https://doi.org/10.2478/s13386-013-0120-y.

Sharp, R.V., Rymer, M.J., and Morton, D.M., 1986, Trace-fractures on the Banning fault created in association with the 1986 North Palm Springs earthquake: Bulletin of the Seismological Society of America, v. 76, no. 6, p. 1838–1843.

Sieh, K.E., and Williams, P.L., 1990, Behavior of the southernmost San Andreas fault during the past 300 years: Journal of Geophysical Research, v. 95, p. 6629–6645, https://doi.org/10.1029/JB095iB05p06629.

Spinler, J.C., Bennett, R.A., Anderson, M.L., McGill, S.F., Hreinsdóttir, S., and McCallister, A., 2010, Present-day strain accumulation and slip rates associated with southern San Andreas and Eastern California shear zone faults: Journal of Geophysical Research, v. 115, B11407, https://doi.org/10.1029/2010JB007424.

Stuiver, M., and Polach, H., 1977, Discussion: Reporting of ^{14}C data: Radiocarbon, v. 19, p. 355–363, https://doi.org/10.1017/S0033822200003672.

Toppozada, T.R., Branum, D.M., Reichle, M.S., and Hallstorm, C.L., 2002, San Andreas fault zone, California: M ≥ 5.5 earthquake history: Bulletin of the Seismological Society of America, v. 92, no. 7, p. 2555–2601, https://doi.org/10.1785/0120000614.

U.S. Geological Survey and California Geological Survey, 2018, Quaternary Fault and Fold Database for the United States: U.S. Geological Survey, https://www.usgs.gov/natural-hazards/earthquake-hazards/faults (accessed May 2020).

Weldon, R.J., II, Fumal, T.E., Powers, T.J., Pezzopane, S.K., Scharer, K.M., and Hamilton, J.C., 2002, Structure and earthquake offsets on the San Andreas faults at the Wrightwood, California, paleoseismic site: Bulletin of the Seismological Society of America, v. 92, no. 7, p. 2704–2725, https://doi.org/10.1785/0120000612.

Wesnousky, S.G., 2008, Displacement and geometrical characteristics of earthquake surface ruptures: Issues and implications for seismic-hazard analysis and the process of earthquake rupture: Bulletin of the Seismological Society of America, v. 98, no. 4, p. 1609–1632, https://doi.org/10.1785/0120070111.

Williams, P.L., McGill, S.F., Sieh, K.E., Allen, C.R., and Louie, J.N., 1988, Triggered slip along the San Andreas fault after the 8 July 1986 North Palm Springs earthquake: Bulletin of the Seismological Society of America, v. 78, p. 1112–1122.

Wintle, A., and Murray, A., 2006, A review of quartz optically stimulated luminescence characteristics and their relevance in single-aliquot regeneration dating protocols: Radiation Measurements, v. 41, p. 369–391, https://doi.org/10.1016/j.radmeas.2005.11.001.

Wolff, L., 2018, 6000-Year Record of Large, Infrequent Earthquakes on the San Andreas Fault System in San Gorgonio Pass, near Cabazon, California [Master's thesis]: Northridge, California, California State University, 106 p.

Yule, J.D., and Sieh, K., 2003, Complexities of the San Andreas fault near San Gorgonio Pass: Implications for large earthquakes: Journal of Geophysical Research, v. 108, no. B11, p. ETG 9-1–9-23, https://doi.org/10.1029/2001JB000451.

Yule, J.D., Maloney, S.J., Cummings, L.S., Prentice, C., Ellsworth, W., and Hellweg, P., 2006, Using pollen to constrain the age of the youngest rupture of the San Andreas fault at San Gorgonio Pass: Seismological Research Letters, v. 77, no. 2, p. 245.

Downloaded from http://pubs.geoscienceworld.org/gsa/geosphere/article-pdf/17/3/685/5319464/685.pdf
by 19162

DAY 3 PAPERS

Recently discovered warm springs at Obsidian Butte, Imperial County, California

Paul M. Adams[1] and David K. Lynch[2]
[1]126 South Helberta Ave. #2, Redondo Beach, CA 90277, paul.m.adams@aero.org
[2]Thule Scientific, P. O. Box 953, Topanga, CA

ABSTRACT—Obsidian Butte is one of the Salton Buttes, which are five Holocene rhyolitic volcanic domes associated with a relatively shallow (~4 km) magma body in the Salton Sea Geothermal System. Late in 2020, several small springs were discovered flowing into the sea along the shore north of Obsidian Butte. The springs span about 150 m along the shore and were recently exposed as the sea level has dropped. They have water temperatures as high as 27°C and form small channels that cross mud flats and bars before entering the sea. Over the period of one year the outflow channels from the springs have changed as the sea level has further dropped, as have the flow rates and temperatures of some of the springs. The combined flow of several of the springs in the main outflow channel is significant (~400 liters/min) with a velocity of nearly 30 cm/s. Thermal imagery showed that water in spring channels with significant flow retained elevated temperatures as it traversed the mud flats. In view of the many geothermal features in the vicinity, the springs' slightly elevated temperatures may be geothermal in origin. We note, however, that spring temperature may be influenced by the region's mean annual temperature of 25°C, which controls the near-surface temperature of the rock and sediment through which the water flows before emerging.

1. Introduction

The Salton Buttes are five rhyolitic volcanic domes associated with the Salton Sea Geothermal System (SSGS) located near the southeast shore of the Salton Sea in Imperial County, California. The SSGS lies in the Salton Trough, a pull-apart basin located at a tectonic stepover between the San Andreas and Imperial faults (Gurbuz, 2010) and has a high geothermal gradient anomaly that is related to the numerous geothermal plants of the Salton Sea Geothermal Field (SSGF) (Hulen et al., 2002). The Salton Buttes, from north to south, are Mullet Island, north and south Red Hill, Rock Hill, and Obsidian Butte. They collectively form a roughly north-northeast trending line about 7 km long. The buttes were thought to have formed during the late Pleistocene (Muffler and White, 1969), but recent work suggests eruptions as recent as 2.45 ka for Red Hill and Obsidian Butte (Schmitt et al., 2013; Wright et al., 2015). Hulen et al. (2003) give a detailed description of the subsurface geology of the Obsidian Butte sector of the SSGF based on analysis of several thousand feet of borehole rock samples. Obsidian Butte is the surface expression of the Obsidian Butte flow-dome-tuff complex (Robinson et al., 1976) which consists of glassy to stony, sparsely porphyritic, flow-banded and pumiceous to perlitic rhyolite. It is underlain by the Pleistocene to Holocene Brawley Formation and uppermost Borrego Formation. The former contains a several-hundred-meter-thick evaporitic anhydrate-bearing mudstone that forms a natural cap to the geothermal system. In the conceptual model of Hulen et al. (2003), the source of the geothermal energy for the Obsidian Butte sector of the SSGF is a still-cooling granitic pluton 2 km in diameter and 3.5 km below the surface. The production fluids are circulating hypersaline brines with temperatures generally greater than 290°C. At depth, the interaction of the brines with the wall rocks has led to hydrothermal alteration and development of epidote, actinolite and clinopyroxene.

Obsidian Butte is located in the Brawley seismic zone and from 28 August to September 2, 2005 a swarm of more than 550 earthquakes with magnitude 1.0 or greater occurred near Obsidian Butte (https://www.cisn.org/special/evt.05.09.01/). Eight events were greater than magnitude 4.0 with the largest being 5.1. Its epicenter was 9.7 km deep and was located 1.6 km south of the butte and 2.3 km south of the wells. Analysis of earthquake data indicated that seismic faulting was restricted to a depth of about 4–6 km along a 10 km-long NE striking near-vertical fault segment. In a cross section based on drill core data, Hulen et al. (2003) show a high angle fault near the zone defined by the earthquake epicenters. Surface deformation was observed by two nearby GPS stations, as were some surface breaks in the field (Lohman and McGuire, 2007).

Obvious surface expressions of geothermal activity in the SSGS occur at fumarole fields 1 km SE of Mullet Island (Lynch et al., 2013; Adams et al., 2017) and at the intersections of Davis and Schrimpf Roads, 4 km SE of Mullet Island (Onderdonk et al., 2011), with the former being currently the most active. The fumarole field 1 km SE of Mullet Island consists of vents with boiling water and mud and small gryphons that are emitting ammonia (Tratt et al., 2016), which produced

Table 1. Dates of observations and measurements.

Date	Sea Level (m)	Measurements	Observations/Comments
12/25/2020	-72.695	Brief photo survey	Initial discovery of springs
01/17/2021	-72.664	Drone (DJI Mavic Pro) survey (DKL)	
02/21/2021	-72.603	IR camera survey, photo survey, water sample	Five major springs located (OB1–OB5) Temperatures 27°C, Total dissolved solids = 1.3%
04/10/2021	-72.542	IR camera survey, photo survey	OB1–OB5 27°C
11/27/2021	-72.926	Pole-Cam images, photo survey, flow rate measurements, water sample	Springs 7°–27°C, Total dissolved solids = 0.34%
12/29/2021	-72.902	IR camera survey, photo survey	
01/15/2022	-72.869	Drone survey (DKL)	
02/01/2022	-72.838	Limited photo survey, flow rate measurement	Algae in spring discharge very pronounced

an interesting assemblage of ammonium sulfate minerals (Adams et al., 2017). The fumarole field was submerged under the Salton Sea as recently as 2007 but the dropping sea level exposed it (Lynch et al., 2013). During the 2016 timeframe, an extensive array of airborne dust mitigation trenches was dug near the fumarole fields (F1 and F2 of Adams et al., 2017) and the area was partially flooded. This accelerated impenetrable vegetation growth and the fumarole field is no longer accessible, but steam clouds can still be observed from a distance. The Davis-Schrimpf fumarole field is less extensive and consists of about a dozen gryphons, up to 2 m tall with intermittent mud eruptions and temperatures of 40°–70°C (Svensen et al., 2009; Mazzini et al., 2011; Onderdonk et al., 2011). Lynch and Adams (2014) conducted a thermal survey of the five buttes in 2014 with an infrared camera and discovered five small low-temperature (to 38°C) thermal vents between crevasses in rocks on the south flank of north Red Hill. They did not observe any thermal anomalies on Obsidian Butte, Rock Island or Mullet Island. On December 25, 2020, while hiking the Salton Sea shoreline north of Obsidian Butte, numerous small rivulets were observed emerging from accumulations of loose barnacle shells or mud between cobbles. These had the appearance of small springs which flowed from near a recent shoreline onto a mudflat and into the Salton Sea. There was no evidence of an upslope channel that supplied the water. At their sources they were found to be warm to the touch and an uncalibrated thermometer suggested the water temperature was 27°C. This initiated a more detailed study (Table 1).

2. Observations

Lynch and Adams (2014) did not detect any thermal anomalies on Obsidian Butte (elevation -39.62 m) when they surveyed it in January of 2014, but they concentrated on rock outcrops similar to those that had thermal vents on Red Hill and did not survey the shoreline (sea level = -70.90 m). Since that time, the Salton Sea level has dropped about 1.83 m (Figure 1), recently exposing several areas (OB1-OB6) discharging water (springs). Table 2 gives their locations. Figure 2 shows the locations of the springs superimposed on a 2019 Google Earth image. Figure 3 shows a drone image of the shoreline on January 17, 2021.

In February 2021, a survey of the shoreline surrounding Obsidian Butte was made and the only area detected with flowing water spanned about 150 m between the points OB1 and OB2. About 10 easily recognizable springs emerged from loose barnacle shells and mud between cobbles. Upslope from the springs

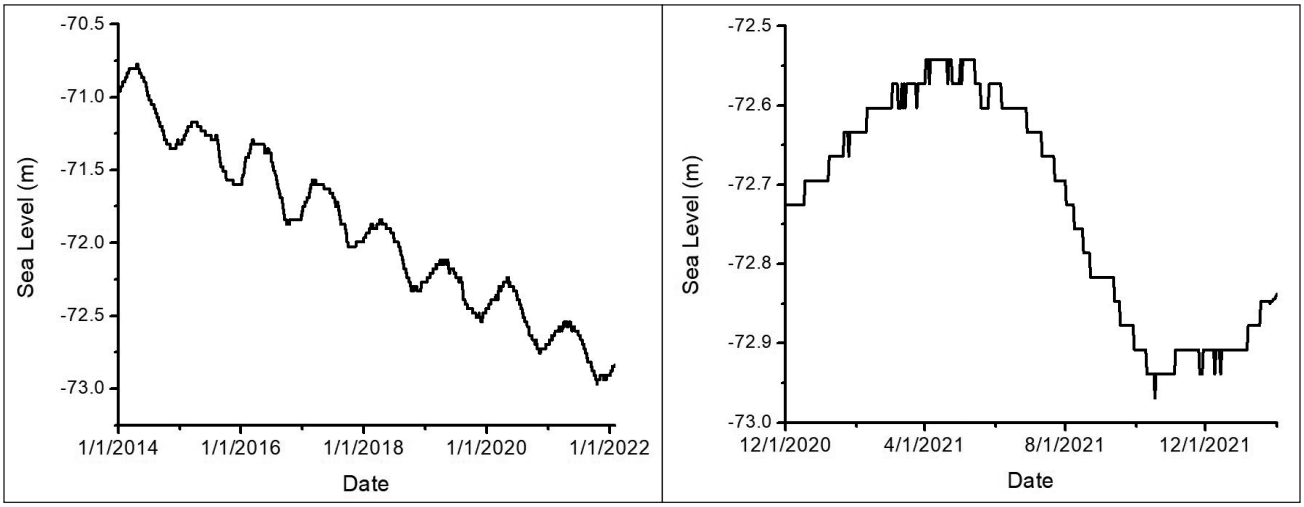

Figure 1. Variation in the Salton Sea level (m) from 12/1/2014 to 2/1/2022. From: (waterdata.usgs.gov/nwis/dv?referred_module=sw&site_no=10254005). The sea level fluctuations are periodic because of seasonal variations in temperature, rainfall, and agricultural runoff.

Table 2. GPS coordinates of discharge sites (OBs) and baseline (BL) Salton Sea measurement sites.

Sites	Latitude	Longitude
OB1	N 33° 10.48'	W 115° 38.46'
OB2	N 33° 10.50'	W 115° 38.37'
OB3	N 33° 10.49'	W 115° 38.42'
OB4	N 33° 10.49'	W 115° 38.41'
OB5	N 33° 10.49'	W 115° 38.40'
OB6	N 33° 10.48'	W 115° 38.51'
BL1	N 33° 10.43'	W 115° 38.57'
BL2	N 33° 10.48'	W 115° 38.52'

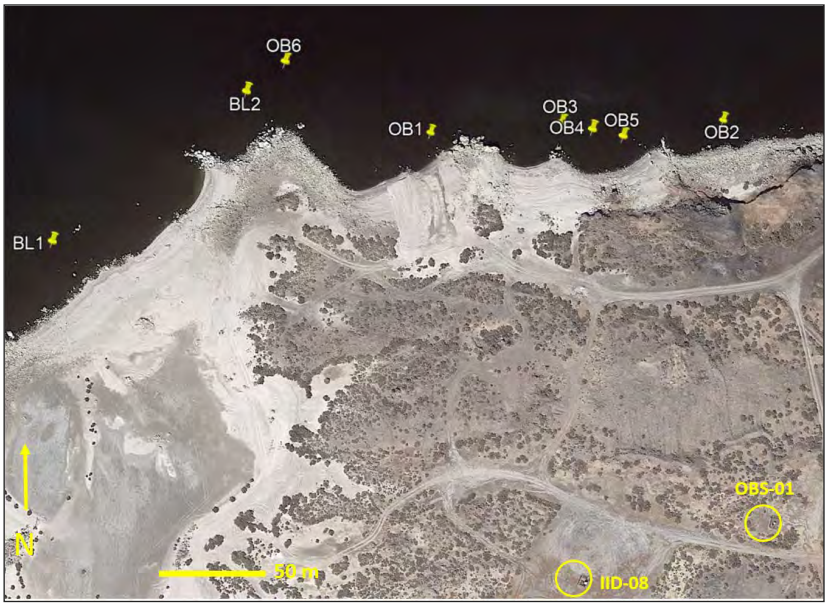

Figure 2. Locations of springs (2/2021) superimposed on 2019 Google Earth image. Locations OB1 and OB2 represented the western- and eastern-most locations, respectively (1/2021 to 4/2021). OB6 was subsequently exposed and OB2 was inactive on 11/ 2021. BL1 and BL2 are locations for Salton Sea baseline measurements. OBS-01 and IID-08 are capped geothermal wells. See Table 2 for GPS coordinates.

there were no recognizable drainage channels that could supply the water. About 25 m south of OB3- OB5 there were outcrops of obsidian and rhyolite to 6 m high that would serve as a barrier to drainage from the butte. At the points of emergence, the springs formed small channels 2–20 cm wide and 1–5 cm deep that merged to form larger shallow channels 10–40 cm wide and 2–10 cm deep that flowed north across sand bars consisting of barnacle shells or mud flats to the open sea (Figure 3–5). There was common enhanced vegetation growth at the source of the springs. Scattered intermittent small bubbles were observed emanating from the spring sources, as well as locations up to several meters from the points of emergence. The temperatures of the five major springs (OB1-OB5) at their sources was 27°C. Water temperatures were measured with a Taylor digital thermometer with a two-meter-long cable probe. The Salton Sea water temperature, measured 40 cm from the shoreline at BL2 away from the springs, was 14°C on 2/20/2021. The temperatures of the Obsidian Butte springs are considerably less than the mudpots 1km SE of Mullet Island (to 100° C) and the Davis-Schrimpf gryphons (40°–70°C) and less than the temperature of the thermal vents on Red Hill (38°C). The total dissolved solids (TDS) content of water collected from OB5 on 2/21/2021 was 1.3%, which compares with 7.4% for Salton Sea water taken from location BL1 in November 2021. The residue was analyzed by X-ray diffraction and was found to be primarily halite with minor anhydrite and a trace of hexahydrite.

When the area was visited in April 2021 the sea level was slightly higher than in February and there appeared to be more water on the mud flats between the sources of the springs and the open sea. This made the outflow channels less distinct. The temperatures of OB1–OB5 were still 27°C with the exception of OB2, which was 17 °C. The open sea water was 20°C.

On November 27, 2021, the level of the Salton Sea had dropped 3.3 cm compared with the last visit in April and the appearance of the shoreline and the configuration of the springs had changed

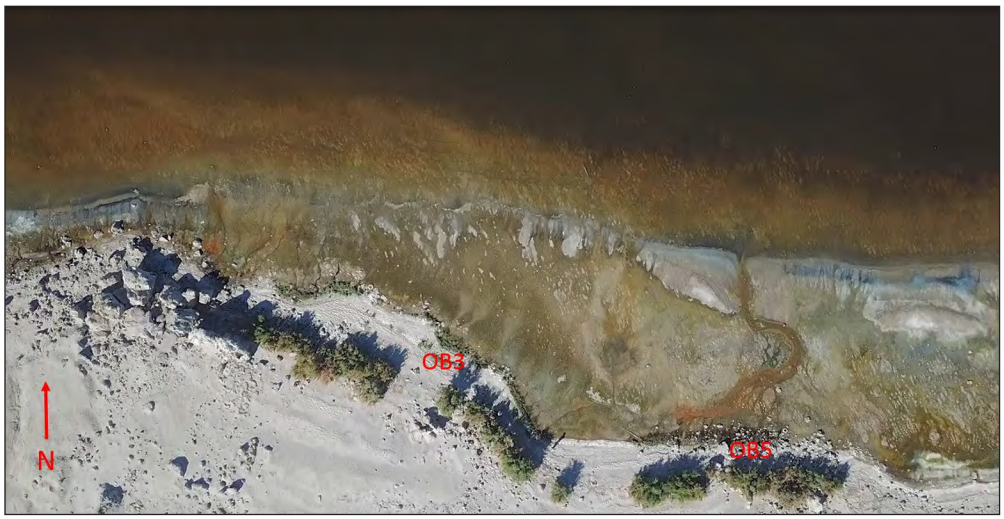

Figure 3. Overhead drone (altitude ~20 m) image of sources of springs OB3 to OB5 (1/17/2021). The outflow channel from OB5 forms a horseshoe-shaped bend through a mudflat before crossing a bar. Reddish brown coloration in the sea is from an algal bloom. See Figure 4 for an oblique view. Compare shoreline in Figure 2.

Figure 4. Oblique drone image of OB5 discharge channel looking east (1/17/2021). Compare with Figure 3.

Figure 5. Western most spring OB1 forming a channel across a bar consisting of barnacle shells. Image taken 2/21/2021, view looking north. GPS receiver (15 cm high) in foreground for scale.

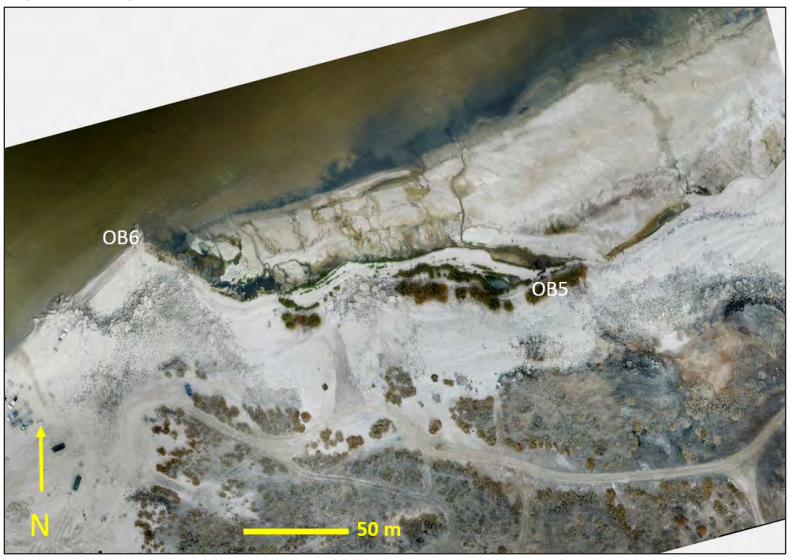

Figure 6. Overhead drone (altitude ~120 m) image of sources of springs OB6 to OB5 (1/15/2022). Compare the shoreline in Figure 3.

dramatically. At this time, images of the shoreline were taken with a point and shoot camera (Olympus TG-3, 12s timer delay) mounted on a 7-m-long telescoping pole (Pole Cam), in order to provide an elevated panoramic perspective when the drone was unavailable. Earlier in 2021, the exact shoreline in this area was difficult to firmly establish. There appeared to be a shallow sand bar and a partially water-covered mud flat separating the springs from open water (Figure 4). It was unclear if the water on the mud flat was from the Salton Sea or an accumulation from the numerous springs. In November 2021, and subsequent visits, the shoreline was much better defined (Figure 6). Proceeding north from the area between OB3 and OB5, there were: 10 m of 15-30 cm-deep loose barnacle shells, a 1m-wide outflow channel with rapidly flowing water, 15 m of salt encrusted firm mud, 15 m of moist mud and 15 m of wet mud that was too soft to walk on.

A new area of flowing small springs (OB6 in Figures 2, 6), that had previously been under water, was also discovered further west from OB1 which earlier had been the western-most. This consisted of 3–4 small (1–3 cm wide) flows emanating from the mud between cobbles within 2 m of the shoreline. Several of the areas previously identified with well-defined springs of flowing water (OB2, OB3) no longer showed evidence of flow but did contain pooled water. When the ambient air temperature was 7°C, the temperature of OB5 and OB6 was 27°C while OB1 = 21°C, OB2 = 7°C, OB3 = 23°C and OB4 = 11°C. The total dissolved solids content of OB5 at the source was 0.34%, which was considerably lower than that measured on February 2021 when the sea level was higher.

The channel leading from OB5 had undergone significant changes. Early in 2021 it wandered in a northerly direction (Figure 3) but in November 2021, and in subsequent visits, it travelled for ~40 m west along the old shoreline in a well-defined channel before making a right-angle bend north to open water (Figures 6, 8). Figure 7 shows OB5 on December 2020 and December 2021. On the later date, OB5 showed two main areas emanating flowing water. Much of the area surrounding the springs was now covered in deep (> 15 cm) loose barnacle shells which covered most of the larger cobbles. In OB5's larger emergence point, the loose barnacle shells could be seen jostling/levitating in the

Figure 7. Spring OB5 on December 26, 2020 (top) and December 29, 2021 (bottom) looking NE. The same large rock is on the lower right corner in each image. In the lower image it is partially obscured by vegetation. The flow rate at (a) was measured on November 26, 2021. There is another small flowing source (b) at the left center margin of the December 2021 image (see Figure 10).

flow. There was also noteworthy vegetation growth. This was typical of the areas around the other earlier identified springs and in many cases it was not possible to precisely locate the earlier locations because points of reference (cobbles) had been covered by barnacle shells or obscured by vegetation (tamarisk and a form of rush). In the swiftly flowing OB5 outflow channel, there was abundant aquatic insect activity (water boatmen, water striders) along with a school of 3 cm-long fish that resembled pupfish.

Measurements of the flow rate from OB5 were made at two locations in November 2021; at the larger of its two emergence points (Figure 7) and in the fast moving outflow channel (Figure 8). Bamboo stakes were placed along the side of the channels at 25 cm intervals and the cross-sectional areas of the flow were measured at three locations. A video camera was used to record the movement of a Styrofoam packing peanut carried by the flow and analysis of the video was used to determine the velocity. At the emergence point, the mean cross-sectional area for the first 0.75 m was 542±57 cm^2 and the velocity was 3.2 cm/s which represents a mean flow rate of 104±11

Figure 8. Pole Camera view of the outflow channel from OB3-OB5 where discharge measurements were made (x).

liters per minute. Further along the channel (Figure 8) the water temperature was 25°C and the mean cross-sectional area of the flow was 219.4 ± 12 cm^2 with a velocity of 29.4 cm/s which represents a mean flow rate of 387±21 liters/min. This is significantly greater than the flow rate at the source of OB5 but there were several other small flowing sources to the west of OB5 that contributed to the flow along with any combined diffuse seepage. The flow rate at the location in Figure 8 was remeasured on February 1, 2022. At that time, the mean cross-sectional area of the flow was 229.37 ± 42.6 cm^2 with a velocity of 33.3cm/s which represents a mean flow rate of 458.3 ± 85.1 liters/min. While this was greater than in November, there was greater uncertainty because of variations in the cross-sectional area. It was not possible to remeasure the flow rate at the emergence point of OB5 (Figure 7) because by February 2022 the surface had become nearly completely covered with filamentous algae. In general, algae was much more common in the spring fed waters on February 1, 2022 and in many places formed mats completely covering the surface.

To better understand the springs, on February 21, 2021, April 10, 2021 and December 29, 2021, infrared surveys of the area were made with an Agema Thermo-Vision 570 camera (wavelengths ~8–13 micrometers) using 12° and 45° lenses. To have maximum thermal contrast between the springs and surroundings, the surveys were conducted at dawn. This also allowed visible images to be taken for reference. The ambient air temperature during the surveys was 5°-7°C. The thermal images covered only a limited field of view, so overlapping images were taken and mosaics of the area were constructed. Thermal and visible images taken of OB1 on 2/20/2021 are presented in Figure 9. They clearly show that the water issuing from the spring remains confined to relatively narrow channels as it crosses the bars and mud flats and is significantly warmer than the surrounding waters. Rock outcrops 25 m south of the springs were imaged with the infrared camera but no thermal anomalies were observed. The

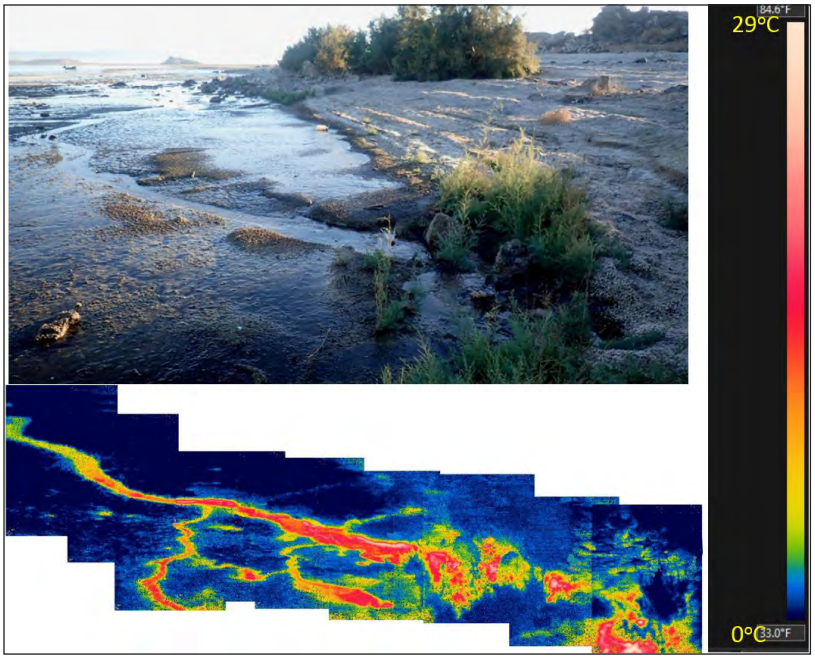

Figure 9. Visible (top) and infrared thermal (bottom) images of spring OB1 taken 2/21/2021. View looking east.

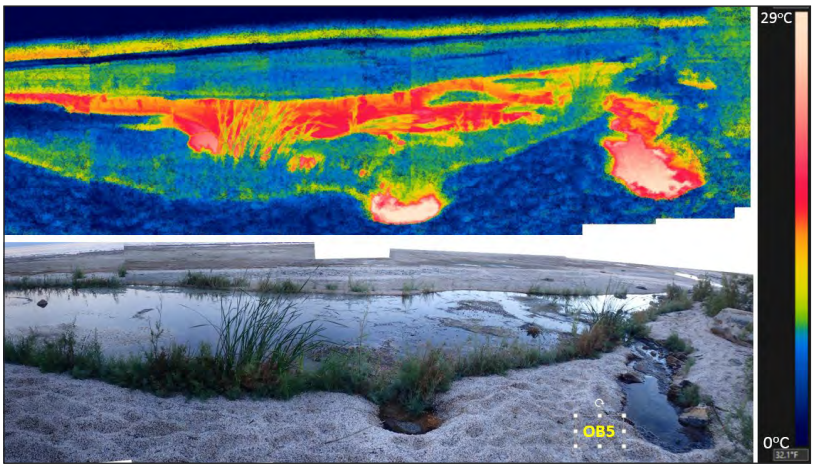

Figure 10. Infrared (top) and visible (bottom) images of spring OB5 taken 12/29/2021. View looking northeast.

survey of the outcrops was not comprehensive. In general, the channels that were well defined in February were less evident in April. The thermal images had less contrast because the temperature differences between the ambient air (13°C), the sea water (20°C) and the spring water 27°C were smaller. Thermal and visible images taken of OB5 and OB1 on 12/29/2021 are presented in Figures 10 and 11, respectively. OB5 is warmest (27°C) at its dual sources but the outflow channel remains well above ambient (23°C vs 7°C) based on the thermal images and physical measurements. At OB1, which no longer showed obvious flow, elevated temperatures (21°C) were generally limited to near the source and the majority of the channels through the mud flats were at ambient.

3. Discussion

Based on the most recent eruption date of 2.45 ka for the Salton Buttes (Schmitt et al., 2013), the U. S. Geological Survey has classified them as active volcanoes (https://www.usgs.gov/volcanoes/salton-buttes). Obsidian Butte potentially could be considered as a geothermal source for the elevated temperature of the springs.

Two capped geothermal test wells (IID-8 and OBS-01) drilled by Cal Energy Operating Corporation are located 200 m south of, and upslope from, the springs (Figures 2 and 12). Observation well IID 8 was drilled in 1990 to a depth of 1988 m, with a bottom-hole temperature of 288° C, had TDS of 22% and showed a pressure drop of 55.2 kPa per year (Woods, 2002). OBS-01 was a shallow (30–90 m) temperature-gradient hole drilled between 1984 and 1986 (Woods, 2002). The wells are listed in the California Department of Conservation Well Finder well records (https://maps.conservation.ca.gov/doggr/wellfinder/#openModal/-115.63329/33.16986/16) but there was no record of depth to the water table. In the California Department of Water Resources Database (https://cadwr.app.box.com/v/WellCompletionReports/folder/77225216507), the nearest well with a reported water table depth was located about 1.5 km away at the SW corner of Boyle and McNerney Roads at an elevation of -68.88 m. The well was drilled in 1989 and standing water was encountered at 2.13–2.90 m below the surface. At that time the Salton Sea level was -70.10 m. It is unclear if this can be related to current conditions if the water table is linked to the sea level.

However, there may be a nongeothermal explanation for the elevated temperatures of the springs. It is possible that the rock through which the springs are flowing is warmer than the sea. If so, the springs should show thermal contrast when the ambient temperature is low, such as before sunrise during the winter or early spring when many of our observations were made. The temperature of spring water is controlled in large part by the discharge rate (Manga and Kirchner, 2004). If the groundwater velocity is high, the heat added by geothermal warming is diluted into a large volume of water, thereby cooling the spring temperature. In contrast, if the discharge velocity is low, the subsurface temperature gradient is little affected by the ground water flow and the discharge temperature will be close to the mean annual surface temperature (Manga and Kirchner,

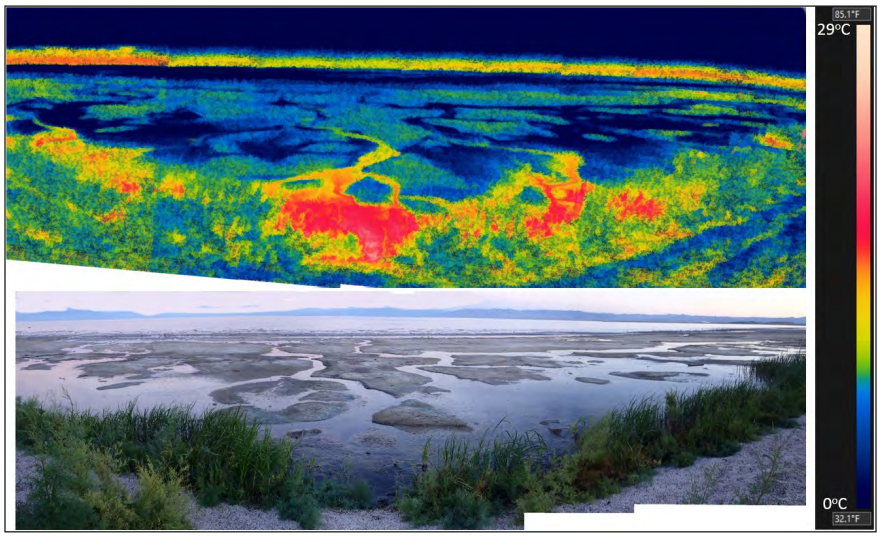

Figure 11. Infrared (top) and visible (bottom) images of spring OB1taken 12/29/2021. View looking north.

2004). For Niland, which is 15 km from Obsidian Butte, the mean daily temperature ranges from 15°C to 35°C (https://www.weather-us.com/en/california-usa/niland-climate#temperature) so that the mean annual temperature is on the order of 25°C, similar to the observed temperature of the springs.

Meinzer (1923) divided non-thermal springs into two categories: 1) those with temperatures approximating the mean annual air temperature and 2) cold springs, with temperatures colder than the mean annual air temperature. Nathenson et al. (2003) proposed the term "slightly-thermal" springs for those that do not meet the requirement for thermal springs (temperature > 10°C above mean annual air temperature) but which have dissolved constituents characteristic of thermal waters. This description possibly fits the springs on the north side of Obsidian Butte. However, it may be difficult to distinguish the dissolved constituents as being from deep geothermal brines, Salton Sea water, agricultural runoff, or some combination of all three. The most recently measured TDS content of the main OB5 spring (0.34%) is considerably less than that of the deep brines (22%) or Salton Sea water (7.4%). However, Williams and McKibben (1989) report that the salinities of geothermal brines in the SSGF are distinctly bimodal, with one population with TDS > 20% and another with low TDS. In the latter, they report TDS contents of about 1.5% for some mudpots. TDS contents similar to OB5 have been measured (0.3%) from some boiling pools (at F1) in the fumarole field 1 km SE of Mullet Island (Adams and Lynch, 2014).

Figure 12. Capped geothermal well OBS-1 operated by Cal Energy Operating Corporation.

4. Summary and conclusions

This paper describes the discovery of small springs along the shore of the Salton Sea north of Obsidian Butte that were recently exposed as the level of the Salton Sea dropped. The springs have temperatures as high as 27°C. Over the period of one year, the outflow channels from the springs have changed as the sea level has further dropped, as have the flow rates and temperatures of some of the springs. The combined flow rate of several of the springs is significant (~400 liters/min) with the main outflow channel having a velocity of nearly 30 cm/s. There are a number of springs in the Salton Buttes area that range in temperature from boiling, at the fumarole fields 1 km SE of Mullet Island (Lynch et al., 2013; Adams et al., 2017), to much lower temperature mound springs at the intersection of Davis Road and State Route 111 (Lynch and Hudnut, 2008; Adams and Lynch, 2014), including an enigmatic moving spring (Lynch and Deane, 2019; Deane and Lynch, 2020), previously known as W9 (Lynch and Hudnut, 2008). The temperature of the latter has ranged from 22°–24°C (D. Lynch, pers. comm.) with a TDS content of 1.8% measured in October 2021. Even though their temperatures are significantly different, the springs all appear to be partly driven by rising carbon dioxide produced by the decomposition of carbonate sediments by the magma body underlying the Salton Sea Geothermal System (Muffler and White, 1969). The temperatures and TDSs of the springs at Obsidian Butte are similar to those of W9 but show only traces of gas escape. The temperature of the springs may not be completely geothermal in nature since the mean annual temperature of the area is so high and influences the temperature of the surface rocks through which the springs flow, creating thermal contrast during colder times of the year. They may possibly be described as slightly-thermal springs.

References

Adams, P.M., Lynch, D.K., 2014. A mineralogical inventory of geothermal features southeast of the Salton Sea, Imperial County, California. In: Reynolds, R. (Ed.), 2014. Desert Symposium Field Guide and Proceedings. Cal. State Univ. Fullerton Desert Studies Consortium, 100–111. http://nsm.fullerton.edu/dsc/images/DSCdocs/2014Notadroplefttodrink.pdf#page=100.

Adams, P. M., Lynch, D. K., Buckland, K. N., Johnson, P. D. and Tratt, D., 2017. Sulfate mineralogy of fumaroles in the Salton Sea Geothermal Field, Imperial County, California, J. Volcanology Geotherm. Res., 347, 15–43.

Deane, R. T. and Lynch, D. K., 2020. A Moving Mud Spring Threatening Critical Infrastructure, Imperial County, California, ASCE Geo-Congress 2020 GSP #316 p717.

Gurbuz, A., 2010. Geometric characteristics of pull-apart basins. Lithosphere 2, 199-206. http://doi.org/10.1130/L36.1.

Hulen, J., Kaspereit, D.,Norton, D., Osborn, W. and Pulka, F. S., 2002. Refined Conceptual Modeling and a New Resource Estimate For the Salton Sea Geothermal Field, Imperial Valley, California, Geothermal Resources Council Transactions, 26, 22–25.

Hulen, J., Norton, D., Kaspereit, D., Murray, L., van de Putte, T. and Wright, M., 2003. Geology and working conceptual model of the Obsidian Butte (Unit 6) sector of the Salton Sea geothermal field, California. Geothermal Resources Council Transactions, 27, 227–240.

Lohman, R. B. and McGuire, J. J., 2007. Earthquake swarms driven by aseismic creep in the Salton Trough, California. J. Geophys. Res., 112, B04405, doi:10.1029/2006JB004596.

Lynch, D. K. and Deane, R. T., 2019. A Moving Mystery, Civil Engineering, July/August, 54-63.

Lynch, D.K., Hudnut, K.W., 2008. The Wister mud pot lineament: Southeastward extension or abandoned strand of the San Andreas Fault? Bull. Seismol. Soc. Amer. 98 (4), 1720-1729. http://doi.org/10.1785/0120070252.

Lynch, David K., Kenneth W. Hudnut and Paul M. Adams, 2013. Recently-Exposed Fumarole Fields near Mullet Island, Imperial Valley, California, Geomorphology. 195, 27–44.

Lynch, D.K., Adams, P.M., 2014. Hot volcanic vents on Red Island, Imperial County, California. In: Reynolds, R. (Ed.), 2014 Desert Symposium Field Guide and Proceedings. Cal. State Univ. Fullerton Desert Studies Consortium, 117–120. (http://nsm.fullerton.edu/dsc/images/DSCdocs/2014Notadroplefttodrink.pdf#page=117).

Lynch, D. K., Deane, T., Rogers, J., Zamora, C., Bailey, J. S., Francuch, D., Allen, C. W., Gouger, C., Dearborn, D., Adams, P. M. and Donnellan, A., 2019. A mysterious moving mud spring near Niland, Imperial County, California. In: Miller, D. (Ed.) 2019 Desert Symposium Field Guide and Proceedings. Cal. State Univ. Fullerton Desert Studies Consortium, 168-175.

Manga, M. and Kirchner, J. W., 2004. Interpreting the temperature of water at cold springs and the importance of gravitational potential energy. Water Resource Research, 40, W05110. doi: 10.1029/2003WR002905.

Mazzini, A., Svensen, H., Etiope, G., Onderdonk, N., Banks, D., 2011. Fluid origin, gas fluxes and plumbing system in the sediment-hosted Salton Sea geothermal system (California, USA). J. Volcano. Geotherm. Res., 205, 67-83. http://doi.org/10.1016/j.jvolgeores.2011.05.008.

Meinzer, O.E., 1923. Outline of ground-water hydrology with definitions. U.S. Geol. Surv. Water-Supply Pap. 494, 71 pp.

Muffler, L. J. P and D. E. White, 1969. Active Metamorphism of Upper Cenozoic Sediments in the Salton Sea Geothermal Field and the Salton Trough, Southeastern California, Bull. Geo. Soc. Am. 80, 57–182.

Nathenson, M. L., Thompson, J. M. and White, L. D. (2003) Slightly thermal springs and non-thermal springs at Mount Shasta, California: Chemistry and recharge elevations. J. Volcanol. Geotherm. Res., 121, 137-153.

Onderdonk, N., Shafer, L., Mazzini, A., Svenson, H., 2011. Controls on the expression and evolution of gryphons, mud pots, and caldera features at hydrothermal seeps in the Salton Sea Geothermal Field, Southern California. Geomorphology 130 (3-4), 327-342. http://doi.org/10.1016/j.geomorph.2011.04.014.

Robinson, P. T., Elders, W. A. and Muffler, L. J. P., 1976. Quaternary volcanism in the Salton Sea geothermal field, Imperial Valley, California. Geol. Soc. America Bull., 87, 347-360.

Schmitt, A.K., Martín, A., Stockli, D. F., Farley, K. A. and Lovera, O. M., 2013. (U–Th)/He zircon and archaeological ages for a late prehistoric eruption in the Salton Trough (California, USA) Geology, 41, 7–10. doi:10.1130/G33634.1

Svensen, H., Hammer, Ø., Mazzini, A., Onderdonk, N., Polteau, S., Planke, S., Podladchikov, Y.Y., 2009. Dynamics of hydrothermal seeps from the Salton Sea geothermal system (California, USA) constrained by temperature monitoring and time series analysis. J. Geophys. Res. 114 (B9), B09201. http://doi.org/10.1029/2008JB006247.

Tratt, D.M., Young, S.J., Johnson, P.D., Buckland, K.N., Lynch, D.K., 2016. Multi-year study of remotely-sensed ammonia emission from fumaroles in the Salton Sea geothermal field. Proceedings, 8th IEEE Workshop on Hyperspectral Image and Signal Processing: Evolution in Remote Sensing – WHISPERS (Los Angeles, CA, August 21-24, 2016).

Williams, A. E. and McKibben, M. A., 1989. A brine interface in the Salton Sea Geothermal System, California: Fluid geochemical and isotopic characteristics, Geochimica et Cosmochimica Acta, 53, 1905-1920.

Woods, M., 2002. Salton Sea Unit 6 Project Geothermal Resource Evaluation. California Energy Commission: Black Rock 1,2 and 3 geothermal power project licensing case : Docket No. 02-AFC-02. (https://ww2.energy.ca.gov/sitingcases/saltonsea/documents/2002-11-15_WOODS_TESTIMONY.PDF).

Wright, H. M., Vazquez, J. A., Champion, D. E., Calvert, A. T., Mangan, M. T., Stelten, M., Cooper, K. M., Herzig, C. and Schriener, A. Jr., 2015. Episodic Holocene eruption of the Salton Butte rhyolites, California, from paleomagnetic, U-Th, and Ar/Ar dating, AGU Publications: Geochemistry, Geophysics, Geosystems, http://doi.org/10.1002/2015GC005714.

Article

Major southern San Andreas earthquakes modulated by lake-filling events

https://doi.org/10.1038/s41586-023-06058-9

Received: 15 July 2022

Accepted: 5 April 2023

Published online: 07 June 2023

Check for updates

Ryley G. Hill[1,2]✉, Matthew Weingarten[1], Thomas K. Rockwell[1] & Yuri Fialko[2]

Hydrologic loads can stimulate seismicity in the Earth's crust[1]. However, evidence for the triggering of large earthquakes remains elusive. The southern San Andreas Fault (SSAF) in Southern California lies next to the Salton Sea[2], a remnant of ancient Lake Cahuilla that periodically filled and desiccated over the past millennium[3–5]. Here we use new geologic and palaeoseismic data to demonstrate that the past six major earthquakes on the SSAF probably occurred during highstands of Lake Cahuilla[5,6]. To investigate possible causal relationships, we computed time-dependent Coulomb stress changes[7,8] due to variations in the lake level. Using a fully coupled model of a poroelastic crust[9–11] overlying a viscoelastic mantle[12,13], we find that hydrologic loads increased Coulomb stress on the SSAF by several hundred kilopascals and fault-stressing rates by more than a factor of 2, which is probably sufficient for earthquake triggering[7,8]. The destabilizing effects of lake inundation are enhanced by a nonvertical fault dip[14–17], the presence of a fault damage zone[18,19] and lateral pore-pressure diffusion[20,21]. Our model may be applicable to other regions in which hydrologic loading, either natural[8,22] or anthropogenic[1,23], was associated with substantial seismicity.

The SSAF is the only historically quiescent seismogenic section of the San Andreas Fault system (Fig. 1) and is believed to pose the largest seismic hazard in California[14,24,25]. The last major earthquake on the SSAF occurred around 1726 (ref. 26). The modern open interval of about 300 years is well in excess of the average recurrence interval of 180 ± 40 years over the past millennium[4,5,26]. Previous studies suggested that at least some large events on the SSAF may have occurred during highstands of ancient Lake Cahuilla[3,27,28]. Lake Cahuilla was a prehistoric lake that formed from periodic meandering of the Colorado River north into the Salton Trough and had an estimated maximum volume of 236 km^3 (ref. 5). Filling and draining of the lake subjected the SSAF system to surface loads corresponding to a roughly 100-m-deep body of water[3,27,28]. Previous studies suggested that loading owing to ancient Lake Cahuilla inhibited failure on most of the SSAF, except maybe for a small portion within the lake boundary[29], or that triggering of large events on the SSAF was mediated by slip on nearby extensional stepover faults[30]. Here we combine new palaeoseismic and geologic data with state-of-the-art numerical modelling to investigate the relationship between lake loading and major earthquakes on the SSAF over the past approximately 1,100 years.

Palaeoseismic evidence is critically important in determining both the timing of large earthquakes and lake history. Previous work at the Coachella palaeoseismic site, just below the ancient Lake Cahuilla shoreline (Fig. 1), suggested five probable and two possible earthquakes over the past millennium[4]. Recently, Rockwell et al.[6] reinterpreted the stratigraphy at the Coachella site, building on the results developed for the past two full lake inundations, which consider both the historical record and drowned stump ages[5]. Three different lake-level models, varied by different sampling assumptions, were constrained by more than 122 radiocarbon dates across several palaeoseismic sites in the ancient Lake Cahuilla inundation zone. The resulting nearly 2,000-year history of ancient Lake Cahuilla is based on an extensive compilation and review of radiocarbon samples throughout the lake basin and on the unique character of some stratigraphic unit interpretations. Distinct organic layers, measuring 1–2 cm in thickness and originally described as 'soils', were reinterpreted to be the result of lake inundations. These organic-rich layers record where organic materials floated to near the shoreline and were incorporated into a lake sequence during rising lake waters. Supporting this interpretation is the fact that organic soils are not present in the hyper-arid environment of the Lake Cahuilla basin and that such organic layers have been identified only at or below the shoreline of Lake Cahuilla[6,27,31]. Similar observations have also been made along the Laguna Salada Fault further to the south[32].

On the basis of these insights into the palaeolake chronology, we infer that six of the past seven SSAF earthquake horizons lie within lacustrine sediments. This is critical, as new palaeoseismic data that refine the history of lake ages[6] also place tighter constraints on the timing of past earthquakes. We converted the ^{14}C radiocarbon ages of organic material to calendar years CE using the OxCal algorithm v.4.4 and the history of atmospheric ^{14}C concentrations[33,34]. The OxCal algorithm produces probability density functions (PDFs) of each date by convolving uncertainties in the radiocarbon measurements. An ordered sequence based on the stratigraphic layering provides further constraints to the radiocarbon age PDFs. The statistically consistent earthquake PDFs are calculated on the basis of the interpretation of their timings in conjunction with the full sequence. The details of our

[1]Department of Geological Sciences, San Diego State University, San Diego, CA, USA. [2]Scripps Institution of Oceanography, University of California San Diego, La Jolla, CA, USA.
✉e-mail: ryleyghill@gmail.com

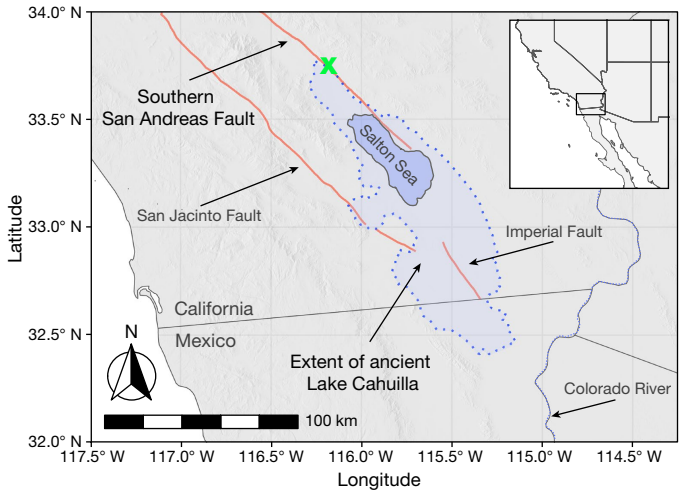

Fig. 1 | Regional context. Map of the Salton Trough and present-day Salton Sea (9.5 m average water depth). Dotted blue line denotes the historical extent of ancient Lake Cahuilla (13 m above sea level; 97.2 m maximum water depth)[29]. Red lines denote traces of several major faults[48]. Green X marks the location of the Coachella palaeoseismic site[4].

interpretation of the palaeoseismic record and OxCal model are provided in the Supplementary Information. Our interpretations of where earthquake horizons lie in the stratigraphy are mostly unchanged from those of Philibosian et al.[4]. The main differences in earthquake ages are a result of reclassifying which sediments are lacustrine, as well as assuming that most charcoal and all organic layers are from material that grew within the lake perimeter, and therefore have ages corresponding to the preceding dry periods between lakes[6]. Figure 2 shows the calculated PDFs for major seismic events that occurred on the SSAF over the past approximately 1,100 years (see Extended Data Table 1 for earthquake dates). Also shown in Fig. 2 is the preferred history model of Lake Cahuilla[6] that includes the following six highstands: 1731–1733 CE (lake A), 1618–1636 CE (lake B), 1486–1503 CE (lake C), 1192–1241 CE (lake D), 1007–1070 CE (lake E) and 930–966 CE (lake F). Highstands are preceded by a 13-year-long inundation period and followed by a 50-year-long dessication period, consistent with previous lake models[5]. The same radiocarbon dates are used to inform the timing of the earthquake and lake ages, but the lake timings are further constrained by climate data[6]. Although previous studies were inconclusive about temporal correlation of the earthquakes and lake episodes over the past millennium[4], the new earthquake history strongly suggests that all lake-filling events were accompanied by large earthquakes (Fig. 2).

Such a correlation between the earthquake and lake timings is probably not coincidental. A Monte Carlo statistical test of the lake and earthquake timings confirms a nonrandom relationship with >97% confidence (Extended Data Fig. 1). Also, hydrologic loads are known to stimulate seismicity[1,23,35–37]. Possible mechanisms include increases in pore pressure, flexural stresses and poroelastic effects[29,30]. Seismicity may be triggered shortly after reservoir impoundment by the poroelastic load of the lake at the Earth's surface, as well as on longer timescales by the time-dependent diffusion of pore pressure to greater depths[1,35,38]. Increases in pore-fluid pressure, in general, bring faults closer to failure and may potentially advance the timing of large events[1,39,40]. Another factor relevant to triggering of seismicity is the presence of fluid pathways resulting from rock damage. Faults are commonly associated with damage zones[18,19], resulting in enhanced permeability that decays with distance away from the fault core[41–45]. Fault damage zones can therefore substantially facilitate fluid transport to seismogenic depths[20,21]. There is evidence for an extensive SSAF damage zone from field observations at surface exposures, borehole data and Earth tidal analyses[46,47]. Models of lake loading therefore need to account for the fully coupled poroelastic response and the heterogeneous hydromechanical properties of the fault zone and ambient crust.

To quantify the effects of lake loading, we built a fully coupled, 3D finite-element model of the Salton Trough that accounts for time-varying surface loads, a realistic fault geometry, crustal poroelasticity and viscoelastic relaxation in the ductile substrate (see Methods and Extended Data Fig. 2). We performed numerical simulations in which we varied material properties of the host rocks and damage zone to constrain a plausible range of pore pressure and stress evolution owing to ancient Lake Cahuilla (Extended Data Fig. 3 and Supplementary Figs. 1–4). The temporal evolution of the lake load, which is ascribed as both pore pressure and vertical stress boundary conditions at the Earth's surface, is constrained by the latest geologic data[6] (Fig. 2). Unless otherwise noted, the models presented below assume the lake depth of 97 m, consistent with previous studies[29], but we also considered a spatially variable surface load controlled by bathymetry. Each lake episode consists of a unique filling, highstand, desiccation and consolidation history. We resolve the coupled deformation transient from the refined approximately 1,100-year lake history with about 200 adaptive time steps across our numerical-model domain. The increase in pore pressure within the basement is highly dependent on the assumed parameters of the fault zone, in particular the damage-zone permeability (Extended Data Table 2). For a given loading history, higher values of permeability give rise to greater pore pressures at depth (Extended Data Fig. 3). Furthermore, similar to the analytic solution (see Methods and Extended Data Fig. 4), we observe the 'memory' effect of pore pressure at depth, whereby subsequent lakes can contribute to higher pore pressure owing to the diffusive time lag of a previous lake superimposing on the next (Fig. 3).

The evolution of faults towards (or away from) failure is commonly described in terms of the Coulomb failure stress (ΔCFS)[7,8,35] (also see Methods). The calculated values of ΔCFS resolved on a potential failure plane (Supplementary Figs. 3 and 6) exhibit a strong sensitivity

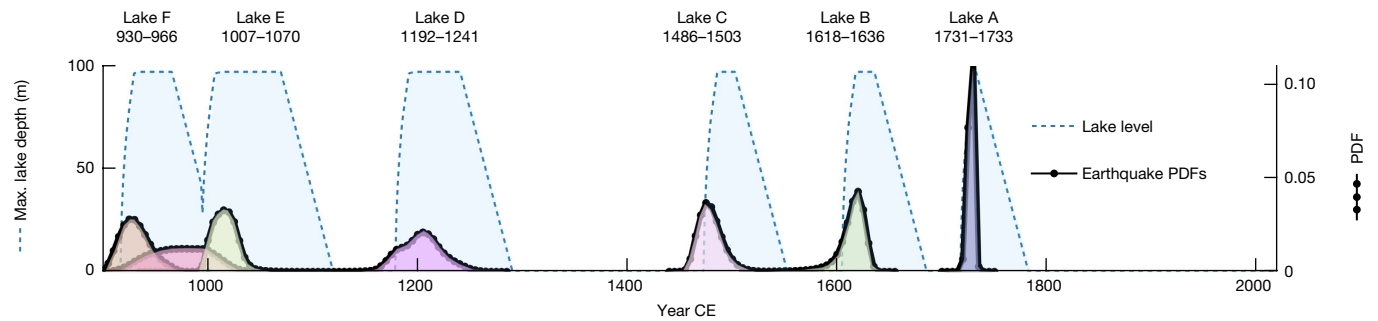

Fig. 2 | Lake and earthquake history. Earthquake PDFs (dotted black lines, right axis) calculated in this study (see Methods) and the relative lake-loading history (dashed blue lines, left axis) from ref. 6. PDFs of prehistoric earthquakes (see Extended Data Table 1) are colour-coded as follows: Coa-1 is blue, Coa-2 is green, Coa-3 and Coa-4 are pink, Coa-5 is magenta, Coa-6 is yellow, Coa-7 is red and Coa-8+ is orange.

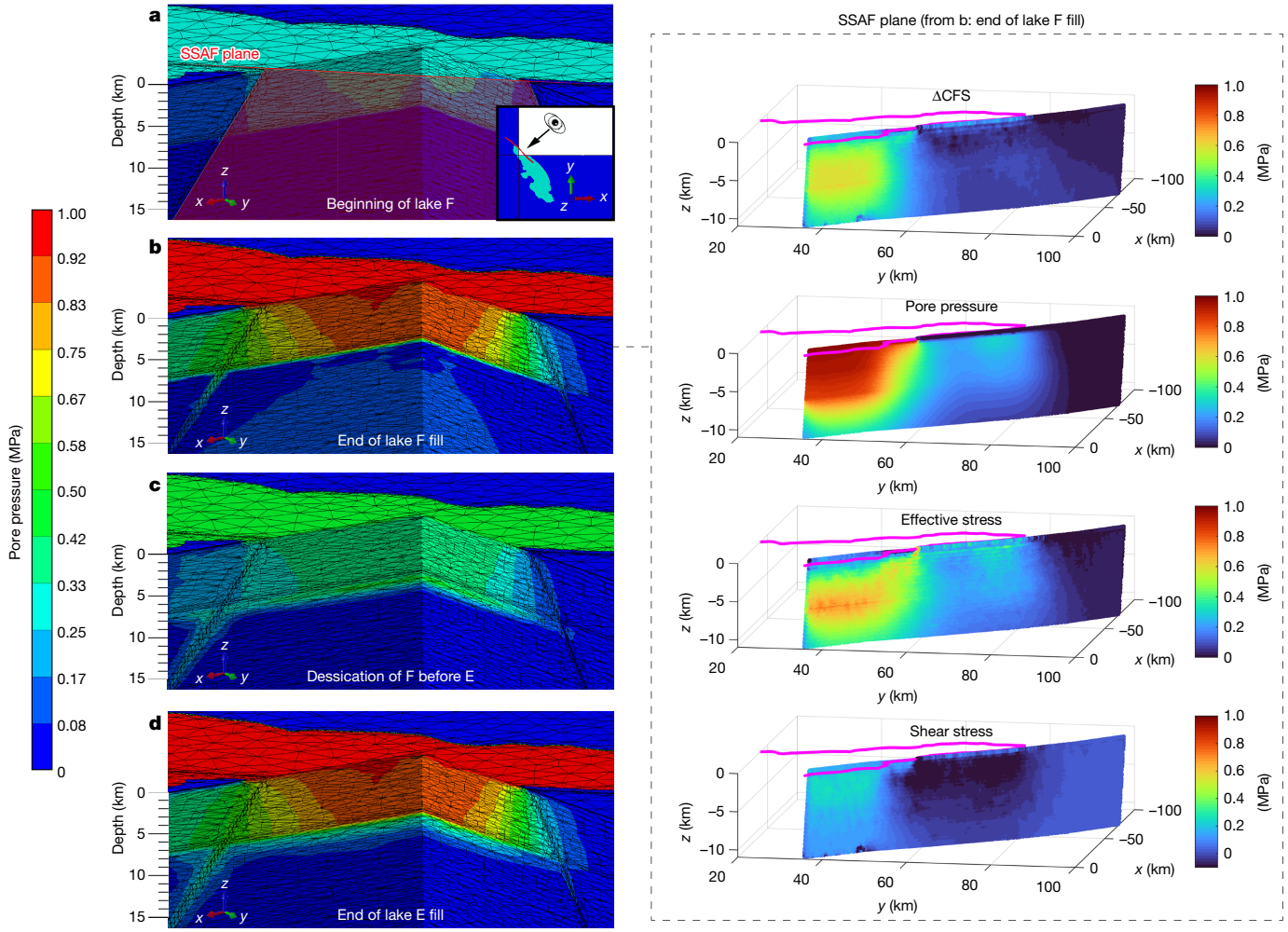

Fig. 3 | Finite-element-model results. Left, spatiotemporal evolution of pore pressure for a single lake cycle of ancient Lake Cahuilla. Calculations assume a constant lake depth of 97.2 m. The cross-section cuts through the northwestern end of the lake and through the embedded dipping fault. **a**, Pore pressure immediately increases as the lake begins to inundate. **b**, At the time of lake highstand, the pore pressure has diffused down much of the higher permeable fault but is more slowly varying elsewhere because of the low-permeability basement. **c**, As the lake desiccates, higher pore pressures remain in and around the fault. **d**, Subsequent lakes further increase the previously elevated pore pressure at basement depth. Right, the Coulomb stress change (ΔCFS), pore pressure (P), effective stress ($\bar{\sigma}_n$) and absolute shear stress (τ_s) perturbations on the SSAF fault plane for a single time frame in the lake cycle. The magenta line represents the outline of ancient Lake Cahuilla at the surface.

to the fault geometry and, in particular, the fault dip angle. We assume an average strike of 313° based on the fault trace[48] (Fig. 1) and a fault dip of 60° NE, which is constrained by geodetic and seismic data[14–16,49]. ΔCFS values are inversely proportional to the fault dip angle: a steeper fault experiences a smaller change in the Coulomb stress and a more shallowly dipping fault experiences a larger change in the Coulomb stress (Supplementary Fig. 1). Another factor affecting ΔCFS is a time-dependent flexure owing to the varying surface load and the associated viscoelastic relaxation in the underlying ductile substrate. For a range of possible substrate viscosities suggested by previous work[29], the effects of viscoelastic relaxation on ΔCFS are relatively minor (Supplementary Fig. 2). Our simulations indicate that variations in the pore pressure are the dominant contributor to the total ΔCFS (Supplementary Figs. 3 and 4). Models that used a simplified representation of only the elastic crust suggested higher values of ΔP but lower values of the effective ΔCFS (Supplementary Figs. 3 and 4).

We find that the magnitude of shear stress ($\Delta\tau_s$), effective normal stress ($\Delta\bar{\sigma}_n$), pore pressure (ΔP) and ΔCFS increase throughout the sequence of flooding cycles (Fig. 4a). Most notably, ΔCFS remains predominantly positive across the fault surface during each cycle (Fig. 4a and Supplementary Videos 1–3). Positive ΔCFS outside the lake boundary, albeit smaller in magnitude, is a consequence of lateral pore-pressure diffusion (Fig. 3 and Supplementary Videos 1–3). When the lake is at highstand, shear stress is positive (that is, encouraging failure) in parts of the fault closest to the lake centre and slightly negative (that is, inhibiting failure) outside the lake. By contrast, the normal stress is negative (that is, inhibiting failure) directly below the lake owing to the increased vertical compression during lake impoundment. However, the effective normal stress stays positive on much of the fault because of increases in pore pressure. The modelled compression directly below the lake simply moderates the magnitude of the Coulomb stress in that region. Models with lower permeability show a similar evolution, although the spatial extent of pore-pressure diffusion is smaller.

Figure 4 depicts the evolution of ΔCFS for a single point on the fault plane near the centre of the lake at the representative seismogenic depth of 7 km (point 21 in Supplementary Fig. 5) for a range of models (models 1–5; see Extended Data Table 2) with different permeabilities of the fault damage zone[15,30]. In each model, as the lake fills, the ΔCFS increases rapidly owing to the initial lake impoundment (that is, undrained response). During the desiccation phase of the lakes, the overall ΔCFS decreases but remains mostly positive except for the

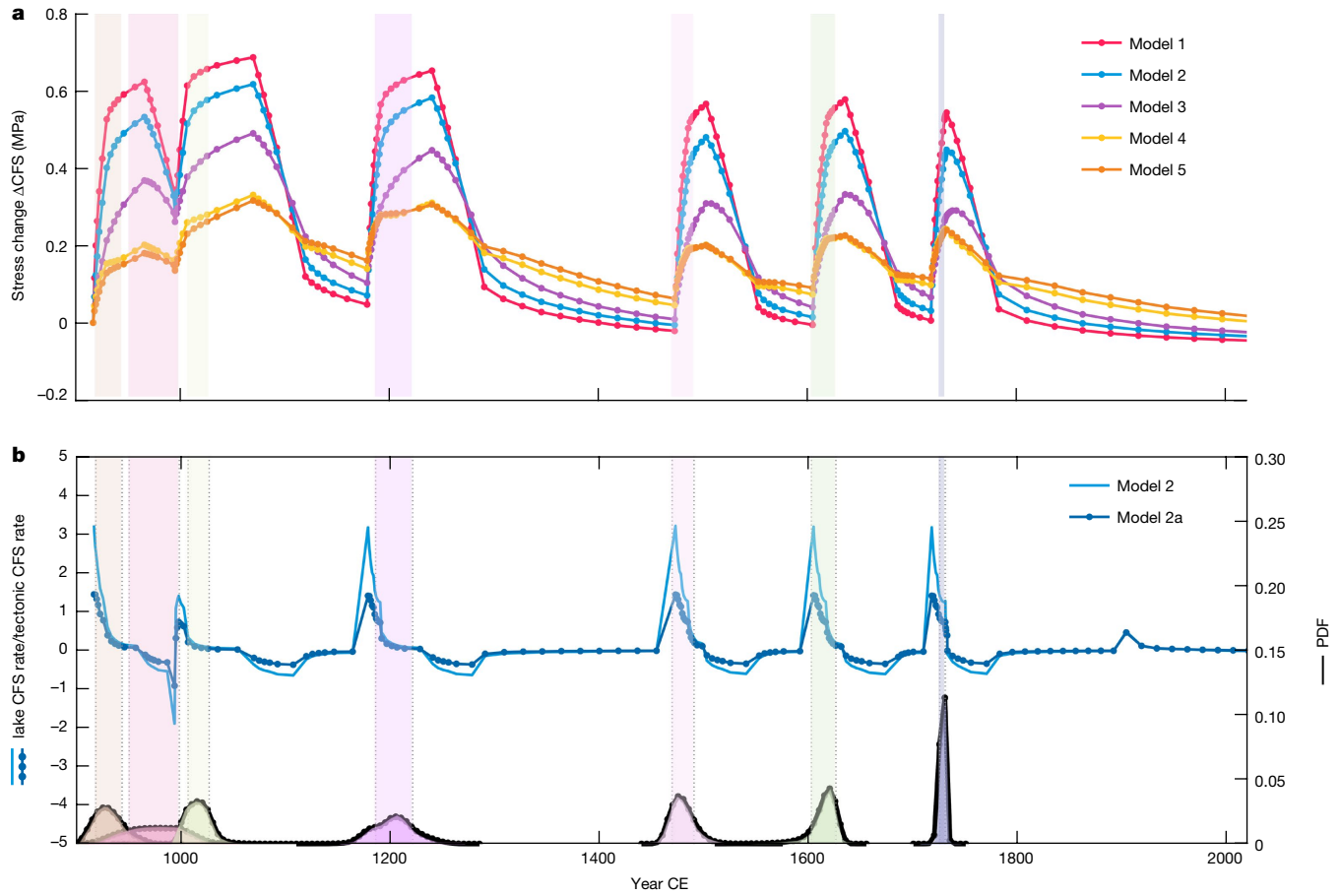

Fig. 4 | Stress effects of lake loading. a, ΔCFS (MPa) on the SSAF as a function of time (year CE) at 7 km depth for location 21, a point on the fault near the centre of the lake (see Supplementary Fig. 5). Coloured lines correspond to models assuming different permeability of the fault zone (see Methods and Extended Data Table 2), from highest (model 1) to lowest (model 5, no permeability contrast with the host rocks). The same plot for a point farther from the lake centre also shows predominantly positive ΔCFS, albeit of lower magnitude (Extended Data Fig. 5). **b**, The Coulomb stressing rate owing to the lake loading normalized by the tectonic loading rate (16 kPa year^{-1}; see Methods). Light blue line represents predictions of model 2 (same as in panel **a**) and dark blue dotted line represents predictions of model 2a, which considers a spatially variable surface load based on a local bathymetry. The small peak in 1905 is because of the inundation of the Salton Sea (see Supplementary Figs. 5–11). Models 1–5 do not include Salton Sea inundation. Vertical colour bars denote ±2 standard deviations of the estimated earthquake dates.

current dry period from about 1733 to the present and the dry period between lakes C and D. The models at the high end of the assumed damage stay positive in most parts of the fault-zone permeability, showing a relatively rapid diffusion of pore pressure from the surface to seismogenic depths. The increased rate of ΔCFS during the lake highstands is indicative of the higher permeability. Furthermore, the results depict how the short time interval between highstands in the first two or three lakes contributes to an overall cumulative increase in the Coulomb stress for the second (lake E) and sometimes the third (lake D) lakes, depending on the modelled fault permeability and depth. The remnant diffusion of pore pressure because of the first lake (lake F) coincides with the impoundment of the subsequent lake, producing a larger overall ΔCFS. This additive effect is even more pronounced for lower fault-zone permeabilities. We acknowledge that shorter lake highstands would reduce the additive effect on ΔCFS discussed in this paper, as we use the maximum durations for the lake highstands[6]. We also performed simulations in which the surface load is controlled by a local bathymetry. The results are similar to the reference model assuming a constant depth of 97 m, except that the calculated stress changes and stressing rates are reduced by around 40%. This is because the average lake depth is less than the maximum depth of 97 m. Predictions of the reference model therefore should be considered an upper bound. Depending on the rate of diffusion, depth of interest and time interval between lakes, the effect of previous lakes may persist during subsequent impoundments. This memory effect is more pronounced for models 3 and 4 owing to lower permeability at depth (Extended Data Fig. 5). All models, including model 5, which does not include a fault damage zone, produce positive ΔCFS values greater than about 0.1 MPa, which is probably large enough for earthquake triggering[7,50,51].

As well as the magnitude of stress changes, earthquake triggering may be affected by variations in the stressing rate[52,53]. We evaluate the ratio of the calculated stressing rate from the lake load to the average tectonic loading rate over time (Fig. 4b). The latter is calculated using a geodetically constrained dislocation model assuming a secular slip rate of 18 mm year^{-1} (ref. 54), which is in agreement with the most recent constraints on the long-term geologic slip rate[55] (and references therein). The estimated tectonic stressing rate at seismogenic depth is $\dot{\sigma}_{13}$ = 16 kPa year^{-1} (see Methods). We find that the largest perturbations in stressing rates occur, as expected, during the early flooding stages of each of the past six lakes (Fig. 4b). For six of the past seven earthquake events on the SSAF (±2σ uncertainties; Extended Data Table 1), the resolved stressing rate from lake loading was greater than the tectonic loading rate. The respective perturbations remain positive through the lake highstands until dessication begins, during which the stressing rates drop below the average interseismic stressing rate. Over

the past approximately 1,100 years, the fault-stressing rate during lake loading increased by more than a factor of 2 (Fig. 4b). These high stressing rates from lake loading persisted for several decades during each lake cycle. The relationship between lake cycles and earthquakes is potentially known at higher precision exclusively from the stratigraphy. There is evidence to suggest that events Coa-5 and Coa-8+ may have occurred during lake-filling phases, whereas Coa-1, Coa-2, Coa-3 and Coa-4, and Coa-6 occurred during highstands (see Methods).

Loading from ancient Lake Cahuilla induced stress changes capable of triggering events on the SSAF, increased ΔCFS across most of the fault and, on average, increased peak stressing rates during lake flooding well above the tectonic stressing rate (Fig. 4b and Supplementary Videos 1–3). Larger fault locking depths[17] and smaller earthquake nucleation depths[56] and elastic moduli of the host rocks[57] would result in a lower tectonic stressing rate and a correspondingly higher contribution of the lake loading. Our model does not account for possible memory effects from earthquakes that occurred more than about 1,000 years ago, as such effects are probably negligible if the interseismic interval exceeds several hundred years (see Fig. 4a; also see ref. 58). We also do not account for stress transfer resulting from slip on subsidiary faults that could potentially amount to ΔCFS on the order of 1 MPa (ref. 30). Our models thus provide a conservative estimate for the modulation of stress on the SSAF by the filling and desiccation of ancient Lake Cahuilla.

Our results bear on the current 300-year-long quiescent period on the SSAF. Variations in stress and stressing rate on the SSAF owing to the lake load suggest that a gradual decline in water level since ancient Lake Cahuilla's last highstand may affect the timing of the SSAF's next event. Indeed, our model predicts predominantly negative ΔCFS for sufficiently long dry periods. The negative ΔCFS during dry periods is primarily because of the flexure of the upper crust caused by a decreased lake level and, to a lesser degree, viscoelastic relaxation below the brittle–ductile transition. A gradual decrease in the ΔCFS since the last highstand was briefly reversed in 1905–1907 because of an overflow of the Colorado River into Salton Basin, which led to formation of the present-day Salton Sea[30]. Our model predicts a sharp increase in ΔCFS, on the order of 0.1 MPa, for most of the fault during the filling phase of the Salton Sea from 1905 to 1907 (Supplementary Figs. 5–11). This increase in ΔCFS was accompanied by the 18 April 1906 M_l 6.1 (MMI 8) event in the Salton Trough near Brawley, CA. This event was previously argued to be triggered by the great 1906 California earthquake near San Francisco that occurred 11 h before and 700 km away from the M_l 6.1 event[59]. It is possible that such distant triggering was facilitated by the lake load. After 1907, the model predicts a subsequent decrease in ΔCFS as the Salton Sea started to decline below the 0.1 MPa triggering threshold (Supplementary Figs. 5–11 and Supplementary Videos 1–3). Further desiccation of the Salton Sea in the future will continue to have a stabilizing effect on the SSAF, but potentially increase the stress to be released in a future event (or a sequence of events).

Our results demonstrate how improved palaeoseismic and palaeolake records, together with advanced models of hydrologic loading of a heterogeneous poroelastic crust, provide new insights into the relationship between water-level variations of ancient Lake Cahuilla and the past seven major earthquakes on the SSAF. We find that increases in lake level result in positive Coulomb stress changes on most of the SSAF, with stressing rates as high as two to three times the tectonic loading rate. Positive ΔCFS values are also seen on sections of the SSAF that are outside the lake owing to lateral diffusion of pore pressure along a permeable fault zone. This indicates that our model predictions are not strongly sensitive to uncertainties in the location of nucleation sites of past (as well as future) large events on the SSAF (see Supplementary Figs. 5–11 and Supplementary Videos 1–3). The pore-pressure 'memory effect' amplifies the contribution of successive lakes provided that intervals between inundations do not substantially exceed the characteristic diffusion time within the seismogenic layer. Our model may also be applicable to other areas in which seismogenic faults are subject to hydrologic loads from natural or anthropogenic sources[1,22,37].

Online content

Any methods, additional references, Nature Portfolio reporting summaries, source data, extended data, supplementary information, acknowledgements, peer review information; details of author contributions and competing interests; and statements of data and code availability are available at https://doi.org/10.1038/s41586-023-06058-9.

1. Talwani, P. On the nature of reservoir-induced seismicity. *Pure Appl. Geophys.* **150**, 473–492 (1997).
2. Tostrud, M. B. *The Salton Sea, 1906-1996, Computed and Measured Salinities and Water Levels*. Draft Report, Colorado River Board of California (1997).
3. Waters, M. R. Late Holocene lacustrine chronology and archaeology of ancient Lake Cahuilla, California. *Quat. Res.* **19**, 373–387 (1983).
4. Philibosian, B., Fumal, T. & Weldon, R. San Andreas fault earthquake chronology and Lake Cahuilla history at Coachella, California. *Bull. Seismol. Soc. Am.* **101**, 13–38 (2011).
5. Rockwell, T. K., Meltzner, A. J. & Haaker, E. C. Dates of the two most recent surface ruptures on the southernmost San Andreas fault recalculated by precise dating of Lake Cahuilla dry periods. *Bull. Seismol. Soc. Am.* **108**, 2634–2649 (2018).
6. Rockwell, T. K., Meltzner, A. J., Haaker, E. C. & Madugo, D. The late Holocene history of Lake Cahuilla: two thousand years of repeated fillings within the Salton Trough, Imperial Valley, California. *Quat. Sci. Rev.* **282**, 107456 (2022).
7. King, G. C. P., Stein, R. S. & Lin, J. Static stress changes and the triggering of earthquakes. *Bull. Seismol. Soc. Am.* **84**, 935–953 (1994).
8. Cocco, M. Pore pressure and poroelasticity effects in Coulomb stress analysis of earthquake interactions. *J. Geophys. Res. Solid Earth* **107**, 2030 (2002).
9. Rice, J. R. & Cleary, M. P. Some basic stress diffusion solutions for fluid-saturated elastic porous media with compressible constituents. *Rev. Geophys.* **14**, 227–241 (1976).
10. Wang, H. *Theory of Linear Poroelasticity: With Applications to Geomechanics and Hydrogeology* (Princeton Univ. Press, 2000).
11. LaBonte, A., Brown, K. & Fialko, Y. Hydrogeologic detection and finite-element modeling of a slow slip event in the Costa Rica prism toe. *J. Geophys. Res. Solid Earth* **114**, B00A02 (2009).
12. Segall, P. *Earthquake and Volcano Deformation* (Princeton Univ. Press, 2010).
13. Barbot, S. & Fialko, Y. A unified continuum representation of post-seismic relaxation mechanisms: semi-analytic models of afterslip, poroelastic rebound and viscoelastic flow. *Geophys. J. Int.* **182**, 1124–1140 (2010).
14. Fialko, Y. Interseismic strain accumulation and the earthquake potential on the southern San Andreas fault system. *Nature* **441**, 968–971 (2006).
15. Lin, G., Shearer, P. M. & Hauksson, E. Applying a three-dimensional velocity model, waveform cross correlation, and cluster analysis to locate southern California seismicity from 1981 to 2005. *J. Geophys. Res. Solid Earth* **112**, B12309 (2007).
16. Fuis, G. S., Scheirer, D. S., Langenheim, V. E. & Kohler, M. D. A new perspective on the geometry of the San Andreas fault in Southern California and its relationship to lithospheric structure. *Bull. Seismol. Soc. Am.* **102**, 236–251 (2012).
17. Lindsey, E. O. et al. Interseismic strain localization in the San Jacinto fault zone. *Pure Appl. Geophys.* **171**, 2937–2954 (2014).
18. Fialko, Y. et al. Deformation on nearby faults induced by the 1999 Hector Mine earthquake. *Science* **297**, 1858–1862 (2002).
19. Cochran, E. S. et al. Seismic and geodetic evidence for extensive, long-lived fault damage zones. *Geology* **37**, 315–318 (2009).
20. Caine, J. S., Evans, J. P. & Forster, C. B. Fault zone architecture and permeability structure. *Geology* **24**, 1025–1028 (1996).
21. Bense, V., Gleeson, T., Loveless, S., Bour, O. & Scibek, J. Fault zone hydrogeology. *Earth Sci. Rev.* **127**, 171–192 (2013).
22. Nof, R. et al. Rising of the lowest place on Earth due to Dead Sea water-level drop: evidence from SAR interferometry and GPS. *J. Geophys. Res. Solid Earth* **117**, B05412 (2012).
23. Gupta, H. K. *Reservoir Induced Earthquakes* (Elsevier, 1992).
24. Weldon, R. J., Fumal, T. E., Biasi, G. P. & Scharer, K. M. Past and future earthquakes on the San Andreas fault. *Science* **308**, 966–967 (2005).
25. Field, E. H. et al. Uniform California Earthquake Rupture Forecast, version 3 (UCERF3)—the time-independent model. *Bull. Seismol. Soc. Am.* **104**, 1122–1180 (2014).
26. Fumal, T. E. Timing of large earthquakes since AD 800 on the Mission Creek strand of the San Andreas fault zone at Thousand Palms Oasis, near Palm Springs, California. *Bull. Seismol. Soc. Am.* **92**, 2841–2860 (2002).
27. Gurrola, L. D. & Rockwell, T. K. Timing and slip for prehistoric earthquakes on the Superstition Mountain fault, Imperial Valley, southern California. *J. Geophys. Res. Solid Earth* **101**, 5977–5985 (1996).
28. Thomas, A. P. & Rockwell, T. K. A 300- to 550-year history of slip on the Imperial fault near the U.S.-Mexico border: missing slip at the Imperial fault bottleneck. *J. Geophys. Res. Solid Earth* **101**, 5987–5997 (1996).
29. Luttrell, K., Sandwell, D., Smith-Konter, B., Bills, B. & Bock, Y. Modulation of the earthquake cycle at the southern San Andreas fault by lake loading. *J. Geophys. Res. Solid Earth* **112**, B08411 (2007).
30. Brothers, D., Kilb, D., Luttrell, K., Driscoll, N. & Kent, G. Loading of the San Andreas fault by flood-induced rupture of faults beneath the Salton Sea. *Nat. Geosci.* **4**, 486–492 (2011).

31. Sieh, K. Slip rate across the San Andreas fault and prehistoric earthquakes at Indio, California. *Eos Trans. AGU* **67**, 1200 (1986).
32. Mueller, K. *Neotectonics, Alluvial History and Soil Chronology of the Southwestern Margin of the Sierra de Los Cucapas, Baja California Norte*. Master's thesis, San Diego State Univ. (1984).
33. Bronk Ramsey, C. Bayesian analysis of radiocarbon dates. *Radiocarbon* **51**, 337–360 (2009).
34. Reimer, P. J. et al. The IntCal20 Northern Hemisphere radiocarbon age calibration curve (0–55 cal kBP). *Radiocarbon* **62**, 725–757 (2020).
35. Roeloffs, E. Fault stability changes induced beneath a reservoir with cyclic variations in water level. *J. Geophys. Res. Solid Earth* **93**, 2107–2124 (1988).
36. Segall, P. Earthquakes triggered by fluid extraction. *Geology* **17**, 942–946 (1989).
37. Gupta, H. K. A review of recent studies of triggered earthquakes by artificial water reservoirs with special emphasis on earthquakes in Koyna, India. *Earth Sci. Rev.* **58**, 279–310 (2002).
38. Rajendran, K. & Talwani, P. The role of elastic, undrained, and drained responses in triggering earthquakes at Monticello Reservoir, South Carolina. *Bull. Seismol. Soc. Am.* **82**, 1867–1888 (1992).
39. Simpson, D., Leith, W. & Scholz, C. Two types of reservoir-induced seismicity. *Bull. Seismol. Soc. Am.* **78**, 2025–2040 (1988).
40. Tao, W., Masterlark, T., Shen, Z. & Ronchin, E. Impoundment of the Zipingpu reservoir and triggering of the 2008 M_w 7.9 Wenchuan earthquake, China. *J. Geophys. Res. Solid Earth* **120**, 7033–7047 (2015).
41. Mitchell, T. & Faulkner, D. The nature and origin of off-fault damage surrounding strike-slip fault zones with a wide range of displacements: a field study from the Atacama fault system, northern Chile. *J. Struct. Geol.* **31**, 802–816 (2009).
42. Dor, O., Ben-Zion, Y., Rockwell, T. & Brune, J. Pulverized rocks in the Mojave section of the San Andreas Fault Zone. *Earth Planet. Sci. Lett.* **245**, 642–654 (2006).
43. Rockwell, T. et al. Chemical and physical characteristics of pulverized Tejon Lookout granite adjacent to the San Andreas and Garlock faults: implications for earthquake physics. *Pure Appl. Geophys.* **166**, 1725–1746 (2009).
44. Morton, N., Girty, G. H. & Rockwell, T. K. Fault zone architecture of the San Jacinto fault zone in Horse Canyon, southern California: a model for focused post-seismic fluid flow and heat transfer in the shallow crust. *Earth Planet. Sci. Lett.* **329**, 71–83 (2012).
45. Rempe, M. et al. Damage and seismic velocity structure of pulverized rocks near the San Andreas Fault. *J. Geophys. Res. Solid Earth* **118**, 2813–2831 (2013).
46. Morrow, C., Lockner, D., Moore, D. & Hickman, S. Deep permeability of the San Andreas fault from San Andreas fault observatory at depth (SAFOD) core samples. *J. Struct. Geol.* **64**, 99–114 (2014).
47. Xue, L., Brodsky, E. E., Erskine, J., Fulton, P. M. & Carter, R. A permeability and compliance contrast measured hydrogeologically on the San Andreas Fault. *Geochem. Geophys. Geosyst.* **17**, 858–871 (2016).
48. USGS and California Geological Survey. *Quaternary Fault and Fold Database for the United States* (accessed 10 July 2019); https://www.usgs.gov/natural-hazards/earthquake-hazards/faults/.
49. Schulte Pelkum, V., Ross, Z. E., Mueller, K. & Ben Zion, Y. Tectonic inheritance with dipping faults and deformation fabric in the brittle and ductile southern California crust. *J. Geophys. Res. Solid Earth* **125**, e2020JB019525 (2020).
50. Goebel, T., Weingarten, M., Chen, X., Haffener, J. & Brodsky, E. The 2016 Mw5.1 Fairview, Oklahoma earthquakes: Evidence for long-range poroelastic triggering at >40 km from fluid disposal wells. *Earth Planet. Sci. Lett.* **472**, 50–61 (2017).
51. Verdecchia, A., Cochran, E. S. & Harrington, R. M. Fluid-earthquake and earthquake-earthquake interactions in Southern Kansas, USA. *J. Geophys. Res. Solid Earth* **126**, e2020JB020384 (2021).
52. Toda, S., Stein, R. S. & Sagiya, T. Evidence from the AD 2000 Izu islands earthquake swarm that stressing rate governs seismicity. *Nature* **419**, 58–61 (2002).
53. Qin, Y., Chen, T., Ma, X. & Chen, X. Forecasting induced seismicity in Oklahoma using machine learning methods. *Sci. Rep.* **12**, 9319 (2022).
54. Lindsey, E. & Fialko, Y. Geodetic slip rates in the southern San Andreas Fault system: effects of elastic heterogeneity and fault geometry. *J. Geophys. Res. Solid Earth* **118**, 689–697 (2013).
55. Blanton, C. M., Rockwell, T. K., Gontz, A. & Kelly, J. T. Refining the spatial and temporal signatures of creep and co-seismic slip along the southern San Andreas Fault using very high resolution UAS imagery and SfM-derived topography, Coachella Valley, California. *Geomorphology* **357**, 107064 (2020).
56. Jin, Z. & Fialko, Y. Finite slip models of the 2019 Ridgecrest earthquake sequence constrained by space geodetic data and aftershock locations. *Bull. Seismol. Soc. Am.* **110**, 1660–1679 (2020).
57. Eissa, E. & Kazi, A. Relation between static and dynamic Young's moduli of rocks. *Int. J. Rock Mech. Min. Geomech. Abstr.* **25**, 479–482 (1988).
58. Salditch, L. et al. Earthquake supercycles and long-term fault memory. *Tectonophysics* **774**, 228289 (2020).
59. Meltzner, A. J. & Wald, D. J. Aftershocks and triggered events of the great 1906 California earthquake. *Bull. Seismol. Soc. Am.* **93**, 2160–2186 (2003).

Publisher's note Springer Nature remains neutral with regard to jurisdictional claims in published maps and institutional affiliations.

Springer Nature or its licensor (e.g. a society or other partner) holds exclusive rights to this article under a publishing agreement with the author(s) or other rightsholder(s); author self-archiving of the accepted manuscript version of this article is solely governed by the terms of such publishing agreement and applicable law.

© The Author(s), under exclusive licence to Springer Nature Limited 2023

Methods

Calculation of the Coulomb stress changes

The change in ΔCFS is defined as[7,8,35]:

$$\Delta \mathrm{CFS} = \Delta\tau_s + \mu(\Delta\sigma_n + \Delta P) \quad (1)$$

in which $\Delta\tau_s$ is the change in shear stress, μ is the coefficient of friction, $\Delta\sigma_n$ is the change in normal stress (increases in compression are deemed negative) and ΔP is the change in pore-fluid pressure (increases in fluid pressure are deemed positive). The sign convention indicates that a positive change in the effective stress $\overline{\sigma_n} = \sigma_n + P$, as well as a positive change in shear stress $\Delta\tau_s$, promote failure. In this paper, we assume a typical value for static friction of $\mu = 0.6$ (refs. 60–63), although it may vary considerably depending on the rock type and ambient conditions[64–66]. The Coulomb stress changes ΔCFS are computed by resolving the normal and absolute shear-stress components using a full stress tensor, the prescribed fault geometry and sense of slip. Calculations were performed using the MATLAB toolbox Abaqus2Matlab[67].

Both the magnitude and the sign of the estimated ΔCFS is sensitive to several parameters in the context of poroelastic deformation, including: (1) the fault-zone permeability, width and connectivity to regions in which large seismic events nucleate. Higher permeability values allow for pore pressure to diffuse faster, increasing pore pressure and ΔCFS at depth[68,69]. A larger fault zone width and pore connectivity may also increase pore pressure and ΔCFS on the fault at greater depths[70]. (2) The fault dip angle[14,16], the varying geometry of the lake and the concomitant surface load[29]. The lake load produces regions of relative compression and extension within the seismogenic crust (Extended Data Fig. 6). Regardless of the fault attitude and sense of slip, increases in the fault-normal compressive stress are expected to inhibit failure and decreases in compressive stress are expected to promote failure. (3) The undrained pore-pressure effect, without which the total pore pressure will be underestimated[40,71] (Extended Data Fig. 6).

Fully coupled 3D finite-element models

The governing equations for a fully coupled linear poroelastic 3D medium are defined as[9,10,72]:

$$G\nabla^2 u_i + \frac{G}{1-2\nu}\frac{\partial^2 u_j}{\partial x_i \partial x_j} = \alpha\frac{\partial P}{\partial x_i} - F_i \quad (2)$$

$$\alpha\frac{\partial \epsilon_{ii}}{\partial t} + S_\epsilon\frac{\partial P}{\partial t} = \frac{k}{\mu}\nabla^2 P + Q \quad (3)$$

in which G is the shear modulus, u the displacement, υ the Poisson's ratio, α the Biot–Willis coefficient, F the body force, k the permeability, μ the fluid viscosity, S_ϵ the constrained specific storage, ϵ_{ii} the dilatancy (trace of the strain tensor), P the pore pressure and Q the fluid source[10]. Equations (2) and (3) are nearly identical to the classic equations for linear elasticity and diffusion of pore pressure, except for the coupling of pore pressure in the conservation of momentum equation (2) and the fluid flow coupled to strain by the requirement of fluid continuity equation (3). Analytic solutions to the system in equations (2) and (3) are restricted to a few highly idealized cases. We solve the respective equations numerically using the 3D finite-element software Abaqus SIMULIA[11,73].

As a preliminary cross-check, we considered a 1D analytic solution for a periodic fluctuation of a surface load in a poroelastic half-space[35] (see Methods). For a reasonable choice of model parameters, the analytic solution shows a cumulative increase in pore pressure at depth through several inundation events. This 'memory effect' is because of the fact that the maximum pore-pressure increase at depth is delayed owing to diffusion and does not completely vanish before the next flooding event. The timing of the superposition depends on the depth, permeability and wavelength of the lake load. One important caveat is that the memory effect only emerges when one considers several lake cycles.

To account for spatial heterogeneity and anisotropy of the hydraulic properties of the lake sediments, upper crust and the fault zone, we construct a 3D hydromechanical model based on parameters constrained by previous studies. Tompson et al.[74] developed and arranged the hydrostratigraphy of the Salton Trough sediments into three broad classes in order of increasing depth: Brawley, Palm Spring and Imperial formations. The composition of these formations vary from sandstones to shales, shaley sandstones, conglomeratic and arkosic sandstones (see Extended Data Table 2). The Salton Trough sediments directly overlie a basement formation and upper mantle layer. The elastic parameters of the basement formation are based on inference from seismic-wave velocities and hydrological parameters are based on crustal-depth dependencies, which produce material properties close to those of Westerly granite[10,75,76] (Extended Data Table 2). A crustal thickness of 18 km is assumed on the basis of seismic observations of the region[77]. We modelled the upper mantle both as an elastic (Supplementary Figs. 6 and 7) and a viscoelastic layer. The viscoelastic mantle is modelled similarly to previous studies as a simple linear Maxwell material[29,78–80]. We use a nonlinear geometry option in Abaqus (NLGEOM) based on the results of Hampel et al.[81], who recommended it for models involving isostatic effects[81].

The fault damage zone is modelled in accordance with field hydrogeologic estimates of San Andreas Fault permeability[47]. Xue et al.[47] estimated a relatively high permeability (10^{-14} m^2) constrained by borehole tidal responses using Earth tidal analysis compared with inferred permeability in the region and laboratory values[46,82,83]. We use this estimate of permeability as a high-end value and explore a range of fault-damage-zone permeabilities between the high-end value and permeability of the ambient crust (that is, no contrast in permeability between the fault-zone material and the host rocks; Extended Data Table 2). Therefore, we test the sensitivity of our model results to a range of fault permeabilities from $k = 10^{-14}$ m^2 (model 1) to values consistent with the intact crystalline basement $k = 10^{-18}$ m^2 (model 5)[76]. The fault permeability in model 1 is considered high when compared with other fault zones worldwide or laboratory measurements. Thus, our preferred model (model 2) uses $k = 10^{-15}$ m^2, which is more consistent with regional measurements and laboratory data[46,82,83]. Observations also show that the effective shear modulus of rocks within a fault zone may be lower than that of the host rock by as much as a factor of 2 (refs. 17–19,84). In our model, the shear modulus of rocks in the fault zone is taken to be a factor of 2 smaller than the shear modulus of the host rocks (Extended Data Table 2).

The numerical domain was developed and discretized in Abaqus CAE[73]. The numerical domain has horizontal dimensions 600 km × 600 km and a depth of 50 km, with the y axis corresponding to north for the Universal Transverse Mercator 11N zone (Extended Data Fig. 2). The finite-element mesh consists of nearly 2 million first-order linear tetrahedral elements. Characteristic element sizes vary from 30,000 m in the far field to less than 100 m on the fault and lake edges. The SSAF fault trace is based on the USGS Quaternary fault database[48]. We model a 60° northeast dip for the SSAF, which is consistent with geodetic slip models, seismicity and seismic tomography data[49,54]. We consider a 200-m-wide damage zone centred on the SSAF slip interface[19,46,84]. The lake shoreline is based on coordinates used by Luttrell et al.[29] and a similar assumption in lake depth (97.2 m) across the entire lake footprint to maintain consistency in model comparisons[5,29]. Models that considered spatially variable lake depth used the SRTM digital elevation model[85] and bathymetry of the Salton Sea to assign the vertical stress and pressure boundary conditions at the nodes within the lake boundaries.

The evolution of the poroelastic effects requires a careful consideration of the model boundary and initial conditions. We assume initial

conditions of equilibrium stress and pore pressure (chapter 9 in ref. 12). These conditions imply that the model only considers the effect of the lake and does not include any loading from tectonic stress. Gravity is included, with stress and pore pressure calculated as relative change from geostatic equilibrium. This is an important consideration, as neglecting gravity in the viscoelastic model may overestimate surface displacements on timescales that exceed the characteristic relaxation time[13,86]. The bottom and sides of the model are fixed in the surface-normal direction and free of shear stress (a 'roller' condition). The bottom of the poroelastic domain is considered to be insulated (zero-flux boundary condition), whereas the sides and top of the model are considered to be permeable and subject to vanishing pore pressure ($P = 0$). The top surface of the model is stress-free outside the lake area. The lake extent is the only boundary condition that varies over time.

Tectonic loading

We approximate the secular tectonic loading using a model of a screw dislocation in an elastic half-space[87] (see equation (2.25) in ref. 12). The respective interseismic shear strain rate is given by:

$$\dot{\epsilon}_{13} = \frac{-\dot{s}}{4\pi}\left[\frac{x_2 - d_2}{(x_2 - d_2)^2 + x_1^2} - \frac{x_2 + d_2}{(x_2 + d_2)^2 + x_1^2}\right] \quad (4)$$

in which $\dot{s}$ is the fault slip rate (taken to be 18 mm year^{-1} (ref. 54)), x_1 is the horizontal coordinate with respect to the centre of the fault damage zone, x_2 is the assumed depth of nucleation of large events and $d = 10$ km is the estimated locking depth of the SSAF[54,88].

For typical values of the shear modulus of the upper crust $G = 28–32$ GPa (ref. 54), the stressing rate predicted by equation (4) at the bottom of the seismogenic zone ($x_2 = 6–8$ km) is $\dot{\sigma}_{13} = 2G(\dot{\epsilon}_{13}) = 25 - 51$ kPa year^{-1}. However, the distribution of stressing rates throughout the seismogenic layer depends on details of a transition between the locked and creeping parts of the fault (for example, ref. 89), as well as the degree of strain localization below the brittle–ductile transition (for example, ref. 90). A dislocation model overpredicts the stressing rate, especially at the bottom of the seismogenic zone, owing to a strong stress singularity. Also, the depth distribution of earthquakes in California shows that most earthquakes nucleate at depths of 3–4 km (ref. 56). Therefore, we use the stressing rate at the free surface ($x_2 = 0$), $\dot{\sigma}_{13} \approx 16$ kPa year^{-1}, as a conservative lower bound for the entire seismogenic layer.

San Andreas Fault, Coachella site earthquake history

The Coachella palaeoseismic site (33.72722° N, 116.16976° W) trenches provide evidence of six or seven lake phases and five to seven earthquakes on the SSAF over the past millenium[6]. Four types of stratigraphy have been identified at the Coachella site: lake clay/silt, recessional sand, aeolian sand and fluvial alluvium. The distinction between aeolian sand and recessional sand may be difficult, as the aeolian sand can be derived entirely from the recessional and shoreline sand deposits. See Fig. 5 in Philibosian et al.[4] for a generalized view of the stratigraphic section and brief descriptions of each unit.

An 'organic-rich layer' is described near the top of unit 1L, which is markedly similar to other organic mats from near-shoreline sites that are interpreted as the debris that accumulates near the shoreline from the inundation of the lake basin. Unit 1L is described as a massive silt layer of lacustrine origin. An alternative interpretation is that unit 1L represents deltaic sedimentation during flooding of the site. In either case, 1L and 1S collectively represent regional lake A at the Coachella site[6] (see their supplementary materials). The most recent event occurred during the highstand of Lake Cahuilla in 1726 ± 7 CE (refs. 5,31).

The penultimate lake earthquake, Coa-2, clearly occurs during deposition of unit 2L, which represents the lacustrine phase of lake B, based on extensive liquefaction (only possible with water present) and upward fault terminations[4,6]. That places Coa-2 to have occurred during lake B.

Coa-3 was interpreted to have occurred during lake C based on weak evidence of sediment (unit 3L) filling a structural trough. Coa-4 was interpreted as occurring before lake C but between two organic layers in unit 4S. However, the reinterpretation is that these organic layers were deposited during the rising stages of lake C along with fine sand deposits (probably of deltaic origin), implying that Coa-4 occurred during the early phase of lake C and that the structural trough formed by Coa-4 was filled by the same lake phase, lake C (ref. 6). Belle Philibosian agrees with this reinterpretation (Rockwell, personal communication, 2022). This means that the evidence for Coa-3 and Coa-4 are the same and that there was only one rupture, which occurred during the filling phase of lake C, but when the water had essentially reached the highstand shoreline (as the Coachella site lies at 9 m, only 4 m below the highstand).

Coa-5 was interpreted by Philibosian et al. as having occurred between the deposition of units 5S and 4L, with the units 5S and 5L folded and capped by undeformed unit 4L (ref. 4). Rockwell et al. interpret the organic unit at the top of unit 5S to represent the inundation and accumulation of organics associated with the drowning phase of lake D (ref. 6). Coa-5 deforms the organic layer along with the underlying lake deposits, implying that the earthquake occurred after its deposition during the rising stages of lake D. Supporting this interpretation, the strata of units 5L and 5S are plastically deformed, which—in this arid environment—almost certainly required the presence of water, which will only be present during a lake stand. Hence, Coa-5 is interpreted to have occurred during lake D and probably during the late filling stage, as the event is capped by fine-grained deposition associated with the highstand of lake D.

Coa-6 is interpreted to have occurred during deposition of unit 5L (lake E) based on apparent upward terminations and a possible colluvial wedge of material derived from unit 5L. This evidence was considered weak, but the presented images look convincing, so we confirm the occurrence of a rupture during the highstand of lake E.

Event Coa-7 is interpreted to have occurred between units 6S and 5L based on upward terminations and displaced strata capped by undeformed strata. This would potentially place this earthquake to between lakes E and F, as there is no evidence of the presence of water at that time (no documented liquefaction).

A seventh event, Coa8+, is interpreted to have occurred in unit 7S, which Philibosian et al. describe as "coarse sand, gravel, and rounded cobbles form cross-cutting channel deposits", which are obviously fluvial in origin[4]. Unit 7L is bedded fine sand and is only exposed at the very base of the section. It is interpreted by Philibosian et al. as 'likely lacustrine' but a lake affiliation is not clearly demonstrated. An alternative interpretation is that unit 7L is a deltaic section that was buried by a large fluvial flood event (not a lake-filling flood event) during rising lake level. The rationale for this is that unit 7S is several metres thick and dating a charcoal sample from unit 7S returned an age of 1185 ± 30 RCYBP (radiocarbon years before present; sample Sb4m14A-c), which is consistent with lake F or the dry period immediately preceding lake F and not the much older lake G.

Furthermore, the unit does not show the oxidation that is characteristic for sediments of unit G, which were exposed at the surface for nearly a thousand years. Hence, we interpret the charcoal date as indicating that 7L may actually be the lower part of lake F (deltaic rising lake phase). If correct, an earthquake occurred during the early depositional phase of lake F, followed by a large depositional event and then more lacustrine sediments. The well-sorted sand of the base of unit 7S seems to extend down through unit 7L and may represent a feeder pipe, with the lowest part of unit 7S possibly a liquefaction deposit.

Periodic loading of a poroelastic half-space

As a preliminary, we consider an analytical solution for a periodic fluctuation of water level over a poroelastic half-space[35]. For a half-space extending in the positive direction of the z (vertical) axis from $z = 0$ to $z = \infty$ with a periodic water load of amplitude p_s at the surface given as both vertical stress and pore-pressure boundary conditions $\sigma_{zz}(z = 0, t) = -p(z = 0, t) = p_s \exp(iwt)$ leads to the following solution[10]:

$$\bar{p}_z = \gamma p_s + (1 - \gamma) p_s \exp\left(-z\sqrt{(w/2c)}\right) \exp\left(-\mathrm{i}z\sqrt{(w/2c)}\right) \quad (5)$$

in which $\gamma = \frac{B(1+\upsilon_u)}{3(1-\upsilon_u)}$ is the loading efficiency and c is the diffusivity. If we assume incompressible grains and fluid ($\gamma = 1$), then the response is entirely the vertical stress associated with water load and constant at all depths (undrained response) (Extended Data Fig. 6). The other endmember ($\gamma = 0$) assumes that the pore pressure is uncoupled from the applied stress and is given by the pore-pressure-diffusion solution (drained response)[10,91] (equation (5)) (Extended Data Fig. 6). Moreover, equation (5) is linear with respect to p_s. If $p(0, t)$ is known, the solution for $p(z, t)$ may be parameterized in the frequency domain with the Green's function that carries a pressure disturbance for frequency w at $z = 0$ to $z > 0$:

$$p(z, t) = \int G(z, w) H(w) \mathrm{e}^{-\mathrm{i}wt} \mathrm{d}w \quad (6)$$

in which

$$G(z, w) = \gamma + (1 - \gamma) \exp\left(-z\sqrt{w/2c}\right) \exp\left(-\mathrm{i}z\sqrt{w/2c}\right)$$

and $H(w)$ is the Fourier transform of the surface ($z = 0$) history of the pressure:

$$p(0, t) = \int H(w) \mathrm{e}^{-\mathrm{i}wt} \mathrm{d}w$$

Therefore, if we know the lake-loading history at the surface, $p(0, t)$, we can simply take its Fourier transform, multiply this pore-pressure distribution with the Green's function (equation (6)) in the frequency domain and take the inverse Fourier transform of the product to arrive at the solution to the pore-pressure distribution for all depths and times (Extended Data Fig. 4).

Given a quasi-periodic lake-loading history[6], the distribution of pore pressure shows an interesting effect. Although the shape of the pore-pressure distribution beyond the Earth's surface is entirely dependent on the poroelastic constants in equation (5), for reasonable values of poroelastic constants of rocks comprising the upper crust (Extended Data Table 2), the high frequency of the surface lake levels show a gradual increase of pore-pressure magnitude. This effect would not be present in a 'single-lake' simulation, as the amplitude of the maximum P would just decay exponentially. Instead, with several lakes, the 'memory' pore-pressure effect is the result of a superposition of each independent Fourier component of $p(0, t)$. For example, the diffusive (drained) component of the poroelastic response of lake F (Supplementary Fig. 5) lags its surface response at depth. This is readily observed at greater depth (9 km), at which essentially only the instantaneous (undrained) response to the surface load is felt through the entire load of a single lake cycle. Consequently, the lag of the maximum (drained) response of pore pressure can coincide with the maximum (undrained) response of pore pressure for subsequent lakes, thus leading to larger pore pressures compared with a single-lake response. Therefore, with several lakes, there is an inherent temporal dependence of the maximum pore pressure. A point in our finite-element model (model 2) below the lake at a depth of 7.2 km that lies within our fault is more coincident to the 1D model at shallower 1 km depth (Extended Data Fig. 5). This 1D solution serves to conceptualize the important delayed memory effects of variable pore pressure. Although the analytical 1D solution is a useful first-order approximation, especially for locations directly below the lake, it fails to account for other potentially important factors affecting stress on the fault, such as crustal heterogeneities, viscoelastic relaxation and lateral pore-fluid diffusion.

Data availability

The Abaqus data files, Lake Cahuilla and Salton Sea data files and processed model results are available on Zenodo (http://doi.org/10.5281/zenodo.7714217). Source data are provided with this paper.

Code availability

All relevant MATLAB post-processing codes and sample-plotting codes are available on Zenodo (http://doi.org/10.5281/zenodo.7714217).

60. Byerlee, J. Friction of rock. *Pure Appl. Geophys.* **116**, 615–626 (1978).
61. Sibson, R. H. An assessment of field evidence for 'Byerlee' friction. *Pure Appl. Geophys.* **142**, 645–662 (1994).
62. Fialko, Y. & Jin, Z. Simple shear origin of the cross-faults ruptured in the 2019 Ridgecrest earthquake sequence. *Nat. Geosci.* **14**, 513–518 (2021).
63. Fialko, Y. Estimation of absolute stress in the hypocentral region of the 2019 Ridgecrest, California, earthquakes. *J. Geophys. Res. Solid Earth* **126**, e2021JB022000 (2021).
64. Lockner, D. A., Morrow, C., Moore, D. & Hickman, S. Low strength of deep San Andreas fault gouge from SAFOD core. *Nature* **472**, 82–85 (2011).
65. Mitchell, E., Fialko, Y. & Brown, K. M. Temperature dependence of frictional healing of Westerly granite: experimental observations and numerical simulations. *Geochem. Geophys. Geosyst.* **14**, 567–582 (2013).
66. Mitchell, E., Fialko, Y. & Brown, K. Frictional properties of gabbro at conditions corresponding to slow slip events in subduction zones. *Geochem. Geophys. Geosyst.* **16**, 4006–4020 (2015).
67. Papazafeiropoulos, G., Muñiz-Calvente, M. & Martínez-Pañeda, E. Abaqus2Matlab: a suitable tool for finite element post-processing. *Adv. Eng. Softw.* **105**, 9–16 (2017).
68. Durham, W. B. Laboratory observations of the hydraulic behavior of a permeable fracture from 3800 m depth in the KTB pilot hole. *J. Geophys. Res. Solid Earth* **102**, 18405–18416 (1997).
69. Miller, S. A. The role of fluids in tectonic and earthquake processes. *Adv. Geophys.* **54**, 1–46 (2013).
70. Chang, K. W. & Segall, P. Injection-induced seismicity on basement faults including poroelastic stressing. *J. Geophys. Res. Solid Earth* **121**, 2708–2726 (2016).
71. Ge, S. Comment on "Evidence that the 2008 Mw 7.9 Wenchuan earthquake could not have been induced by the Zipingpu Reservoir" by Kai Deng, Shiyong Zhou, Rui Wang, Russell Robinson, Cuiping Zhao, and Wanzheng Cheng. *Bull. Seismol. Soc. Am.* **101**, 3117–3118 (2011).
72. Biot, M. A. General theory of three dimensional consolidation. *J. Appl. Phys.* **12**, 155–164 (1941).
73. Dassault Systèmes. *Abaqus 2019* (Dassault Systèmes, 2019, 2020).
74. Tompson, A. et al. *Groundwater Availability Within the Salton Sea Basin Final Report* (Lawrence Livermore National Laboratory, 2008).
75. Allam, A. A. & Ben-Zion, Y. Seismic velocity structures in the southern California plate-boundary environment from double-difference tomography. *Geophys. J. Int.* **190**, 1181–1196 (2012).
76. Shmonov, V., Vitiovtova, V., Zharikov, A. & Grafchikov, A. Permeability of the continental crust: implications of experimental data. *J. Geochem. Explor.* **78-79**, 697–699 (2003).
77. Richards-Dinger, K. B. & Shearer, P. M. Estimating crustal thickness in southern California by stacking *PmP* arrivals. *J. Geophys. Res. Solid Earth* **102**, 15211–15224 (1997).
78. Lundgren, P. E., Hetland, A., Liu, Z. & Fielding, E. J. Southern San Andreas-San Jacinto fault system slip rates estimated from earthquake cycle models constrained by GPS and interferometric synthetic aperture radar observations. *J. Geophys. Res. Solid Earth* **114**, B02403 (2009).
79. Pearse, J. & Fialko, Y. Mechanics of active magmatic intraplating in the Rio Grande Rift near Socorro, New Mexico. *J. Geophys. Res. Solid Earth* **115**, B07413 (2010).
80. Johnson, K. Slip rates and off-fault deformation in Southern California inferred from GPS data and models. *J. Geophys. Res. Solid Earth* **118**, 5643–5664 (2013).
81. Hampel, A., Lüke, J., Krause, T. & Hetzel, R. Finite-element modelling of glacial isostatic adjustment (GIA): use of elastic foundations at material boundaries versus the geometrically non-linear formulation. *Comput. Geosci.* **122**, 1–14 (2019).
82. Brace, W. F. Permeability of crystalline and argillaceous rocks. *Int. J. Rock Mech. Min. Sci. Geomech. Abstr.* **17**, 241–251 (1980).
83. Ross, Z. E., Cochran, E. S., Trugman, D. T. & Smith, J. D. 3D fault architecture controls the dynamism of earthquake swarms. *Science* **368**, 1357–1361 (2020).
84. Jeppson, T. N., Bradbury, K. K. & Evans, J. P. Geophysical properties within the San Andreas Fault Zone at the San Andreas Fault Observatory at Depth and their relationships to rock properties and fault zone structure. *J. Geophys. Res. Solid Earth* **115**, B12423 (2010).
85. Farr, T. & Kobrick, M. Shuttle Radar Topography Mission produces a wealth of data. *Eos* **81**, 583–585 (2000).
86. Pollitz, F. F. & Sacks, I. S. The 1995 Kobe, Japan, earthquake: a long-delayed aftershock of the offshore 1944 Tonankai and 1946 Nankaido earthquakes. *Bull. Seismol. Soc. Am.* **87**, 1–10 (1997).
87. Savage, J. & Burford, R. Geodetic determination of relative plate motion in central California. *J. Geophys. Res.* **78**, 832–845 (1973).

88. Lin, G., Shearer, P. M. & Hauksson, E. Applying a three-dimensional velocity model, waveform cross correlation, and cluster analysis to locate southern California seismicity from 1981 to 2005. *J. Geophys. Res. Solid Earth* **112**, B12309 (2007).
89. Lindsey, E. O. & Fialko, Y. Geodetic constraints on frictional properties and earthquake hazard in the Imperial Valley, Southern California. *J. Geophys. Res. Solid Earth* **121**, 1097–1113 (2016).
90. Takeuchi, C. & Fialko, Y. Dynamic models of interseismic deformation and stress transfer from plate motion to continental transform faults. *J. Geophys. Res. Solid Earth* **117**, B05403 (2012).
91. Turcotte, D. L. & Schubert, G. *Geodynamics* 2nd edn (Cambridge Univ. Press, 2002).

Acknowledgements This work was supported by the Southern California Earthquake Center (grant 21091) to M.W. and NSF (EAR-1841273), NASA (80NSSC22K0506) and USGS (G20AP00051) to Y.F. This research benefited from correspondence with R. Guyer. This project used Quaternary fault data from the USGS. We acknowledge use of the CSRC high-performance computing cluster at San Diego State University.

Author contributions R.G.H. constructed the finite-element model, performed analysis of the model results and wrote the manuscript. M.W. managed the study, assisted with building the model, provided access to the modelling software, acquired funding, helped conceive the experiment and commented on the manuscript. T.K.R. carried out the palaeoseismic analysis, conceived the experiment and contributed to the manuscript. Y.F. provided advice on modelling and interpretation of the model results and contributed to the manuscript.

Competing interests The authors declare no competing interests.

Additional information

Supplementary information The online version contains supplementary material available at https://doi.org/10.1038/s41586-023-06058-9.

Correspondence and requests for materials should be addressed to Ryley G. Hill.

Peer review information *Nature* thanks the anonymous reviewers for their contribution to the peer review of this work. Peer reviewer reports are available.

Reprints and permissions information is available at http://www.nature.com/reprints.

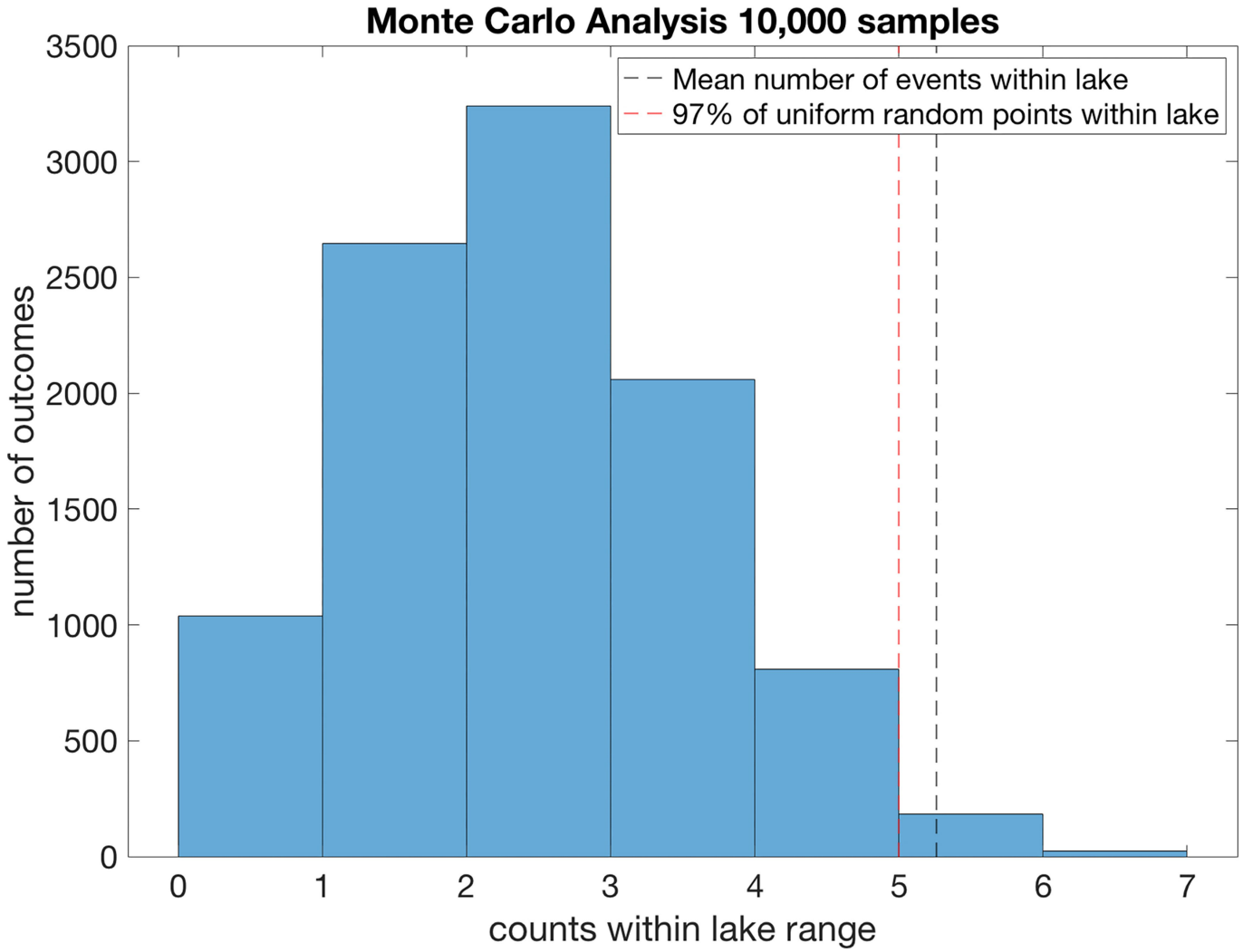

Extended Data Fig. 1 | Monte Carlo statistical test of the lake and earthquake timings. Results of Monte Carlo statistical testing (10,000 samples) based on sampling earthquake PDF distributions and lake timings. After sampling the earthquake PDFs, we determine how many fall inside the lake timings when the lake was greater than 70% full. We compare these timings to a uniform random distribution of seven times across the same lake-loading-time range. We find that the mean timings that occur within lakes is >97% of the earthquake timings of a uniform random distribution that occur within lakes.

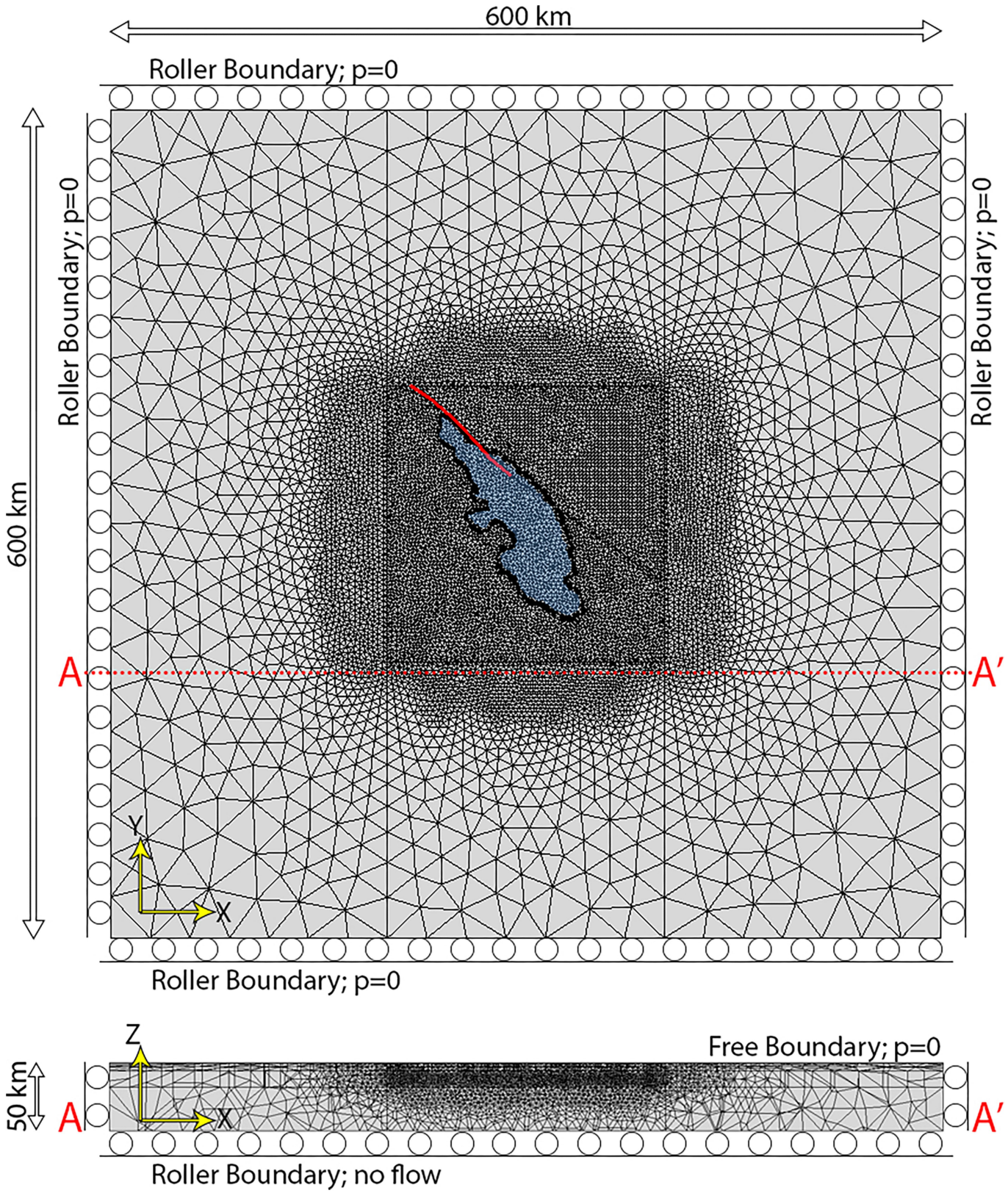

Extended Data Fig. 2 | Numerical domain. 3D finite-element method model domain. The model mesh contains about 2 million tetrahedron elements. The light blue colour represents the extent of ancient Lake Cahuilla. The prescribed vertical load is hydrostatic, to the lake maximum water head (97.2 m). The solid red line is the SSAF fault trace. The fault zone is modelled as a slab dipping to the northeast at 60° (ref. 54), with the assumed thickness of 200 m (refs. 19,46,84).

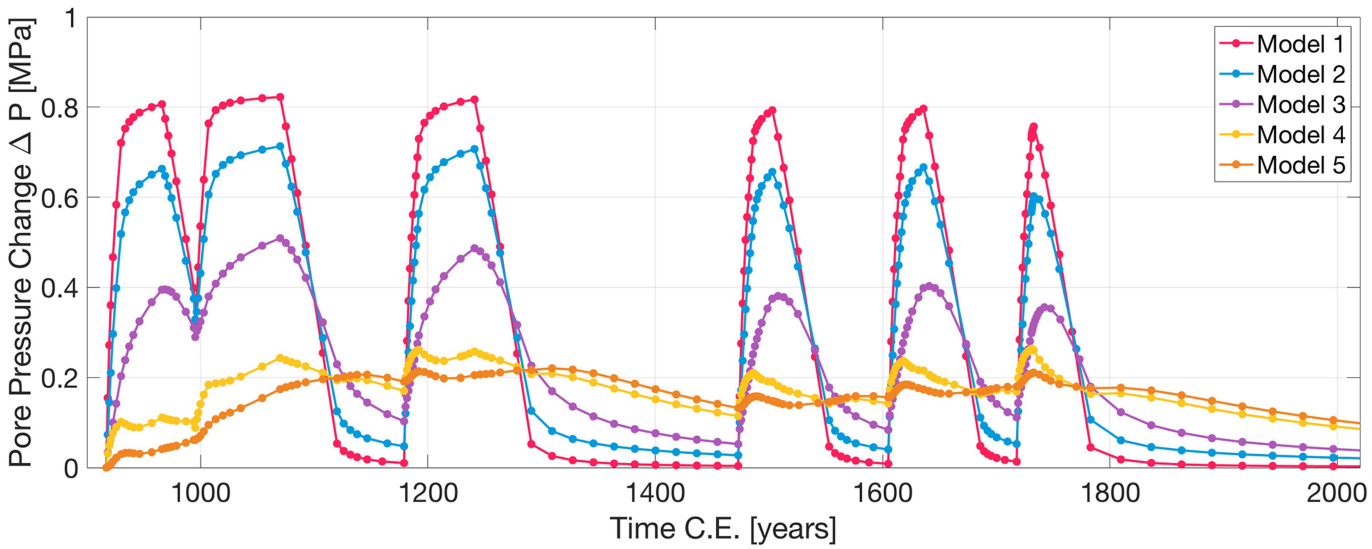

Extended Data Fig. 3 | Pore-pressure effects of lake loading. Pore pressure (MPa) on the SSAF as a function of time (year CE) at 7 km depth for location 21, a point on the fault near the centre of the lake (see Supplementary Fig. 5). Each model is based on the variable fault permeability, with model 1 as the most permeable and model 5 as the no damage zone (Extended Data Table 2).

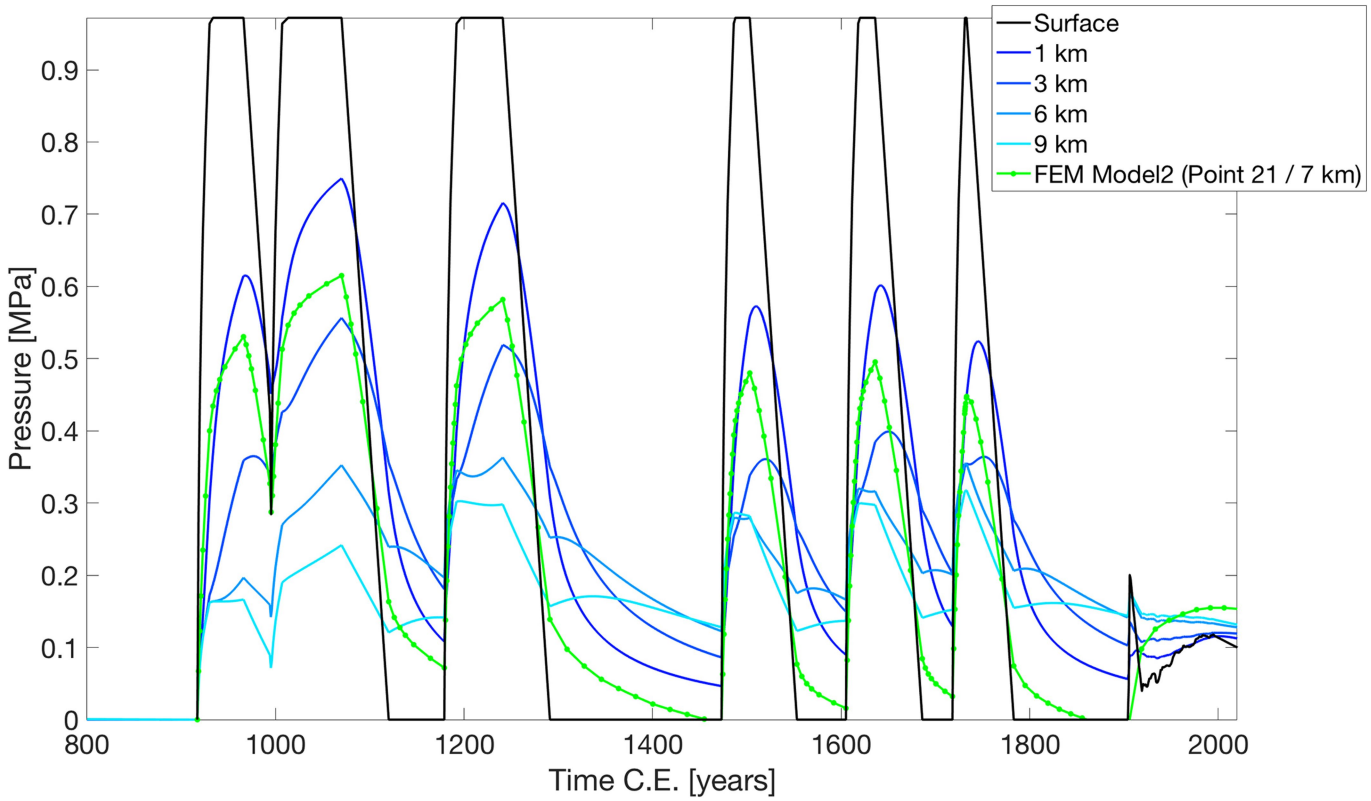

Extended Data Fig. 4 | Analytic solution for periodic loading of a poroelastic half-space. 1D analytical model of pore pressure for a variety of different depths (blue) with surface lake-level pore pressure (black). The smaller surface profile from 1905 to the present is the Salton Sea[2]. Finite-element method model 2 at 7.2 km depth (green line) shows the effect of 3D diffusion with a high-permeability fault damage zone embedded in a lower-permeability host rock. The finite-element method model at 7.2 km resembles pore pressure in the 1D analytical case at 1 km, demonstrating how a fault damage zone can transmit pore pressure to depth effectively. $\gamma = 0.1685$; $k_{fault} = 1e^{-15}$ (m^2); $k_{host/1Dmodel} = 1e^{-18}$ (m^2).

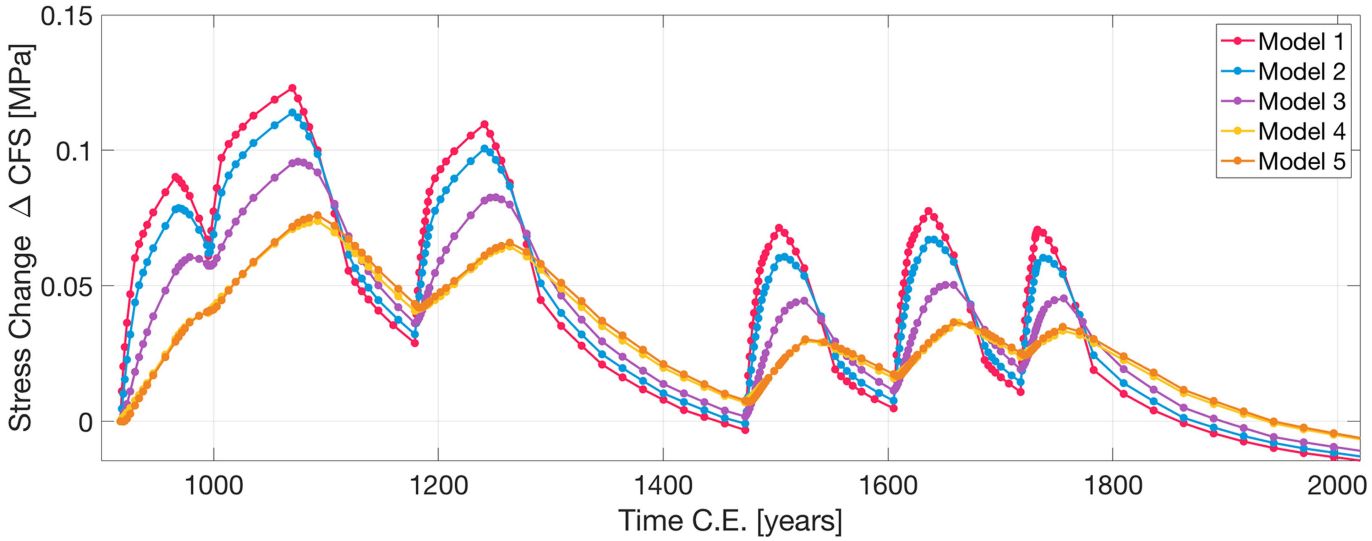

Extended Data Fig. 5 | Stress effects of lake loading. Similar to Fig. 4a but for a point farther away from the lake centre (point 24 in Supplementary Fig. 5).

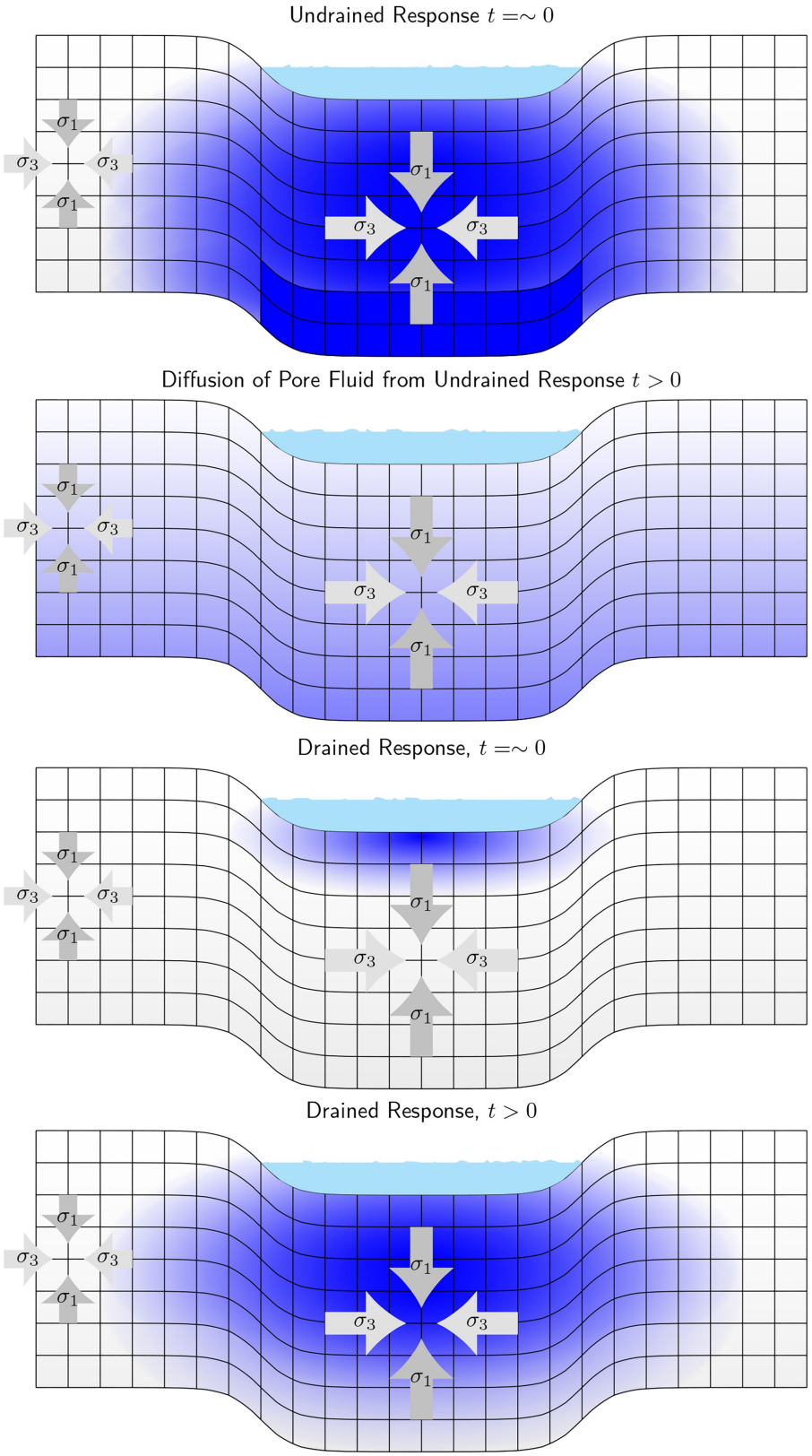

Extended Data Fig. 6 | Conceptual model of the undrained and drained effects from a lake load. The instantaneous and transient effects of the undrained and drained effects. At $t = 0$, the undrained effect is felt almost instantaneously throughout the poroelastic medium beneath the lake. As time progresses, this effect attempts to equilibrate at depth. At $t = 0$, the drained effect is not felt except for the surface poroelastic medium and the bottom of the lake. As time progresses, this effect increases pore pressure as diffusion drives fluid from the surface down. Furthermore, as the lake load is applied, areas of compression form immediately beneath the lake, whereas areas of extension are formed near the edges.

Extended Data Table 1 | Earthquake dates

Earthquake	Year	95% Confidence Range
Coa-1	1730	1721-1731
Coa-2	1610	1586-1636
Coa-3/4	1480	1459-1503
Coa-5	1200	1165-1244
Coa-6	1020	995-1040
Coa-7	970	923-1022
Coa-8	930	905-961

Best estimates (to the nearest decade) and 95% confidence ranges of earthquake dates from the OxCal model.

Extended Data Table 2 | Material properties

Hydrostratigraphy Unit	Post Brawley / Brawley	Palm Springs / Borrego	Imperial	Crystalline Basement	Mantle*	Fault Zone
Depth Range [km]	0-0.5	0.5-3	3-7	7-18	18-50	0-18
Poisson's Ratio	0.25	0.25	0.25	0.25	0.36	0.25
Young's Modulus [GPa]	50	50	50	58.4	140	1/2 host rock
Permeability [m^2]	$2{\cdot}10^{-13}$	$1.2{\cdot}10^{-12}$	$9{\cdot}10^{-14}$	10^{-18}	/	10^{-14},10^{-15},10^{-16},10^{-17}
Bulk Modulus of Solid Grains [GPa]	33	33	33	39	/	host rock
Reference	(74)	(74)	(74)	(76)	(91)	(18,54)

*The mantle is modelled as a simple linear viscoelastic material with 3×10^{19} Pa s viscosity[29]. Bulk modulus of permeating fluid (water) is assumed to equal 2.2×10^{9} Pa. Several simulations were performed to evaluate the model sensitivity to the assumed parameters. Models 1–4 considered the effect of fault-zone permeability for the assumed permeability values 10^{-14}, 10^{-15}, 10^{-16} and 10^{-17} m^2, respectively. Model 5 corresponds to a case of no damage zone (permeability and Young's modulus are the same as those of the host rock). Model 2a uses the same material properties as model 2 but assumes a spatially variable surface load controlled by a local bathymetry.

AGU PUBLICATIONS

Geochemistry, Geophysics, Geosystems

RESEARCH ARTICLE
10.1002/2015GC005714

Episodic Holocene eruption of the Salton Buttes rhyolites, California, from paleomagnetic, U-Th, and Ar/Ar dating

Heather M. Wright[1], Jorge A. Vazquez[2], Duane E. Champion[2], Andrew T. Calvert[2], Margaret T. Mangan[2], Mark Stelten[2,3], Kari M. Cooper[3], Charles Herzig[4], and Alexander Schriener Jr.[5]

[1]U.S. Geological Survey, Cascades Volcano Observatory, Vancouver, Washington, USA, [2]U.S. Geological Survey, Volcano Science Center, Menlo Park, California, USA, [3]Department of Earth and Planetary Sciences, University of California-Davis, Davis, California, USA, [4]Department of Earth Sciences, El Camino Community College, Torrance, California, USA, [5]CalEnergy Operating Corporation, Calipatria, California, USA

Abstract In the Salton Trough, CA, five rhyolite domes form the Salton Buttes: Mullet Island, Obsidian Butte, Rock Hill, North and South Red Hill, from oldest to youngest. Results presented here include $^{40}Ar/^{39}Ar$ anorthoclase ages, ^{238}U-^{230}Th zircon crystallization ages, and comparison of remanent paleomagnetic directions with the secular variation curve, which indicate that all domes are Holocene. ^{238}U-^{230}Th zircon crystallization ages are more precise than but within uncertainty of $^{40}Ar/^{39}Ar$ anorthoclase ages, suggesting that zircon crystallization proceeded until shortly before eruption in all cases except one. Remanent paleomagnetic directions require three eruption periods: (1) Mullet Island, (2) Obsidian Butte, and (3) Rock Hill, North Red Hill, and South Red Hill. Borehole cuttings logs document up to two shallow tephra layers. North and South Red Hills likely erupted within 100 years of each other, with a combined ^{238}U-^{230}Th zircon isochron age of: 2.83 $\pm$ 0.60 ka (2 sigma); paleomagnetic evidence suggests this age predates eruption by hundreds of years (1800 cal BP). Rock Hill erupted closely in time to these eruptions. The Obsidian Butte ^{238}U-^{230}Th isochron age (2.86 $\pm$ 0.96 ka) is nearly identical to the combined Red Hill age, but its Virtual Geomagnetic Pole position suggests a slightly older age. The age of aphyric Mullet Island dome is the least well constrained: zircon crystals are resorbed and the paleomagnetic direction is most distinct; possible Mullet Island ages include ca. 2300, 5900, 6900, and 7700 cal BP. Our results constrain the duration of Salton Buttes volcanism to between ca. 5900 and 500 years.

Key Points:
- Five rhyolite obsidian domes form the Salton Buttes, CA
- We use Ar/Ar, U-Th, and paleomagnetism to date all five domes
- All domes are mid-late Holocene in age, erupted in three separate episodes

Supporting Information:
- Supporting Information S1
- Table S1
- Table S2
- Table S3

Correspondence to:
H. M. Wright,
hwright@usgs.gov

Citation:
Wright, H. M., J. A. Vazquez, D. E. Champion, A. T. Calvert, M. T. Mangan, M. Stelten, K. M. Cooper, C. Herzig, and A. Schriener Jr. (2015), Episodic Holocene eruption of the Salton Buttes rhyolites, California, from paleomagnetic, U-Th, and Ar/Ar dating, *Geochem. Geophys. Geosyst.*, *16*, 1198–1210, doi:10.1002/2015GC005714.

Received 2 JAN 2015
Accepted 12 MAR 2015
Accepted article online 20 MAR 2015
Published online 30 APR 2015

© 2015. American Geophysical Union. All Rights Reserved.

1. Introduction

Age determination of Holocene volcanic rocks is inherently difficult, especially where carbon that could be used for ^{14}C dating is not present or the relation of the organic material to the eruption is difficult to establish [e.g., *Schmitt et al*., 2010a; cf. *Capra et al*., 2007]. At monogenetic volcanic fields, where there is only one phase of eruptive activity at each center, eruptive deposits from all centers likely do not form a single stratigraphic section. Thus, detailed mapping is required in order to resolve relative age relationships, if at all possible. Indeed, the use of a variety of dating techniques in combination with geologic mapping may be required in order to resolve the eruptive chronology at monogenetic volcanic fields in general [*Connor and Conway*, 2000]. Apart from ^{14}C dating, radioisotope dating of Holocene rocks is challenging due to small accumulated quantities of radioactive decay daughters, but analytical advances and high-resolution sampling techniques yield meaningful dates for late Pleistocene-Holocene eruptions [e.g., *Lanphere et al*., 2007; *Vazquez and Lidzbarski*, 2012]. In cases where uncertainties are large, paleomagnetic directions of primary volcanic deposits can be used to refine age determinations [*Hagstrum and Champion*, 2002]. Here we use the results from multiple dating techniques to resolve the timing and episodicity of rhyolitic volcanism that generated the five obsidian domes that compose the Salton Buttes, southern California, and scrutinize the advantages and shortfalls of each geochronologic technique.

2. Salton Trough Magmatism

The Salton Buttes consist of five rhyolitic obsidian domes located at the southern margin of the Salton Sea, California, USA. The domes are aligned subparallel to the axis of spreading along the boundary between the

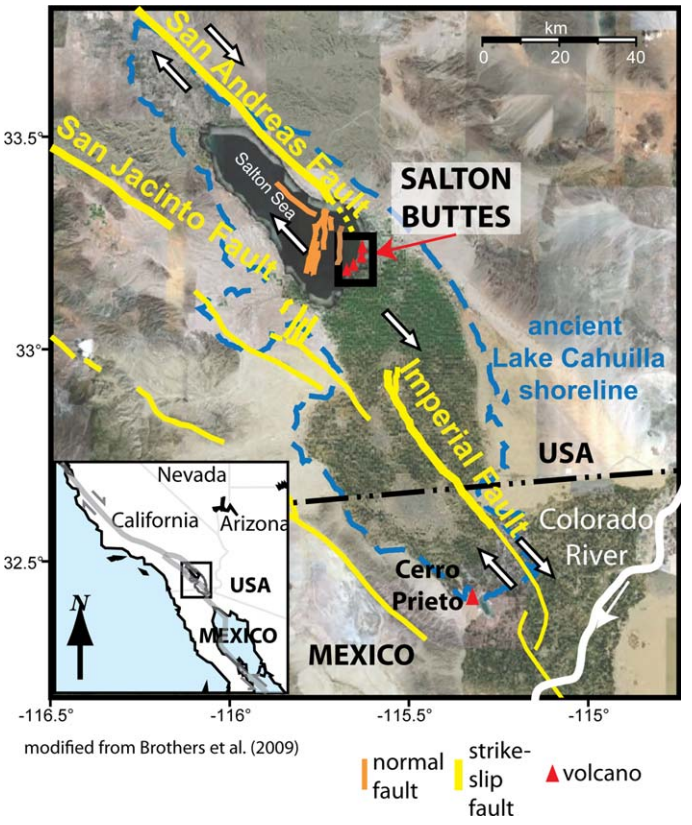

Figure 1. Location of Salton Buttes domes in a pull-apart basin between right-lateral strike slip faults along the Pacific-North American plate boundary. The location of ancient Lake Cahuilla shoreline (precursor to current Salton Sea) is shown for reference, as is the current path of the Colorado River in the southeastern corner of the figure.

North American and Pacific plates [*Brothers et al*., 2009] (Figure 1). Heat flow in the Salton Trough is high [*Lachenbruch et al*., 1985] and the locations of the Salton Buttes are coincident with positive magnetic and gravity anomalies [*Griscom and Muffler*, 1971; *Mariano et al*., 1986; *Langenheim et al*., 2012]. The five domes, from northeast to southwest, include Mullet Island (now a peninsula: *Lynch et al*. [2014]), North Red Hill, South Red Hill, Rock Hill, and Obsidian Butte (Figure 2). They range in vertical relief from 13 to 31 m above the adjacent Salton Sea, which itself lies 69 m below sea level (as of 2010 USGS lidar survey; Figure 2). The Salton Trough has repeatedly been submerged beneath the ancient Lake Cahuilla (predecessor to Salton Sea) and exposed over thousands of years, where at least five lake highstands have occurred since 800 CE [*Philibosian et al*., 2011]. The total volume of all five domes has been estimated at <5 km^3 [*Robinson et al*., 1976]. A young age (Holocene or late Pleistocene) for the small volume buttes is required by their subaerial exposure in an area of rapid sedimentation largely derived from the Colorado River (average 2.2–3.8 mm/yr over the past 420 ka) [*Schmitt and Hulen*, 2008]. However, the exact age of the buttes and the timespan required to produce all five dome-forming eruptions is more difficult to determine.

Previous eruption age determinations have largely focused on South Red Hill and Obsidian Butte. *Muffler and White* [1969] cite a whole-rock K-Ar age of Obsidian Butte of ca. 16 ka by R. W. Kistler and J. Obravodich (unpublished data), whereas obsidian hydration rind ages (fraught with errors) [e.g., *Anovitz et al*., 1999] placed Obsidian Butte at ca. 6.7–8.4 ka and Red Island (Red Hill) at ca. 2.4 ka [*Friedman and Obradovich*, 1981]. U-Th crystallization ages of zircon crystals in Obsidian Butte and South Red Hill span a range of ages, depending upon the component analyzed: granophyre xenoliths at South Red Hill contain ca. 26.2–20.5 ka and one 3 ka zircon (zircon isochron and zircon-whole rock model ages: *Schmitt and Vazquez* [2006] and *Schmitt et al*. [2012]), a fine-grained altered felsite xenolith at South Red Hill contains 18.3 ka zircon (zircon isochron age: *Schmitt and Vazquez* [2006]), rhyolitic partial melt pockets in basalt contain ca. 30.1 and 9.2 ka zircon (zircon isochron ages: *Schmitt and Vazquez* [2006]), and lava from Obsidian Butte and South Red Hill contains zircon cores *and* rims with age peaks at ca. 12.1 and 5.5 ka with minor inherited pre-Quaternary zircons (unmixed zircon model ages: *Schmitt et al*. [2012]). *Schmitt et al*. [2012] determined a 2.48 $\pm$ 0.47 ka (U-Th)/He eruption age (95% confidence interval) from analysis of zircon in a granophyre xenolith at South Red Hill. Consistent with the young age found for South Red Hill, *Schmitt et al*. [2012] compiled a list of dated artifacts sourced at Obsidian Butte and found that the oldest Obsidian Butte artifact was excavated above 1497 and 2259 cal BP age hearths [*Kyle*, 1996] (recalibrated here using OxCal v.4.2.3 *Bronk Ramsey* [2009] using the IntCal13 calibration curve of *Reimer et al*. [2013]), under about 1 m of sediment. Finally, *Perrine et al*. [2013] report a combined infrared stimulated luminescence age of sediment underlying Obsidian

15252027, 2015, 4, Downloaded from https://agupubs.onlinelibrary.wiley.com/doi/10.1002/2015GC005714, Wiley Online Library on [29/08/2023]. See the Terms and Conditions (https://onlinelibrary.wiley.com/terms-and-conditions) on Wiley Online Library for rules of use; OA articles are governed by the applicable Creative Commons License

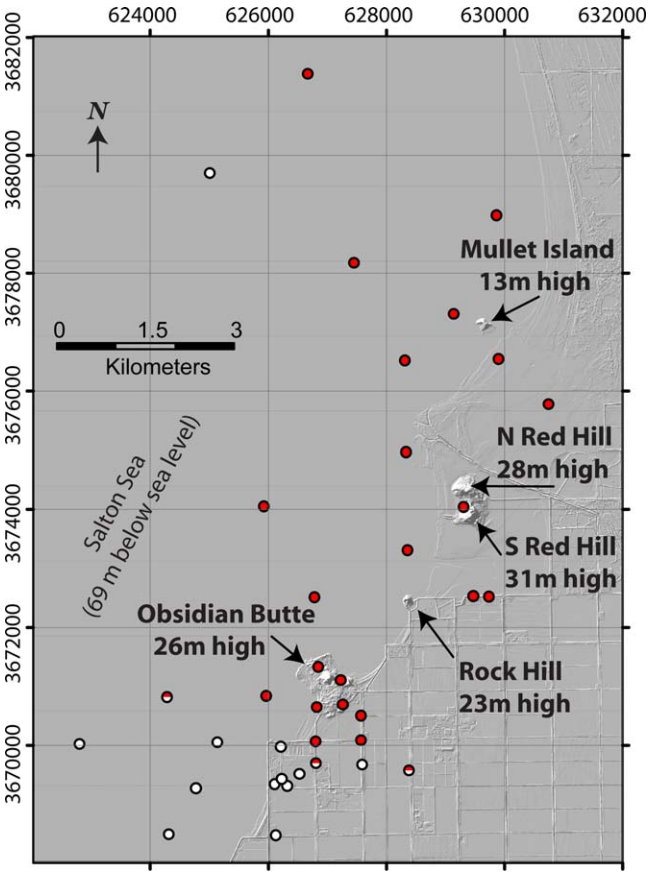

Figure 2. Shaded relief image of the southern margin of the Salton Sea and Salton Buttes from 2010 USGS LIDAR survey. Dispersal of tephra around buttes as recorded in shallow drill holes, where white dots indicate absence of tephra and red dots indicate that tephra is present. Two dots are half red, indicating the presence of tephra that is likely contamination in the hole. UTM coordinate system, see supporting information for complete well log data.

Butte at 3.3 ± 0.5 ka (2 sigma uncertainty), placing a maximum limit on the age of the Obsidian Butte eruption.

2.1. Geologic Context of Salton Buttes Volcanism

Eruptions at all five Salton Buttes consisted of an effusive eruptive phase, but at least two of these volcanoes also experienced explosive eruptions. Pyroclastic deposits from Obsidian Butte and South Red Hill are found in boreholes drilled through or in close proximity to the Salton Buttes. Six of these holes (including continuous core hole and rotary-drilled cuttings holes) intersect rhyolite flows at Obsidian Butte (five holes: 86-1, 86-2, 86-3, 84-3, and IID-8; California Department of Conservation well records: Figure 2) and South Red Hill (one hole: IID-14) in the shallow parts of the holes. There, effusive dome deposits are underlain by pumice fall deposits that are more laterally extensive than the effusive counterparts. Pumice fall deposits in these holes are found at 20–87 m depth and are thickest closest to the volcanic vent. These pumice deposits were quarried from the vicinity of Obsidian Butte as early as 1918, where quarried pumice bed thickness exceeded 3 m [*Chesterman*, 1956]. At South Red Hill, a pumice fall deposit is found at 24–85 m depth. Shallow rotary-drilled temperature gradient holes around Obsidian Butte (Figure 2) intersect pumice deposits at 20–40 m depth and are thickest on the E side of the dome (cuttings were logged at ~1.5 m intervals). Shallow temperature-gradient boreholes drilled by the Shallow Salton Thermal Gradient Project (Lawrence Livermore National Lab and Sandia National Lab) [*Newmark et al.*, 1988] in the southeastern portion of the Salton Sea intersected tephra deposits as well (cuttings were logged at 3 m intervals). Pumiceous clasts, obsidian fragments, and ash shards were found at depths up to 80 m below the lake-bed. Depths and textural classifications of intersected tephra are recorded in supporting information Table S1. The maximum thickness of primary volcanic material (i.e., not contaminated slough from higher in the hole) is 43 m, and is located north of Obsidian Butte (Well 7F). No tephra is found in holes >1 km southeast of Obsidian Butte (white circles, Figure 2), but is found in holes up to 10 km northward of Obsidian Butte (Hole 6E, ~5 km north-northwest of Mullet Island); based on these and shallow observation wells near Obsidian Butte, tephra dispersal was likely to the northeast (Figure 2). Clear evidence is lacking in these core holes for multiple tephra layers separated by at least several meters of sediments (as would be expected from multiple explosive eruptions separated in time by a period of sedimentation in the lake), except in one hole, 6T (Figure 2 and supporting information Table S1), where tephra is found at 6–25 m and 60–70 m.

In addition to well-sorted fall deposits that underlie effusive deposits (lava and flow margin breccia), volcaniclastic sediments overlie the domes at North and South Red Hills (Figure 3). These deposits are matrix-supported, where the matrix consists of fine clay and quartz sediment and clasts consist of variably vesicular juvenile material. Accretionary lapilli are found in some outcrops on the southwest side of North Red Hill,

15252027, 2015, 4, Downloaded from https://agupubs.onlinelibrary.wiley.com/doi/10.1002/2015GC005714, Wiley Online Library on [29/08/2023]. See the Terms and Conditions (https://onlinelibrary.wiley.com/terms-and-conditions) on Wiley Online Library for rules of use; OA articles are governed by the applicable Creative Commons License

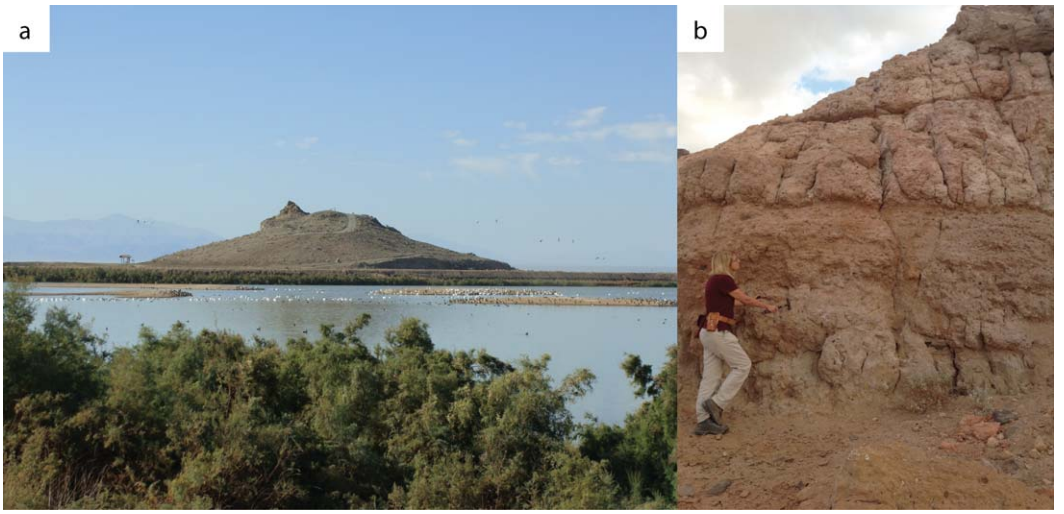

Figure 3. (a) Rock Hill viewed from South Red Hill. Total vertical relief is 23 m above water level as measured from 2010 lidar data. (b) Weakly vertically columnar jointed pyroclastic deposits at South Red Hill. Thermal demagnetization of these sediment laden pyroclastic deposits indicates emplacement temperatures in excess of 500°C, where remanent magnetization is identical to the volcanic dome rock itself.

indicating moist aggregation of ash in the atmosphere. At South Red Hill, these deposits are red-colored, coherent, and weakly columnar to vertically jointed in places.

Eruptive products are high-K rhyolites (73.2–76.4 wt. % SiO_2; unpublished analyses). All five domes are phenocryst-poor, containing <1–2% of anorthoclase and clinopyroxene, accessory magnetite, ilmenite, orthopyroxene, quartz, amphibole, zircon, and apatite. Several xenolith lithologies have been identified in rhyolitic lavas, including low-K tholeiitic, amphibole-bearing basalt, partially melted granophyre, altered rhyolite, and hornfelsic metasediments [*Robinson et al.*, 1976; *Schmitt and Vazquez*, 2006].

3. Geochronologic Techniques

In order to better constrain the timing of eruptive activity three independent geochronologic dating techniques were applied to each of the five Salton Buttes domes.

3.1. ^{238}U-^{230}Th Geochronology

Zircon crystals were extracted from cleaned, crushed obsidian samples using standard magnetic and heavy liquid separation techniques. After separation, zircon crystals were placed in a cold, dilute hydrofluoric acid bath for 5 min to remove adhering glass. Individual grains were then hand-picked and embedded into soft indium metal in order to analyze unpolished zircon rim compositions [*Vazquez and Lidzbarski*, 2012]. Grains were mounted on the same mounts as reference standards. ^{238}U-^{230}Th-^{232}Th compositions of 109 zircon crystals (>17 crystals for each of the five domes) were determined by secondary ion mass spectrometry (SIMS) using the Stanford-USGS SHRIMP-RG ion microprobe following analytical techniques described in *Vazquez and Lidzbarski* [2012]. Measurements were made in 2013, which is the reference year for zircon crystallization age determinations here. All zircon grains were imaged after analysis with a cathodoluminescence (CL) detector to document grain shape and analysis spot position on the crystal face. U and Th isotope compositions of host obsidian glass were determined by multicollector Inductively Coupled Plasma Mass Spectrometer (ICP-MS) for hand-picked glass separates from each dome using standard dissolution techniques and ion-exchange chromatography as described in *Cooper and Donnelly* [2008] and modified in *Stelten and Cooper* [2012]. For each dome, isochron ^{238}U-^{230}Th ages were calculated using respective rim compositions and the measured ^{238}U-^{230}Th composition of host obsidian glass. Model ^{238}U-^{230}Th crystallization ages were calculated as two-point isochrons through individual rim analyses and host obsidian glass [*Reid et al.*, 1997]. Isochron and weighted mean model ages are reported with uncertainty at the 95% confidence level. During the analytical sessions, sectioned zircon from Puy de Dome trachyte, France (PdD), and from a syenite lithic clast erupted at Laacher See, Germany (268 sanidinite), were analyzed for comparison

15252027, 2015, 4, Downloaded from https://agupubs.onlinelibrary.wiley.com/doi/10.1002/2015GC005714, Wiley Online Library on [29/08/2023]. See the Terms and Conditions (https://onlinelibrary.wiley.com/terms-and-conditions) on Wiley Online Library for rules of use; OA articles are governed by the applicable Creative Commons License

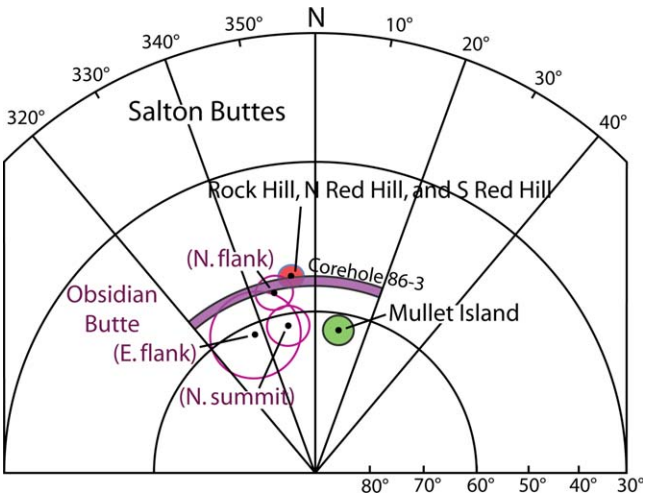

Figure 4. Lower hemisphere equal area plots of mean magnetization directions of Salton Buttes domes with 95% confidence ovals. Data represent two sites on Mullet Island, six sites on Rock Hill, North Red Hill, and South Red Hill, and three sites from Obsidian Butte (purple labels). Purple inclination band centered at 54° inclination is derived from 19 of 22 azimuthally unoriented vertical drill core samples in Obsidian Butte rhyolite from core hole 86-3. The overlap between this band and the orientation of one Obsidian Butte site supports the inference that this site was the least deformed of the three Obsidian Butte sites and thereby most closely represents the original magnetization direction.

to the results from independent studies. Together with U-Th data delimiting the initial $^{230}Th/^{232}Th$ of their host magma [*Condomines*, 1997], Puy de Dome zircon yield an isochron age of 10.1 ± 2.1 ka (n = 9, 95% confidence), which is indistinguishable from the thermal ionization mass spectrometry U-Th age of 12.1 ± 1.0 ka reported for bulk zircon separate [*Condomines*, 1997], and a SIMS age of 14.8 ± 2.4 [*Schmitt et al*., 2010b]. Laacher See zircon yields an isochron age of 17.2 ± 3.1 ka (n = 14, 95% confidence), which is indistinguishable from the SIMS isochron age of 17.1 ± 2.6 ka reported by *Schmitt* [2006].

3.2. $^{40}Ar/^{39}Ar$ Geochronology

Both anorthoclase and glass separates were extracted from obsidian samples for $^{40}Ar/^{39}Ar$ geochronology. Anorthoclase crystals were separated from four of the Salton Buttes domes: Obsidian Butte, North Red Hill, South Red Hill, and Rock Hill. 250–500 μm size whole anorthoclase crystals were extracted from the same cleaned, crushed obsidian samples used for zircon extraction, using standard magnetic and hand separation techniques. After separation, crystals were placed in a cold, dilute hydrofluoric acid bath to remove adhering glass. In addition, 500–1000 μm size anorthoclase crystals were extracted from Obsidian Butte obsidian and 250–355 μm size fresh glass chips were separated from Obsidian Butte and Mullet Island obsidians. Aliquants of anorthoclase weighing 121–161 mg and of glass weighing 104–115 mg were encapsulated in Cu foil and placed in quartz vials along with fluence monitor mineral Bodie Hills sanidine (t = 9.6345 Ma), an internal USGS standard calibrated to Taylor Creek sanidine (TCR-2 = 27.87 Ma). TCR-2 is calibrated to the first principles standard SB-3 (162.9 Ma) [*Lanphere and Dalrymple*, 2000]. Using these standard ages, the commonly employed monitor Fish Canyon sanidine yields an age of 27.63 Ma. The quartz vials were then wrapped with Cd foil and were irradiated for 60 min in the U.S. Geological Survey TRIGA reactor in Denver, Colorado. Samples were irradiated in two sets, IRR314 and IRR315, and were rotated continuously and the package was oscillated through the reactor centerline to minimize the flux gradient. Full details of the irradiation and experimental technique, with special

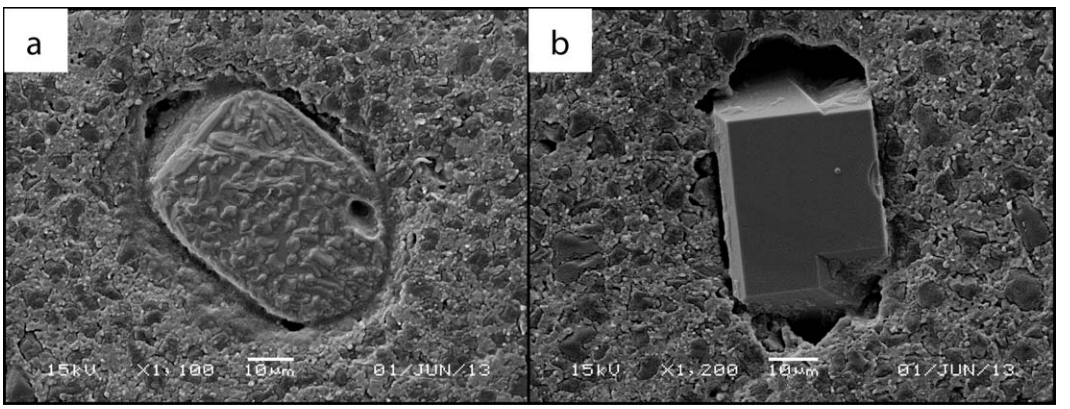

Figure 5. Secondary electron images of unpolished zircon grains mounted in indium metal, (a) Mullet Island zircon: note irregular surface, and (b) Rock Hill zircon. Zircons from Obsidian Butte, North and South Red Hills, and Rock Hill look like Rock Hill zircon shown here.

15252027, 2015, 4, Downloaded from https://agupubs.onlinelibrary.wiley.com/doi/10.1002/2015GC005714, Wiley Online Library on [29/08/2023]. See the Terms and Conditions (https://onlinelibrary.wiley.com/terms-and-conditions) on Wiley Online Library for rules of use; OA articles are governed by the applicable Creative Commons License

Table 1. $^{40}Ar/^{39}Ar$ ages for Saltern Buttas with 2 sigma uncertatinties

			$^{40}Ar/^{39}Ar$ Weighted mean plateau age				$^{40}Ar/^{39}$ isotope correlation (isochom) age				$^{40}Ar/^{39}$total gas	
Sample	Matenal	Experiment	Age (ka)	%^{39}Ar[steps, °C]	MSWD	Age (ka)	%^{39}Ar[steps, °C]	MSWD	$^{40}Ar/^{36}Ar_I$	Age (ka)	Comments
1 2HW-SB08 South Red Hill (250-500μm)	Anorthoclase	13Z0134	*0.9 ± 2.8*	74[700-1250]	1.98	1.7±4.0	74[700-1250]	2.11	293.3 ±6.2	5.8 ± 2.0	Climbing spectrum, acceptable plateau or isochron
12HW-SB09 Rock Hill (250-500μm)	Anorthoclase	13Z0131	6.5±7.6	100[600-1450]	10.88	9.8±7.0	73[600-1250]	1.68	289.1 ±4.0	2.7 ± 2.6	Acceptable isochron
12HW-SB11 North Red Hill (250-500μm)	Anorthoclase	13Z0135	*1.7 ± 1.6*	68[900-1250)	0.78	2.1 ±3.0	68[900-1250]	0.89	293.7 ±9.6	4.4 ± 1.6	Good plateau, isochron
13HW-SB18 Obsidian Butte (250-500μm)	Anorthoclase	13Z0132	*4.9±2.0*	59[900-1200]	0.52	4.9±3.6	59[900-1200]	0.62	295.2±5.6	7.8 ± 2.0	Good plateau, isochron
13HW-SB18 Obsidian Butte (500-1000μm)	Anorthoclase	13Z0137	*4.7±2.4*	66[600-1250]	0.57	3.6±3.8	66[600-1250]	0.59	298.0±8.5	6.9 ± 2.2	Good plateau, isochron
13HW-SBI8 Obsidian Butte	Obsidian	13Z0133	*5.8±1.8*	67[800-1050)	0.29	1.8±15.0	67[800-1050)	0.29	319.4 ± 99.6	9.4 ± 1.8	Good plateau, isochron
1 2HW-SB04 Mullet Island	Obsidian	13Z0136	−119.4 ± 7.6	47[600-850]	1.13	*5.7±335.4*	47[600-850]	1.13	282.2 ±26.9	−93.1 ± 5.2	Low precision isochron ok

[a]Samples irradiated at USGS TRIGA reactor using 9.6345 Ma Bodie Hills sanidine as a neutron flux monitor
Preferred ages in italics

consideration for young volcanic samples with low radiogenic yields, are found in *Calvert and Lanphere* [2006]. The results are presented as age spectrum diagrams and as normal isochron (isotope correlation) plots. All analyses are shown with 2 sigma uncertainties (Table 1).

3.3. Paleomagnetics

Paleomagnetic samples were collected, processed, and interpreted using the methods described by *McElhinny* [1973]. Sites were occupied at 1–3 locations in each of the five obsidian domes. An additional site was taken in syn-eruptive volcaniclastic deposits plastered against the dome at South Red Hill. These volcaniclastic deposits are red-colored, matrix-supported, poorly sorted deposits with a sedimentary matrix (fine clay and quartz silt) surrounding abundant volcanic (pumice and obsidian) clasts. Samples were taken in the field using a handheld, gasoline-powered, 2.5 cm coring drill and were oriented using a sun compass. Eight, 10 cm long samples were taken at each site. 2.5 cm long specimens were measured using an automated cryogenic magnetometer and variously subjected to alternating-field (AF) or thermal demagnetization to remove secondary components of, and reveal the characteristic direction of remanent magnetization. The mean direction of magnetization for each site was calculated using Fisher statistics on data from line fits on vector component diagrams. Site mean directions are presented in Table 2, and illustrated in Figure 4 for each dome as part of an equal-area projection (lower hemisphere) showing mean directions and ovals of 95% confidence (α95).

An additional 28 samples were subcored from vertical (6.4 cm diameter) drill cores taken through Obsidian Dome (Holes 86-1 and 86-3; Department of Conservation well log list: http://geosteam.conservation.ca.gov/WellSearch/GeoWellSearch.aspx), and generously made available to us by CalEnergy Operating Corporation. These samples were not oriented with regard to azimuth and thus can only provide remanent inclination data. They too were measured in an automated cryogenic magnetometer, AF demagnetized, fit with line solutions on vector component diagrams, and average inclination values calculated using an algorithm by *McFadden and Reid* [1982, Table 2.

4. Results

4.1. ^{238}U-^{230}Th Geochronology

All analyzed zircon crystals are euhedral, with the exception of most grains from Mullet Island, which have less distinct crystal edges and vermiform surfaces (Figure 5 and supporting information Figure S1). Isochron ages calculated from zircon populations and matrix glass compositions at North Red Hill, Obsidian Butte, and South Red Hill yield dates of 3.15 ± 0.40, 2.86 ± 0.48, and 2.43 ± 0.47 ka, respectively (±1 sigma, Figure 6, Table 3; supporting information Table S2).

Mean apparent zircon rim model ages for crystallization in order of decreasing age are 8.9 ± 0.5, 4.2 ± 0.4, 3.1 ± 0.4, 2.8 ± 0.5, and

15252027, 2015, 4, Downloaded from https://agupubs.onlinelibrary.wiley.com/doi/10.1002/2015GC005714, Wiley Online Library on [29/08/2023]. See the Terms and Conditions (https://onlinelibrary.wiley.com/terms-and-conditions) on Wiley Online Library for rules of use; OA articles are governed by the applicable Creative Commons License

Table 2. Salton Buttes Paleomagnetic Data

Dome	Site number	LAT	LON	N/No	Exp. type	I (°)	D (°)	A_{95}	k	R	λ_P	Φ_P
Rock Hill	0652B	33.182	244.377	8/8	AF	52.3	354.5	3.3	288	7.9757	85.4	152.4
South Red Hill	0732B	33.194	244.389	8/8	AF	52.7	354.8	2.1	692	7.9899	85.7	156.9
	1132B	33.195	244.389	8/8	AF	52.9	352.9	1.1	2343	7.997	84.1	159.3
	0013B	33.197	244.388	7/8	Th	53.2	351.8	2.2	744	6.99193	83.2	161.7
	average	33.195	244.389	3/3		52.9	353.2	1.4	7288	2.99973	84.3	159.4
North Red Hill	0812B	33.198	244.389	6/8	AF	55.7	347.2	1.7	1621	5.9969	79.1	174.1
	1212B	33.198	244.388	8/8	AF	49.6	355.5	3.2	294	7.97262	85.3	119.7
	average	33.198	244.389	2/2		52.7	351.6	17.3	211	1.99525	83	157.5
Average of Rock and Red Hills	average	33.190	244.380	3/3		52.8	352.9	2.2	925	5.9946	84.1	157.8
Obsidian Butte	1052B	33.170	244.363	7/8	AF	55.4	347.1	3.3	328	6.9817	79	172.6
	0972B	33.171	244.363	7/8	Th	62.1	349.5	3.8	260	6.97695	76.9	208.7
	6982B	33.172	244.364	4/8	Th	61.9	336.5	8.2	126	3.97613	69.1	189.6
Mullet Island	6732B	33.225	244.393	9/9	Th	63	10.5	3.6	206	8.96111	76.1	277.1
	6822B	33.226	244.392	8/8	Th	63.2	7.7	2.2	666	7.98949	77.1	269.6
	average	33.225	244.392	2/2		63.1	9.1	2.8	7982	1.99987	76.6	273.6

[a]Site number is a field and laboratory identification number, all sites were drilled in rhyolite lava except 0013B that was drilled in red fragmental deposits on top of South Red Hill dome; N/No is the number of samples used in calculation of the average divided by the number of samples collected; Exp. type: AF indicates line fits on alternating field demagnetization results, Th indicates line fits on thermal demagnetization results; I, D are in situ inclination and declination directions of mean paleomagnetic directions; R is the resultant vector sum of N unit vectors; k is the concentration parameter (Fisher 1953); A_{95} is the radius of 95% confidence, λP and ΦP are the latitude and longitude of the virtual geomagetic pole, respectively.

2.4 ± 0.5 ka for Mullet Island, Rock Hill, North Red Hill, Obsidian Butte, and South Red Hill, respectively (1 sigma uncertainty; supporting information Table S2). These model ages are well within uncertainty limits of isochron ages for North Red Hill, Obsidian Butte, and South Red Hill. A minority of zircon crystals from three domes (Obsidian Butte, North Red Hill, and Rock Hill) yield individual model ages from ca. 10 to 100 ka.

4.2. $^{40}Ar/^{39}Ar$ Geochronology

For each of the seven aliquants in Table 1, a weighted-mean plateau age, an isotope correlation age, and a total gas age has been calculated, where the preferred age is shown in bold. We define the criteria for selection of the most meaningful incremental heating age following *McDougall and Harrison* [1999] and *Calvert and Lanphere* [2006]. On this basis, weighted mean plateau ages are favored when four criteria are met: a well-defined horizontal plateau for more than 50% of the ^{39}Ar released; a well-defined isochron for the plateau gas fractions; concordant plateau and isochron ages; and a $^{40}Ar/^{39}Ar$ isochron intercept that does not significantly differ from the atmospheric value of 295.5. Where one or more of these criteria are not met, we favor the isochron age for that sample. Weighted mean plateau ages are favored for all samples, except the Rock Hill anorthoclase and the Mullet Island obsidian glass samples (Figure 7, supporting information Figure S2 and Table S3).

In order of decreasing age, our interpreted ages for incremental heating experiments are all Holocene. The Rock Hill anorthoclase yielded a climbing age spectrum with no plateau, but an isochron age for Rock Hill anorthoclase of 9.8 ± 7.0 ka (±2 sigma). Mullet Island contained no separable anorthoclase and obsidian produced all negative apparent ages and yielded a reasonable, but poorly determined isochron age of 5.7 ± 330 ka. Obsidian Butte anorthoclase analyses yielded well-determined weighted mean plateau ages of 4.9 ± 2.0 and 4.7 ± 2.4 ka, and obsidian analyses produced a weighted mean plateau age of 5.8 ± 1.8 ka; these three ages

Table 3. ^{238}U-^{230}Th Zircon-Glass Isochron Ages for Salton Buttes

Sample	Rhyolite	Isochron age (ka)	±1σ	N	MSWD	±95% conf.
SB08	South Red Hill	2.41	0.47	18/18	1.6	0.93
SB11	North Red Hill	3.14	0.40	20/23	1.5	0.79
SB18	Obsidian Butte	2.86	0.48	17/20	0.95	0.94
SB08+SB11	South Red Hill +North Red Hill	2.83	0.30	38/41	1.5	0.76

[a]Isochron and model ages are derived using a ^{230}Th decay constant of 9.1705 (±0.0138)x$10^{-6}a^{-1}$ [*Cheng et al.*, 2013] and reported as years before 2013 (ka) with uncertainty at the 1 sigma and 95% confidence interval. N = number of analyses included for isochron age relative to number analyzed. MSWD = mean square of weighted deviates [*Wendt and Carl*, 1991].

15252027, 2015, 4, Downloaded from https://agupubs.onlinelibrary.wiley.com/doi/10.1002/2015GC005714, Wiley Online Library on [29/08/2023]. See the Terms and Conditions (https://onlinelibrary.wiley.com/terms-and-conditions) on Wiley Online Library for rules of use; OA articles are governed by the applicable Creative Commons License

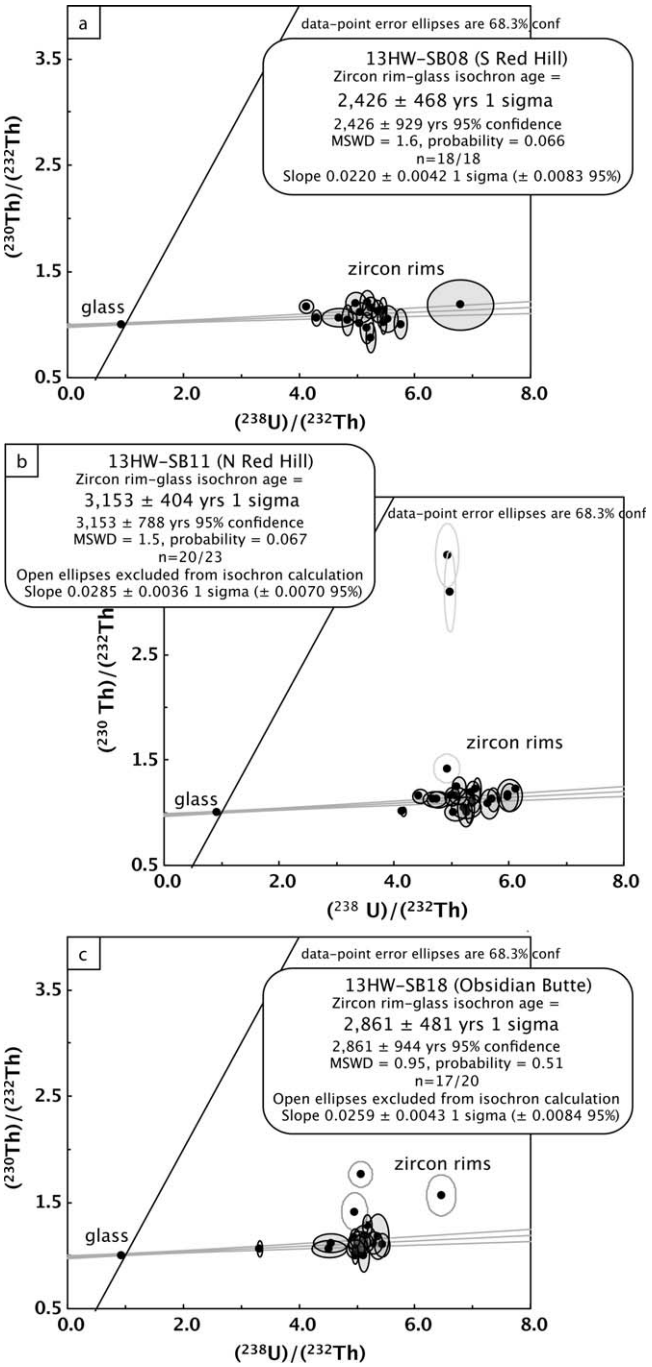

Figure 6. ^{238}U-^{230}Th isochron age diagrams for zircon rims (supporting information Table S2 contains all U-Th data).

are within 2 sigma analytical uncertainty of each other. North Red Hill anorthoclase analyses yielded a weighted mean plateau age of 1.7 ± 1.6 ka and South Red Hill anorthoclase analyses produced a weighted mean plateau age of 0.9 ± 2.8 ka.

4.3. Paleomagnetic Directions

Mean characteristic directions for all sampled sites are shown in Table 2. North Red Hill, South Red Hill, and Rock Hill obsidian domes have identical remanent directions within the calculated uncertainty, with I ~ 53° and D ~ 353°. Samples from red, clastic deposits that overlie South Red Hill also have identical directions, indicating that these deposits were emplaced at temperatures above the Curie point, and must be primary phreatomagmatic deposits (with clay and quartz sedimentary matrix supporting volcanic clasts; Figure 3). Samples from the two sites on Mullet Island are distinct from the above and cluster tightly at I ~ 63° and D ~ 9°.

The remanent directions recorded by samples from the three paleomagnetic sites on Obsidian Butte, however, exhibit significant internal variation (Figure 4). Two sources of variation are possible. The scatter may be a reflection of geomagnetic secular variation occurring over the course of the eruption, or, alternatively, may be an artifact of syn or posteruption dome deformation. Geomagnetic secular variation, which occurs at a rate of 2° to 8° per 100 years [*Merrill et al*., 1996], is dismissed because the time required to produce the observed variation is inconsistent with the characteristic days to tens of years durations of small dome-forming eruptions [*Newhall and Melson*, 1983]. Instead we attribute the variation to sub-Curie point deformation (e.g., at temperatures below 580°C), either by postemplacement fracture and rotation of cold dome rocks, or, by nonuniform, plastic deformation occurring during extrusion (e.g., scatter in single Unzen lava flow directions) [*Tanaka et al*., 2004].

Paleomagnetic inclinations of vertical drill core from Obsidian Butte (core hole 86-3 in Figure 2) can be used to determine which of the surface sample sites most faithfully represent the primary magnetic field direction at the time of eruption. The mean inclination derived from 19 of the 22 Obsidian Butte core samples analyzed is 54.0 ± 0.9°, which is shown in Figure 4 as the purple band reflecting the 95% confidence

15252027, 2015, 4, Downloaded from https://agupubs.onlinelibrary.wiley.com/doi/10.1002/2015GC005714, Wiley Online Library on [29/08/2023]. See the Terms and Conditions (https://onlinelibrary.wiley.com/terms-and-conditions) on Wiley Online Library for rules of use; OA articles are governed by the applicable Creative Commons License

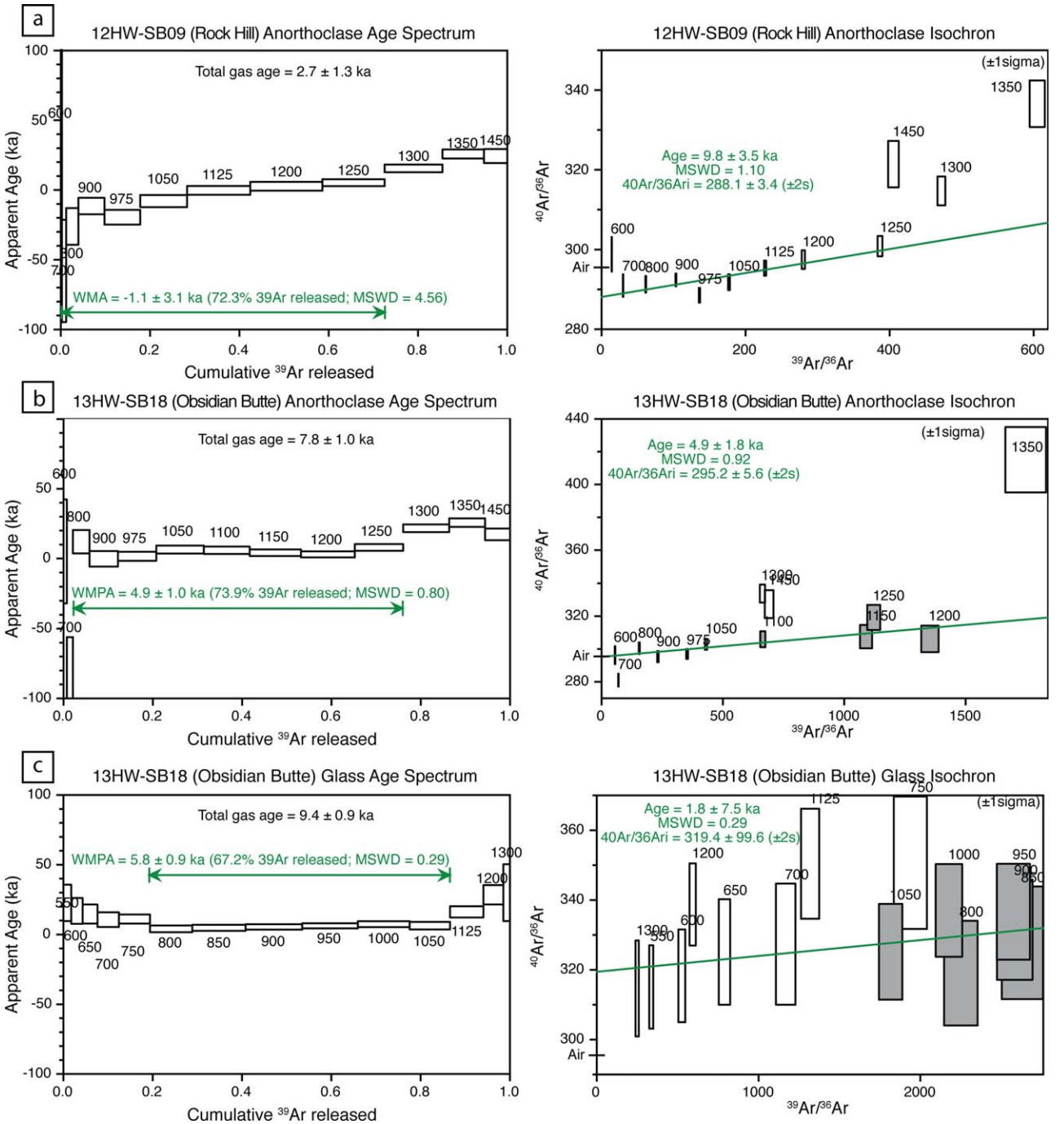

Figure 7. Sample $^{40}Ar/^{36}Ar$ age spectra diagrams and normal isochron plots for anorthoclase and glass separates from Salton Buttes (supporting information Figure S2 contains all plots). Uncertainties for apparent ages and isotopic ratio boxes are all 2 sigma. Interpreted ages, weighted mean plateau ages (WMPA), and $^{40}Ar/^{36}Ar$ ratios are 2 sigma. Horizontal lines with arrows on age spectra show which steps were used in plateau ages, filled symbols on isochron plots show steps used in isochron fit.

interval. The band only intersects the north flank magnetization direction. Data from the other two sites on Obsidian Butte are off by ~8°. The best estimate for the characteristic remanent magnetization of Obsidian Butte is therefore taken as I ~ 55° and D ~ 347°. The Obsidian Butte direction is slightly steeper and more westerly than the mean direction of Rock Hill, North Red Hill, and South Red Hill. The observed 4° angular separation between the two clusters suggests eruptions separated by no more than 200 years. The 13° separation of Mullet Island data from the other domes suggests the entire eruptive episode creating Salton Buttes could have lasted no more than approximately 500 years.

15252027, 2015, 4, Downloaded from https://agupubs.onlinelibrary.wiley.com/doi/10.1002/2015GC005714, Wiley Online Library on [29/08/2023]. See the Terms and Conditions (https://onlinelibrary.wiley.com/terms-and-conditions) on Wiley Online Library for rules of use; OA articles are governed by the applicable Creative Commons License

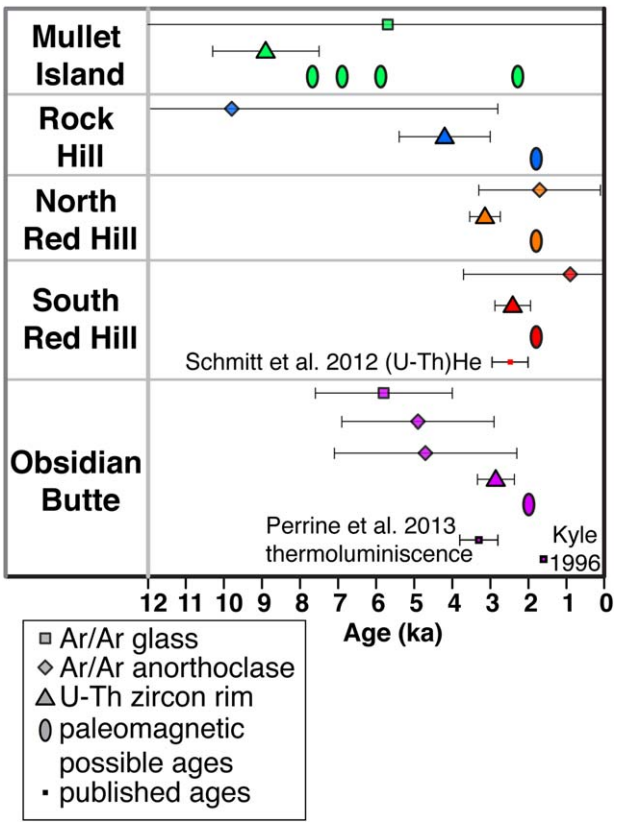

Figure 8. Compilation of $^{40}Ar/^{39}Ar$ and ^{238}U-^{230}Th age results (with 2 sigma uncertainties for Ar ages and 95% confidence intervals for U-Th ages) from this study, including permissible ages for paleomagnetic data within uncertainty limits of other age determinations and previously published age constraints for Salton Buttes surface domes.

5. Discussion

The ^{238}U-^{230}Th isochron ages for the final increment of zircon crystallization provide the most precise radioisotopic ages in this study (Figure 8). Crystallization ages from zircon provide a maximum limit on eruption age because crystal growth necessarily precedes eruption and U and Th are effectively retained in zircon even at magmatic temperatures. Given potential growth rates from diffusion of Zr in a cooling rhyolitic melt [e.g., *Watson*, 1996] and the results from depth profiling of crystallization ages in single zircon [*Schmitt*, 2011; *Storm et al*., 2011], the typical depth of ~5 μm sampled during SHRIMP-RG U-Th analyses [*Vazquez and Lidzbarski*, 2012] may integrate several centuries to millennia of crystal stratigraphy if crystallization was continuous without hiatus or loss of the youngest zircon domains by resorption. Dating studies that directly or effectively sample the outermost rims on euhedral zircon can resolve crystallization ages that precede eruption by several millennia or less [e.g., *Crowley et al*., 2007; *Vazquez and Lidzbarski*, 2012]. Rim ages that precede eruption by tens of thousands of years indicate recycling of antecrysts [e.g., *Storm et al*., 2011].

Rims on zircon from Obsidian Dome, North Red Hill, South Red Hill, and Rock Hill are euhedral (Figure 5), consistent with thermochemical equilibrium with their host rhyolitic melt. The irregular overall morphology of zircon grains in the Mullet Island dome suggests limited dissolution and in turn that this rhyolite batch became undersaturated in zircon prior to eruption. Partial dissolution of outer growth zones is evident in the CL images of some, but not all Mullet Island zircon grains (supporting information Figure S3). Resorption of Mullet Island zircon was rapid, lasting no more than several centuries based on the dissolution kinetics of entire 50–100 μm zircon grains in undersaturated melt [*Harrison and Watson*, 1983] at the 770–790°C temperatures derived from Zr-in-melt geothermometry (H. Wright, unpublished data, 2013). The thin vermiform texture on the crystal faces of the Mullet Island zircon (Figure 5) suggests that this population of crystals may have undergone a final episode of rapid crystallization, likely near the time of eruption [e.g., *Roeder et al*., 2001; *Waters and Lange*, 2013]. The relatively old U-Th model ages for the resorbed Mullet Island zircon can be reconciled with the zircon ages for the other rhyolites if the apparent episode of dissolution removed a sequence of the crystal stratigraphy equivalent to several millennia of growth. Accordingly, the Mullet Island zircon U-Th ages are likely to predate eruption by a greater interval of time than for the other domes. The ages for the resorbed Mullet Island zircon are consistent with the isochron ages reported by *Schmitt and Vazquez* [2006] for zircon cores from Obsidian Butte and South Red Hill (ca. 12.1 ka) that reflect the onset of zircon saturation or recycling of antecrysts.

$^{40}Ar/^{39}Ar$ ages are less precise than ^{238}U-^{230}Th isochron ages; we find that $^{40}Ar/^{39}Ar$ ages agree with ^{238}U-^{230}Th crystallization ages within 2 sigma uncertainty levels. The overlap in the two age determinations validates the assumption that zircon crystallization proceeded to sometime shortly before eruption (i.e., zircon rim crystallization ages are not thousands of years older than the eruption). These results inform our ultimate interpretation that all five Salton Buttes erupted in the Holocene, and at least four of the five

15252027, 2015, 4, Downloaded from https://agupubs.onlinelibrary.wiley.com/doi/10.1002/2015GC005714, Wiley Online Library on [29/08/2023]. See the Terms and Conditions (https://onlinelibrary.wiley.com/terms-and-conditions) on Wiley Online Library for rules of use; OA articles are governed by the applicable Creative Commons License

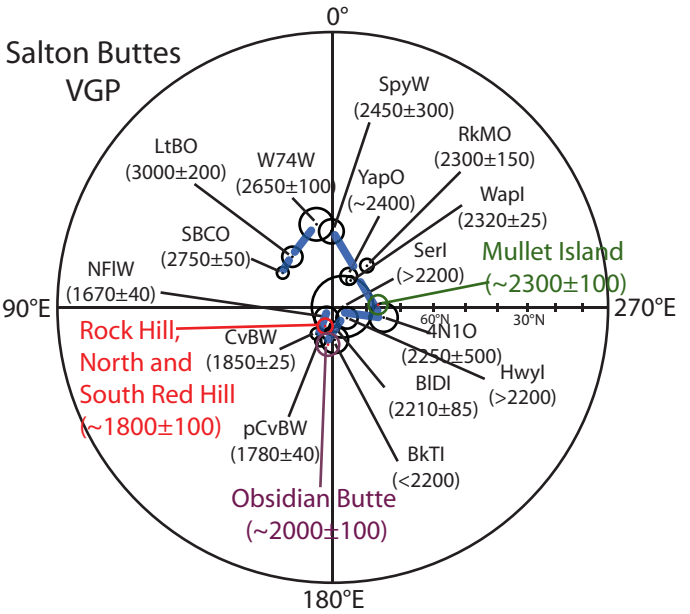

Figure 9. North polar equal area plot showing Virtual Geomagnetic Poles (VGP) from Salton Buttes units (in red, purple, and green), and calibrated ^{14}C dated reference VGP principally from *Hagstrum and Champion* [2002], but also unpublished Mount St. Helens area data from Clynne and Champion (written communication). Ages in parentheses are calibrated ^{14}C ages ±1 sigma uncertainty for the reference flow VGP. Thick dashed blue line shows generalized path of geomagnetic secular variation through about 1000 years. Abbreviations of reference VGP in decreasing age order are SBCO: South Belknap Cone flow; LtBO: Little Belknap flow; W74W: W74-type basaltic andesite, Castle Creek episode, Mount St. Helens; SpyW: South Puyallup pyroclastic flow; RkMO: Rock Mesa pyroclastic flow; YapO: Yapoah lava flow; WapI: Wapi and Kings Bowl lava fields; 4N1O: Four-in-One flow; SerI: Serrate flow; HwyI: highway flow; BlDl: Blue Dragon flows; BkTl: Broken Top flows; pCvBW: pre-Cave basalt flows, Mount St. Helens; CvBW: Cave Basalt flows, Mount St. Helens; and NFlW: North flank basalts, Mount St. Helens.

erupted in the mid to late-Holocene. We can further refine these estimates, however, using paleomagnetic data. A comparison of paleomagnetic directions in the flows allows us to better understand the differences between eruption ages, where paleomagnetic results provide evidence for three different eruption intervals.

On their own, remanent paleomagnetic directions can discriminate between times of eruptions, but cannot provide eruption ages. However, eruption ages can be inferred through comparisons with the established Holocene paleomagnetic secular variation curve derived from ^{14}C-dated magnetic reference points for the western U.S. [*Hagstrum and Champion*, 2002]. This comparison is made on plots of virtual geomagnetic poles (VGP), calculated from the original site directional data, in order to remove gradients in direction inherent to the dipolar geomagnetic field, and allow regional comparisons to be made.

In Figure 9, two distinct eruption periods are evident (two clusters of VGP positions). Reference to the calibrated ^{14}C ages on this curve assigns ages of 2000 ± 100 cal BP for Obsidian Butte, and 1800 ± 100 cal BP for Rock Hill, and South and North Red Hills. Using approximate depths to tephra in shallow drill holes near Obsidian Butte of 15–18 m and an age of 2000 BP for the Obsidian Butte eruption, implies an average sedimentation rate of 8–9 mm/yr. Reference to calibrated ^{14}C ages gives an eruption age of 2300 ± 100 cal BP for Mullet Island. The inferred eruption ages are consistent with the approximately 500 year duration of Salton Butte volcanism indicated by the site mean directions in Figure 4.

Despite textural evidence for late-stage resorption of Mullet Island zircons, the 8.9 ± 1.4 ka ^{238}U-^{230}Th mean apparent model age of those crystals allows for the possibility that Mullet Island erupted much earlier than the other domes. By comparison to calibrated ^{14}C dated reference VGP available from the western US, and younger than ca. 9 ka, three older (than the 2300 ± 100 cal BP age listed above) possible paleomagnetic age assignments for Mullet Island (ca. 5900, 6900, and 7700 years cal BP) are suggested (Figure 10). A significantly older eruption age for the Mullet Island rhyolite may explain the apparent presence of two tephra layers separated by >20 m of sediment in shallow drill hole 6T west of Mullet Island (Figure 2).

The combination of paleomagnetism with ^{238}U-^{230}Th and ^{40}Ar/^{39}Ar dating reveals that episodic volcanism generated the rhyolites at Salton Buttes. Paleomagnetic characteristics require three distinct episodes of volcanism separated by several years to hundreds of years, despite similar compositions for the rhyolites. If Mullet Island is young (ca. 2 ka, Figure 8), then Salton Buttes volcanism extended over an interval of approximately 500 years, but could be as long as approximately 5000 years if older (i.e., if zircon crystallization ages are close in time to eruptions, despite resorbed surfaces, ca. 8 ka, Figure 8). Hence, the Holocene eruptive activity that produced the five obsidian domes and pyroclastic volcanic deposits was not constrained to a single episode of eruption.

15252027, 2015, 4, Downloaded from https://agupubs.onlinelibrary.wiley.com/doi/10.1002/2015GC005714, Wiley Online Library on [29/08/2023]. See the Terms and Conditions (https://onlinelibrary.wiley.com/terms-and-conditions) on Wiley Online Library for rules of use; OA articles are governed by the applicable Creative Commons License

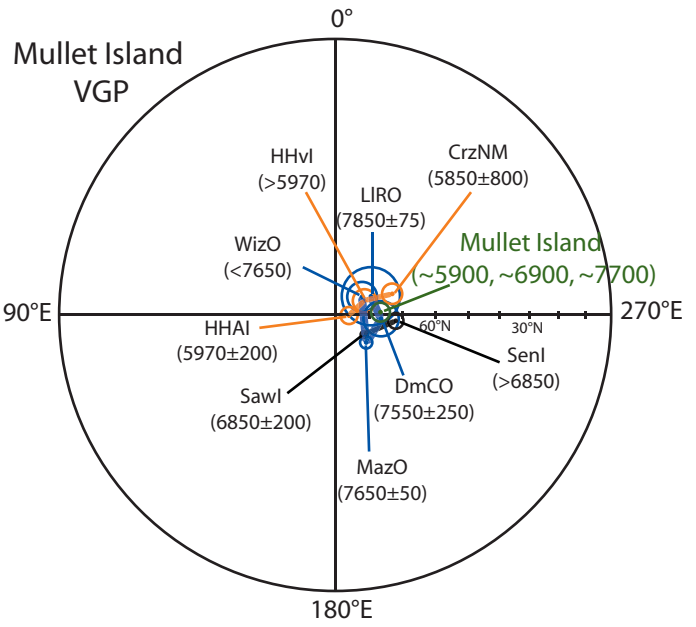

Figure 10. North polar equal area plot showing Virtual Geomagnetic Poles (VGP) from Mullet Island (in green), and calibrated ^{14}C dated reference VGP principally from *Hagstrum and Champion* [2002], but also from *Sherrod et al*. [2012]. Ages in parentheses are calibrated ^{14}C ages ±1 sigma uncertainty for the reference flow VGP. Thick tan (~5900 years), black (~6900 years), and blue (~7700 years) lines show generalized paths of geomagnetic secular variation through those three different time spans. Abbreviations of reference VGP in decreasing age order are: HHAI: Hells Half Acre lava field; HHvI: Hells Half Acre vent area; CrzNM: Carrizozo lava field; SawI: Sawtooth flow; SenI: Sentinel flow; LIRO: Llao flow; DmCO: Diamond Craters lava field; MazO: climactic pyroclastic flows of Mount Mazama; and WizO: Wizard Island.

6. Conclusions

All five Salton Buttes dome-forming eruptions occurred in Holocene time, likely mid to late-Holocene. Based on the overlap in paleomagnetic directions, the overlap in ^{238}U-^{230}Th ages, and the overlap in ^{40}Ar/^{39}Ar ages, North and South Red Hills likely erupted within a century of each other. Slightly younger South Red Hill appears to be the only butte (of the five) clearly erupted through water. A combined U-Th isochron age for these two domes is 2.83 ± 0.60 ka (2 sigma), but paleomagnetic evidence suggests that this age predates eruption by hundreds of years, where an age of 1800 ± 100 cal BP is found for other volcanics with identical paleomagnetic directions to South and North Red Hills. The similarity in paleomagnetic direction, the overlap in ^{238}U-^{230}Th age, and to a lesser degree the overlap in ^{40}Ar/^{39}Ar age suggests that Rock Hill erupted closely in time to the Red Hill eruptions as well. Note that although the Obsidian Butte ^{238}U-^{230}Th isochron age (2.86 ± 0.48 ka) is nearly identical to the combined Red Hill age, its paleomagnetic direction is just outside the 95% confidence radius of North and South Red Hills and Rock Hill domes. This difference and the relative location of its VGP pole suggest a slightly older age (years to one hundred years) for Obsidian Butte relative to the Red Hills. Reference to the calibrated ^{14}C ages on the secular variation curve assigns an age of 2000 ± 100 cal BP for Obsidian Butte. These age constraints are consistent with the 2.48 ± 0.47 ka (U-Th)/He age of South Red Hill and thermoluminescence (<3.3 ± 0.5 ka) constraints on the Obsidian Butte age. The difference in paleomagnetic direction and older ^{238}U-^{230}Th and ^{40}Ar/^{39}Ar ages suggest that Mullet Island dome is older than the other domes, as little as 500 years older than the Red Hill eruptions or as much as ~5000 years older.

Acknowledgments

Supplementary data for this paper are available in supporting information Figures S1–S3 and Tables S1–S3. Kari Cooper would like to acknowledge funding from NSF award EAR-1144945 for U-Th analyses of glasses. We would like to acknowledge CalEnergy for access to drillcore samples from Obsidian Butte and for discussions about the geology of the volcanic buttes. We thank Marsha Lidzbarski for assistance with sample preparation, and Brad Ito for technical assistance in the SHRIMP laboratory. We thank Axel Schmitt and Erik Klemetti for helpful reviews.

References

Anovitz, L. M., J. M. Elam, L. R. Riciputi, and D. R. Cole (1999), The failure of obsidian hydration dating: Sources, implications, and new directions, *J. Archaeol. Sci.*, *26*, 735–752.

Bronk Ramsey, C. (2009), Bayesian analysis of radiocarbon dates, *Radiocarbon*, *51*, 337–360.

Brothers, D. S., N. W. Driscoll, G. M. Kent, A. J. Harding, J. M. Babcock, and R. L. Baskin (2009), Tectonic evolution of the Salton Sea inferred from seismic reflection data, *Nat. Geosci.*, *2*(8), 581–584.

Calvert, A. T., and M. A. Lanphere (2006), Argon geochronology of Kilauea's early submarine history, *J. Volcanol. Geotherm. Res.*, *151*(1–3), 1–18.

Capra, L., C. Siebe, J. L. Macías, and J. M. Espíndola (2007), Comment on: *Schmitt*, AK et al. (2006): Eruption and magma crystallization ages of Las Tres Vírgenes (Baja California) constrained by combined ^{230}Th/^{238}U and (U-Th)/He dating of zircon [J. Volcanol. Geotherm. Res. V. 158: 281–295], *J. Volcanol. Geotherm. Res.*, *163*(1), 98–101.

Chesterman, C. W. (1956), Pumice, pumicite, and volcanic cinders in California, *Calif. Div. Mines Bull.*, 81–87.

Condomines, M. (1997), Dating recent volcanic rocks through ^{130}Th-^{238}U disequilibrium in accessory minerals: Example of the Puy de Dome (French Massif Central), *Geology*, *25*, 375–378.

Connor, C. B., and F. M. Conway (2000), Basaltic volcanic fields, in edited by H. Sigurdsson, *Encyclopedia of Volcanoes*, pp. 331–343, Academic Press, San Diego, Calif.

Cooper, K. M., and C. T. Donnelly (2008), ^{238}U-^{230}Th-^{226}Ra disequilibria in dacite and plagioclase from the 2004–2005 eruption of Mount St. Helens, in *A Volcano Rekindled: The Renewed Eruption of Mount St. Helens, 2004–6, U.S. Geol. Surv. Prof. Pap., 1750*, edited by D. R. Sherrod, W. E. Scott, and P. H. Stauffer, pp. 827–846.

15252027, 2015, 4, Downloaded from https://agupubs.onlinelibrary.wiley.com/doi/10.1002/2015GC005714, Wiley Online Library on [29/08/2023]. See the Terms and Conditions (https://onlinelibrary.wiley.com/terms-and-conditions) on Wiley Online Library for rules of use; OA articles are governed by the applicable Creative Commons License

Crowley, J. L., B. Schoene, and S. A. Bowring (2007), U-Pb dating of zircon in the Bishop Tuff at the millennial scale, *Geology*, *35*, 1123–1126.
Friedman, I., and J. Obradovich (1981), Obsidian hydration dating of volcanic events, *Quat. Res.*, *47*, 37–47.
Griscom, A., and P. Muffler (1971), Aeromagnetic map and interpretation of the Salton Sea Geothermal Area, California, *Geophys. Invest. Map, GP-754*, U.S. Geol. Surv., Washington, D. C.
Hagstrum, J. T., and D. E. Champion (2002), A Holocene paleosecular variation record from ^{14}C-dated volcanic rocks in western North America, *J. Geophys. Res.*, *107*(B1), 2025, doi:10.1029/2001JB000524.
Harrison, T. M., and E. B. Watson (1983), Kinetics of zircon dissolution and zirconium diffusion in granitic melts of variable water content, *Contrib. Mineral. Petrol.*, *84*, 66–72.
Kyle, C. E. (1996), A 2,000 year old milling tool kit from CA-SDI-10148, San Diego, California, *Pac. Coast Archaeol. Soc. Q.*, *32*, 76–87.
Lachenbruch, A. H., J. H. Sass, and S. P. Galanis Jr. (1985), Heat flow in southernmost California and the origin of the Salton Trough, *J. Geophys. Res.*, *90*, 6709–6736.
Langenheim, V. E., N. D. Athens, D. S. Scheirer, and G. S. Fuis (2012), Width and dip of the southern San Andreas fault from modeling of magnetic and gravity data, paper presented at Southern California Earthquake Center Annual Meeting, NSF and USGS, Palm Springs, CA.
Lanphere, M., D. Champion, L. Melluso, V. Morra, A. Perrotta, C. Scarpati, D. Tedesco, and A. Calvert (2007), ^{40}Ar/^{39}Ar ages of the AD 79 eruption of Vesuvius, Italy, *Bull. Volcanol.*, *69*(3), 259–263.
Lanphere, M. A., and G. B. Dalrymple (2000), First-principles calibration of ^{38}Ar tracers: Implications for the ages of ^{40}Ar/^{39}Ar fluence monitors, *U.S. Geol. Surv. Prof. Pap., 1621*, 10 p.
Lynch, D. K., P. M. Adams, and D. M. Tratt (2014), Mullet Island has become a peninsula, in *2014 Desert Symposium*, pp. 113–116, Fullerton, Calif. State Univ. Desert Stud. Cent. [Available at http://nsm.fullerton.edu/dsc/images/DSCdocs/2014Notadroplefttodrink.pdf.]
Mariano, J., M. G. Helferty, and T. B. Gage (1986), Bouguer and isostatic residual gravity maps of the Colorado River Region, including the Kingman, Needles, Salton Sea, and El Centro Quadrangles, *U.S. Geol. Surv. Open File Rep., 86–347*, plates 3–4.
McDougall, I., and T. M. Harrison (1999), *Geochronology and Thermochronology by the ^{40}Ar/^{39}Ar Method*, 2nd ed., 269 pp., Oxford Univ. Press, Oxford, U. K.
McElhinny, M. W. (1973), *Paleomagnetism and Plate Tectonics*, 368 pp., Cambridge Univ. Press, Cambridge, U. K.
McFadden, P. L., and A. B. Reid (1982), Analysis of paleomagnetic inclination data, *J. R. Astron. Soc. Can.*, *69*, 307–319.
Merrill, R. T., M. W. McElhinny, and P. L. McFadden (1996), *The Magnetic Field of the Earth*, 527 pp., Academic. Press, San Diego, Calif.
Muffler, L. J. P., and D. E. White (1969), Active metamorphism of Upper Cenozoic sediments in the Salton Sea geothermal field and the Salton Trough, Southeaster California, *Geol. Soc. Am. Bull.*, *80*, 157–182.
Newhall, C. G., and W. G. Melson (1983), Explosive activity associated with the growth of volcanic domes, *J. Volcanol. Geotherm. Res.*, *17*, 111–131.
Newmark, R. L., P. W. Kasameyer, and L. W. Younker (1988), Shallow drilling in the Salton Sea region: The thermal anomaly, *J. Geophys. Res.*, *93*, 13,005–13,023.
Perrine, A. R., A. K. Schmitt, and E. J. Rhodes (2013), Infrared stimulated luminescence emplacement ages for Obsidian Butte rhyolite dome (Imperial County, California), *Geol. Soc. Am. Abstr. Programs*, *45*(7), 337.
Philibosian, B., T. Fumal, and R. Weldon (2011), San Andreas fault earthquake chronology and Lake Cahuilla history at Coachella, California, *Bull. Seismol. Soc. Am.*, *101*(1), 13–38.
Reid, M. R., C. D. Coath, T. M. Harrison, and K. D. McKeegan (1997), Prolonged residence times for the youngest rhyolites associated with Long Valley Caldera: ^{230}Th-^{238}U ion microprobe dating of young zircons, *Earth Planet. Sci. Lett.*, *150*, 27–39.
Reimer, P. J., E. Bard, A. Bayliss, J. W. Beck, P. G. Blackwell, C. B. Ramsey, C. E. Buck, H. Cheng, R. L. Edwards, and M. Freidrich (2013), IntCal13 and Marine13 radiocarbon age calibration curves 0–50,000 years calBP, *Radiocarbon*, *55*, 1869–1887.
Robinson, P. T., W. A. Elders, and L. J. P. Muffler (1976), Quaternary volcanism in the Salton Sea geothermal field, Imperial Valley, California, *Geol. Soc. Am. Bull.*, *87*, 347–360.
Roeder, P. L., A. Roustovetov, and N. Oskarsson (2001), Growth forms and composition of chromian spinel in MORB magma: Diffusion-controlled crystallization of chromian spinel, *Can. Mineral.*, *39*, 397–416.
Schmitt, A. K. (2006), Laacher See revisited: High-spatial-resolution zircon dating indicates rapid formation of a zoned magma chamber, *Geology*, *34*(7), 597–600.
Schmitt, A. K. (2011), Uranium series accessory crystal dating of magmatic processes, *Annu. Rev. Earth Planet. Sci.*, *39*, 321–349.
Schmitt, A. K., and J. B. Hulen (2008), Buried rhyolites within the active, high-temperature Salton Sea geothermal system, *J. Volcanol. Geotherm. Res.*, *178*(4), 708–718.
Schmitt, A. K., A. Martin, D. F. Stockli, K. A. Farley, and O. M. Lovera (2012), (U-Th)/He zircon and archaeological ages for a late prehistoric eruption in the Salton Trough (California, USA), *Geology*, *41*(1), 7–10.
Schmitt, A. K., and J. A. Vazquez (2006), Alteration and remelting of nascent oceanic crust during continental rupture: Evidence from zircon geochemistry of rhyolites and xenoliths from the Salton Trough, California, *Earth Planet. Sci. Lett.*, *252*(3–4), 260–274.
Schmitt, A. K., D. F. Stockli, S. Niedermann, O. M. Lovera, and B. P. Hausback (2010a), Eruption ages of Las Tres Vírgenes volcano (Baja California): A tale of two helium isotopes, *Quat. Geochronol.*, *5*(5), 503–511.
Schmitt, A. K., F. Wetzel, K. M. Cooper, H. Zou, and G. Worner (2010b), Magmatic longevity of Laacher See Volcano (Eifel, Germany) indicated by U-Th dating of intrusive carbonatites, *J. Petrol.*, *51*, 1053–1085.
Sherrod, D. R., D. E. Champion, and J. P. McGeehin (2012), Age and duration of volcanic activity at Diamond Craters, southeastern Oregon, *J. Volcanol. Geotherm. Res.*, *247*, 108–114.
Stelten, M. E., and K. M. Cooper (2012), Constraints on the nature of the subvolcanic reservoir at South Sister volcano, Oregon from U-series dating combined with sub-crystal trace-element analysis of plagioclase and zircon, *Earth Planet. Sci. Lett.*, *313–314*, 1–11.
Storm, S., P. Shane, A. K. Schmitt, and J. M. Lindsay (2011), Contrasting punctuated zircon growth in two syn-erupted rhyolite magmas from Tarawera volcano: Insights to crystal diversity in magmatic systems, *Earth Planet. Sci. Lett.*, *301*(3–4), 511–520.
Tanaka, H., H. Hoshizumi, Y. Iwasaki, and H. Shibuya (2004), Applications of paleomagnetism in the volcanic field: A case study of the Unzen Volcano, Japan, *Earth Planets Space*, *56*, 635–647.
Vazquez, J. A., and M. I. Lidzbarski (2012), High-resolution tephrochronology of the Wilson Creek Formation (Mono Lake, California) and Laschamp event using ^{238}U-^{230}Th SIMS dating of accessory mineral rims, *Earth Planet. Sci. Lett.*, *357–358*, 54–67.
Waters, L. E., and R. A. Lange (2013), Crystal-poor, multiply saturated rhyolites (obsidians) from the Cascade and Mexican arcs: Evidence of degassing induced crystallization of phenocrysts, *Contrib. Mineral. Petrol.*, *166*, 731–754.
Watson, E. B. (1996), Dissolution, growth and survival of zircons during crustal fusion: Kinetic principles, geological models and implications for isotopic inheritance, *Geol. Soc. Am. Spec. Pap.*, *315*, 43–56.

15252027, 2015, 4, Downloaded from https://agupubs.onlinelibrary.wiley.com/doi/10.1002/2015GC005714, Wiley Online Library on [29/08/2023]. See the Terms and Conditions (https://onlinelibrary.wiley.com/terms-and-conditions) on Wiley Online Library for rules of use; OA articles are governed by the applicable Creative Commons License

A mysterious moving mud spring near Niland, Imperial County, California

D. K. Lynch,[1] Travis Deane,[1] Justin Rogers,[2] Carolina Zamora,[1] James S. Bailey,[1] Dean Francuch,[1] Christopher W. Allen,[1] Cassandra Gouger,[2] David Dearborn,[3] Paul Adams,[4] and Andrea Donnellan[5]
1 Shannon and Wilson, Inc.; 2 Union Pacific Railroad; 3 Lawrence Livermore National Laboratory; 4 126 South Helberta Ave. #2, Redondo Beach, CA; 5 Jet Propulsion Laboratory

ABSTRACT—Along the southeastern edge of the Salton Sea, California, there are several areas with geothermal mud pots and mud volcanoes. These features may change shape, but their locations remain fixed. In 2016, adjacent to an older mound spring near Niland, a large, muddy CO_2-driven spring developed and began moving southwest. By early 2018 it was threatening local infrastructure; railroad tracks, petroleum pipeline, fiber optic cables and California State Route CA SR 111. On Oct 4, 2018 a sinkhole suddenly opened up, undermining part of the railroad tracks, that by then had been abandoned as a precaution. The Union Pacific Railroad has built two detour tracks and Kinder Morgan has rerouted its pipeline. The mud spring showed a variety of curious behaviors and movement patterns. Current projections are that the mud spring will reach CA SR111 in a few years.

Introduction

Mud pots and mud volcanoes (gryphons) are common in geothermal areas of the world. One place they are found is the Salton Sea Geothermal Field in southern California.[1-6] In this area, mud pots and mud volcanoes form when upward moving gases (primarily CO_2) produced below the water table entrains water and carries it to the surface, usually through sediment. If the sediment load is low and the muddy water is inviscid, mud pots form. If the mud is viscous enough to support itself, mud volcanoes form. In both cases, water is brought to the surface by rising CO_2, not by hydrostatic pressure as in artesian springs.

The Salton Sea Geothermal Field and the moving mud spring described here are in the Salton Trough, California. The trough is an active tectonic pull-apart basin,[1.] the result of right-hand steps in three right lateral transform faults of southern California and northern Baja, Mexico: San Andreas, Imperial and Cerro Prieto.[2] The area is seismically active and experiences frequent earthquakes and earthquake swarms. Much of the trough is below sea level. A number of geothermal electricity generating facilities have taken advantage of the high geothermal gradient.[2]

The Salton Trough is filled with several kilometers-deep Colorado River sediments that have been deposited in the trough during the last 5 million years.[2] Mineralogically the sediment is mostly very fine grained quartz with virtually no clay minerals, but the submicron particles produce clay-like plastic properties: slippery mud when wet and hard, earth when dry. Basement is several km down and rocks or boulders in the sediments are rare except near the Salton Buttes. In historic times, the trough has undergone periods of flooding, both naturally (Lake Cahuilla[7]) and manmade (Salton Sea[8]).

Carbon dioxide is the most common gas that seeps out of the soil, and commercial mining of CO_2 was carried out in the early part of the 20th century. Such emissions are widely distributed in the trough but go largely unnoticed except where CO_2 bubbles are apparent in surface water. The origin of the CO_2 has not been definitively identified: it could be hydrothermal alteration of carbonates to diagenetic greenschist facies[9,10] or plutonic CO_2 from the shallow magma body[10] producing the high geothermal gradients. H_2S is also present in the area, and ammonia occurs in and around the Salton Sea's geothermal features. Methane is rare but not unknown.

While mud pots and mud volcanoes can change shape as more fluid is brought to the surface, or precipitation and wind erode them, their locations remain largely unchanged. In 2016, however, a moving mud spring developed[11] on private land that threatened local infrastructure: railroad tracks, petroleum pipeline, fiber optic cables, and a highway. It soon became clear that the spring was not going to stop and would eventually reach the railroad tracks and beyond. As a result, the railroad's attempted mitigation was forced by circumstances to become accommodation. In this paper we report the chronological development of the mud spring, and many aspects of its geology, hydrology and behavior.

Historical developments.

The origin of the mud spring is as murky as its water. The landowner of the property near the southeast corner of California State Route 111 (CA SR111) and Gillespie Road in Imperial County (Figure 1) reported that a small spring had been present at this location for decades, and only grew to ~80 ft across in the early part of the 21st century. Google Earth historic imagery shows a large pond appearing between 2002 and 2005. Lynch and Hudnut[3] labeled this large shield-like mound spring "W9".

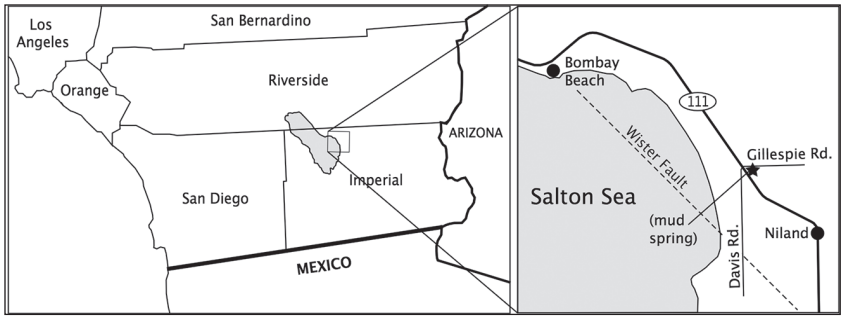

Figure 1. Map of the mud spring's area and its relation to the Salton Sea and Wister Fault.

It is one of about 30 seeps, mud pots and other hydrologic structures defining a NW striking lineament called the Wister Fault.[3] The Wister Fault is probably a southeast extension or abandoned strand of the San Andreas Fault.

In about 2005 when W9 became apparent in Google Earth, surface water and moisture also appeared west of W9 on either side of the railroad tracks and adjacent to the highway (Figure 2). By 2017, much of the soil in a parking lot of the Wister Unit of the Imperial Valley Wildlife Area located west of the highway began to show areas of surface moisture along WSW lineaments (Figure 3). These moist areas were thought to be water that was related to the mud spring. Their WSW trends suggested cross faults through which water could come to the surface.

From 2005 to2016, water from W9 flowed west and south and came within about 60 ft of the Union Pacific Railroad (UPR) tracks. In 2014 the Imperial Irrigation District cut a trench on the NE side of the W9's caldera to redirect the water away from the tracks. Yet the water soon found a way to come even closer and was redirected south and west toward the Salton Sea.

The moving mud spring appears

In mid 2016, an ambient temperature CO_2-driven mud spring appeared that partially overlapped W9. Gas sampling confirmed CO_2 with minor H_2S. The mud spring began moving southwest toward the UPR tracks and CA SR111 at about 16 ft per month (very uncertain). The new spring, called W9a, is less than a mile NE of the Wister Fault and it was moving perpendicular to it, as though along a cross fault.

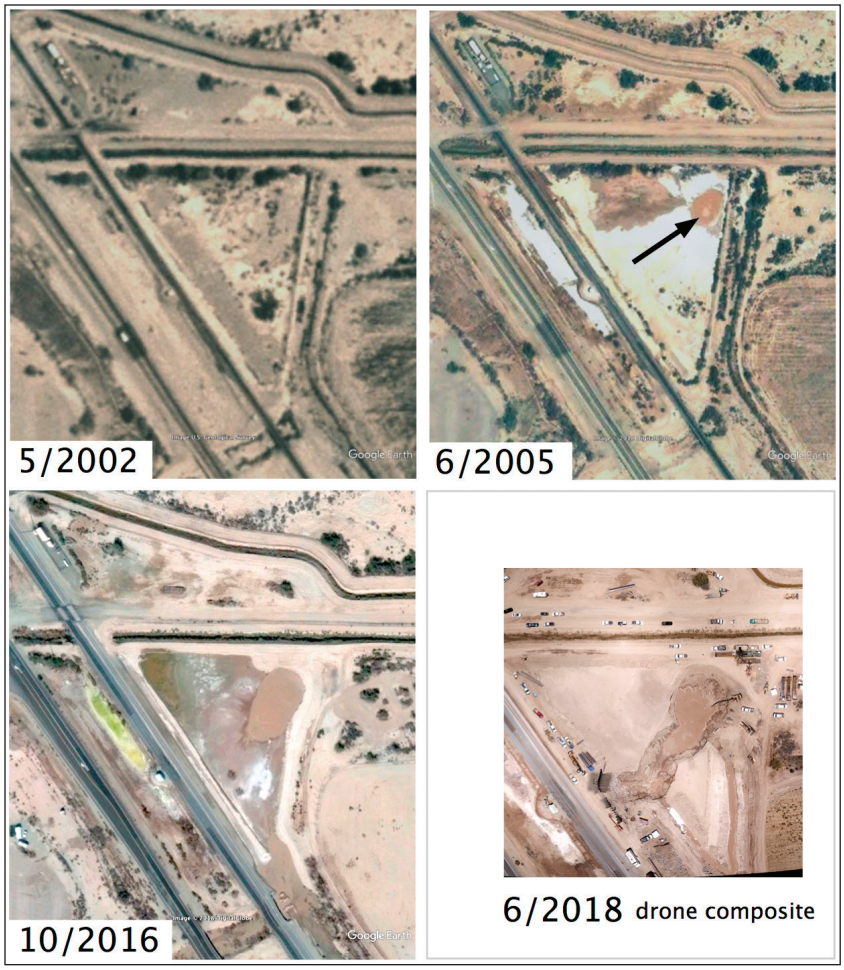

Figure 2. Time series from Google Earth showing the appearance of W9 (arrow) and the first detection of the moving mud spring (2016) as a southwestern elongation of W9. The moving mud spring only appears here after 10/2016. Moist areas are obvious after 2005.

UPR hired Shannon and Wilson, Inc. in May 2018 to manage the site and mitigate the threat. By this time W9a had carved out a large basin about 11 ft deep that was filled with muddy water (Figure 3). A number of acoustic imaging studies were carried out and riprap was dumped into W9a to "plug the hole" but this didn't work. Most of the rock sank into the mud and vanished below the water's surface.

A 140 ft long sheet pile wall was constructed in May and June 2018 down to a refusal depth of about 75 ft (Figure 3). The goal was to stop or slow down W9a's southwesterly movement and to maintain the integrity of the sediment between the piles and tracks. Around this same time, the mud spring seemed to changed direction and began moving more westerly.

As W9a advanced, it fluidized the sediment and grew to a ~24,000 sq ft basin about 11 ft deep, representing the removal of 250,000 cf of sediment (Figure 3). Water sampling revealed that the sediment-to-water ratio was 0.051 by volume, and the sediment particles in the water were small, on average less than a micron in diameter. Moving in a fairly straight line, the spring remained

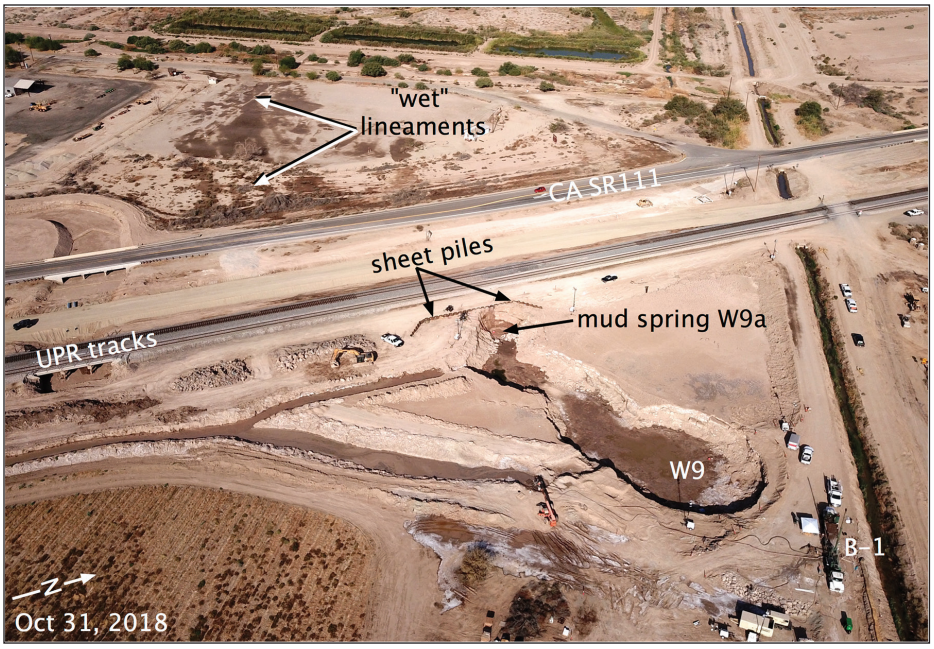

Figure 3. Aerial view of the area around the mud spring W9a. View looking west. The elongated basin is evident as are the two diversion channels leading southward that carried water from the basin to the Salton Sea. The UPR railroad tracks and CA SR111 are shown, along with the wet soil lineaments in the California Department of Fish and Wildlife parking lot west of the highway. Photo taken 31 Aug. 2018, after the basin was drained in June 2018.

a discrete, point-like structure and did not develop into a linear trench-like source as might be expected.

In June a well was drilled NE of W9's former location and about 350 ft from W9a in the hope that it would decompress the aquifer that was powering the spring. When the drill reached a depth of 326 ft below grade, there was a blowout. Mud, CO_2 and water shot from the well to a height of around 100 ft. In a few hours the blowout gradually subsided, though the well produced water for many days afterwards. No discernable effect on W9a was detected following the blowout.

As a precaution, UPR constructed a shoofly (detour track) west of the existing tracks in July 2018. Owing to surface moisture and scattered standing water with alkaline deposits, a 500 ft long section of soil was first dewatered and stabilized using engineering lime down to a depth of about two ft along the planned path. An elevated railroad bed was prepared followed by deposition of ballast and laying the tracks. The plan was to use the shoofly temporarily if the mud spring started to undermine the existing tracks. Consideration was also given to building a bridge over any failed tracks if necessary.

In late June 2018, UPR decided to drain the basin in order to reduce hydrostatic pressure on the sheet piles and water diffusion through the sediment toward the tracks (Figure 3). It also allowed for better monitoring of the spring. Pumping involved disposing of 5 million cubic feet of water. When drained, the basin was found to have a flat bottom 10-15 ft deep, though a little deeper at the spring. Draining the basin obliterated W9 but its original CO_2 sources remained evident: dozens of small, bubbling mud pots and mud volcanoes at the bottom of the basin at the NE end. Pumping W9a itself continued, the discharge being somewhat variable but averaging around 40,000 gallons per day (5100 cf/day). Daily pumping is carried out.

By mid July 2018, W9a had reached the sheet piles, 40 ft from the tracks. Bubbling water began to erode the sediment and expose the east side of the piles (Figure 4). The sediment on the west side remained in place and continued to support the eastern railroad track. At this time the spring remained more-or-less fixed immediately adjacent to the east side of the sheet piles, though it wandered a bit. There was concern that the spring's subsurface source was continuing to move westward under the sheet piles. This would eventually undermine the sediment between the sheet piles and the tracks. The fact that W9a appeared to remain stationary

Figure 4. Photograph of W9a with view looking northwest, with railroad tracks just beyond the exposed sheet piles. Centers of the sheet piles are 56 inches apart. Photo taken 12 Sept. 2018 by Carol Zamora.

east of the sheet piles was because this location was the only conduit though which the spring's pressure could be relieved. As we later found out, the spring was indeed carving out a hollow in the sediment west of the sheet piles.

In August 2018, UPR authorized drilling of two more decompression wells, both east of the tracks. Well B-2 was 100 ft NNW of the spring (now hard against the sheet piles) and well B-3 was 100 ft SW of the spring. B-2 was advanced to a depth of 800 feet. It encountered predominately dense to plastic clays with interbeds of fine to medium sand and silt. No significant water-bearing zones were found. One region of high pressure CO_2 gas was encountered around 550 feet. This zone was sealed off with steel casing when the hole was drilled deeper. B-3 was drilled to about 405 feet and revealed similar dense to plastic clays with interbeds of fine to medium sand and silt. A high pressure CO_2 gas zone was encountered near 400 feet that stopped the drilling for several days. Upon the resumption of drilling, B-3 continued to vent CO_2 gas continuously when the wellhead valve was open. When the valve was shut, CO_2 pressure built up to at least 140 psi after several days. Regardless of whether either valve was open or closed, there was no discernable effect on the mud spring.

In mid August 2018, W9a's behavior changed dramatically. Instead of a constant, vigorous bubbling flow, it would stop for a few seconds or minutes, only to resume. In the following three weeks, the spring began cycling between the sudden onset of a violent, splashing outburst and a more gradual lessening of activity leaving the spring nearly quiescent for several minutes, except for minor flow and isolated bubbles. Initially the period was 4–5 minutes but by late August had dropped to around a minute. Soon the outbursts became hardly perceptible and by early September the spring resumed its constant flow as it had been doing in previous years. By then, many of the sheet piles had become exposed down to a depth of 22 ft (Figure 4), the average water level maintained by pumping.

Gas and water pumped from W9a were measured every day. CO_2 levels at the surface near the spring were almost always within safe levels, rarely (and temporarily) rising enough to be of concern. H_2S levels were always within safe limits. On August 26 (2018), a gas monitor was lowered down along the sheet piles to within 2 ft of the spring's surface. Here CO_2 was off scale (high), O_2 was 2.4%, H_2S was 61.7 ppm and SO_2 was zero.

Sheet pile breach

During August and September 2018, W9a remained fixed relative to the sheet piles and continued to erode the pool's periphery east of the sheet piles until the walls were vertical. Bouguer microgravity measurements revealed an area of reduced gravitation, suggesting that a cavity was forming just west of the sheet piles. On October 3 gurgling was heard coming from a surface crack that opened up immediately west of the sheet piles. Jets of muddy water were also seen squirting to the east.

The next morning (October 4, 2018), a shallow, three foot wide, bubbling mud puddle was seen about 3 ft west of the sheet piles, an ominous sign. At 1:15p that afternoon, a ~60 ft diameter, 25 ft deep sinkhole suddenly opened up (Figure 5). It spanned the ground between the sheet piles and the eastern most railroad track, which at

Figure 5. Before-and-after aerial photographs of the sinkhole. North is up. On September 20th (upper) W9a had not breached the sheet piles. On October 4th when it appeared (lower picture taken October 5), the sinkhole was roughly the same width as the mud spring basin east of the sheet piles (lower, photo on 5 October 2018). The southwest lip of the sinkhole was just touching the eastern track, which by this time had already been taken out of service. A small spring was visible on the 5 Oct image northwest of the main spring in a ~2ft diameter crater (white arrow pointing to dark spot on the NW crater wall). This would grow to become the dominant spring by early 2019.

the time had stationary railroad cars on it. Travis Deane witnessed the collapse and reported:

> "In preparation of the scheduled 1330 call with UPRR and other team representatives, I approached the new mud spring from the NE at about 1315 to make observations before the call. When I approached the area, I observed jets of dust shooting approximately 5 feet vertically into the air where the new mud spring had previously been observed. The jets stopped after about 15 seconds followed by loud rattling of the sheet piles. I ran over to the north end of the sheet piles to observe the geyser [mud spring] in the caldera area and the sheet piles when an explosive release of gas and dust occurred between the sheet piles and Main 1 track. I did not observe water being released during the explosion. Several nearby people from the railroad observed the gas explosion and began recording video of the event with their cell phones. The ground collapsed about 20 to 25 feet between the sheet piles and the ballast shoulder, measuring approximately 35 feet wide by 70 feet long. The entire event occurred in less than five minutes. The sinkhole ….. continued to cave on the sides."

With W9a exposed west of the sheet piles, its true location could now be measured. It was 20 ft SW of the sheet piles. Based on its location of 40 ft NE of the sheet piles in early July 2018, the spring had moved about 60 ft SW, a rate of about 110 ft/yr. Some measurements suggest that the speed the spring is moving is not constant.

Riprap was immediately dumped into the sinkhole, this time *west* of the sheet piles. As before, this was done to keep the sediment in place that was supporting the eastern shoofly. Soon individual piles began to sink into the mud and they began to tilt westward into the sinkhole. So more rip rap was placed in the sinkhole against the sheet piles. In late October 2018 the sink hole was excavated to the southwest by about 40 ft in order to monitor the spring's movement and help predict its future path (Figure 6).

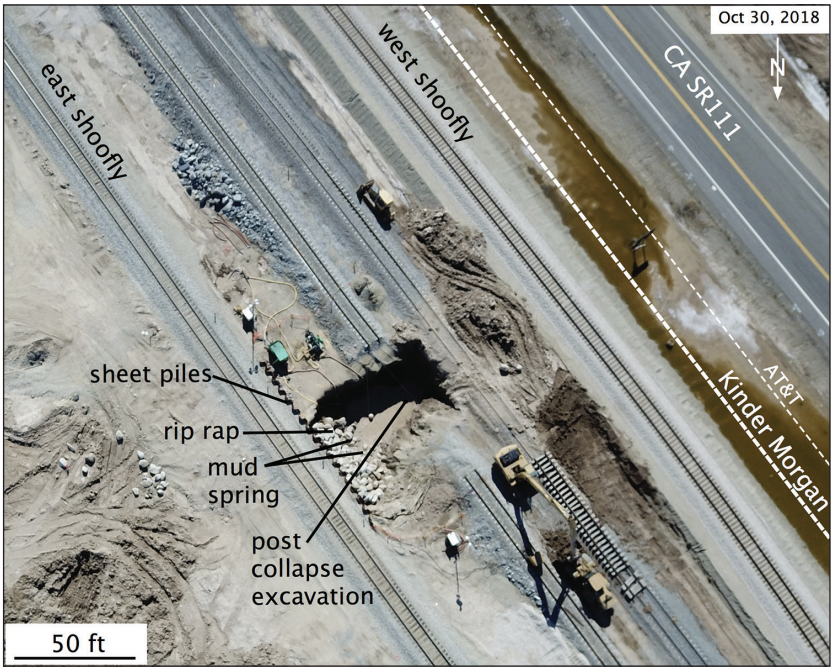

Figure 6. Infrastructure near the mud spring. Railroad track locations are evident and the approximate location of the Kinder Morgan pipeline and AT&T fiber optic cables are shown.

Accommodation and later developments

By mid October 2018, work crews refilled the basin with sediment because it was dangerous, with steep sides and containing much CO_2. This allowed UPR to build a second shoofly east of the mud spring, so that they once again had two operational tracks. Owing to the relatively sharp

Figure 7. Aerial photograph of the mud spring areas showing the two shooflies curving around the two formerly active tracks. View looking northwest on 31 Oct 2018.

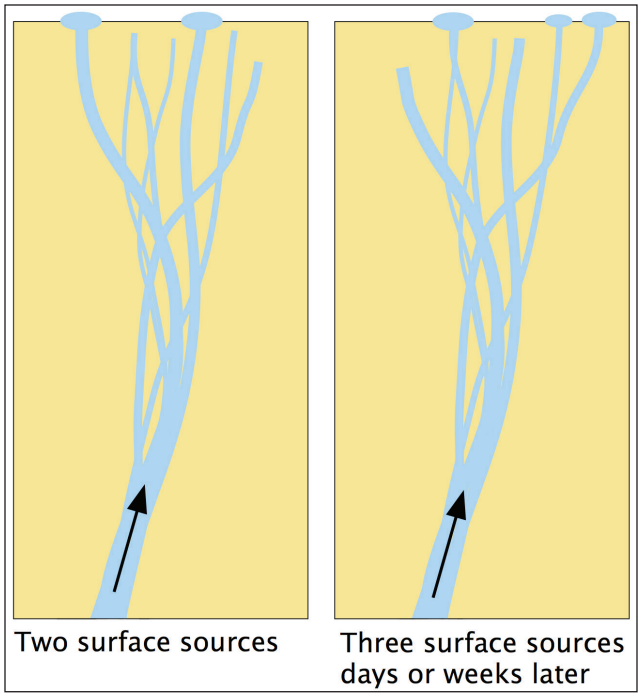

Figure 8. "Hydra" structure in water rising through sediment. As internal erosion causes sediment to collapse in a conduit, upward flow is blocked. This creates excess pressure which forces the flow to shift to another conduit or make a new one. Although the spring appears to "hop" around, the underlying source is not changing.

curvatures of the shoofly tracks, trains were required to slow down to about 30 mph to pass the mud spring.

In late October 2018, two boreholes were drilled west of the west shoofly for Kinder Morgan, whose petroleum/gasoline pipeline was now only 150 ft from the spring. Both reached a depth of 100 ft and produced very wet mud at a depth of about five feet, probably residual moisture from when W9a first appeared (Figure 2). Below that only interbedded dry sediment and sand were encountered.

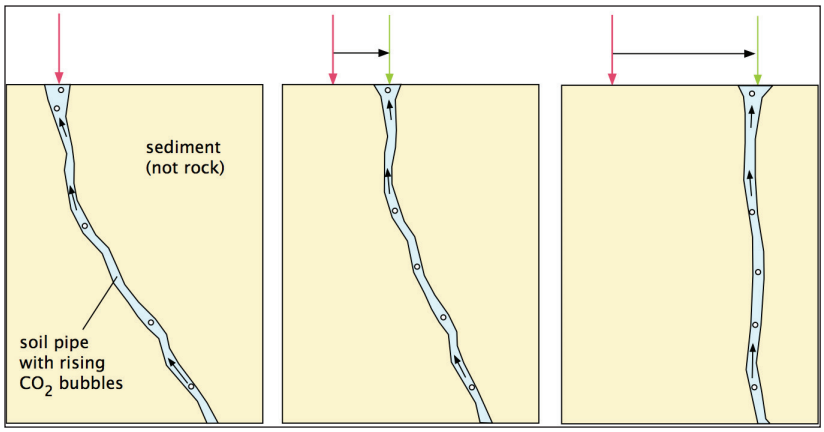

Figure 9. A tilted soil pipe with water entrained by rising CO_2 would be expected to erode the walls of the pipe. This would remove sediment from the upper (right hand) part of the pipe and deposit it on the lower (left hand) part, leading to a gradual migration of the surface spring to the right, and toward a point on the surface that is directly above the deep source. At this juncture, movement of the spring would cease.

Between October 2018 and March 2019, a curious thing happened. The main mud spring on the southeast side of the sinkhole grew less active while the tiny spring on the northwest flank expanded and became more active. By January both springs were producing at about the same rate and by March, the NW spring had become clearly dominant. Such behavior had been seen before and was interpreted as the spring "hopping around." In this case, however, it was clear that there were two separate springs (at the surface) and their water production varied inversely with one another.

Speculation on the causes of mud spring motion

Mud spring W9a has shown two kinds of movement: (1) a short-term (weeks to months), where the spring appears to hop around by 10–20 ft. and (2) a long-term southwesterly displacement of hundreds of feet over a period of years. Though the reason for the movement remains a mystery, we suggest two related mechanisms that can to explain the movement and are consistent with the observed geology and hydrology in the area. Both involve subsurface sediment collapse.

The short-term motion might be explained by a "hydra" structure (Figure 8), analogous to the "flower" structure found in faults. As water approaches the surface, it becomes progressively less constrained by hydrostatic pressure from the overlying sediments. Weak portions of the near-surface sediment allow the spring to split into many branches. Being in sediment that is being eroded by rising water and CO_2, there are occasional sediment collapses beneath the surface that block flow and locally create extra pressure. The extra pressure causes the flow to push into or shift to another branch that reaches the surface. In this way, several surface springs may be present. As one wanes and another one grows, the spring appears to "hop around."

To explain the long-term motion of the spring, consider a structure called a *soil pipe*.[12,13] Soil pipes are tubular flows through sediment driven by gravity. While this spring is driven by buoyant CO_2 gas bubbles, both would be expected to undergo internal erosion of the enclosing sediments. This could result in soil collapse that blocks the flow and redirects it, thus moving the surface location of the spring. The CO_2 variant of the soil pipe model is shown in Figure 9. If the conduit through which water is brought to the surface is tilted, erosion would tend to remove sediment from the upper parts of the pipe and deposit it on the lower parts. This would lead to a gradual movement of the spring that would also maintain the spring as a discrete source. This model predicts that the spring would move toward a point on the surface directly above the deep source.

When this location is reached, the spring would stop moving.

For this mechanism to work, the sediment must fall to the bottom of the pipe, rather than be carried upward by the water. This places some conditions on how the soil collapses, the speed of the water, and particle size of the sediment. Erosion could occur as a collapse of larger, more intact chunks of sediment. Otherwise the small particles might be carried upward and away, perhaps later settling to the bottom when the flow slows down.

Discussion

The inverse production between the SE and NW springs in the sinkhole after Oct 2018 supports the hydra structure model. As the two springs varied, water production remained constant, about 40,000 gallons per day. This suggests an unchanging deep source whose gas and water find their way to the surface by any route possible. Production is conserved, whether through a singe spring or several.

Regarding the hydrology of the area, we can only say that the water table—if such a concept makes sense here—is patchy and inhomogeneous. This seems reasonable because there are two dry wells within 100 ft of W9a, which is producing 40,000 gallons of water a day. The explanation may be that the water source is not moving, but rather the CO_2 source is moving, and this is what is driving the mud spring. If there is no major CO_2 source on either side of the spring, no water would be brought to the surface and therefore the CO_2 emission would pass unnoticed.

Could W9a (or the CO_2 source) be moving along a northeast striking fault? It seems likely. The spring's movement in a southwesterly direction is nearly perpendicular to the controlling faults in the area, mainly the San Andreas, as though moving along a cross fault. Cross faults are well known in the area, though none have been mapped at the spring's location, primarily because the land surface has been heavily modified by agriculture and conservation efforts. Scarps and other tectonic structures have been largely erased. There is nothing in the seismicity to suggest an active fault. The moist soil lineaments in the parking lot of the California Department of Fish and Wildlife parking lot west of CA SR111 may be revealing an increase in near-surface water in the last few years. Their SSW trends could be indicative of cross faulting by which water reaches the surface.

Another fault geometry could also produce SW moving spring (Figure 10). Instead of a cross fault striking NE, suppose that a shallow dipping fault striking NW and dipping SW was present. Such a fault might be a growth fault, a nontectonic fault found in deltaic sediments.[14,15] When rising water reached the fault plane, it would be diverted along the fault in a SW direction. Even though it would encounter a planar fault, the water would move upward at an angle along the fault following the steepest possible path (SW), thereby carving out a soil pipe, like the ones shown in Figure 9.

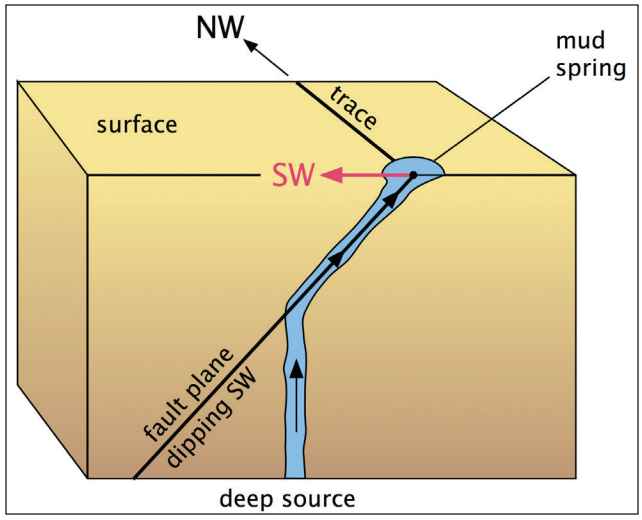

Figure 10. A northwest striking, southwest dipping shallow angle fault could provide the necessary conditions to explain the direction of the mud spring's motion. Water from a deep source rises vertically until it reaches the fault. The fault—having fractured sediment along its plane—provides the easiest route of ascent. The direction of flow changes from vertical to obliquely upward when it reaches the fault. Water rises along the steepest angle of inclination, in this case southwest.

As of this writing (March 2019), the situation is more or less like that shown in Figure 7, except Kinder Morgan has done significant excavation to reroute their pipeline around W9a and the former location of W9.

Stay tuned!

If W9a's movement remains unchanged, it is expected to reach the western shoofly by the end of 2019. The pipeline and fiber optic cables will be affected by mid 2020 and SR111 by 2021. Exact predictions are impossible to make because this spring is a unique geological mystery.

As interesting as the mud spring is, the railroad is not amused. Nor are the pipeline, fiber optic cable, and highway people, all of whom must deal with the time, effort and cost to accommodate the apparently unstoppable threat. At its current rate of movement—about 110 ft per year southwest—W9a will remain a fascinating headache for several years to come—maybe more.

A moving mud pot is unique in our experience and in this case, it appears to be unstoppable. We have described its behavior and attempts at mitigation. Even though we know a fair bit about the spring and its machinations, there still remain a number of fundamental, unanswered questions:

1. How can a spring move?
2. How can it move and remain a discrete source?
3. Why was the bottom of the basin (after emptying it) flat and horizontal?

4. What is the chemical source of the CO_2 and from what depth does it originate?
6. Why did the spring undergo periodic cycling?
7. What is the subsurface geometry of the spring?
8. What is the water table geometry, in light of the fact that virtually no water was found within a hundred feet of the mud spring down to a depth of over 500 ft?

Acknowledgements

The authors would like to thank David Buesch for heroically thorough comments that helped make this paper better. We also recognize and appreciate the many people from many organizations who worked on this project.

References

1. https://en.wikipedia.org/wiki/Salton_Trough

2. Alles, David L., 2011, Geology of the Salton Trough, http://fire.biol.wwu.edu/trent/alles/GeologySaltonTrough.pdf

3. Lynch, D.K., Hudnut, K.W., 2008, The Wister mud pot lineament: Southeastward extension or abandoned strand of the San Andreas Fault?: Bulletin of the Seismological Society of America,, v. 98, no. 4, p. 1720-1729,

4. Sturz, A., Kamps, R., and Earley, P., 1992, Temporal changes in mud volcanos, Salton Sea geothermal area: in Water-Rock Interaction, edited by Y. Kharaka, and A. Maest, , Balkema, Rotterdam, Netherlands p. 1363–1366.

5. Onderdonk, N., Shafer, L, Mazzini, A. and Svenson, H., 2011 Controls on the expression and evolution of gryphons, mud pots, and caldera features at hydrothermal seeps in the Salton Sea Geothermal Field, Southern California, Geomorphology, 130, 327-342.

6. Svensen, H., Karlsen, D.A., Sturz, A., Backer-Owe, K., Banks, D.A., Planke, S., 2007, Processes controlling water and hydrocarbon composition in seeps from the Salton Sea geothermal system, California, USA: Geology, v. 35, no. 1, p. 85–88

7. https://en.wikipedia.org/wiki/Lake_Cahuilla

8. https://en.wikipedia.org/wiki/Salton_Sea

9. Keith, Terry E. C, L. J. Patric Muffler, and Marcelyn Cremer, 1968, Hydrothermal Epidote formed in the Salton Sea Geothermal System, California, The American Mineralogist, 53, 1635-1644.

10. Maseki Enami, Juhn G. Liou and Dennis K. Bird, 1992, Cl-Bearing Amphibole in the Salton Sea Geothermal system, California, Canadian Minerologist, 30, 1077-1092

11. Lynch et al., 2018, A Moving Mud Pot Threatening Railroad Tracks and a Highway, Imperial County, California, Southern California Earthquake Center Annual meeting, Palm Springs.

12. Wilson, G., J. Nieber, R. Sidle, and G. Fox. 2013, Internal Erosion During Soil Pipe Flow: State of Science for Experimental and Numerical Analysis. Transactions of the American Society of Agricultural Engineers, St Joseph, MI, 56(2):465-478

13. Schneider, C. 2015. From Pores to Pipes: The Problem of Underground Erosion in Soils. Soil Horizons, 55, 1-3

14. Susanna K. Taylor, Andrew Nicol and John J. Walsh, 2000 Displacement loss on growth faults due to sediment compaction, J. Structural Geology, 30(3,) 394-405

15. Lerche, I. 1994 Notes on growth faults and sedimentary bed motions, Mathematical Geology, 26(6), 677–715

Journal of Volcanology and Geothermal Research 347 (2017) 15–43

Contents lists available at ScienceDirect

Journal of Volcanology and Geothermal Research

journal homepage: www.elsevier.com/locate/jvolgeores

Sulfate mineralogy of fumaroles in the Salton Sea Geothermal Field, Imperial County, California

Paul M. Adams *, David K. Lynch, Kerry N. Buckland, Patrick D. Johnson, David M. Tratt

The Aerospace Corporation, P. O. Box 92957, Los Angeles, CA 90009, United States

ARTICLE INFO

Article history:
Received 4 March 2017
Received in revised form 8 August 2017
Accepted 26 August 2017
Available online 31 August 2017

Keywords:
Salton Sea
Fumaroles
Sulfates
Mascagnite
Remote sensing
Mako

ABSTRACT

The Salton Trough lies in the transition between the San Andreas Fault and oblique spreading centers and transform faults in the Gulf of California. The Salton Sea Geothermal Field is the northernmost expression of those spreading centers. In ~2007 two ammonia-emitting fumarole fields that had been submerged beneath the Salton Sea were exposed for the first time in nearly 50 years. As the sea level continued to drop these fields have developed a number of boiling pools, mud pots, gryphons and a unique suite of ammonium sulfate minerals. These have been studied over time with long-wave infrared remote sensing coupled with ground truth surveys backed by laboratory analyses of the minerals. Many vents lie at the center of concentric rings of mineralization with systematic occurrence of different minerals from center to edge. Three semi-concentric zones (fumarole, transition and evaporite) have been defined with respect to ammonia-emitting vents and bubbling pools. The scale of these zones range from several meters, localized around individual vents, to that of the fumarole fields as a whole. The fumarole zone is closest to the vents and locally contains cavernous sulfur crystals and significant deposits of gypsum, mascagnite, boussingaultite and other ammonium sulfates. The transition zone comprises a dark brown surficial band of inconspicuous sodium nitrate underlain by anhydrite/bassanite that is thought to have formed by ammonia-oxidizing microbes interacting with the ammonium sulfates of the outer fumarole zone. The evaporite zone is the outermost and contains blödite, thenardite and glauberite, which are typical of the sulfates associated with the shoreline of the Salton Sea. Remote sensing has shown that the mineral zones have remained relatively stable from 2013 to 2017, with minor variations depending on rainfall, temperature and levels of agricultural runoff.

© 2017 Elsevier B.V. All rights reserved.

1. Introduction

The Salton Trough is a topographic low in southern California and northern Baja California, Mexico that represents a tectonically active, sedimentary pull apart basin (Lonsdale, 1989; Brothers et al., 2009; Gurbuz, 2010). Except for minor contributions from the surrounding mountains and aeolian sources, most of the sediments in the Salton Trough represent Colorado River sediments and are as thick as 6 km (Muffler and White, 1969). The trough is structurally controlled and lies in the transition between the right lateral San Andreas Fault system to the north and a series of oblique spreading centers and transform faults in the Gulf of California to the south (Macdonald, 1982). The area is dominated by a number of contiguous right lateral, right stepping (releasing) transform faults including the Imperial and Cerro Prieto faults (Meltzner et al., 2006) and those of the Sierra Cucapah in Mexico (Hauksson et al., 2011).

Within the Salton Trough lies the Salton Sea Geothermal Field where the geothermal gradient averages ~0.3 °C/m (Younker et al., 1982), reaching a maximum of 4.3 °C/m (Lee and Cohen, 1979). About 11 commercial geothermal electricity generating plants operate in the area with a combined output of about 340 MW. The high geothermal gradient is the result of a shallow magma body from one or more spreading centers (Lachenbruch et al., 1985; Schmitt and Vazquez, 2006). Extruded magma produced the Salton Buttes, five late Quaternary rhyolitic volcanic necks near the southeastern end of the Salton Sea (Robinson et al., 1976; Newark et al., 1988). From south to north they are Obsidian Butte, Rock Hill, Red Island (north and south) and Mullet Island. The age of some of these volcanic structures has recently been dated to 2400 ybp (Schmitt et al., 2013). Recent thermal surveys have located moderate temperature (30 °C) thermal vents on Red Island north (Lynch and Adams, 2014) but the majority of higher temperature surface thermal features are concentrated southeast of Mullet Island (Lynch et al., 2013).

The Salton Sea occupies the lowest part of the Salton Trough. It is a saline, eutrophic, endorheic rift lake (Dangermond, 2003; Hurlbert, 2008) that was created when a canal breach diverted the Colorado River into the Salton Trough in March 1905 and fresh water flowed north through the New and Alamo Rivers (Kennan, 1917). After the canal was repaired in Feb 1907, the high water level of -59 m MSL decreased rapidly to around -76 m MSL in 1917. Rain and agricultural

* Corresponding author.
E-mail address: paul.m.adams@aero.org (P.M. Adams).

https://doi.org/10.1016/j.jvolgeores.2017.08.010
0377-0273/© 2017 Elsevier B.V. All rights reserved.

runoff gradually raised the sea level, reaching a high of about -70 m MSL in the mid-1980s, after which legislation resulted in a gradual lowering of the sea level that continues to this day (Lynch, 2011).

Where the Salton Sea overlaps the Salton Sea Geothermal Field, the interaction of rising gas and hot water with sea floor sediments has produced a number of fumaroles, gryphons and salses (LeConte, 1855; Veatch, 1858; Veatch, 1860; Hanks, 1882; Muffler and White, 1968; Helgeson, 1968; Sturz et al., 1992; Svensen et al., 2007, Svensen et al., 2009; Lynch and Hudnut, 2008; Onderdonk et al., 2011; Manga et al., 2009; Rudolph and Manga, 2010). Much of the activity involves rising CO_2 produced by hydrothermal alteration of calcareous components of the Colorado River sediments (Muffler and White, 1969). When bubbling water sometimes stands in the calderas of gryphons, they are termed salses. Salses are often called mud pots, and may vary in fluid content between water with small amounts of sediment to thick, viscous mud. Gryphons are relatively rare geological structures and tend to occur at active plate margins like the Salton Trough. Fumaroles, gryphons and salses with elevated temperatures often emit gasses such as CO_2, H_2O, SO_2, H_2S, NH_3, and CH_4 (Dimitrov, 2002).

The Salton Sea level began dropping about 1983, and around 2007 the fumarole fields in this study were exposed along the southeast shore for the first time since about 1945. The Salton Sea level varies seasonally in a sinusoidal fashion with a difference of about 0.35 to 0.55 m over the year with the maximum in March and the minimum in November (Fig. 1). This depends on rainfall and temperature but the Imperial Irrigation District (IID) also delivers water to the Salton Sea, and removes water from it according to their needs. Over the period of this study (2009–2017) the sea level dropped about 1.4 m. The average yearly rainfall is about 5 cm with the majority being recorded in 1–2 major events (1.5–3.5 cm) related either to late summer monsoonal or winter storms (National Weather Service, 2017).

The area to be described is an active moderate temperature (to 100 °C) ammonia-emitting and sulfate-rich fumarole area (N 33.2184, W 115.601) which has an unusual assemblage of ammonium sulfate minerals that is located 8.1 km WSW of Niland, Imperial County, California. Ammonium sulfates are uncommon and are typically associated with fumaroles (Koenig, 1969; Dunning and Cooper, 1993) or burning coal heaps (Lapham et al., 1980; Parafiniuk and Kruszewski, 2010; Masalehdani et al., 2009). There are five fumarole fields in the general area (F1–F5) (Lynch et al., 2013) and the Davis-Schrimpf fumarole field lies 3.2 km to the southeast on the same trend (Mazzini et al., 2011; Onderdonk et al., 2011). The latter field is located at the corner of Davis and Schrimpf roads. The F1 and F2 fumarole fields (Fig. 2) are the largest and most accessible and are located on a sand spit southeast of what was Mullet Island (Lynch et al., 2014), and have been described in detail by Lynch et al. (2013). Based on historic imagery available in Google Earth, F2 was exposed sometime between August 2006 and February 2008. The area was visited by airboat on June 8, 2007 and the F2 region was found to be partially exposed. Owing to seasonal changes in Salton Sea water levels (Fig. 1), F1 and F2 have probably experienced several episodes of submersion and subaerial exposure between 2006 and 2008. Surface mud flow patterns changed markedly between the two dates. Between August 2010 and January 2011 the water level had dropped sufficiently to expose F1. In September 2011 native sulfur producing vents at F1 and F2 were confirmed for the first time. Since the vents were not noted in January 2011 it is clear that many of them surfaced during the eight month period between visits. At that time several unusual ammonium sulfates were identified, including boussingaultite and lecontite (Lynch et al., 2013). More detailed follow on field studies were conducted between October 2013 and February 2017 (Adams and Lynch, 2014). A compilation of all field visits is presented in Table 1.

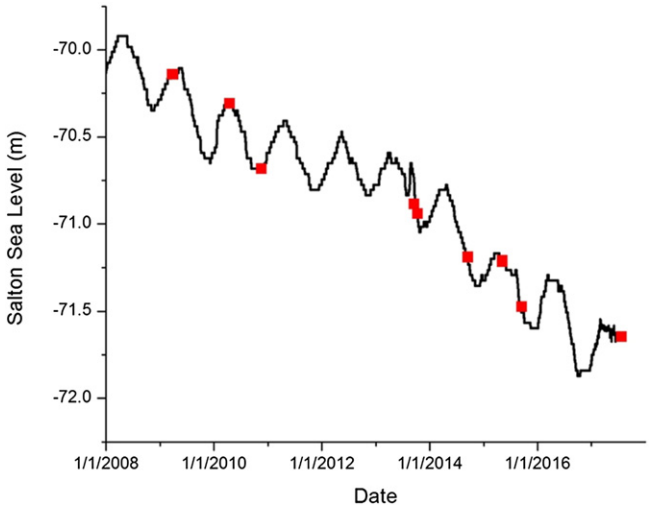

Fig. 1. Salton Sea level (above NGVD 1929) measured from the USGS Westmorland Gauging station. Larger squares are dates of remote sensing data collects. (https://waterdata.usgs.gov/nwis/dv?referred_module=sw&site_no=10254005.)

There recently (2016) has been significant activity by the IID to control both irrigation runoff and more importantly windblown dust emissions. This has resulted in a significant change to the local fumarole landscape (Fig. 3). As part of a pilot project under the Salton Sea Management Program to mitigate windblown dust the IID has constructed a field of north-south oriented, 0.5 m-deep trenches, spaced about 2–3 m apart, that closely surrounds F2 on three sides and F1 on two sides. The purpose for the trenches was to trap low lying windblown sand and collect water for waterfowl habitat. Many of these trenches have acted as irrigation ditches which bring water from the marsh area to the east of the fumaroles westward and have inundated a source for windblown sand. The net result has been that while the Salton Sea level has dropped, F1 is now (based on a February 2017 visit) closely surrounded by shallow water on all sides and is difficult to approach because of very soft mud. During the spring of 2017 the 4 km trail to the fumaroles was blocked with a locked gate and "No Trespassing" signs were posted thereby restricting access. The long term existence of the fumarole field is also in jeopardy as the area has recently been leased from IID by a commercial entity as a site for a future large scale geothermal generating facility. Preliminary plans place the facility directly on top of the fumarole fields.

This study describes the sulfate mineralogy of the F1 and F2 fumarole areas in detail based on field observations from 2013 to 2017 supported with laboratory analyses of collected samples. It is coupled with long wave infrared (LWIR — nominally 7.5–13.5 μm) remote sensing studies from 2009 to 2017 which were used to map the large scale distribution of minerals over the evolution of the fumarole fields from shortly after they emerged from the Salton Sea. Ground truth surveys in 2014 and 2015 verified the remote sensing mineral identifications. There have been relatively few studies of this type which have combined extensive field collection and laboratory analysis to validate the LWIR remote sensing retrievals. Vaughan et al. (2005) performed ground truth sample collection with laboratory analyses for the Steamboat Springs, NV geothermal area. Reath and Ramsey (2013) performed a remote sensing study of the nearby Davis-Schrimpf fumarole field with limited coverage of the F2 field in this study but with limited ground truthing. This study serves as important documentation of the fumarole field mineralogy since its long term accessibility is in question as a result of dust mitigation efforts by the Imperial Irrigation District and the potential development of a large scale geothermal facility directly on the site.

2. Methods

2.1. Remote sensing

The fumarole areas have been studied by airborne LWIR hyperspectral remote sensing using the SEBASS (Hackwell et al., 1996)

Fig. 2. Google Earth image (2015) showing the F1 and F2 fumarole fields in relation to Mullet Island (MI) and the Alamo River (AR). There is additional fumarole activity at F3 and offshore northwest of Mullet Island.

and Mako (Warren et al., 2010; Hall et al., 2011) sensors in nine data collects between 2009 and 2017 (Table 1). Mako and its predecessor SEBASS have been widely used for passive remote sensing and identification of gasses and minerals (Tratt et al., 2011; Buckland et al., 2017; Kirkland et al., 2002, 2003). SEBASS has been used in the study of other geothermal systems including the nearby Davis-Schrimpf fumarole field (Reath and Ramsey, 2013) and Steamboat Springs, Nevada (Vaughan et al., 2005). The spectroscopic observation and identification of sulfates by remote sensing is of considerable interest based on the detection of Mg and Fe sulfates on Mars (Cluotis et al., 2006; Chou et al., 2013) and the environmental consequences of acid mine runoff on Earth, which produces sulfates as a byproduct (e.g., Kim et al., 2002; McCauley et al., 2009).

These sensors operate in the nominal 7.5–13.5 μm atmospheric window. SEBASS is a nadir-viewing roll-stabilized push-broom system with an 8° swath width and 1.1-mrad instantaneous pixel field of view (IFOV), while Mako is a 3-axis stabilized whisk-broom system with a swath width programmable up to 110° and 0.55-mrad pixel IFOV. Both systems have approximately the same spectral resolution (~46 nm in 128 channels) but Mako offers superior radiometric sensitivity. The spatial resolution (ground sampling distance) of SEBASS and Mako is determined from the altitude and for these studies ranged from 0.5 m to 2 m (Table 1).

The fumarole areas were visited 19 times between 2009 and 2017 (Table 1). This included two ground truth surveys that were performed at the same time as remote sensing collects since many of the mineral growths were ephemeral and changed over time depending on rainfall, temperature, the level of the Salton Sea and agricultural irrigation runoff. An additional ground truth field operation was performed within one month of the remote data collect in 2013. Comprehensive field collects in 2013 prior to the ground truths, and subsequent mineral identifications provided the list of known minerals, from which the eight dominant minerals were plotted in the final remote sensing mineral maps. During ground truth surveys each collection site was located using a handheld Garmin 60csx GPS receiver. The accuracy of the Garmin was on the order of ±1–2 m. As a result of the 19 field collects, over 300 samples were collected and analyzed by XRD and a similar number of Exoscan FTIR spectra were collected in the field.

The procedure for correlating remote sensing mineral maps and sample locations evolved over time since early ground truth surveys yielded equivocal results. The final method (September 2015) involved placing 25 1 m × 1 m aluminum foil (0.05 mm thick) panels around areas of interest at the margins of the various fumarole fields and near areas of mineralogical interest. This was accomplished the day before the remote data collect. Accuracy of the GPS coordinates at the Al panel end points of Exoscan traverses were ±1 m while all others were ±2 m. The bright panels are readily visible in context images taken from the aircraft with a Canon 5D Mk II camera (Fig. 4a). Between a combination of the Al panels, thermal vents and vegetation it was relatively easy to correlate field observations of mineral deposits with the context visible images, LWIR images and Tactical Analysis Report (TAR) mineral images (Fig. 4). The latter were provided to the field crew within 3 h of the flight (at the Brawley airport, BWC) and guided ground truth sampling locations for the next 1–2 days. A detailed description of the TAR is given below. The Al panels were easily discerned in the LWIR images as black "cold" pixels while thermal vents appeared light and vegetation appeared slightly darker than background. Finalized multicomponent mineral maps were typically not available until about a week after the remote collect. Larger areas (5 m^2) of minerals identified in the TAR images were selected for ground truth sampling in order to maximize the chances of correct sampling considering errors in relating features in the field with context camera, LWIR and TAR mineral images. This typically limited the minerals sought in ground truth surveys to mascagnite, gypsum, nitratine and blödite, since they were the most abundant.

Table 1
Summary of field visits and remote sensing data collects.

Date	Method[a]	GSD[b] (m)	Rainfall in preceding 3 months,[c] date (m/d) (cm): daily **max/min** temperature (°C)[d]	Local time of remote collect; comments
6/24/2017	Mako	1	6/02(0.05), 5/27(0.15), 5/10(0.15): **48/26** °C	6:00 PM
2/11/2017	Field			F1 nearly surrounded by shallow water
11/25/2016	Field			Vehicular access no longer possible, dust abatement trenching completed
12/26/2015	Field			Exoscan surveys, limited dust abatement trenches present
11/26/2015	Field			Standing water returns
9/24/2015[e]	Mako/field	0.5, 1	7/20(0.28), 7/19(0.38): **42/25** °C	11:30 AM; very little standing water, mud is thick and ground dry
4/22/2015	Mako	1	3/3(0.15), 3/2(1.27), 1/30(0.08), 1/27(0.23): **28/16** °C	12:00 PM
11/27/2014	Field			Exoscan surveys
7/23/2014[e]	Mako/field	1	No rainfall: **47/28** °C	9:45 AM
1/18/2014	Field			Exoscan surveys
12/20/2013	Field			Exoscan surveys
11/6/2013[e]	Field			
10/12/2013	Field			
9/24/2013	Mako	2	9/8(0.97), 9/8(0.05), 9/5(0.33), 8/29(0.23), 8/27(0.43), 8/26(0.69): **37/18** °C	4:00 PM
8/28/2013	Mako	1	8/27(0.43), 8/26(0.69): **41/27** °C	5:00 PM
9/10/2012	Field			
2/12/2012	Field			
10/12/2011	Field			
9/15/2011	Field			Sulfur found at F1and F2 vents
7/28/2011	Aircraft			Low altitude imaging
1/26/2011	Field			F1 exposed, lab samples collected
1/18/2011	Field			F1 exposed
11/19/2010	Aircraft			USGS Lidar study
9/18/2010	Mako	1	8/28(0.41): **42/18** °C	7:30 PM; night time remote collect
8/13/2010	Field			F2 exposed with mudflows
4/6/2010	SEBASS	1	4/2(0.18), 3/08(1.68), 2/20(0.15), 2/10(0.43), 2/7(0.53): **25/9** °C	8:40 AM; F2 exposed with mudflows
3/26/2009	SEBASS	1	2/17(0.53), 2/8(0.41): **31/13** °C	3:00 PM
7/8/2007	Airboat			F1, F2 covered with a few cm's of water
2006	Field			F1, F2 covered by Salton Sea

[a] Field collect or remote sensor
[b] Remote sensing ground sampling distance (GSD).
[c] From: www.cnrfc.noaa.gov/archivePrecipMap.php?area=rsa&month=11&day=23&year=13.
[d] At Imperial Airport; https://www.wunderground.com/history/airport/KIPL.
[e] Ground truth survey.

Details of the custom data processing developed for Mako are provided in Buckland et al. (2017). Spectral calibration is accomplished by viewing blackbody sources through a NIST SRM 1921b polystyrene film that has known absorption features and performing a least-squares fit across the entire focal plane array. Radiometric calibration, determined by observing calibrated blackbody sources at different known temperatures, is used to convert the raw instrument output to useful radiance units. Georeferencing of images is accomplished by the instrument flight software continuously recording sensor position (latitude, longitude, and altitude) from the global positioning system (GPS) and attitude (roll, pitch, and heading) from the inertial navigation system (INS) and the scan mirror encoder angles. The measured sensor radiance includes contributions from the atmospheric transmission and upwelling radiance which impose spectral features (primarily due to H_2O, CO_2, O_3, CH_4, and N_2O) onto the data. Atmospheric compensation to remove these features is accomplished through the ISAC (In-Scene

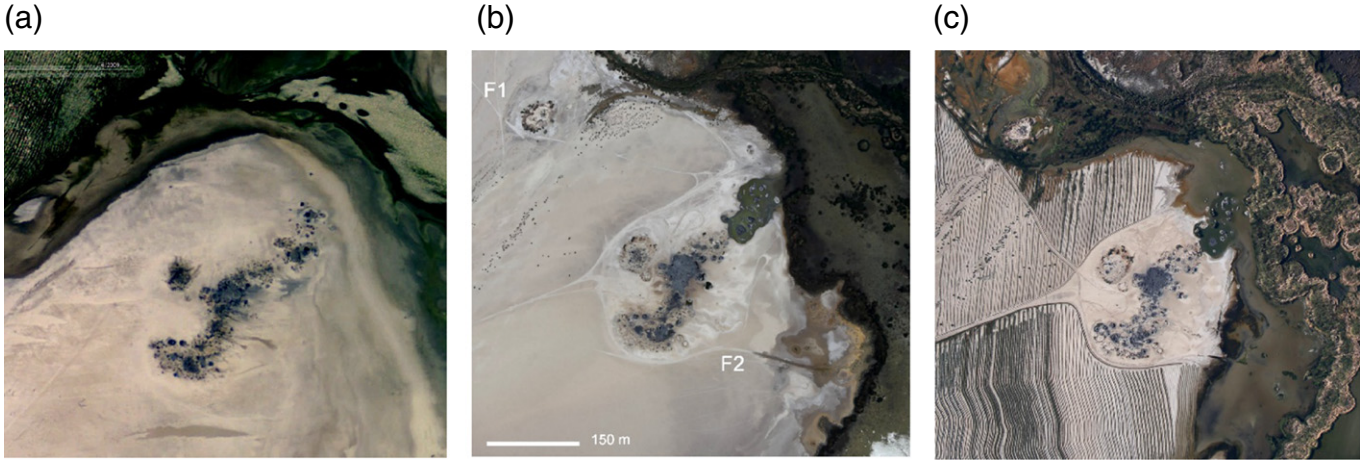

Fig. 3. Evolution of the F1 and F2 fumarole fields between 2009 and 2017. (a) Google Earth image from 2009 before the emergence of F1, (b) Context camera image, remote sensing collect April 22, 2015, (c) Context camera image, remote sensing collect June 24, 2017 after completion of the dust mitigation trenching program.

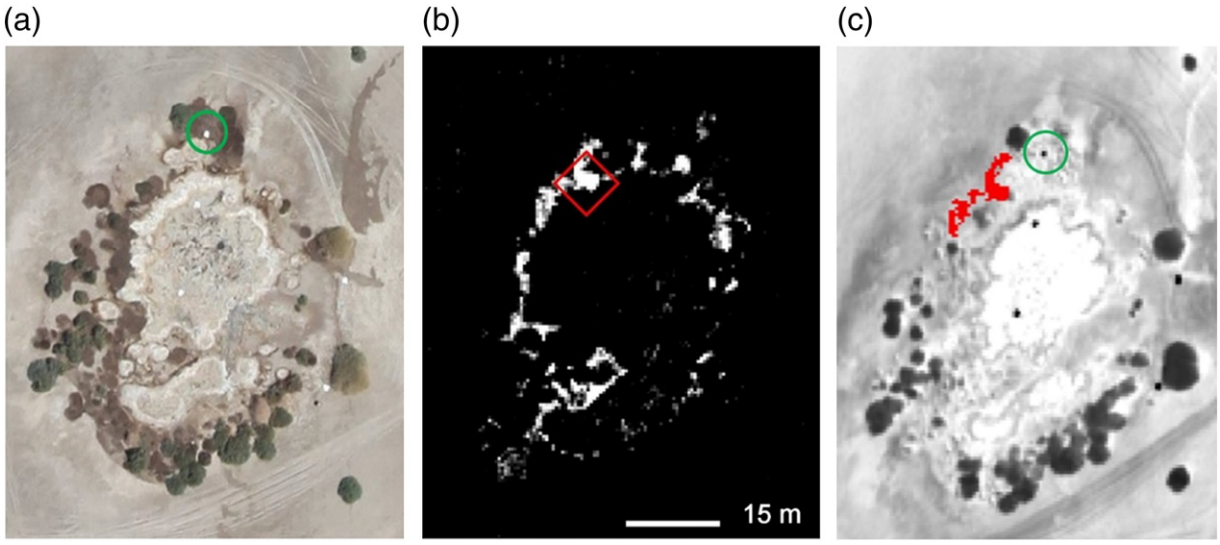

Fig. 4. F1 fumarole field (9/24/2015). Comparison of (a) context camera image, (b) ACE filter output (nitratine) extracted from TAR and (c) LWIR image (~11 μm) with a nitratine ROI used to locate sampling areas for ground truthing. Green circle denotes one of five 1 m × 1 m aluminum foil panels in the scene which appear bright in the context image and black in the LWIR image. Red diamond is centered on the pixel in the ROI with the greatest filter output value. The red ROI comprises connected pixels with filter output values above a specified threshold value used for ID, and in combination returned a nitratine identification in the tactical analysis.

Atmospheric Compensation) algorithm (Young et al., 2002) which makes use of the natural occurrence of blackbody (or near blackbody) surfaces within the scene (e.g., areas covered by healthy vegetation or water) and exploits the natural temperature variations over these surfaces to extract transmission and upwelling contributions directly from the measured data.

The Aerospace solids library currently in use contains 4186 reflectance signatures that have spectral features in the LWIR region and is compiled primarily from Aerospace, USGS (Clark et al., 2007), UCSB-MODIS (University of California, Santa Barbara), ASU 1.1 (Christensen et al., 2000), ASTER 2.0 (Baldridge et al., 2009), and USGS-VEG (Ribeiro da Luz and Crowley, 2010) libraries with the addition of signatures of special origin (PNNL 3.0 and NEF 9.7). The spectral library signatures are organized into family categories. The user supplies a compounds (families) of interest list (COI) and the TAR is automatically generated and subsequently updated whenever a detection and identification result contains a signature belonging to a family within this COI list. This list was based on minerals previously identified from the fumaroles (Adams and Lynch, 2014).

Solid signature variability in the LWIR is common and can be produced by variations in particle size, moisture content and aging in some cases. It is not necessary (or desirable) to produce detection filters for all of the signatures that are contained within a family. Only the spectrally unique signatures within a family are required, and the software automatically interrogates each requested family to provide a series of distinct signatures that serve as representative surrogates for the entire family. These signatures are then used to create the detection filters.

Target detection is accomplished through the use of the adaptive coherence estimator (ACE; Manolakis et al., 2003) spectral filter which provides a fast and robust method for detecting the presence of pixels with spectral similarities to known target signatures within the data with a minimal amount of user input and preparation. This filter outputs the cosine of the spectral angle in whitened space between the atmospherically compensated radiance for each pixel (after removing the scene mean vector) and the library signature under investigation. (The concept underlying data whitening in the context of hyperspectral imagery is outlined in Manolakis et al., 2003.) The whitening transformation is constructed from the full-scene covariance matrix of the data and is used to produce spectrally uncorrelated data with unit variance across the spectral channels. In the case of the fumarole area, the spectral mean scene vector represents quartz sand and halite mixtures and the consequence of the mean scene removal process means that quartz/halite cannot be identified/mapped.

Each of the spectral filter output images (ACE) are automatically assessed for the presence of target signatures by requiring that the filter output values exceed some predefined threshold value within a specified region of pixel connectivity. These region of interest (ROI) specifications are each encoded with the location (pixel coordinates, latitude and longitude) corresponding to the pixel with the largest magnitude of filter output within the ROI, the number of pixels contained within the ROI and the mean spectrum of the ROI pixels. The mean spectrum of each ROI is then passed to the identification stage for further processing. Until this final step the ACE images only represent regions with spectral similarities to the signatures used to create the various filters.

The goal of target identification is to uniquely determine the composition of the mean spectral vector for each ROI, using a library of possible reference spectral signatures. This is done by applying the *stepwise* generalized least-squares (GLS) algorithm (Draper and Smith, 1998) coupled with a large spectral library database that currently contains 4186 solid signatures. Once the ID is complete, a tactical analysis report (TAR) entry is generated and subsequently updated whenever the ID results contain a requested compound (signature) included within the COI list. These TAR entries display an ACE filter output as gray-scale using a specified linear stretch with red-diamond target designator overlaid (Fig. 4b), and a ROI image that shows the pixels selected for ID superimposed in red onto the thermal image (~11 μm, Fig. 4c). A real-space representation of the spectral fit using the combination of signatures that were identified in whitened-space is also returned by the ID algorithm (e.g., Fig. 5). The TAR report contains the sum of the entries for all the ROIs for each mineral for each whisk. For scattered mineral occurrences with poor connectivity there may be a considerable number of ROIs and TAR entries for each mineral.

Examples for a nitratine TAR entry at F1 are given in Fig. 4 where the red diamond is centered on the pixel in the ROI with the greatest ACE filter output value (highest spectral correlation to signature). The ACE filter output images are displayed using a linear stretch of 2σ to 6σ which translates to brightness of the pixels corresponding directly to filter output strength in this range. The red ROI comprises connected pixels with filter outputs exceeding a specified threshold value. The

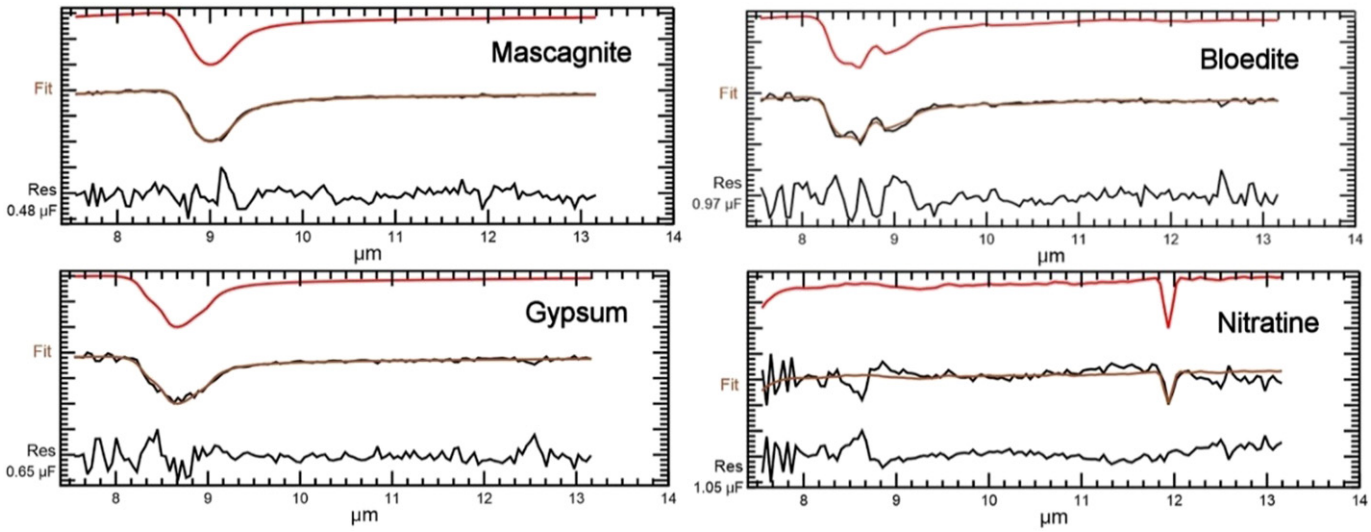

Fig. 5. Example comparisons of library reference spectra (top), real-space representation of the spectral fit using the combination of signatures that were identified in whitened-space (middle) and the spectral residuals (with RMS value) of the spectral fit (bottom). The scale of the spectral residual has been expanded to show detail. From the 9/24/2015 Mako data collect.

mean spectrum of these ROI pixels returned a nitratine identification in the tactical analysis.

Fig. 5 shows examples of library reference spectra along with a real-space representation of the spectral fit using the combination of signatures that were identified in whitened-space. The middle plot displays the atmospherically corrected (minus background and mean scene vector) ROI spectrum superimposed with the best spectral fit from the library. The spectral residuals (with RMS value) of the spectral fit are also shown with the scale expanded to show detail.

The SEBASS/Mako GSD (ground sample distance) ranged from 0.5 to 2 m depending on altitude. Therefore in most cases the measured radiance was integrated over regions containing a variety of surface materials, often significantly so. The ID algorithm is capable of returning up to 10 compounds from the library through linear unmixing in whitened space (if necessary) to successfully fit the data of mixed pixels.

Large scale false-color multi-mineral maps compiled from georeferenced whisk mosaics are created by following a similar procedure with the ID done on each pixel (rather than selected ROI's). These maps are generated by ignoring all but the dominant spectral (not spatial) component. Typically about 8 minerals are mapped so that individual colors (minerals) can be easily discriminated. The generation of these maps was more time consuming since an identification must be performed for each pixel rather than the individual ROIs in the TAR, and this process was not generally completed until about a week after the data collect. Estimation of pixel fill fraction is generally not possible since many of the spectra in the solids spectral library are not calibrated for absolute measurements.

2.2. Laboratory and field studies

Mineral identifications were made using powder X-ray diffraction (XRD), coupled with energy dispersive X-ray spectroscopy (EDS) in the scanning electron microscope (SEM). XRD was performed with a PANalytical X'Pert Pro diffractometer using copper radiation. A small amount of material (typically 0.05 g) was scraped from the surface and ground in a mortar and pestle and pressed against a zero background plate (quartz crystal cut so as to produce no XRD reflections). In the scraping process it was common to incorporate some underlying material (typically quartz sand). Most samples were analyzed in θ–2θ

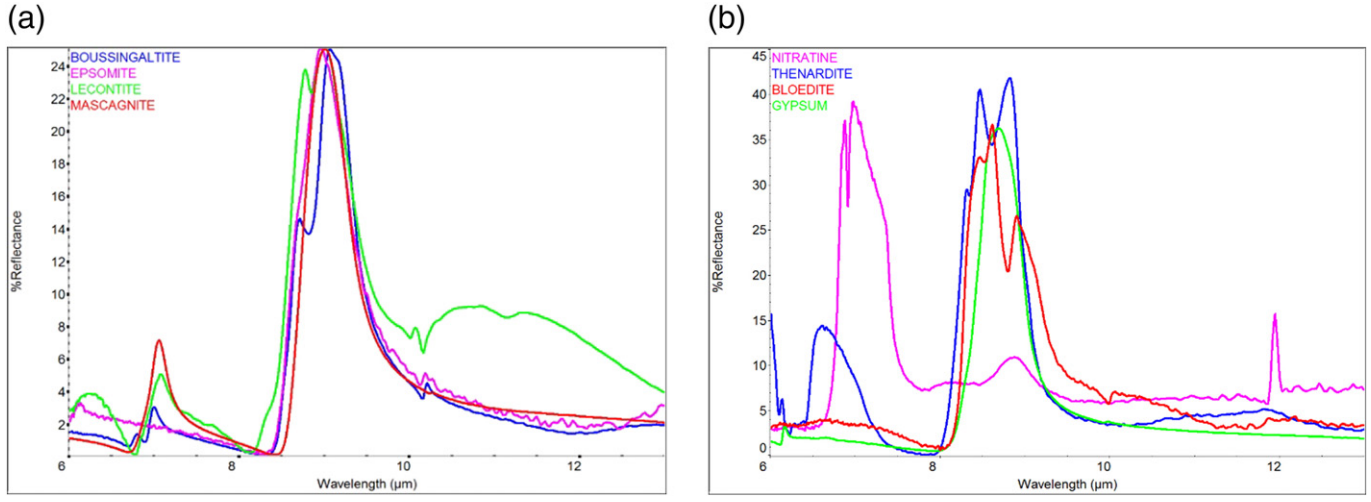

Fig. 6. Comparison of biconical reflectance spectra of minerals from the fumarole fields. Spectra scaled for better comparison. (a) Boussingaultite, mascagnite, lecontite, and epsomite. (b) Nitratine, blödite, gypsum and thenardite.

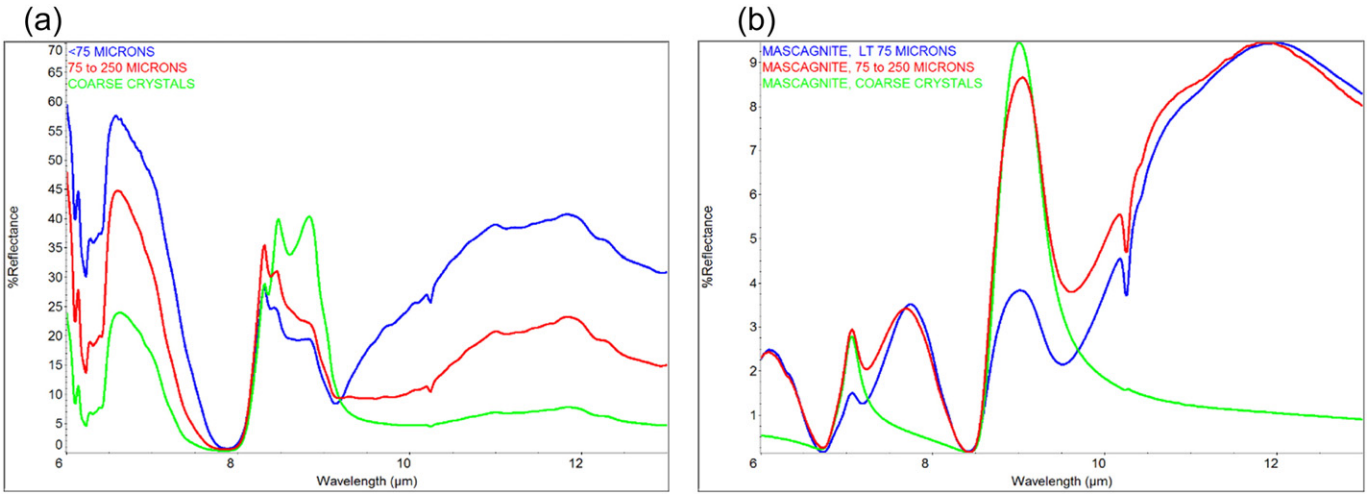

Fig. 7. Comparison of biconical reflectance spectra as a function of particle size. (a) reagent sodium sulfate (thenardie). (b) reagent ammonium sulfate (mascagnite).

mode with an X'Celerator strip detector for quick analysis. Selected surfaces were analyzed directly with parallel beam optics (X-ray mirror and parallel plate collimator). This method was more surface sensitive (10s of μm) with less chance of incorporating underlying material but was more time consuming. It can also analyze irregular surfaces without introducing peak shifts or peak broadening from sample topography and displacement. Interpretation is more complicated as a result of fewer crystallites being present and the likelihood of preferential mineral growth directions, both of which produce different relative peak intensities compared to reference patterns.

SEM/EDS was performed with a JEOL model 6460LV variable pressure SEM (base pressure 35 Pa) equipped with an Oxford Xtreme EDS operated with INCA software. Cross sections of selected samples were prepared for SEM/EDS analysis in order to better understand mineral distribution as a function of depth. After pulling a vacuum to evaporate any remaining fluid, samples were potted and impregnated with epoxy. They were then sectioned dry with a band saw and ground and polished (120–1200 grit SiC) using mineral oil so as not to dissolve water soluble phases. The oil residue was removed with methanol and the samples were carbon coated to prevent charging in the SEM.

Laboratory Fourier transform infrared (FTIR) measurements were made at 4 cm^{-1} resolution with a dry nitrogen purged Thermo Nicolet model 6700 FTIR spectrometer equipped with DTGS and MCT-A detectors. Biconical diffuse reflectance measurements were performed using a Harrick "praying mantis" accessory. Labsphere Infragold was used as the background reference. Biconical reflectance (R) spectra can be related to remotely collected emissivity (ε) spectra by Kirchhoff's Law ($\varepsilon = 1 - R$) (Hunt and Vincent, 1968; Salisbury et al., 1994). Such measurements reproduce spectral shapes accurately but are not quantitative. Reference spectra were measured from selected samples identified by XRD as relatively pure materials. These reference spectra were added to the Aerospace Solids spectral library. Limited attenuated total reflectance (ATR) analyses were made with a Durascope single-bounce diamond ATR accessory. Laboratory measurements were ideally made within one week of field collects in order to minimize changes to the samples resulting from desiccation or subsurface fluids wicking to the surface by capillary action and dissolving existing species or precipitating new minerals.

An Agilent Technologies model 4100 Exoscan portable FTIR was used to make selected diffuse reflectance measurements. In the field the Exoscan was interfaced with a personal computer (PC) for data collection with both located under large umbrellas to provide cooling shade (daytime highs to 45 °C) and to make the PC screen visible in otherwise bright sunlight. Field samples typically had very rough surfaces which required the use of the 100 μm diffuse standard and maximum gain settings on the Exoscan in order to record spectra. Concentric mineral growths are commonly observed around thermal vents. In order to better understand these, sampling "traverses" were conducted and specimens were analyzed using the Exoscan. The traverses were oriented radially from the central vent and across mineral zones. Each traverse was marked with stakes beginning as close to a central sulfur producing vent or bubbling pool as possible and ending in sand/halite where there was no obvious mineral growth of interest. The locations of the stakes were recorded with GPS. A tape measure between the stakes was used to record the locations of samples which were collected and returned to the Exoscan for immediate analysis. This aided in the selection of material to be returned to the lab for further XRD analyses. Generally only those samples that produced a significant sulfate signature were considered for further XRD analysis since many of the minerals of interest mapped by airborne LWIR remote sensing were sulfates. During later ground truth surveys the ending traverse location was also marked with an aluminum foil panel which could be readily located in the airborne LWIR images. The Exoscan diamond ATR attachment, which produces transmission-like spectra, was also used to make selected mineral identifications in the field.

Fig. 8. F1 fumarole field from 8 m elevation looking south towards Red Island (11/26/15). Note vehicle for scale and steam from boiling pools and zoned mineralized satellite vents.

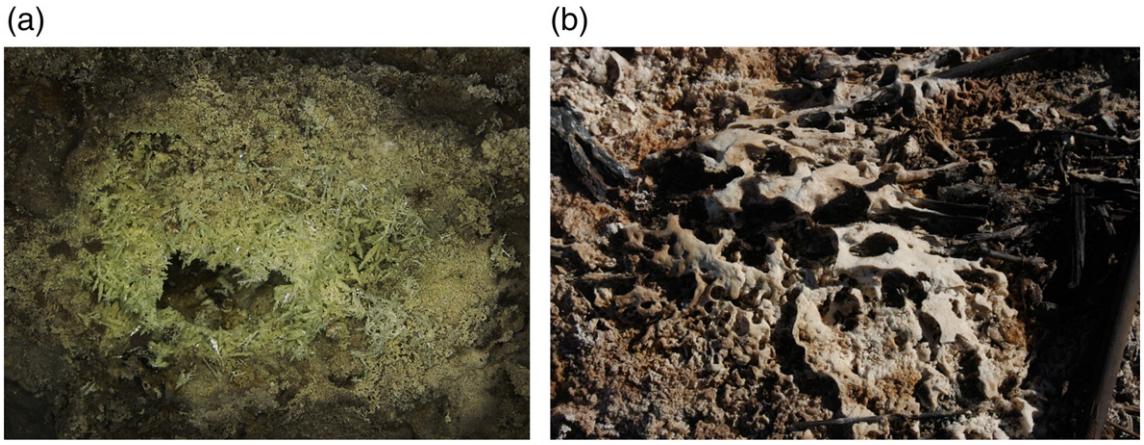

Fig. 9. (a) Sulfur producing vent at F1. Field of view is 8 cm. (b) Mascagnite growth on dead vegetation near a vent at F1. Field of view is 30 cm.

3. Infrared spectroscopy of sulfates

Sulfates, which are common at the fumarole fields, have characteristic absorption bands between 8.5 μm and 9.5 μm in the infrared that are attributable to ν_3 S-O bending and ν_1 S-O stretching (Cluotis et al., 2006; Lane, 2007). In diffuse reflectance (DR) spectra they appear as reflectance maxima (reststrahlen bands). Reference DR spectra were measured from selected samples identified by XRD to be relatively pure materials. Fig. 6 shows examples of representative spectra used for screening samples for further investigation. These reference spectra were subsequently added to the Aerospace Solids Library. The sulfate spectra are all very similar but show slight wavelength shifts and distinctive lobes and shoulders that can be used in identification. Boussingaultite, lecontite, mascagnite and epsomite have reflectance maxima from 9.07 μm to 8.96 μm, respectively, in descending order. Lecontite and boussingaultite can be distinguished by their subsidiary maxima at 8.78 μm and 8.71 μm, respectively. The nitrate band at 12 μm in the nitratine spectrum is distinctive along with the complex band at 7 μm, the latter of which cannot be observed in remote sensing spectra because it is outside the atmospheric window.

Reflectance spectra show variations which are dependent on particle size or surface roughness as the contribution from volume scattering over surface scattering increases with decreasing particle size (Hunt and Vincent, 1968; Salisbury and Wald, 1992; Mustard and Hays, 1997). Examples are shown in Fig. 7. In general, spectral contrast decreases with decreasing particle size and the intensity from the broad transparency feature at longer wavelength increases with respect to the reststrahlen band (Salisbury and Wald, 1992). This complicates remote sensing identifications since multiple spectra for individual minerals must be present in spectral libraries in order to cover a range of particle sizes. It was not possible to obtain fine grained (<75 μm) reference spectra for many of the fumarole sulfates and the only library spectrum for lecontite (Fig. 6a) most likely represents fine grained material based on the strong reflectance transparency feature at 11 μm.

Table 2
Total dissolved solids (TDS) content in pools from F1 and F2.

Location	Sample	TDS (g/l)	Residue determined by XRD
F1	A	3	GYPSUM, Halite, Sal ammoniac, lecontite, boussingaultite
F1	B	3	HALITE, Gypsum, lecontite, boussingaultite, sal ammoniac
F2	WP303	3	HALITE, Sal ammoniac, Gypsum, lecontite
F2	WP450	3	GYPSUM, Mascagnite, boussingaultite, lecontite
F2	WP451	34	HALITE, gypsum, sal ammoniac, sylvite, calcite?
F2	N Pool	87	HALITE, gypsum, unknown?
F2	SE Pool	3	HALITE, Gypsum, Sal ammoniac, boussingaultite
Salton Sea		48	HALITE, gypsum, blödite, hexahydrite

Abundance: MAJOR, Minor, trace.

4. Fumarole field mineralogy

4.1. Overview

F1, the westernmost fumarole field, is about 650 m SE of what was Mullet Island (Lynch et al., 2013) and 400 m NW of F2 (Figs. 2, 8). It is elliptical, about 25 m × 50 m, and has abundant small clear to thin muddy boiling pools, sulfur producing vents and associated sulfate accumulations (Fig. 9a, b). It has no elevated structures (gryphons) (Fig. 8). The subsurface generally consists of dark gray to black mud, sand and locally has hard deposits of cemented small pelecypod shells and remnants of plant stems. Unlike F2, F1 is surrounded by vegetation, predominantly iodine bush (*Allenrolfea occidentalis*). Living plants are in close proximity to the fumaroles and dead plant material is common and often mixed in with the mud and ammonium sulfates (Fig. 9b). Water temperatures were typically boiling (100 °C) and the total dissolved solids were 3 g/l compared with 48 g/l for Salton Sea water (Table 2).

The F2 field is roughly 120 m × 400 m and irregular in shape. It is subdivided into the F2 north complex (F2NC), a small outlier to the northwest and the F2 base complex (F2BC). Fluids at F2 are more viscous than at F1 which has allowed the development of hundreds of mud pots and gryphons to 1.5 m high, though the height varies with time and seasonal ground-water levels (Fig. 10a). Their base diameters varied from a few cm to up to 10 m. Some are single structures, others are composites of several gryphons that grew and merged together. F2 also contains hundreds of "mud towers", which consist of slender vertical tubes with central vents emitting hot gas and relatively thin mud (Lynch et al., 2013) (Fig. 10b). They ranged in height from a few cm to over 0.5 m, and were between 3 cm and 20 cm wide. Isolated mud towers were the most common, but many were also formed inside or atop composite gryphons. Water temperatures ranged from boiling to ambient for areas of some larger pools on the eastern margin of the field.

Laboratory analysis revealed that the main component of the mud from the gryphons was quartz (~60–80%). Gypsum, halite, calcite, dolomite and various minor feldspars were also present. Despite the variation in mud color, there was little if any difference in composition. A number of common sulfate minerals, including glauberite, bassanite, anhydrite, thenardite, and blödite, were present in minor amounts. The minerals found at F1 and F2 are similar. Ammonium sulfates are present at both fields but are much more common at F1. Sulfur producing vents and living and dead vegetation are more common at F1,

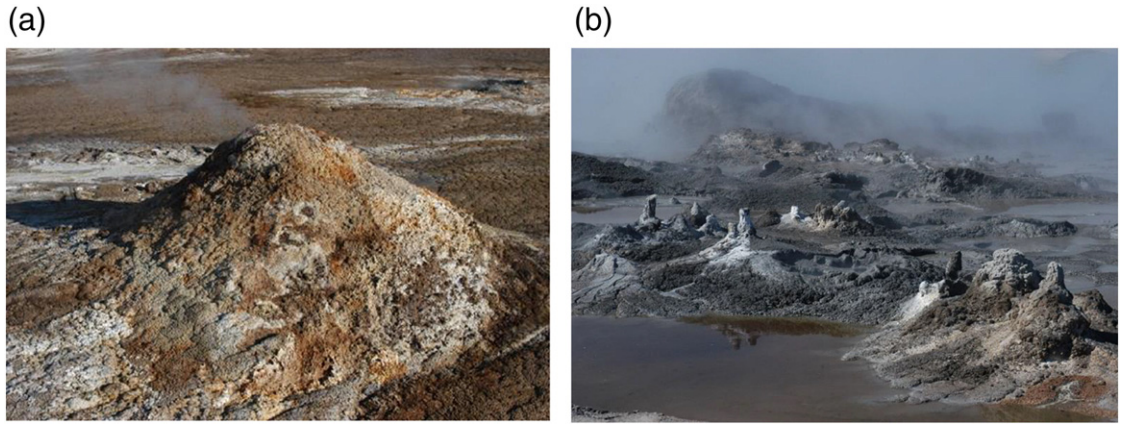

Fig. 10. (a) Sulfate encrusted gryphon (1 m high) from west side of F2 base complex fumarole field. (b) Field of mud towers from the southeast side of F2. Height of tubes is about 20 cm.

compared with F2. The fumaroles at F1 are less extensive but were more accessible than F2. Brown rings containing nitratine and anhydrite typically form around the ammonium sulfates at both F1 and F2 (Fig. 11).

Plumes of ammonia gas have been observed emerging from the F1 and F2 fields (Tratt et al., 2011, 2016) and are thought to produce the ammonium sulfates. The source of the ammonia had originally been assumed to originate from thermal decomposition of plant matter or fertilizer residues from agricultural runoff (Tratt et al., 2011 and references therein). However, it is noted that elevated levels of dissolved ammonia have been measured in the deep seated hypersaline brines beneath the region (Bishop and Bricarello, 1978; McKibben, 2008) and that ammonium salts were suspected far earlier than agricultural development (LeConte, 1855). Ammonia has not been detected from the nearby Davis-Schrimpf fumarole fields (Mazzini et al., 2011) but emissions of ammonia from the cooling towers of the associated Energy Sources Featherstone geothermal plant point to a more deep seated origin (Tratt et al., 2016). Ammonium sulfates have been found at other fumarole fields where irrigation and agricultural runoff are not a potential source of ammonia. This includes ammonioalunite, ammoniojarosite, boussingaultite, letovicite, mascagnite, and tschermigite from the Geysers in Sonoma County, CA (Dunning and Cooper, 1993; Koenig, 1969); tschermigite and boussingaultite from a geyser in Peru (Ciesielczuk et al., 2013) and boussingaultite from Coso Hot Springs, Inyo County, CA (Ross and Yates, 1942). A suite of rare ammonium-containing minerals have also been found at La Fossa crater, Vulcano, Sicily (DeMartIn et al., 2009). Ammonium-bearing feldspar and alunite have been observed at gold- and mercury-bearing hot springs deposits in Nevada, and California, as well as at several other hydrothermal systems in the western United States (Krohn et al., 1993). Ammonium sulfates are also commonly associated with exhalations from underground coal fires (Lapham et al., 1980; Parafiniuk and Kruszewski, 2010; Masalehdani et al., 2009).

The pH of the water in the bubbling and boiling pools (measured with colorpHast pH strips) is nominally neutral (6.5–7.5). The pH of pools at the nearby Davis-Schrimpf fumarole field, which were measured more accurately with a digital pH meter, ranged from 5.2 to 6.8 (Svensen et al., 2007, 2009; Mazzini et al., 2011). The total dissolved solids in 2 clear pools at F1 was 3 g/l and 5 clear to milky pools at F2 ranged from 3 to 87 g/l compared with 48 g/l for Salton Sea water (Table 2). Residues remaining after evaporation consist primarily of halite though gypsum was the main constituent of two pools. Minor to trace amounts of ammonium salts, such as sal ammoniac, lecontite, mascagnite and boussingaultite occur in some residues. The major residue from Salton Sea water is halite with trace amounts of gypsum, blödite and hexahydrite. It is interesting to note that mascagnite was not more common in the residues from the fumarole water considering how prevalent it is surrounding the pools and vents. As a result, it is clear that the extensive ammonium sulfate salts do not form from the simple evaporation of the water from the bubbling and boiling pools. Instead it is conjectured that ammonia and SO_2/H_2S percolating through the wet sand and mud near gas vents react to form ammonium sulfate solutions that are concentrated and then brought to the surface by capillary action to form the efflorescent growths (Fig. 9b). In fact, ammonia has been suggested as an effective agent for scrubbing SO_2 from the stacks of coal fired power plants (Shale, 1974).

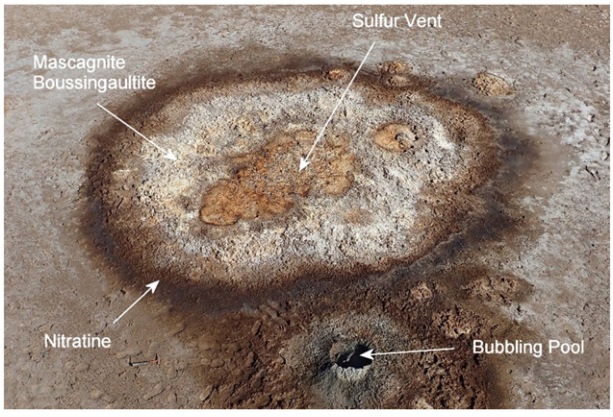

Fig. 11. Satellite vent at F2 showing mineral zonation from 6 m elevation. Field of view is 4 m. White areas and brown rings contain ammonium sulfates and nitratine, respectively.

4.2. Remote sensing results

4.2.1. Overview

The context camera image of the F1 and F2 fumarole fields from July 2014 is shown in Fig. 12a along with the brightness temperature image (Fig. 12b) computed from the radiance data. Temperatures >60 °C were recorded from a large area located in the center of F2. This corresponds with an area of bubbling mud (Fig. 13). Temperatures of up to 100 °C have been measured on the ground from selected mud pots and clear boiling pools at F1 and F2. A map of ammonia emissions is presented in Fig. 14a and shows four major sources. The ammonia abundances were determined by the procedure described in Buckland et al. (2017). The prevailing wind direction was to the SE so the sources of the plumes are at the western most points. The largest plume is correlated with the large high-temperature bubbling mud pot field in F2 (Fig. 13) which is relatively devoid of sulfate mineralization. Other significant ammonia emissions are located at F1, F2NC and F2BC. Fig. 14b is a map showing the eight most common sulfate minerals associated with the F1 and F2 fumarole fields superimposed on the thermal radiance image for reference. Only the dominant mineral in each pixel is plotted. This map was

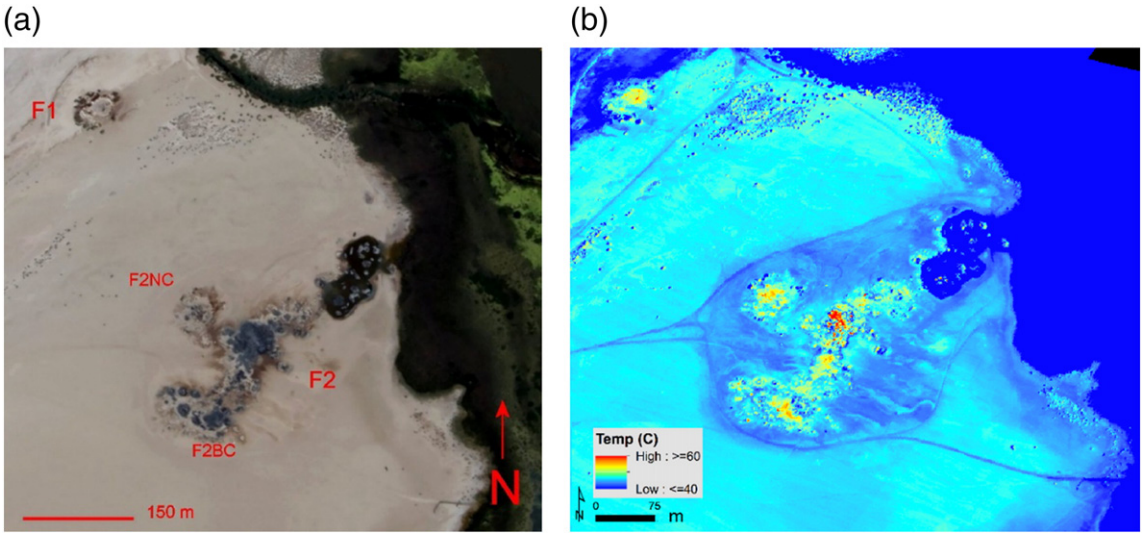

Fig. 12. (a) Context camera image of the fumarole fields on 7/23/2014. (b) Brightness temperature image of the F1 and F2 fumarole fields (7/23/2014).

created by combining 9 whisks. The sulfate minerals are not only associated with the areas of ammonia discharge in the F1 and F2 fumaroles but also occur along the brush/shore line bordering the marsh at the right of the image. A map of ten other sulfate minerals, including: alum-(Na), alunite, bassanite, glauberite, gwihabaite (ammonium nitrate) lecontite, mirabilite, sal ammoniac, sodium alum, tschermigite and urea was also generated. These other minerals, when present, generally only represented a few pixels and were difficult to locate and verify by ground truth.

Fig. 15 compares a more detailed view of the sulfate mineral map for F1 compared with the ammonia plume. The plume originates from a small area of boiling pools in the center of an area of gypsum but the ammonium sulfate and nitrate mineralization has developed a series of concentric zones a considerable distance (~20–30 m) from the greatest ammonia emissions.

An enlarged view of the mineral map showing the F2NC field along with the context camera image from September 24, 2015 are shown in Fig. 16. Darker rounded features which are not mapped as minerals are clumps of vegetation. At F2NC the minerals tend to define a series of somewhat concentric rings. Mascagnite [$(NH_4)_2SO_4$] and boussingaultite [$(NH_4)_2Mg(SO_4)_2 \cdot 6H_2O$] are found near the center, closest to the area of ammonia emission. These are followed outwardly by gypsum [$CaSO_4 \cdot 2H_2O$], nitratine [$NaNO_3$] and blödite [$Na_2Mg(SO_4)_2 \cdot 4H_2O$]. The blödite is more concentrated on the west side of the field while the nitratine is developed preferentially on the east side. Halite is usually found beyond the blödite ring but it does not have a LWIR signature that can be mapped (for a more detailed discussion of the spectral signature associated with halite areas see Section 4.2.4). There is a similar nearly concentric zonation of minerals at F1 (Fig. 15) except that the order of gypsum and mascagnite zones is reversed and the nitratine ring is incomplete. Based on these results and field observations the mineralization is divided into three roughly concentric zones. Outwardly from the central boiling pools and fumarole vents the zones are: fumarole, transition and evaporite. For the purposes of the remote sensing mineral maps the dominant minerals in each zone are (in parentheses): fumarole (mascagnite, boussingaultite and gypsum), transition (nitratine) and evaporite (blödite and thenardite). More detailed descriptions of the minerals in each of the zones are described in Section 5.

4.2.2. Ground truth results

Fig. 16 shows locations at F2NC where ground truth sampling was performed. Way points (WPs) in Fig. 16a can be related to samples identified in the laboratory by XRD (Table 3) and additional ground truth results for F2BC are presented in Table 4. The X's in Fig. 16b note locations

Fig. 13. Large field of boiling mud pots at the center of the F2 fumarole field.

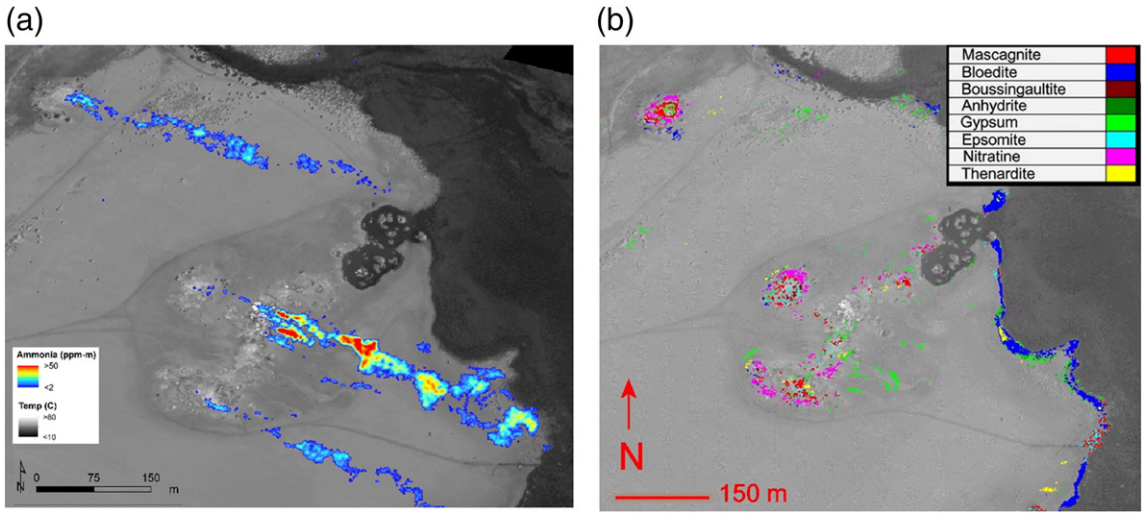

Fig. 14. (a) LWIR hyperspectral false color ammonia column density at the F1 and F2 fumarole fields superimposed on gray scale surface brightness temperature image (7/23/2014). Image shows four principal centers of ammonia emission. (b) LWIR hyperspectral map of the eight most common minerals for the F1 and F2 fumarole fields superimposed on gray-scale thermal radiance image (7/23/2014).

at F2NC where ground truth specimens returned to the laboratory confirmed the remote sensing identifications.

Typically more than one mineral was identified in the ground truth samples, which may have included subsurface minerals being incorporated into the material being analyzed. Mineralogical inhomogeneities also certainly existed on the scale of the SEBASS/Mako GSD (0.5–1 m). In general the spectrally dominant mineral identified by Mako represented the major mineral identified by XRD, with the exception of blödite. The first two ground truth surveys failed to identify any blödite based on random sampling, including when multiple spectra were recorded with the Exoscan in the field. The verification of blödite was somewhat problematical because the blödite formed scattered subtle mm-sized growths that were not obvious when sampling the surface that was predominantly quartz sand and halite. It covered only a small fraction of the area of the pixels mapped as blödite but was more obvious beneath the surface in cross sections. In contrast, the other sulfate minerals formed substantial easily recognizable accumulations. It was not until the inconspicuous blödite could be recognized in the field that successful ground truth samples were collected. In areas mapped as blödite, quartz sand and halite represented the mean scene vector in the remote sensing data which was subtracted before mineral identification. This is the likely reason why blödite was identified as the spectrally dominant mineral present in these areas even though it represented a very small pixel fill fraction.

The results of ground truth surveys by Vaughan et al. (2005) for SEBASS data from the Steamboat Springs geothermal field were similar to ours from the Salton Sea fumaroles. They found that XRD generally identified the major mineral mapped remotely as the dominant component in a mixture of minerals. Failures of the ground truth could be attributed to spectra of minerals identified by XRD not being in the remote spectral library, inhomogeneities at the sampling site and the drastically different length scales between the collected samples and remote ground sampling distance.

The ground truth survey verification of the minerals (blödite, thenardite, mascagnite) identified along the brush line was only partially successful, in part because the area was saturated with briny water and very soft and muddy. Collected samples that were returned to the lab tended to crystallize halite and were not representative of the material present on the surface at ~41 °C when the Mako flight was conducted. SEM/EDS of cross sections was helpful in identifying blödite and thenardite that was below the surface of collected samples. It was not practical to perform Exoscan traverses to prescreen samples in real time for return to the lab because of the distance between the collection area and a base lab on solid ground. Mascagnite was not expected along the brush line since there were no obvious white deposits like at F1 and to a lesser degree F2. It is noted that there are small areas of gaseous emissions along the brush line as evidenced by slow bubbling.

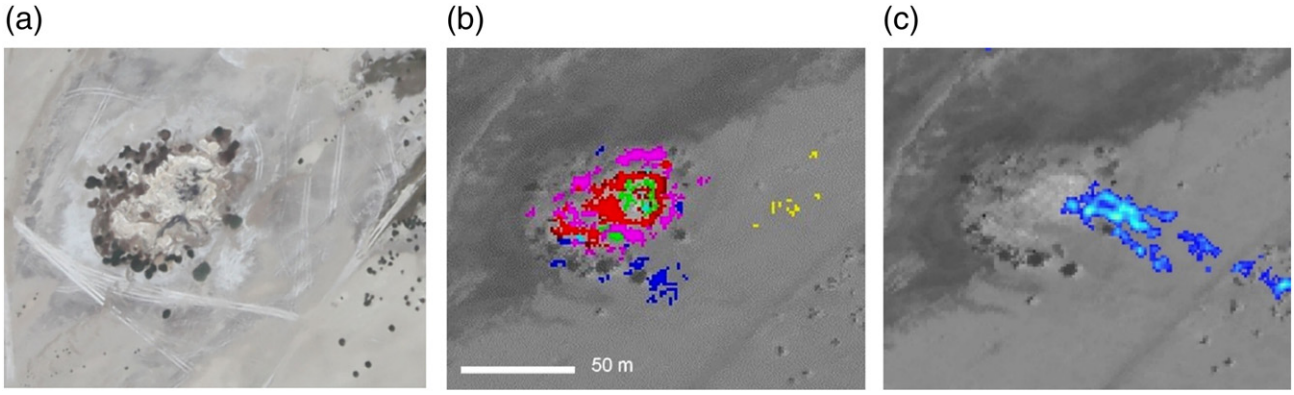

Fig. 15. (a) Context camera view of fumarole field F1 (4/22/2015). (b) Detail of mineral map of F1 superimposed on gray scale surface brightness temperature image (7/23/2014). Red = mascagnite, green = gypsum, magenta = nitratine, blue = blödite and yellow = thenardite. (c) Map of ammonia plume. Plume originates at left-most spot centered in the gypsum zone (green) and is blown to the southeast.

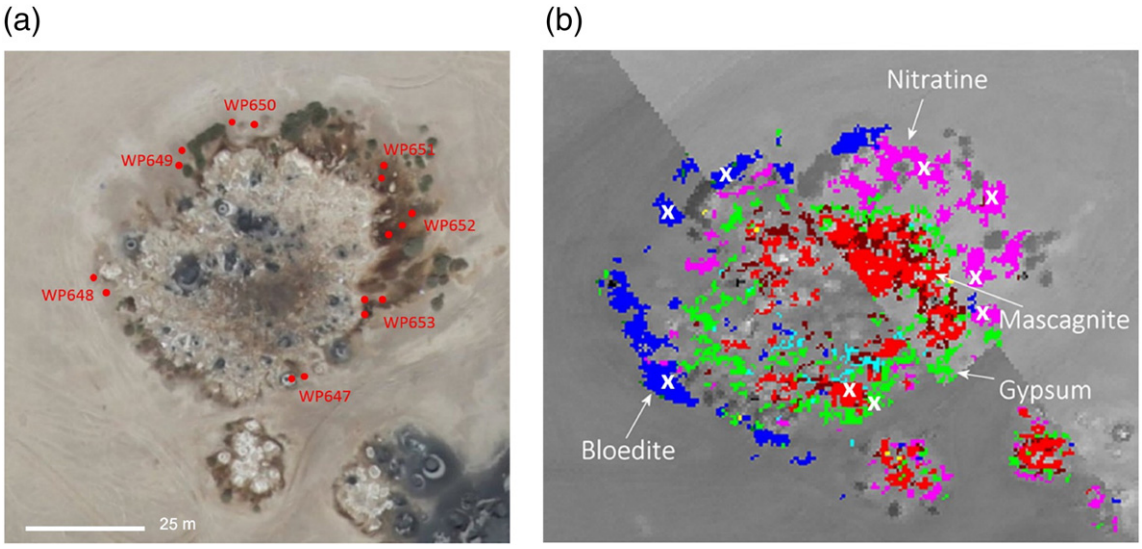

Fig. 16. (a) Context camera view of F2NC fumarole field (9/24/2015). (b) Detailed LWIR hyperspectral mineral map for the F2NC fumarole field superimposed on gray-scale thermal radiance image (9/24/2015). Red = mascagnite, green = gypsum, magenta = nitratine, blue = blödite, brown = boussingaultite and cyan = epsomite. X's mark locations where ground truth/laboratory analyses verified remote sensing identifications. Note distortion of the mineral map as a result of georeferencing errors between the two stitched flight lines.

Based on these confirmations we are confident in interpreting the remote sensing results over the evolution of the fumarole fields. The successful ground truth survey in September 2015 was in part a result of lessons learned from previous less fruitful attempts. The first attempt in October 2013 was the least successful. It relied upon using GPS coordinates from completed georeferenced mineral maps coupled with GPS location of sampling locations in the field. Georeferencing errors in producing the maps (±10 m), errors in GPS location in the field (±2 m) and the fact that the ground truth survey was conducted one month after the remote collect all contributed to the poor verification results. The use of the aluminum foil panels in September 2015, which were visible in both the context camera and LWIR images, made locating specific areas for sampling more accurate than depending on georeferencing the mineral maps and relying on the ±1–2 m resolution of handheld GPS. Having the TAR single component mineral images delivered the same day as the data collect also made locating particular mineral zones easier. When areas were inhomogeneous the use of the Exoscan made it possible to do near real time preliminary mineral identifications in the field, thereby increasing the probability of collecting the correct material for lab identification by XRD. Prompt laboratory analyses also minimized the possibility that sample mineralogy could change over time. All of these factors are important for these evaporite minerals because of the inhomogeneity of the deposits (both on the surface and subsurface) and their ephemeral nature. The latter, on the scale of weeks to months, is dependent on rainfall, temperature, and agricultural runoff levels. On much shorter time scales one must be aware that the temperature of the actual ground surface (outer 10s of microns) during the remote sensing collect may have easily been >60 °C (maximum air temperatures were 42–47 °C). Ground surface temperatures as high as 71 °C have been recorded in several places in Death Valley, CA with the record being 88 °C (Robinson and Hunt, 1961). The sand/mud substrates, part of which are collected with samples returned to the lab, may have been saturated with brine. Once returned to the lab where the temperature was about 20 °C the brine has the opportunity to migrate to the surface through capillary action and dissolve existing minerals or precipitate new species. Most of the sulfate minerals are highly water soluble, with the solubility

Table 3
Ground truth mineral identifications for fumarole field F2NC from Fig. 16 (9/24/2015).

Way point	Sample	Mako ID	Exoscan ID	XRD ID
647	A	Mascagnite	Mascagnite	**MASCAGNITE**, lecontite
	B	Gypsum	Gypsum	**GYPSUM**, QUARTZ, mirabilite
648	A	Blödite	Blödite	QUARTZ, Halite, **blödite**
	B	Blödite	Blödite	QUARTZ, Glauberite, **blödite**
649	A	Blödite	Quartz, Halite	HALITE, Quartz
	B	Blödite	Blödite	QUARTZ, halite, **blödite**
650	A	Blödite	Quartz, Halite	QUARTZ, Halite
	B	Blödite	Blödite	HALITE, Quartz, **blödite**
651	A	Nitratine	Nitratine	QUARTZ, **NITRATINE**, Glauberite, Anhydrite
	B	Nitratine	Nitratine	**NITRATINE**, Quartz, Anhydrite
652	A	Nitratine	Nitratine	**NITRATINE**, Quartz, Anhydrite
	B	Nitratine	Nitratine?	ANHYDRITE, **NITRATINE**, QUARTZ, gypsum
	C	Nitratine	Nitratine	**NITRATINE**, Quartz, Anhydrite
653	A	Nitratine	Nitratine +?	QUARTZ, ANHYDRITE, Halite, nitratine?
	B	Nitratine	Blödite?	QUARTZ, HALITE, glauberite, bassanite
	C	Nitratine	Nitratine +?	**NITRATINE**, Anhydrite, quartz

XRD Abundance: MAJOR, Minor, trace.
Bold = XRD verification of Mako mineral map.

Table 4
Ground truth mineral identifications for northwest fumarole field F2BC (9/24/2015).

Way point	Sample	Mako ID	Exoscan ID	XRD
654	A	Blödite	?	QUARTZ, Halite, **blödite**
	B	Blödite	?	QUARTZ, Halite, **blödite**
	C	Blödite	Quartz	QUARTZ, Halite, **Blödite**
655	A	Boussingaultite		**BOUSSINGAULTITE**, Koktaite
	B	Boussingaultite		**BOUSSINGAULTITE**
	C	Nitratine	Quartz, Nitratine	QUARTZ, **NITRATINE**, Blödite
	D	Nitratine	Quartz	QUARTZ, Hexahydrite
656	A	Boussingaultite	NA	QUARTZ, Koktaite, **Boussingaultite**
	B	Boussingaultite	NA	**BOUSSINGAULTITE**
657	A	Boussingaultite	NA	MASCAGNITE,QUARTZ, sal ammoniac, koktaite
	B	Boussingaultite	Gypsum	GYPSUM
	C	Boussingaultite	NA	QUARTZ, **Boussingaultite**, lecontite

XRD abundance: MAJOR, Minor, trace.
Bold = XRD verification of Mako mineral map.
NA = not analyzed.

Table 5
Solubilities[a] in pure water at 25 °C of the most common fumarole field minerals.

Mineral	Solubility (g/kg)
Gypsum	2.08
Anhydrite	3.11
Glauberite	118.2
Boussingaultite[b]	179
Mirabilite	273.5
Halite[b]	357
Epsomite	358.3
Thenardite	519.9
Blödite	522.5
Mascagnite[b]	706
Nitratine[b]	921

[a] Spencer (2000).
[b] Handbook of Chemistry and Physics, CRC Press.

dependent on temperature (Table 5) so the possibility exists for dissolution or precipitation after samples were collected. There were early examples where field Exoscan spectra of samples could not be duplicated several weeks after the samples had been returned to the lab.

4.2.3. Evolution of fumarole mineral fields

As stated earlier there is a concentric distribution of minerals centered on areas with the boiling pools and sulfur forming vents (Figs. 11, 15b, 16b). Outwardly from the pools/vents they have been divided into the following three zones where the dominant minerals are given in parentheses: fumarole (mascagnite, gypsum, boussingaultite), transition (nitratine) and evaporite (blödite, thenardite).

Fig. 17 presents the mineral maps for F2NC for the period of 2009 through 2017. Blödite, thenardite and gypsum are the first minerals to form (2009) and significant amounts of ammonium containing minerals (mascagnite, boussingaultite) do not appear until 2013 even though ammonia emissions from the location were noted as early as

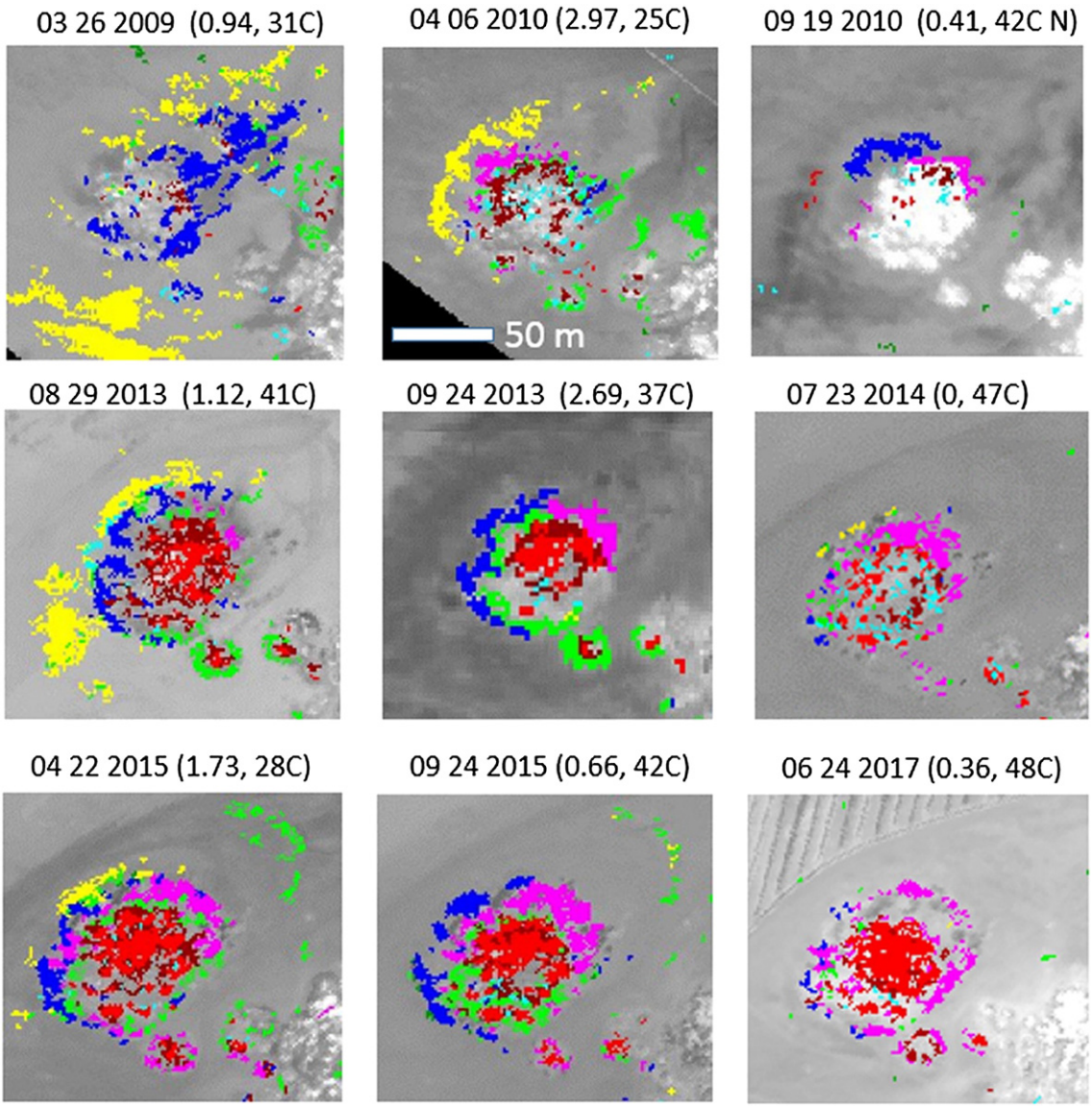

Fig. 17. Time series of mineral maps for the F2NC fumarole field superimposed on gray-scale thermal radiance images. Dates of data collects are given along with total rainfall (in cm) in the prior three months and the daily high temperature (°C), respectively, in parentheses. Note that 9/19/2010 was a night time collect (N). Red = mascagnite, green = gypsum, magenta = nitratine, blue = blödite, brown = boussingaultite, cyan = epsomite and yellow = thenardite.

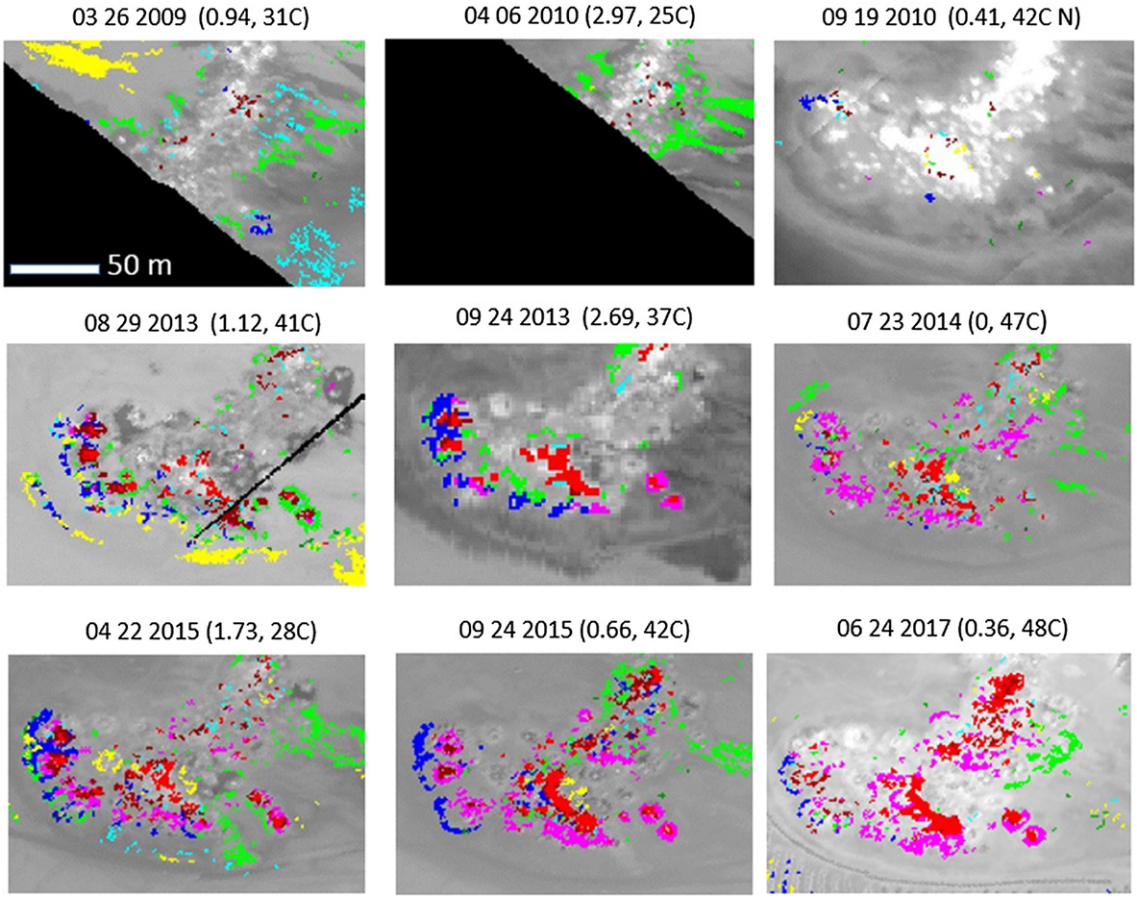

Fig. 18. Time series of mineral maps for the F2BC fumarole field superimposed on gray-scale thermal radiance images. Dates of data collects are given along with total rainfall (in cm) in the prior three months and the daily high temperature (°C), respectively, in parentheses. Note that 9/19/2010 was a night time collect (N). Red = mascagnite, green = gypsum, magenta = nitratine, blue = blödite, brown = boussingaultite, cyan = epsomite and yellow = thenardite.

2009 (Tratt et al., 2011). This is consistent with ground observations. The previously mentioned concentric ring structure is even present at that time and in general there are only subtle changes in its structure over time. The most noticeable difference was on 23 July 2014 when the amounts of mascagnite, gypsum and particularly blödite were greatly diminished. This corresponded to a time with no appreciable rainfall (0.05 cm) in the preceding seven months and relatively high temperatures (>40 °C) at the time of the collect, which implied that the fumarole field was relatively dry. Epsomite also appeared to be more common in that time frame. The observations on 6/24/17 are somewhat similar to those of 7/23/17 in that the occurrence of gypsum and blödite are very low but mascagnite is still common. Both dates had the highest temperatures of all the collects and followed periods of relatively low rainfall.

A time series of mineral maps for the F2BC field is presented in Fig. 18. The same general trends from F2NC are repeated here with gypsum appearing as early as 2009. Similar concentric rings of minerals are also seen at the southwestern end of F2 but they are not as completely developed as in F2NC (Figs. 16b, 17). Gypsum, epsomite and thenardite are the first minerals to appear in significant quantities. Boussingaultite is the first ammonium mineral to form (along with nitratine) and is found with the other magnesium-containing sulfate — epsomite. Mascagnite does not appear in quantity until 2013. As with F2NC there is less sulfate mineralogy present during July 2014 and June 2017 with blödite being nearly absent. A distinctive feature of the rings is that they are commonly incomplete. At both the F2NC and F2BC fields blödite is typically only found on the west side, while at the F2NC field nitratine is more concentrated on the NE side.

The F1 field also shows mineral zonation (Fig. 19) but it is slightly different from F2. The first presence of ammonium minerals (mascagnite) was mapped in September 2010 which is consistent with the first field observations in 2011 but is earlier than that observed at F2. Nitratine did not become a prominent mineral until 2013 and there is a considerable difference between August and September 2013 with the latter having considerably more nitratine and being just after a much wetter period. In June 2017 nitratine is nearly absent as a result of the former transition zone being submerged under several cm's of water. Unlike at F2, gypsum periodically (7/2014, 9/2015) forms the core of the concentric rings and appears to be more prevalent during drier periods (7/2014, 9/2015). While being common in 2010, blödite was subsequently more scattered and intermittent and in 2017 its occurrence shifted from the east side to the west side as a result of flooding of the area surrounding F1.

Fig. 20 shows the mineral maps for the F2 eastern brush/shore line area. This area does not show obvious fumarole activity or significant non-halite salt accumulations and the shoreline has changed significantly from 2013 to 2015. While the overall Salton Sea level has dropped during this period, the area of the marsh has increased and migrated westward since late 2014. The Sonny Bono National Wildlife Refuge is located several kilometers south of the fumaroles and the area in general has a high population of waterfowl. As the Salton Sea level has dropped there has been a large decrease in waterfowl habitat and sportsmen (duck hunters) have attempted to reverse this trend by damming agricultural runoff, thereby increasing the marsh area to the east of the fumaroles. Subsequent to 2015 the development of dust mitigation trenching has greatly expanded the marsh westward.

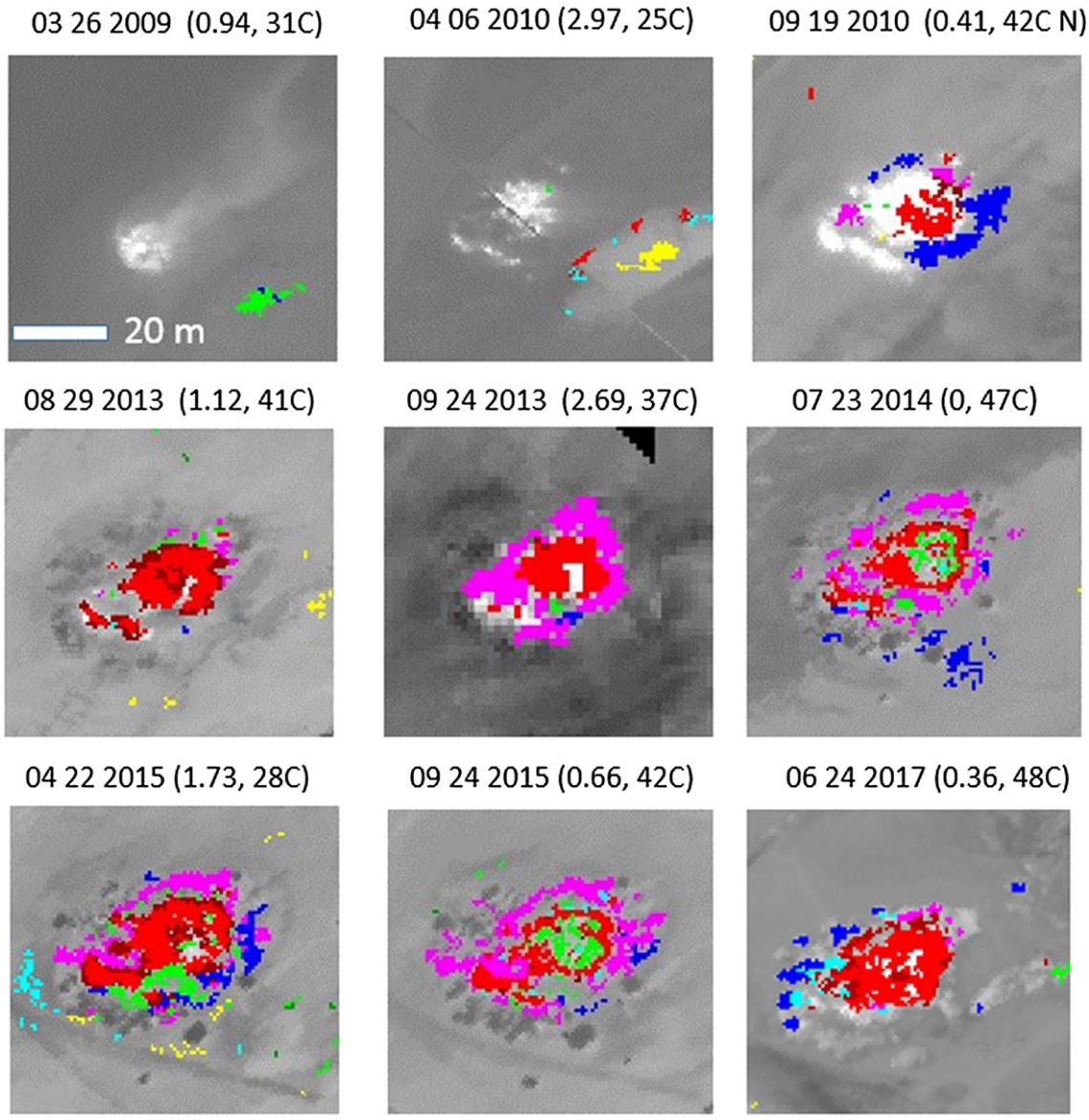

Fig. 19. Time series of mineral maps for the F1 fumarole field superimposed on gray-scale thermal radiance image. Dates of data collects are given along with total rainfall (in cm) in the prior three months and the daily high temperature (°C), respectively, in parentheses. Note that 9/19/2010 was a night time collect (N). Red = mascagnite, green = gypsum, magenta = nitratine, blue = blödite, brown = boussingaultite, cyan = epsomite and yellow = thenardite.

Blödite, thenardite and gypsum have commonly been mapped along the brush/shore line. Mascagnite has also been locally mapped but has not been ground truth verified and in general, ground truth surveys of this area have been less successful because the area is very muddy with very shallow standing water (see Section 4.2.2). In very shallow water small bubbles have locally been seen indicating there are limited gas emanations in the area. On November 23, 2013 extensive crusts of thenardite, often with or after mirabilite were observed on the west side of F2 complex and the F2 SE brush line mud flats. Along the latter they usually encrusted the stems of dead vegetation. This time period was shortly after a very heavy rainfall (2.7 cm). This indicates that it is not unreasonable to expect these minerals along the brush line.

Fig. 21 shows the context camera image and mineral map for the wind borne dust mitigation trenches and the brush/shore line area south of F2 on 6/24/2017. The easternmost trenches have been partially filled with water as shown by the dark coloration in both the visible and LWIR images. Along the southeast shoreline a variety of sulfates have been identified, including anhydrite, gypsum, thenardite, blödite and mascagnite similar to those seen in Fig. 20. Surprisingly gypsum and, to a lesser degree blödite, were identified along some of the trenches. It is not known whether these were present subsurface and were exposed in the trenching process or if they formed by precipitation from newly introduced fluids brought to the surface by capillary action.

4.2.4. Comparison with other remote sensing studies

Reath and Ramsey (2013) published a partial mineral map for the F2 fumarole field from the same SEBASS data presented in this paper, referring to the area as the "Sand Bar" field. A direct comparison with our data is shown in Fig. 22. There is satisfactory agreement in the areas identified as gypsum between our map and Reath and Ramsey (2013), but there are also two significant respects in which the two analyses diverge and that merit further discussion. Firstly, we did not identify significant amounts of anhydrite in the F2 region of interest but some of the areas identified as anhydrite by Reath and Ramsey (2013) were mapped as blödite or thenardite. It is noted that we did identify small regions of anhydrite on the surface along the brush line east of F2. This was not verified by ground truth but anhydrite was identified by XRD in subsurface material from the transition zone. Secondly, one of Reath and

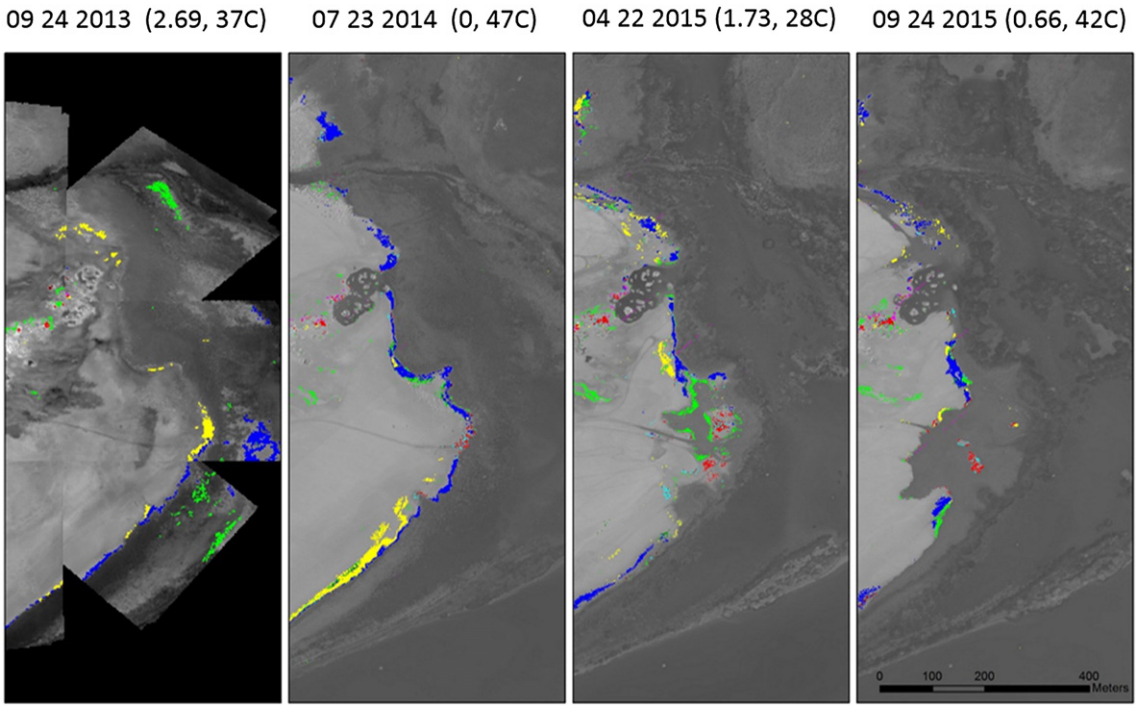

Fig. 20. Detailed LWIR hyperspectral mineral maps for the brush line area from 9/24/2013 to 9/25/2015. Dates of data collects are given along with total rainfall (in cm) in the prior three months and the daily high temperature (°C), respectively, in parentheses. Dark area to the east is water. Red = mascagnite, green = gypsum, magenta = nitratine, blue = blödite, cyan = epsomite and yellow = thenardite.

Ramsey's (2013) major conclusions was that an unidentified Mg-sulfate was prevalent at the Davis-Schrimpf and F2 fumarole fields (red in Fig. 22, center). Their tentative identification of a probable Mg-sulfate was based on the presence of an 8.2 μm-doublet emissivity minimum in the SEBASS data, however they were unable to identify any Mg-containing sulfates during laboratory analyses that were carried out on material collected from those areas.

To explain these discrepancies it is instructive to review how the data were processed. In contrast to how mineral maps were generated for this paper (Section 2.1), Reath and Ramsey (2013) processed the SEBASS data in the following manner: after atmospheric compensation a decorrelation stretch (DCS) was used to display variations in emissivity (composition). Spectral variability within the SEBASS scene was then compared with sulfate spectra in the ASU and ASTER spectral libraries. Using the pixel purity index function in ENVI, a spectrum representing the unidentified hydrated Mg-sulfate mineral was identified in the SEBASS scene and incorporated into the end member suite of candidate minerals based on those reported from the Salton Sea area and observed in the SEBASS data. This spectral end member suite was then applied to the SEBASS emissivity data using the linear deconvolution modeling approach of Ramsey and

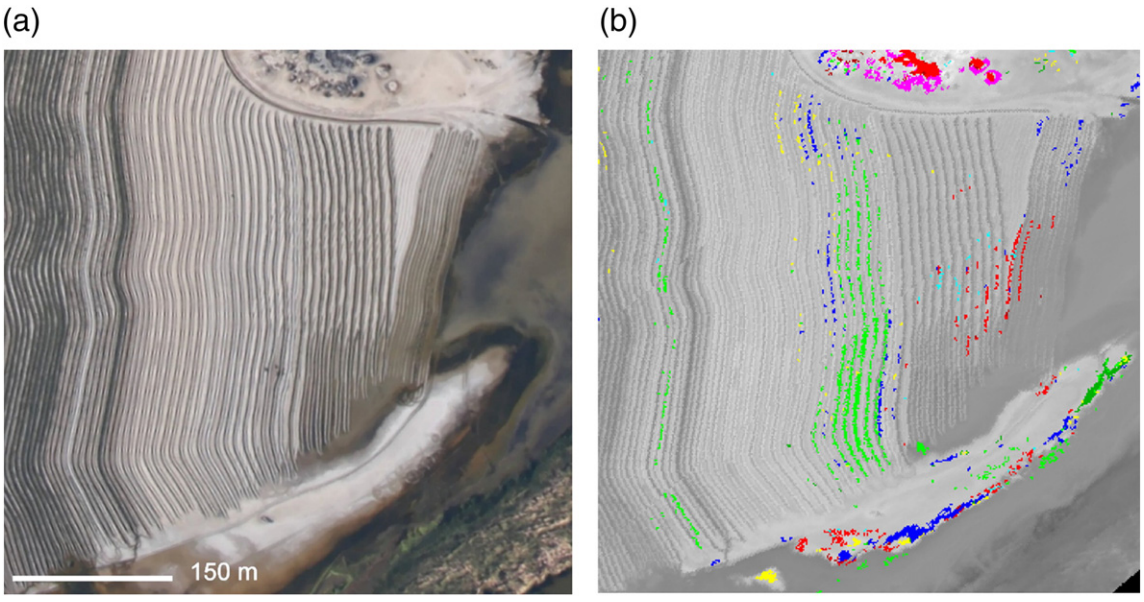

Fig. 21. Brush line area and dust mitigation trenches south of F2BC from 6/24/2017. (a) Context camera image. (b) Detailed LWIR hyperspectral mineral maps for the trenches. Red = mascagnite, lime green = gypsum, magenta = nitratine, blue = blödite, cyan = epsomite, dark green = anhydrite and yellow = thenardite.

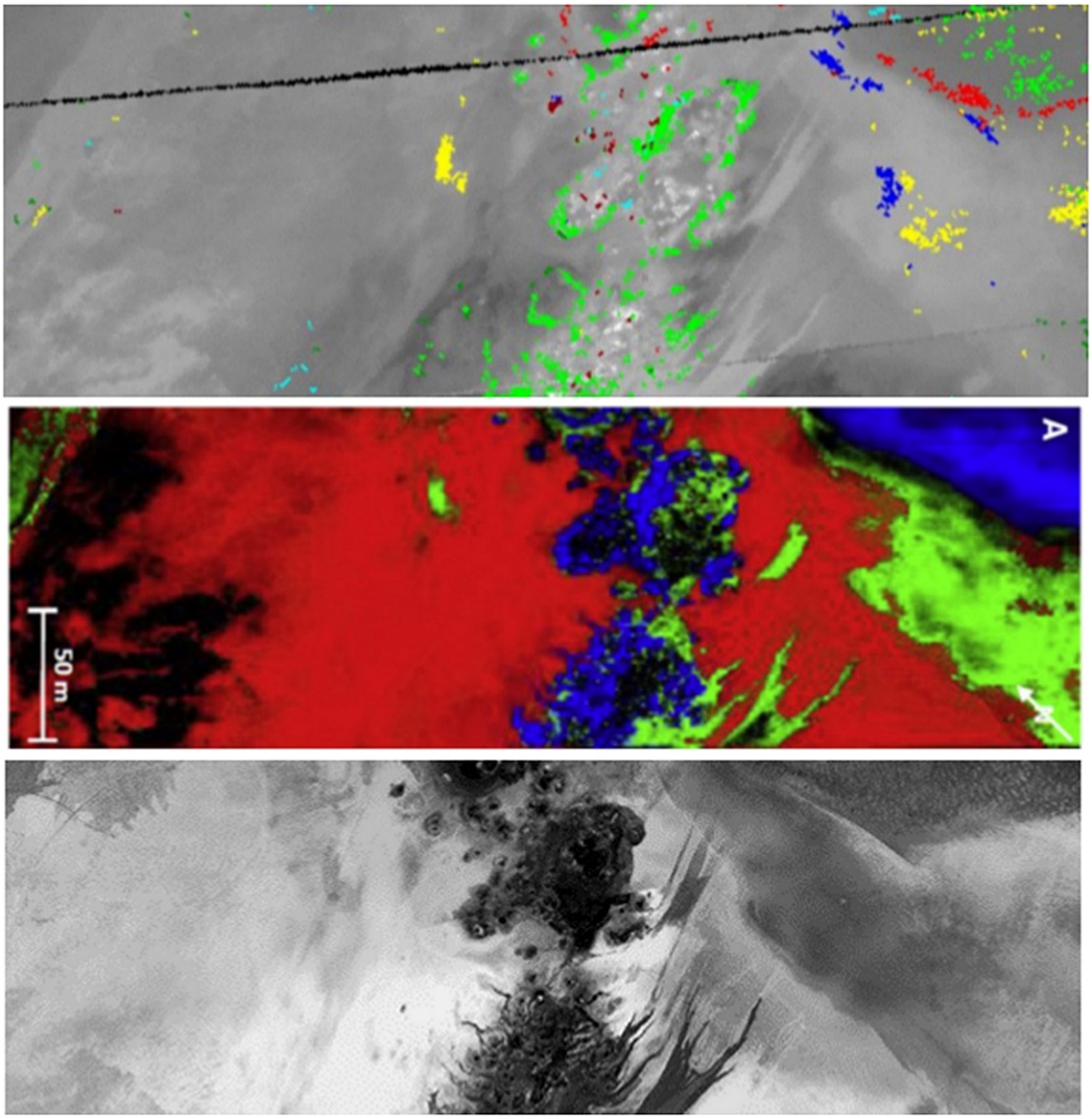

Fig. 22. Northeast fumarole field F2BC 4/6/2010 SEBASS data collect. (top) Aerospace SEBASS mineral map superimposed on gray-scale thermal radiance image. Red = mascagnite, lime green = gypsum, magenta = nitratine, blue = blödite, brown = boussingaultite, cyan = epsomite, dark green = anhydrite and yellow = thenardite. (center) Mineral map from Reath and Ramsey (2013) of the same SEBASS scene. Red = unknown Mg sulfate, green = anhydrite and blue = gypsum. (bottom) Aerospace panchromatic context camera image.

Christensen (1998). Spectral variability (e.g. DCS) within the SEBASS/Mako data were not evaluated before creating our maps so that regions with spectra not accounted for in the Aerospace solids library could not be identified. Since the solids library only contains spectra of known minerals, regions such as the putative Mg-sulfate would not be mapped.

Fig. 23 compares the spectra derived from the SEBASS data for areas identified as gypsum, anhydrite and the unknown Mg-sulfate by Reath and Ramsey (2013) in Fig. 22. It can be seen that gypsum areas have a very strong band with significant spectral contrast and it was mapped by both us and Reath and Ramsey (2013). In contrast, the anhydrite signature is very weak and shows very little spectral contrast with two broad poorly defined features. It is conjectured that in producing their mineral map Reath and Ramsey (2013) deconvoluted a fine grained anhydrite spectrum from this data since it also has very low spectral contrast. They indicated that anhydrite is expected in the Salton Sea area but provided no ground truth verification, whereas our mineral identification algorithm registered an insufficient signal to noise ratio to retrieve a positive identification with acceptable confidence.

Turning now to the 8.2 μm feature that Reath and Ramsey (2013) hypothesized as a probable unidentified Mg-sulfate, we advance an alternative explanation. This area is part of what we have referred to as the evaporite zone which, with the exception of localized areas of blödite and thenardite, typically has a thin halite crust overlying quartz sand. Representative examples of Exoscan spectra from this zone (albeit from a slightly different location and at a much later date) are presented in Fig. 24a. In some of the spectra a reflectance maximum near 8.16 μm is present. This is very close to the feature reported by Reath and Ramsey (2013) but is not a doublet. Our interpretation hinges on the observation that halite can modify the characteristic quartz spectrum in such a way that a shoulder results at 8.16 μm. We did not perform a ground collect in the 2010 time frame but a color aerial image (Fig. 25) shows the area surrounding F2 to be bright white similar to a halite covered salt pan. This further supports the idea that halite is present in the area at that time.

Fine-grained wind-blown quartz, or another silicate such as a clay entrapped in the halite, may be responsible for the observed spectra.

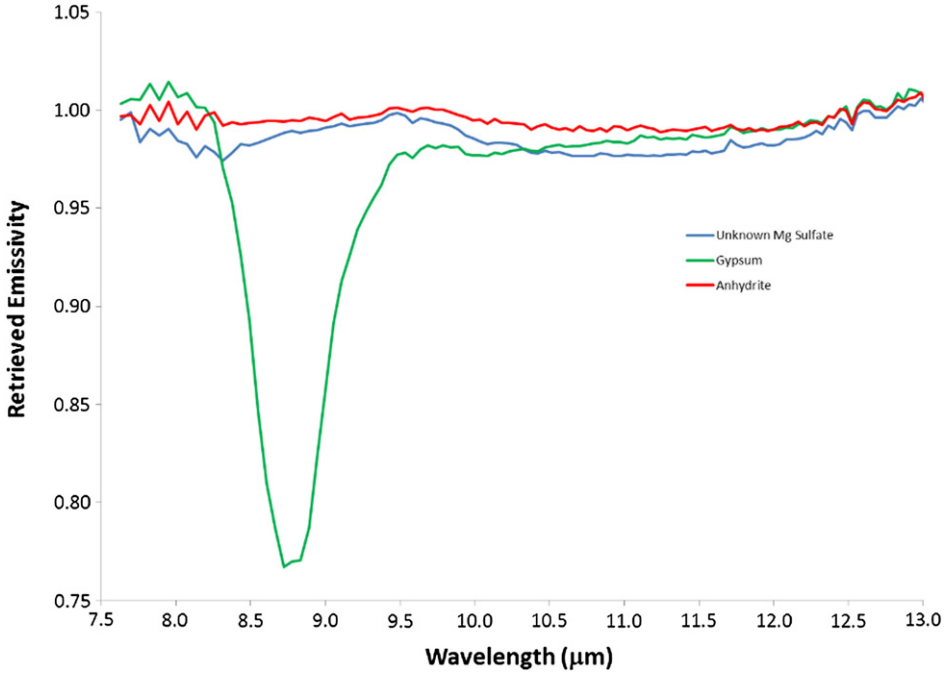

Fig. 23. Spectra derived from SEBASS data for areas identified as gypsum, anhydrite and unknown Mg-sulfate by Reath and Ramsey (2013) in Fig. 22b. Spectra are an average of 10–20 pixels.

Halite is spectrally featureless in the LWIR (Eastes, 1989) but its presence does appear to influence the spectrum of quartz sand, which is ubiquitous in the areas surrounding the fumaroles. The amount of halite/fine grained quartz modifies the quartz spectrum to differing degrees. In particular, the lobe of the quartz band at 9.65 μm decreases with increasing amounts of halite/fine grained quartz while the lobe at 8.4 μm remains relatively unchanged. Fine grained powders, dilutely dispersed in an IR transparent medium (KBr, NaCl), produce transmission-like features in diffuse reflectance of spectra (Fuller and Griffiths, 1978; Sobkowiak and Painter, 1995).

This can be better understood by considering the diffuse reflectance infrared Fourier transform (DRIFT) spectroscopy technique (Fuller and Griffiths, 1978). In this method a fine-grained powder is dispersed and diluted in an infrared transparent matrix (typically KBr). The diffuse reflectance spectrum of this mixture produces a transmission-like spectrum as a result of the IR beam passing through the fine powder and diffusely reflecting off the KBr matrix particles. This phenomenon has been demonstrated by Eastes (1989) for halite mixtures with calcite, gypsum, quartz and montmorillonite. In contrast Berger et al. (2015) investigated the effect of pure halite coatings on materials and noted that the main result was to reduce spectral contrast and overall reflectance. In the case of the fumarole fields, very fine grained quartz may become trapped in NaCl, which then overlays coarse grained sand.

Laboratory spectra were recorded to test the fine grained quartz/halite hypothesis. Approximately 5 wt.% of <75 μm quartz powder was dispersed in fine-grained KBr (Sigma-Aldrich, FTIR grade). The diffuse reflectance spectrum of this mixture is shown in Fig. 24b (green) and is similar to that reported by Eastes (1989). Rather than a reflectance

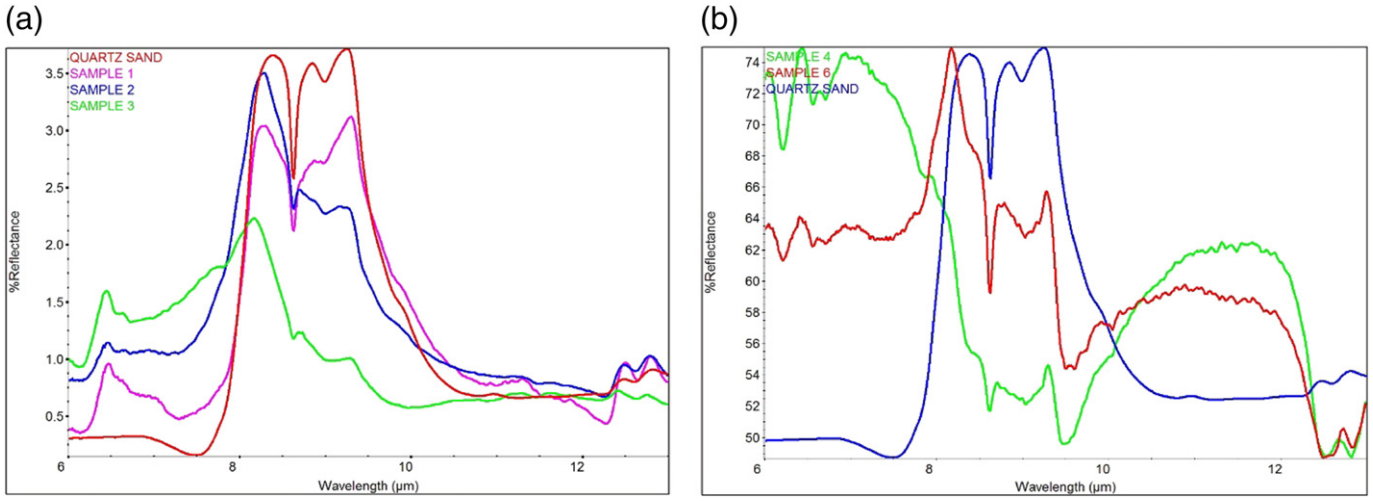

Fig. 24. (a) Exoscan reflectance spectra from the distal halite-containing portion of the evaporite zone from F2BC. Samples 1–3 contain varying amounts of what are assumed to be fine-grained quartz entrapped in halite on quartz sand. Scales have been adjusted for better comparison. The intensity of the 9.65 μm band decreases as the amount of entrapped fine grained quartz in halite, which has an absorption signature, increases. (b) Biconical reflectance spectra of coarse quartz sand (blue), dilute fine quartz (<75 μm) dispersed in KBr (green) and dilute fine quartz (<75 μm) dispersed in KBr dispersed on sand (red). Spectra scaled for better comparison.

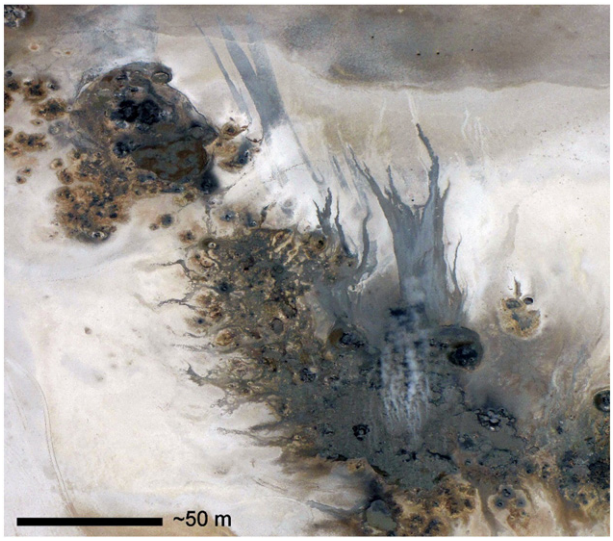

Fig. 25. Color aerial image of F2 fumarole field in Fig. 3 (Lynch et al., 2013). Note outflow of thin gray mud from bubbling pools and fumarole vents onto the white salt pan. Compare with Fig. 22 (bottom).

maximum, a reflectance minimum is produced at the location of the quartz reststrahlen band but it is shifted to slightly longer wavelength. When this feature is combined with the diffuse reflectance spectrum of coarse quartz sand the net effect is to drastically reduce the depth of the 9.65 μm band, with less of an influence on the 8.4 μm lobe, thus producing spectra similar to those shown in Fig. 24a. This was accomplished experimentally by placing a thin layer (<0.5 mm) of the <75 μm quartz and KBr mixture over the coarse quartz sand (red in Fig. 24b). By changing the thickness of the mixture the degree of the effect can be varied. Fig. 26 compares the results from the laboratory mixture (red) with an Exoscan spectrum (blue) in the field and a converted SEBASS spectrum from the unknown Mg-sulfate area. They are very similar considering that the exact composition and particle size of silicates mixed with halite in the field is not known. We believe that this phenomenon is responsible for the 8.2 μm feature Reath and Ramsey (2013) mapped and tentatively identified as a Mg-sulfate and furthermore is consistent with their not

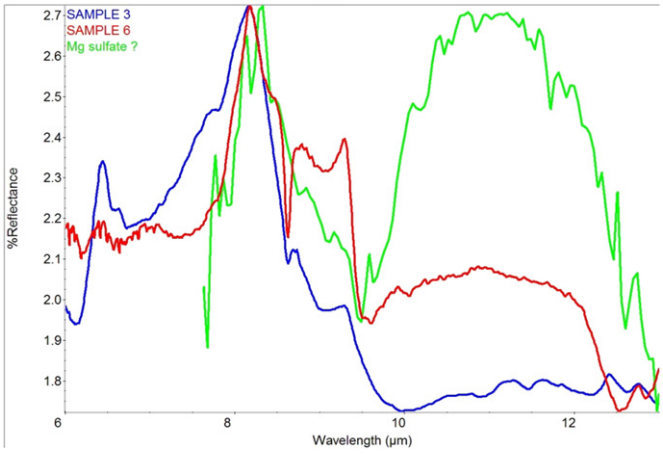

Fig. 26. Comparison of SEBASS spectrum of putative unknown Mg-sulfate with laboratory and field spectra. Spectra scaled for better comparison. SEBASS spectrum (green) was converted to reflectance using Kirchhoff's Law ($R = 1 - \varepsilon$). Sample 3 (blue) is an Exoscan reflectance spectrum from the distal halite-containing portion of the evaporite zone and contain varying amounts of what are assumed to be fine-grained quartz entrapped in halite on quartz sand. Sample 6 (red) is a laboratory biconical reflectance spectrum of dilute fine quartz (<75 μm) dispersed in KBr and dispersed on quartz sand.

being able to identify a Mg-sulfate in laboratory analyses of the ground truth samples. They noted only that XRD failed to identify any minerals consistent with the LWIR signature. The 8.2 μm feature was not a doublet and was slightly shifted in their emissivity measurements, which they attributed to the elevated temperatures associated with the analysis, possibly dehydrating the mineral of interest.

Eastes (1989) concluded that the spectral properties of minerals mixed with NaCl can be significantly different from the pure materials and the spectral behavior cannot be predicted with confidence from the transmission or reflectance spectra of the separate constituents. Furthermore they indicate that remote sensing of highly saline environments may need to consider the potential spectral effects of NaCl since it is common to those regions.

4.3. Field infrared spectroscopy

A total of 11 diffuse reflectance Exoscan traverses were performed. In many instances it was difficult to obtain spectra because of the very low signal resulting from the very irregular surfaces. Fig. 27 shows the location of an Exoscan traverse at the F1 field with the corresponding spectra in Fig. 28. This duplicates the zonation observed on a much larger scale in the remote sensing data. Gypsum was found closest to the sulfur producing vent followed by zones of boussingaultite, nitratine and blödite followed by quartz/halite. In other traverses the same general zonation was observed with the exception that blödite was often not observed.

5. Detailed mineral descriptions

The following mineral descriptions are arranged by zones approximately in the order they appear with distance from bubbling pools and sulfur producing vents.

5.1. Fumarole zone

The fumarole zone is located closest to ammonia emitting vents, boiling pools and gryphons. It is characterized by conspicuous accumulations of several different white ammonium sulfates, which are difficult to distinguish in the field, and gypsum.

5.1.1. Sulfur S

Dry hissing thermal vents up to 5 cm in diameter commonly have intergrowths of yellow bladed sulfur crystals associated with them (Fig. 9a) that appear to have formed by sublimation. The temperature measured in some of these vents was 100 °C. Dendritic growths of sulfur crystals have also been seen growing on dead vegetation (Fig. 29a). These vents are at ground level at F1 but at F2 they may also be near the summits, or on the flanks, of gryphons. Vents at F2 showing sulfur crystal growths became more common in 2014. The individual crystals range up to 3 mm in length and have a skeletal appearance (Fig. 29b). Beneath the surface, close to the vents, cavities (to 8 cm) in wet black mud often have a thin lining of sulfur crystals. Crude bladed gypsum crystals (to 0.5 mm) are often associated with, or in close proximity to, the sulfur crystals. Sulfur crystals associated with these fumarole vents have been documented as early as the late 1800s (Hanks, 1882).

5.1.2. Gypsum $CaSO_4 \cdot 2H_2O$

Gypsum appears to form in two different environments, one fumarole related and the other evaporite. Mats of white to cream-colored crude bladed gypsum crystals (to 1 mm) are often associated with sulfur producing vents and mascagnite (Fig. 30). Gypsum may also occur as fibrous aggregates and as clear thin fibers found underneath other sulfate crusts. Other associated species include boussingaultite, tschermigite and koktaite. Some gypsum-containing areas several meters from vents at F2 have been identified by remote sensing along with areas along the eastern brush/shore line.

Fig. 27. Northeast corner of fumarole field F1 with Exoscan traverse EX2 (1/2014) marked with arrows (0 m and 10 m relate to location distances of spectra in Fig. 28). White efflorescence at 0 m contains gypsum and boussingaultite and dark brown patch just left of center contains sodium nitrate (nitratine). White salt pan in the distance is primarily a surface coating of halite.

5.1.3. Mascagnite $(NH_4)_2SO_4$

White, cream or light gray botryoidal crusts of mascagnite covering areas of several square meters are relatively common and are often found close to sulfur producing vents and boiling pools at both F1 and F2 and may also be found growing on dead vegetation (Fig. 9a). The deposits can be up to several cm thick (Fig. 31a) and can vary from columnar growths with mushroom-like tops to unconsolidated material with the consistency of fresh snow. The mascagnite is typically very fine grained but bladed crystals to 0.2 mm have been observed (Fig. 31b). Mascagnite may also be associated with lecontite, boussingaultite, koktaite or sal ammoniac. Subsurface, the mascagnite often has a fibrous-columnar structure with fibers to several cm (Fig. 32a).

A specimen of columnar/fibrous mascagnite (including the substrate) approximately 2 m from a sulfur producing vent at F1 was sampled and cross sectioned. The results are presented in Fig. 32. The subsurface consists primarily of sand grains (quartz with minor plagioclase and potassium feldspar) and elemental sulfur (to 0.20 mm) cemented with massive mascagnite. The base of the columnar mascagnite includes koktaite blades (to 0.40 mm) while the upper 30 mm consists of fibrous mascagnite with minor boussingaultite.

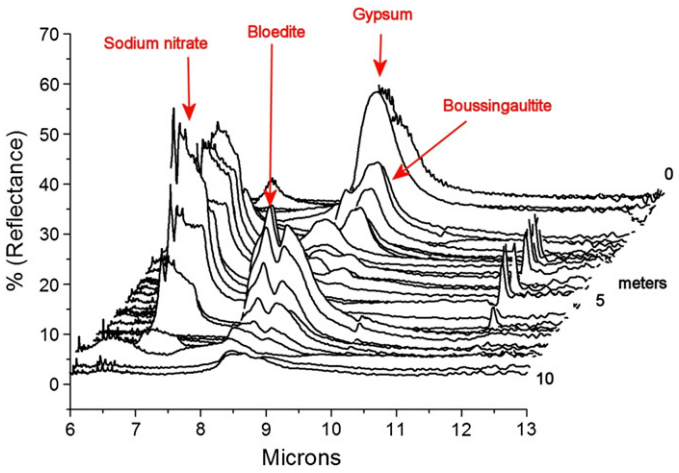

Fig. 28. Exoscan spectra from 10 m traverse EX2 (1/2014) in NE corner of F1 (refer to Fig. 27). A sulfur producing vent is located at 0 m. Sampling interval from 0 to 5 m was 15 cm; from 5 to 10 m interval was 30 cm.

Mascagnite from other localities has been formed from sublimation from volcanic fumaroles and coal fires (Dunning and Cooper, 1993; Parafiniuk and Kruszewski, 2010; Masalehdani et al., 2009). The thickness (to 6 cm) of fibrous deposits at the Salton Sea fumaroles suggests that precipitation from solutions drawn to the surface by capillary action (efflorescence) may also play a part, considering the high solubility of mascagnite (Table 5). The fact that the area experiences up to 5 cm of rain annually also supports the idea that there can also be dissolution and reprecipitation of mascagnite.

5.1.4. Boussingaultite $(NH_4)_2Mg(SO_4)_2 \cdot 6H_2O$

Boussingaultite is often a constituent of botryoidal crusts associated with sulfur producing vents. It commonly occurs with mascagnite, lecontite, tschermigite, koktaite and blödite. Crystals are typically only a few tenths of a mm long but larger corroded bladed crystals (to 4 mm) have been found in unconsolidated material below other crusts at F1 (Figs. 30b, 33a). In limited cross sections, boussingaultite crusts formed over loosely consolidated sand and gypsum (anhydrite/bassanite) (Fig. 33b). Boussingaultite can form from the evaporation of solutions of ammonium and magnesium sulfates (Faust and Bloss, 1963) and may be the result of dissolved mascagnite interacting with magnesium sulfate solutions derived from the evaporite zone. However, minor amounts of boussingaultite were observed in evaporation residues from clear pools.

5.1.5. Lecontite $(NH_4,K)Na(SO_4) \cdot 2H_2O$

Botryoidal mascagnite crusts from F1 and F2 occasionally contain minor amounts of lecontite. It also occurs with boussingaultite at F2. Euhedral lecontite crystals (to 0.1 mm) have only been recognized in a few specimens of more pure lecontite from F1 (Fig. 34a). Lecontite can form from evaporation of solutions of $(NH_4)_2SO_4$ and sodium sulfates (Corazza et al., 1967) which may have resulted from dissolved mascagnite mixing with sodium sulfates from the evaporite zone.

5.1.6. Koktaite $(NH_4)_2Ca(SO_4) \cdot 2H_2O$

Minor amounts of koktaite have been identified with boussingaultite and mascagnite by XRD in samples from F1 and F2. It occurs as bladed crystals to 200 μm (Figs. 32b, 34b). It has not been recognized in hand

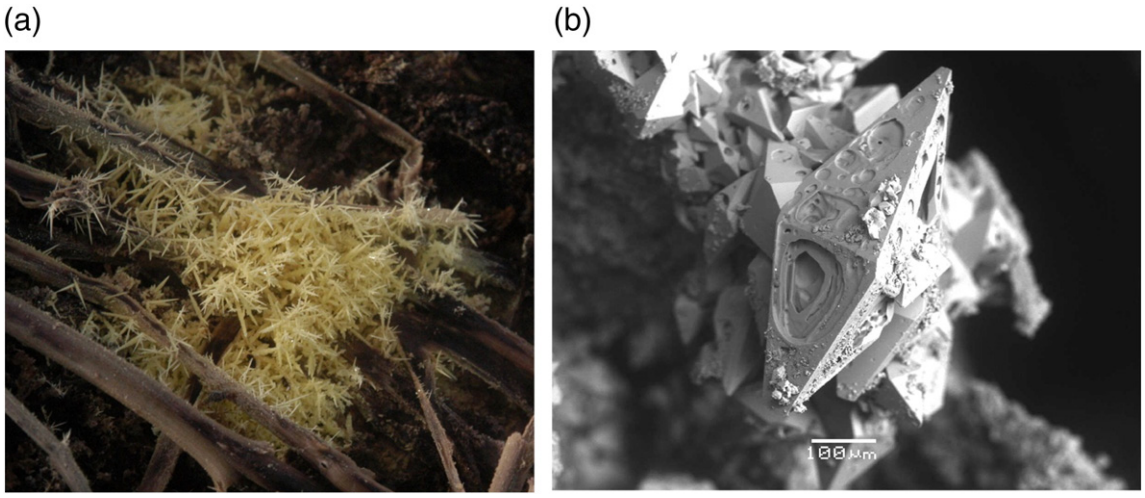

Fig. 29. (a) Dendritic sulfur growing on dead vegetation near an F1 thermal vent. Field of view is 9 cm. (b) SEM image of sulfur crystals.

specimens. It is assumed that it forms in a similar manner to boussingaultite and lecontite — by evaporation of solutions of ammonium and calcium sulfates.

5.1.7. Tschermigite $(NH_4)Al(SO_4)_2 \cdot 12H_2O$

XRD and SEM/EDS analyses have indicated that minor amounts of tschermigite occur with boussingaultite, lecontite and gypsum in samples from F1 and F2 (Fig. 35a, b). It has not been recognized in hand specimens.

5.1.8. Natrojarosite $NaFe_3^{3+}(SO_4)_2(OH)_6$

Small areas around vents at F1 and F2 have a yellow to light orange color. Natrojarosite occurs here as thin crusts of microscopic hexagonal plates (Fig. 36a).

5.1.9. Sal ammoniac NH_4Cl

Minor amounts of sal ammoniac have been identified with mascagnite by EDS from F2 (Fig. 36b). It also occurs in evaporation residues of water collected from hot milky pools at F2 (Table 2). It has not been recognized in hand specimens. Sal ammoniac specimens from the fumaroles were identified as early as 1850, by the subjective method of "the sharpness of their taste" (LeConte, 1855). Sal ammoniac is commonly produced by sublimation at fumaroles at many other worldwide occurrences (Parafiniuk and Kruszewski, 2010; Masalehdani et al., 2009).

5.1.10. Tamarugite $NaAl(SO_4)_2 \cdot 6H_2O$

Tamarugite was identified by XRD from one specimen with alum-(Na) in a sulfate patch at the SE end of F2 that also contained lecontite, mascagnite and boussingaultite. It has not been recognized in hand samples.

5.2. Transition zone

The transition zone is a typically brown nitrate-containing band on the surface that separates the ammonium sulfates of the fumarole zone from other sodium and magnesium sulfates of the evaporite zone.

5.2.1. Nitratine $NaNO_3$

In January 2014 an Exoscan FTIR survey of sulfate patches in the SE corner of F2 revealed the presence of nitratine. It was found in black and brown areas just outside of the ammonium sulfate growths around small bubbling pools and vents. These brown rings containing nitratine are very common and are associated with the more distal regions of small fumarole vents and the fumarole fields as a whole (Fig. 11). They constitute one of the more prominent remotely sensed mineral map units. Crystalline deposits, however, were inconspicuous in these

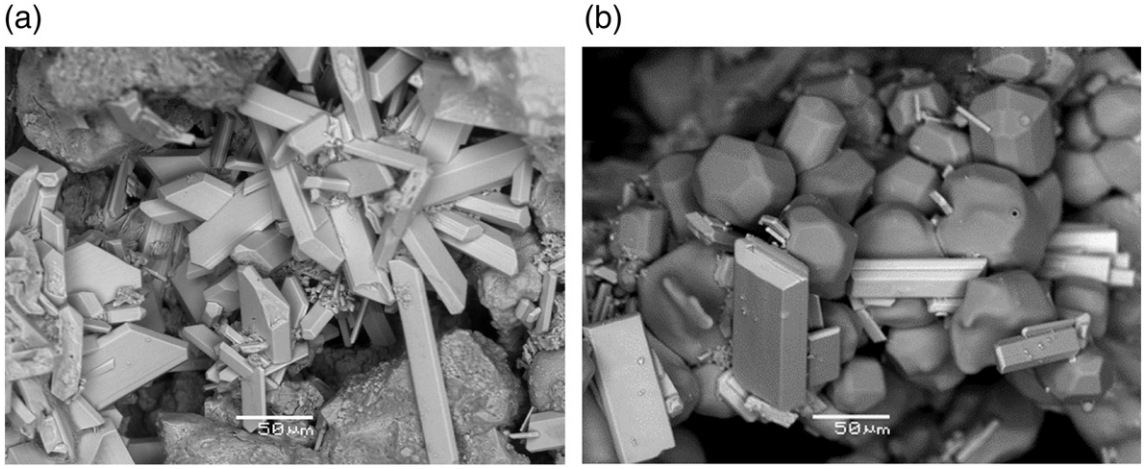

Fig. 30. (a) SEM image of bladed gypsum crystals from F2. (b) SEM image of boussingaultite and bladed gypsum crystals from F2.

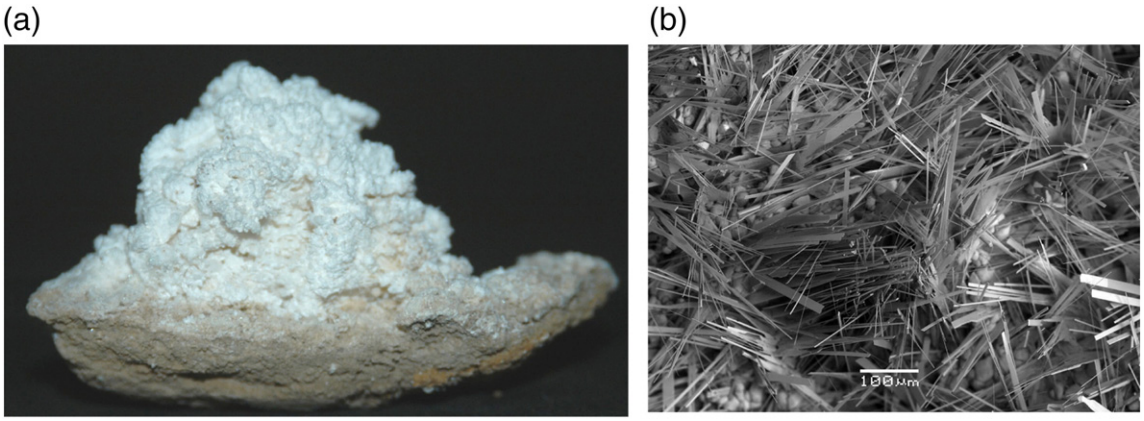

Fig. 31. (a) Side view of fibrous mascagnite efflorescence from F1. Sand substrate is at the bottom. Horizontal field of view is 9 cm. (b) SEM image of bladed mascagnite crystals.

rings and they were overlooked in early sampling campaigns. More rarely nitratine occurs as thin white crusts of delicate branching intergrowths of white to clear 0.05 mm crystals (Fig. 37a) that may be up to 100 μm in thickness (Fig. 37b). Nitratine had been identified as early as 1902 from along the old beach lines of the Salton Sea east of the "Mud Volcanoes" in T.10S. R.14E. (Bailey, 1902).

Ammonium sulfate is a common fertilizer and the process of nitrification, how ammonium is broken down to produce useable nitrate, has been attributed to bacterial action (Praveen-Kumar et al., 1989). In particular *Nitrosomonas* oxidizes ammonia (and ammonium) into nitrite while *Nitrobacter* converts the nitrite to nitrate. Similar moderately thermophilic nitrifying bacteria (*Nitrosomonas* and *Nitrospira*) have been found associated with hot springs (Lebedeva et al., 2005). They showed that the ammonia- and nitric-oxidizing bacteria were able to be cultured in the temperature ranges of 27°–55 °C and 40°–60 °C, respectively. Ammonia-oxidizing Archea (*Candidatus*, *Crenarchaeota*) have also been found associated with hot springs (Chen et al., 2016; Reigstad et al., 2008).

The location of the brown nitratine-containing deposits infers that ammonium sulfate solutions are diffusing outward from the mascagnite rich central zone. The location of the nitratine zone away from the fumaroles may in part be due to a reduced concentration of ammonium

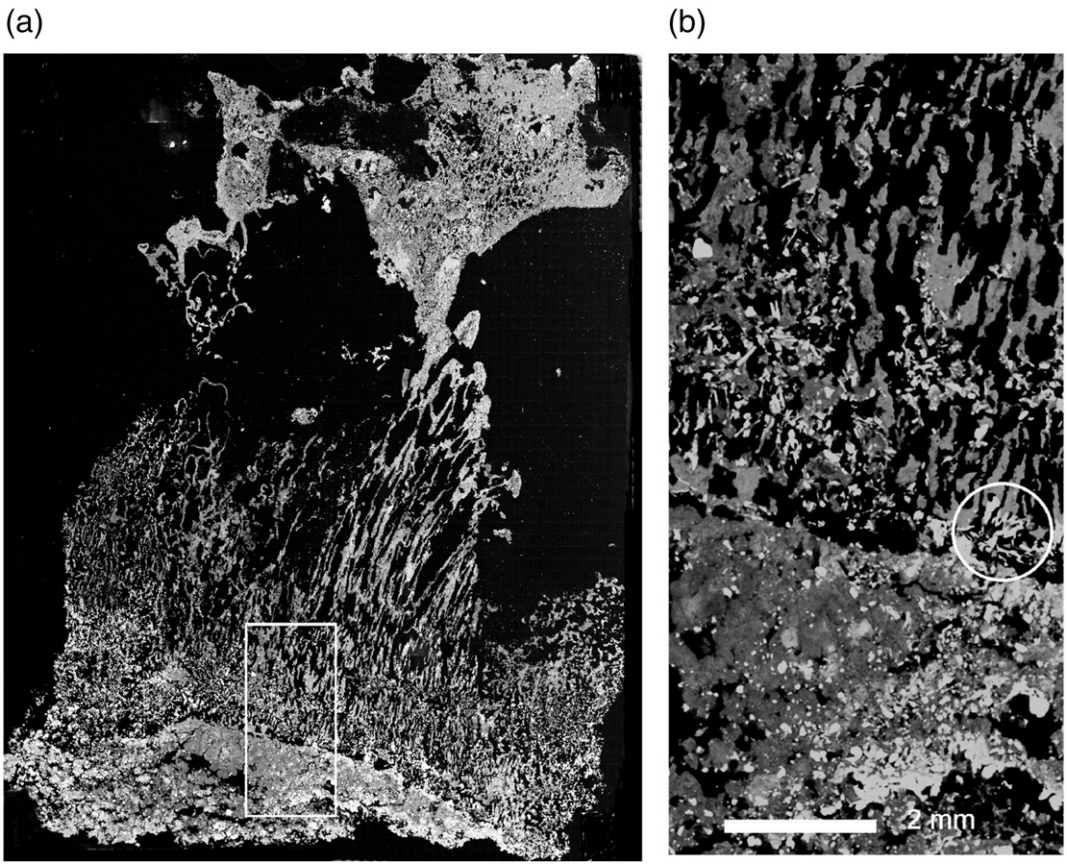

Fig. 32. Backscatter SEM images of a cross section through a fibrous columnar mascagnite growth. (a) Field of view is 4 cm × 6 cm, surface is at top. Base consists of quartz sand cemented by massive mascagnite. Bright grains at bottom are elemental sulfur and sand in a solid mascagnite matrix. (b) Close up of base of mascagnite columns — enlarged view of box in (a). Base of columns include bladed koktaite (bright grains — circled).

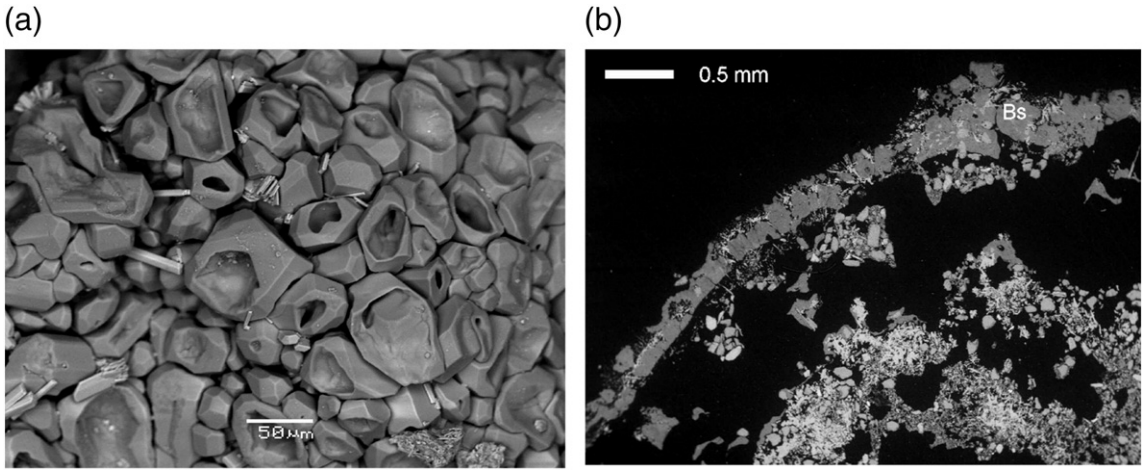

Fig. 33. (a) SEM image of cavernous boussingaultite crystals from F1. (b) Backscatter SEM image of cross section through boussingaultite (Bs) crust from F2. Underlying material is quartz sand and bladed gypsum.

coupled with lower temperatures that are more favorable for microbial activity. The dark brown color of the nitratine rings also suggests that decomposition of vegetation may also contribute to its formation.

5.2.2. Anhydrite $CaSO_4$; Bassanite $2CaSO_4 \cdot H_2O$

Fine grained anhydrite and bassanite are commonly found in loosely consolidated material just beneath the surface in brown nitratine areas (Figs. 11, 37b). This is surprising since the temperature for the transformation of gypsum to anhydrite has been reported to occur between 42 °C and 58 °C (Blount and Dickson, 1973) and the transition zone is a significant distance from the higher temperatures in the fumarole zone where gypsum has been found to occur very close to sulfur producing vents. The fact that anhydrite is subsurface implies that solar heating cannot be responsible for its formation. However, it has been shown that the transformation temperature from gypsum to anhydrite can be much lower (20–30 °C) in highly concentrated NaCl solutions (Blount and Dickson, 1973). It is noted that microbial activity has been implicated in the formation of nitratine in the transition zone. Gunatilaka (1990) describes how halophyte vegetation and a microbial community is associated with the preferential formation of anhydrite over gypsum in a sabkha environment in Kuwait. At that locality cyanobacteria consisting primarily of *Anabaena constricta*, *Spirolina* sp. and *Synechocystis* sp. along with some fungi and halophylic bacteria formed a thin surface layer (~0.6 cm) overlying a black layer rich in sulfate reducing coccoid bacteria.

5.2.3. Hexahydrite $MgSO_4 \cdot 6H_2O$; Epsomite $MgSO_4 \cdot 7H_2O$

Hexahydrite and epsomite have been found associated with anhydrite and nitratine at F1 where epsomite was a major constituent of a small light gray ring around a 1 m orange patch of boussingaultite.

5.3. Evaporite zone

The evaporite zone comprises those areas adjacent to the transition zone around fumaroles and the brush line along the marsh to the east of the fumaroles. The mineralogy is more typical of that found in arid closed sedimentary basins. Many of the sulfate minerals in this zone (blödite, glauberite, thenardite, mirabilite) are relatively common along the shoreline of the Salton Sea (Buck et al., 2011).

5.3.1. Blödite $Na_2Mg(SO_4)_2 \cdot 4H_2O$

Large areas containing blödite had been identified by remote sensing but ground truth verification was initially elusive. It was finally determined that the blödite was present in small amounts as 2–3 mm granular clusters (micro-snowballs) scattered on the surface at F1 and F2 (Fig. 38a). This morphology is common for sulfates of pedogenic origin (Buck et al., 2006). More rarely it occurs as corroded euhedral

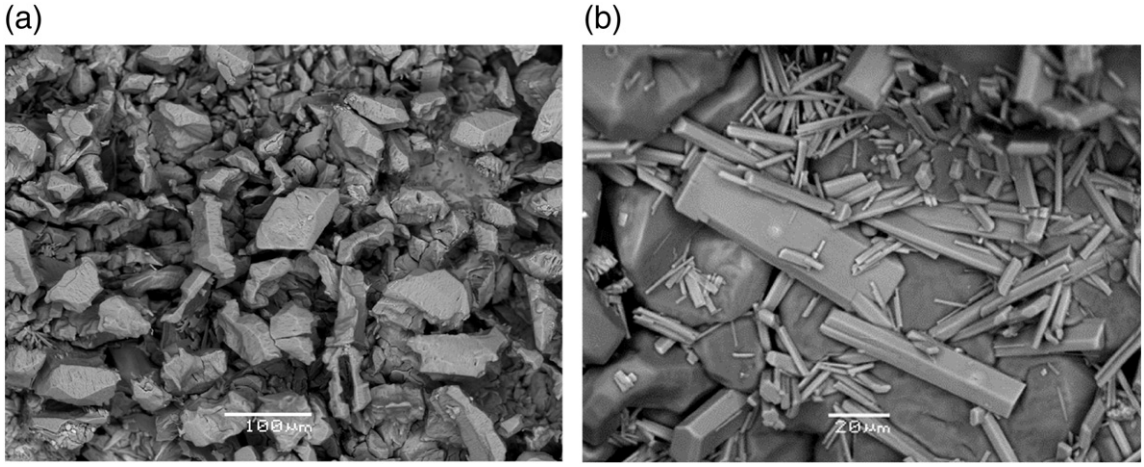

Fig. 34. (a) SEM image of lecontite crystals from F1. (b) SEM image of koktaite crystals on boussingaultite from F1.

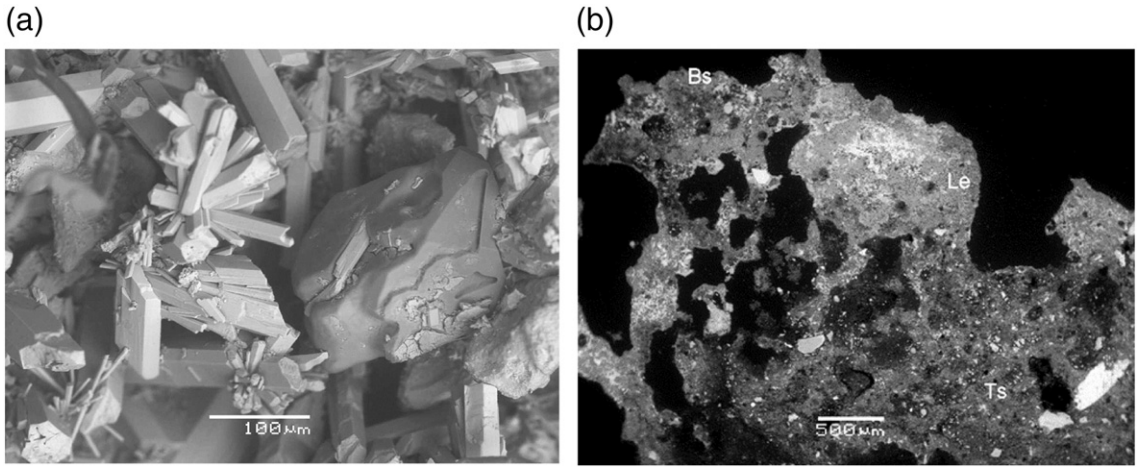

Fig. 35. (a) SEM image of blocky tschermigite crystal with bladed gypsum. (b) Backscatter SEM image of cross section of yellow efflorescence from F1. Top zone is a mixture of boussingaultite (Bs), lecontite (Le) and an unidentified Na–K–Fe sulfate (white). Bottom darker zone is tschermigite (Ts).

crystals to 0.3 mm (Fig. 38b). Cross sections of these samples revealed a blödite crust up to 1 mm thick which was underlain by sand that was poorly consolidated with minute (0.05 mm) acicular glauberite (Fig. 39). Blödite has also been mapped (and verified) along the brush line. Blödite crystallizes between -6.2 °C and 21.6 °C from solutions containing its constituent ions. At -6.3 °C it is in equilibrium with epsomite [$MgSO_4 \cdot 7H_2O$] and mirabilite [$Na_2SO_4.10H_2O$] and at 21.6 °C with vanthoffite [$MgNa_6(SO_4)_4$] and löweite [$Mg_2Na_4(SO_4)_4 \cdot 5H_2O$] while from solutions saturated in NaCl it may form at temperatures between -15.3 °C and 15.3 °C (Palache et al., 1951).

5.3.2. Konyaite $Na_2Mg(SO_4)_2 \cdot 5H_2O$

On November 28, 2013 botryoidal efflorescent konyaite occurred in growths collected from several centimeter-deep boot prints following a heavy rain that occurred 5 days earlier. On a later trip it formed more extensive deposits at the base of a small gryphon (at F2). Konyaite is relatively unstable and under low humidity conditions alters to blödite (Van Doesburg et al., 1982). However, it has been shown that synthetic konyaite completely decomposes to a mixture of thenardite, hexahydrite, blödite and löweite (Mills et al., 2010).

5.3.3. Glauberite $Na_2Ca(SO_4)_2$

Glauberite was identified by XRD as a minor constituent in areas containing blödite at F1 and F2NC. It occurs as acicular crystals (to 50 μm) in loosely consolidated material below blödite crusts (Fig. 39b, 40a). It has not been recognized visually.

5.3.4. Thenardite Na_2SO_4

The presence of conspicuous thenardite appears to be ephemeral. About a month after a heavy rain (2.4 cm) on November 23, 2013 extensive crusts of thenardite, often with or after mirabilite (Fig. 40b), were observed on the west side of F2 complex and the F2 SE brush line mud flats. These crusts were not present on previous visits. Isolated patches of thenardite have also been identified from the outer portions of the F2 north complex. Thenardite and blödite have typically been identified by remote sensing along the brush line. It has been difficult to identify in hand samples. A cross section of material from the brush line revealed thenardite intergrown with blödite and minor glauberite (Fig. 41a). In January 2014 extensive regions of halite around F1 were identified as containing minor amounts of thenardite and blödite.

5.3.5. Mirabilite $NaSO_4 \cdot 10H_2O$

The existence of mirabilite is also ephemeral and extensive crusts altering to thenardite were observed in late December 2013 on the west side of the F2 field and along the brush line SE of F2. Bladed crystals of mirabilite, about 4 mm × 20 mm, altering to thenardite were found in deep boot prints and tire tracks at F2 (Fig. 41b). At some point after

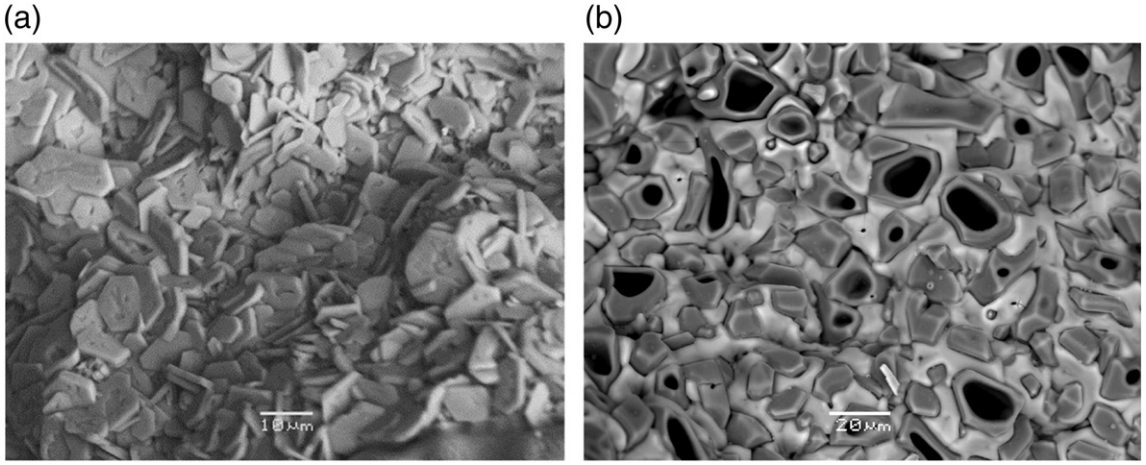

Fig. 36. a) SEM image of pseudohexagonal natrojarosite crystals. b) SEM image of cavernous mascagnite surrounded by sal ammoniac from F1.

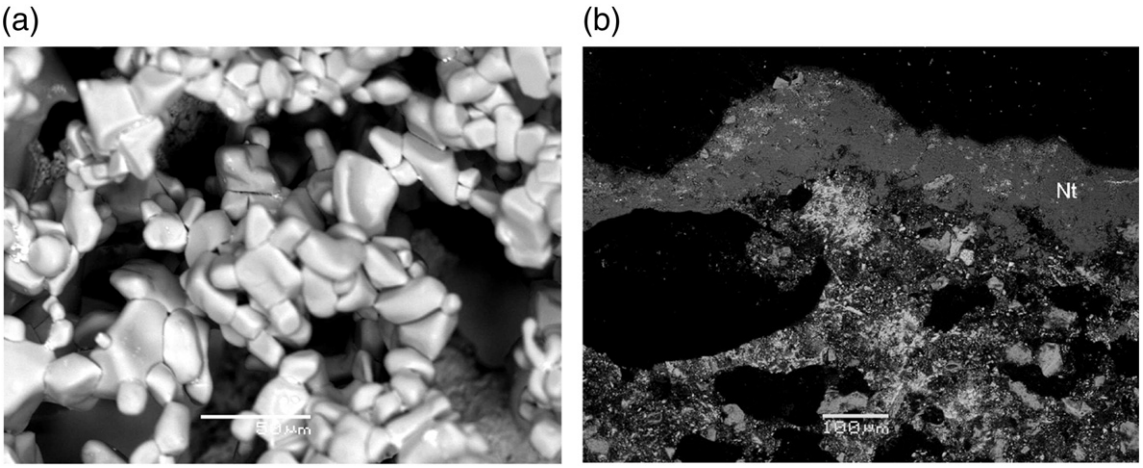

Fig. 37. (a) SEM image of nitratine crystals from F1. (b) Backscatter SEM image of polished cross section of nitratine crust (Nt) from F1. Bright areas under crust are anhydrite/bassanite.

the visit on November 29, 2013 these depressions evidently partially filled with saturated fluids from which the mirabilite crystallized. The thenardite forms pseudomorphic hollow casts after the mirabilite crystals. These casts are very delicate and are probably easily disturbed and redistributed by wind and blowing sand.

5.3.6. Bischofite $MgCl_2 \cdot 6H_2O$

Granular bischofite, associated with acicular glauberite, was found in material collected from the brush line in 2015 that was identified by remote sensing as containing blödite (Fig. 41b).

5.3.7. Halite NaCl

Halite is ubiquitous as thin white surface films and crystalline crusts away from the gryphons and fumaroles. The extent of the halite efflorescence varies depending on how recently it rained and the amount of time to draw saline solutions to the surface from capillary action. Cubic crystals of halite to 3 mm have been observed in boot prints and tire tracks where water accumulated after heavy rains.

6. Comparison with the Davis-Schrimpf fumarole field

The Davis-Schrimpf (DS) fumarole field lies 3.2 km to the southeast on the same trend as the F1 and F2 fields. Since it is further from the Salton Sea it is drier and because the mud has a thicker consistency much taller gryphons (to 3 m) have developed (Mazzini et al., 2011; Onderdonk et al., 2011). Water dominated seeps have temperatures between 15 °C and 32 °C while mud pots and seeps are hotter (22–62 °C) (Svensen et al., 2007). In contrast many of the clear pools at F1 and the main mud pot area at F2 are boiling, but distal pools at F2 are near ambient. The water from DS has pH that varies from 5.2 to 6.8 and the salinity (total dissolved solids) ranges from 1.5 to 134 g/l (Svensen et al., 2007, 2009; Mazzini et al., 2011). These are comparable with what has been observed at F1 and F2, but from limited measurements, the maximum TDS content at F2 was 87 g/l. Significant ammonia emissions have been mapped at F1 and F2 (Tratt et al., 2011) but the exact gas composition has not been determined. No ammonia has been detected from the fumaroles at DS where the main gaseous species are carbon dioxide and to a much lesser extent — methane (<2 vol.%) (Svensen et al., 2007; Mazzini et al., 2011). It is not surprising that no ammonium-containing minerals have been identified at DS. There appears to be a much deeper source of ammonia at DS since it has been observed in the cooling tower emissions from the adjacent geothermal power plant (Tratt et al., 2016). The most obvious difference between DS and F1–F2 is related to the ammonia emissions in the latter which are responsible for the significant development of ammonium-containing sulfates (mascagnite, boussingaultite, lecontite and koktaite). Sulfates at DS are poorly developed and limited to a ~20 cm diameter area at the summit of a small (1 m high) gryphon at the

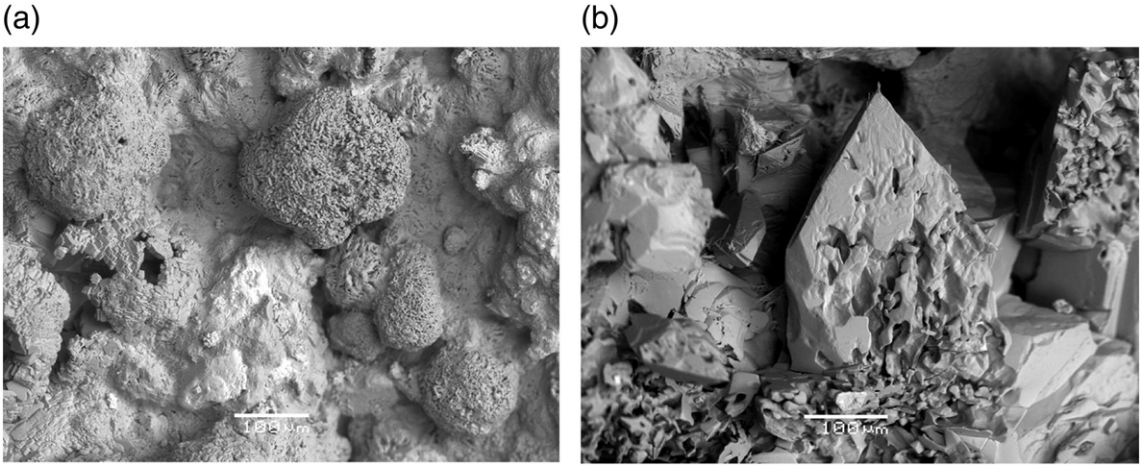

Fig. 38. (a) SEM image of clusters of blödite micro-snowballs from F2. (b) Corroded blödite crystal from F2.

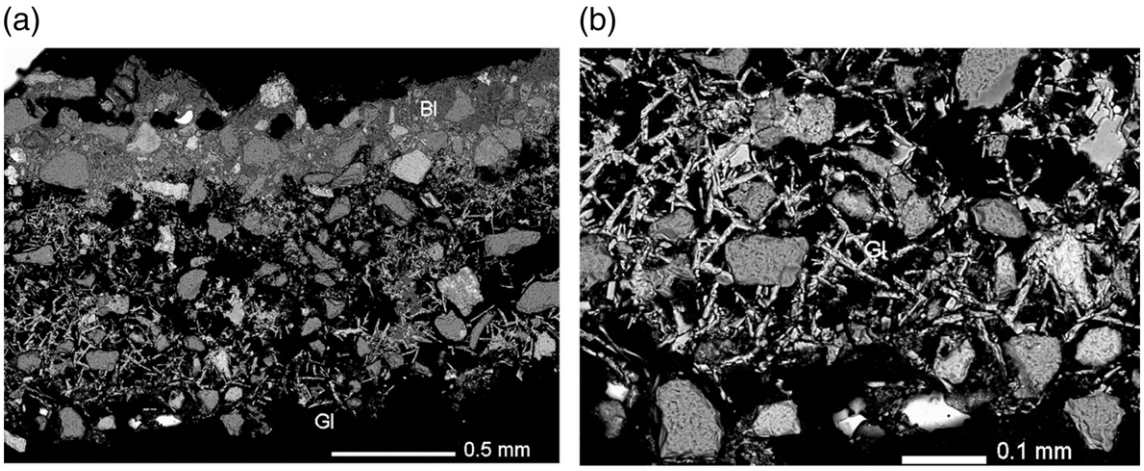

Fig. 39. (a) Backscatter SEM cross section through surface blödite (Bl) crust (top). (b) Close up of poorly consolidated sand under blödite crust with acicular grains of glauberite (Gl).

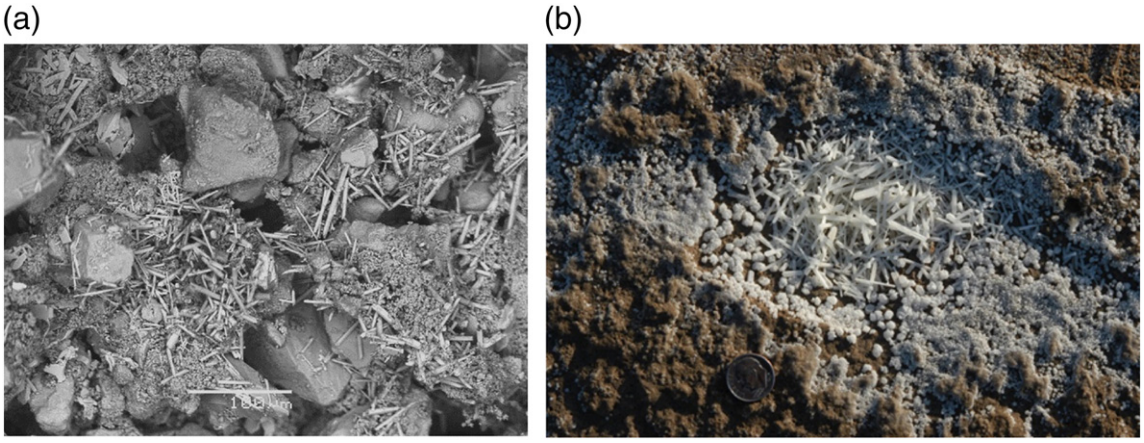

Fig. 40. (a) SEM image of acicular glauberite crystals on sand grains below crust of blödite from F2. (b) Thenardite after mirabilite precipitated from solution collected in a boot print. FOV 15 cm.

south side of the field and two nearby surface patches (to 3 m × 3 m). Mazzini et al. (2011) trenched one of the surface exposures and found tamarugite and blödite. Adams and Lynch (2014) performed a more extensive study and additionally found limited quantities of hexahydrite, starkeyite, epsomite, gypsum, anhydrite, pickeringite, halotrichite, natrojarosite, alum-K, thenardite, voltaite, cinnabar and sulfur. Reath and Ramsey (2013) mapped extensive fields of anhydrite, gypsum and their unknown Mg-sulfate at DS. We were unable to corroborate this latter observation, which we believe may be interpreted differently as discussed in Section 4.2.4.

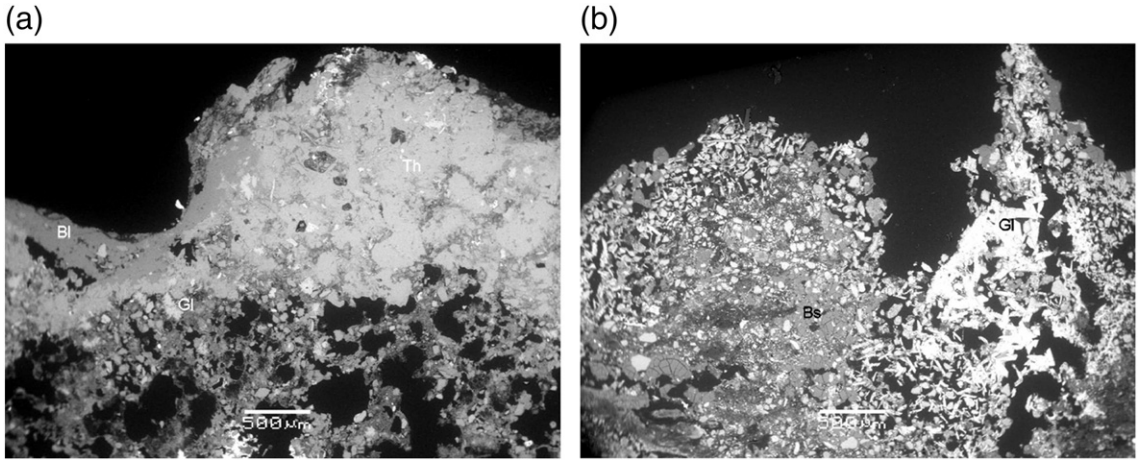

Fig. 41. a) Backscatter SEM image of a cross section of thenardite (Th)–blödite (Bl)–glauberite (Gl) crust from the brush line area. The glauberite forms small (200–300 μm) radiating clusters of crystals. b) Backscatter SEM image of cross section of bischofite (Bs) and acicular glauberite (Gl).

Table 6
Summary of major surface and subsurface mineralogy of fumarole zones.

	Fumarole zone	Transition zone	Evaporite zone
Surface	Mascagnite, boussingaultite, gypsum, lecontite, koktaite, sulfur[a]	Nitratine	Blödite, thenardite, mirabilite, halite
Sub-surface[b]	Quartz, sulfur	Quartz, anhydrite, bassanite	Quartz, glauberite

[a] Localized to active vents.
[b] Based on limited sampling.

7. Summary/conclusions

We have described an active moderate-temperature ammonia-emitting fumarole area which has an unusual assemblage of ammonium sulfate minerals that formed following the drop in the Salton Sea level from 2009 to 2017. This study is significant since recently access to the area has been restricted and there have been large scale changes to the landscape and hydrology as a result of wind-borne dust mitigation efforts. Plans for a large scale geothermal plant on the site further endanger the long term fate of the fumaroles.

The large scale mineral zonation mapped by SEBASS and Mako was verified by ground truth sampling. The zonation has been sustained and relatively consistent since about 2013 when the fumaroles had become fully emerged and relatively dry. Recently this trend has been reversed for F1 which now is surrounded by shallow water and much of the evaporite and transition zone has been resubmerged. Minor variations in mineralogy are probably a result of differences in rainfall which can dissolve and transport highly soluble salts (Table 5), ground water level (a function of Salton Sea level and irrigation runoff) and recent daytime temperatures. The latter two may influence the level of the capillary fringe and the formation of evaporative crusts. Other factors such as wind and wind-blown sand may also modify the surface mineralogy by sandblasting, transport or burial. The large scale mineral rings also reproduce the much smaller zonation seen around individual satellite fumarole vents (Fig. 11). In these cases sulfur crystals are found surrounding the vents, usually in close association with gypsum. Outwardly there is a zone closely associated with the fumaroles consisting of ammonium sulfates (mascagnite, lecontite, koktaite and boussingaultite) followed by a transition zone containing a dark brown zone of nitratine and subsurface anhydrite/bassanite (Table 6). The outermost zone is more related to evaporites. This zone with blödite, and to a lesser extent thenardite, is usually not observed around smaller vents. An example of the small scale zonation is shown in Fig. 28, which was constructed from diffuse reflectance FTIR spectra obtained with the Exoscan.

The mineral zonation may be a result of chemical and temperature gradients from the ammonia emitting vents and mineral solubilities probably also contribute. In the evaporation of complex salt mixtures from hypersaline lakes, typically the least soluble minerals sequentially precipitate first and form the outer-most rings of the concentric structures (Hardie, 1968; Hunt et al., 1966; Jones, 1965). At the fumaroles gypsum is usually associated with sulfur closest to the vents and it along with anhydrite are the least soluble sulfates present. The ammonium sulfates mascagnite, boussingaultite and lecontite are closely associated with the vents but are much more water soluble and form thick efflorescent growths on the surface. Surrounding this ammonium dominated fumarole zone is a transition region where nitrates form from the ammonium salts, probably assisted by microbial action. This is characterized by a dark brown zone which contains nitratine at the surface. Outward from this is a less recognizable zone with sulfate minerals (blödite, thenardite) more representative of the end stage of evaporite sequences from neutral brines such as in the Saline Valley, CA (Hardie, 1968) or pedogenic soils in arid environments (Buck et al., 2006). In the latter case the sulfates form a surface crust resulting from high evaporation rates along the top of the capillary fringe. Blödite, thenardite and glauberite are relatively common along the shoreline of the Salton Sea (Buck et al., 2011), and other dry saline lakes (Mees et al., 2011; Orti et al., 2002).

One of the significant findings of this study is field and remote sensing verification that fine grained quartz or other silicates entrapped in halite can produce unexpected modifications to the reflectance/emissivity spectra of underlying minerals, in this case to quartz, in the outer evaporite zone. The result is a range of spectra that do not resemble end member spectra in remote sensing spectral libraries. This greatly complicates the correct identification and mapping of these areas and points to the importance of performing ground truth sampling of such halite-rich areas.

Acknowledgements

This research was supported in part by The Aerospace Corporation's Independent Research and Development program. G. Rossman and J. Leadbetter are thanked for reviewing the microbiological content. Christian Schoneman of the US Fish and Wildlife Service provided valuable logistical support. H. Svensen and an anonymous reviewer are thanked for constructive comments that improved the contents and flow of the paper.

References

Adams, P.M., Lynch, D.K., 2014. A mineralogical inventory of geothermal features southeast of the Salton Sea, Imperial County, California. In: Reynolds, R. (Ed.), 2014 Desert Symposium Field Guide and Proceedings. Cal. State Univ. Fullerton Desert Studies Consortium:pp. 100–111 (http://nsm.fullerton.edu/dsc/images/DSCdocs/2014Notadroplefttodrink.pdf#page=100.).
Bailey, G.E., 1902. The saline deposits of California. Calif. State Min. Bur. Rpt. 24, 178–180.
Baldridge, A.M., Hook, S.J., Grove, C.I., Rivera, G., 2009. The ASTER spectral library version 2.0. Remote Sens. Environ. 113 (4):711–715. https://doi.org/10.1016/j.rse.2008.11.007.
Berger, J.A., King, P.L., Green, A., Craig, M.A., Spilde, M.N., Wright, S.P., Kunkel, T.S., Lee, Rachel J., 2015. Effect of halite coatings on thermal infrared spectra. J. Geophys. Res. Solid Earth 120:2162–2178. https://doi.org/10.1002/2014JB011712.
Bishop, H.K., Bricarello, J.R., 1978. Scaling and corrosion in an experimental geothermal power plant. J. Pet. Technol. 30 (9):1240–1242. https://doi.org/10.2118/6612-PA.
Blount, C.W., Dickson, F.W., 1973. Gypsum-anhydrite equilibria in the systems $CaSO_4$-H_2O and $CaCO_4$-NaCl-H_2O. Am. Mineral. 58, 323–331.
Brothers, D., Driscoll, N., Kent, G., Harding, A., Babcock, J., Baskin, R., 2009. Tectonic evolution of the Salton Sea inferred from seismic reflection data. Nat. Geosci. 2:581–584. https://doi.org/10.1038/ngeo590.
Buck, B.J., Wolff, K., Merkler, D.J., McMillan, N.J., 2006. Salt mineralogy of Las Vegas Wash, Nevada: morphology and subsurface evaporation. Soil Sci. Soc. Am. J. 70 (5): 1639–1651. https://doi.org/10.2136/sssaj2005.0276.
Buck, B.J., King, J., Etyemezian, V., 2011. Effects of salt mineralogy on dust emissions, Salton Sea, California. Soil Sci. Soc. Am. J. 75 (5):1958–1971. https://doi.org/10.2136/sssaj2011.0049.
Buckland, K.N., Young, S.J., Keim, E.R., Johnson, B.R., Johnson, P.D., Tratt, D.M., 2017. Tracking and quantification of gaseous chemical plumes from anthropogenic emission sources within the Los Angeles Basin. Remote Sens. Environ. 201:275–296. https://doi.org/10.1016/j.rse.2017.09.012.
Chen, S., Peng, X., Xu, H., Ta, K., 2016. Nitrification of archaeal ammonia oxidizers in a high-temperature hot spring. Biogeosciences 13 (7):2051–2060. https://doi.org/10.5194/bg-13-2051-2016.
Chou, I.-M., Seal II, R.R., Wang, A., 2013. The stability of sulfate and hydrated sulfate minerals near ambient conditions and their significance in environmental and planetary sciences. J. Asian Earth Sci. 62:734–758. https://doi.org/10.1016/j.jseaes.2012.11.027.
Christensen, P.R., Bandfield, J.L., Hamilton, V.E., Howard, D.A., Lane, M.D., Piatek, J.L., Ruff, S.W., Stefanov, W.L., 2000. A thermal emission spectral library of rock-forming minerals. J. Geophys. Res. 105 (E4):9735–9739. https://doi.org/10.1029/1998JE000624.
Ciesielczuk, J., Zaba, J., Bzowska, G., Gaidzik, K., Glogowska, M., 2013. Sulphate efflorescences at the geyser near Pinchollo, southern Peru. J. S. Am. Earth Sci. 42, 186–193.
Clark, R.N., Swayze, G.A., Wise, R., Livo, K.E., Hoefen, T.M., Kokaly, R.F., Sutley, S.J., 2007. USGS Digital Spectral Library splib06a. U.S. Geological Survey, Data Series 231 (http://speclab.cr.usgs.gov/spectral.lib06/ds231/datatable.html).
Cluotis, E.A., Hawthorne, F.C., Mertzman, S.A., Krenn, K., Craig, M.A., Marcino, D., Methot, M., Strong, J., Mustard, J.F., Blaney, D.L., Bell III, J.F., Vilas, F., 2006. Detection and discrimination of sulfate minerals using reflectance spectroscopy. Icarus 184 (1): 121–157. https://doi.org/10.1016/j.icarus.2006.04.003.

Corazza, E., Sabelli, C., Giuseppetti, G., 1967. The crystal structure of lecontite, $NaNH_4SO_4 \cdot 2H_2O$. Acta Cryst. 22:683–687. https://doi.org/10.1107/S0365110X67001355.

Dangermond, J., 2003. Salton Sea Atlas. ESRI Press (136 pp.).

DeMartIn, C., Gramaccolli, C.M., Campostrini, I., 2009. Brontesite, $(NH_4)_3PbCl_5$, a new product of fumarolic activity from La Fossa crater, Aeolian Islands, Italy. Can. Mineral. 47 (5):1237–1243. https://doi.org/10.3749/canmin.47.5.1237.

Dimitrov, L., 2002. Mud volcanoes—the most important pathway for degassing deeply buried sediments. Earth-Sci. Rev. 59 (1–4):49–76. https://doi.org/10.1016/S0012-8252(02)00069-7.

Draper, N.R., Smith, H., 1998. Applied regression analysis. Wiley Series in Probability and Statistics, 3rd edition.

Dunning, G.E., Cooper Jr., J.F., 1993. History and minerals of The Geysers, Sonoma County, California. Mineral. Rec. 24 (5), 339–354.

Eastes, J.W., 1989. Spectral properties of halite-rich mineral mixtures: Implications for remote sensing of highly saline environments. Remote Sens. Environ. 27:289–304. https://doi.org/10.1016/0034-4257(89)90089-8.

Faust, R.J., Bloss, D.F., 1963. X-ray study of lecontite. Am. Mineral. 48 (1–2):180–188 (http://www.minsocam.org/ammin/AM48/AM48_180.pdf).

Fuller, M.P., Griffiths, P.R., 1978. Diffuse reflectance measurements by infrared Fourier transform spectrometry. Anal. Chem. 50 (13):1906–1910. https://doi.org/10.1021/ac50035a045.

Gunatilaka, A., 1990. Anhydrite diagenesis in a vegetated sabkha, Al-Khiran, Kuwait, Arabian Gulf. Sedimentary Geology 69:95–116. https://doi.org/10.1016/0037-0738(90)90103-Z.

Gurbuz, A., 2010. Geometric characteristics of pull-apart basins. Lithosphere 2 (3): 199–206. https://doi.org/10.1130/L36.1.

Hackwell, J.A., Warren, D.W., Bongiovi, R.P., Hansel, S.J., Hayhurst, T.L., Mabry, D.J., Sivjee, M.G., Skinner, J.W., 1996. LWIR/MWIR imaging hyperspectral sensor for airborne and ground-based remote sensing. Proc. SPIE 2819:102–107. https://doi.org/10.1117/12.258057.

Hall, J.L., Boucher, R.H., Gutierrez, D.J., Hansel, S.J., Kasper, B.P., Keim, E.R., Moreno, N.M., Polak, M.L., Sivjee, M.G., Tratt, D.M., Warren, D.W., 2011. First flights of a new airborne thermal infrared imaging spectrometer with high area coverage. Proc. SPIE 8012:801203. https://doi.org/10.1117/12.884865.

Hanks, H.G., 1882. Mud volcanoes and the Colorado Desert. Second annual report of the State Mineralogist of California; from December 1, 1880 to October 1, 1882. Calif. Min. Bur. Rep. 2, 227–240.

Hardie, L.A., 1968. The origin of the recent non-marine evaporite deposit of Saline Valley, Inyo County, California. Geochim. Cosmochim. Acta 32 (12):1279–1301. https://doi.org/10.1016/0016-7037(68)90029-X.

Hauksson, E., Stock, J., Hutton, K., Yang, W., Vidal-Villegas, A., 2011. The 2010 M_w 7.2 El Mayor-Cucapah earthquake sequence, Baja California, Mexico and Southernmost California, USA: active seismotectonics along the Mexican Pacific Margin. Pure Appl. Geophys. 168 (8):1255–1277. https://doi.org/10.1007/s00024-010-0209-7.

Helgeson, H., 1968. Geologic and thermodynamic characteristics of the Salton Sea geothermal system. Am. J. Sci. 266 (3):129–166. https://doi.org/10.2475/ajs.266.3.129.

Hunt, G.R., Vincent, R.K., 1968. The behavior of spectral features in the infrared emission from particulate surfaces and various grain size. J. Geophys. Res. 73:6039–6046. https://doi.org/10.1029/JB073i018p06039.

Hunt, C.B., Robinson, T.W., Bowles, W.A., Washburn, A.I., 1966. Hydrologic Basin, Death Valley, California. USGS Prof. Paper 494B (https://pubs.usgs.gov/pp/0494b/report.pdf).

The Salton Sea Centennial Symposium. In: Hurlbert, S.H. (Ed.), Proceedings of a Symposium Celebrating a Century of Symbiosis Among Agriculture, Wildlife and People, 1905–2005, Held in San Diego, California, USA, March 2005 (Reprinted from Hydrobiologia 604 (1). http://rd.springer.com/journal/10750/604/1/page/1).

Jones, B.F., 1965. Hydrology and mineralogy of Deep Springs Lake, Inyo County California. USGS Prof. Paper 502A (https://pubs.usgs.gov/pp/0502a/report.pdf).

Kennan, G., 1917. The Salton Sea: An Account of Harriman's Fight with the Colorado River. The MacMillan Company, New York (106 pp.).

Kim, J., Kim, S., Tazaki, K., 2002. Mineralogical characterization of microbial ferrihydrite and schwertmannite, and non-biogenic Al-sulfate precipitates from acid mine drainage in the Donghae mine area, Korea. Environ. Geol. 42 (1):19–31. https://doi.org/10.1007/s00254-002-0530-2.

Kirkland, L., Herr, K., Keim, E., Adams, P., Salisbury, J., Hackwell, J., Treiman, A., 2002. First use of an airborne thermal infrared hyperspectral scanner for compositional mapping. Remote Sens. Environ. 80 (3):447–459. https://doi.org/10.1016/S0034-4257(01)00323-6.

Kirkland, L.E., Herr, K.C., Adams, P.M., 2003. Infrared stealthy surfaces: why TES and THEMIS may miss some substantial mineral deposits on Mars and implications for remote sensing of planetary surfaces. J. Geophys. Res. 108 (E12):5137. https://doi.org/10.1029/2003JE002105.

Koenig, J.B., 1969. Geysers geothermal field. Calif. Div. Mines, Geol., Mineral Info. Serv. 22 (8), 123–128.

Krohn, M.D., Kendall, C., Evans, J.R., Fries, T.L., 1993. Relations of ammonium minerals at several hydrothermal systems in the western US. J. Volcanol. Geotherm. Res. 56 (4):401–413. https://doi.org/10.1016/0377-0273(93)90005-C.

Lachenbruch, A., Sass, J., Galanis, S., 1985. Heat flow in southernmost California and the origin of the Salton Trough. J. Geophys. Res. 90 (B8):6709–6736. https://doi.org/10.1029/JB090iB08p06709.

Lane, M.D., 2007. Mid-infrared emission spectroscopy of sulfate and sulfate-bearing minerals. Am. Mineral. 92:1–18. https://doi.org/10.2138/am.2007.2170.

Lapham, D.M., Barnes, J.H., Downey Jr., W.F., Finkelman, R.B., 1980. Mineralogy Associated with Burning Anthracite Deposits of Eastern Pennsylvania. vol. 78. Commonwealth of Pennsylvania, Department of Environmental Resources, Bureau of Topographic and Geologic Survey (https://ia801907.us.archive.org/5/items/mineralogyassoci00laph/mineralogyassoci00laph.pdf).

Lebedeva, E.V., Alawi, M., Fiencke, C., Namsaraev, B., Bock, E., Spieck, E., 2005. Moderately thermophilic nitrifying bacteria from a hot spring of the Baikal rift zone. FEMS Microbiol. Ecol. 54 (2):297–306. https://doi.org/10.1016/j.femsec.2005.04.010.

LeConte, J.L., 1855. Account of some volcanic springs in the desert of the Colorado, Southern California. Am. J. Sci. Arts (2nd Ser.) 19 (55), 1–6.

Lee, T.C., Cohen, L.H., 1979. Onshore and offshore measurements of temperature gradients in the Salton Sea geothermal area, California. Geophysics 44 (2):206–215. https://doi.org/10.1190/1.1440962.

Lonsdale, P., 1989. Geology and tectonic history of the Gulf of California. In: Winterer, E.L., Hussong, D.M., Decker, R.W. (Eds.), The Eastern Pacific Ocean and Hawaii. Geological Society of America, The Geology of North America, N:pp. 499–521 https://doi.org/10.1130/dnag-gna-n.499.

Lynch, D.K., 2011. The coming land bridge to Mullet Island. In: Reynolds, R. (Ed.), 2011 Desert Symposium Field Guide and Proceedings. Cal. State Univ. Fullerton Desert Studies Consortium:pp. 96–100 (http://nsm.fullerton.edu/dsc/images/DSCdocs/2011shrinkingpliocene.pdf#page=97).

Lynch, D.K., Adams, P.M., 2014. Hot volcanic vents on Red Island, Imperial County, California. In: Reynolds, R. (Ed.), 2014 Desert Symposium Field Guide and Proceedings. Cal. State Univ. Fullerton Desert Studies Consortium:pp. 117–120 (http://nsm.fullerton.edu/dsc/images/DSCdocs/2014Notadroplefttodrink.pdf#page=117).

Lynch, D.K., Hudnut, K.W., 2008. The Wister mud pot lineament: southeastward extension or abandoned strand of the San Andreas Fault? Bull. Seismol. Soc. Am. 98 (4):1720–1729. https://doi.org/10.1785/0120070252.

Lynch, D.K., Hudnut, K.W., Adams, P.M., 2013. Development and growth of recently-exposed fumarole fields near Mullet Island, Imperial County, California. Geomorphology 195:27–44. https://doi.org/10.1016/j.geomorph.2013.04.022.

Lynch, D.K., Adams, P.M., Tratt, D.M., 2014. Mullet Island has become a peninsula. In: Reynolds, R. (Ed.), 2014 Desert Symposium Field Guide and Proceedings. Cal. State Univ. Fullerton Desert Studies Consortium:pp. 113–116 (http://nsm.fullerton.edu/dsc/images/DSCdocs/2014Notadroplefttodrink.pdf#page=113).

Macdonald, K.C., 1982. Mid-ocean ridges: fine scale tectonic, volcanic and hydrothermal processes within the plate boundary zone. Annu. Rev. Earth Planet. Sci. 10: 155–190. https://doi.org/10.1146/annurev.ea.10.050182.001103.

Manga, M., Brumm, M., Rudolph, M., 2009. Earthquake triggering of mud volcanoes. Mar. Pet. Geol. 26 (9):1785–1798. https://doi.org/10.1016/j.marpetgeo.2009.01.019.

Manolakis, D., Marden, D., Shaw, G.A., 2003. Hyperspectral image processing for automated target detection applications. Lincoln Lab. J. 14 (1): 79–116 (http://www.ll.mit.edu/publications/journal/pdf/vol14_no1/14_1hyperspectralprocessing.pdf).

Masalehdani, M.N.-N., Mees, F., Dubois, M., Coquinot, Y., Potdevin, J.-L., Fialin, M., Blanc-Valleron, M.-M., 2009. Condensate minerals from a burning coal-waste heap in Avion, northern France. Can. Mineral. 47 (3):865–884. https://doi.org/10.3749/canmin.47.3.573.

Mazzini, A., Svensen, H., Etiope, G., Onderdonk, N., Banks, D., 2011. Fluid origin, gas fluxes and plumbing system in the sediment-hosted Salton Sea geothermal system (California, USA). J. Volcanol. Geotherm. Res. 205 (3–4):67–83. https://doi.org/10.1016/j.jvolgeores.2011.05.008.

McCauley, C.A., O'Sullivan, A.D., Milke, M.K., Weber, P.A., Trumm, D.A., 2009. Sulfate and metal removal in bioreactors treating acid mine drainage dominated with iron and aluminum. Water Res. 43 (4):961–970. https://doi.org/10.1016/j.watres.2008.11.029.

McKibben, M.A., 2008. The Salton Sea geothermal brines. In: Reynolds, R. (Ed.), 2008 Desert Symposium Field Guide and Proceedings. Cal. State Univ. Fullerton Desert Studies Consortium:pp. 102–106 (http://nsm.fullerton.edu/dsc/images/DSCdocs/2008troughtotrough.pdf#page=102).

Mees, F., Castañeda, C., Herrero, J., Van Ranst, E., 2011. Blödite sedimentation in a seasonally dry saline lake (Salada Mediana, Spain). Sediment. Geol. 238 (1–2):106–115. https://doi.org/10.1016/j.sedgeo.2011.04.006.

Meltzner, A.J., Rockwell, T.K., Owen, L.A., 2006. Recent and long-term behavior of the Brawley fault zone, Imperial Valley, California: an escalation in slip rate? Bull. Seismol. Soc. Am. 96 (6):2304–2328. https://doi.org/10.1785/0120050233.

Mills, S.J., Wilson, S.A., Dipple, G.M., Raudsepp, M., 2010. The decomposition of konyaite: importance in CO_2 in mine tailings. Mineral. Mag. 74:903–917. https://doi.org/10.1180/minmag.2010.074.5.903.

Muffler, L.J.P., White, D.E., 1968. Origin of CO_2 in the Salton Sea geothermal system, southeastern California, USA. Proc. 23rd Intl. Geol. Congress 97, 185–194.

Muffler, L.J.P., White, D.E., 1969. Active metamorphism of the upper Cenozoic sediments in the Salton Sea geothermal field and the Salton Trough, southern California. Geol. Soc. Am. Bull. 80 (2):157–182. https://doi.org/10.1130/0016-7606(1969)80[157:AMOUCS]2.0.CO;2.

Mustard, J.F., Hays, J.E., 1997. Effects of hyperfine particles on reflectance spectra from 0.3 to 25 μm. Icarus 125:145–163. https://doi.org/10.1006/icar.1996.5583.

National Weather Service, 2017. Advanced Hydrologic Prediction Service. http://water.weather.gov/precip/.

Newark, R., Kasmeyer, P., Younker, L., 1988. Shallow drilling in the Salton Sea region: the thermal anomaly. J. Geophys. Res. 93 (B11):13005–13023. https://doi.org/10.1029/JB093iB11p13005.

Onderdonk, N., Shafer, L., Mazzini, A., Svensen, H., 2011. Controls on the expression and evolution of gryphons, mud pots, and caldera features at hydrothermal seeps in the Salton Sea Geothermal Field, Southern California. Geomorphology 130 (3–4): 327–342. https://doi.org/10.1016/j.geomorph.2011.04.014.

Orti, F., Gundogan, I., Helvaci, C., 2002. Sodium sulphate deposits of Neogene age: the Kirmir Formation, Beypazari Basin, Turkey. Sediment. Geol. 146 (3–4):305–333. https://doi.org/10.1016/S0037-0738(01)00140-3.

Palache, C., Berman, H., Frondel, C., 1951. The System of Mineralogy. 7th edition. John Wiley, New York, pp. 449–450.
Parafiniuk, J., Kruszewski, L., 2010. Ammonium minerals from burning coal-dumps of the Upper Silesian Coal Basin (Poland). Geol. Q. 53:341–356 (https://gq.pgi.gov.pl/gq/article/viewFile/7524/6174).
Praveen-Kumar, Aggarwal, R.K., Sharma, B.M., 1989. Nitrification and nitrate movement from ammonium sulphate and urea in sandy soils as affected by their previous applications. Fertil. Res. 21 (1):29–36. https://doi.org/10.1007/BF01054733.
Ramsey, M.S., Christensen, P.R., 1998. Mineral abundance determination: quantitative deconvolution of thermal emission spectra. J. Geophys. Res. 103B:577–596. https://doi.org/10.1029/97JB02784.
Reath, K.A., Ramsey, M.S., 2013. Exploration of geothermal systems using hyperspectral thermal infrared remote sensing. J. Volcanol. Geotherm. Res. 265:27–38. https://doi.org/10.1016/j.jvolgeores.2013.08.007.
Reigstad, L.J., Richter, A., Daims, H., Urich, T., Schwark, L., Schlepe, C., 2008. Nitrification in terrestrial hot springs of Iceland and Kamchatka. FEMS Microbiol. Ecol. 64 (2): 167–174. https://doi.org/10.1111/j.1574-6941.2008.00466.x.
Ribeiro da Luz, B., Crowley, J.K., 2010. Identification of plant species by using high spatial and spectral resolution thermal infrared (8.0–13.5 μm) imagery. Remote Sens. Environ. 114 (2):404–413. https://doi.org/10.1016/j.rse.2009.09.019.
Robinson, T.W., Hunt, C.B., 1961. Some extremes of climate in Death Valley, California. Short Papers in the Geologic and Hydrologic Sciences, Articles 1–146: Geological Survey Research 1961. U. S. Geological Survey Prof. Paper 424-B, pp. 192–194.
Robinson, P.T., Elders, W.A., Muffler, L.J., 1976. Quaternary volcanism in the Salton Sea geothermal field, Imperial Valley, California. Geol. Soc. Am. Bull. 87 (3):347–360. https://doi.org/10.1130/0016-7606(1976)87<347:QVITSS>2.0.CO;2.
Ross, C.P., Yates, R.G., 1942. The Coso quicksilver district, Inyo County, California. USGS Bull. 936-Q:394–415 (https://pubs.usgs.gov/bul/0936q/report.pdf).
Rudolph, M.L., Manga, M., 2010. Mud volcano response to the 4 April 2010 El Mayor–Cucapah earthquake. J. Geophys. Res. 115 (B12), B12211. https://doi.org/10.1029/2010JB007737.
Salisbury, J.W., Wald, A., 1992. The role of volume scattering in reducing spectral contrast of reststrahlen bands in spectra of powdered minerals. Icarus 96:121–128. https://doi.org/10.1016/0019-1035(92)90009-V.
Salisbury, J.W., Wald, A., D'Aria, D.M., 1994. Thermal-infrared remote sensing and Kirchhoff's law 1. Laboratory measurements. J. Geophys. Res. 99B (11):897–11911. https://doi.org/10.1029/93JB03600.
Schmitt, A.K., Vazquez, J., 2006. Alteration and remelting of nascent oceanic crust during continental rupture: evidence from zircon geochemistry of rhyolites and xenoliths from the Salton Trough, California. Earth Planet. Sci. Lett. 252 (3–4):260–274. https://doi.org/10.1016/j.epsl.2006.09.041.
Schmitt, A.K., Martín, A., Stockli, D.F., Farley, K.A., Lovera, O.M., 2013. (U-Th)/He zircon and archaeological ages for a late prehistoric eruption in the Salton Trough (California, USA). Geology 41 (1):7–10. https://doi.org/10.1130/G33634.1.
Shale, C.C., 1974. Ammonia injection: a route to clean stacks. Pollution Control and Energy Needs. Adv. Chem 127:pp. 195–205. https://doi.org/10.1021/ba-1973-0127.ch017 (Ch. 17).
Sobkowiak, M., Painter, P., 1995. A comparison of Drift and KBr pellet methodologies for the quantitative analysis of functional groups in coal by infrared spectroscopy. Energy Fuel 9:359–363. https://doi.org/10.1021/ef00050a022.
Spencer, R.J., 2000. Sulfate minerals in evaporate deposits. In: Alpers, C.N., Jambor, J.L., Nordstrom, D.K. (Eds.), Sulfate Mineralogy — Crystallography, Geochemistry and Environmental Science. Reviews in Mineralogy and Geochemistry 40:pp. 173–192. https://doi.org/10.2138/rmg.2000.40.3.
Sturz, A., Kamps, R., Earley, P., 1992. Temporal changes in mud volcanoes, Salton Sea geothermal area. In: Kharaka, Y., Maest, A. (Eds.), Water-Rock Interactions 2. Balkema, Rotterdam, Netherlands, pp. 1363–1366.
Svensen, H., Karlsen, D., Sturz, A., Backer-Owe, K., Banks, D., Planke, S., 2007. Processes controlling water and hydrocarbon composition in seeps from the Salton Sea geothermal system, California, USA. Geology 35 (1):85–88. https://doi.org/10.1130/G23101A.1.
Svensen, H., Hammer, Ø., Mazzini, A., Onderdonk, N., Polteau, S., Planke, S., Podladchikov, Y.Y., 2009. Dynamics of hydrothermal seeps from the Salton Sea geothermal system (California, USA) constrained by temperature monitoring and time series analysis. J. Geophys. Res. 114 (B9), B09201. https://doi.org/10.1029/2008JB006247.
Tratt, D.M., Young, S.J., Lynch, D.K., Buckland, K.N., Johnson, P.D., Hall, J.L., Westberg, K.R., Polak, M.L., Kasper, B.P., Qian, J., 2011. Remotely-sensed ammonia emission from fumarolic vents associated with a hydrothermally active fault in the Salton Sea Geothermal Field, California. J. Geophys. Res. 116 (D21), D21308. https://doi.org/10.1029/2011JD016282.
Tratt, D.M., Young, S.J., Johnson, P.D., Buckland, K.N., Lynch, D.K., 2016. Multi-year study of remotely-sensed ammonia emission from fumaroles in the Salton Sea geothermal field. Proceedings, 8th IEEE Workshop on Hyperspectral Image and Signal Processing: Evolution in Remote Sensing — WHISPERS (Los Angeles, CA, August 21–24, 2016).
Van Doesburg, J.D.J., Vergouen, L., van der Plas, L., 1982. Konyaite, $Na_2Mg(SO_4)_2 \cdot 5H_2O$, a new mineral from the Great Konya Basin, Turkey. Am. Mineral. 67 (9–10), 1035–1038.
Vaughan, R.G., Hook, S.J., Calvin, W.M., Taranik, J.V., 2005. Surface mineral mapping at Steamboat Springs, Nevada, USA, with multi-wavelength thermal infrared images. Remote Sens. Environ. 99 (1–2):140–158. https://doi.org/10.1016/j.rse.2005.04.030.
Veatch, J.A., 1858. Notes of a visit to the mud volcanoes in the Colorado Desert in the month of July 1857. Am. J. Sci., 2nd Ser. 26, 288–295.
Veatch, J., 1860. Salses or mud volcanoes of the Colorado Desert. Hesperian 3 (5), 481–489.
Warren, D.W., Boucher, R.H., Gutierrez, D.J., Keim, E.R., Sivjee, M.G., 2010. MAKO: a high-performance, airborne imaging spectrometer for the long-wave infrared. Proc. SPIE 7812:78120N. https://doi.org/10.1117/12.861374.
Young, S.J., Johnson, B.R., Hackwell, J.A., 2002. An in-scene method for atmospheric compensation of thermal hyperspectral data. J. Geophys. Res. 107 (D24):4774. https://doi.org/10.1029/2001JD001266.
Younker, L.W., Kasameyer, P.W., Tewhey, J.D., 1982. Geological, geophysical, and thermal characteristics of the Salton Sea geothermal field, California. J. Volcanol. Geotherm. Res. 12 (3–4):221–258. https://doi.org/10.1016/0377-0273(82)90028-2.

CRUSTAL STRUCTURE AND TECTONICS OF THE SALTON TROUGH
A SUMMARY

Gary Fuis and many collaborators

Seismic imaging of the Salton Trough (Fig. 1) began with the publication of Biehler et al. (1964) and continued with surveys conducted by the U.S. Geological Survey in 1979 (Fuis et al., 1984; Fig. 2), 1992 (Parsons and McCarthy, 1996; Fig. 2), and 2011 (Fuis et al., 2017; Fig. 3).

Key discoveries in the first USGS survey were 1) "basement" beneath the Imperial Valley is relatively low in velocity (5.6-5.8 km/s), 2) there is no reflection between sedimentary rocks and basement, and 3) basement shoals beneath known geothermal areas (Fig. 4). These discoveries led to the interpretation that "basement" was not pre-Cenozoic granitic metamorphic rocks, as exposed on the flanks of the Imperial Valley, but young metamorphosed Colorado river sedimentary rocks. Another discovery was that there was a "subbasement" at ~ 10-km depth beneath the Imperial Valley with velocities of mafic rocks (6.8-7.2 km/s); this layer could be modeled with a density of 3.1 g/cc (Fig. 5; purple layer), that compensated for the relatively low-density sedimentary and metasedimentary rocks above and could be interpreted as gabbroic rocks of an oceanic spreading center. Seismicity in the "Brawley Seismic zone" (Johnson and Hadley, 1976; Lin et al., 2007), extending between the Imperial fault and San Andreas fault (SAF), and also in the Cerro Prieto geothermal area of Mexico, are interpreted as surface manifestations of such spreading centers (Figs. 1, 2).

Key discoveries in the third USGS survey were that the subsurface geometry of the SAF, in the Coachella Valley, is not vertical or even planar. The fault dips steeply in the upper 6 km of the crust and then dips moderately NE below that (Fig. 6). This shape was revealed by at least 4 independent data sets, including seismic refraction and reflection data, gravity and aeromagnetic data, and seismicity data. This geometry is a refinement of the subsurface geometry of the southeast "blade" of the propeller-shaped SAF that had been interpreted in Fuis et al. (2012). Flower-structure faults in the hanging wall of the SAF include the Painted Canyon and Platform faults. A similar subsurface geometry is seen for the Banning branch of the SAF in the northern Coachella Valley.

Figures 7a and 7b represent a summary of the crustal structure and tectonics of the southern Coachella, Imperial, and Mexicali Valleys. Figure 7a is an older, colored interpretation. Figure 7b is an updated interpretation, where 1) the "Extra fault zone" of Brothers et al., (2009, 2011) has been added and 2) well data in Mexico has been added and the interpretation of buried pre-Cenozoic basement rocks has been extended into Mexico.

Figure 8 represents an updated version of the crustal and upper-mantle structure along a NW-SE cross section extending through the Coachella Valley, Salton Sea, Imperial Valley, Mexicali Valley, and Altar basin from Han et al. (2016a). Note that a thin (~ 5-km) layer of stretched continental crust, perhaps intruded by sparse mafic rocks, may or may not be present between the young metasedimentary rocks constituting "basement" in the Imperial Valley and

the prominent lower-crustal layer of mafic rocks above the mantle. Similar stretched continental crust is interpreted farther south in the Gulf of California as well as blocky extended continental crust observed in both the Imperial Valley (above this layer) and farther south (Gonzalez-Fernandez et al., 2005; Lizarralde et al., 2007; Martin-Barajas et al., 2013). The Conclusions of Han et al. (2016a) are reproduced below describing a revised interpretation of lower crustal structure in the Salton Trough.

Conclusions of Han et al. (2016a):

"The SSIP data constrain the crust to be 17–18 km thick and roughly one-dimensional from the northern Salton Sea to the southern end of the Imperial Valley. In the central Salton Trough, crystalline rocks (>5 km/s) occur at ~4 km depth and are interpreted to be sediment metamorphosed by high heat flow to ~8 km depth. Crystalline rocks with velocity of ~6.2–6.6 km/s are ~4.5 km thick and are interpreted to be either stretched preexisting continental crust or high-grade metamorphosed sediment, with possible minor basaltic intrusion. A high velocity of 6.7–6.8 km/s in the lower crust is interpreted as rift-related mafic intrusion by underplating. The upper mantle velocity is 7.85 km/s, indicative of high heat and partial melting. In contrast, in the Coachella Valley, sediment thins to the north, the crust thickens, and the basement is interpreted to be granitic continental crust. The Mexicali Valley is also interpreted to be underlain by thicker stretched continental crust. North American crust has been essentially rifted apart with steep continental margins. Since breakup, an ~100 km wide zone of new crust in the extensional direction has been created by magmatism from below, sedimentation from above, and metamorphism of the sediment. The active rift zone is interpreted to be at least ~100 km wide in the lower crust and upper mantle, despite the much narrower volcanic, thermal, and seismic features in the uppermost crust. The Salton Trough and northern Gulf of California emphasize the important role of river delta sedimentation upon late-stage rifting."

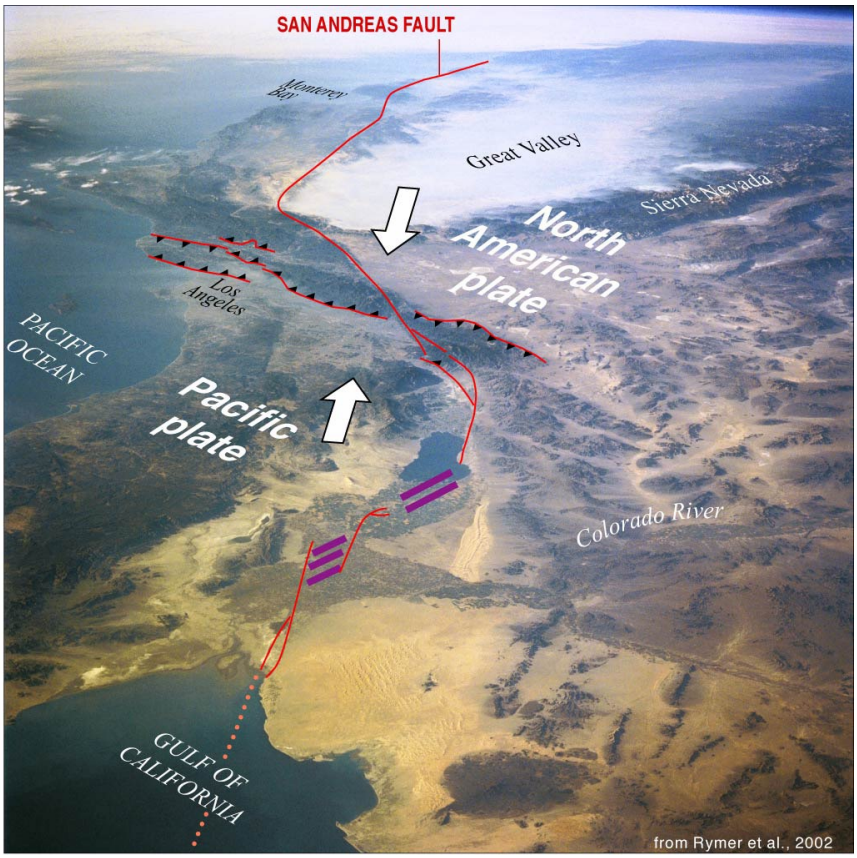

Figure 1. Oblique shuttle photo of southern California and northern Baja. Red lines, faults; teeth on upper plate. Purple lines, spreading centers, located within the Salton Trough.

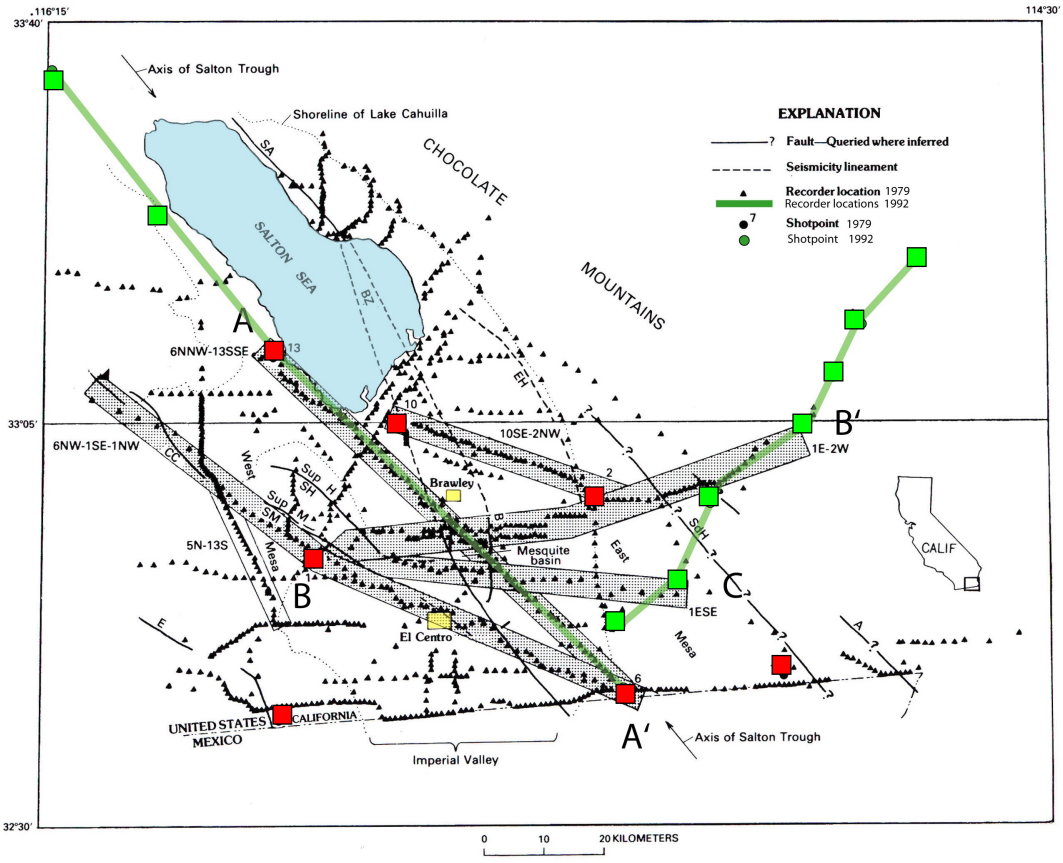

Figure 2. Explosion seismic surveys of 1979 and 1992. 1979 shotpoints, red with numbers; receivers, black triangles. 1992 shotpoints, green; receivers, deployed along green line. Stippled strips, chief profiles for 1979 along with abbreviations (6NW-1SE-1NW, etc). A, Algodones f.; BZ, Brawley seismic zone; E, Elsinore f.; EH, East Highline canal seismicity lineament; SA, San Andreas f.; SdH, Sand Hills f.; SH, Superstition Hills f.; SM, Superstition Mountains f. See Fuis et al. (1984) and Parsons and McCarthy (1996).

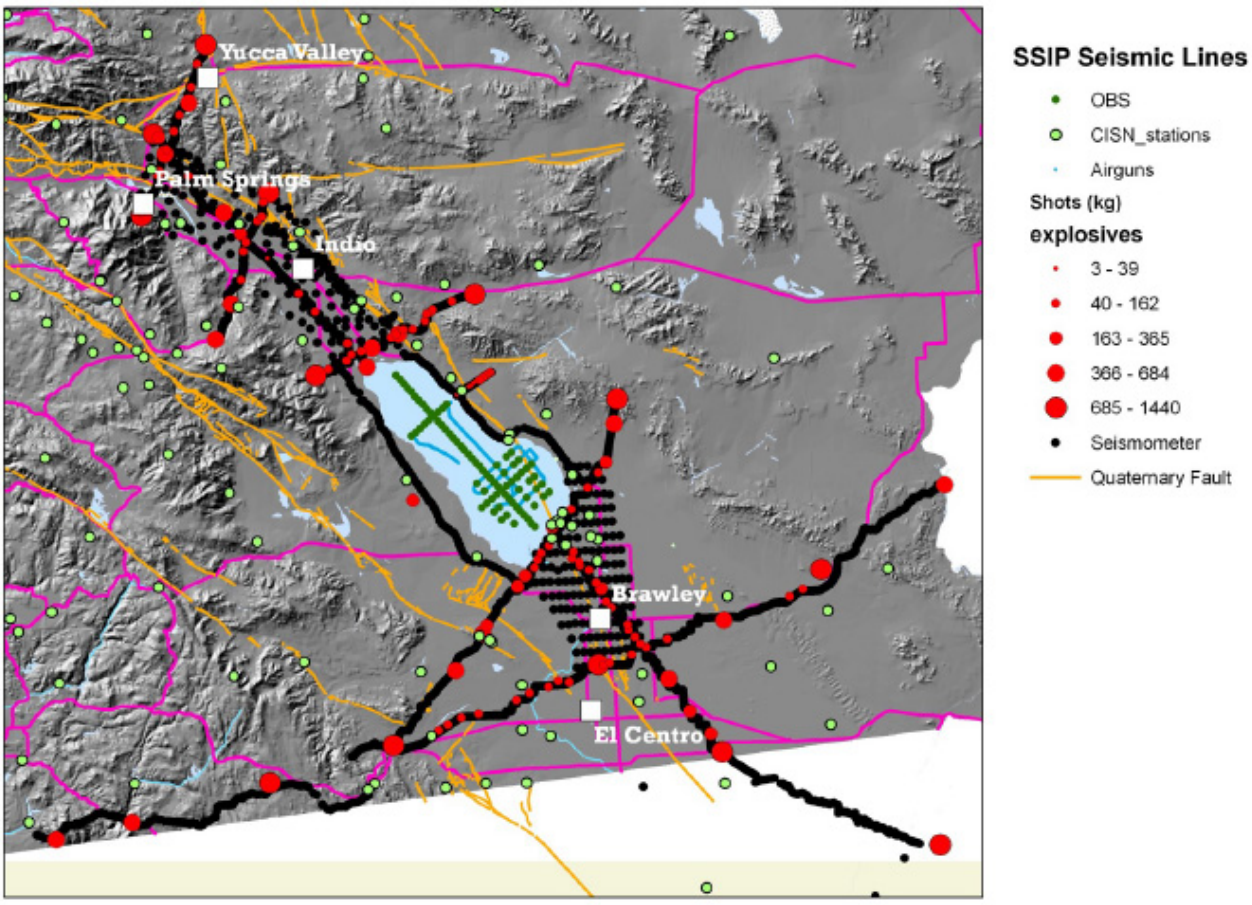

Figure 3. Explosion seismic survey for 2011 Salton Seismic Imaging Project. Salton Sea, large light blue feature. Quaternary faults, orange lines. Major roads, magenta lines. See Fuis et al. (2017).

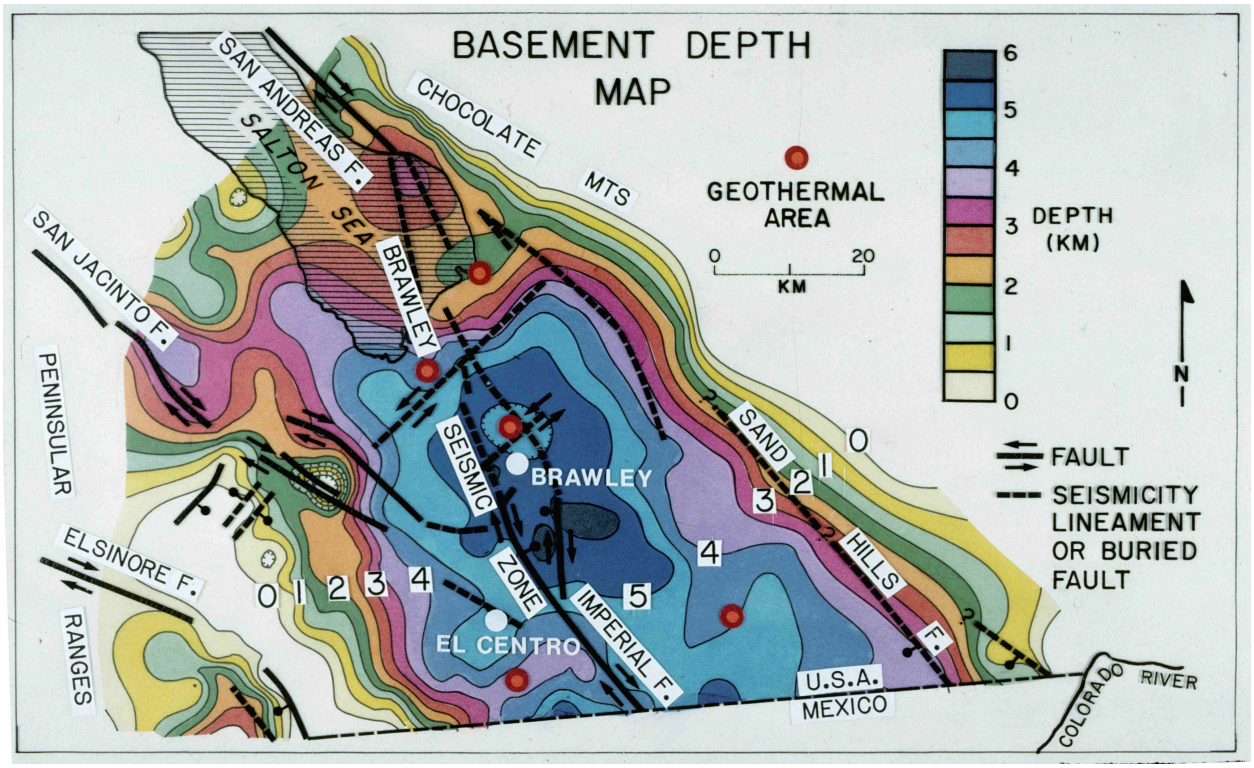

Figure 4. Basement-depth map interpreted from time-term analysis. See Kohler and Fuis (1986).

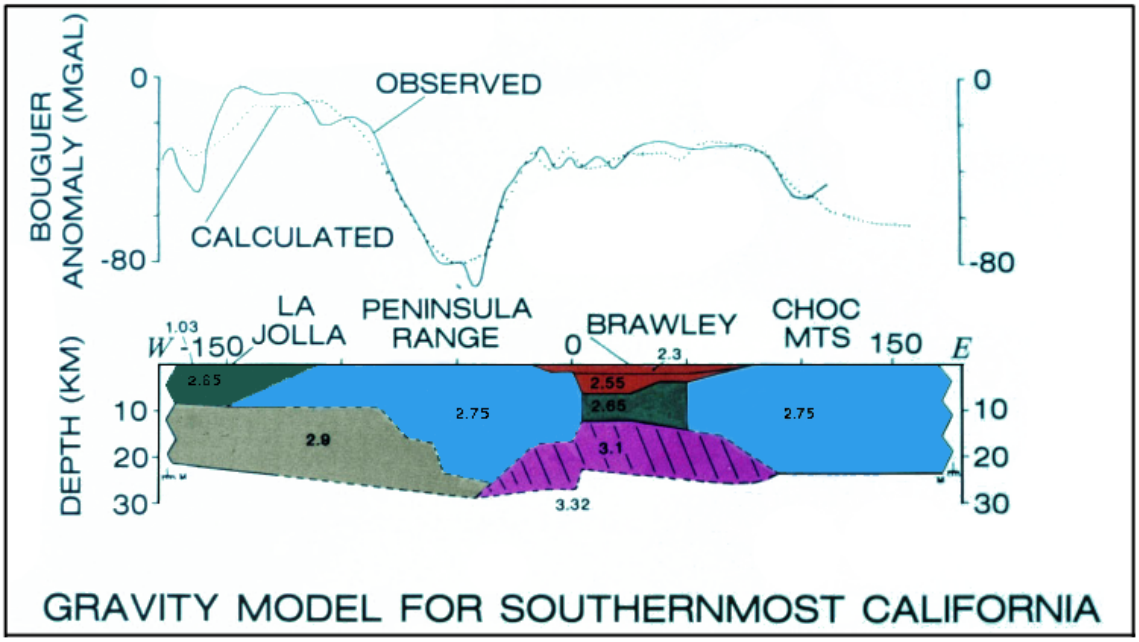

Figure 5. Gravity model for southernmost California. Densities, in g/cc. See Fuis et al. (1984).

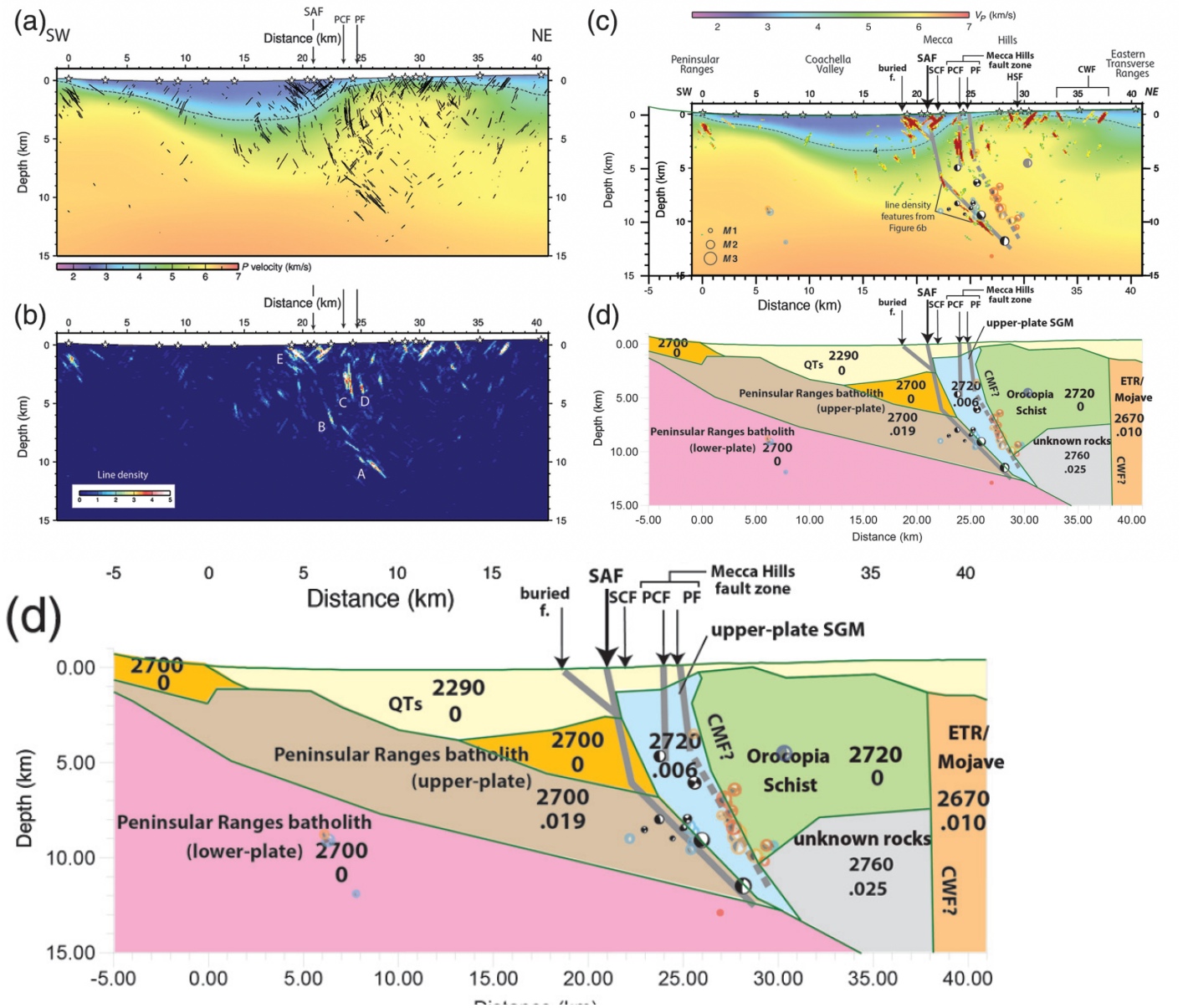

Figure 6. Seismic models along NE-SW profile immediately N of Salton Sea in Figure 5 (same as fig. 6 of Fuis et al., 2017). (a) Line-drawings of reverse-moveout reflections detected and migrated using algorithms of Bauer et al. (2013) and velocity model derived using the inversion algorithm of Hole (1992). White stars, shotpoints. (b) Line-drawing density diagram of reflections shown in (a). Line-drawing density is the number of migrated line segments in 100 m × 100 m grid cells weighted by their underlying waveform coherencies. Features A through E are the chief reflection packages repeated in (c). (c) Velocity model for profile with line-density features from (b) (using slightly different colors for line density), earthquakes (focal

mechanisms), and interpreted faults (heavy gray lines). M, magnitude. Far-hemisphere focal mechanisms (fm) from Yang et al. (2012) using hypocenters of Hauksson et al.(2012): black, fm within 2 km of line 4; dim gray and blue, fm from 2 to 10 km northwest of line 4; dim orange and red, fm from 2 to 10 km southeast of profile. Focal mechanisms are from the period 1981–2011. The focal mechanism solutions displayed are from the three highest quality categories (A, B, C) of Yang et al. (2012). CWF, ClemensWell fault (buried); PCF, Painted Canyon fault; PF, Platform fault; SAF, San Andreas fault; SCF, Skeleton Canyon fault. (d) Joint model of gravity and aeromagnetic data along profile. Interpreted faults (gray) and focal mechanisms are repeated from (c). Density (kg/m^3; top numbers); magnetic susceptibility (10^{-3} SI; bottom numbers). QTs, Quaternary-Tertiary sediments; CMF?, Chocolate Mountains fault? (buried, overturned?); ETR, eastern Transverse Ranges rocks; and SGM, San Gabriel Mountains rocks (see Powell, 1993). Figure 6c and 6d shows that the deep part of the SAF dips moderately northeast. A flowerlike structure, consisting of steeply dipping faults, is developed above ~ 6-km depth including the upper part of the SAF itself, the Painted Canyon and Platform faults, and possibly a buried fault at 18.5 km range. The upper, steeply dipping part of the SAF (above ∼6 km depth) is neither imaged by reflections or earthquakes. Its connection to the deeper, moderately dipping fault is inferred from the reflection pattern.

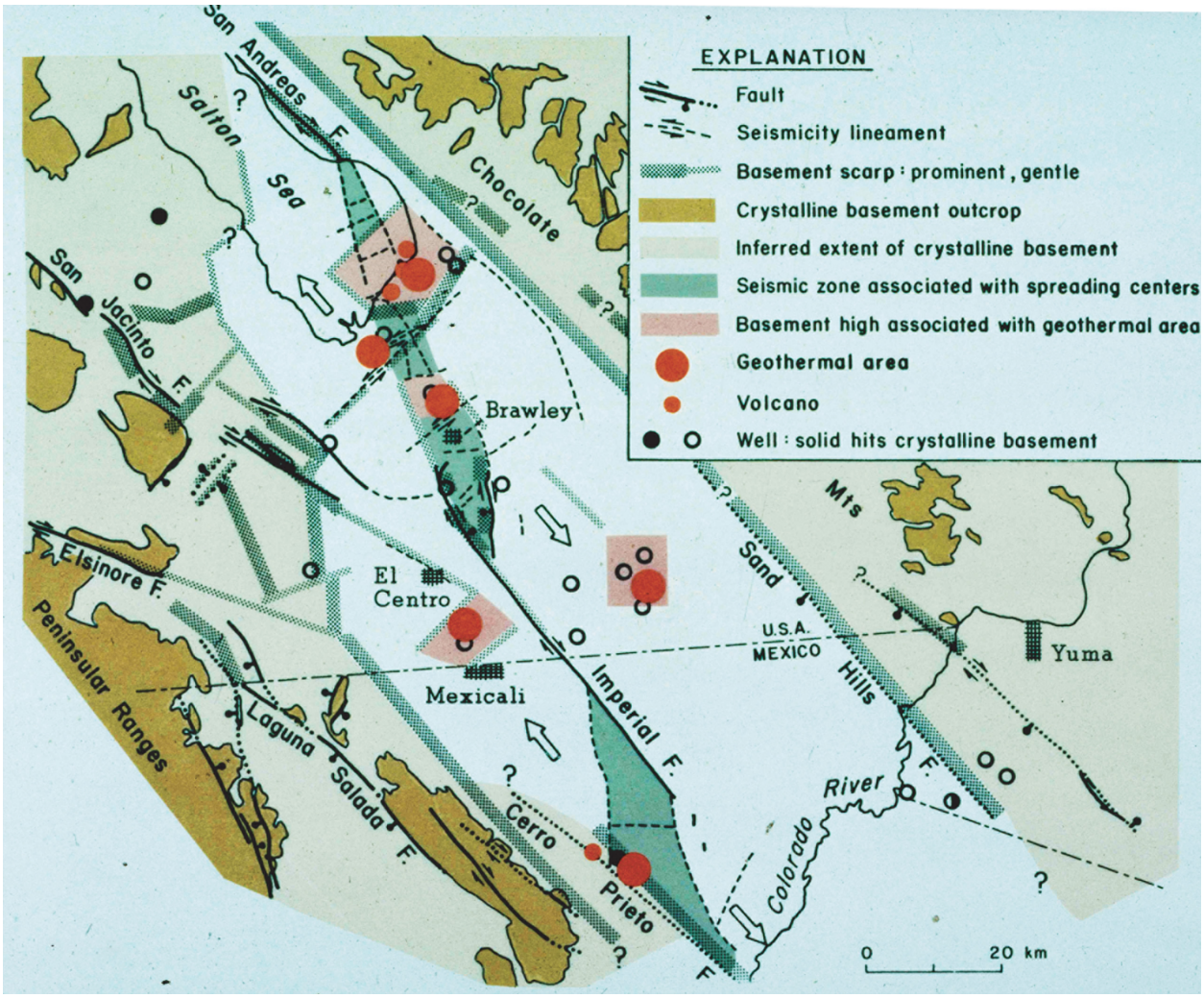

Figure 7a. Basement of the Salton Trough (exposed and inferred), faults (exposed and inferred), volcanoes, seismicity zones, and geothermal areas. Exposed pre-Cenozoic basement, darker brown; buried pre-Cenozoic basement, light brown; young metamorphic sedimentary basement, interpreted to be mostly sediment from the Colorado River, uncolored; faults, black lines; buried steep gradients in basement-depth contour map (see Figure 3), interpreted as possible faults, stippled lineaments (thicker lineaments, steeper gradients); seismicity zones, interpreted as spreading centers, gray lens-shaped features; volcanoes, small red dots; geothermal areas, large red dots surrounded by pink, representing basement highs. See Fuis and Kohler (1984).

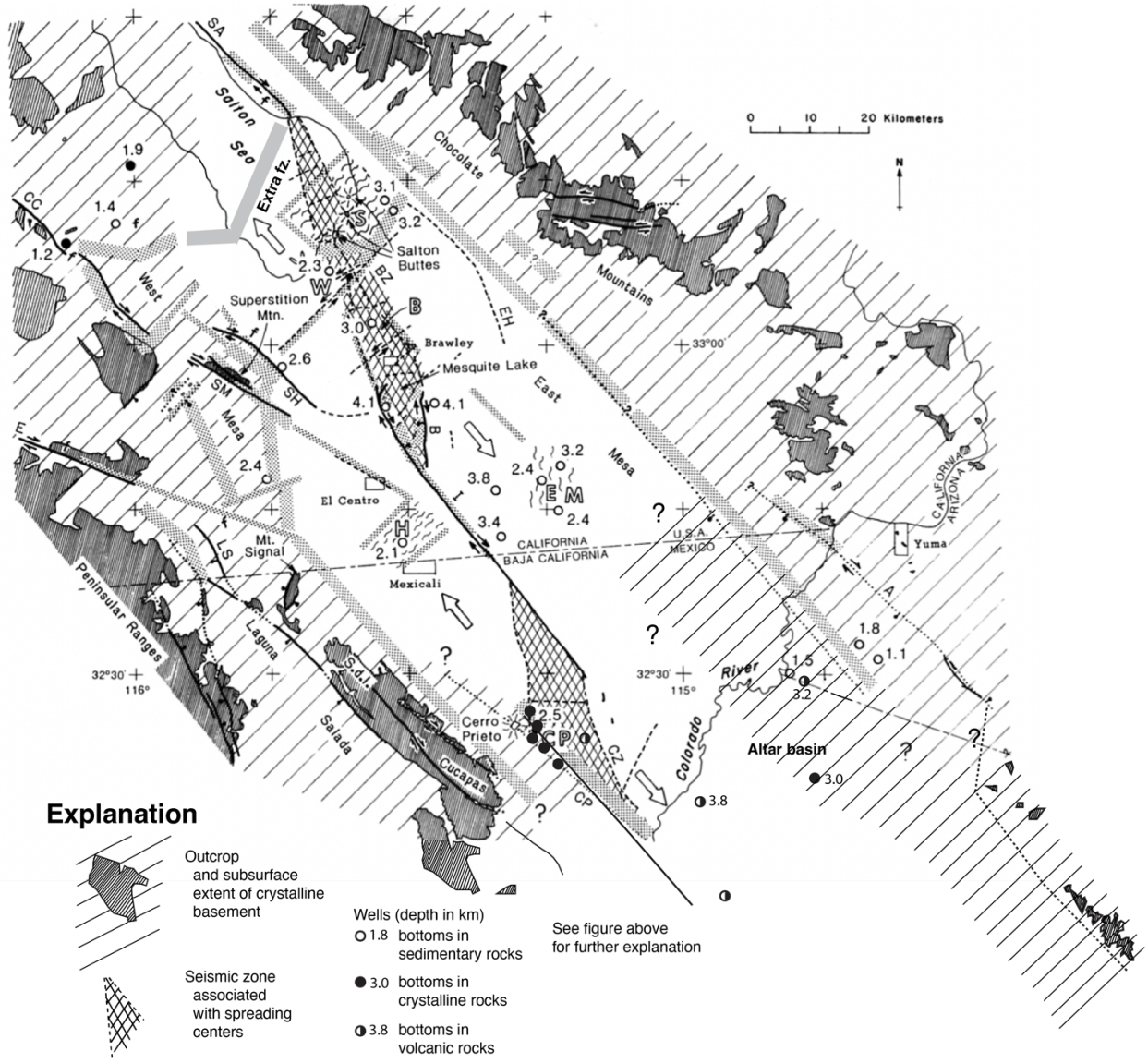

Figure 7b. Same as Figure 7a but (1) extended farther into Mexico from Pacheco et al. (2006) and Martinez et al (2021) and (2) modified around the Extra fault zone of Brothers et al. (2009) in the middle of the Salton Sea. Note that the Extra fault zone may or may not be a discreet boundary between buried pre-Cenozoic basement, to the northwest and young metasedimentary basement, to the southeast. Han et al. (2016a) interpret no discreet boundary in this region but rather a layer of stretched continental crust extending from the Coachella Valley into the Imperial Valley beneath young metasedimentary rock (Fig. 8). Flores et al. (2023) model the Extra fault zone as a normal fault capable of triggering rupture on the SAF, as in scenarios proposed by Brothers et al. (2011) and more recently by Hill et al. (2023). Geothermal areas are labeled S, W, B, H, EM, CP, for Salton, Westmorland, Brawley, Heber, East Mesa, and Cerro Prieto geothermal areas, respectively.

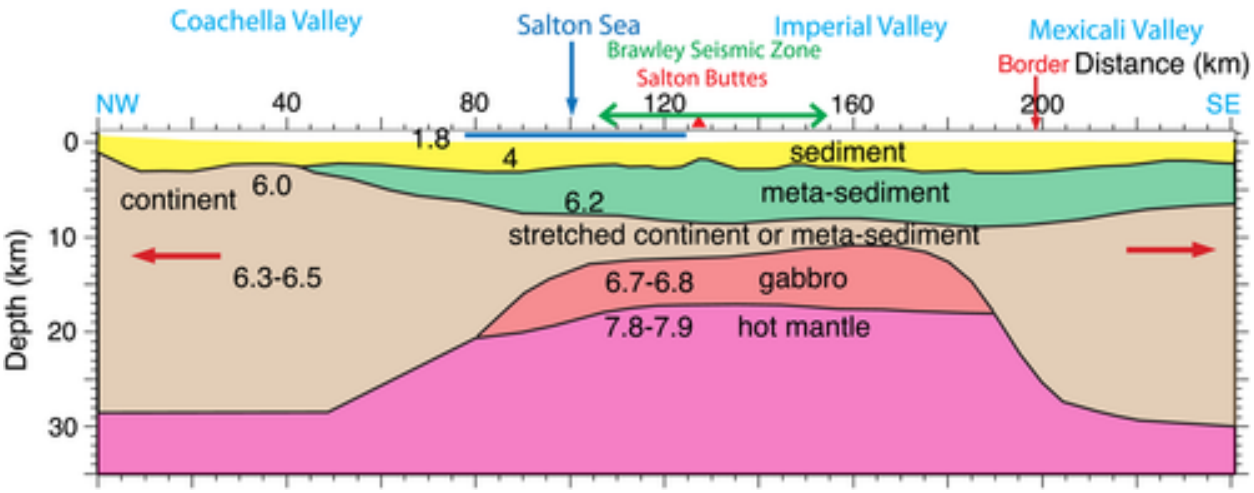

Figure 8. Same as Figure 12 of Han et al. (2016a) showing a revised interpretation of lower crustal structure in the Salton Trough.

References cited:

Bauer, K., T. Ryberg, G. S. Fuis, and S. Lueth (2013). Seismic imaging of the Waltham Canyon fault, California: Comparison of ray-theoretical and Fresnel volume prestack depth migration, Bull. Seismol. Soc. Am. 103, 340–352, doi: 10.1785/0120110338.

Biehler, S., R. W. Kovach, and C. R. Allen (1964). Geophysical framework of the northern gulf province, in Marine Geology of the Gulf of California, T. H. van Andel and G. G. Shor Jr. (Editors), Mem. Amer. Assoc. Petrol. Geol., 3, 126–143.

Brothers, D.S., N.W. Driscoll, G.M. Kent, A.J. Harding, J.M. Babcock, and R.L. Baskin (2009). Tectonic evolution of the Salton Sea inferred from seismic reflection data, Nature Geoscience, DOI: 10.1038/NGEO590.

Brothers, D., D. Kilb, K. Luttrell, N. Driscoll, and G. Kent (2011). Loading of the San Andreas fault by flood-induced rupture of faults beneath the Salton Sea, Nature Geoscience, 4, DOI: 10.1038/NGEO1184.

Luis Iván Bazán Flores, Christodoulos Kyriakopoulos, David Oglesby, Aaron Meltzner, Thomas Rockwell, John Fletcher, and Daniel Brothers (2023). Normal Fault Displacement History Provides Clues on Ruptures Along the Southern San Andreas Fault, Southern California Earthquake Center annual meeting poster #108.

Fuis, G. S., and W. M. Kohler, (1984). Crustal structure and tectonics of the Imperial Valley region, California, in Rigsby, C. A., ed., The Imperial Basin--tectonics, sedimentation, and thermal aspects: Society of Economic Paleontogists and Mineralogists (SEPM), Pacific Section, p. 1-13.

Fuis, G. S., and W. M. Mooney, J. H. Healy, G. A. McMechan, and W. J. Lutter (1984). A seismic refraction survey of the Imperial Valley region, California, J. Geophys. Res., 89, 1165–1189, doi:10.1029/JB089iB02p01165.

Fuis, G. S., K. Bauer, M. R. Goldman, T. Ryberg, V. E. Langenheim, D. S. Scheirer, M. J. Rymer, J. M. Stock, J. A. Hole, R. D. Catchings, et al. (2017). Subsurface geometry of the San Andreas fault in southern California: Results from the Salton Seismic Imaging Project (SSIP) and strong ground motion expectations, Bull. Seismol. Soc. Am. 107, 1642–1662, doi: 10.1785/0120160309.

Fuis, G. S., D. S. Scheirer, V. E. Langenheim, and M. D. Kohler (2012). A new perspective on the geometry of the San Andreas fault in southern California and its relationship to lithospheric structure, Bull. Seismol. Soc. Am. 102, no. 1, 236, doi: 10.1785/0120110041.

Gonzalez-Fernandez, A., J. J. Danobeitia, L. A. Delgado-Argote, F. Michaud, D. Cordoba, and R. Bartolome (2005). Mode of extension and rifting history of upper Tiburon and upper Delfin basins, northern Gulf of California, J. Geophys. Res., 110, B01313, doi:10.1029/2003JB002941.

Han, L., J. A. Hole, J. M. Stock, G. S. Fuis, C. F. Williams, J. R. Delph, K. K. Davenport, and A. J. Livers (2016a). Continental rupture and the creation of new crust in the Salton Trough rift, southern California and northern Mexico: Results from the Salton Seismic Imaging Project, J. Geophys. Res. Solid Earth, 121, doi:10.1002/2016JB013139.

Han, L., J. A. Hole, J. M. Stock, G. S. Fuis, C. F. Williams, J. R. Delph, K. K. Davenport, and A. J. Livers (2016b). Seismic imaging of the metamorphism of young sediment into new crystalline crust in the actively rifting Imperial Valley, California, Geochem. Geophys. Geosyst., 17, doi:10.1002/ 2016GC006610.

Hill, R.G., Weingarten, M., Rockwell, T.K. (2023). Major southern San Andreas earthquakes modulated by lake-filling events, Nature, 618, 761–766 https://doi.org/10.1038/s41586023-06058-9.

Hole, J. (1992). Nonlinear high-resolution three-dimensional seismic travel time tomography, J. Geophys. Res. 97, 6553–6562.

Johnson, C.E., and D.M. Hadley (1976). Tectonic implications of the Brawley earthquake swarm, Imperial Valley, California January 1975, Bull. Seismol. Soc. Am., 66, 1133-1144.

Kohler, W. M., and G. S. Fuis (1986). Traveltime, time-term, and basement depth maps for the Imperial Valley region, California, from explosions: Seismological Society of America Bulletin, v. 76, p. 1289-1303.

Lin, G., P. M. Shearer, and E. Hauksson (2007). Applying a threedimensional velocity model, waveform cross correlation, and cluster analysis to locate southern California seismicity from 1981 to

2005, J. Geophys. Res. 112, no. B12309, doi: 10.1029/ 2007JB004986.

Lizarralde, D., et al. (2007). Variation in styles of rifting in the Gulf of California, Nature, 448, 466–469, doi:10.1038/nature06035.

Lomnitz, C., C. R. Mooser, C. R. Allen, J. N. Brune, and W. Thatcher (1970). Seismicity and tectonics of the northern Gulf of California region, Mexico. Preliminary results, Geofis. Int. 10, 37–48.

Martin-Barajas, A., M. Gonzalez-Escobar, J. M. Fletcher, M. Pacheco, M. Oskin, and R. Dorsey (2013), Thick deltaic sedimentation and detachment faulting delay the onset of continental rupture in the Northern Gulf of California: Analysis of seismic reflection profiles, Tectonics, 32, 1294–1311, doi:10.1002/tect20063.

Pacheco, Martín, A. Martín-Barajas, Wilfred Elders, J.M. Espinosa-Cardeña, J. Helenes, and A. Segura (2006). Stratigraphy and structure of the Altar basin of NW Sonora: implications for the history of the Colorado river delta and the Salton Trough, Revista Mexicana de Ciencias Geológicas, 23, 1- 22.

Parsons, T., and J. McCarthy (1996). Crustal and upper mantle velocity structure of the Salton Trough, southeast California: Tectonics, 15, 456-471.

Powell, R. E. (1993). Balanced palinspastic reconstruction of pre-late Cenozoic paleogeology, southern California: Geologic and kinematic constraints on evolution of the San Andreas fault system, in The San Andreas Fault System: Displacement, Palinspastic Reconstruction, and Geologic Evolution, R. E. Powell, R. J. Weldon II, and J. C. Matti (Editors), Geol. Soc. Am. Memoir, Vol. 178, 1–106.

Carlos Simon Reyes-Martínez, Mario Gonzalez-Escobar, Juan Carlos Montalvo-Arrieta, Fernando Velasco Tapia, Uwe Jenchen (2021). Extension in geothermal fields between the Imperial and Mexicali Valleys revealed by 2D seismic imaging and joint gravity-aeromagnetic modeling, Geothermics, 89, https://doi.org/10.1016/j.geothermics.2020.101984.

Yang, W., E. Hauksson, and P. M. Shearer (2012). Computing a large, refined catalog of focal mechanisms for southern California (1981–2010): Temporal stability of the style of faulting, Bull. Seismol. Soc. Am. 102, 1179–1194.

On the origin and evolution of the Salton Sea

David K. Lynch[1] and Brian McNeece
[1]*dave@caltech.edu*

ABSTRACT—It is widely written and generally believed that the Salton Sea was created by an engineering accident. Many called it a blunder, gross negligence by Charles Rockwood. But we argue that the catastrophic inundation of 1905 was a natural event. Triggered by the Gila River's largest flood on record, Colorado River water would have reached into the Salton Trough whether or not Rockwood's California Development Company (CDC) had been there at all. Indeed, historical records show that the Colorado River flowed into the trough as early as 1840, long before the CDC. After the 1905-1907 flood subsided, the Salton Sea might have been expected to evaporate and percolate away in a few years. And it would have if the Alamo Canal had not continued to bring in river water, more in fact than was needed. For the past 115 years, the sea has been maintained by river water, not as the primary goal, but as the only practical way to dispose of irrigation runoff. The original Salton Sea may have been formed catastrophically, but the modern sea's existence is intentional, an inevitable result of Imperial Valley agriculture. Today's Salton Sea has little or nothing to do with the 1905 flood and should not be called an accident.

1. Introduction

The dramatic formation of the Salton Sea in 1905 has been much discussed and extensively studied[1-7]. The usual story is this: poor water management of the Colorado River and Alamo Canal near Yuma diverted the river water into the Salton Trough, creating the Salton Sea. Many narratives assign blame to Charles Rockwood, who allowed water from the river to flow into the Alamo Canal through open cuts without constructing head gates to control the flow. When the Colorado flooded as a result of floods on the tributary Gila River, it coursed unchecked through Rockwood's Lower Mexican Heading and into the Imperial Valley. This is the basis for the prevalent notion that the sea was Rockwood's fault. Yet the story is more complicated, and an examination of historical records leaves room for other interpretations.

We will not repeat the many fascinating accounts of the 1905 floods and subsequent return of the Colorado River to its natural bed in Mexico. Instead we will investigate two different though related topics: (1) The cause of the sea's 1905 inundation, and (2) some seldom-considered aspects of the sea's continued existence.

2. Origin of the Salton Sea

Water in the Salton Trough is nothing new. The geological record reveals that as a major body of water, Lake Cahuilla existed there episodically during the late Pleistocene and

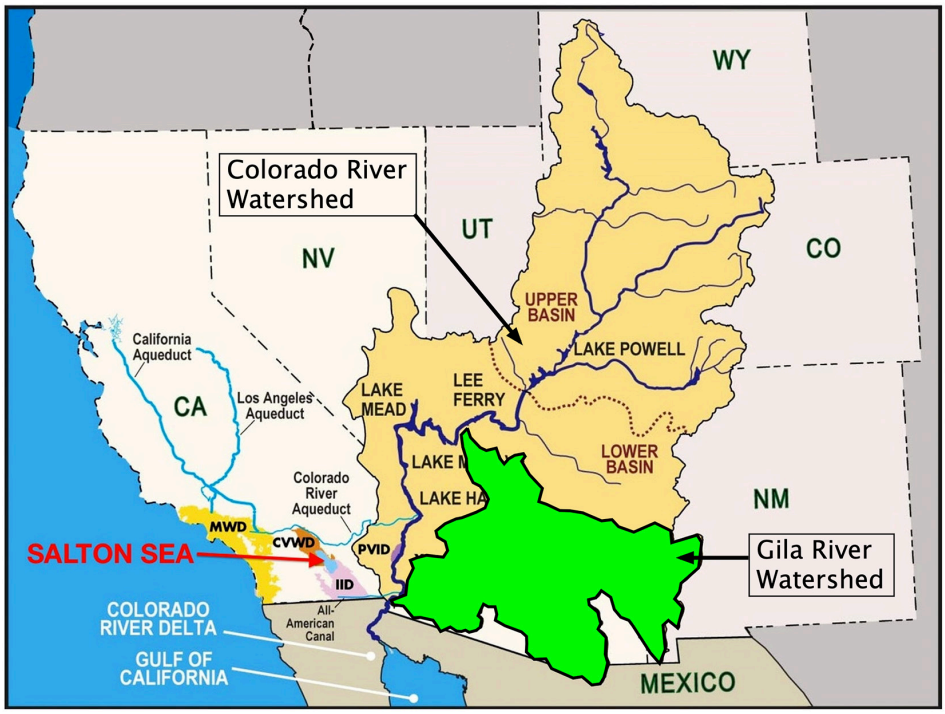

Figure 1. Drainage Basins of the Colorado and Gila rivers. Colorado River watershed includes the Gila's. Due to elevation, climate and latitude differences, the Gila River watershed is much warmer than the Colorado's. In winter, rain in the Gila's drainage basin runs off, but snow in the Colorado drainage basin stays on the ground. In summer, the Gila basin often experiences flash floods due to monsoons, less so in the upper Colorado basin because it is farther north and less likely to have monsoons. Figure adapted from the Central Basin Water District.

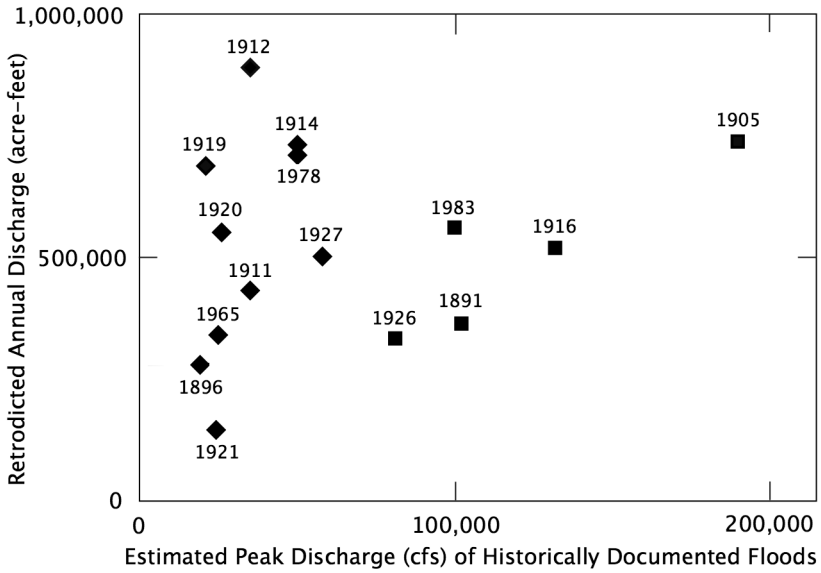

Figure 2. Historic Floods on the middle Gila River (adapted from Woodson, 2015)[18]. The earliest floods for which discharges and could be estimated ("retrodicted") were in 1891, 1896 and 1905. All three carried Colorado River Water into the Salton Trough. Given that the 1905 flood was much larger than the earlier ones, it seems certain that it produced a Lake Cahuilla, later called the Salton Sea. Squares are major floods.

Holocene at irregular intervals of between 500–1000 years[8]. Based on historical accounts[9], the last event was around 1540. Yet at least nine times in the 19th century (1840, 1842, 1852, 1859, 1867, 1862, 1884, 1891 and 1896)[10-13], there were reports of significant water in the trough, some with areas greater than the modern-day Salton Sea. In most cases, the water appeared after well-documented, natural floods on the Colorado River. The resulting short-lived lakes evaporated within a few years and had no enduring names, though some locals called them "inland seas". If we call natural occurrences "Lake Cahuilla" and manmade ones "Salton Sea", these 19th century bodies of water should have been called Lake Cahuilla. Thus, the lake's last highstand was 1896. If it can be established that the 1905 flood was a natural event, Lake Cahuilla's last highstand would be reckoned as February 1907.

As a manmade body of water, the Salton Sea formed in 1901, not 1905 as is usually cited[14-15]. In May 1901, water began flowing from the river along the newly constructed Alamo (Imperial) Canal and reached the Imperial Valley in June[1-7]. It seems that no one considered what to do with the water after it was used for irrigation, so it simply trickled down to the bottom of the sink. It was little more than a transitory wetland that didn't bother anyone. But it quietly marked a historic event for southern California's water saga: the birth of the Salton Sea.

The sea's catastrophic growth in 1905 is best understood by examining the source of the lower Colorado River's water before damming in the 20th century. Figure 1 shows its drainage basin, which includes that of the Gila River basin. Both watersheds reached their present configuration about 5 million years ago (early Pliocene). The Gila River's 58,000 sq mi drainage basin is mostly in Arizona, while the much larger Colorado drainage basin (246,000 sq mi, which includes the Gila's) extends as far north as Wyoming and as far east as Colorado and the Rocky Mountains. On average, the Gila watershed is at a lower elevation (2800 ft estimated) than the Colorado's (5500 ft), and is more southerly. Thus the Gila watershed is warmer than the Colorado's. Assuming a mean temperature drop off with elevation (adiabatic lapse rate[16]) of 18°F/mile, it is on average 9°F colder in the Colorado watershed than in the Gila's: When both climate and latitude are considered, another ~20°F is added. As an example, when it's 40°F and raining in Yuma, it's 11°F in Laramie and snowing.

The rivers have different seasonal variations. During winter, the Colorado River's discharge is low because precipitation in its upper drainage basin tends to be snow, which sticks to the ground and does not run off. Winter floods from the upper Colorado are rare but they occasionally occur on the lower, warmer Gila. Precipitation in the Gila watershed is mainly rain and it runs off to join the lower Colorado, but the discharge is normally small.

In the summer, weather patterns are different. Rain and snowmelt runoff from the Colorado swells the river from April to August and is fairly predictable. Monsoon[17] rains over the Gila watershed are unpredictable. They only occur in summer and affect relatively small areas, not the entire watershed. Monsoons can dump enormous amounts of water on the desert, enough to create flash floods.

Snowmelt and monsoons would seem to make summer the season for floods. But in 1905, the floods came in winter. And not from the Colorado River *per se*, but rather from its tributary, the Gila River[1-7]. What sparse data exists on Gila River floods is sufficient to gain some insight into its influence on the Colorado River.

Historic floods on the Gila[18] have been characterized by their *total discharge* and *peak discharge* (Figure 2). Prior to modern instrumentation, these values could only be estimated, but Figure 2 reveals that the 1891 and 1896 Gila floods, both being natural events, sent river water into the trough. Since the 1905 flood was much larger than the previous two, it seems certain this flood would have also overwhelmed the Colorado and created a Lake Cahuilla.

To see the actual timing, consider Figure 3, which shows the daily discharge of the Colorado and Gila Rivers in 1905, along with the typical daily discharge of

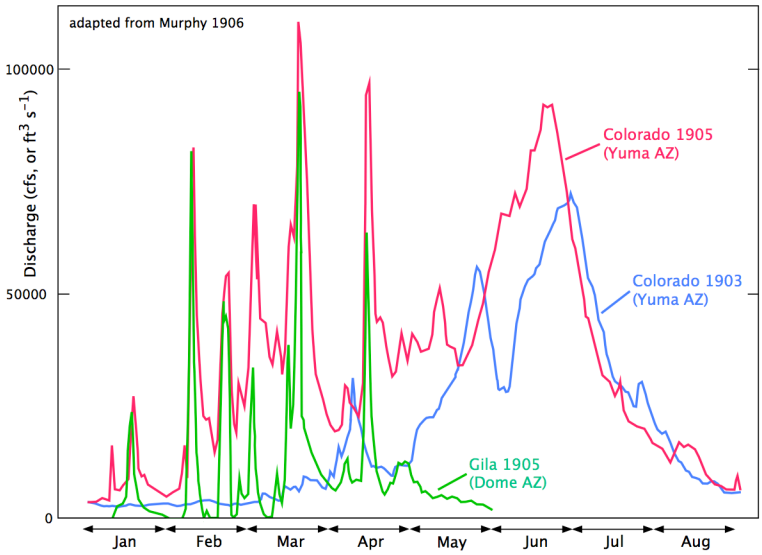

Figure 3. Colorado River discharges at Yuma, AZ and Gila River discharges at Dome, AZ. In normal years (1903), the Colorado River discharge peaks in summer. The Gila is usually very low or dry. In 1905, however, the Gila flooded at least 5 times, pushing the Colorado to record levels. Each flood on the Colorado was preceded (by a few hours) by floods on the Gila. Figure adapted from Murphy (1906).

the Colorado in 1903[19]. Normally the Colorado and Gila were low in the winter and early spring. While the Gila remained low all year, the Colorado discharge increased ~ten-fold from snowmelt in spring and summer. Since the Gila flows into the Colorado above Yuma, pulses of water on the Gila eventually reach the Colorado. Indeed, Figure 3 shows that in 1905, each flood on the Gila reached the Colorado a few hours later. Considering the total discharge in 1905—the area under the 1905 Colorado curve—it seems that the unusual but still natural floods on the Colorado were by themselves sufficient to inundate the trough.

If the 1905 floods were natural events, why hasn't the Colorado flowed into the trough again? After all, in 1909, the discharge was enormous[20], larger than any during 1905–1907, yet no water found its way to the trough. The answer is that Rockwood and Cory had learned their lesson and greatly enlarged the levees surrounding the Alamo Canal[21].

To summarize, the 1905–1907 Colorado River flood waters came through Rockwood's open cut in Mexico. This was the basis for believing the Salton Sea was the result of an engineering accident. But water reached the trough through the cut simply because it was the most efficient route at the time. Had this opening not been present, the 1905 Gila flood would have overflowed the Colorado, breached a levee somewhere else and made its way to the Salton Trough.

3. The enduring Salton Sea

What happened to the Salton Sea (not yet named) in 1905 is a matter of historical record[1-7]. By June a shallow body of water covering 150 sq mile (~12 x 12 miles) had collected at the bottom of the trough as 80,000 CFS flowed in. By October, the entire river reached the trough. The Salton Sea grew rapidly as the entire Colorado River flowed into the Salton Trough. Surging across the desert, the flood overran huge portions of the Mexicali Valley in a sheet of braided channels 8–10 miles wide (Figure 4). It reached Volcano Lake at the foot of Cerro Prieto and was channeled north to the New River, turning a shallow brush-filled depression into a torrent. Ultimately, Harry Thomas Cory, who made many courageous decisions concerning the flood and who probably convinced E. H. Harriman to fund the effort, took over. He closed the cut and finally put the Colorado River back where it belonged on February 10, 1907.

Figure 4. Published reports refer to a broad 8–10 mile wide shallow flood in 1905 as a sheet-like flow or shallow braided channels. No maps of the flood flow were produced because there were no surveyors in the areas during 1905-1907. This image is consistent with historic reports. Adapted from the Salton Sea Atlas, Redlands Institute (2002).

Once the Colorado River was returned to its former bed, the disaster was over but the Salton Sea remained. Left to itself, it would have vanished by about 1917 (Figure 5), losing about 6 ft per year to evaporation and percolation[22]. But with agriculture once again flourishing, the CDC kept the water flowing. After irrigating the fields, water was left to drain into the sink. While the flooding of 1905-1907 was a surprise, today's Salton Sea is not. It is there because farmers want it there. Not because they particularly like it, but because the sink was the natural sump for

their irrigation water. Indeed, President Coolidge formalized this in 1924 by an executive order setting aside land under the sea as a permanent drainage reservoir[23].

As Figure 5 shows, the Salton Sea grew steadily between 1924 and 1983. Part of its enlargement occurred because more and more water was needed to supply the growing acreage of farmland. But there was another reason. Farmers were taking more water than they needed to grow crops because they were trying to desalinate the soil and thereby improve crop yields. As an endorheic basin, sediments in the trough have accumulated salt and other evaporites from thousands of years of evaporation. Most evaporites are on or near the surface because the clay-like soil is poorly drained. To remove it, farmers began using an ancient desalination technique known to the Indus Valley Civilization[24], and this requires a lot of extra water; *deep drainage*.[25-27]. In 1920s, the Imperial Irrigation District (IID) began a massive program to desalinate the soil.

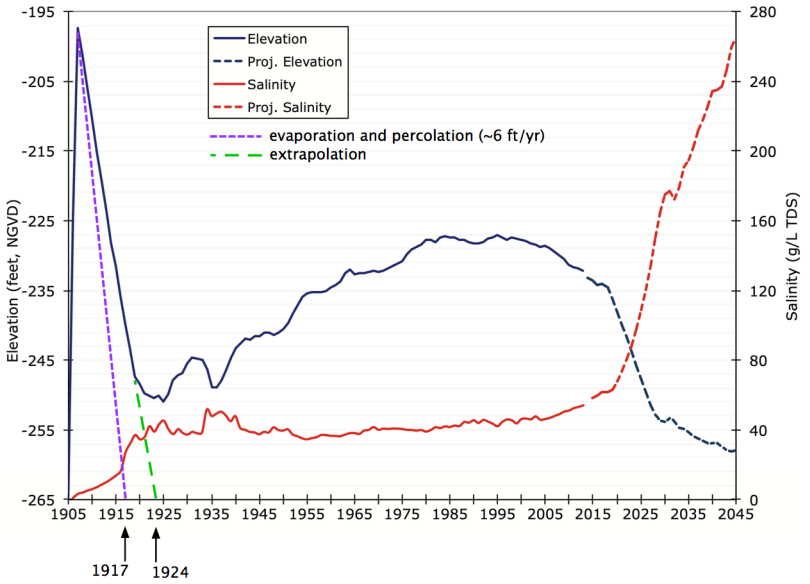

Figure 5. After the flood was stopped, the Sea level dropped sharply. This was due mostly to evaporation and percolation. Had the CDC not allowed Colorado River water to enter the trough through the Alamo Canal, the Salton Sea would have disappeared by about 1917. But the continuing growth in agriculture required more water than ever and the Sea level rose from 1925 until 1983.

In deep drainage (Figure 6), long lines (miles) of perforated or porous pipes are placed at a slight inclination a meter or so below ground, then covered. Though the soil is poorly drained, water eventually makes its way down to the pipes and is carried down to the sea by gravity, primarily through the Alamo and New rivers. This water carries salt and agricultural fertilizer from the topsoil and soil in the vadose zone to the drain pipes. For deep drainage to be efficient, however, farmers had to use more water than they had taken earlier. For every three acre-feet of water that a farmer applied to the ground, one acre-foot ended up in the Salton Sea[28]. This practice of using extra water caused the Salton Sea level to rise even faster.

Deep drainage in the Imperial Valley does three things: it lowers a high water table, removes surface salt, and also dumps salt into the Salton Sea. This is why the Sea is so salty, almost twice that of the ocean in 2019[29]. Drain water also contains large amounts of fertilizer including nitrogen and selenium[30] (selenium is also found

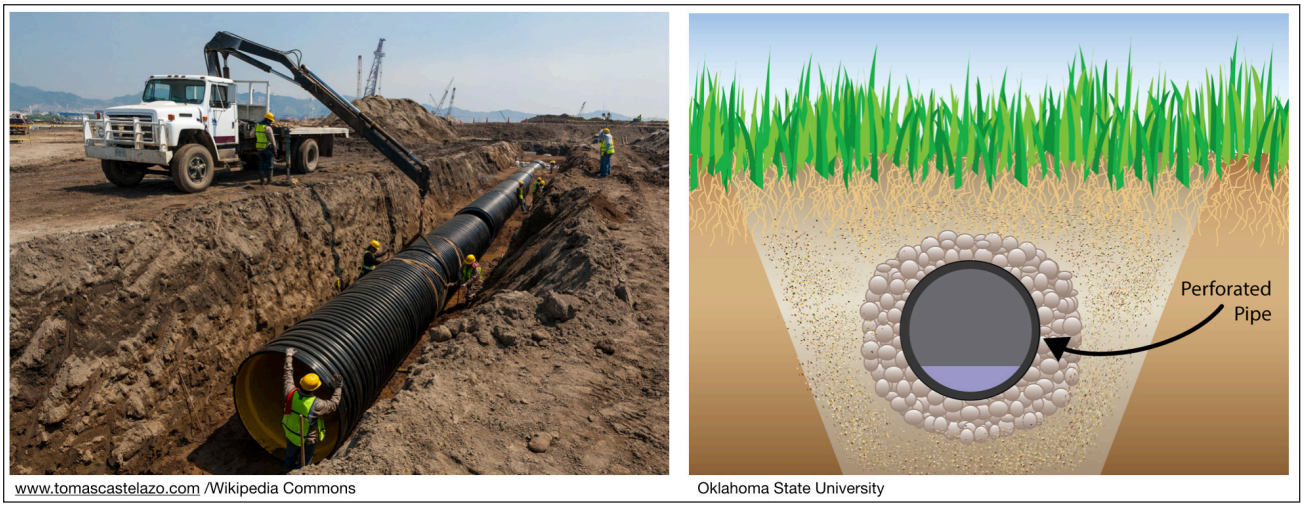

Figure 6. Deep drainage is a way to desalinate surface soils so that crops grow better. Perforated pipe inclined slightly downward toward the Sea are buried. Salt-laden water percolating down from the surface removes salt from the topsoil. This water and salt (and fertilizer), however, increase the salinity of the sea and raises its level. Deep drainage desalination requires more water than crops need.

in Colorado River water and sediments). Pollution from the Alamo and New rivers, the latter once called the most polluted river in the world, additionally adds to the sea's chemical soup.

Until the urban areas of Phoenix, Tucson, Los Angeles, and San Diego grew beyond water supplies, farmers in the Imperial Valley had no reason to limit their use of water. The IID receives its water from the Bureau of Reclamation for free; farmers are merely charged the cost to deliver the water. And since water is delivered by gravity, delivery is cheap. As a result, Imperial Valley farmers have paid some of the lowest rates in the nation. Today, they pay $20 for an acre-foot of water. In contrast San Diego area farmers pay above $900 for an acre-foot.[31]

Deep drainage, along with surface drainage known as *tailwater*, turned out to be a doubled-edged sword. Crops grew better, but in the late 1970s, agricultural drainage into the sea caused its level to rise enough to flood some productive agricultural land. The flooded farmers sued the IID. After years of litigation, the court ruled that the IID was wasting water and was ordered to begin conserving water in order to lower the elevation of the Salton Sea[32]. In 1984, Decision 1600 of the California State Water Resources Control Board forced the IID to limit water delivery to the Salton Sea and to accept funding from the Metropolitan Water District (MWD) of Los Angeles. MWD would pay for system improvements so the IID would use less water. In return, the MWD would receive 104,000 acre-feet of water annually. This was the first large agriculture-to-urban water transfer[33]. As of January of 2020, the IID now transfers nearly 500,000 acre-feet to Los Angeles, San Diego, Coachella, and Native American water districts. Because of these transfers, the Salton Sea, after decades of rising, is now falling.

Water will continue to flow into the Imperial Valley and maintain the Salton Sea for the foreseeable future because farmers need water. There are plans to shrink the sea but not to dry it up[34]. Eliminating the sea would mean eliminating Imperial Valley agriculture.

Summary and conclusions

The Salton Sea's origin and evolution have been a source of ridicule, uncertainty, misinformation, and speculation. While most people believe the initial formation took place in 1905 as the result of an engineering accident, it actually started in 1901 as man-made runoff from irrigation water brought from the Colorado River by the Alamo Canal. *We argue that the Salton Sea's 1905 "formation" was simply another natural inundation from a Colorado River flood, triggered by floods on the Gila.* The sea's beginning was inevitable, if not intentional. Nor is the sea's continued existence an accident. Rather it is a deliberate, even desirable, result of agriculture in the Imperial Valley and its farmers' efforts to desalinate the soil.

References

1. Kennan, George, *The Salton Sea; an account of Harriman's fight with the Colorado River*, New York, The Macmillan Company (1917). https://catalog.hathitrust.org/Record/006205158
2. Rockwood, Charles, Born of the Desert, Calexico Chronicle (1909) https://books.google.com/books?id=S-41AQAAMAAJ
3. https://en.wikipedia.org/wiki/Charles_Robinson_Rockwood Excellent account and many good references.
4. Cory, Harry T., *The Imperial Valley and Salton Sink,* San Francisco, John J. Newbegin (1915) https://www.google.com/url?sa=t&rct=j&q=&esrc=s&source=web&cd=17&ved=2ahUKEwjquum1wfnmAhUVrp4KHQBJBb4QFjAQegQICBAC&url=https%3A%2F%2Fnrm.dfg.ca.gov%2FFileHandler.ashx%3FDocumentID%3D9257&usg=AOvVaw3XgKu-thHpRTRIAVWdnIR4
5. Tout, Otis B., *The First Thirty Years, An Account of the Principal Events in the History of Imperial County, Southern California, USA*, Otis B. Tout. Publisher, 4612 Terrace Drive, San Diego, Calif., Produced by Arts & Crafts Press, San Diego, Calif. (1931) https://books.google.com/books?id=RskuAAAAIAAJ
6. Farr, Finnis, *The History of Imperial County California*, Berkley, CA, USA: Elms and Franks. pp. 311, 312. (1918)
7. McNeece, B., *The Early History of Water in the Imperial Valley*, Video script, Imperial Irrigation District (2015) https://www.iid.com/home/showdocument?id=13967, Video: https://www.youtube.com/watch?v=KAsntugo710 .
8. Waters, M. R., Late Holocene lacustrine chronology and archaeology of ancient Lake Cahuilla, California. Quaternary Research 19, 373-387 (1983)
9. Wilke, Phillip J., Late Prehistoric Human Ecology at Lake Cahuilla, Coachella Valley, California, University of California Archaeological Research Facility Contributions No. 38 (1978)
10. http://saltonseaauthority.org/get-informed/history/
11. Sykes, G. The Colorado Delta, Publication no. 460, Carnegie Institution, Washington D.C., (1937), https://babel.hathitrust.org/cgi/pt?id=uc1.31822010629376&view=1up&seq=6
12. Sykes, G., The delta and estuary of the Colorado River. Geog. Rev., vol. 16, p. 232–255. (1937)
13. Cecil-Stephens, B. A., The Colorado Desert and its recent flooding. Amer. Geog. Soc., Bull., vol. 23, p. 367–377 (1891)
14. https://water.ca.gov/LegacyFiles/pubs/conservation/salton_sea_history/history.pdf
15. https://www.parks.ca.gov/?page_id=639
16. https://en.wikipedia.org/wiki/Lapse_rate
17. https://en.wikipedia.org/wiki/North_American_Monsoon
18. Woodson, K., The Impact of Flooding on Hohokam Canal Irrigation Agriculture, in

Traditional Arid Lands Agriculture: Understanding the Past for the Future, Scott E. Ingram and Robert C. Hunter (eds), University of Arizona Press, 180-216 (2015)

19. Murphy, Edward C. (and others), Destructive Floods in the United States in 1905 with a Discussion of Flood Discharge and Frequency and an Index to Flood Literature, Water Supply and Irrigation Paper No. 162, Series M, General Hydrographic Investigations, 17, U.S. Government Printing Office (1906)

20. Fall, A. B. and Davis, A.P., Problems of Imperial Valley and Vicinity, US Bureau of Reclamation, Document No. 142, 87th Congress (Senate), Government Printing Office (1922)

21. Dowd, M. J., IID: THE FIRST 40 YEARS, IID (1956). https://www.iid.com/home/showdocument?id=6000

22. https://www.iid.com/home/showdocument?id=17297.

23. http://resources.ca.gov/docs/salton_sea/Salton_Sea_Chronology_(Prehistory-2015).pdf

24. https://en.wikipedia.org/wiki/Indus_Valley_Civilisation

25. https://www.agric.wa.gov.au/water-management/deep-drainage-salinity-management

26. https://en.wikipedia.org/wiki/Drainage#Early_history

27. Kovulek, Paul, Irrigation and Drainage Practices in the Colorado River Basin of California, paper prepared for the California Irrigation Institute, Fresno, California, (1964)

28. Author's personal conversation (McNeece) with Wally Leimgruber, Holtville farmer and former Imperial County Supervisor, January 28, 2020.

29. Cohen, Michael, Salton Sea +20, (2019) https://pacinst.org/salton-sea-20/

30. Selenium and the Salton Sea, https://www.google.com/url?sa=t&rct=j&q=&esrc=s&source=web&cd=2&ved=2ahUKEwiSzLfdvZPnAhWWlp4KHfPzB4AQFjABegQIAhAB&url=https%3A%2F%2Fnrm.dfg.ca.gov%2FFileHandler.ashx%3FDocumentID%3D9091&usg=AOvVaw2mXPvBQG0i7YMPPj1Sgtm1.

31. Author's personal conversation (McNeece) with Dennis Cushman, San Diego County Water Authority Assistant General Manager, March 7, 2019

32. Alleged waste and unreasonable use of water by Imperial Irrigation District. http://www.sci.sdsu.edu/salton/iidAllegedWasteofWater.html

33. This is the transfer of water rights from agricultural use to urban use, not the transfer of water that has reached farmland and then moving it to cities.

34. Salton Sea Hydrological Modeling and Results, Technical report by CH2M Hill, (2018) https://www.iid.com/home/showdocument?id=17299

Nelson, S. M., Lynch, D. K.,and Rivas, T., 2023 The Colorado River (Mexico) tidal bore: persistent phenomenon in a changing estuary , in Mines of the Mojave, D. Miller and S. Rowland (eds), Proceedings of the 2023 Desert Symposium, April 21-24, 2023, Zzyzx, 143-153

The Colorado River (Mexico) tidal bore: persistent phenomenon in a changing estuary

Steven M. Nelson,[1,*] David K. Lynch,[2] and Tomás E. Rivas Salcedo [3]
[1] *Independent Scientist, 6101 NE 102nd Avenue, Apt. 5, Vancouver, WA 98662-6321,* snelson467@gmail.com
[2] *Thule Scientific, P. O. Box 953, Topanga CA 90290*
3 Sonoran Institute, Blvd. López Mateos SN, Zona Industrial, Mexicali, Baja California, C.P. 21010, Mexico

ABSTRACT — The macro-tidal estuary of the Colorado River, Mexico has been disconnected from the river's fluvial supply by the operation of upstream dams and diversions. Since the last major period of fluvial delivery in the 1980s and 90s an emergent and growing tidal sandbar has obstructed the river channel 40 km upstream from the Gulf of California. The estuary has assumed the characteristics of a blind tidal channel system where tidal sediment is transported landward, leading to decreased channel depth and width. Loss of fluvial flow diminished but did not eliminate tidal bores which continue to ascend the estuary channel at the head of flooding spring tides. Spring tide flood currents saw increased power after a large area of the intertidal mudflats subsided up to 1m following the 2010 M7.2 El Mayor-Cucapah earthquake, resulting in extensive channel bank erosion and headcut incision of new tidal channels. We conducted field visits and used satellite imagery to detect tidal bores over the 12-year post-earthquake period in order to estimate the frequency of tidal bores and gain a better understanding of their contribution to both erosion and aggradation of estuary channels and the surface of the intertidal flats.

1. Introduction

The estuary

The Colorado River estuary is situated at the northern end of the Gulf of California (Figure 1). The mean spring tide range in the upper Gulf is 6.4 m (Lavin and Marinone, 2003), reportedly increasing to 8 to 10 m within the estuary (Thompson, 1968) although no tide monitoring stations are maintained therein. In the mixed semidiurnal tidal regime of the upper Gulf, each day's lower low tide immediately precedes the higher high, contributing a maximum range to one of the day's tides. The convergent estuary is hypersynchronous, compressing the flood tidal wave into a smaller cross-sectional area as it ascends the narrowing/shallowing estuary channel, enhancing tidal effects until friction ultimately dissipates the wave at the tidal limit. Compression of the flood wave also steepens it and delays its arrival, resulting in highly asymmetrical flood-dominant tide cycles: the authors' observations at various locations within the estuary have recorded spring-tide flood periods ranging from 2.5 to 4 hours, with the ebb lasting 8 to 9.5 hours. These factors combine to create conditions favoring the formation of a tidal bore wave at the head of one and sometimes both daily flood tides during spring tide (full and new moon) periods.

Figure 1. Regional map showing the study area in the Colorado River Estuary.

The tidal bore

Lynch (1982) and Graber (2012) provide introductory information and scientific theory of tidal bores. A bore is a tidally generated water wave advancing upstream and represents the instantaneous turning of the tide from ebb to flood. It occurs during spring tides when the tidal range is at its monthly maximum. Tidal bores have been documented in the Colorado River estuary since the earliest Spanish explorers visited the area in the 16th century (Freeman, 1923).

Perhaps the best introduction to the Colorado River bore is found in the description provided by James H. Gordon of the U.S. Weather Bureau who witnessed a bore at the tiny seaport of La Bomba on the south bank of

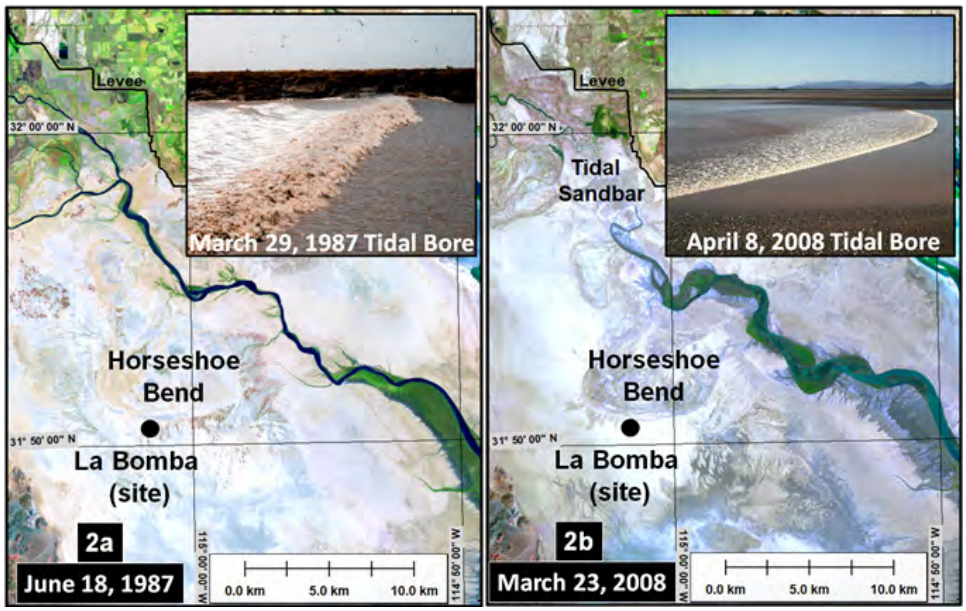

Figure 2. Estuary changes in the two decades prior to the 2010 El Mayor-Cucapah Earthquake (Landsat 5 images). Both pictured bores are advancing left to right. Fig. 2a: In 1987-88, Nelson observed tidal bores along the reach between the La Bocana fish camp and a tide gage 4 km to the south. Fluvial flow to the Gulf was occurring, producing classic river-channel tidal bores. Note the opposite channel bank just 100 m away. Fig. 2b: Fluvial flow to the Gulf was curtailed after 2000 as drought conditions developed throughout the Colorado River Basin. By 2006 a tidal sandbar (upper left) blocked the river channel and the estuary once again became a strictly tidal system. Bores in the tidal channel became smaller and appeared only intermittently in deeper and more constricted sections where the flood met opposing ebb current. 1987 photo by Lynn C. Anderson, 2008 photo by Steven Nelson.

Horseshoe Bend, a now-abandoned meander of the river (Figure 2) on December 9, 1923:

> The coming of the bore was first called to our attention by the disturbance among a big flock of white pelicans fully 6 miles away. Fish always follow the bore in, we were told. The brown line of the bore itself was visible with the glass at perhaps 3 miles. Its speed appeared to be nearly 8 miles an hour. As a spectacle it was disappointing. This was doubtless due in some measure to the strong north wind that had been fighting the tide all the way up the Gulf. Up to the moment that the bore, or first wave, arrived the current was running strongly seaward. In an instant it was reversed and racing up the river. The bore was not over 3 feet high, a racing wave fully a mile long, foam crested and perhaps a foot higher over the shallows and sand bars…. The lack of turmoil between the two opposite currents was surprising. The level of the river rose 3 feet in the first minute and 5 feet in 15 minutes. The bank was 15 feet high at low tide. The high tide of two nights previous had filled the channel and overflowed the surrounding country 6 inches deep. Probably a full half mile behind the first wave something similar to a tide rip appeared, waves 3 to 4 feet high probably not over 20 feet from crest to crest racing up the river. They would have made very rough going for a small boat (Gordon, 1924).

Gordon may have been underwhelmed by the observed bore because of a newspaper report (Henderson, 1922a) of a bore "15 to 20 ft" high that had capsized a small ship as it lay at anchor off La Bomba. A later statement by the ship's engineer (Henderson, 1922b) said a bore "about 8 ft" high had pushed the ship onto a bar and caused it to list so severely that many people jumped or fell into the river and were drowned. The actual size of the bore would have been very hard to judge because it approached in darkness just two nights past the new moon (night of November 19–20, 1922), despite a later account claiming the victims watched the "nearly 15 ft" bore approach in bright moonlight (Waters, 1946).

The Colorado River estuary is so remote that few people have actually witnessed a tidal bore there, which complicates accurate reporting. A survey of eyewitness accounts indicates that historical bores were generally considerably smaller than 15 ft or even 8 ft: Gordon (1924) and Sykes (1937) reported 3 ft[1] bores, Derby (1852) and Waters (1946) 4 ft bores, Leigh (1941) a 4.5 ft bore, and Ives (1861) a bore "several" feet high. The best historical photo of a bore taken by Sykes[2] shows one about 2–3 ft high in Horseshoe Bend, circa 1904.

While the Colorado River tidal bores are not among the world's largest (Bartsch-Winkler and Lynch, 1988), they share with all tidal bores an important function in mixing and dispersion of sediments as the wave propagates upstream (Chanson, 2004). Understanding the occurrence and frequency of tidal bores within the estuary as modified by the 2010 El Mayor-Cucapah earthquake is an important first step in understanding erosion and sedimentation processes.

1 Sykes added that bores could "swell up to 6 or 7 feet" at constrictions in the channel or irregularities in the shoreline.
2 Sykes Family Collection PC240, Box 8, Folder 147 "Tidal Bore on Colorado River" , Arizona Historical Society Library and Archives, Tucson, Arizona

Tidal bores in the three decades prior to the 2010 El Mayor-Cucapah earthquake

Nelson (2007) observed several tidal bores in 1987 and 1988 during a period of fluvial discharge to the estuary and Gulf (Fig. 2a). River flow in the 100 m-wide channel was sufficient to keep all channel bars submerged even at low tide, and in mid-channel the bore wave was typically undular (non-breaking). Although river discharge can have a dampening effect on bore formation if the water in the channel becomes too deep (Bonneton et al., 2015), fluvial discharge in early 1987 resulted in bores similar in size to the eyewitness reports from the 19th and early 20th centuries.

Flood-dominant estuaries typically experience net landward bedload transport as fine-grained sediments mobilized by the flood tides are deposited on inundated surfaces during the long slack tide preceding the extended ebb (Dalrymple, 2010; Wells, 1995). When fluvial flow reaches the estuary, these tide-mobilized sediments are deposited near the river's mouth, but in the absence of such flow the sediments are carried inland. After fluvial flow to the estuary was curtailed in the 1960s and 70s following installation of upstream dams and diversions, landward transport of tidal sediments caused a tidal sandbar to form in the Colorado River channel 40 km above the river's mouth (ACOE, 1982). The channel reopened when fluvial flow was temporarily restored in the 1980s (Nelson et al., 2020), only to close again after 2000 as drought conditions once again curtailed fluvial flow. By 2006 a new tidal sandbar (Fig. 2b) had developed in the same location as the previous one (Nelson et al., 2013b; Zamora et al., 2013). The estuary downstream from the sandbar became a "blind" (tapering to a dry upstream terminus) tidal channel.

The blind estuary channel was significantly wider and more sinuous than the riparian channel had been in the 1980s. Bank erosion and retreat, which had begun in the 1990s, continued after the fluvial supply was cut off, indicating that it was driven by tidal currents. Much of the sediment eroded from the banks was retained in channel bars (Nelson et al., 2013b). In contrast to the 1980s channel morphology, which had been dominated by fluvial flow, channel bedforms were now defined by bi-directional flow. A system of parallel "mutually evasive" flood and ebb dominated channels developed, meandering independently of each other with frequent intersections and interconnections as is common in tidal channels (Hughes, 2012; Wells, 1995). Tidal bores (inset, Fig. 2b) diminished in size from those seen in the 1980s, forming intermittently in places where the flood and ebb channels coincided.

Subsidence Impact of the 2010 El Mayor-Cucapah earthquake

The mainshock of the Mw 7.2 El Mayor-Cucapah earthquake occurred on Easter Sunday, April 4, 2010, producing a nearly continuous fault trace extending 120 km from the U.S.-Mexico international boundary to the Gulf of California (Fletcher et al., 2014). The current study area is at the far southern end of the rupture zone where movement occurred along previously unidentified faults, causing coseismic and post-seismic subsidence of up to 1 m (Huang et al., 2017; Nelson et al., 2013a).

Figure 3 illustrates spring tidal inundation patterns in the study area 8 months prior to and 6 months after the earthquake. Prior to the earthquake (Fig. 3a) a spring tide predicted to reach ~5.5m (at Puerto Peñasco, Sonora) inundated an area mainly aligned along the estuary

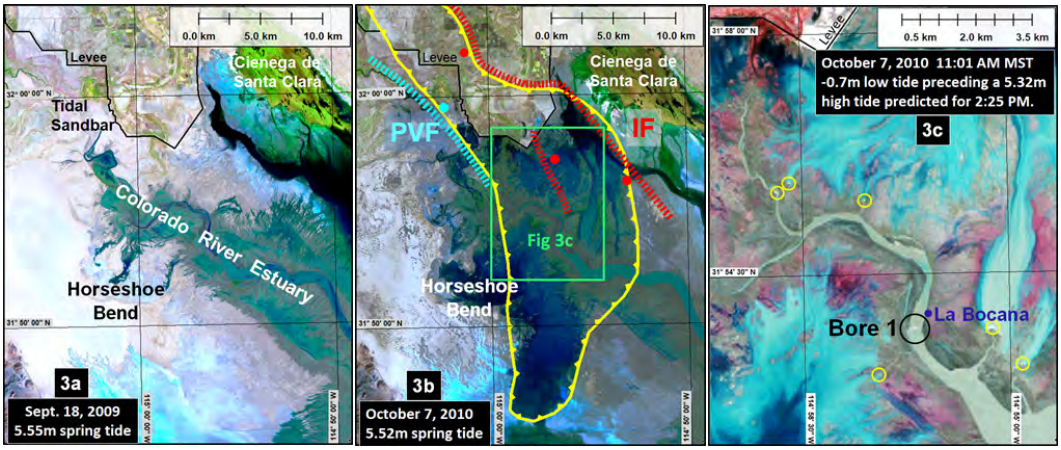

Figure 3. Changes in tidal inundation following the 2010 El Mayor-Cucapah Earthquake. Figs. 3a and 3b show the areas of tidal inundation by ~5.5m spring tides before and after the earthquake. Fig 3a. Pre-earthquake spring tides primarily inundated areas adjacent to the main estuary channel between natural levees created by the deposition of fluvial and tidal sediment on the channel banks. Some water escaped southwest toward Horseshoe Bend or east toward the Santa Clara Slough (inundated area south of Cienega de Santa Clara) through low sections of the levees. Spring tides rarely reached the flood control levee (black line upper left). Fig 3b. The area between the Pangas Viejas Fault (PVF) and Indiviso Fault (IF) subsided up to 1m over a six month period following the earthquake. The yellow raked line shows the limits of coseismic and post seismic subsidence. Subsidence of the estuary channel's natural levees allowed most spring tides to inundate more of Horseshoe Bend than previously. Fig 3c. The area within the rectangular inset shown in 3b has been processed using false color infrared bands to accentuate water ponded on the tide flats well as whitewater rapids at headcut erosion points (small circles). A tidal bore spanning the entire 350m-wide channel (Bore 1, large circle) is moving up the channel at the head of the flood tide.

channel. The flood was mostly contained within the natural levees/berms that had developed along the channel from deposition of fluvial and tidal sediments. Overflow occurred at a few low spots, allowing some tidal water to flow southwest toward the old Horseshoe Bend meander and east toward the Santa Clara Slough (dark blue standing water south of the Cienega de Santa Clara). Spring tides rarely flooded all the way north to the flood control levee.

The previously unidentified Pangas Viejas and Indiviso faults (Figure 3b) mark the southernmost extent of the rupture zone (Chanes-Martínez, 2012; Fletcher et al., 2014). These two faults form the western and eastern margins of an extensional strike-slip duplex system that underlies the alluvial surface in the subsidence zone (Sánchez García, 2013). The zone of subsidence extends north of the flood control levee which now marks the northern limit of tidal inundation by most spring tides. Although the western part of the Horseshoe Bend meander is outside the area of seismic subsidence, the earthquake caused subsidence of the natural levees which had prevented full inundation of the abandoned meander prior to the earthquake, causing the new area of inundation to extend into Horseshoe Bend west of the subsidence zone.

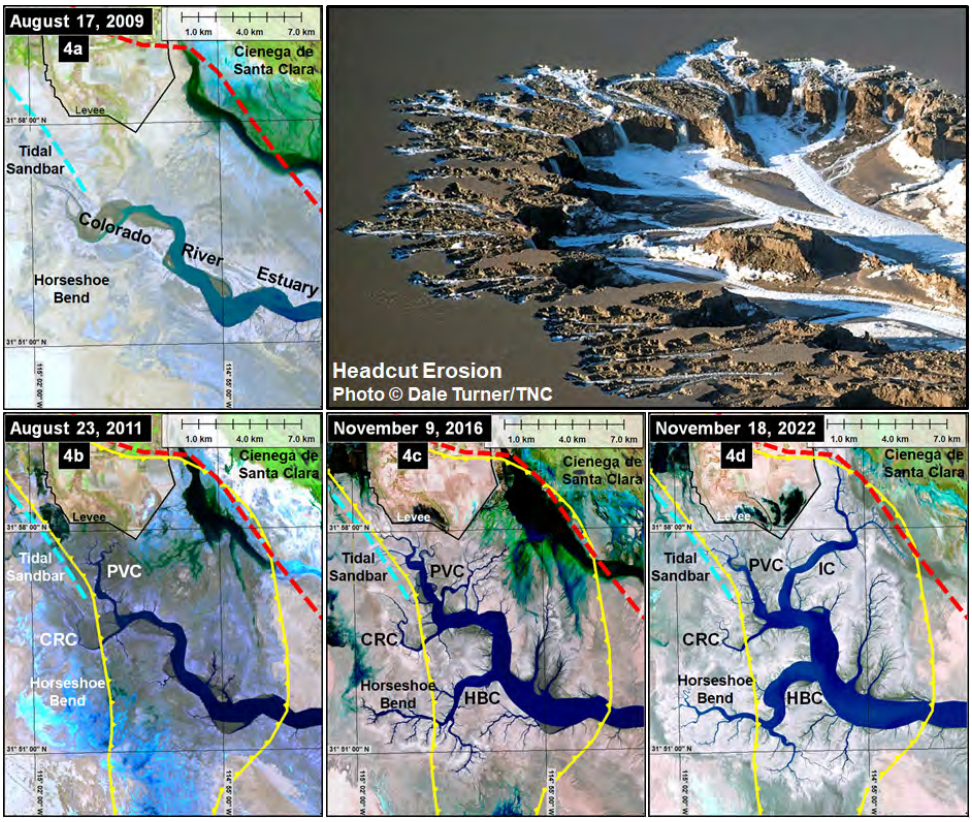

Figure 4. Headcut erosion of tidal drainage channels, 2010-2022. Red dashed line: Indiviso Fault. Aqua dashed line: Pangas Viejas Fault. Yellow raked line: Zone of earthquake subsidence. CRC: Colorado River Channel. PVC: Pangas Viejas Channel. HBC: Horseshoe Bend Channel. IC: Indiviso Channel. Images 4b, 4c, and 4d were acquired at times when the water surface in mid-estuary was estimated to be at approximately the same elevation. Fig. 4a: Pre-earthquake conditions. Fig. 4b: Sixteen months after the 2010 earthquake a new tidal drainage channel PVC has been headcut north along the east side of the Pangas Viejas Fault. The CRC upstream from the PVC is outside the subsidence zone and has not been significantly headcut. Fig. 4c: By 2016 the HBC system of drainage channels has been headcut into Horseshoe Bend and headcuts are advancing to the northeast toward the large area of impounded water west of the Indiviso Fault. Fig. 4d: The most recent major tidal channel IC now drains the low area west of the Indiviso Fault. As of 2022 a network of tidal channels insures rapid drainage of the entire tide flat surface within the subsidence zone, which now completely floods in 3-4 hours and drains in 8-9 hours during spring tides. Note the increase in width of the main estuary channel between 2011 and 2022. Figs 4a and 4b: Landsat 5 TM. Figs 4c and 4d: Sentinel 2. All satellite images processed with short wave infrared bands.

As a result of the earthquake a new intertidal basin up to 1 m deep and 260[3] sq km in area developed, increasing spring tide inundated area by about 190 sq km from the average pre-earthquake situation. The new intertidal basin was subject to rapid inundation and more gradual drainage during each asymmetrical spring tide cycle.

Incision of new tidal drainage channels began as headcut erosion occurred at points where water drained over existing channel banks during the long ebb tide (Figure 3c). Figure 3c has been processed using false color infrared bands to accentuate both standing water and whitewater rapids at headcutting points (small yellow circles). It also reveals a tidal bore (Bore 1, inside the larger black circle) at the head of the incoming flood. The bore extended across the entire 350 m-wide low-tide channel and must have been a substantial breaking wave to be detectable at the 30m spatial resolution of Landsat 5.

Development of tide flat drainage channels

Since there were no pre-existing drainage channels in much of the subsided area, large areas of the tide flats initially remained inundated with residual sea water for

3 This includes 230 sq km of newly subsided tide flats and an additional 30 sq km of pre-existing low ground in the Horseshoe Bend which had not been subject to regular inundation prior to the 2010 earthquake.

days following spring tides, and some areas remained inundated for years until drainage channels reached them. The progress of drainage channel development is shown in Figure 4. Figure 4a shows the situation prior to the earthquake. Note the linear area of inundation nearly parallel to and just west of the (at the time unidentified) Indiviso Fault (red dashed line). This linear feature may be an indication of earlier movement of the Indiviso Fault. Prior to the 2010 earthquake it was inundated whenever the adjacent Santa Clara Slough (out of view to the southeast) was flooded, but otherwise dry.

By August 2011, 16 months after the 2010 earthquake, the first major new drainage channel ("PVC" for Pangas Viejas Channel in Figure 4b) had developed along a linear subsidence feature just east of the Pangas Viejas Fault. Drainage from this newly subsided area flowed directly into the existing Colorado River Channel (CRC), and the Pangas Viejas Channel grew quickly. Headcuts did not significantly advance up the Colorado River Channel beyond the western limit of subsidence, and the pre-existing tidal sandbar in that channel continued to aggrade.

By November 2016 another major tidal channel had been headcut into the Horseshoe Bend ("HBC", Horseshoe Bend Channel, in Figure 4c). A third network of channels was headcutting northeastward toward the large inundated area just west of the Indiviso Fault and Cienega de Santa Clara. This area had been continuously inundated since the 2010 earthquake and remained so until a headcut channel finally reached and began to drain it in late 2017. As of late 2022 (Figure 4d) the Indiviso channel (IC) was fully developed and the entire 260 sq km subsidence zone was now well drained. Spring tides continue to inundate most of the subsidence zone during the 3–4 hour flood, and nearly all tidal waters are returned to the estuary channel during the 8–9 hour daily ebb.

Methods

Estimating bore occurrence

In order to determine which satellite imagery to examine for possible bore occurrence between 2010 and 2022, we first made an initial estimate of dates and times by querying tidal prediction data for Puerto Peñasco[4] using parameters from Nelson (2007) and more recent field observations:

1. Minimum flood tide range at Puerto Peñasco: 5.2 m
2. Select daytime flood tides only.
3. Low tide correction factor for La Bocana (Figure 3c): Puerto Peñasco low + 4 hours

Nobeltec Tides and Currents v3.6, using United Kingdom Hydrographic Office (UKHO) data for the Puerto Peñasco harmonic station, was utilized for queries of tidal events. However, all tidal information presented in this article utilizes the times and heights as calculated by the MAR V1.0 software issued by the Centro de Investigación Cientifica y de Educación Superior de Ensenada, Baja California (CICESE). The two prediction databases yield similar results, but the CICESE numbers are reported here to be consistent with most other Gulf of California research.

An initial Tides and Currents query on daytime floods with a range greater than 5.2m predicted 524 events for the period April 4, 2010-December 31, 2022. These were sorted by time of predicted arrival at La Bocana. To be visible in a satellite image a bore must be present somewhere in the estuary between 11:00AM and 11:35AM MST when the images are acquired. To account for variations in bore arrival time, 449 days with predicted low tide between 10:00 AM and 12:15 PM were selected for further evaluation.

Satellite Imagery

This analysis used an existing library of Landsat and Sentinel 2 imagery maintained by the corresponding author. In conjunction with ongoing monitoring of the estuary since 2009, all Landsat and Sentinel 2 imagery covering the study area has been downloaded and processed, usually within 48 hours of acquisition by the satellite. Landsat imagery is obtained from the https://earthexplorer.usgs.gov/ website. Sentinel 2 imagery is downloaded from Amazon Web Services (public bucket **sentinel-s2-l1c**): https://registry.opendata.aws/sentinel-2/ . Imagery is processed using the Spectral Discovery for Landsat 8 Imagery and Spectral Discovery for Sentinel 2 Imagery programs (https://www.geosage.com/) to produce false color near-infrared (NIR) and Short Wave Infrared (SWIR) products as follows:

Table 1. Satellite image products
band number, (characterized wavelength), spatial resolution

	Landsat 5 TM	Landsat 8/9 OLI	Sentinel 2 MSI
NIR Bands:	2 (green) 30m	3 (green) 30m	B3 (green) 10m
	3 (red) 30m	4 (red) 30m	B4 (yellow) 10m
	4 (NIR) 30m	5 (NIR) 30m	B8 (NIR) 10m
		8 (Panchromatic) 15m	
SWIR Bands:	1 (blue) 30m	4 (red) 30m	B05 (red edge) 20m
	4 (NIR) 30m	5 (NIR) 30m	B8A (NIR) 20m
	5 (SWIR) 30m	6 (SWIR) 30m	B11 (SWIR) 20m
		8 (Panchromatic) 15m	B4 (yellow) 10m

4 Puerto Peñasco was used as the base station to maintain consistency with prior studies.

Landsat 8/9 and Sentinel 2 SWIR images are pan-sharpened using the higher resolution bands shown. For the figures in this article SWIR images are employed to emphasize water and wet features such as the estuary channels and subsidence zone. NIR images were used in the search for bores because they provide good contrast for whitewater features and the turbulent water following the bore, and because of the native 10 m spatial resolution of these bands in Sentinel 2 images.

Satellite imagery was available for 111 of the 449 days selected for evaluation. All 111 images were examined for bores, using elements of analog image interpretation. Bores were detected in 14 of the images. In some cases, multiple bores were visible in a single image as they ascended the estuary's several arms.

Field visits

Prior to the 2010 earthquake it was normally possible to drive a motor vehicle directly to the bank of the estuary channel to observe tidal bores and other characteristics of the tides (Nelson, 2007). Such easy access ended soon after the earthquake as the tidal flats subsided and became subject to regular inundation. For this reason, only three field visits to monitor tidal conditions were completed following the earthquake.

Kayak

The corresponding author accessed the main estuary channel by kayak on March 9, 2012, to observe a bore at close range, measure the rate of vertical rise of the flood tide (up to the point when the landing spot was inundated), and measure the speed of the flood current. This mode of access also facilitated a keen appreciation of the extreme turbulence of a spring-tide flood under post-earthquake conditions.

Motor vehicle

The main channel was accessed by motor vehicle on April 28, 2013, using a causeway constructed by the State of Baja California to provide access for the Gulf Corvina fishery. This was the only motorized visit to the main channel that could be completed before the causeway was cut by the advancing Indiviso Channel in 2014. A second visit was conducted on April 19, 2015, using the surviving portion of the causeway to observe tidal conditions in the Indiviso Channel.

Table 2. Tidal Bores in the post-2010 El Mayor-Cucapah Earthquake Colorado River Estuary as detected in satellite imagery and observed during a field visit. E: Main estuary channel. PVC: Pangas Viejas Channel. CRC: Colorado River channel upstream from the subsidence zone. HBC: Horseshoe Bend Channel. IC: Indiviso Channel.

Bore Number	Date	Location		Channel	Flood tide range (m) at Puerto Peñasco (CICESE)	Time (MST)	Time Offset from Puerto Peñasco Low Tide	Sensor
	M/D/Y	Latitude	Longitude				Add	
1	10/7/2010	31.8951	-114.9435	E	6.05	11:01	3:47	TM
2	7/13/2011	31.9220	-114.9605	E	5.62	11:06	4:29	TM
3	3/9/2012	31.9206	-114.9481	E	6.38	12:42	4:12	Field Obs
4	5/24/2013	31.9168	-114.9515	E	6.66	11:13	4:12	OLI
5	5/24/2013	31.8857	-114.9617	HBC	6.66	11:13	4:12	OLI
6	6/12/2014	31.9206	-114.9481	E	6.32	11:10	4:07	OLI
7	8/4/2016	31.8635	-114.9049	E	5.55	11:33	2:52	MSI
8	9/18/2017	31.9463	-114.9961	PVC	5.91	11:33	4:50	MSI
9	7/12/2018	31.9220	-114.9810	PVC	6.73	11:24	4:29	MSI
10	7/12/2018	31.9144	-114.9785	CRC	6.73	11:24	4:29	MSI
11	5/6/2019	31.8660	-114.9134	E	5.75	11:36	3:09	MSI
12	8/1/2019	31.9243	-114.9492	E	6.85	11:26	3:35	MSI
13	8/14/2019	31.8662	-114.9830	HBC	5.19	11:36	4:17	MSI
14	8/14/2019	31.9229	-114.9803	PVC	5.19	11:36	4:17	MSI
15	8/14/2019	31.9162	-114.9777	CRC	5.19	11:36	4:17	MSI
16	9/28/2019	31.9395	-114.9627	IC	6.78	11:35	4:11	MSI
17	9/28/2019	31.8698	-114.9955	HBC	6.78	11:35	4:11	MSI
18	5/7/2020	31.9171	-114.9484	E	7.06	11:26	3:43	MSI
19	10/17/2020	31.9189	-114.9573	E	5.99	11:35	3:38	MSI
20	4/27/2021	31.9030	-114.9504	E	7.1	11:25	3:31	MSI
21	4/27/2021	31.9055	-114.9362	E	7.1	11:25	3:31	MSI
22	3/31/2022	31.9464	-114.9551	IC	5.73	11:35	3:47	MSI
23	5/15/2022	31.9590	-114.9311	IC	6.56	11:36	4:30	MSI
24	5/15/2022	31.9299	-114.9853	PVC	6.56	11:36	4:30	MSI
25	5/15/2022	31.9125	-114.9832	CRC	6.56	11:36	4:30	MSI
26	5/15/2022	31.8657	-114.9852	HSC	6.56	11:36	4:30	MSI
27	10/9/2022	31.9566	-114.9456	IC	5.81	11:26	3:59	MSI

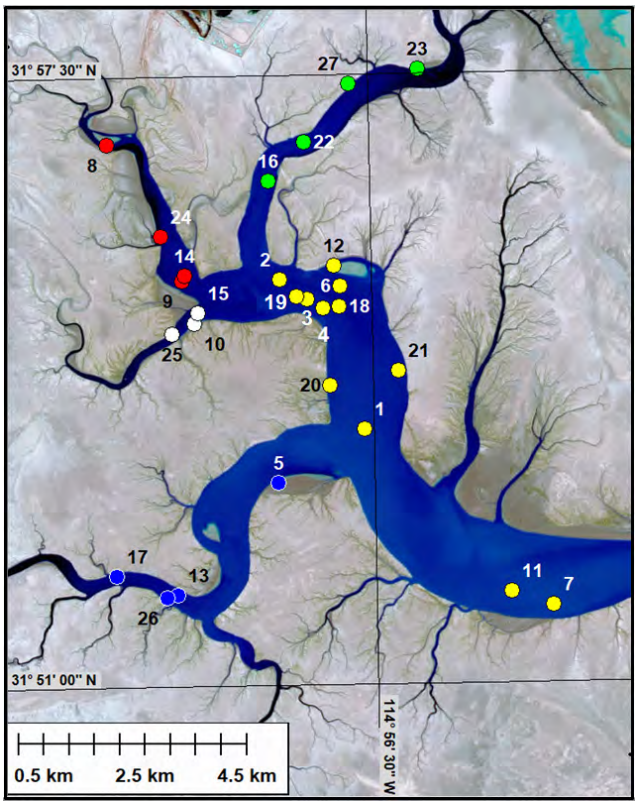

Figure 5. Map of Tidal Bores. See Table 2 for more information. All bores were detected in satellite imagery with the exception of Bore 3 which was observed in the field. Bore locations are color coded by the channel in which they were detected. Yellow: Main estuary. Red: Pangas Viejas Channel. Blue: Horseshoe Bend Channel. Green: Indiviso Channel. White: Colorado River Channel.

Results

The tidal bores

Detected tidal bores are listed chronologically by date of occurrence in Table 2. The location of each is plotted on a map in Figure 5. Satellite views of bores selected for discussion in this section are found in Figure 6.

More bores were detected in the later years of the 12 years studied because both spatial and temporal resolution of satellite imagery improved dramatically during the study period, which spanned the transition from Landsat 5 to Landsats 8/9 and Sentinel 2a/b. There were no functional Landsat satellites in 2012. Landsat 8 became operational in 2013, followed by Sentinel 2a in 2015, Sentinel 2b in 2017, and Landsat 9 in 2021, so the increased detection in later years is to be expected.

Bores 4 and 5 detected in a Landsat 8 OLI image acquired May 24, 2013 are the first for which high resolution imagery is available, and are also representative of the bores that occurred in the estuary prior to extensive development of alternate channels. Bore 4 was very similar to Bore 3 which was observed nearby on March 9, 2012. The 2012 field trip was conducted by kayak, with a 4:40 AM departure from the flood control levee to ride the ebb down the Pangas Viejas Channel to an observation point in the estuary on the east bank just upstream from the location of Bore 4. The water level in the estuary channel dropped 3 m between the 8:15 AM landing and low tide (arrival of the flood tide) at 12:42 PM. The flood approached with a roar but without a defined bore wave until it encountered a shallow bar which produced a breaking wave ~0.6m high. After passage of the bore front, the water rose 3 m in 12 minutes to inundate the observation point, and the kayaker was afloat again. The objective for the return trip was to float with the flood to determine its speed. The GPS immediately registered 7.4 knots (13.7 km/hr). The paddle was used only to maneuver away from ~1m standing wave sets which developed without warning as the water level rose over submerged bars. Similar zones of flood turbulence can be seen as white areas extending about 2 km behind Bore 4 and other bores in Figure 6. Sections of bank collapsed into the channel and numerous uprooted shrubs were seen rolling upstream in the shallows. The observer floated 9 km with the flood in just over an hour, though this included about 5 minutes waiting in an eddy for turbulence to subside. High tide back at the levee occurred at 4 PM.

The observer returned to the estuary on April 28, 2013, to record a tide change at the El Zanjon fish camp (Z1 in Figure 6), which was temporarily accessible by auto using

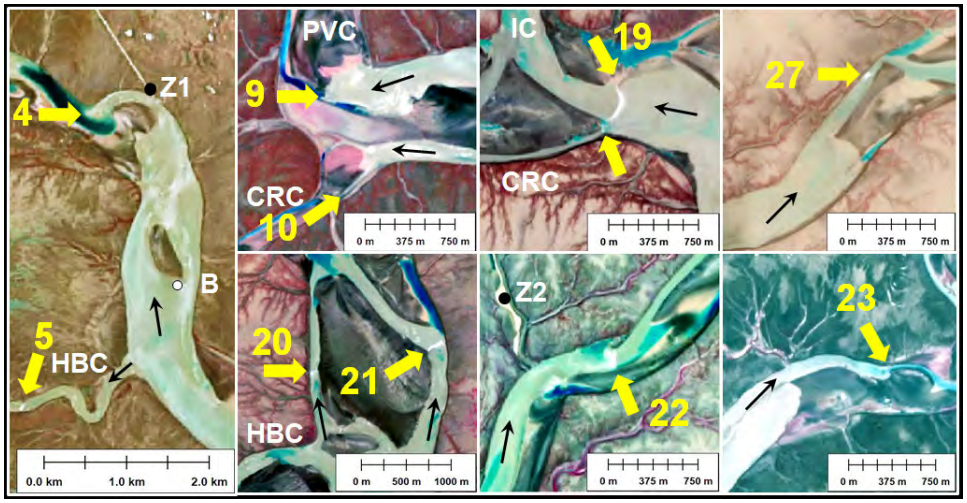

Figure 6. A selection of bores as seen in satellite imagery. See Fig. 5 for location context and Table 2 for additional information about each bore. Yellow arrows point to the bore front. Black arrows indicate the direction of flood current. B: Site of La Bocana. Z1: First location of El Zanjon. Z2: Second location of El Zanjon. CRC: Colorado River Channel. PVC: Pangas Viejas Channel. HBC: Horseshoe Bend Channel. IC: Indiviso Channel. See text for discussion.

a recently constructed elevated causeway. The 4 m-high bank at the fish camp was undergoing active erosion with large sections of collapsed bank slumped at the water's edge, though there was little sign of erosion during the gentle ebb. Despite a predicted 5.8 m tide range there was no bore although the tide turned abruptly at 1:16 PM. Small pieces of the bank began calving off immediately following the tide change. This erosion continued and intensified with the growing flood. The site of the former La Bocana fish camp (B in Figure 6) gives an idea of the extent of bank erosion underway in the estuary following the 2010 earthquake. The La Bocana site had been on the bank in 2010. By 2013 it was 250 m out in the channel. The causeway to the Z1 site was cut by the advance of the Indiviso Channel in the summer of 2013, so El Zanjon was moved to site Z2 (panel for Bore 22 in Figure 6), using the growing Indiviso Channel for fishing access.

Although a bore was not seen at Z1 on April 28, 2013, one could have formed elsewhere in the estuary on that day or on the two previous days when the flood tide range was greater. The channel at Z1 was wide and its bottom braided with bars, creating an irregular channel bed unconducive to bore wave formation. More favorable conditions, (mainly the presence of a better-defined common flood/ebb channel) could have produced a bore elsewhere. Bore pairs 9/10 and 20/21 are examples of that phenomenon. In the instance of Bores 9/10, the flood advanced over a relatively wide channel bed, probably without formation of a bore wave, but the flow was funneled into two narrow channels just as the satellite passed over. In the case of 20/21, a large bar obstructed most of the channel, causing the flood to be constricted in narrow channels on each side.

Bore 19 is second in size only to Bore 1, spanning a channel 313 m wide. It also has an unusual inverted leading edge. In a channel that is deeper in the center and shallow along the banks, a bore wave usually advances upstream faster in the deep water in mid-channel. The leading edge of Bore 19 is inverted, with the wave moving faster close to the banks. This probably indicates the presence of a shallow mid-channel bar. Note also that Bore 19 is in the process of splitting into two bore waves, with the smaller wave moving up the Colorado River Channel.

Bores 22, 23, and 27 are all advancing up the Indiviso Channel, which has recently become the focus of tidal energy. Fewer bores are advancing into the other channels for reasons that will be discussed in the following section. Bore 22 is just passing the relocated El Zanjon fish camp (Z2). Bores 23 and 27 illustrate a common pattern seen in the flood tide. The flood front, including the bore wave, surges out ahead in a narrow channel while taking longer to cover a higher mid-channel bar. An unfavorable sun angle creating a strong reflection from the water's surface makes it harder to see a distinct bore wave in the case of Bore 23, but the forces at work on the flood front are the same in both cases.

Discussion

How common are tidal bores in the blind channels of the Colorado River Estuary?

The tidal bores detected in this study represent a small subset of the bores that likely form in the estuary. Most of the bores reported here were detected during the roughly 10 minute period of the day (11:25 to 11:35AM) when Sentinel 2 satellites pass over the estuary. A query of the CICESE tidal prediction database using the criteria specified in Section 2.1 (excluding the daytime restriction) predicted acceptable conditions for bore formation on 130 occasions (64 in daylight hours, 66 at night) in 2023, with daytime bores occurring in the study area as early as 9:10 AM and as late as 1 PM. Clearly we documented only a small sample. Tidal bores are much more common in the Colorado River Estuary than opportunities to see them!

How common are tidal bores in blind tidal channels?

While most of the world's tidal bores are reported from tidal rivers, they are also known to occur in other blind (or nearly blind) channels, most notably the North Branch of the Changjiang (Yangtze) Estuary, China (Chen, 2003; Guo et al., 2022) and blind channels of the Sittaung River Estuary, Myanmar (Choi et al., 2021; Jo et al., 2022).

Tidal bores as agents of aggradation

Tidal bore waves, and the turbulence following them, mobilize sediment and contribute to bank erosion. Where has the sediment mobilized after the 2010 El Mayor-Cucapah earthquake gone? Landward movement of sediment in macrotidal estuaries with limited or no fluvial input is common worldwide (Dalrymple and Choi, 2007; Gugliotta and Saito, 2019; Nienhuis et al., 2018). Zamora et al. (2013) estimated a rate of deposition of tidal sediment of 10–21 cm/year as the tidal sandbar developed in the Colorado River Channel in the early 2000s. In the absence of a rigorous monitoring program, can we establish that channel beds and tide flat surfaces are aggrading elsewhere in the subsidence zone? Perhaps not with a great level of precision, but there are indications.

Changes in the pattern of tidal inundation and the movement of tidal bores (Figure 7) suggest that the Colorado River Channel, Pangas Viejas Channel, and Horseshoe Bend Channel are all aggrading. Bores 8 (Figure 7a) and 22 (Figure 7b) occurred on days with a similar tide range (~5.9 m vs 5.7 m), and the bores have advanced similar distances into the estuary. Caution should be used in directly comparing the water levels between images. Although the tide range was similar on both days, low tide on the 2017 date was predicted to be 0.3 m higher than on the 2022 date—so more water was likely present when the 2017 image was acquired. The significance of the comparison is that the channel bottom of the Pangas Viejas Channel is clearly higher than the channel bottom of the Indiviso Channel in 2022. The original headcutting of both channels started

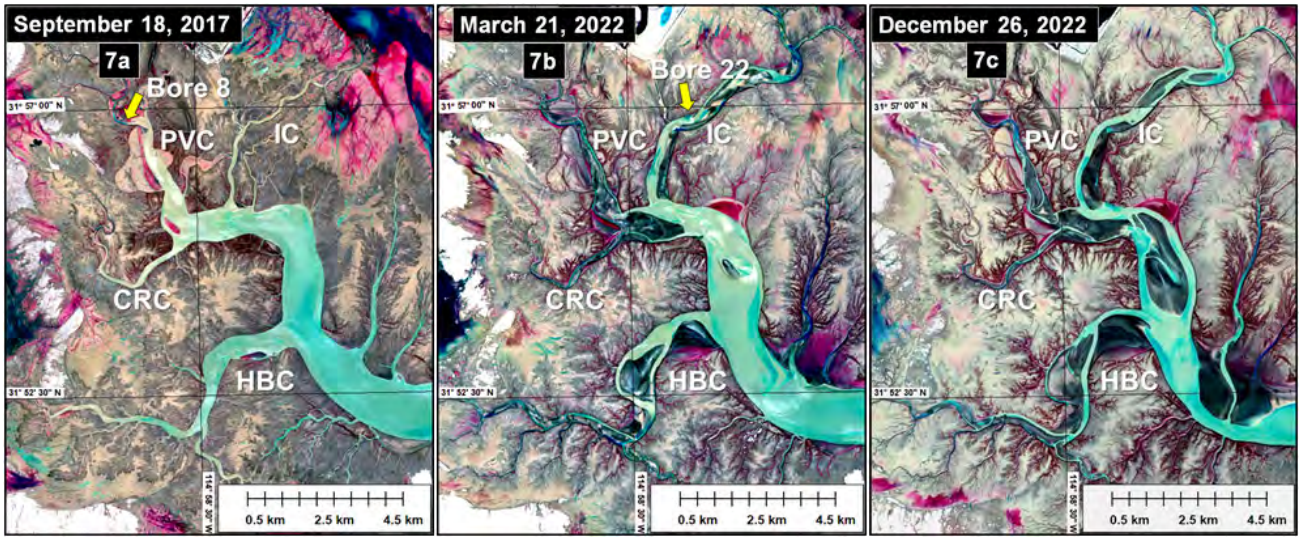

Figure 7. Aggradation of the Pangas Viejas, Colorado River, and Horseshoe Bend channels. CRC: Colorado River Channel. PVC: Pangas Viejas Channel. HBC: Horseshoe Bend Channel. IC: Indiviso Channel. Bores 8 and 22 occurred on days with a similar tidal range (~5.9m vs 5.7m). Fig. 7a: In 2017 most tidal energy was directed into the PVC, and tidal bores moved from the main estuary channel into the PVC. Fig. 7b: By 2022 most tidal energy was directed into the IC and most tidal bores moved from the main estuary into the IC. At present the PVC and HBC do not fully inundate until later in the flood, indicating that their channel bottoms have been aggraded. Since 2017 all tidal bores detected in the PVC were located near its lower connection to the estuary. The frequency of tidal bores in the HBC also seems to have diminished, although a bore did occur in 2022 on a day with a 6.6m tide swing. The tidal sandbar in the CRC continues to grow. Fig. 7c: The estuary during an ebbing spring tide revealing channel bottom conditions.

at a common base level in the estuary, so the Pangas Viejas Channel must have aggraded. Figure 7c shows the estuary on a falling spring tide, giving a clear indication of the relative levels of the channel bottoms in 2022. The Indiviso Channel is the newest channel and is less aggraded than the others, but by virtue of its lower bed elevation it is now the focus of tidal bore activity, which mobilizes sediments for upstream transport on the flood. It will most likely experience aggradation just as the other channels have.

What about the general surface of the tidal flats? Is that also aggrading? This is more difficult to establish, but there are indications that some parts of the subsided tidal flats are not being inundated as often as they were immediately after the earthquake. A case in point is an area near the flood control levee where Palmer's saltgrass (*Dishtichlis palmeri*) became established shortly after the area subsided following the earthquake (See Lynch et.al 2023, Plant Rings of the Colorado River Delta: Clones, Ghosts, and Zombies, this volume). It did well for several years but has declined recently. A possible reason is that the area is not being inundated by the tides as often as it was immediately following the earthquake. Aggradation of the Pangas Viejas Channel which delivers flood tides to this area may reduce the frequency of inundation. Fluid mud deposits 2-3 cm thick have been noted by the authors on the surface of the tidal flats in this area following spring tide inundation. These mud drapes dry back to much thinner layers, but each contributes to gradual aggradation.

Aggradation has been documented by the authors from the area between the Colorado River and Pangas Viejas channels where a connecting channel was dredged in 2016 in an effort to reintroduce limited fluvial flow to the lower estuary. Originally dredged to a depth of 2m, the channel had completely filled with tidal sediment by 2021.

How much of this aggradation might be attributable specifically to tidal bores? Sedimentary research has begun to examine the recognition of tidal bore signatures preserved in sedimentary successions. Tessier et al. (2017) discussed such tidal signatures and their record of the direct impact of tidal bores on the sediment bottom as well as their indirect impact in inducing very high suspended sediment concentrations. Recent studies have begun to quantify the contribution of tidal bores. Dalrymple (2021) studied the Salmon River Estuary in the Bay of Fundy and found that deposits from the small (~30 cm) tidal bores there comprise approximately 15% of the deposits in the upper-flow-regime sand flats in the inner part of the estuary. Jo et al. (2022) found that tidal bores in blind tidal channels induce less turbulent internal mixing than tidal bores in fluvial channels because of the lower intensity of the bore wave, but that they nevertheless convey a turbid plume to the tide flats in the upper intertidal zone of the Sittaung River, Myanmar. They also reported that the turbidity peak of blind channel bores coincides with the bore front, but the sedimentation rate is relatively lower than for bores in fluvial channels. This is because the peak current speed is reached about an hour after bore passage, instead of coinciding with bore passage as is normally the case with river bores. Thus, in the case of the blind channel bores currently ascending the Colorado River estuary, the intense turbulence in the hour following passage of the bore may be as important as

the bore wave itself in mobilizing sediment for landward transport.

Acknowledgements

The authors thank Lynn C. Anderson for permission to use the 1987 tidal bore photo in Figure 2 and Dale Turner and The Nature Conservancy for permission to use the photo of headcut erosion in Figure 4.

References

ACOE U. S. Department of Defense, Army Corps of Engineers, Los Angeles District. 1982. Colorado River Basin, Hoover Dam, Review of flood control regulation, final report. Government Printing Office, Washington, D.C., USA.

Bartsch-Winkler, S., Lynch, D.K., 1988. Catalog of worldwide tidal bore occurrences and characteristics. US Geological Survey Circular 1022. US Government Printing Office, Washington, D.C.

Bonneton, P., Bonneton, N., Parisot, J.P., Castelle, B., 2015. Tidal bore dynamics in funnel-shaped estuaries. Journal of Geophysical Research: Oceans. 120 (2), 923-941. https://doi.org/10.1002/2014JC010267

Chanes-Martínez, J.J. 2012. Características estructurales y sismoestratigráficas en un sector del delta del Río Colorado, noroeste de México, a partir de sísmica de reflexión. Centro de Investigación Científica y de Educación Superior de Ensenada, Departamento de la Ciencias de la Tierra, Ensenada.

Chanson, H. 2004. Mixing and dispersion role of tidal bores, in: Mossa M., Yasuda Y., Chanson H., eds. Fluvial, Environmental and Coastal Developments in Hydraulic Engineering. Taylor and Francis, London, pp. 223-232.

Chen, S. 2003. Tidal bore in the north branch of the Changjiang estuary. Proc. Intl Conf. on Estuaries & Coasts ICEC-2003. Zhejiang University Press, pp. 233-239.

Choi, K., Jo, J., Kim, D., 2021. Tidal and seasonal controls on the stratigraphic architecture of blind tidal channel deposits in the fluvial-tidal transition of the macrotidal Sittaung River estuary, Myanmar. Sediment. Geol. 426, 106029. https://doi.org/10.1016/j.sedgeo.2021.106029

Dalrymple, R.W. 2010. Tidal Depositional Systems, in: James N.P., Dalrymple R.W., eds. Facies Models 4. SEPM Society for Sedimentary Geology, pp. 201-231.

Dalrymple, R.W., 2021. Sedimentation on high-energy sand flats in the Bay of Fundy: The record of tidal-bore activity and deposition from high-concentration suspensions of sand. Sedimentology. 68 (5), 2195-2226.

Dalrymple, R.W., Choi, K., 2007. Morphologic and facies trends through the fluvial–marine transition in tide-dominated depositional systems: A schematic framework for environmental and sequence-stratigraphic interpretation. Earth-Sci. Rev. 81 (3-4), 135-174. 10.1016/j.earscirev.2006.10.002

Derby, G.H., 1852. Report of the Secretary of War communicating, in compliance with a resolution of the Senate, a reconnoissance of the Gulf of California and the Colorado river by Lieutenant Derby. Department of War, Washington, D.C.

Fletcher, J.M., Teran, O.J., Rockwell, T.K., Oskin, M.E., Hudnut, K.W., Mueller, K.J., Spelz, R.M., Akciz, S.O., Masana, E., Faneros, G., Fielding, E.J., Leprince, S., Morelan, A.E., Stock, J., Lynch, D.K., Elliott, A.J., Gold, P., Liu-Zeng, J., González-Ortega, A., Hinojosa-Corona, A., González-García, J., 2014. Assembly of a large earthquake from a complex fault system: Surface rupture kinematics of the 4 April 2010 El Mayor–Cucapah (Mexico) Mw 7.2 earthquake. Geosphere. 10 (4), 797-827. 10.1130/GES00933.1

Freeman, L.R., 1923. The Colorado River yesterday, today, and tomorrow. Dodd, Mead, and Company, Rahway, NJ.

Gordon, J.H., 1924. Tidal bore at the mouth of the Colorado River. Monthly Weather Review. 52 (February 1924), 98-99.

Graber, S.D. 2012. Perspective on the tidal bore: Background and initiation. Proceedings of the American Society of Mechanical Engineers 2012 Fluids Engineering Summer Meeting. Rio Grandi, Puerto Rico. pp. 211-221.

Gugliotta, M., Saito, Y., 2019. Matching trends in channel width, sinuosity, and depth along the fluvial to marine transition zone of tide-dominated river deltas: The need for a revision of depositional and hydraulic models. Earth-Sci. Rev. 191, 93-113. 10.1016/j.earscirev.2019.02.002

Guo, L., Xie, W., Xu, F., Wang, X., Zhu, C., Meng, Y., Zhang, W., He, Q., 2022. A historical review of sediment export–import shift in the North Branch of Changjiang Estuary. Earth Surface Processes and Landforms. 47 (1), 5-16. https://doi.org/10.1002/esp.5084

Henderson, R. 1922a. Seventy Drowned at La Bomba: Tide Capsizes Boat Filled with Cotton Pickers from Guymas; Only Few Survive. Calexico Chronicle, Calexico, California. November 20, 1922.

Henderson, R. 1922b. Less Than Forty Are Drowned. Engineer Tells Story of Ship Wreck. Calexico Chronicle, Calexico, California. November 22, 1922.

Huang, M.-H., Fielding, E.J., Dickinson, H., Sun, J., Gonzalez-Ortega, J.A., Freed, A.M., Bürgmann, R., 2017. Fault geometry inversion and slip distribution of the 2010 Mw 7.2 El Mayor-Cucapah earthquake from geodetic data. Journal of Geophysical Research: Solid Earth. 122 (1), 607-621. https://doi.org/10.1002/2016JB012858

Hughes, Z.J. 2012. Tidal channels on tidal flats and marshes, in: Davis R.A., Dalrymple R.W., eds. Principles of tidal sedimentology. Springer, New York, pp. 269-300.

Ives J.C., 1861. Report upon the Colorado River of the west, explored in 1857 and 1858 by Lieutenant Joseph C. Ives. Government Printing Office, Washington, D.C.

Jo, J.H., Kim, D.H., Choi, K.S. 2022. Morphologic and hydrodynamic controls on the occurrence of tidal-bore deposits in the inshore tidal flats, Sittaung River Estuary, Myanmar (Poster). Tidalites 2022 10th International Congress of Tidal Sedimentology. Matera, Italy.

Lavin, M.F., Marinone, S.G. 2003. An overview of the physical oceanography of the Gulf of California, in: Valasco Fuentes, O.U., Shenbaum J., Ochoa J., eds. Nonlinear processes in geophysical fluid dynamics. Springer, pp. 173-204.

Leigh, R., 1941. Forgotten Waters; Adventure in the Gulf of California. J. B. Lippincott, Philadelphia.

Lynch, D.K., 1982. Tidal bores. Sci. Am. 247 (4), 146-157.

Nelson, S. 2007. In search of El Burro, the tidal bore of the Rio Colorado Delta, in: Felger R.S., Broyles B., eds. Dry borders: Great Natural Reserves of the Sonoran Desert. University of Utah Press, Salt Lake City, UT, pp. 519-529.

Nelson, S.M., Fielding, E.J., Zamora-Arroyo, F., Flessa, K., 2013a. Delta Dynamics: Effects of a major earthquake, tides, and river flows on Ciénega de Santa Clara and the Colorado River Delta, Mexico. Ecol. Eng. 59 (2013), 144-156. https://doi.org/10.1016/j.ecoleng.2012.09.004

Nelson, S.M., Kendy, E., Flessa, K.W., Rodríguez-Burgueño, J.E., Ramírez-Hernández, J., Rivas-Salcedo, T.E., 2020. Channel incision by headcut migration: Reconnection of the Colorado River to its estuary and the Gulf of California during the floods of 1979–1988. Hydrological Processes. 2020 (34), 4156-4174. 10.1002/hyp.13858

Nelson, S.M., Zamora-Arroyo, F., Ramirez-Hernandez, J., Santiago-Serrano, E., 2013b. Geomorphology of a recurring tidal sandbar in the estuary of the Colorado River, Mexico: Implications for restoration. Ecol. Eng. 59 (2013), 121-133. https://doi.org/10.1016/j.ecoleng.2012.12.095

Nienhuis, J., Hoitink, A.J.F., Törnqvist, T., 2018. Future change to tide-influenced deltas. Geophys. Res. Lett. 45, 3499-3507. 10.1029/2018GL077638

Sánchez García, A.C. 2013. Rasgos estructurales en el suroeste del delta del Río Colorado : interpretación de perfiles de sísmica de reflexión. Centro de Investigación Científica y de Educación Superior de Ensenada, Tesis para obtener el grado de Maestro en Ciencias de la Tierra con orientación en Geofísica Aplicada,

Sykes, G., 1937. The Colorado River Delta. American Geographical Society, New York.

Tessier, B., Furgerot, L., Mouazé, D., 2017. Sedimentary signatures of tidal bores: a brief synthesis. Geo-Mar. Lett. 37, 10.1007/s00367-016-0479-x

Thompson, R.W., 1968. Tidal flat sedimentation on the Colorado River Delta, northwestern Gulf of California. Bull. Geol. Soc. Am. Memoir 107, 1-133.

Waters, F., 1946. The Colorado. Rinehart & Company, New York.

Wells, J.T. 1995. Tide-Dominated Estuaries and Tidal Rivers, in: Perillo G.M.E., ed. Geomorphology and Sedimentology of Estuaries. Elsevier, Amsterdam, pp. 179–205.

Zamora, H.A., Nelson, S.M., Flessa, K.W., Nomura, R., 2013. Post-dam sediment dynamics and processes in the Colorado River estuary: Implications for habitat restoration. Ecol. Eng. 59 (2013), 134-143. https://doi.org/10.1016/j.ecoleng.2012.11.012